

PROCEEDINGS OF SPIE



SPIE—The International Society for Optical Engineering

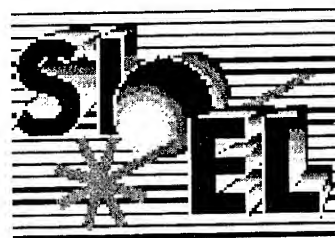
Final Report

F61775-99-WF061

SIOEL '99

Sixth Symposium on Optoelectronics

Teodor Necsoiu
Maria Robu
Dan C. Dumitras
Editors



22-24 September 1999
Bucharest, Romania

Sponsored by

National Agency for Science, Technology and Innovation (Romania)
Romanian Academy
Romanian Ministry of National Defence
EOS—European Optical Society
SPIE—The International Society for Optical Engineering
EOARD—European Office of Aerospace Research and Development

Organized by

IOEL-SA—Institute of Optoelectronics (Romania)
University Politehnica Bucharest (Romania)
Faculty of Physics/University of Bucharest (Romania)
Romanian Physical Society
SPIE Romania Chapter



20000913 067

Volume 4068

REPORT DOCUMENTATION PAGE

Form Approved OMB No. 0704-0188

Public reporting burden for this collection of information is estimated to average 1 hour per response, including the time for reviewing instructions, searching existing data sources, gathering and maintaining the data needed, and completing and reviewing the collection of information. Send comments regarding this burden estimate or any other aspect of this collection of information, including suggestions for reducing this burden to Washington Headquarters Services, Directorate for Information Operations and Reports, 1215 Jefferson Davis Highway, Suite 1204, Arlington, VA 22202-4302, and to the Office of Management and Budget, Paperwork Reduction Project (0704-0188), Washington, DC 20503.

1. AGENCY USE ONLY (Leave blank)		2. REPORT DATE 1999	3. REPORT TYPE AND DATES COVERED Conference Proceedings	
4. TITLE AND SUBTITLE The 6th Symposium of Optoelectronics - SIOEL '99			5. FUNDING NUMBERS F61775-99-WF	
6. AUTHOR(S) Conference Committee				
7. PERFORMING ORGANIZATION NAME(S) AND ADDRESS(ES) Institute of Optoelectronics PO Box MG-22 Bucharest - Magurele 76900 Romania			8. PERFORMING ORGANIZATION REPORT NUMBER N/A	
9. SPONSORING/MONITORING AGENCY NAME(S) AND ADDRESS(ES) EOARD PSC 802 BOX 14 FPO 09499-0200			10. SPONSORING/MONITORING AGENCY REPORT NUMBER CSP 99-5061	
11. SUPPLEMENTARY NOTES Proceedings are on CD.				
12a. DISTRIBUTION/AVAILABILITY STATEMENT Approved for public release; distribution is unlimited.			12b. DISTRIBUTION CODE A	
13. ABSTRACT (Maximum 200 words) The Final Proceedings for The 6th Symposium of Optoelectronics - SIOEL '99, 22 September 1999 - 24 September 1999 This is an interdisciplinary conference. Topics include materials for optoelectronics; optoelectronic components and devices, and optoelectronic applications to communications, analytical instrumentation, and medicine.				
14. SUBJECT TERMS EOARD, Opto-electronic Materials, Optoelectronic components, Optoelectronic applications			15. NUMBER OF PAGES 845	
			16. PRICE CODE N/A	
17. SECURITY CLASSIFICATION OF REPORT UNCLASSIFIED	18. SECURITY CLASSIFICATION OF THIS PAGE UNCLASSIFIED	19. SECURITY CLASSIFICATION OF ABSTRACT UNCLASSIFIED	20. LIMITATION OF ABSTRACT UL	

NSN 7540-01-280-5500

Standard Form 298 (Rev. 2-89)
Prescribed by ANSI Std. Z39-18
298-102



PROCEEDINGS OF SPIE

SPIE—The International Society for Optical Engineering

SIOEL '99

Sixth Symposium on Optoelectronics

**Teodor Necsoiu
Maria Robu
Dan C. Dumitras**
Editors

**22–24 September 1999
Bucharest, Romania**

Sponsored by

National Agency for Science, Technology and Innovation (Romania)
Romanian Academy
Romanian Ministry of National Defence
EOS—European Optical Society
SPIE—The International Society for Optical Engineering
EOARD—European Office of Aerospace Research and Development

Organized by

IOEL-SA—Institute of Optoelectronics (Romania)
University Politehnica Bucharest (Romania)
Faculty of Physics/University of Bucharest (Romania)
Romanian Physical Society
SPIE Romania Chapter

Published by

SPIE—The International Society for Optical Engineering



Volume 4068

SPIE is an international technical society dedicated to advancing engineering and scientific applications of optical, photonic, imaging, electronic, and optoelectronic technologies.

AQ F00-12-3866



The papers appearing in this book compose the proceedings of the technical conference cited on the cover and title page of this volume. They reflect the authors' opinions and are published as presented, in the interests of timely dissemination. Their inclusion in this publication does not necessarily constitute endorsement by the editors or by SPIE. Papers were selected by the conference program committee to be presented in oral or poster format, and were subject to review by volume editors or program committees.

Please use the following format to cite material from this book:

Author(s), "Title of paper," in *SIOEL '99: Sixth Symposium on Optoelectronics*, Teodor Necsoiu, Maria Robu, Dan C. Dumitras, Editors, Proceedings of SPIE Vol. 4068, page numbers (2000).

ISSN 0277-786X
ISBN 0-8194-3705-0

Published by
SPIE—The International Society for Optical Engineering
P.O. Box 10, Bellingham, Washington 98227-0010 USA
Telephone 360/676-3290 (Pacific Time) • Fax 360/647-1445

Copyright ©2000, The Society of Photo-Optical Instrumentation Engineers.

Copying of material in this book for internal or personal use, or for the internal or personal use of specific clients, beyond the fair use provisions granted by the U.S. Copyright Law is authorized by SPIE subject to payment of copying fees. The Transactional Reporting Service base fee for this volume is \$15.00 per article (or portion thereof), which should be paid directly to the Copyright Clearance Center (CCC), 222 Rosewood Drive, Danvers, MA 01923. Payment may also be made electronically through CCC Online at <http://www.directory.net/copyright/>. Other copying for republication, resale, advertising or promotion, or any form of systematic or multiple reproduction of any material in this book is prohibited except with permission in writing from the publisher. The CCC fee code is 0277-786X/00/\$15.00.

Printed in the United States of America.

Contents

xiii	<i>Conference Committees</i>
xv	<i>Introduction</i>

SESSION I MATERIALS FOR OPTOELECTRONICS AND RELATED FIELDS

- 2 **InGaAsP/AlGaAs multiple-wavelength vertical-cavity lasers and arrays in the 1.5- μ m band fabricated by localized wafer fusion technique (Invited Paper) [4068-01]**
A. V. Syrbu, V. P. Iakovlev, A. P. Rudra, C.-A. Berseth, E. E. Kapon, Swiss Federal Institute of Technology Lausanne; A. Z. Mereuta, I. Sagnes, A. Ougazzaden, France Telecom-CNET

- 6 **Calibration-free laser-induced plasma spectroscopy: a new frontier for material analysis, environmental protection, and cultural heritage conservation (Invited Paper) [4068-02]**
L. Bolognesi, M. Corsi, V. Palleschi, E. Tognoni, A. Salvetti, Istituto di Fisica Atomica e Molecolare (Italy)

- 17 **Mixed-valence ion-doped PVA as potential materials for real-time holography (Invited Paper) [4068-03]**
M. Bulinski, Univ. of Bucharest (Romania); V. Kuncser, National Institute for Physics of Materials (Romania); I. Iova, A. Bela, Univ. of Bucharest (Romania); H. Franke, Univ. Gesamthochschule Duisburg (Germany); U. Russo, Univ. degli Studi di Padova (Italy); G. Filoti, National Institute for Physics of Materials (Romania)

- 26 **Local electric fields in optical glasses during field-assisted ionic exchanges [4068-04]**
A. I. Lupascu, Univ. Politehnica Bucharest (Romania); A. P. Kevorkian, TeemPhotonics (France); C. P. Cristescu, I. M. Popescu, Univ. Politehnica Bucharest (Romania)

- 33 **Influence of the precrystallization zone on the dopant field in microgravity [4068-05]**
A. M. Balint, D. G. Bălcean, M. Mihailovici, A. Neculae, Ș. Balint, Univ. of the West Timișoara (Romania)

- 45 **Electro-optic and phase transition studies on polymer-dispersed liquid crystal films [4068-06]**
D. Manaila-Maximean, Univ. Politehnica Bucharest (Romania); M. Furlani, Chalmers Univ. of Technology (Sweden) and Göteborg Univ. (Sweden); R. Bena, V. Stoian, C. Rosu, Univ. Politehnica Bucharest (Romania)

- 52 **C-Ni multilayer reflectors: an AFM roughness study [4068-07]**
M. Ulmeanu, G. Radu, National Institute for Laser, Plasma and Radiation Physics (Romania); P. Budau, Univ. of Bucharest (Romania); M. Enachescu, Lawrence Berkeley National Lab. (USA)

- 59 **Preparation of a copolymer for second-order nonlinear optics [4068-08]**
A.-M. Albu, B. Marculescu, D. Manaila-Maximean, Univ. Politehnica Bucharest (Romania); A. Trouillet, Univ. Jean Monnet/Saint Etienne (France)

- 65 **Influence of the stresses of predeformed InP crystals on acoustic emission under microindentation [4068-09]**
R. Zhitaru, V. Rahvalov, Institute of Applied Physics (Moldova)

- 72 **Phosphors with sulphide matrix: synthesis parameter influence on optical properties**
[4068-10]
C. Onose, S. Jinga, C. Onose, MATPUR SA (Romania)

- 78 **Transparent ferroelectric ceramic from chemically synthesized powders** [4068-11]
S. Jinga, C. Onose, MATPUR SA (Romania)

- 84 **Indium antimonide semiconductor material preparation for thermoelectric applications**
[4068-12]
M. Simion, A. I. Stanculescu, MATPUR SA (Romania); M. Tilica, M. Vasilescu, BIOTEHNOS
SA (Romania)

- 90 **Aluminophosphate-doped glasses with rare-earth ions** [4068-13]
R. Rogojan, MATPUR SA (Romania); P. E. Sterian, Univ. Politehnica Bucharest (Romania);
M. Elisa, MATPUR SA (Romania)

- 97 **Influence of growth conditions on the physical properties of an organic crystalline material
for optical application** [4068-14]
A. I. Stanculescu, F. G. Stanculescu, MATPUR SA (Romania)

- 104 **Electric field effect on the electronic states in a GaAs spherical quantum dot** [4068-15]
E. C. Niculescu, Univ. Politehnica Bucharest (Romania); E. Lengyel, National Institute
for Physics of Materials (Romania); M. Cristea, Univ. Politehnica Bucharest (Romania)

- 111 **Synthesis of luminescent strontium-magnesium orthophosphate activated with cerium
and manganese** [4068-16]
M. Vădan, E. J. Popovici, L. Ungur, Institute of Chemistry (Romania); M. Vasilescu, Institute
of Physical Chemistry (Romania); D. Macarovici, Institute of Chemistry (Romania)

- 117 **Thin film CdTe/CdS structures** [4068-17]
L. Pascu, E. J. Popovici, Institute of Chemistry (Romania); E. Indrea, National Institute of
Isotopic and Molecular Technology (Romania); R. Grecu, L. Păcurar, Institute of Chemistry
(Romania)

- 124 **Calcium tungstate phosphors with well-defined particle sizes** [4068-18]
F. Forgaciu, E. J. Popovici, C. Ciocan, L. Ungur, M. Vădan, Institute of Chemistry (Romania)

- 130 **Synthesis of copper-activated zinc sulphide phosphors sensitive to β radiation** [4068-19]
E. J. Popovici, F. Forgaciu, C. Ciocan, L. Pascu, Institute of Chemistry (Romania); D. Angelescu,
Institute of Physical Chemistry (Romania); C. Postolache, Institute of Physics and Nuclear
Engineering (Romania)

- 136 **Macroscopic model of PZT ceramics: linear piezoelectric equations** [4068-20]
M. V. Lazar, Institute of Optoelectronics (Romania)

- 143 **Negative magnetoresistance of granular Co-Cu films prepared by electrochemical deposition**
[4068-21]
V. M. Hutanu, Institute of Optoelectronics (Romania); V. Dolocan, Univ. of Bucharest
(Romania)

- 149 **Preparation and magnetotransport properties of Ni-Bi and Ni-Cu magnetic multilayers** [4068-22]
V. M. Hutanu, Institute of Optoelectronics (Romania); V. Dolocan, Univ. of Bucharest (Romania)

SESSION II LASERS AND APPLICATIONS

- 156 **Upconversion violet emission in diluted Er:YAG crystals (Invited Paper)** [4068-23]
S. Georgescu, V. Lupei, A. Petraru, C. Hapenciuc, National Institute for Lasers, Plasma and Radiation Physics (Romania); C. Florea, Ecole Supérieure d'Ingénieurs en Electrotechnique et Electronique (France); C. Naud, C. Porte, Univ. Paris VI (France)
- 166 **Resonant photodetection with long-wavelength double-fused InGaAsP/AlGaAs vertical-cavity lasers (Invited Paper)** [4068-24]
V. P. Iakovlev, A. V. Syrbu, C.-A. Berseth, A. P. Rudra, G. I. Suruceanu, E. E. Kapon, Swiss Federal Institute of Technology Lausanne
- 172 **High-precision towers for support of an optoelectronic detector** [4068-25]
B. Comanescu, A. Ighigeanu, D. Oancea, M. Petcu, B. Tatulea, Institute of Optoelectronics (Romania); G. Chelkov, D. Dedovich, P. Evtoukhovitch, A. Gongadze, S. Podkladkin, E. Tskhadadze, Joint Institute for Nuclear Research (Russia)
- 178 **Launch of the LP₀₁ mode on an optical fiber: a model based on Gaussian beam notion** [4068-26]
C. L. Schiopu, P. Schiopu, Univ. Politehnica Bucharest (Romania)
- 184 **Launch of the guided modes on an optical fiber: a model based on Gaussian beam notion** [4068-27]
C. L. Schiopu, P. Schiopu, Univ. Politehnica Bucharest (Romania)
- 191 **Power-related frequency shift determinations of an iodine-stabilized He-Ne laser at 633-nm wavelength by using a master-slave laser system** [4068-28]
G. Popescu, National Institute for Laser, Plasma and Radiation Physics (Romania)
- 198 **Evaluation method for the dynamics of an erbium-doped fiber laser** [4068-29]
F. I. Vasile, Siemens Co. (Romania); P. Schiopu, Univ. Politehnica Bucharest (Romania)
- 207 **Influence of cross-relaxation parameter on the sensitized photon avalanche** [4068-30]
E. Osiac, V. Lupei, National Institute for Laser, Plasma and Radiation Physics (Romania)
- 213 **Characterization of coated optical components by laser calorimetry** [4068-31]
T. Visan, D. G. Sporea, National Institute for Laser, Plasma and Radiation Physics (Romania)
- 219 **Execution of chemical metallizing of the inlet opening of a puncture in material** [4068-32]
E. Petrescu, Univ. Politehnica Bucharest (Romania); P. Penciu, C. Petrescu, M. Catrinciuc, Research and Development Institute for Electrical Engineering (Romania)
- 226 **Plasma analysis in the process of pulsed laser deposition of aluminium nitride and titan nitride thin films** [4068-33]
C. Grigoriu, I. Apostol, R. Rizea, A. Marcu, D. Dragulinescu, National Institute for Laser, Plasma and Radiation Physics (Romania)

- 232 **Optical phonon effects on linewidth of several laser active ions in YAG [4068-34]**
A. Lupei, V. Lupei, T. G. Sorop, E. Osiac, A. Petraru, National Institute for Laser, Plasma and Radiation Physics (Romania)
- 240 **Evaluation of some nonlinear parameters of $\text{Er}^{3+}:\text{Ti}:\text{LiNbO}_3$ waveguides from interferometric and near-field measurements [4068-35]**
N. N. Puscas, Univ. Politehnica Bucharest (Romania)
- 247 **He-Ne laser gain dependence on discharge current and gas pressure from resonant Faraday effect [4068-36]**
A. Gearba, C. Negutu, G. Cone, I. M. Popescu, Univ. Politehnica Bucharest (Romania)
- 255 **Global symmetries for laser radiation [4068-37]**
R. Constantinescu, C. Ionescu, R. Popa, Univ. of Craiova (Romania)
- 261 **Characterization of a resonant photoacoustic cell using the acoustic transmission line model [4068-38]**
S. M. Cristescu, D. C. Dumitras, D. C. A. Dutu, National Institute for Laser, Plasma and Radiation Physics (Romania)
- 271 **Accurate method to calculate some periodic integrals occurring in electromagnetic field analysis [4068-39]**
C. V. Atanasiu, I. G. Miron, National Institute for Laser, Plasma and Radiation Physics (Romania)
- 278 **Absorption in a self-heating He-Se laser tube [4068-40]**
M. Ristici, E. Ristici, M. Tivarus, National Institute for Laser, Plasma and Radiation Physics (Romania); B. Iliescu, National Institute for Physics of Materials (Romania); C. Cotirlan, Institute of Optoelectronics (Romania)
- 284 **Simple method for characterizing the up-conversion processes governing 3- μm generation in concentrated erbium crystals [4068-41]**
S. Georgescu, C. Hapenciuc, National Institute for Laser, Plasma and Radiation Physics (Romania)
- 290 **1D algorithm for automatic fringe spacing measurement in a straight equispaced parallel fringe pattern [4068-42]**
V. Nascov, A. Dobroiu, D. Apostol, V. Damian, National Institute for Laser, Plasma and Radiation Physics (Romania)
- 297 **Ultrashort-pulse generation and subharmonic bifurcation in directly modulated MQW lasers [4068-43]**
M. D. Guina, M. M. Dumitrescu, Tampere Univ. of Technology (Finland)
- 303 **Metal grating efficiencies for Smith-Purcell radiation in a relativistic regime [4068-44]**
F. Scarlat, M. Facina, C. D. Dinca, National Institute for Laser, Plasma and Radiation Physics (Romania); V. Manu, National Institute for Physics and Nuclear Engineering (Romania); A. Karabarounis, C. Trikalinos, E. Stiliaris, I. Papadakis, Univ. of Athens (Greece)
- 310 **High-performance 980-nm emission wavelength InGaAs/AlGaAs/GaAs laser diodes [4068-45]**
G. I. Suruceanu, A. N. Caliman, S. F. Vieru, V. P. Iakovlev, A. V. Sarbu, A. Z. Mereuta, Technical Univ. of Moldova

- 317 **Tunable laser diode sources for 830-nm and 980-nm wavelength range [4068-46]**
G. I. Suruceanu, Technical Univ. of Moldova

SESSION III OPTOELECTRONIC COMPONENTS: ANALYSIS AND CONTROL METHODS

- 324 **Solar cell optimization from spectral response [4068-47]**
G. Stoenescu, Univ. of Craiova (Romania)
- 330 **Improved measurement precision through continuous optical focusing on optoelectronic detection devices [4068-48]**
C. A. Spulber, G. E. Constantinescu, Pro Optica SA (Romania)
- 336 **Photoconductive frequency-resolved spectrometer [4068-49]**
I. Burda, S. Simon, G. Cristea, G. Cerbanic, L. Cociu, M. Todica, Babes-Bolyai Univ. (Romania)
- 342 **Improved method for processing Newton's rings fringe patterns [4068-50]**
A. Dobroiu, National Institute for Laser, Plasma and Radiation Physics (Romania);
A. Alexandrescu, Univ. Politehnica Bucharest (Romania); D. Apostol, V. Nascov, V. Damian,
National Institute for Laser, Plasma and Radiation Physics (Romania)
- 348 **Computer-assisted electropneumatic system to compensate for the sag of an optoelectronic detector [4068-51]**
M. Blejan, P. Drumea, I. Enache, M. Marin, Hydraulics and Pneumatics Research Institute
(Romania); B. Comanescu, D. Oancea, Institute of Optoelectronics (Romania)
- 355 **Optoelectronic systems: design of world-class products [4068-52]**
L. Tanase, Institute of Optoelectronics (Romania); M. Cucu, Research and Design Institute
for Production Systems (Romania)
- 364 **Quality control of product/process using nondestructive control and possibilities of robotic investigation [4068-53]**
L. Tanase, M. Margaritescu, EUROTEST 2000 SRL (Romania)
- 375 **Precision improvement in ellipsometric-type measurements for the refraction index using numerical code processing [4068-54]**
A. Belea, M. Bulinski, Univ. of Bucharest (Romania)
- 381 **Temperature and dopant concentration in single-mode 5- μ m diameter optical fiber—cooling through the die: implications for Laguerre orders in optical refractive synchronization [4068-55]**
J. R. Palmer, SilkRoad, Inc. (USA)
- 401 **Joined optical channels [4068-56]**
G. Copot, R. Copot, Institute of Optoelectronics (Romania)
- 407 **Thermovision used for determination of thermal losses in thermoelectric plants [4068-57]**
R. Pascu, A. Caramizoiu, Institute of Optoelectronics (Romania)
- 413 **Simple effective tests for beam propagation method programs [4068-58]**
M. M. Dumitrescu, Tampere Univ. of Technology (Finland); O. D. Iancu, Univ. Politehnica
Bucharest (Romania); J.-M. Karam, Institut National Polytechnique de Grenoble (France)

- 423 **Growth and spectral characteristics of Nd³⁺ in calcium lithium niobium gallium garnet (CLNKG) crystals [4068-59]**
A. Lupei, V. Lupei, E. Osiac, L. Gheorghe, M. Petrache, C. Stoicescu, A. Petraru, National Institute for Laser, Plasma and Radiation Physics (Romania)
- 429 **Numerical algorithm for complex field reconstruction [4068-60]**
M. Bulinski, A. Belea, Univ. of Bucharest (Romania)
- 436 **Analysis of the third order harmonic generation process in optical organic waveguides [4068-61]**
N. N. Puscas, Univ. Politehnica Bucharest (Romania)
- 442 **Pointing out the structure of double layers through spectroscopic methods [4068-62]**
B. Opreescu, Univ. of Pitești (Romania); M. Sanduloviciu, Univ. of Iasi (Romania)
- 448 **MOS transistor microscopic analysis [4068-63]**
G. Stoenescu, Univ. of Craiova (Romania); N. Baltateanu, Hyperion Institute for Research and Development (Romania)
- 454 **Temperature dependencies of optical parameters from EBBA channeled spectra [4068-64]**
M. Ursache, M. Socaciu, V. Calian, Univ. of Craiova (Romania)
- 460 **Antisymmetrized molecular dynamic simulations for conduction mechanisms in CdSe thin films [4068-65]**
V. Calian, G. Stoenescu, Univ. of Craiova (Romania)
- 466 **Calculations of the near-field enhancement in surface-enhanced Raman scattering on periodically structured metallic substrates [4068-66]**
M. Palamaru, S. Astilean, Babes-Bolyai Univ. (Romania)
- 472 **Electrical properties of irradiated CdSe thin films [4068-67]**
G. Stoenescu, Univ. of Craiova (Romania)
- 478 **Experimental investigation on multimode quartz fiber phase conjugation using SBS [4068-68]**
A. Mocofanescu, M. Zamfirescu, C. G. Fenic, A. Stratan, T. Visan, National Institute for Laser, Plasma and Radiation Physics (Romania)
- 485 **Numerical method for nonlinear optical devices [4068-69]**
V. Calian, M. Ursache, M. Socaciu, Univ. of Craiova (Romania)
- 491 **Optoelectronic visualization and study of heat transfer from metal wires to water by a compact Schlieren system [4068-70]**
A. Petris, National Institute for Laser, Plasma and Radiation Physics (Romania); D. Popa, Univ. Politehnica Bucharest (Romania); A. Jianu, National Institute for Laser, Plasma and Radiation Physics (Romania); C. Popa, Univ. Politehnica Bucharest (Romania); V. I. Vlad, National Institute for Laser, Plasma and Radiation Physics (Romania)
- 497 **Wavelength assignment algorithms in all-optical networks [4068-71]**
C. Bulaceanu, Pricewaterhouse Coopers (Romania)

SESSION IV TECHNOLOGIES IN OPTOELECTRONICS AND RELATED FIELDS

- 506 **Ultrasonic investigation of pulsed laser interaction with solid targets (Invited Paper)** [4068-72]
I. G. Apostol, R. Stoian, R. V. Dabu, A. Stratan, National Institute for Laser, Plasma and Radiation Physics (Romania); A. Serbanescu Oasa, Technical Univ./Sibiu (Romania); C. Angelescu, National Institute for Laser, Plasma and Radiation Physics (Romania)
- 513 **Resonance-enhanced light transmission through metal nanochannels (Invited Paper)** [4068-73]
S. Astilean, Babes-Bolyai Univ. (Romania); Ph. Lalanne, Institut d'Optique-CNRS (France); M. Palamaru, Babes-Bolyai Univ. (Romania)
- 520 **Modern procedures for chemical cleaning of corroded carbon steel equipment** [4068-74]
I.-H. Plonski, S.-F. Spiridon, M. Robu, Institute of Optoelectronics (Romania); C. Doman, M. Tudorache, M. Bobu, E. Mateescu, S. C. Thermoelectrica SA (Romania); F. Schneider, Institute of Solid State and Material Research (Germany)
- 526 **Evaluating smoke screens' masking ability in infrared using thermovision equipment** [4068-75]
M. Tomescu, R. Marginean, Institute of Optoelectronics (Romania); E. Nitis, M. Negosanu, M. Vizireanu, UM 02512C (Romania)
- 535 **Computer designing of the shot-range order structure of vitreous $\text{As}_2(\text{S,Se})_3\text{Sn}_{0.1}$ semiconductors before and after illumination** [4068-76]
A. M. Andriesh, A. I. Buzdugan, V. Dolghier, M. S. Iovu, A. N. Popescu, Institute of Applied Physics (Moldova)
- 543 **Fiber gyroscopes for strapdown technology** [4068-77]
O. Novac, F. Jitescu, Military Equipment and Technologies Research Agency (Romania)
- 549 **Peculiarities of the solidification mechanism of steel after Nd:YAG long-pulse laser welding** [4068-78]
V. Iov, F. Costache, A. Marian, D. M. Buca, National Institute for Laser, Plasma and Radiation Physics (Romania)
- 555 **Selective laser sintering processing of metallic components by using a Nd:YAG laser beam** [4068-79]
F. Costache, A. Marian, D. M. Buca, V. Iov, National Institute for Laser, Plasma and Radiation Physics (Romania)
- 562 **Optical refractive synchronization frequency sampling ratio amplitude ratio between the clock frequency and the modulated frequency** [4068-80]
J. R. Palmer, SilkRoad, Inc. (USA)
- 570 **Polishing of optical fibers using a CO_2 laser** [4068-81]
H. Orun, Middle East Technical Univ. (Turkey); M. V. Udrea, National Institute for Laser, Plasma and Radiation Physics (Romania); A. Alacakir, Ankara Nuclear Research and Training Ctr. (Turkey)
- 576 **Plume behavior and thin film deposition by laser ablation using a hellicoidal shadow mask** [4068-82]
A. Marcu, C. Grigoriu, National Institute for Laser, Plasma and Radiation Physics (Romania); W. Jang, K. Yatsui, Nagaoka Univ. of Technology (Japan)

SESSION V OPTOELECTRONIC DEVICES

- 584 **Combinational logic circuits with photonic devices [4068-83]**
P. Schiopu, Univ. Politehnica Bucharest (Romania); V. Degeratu, S. C. Banease SA (Romania); S. Degeratu, Univ. of Bucharest (Romania)
- 591 **Optimization of the number of detectors for the laser irradiation alert station [4068-84]**
M. Olariu, Military Equipment and Technologies Research Agency (Romania)
- 597 **Resonant cavity light-emitting diodes: modeling, design, and optimization [4068-85]**
M. M. Dumitrescu, P. Sipilä, V. Vilokkinen, L. Toikkanen, P. Melanen, M. J. Saarinen, S. L. Orsila, P. Savolainen, M. Toivonen, M. Pessa, Tampere Univ. of Technology (Finland)
- 608 **MQW laser dynamic behavior analysis based on small signal modulation regime simulation [4068-86]**
M. D. Guina, M. M. Dumitrescu, Tampere Univ. of Technology (Finland); O. D. Iancu, Univ. Politehnica Bucharest (Romania)
- 615 **Magnetic field sensors utilizing diluted magnetic semiconductors [4068-87]**
A. Gh. Podoleanu, R. G. Cucu, D. A. Jackson, Univ. of Kent at Canterbury (UK)
- 621 **LabVIEW remote control for a laser power/energy meter [4068-88]**
G. Ivan, D. G. Sporea, National Institute for Laser, Plasma and Radiation Physics (Romania)
- 627 **Multiconfiguration optical system with applications in night vision devices [4068-89]**
M. Mirzu, Military Equipment and Technologies Research Agency (Romania); G. Copot, Institute of Optoelectronics (Romania)
- 633 **Some aspects concerning optically powered intelligent sensors [4068-90]**
M.-A. Chita, S.-D. Anghel, I. Iorga-Siman, Univ. of Pitești (Romania)
- 639 **Staring infrared focal plane arrays for thermal imaging technology [4068-91]**
F. Jitescu, O. Novac, Military Equipment and Technologies Research Agency (Romania)
- 645 **First results of the cesium atomic fountain at INFLPR [4068-92]**
C. Mandache, T. Acseente, M. Ungureanu, National Institute for Laser, Plasma and Radiation Physics (Romania)
- 651 **Measurement of the ^{87}Rb ground-state hyperfine splitting in an atomic fountain [4068-93]**
S. Bize, Y. Sortais, Observatoire de Paris (France); M. S. Santos, Univ. de Sao Carlos (Brazil); C. Mandache, National Institute for Laser, Plasma and Radiation Physics (Romania); A. Clairon, Observatoire de Paris (France); C. Salomon, Lab. Kastler Brossel (France)
- 657 **Small-power-pulsed and continuous longitudinal CO_2 laser for material processing [4068-94]**
M. V. Udrea, National Institute for Laser, Plasma and Radiation Physics (Romania); A. Alacakir, Ankara Nuclear Research and Training Ctr. (Turkey); A. Esendemir, Middle East Technical Univ. (Turkey); O. Kusdemir, O. Pervan, Ankara Nuclear Research and Training Ctr. (Turkey); S. Bilikmen, Middle East Technical Univ. (Turkey)
- 663 **Wide-band acoustic transducer [4068-95]**
O. Robu, Marine Equipment Scientific Research Ctr. (Romania); M. Robu, Institute of Optoelectronics (Romania)

- 669 **Equipment for gluing the parts of an optoelectronic detector [4068-96]**
B. Comanescu, A. Ighigeanu, D. Oancea, M. Petcu, B. Tatulea, Institute of Optoelectronics (Romania); G. Chelkov, D. Dedovich, P. Evtoukhovitch, A. Gongadze, S. Podkladkin, E. Tskhadadze, Joint Institute for Nuclear Research (Russia); D. Vasile, M. Vlad, Electronics and Automatics Co. (Romania)
- 676 **Method for calculus of the sag of the frame of an optoelectronic detector [4068-97]**
B. Comanescu, A. Ighigeanu, D. Oancea, M. Petcu, B. Tatulea, Institute of Optoelectronics (Romania); G. Chelkov, D. Dedovich, P. Evtoukhovitch, A. Gongadze, S. Podkladkin, E. Tskhadadze, Joint Institute for Nuclear Research (Russia)

SESSION VI OPTOELECTRONICS IN ANALYTICAL INSTRUMENTATION AND MEDICINE

- 686 **Advances in low-coherence interferometry for tissue imaging (Invited Paper) [4068-98]**
A. Gh. Podoleanu, D. A. Jackson, Univ. of Kent at Canterbury (UK)
- 695 **Digital speckle-interferometry camera for nondestructive testing (Invited Paper) [4068-99]**
D. Apostol, V. Damian, A. Dobroiu, V. Nascov, National Institute for Laser, Plasma and Radiation Physics (Romania)
- 706 **Holographic interferometry study of phenol diffusion [4068-100]**
M. Kurzeluk, Technical Univ. of Construction (Romania); A. Guzun, Univ. Politehnica Bucharest (Romania); L. Stefan, Univ. of Bucharest (Romania)
- 712 **Spectrophotometric characterization of useful dyes in laser photodynamic therapy [4068-101]**
L. Danaila, Institute of Cerebrovascular Diseases (Romania); M. L. Pascu, A. Popescu, National Institute for Laser, Plasma and Radiation Physics (Romania); M. Pascu, Prof. Dr. Dimitrie Gerota Hospital (Romania); R. Ion, S.C. ZECASIN SA (Romania)
- 721 **Medical diagnosis using thermal flux sensors of a thermoelectric type [4068-102]**
R. Marginean, V. M. Hutanu, Institute of Optoelectronics (Romania)
- 726 **Soil-vegetation discrimination and assessment in satellite imagery [4068-103]**
A. Caramizoiu, C. Aiftimiei, A. D. Stoica, Institute of Optoelectronics (Romania)
- 733 **Optoelectronic associative neural network for recognition of some graphical patterns [4068-104]**
I. Ileană, 1 Decembrie 1918 Univ. (Romania); O. C. Iancu, Univ. Politehnica Bucharest (Romania)
- 740 **Stabilization system for the viewing field of sighting optical devices installed on vehicles [4068-105]**
A. D. Stoica, A. Caramizoiu, C. Aiftimiei, Institute of Optoelectronics (Romania)
- 751 **Analysis of some specific errors in infrared thermometry [4068-106]**
C. A. Spulber, G. E. Constantinescu, Pro Optica SA (Romania)
- 758 **Biostimulation effects of low-energy laser radiation on yeast cell suspensions [4068-107]**
S.-D. Anghel, C. S. Stănescu, D. Giosanu, I. Neagu, Univ. of Pitești (Romania); G. Săvulescu, Wine-Growing Research Station (Romania); I. Iorga-Simăn, Univ. of Pitești (Romania)

- 764 **Design consideration and performance of a digital lock-in amplifier with 68HC11 microcontroller [4068-108]**
I. Burda, S. Simon, M. Todica, G. Cristea, G. Cerbanic, L. Cociu, Babes-Bolyai Univ. (Romania)
- 770 **Environmental diagnosis and supervision mobile system for emergency cases [4068-109]**
M. Rosca, S. Geanta, G. Manoliu, Civil Protection Command (Romania); O. Logofatu, Arsenalul Armatei (Romania)
- 776 **Low-power radio-frequency capacitively coupled plasma in air: an alternative spectral source? [4068-110]**
S.-D. Anghel, A. Simon, T. Frentiu, E. A. Cordos, Babes-Bolyai Univ. (Romania)
- 786 **Spectral study of some fatty acid-cholesterol mixtures [4068-111]**
M. Honciuc, E. G. Carbunescu, C. Popa, E. Slavnicu, I. Badragan, Univ. Politehnica Bucharest (Romania)
- 792 **Single-particle optical sensing (SPOS) using optical fiber intensity-modulation sensors [4068-112]**
T. Nicula, Military Chemistry Application School (Romania)
- 800 **Remote sensing studies on seismic activity [4068-113]**
C. Aiftimiei, A. Caramizoiu, A. D. Stoica, Institute of Optoelectronics (Romania); A. Aiftimiei, Ministry of Defense (Romania)
- 806 **Neural networks for vegetation stress assessment [4068-114]**
C. Aiftimiei, A. Caramizoiu, A. D. Stoica, Institute of Optoelectronics (Romania); A. Aiftimiei, Ministry of Defense (Romania)
- 812 **Quality audit of optoelectronics systems [4068-115]**
L. Tanase, Institute of Optoelectronics (Romania)
- 824 **Mobile system for locating and tracking vehicles in distress [4068-116]**
G. Landi, HAL 9000 ID Systems srl (Italy); A. D. Stoica, Institute of Optoelectronics (Romania)
- 834 **Temporal resolution spectroscopy applied in the study of an LTE arc plasma [4068-117]**
I. Iova, S. Levai, F. Iova, C. Biloiu, Gh. Ilie, M. Băzăvan, M. Bulinski, Univ. of Bucharest (Romania)
- 844 *Author Index*

Conference Committees

Conference Chair

Teodor Necsoiu, Institute of Optoelectronics (Romania)

Organizing Committee Chair

Maria Robu, Institute of Optoelectronics (Romania)

Scientific Committee

L. Anaticiuc (Ukraine)
A. Andries (Rep. Moldova)
A. Balaban (Romania)
D. Botez (USA)
E. Curatu (Canada)
S. Diaconescu (Romania)
K. L. Dickson (USA)
S. Miyazawa (Japan)
I. Mogos (Romania)
T. Necsoiu (Romania)
T. Niculescu (Romania)
M. Peculea (Romania)
I. I. Popescu (Romania)
I. M. Popescu (Romania)
A. Sandulescu (Romania)
E. Stefanescu (Romania)
A. Stoica (Romania)
M. Strzelec (Poland)
F. Tanasescu (Romania)
V. Vlad (Romania)

Program Committee

V. Babin (Romania)
M. Bertolotti (Italy)
V. Bivol (Rep. Moldova)
A. Cavaleru (Romania)
V. Ciumas (Rep. Moldova)
E. Cordos (Romania)
D. Dumitras (Romania)
D. Haseganu (Romania)
I. Iova (Romania)
I. Jelev (Romania)
M. Kopica (Poland)
S. Levai (Romania)
G. Marmureanu (Romania)
M. Marzu (Romania)
R. Medianu (Romania)
A. Moldovan (Romania)
I. Munteanu (Romania)
D. Oancea (Romania)
M. Pusca (Romania)
M. Robu (Romania)
P. Sterian (Romania)
A. Stoica (Romania)

Technical Committee

A. Caramizoiu (Romania)
O. Curcan (Romania)
C. Dragomirescu (Romania)
M. Ionescu (Romania)
R. Marginean (Romania)
V. Stan (Romania)
A. Vlasceanu (Romania)

Introduction

The Symposium on Optoelectronics (SIOEL) is a series of international conferences dedicated to the optoelectronics field. Held each year in Bucharest, the symposium summons engineers, physicists, and researchers from Romania and abroad who have contributed to the development of optoelectronics.

The aim of this sixth symposium was to share and promote the progress achieved in optoelectronics in recent years. These achievements have had a significant impact on microtechnologies, information technology, automation of industrial processes, measuring and control equipments, miniaturizing, etc. There is practically no industry that has not benefited from the results of research in optoelectronics.

This year the symposium covered various topics including, but not limited to, materials for optoelectronics, lasers and their applications, optoelectronic components, technologies in optoelectronics, optoelectronic devices, optoelectronics in medicine, and analytical instrumentation.

The SIOEL '99 Scientific Committee selected for presentation 165 papers submitted by authors from 14 countries. We are confident that the 4 plenary sessions, 10 invited papers, 29 oral papers, and 122 poster papers gave an overview of the newest and most important results in optoelectronics. The editors selected 117 papers to be published; the most important contributions to the symposium are included, due to the limit in number of pages for this SPIE Proceedings volume.

The organization of the Optoelectronics Symposium was made possible only through the joint action and support of several domestic and international institutions. We also owe much to the institutions that sponsored this event. All these organizations are listed on the cover and title page of this volume.

Our acknowledgements are also due to the referees, to the invited professors, and to all of the participants for their outstanding contribution to the success of the symposium. Lastly, we would like to express our thanks to the members of the Organizing Committees, to colleagues and members of the other committees, and to the Secretariat for their effort and creativity.

We do hope that the participants attending the 1999 Optoelectronics Symposium enjoyed the sessions and their time spent during this event. We believe that this symposium provided an opportunity to renew friendships or to start new ones.

On behalf of the Organizing Institutions, we would like to extend our warmest thanks to all participants of the Sixth Symposium on Optoelectronics and to invite them to take part, through their important and valuable contributions, in the next conference in 2000.

Teodor Necsoiu
Maria Robu
Dan C. Dumitras

SESSION I

Materials for Optoelectronics and Related Fields

InGaAsP/AlGaAs multiple wavelength vertical cavity lasers and arrays in the 1.5- μ m band fabricated by localized wafer fusion technique

A.V. Syrbu^{*a}, V.P. Iakovlev^a, A. Rudra^a, C.-A. Berseth^a, E. Kapon^a, A. Mereuta^b, I. Sagnes^b, A. Ougazzaden^b

^aDepartment of Physics, Swiss Federal Institute of Technology Lausanne, CH-1015 Lausanne, Switzerland

^bFrance Telecom-CNET, 196 Avenue Henri Ravera, BP 107, 92225 Bagneux, France

ABSTRACT

We have demonstrated InGaAsP/AlGaAs double fused 1.5 μ m multiple wavelength vertical cavity lasers and arrays in which element definition is obtained by localized fusion. Laser elements emit in continuous wave under electrical and optical pumping. Multiple wavelength single element VCSELs have been fabricated in the same batch taking advantage of layer thickness nonuniformity of InGaAsP/InP material close to the edge of the wafer. To obtain multiple wavelength arrays a controllable cavity length variation using anodic oxidation has been performed. The wavelength span in an 8x1 laser array is 10 nm. Single mode operation with more than of 40 dB side mode suppression ratio is characteristic for laser elements in the array.

INTRODUCTION

Recent developments in the field of 1.5 μ m-wavelength vertical cavity surface emitting lasers (VCSELs) show considerable progress in improving operation characteristics and manufacturability of both electrically pumped and optically pumped devices¹⁻⁷. Maximum operating temperature of electrically pumped VCSELs in excess of 70 °C¹ and novel simplified fabrication techniques based on double fused^{2,3}, single fused^{4,5} and all-grown⁶⁻⁸ 1.5 μ m VCSEL structures demonstrate that present fabrication technologies have the potential to produce low cost, uncooled light sources for fiber optic networks. On the other hand, continuous wavelength tuning over 50 nm, very recently obtained on microelectromechanical optically pumped VCSELs⁹ targets the important market of wavelength division multiplexed (WDM) communication systems.

So far all published results in this field refer to single element devices emitting at a given wavelength and in the literature there are no reports on 1.5 μ m VCSEL arrays fabrication. Yet, multiple wavelength 1.5 μ m VCSELs and VCSEL arrays could be also attractive for WDM applications, especially in low cost local and metropolitan WDM networks. In this paper we demonstrate multiple wavelength 1.5 μ m VCSELs and monolithic arrays fabricated using the localized wafer fusion technique².

FABRICATION APPROACH

We are using the double wafer fusion to assemble the VCSEL structure which consists of an InGaAsP/InP active cavity material sandwiched between two (top and bottom) AlGaAs/GaAs distributed Bragg reflectors (DBRs). Element definition (electrical and optical lateral confinement) is obtained in-situ by localized fusion of one of the AlGaAs/GaAs wafers to the InGaAsP/InP active cavity material. This approach is different from the traditional one^{1,3,4} which is based on lateral Al(Ga)As wet oxidation (See Fig. 1) and offers a number of advantages which are described elsewhere². In the new approach the size of VCSEL elements is defined by the size of the mesa etched on the GaAs-based wafer before performing the localized fusion. Thus VCSEL elements with the aperture of 5 μ m and less can be reproducibly defined with a very good uniformity on the wafer, which we believe is another advantage compared with the traditional method of element definition by lateral Al(Ga)As oxidation.

Precise aperture definition is important both for wavelength control and reproducibility of single mode operation and of all other parameters of VCSEL elements.

In this study we have used InGaAsP/InP active cavity material, p-, n- type and undoped AlGaAs/GaAs DBRs - all grown

Correspondence: Email: sirbu@dpmail.epfl.ch

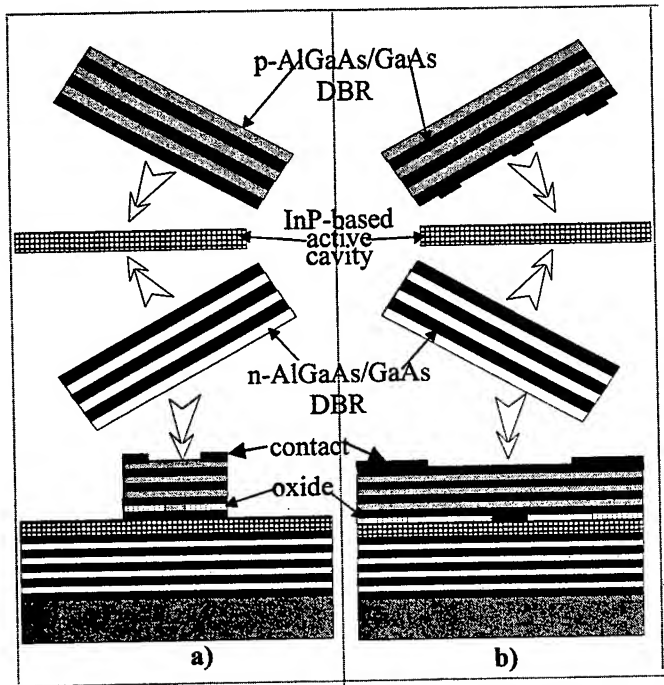


Fig. 1. a) traditional and b) localized fusion approach to element definition (electrical and optical lateral confinement) in VCSELs

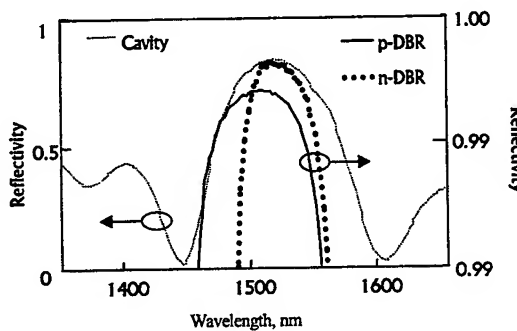


Fig. 2. Typical results of InGaAsP/InP active cavity material, n- and p- AlGaAs/GaAs DBRs reflectivity measurements.

ELECTRICALLY PUMPED MULTIPLE WAVELENGTH SINGLE-ELEMENT 1.5 μm VCSELs.

To obtain multiple wavelength 1.5 μm optical communication lasers, which at present are mostly distributed feedback (DFB) edge emitting lasers diodes, the common approach is to change the grating pitch that defines the emitting wavelength. For example, to obtain laser diodes with 8 different wavelengths it is necessary to process 8 different wafers and slightly changing the grating pitch on each wafer. In the case of VCSELs it is possible to obtain multiple wavelength devices on the same wafer by taking advantage of layer thickness nonuniformity which translates into nonuniformity of cavity length. This is normally the case when using material close to the edge of the wafer. Fig. 3 shows spectral characteristics of 8 VCSELs with an aperture of 5 μm taken from the same batch of devices. These devices operate in continuous wave at room temperature and have

by metal organic chemical vapor deposition (MOCVD) at 650°C. InGaAsP/InP material is grown with a constant group V elements composition throughout the structure and has an optical thickness of $3/2 \lambda$. It includes a strain compensated 6 quantum well structure with 1% compressive strain in the wells and 0.8 % tensile strain in the barriers. The peak of the photoluminescence spectrum is at 1550 nm. N-AlGaAs/GaAs DBRs with either abrupt or graded AlGaAs/GaAs interfaces are uniformly doped at about 10^{18} cm^{-3} . For p-DBRs it is important to have graded AlGaAs/GaAs interfaces and a special doping scheme in order to obtain acceptable optical and electrical properties.

Before assembling the double fused structure we carefully measure the reflectivity spectra of the VCSEL components. Fig. 2 shows some typical results of InGaAsP/InP active cavity material and n- and p- AlGaAs/GaAs DBR reflectivity measurements. Reflectivity spectrum of InGaAsP/InP material has a maximum indicating the position of the cavity mode. AlGaAs/GaAs DBRs are measured using a high resolution multiple reflections method¹⁰. Typically 99.8 % and 99.7 % reflectivity values are obtained on n- and p- type DBRs, respectively. Optical absorption values of p-DBRs are in the range of $30\text{-}50 \text{ cm}^{-1}$ and are about 5 times higher than respective values of n-DBRs.

In the first fusion process the structured p-DBR is fused to the active cavity material at 650°C using the wafer fusion technique described in Ref.11. Before performing the second fusion we selectively etch the InP wafer and measure the photoluminescence of the fused structure. Compared with InGaAs/InP multiquantum well material used in our previous work, which was grown at low temperature (below 500°C) by chemical beam epitaxy (CBE)¹¹ and gas source molecular beam epitaxy (GSMBE)², the present material grown by MOCVD at 650°C does not show any post-diffusion degradation. After the second fusion process we selectively etch one of the GaAs substrates and deposit n- and p-ohmic contacts on those structures that are designed for electrical pumping.

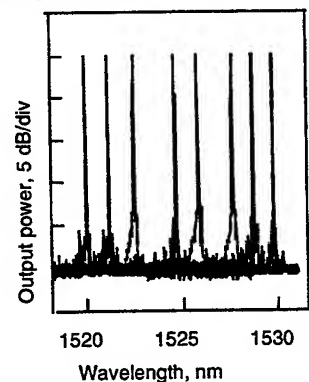


Fig. 3. Spectral characteristics of 8 VCSELs taken from the same batch of devices.

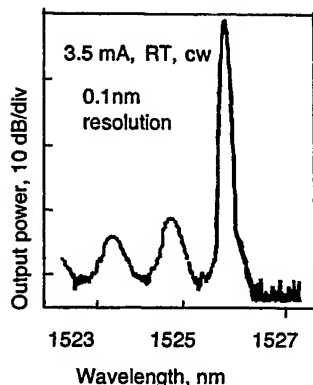


Fig.4. Typical high resolution spectrum of an electrically Pumped VCSEL

In this structure the top and bottom AlGaAs/GaAs DBRs are undoped and comprise 35 pairs of AlGaAs (70% AlAs) and GaAs quarter-wavelength layers with the Bragg wavelength centered at 1.53 μm . Fabrication process starts with etching on one AlGaAs/GaAs DBR 5 μm diameter mesas with 250 μm spacing through the top GaAs quarter-wavelength layer. This is followed by precise mesa etching applying photolithography and anodic oxidation steps using a technique similar to that described in Ref. 12. This allows us to obtain sets of 8x1 mesas with different heights within about 20 nm. After the second fusion one of the GaAs wafers is selectively etched and the double fused structure is cleaved into linear arrays of 8x1 elements. These arrays have been tested by optical pumping using standard 980 nm pump laser diodes. Lasing is obtained only when the pumping light illuminates the double fused structure in the mesa region. Fig. 6 shows the measured wavelength distribution in one of the 8x1 arrays. The wavelength span is 10 nm. All laser elements operate under continuous optical pumping. Fig. 7 depicts the emission spectrum of an element in the center of the array measured at 3 mW optical pumping level. Single mode emission with side mode suppression ratio in excess of 40 dB is obtained.

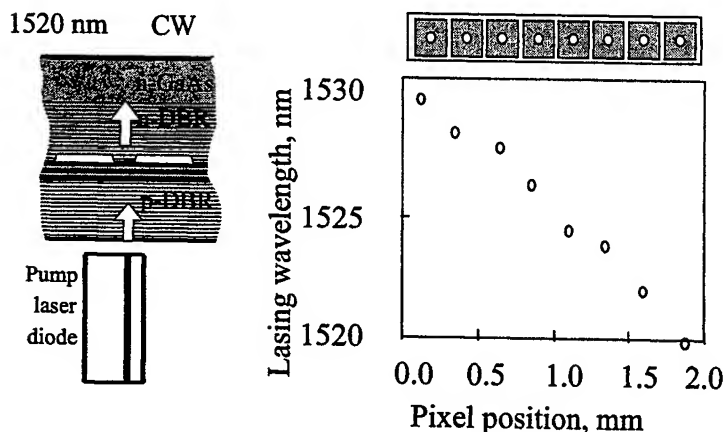


Fig. 6. Pumping scheme and lasing wavelength distribution in a 8x1 array.

different wavelength values in the range 1520-1530 nm. Threshold current of these devices increases from 3 mA to 7 mA with decreasing wavelength because of increasing detuning between the maximum of gain spectrum and cavity mode. Typical high resolution spectrum of a VCSEL (Fig.4) shows that emission consists of a dominant mode with side-mode suppression ratio of about 30 dB.

OPTICALLY PUMPED MULTIPLE WAVELENGTH VCSEL ARRAYS

As in our previous 1.5 μm single element devices, we are using double fused InGaAsP/AlGaAs structures in which element definition is obtained by localized wafer fusion. InGaAsP/InP material is taken from the central part of the wafer where layer thickness is constant. To produce a controllable cavity length variation in neighboring elements we perform a precise mesa «trimming» using anodic oxidation as schematically shown in Fig. 5.

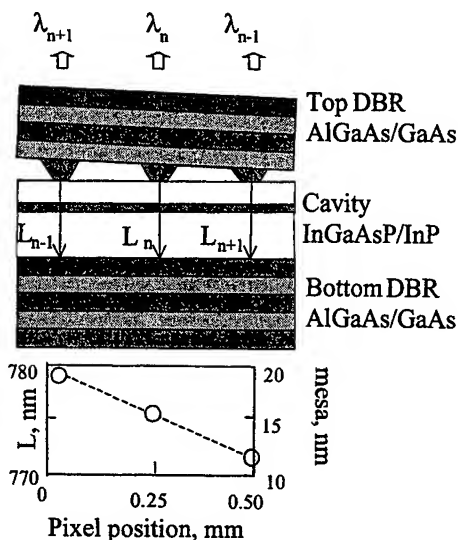


Fig. 5. Schematic of the VCSEL array structure with pixels obtained by localized fusion. Precise mesa «trimming» using anodic oxidation was performed on the top DBR to produce a controllable cavity length variation.

Lower part of the figure shows effective cavity thickness vs. pixel position

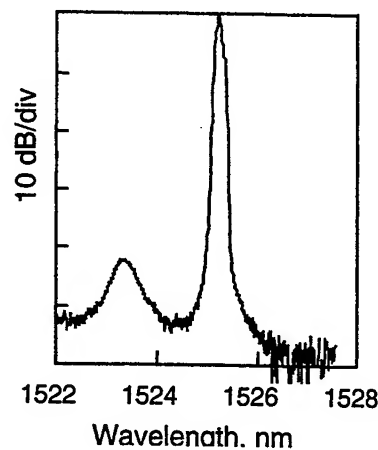


Fig. 7. Emission spectrum of the center element in the array measured at 3 mW optical pumping level.

CONCLUSION

We have demonstrated InGaAsP/AlGaAs double-fused 1.5 μm multiple wavelength vertical cavity lasers and arrays in which element definition is obtained by localized fusion. Laser elements emit in continuous wave under electrical and optical pumping. Multiple wavelength single element VCSELs have been fabricated in the same batch taking advantage of layer thickness nonuniformity of InGaAsP/InP material close to the edge of the wafer. To obtain multiple wavelength arrays a controllable cavity length variation using anodic oxidation has been performed. The wavelength span in a 8x1 laser array is 10 nm. Single mode operation with more than 40 dB side mode suppression ratio is characteristic for the laser elements in the array.

ACKNOWLEDGMENT

Authors gratefully acknowledge C. Harder and B. Schmidt from Uniphase Laser Enterprise, Zurich, Switzerland, for providing 980 nm pump laser diodes.

REFERENCES

1. K.A. Black, P. Abraham, A. Keating, Y.J. Chiu, E.L. Hu, and J.E. Bowers, "Long wavelength vertical cavity lasers", 11th International Conference on Indium Phosphide and Related Materials, 16-20 May 1999, Davos, Switzerland, pp. 271-6.
2. A.V. Syrbu, V.P. Iakovlev, C.A. Berseth, O. Dehaese, A. Rudra, E. Kapon, J. Jacquet, J. Boucart, C. Stark, F. Gaborit, I. Sagnes, J.C. Harmand and R. Raj, "30 C operation of 1.52 μm InGaAsP/AlGaAs vertical cavity lasers with in situ built-in lateral current confinement by localised fusion", *Electron. Lett.* 34 (18), 1744-5 (1988).
3. H.W. Song, D.S. Song, I.Y. Han, C.K. Kim, H.Y. Ryu and Y.H. Lee, "1.5 μm vertical cavity surface-emitting lasers utilising low loss $\text{Al}_x\text{O}_y/\text{GaAs}$ mirrors", *Electron. Lett.* 35 (4), pp. 296-7 (1999)
4. Y. Ohiso, C. Amano, Y. Itoh, K. Tatenno, T. Tadokoro, H. Takenouchi, T. Kurokawa, "1.55 μm vertical-cavity surface-emitting lasers with wafer-fused InGaAsP/InP-GaAs/AlAs DBRs". *Electron. Lett.*, 32, (16), pp. 1483-4, (1996)
5. Rapp, F. Solomonson, J. Bentell, I. Sagnes, H. Moussa, C. Meriadec, R. Raj, K. Streubel and M. Hammar, "Near room temperature continuous-wave operation of electrically pumped 1.55 μm vertical cavity lasers with InGaAsP/InP bottom mirror", *Electron. Lett.* 35 (1), pp. 49-50, (1999)
6. C. Stark, J. Boucart, A. Plais, N. Bouche, E. Derouin, A. Pinquier, F. Gaborit, "Novel 1.55 μm VCSELs with top metamorphic GaAs/AlGaAs and bottom InP/InGaAsP Bragg Reflectors", IEEE OFC Conference proceedings, San Diego, USA, Feb 22-26 1999.
7. J.K. Kim, E. Hall, O. Sjolund, G. Almuneau and L.A. Coldren, "Room temperature, electrically pumped multiple-active-region VCSELs with high differential efficiency at 1.55 μm ", *Electron. Lett.* 35 (13), pp. 1084-5, (1999).
8. Kazmierski, C, Debray, J.P., Madani, R., Boudma, M., Etrillard, J, Sagnes, I., Alexandre, F., and Quillec, M: "First all-monolithic VCSELs on InP: 55 C pulse lasing at 1.56 μm with GaInAlAs/InP system", IEEE-ISLC 98, Nara, Japan, 4-8 October 1998, Postdeadline Paper.
9. D. Vakhshoori, P. Tayebati, Chih-Cheng Lu, M. Azimi, P. Wang, Jiang-Huai Zhou and E. Canoglu, "2 mW CW singlemode operation of a tunable 1550 nm vertical cavity surface emitting laser with 50 nm tuning range", *Electron. Lett.* 35 (11) pp. 900-901, (1999).
10. Berseth, C.A., Syrbu, A.V., Iakovlev, V.P., Dehaese, O., Rudra, A., Kapon, E. "Highly accurate measurement of reflectivity and optical absorption in distributed Bragg reflectors using wafer fused resonator" *Electron Lett.*, 34, (18), pp. 1666-7, (1998).
11. A. V. Syrbu, J. Behrend, J. Fernandez, J.F. Carlin, C.-A. Berseth, V.P. Iakovlev, A. Rudra and E. Kapon, "Thermal stability of InP based structures for for wafer fused laser diodes", *J. Cryst. Growth*, 188, pp. 338-342, (1998).
12. T. Wipiejewski, J. Ko, B.J. Thibeault and L.A. Coldren, "Multiple wavelength vertical-cavity laser array employing molecular beam epitaxy regrowth", *Electron. Lett.* 32 (4), 340-2, (1996)

Calibration free laser induced plasma spectroscopy: a new frontier for material analysis, environmental protection and cultural heritage conservation

Luca Bolognesi, Michela Corsi, Vincenzo Palleschi*, Elisabetta Tognoni, Azenio Salvetti

Pulsed Laser Spectroscopy Group, Istituto di Fisica Atomica e Molecolare del CNR
Via del Giardino, 7 – I-56127 PISA, Italy

ABSTRACT

A new calibration free procedure (CF-LIPS) for quantitative elemental analysis of material, based on Laser Induced Plasma Spectroscopy technique, has been developed and patented by the Pulsed Laser Spectroscopy Group at IFAM/CNR (Pisa). This procedure allows for fast and reliable quantitative analysis of materials in solid, liquid or gaseous phase. Precision of order of a few parts percent can be obtained, for all the elements in the sample, with typical sensitivities of one part per million (ppm) or better. Major constituents, trace elements and impurities are all measured in the same run. The two major advantages of the CF-LIPS technique, compared with conventional chemical analysis methods, are the independence on sample pretreatment and calibration curves. The problems related to the so called 'matrix effect', which produces a lack of linearity in emission spectra, are completely overcome by the application of this standardless analytical procedure, which is based on the measure of the relevant physical quantity characterizing the plasma. These features make CF-LIPS an eligible method for on line elemental analysis or in field quantitative measurements. In fact, CF-LIPS is the only existing technique which gives precise quantitative results, comparable with laboratory chemical analysis, in real time and *in situ*. The comparatively low cost of the system, along with its intrinsic speed and ease of use, will probably help, in next few years, a further diffusion of the Calibration-free LIPS technique for material analysis, environmental protection and Cultural Heritage conservation and study.

Keywords: LIBS, laser, spectroscopy, material analysis, environmental protection, cultural heritage

1. INTRODUCTION

The first applications of Laser Induced Plasma Spectroscopy (LIPS) for material analysis have been proposed in the early 80's¹⁻⁶. Since then, many LIPS-based diagnostic systems have been developed for research and industrial applications⁷⁻²⁸, taking advantage of the intrinsic characteristics of this technique, such as quickness, sensitivity and feasibility of *in situ* measurements. In particular, LIPS has been extensively used as a reliable analysis technique for trace element detection in atmosphere⁸⁻⁹ as well as in liquid effluents¹¹⁻¹² or in metallic alloys¹³⁻¹⁴. Applications to Cultural Heritage conservation and study have been also proposed¹⁵⁻¹⁸.

LIPS is a fast and essentially non-destructive diagnostic method, based on the analysis of the spectral emission of the plasma produced by focusing an intense laser beam on the sample to be investigated. Typical temperatures and electron densities in the induced plasma can reach several eV and 10^{18} electrons/cm³. After irradiation, the de-excitation of the atoms and ions in the focal spot produces characteristic emission lines; the spectral region of interest for LIPS analysis is typically in the 200-800nm range.

The LIPS technique doesn't require sample preparation and can be applied on samples of arbitrary shapes in solid, liquid or gaseous state. One of the principal advantages of this technique is its independence from laser source wavelength: the plasma formation process in fact is mainly related to the high energy of the laser pulse. The measuring time is very short (seconds); moreover, with the use of new spectral detection systems (Echelle spectrometers) a fast mapping of the sample surface, when required, can be performed in a short time. The dynamic range of LIPS technique is also remarkably wide: the

* Correspondence: E-mail: vince@ifam.pi.cnr.it; WWW: <http://www.ifam.pi.cnr.it/libr.htm>, Tel: +39 050 3139007
Fax: +39 050 3139036

technique gives simultaneously information about elements with concentrations ranging from 100 % down to parts per million.

In last years, several works have studied the possibility of LIPS application to quantitative elemental analysis of materials, by comparing the LIPS signal obtained for a given element to a suitable calibration curve¹⁹⁻²⁵. However, the LIPS signal emitted by the same element depends on the matrix in which it is embedded²³⁻²⁴; this 'matrix effect' leads to the necessity of many calibration curves, in principle one for any substrate composition. In case of samples of unknown composition, this would lead to the paradoxical need for an exact knowledge of the sample composition in order to build the proper calibration curve required for the measurement. This problem has been studied in recent papers by Xu et al.²⁷ and Chaléard et al.²⁸, where two different approaches have been suggested in order to alleviate the matrix effect in LIPS analysis.

However, at present time, no exhaustive approach has been suggested which is able to completely overcome this problem. In practical situations, the use of empirical calibration curves might be useful for measurements of the concentration of a single specie in a well defined matrix⁸⁻¹²; however, this procedure would be inappropriate in more complex cases, such as multi-elemental analysis in *a priori* unknown environments.

Hopefully, the basic physics of the laser induced plasma process allows us to build up a measurement protocol which is not affected by the above mentioned effects. Assuming that some simple conditions are verified, a quantitative analysis of the atomic species constituting the sample is possible, without calibration curves. This calibration-free procedure, applicable to solids, liquids, particulate and gaseous samples, will be described in the next section.

2. DESCRIPTION OF THE PROCEDURE

Preliminary data processing

The calibration-free procedure requires all the atomic components of a sample to be detected by measuring at least one of their characteristic spectral lines. Therefore, an unknown sample should be investigated in detail by recording the whole spectrum within the sensitivity range of the spectral detector (2000 to 8000 Å, typically).

The spectral signal collected by the detector is stored on a computer and the data are processed using a dedicated programme developed at IFAM-CNR.

Working hypothesis

In order to develop a calibration-free measurement protocol we should make some reasonable assumptions, concerning both the experimental way of operation and the theoretical representation of the plasma conditions.

First of all, we will assume that the plasma composition is representative of the actual material composition prior of the ablation (this is the basic assumption for application of LIPS technique, which is well realized in the range of the laser energies used in LIPS experiments). Moreover, we assume that in the actual temporal and spatial observation window, the plasma is in Local Thermal Equilibrium (LTE) condition and the radiation source is optically thin (this hypothesis is in general fulfilled in LIPS experiments, where the main ionization process is produced through impact excitation by thermal electrons).

Although these requirements might seem strong, experimental results obtained in our laboratory showed that the population of the excited atomic levels (with typical energy between 3 eV and 8 eV) obeys to a Boltzmann distribution. This is a good a posteriori demonstration that the plasma produced is close to LTE conditions. In normal LIPS operating conditions, the assumption of optically thin plasma is fulfilled for trace elements, while in a few cases it may become critical for intense resonance lines of the primary components. The self-absorption effect can be theoretically modeled, and a forthcoming paper will be published by the authors on this topic. At the moment, our analysis will consider only the spectral lines that are not self-absorbed.

In LTE approximation, the line integral intensity corresponding to the transition between two levels E_k and E_i of an atomic specie s can be expressed as:

$$I_{\lambda}^{ki} = N_s A_{ki} \frac{g_k e^{-\frac{E_k}{K_B T}}}{U_s(T)} \quad (1)$$

where λ is the wavelength of the transition, N_s is the number density (particle/cm³) of the emitting atoms for each specie, A_{ki} is the transition probability for the given line, g_k is the k level degeneracy, K_B the Boltzmann constant, T the plasma temperature and $U_s(T)$ is the partition function for the emitting specie at the plasma temperature. The emitted intensity is expressed in photons/(sec·cm³). In actual measurements, the efficiency of the collecting system affects as a scale factor the measured intensity of the line, so that we can write:

$$\overline{I_{\lambda}^{ki}} = FC_s A_{ki} \frac{g_k e^{-\frac{E_k}{K_B T}}}{U_s(T)} \quad (2)$$

where $\overline{I_{\lambda}^{ki}}$ represents the measured integral line intensity, C_s is the concentration of the emitting atomic specie and F is an experimental parameter which takes into account the optical efficiency of the collection system as well as the plasma density and volume.

In eq.(2), the line integral intensity $\overline{I_{\lambda}^{ki}}$ is the result of LIPS measurement, the spectroscopic parameters A_{ki} , g_k , E_k can be retrieved from spectral databases (in our case we got the relevant information from the NIST Database for Atomic Spectroscopy), and the F , C_s , T values have to be determined from the experimental data. The partition function of each specie can be calculated from the spectroscopic data, once the plasma temperature is known.

Let us now define the following quantities:

$$y = \ln \frac{\overline{I_{\lambda}^{ki}}}{g_k A_{ki}}, \quad x = E_k, \quad m = -\frac{1}{K_B T}, \quad q_s = \ln \frac{C_s F}{U_s(T)} \quad (3)$$

Taking the logarithm of eq.(2) and substituting the above definitions, we obtain the following relationship between the x and y parameters:

$$y = mx + q_s \quad (4)$$

The two-dimensional space identified by the above defined x and y co-ordinates is called Boltzmann plane. We can write a similar relation for each species in the plasma.

Using the definitions of eq.(3), we can represent each experimental LIPS line as a point in the Boltzmann plane. Thus, the entire data set of line intensity can be graphically represented as a Boltzmann plot²⁹, where the different points lie on several parallel straight lines, with slope m and intercept q_s , each one corresponding to a different atomic specie.

According to eq.(4), the slope m of the plots is related to the plasma temperature, while the intercept q_s is proportional to the logarithm of the specie concentration.

Let us assume that experimental data are available for each specie present in the plasma, that is, in our experimental conditions, for both the neutral and ionized species of each atomic element. In principle, with the hypothesis of LTE, after determination of the plasma temperature, the concentration of a specie can be obtained from the measurement of just one experimental line. However, because of the rather large uncertainties existing in the literature on the A_{ki} coefficients, a precise concentration measure must be obtained using several spectral lines at different energies. Then, the F factor can be determined by normalizing to unit the species concentration C_s :

$$\sum_s C_s = \frac{1}{F} \sum_s U_s(T) e^{q_s} = 1 \quad (5)$$

Finally, the concentration of all the atomic species of the sample can be obtained as:

$$C_s = \frac{U_s(T)}{F} e^{q_s} \quad (6)$$

where all the factors are known. The concentration value determined by eq.(6) refers to one specie; in order to obtain the elemental composition, it is sufficient to add the values corresponding to the neutral and single ionised species of the same element, i.e. the total concentration for a given element M is given by:

$$C_M^{TOT} = C_{M(I)} + C_{M(II)} \quad (7)$$

3. SOME APPLICATIONS OF THE CF-LIPS PROCEDURE

The new CF-LIPS method developed at IFAM is proposed as a viable alternative to the traditional analytical procedures (AAS, ICP). A number of applications have already been suggested: as an example, automatic control in industrial processes or monitoring of polluted soils can be mentioned. The technique has already been tested at IFAM on polluted soils, yielding excellent results with respect to measurement quickness (a few seconds), sensitivity (1 ppm), precision (around 1 %), possibility of in situ operation, cheapness. The technique has also been applied in the field of Cultural Heritage conservation for determining analytical composition of pigments, ancient bronze objects and ceramic glazes.

3.1 Experimental setup

The CF-LIPS experimental setup is analogous to the apparatus required for a traditional LIPS measurement. The experimental prototype for LIPS analysis, operating since several years at IFAM-CNR Institute in Pisa⁷⁻¹⁵, is sketched in Fig. 1.

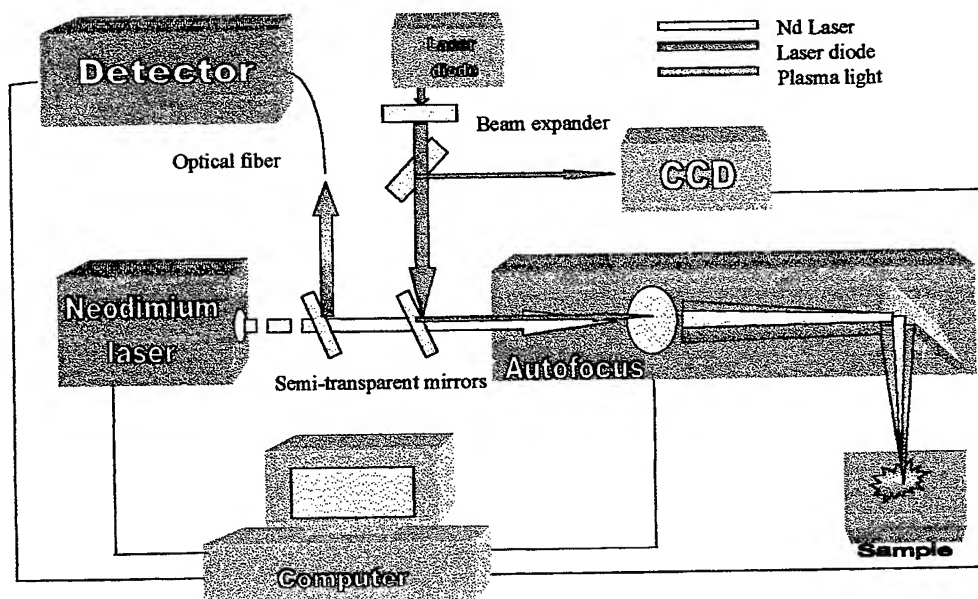


Fig.1 Experimental CF-LIPS setup

The prototype uses a Quanta System Q-switched Nd-Yag laser (Handy 101E), delivering about 600 mJ at 1064 nm in 7ns pulses, at a maximum repetition rate of 10Hz, for generating a micro-plasma at the sample surface. The laser beam is focused on the sample by a lens of 20 cm focal length. The light emitted by the sample is collected using an optical system and then sent through an optical fibre to a Mechelle 7500 spectrometer by Multichannel Instruments AB. The spectrometer acquisition is triggered a couple of microseconds after the laser pulse, in order to reduce the contribution of the continuum *Bremsstrahlung* radiation to the LIPS signal. In typical experimental conditions we use a gate width of about 1 μ s, which allows to obtain a good LIPS signal in a regime where space and time variations of plasma parameters are almost negligible. The resulting LIPS spectrum is analyzed by computer using specialized software developed at IFAM. The tagging of a peak to an atomic species is performed by means of the comparison with the set of wavelength and intensity data available on the NIST electronic database (NIST DB 38). The data set corresponding to the different lines observed are then represented as a Boltzmann plot, from which the plasma temperature and the species concentration are determined.

3. 2 Applications

The procedure here proposed can be applied for the analysis of solid, liquid and gaseous samples. A few results are described in the following as an example of different fields of application which could get benefits from the features of CF-LIPS technique.

Environmental Protection: Quantitative Analysis of Heavy Metals in Off-Stack Emissions from Power Plants

At present time, the concentration of metals coming from stack emissions is measured by off-line analysis of samples extracted at the chimney. The low quantity of solid emissions requires long sampling periods and errors can easily occur; moreover, the monitoring of volatile compounds, like mercury, are more difficult. It is thus evident the usefulness of an instrument able to perform continuous monitoring of metal emissions from industrial plants³⁰⁻³³.

The field measurements have been carried out on a 150 MW oil-fired power plant. Smoke temperature was about 150 °C, with a solid particulate volume fraction of about 10^{-8} .

The laser beam was focused into the flue duct by means of an optical system; the UV-visible light emitted by the plasma was collected on axis and focused through a small lens onto a fiber optic, which transmitted the light to the entrance slit of the spectrometer. No optical windows were needed since the plant was operating at low pressure.

Before starting the measurements inside the duct, a number of acquisitions outside the duct were performed in order to evaluate the background signal and to be sure that the spectral lines detected were in fact emitted by metals present in the smokes. Fig.2 shows the quantitative analysis of atmospheric air; it's clear that the CF-LIPS results are in very good agreement with the known elemental composition of the atmosphere.

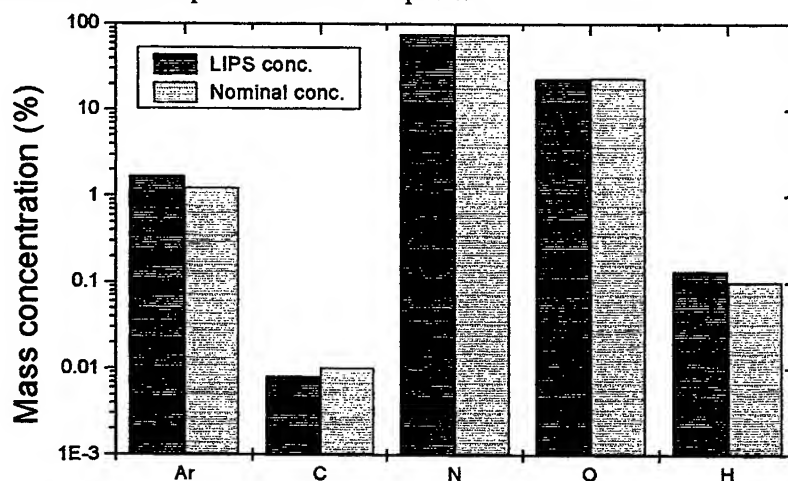


Fig. 2 LIPS quantitative analytical results for clean air, compared with the known composition. For what concerns the hydrogen (from H₂O) and carbon (from CO₂) reference concentration, average values are used corresponding to a typical atmosphere composition.

The analysis of the spectra taken in the flue duct shows that many metallic elements are clearly identifiable in the power plant smokes: among them it's worth to mention Ni, V, Ti, Mg, Fe.

The Figs. 3a-3c shows some experimental LIPS spectra resulting from the averaging of 250 laser pulses in the centre of the flue duct.

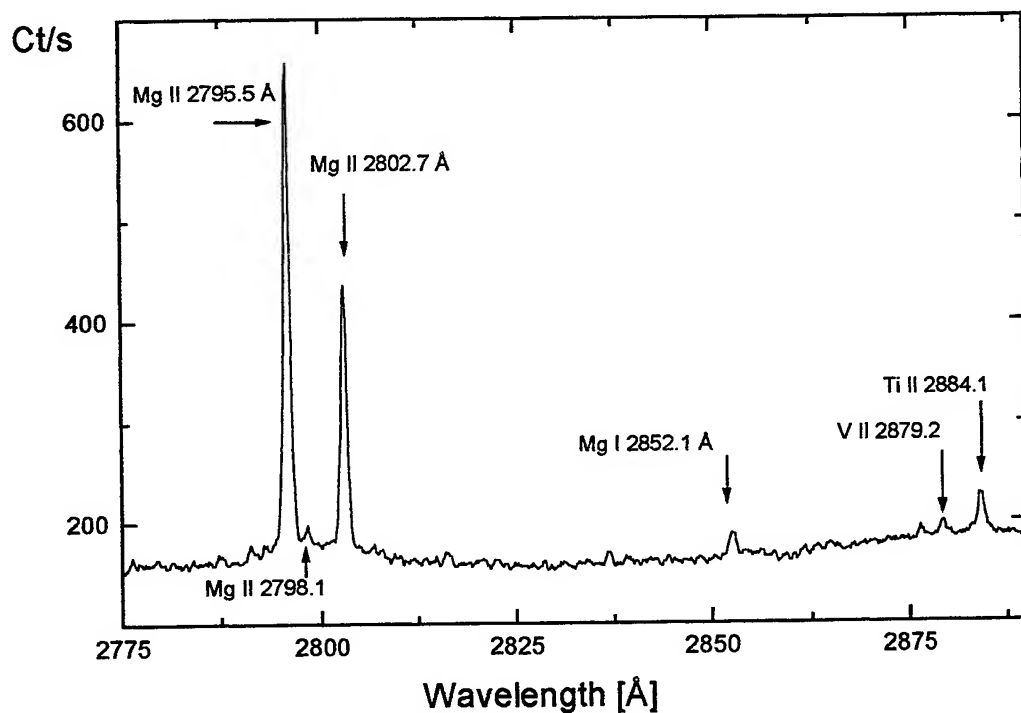


Fig. 3 a) Experimental LIPS spectrum showing characteristic lines of Mg, Ti and V

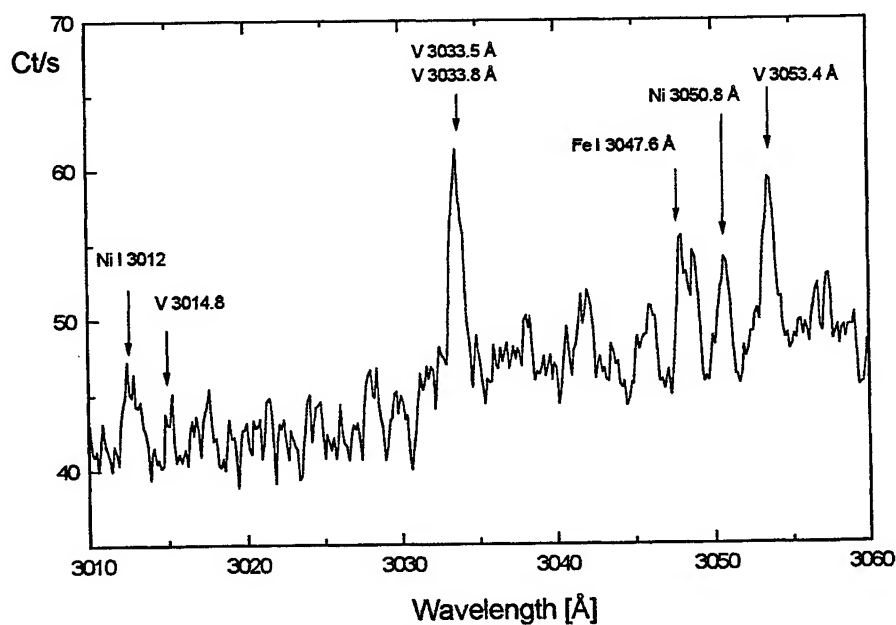


Fig. 3 b) Experimental LIPS spectrum showing characteristic lines of Ni, Fe and V

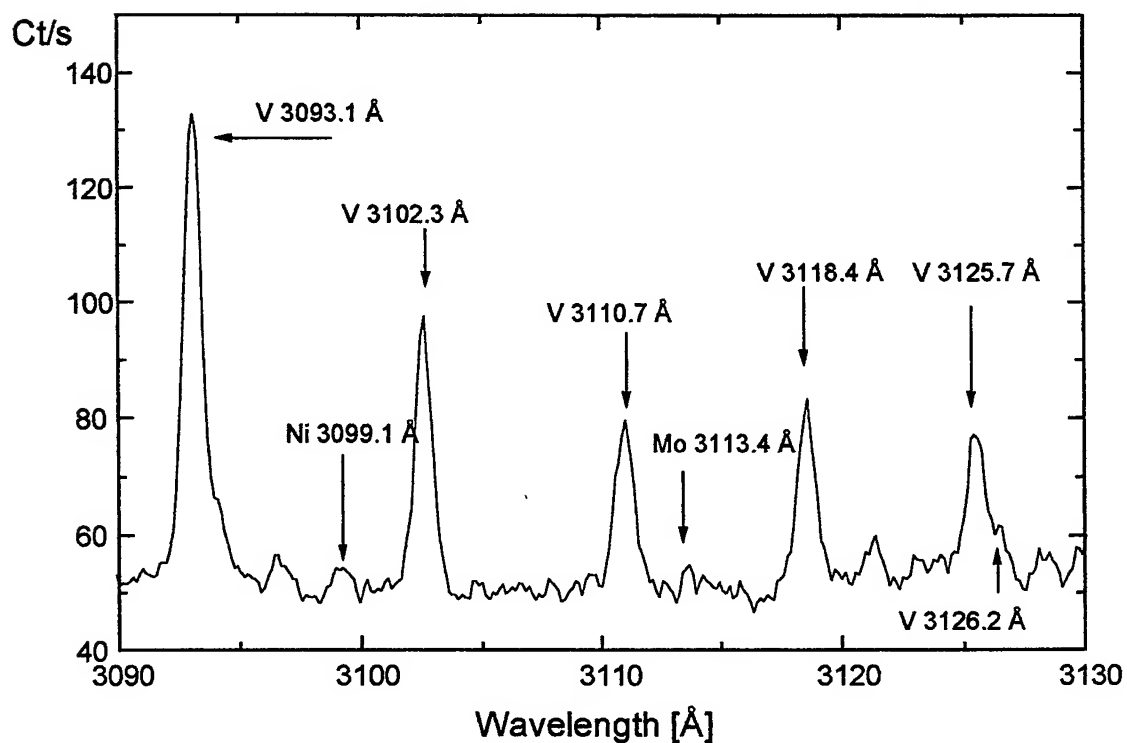


Fig. 3 c) Experimental LIPS spectrum showing characteristic lines of Ni, Mo and V

The laboratory analysis of a sample of the heavy oil confirmed the presence of the same elements (see Fig. 4).

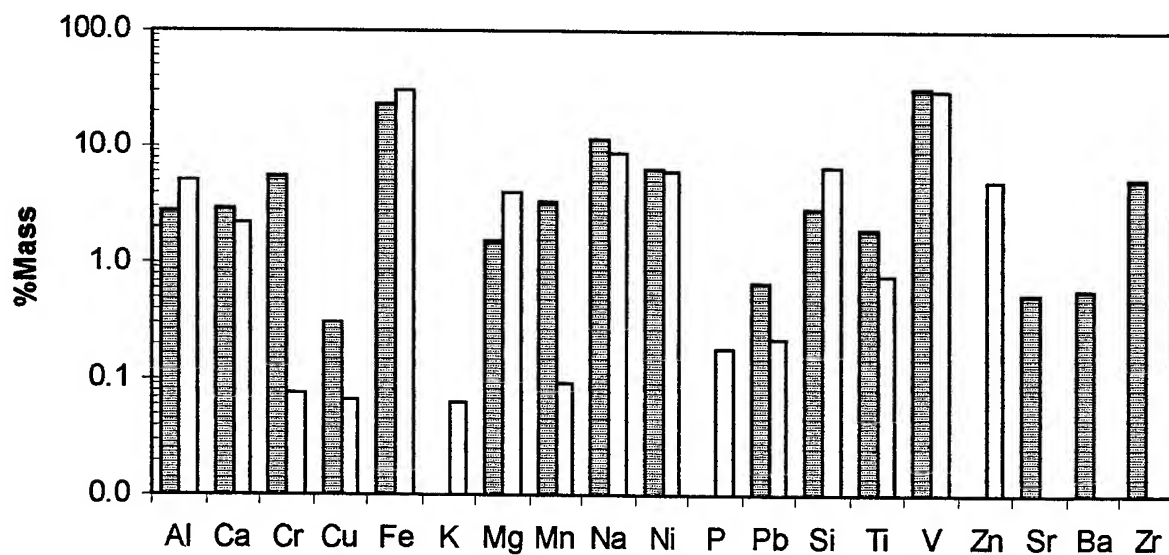


Fig. 4 Comparison between LIPS (gray bars) and ICP/Mass (white bars) analysis of the combustion products

Material Analysis: Determination of Gold caratage of precious alloys

The problem of determining the composition of precious alloys is particularly important for jewel manufacturers and their suppliers of the raw materials. In fact, the manufacturing process, in compliance with domestic and international regulations, requires a careful quality control and certification of the products which, up to now, can only be achieved by application of the traditional "Fire assay" method. This kind of analysis, though very accurate (around 0.01 % in gold concentration determination) is essentially destructive and requires a number of critical measuring stages – including weighing of the sample up to fifth decimal digit, acid attack of the sample and successive weighing of the gold residual – and can be performed, therefore, only by highly skilled operators.

In recent years the need for fast determination of precious alloys composition stimulated the proposals of different alternative techniques for caratage determination, among which the following are worth mentioning: Atomic Absorption Spectrometry (AAS), Inductively Coupled Plasma-Atomic Emission Spectrometry (ICP-AE), Inductively Coupled Plasma-Mass Spectrometry (ICP-MS), Neutron Activation Analysis (NAA) and X-Ray Fluorescence Spectrometry (XRF) techniques.

However, it's common opinion that none of these techniques can be considered, at present time, as a valid alternative to the "Fire assay" method. In particular, the only non-destructive technique (XRF) gives information exclusively about the composition of the sample surfaces (about 2 μm penetration depth) and is therefore very limited in its applications. Moreover, all the above mentioned techniques require a calibration of the system with a reference sample of similar composition; unfortunately, the composition of precious alloys may greatly vary in function, for example, of the desired colour or of their physical and mechanical properties. On the contrary, the CF-LIPS technique does not require any *a priori* knowledge of the sample composition, and thus it seems to be the ideal solution to the problem of caratage determination of precious alloys.

In order to test the accuracy of the CF-LIPS technique, we analyzed five precious alloy samples, in the form of irregular foils of about 10mm x 10mm x 0.5mm, corresponding to gold concentrations ranging from 200/1000 up to 1000/1000 in weight. Four of them were ternary alloys (Au, Ag and Cu) and one was a quaternary alloy (Au, Ag and Cu with addition of palladium).

The correlation between CF-LIPS determined gold caratage and the nominal caratage is shown in Fig. 5. It should be noted that the standard deviation of the CF-LIPS determined caratage from the 'perfect correlation' line is about 0.1%; the accuracy of the CF-LIPS measurements thus lies in the same range as that of "Fire assay" technique. Moreover, the CF-LIPS analysis gives almost identical results for the ternary and quaternary alloy (both samples correspond to the same gold concentration of 750/1000 in weight); the matrix effect does not affect, thus, the accuracy of CF-LIPS measurements. It's interesting to compare these results with those obtained from the same experimental data by using the conventional calibration technique, i.e. taking the 2676 Å Au line intensity of a pure gold sample as a calibration reference (see insert in Fig. 5)

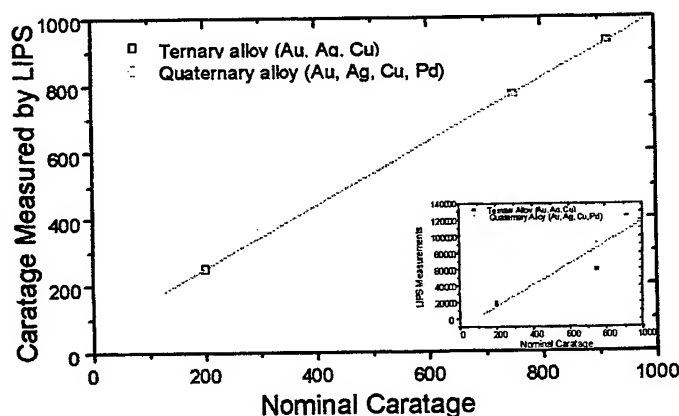


Fig.5 Correspondence between nominal and CF-LIPS measured gold caratage. In the insert are reported the same data obtained using standard calibration.

It is clear from the figure that in this case the scattering of the experimental data with respect to the perfect correlation line is very high, and the data corresponding to the same gold caratage for ternary and quaternary alloys do not coincide at all. These results reinforce our considerations on the difficulty of overcoming the matrix effect problems with conventional analysis techniques on unknown samples.

Cultural Heritage conservation and study: Analysis of Ancient Bronze Samples

In order to validate the use of Calibration-free LIPS technique for ancient metallic alloys analysis, we performed a detailed comparison of the results obtained at IFAM laboratory with the results supplied by other established techniques. Several bronze samples were analysed using CF-LIPS, whose composition had already been measured by means of a series of well known analytical technique: AAS (Atomic Absorption Spectroscopy), ICP (Inductively Coupled Plasma), EPMA (Electron Probe Micro Analysis), XRF (X-Ray Fluorescence), SEM (Scanning Electron Microscopy), PIXE (Particle Induced X-Ray Emission).

The samples to be investigated included a set of bronze alloys prepared on purpose and two ancient samples from bronze artworks: the first coming from the "Stories from the life of Jacob and Esau" (panel from the eastern door, author Lorenzo Ghiberti, 1425-52, Baptistery, Florence) and the second from "Doubting Thomas" (author Andrea del Verrocchio, 1476-83 from Orsanmichele, Florence). The major components of the prepared alloys were copper, tin and lead; two samples were also prepared adding a small percentage of zinc. The compared results are reported in figure 6. The composition measured by the different techniques was obtained by normalising to 100 the sum of the major elements concentration. The labels identifying the samples are derived from¹⁸.

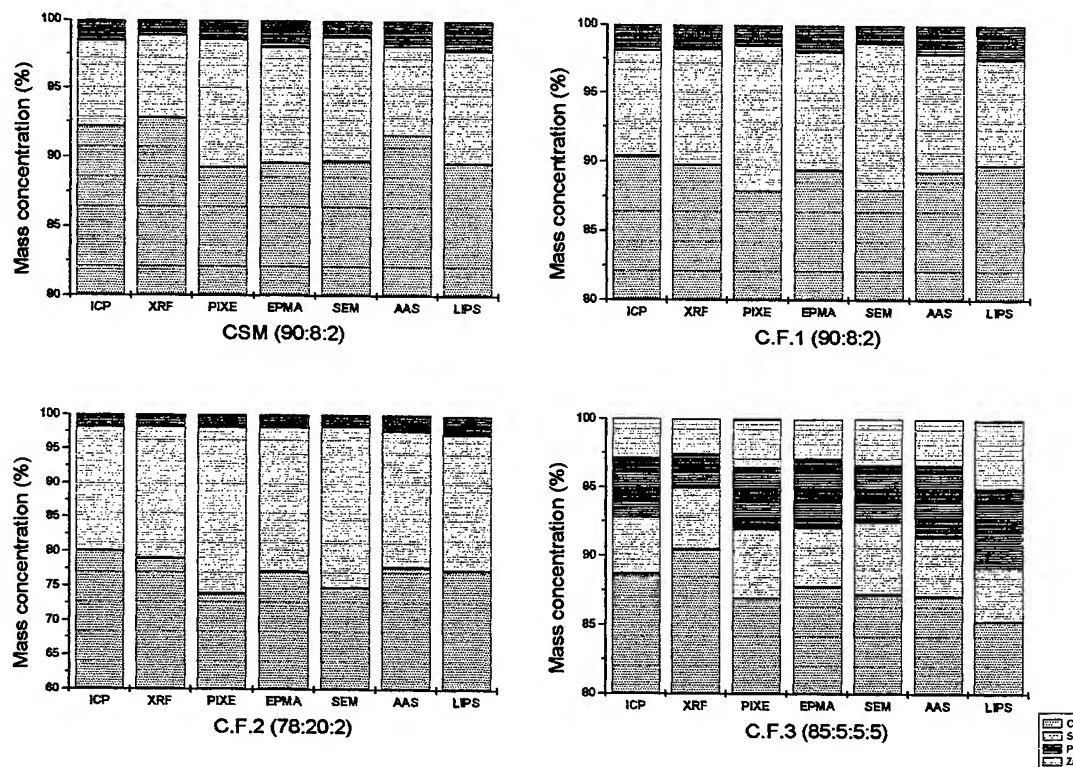


Fig. 6 Comparison of elemental composition of the bronze samples, obtained using different techniques

It is clear from the figures that the CF-LIPS technique gives results in a very good agreement with the results of the other techniques. Moreover, these results have been obtained without any previous knowledge of the nature of the sample (CF-LIPS is a 'blind' technique - in other words, the information that the analysed sample is a bronze alloy is not used for

obtaining the quantitative determination of the elemental composition of the alloy itself), without pre-treatment of the sample, in a few minutes.

For what concerns the two historical samples, with CF-LIPS it was possible to obtain, with the same measurement, both the major and minor components concentration in the alloy. The results are shown in Fig. 7, compared with the results of the other techniques.

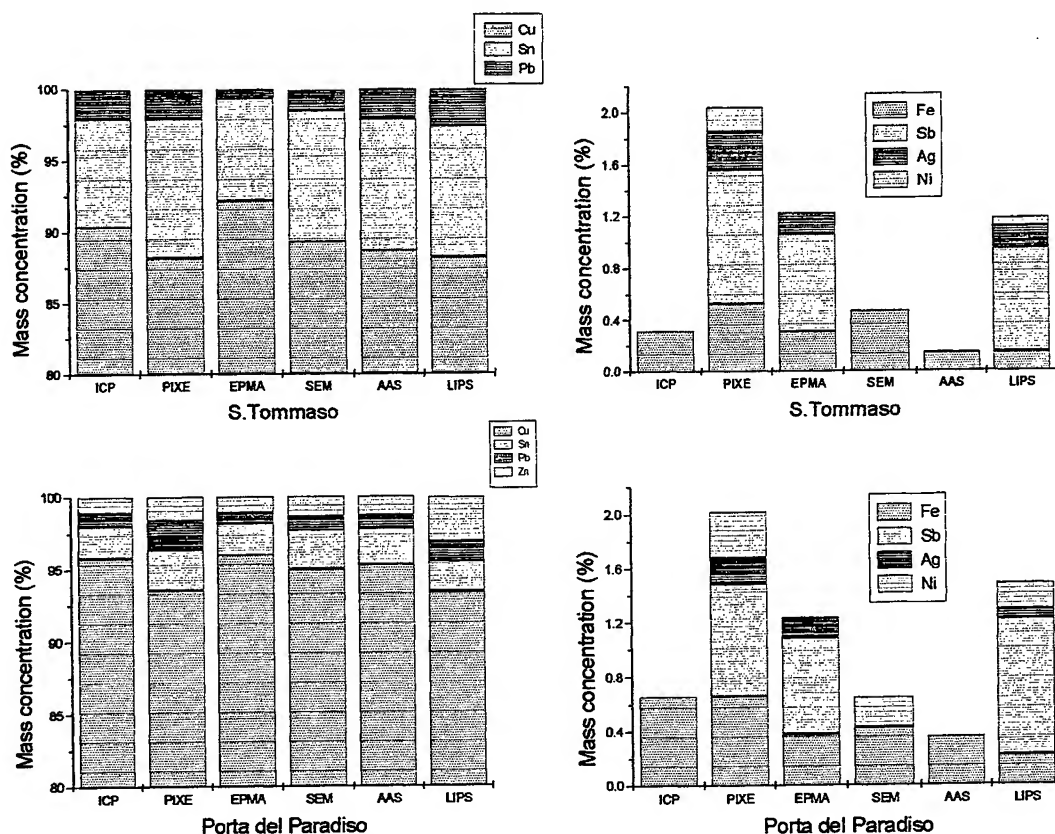


Fig. 7 Comparison of elemental composition of the "St. Thomas" and "Porta del Paradiso" bronze samples, obtained using different techniques

Considering that the errors on the minor components concentration can be rather high, the results of CF-LIPS are comparable in precision with the results obtained with the other techniques.

4. CONCLUSION

The Pulsed Laser Spectroscopy Group at Istituto di Fisica Atomica e Molecolare (Pisa) has recently developed and patented an innovative LIPS-based self-calibrated analytical procedure, called Calibration-Free LIPS (CF-LIPS). CF-LIPS is a fast and essentially non-destructive diagnostic method, and can be applied on samples of arbitrary shapes. The principle of this technique relies in determining sample composition by means of the spectral analysis of the emission of the plasma produced by an intense laser beam focused on the sample surface, without need for calibration curves or reference samples. Using the proposed calibration-free procedure, precise quantitative results can be obtained in a few minutes without need of reference samples. Both majority components and trace elements (down to concentrations of order of 1 ppm) can be simultaneously measured.

The application of this new measurement protocol allows to overcome the so called 'matrix effect', which has been up to now the major obstacle to practical LIPS applications to multi-elemental quantitative analysis. The improvement in the

analytical procedure achieved by means of this algorithm makes the CF-LIPS technique particularly useful for field measurement, in which the material composition is in principle unknown.

REFERENCES

1. L.J.Radziemsky, T.R.Loree, D.A.Cremers and N.M.Hoffman, *Anal.Chem.*, **55**, p. 1246, 1983.
2. D.A.Cremers and L.J.Radziemsky, *Anal.Chem.*, **55**, p. 1252, 1983.
3. J.Belliveau, L.Cadwell, K.Coleman, L.Huvel. and H. Griffin., *Appl. Spectrosc.*, **39**, p. 727, 1985.
4. L.J.Radziemsky, D.A.Cremers. and T.R.Loree, *Spectrochim. Acta*, **38 B**, p. 349, 1983.
5. T.R.Loree and L.J.Radziemsky, *Plasma Chem. and Plasma Processing*, **1**, p. 271, 1981.
6. D.A.Cremers, L.J.Radziemsky and T.R. Loree, *Appl. Spectrosc.*, **38**, p. 721, 1984.
7. M.Casini, M.A. Harith, V. Palleschi, A. Salvetti, D.P. Singh and M. Vaselli, *Laser and Particle Beams*, **9**, p. 633, 1991.
8. C.Lazzari, M. De Rosa, S. Rastelli, A.Ciucci, V.Palleschi and A.Salvetti, *Laser and Particle Beams*, **12**, p. 525, 1994.
9. G.Arca, A.Ciucci, V.Palleschi, S.Rastelli and E.Tognoni, *Detection of environmental contaminants by time resolved Laser Induced Breakdown Spectroscopy technique, Proceedings of International Geoscience and Remote Sensing Symposium*, 27-31 May 1996, Lincoln, Nebraska, p. 854, 1996.
10. A.Ciucci, S.Rastelli, V.Palleschi, R.Barbini, F.Colao, R.Fantoni, A.Palucci, S.Ribezzo and H.J.L. Van Der Steen, *Appl. Phys. B*, **63**, p. 185, 1996.
11. G.Arca, A.Ciucci, V.Palleschi, S.Rastelli and E.Tognoni, *Detection of pollutants in liquids by Laser Induced Breakdown Spectroscopy Technique*, Proceedings of International Geoscience and Remote Sensing Symposium, 27-31 May 1996, Lincoln, Nebraska, p. 520, 1996.
12. G.Arca, A.Ciucci, V.Palleschi, S.Rastelli and E.Tognoni, *Appl. Spectrosc.*, **51**, p. 1102, 1997.
13. A.Ciucci, V.Palleschi, S.Rastelli, A.Salvetti and E.Tognoni, *A New Calibration-free Method for Quantitative Analysis of Materials Using Laser Ablation Spectroscopy*, Proceedings of the European Conference on Laser Interaction with Matter (ECLIM), May 4-8 1998, Formia, Italy, 1998
14. A. Ciucci, M. Corsi, V. Palleschi, S. Rastelli, A. Salvetti and E. Tognoni, "A New Procedure For Quantitative Elemental Analysis By Laser Induced Plasma Spectroscopy", *Appl. Spectrosc.*, in press 1999.
15. V.Palleschi, G.Arca, S.Rastelli, A.Ciucci and E.Tognoni, "Verso il laser intelligente: applicazione alla pulitura di monumenti", *Internal Report IFAM B01LS/96*, 1996.
16. D.Anglos, S.Couris and C.Fotakis, *Appl. Spectrosc.*, **51**, p. 1025, 1997.
17. P.V.Maravelaki, V.Zafriopoulos, V.Kilikoglou, M.Kalaitzaki and C.Fotakis, *Spectrochim. Acta B*, **52**, p. 41, 1997.
18. M.C.Squarcialupi, G.P.Bernardini, P.A.Mandò, M.Matteini, F.Olmi and R.Trosti-Ferroni, *Analysis of alloys in ancient bronze objects: preliminary comparison of different methods and techniques*, Proceedings of the VI International Conference on Non-destructive testing and microanalysis for the diagnostic and conservation of the Cultural and the Environmental Heritage, Rome, May 17-20 1999, p. 1917, 1999.
19. D.R.Alexander, D.E.Poulain, M.S.Khlif and E.R.Cespedes, *Proceedings of International Geoscience and Remote Sensing Symposium*, 27-31 May 1996, Lincoln, Nebraska, p. 857, 1996.
20. D.A.Cremers, *Appl. Spectrosc.*, **41** (4), p. 572, 1987.
21. A.González, M.Ortiz and J.Campos, *Appl. Spectrosc.*, **49** (11), p. 1632, 1995.
22. T.L.Thiem, R.H.Salter, J.A.Gardner, Y.I.Lee and J.Sneddon, *Appl. Spectrosc.*, **48** (1), p. 58, 1994.
23. A.S.Eppler, D.A.Cremers, D.D.Hickmott, M.J.Ferris and A.C.Koskelo, *Appl. Spectrosc.*, **50** (9), p. 1175, 1996.
24. D.A.Cremers, M.J.Ferris and M.Davies, *SPIE vol. 2835*, 0-8194-2223-1/96, p. 190, 1996.
25. H.Schroeder, I.Schechter, R.Wisbrun and R.Niessner, *Excimer lasers and applications*, ed. by L.D. Laude (Kluwer Academic Publishers Dordrecht The Netherlands), p. 269, 1994.
26. R.Wisbrun, I.Schechter, R.Niessner and H.Schroeder, *SPIE vol. 1716*, 0-8194-0881-6/93, 2, 1992.
27. N.Xu, V.Bulatov, V.V.Gridin and I.Schechter, *Anal. Chem.*, **69**, p. 2103, 1997.
28. C.Chaléard, P.Mauchien, N.Andre, J.Uebbing, J.L. Lacour and C.Geertsens, *J.Anal.At.Spectrom.*, **12**, p. 193, 1997.
29. M.Sabsabi and P.Cielo, *Appl. Spectrosc.*, **49** (4), p. 499, 1995.
30. D.A.Cremers, *Appl. Spectrosc.*, **41** (4), p. 572, 1987.
31. W.L.Flower et al., *Fuel Processing Technology*, **39**, p. 277, 1994.
32. K.J.Grant, G.L.Paul and J.A.O'Neill, *Appl. Spectrosc.*, **44** (10), p. 1711, 1990.
33. D.K.Ottesen, *The Development Of Laser Spark Emission Spectroscopy For The Characterization Of Ash Deposits*, Proceedings of the Twenty-Fourth Symposium (International) on Combustion, The Combustion Institute, p. 1579, 1992.

Mixed valence ion doped PVA as potential materials for real time holography

M.Bulinski^{a*}, V.Kuncser^b, I.Iova^a, A.Bela^a, H.Franke^c, U.Russo^d, G.Filoti^b

^aFaculty of Physics, University of Bucharest, P.O.Box MG 11, 76900, Bucharest-Magurele, Romania

^bNational Institute for Physics of Materials, P.O.Box MG 07, 76900, Bucharest-Magurele, Romania

^cLaboratorium für Angewandte Physik, Universität GH-Duisburg, Lotharstrasse 1-21, D-47048, Duisburg, Germany

^dDipartimento di Chimica Inorganica, Metallorganica e Analitica, Università di Padova, Via Loredan 4, I-35131 Padova, Italy

ABSTRACT

Mixed valence ion doped polymers are potential materials for the real time holography. We review the intimate mechanisms imposing suitable optical properties in Fe:PVA, stressing on the main role played by the Fe ions. Under the UV exposure, both the refractive index and the absorption coefficient are changing due to a local electron transfer from the PVA matrix to the Fe³⁺ ions. The absorption coefficient proved to be dependent on a new-formed low spin Fe²⁺ state whereas the refractive index is related to the total content of the high spin Fe²⁺ state. The diffraction efficiency data are explained in terms of the Fe²⁺/Fe³⁺ ratio. Additional data concerning the electron transfer in Sn:PVA thin films are also discussed.

1. INTRODUCTION

Polymer materials are of growing interest for the optical data processing technologies. There are potential applications as permanent and transient data storage materials or as basic materials for the fabrication of the active and passive light guides. The metal ion doped polymers represent a new class of organic materials for non-linear optics. Among such materials, the ferric chloride doped polyvinyl alcohol (Fe:PVA) and the dichromate polyvinyl alcohol (DCPVA) are suitable for real time holography in the UV range. In spite of a very good diffraction efficiency (around 80 %), they present a quite low sensitivity (10 J.cm⁻² for Fe:PVA and 2 J.cm⁻² for DCPVA)^{1,2}.

In order to find new materials with improved properties it was necessary to find out the electronic mechanisms involved in the optical behavior. Therefore the optical data obtained by absorption or m-line spectroscopy were related to those obtained by the powerful tool of the Mossbauer spectroscopy. Consequently such studies are limited only to materials containing usual Mossbauer isotopes. Fortunately Fe is one of them and this is the reason we started the study on the Fe:PVA thin films. In the following there is evidence for the main role played by the iron ions in the microscopic mechanism related to the real time recording process. The mechanism consisting in an electron transfer from the PVA matrix to the iron ion is explained in detail starting from the correlation of the optical and Mossbauer data. The experimental diffraction efficiency behavior was successfully described with our proposed mechanism. The studies are extended to the Sn:PVA thin films, where another type of electron transition takes place, with a lower probability than for the Fe:PVA.

2. EXPERIMENTAL

The Fe:PVA and Sn:PVA solutions were obtained starting from ferric chloride or tin chloride and a pure solution of PVA dissolved in water^{1,2}. The PVA-water mixture was initially warmed at 30-40 °C and finally brought to 70 °C for more than 30 minutes in order to achieve homogeneity. Three solutions of PVA in water were prepared (5 %, 8 % and 11 % wt of PVA). Four Fe:PVA ratios were considered (1 %, 2 %, 4 %, 6 %wt of FeCl₃, denoted in the following as 1 %, 2 %, 4 %, 6 %wt Fe). Four other equivalent solutions of Fe:PVA with the same iron concentrations were prepared starting from FeCl₂. Only a solution 4 %wt Sn in 5 %wt PVA was prepared.

*Correspondence: Phone (401)780.47.70

Tab. 1 The investigated systems

Code	%wt. FeCl ₃	%wt. FeCl ₂	%wt. SnCl ₂	%wt. PVA	Thickness (μm)
1,2,3-PVA	-	-	-	5, 8, 11	30-50
1,2,4-5- <i>oa</i>	1, 2, 4	-	-	5	1-2
1,2,4-8- <i>oa</i>	1, 2, 4	-	-	8	1-2
1,2,4-11- <i>oa</i>	1, 2, 4	-	-	11	1-2
Fe-III- <i>ml</i>	0, 1, 2, 4, 6	-	-	11	4-6
Fe-II- <i>ml</i>	-	0, 1, 2, 4, 6	-	11	4-6
6-11- <i>ml</i>	6	-	-	11	4-6
1,2,4-5- <i>ms</i>	1, 2, 4	-	-	5	30-50
1,2,4-8- <i>ms</i>	1, 2, 4	-	-	8	30-50
1,2,4-11- <i>ms</i>	1, 2, 4	-	-	11	30-50
SI	4	-	-	8	30-50
SII	6	-	-	8	30-50
SIII	6	-	-	11	30-50
SIV	-	-	4	5	10-20

For the Mossbauer measurements, the polymer films were obtained by gravity deposition on glass plates, the films thickness being between 20 and 50 μm. The absorption spectra obtained on such thick samples³ are saturated below 450 nm, evidencing only a strong absorption between 250 and 450 nm. In order to obtain the band structure in this domain, new thinner films (1-2 μm thickness, depending on the preparation conditions) were deposited by spin coating method. For the m-line spectroscopy measurements of the refraction index, thin films with intermediate thickness (4-6 μm) were obtained by spin coating method too, starting from both the Fe³⁺/PVA and Fe²⁺/PVA solutions. The reference films obtained from the solutions of PVA in water were also prepared. The thinner films seem to be dried in few hours after deposition, while the thicker ones in few days. All the investigated systems are presented in Tab. 1. Films from few selected series were subject to various exposure energies. The UV exposure was performed with a photo-resist illuminator for UV light (300 nm < λ < 500 nm) of about 25 mW*cm⁻² intensity on the film surface. The exposure time was extended up to 60 minutes.

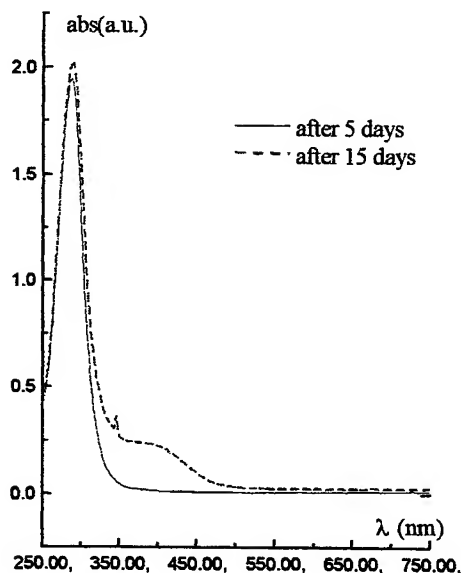


Fig. 1 The optical absorption spectra of the PVA (8wt%) thick film

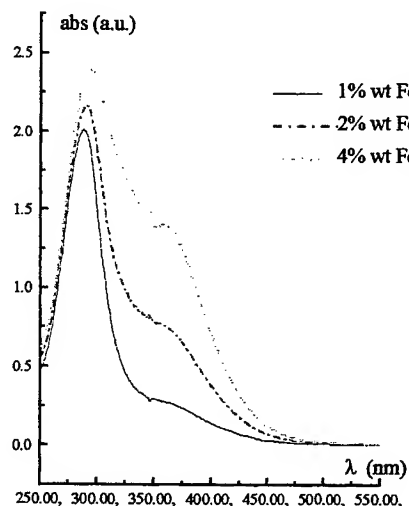


Fig. 2 The absorption spectra obtained on the 1,2,4-8-*oa* series

For the optical measurements the Fe:PVA films have remained coated on the glass slides. The absorption spectra were recorded with a standard SHIMADZU UV-VIS Spectrometer, with an identical glass slide in the reference beam. For the Mossbauer measurements the Fe:PVA films have been scraped from the slides and stacked into a suitable holder. A conventional Mossbauer set-up in transmission geometry with symmetrical waveform and the sample placed in a standard

exchange gas type cryostat was used. The m-line spectroscopy measurements were recorded with laboratory-made set-up, using the prism coupling technique and a He-Ne laser.

3. RESULTS AND DISCUSSION

3.1. The main role played by the iron neighborhoods in the optical absorption

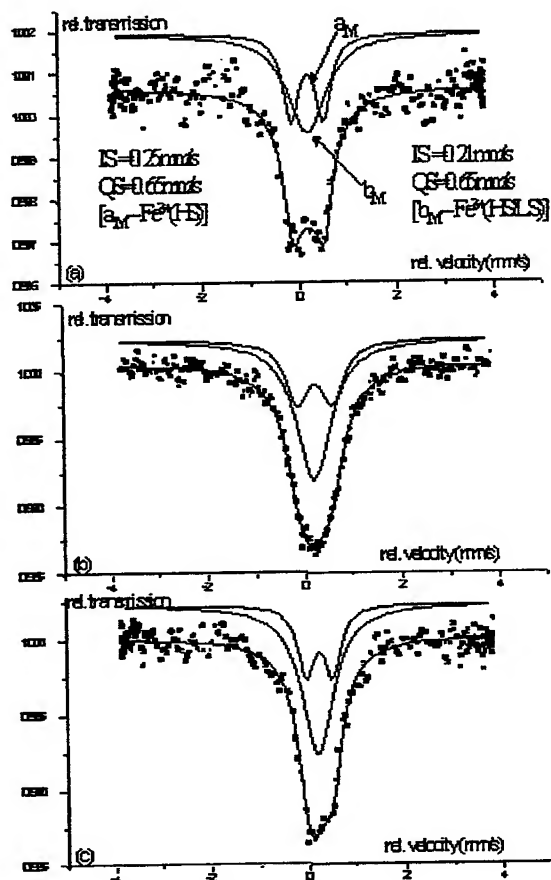


Fig. 3 The room temperature Mossbauer spectra for the 1,2,4-8-ms series (2 % wt Fe(a), 4 % wt Fe(b), 6 % wt Fe(c))

The optical absorption spectrum obtained on a thick PVA film (2-PVA) is presented in Fig. 1. Two absorption regions appeared after more than 5 days, when the absorption properties become stables. As previously mentioned, the absorption spectra obtained on Fe:PVA films with such a thickness are saturated and hence the necessity for preparing much thinner films. The absorption spectra obtained on the 1,2,4-8-0a series (Fig. 2) evidence also 2 absorption peaks superposed on the peaks shown by the PVA films.

The data suggest new excited levels introduced in the PVA absorption band by the Fe ions. A strong evidence for this can be obtained by corroborating the optical data with the Mossbauer ones⁴.

The room temperature Mossbauer spectra (see Fig. 3, for the 1,2,4-8-ms series) consist in an asymmetrical broad doublet, generally well evidenced for low iron content. At higher iron content, a structured central pattern can be underlined, stressing finally a superposition of two Mossbauer lines. Consequently, all the room temperature Mossbauer spectra were fitted with a broad singlet together with a broad doublet (Fig. 3) each pattern being attributed to a specific iron mean configuration. Their hyperfine parameters stand for Fe³⁺ ions. Because both the optical absorption and Mossbauer spectra can be decomposed in two patterns and taking into account that from the Mossbauer spectroscopy these correspond to two iron mean positions, it results that the absorption peaks might be correlated to the same iron positions. An increased contribution of the second absorption peak (at higher wavelengths) vs. the iron content, as well as of the singlet pattern in the Mossbauer spectra, are evidenced by comparing the Figs. 2 and 3. In terms of the above assumption, the Mossbauer singlet and the second absorption peak has to correspond to the same iron position. The ratio between the areas of the two components is expressed function on the iron content n_I and n_{II} on each position for both type of measurements⁴:

$$R_i^{opt} = \left(\frac{A_{II}}{A_I} \right)_i = \left(\frac{n_{II} P_{II}}{n_I P_I} \right)_i ; \quad R_i^{Mossb} = \left(\frac{A_{II}}{A_I} \right)_i = \left(\frac{n_{II} f_{II}}{n_I f_I} \right)_i \quad (1)$$

In the above relations, "P" refers to the absorption probability on the excited electron levels associated to a mean iron position and "f" to the Debye-Waller factor of the iron position. Considering the ratio of the absorption probabilities and Debye-Waller factors on the two iron positions are not changing at two i and $i+1$ iron consecutive concentrations (e.g in 1-8 and 2-8 films), the following theoretical relation is valid for $R_{i+1,i} = R_{i+1} / R_i$

$$R_{i+1,i}^{op} = \left(\frac{n_{II}}{n_I} \right)_{i+1} \left(\frac{n_{II}}{n_I} \right)_i^{-1} = R_{i+1,i}^{Mossb} \quad (2)$$

The experimental results produced the $R_{i+1,i}$ ratios which showed a 7 % range between the values obtained from the optical

data and Mossbauer data respectively⁴. The good agreement between these data confirm the initial assumption that the absorption spectra are strongly correlated with the two Fe^{3+} positions.

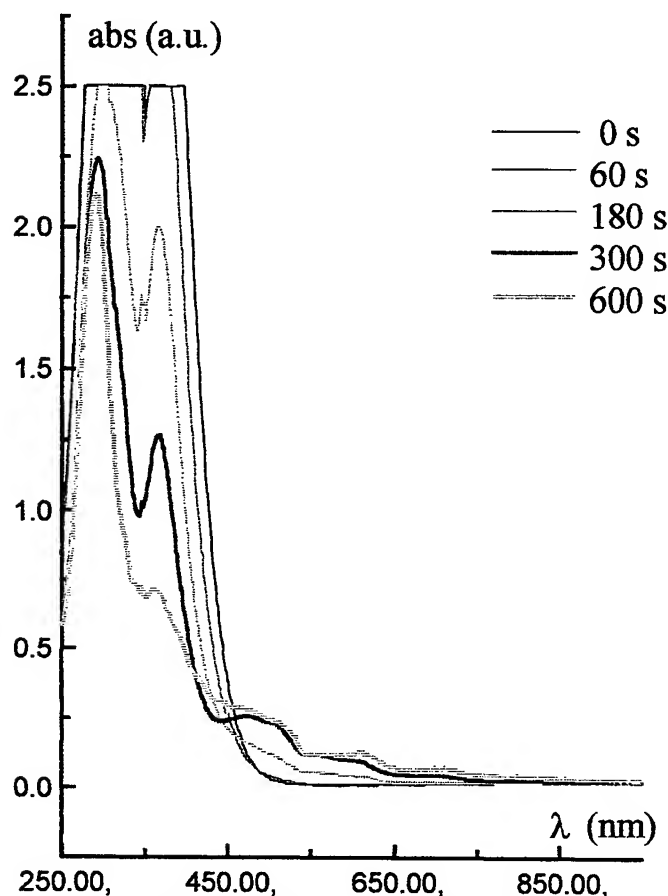


Fig. 4 The absorption spectra obtained on the 1,2,4-8-0a series

3.2. The effect of the UV light exposure

In order to study the mechanisms involved in the holographic recording process, a 6-11-ml film, with suitable thickness for both optical absorption and m-line spectroscopy, was exposed to UV light up to 10 min. After different exposure times the absorption spectra and the refractive index were measured. The absorption spectra are shown in Fig. 4. The two already known bands at wavelengths less than 450 nm that are decreasing with the exposure time. Besides them we have noticed new bands between 500 to 700 nm.

We took as a quantitative parameter, describing the absorption in the reconstruction wavelength range, the value of the absorption coefficient at the maximum intensity for the most representative -610nm peak-noted in the following as Abs(610nm). The dependencies of the Abs(610nm) and of the refractive index vs. the exposure time are presented in the Figs. 5 and 6. The absorption coefficient in the reconstruction wavelength range increases and the refractive index decreases vs. the exposure energy. Moreover, after a 300s exposure, the absorption coefficient continue to increase whereas the refractive index reach his stationary value. Consequently, the refractive index has a higher sensitivity. The microscopic influence of the UV exposure was analyzed by Mossbauer spectroscopy. Thicker films from the SIII series (with identical composition as for 6-11-ml) were exposed to different time and afterworld measured by Mossbauer spectroscopy. The spectra are presented in Fig. 7.

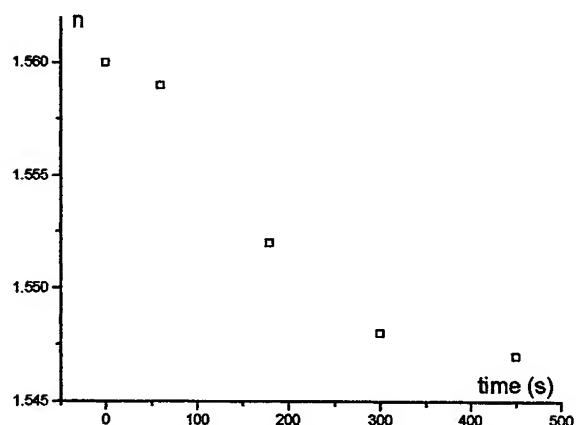


Fig. 5 The dependencies of the refractive index (648nm) vs. the exposure time for the same film as in Fig. 4

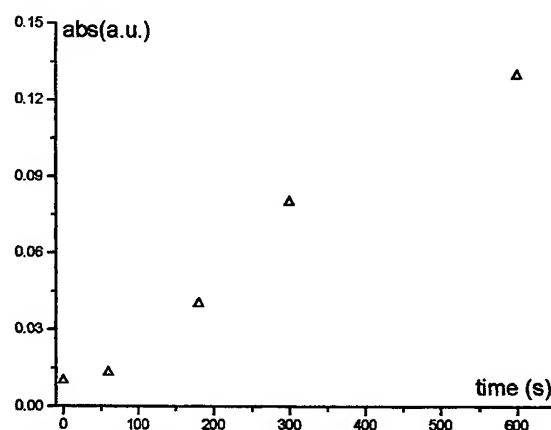


Fig. 6 The dependencies of the Abs (610nm) vs. the exposure time for the same film as in Fig. 4

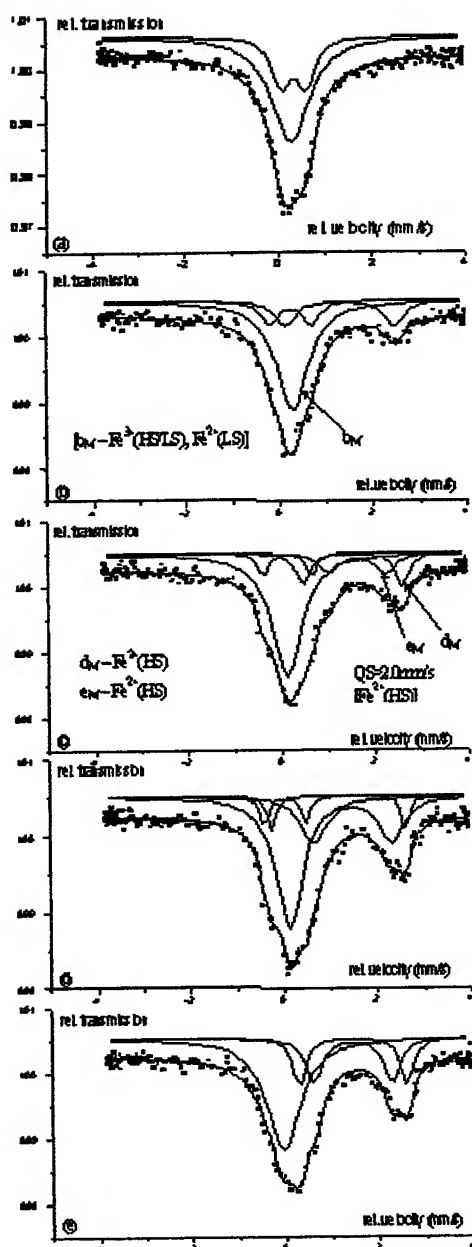


Fig.7 Mossbauer spectra for SIII series (identical composition as for 6-11-ml) vs. the exposure time: a) and b),c),d), e) for unexposed and respectively exposed for 400s, 800s, 1500s 2500s.

mentioned connection thin films of the Fe-III-ml (obtained starting from FeCl_3) and Fe-II-ml (obtained starting from FeCl_2) series were measured using m-line spectroscopy. The dependencies of the refractive indices vs. the Fe content are presented in Fig. 12. One observes that beginning with an iron content of 4 %wt, the refractive indices are in the Fe^{2+} :PVA films sensible lower than in the Fe^{3+} :PVA ones. These results support the hypothesis that the refractive index decreases by the partial reduction of the metal ions via electron transfer from the PVA matrix.

Supplementary doublets with higher quadrupole splitting (around 3 mm.s^{-1}) appeared in the spectra of the exposed samples. Taking into account their typical hyperfine parameters, the new pattern can be indubitably assigned to Fe^{2+} species in high spin (HS) configuration. The main microscopic effect of the UV exposure is an electronic transfer from the PVA matrix to the Fe ions. The content in Fe^{2+} ions is dependent on the exposure energy (or time). Both the absorption and the refractive index variation have to be related to this electronic transition.

As an important point, the decrease in the intensity of the absorption bands below 400nm has to be correlated with the relative decrease of the Fe^{3+} content under the UV exposure, as we previously shown. The electron transition can be understood related to the local Fe-PVA complex forming a donor-acceptor system, with the Fe ions behaving as acceptors.

3.3. A proposed electronic mechanism for the optical absorption in the reconstruction wavelength

In Fig. 8, we present as an exemplification, the evolution of the $\text{Abs}(610\text{nm})$ vs. the exposure time on films from the series SII and SIII. On the other hand, the evolutions of the Fe^{2+} relative content vs. the exposure time/energy are shown for all the three series in Fig.9. Comparing the two curves corresponding to the SIII series it is noticed that after 2500s of exposure, the absorption coefficient is strongly increasing whereas the Fe^{2+} content becomes quite saturated.

Such discrepancies suggest the absorption in the recording range is not directly connected with the total content of the HS Fe^{2+} phase. A hyperfine parameter very sensitive to the electronic distribution around the iron atoms is the isomer shift.

A surprising result was obtained by plotting the singlet associated isomer shift in the Mossbauer spectra vs. the exposure energy (Fig.10). The dependencies are quite similar to the ones corresponding to $\text{Abs}(610\text{nm})$, inferring a direct connection with iron phases described by singlet pattern. The isomer shift values suggest high spin Fe^{3+} , low spin (LS) Fe^{3+} and low spin (LS) Fe^{2+} as rising the singlet. In a detailed discussion presented in ref.⁴, it was shown that the decrease of the isomer shift might be due to the balance between the phases rising the singlet pattern under the UV exposure, namely due to the formation of the new LS Fe^{2+} on the account of the initial LS Fe^{3+} . It is worth noticing that following the exposure, the new formed low spin Fe^{2+} phase is in a metastable excited state according to a relaxation time of tenth of minutes, as it can be observed from Fig. 11.

3.4. The refractive index variation

The saturation of both the refractive index (Fig.5) and the HS Fe^{2+} content, p, (Fig. 9, SIII curve) vs. the exposure energy suggest a direct relation between these two parameters. In order to prove the above

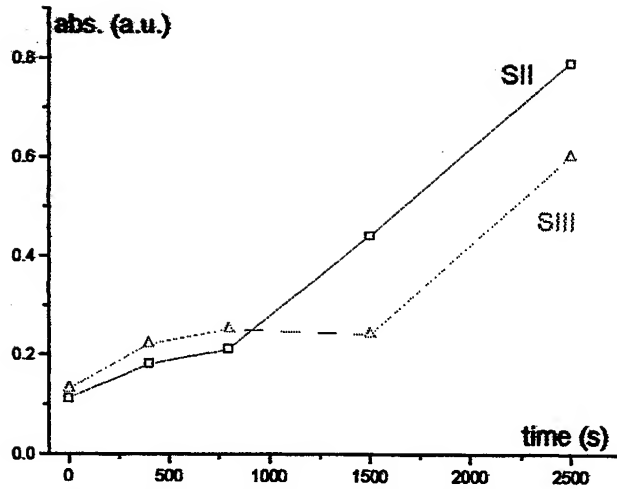


Fig. 8 The Abs(610nm) vs. the exposure time for the SII and SIII series.

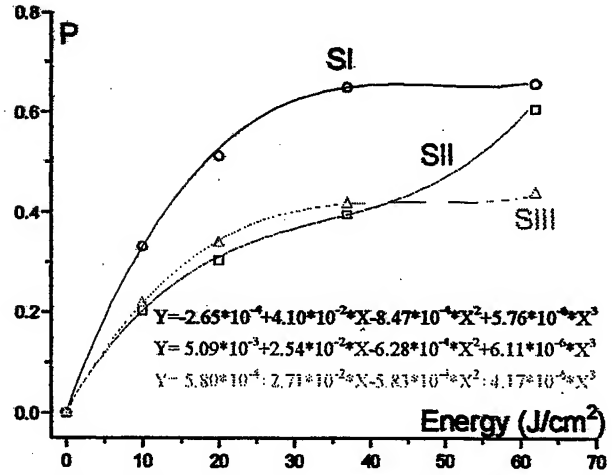


Fig. 9 The Fe²⁺ relative content vs. the exposure energy for all the three series

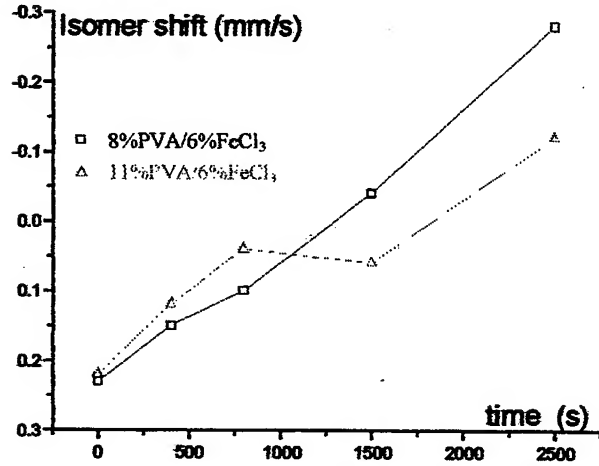


Fig. 10 The isomer shift for the Mossbauer singlet vs. the exposure time for the SII and SIII series.

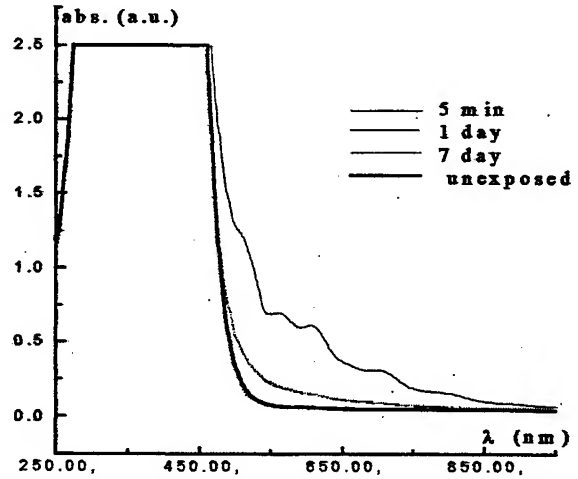


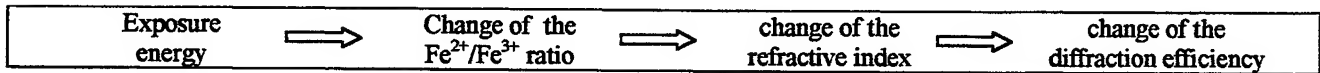
Fig. 11 The absorption spectra of thick films (exposed 2500 s) of Fe:PVA (SIII series) measured after various time.

3.5. Fe:PVA as phase hologram recording material

It is known that for a "phase hologram", the diffraction efficiency can be expressed as

$$\eta = \eta_{\max} \frac{\pi \Delta n}{\lambda \cos(\alpha)} \quad (3)$$

where: t is the film thickness, λ is the reconstruction wavelength, 2α is the inter-beams angle during the recording process, Δn is the difference between the maximum and the minimum value of the refractive index and η_{\max} is the maximum value of the diffraction efficiency for the storage material. The following mechanism explaining the diffraction efficiency is considered (see section 3.4)



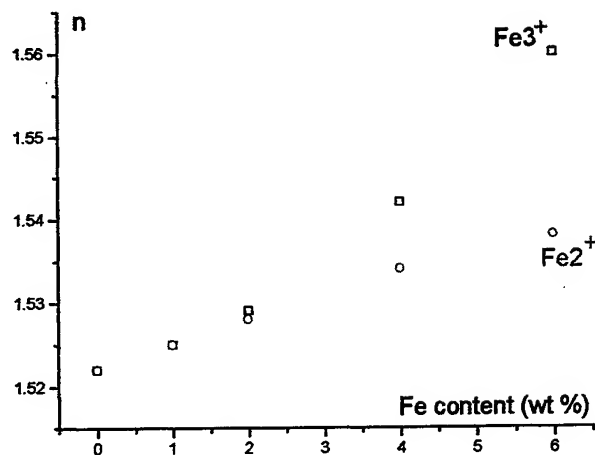


Fig. 12 The dependencies of the refractive indices vs the Fe content

In fact the difference of the refractive indices introduced by UV exposure can not be directly measured on the holographic media using the m-line spectroscopy due to the high film thickness (40-60 μ m) which produce strong overlapping modes. Fortunately, all these thickness are suitable for Mossbauer measurements giving the fraction of the Fe^{2+} phase. The refractive index of an exposed Fe:PVA thin film, $n_{\text{Fe:PVA}}$, will be considered as a linear combination of the refractive indexes of the two species simultaneously contained^{5,6}:

$$n = (1 - p)n_{\text{Fe}^{3+}:\text{PVA}} + pn_{\text{Fe}^{2+}:\text{PVA}} \quad (4)$$

where p is the fraction of Fe^{2+} phase formed under UV exposure. The refractive indices for the pure $\text{Fe}^{3+}:\text{PVA}$ and $\text{Fe}^{2+}:\text{PVA}$ (supposed as independent on the film thickness) can be obtained from m-line measurements on thin films.

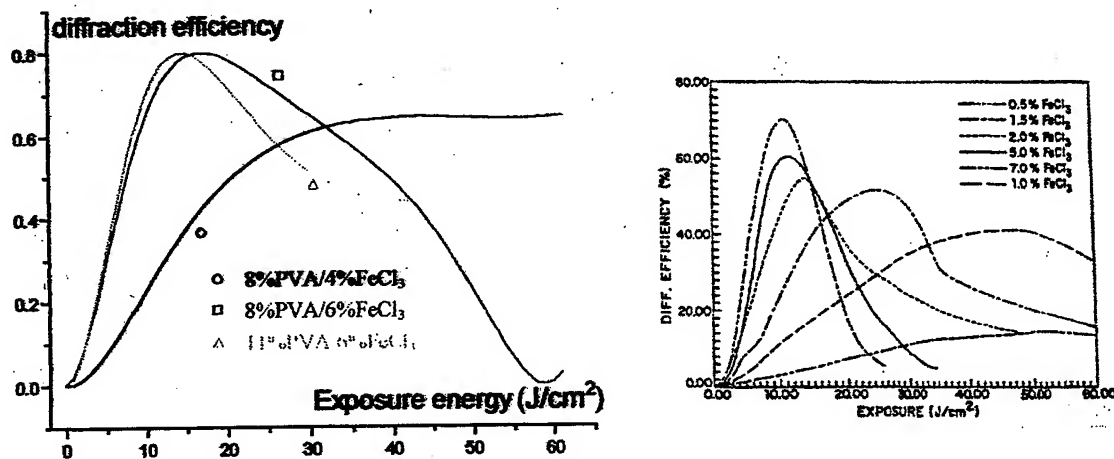


Fig. 13 The numerical dependencies of the diffraction efficiency vs. the exposure energy

Starting from relations (3) and (4) the diffraction efficiency vs. the exposure energy may be estimated for all the SI, SII and SIII sample where Mossbauer data on the p fraction are available. Tacking into account that the unexposed films contain only the Fe^{3+} species, relation (3) can be expressed function on the p fraction as⁷

$$\eta = \eta_{\text{max}} \sin^2 kp \quad (5)$$

where k is a constant parameter, depending on the experimental set-up and the recording material properties.

$$k = \frac{\pi(n_{Fe^{3+}:PVA} + pn_{Fe^{2+}:PVA})}{\lambda \cos \alpha} \quad (6)$$

The numerical calculations of the diffraction efficiency vs. the exposure energy for all the analyzed series are presented in Fig. 13 ($\alpha = 20^\circ$, $\lambda = 647\text{nm}$ as in ref.¹ and $t = 40\mu\text{m}$). The numerical data plotted in Fig. 9 were considered for the dependencies of the p -parameter vs. the exposure energy. The similar trends between the above evaluated diffraction efficiency curves and the experimental ones¹ (inset of Fig. 13) confirm the proposed electronic mechanism and the phase hologram behavior of the Fe:PVA at relatively low exposure energy ($<20\text{-}25\text{J.cm}^{-2}$)^{6,7}.

3.6. Sn:PVA thin films

The results obtained on the Fe:PVA thin films have shown that the main electronic mechanism involved in the variation of the refractive index consist of the local transfer of one electron from the PVA matrix to the metal ion, under the UV exposure. In the following we'll see that an opposite transfer, from the metal ion to the PVA matrix could be also possible. Two sample of Sn:PVA thin films from the SIV series were considered. One of them was exposed to the UV light for around 500s and the other one was kept unexposed. The absorption spectra are presented in Fig. 14 and the Mossbauer spectra in Fig. 15.

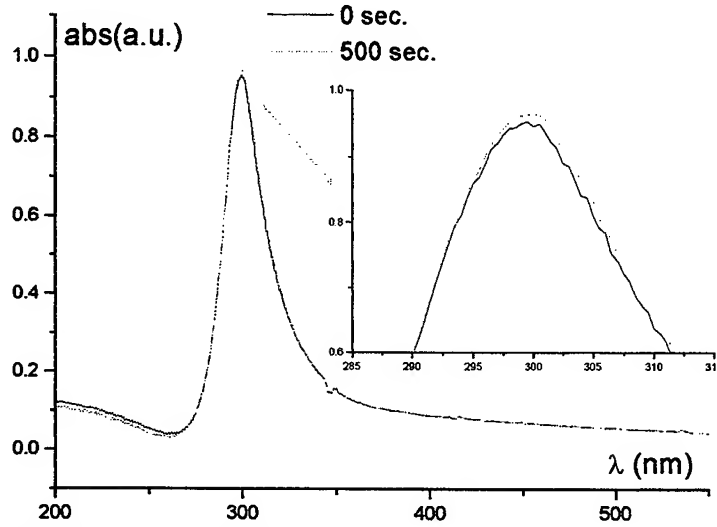


Fig. 14 The absorption spectra of the Sn:PVA thin films (from the SIV series)

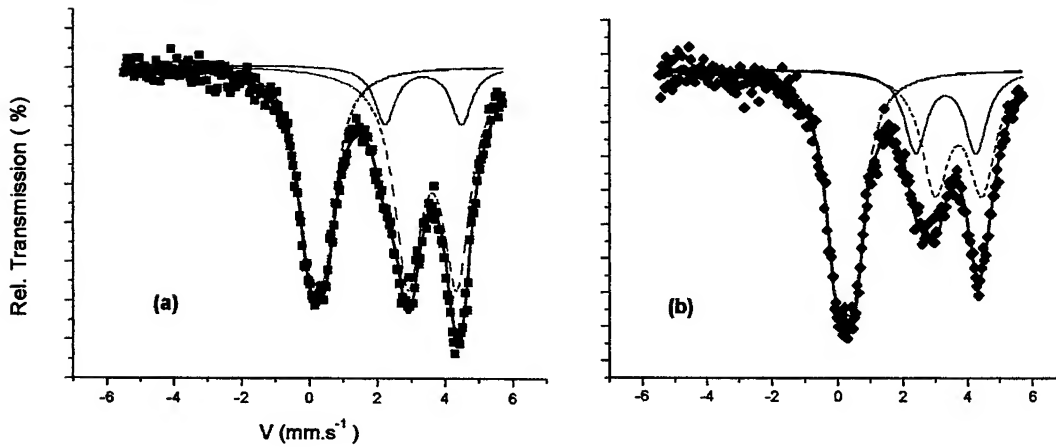


Fig. 15 ¹¹⁹Sn Mossbauer spectra obtained on unexposed (a) and exposed (b) samples of the SIV series

It is worth noticing that comparing with the Fe:PVA case, the absorption pattern consist of a relatively narrow line centered around 300 nm which increase slowly in intensity under the UV exposure. A such behavior can be understood again by the analyze of the Mossbauer spectra which consist in 3 paramagnetic patterns: two doublets with quite high quadrupole splitting and isomer shift, both assigned to Sn^{2+} species and a third one (less splitted) and assigned to a Sn^{4+} specie. The relative content of the Sn^{4+} ions (proportional with the relative area of the third doublet) increases under the UV exposure from 33 % to 43 %. Such a result shows directly, that contrary to the Fe:PVA case, this time two electrons are transferring from the metal ion to the PVA matrix. As we learned from the Fe:PVA films, the absorption peaks in the UV range are related to the ions in the high valence state and so the increase of the Sn^{4+} content under the UV exposure can also explain the increase of the absorption peak at 300 nm. A variation of the refractive index vs. the exposure energy is expected in Sn:PVA films due to the balance of the two Sn species, but m-line spectroscopy measurements are not yet available. In any case, the UV induced fraction of the Sn^{4+} species is much lower than in the Fe case (around 10 % compared with 60 %), but the sensitivity of the material has to be increased due to the change induced by the transfer of the two involved electrons.

4. CONCLUSIONS

The main optical parameters, important for practical use of the real time holographic media were related to local electronic mechanisms by using a combined investigation with optical and Mossbauer spectroscopy.

Both the real and the complex part of the refractive index are changing for the Fe:PVA thin films. The real part is more sensible at low exposure energy whereas the imaginary one (the absorption coefficient) at higher energy. The refractive index changes induced by the UV exposure are the result of an acceptor-donor mechanism and depend on the $\text{Fe}^{2+}/\text{Fe}^{3+}$ content. The behavior of the diffraction efficiency vs. the exposure energy was pretty well described using a linear combination of the refractive indices belonging to each valence state of iron.

The complexity of the electronic mechanism was proved by comparing two different media Fe:PVA and Sn:PVA. Contrary to the Fe:PVA case where under the UV exposure one electron is transferring from the PVA matrix to the mixed valence ion, in the Sn:PVA case two electrons are transferring from the ion specie to the PVA matrix.

The efficiency should be higher for a higher number of electrons transferred between the PVA and the metal ion.

ACKNOWLEDGEMENTS

The financial supports of the Romanian National Agency for Science and Technology by the grant " Electronic Processes in New Real Time Holographic Media " as well as the joint research project " New oxides and coordination compounds. Structure and hyperfine interactions " in frame of the 13-th Protocol for the scientific and technological cooperation between Italy and Romania are gratefully acknowledged.

REFERENCES

1. R.A. Lessard, R. Changkakoti and G. Mannivannan, "Metal Ion Doped Polymer Systems for Real-Time Holographic Recording", *SPIE* Vol. 1559, pp. 438-447, 1991
2. G. Manivannan, O. Nikolov, T. Kardinahl, W. Keune, H. Franke, R. Changkakoti and R.A. Lessard, "Charge Transfer Phenomenon in Optical Storage Material Fe^{3+} Doped Poly(Vinil Alcohol)" *SPIE Proc.* 2042, pp. 98-109, 1993.
3. G. Filoti, V. Kuncser, H. Franke, T. Kardinahl and G. Mannivannan, "Optical Induced Modification in the Films of Fe:PVA", *J. Radioanal. Nucl. Chem. Art.* 190, pp. 315-320, 1995
4. V. Kuncser, A. Avramescu, G. Filoti, P. Rotaru, R. Podgorsek, M. Biebricher and H. Franke, "Optical and Mossbauer Study of the Holographic Organometallic Material Fe:PVA", *J. Alloys Comp.* 256, pp. 269-245, 1997
5. V. Kuncser, G. Filoti, R. Podgorsek, M. Biebricher and H. Franke, "The Diffraction Efficiency in Fe:PVA explained by Mossbauer Spectroscopy" *J Phys. D. Appl. Phys.* 31, pp. 2315-2318, 1998
6. M. Bulinski, I. Iova, A. Belea, V. Kuncser and G. Filoti, "Fe:PVA As s Potential Material for the Real Time Holography" *Anal. Univ. Buc. Vol. XLVII*, pp. 57-59, 1998

Local electric fields in optical glasses during field-assisted ionic exchanges

Alexandru Lupascu^{*a}, Antoine Kevorkian^b, Constantin P. Cristescu^a, Ion M. Popescu^a

^aPhysics Department, University "Politehnica", 313 Spl. Independentei, 77 206 Bucharest, Romania

^bTeemPhotonics, 13 Chemin du Vieux Chêne, 38240, Meylan, France

ABSTRACT

We study the phenomena connected with high concentration of incoming ions emerging during field-assisted migration in optical glass. We find that ion dynamics are very different at concentrations higher and lower than a certain parameter called the transition concentration. To explain anomalies at high ionic concentrations, we introduce a supplementary local electric field. This field opposes to the field E_0 existing in the glass at all concentrations of incoming ions and is connected with a local space charge. We investigate its dependence on concentration and on E_0 . These effects are studied using a model with concentration-dependent diffusion coefficients and mobilities. We present a method to obtain the concentration dependence of the relevant quantities. Theoretical curves are compared with experimental results measured in usual silicate glasses, during $\text{Ag}^+ - \text{Na}^+$ exchanges.

Keywords: Optical integrated circuits in glass, ionic inter-diffusion, local electric fields

1. INTRODUCTION

Optical guides in glass may be built using ionic inter-diffusion; processes are purely thermal, or field-assisted. Electric fields are used as a second step, to bury the surface waveguides obtained by thermal diffusion, or they may force from the beginning the ionic penetration in the glass. The last technique is called field-assisted migration (FAM). We have studied $\text{Ag}^+ - \text{Na}^+$ inter-diffusion in various silicate glasses, under very different conditions. We have established a complex model of this process, using concentration-dependent diffusion coefficients and mobilities¹. The model is able to predict very different ionic profiles, mono-mode structures, as well as skewed multi-mode structures, built under strong burying electric fields (current densities up to 150 Am^{-2}). The successful application of the model in such extreme conditions suggested the possibility to apply it to all diffusion processes. However, efforts attempting to characterize FAM fell short.

Ionic profiles given by FAM's are steeper than the thermal ones, and, more important, a very significant part occurs at high concentrations of incoming ions. A criterion for such regimes is given by the *transition concentration* c_t , defined in Eq. (9). At concentrations of incoming ions higher than c_t new phenomena appear, unobserved during thermal diffusions or during field-assisted burying. An example is the anomalous behavior of drift mobilities; the Nernst-Einstein relation between mobilities and diffusion coefficients becomes improper². We explain these anomalies introducing a *supplementary local electric field*, denoted by $E_{\text{sup pl}}$, whose action manifests only at high concentrations of incoming ions. The second section contains a short presentation of the model, with emphasize on the important physical quantities. The third section presents in detail an original method to obtain the concentration dependence of the diffusion coefficients. We introduce here a very important parameter, namely the transition concentration c_t . It also contains a comparison between our model, the usual model with constant coefficients, and experimental data. In the fourth section, introducing the supplementary electric field, we explain the phenomena arising during FAM. Anomalies seem to manifest themselves at concentrations higher than c_t . The last section contains discussion and conclusions.

2. MODELING IONIC EXCHANGE IN GLASS

^{*}We study a glass, containing initially only *b*-type mono-valent cations (e. g. Na^+), put in contact with a molten salt bath, which contains the *a*-type foreign ion (e. g. Ag^+). Pure thermal or field-assisted diffusion brings *a*-type ions into the glass, thus forming a wave-guide. The model of this process is based on Fick's laws and rests upon the following assumptions:

^{*} Correspondence: E-mail: lupascu@physics2.physics.pub.ro; Telephone: 401-410 45 42 extension 102; Fax: 401-411 61 71

- i)- only mono-valent cations participate to the process; this hypothesis is supported by nuclear measurements
- ii)- mechanical stress is neglected; this is true for $\text{Ag}^+ - \text{Na}^+$ exchanges
- iii)- the mechanism of thermal diffusion and of electric drift are similar; this assumption allows the use of Nernst-Einstein relationship between mobilities and diffusion coefficients³
- iv)- local neutrality is respected in the glass during all the fabrication steps.

The Nernst-Einstein relations between the diffusion coefficients of the two ionic species, D_a and D_b , and their drift mobilities μ_a and μ_b are:

$$\mu_i(c_i, T) = \frac{eD_i(c_i, T)}{HkT} \quad i = a, b \quad (1)$$

where c_a, c_b are the doping and host ion concentrations, e is the electronic charge, k the Boltzmann constant and H the Haven ratio. The quantities have an Arrhenius-type dependence on the temperature:

$$D_i(c_i, T) = D_{0i} \exp\left(-\frac{\Delta E_i}{RT}\right) f_i(c_i) \quad i=a, b \quad (2)$$

where ΔE_i are activation energies (J/mole), R the constant of perfect gases, and $f_i(c_i)$ functions depending on the particular exchange. As the concentration dependence of the parameters is very important, we present in the third section an original method to obtain these functions.

The inter-diffusion is mathematically described by Fick's equations, one for each ionic species, supplemented by Gauss law^{1, 4}. This system of three coupled equations may be reduced to a single one using the assumption iv) above, namely the local electric neutrality. Actually, this conjecture is incorrect for all field-assisted processes⁴. It is easy to show that, whenever an electric current flows through an inhomogeneous material a local space charge density (SCD) appears. The process is manifest even in stationary conditions. Indeed, suppose a constant current density J_0 flows through a material, described by the conductivity $\sigma(r, t)$ and by the dielectric permittivity $\epsilon(r, t)$. The laws of Gauss and Ohm give:

$$\nabla(\epsilon(r, t)\mathbf{E}) = \nabla\left[\frac{\epsilon(r, t)\mathbf{J}_0}{\sigma(r, t)}\right] = \mathbf{J}_0 \nabla\left[\frac{\epsilon(r, t)}{\sigma(r, t)}\right] = \rho(r, t) \neq 0 \quad (3)$$

The SCD is non-zero for all compound materials, especially for glasses, where the mixed alkali effect is present. This charge is not annihilated by an electric field, until the electric current is switched off. Therefore, only at the end of the process a relaxation occurs, and the final sample has no more local SCD. However, this SCD is zero for thermal diffusion, because $J_0 = 0$, and it turns out that it has negligible effects in burying processes⁵. Its influence reveals only in FAM's, as we shall see in section 4. Therefore, assumption iv) is valid for all processes, except FAM; using it, we obtain the equation governing the inter-diffusion:

$$\frac{\partial c}{\partial t} = \nabla \left[\tilde{D}_a(c, T) \left(\nabla c - \frac{J_0}{c_0 D_b(c, T)} c \right) \right] \quad (4)$$

where $c = c_a/c_0$ is the relative concentration of incoming ions, c_0 the initial, constant concentration of host ions in the glass, and $\tilde{D}_a(c, T)$ the inter-diffusion coefficient, defined by:

$$\tilde{D}_a(c, T) = \frac{D_a(c, T)}{1 - \alpha(c, T)c} \quad (5)$$

The quantity $\alpha(c, T)$ is defined by:

$$\alpha(c, T) = 1 - \frac{D_a(c, T)}{D_b(c, T)} \quad (6)$$

In this approximation of zero space charge, the local electric field E_0 has the form:

$$E_0(r, t) = \frac{HkT}{e} \frac{J_0}{c_0 D_b(c)} \frac{1}{1 - \alpha(c)c} - \frac{HkT}{e} \frac{\alpha(c) \nabla c}{1 - \alpha(c)} = E_{\text{ext}} + E_{\text{diff}} \quad (7)$$

As the diffusion proceeds, the local concentration c varies in time, being actually a function of r and t . The expression (7) has the same form as the field obtained without taking into account the concentration dependence of the parameters⁶. The first term is known as the external field, the second one as the diffusion field. These two fields have the same direction, namely towards the bulk, for all processes except FAM.

3. APPLICATION TO THERMAL DIFFUSION AND TO FIELD-ASSISTED BURYING

An important point of the model is the concentration dependence of the quantities. Usually one uses the Boltzmann method⁷, which has, however, a limitation: it can be applied only to monotonous diffusion profiles. We have introduced an original method free from this restriction¹; we shall present it here in detail. It has a marked resemblance with the variational method used e. g. in analytical mechanics.

Our method requires the record of two experimental profiles, at the same temperature, but for different times. The first process, obtained during the time τ , may be pure thermal, or a field-assisted one. The second one is a pure thermal re-diffusion, from τ to $\tau + \delta\tau$. The interval $\delta\tau$ must be short compared with τ ; typical figures, shown in Fig. 1, are $\tau = 20$ min., $\delta\tau = 5$ min.

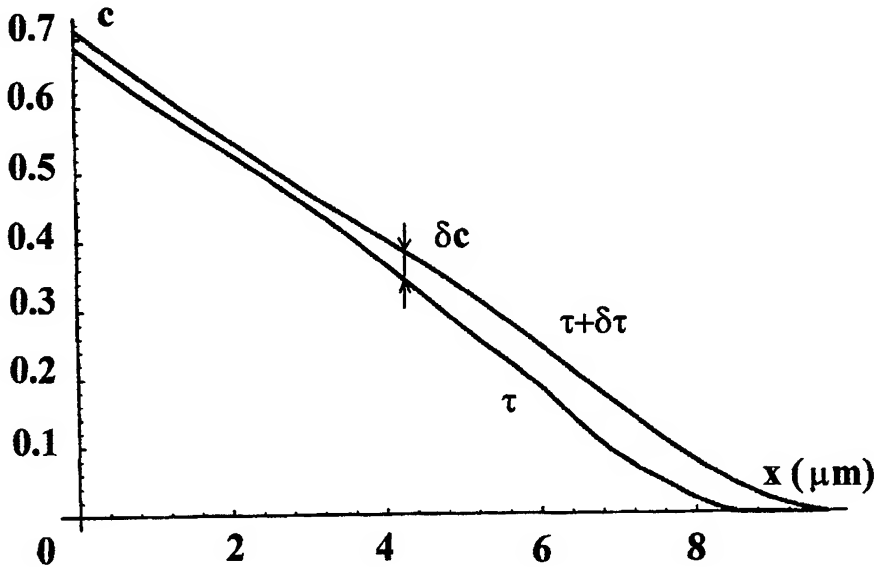


Fig. 1 The two profiles used for computing $D(c)$; $\tau=20$ min., $\delta\tau=5$ min.; diffusion of silver ions in sodium containing silicate glass at 330 °C

Under this condition, we can approximate the partial derivative $\partial c / \partial t$ by the variation $\delta c / \delta t$. Integrating Eq. (4), with $J_0 = 0$, from x to ∞ ($x = \infty$ is a point in the glass far beyond the diffusion front), we obtain:

$$\tilde{D}_a(x') \frac{\partial c}{\partial x'} \Big|_x^\infty = \int_x^\infty \frac{\partial c(x')}{\partial t} dx'$$

At the upper limit, $c(\infty) = 0$, $\partial c / \partial x'(x' = \infty) = 0$. Replacing the time derivative by the variation, we find the approximation:

$$\tilde{D}_a(x) \approx - \frac{x}{\frac{\partial c}{\partial x}} \frac{\int_x^\infty \frac{\delta c(x')}{\delta t} dx'}{\delta c(x)} \quad (8)$$

The derivative $\partial c / \partial x$ and the variation $\delta c(x')$ are measured from the experimental curves in Fig. 1. Relation (8) and the curve $c(x)$ give easily the function $\tilde{D}_a(c)$ (a typical dependence is shown with a dashed line in Fig. 4). Theoretical profiles using the function $\tilde{D}_a(c)$ obtained as above are in very good agreement with experimental points measured by scanning electron microscopy (SEM), or by other methods. Fig. 2 shows how close theoretical curves match experimental points, even in extreme conditions of skewed multi-mode waveguides.

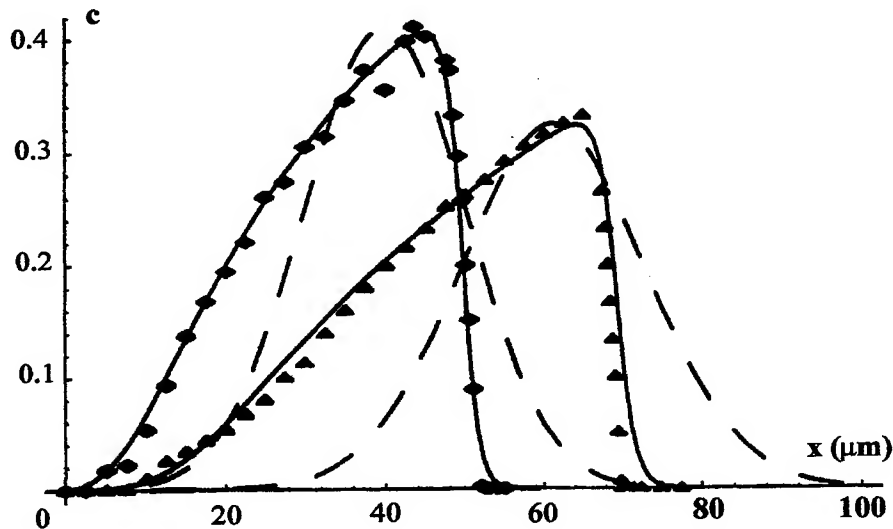


Fig. 2 Comparison between experimental points measured by SEM, the model with constant diffusion coefficients – dashed lines, and our model – continuous line. Rhombs – thermal diffusion during 20 min. at 330 °C, followed by 20 min. burying, at 50 Am⁻²; triangles – thermal diffusion during 20 min. at 330 °C, followed by 40 min. burying, at 50 Am⁻²

4. FIELD ASSISTED MIGRATION

A typical FAM profile is shown in Fig. 3, together with a theoretical curve, shown as the continuous line. This theoretical curve is not obtained using our preceding model, which fails in this specific case. We have shown² that the main reason for this failure is the anomalous behavior of drift mobilities during FAM processes. To be specific, the inter-diffusion $\tilde{D}_a(c)$ may vary more than 10 times, while the inter-mobility remains almost constant.

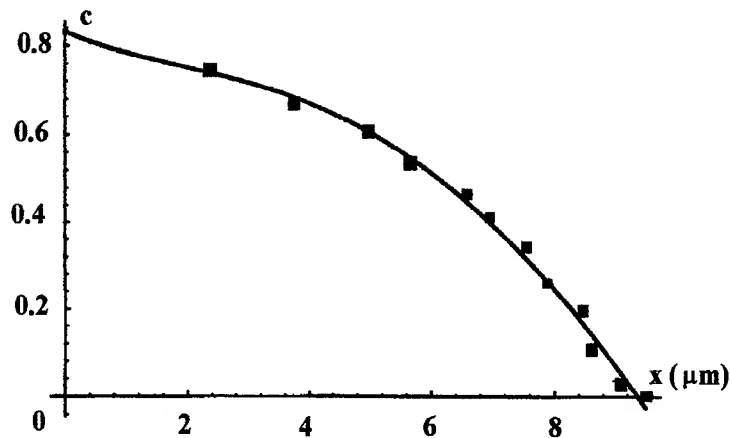


Fig. 3 Diffusion profile for 3 min. field-assisted migration at 330 °C, under a current density $J_0=23 \text{ Am}^{-2}$. Theoretical curve is draw assuming an anomalous behavior of the inter-mobility for $c > c_t$.

We show in Fig. 4 these very different behaviors of the two curves, which clearly contradict the Nernst-Einstein relation (1). As these deviations appear only in FAM, we stress that they are manifest only when foreign ion concentrations are higher than the *transition concentration*.

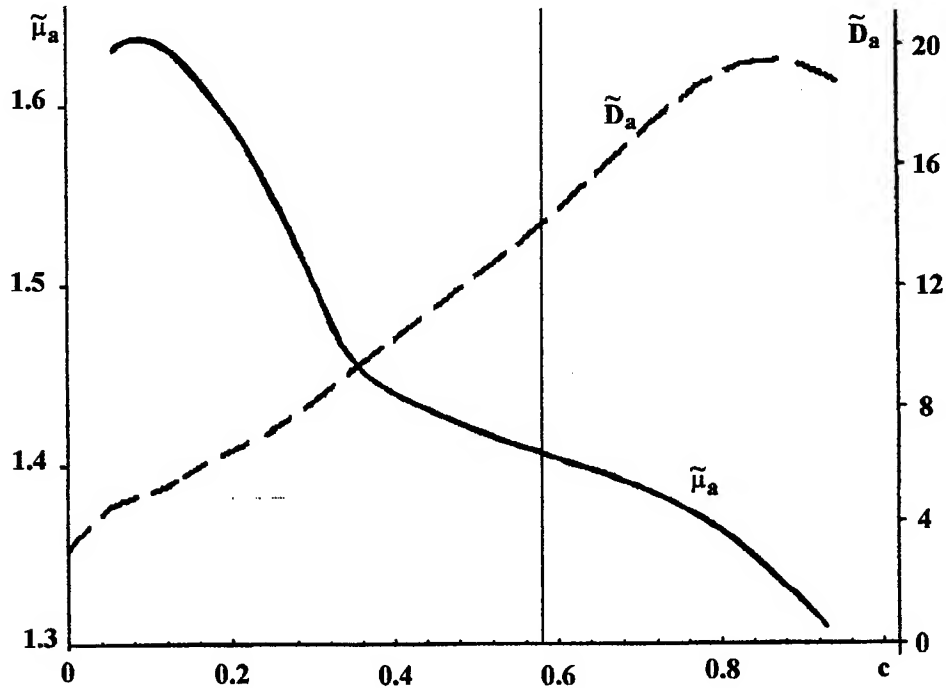


Fig. 4 Inter-mobility $\tilde{\mu}_a(c)$ and inter-diffusion coefficient $\tilde{D}_a(c)$ versus the relative concentration c . The transition concentration for this case is $c_t=0.58$. The relevant parts of the curves are placed at the right of the vertical line going through c_t .

The explanation is based on Eq. (7). The denominators are positive for all concentrations, hence E_{ext} points always towards the bulk, as does J_0 . However, $\alpha(c)$ changes its sign around the *transition concentration* c_{tr} defined as the concentration at which the two ionic species have equal diffusion coefficients:

$$D_a(c_{\text{tr}}) = D_b(c_{\text{tr}}), \quad \text{or} \quad \alpha(c_{\text{tr}}) = 0 \quad (9)$$

For thermal diffusion or for FAM, the concentration gradient is negative, hence E_{diff} is omo-parallel to E_{ext} for $c < c_{\text{tr}}$, but anti-parallel for $c > c_{\text{tr}}$. E_{diff} points towards the surface at high concentrations of incoming ions, consequently opposing the main ionic flux and facilitating charge accumulation. There is a space charge density, which, if $c > c_{\text{tr}}$, has measurable effects, e. g. the inadequacy of the Nernst-Einstein relation. We explain the differences between the two curves in Fig. 4 by the appearance of a *supplementary local electric field* E_{suppl} . Its effect is to make almost constant the apparent inter-mobility. We may write then, as a first approximation:

$$c\tilde{\mu}_{\text{const}} E_0 = c\tilde{\mu}(c)(E_0 + E_{\text{suppl}}) \quad (10)$$

This relation holds for $c > c_{\text{tr}}$, while for lower concentrations the mobility and the diffusion coefficient are proportional to each other. From Eq. (10), and using Eqs. (5-8), one finds the expression of the supplementary field in terms of the field E_0 :

$$E_{\text{suppl}} = E_0 \left[\frac{\tilde{D}_a(c_{\text{tr}})}{\tilde{D}_a(c)} - 1 \right] = E_0 \left[\frac{D_a(c_{\text{tr}})}{D_a(c)} (1 - \alpha(c)c) - 1 \right] \quad (11)$$

The first term is smaller than 1 for $c > c_{\text{tr}}$, hence E_{suppl} points in the direction opposite to E_0 . Fig. 5 shows the dependence of the ratio E_{suppl}/E_0 in the interesting region of high concentrations.

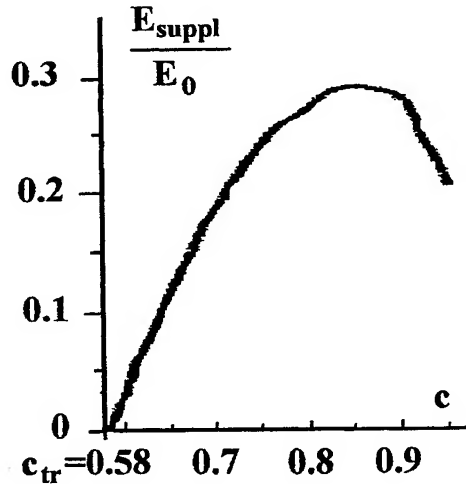


Fig. 5 The ratio E_{suppl}/E_0 as a function of the relative concentration, for $c > c_{\text{tr}}$. The curve is constructed using relation (11) and the dependence $\tilde{D}_a(c)$ from Fig. 4

5. DISCUSSION AND CONCLUSIONS

As is well known, local space charges are negligible in field-assisted burying, and zero in thermal processes. It turns out that in FAM some anomalies are manifest at concentrations higher than c_{tr} . The apparent constant value of the inter-mobility may have two motives:

- a local electric charge builds up, because for $c > c_{tr}$ the field E_{diff} opposes to the main ionic flux
- not all the ions participate to the conduction.

The two causes can not be discriminated by diffusion measurements, because the equations contain the product $c\mu E$. On the other hand, they are connected together, because an additional electric field opposing to ionic motion helps charge accumulation. The distinction between the cations participating to the drift process and the others is difficult, but could be done e. g. using ionic Hall effect⁸.

We have proposed a way out, based on a supplementary electric field, which manifests itself only at concentrations higher than c_{tr} . This field opposes to the local field E_0 computed by Eq. (7) in the zero space-charge approximation. In our example E_{suppl} points towards the surface, hence it helps charge accumulation. It would be interesting to search for a glass and for conditions such as E_0 would change its sign. This would happen for $E_{ext}=E_{diff}$ i. e.

$$J_0 = (D_a - D_b) \frac{\nabla c}{c_0} \quad (12)$$

In such conditions the local ionic arrangements could show interesting features.

A very important physical quantity for field-assisted ionic exchanges is the concentration transition c_{tr} . This parameter appears only in models with concentration-dependent diffusion coefficients. The profile dynamics is very different at concentrations lower and higher than c_{tr} . Following Abou-El-Leil and Cooper⁹, we may say that at lower concentrations the profile is stable, and for $c > c_{tr}$ it is unstable. These two cases co-exist for FAM profiles.

REFERENCES

1. A. Lupascu, A. Kevorkian, T. Boudet, F. Saint-André, D. Persegol, and M. Lévy, "Modeling ion exchange in glass with concentration-dependent diffusion coefficients and mobilities", *Optical Eng.* **35**, pp. 1603-1610, 1996.
2. A. Lupascu, C. P. Cristescu, A. Kevorkian and I. M. Popescu, "Anomalous behavior of drift mobilities during field-assisted ionic migration in optical glass", *Sci. Bull. of the Polytechnic Univ. Bucharest* **60**, pp. 69-80, 1998.
3. Ch. Desportes et. al., *Electrochimie des solides*, pp. 73-83, Presses Universitaires de Grenoble, 1994.
4. A. Lupascu and A. Kevorkian, "Local electric effects during ionic exchanges in optical glasses", *Rom. Repts. in Phys.* **49**, pp. 907-917, 1997.
5. R. V. Ramaswami and R. Srivastava, "Ion-exchanged glass waveguides: a review", *J. Lightwave Technol.* **6**, pp. 984-1002, 1988.
6. J. Albert and J. W. Y. Lit, "Full modeling of field-assisted ion exchange for graded index buried channel optical waveguides", *Appl. Opt.* **29**, pp. 2798-2804, 1990.
7. J. Crank, *The Mathematics of Diffusion*, Chapter 8, Clarendon Press, Oxford, 1956.
8. Ref. 3, page 140.
9. M. Abou-El-Leil and A. R. Cooper, "Analysis of Field-Assisted Binary Ion Exchange", *J. Am. Ceram. Soc.* **62**, pp. 390-395, 1979.

The influence of the precrystallization-zone on the dopant field in microgravity

Agneta M. Balint^{*a}, Diana G. Bălțean^b, Monica Mihailovici^{ab}, Adrian Neculae^a, Ștefan Balint^b

^aDepartment of Physics, University of the West Timișoara

^bDepartment of Mathematics, University of the West Timișoara

ABSTRACT

In this paper we present the computed dopant field in the neighborhood of the melt/solid interface in the case of Bridgman-Stockbarger semiconductor crystal growth system in microgravity. The computation is made in quasi-steady state approximation for crystal and melt with thermophysical properties similar to those of gallium-doped germanium, using the "precristallization-zone" model. In the quasi-steady state approximation the translation of the ampoule is replaced by supplying melt into the ampoule with velocity V_l and removing crystal at the other end of the ampoule at the rate $V_s = V_l$. The "precristallization-zone" is considered to be a thin layer masking the crystal in which exists a periodical microstructure created by the periodical structure of the crystal which governs the arranging of the own atoms into a specific crystalline lattice. In fact, in this layer we have periodically distributed places which are not available for the dopant. Using this approximation and model, we find relevant radial segregation due to the precristallization-zone. We also find that reducing the diameter of the rod a lower radial segregation appears. Therefore the influence of the precristallization-zone is relevant even in microgravity and there is no reason to ignore this zone in general.

Keywords: Dopant field, precristallization-zone, microgravity, homogenization, melt/solid interface

1. INTRODUCTION

In the semiconductor crystal growth process by vertically-stabilized Bridgman-Stockbarger method, the heat and mass transfer in the ampoule are time dependent. These dependences are caused mainly by the steady decrease in the ratio of melt to crystal in the ampoule. For semiconductor materials, the decrease is slow. Therefore, in modelling, the true unsteady process is replaced by a quasi-steady state process viewed from a stationary reference frame and is described in a cylindrical polar coordinate system shown in Fig. 1.^{1,2}

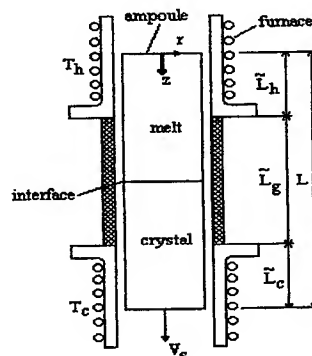


Fig. 1 Geometry of prototype vertical Bridgman-Stockbarger growth system

* Correspondence: Email: balint@balint.uvt.ro or sbalint@mail.dnttm.ro; Telephone: +4056201105 or +4056167544; Fax: +4056201105 or +4056167544

The translation of the ampoule is replaced by supplying melt into the ampoule at $z = 0$ with velocity $v_z = V_l$ and removing crystal at the other end of the ampoule at the rate $V_s = V_l$ ^{1,2}. For long ampoules and melts with low Prandtl numbers the transient effects on heat and mass transfer are small^{1,2}. Consequently, a numerical computation made in quasi-steady state approximation corresponds to the computation made for a position of the ampoule inside the furnace which corresponds to a time step in the growth experience^{1,2}. Changes in the length of the melt caused by translating the ampoule lead to an increase of the average concentration of dopant in the melt. This effect is ignored in the quasi-steady state approximation^{1,2}.

In the quasi-steady state approximation, the phase field equations governing fluid flow in the melt, heat transfer in the melt and in the crystal in axisymmetric and dimensionless form are the following:

$$\nabla \mathbf{v} = 0 \quad (1)$$

$$(\mathbf{v} \cdot \nabla) \mathbf{v} = -\nabla p + Pr \nabla^2 \mathbf{v} + Ra Pr \theta \mathbf{e}_z \quad (2)$$

$$\mathbf{v} \cdot \nabla \theta = \nabla^2 \theta \quad (3)$$

$$Pe \mathbf{e}_z \cdot \nabla \theta = \gamma \nabla^2 \theta \quad (4)$$

The interface condition in dimensionless form is:

$$(\mathbf{N} \cdot \nabla \theta)_l - K(\mathbf{N} \cdot \nabla \theta)_s = S Pe \mathbf{N} \cdot \mathbf{e}_z \quad (5)$$

where

$$\theta(r, h(r)) = \frac{\tilde{T}_m - T_c}{T_h - T_c} \quad (6)$$

We used the following notations:

$\mathbf{v}(r, z) = \tilde{\mathbf{v}}(r, z) L / \alpha_l$ – dimensionless velocity field

$\tilde{\mathbf{v}}(r, z)$ – velocity field

L – height of the ampoule

α_l – thermal diffusivity in the melt

$p(r, z) = \tilde{p}(r, z) L^2 / \rho_l \alpha_l^2$ – dimensionless pressure field

$\tilde{p}(r, z)$ – pressure field

$\rho_{l,s}$ – melt/solid density

$\theta(r, z) = (\tilde{T}(r, z) - T_c) / (T_h - T_c)$ – dimensionless temperature field

$\tilde{T}(r, z)$ – temperature field

\tilde{T}_m – melting temperature

$T_{h,c}$ – temperature of the hot/cold region of the furnace

R – radius of the ampoule

$\Lambda = R/L$ – aspect ratio

$L_{h,g} = \tilde{L}_{h,g} / L$ – dimensionless length of the hot/gradient zone

$z = h(r)$, $0 < r < \Lambda$ – location of the melt/solid interface

$\mathbf{N} = (\mathbf{e}_z - h_r \mathbf{e}_r) / (1 + h_r^2)^{1/2}$ – unit normal vector at the interface

$\mathbf{t} = (\mathbf{e}_r + h_r \mathbf{e}_z) / (1 + h_r^2)^{1/2}$ – unit tangent vector at the interface

$h_r = dh/dr$

$\mathbf{e}_{r,\theta,z}$ – unit vectors for the cylindrical polar coordinate system

$\nabla = \mathbf{e}_r \partial/\partial r + \mathbf{e}_z \partial/\partial z$

$Pr = \nu/\alpha_l$ – Prandtl number

$Ra = \beta g (T_h - T_c) L^3 / \nu \alpha_l$ – Rayleigh number

ν – kinematic viscosity of melt

β – thermal expansion coefficient
 g – gravity acceleration
 $\gamma = \alpha_s / \alpha_l$ – ratio of thermal diffusivities in solid and melt
 $Pe = V_s L / \alpha_l$ – Peclet number of convective heat transfer
 $S = \Delta H_f / [\rho_l c_{pl} (T_h - T_c)]$ – Stefan number
 ΔH_f – heat of fusion
 c_{pl} – heat capacity of the melt
 $K = k_s / k_l$ – conductivity ratio

Boundary conditions on velocity at the interface insure no slip tangential to the crystal and the solidification of the melt at a rate proportional to the growth rate V_s . The top surface and sidewall of the ampoule are assumed to be no slip surfaces so that $v_r = 0$ and $v_z = Pe$ in the melt^{1,2}.

The symmetry boundary conditions at the axis of the cylinder are^{1,2}.

$$v_r = \frac{\partial v_z}{\partial r} = \frac{\partial \theta}{\partial r} = 0, \quad 0 \leq z \leq 1, r = 0 \quad (7)$$

The thermal boundary conditions incorporate the assumption that the ampoule has negligible thermal mass, the adiabatic region is a perfect insulator, the ampoule has the temperature of the surrounding furnace and the ends of the ampoule are perfectly insulated^{1,2}.

The convective-diffusive equation for the concentration $c = c(r, z)$ of the dilute dopant is:

$$\frac{Sc}{Pr} \nabla c = \nabla^2 c \quad (8)$$

where $Sc = v/D$ is the Schmidt number and D is the diffusivity of the dopant in the melt^{1,2}.

The boundary conditions for eqn. (8) are:

$$\frac{\partial c}{\partial z} = \frac{Pe Sc}{Pr} (c - 1), \quad z = 0, \quad 0 \leq r \leq \Lambda \quad (9)$$

$$\mathbf{N} \nabla c = \frac{Pe Sc}{Pr} (\mathbf{N} \mathbf{e}_z)(1 - k) c, \quad z = h(r), \quad 0 \leq r \leq \Lambda \quad (10)$$

$$\frac{\partial c}{\partial r} = 0, \quad 0 \leq z \leq 1, r = 0, \Lambda \quad (11)$$

where k is the segregation coefficient^{1,2}.

If we ignore the precrystallization-zone, assuming that the melt is homogenous, the value of the Schmidt number is the same in eqn. (8), (9) and (10). But if we take into account the precrystallization-zone, then, due to the microstructures in the precrystallization-zone, the diffusivity of the dopant decreases with z which leads to an increase of the value of Sc . Therefore, we must take in eqn. (10) a bigger value for Sc than the value in (8) and (9).

2. THE PRECRYSTALLIZATION-ZONE

Starting from the fact that the "uniform-diffusion-layer" and "global-thermal-convection" models used in^{1,2} to compute the dopant field ignore the "precrystallization-zone", we have developed^{3,4} a so called "precrystallization-zone-model" in which we obtained, using homogenization method, a new convective-diffusive equation for the dopant. Concerning this model we assume that there exists a thin layer masking the crystal where we have a weak form of the periodic structure of

the crystal. This periodic microstructure is created by the crystal of which structure like a matrix governs the arranging of the atoms from the melt into a specific crystalline lattice. Consequently, in a thin layer masking the crystal we have periodically distributed places which are not available for the dopant. These places can be imagined as some small "solid inclusions" (small with respect to the distance between two neighboring inclusions and small also with respect to a critical size⁵). In these conditions the velocity field in the effective dopant-transport equation (8) is not influenced⁵, but the diffusive term changes. Therefore we will have for the dopant a new not constant diffusion coefficient in isotropic case and a diffusion tensor in anisotropic case. The new diffusion coefficient or tensor depend on z , on the concentration of the "solid inclusions" and on the geometry of these inclusions⁶. At the level of the melt/solid interface this coincides with the diffusion coefficient or tensor in the crystal⁷. In the precrystallization-zone the diffusion coefficient which appears in eqn. (8) decreases with z and influences the dopant field⁶. We have estimated this influence in isotropic case changing the Schmidt number just in eqn. (10) in agreement with the decrease of D ^{6,8}. The effect of this change was calculated for microgravitational conditions and is shown beyond.

3. NUMERICAL COMPUTATION OF STREAMLINES, VELOCITY FIELDS AND TEMPERATURE FIELDS IN MICROGRAVITY ($Ra = 10$)

Streamlines, velocity fields and isotherms in microgravitational conditions are computed using the software called "Cosmos". Calculus has been made for melt and crystal with thermophysical properties similar to those of gallium-doped germanium. The interface is planar and fixed at the middle of the gradient region.

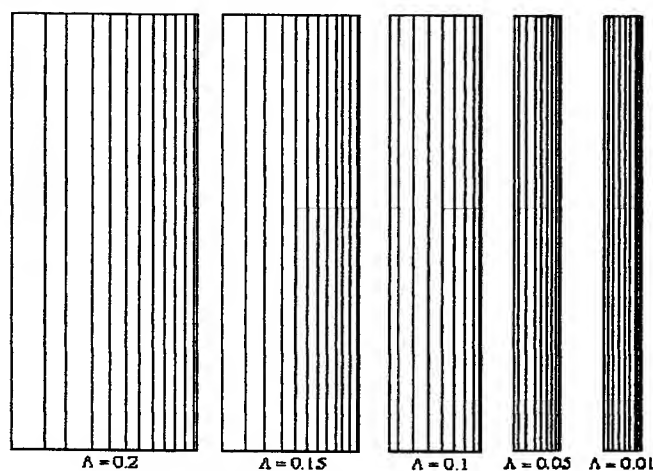


Fig. 2a) Streamlines in the melt region for $Ra = 0$

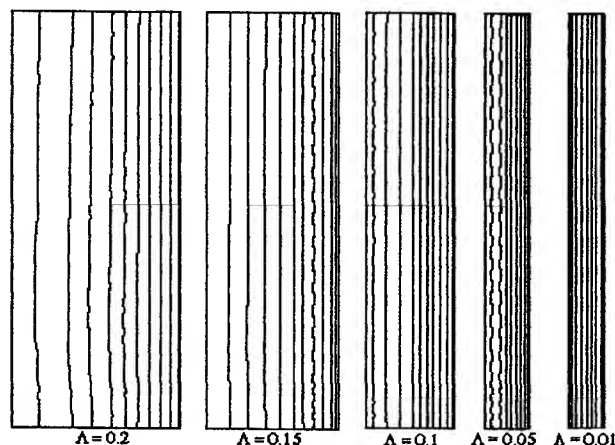


Fig. 2b) Streamlines in the melt region for $Ra = 10$

Streamlines computed for various values of the aspect ratio Λ are shown on Fig. 2b). These lines are rectilinear and are very slightly distorted by thermal convection. These distortions get weaker with decreasing aspect ratio.

Velocity fields computed for the same values of Λ as above are shown on Fig. 3b). These fields differ from those computed in strictly zero-gravity (see Fig. 3a)) somewhat by 10^{-4} . This shows, that under microgravity ($Ra = 10$) the influence of the thermal convection on the velocity field is of range 10^{-4} . It must be mentioned, that this difference decreases with Λ and practically disappears for $\Lambda = 0.01$.

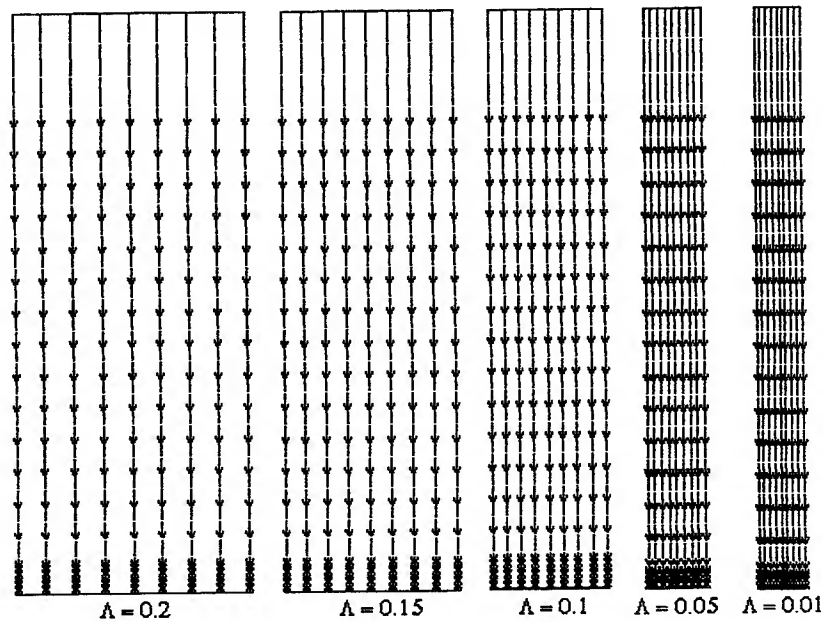


Fig. 3a) Velocity fields in the melt region for $Ra = 0$

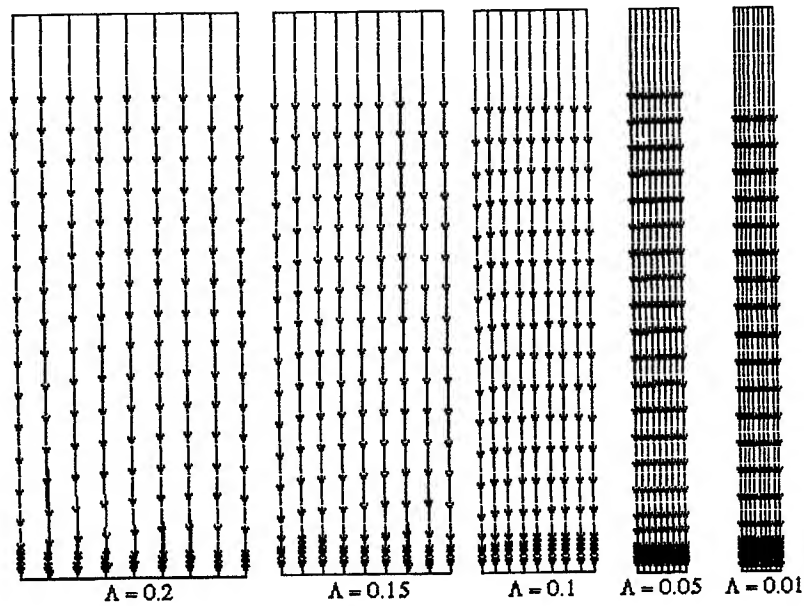


Fig. 3b) Velocity fields in the melt region for $Ra = 10$

Figs. 4 show the temperature fields computed for the same values of Λ as in the previous figures. For $\Lambda = 0.01$ there is no difference between the temperature fields in strictly zero-gravity and those in microgravity ($Ra = 10$).

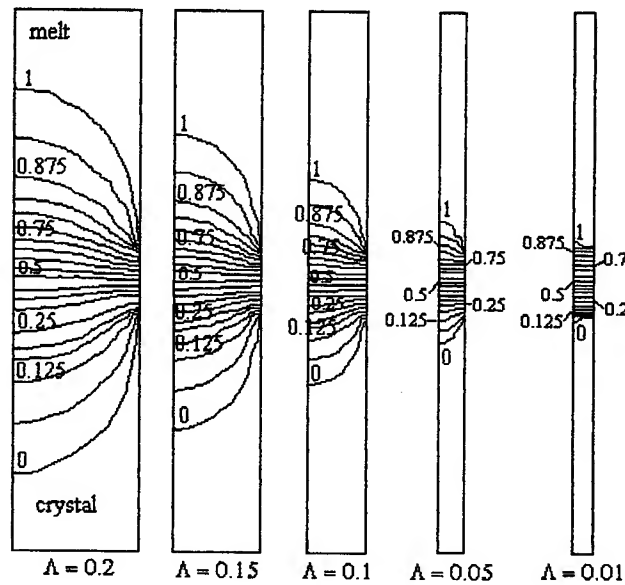


Fig. 4a) Temperature fields (melt and crystal) for $Ra = 0$

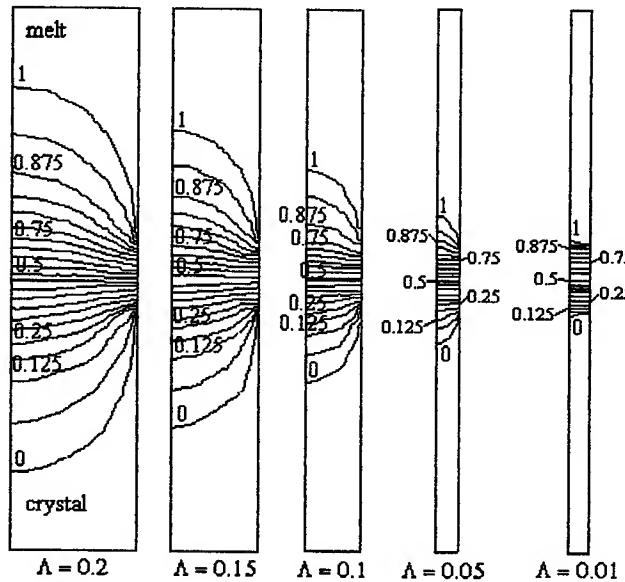


Fig. 4b) Temperature fields (melt and crystal) for $Ra = 10$

4. NUMERICAL COMPUTATION OF DOPANT FIELDS IGNORING THE MICROSTRUCTURE NEAR THE INTERFACE

Figs. 5 show the dopant fields computed in strictly zero-gravity (Fig.5a)) and microgravity (Fig.5b)) for various values of Λ . These computations have been made assuming that the diffusion coefficient D has the same value in eqn. (8), (9) and (10). This means, that we ignore the precrystallization-zone and implicit the microstructure in the neighborhood of the

interface. The iso-concentration lines are parallel to the interface and those in microgravity are similar to those in strictly zero-gravity.

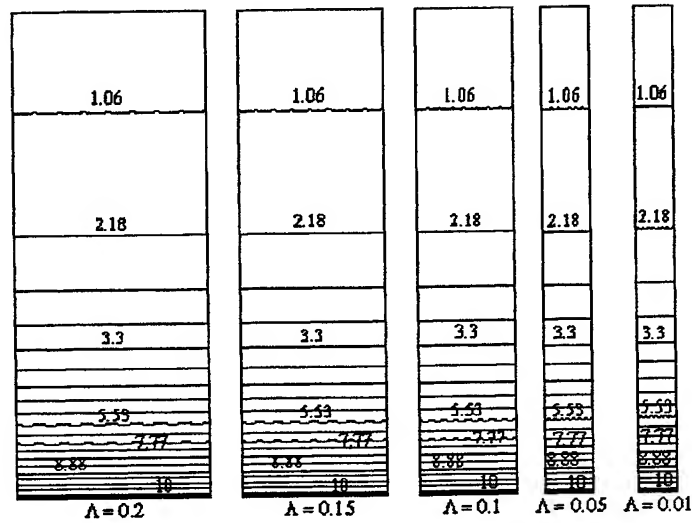


Fig. 5a) Dopant concentration fields for flow fields shown in Fig.2a); $Sc=10$ and $k=0.1$

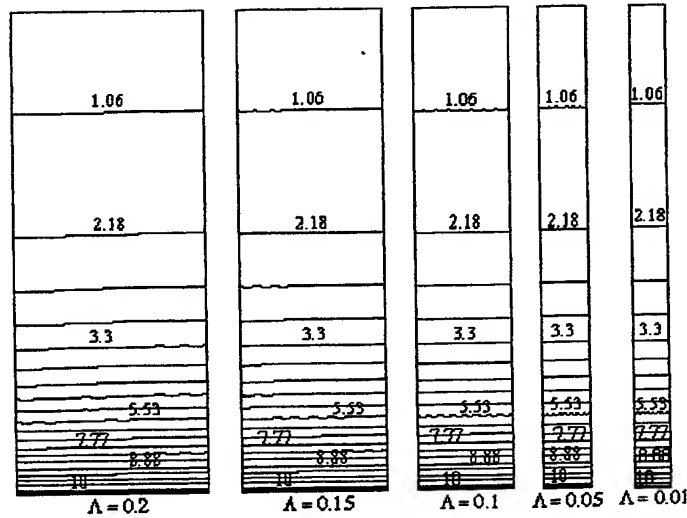


Fig. 5b) Dopant concentration fields for flow fields shown in Fig.2b); $Sc=10$ and $k=0.1$

5. NUMERICAL COMPUTATION OF THE DOPANT CONCENTRATION AT THE AXIS OF THE CYLINDER IN THE PRESENCE OF MICROSTRUCTURES

Figs. 6 to 10 show the computed values of the dopant concentration at the axis of the cylinder for five different values of Λ and five different values of the volumic concentration ϕ of "solid inclusions" which describes the microstructure in the precrystallization-zone. For each value of Λ one observes that an increase of ϕ leads to modifications in the dopant concentrations at the axis of the cylinder. More precisely, the concentration increases with ϕ near the interface. This increase is significant, because for a variation of ϕ from 0 % to 5 %, the concentration of the dopant at the axis near the interface increases five times. The scale factor of dopant concentration is the same for all Λ values.

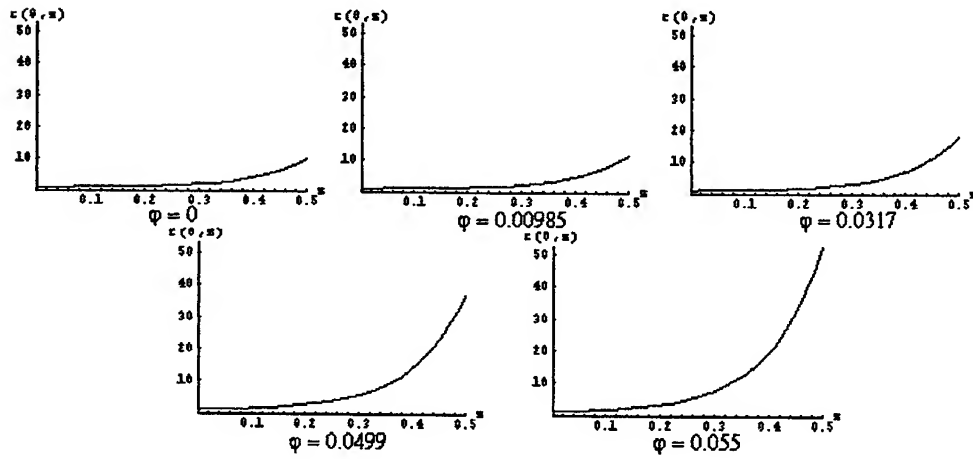


Fig. 6 Dopant concentration at the axis of the cylinder for $\Lambda = 0.2$ and $Ra = 10$ for several values of the volumic concentration φ of "solid inclusions"

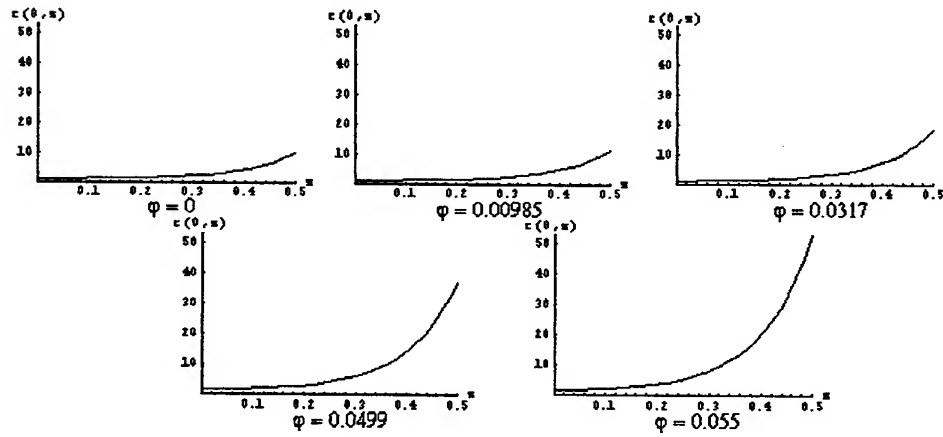


Fig. 7 Dopant concentration at the axis of the cylinder for $\Lambda = 0.15$ and $Ra = 10$ for several values of the volumic concentration φ of "solid inclusions"

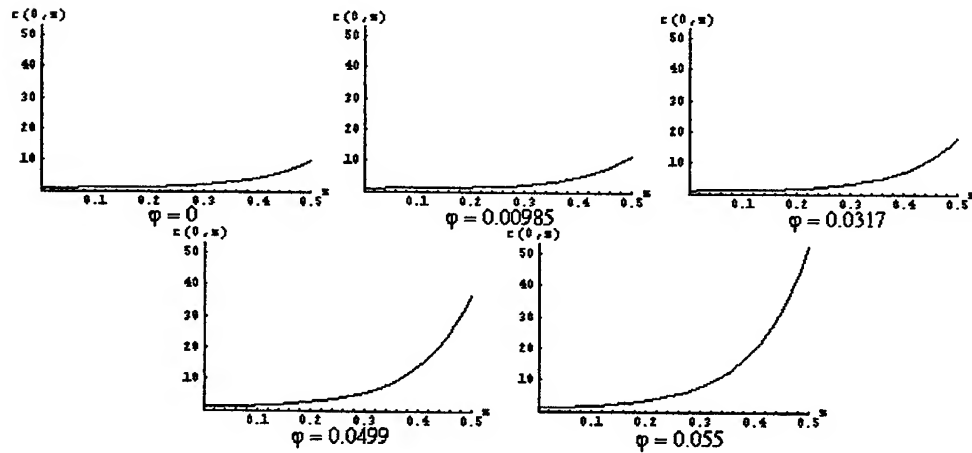


Fig. 8 Dopant concentration at the axis of the cylinder for $\Lambda = 0.1$ and $Ra = 10$ for several values of the volumic concentration φ of "solid inclusions"

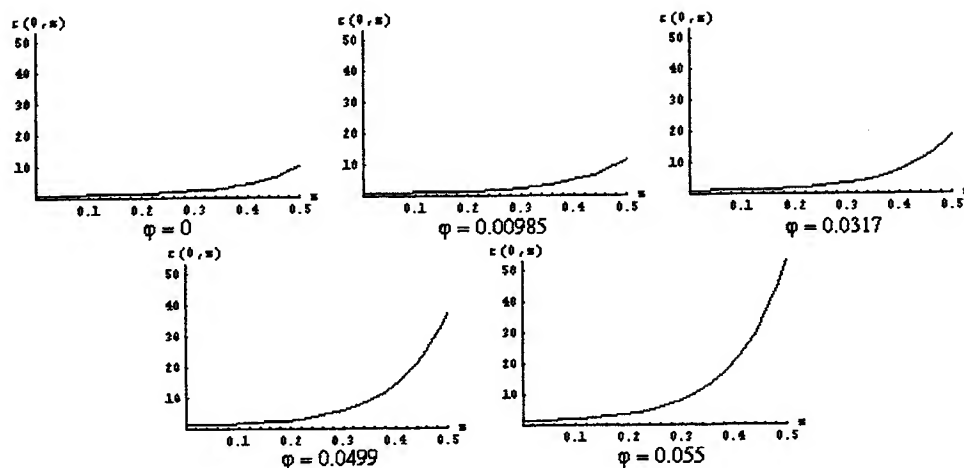


Fig. 9 Dopant concentration at the axis of the cylinder for $\Lambda = 0.05$ and $Ra = 10$ for several values of the volumic concentration ϕ of "solid inclusions"

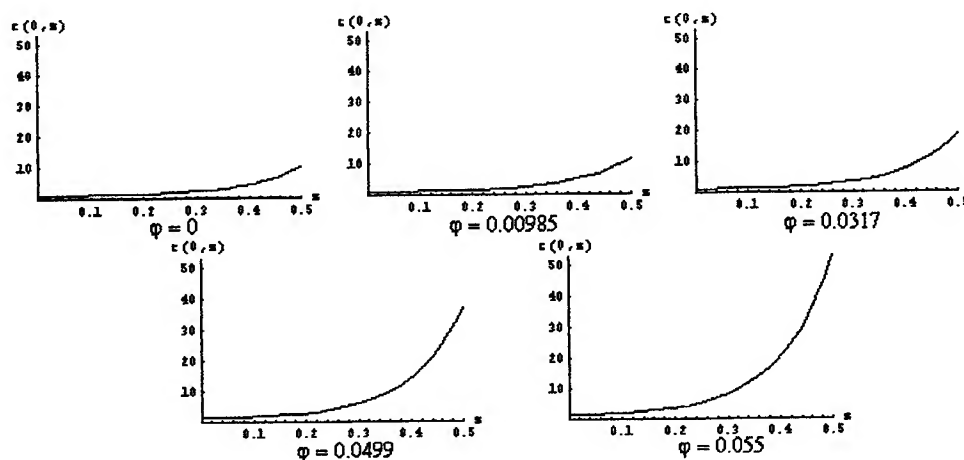


Fig. 10 Dopant concentration at the axis of the cylinder for $\Lambda = 0.01$ and $Ra = 10$ for several values of the volumic concentration ϕ of "solid inclusions"

6. NUMERICAL COMPUTATION OF THE RADIAL VARIATION OF DOPANT CONCENTRATION AND PERCENT RADIAL SEGREGATION IN THE PRECRYSTALLIZATION-ZONE

Figs. 11 to 14 show the radial variations for various values of Λ and ϕ . This variation is not zero like in section 4. For a given value of Λ , the radial variation increases with ϕ . For a given ϕ , the radial variation decreases with Λ and disappears completely for $\Lambda = 0.01$. Therefore, under microgravitational conditions, in precrystallization-zone model we have radial variation of the dopant concentration due to the residual gravity and it attenuates for small aspect ratios Λ (see Fig. 15).

For a given Λ , the percent radial segregation is an increasing function of ϕ (see Fig. 15). For a given ϕ , the percent radial segregation is an increasing function of Λ (see Fig. 16).

Therefore in precrystallization-zone model we have radial segregation due to the residual gravity. This segregation is significant for $\Lambda = 0.2$ and insignificant for $\Lambda = 0.05$.

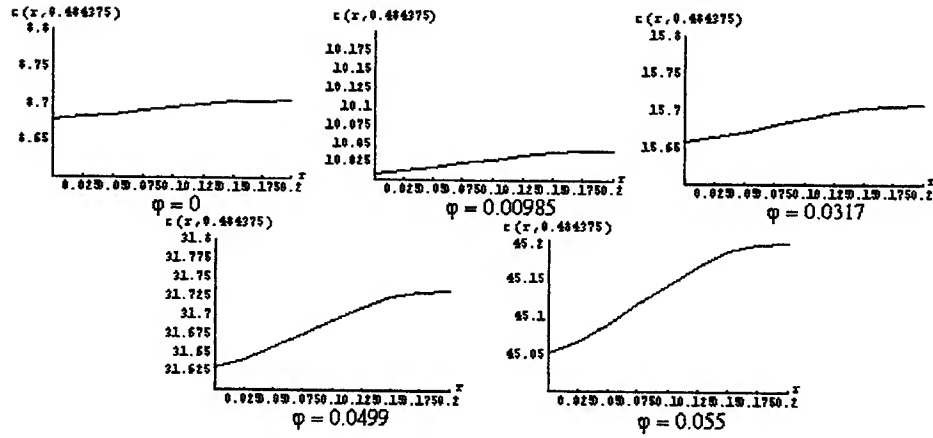


Fig. 11 Radial variation of the dopant concentration for $\Lambda = 0.2$ and $Ra = 10$ and several values of the volumic concentration ϕ of "solid inclusions"

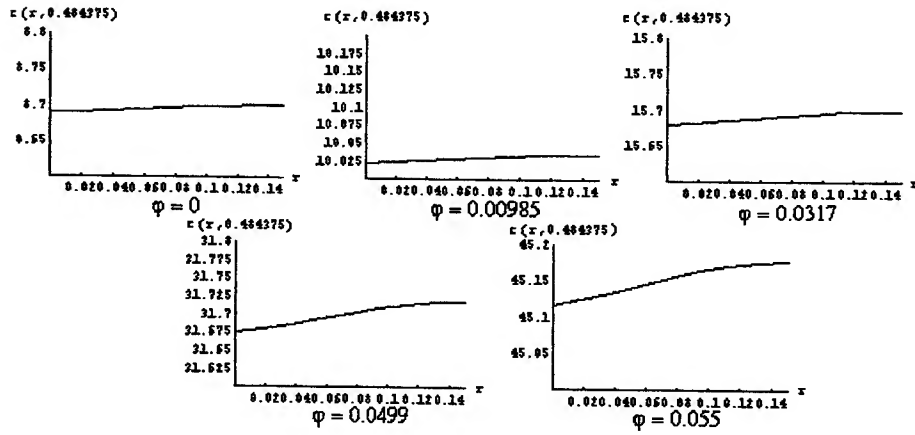


Fig. 12 Radial variation of the dopant concentration for $\Lambda = 0.15$ and $Ra = 10$ and several values of the volumic concentration ϕ of "solid inclusions"

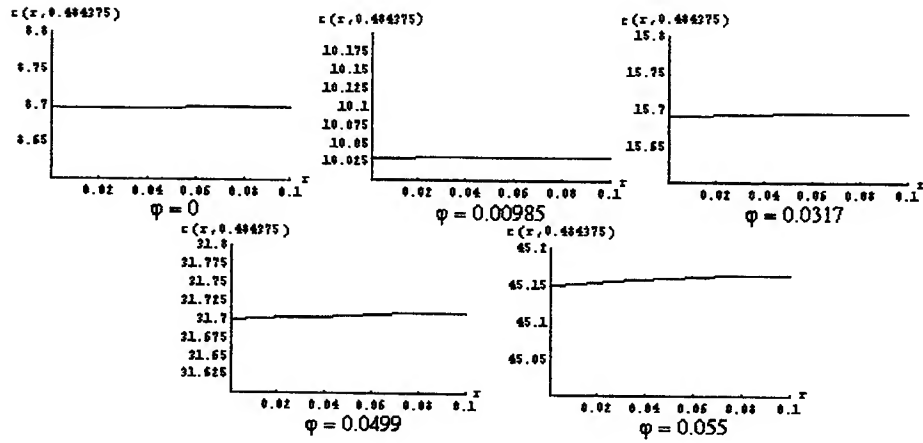


Fig. 13 Radial variation of the dopant concentration for $\Lambda = 0.1$ and $Ra = 10$ and several values of the volumic concentration ϕ of "solid inclusions"

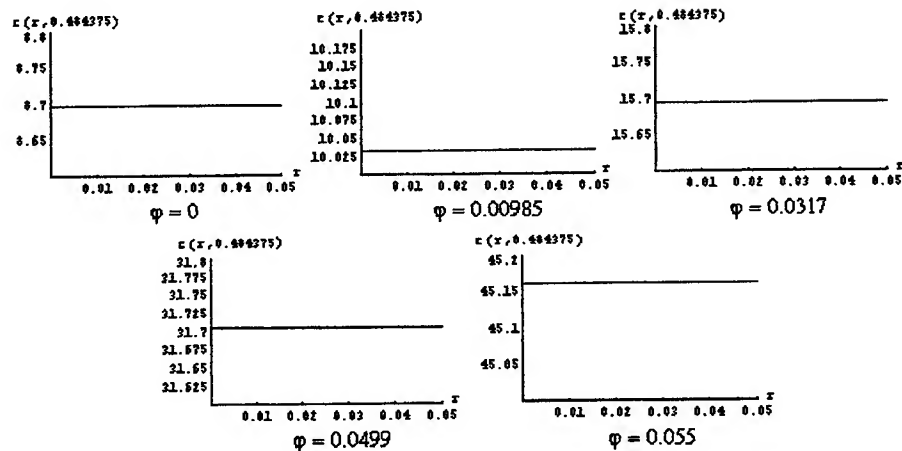


Fig. 14 Radial variation of the dopant concentration for $\Lambda = 0.05$ and $Ra = 10$ and several values of the volumic concentration ϕ of "solid inclusions"

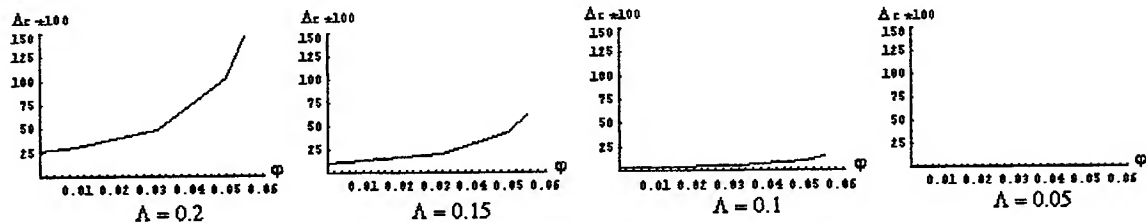


Fig. 15 Percent radial segregation as a function of volumic concentration ϕ of "solid inclusions" for different values of Λ ; $k = 0.1$, $Ra = 10$

The variation of the percent radial segregation with Λ for given values of ϕ is shown on Figure 16.

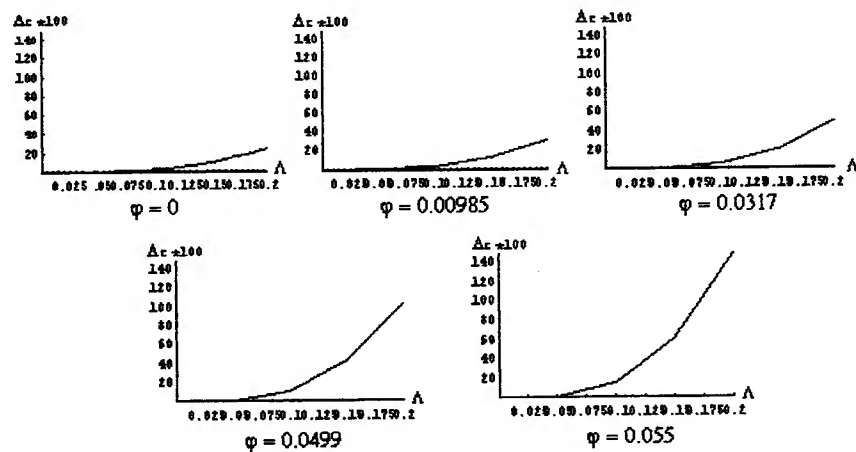


Fig. 16 Percent radial segregation as a function of aspect ratio Λ for different values of volumic concentration ϕ of "solid inclusions"; $k = 0.1$, $Ra = 10$

7. CONCLUSIONS

The microstructure in the precrystallization-zone has an important influence on the dopant concentration in the precrystallization-zone. An increase from 0 % to 5 % of the volumic concentration ϕ of these microstructures leads to a five time bigger dopant concentration at the interface on the axis of the cylinder. Even in microgravity there is no reason to ignore the microstructure in the precrystallization-zone.

For a given volumic concentration of "solid inclusions" the axial dopant concentration doesn't vary significant with the aspect ratio.

Radial variations of dopant concentration exist even in microgravity conditions. These variations are strongly dependent on the volumic concentration of "solid inclusions", i.e. they increase with ϕ . Though, these radial variations decrease with decreasing aspect ratio.

For $\Lambda = 0.05$, radial variations of the dopant concentration are almost inexistent, even for higher volumic concentration of "solid inclusions" (for ex., at $\phi = 0.055$). In the case of very thin rods ($\Lambda = 0.01$), radial variations disappear completely.

The percent radial segregation, defined as

$$\Delta c = |c(0, 0.484375) - c(\Lambda, 0.484375)| \times 100/k,$$

for a given aspect ratio is an increasing function of the volumic concentration ϕ of "solid inclusions".

For a given value of the volumic concentration ϕ of "solid inclusions" the percent radial segregation is an increasing function of the aspect ratio Λ . Radial segregation is important for higher values of Λ ($\Lambda = 0.2, 0.15$), insignificant for $\Lambda = 0.05$ and disappears completely in the case of very thin rods ($\Lambda = 0.01$).

Even in microgravity the influence of the precrystallization-zone on the dopant dispersion is relevant and there is no reason to ignore this zone in general.

REFERENCES

1. C.J. Chang and R.A. Brown, "Radial Segregation induced by Natural Convection and Melt/Solid Interface Shape in Vertical Bridgman Growth", *J. of Crystal Growth* **63**, pp. 343-364, 1983.
2. P.M. Adornato and R.A. Brown, "Convection and Segregation in Directional Solidification of Dilute and Non-Dilute Binary Alloys: Effects of Ampoule and Furnace Design", *J. of Crystal Growth* **80**, pp. 155-190, 1987.
3. Șt. Balint, A.M. Balint, D.G. Bălțean and A. Neculae, "The Dopant Transport by Convection and Diffusion During Melt Growth of Semiconductor Crystals in the context of the Bridgman-Stockbarger Crystal Growth Configuration", *International Conference on Analysis and Numerical Computation of Solutions of Nonlinear Systems Modelling Physical Phenomena*, Șt. Balint, pp. 225-239, Mirton Publishing House, Timișoara, 1997.
4. Șt. Balint, A.M. Balint, D.G. Bălțean and A. Neculae, "Analysis of the convective-diffusive transport equation of the dopant in the neighborhood of the growth interface in the context of Bridgman-Stockbarger crystal growth configuration", *Second International Conference on Nonlinear Problems in Aviation and Aerospace*, S. Sivasundaram, **1**, pp. 63-72, European Conference Publications, Cambridge, 1999.
5. Th. Lévy, *C.R. Acad. Sci.Paris* **292**, Serie II, p. 871, 1981.
6. D.G. Bălțean, Th. Lévy and Șt. Balint, *C.R. Acad. Sci.Paris* **326**, Serie II b, pp. 821-826, 1998.
7. A. Neculae, A.M. Balint, D.G. Bălțean and Șt. Balint, "Diffusion in periodic structures (I)", *Analele Universității din Timișoara, Seria Științe Fizice*, **XXXVIII**, pp. 53-64, 1998.
8. C. Moutsopoulos and S. Bories, *C.R. Acad. Sci.Paris* **316**, Serie II b, pp. 1667-1672, 1993.
9. A.M. Balint, D.G. Bălțean, Th. Lévy, M. Mihailovici, A. Neculae and Șt. Balint, "The dopant fields in "uniform-diffusion-layer", "global-thermal-convection" and "precrystallization-zone" models", *The European Material Conference*, Strasbourg, June 1- 4, 1999.
10. C. Barat, *Ph.D. Thesis*, Université de Rennes I, 1995.

Electro-optic and phase transition studies on polymer dispersed liquid crystal films

Doina Manaila-Maximean^{a*}, Maurizio Furlani^b, Rodica Bena^a, Victor Stoian^a, Constantin Rosu^a

^aUniversity "Politehnica" Bucuresti, Department of Physics,
Spl. Independentei 313, 77206, Bucharest, Romania

^bChalmers University of Technology and Göteborg University - Department of Physics and
Engineering Physics 41296 Göteborg - Sweden.

ABSTRACT

We obtained polymer dispersed liquid crystal (PDLC) films using a nematic liquid crystal E7 and polymethyl methacrylate (50% by weight) by the Solvent Induced Phase Separation method. Using the Thermally Stimulated Depolarization Current method we determined the clearing point of the pure liquid crystal and of the PDLC films. The glass transition temperature of the PMMA matrix has also been determined. The results have been compared with those obtained by Differential Scanning Calorimetry. During the TSDC measurements we registered the optical transmission as a function of temperature, thus the thermal switch operation being demonstrated.

Keywords: liquid crystal, polymer dispersed liquid crystal, phase transition, thermally stimulated depolarization currents

1. INTRODUCTION

Polymer dispersed liquid crystal (PDLC) composite materials consist of micrometer sized liquid crystal (LC) droplets embedded in a solid polymer matrix¹. There are two different types of such materials: a. Plastic materials with open or connected micropores which can be filled with a nematic liquid crystal. b. Materials containing encapsulated liquid crystals, that is a polymeric continuum in which the liquid crystal micro-droplets are randomly fixed in position, but are not connected to each other. The unifying theme in polymer dispersed liquid crystals is the formation of systems with high surface-to-volume ratios. Traditional liquid crystal devices are formed as thin films between two parallel substrates. The substrates are usually treated to obtain uniform alignment of the liquid crystal at each surface. Anchoring effects are relegated to the two bounding substrates. In the PDLC systems there is a large increase in the relative surface area. As a result, the interfacial effects become more important, because of the anchoring properties of the liquid crystal at the surface and of the hydrodynamic flow characteristics of the liquid crystal in close proximity to a surface.

PDLC devices exhibit an electro-optical effect because of optical heterogeneity between the polymer and the LC domains. One achieves switching between an opaque field-"off" and a transparent field-"on" state by matching the ordinary refractive index of the LC to the refractive index of the polymer matrix.

PDLC films have various applications: displays, bistable devices, polarizers, memory devices, selective permeable membranes, thermal switches, etc., their properties varying strongly with the temperature.

Methods of preparation:

1. *Emulsion methods for PDLC films* - emulsification of a liquid crystal in a film forming polymer (polyvinyl alcohol, latex). This emulsification is coated onto a conductive substrate and allowed to dry. As the film dries, the polymer forms a solid phase which contains the dispersed LC droplets.

2. *Phase separation methods for PDLC films:*

-*PIPS- polymerisation - induced phase separation:* LC is mixed with low molecular weight monomers or oligomers, which act as a solvent for the LC. Polymerization is induced by heat or electromagnetic radiations. The growing polymer chains phase separate from the LC to form a matrix surrounding discrete liquid crystalline

*Correspondence:

Email: manaila@physics2.physics.pub.ro

domains. The phase separation process is sensitive to: temperature, light intensity (in photo-cured systems), presence of impurities, solubility characteristics and molecular weight of the starting materials.

-TIPS- thermally - induced phase separation : thermoplastic polymer heated into a melt and mixed with a LC to form a single phase solution. The LC phase separates into droplets as the system is cooled back to room temperature. The droplet size in TIPS films can be controlled to an extent by the rate of cooling, with rapid cooling leading to smaller droplet sizes.

-SIPS- solvent evaporation- induced phase separation: the polymer is mixed with the LC and an organic solvent to form a single phase mixture. Evaporation of the solvent causes phase separation of the polymer and liquid crystalline phases. The droplet size can be controlled by controlling the rate of solvent evaporation, a smaller cooling rate leading to bigger droplets.

3. *Imbibing porous structures with LC :* organic membranes with open fibrous microstructure are imbibed with LC. (they need high voltages to orient an operate; the domain size of LC is very large, so that the zero-field states of these systems possess mediocre scattering properties)

4. *Glass - dispersed systems:* sol-gel chemistry has been used to create dispersed nematic systems within a silica glass matrix.

In this paper we study the phase transitions in E7/PMMA polymer dispersed liquid crystal films by the thermally stimulated depolarisation currents (TSDC)^{2,3,4} method and by differential scanning calorimetry (DSC). Polarized microscopy observations and optical transmission measurements are also used to interpret the phase transition temperatures.

2. EXPERIMENTAL

2.1. Sample preparation

We prepared PDLC films by the solvent induced phase separation method⁵. The polymer and the liquid crystal were mixed in equal ratios by weight. Then chlorophorm was added in a 6:1 weight ratio. After stirring well, the mixture was placed on ITO coated glass plates, and the chlorophorm was evaporated. Then another ITO coated glass plate was used to sandwich the PDLC film. We have used the nematic LC mixture E7 (Merck), having the following phase transition temperatures: - glass transition temperature: $T_g = -62^\circ\text{C}$ and the nematic -isotrop transition temperature: $T_{NI} = 59^\circ\text{C}$. The polymethyl methacrylate (PMMA) was obtained in the laboratory and has the $T_g = 112^\circ\text{C}$. The thickness of the E7 cell was $10\ \mu\text{m}$ and the thickness of the PDLC cell was $225\ \mu\text{m}$. The dimensions of the LC droplets in the PDLC film are $1\text{-}5\ \mu\text{m}$.

For the DSC experiments, the films have been solvent-casted and sealed in aluminium pans.

2.2. Experimental set-up

2.2.1. Thermally Stimulated Depolarization Currents (TSDC)

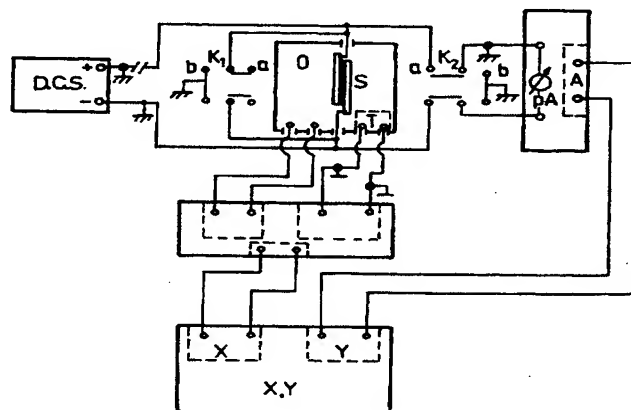


Fig. 1 Experimental set-up for TSDC measurements. D.C.S - D.C. voltage supply; O - thermostated oven; S- sample; T -temperature transducer; K_1 , K_2 - switches, a-measuring position, b - shortcircuit position; pA - picoammeter (TR 1452), A - amplifier; X, Y recorder (current intensity, temperature)

The experimental set-up for the TSDC measurements is shown in Fig.1. A copper thermostated oven with a controlled heating rate ($1^{\circ}\text{C}/\text{min}$) was used. The experimental set-up allows the simultaneous microscopic examination of the sample.

The following heating-cooling cycles were used: From the room temperature, the sample was first heated up to approx. 100°C , without applying polarizing electric field, and then it was cooled down to room temperature. The sample was again heated to 100°C and a field $E_p \neq 0$ was applied for 15 minutes; the sample was then cooled down to room temperature while maintaining $E_p \neq 0$. Finally the sample was short-circuited for 15 minutes to eliminate the accumulated charges, and heated to 110°C . Both heating and cooling cycles were registered when the picoammeter was connected.

2.2.2. The optical transmission measurements have been performed in polarized light (between parallel polarizers – classical Depolarized Light Intensity measurements). The light intensity versus temperature has been registered simultaneous with the TSDC measurements

2.2.3. Differential Scanning Calorimetry (DSC)

The measurements were performed with a Mettler-Toledo 30 DSC - control system TC10A/TC15, calibrated on 6 points over the range of temperature investigated, with glass medium sensor.

The samples have been cooled down from room temperature to -100°C with a rate of $-100^{\circ}\text{C}/\text{min}$ and, after equilibration, they have been heated with a rate of $5^{\circ}\text{C}/\text{min}$. Sequential DSC cycles did not show significant differences.

3. RESULTS AND DISCUSSIONS

After running more cycles of initial depolarization, we have registered the TSDC spectra for fixed polarizing electric fields E_p ^{7,8,9}. In Fig.2. is shown the TSDC spectrum for the pure liquid crystal E7 after applying a polarization field $E_p = 9\text{kV/m}$. A plateau corresponding to the nematic-isotropic transition is between $56-60^{\circ}\text{C}$.

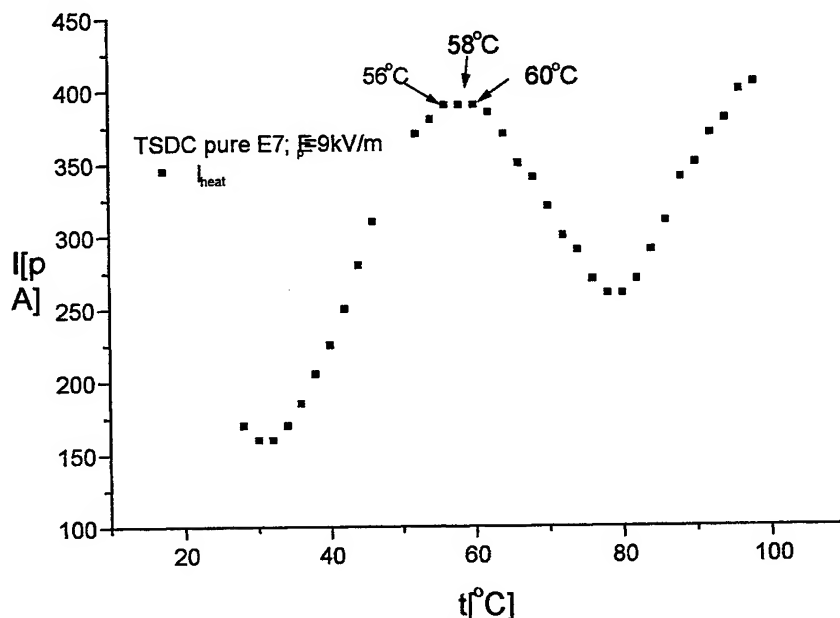


Fig.2. TSDC spectrum for pure E7 after $E_p = 9\text{kV/m}$.

In Fig.3 the depolarization current without polarizing field for the E7/PMMA sample is presented. We notice a shift of the nematic –isotropic transition towards lower temperatures and a higher intensity peak at about 90°C . This peak corresponds to the glass transition of the PMMA matrix.

The TSDC spectra for PDLC E7/PMMA after applying different polarizing fields are presented in Fig. 4 ($E_p=9\text{kV/m}$) and Fig.5 ($E_p=22\text{kV/m}$ and $E_p=40\text{kV/m}$).

During the polarization-depolarization cycles, we have simultaneously registered the transmittance of the samples. In Fig. 6 is shown the optical transmittance versus temperature for the E7/PMMA sample after applying $E_p=40\text{kV/m}$.

In Fig. 7 and in Tab. 2 are presented the results of the DSC measurements.

In Tab. 1 are presented the results of the TSDC measurements.

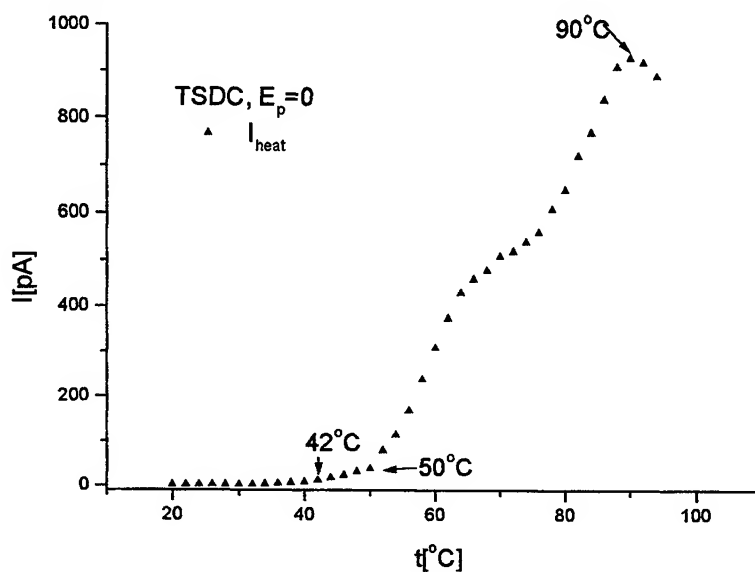


Fig.3 TSDC spectrum for E7/PMMA 50%, without polarizing electric field

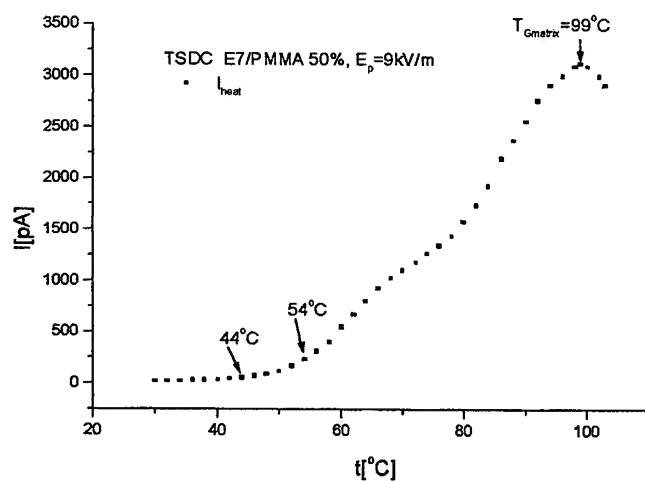


Fig.4 TSDC spectrum for E7/PMMA 50%, after: $E_p=9\text{kV/m}$

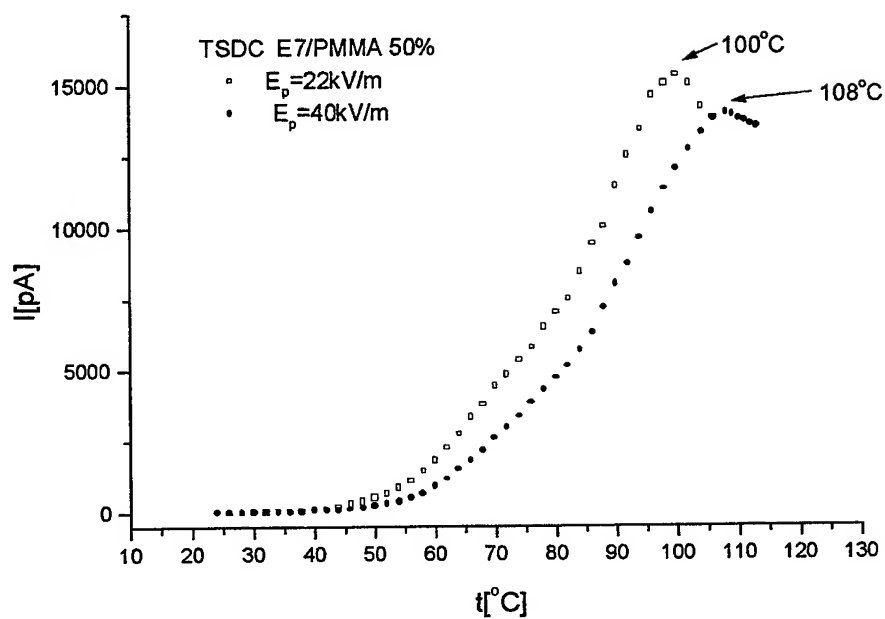


Fig.5 TSDC spectra for E7/PMMA 50%, after: □ $E_p = 22 \text{ kV/m}$, • $E_p = 40 \text{ kV/m}$

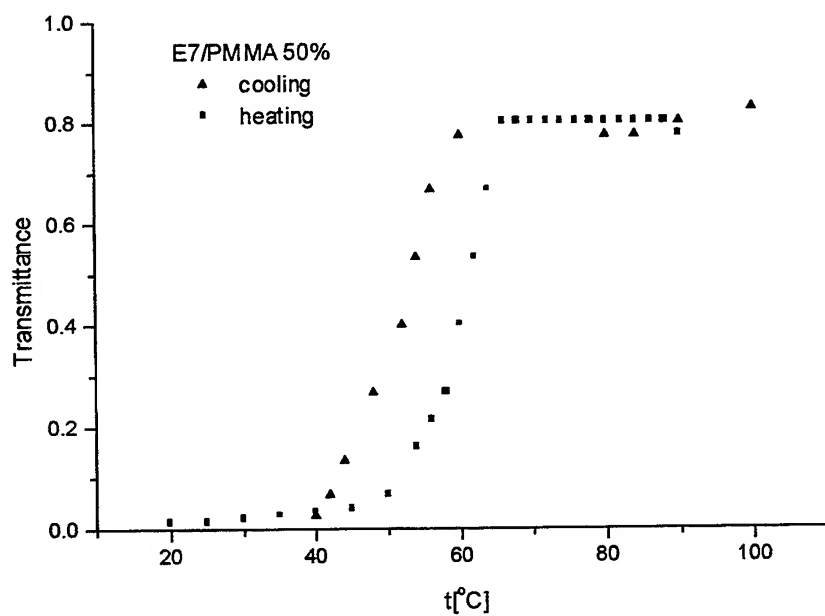


Fig.6 Transmittance versus temperature after $E_p = 40 \text{ kV/m}$. Thermal switch operation

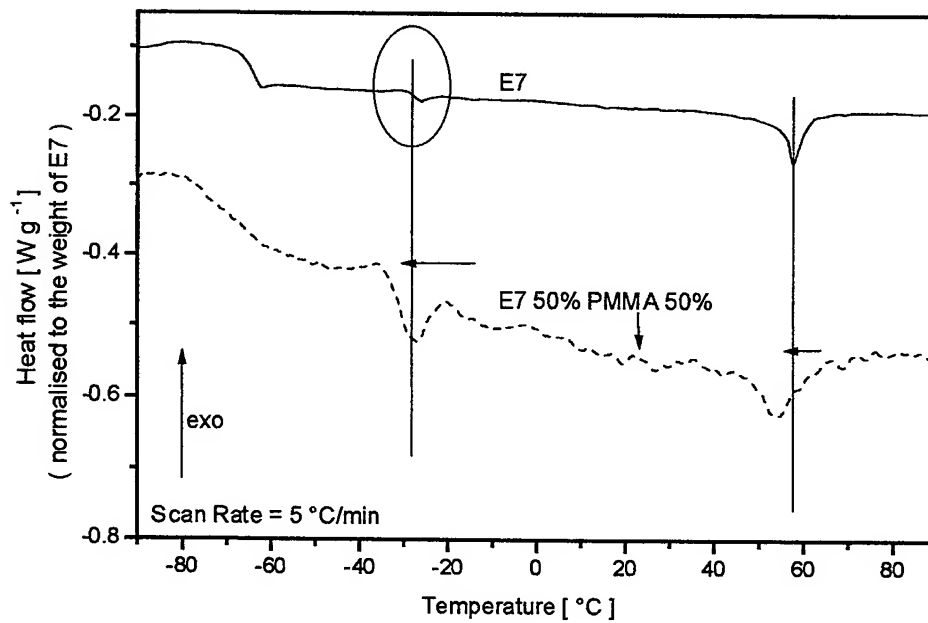


Fig.7 Differential scanning calorimetry on E7 and E7/PMMA 50%

Tab. 1 Results of the TSDC measurements: T_{N-I} and $T_{Gmatrix}$ for E7 and E7/PMMA 50% after different E_p

Composition	E_p [kV/m]	$T_{N-I}(\text{onset})$ [°C]	$T_{Gmatrix}$ [°C] (current peak)
E7 (pure)	0	59	-
E7 (pure)	9	56	-
E7 50% PMMA50%	0	42	90
E7 50% PMMA50%	9	44	99
E7 50% PMMA50%	22	45	100
E7 50% PMMA50%	40	46	108

When the LC is mixed with the PMMA its typical transition temperatures are shifted down a few degrees (see Tabs.1 and 2) and the peaks are broadened which is coherent with the dispersion of microdroplets and the consequential presence of a large interface between the LC and the polymer matrix.

Tab 2. Transition temperatures obtained by differential scanning calorimetry (DSC heating rate = 5 °C/min)

Composition\transition	Tg1 (midpoint)	Tg2 (midpoint)	nem.-isot. (onset)	nem.-isot. (peak)
E7 (pure)	-65.1	-28.6	53.3	57.1
E7 50% PMMA50%	diffuse	-32.4	49.15	53.9

4. CONCLUSIONS

Analyzing the results of the TSDC measurements we conclude:

1. As compared to the pure LC, the phase transition temperatures are lower in the composite material. This is also in good agreement with the DSC measurements.

2. When on the PDLC sample is applied a polarizing electric field (D.C.) the phase transition temperatures increase with the polarizing field. This can be explained as follows: when a polarizing electric field is applied at higher temperatures, the dipoles are oriented. Keeping the field applied during cooling, the dipoles are "frozen in". At the increase of the temperature, thermally stimulated depolarization currents are registered. If the polarizing field is stronger, more dipoles are oriented, and more energy, that is higher temperature will be needed to disorient them and to pass in a "glassy" state.

Analyzing Fig. 6, we observe a high optic transmittance of the sample in the "on" state. The transmittance versus temperature curve also shows a good "on"- "off" ratio and a steep slope of the nematic-isotropic transition. At the decrease of the temperature hysteresis is obtained, the $T_{N-I, cool}$ being lower than $T_{N-I, heat}$. Thus the thermal switch operation is demonstrated.

REFERENCES

1. P.S. Drzaic, "Liquid crystal dispersions" *World scientific*, Singapore, 1995.
2. J. Vanderschueren and J. Gasiot, *Thermally Stimulated Relaxation in Solids*, ed. Braunlich, Springer Verlag, Berlin 1979.
3. R. Sharma and L. V. Sud, "Temperature-dependent currents in unpolarised poly(vinyl alcohol)" *J.Phys. D: Appl. Phys.*, **14**, p. 1671, 1981.
4. M. Honciuc, I. Cuculescu, M. Socaciu, R. Bena and V. Stoian, "Build-up of thermoelectrets at phase transitions in fatty acids", *Phase transitions*, **51**, p. 231, 1994.
5. D. Manaila-Maximean, R. Bena and A. M. Albu, "Electric and electro-optic investigations on polymer dispersed liquid crystal films" *Modern Physics Letters B*, **11**, 9&10, p. 431, 1997.
6. R. Roussel, U. Maschke, X. Coqueret and J.-M. Buisine, "Optical and thermophysical properties of polymer dispersed liquid crystals (PDLC)" *C. R. Acad. Sci. Paris*, **326**, Serie II b, p. 449, 1998.
7. Z. Z. Zhong, D. E. Schuele, W. L. Gordon, K. J. Adamic and R. B. Akins, "Dielectric properties of PMMA/E7 polymer dispersed liquid crystal" *Journal-of-Polymer-Science,-Part-B-(Polymer-Physics)*. **30**, no.13, p. 1443, 1992.
8. D. Manaila-Maximean, M. Furlani, B.-E. Mellander, R. Bena, C. Rosu, T. Pop, and C. Motoc, "Phase transition investigations in polymer/liquid crystal composite materials" *4th Liquid Matter Conference*, Granada, Spain, 3-7 July 1999.
9. D. Manaila-Maximean, M. Furlani, B.-E. Mellander, R. Bena, C. Rosu, T. Pop, and C. Motoc "Phase transition investigations in polymer/liquid crystal composite materials", submitted to *Modern Physics Letters B*, 1999.

C-Ni multilayer reflectors: an AFM roughness study

M. Ulmeanu^a, G. Radu^b, P. Budau^c, M. Enachescu^{d*}

^aNational Institute for Laser, Plasma and Radiation Physics, Department of Lasers,
P.O. Box MG-36, Bucharest-Magurele, Romania

^bNational Institute for Laser, Plasma and Radiation Physics, Electronic Quantum Laboratory,
P.O. Box MG-36, Bucharest-Magurele, Romania

^cUniversity of Bucharest, Faculty of Physics, P.O. Box MG-11, Romania

^dLawrence Berkeley National Laboratory, University of California, Berkeley, CA 94720

ABSTRACT

Amorphous C-Ni superlattice films designed as normal-incidence reflector for 5 nm have been grown on quartz substrates by magnetron sputter deposition in Ar discharge. An extended set of characterization techniques has been applied: Transmission Electron Microscopy (TEM) and Atomic Force Microscopy (AFM) in order to characterize the growth conditions. TEM measurements revealed information about the evolution of smoothness and the uniformity of the multilayer structure function of the distance to the substrate. A new DSP-controlled AFM system has been involved in investigating the surface topography of the final surface of the multilayer structure as well as the substrate. A detailed analysis of AFM topographic images is presented. Special attention has been paid to an important parameter for such mirrors, the surface roughness, for nanometric and micrometric areas, involving AFM tips with different radius of curvature. Roughness analysis as well as the implication of the different radius curvature tips used in AFM-contact experiments are presented together with the power spectral density function calculation.

Keywords: multilayer, RF magnetron sputtering deposition, atomic force microscopy, surface roughness, root-mean-square roughness, power spectral density

1. INTRODUCTION

The interest in producing layered synthetic microstructures has increased continuously in the last years due to the unique properties that many materials combinations have been shown to exhibit. By varying the layer thickness, the number of interfaces and the choice of constituent materials, the multilayer structure offers unique opportunity that is simply not possible with ordinary diffraction elements^{1,2}. These multilayer mirrors offer high flexibility of use because of their ability to choose the spacing parameters, the nature of the constituents and the number of the bilayers.

High reflectivity soft X-ray mirrors require uniform layer thicknesses and densities, high stack regularity, perfectly smooth and sharp interfaces, and substrates that are flat. Different vacuum deposition techniques have been used in the last few years to produce synthetic layered microstructures. An RF magnetron sputtering technique is a good choice providing film purity, process repeatability and uniformity of deposition, ability to cover complex shapes and where numerous periods are needed. The most successful multilayer mirrors reported for 50 Å region are obtained from the transition elements (V, Cr, Mn, Fe, Co, Ni) combined with spacer layers of carbon.

In this paper a detailed study of the C-Ni multilayer surface quality is presented. From Transmission Electron Microscopy (TEM) measurements we learned about the evolution of smoothness and the uniformity of the multilayer structure function of the distance to the substrate. In order to investigate the surface topography of the final surface of the multilayer structure as well as the substrate a new DSP-controlled Atomic Force Microscope (AFM) system has been involved. The comprehensive analysis of AFM topographic images has been performed with emphasis on important parameters for such mirrors, (a) the surface roughness, for nanometric and micrometric areas, involving AFM tips with different radius of

* Correspondence: E-mail: mulm@ifin.nipnc.ro; Fax: (401) 423 17 91

curvature, and on (b) power spectral density function evaluation. Roughness analysis as well as the implication of the different radius curvature tips used in AFM-contact experiments are presented.

2. EXPERIMENTAL

One of the most known and used optical coating deposition technique is that based on RF sputtering. Sputtering is a process operating on an atomic or molecular scale, governed by the momentum transfer of incident atoms to the target material atoms and this momentum transfer can lead to the ejection of a surface atom (sputtering). Since in this kind of process the atoms arrive individually, it is an appropriate technique for growing films of atomic thicknesses or small multiples thereof or molecule-by-molecule also.

The targets used for our depositions were 10 cm diameter disks of 99.9 % pure Ni and C. Plasma was ignited at an operating pressure of ~ 0.6 Pa due to Ar flow of 60 sccm measured with a mass flow controller of 0.2 % accuracy. The power of discharge was 175 W for C deposition and 125 W for Ni. The deposition rates for both Ni and C were approximately 0.2 Å/s, with a target-to-substrate distance of about 8 cm. The deposition rate was measured using quartz crystal of 0.1 Å/s accuracy. A system of individually shutters was used in order to control the deposition process initialisation. To minimize intermixing between layers, a delay of few seconds between the closing of one shutter and the opening of the other was employed.

The quartz substrates were selected because their surface are microscopically smooth. The substrates were initially at room temperature and no effort was made to control their temperature during deposition.

In order to increase reflectivity response, an optical component has to be made using a stack of interfaces set at the right spacing. This lead to a constructive interference obtained from the partially reflected waves of each interface thus the absorption loss should be lower than reflectivity per interface. In designing the best parameters - the optimum thickness and the number of periods required - we followed the first good approximate calculation proposed in 1977 by Vinogradov *et al.* and completed in 1987³. We considered that such simplified formulas could be used with confidence for good predictions.

For the wavelength $\lambda = 5$ nm the optical constants for Ni and C are:

nickel	$\tilde{n}_{Ni} = n_1 - ik_1 = 0.9832 - 0.00903i$
carbon	$\tilde{n}_C = n_2 - ik_2 = 0.996 - 0.000926i$

We assume that the nickel thin film takes the share α of all period l , with $0 < \alpha < 1$. Following the simple transcendental equation we found the optimum value $\alpha = 0.4$. Thus, the number of periods should be 100 and the thickness of the carbon and nickel layers 1.5 nm and 1 nm respectively for maximum reflectivity ($\lambda = 5$ nm) of around 28.4% at 4.5° incidence angle.

For the same reason of maximum reflectivity, it is necessary to form smooth, stable boundaries between thin films. It is known that spacer thin films of carbon are better for X-rays ($4.5 \text{ nm} < \lambda < 10 \text{ nm}$), forming stable interfaces without interdiffusion with most metals and with an effective roughness $\sigma_{rms} = 0.3 \text{ nm}$.

Due to the great number of periods required, at this stage of our work we chose to deposit fewer periods in order to have a prior knowledge about thin films and interface characteristics for this method. The multilayer structure was obtained by growing alternatively C and Ni thin films at a fixed substrate-target distance $D = 8 \text{ cm}$. During the fabrication an initial layer of C (1.5 nm) was deposited on the substrate. Then 16 layers of Ni (1 nm), alternating with 15 layers of C (1.5 nm) were deposited.

3. RESULTS AND DISCUSSION

3.1 Transmission Electron Microscopy results

TEM investigations have been performed on a JEOL 200CX system operating at 200 kV. Samples have been prepared by the extraction replica technique.

The corresponding diffraction pattern of the multilayer structure revealed the complete oxidation of the Ni layers leading to the fcc NiO structure (bunsenite) with the cell parameter $a = 4.1769 \text{ \AA}$. The NiO layers consist of small crystallites (few nanometers size) which determine the diffuse aspect of the diffraction rings.

The micrograph presented in Fig. 1 shows the cross-section of 32 alternative C-Ni multilayers. It is worth to mention that the layers smoothness and the uniformity increase with the distance from the substrate, as it can clearly be observed from the TEM micrograph. These values seem to reach a minimal stationary value after the first 10 deposited layers. Also, the TEM micrograph reveals a regular uniformity in our multilayer structure obtained by alternating the C and Ni layers.

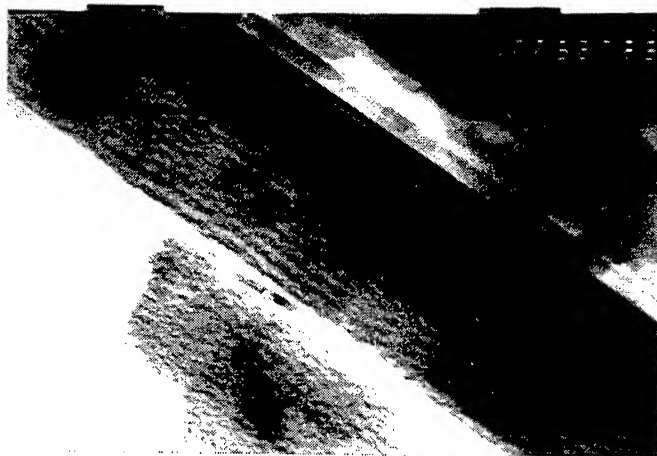


Fig. 1 Cross-sectional TEM image showing C-Ni multilayer on quartz substrate

3.2 Atomic Force Microscopy measurements

Using the capabilities of an AFM system, we started a systematic approach of investigating the surface quality of the final multilayer structure. The AFM measurements were performed at the NANOTECH-21 laboratory using a custom built DSP-controlled system [NANOTECH-21, Magurele-Bucharest, P.O. Box MG-15, Bucharest, Romania]. The optical deflection method is used to measure the bending of the AFM lever sensor by tip-surface forces. For these studies we used commercial available microfabricated cantilevers. Using this system we are able to routinely measure atomic lattice resolution on mica and HOPG samples, under ambient conditions. All results presented in this work were obtained in AFM-contact mode experiments.

In Fig. 2 is presented a large area image of $9.3 \mu\text{m} \times 9.3 \mu\text{m}$ recorded on the C-Ni multilayer structure. It is obvious that the end-layer surface quality depicted in Fig. 2 presents a high level of smoothness correlated with a very low surface roughness.

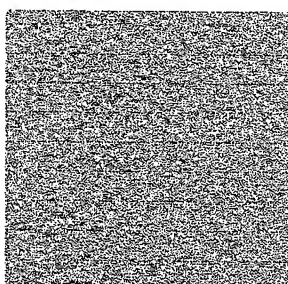


Fig. 2 Top view AFM-contact mode image of a 32-multilayer C-Ni structure. The scanned area is $9.3 \mu\text{m} \times 9.3 \mu\text{m}$

In order to quantify the multilayer surface quality we performed roughness calculations for a very large set of data. In our calculations we involved parameters like standard roughness and root-mean-square roughness. The standard roughness is defined as:

$$R_s = \frac{1}{N} \sum_{i=1}^N |h_i - \bar{h}| \quad (1)$$

where h_i represents the height value at each data point, \bar{h} represents the profile mean value of the surface, and N represents the number of data points in the analyzed profile. Thus, the standard roughness or the arithmetic average roughness-height, represents the arithmetic mean of the deviations in height from the profile mean value, where the profile mean value is defined as:

$$\bar{h} = \frac{1}{N} \sum_{i=0}^N h_i \quad (2)$$

The root-mean-square roughness is defined as:

$$RMS = \sum_{i=1}^N \left[\frac{(h_i - \bar{h})^2}{N} \right]^{1/2} \quad (3)$$

The values of R_s , RMS , average height and maximum height calculated using a large measurements statistics are presented in Tab. 1.

Tab. 1 The measured values of R_s , RMS , average height and maximum height

R_s [nm]	RMS [nm]	Average height [nm]	Maximum height [nm]
0.76	1.07	4.1	6.4

According to the R_s and RMS values obtained the multilayer surface roughness could be characterized as being in the nanometer and sub-nanometer range, representing a high quality ended surface for our reflectors. The values of the average height and maximum height determined from our measurements support strongly the very low surface roughness and the high quality of the reflectors. As can be observed from the Table 1, statistically we obtained a difference of only 2.3 nm between the average height and the maximum height of the surface features for scanned surfaces of $9.3 \mu\text{m} \times 9.3 \mu\text{m}$. This strongly support the smoothness and the low roughness of our mirrors for relatively large investigated areas.

Moreover, trying to characterize and understand more the quality of our reflectors, we performed additional AFM measurements involving tips with different radius of curvature. In Fig. 3 is presented a three dimensional AFM-contact image of $0.5 \mu\text{m} \times 0.5 \mu\text{m}$ acquired with an AFM tip having a radius of curvature of about 50 nm.

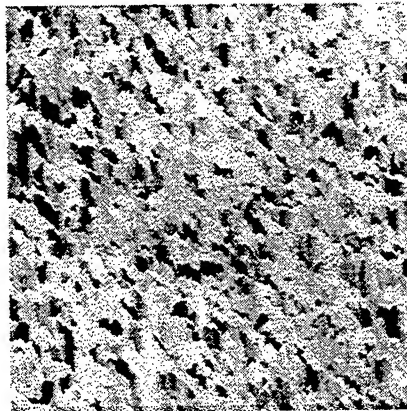


Fig.3 Three dimensional AFM-contact mode image of a 32-multilayer C-Ni structure. The scanned area is $0.5 \mu\text{m} \times 0.5 \mu\text{m}$ and the radius of curvature of the tip used for imaging is about 50 nm

Routinely we determine the characteristics of the AFM tips involved in measurements, consisting of obtaining a full 3-D image of the cantilever tip, the cantilever tip angle and its curvature radius. For AFM-tip characterization we use silicon calibration gratings having tip-like features with symmetry of tip sides, small tip angle (less than 20 degrees), small curvature radius of tip (less than 10 nm) [commercially available from NT-MDT Co., Zelenograd Research Institute of Physical Problems, Moscow, Russia]. Fig. 4 depicts a three-dimensional image of the silicon grating used for the AFM-tip characterization, showing a regular grating of tip-like features with a distance periodicity of about 2.12 μm .

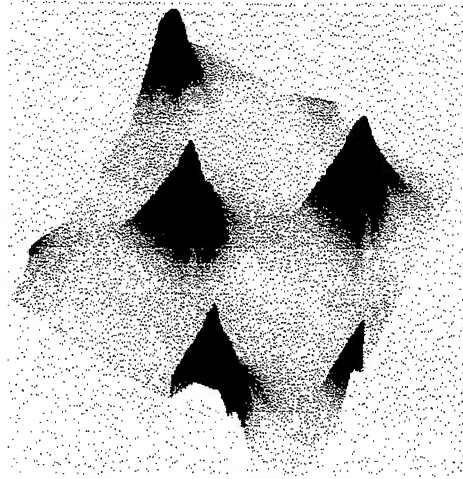


Fig. 4 AFM-contact mode image of a silicon grating used for AFM-tip characterization. The scanned area is 4 μm x 4 μm

The AFM-tip used of taking the image presented in Fig. 4 is the same one used for acquiring the image from Fig. 3. Analyzing images like one presented in Fig. 4 we were able to determine the AFM-tip cone angle, shape, and local radius of curvature. The radius of curvature of the AFM-tips is simply determined by fitting a parabola at the apex of the tip-like features presented in Fig. 4. For the AFM-tip involved in the imaging of Fig. 4 we determined a cone angle of about 57° and radius of curvature of about 50 nm.

In Tab. 2 are presented the results obtained for the surface roughness of the C-Ni multilayers using for measurements AFM-tips with radius of curvature of about 50 nm and of about 250 nm.

Tab. 2. The measured values of R_s and RMS using AFM-tips with different radius of curvature

Lever spring constant [N/m]	Tip radius of curvature [nm]	R_s [nm]	RMS [nm]
0.12	50	0.97	1.23
0.17	250	0.84	1.07

The results presented in Tab. 2 reveal in a new light the fact that the surface quality of our C-Ni deposited reflectors is indeed high. The fact that both the R_s and RMS values for each individual AFM-tip have close values demonstrate the high quality of the surface, i.e. the surface is of a smoothness which gives a roughness almost constant for images recorded with tips having radius of curvature of about five times different in size. This represents a self-explaining test of surface quality and is a good example of AFM imaging where the tip-surface convolution does not play an important role in the surface topography determination. Note also the small increase in the surface roughness detected with the decreasing the tip radius of curvature.

In order to determine the influence of the multilayer surface microstructure on scatter losses we performed power spectral density (PSD) function calculations. The PSD function is defined as the square magnitude of the Fourier Transform of the surface profile. Therefore, from a line profile $h(x)$:

$$PSD(f) = \frac{1}{L} \left| \int e^{2\pi i f x} h(x) dx \right|^2 \quad (4)$$

in units of $\text{\AA}^2/\mu\text{m}$, where: L is the scan length [μm], $h(x)$ is the line profile [\AA], x is the scanning coordinate [μm], and f is the wave number [μm^{-1}].

Following a PSD analysis one can easily determine whether the substrate or the film structure or both are the cause of scatter losses⁴. The PSD curves of the quartz substrate and of C-Ni multilayer structure deposited by RF magnetron sputtering technique are depicted in Fig. 5. In the high frequency region the PSD curves are mainly determined by the intrinsic film structure and in this case are considerably decreased compared with the PSD of the substrate. Toward lower frequencies, the PSD of the film approaches the PSD of the substrate until the curves finally coincide. This means that the substrate structure gives rise to scatter. The fact that the PSD curves decreases in the high frequency region means that the film does not replicated the substrate roughness and the deposition parameters used for the RF sputtering deposition are quite well adjusted. In order to further reduce scatter losses the substrate quality should be improved, either by choosing a new substrate or by special polishing treatment of the present substrate.

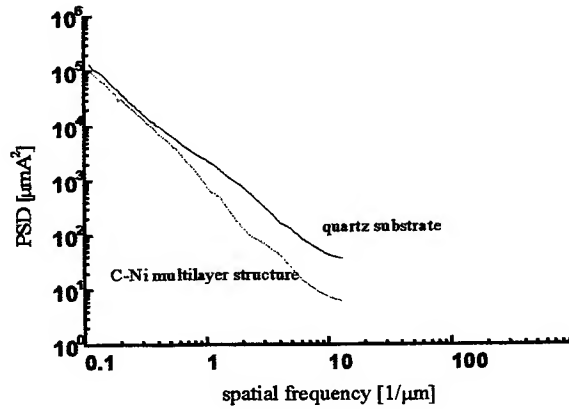


Fig. 5 PSD functions of a quartz substrate and of a C-Ni multilayer structure on this substrate. The PSD functions were obtained from AFM measurements with scan area of $9.3 \mu\text{m} \times 9.3 \mu\text{m}$

4. CONCLUSIONS

Under the deposition conditions described in the experimental details we were able to obtain smooth layers of C and Ni by RF magnetron sputtering technique. The structural characteristics of the multilayer were determined by TEM, the roughness and PSD spectra of the substrate and C-Ni multilayer structure by AFM.

The TEM measurements indicate smooth surfaces, a multilayer structure with a continuous aspect and for larger periods the smoothing effect increases together with the uniformity of the layers. The layers smoothness and the uniformity increase with the distance from the substrate. The roughness and height measurements indicate the C-Ni multilayer surface as being in the nanometer and sub-nanometer range, representing a high quality ended surface for our reflectors. Similar conclusions regarding the reflectors final surface quality were obtained by measurements of surface roughness involving AFM-tips with a large range of tip radius. PSD curves generated with AFM data indicates the substrate microstructure as being the major cause of scatter. The scatter losses can be reduce through the improvement of substrate polish.

We note that with the knowledge about the film characteristics afforded by the complementary characterization techniques used in this work, it should now be possible to improve the quality of the mirrors and its reflectance.

ACKNOWLEDGMENTS

M. Ulmeanu and G. Radu are greatly indebted to NANOTECH-21 laboratory for the continuous supervision and great support provided during this work.

*Permanent address: University of Bucharest, Faculty of Physics, P.O. Box MG-11, Romania

REFERENCES

1. H.P. Klug and L. E. Alexander, *X-Ray Diffraction Procedures*, Wiley, New York, 1990.
2. J.M. Cowley, *Diffraction Physics*, North-Holland, Amsterdam, 1981.
3. A.V. Vinogradov and B. Y. Zeldovich, "X-ray and far UV multilayer mirrors: principles and possibilities," *Appl. Opt.* **16**, pp. 89-93, 1977.
4. S. Jakobs, A. Duparre and H. Truckenbrodt, "Interfacial roughness and related scatter in ultraviolet optical coatings: a systematic experimental approach," *Appl. Opt.* **38**, pp. 1180-1193, 1998.

Preparation of a copolymer for second order nonlinear optics

Ana-Maria Albu^{*a}, Bogdan Marculescu^a, Doina Manaila-Maximean^b, Allain Trouillet^c

^aUniversity "Politehnica Bucuresti", Department of Polymer Science, 149 Calea Victoriei, Bucharest, Romania,

^bDepartment of Physics, 313 Splaiul Independentei, 77206, Bucharest, Romania, Email: manaila@physics2.physics.pub.ro

^cUniversity Jean Monnet of Saint Etienne, 23 rue Francis Bolieu, Saint Etienne, France

ABSTRACT

During the last decade the interest in polymeric materials for second-order nonlinear optical properties has been constantly growing. They combine structural electronic properties, with good thermal and mechanical stability, a relatively low cost and easy processability. The second order nonlinear optical (NLO) properties of such materials have electronic origin, with an ultra-fast response time. In the present paper, we report the preparation and characterisation of a new material with a higher concentration of a NLO chromophore. We have synthesised a new dye monomer by the phase transfer catalysed reaction. We have prepared the copolymer with styrene, by bulk copolymerization; the initiator was di-t-butyl peroxide at 120 °C. We have characterised the monomer and the copolymer by IR; UV-Vis; ¹H-NMR spectroscopy. The glass transition temperature (T_g) and the melting point have been obtained using the differential scanning calorimetry. For studying the NLO properties, the samples have been poled by the Corona poling method, in an electric field of approx. 100V/ μ m. We have appreciated the second-order nonlinear coefficient by comparing the light signal passing through the sample, with the signal passing through a standard quartz plate.

Keywords: nonlinear optics, polymeric materials, second harmonic generation

1. INTRODUCTION

The area of nonlinear optics of organic molecules and polymers offers exciting opportunities both for fundamental and technological development. As a result, in recent years, there has been great interest in the synthesis of novel monomers and polymers with the intention of producing materials having large nonlinear optical properties¹⁻⁵.

The electronic, second-order nonlinearity is closely related to microscopic electronic structure. The efficiency of the nonlinear optical process depends on how easy it is for the optical electric field of the fundamental beam to polarise the valence electrons of the molecule along the field in a nonlinear way⁶.

Materials used in guided optics and optical processing of the information should be characterised by high values of their electrooptical coefficients (both of II-nd and III-rd order). A chromophore segment included in a polymer designed for nonlinear optics should contain the following structural elements^{6,7}:

- a π electron system bearing the non-linear signal of III-rd order;
- an electron donor that strengthen the non-linear signal of second order;
- the acceptor, that orientates the non-linear signal of second order.

On the other hand, chromophores accountable for NLO behaviour must be incorporated into a continuous polymeric matrix; its essential properties have to fulfil the following requirements:

- optimal distribution of NLO chromophore fragments;
- transparency;
- an adequate stiffness (given by a highly enough T_g value) to keep the arrangement of chromophores in electrical

* Correspondence: a.albu@tsocm.pub.ro, Phone: +401 650 25 14

field

- the material should be easily processable, i.e. it should present a reasonable molecular weight (min. 10^4).

The macromolecular structures fulfilling the above mentioned restrictions may be obtained according to alternative strategies⁸:

1. The chromophore fragment may be attached to a pre-formed macromolecular chain, through a polymer-analogous reaction; this solution is satisfactory, provided that both the polymer and the low-molecular reactant, respectively, possess condensable organic functions to assure a quantitative conversion without any secondary reactions.

2. A macromolecular arrangement with a predictable architecture may be obtained through the copolymerisation of some monomers containing incorporated chromophore fragments. In this case, the main restriction that must be satisfied is connected with the intrinsic structure of monomers and their purity that should not impede the copolymerisation process; the chain transfer should also be limited⁹.

The generation of macromolecular structures for NLO applications can be obtained by the copolymerization of comonomers having chromophore fragments chemically incorporated, with classical monomers such as styrene (S), methyl methacrylate (MMA)¹⁰.

In our previous papers, we have highlighted the kinetics of the radical copolymerization of CM with styrene or methyl methacrylate and the primary physical properties of the reaction products. The preliminary data showed that:

- The coloured monomers (CM) can be incorporated in a glass matrix such as polymethyl methacrylate (PMMA) or polystyrene (PS) without major difficulties. The maximum level of CM incorporation is decided only by the intense transfer activity manifested by these monomers in radical polymerisation. From the kinetics point of view, the presence of the CM does not have delaying or inhibition effects. On the contrary, even at low concentrations, they increase the polymerisation rate, thus being possible high conversion rates even for reasonable small time intervals^{11, 12}.
- The incorporation of the monomer units derived from CM in the copolymeric chain preserves the optical properties specific to the chromophore of each structure.

2. EXPERIMENTAL

2.1. Sample preparation and characterisation

We have synthesised the Schiff base type monomer (Fig. 1) by a serial of condensation reactions.

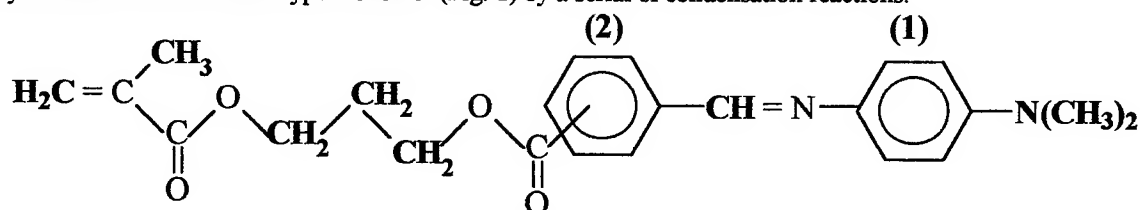


Fig.1 The structure of the azomethynic monomer A1

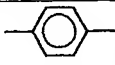
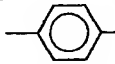
The melting temperature of the monomer was determinate by differential scanning calorimetry, using a DSC92-Seteram calorimeter and the results are presented in Tab. 1. The synthesised monomer was characterised by the UV-VIS absorption spectra using a JASCO spectrophotometer. The IR spectra have been obtained using a FT-IR Bio Rad spectrophotometer. The solvent was chloroform.

Tab. 1 The UV-VIS absorption characteristics and the melting temperatures of the synthesised monomer

monomer	λ_1 (nm)	ϵ_1 (l/mole cm)	λ_2 (nm)	ϵ_2 (l/mole cm)	T_f (°C)
A1	262	19 320	402	21 930	108,9

The coloured monomer has two absorption spectra, one in the UV and the other in the visible range. The molar extinction coefficients are of the order of 10^4 , in full agreement with the chemical structure of the synthesised monomer. The H^1 -NMR spectrums have been obtained using a Bruker WP 300 installation and are presented in Tab. 2.

Tab. 2 The H^1 -NMR spectrum for the A1 monomer

R / δ (ppm)	A1
$H_2C=C$	6,13 and 5,57 (2H)
$CH_2-CH_2-CH_2$	2,5 and 8,35 (2H)
$CH_2-CH_2-CH_2$	4,42 and 4,35 (2H)
$H_3C-C=$	1,95 (3H)
 (1)	7,32 and 6,76 (4H)
 (2)	8,1 and 7,94 (4H)
$-CH=N-$	8,57 (1H)
$-N(CH_3)_2$	3 (6H)

As one can observe from Tab. 2, the interpretation of the H^1 -NMR spectrum is in full agreement with the proposed structure. The values for each monomer characteristic group are determined by $-N(CH_3)_2$.

The synthesis of the polymer was done by the mass polymerisation procedure, using as initiator di-*t*-butyl peroxide, the working temperature was 120 °C. The copolymers have been separated by precipitation in methanol. The characteristics of the substrate and the main features of the synthesised copolymers are presented in Tab. 3.

Tab. 3 The characteristics of the synthesised copolymers. x_2 : molar fraction of CM in the substrate; X_2 molar fraction of CM in the copolymer

code	M_{oT} (mole/l)	x_2	X_2	t_r (hours)	C (%)	T_G (°C)	λ_{max} (nm)	ϵ (l/mole cm)	M_n
S-A1	*9,77	0,24	0,10	18,00	50	92	248 402	28100 20650	6 000
	*9,19	0,11	0,15	22,50	30	68	249 402	35910 19790	10 000

For the evaluation of the optical properties, we measured the absorption spectra in the UV-VIS domain and we evaluated the molar extinction coefficients.

According to the data in Tab. 3, for the two proposed substrates we obtained macromolecular structures with a high content of A1 structural units. The experimental proof that these A1 sequences are included in the polymer chain was obtained by registering the H^1 -NMR spectrum for the synthesised polymers ($CDCl_3$, 300MHz, TMS references). On the basis of these spectra we calculated the molar ratio of coloured monomer (X_2) in the copolymer structure. These values are presented in Tab. 3, together with the initial composition of the reaction substrate (x_2).

For the calculation of the molar extinction coefficients of the copolymer we used the copolymer concentrations and their composition; thus we obtained a molar concentration of the A1 structural units, which determine the total value of the global extinction. The molar extinction coefficients for the copolymers are maintaining the magnitude order of the corresponding monomers. We notice that for the same copolymer structure, at the increase of A1 concentration the molar extinction coefficients are increasing.

2.2. Film preparation for optical measurements

Chloroform solutions of the obtained polymeric material of 12g/dl concentration have been prepared and spread by spinning on ITO (indium tin oxide) covered glass plates. Homogenous films of micrometer widths have been obtained and poled in electric field by the Corona-poling technique at a temperature greater than the polymer glass transition temperature. After a few minutes, the sample was slowly cooled down to the room temperature, maintaining the electric field applied. The value of the electric field inside the sample was of about 100V/ μ m.

2.3. Nonlinear optical measurements¹³

The second order nonlinear coefficients d_{31} and d_{33} of the poled polymeric samples have been measured using the experimental set-up schematically presented in Fig. 2.

The principle of the measurement consists in simultaneously registering the second harmonic signals generated in the reference quartz plate and in the sample. The Nd:YAG laser beam ($\lambda = 1064$ nm) is TM polarised. A small part of the emerging from the prism light is deviated towards a photodiode PD and helps synchronising the oscilloscope.

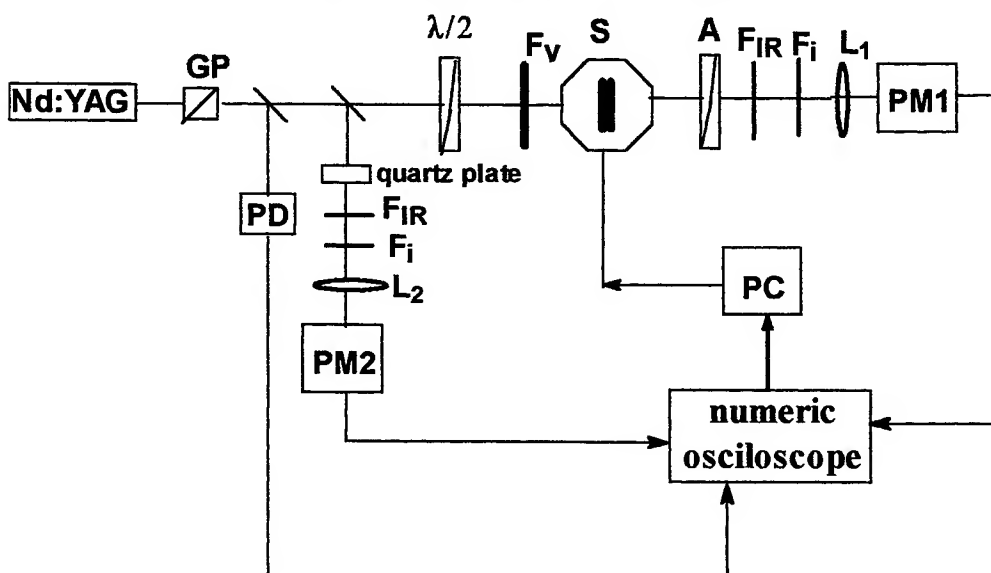


Fig. 2 Second harmonic generation experimental set-up.

GP: Glan prism polarised; PD: photodiode; L1, L2: lenses; FI: interferential filter; FIR: infrared filter, FV: visible filter, HWP: half-wave plate; PM1, PM2: photomultipliers; S: sample; A: analyser

Another part of the light is deviated towards the reference quartz plate ($d_{11} = 0.34$ pm/V), where the second harmonic signal is generated. The emerging from the quartz plate signal is filtered for selecting the wavelength $\lambda = 532$ nm, focused and detected by the photomultiplier PM2. The numerical oscilloscope registered the corresponding electrical signal. Second harmonic is also generated in the rotating sample, the rotation being computer piloted. The emerging optical beam is detected by the photomultiplier PM1, and the electrical signals enter the oscilloscope. The second order nonlinear coefficients have been determined by comparing the intensity of the signals generated in the reference quartz plate and in the samples, the results being presented in Tab. 4.

Tab. 4 Physical characteristics of the S-A1 copolymer

Property	S-A1	quartz
*X ₂	0,15	-
10 ³ M _n	6	-
T _G (°C)	70	-
λ _{max} (nm)	402	-
n ₀ ^{1064 nm **}	-	1,534±0,0001
n _{2ω} ^{532 nm ***}	-	1,547±0,0001
d ₁₁ (pm/V)	-	0,340±0,0400
d ₃₁ (pm/V)	4,2	-
d ₃₃ (pm/V)	12,8	-
d ₃₁ /d ₃₃ (pm/V)	2,95	-

*molar fraction of A1,

**refractive index of the medium at frequency ω,

*** refractive index of the medium at frequency 2ω;

Comparing the data presented in Table 4 with the corresponding data given in literature, we conclude that the S-A1 structure is of great interest for NLO applications, its NLO coefficients being twice as big as the known classical structures^{7, 14, 15}.

Analysing the data presented in Tab. 4, we observe that the nature of the chromophore bond is determinant for the value of the NLO coefficients. Thus, the structure with azomethynic chromophore is characterised by high values of the NLO coefficients. The presence of a great number of methylen groups between the chromophore structure and the methyl methacrylate results in an increase value of the NLO coefficients. A possible explanation of this phenomenon is the greater flexibility of the chromophore segment, thus favouring the orientation of the macromolecular structure.

3. CONCLUSIONS

The monomer A1 has been characterised by the IR, UV-VIS and H¹-NMR spectra, confirming the proposed structure.

The UV-VIS and IR absorption spectra show a shift of the absorption level (UV-VIS) towards the visible range as a result of the conjugation of the bathochrome and hypsochrome effects of the substitutes and a shift of the absorption bands specific to the functional groups as a result of the internal electronic conjugation.

The orienting of the molecular dipole (from left towards right) is determined by the strong electron donor effect showed by the -N(CH₃)₂ group.

To render evident the optical properties, the most accessible analyse is the UV-VIS absorption, and the evaluation of the molar extinction coefficients; their values (of the order 10⁴) are within the limits given in the literature for the conjugate systems.

The copolymers of the A1 monomer with the styrene have been obtained by the mass polymerisation procedure, and are characterised by high molecular mass (10⁴).

Although the coloured monomer fraction is relatively small (15 %), the analyse of the UV-VIS absorption spectrum renders evident the preservation of the absorption wavelength range and of the magnitude order of the molar extinction coefficients. Consequently, the inclusion of the coloured monomers in saturated chains does not attenuates the optical properties, but increases them.

The obtained NLO coefficients for the S-A1 structure are twice as big as the NLO coefficients of the classical known structure.

These results recommend the alchyl-methacrylic structures as support for the structures with NLO applications. Further improvement of the optical properties can be obtained by increasing the monomer concentration in the copolymer and by the "freezing in" the macromolecular structure by the cross linking induced during poling.

REFERENCES

1. J. Williams, D. Pugh, J. O. Morley, J.F.Nicoud and J. R. Twieg "Nonlinear optical properties of organic molecules and crystals", 1, *Academic Press*, New York, 1987.
2. D. R. Kanis, M. A. Rather and T. J. Marks "Design and Construction of Macromolar Assemblies with Large Second-order Optical Nonlinearities. Quantum Chemical Aspects", *Chem. Rev.*, 94, p. 195, 1994.
3. A. E. Stiegman, J. W. Perry and L-T Cheng, "Second-order Nonlinear Optical Properties of Donor-Acceptor Acetylene Compounds in Organic Materials for Non-Linear Optics II" ed. By R. A. Hann & D. Bloor, *Roy. Chem. Soc. Of Chem.*, Cambridge, p. 149, 1991.
4. C. Bosshard, G. Knopfle, S. Follonier, C. Serbutoviez and P. Gunter, "Molecular Crystals and Polymer for Nonlinear Optics", *Optical Engineering*, 34, 7, 1995.
5. D. M. Burland, R. D. Miller and C. A. Walsh, "Second-Order Nonlinearity in Poled-Polymer Systems", *Chem. Rev.*, 94, p. 31, 1994.
6. C. W. Spangler, T. J. Hall, P. -K. Liu, L. R. Dalton, D. W. Polis and L. S. Sapochak, "Organic Materials for Non-Linear Optics II" R. A. Hann and D. Bloor, *Roy. Ed., Soc.; Chem.*, London, p. 260, 1991.
7. G. S'Heeren, A. Persoons, Ph. Rondou, M. van Beylen and C. Samyn, "Synthesis of Nonlinear Optical Polymer Functionalized with 4-amino-4'-cyanostyrene and azobenzene dyes. Second Harmonic Generation in Corona Poled thin Films, *Makromol. Chem.* 194, 17332, 1993;
8. Tomaru, T. Kurihara, H. Suzuki, N. Ooba, T. Kaino and S. Matsumoto "Organic Materials for Non-linear Optics II", R. A. Hann and D. Bloor, Ed., *Roy Soc. of Chem.*, Cambridge, 156, 1991.
9. Pierre Le Barny and Philippe Robin, "*Optoelectronique Molculaire*", Masson, Paris, 1993.
10. A. M. Albu, "Macromolecular structures with potential applications in nonlinear optics", PhD thesis, University "Politehnica Bucuresti", 1998.
11. A. M. Albu, D. Manaila-Maximean, A. Boborodea, B. Marculescu and D. S. Vasilescu, "Macromolecular structures with applications in nonlinear optics. II. Synthesis of macromolecular compounds based on styrene and methyl methacrylate", *Chemistry National Conference*, 2, 46, Bucharest, October (1997).
12. Ana-Maria Albu, B. Marculescu, A. G. Boborodea and D. S. Vasilescu, "Synthesis and Characterisation of some Polymers with Applications in Non-Linear Optics: I. Polymerisation of Styrene and Methyl Methacrylate in the Presence of Coloured Comonomers", *E. Polym. J.*, in press.
13. Trouillet, A., *PhD thesis*, University Jean Monnet, France, 1994.
14. I. McCulloch, R. DeMartino, R. Keosian and T. Leslie, "Side Chain pendant Non-linear Optically Active Polymers Synthesised by Grafting Reactions on Maleic Anhydride Copolymers", *Macromol. Chem. Phys.*, 197, p. 687, 1996.
15. A. Zerroukhi, *PhD thesis*, University Claude Bernard Lyon I, 1993.

Influence of the stresses of predeformed InP crystals on acoustic emission under microindentation

Zhitaru R.^a, Rahvalov V.^{a*}

^aInstitute of Applied Physics., Academy of Sciences,
Academy str. 5, MD-2028, Kishinev, Moldova

ABSTRACT

It was shown that the acoustic emission (AE) intensity decreases with the increase of the temperature and relaxation of the preliminary deformation of the InP crystals and alternatively sharply enhances with the predeformation degree rise. The results obtained allowed to conclude that the emission process of acoustic waves is tightly related to the both the deformation (internal) stresses and structure state of defects, characterizing the starting InP crystals before the AE initiation by microindentation.

Keywords: acoustic emission, InP crystals, preliminary deformation, deformation stresses.

1. INTRODUCTION

Many sections of solid state physics are connected with the propagation processes of waves, including the elastic ones, in the crystal lattice.

Origination and emission of elastic waves are significantly dependent on the material internal stresses: their value, distribution homogeneity, stability and so on¹⁻³. The different types of defects, existing in the crystal lattice, largely determine the internal crystal stresses⁴. The effect on the crystal of different external factors (temperature, deformation, electricity etc.) causes the new defects formation or the transformation of existing ones that leads to the internal stress increase^{1, 5, 6}. As known the acoustic signal emission is connected with the dislocation movement, generation and annihilation of cracks, material failure⁷⁻¹². The method of the acoustic emission (AE) signals registration is especially sensitive to the structure changes in the solids^{2, 7-11}. The analogous result was established for the silicium crystals: the AE signals were occurred on the samples, contained the dislocations and were absent on the samples, free from dislocations¹².

The AE signals occurrence in Si crystals attribute to the failure and movement of the dislocation ensembles under effect of both electrocurrent and thermoelastic stresses¹². The AE signals under indenter loading and unloading were identified with the formation and further progress of cracks^{2, 10, 11}.

So, the data from literature show the interrelation of the crystal defects and emission of the acoustic waves. Therefore the external action on the crystal must be followed by the AE characteristic changes, resulting from the suitable dynamical structure rearrangement. However such relation is yet insufficiently investigated. This problem is especially actual for semiconductors, using as a devices in the different stress fields (mechanical, thermal, electrical, etc.).

In this respect, the influence of preliminary deformation, resulting in the mechanical stress formation in the InP crystals, on the intensity of acoustic emission, arising under indentation, was studied.

2. EXPERIMENTAL PROCEDURE

The investigations were made on the (111) and (001) planes of pure and Fe-doped InP crystals, grown by the Chochralsky technique. The samples size was amounted to 1×9×10 mm. Preliminary deformation of samples was performed by scratching (by moving indenter) along <110> directions. The indenter load for the scratches was equal to 20g. The

* Correspondence: e-mail: rahvalov@phys.asm.md

deformation degree and accordingly the internal stresses were varied by the change of the distance between scratches (d) within 20–120 μm . So, depending on the distance between scratches, the crystal regions with the different strength degree (ϵ) were formed: ϵ is decreased with the d increase. In addition to this the different temperatures of preliminary deformation of samples ($T=293\pm 723\text{K}$) as well as their annealing at 293K (the storage) during the 360-720 hours for the sake of the internal stress change were also employed. The AE signals (N_1) due to the indenter penetration as well as ones during all indentation process (N) were registered by use of special device⁷. Then the $\Delta N=N-N_1$ difference resembles the AE signals in the indenter removing from the sample (indenter unloading). The Vickers diamond pyramid was used as the indenter. The indenter loads were varied within the limits 100-300g.

The direct observation of the structure state of defects was made using electron-microscopy decoration method. The argentine and anthracene were used as the decoration elements. The decoration of the InP surfaces was carried out in vacuum of 10^{-5} mm of mercury. The transmission and scanning electron microscopes were applied for these investigations.

3. RESULTS AND DISCUSSION

3.1. The influence of the preliminary deformation degree on the acoustic emission

From Fig. 1 it is seen that all N , N_1 and ΔN parameters are decreased with the d increase; that means that AE signals number fall with the reduction of the degree of the preliminary deformation at 293K of InP crystals. However the course of the $N(d)$, $N_1(d)$ and $\Delta N(d)$ dependencies is different, Fig. 1. $N(d)$ dependence shows the three-stage character: the AE signals number at the first stage (40-60 μm) weakly changes; sharply falls in the region from 60 to 100 μm (second stage) and increases significantly within the range of 100-120 μm , fig1, curve 1. This result evidences that not only the InP surface layer stress state influences the acoustic waves initiation and propagation, but also other factors take place. The $N_1(d)$ dependence demonstrates other behaviour: the $N_1(d)$ curve practically smoothly falls down, Fig. 1, curve 2.

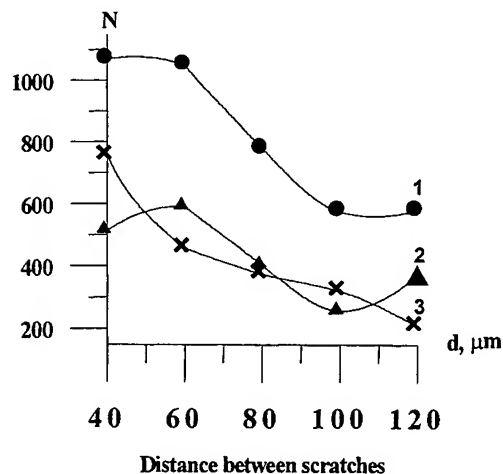


Fig. 1 Dependence of the summary account of AE signals (N) on the preliminary deformation degree for InP crystals during all indentation cycle (1); indenter penetration into sample (2) and indenter lifting (unloading) from InP (3). Predeformation temperature T , K: 293. $P_{\text{indentation}}=100\text{g}$

Such dependence course shows that the number of AE signals, emitted under indenter penetration, and the change of the preliminary deformation degree of InP crystals correlate well: decrease of the predeformation degree leads to the N_1 fall.

The shape of the curve 3, Fig. 1, is analogous to the curve 1: the weak increase on the I and III stages and the sharp fall on the II one were occurred. The established N and ΔN changes evidence that the acoustic waves emission is dependent not only on the stress state degree of the InP crystals preliminary deformation, as N_1 (curve 2, Fig. 1), but also on the type and structure of the deformation defects. The latter is especially principal for the AE signals, arising during indenter unloading, while the impulse relaxation of the deformation stresses occurs.

Electron-microscopy investigations of the InP crystal decorated surfaces shown, that the preliminary deformation significantly changes the deformation defects structure, Fig. 2.

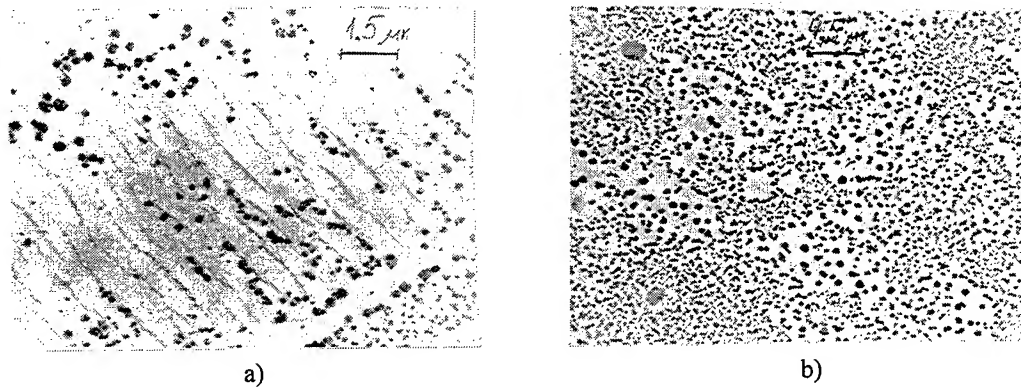


Fig.2 Appearance of decoration surfaces of InP crystals in the deformed region (a) and out of it (b).
The argentum eas used as a decoration element.

It is seen that the distribution of Ag particles is different for crystal deformation region and out of it: more homogeneous distribution of small Ag particles for undeformed crystal region and large aggregation of Ag particles, forming the bent short lines, near the scratches, Fig. 2a, b. It is normal that the different defects structure causes the different stresses state of crystals and therefore leads to the AE signals change.

3. 2. The influence of the preliminary deformation temperature

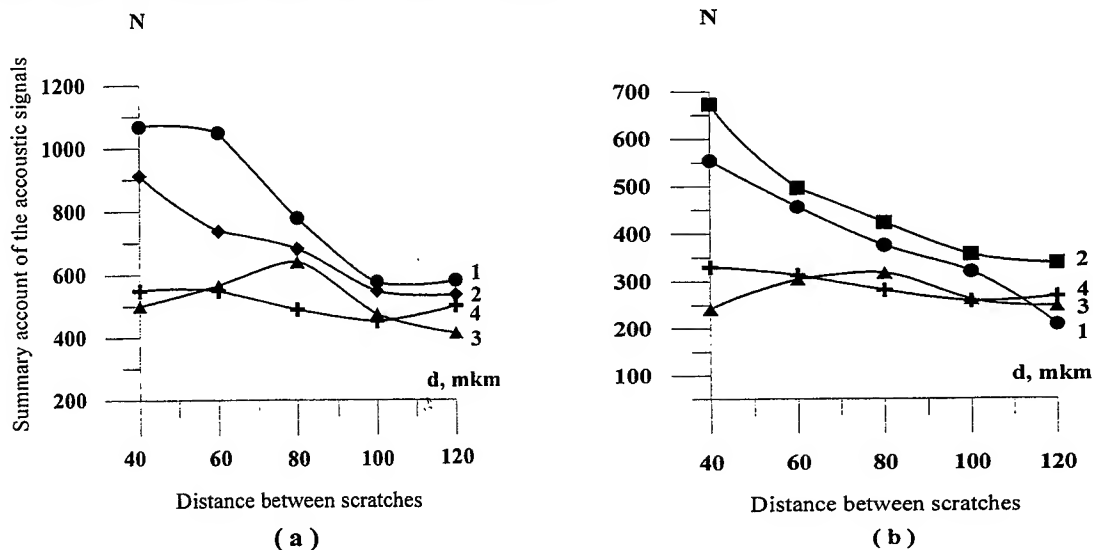


Fig. 3 Dependence of the summary account of acoustic emission signals on the preliminary deformation degree (distance between scratches) for all indentation process (a) and indentor penetration (b)
The preliminary deformation temperature T, K: 293-1; 423-2; 573-3 and 723-4

The state of defects, generated under preliminary deformation, was varied by the scratch temperature change in region from 293 to 723K. The $N(d)$ dependencies at 293; 423; 573 and 723K are presented on the Fig. 3a. As it is seen the $N(d)$ curves are (placed) situated quite well: the higher temperature the lower $N(d)$ curve is placed. Therefore the common regularity for whole predeformation interval is revealed: the number of AE signals is decreased with the preliminary deformation temperature increase, Fig. 3a. The effect established is pronounced in the region of small d (40-80μm), when the preliminary deformation degree of InP crystals in our experiments is maximum; and weak one for low predeformation degree ($d=80-120\mu\text{m}$), Fig. 3a.

These data are more clear-cut on the Fig. 4, which the temperature dependence of N for each of mentioned sample regions, $d=40\mu\text{m}$ (a) and $d=120\mu\text{m}$ (b), presents. It is seen that $N(T)$ dependence is more strong for $d=40\mu\text{m}$, than for $d=120\mu\text{m}$, Fig. 4.

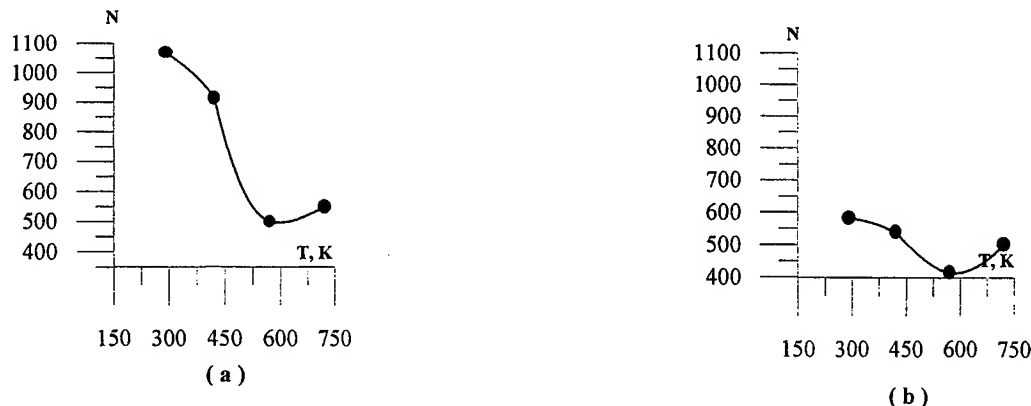


Fig. 4. The temperature dependence of the summary account of acoustic emission signals for sample regions: high preliminary deformation (a) and weak one (b)

From the Fig. 3a it can be also seen that number N is decreased with the d increase for all investigated predeformation temperatures. However this effect is reduced with the T increase and for $T=723\text{K}$ is practically absent, cf. the run of curves 1 and 4, Fig. 3a.

The last shows that the stress state, developed by the preliminary deformation at high temperatures ($T \geq 573\text{K}$), slight influences the acoustic emission signals, investigated under indentation, while the stress state at 293K is significant in such processes, Fig. 3a. Noted well correlates with the data of Fig. 3b: run of the curves 3 and 4 is practically independent of the predeformation degree.

The measurements of the acoustic signals under indenter penetration into the InP sample, in general, demonstrate the regularities analogous to those obtained for the N , Fig. 3a: the N_1 is decreased with the increase of preliminary deformation temperature and with the fall of the mechanical stresses of samples, Fig. 3b. However the certain disagreement takes place: the curve 2 is situated above than curve 1, that is irregular, Fig. 3b. It is possible that the special conditions are formed under preliminary deformation at 423K , which cause the acoustic emission intensification. Latest perhaps leads to the displacement of the curves 1 and 2, Fig. 3b.

The regularities, analogous to the mentioned above for N (Fig. 3a), were obtained for AE signals number ΔN , arising under indenter removal from sample: the discrepancy in this case was not found.

The assumption above that emission of the acoustic waves, arising under indentation of InP crystals, is dependent on the both deformation defects state and mechanical stresses is completely confirmed by the obtained results.

It is known that the type and structure state of deformation defects, internal stresses, homogeneity of their distribution are changed with the test temperature change for all crystals, including InP ones^{5-6, 13-21}.

Especially the surface layer of InP crystals is sensitive to the test temperature: the surface is oxidised and InP crystals are decomposed at $T > 700\text{K}$ ¹⁶. The type, number and structure state of the deformation defects with the test temperature change are affected too. So, under bending of InP crystals in the temperature interval $573-973\text{K}$ the authors of the paper²⁰ did not observed the microtwins, while the twins formation in the mechanical testing is typical of InP crystals. With the temperature rise the dislocations number and their role in the deformation processes under microindentation of the InP crystals are significantly increased, t. e. the dislocation plasticity becomes more appreciable¹⁹.

This fact is correlated with our data, Fig. 5. The structure change of the deformation zone within the indentations with the test temperature variation is demonstrated on the Fig. 5.

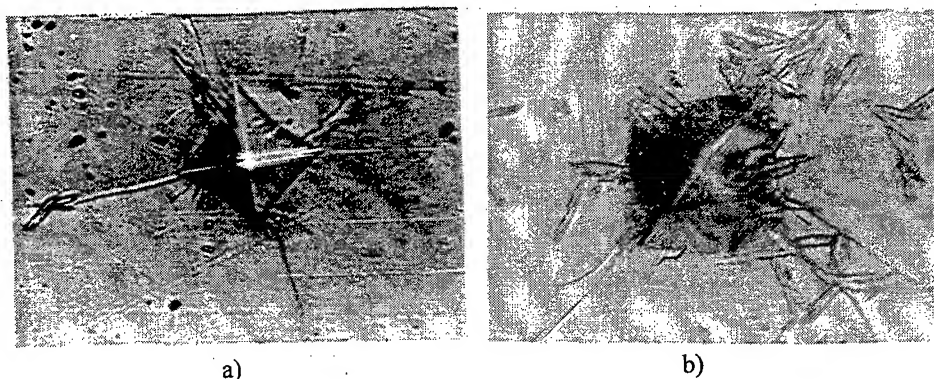


Fig. 5 The (001) plane of the indentation zone at 293 (a) and 603 (b) temperatures. The samples surface was decorated by the antrahion. $P=200$ g

It is seen that the clear slip bands, besides the cracks, in the region within the indentation, made at 603K, are observed, while the similar bands at 293K are absent, Fig. 5. The obtained result the ever-increasing role of the dislocation mechanism under InP indenter deformation with the temperature increase from 293K to 693K evidences and it is well agreed with the conclusion of the article ¹⁹. Alternatively, the plasticity enhancement is followed by the elastic stresses relaxation. Therefore, it can be regarded that the elastic stresses of the predeformed InP crystals are reduced and also the deformation defects spectrum is changed in the test temperature rising. This allows to propose the possibility of the InP crystal elastic supertensions initiation as a result of the predeformation at 423K, that gives rise to the elastic waves emission. That is quite normal that such state of the mechanical stresses influences at first the acoustic emission, arising under indenter penetration. Additional deformation, introduced during indenter penetration, perhaps, assists the stress state change of the predeformed regions of the InP crystals. Accordingly the AE signals number under indenter removal from the samples the other character of the temperature dependence revealed. The last resulted in the same dependence for the N, Fig. 3a.

3. 3. The influence of the crystal storage on the acoustic waves emission

With the sake of the change of stress state, formed during preliminary deformation (scratching), the sample storage at 293K was performed. The storage time was varied in the range from 360 to 720 hours, in certain cases to 5 months. It is known that the storage (annealing at room temperature), as a rule leads to the, leads to the self-correcting of the crystal defects structure, and to the minimising of the mechanical overstresses. Therefore the regularities study of the acoustic signals emission before and after storage of the predeformed InP crystals will be promote the elucidation of the elastic overstresses role for the generation and spread of such waves in the crystals.

It was established that the number of AE signals after crystal storage are significantly decreased, fig. 6. It is seen that the curves, characterizing the emission after storage, are mainly placed lower than those before annealing, fig. 6a, b, c, curves 1 and 2 ^{*)}

The storage of samples, predeformed at 293 and 723K, the AE signals number decrease causes too.

So, it can be concluded that the mechanical overstresses of InP crystals influence the acoustic waves emission and their relaxation leads mainly to the decrease of the AE signals number.

^{*)} It must be mentioned, that this effect for the AE signals under indenter penetration is not clear-cut: for $d=40$ and $100\mu\text{m}$ N_1 is even increased after storage, Fig. 6b.

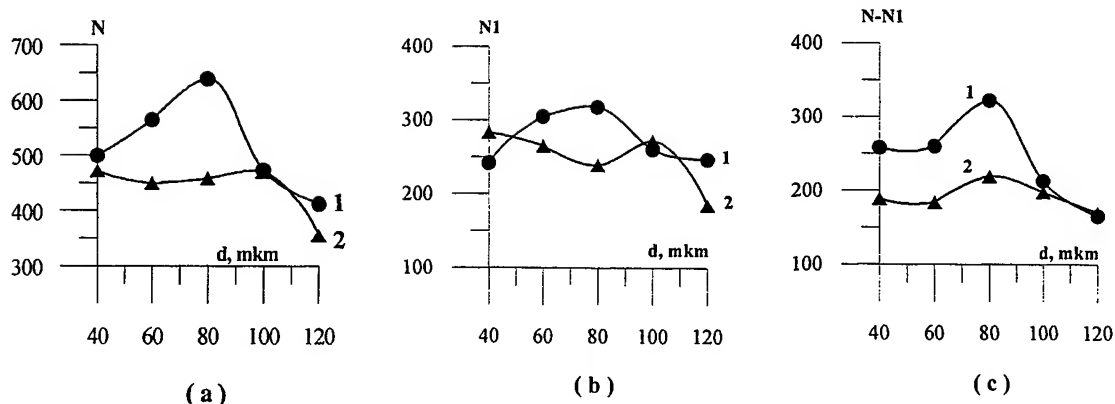


Fig. 6 The AE signals number dependence on the degree of preliminary deformation at 573K for all indentation cycle (a), under indenter penetration into sample (b) and under unloading one (removal from sample) (c).
Curves 1-before and 2-after samples storage during 370 hours.

However the opposite phenomenon for the InP samples, predeformed at 423K, was observed, fig. 7. It is seen that the curves 2 are situated higher, but not lower, than curves 1, fig. 7a, b. The same effect for the N_1 parameter is occurred too. That means that the acoustic signals number under indentation of the aged InP crystals is larger, than that one for the samples before aging. It was mentioned above about the peculiarities of the results, obtained on the InP crystals, predeformed at 423K, Fig. 3b. For explanation unusual phenomenon the assumption about the specific state of the surface layer deformation defects and mechanical stresses, arising during the InP crystals predeformation at 423K, was proposed.

The investigation of the microstructure around the indentations by means the scanning and light microscopes shown that the InP samples, predeformed at 423K, after storage become more fragile, while the samples, predeformed at 293K, 573K and 723K, on the contrary, become more plastic. The last well correlates with data of the paper¹⁹. Unusual behaviour of the InP crystals, heated to the 423K, was also observed under study of the temperature dependence of microhardness H : H was higher at 423K than at 293K¹⁹. It is known that the strength increase, as a rule, is followed by the brittleness enhancement. In this respect our result and data from paper¹⁹ are agreed. Accordingly it can be concluded, that the reason of the acoustic waves emission intensification is the brittleness increase of the InP crystals, preliminary heated and deformed at 423K. This fact is rather connected with the specific state of the mechanical stresses and deformation defects structure, i. e. with the internal stresses.

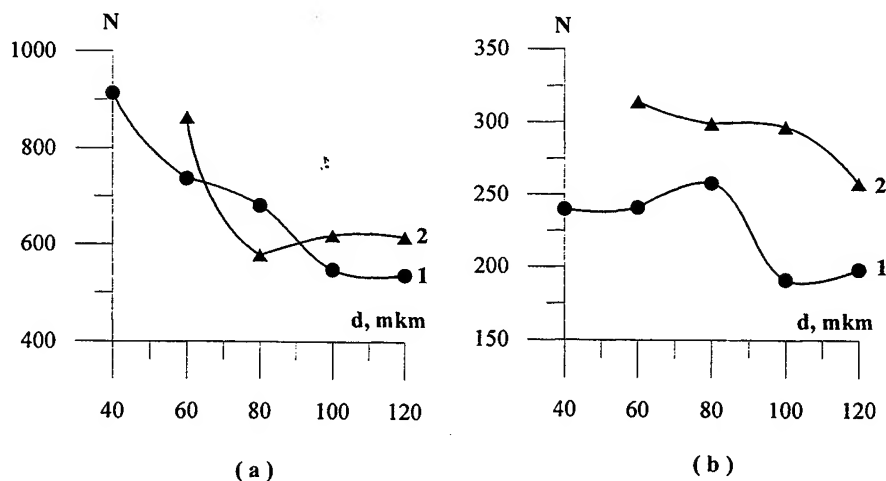


Fig. 7 The AE signals number dependence on the degree of preliminary deformation at 423K for all indentation cycle (a) and under indenter unloading (b).
Curve (1) – before and (2) – after samples storage during 5 months.

The data, obtained under antrahinon decoration of InP-pure and InP-Fe samples, shown that the surface state of InP crystals is connected with their strength and impurity content. It was established that the decoration ratio for pure InP in comparison with the Fe-doped ones is sharply different: the antrahinon particles were not practically deposited on the pure InP crystals surfaces and settled on the InP-Fe surfaces. This fact evidences the unusual surface state of InP crystals, doped by Fe and allows to propose that this phenomenon is probably due to the inadequate surface electrical properties of pure and Fe-doped InP crystals: the impurity introduction leads to the surface change increase for these objects. It is necessary to note that the microhardness and number of AE signals under indentation were higher for InP-Fe than for pure InP.

So, the obtained results allow to conclude that the emission process of acoustic elastic waves is tightly related to the both deformation (internal) stresses and structure state of defects, characterizing the starting InP crystals before the AE initiation and propagation.

REFERENCES

1. Ya. M. Olih, "Akusticheskaya emissia v halkogenidnom stele $\text{Gl}_{0.18}\text{As}_{0.28}\text{Sl}_{0.54}$ ", *FTT*, **40**, №9, pp. 1623-1626, 1998.
2. C. S. Lee, V. M. Rhgim, D. Kwon and K. Ono, "Acoustic emission measurement of fatigue crack closure", *S'er. Met. et mater.*, **32**, №5, pp. 701-706, 1995.
3. Sukanuma Matchiro, "Scanning acoustic microscopy of indentation damage in I_2O_3 -stabilized tetragonal zirconia", *J. Amer. Ceram.*, **78**, №11, pp. 2889-2896, 1995.
4. E. G. Tsvetkov, T. M. Rilov and A. M. Jurkin, "Rol dislokatsionnich obrasovanii v relaxatii lokalnich napreazhenii, vizvannich structurnoi neodnorodnostiyu kristallov", *Kristallografia*, **44**, №2, pp. 308-316, 1999. (in Russian)
5. A. Damask and J. Dins, *Tochechnie defecti v metallach*, Mir, Moskva, 1966, (in Russian)
6. Van Bjuren, *Defecti v kristallah*, IL, Moskva, 1962. (in Russian)
7. Yu. S. Boyarskaya, D. Z. Grabco and M. S. Kats, *Physics of microindentation process*, Stiinta, Kishinev, 1986 (in Russian).
8. Yu. V. Milman, V. A. Goncharuk and V. V. Danilov "Badania vlaschiwosci mechanicznych ceramiki metoda emisji akustycznej", *Ceramics (Polish ceramic bulletin 7, Krakov)*, **45**, pp. 197-211, 1994.
9. Yu. S. Boyarskaya, R. P. Zhitaru, M. S. Kats and E. I. Purich, *Physics of composite material strength*, LINF, Leningrad, 1979 (in Russian).
10. B. V. Tanikella, Scattergood O. Ronald, "Acoustic emission during failure process under indentation", *J. Amer. Ceram. Soc.*, **78**, №6, pp. 1698-1702, 1995.
11. Gul Kim Kwang and Sachse Wolfgang, "Characteristics of acoustic emission signals of Hertzion and unloading cracks in glass", *J. Appl. Phys.*, **55**, №8, pp. 2847-2856, 1984.
12. A. M. Orlov, A. A. Skvortsov and V. A. Frolov, "Akusticheskaya emissia v dislokatsionnom kremnii pri tokovih I teplovich vosdeistviiach", *J. Pisma v ZhTF*, **28**, №3, pp. 28-32, 1999 (in Russian).
13. J. F. Boudet and S. Ciliberto, "Interaction of Sound with Fast Crack Propagation", *Phys. Rev. Let.*, **80**, №2, pp. 341-344, 1998.
14. K. V. Sapozhnikov, S. V. Kustov, "Vlianie temperaturi na amplitudnie zavisimosti akustoplasticheskogo effekta", *FTT*, **38**, №1, pp. 127-132, 1996.
15. Haruo Nadaj, "Dislocation velocities in Indium Phosphide", *JJAP*, **20**, №4, K793-K794, 1981.
16. Johico Iokinaga and Sumino Koji, "Effects of dopants on dynamic behaviour of dislocations and mechanical strength of InP", *J. Appl. Phys.*, **74**, №2, pp. 917-924, 1993.
17. F. G. Evans and M Linder, "Failure Prediction in Structural Ceramics Using Acoustic Emission", *J. Amer. Soc.*, **56**, №11, pp. 575-581, 1973.
18. A. G. Evans, "Residual Stress Measurement Usual Acoustic Emission", *J. Amer. Soc.*, **58**, №5/6, pp. 239-244, 1975.
19. D. Z. Grabco, V. S. Panfilov and E. E. Maronchuk, "Micromechanicheskie svoistva monokristallov phosphida india, legirovannich zhelesom", pp. 251-256, *Phosphid india v poluprovodnikovoi elektronike*, Stiinta, Kishinev, 1988.
20. Le Bourhis, A. Zozime, A. Reviere and C. Vameulin, "Investigation of the plasticity of InP as a function of temperature" *J. Phys. Soc.* **3**, **5**, №11, pp. 1795-1801, 1995.
21. H Siethoff, J. Volkl, D. Gerthsen and H. G. Brion, "The lower Yield Point of InP and GaAs", *Phys. Stat. Sol. (a)*, **101**, K13, 1987.

Phosphors with sulphide matrix. Synthesis parameters influence on optical properties

C. Onose*, S. Jinga, Carmen Onose

MATPUR, Sos. Garii Catelu, nr.5, 73611, Bucharest, Romania

ABSTRACT

These paper present the wet synthesis method of high purity cadmium and zinc sulphides for phosphors. As row materials are used zinc sulphide, cadmium sulphide and cadmium-zinc sulphide in order to obtain a large types of phosphors. These phosphors have incorporated in base structure well-defined quantities of dopants. Changes of dopants and thermal treatment must be obtained different wavelength of emitted radiation and different optic efficiency. Thus, ZnS hex:Cu emits at 561nm (green colour) with optical efficiency 90 % opposite to zinc silicate, ZnS cub:Cu,Ag emits at 528 nm (green colour) with optical efficiency 200 %, ZnS hex:Cu emits at 516 nm (green colour) with optical efficiency 100 %, ZnS cub:Zn emits at 470 nm (blue colour) with optical efficiency 190 %, ZnS cub:Ag emits at 455 nm (dark-blue colour) with optical efficiency 220 %, (Zn,Cd)S:Ag emits at 565 nm (yellow colour), 556 nm (yellow-green colour), 550 nm (yellow colour), 540 nm (green colour), 537 nm (green colour) or 528 nm (green colour) with optical efficiency 370 % opposite to zinc silicate, (ZnS, Cd):Cu emits at 530 nm and 528 nm (green colour) with optical efficiency 140 % opposite to zinc silicate.

The utilised zinc sulphide must have a special purity. Was established that any impurities with greater concentration than 10^{-6} - 10^{-5} % modify more or less the properties of product. Practically was established that materials utilised for above-mentioned purpose must have 99.99 – 99.999 % level purity. The control of reaction mechanism in order to achieve the best yield reaction, in the same time with an advanced purification was experimented. Were achieved phosphors with 400 – 600 nm emission ranges. Also, influence of material parameters (particle size distribution, chemical homogeneity, structure) on luminescence emission parameters was studied.

Keywords: luminescence, phosphors, high purity, zinc sulphides, cadmium sulphides, cadmium and zinc sulphides

1. INTRODUCTION

The researches in this field are oriented toward the obtaining of phosphors panels, plate colour TV display and fool-colour panels. The purpose of this study is the investigation of chemical equilibrium and synthesis reactions of base zinc sulphide phosphors and the doping of crystalline structure for obtaining optimal optical properties.

The luminescence is a radiation process in which, by absorption of energy, the materials generate a characteristic nonthermic radiation.

We tried many methods for zinc sulphide synthesis and finally was used the obtaining method by ZnSO_4 and $\text{Na}_2\text{S}_2\text{O}_3$. The method is very simple without complicated installations. The starting solutions was purified in many stages with porpoise to reach an impurities level better than 10^{-5} .

The blend of zinc sulphide and/or cadmium sulphide, sulphur, fondants and activators were calcinated in nitrogen atmosphere at 600-900 °C. After quenching at room temperature, the powder was grided with 1 % sulphur in wet medium, was dried and calcinated again in nitrogen atmosphere. This treatment is made at 900-1250 °C and different times, taking into accounts the type of phosphorous.

The utilised compositions in experiments are:

- cub-ZnS:Cu 100g ZnS + 2g NaCl + 0,01g CuCl₂
- hex-ZnS:Cu 100g ZnS + 2g NaCl + 0,01g CuCl₂

*Correspondence: Email: cristi@matpur.ro; Fax: (401)255 01 48; Telephone: (401) 255 69 00/188

• hex-ZnS:Cu	100g ZnS + 2g NaCl + 0,01g CuCl ₂
• hex-ZnS:Cu,Ag	100g ZnS + 2g NaCl + 0,02g CuCl ₂ + 0,032g AgNO ₃
• cub-ZnS:Ag	100g ZnS + 2g NaCl + 0,016g AgNO ₃
• hex-ZnS:Ag	100g ZnS + 4g NaCl + 0,016g AgNO ₃ + 2g BaCl ₂
• hex-ZnS(48)CdS(52):Ag	48g ZnS + 52g CdS + 2g NaCl + 0,016g AgNO ₃
• hex-ZnS(86)CdS(14):Ag	86g ZnS + 14g CdS + 1g NaCl + 0,015g CuCl ₂ + 2g BaCl ₂

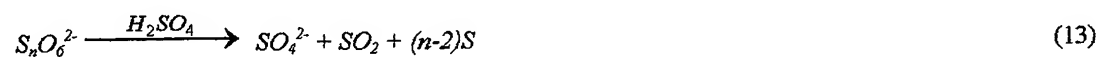
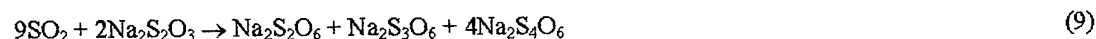
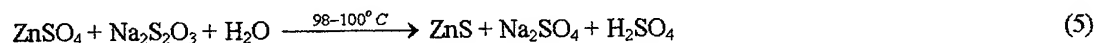
2. EXPERIMENTS

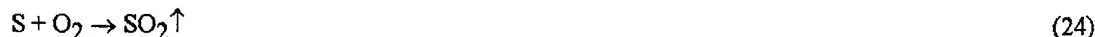
Cadmium and zinc sulphide preparation for phosphors is a hard operation because of required high purity level. Synthesis reactions are:



This method is preferred because of small reagent necessary and a good possibility of separation of products. Was utilised a molar ratio $\text{MSO}_4 / \text{Na}_2\text{S}_2\text{O}_3 = 1/2$ ($M = \text{Zn, Cd}$). Used raw materials are successively purified at 99.99 % - 99.999 %.

Reaction mechanism is very complicated and controversed ¹.





By thermic and dynamic control of process was achieved the slowness of reaction (9) and the enhance of reactions (10,13), decreasing $\text{Na}_2\text{S}_2\text{O}_3$ used quantity. On the other hand NH_4OH introducing in reaction (21) facilitate reaction (5) and limit reaction (6), SO_2 emission and reaction (9).

Using as reagent a mixture of ZnSO_4 and CdSO_4 (with required Zn/Cd ratio), result a cadmium-zinc sulphide with 30 % sulphur and a small quantities of hydroxide in saturated sodium sulphate solution. The precipitate was washed with deionized water until total removing of ions sulphate. The precipitate was calcinated at 400-800 °C in nitrogen stream for sulphur removing (reactions 23, 24). The achieved product was washed with acetic acid for traces zinc oxide removing, then with water to neutral pH and finally with acetone. Drying was made at 100-120 °C.

This method is able to obtain a stoichiometric zinc and cadmium sulphide with 99.99-99.999 % purity and submicronic grains². This powder was used for phosphors synthesis.

Starting from several well-known compositions, was realised a mixture of sulphides and dopants, with was wet grided, dried and again dry grided. The powder was calcinated at 700-900 °C. After the powder was grided with 1 % sulphur and again calcinated in nitrogen stream at 900-1200 °C and different times related to types of phosphor.^{3,4}

Was obtained zinc sulphide and cadmium-zinc sulphide phosphors doped with copper and/or silver and was characterised regarding composition, particle size distribution and optical efficiency, UV excited.

3. RESULTS

The results presented in this paper were obtained in MATPUR laboratory.

The characterisation was made with PERKIN-ELMER and KARL ZEISS-JENA spectrophotometers. Particle size distribution was determinate with LAUC laser analyser. Microstructure was determinate with KARL ZEISS-JENA optical microscope. Chemical analyses for impurities were made with induced coupled plasma spectrometer ICP 3000.

Tab. 1 Optical parameters variation (λ_{max} – maximum of emission curve excited at 365 nm; H – brightness compare with antracen etalon; A – optical efficiency compare with antracen etalon) function of dopants, treatment temperature and treatment time.

Nr. crt.	Phosphor	Synthesis temperature [°C]	Treatment time [hours]	Dopants		λ_{\max}	H	A
				[ml]		[nm]	[%]	[%]
1	2	3	4	5	6	7	8	9
1.	ZnS	940	2	AgNO ₃ (0.56)	NaCl (8.3)	450	36	74
2.	ZnS	950	1	AgNO ₃ (0.44)	NaCl (6.6)	455	72	96
3	ZnS	950	2	AgNO ₃ (0.44)	NaCl (6.6)	455	80	102
4	ZnS	950	4	AgNO ₃ (0.44)	NaCl (6.6)	455	95	148
5	ZnS	950	4	AgNO ₃ (0.44)	NaCl (6.6)	455	96	157
6.	ZnS	950	4	AgNO ₃ (0.44)	NaCl (8.6)	455	86	137
7.	ZnS	980	2	AgNO ₃ (0.50)	NaCl (7.8)	455	90	150
8.	ZnS	1000	4	AgNO ₃ (0.70)	NaCl (11.1)	435	23	45
9.	ZnS	1050	2	AgNO ₃ (0.28)	NaCl (5.3)	440	59	78

1	2	3	4	5	6	7	8	9
10.	ZnS	1100	1	AgNO ₃ (0.56)	NaCl (8.3)	430	54	56
11	ZnS	1200	2	AgNO ₃ (0.44)	NaCl (6.6)	435	105	170
12.	ZnS	850	1	CuCl ₂ (2.55)	NaCl (6.6)	526	36	70
13.	ZnS	900	1	CuCl ₂ (2.55)	NaCl (6.6)	526	62	96
14.	ZnS	900	2	CuCl ₂ (2.55)	NaCl (6.6)	526	80	102
15.	ZnS	900	4	CuCl ₂ (2.55)	NaCl (6.6)	526	95	148
16.	ZnS	950	1	CuCl ₂ (2.55)	NaCl (6.6)	526	86	137
17.	ZnS	950	2	CuCl ₂ (2.55)	NaCl (6.6)	526	96	157
18.	ZnS	1000	1	CuCl ₂ (2.55)	NaCl (6.6)	526	90	155
19.	ZnS	1000	2	CuCl ₂ (2.55)	NaCl (6.6)	526	98	145
20.	ZnS	1000	1	CuCl ₂ (2.55)	NaCl (6.6)	526	97	150
21.	ZnS	1000	2	CuCl ₂ (2.55)	NaCl (6.6)	526	85	100
22.	ZnS	1050	1	CuCl ₂ (2.55)	NaCl (6.6)	526	90	138
23.	ZnS	1200	1	CuCl ₂ (2.55)	NaCl (6.6)	516	80	112
24.	ZnS	1200	2	CuCl ₂ (2.55)	NaCl (6.6)	516	73	98
25.	ZnS	1250	1	CuCl ₂ (2.55)	NaCl (6.6)	516	66	89
26.	ZnS	1250	2	CuCl ₂ (2.55)	NaCl (6.6)	516	59	85
27.	ZnS	1300	1	CuCl ₂ (2.55)	NaCl (6.6)	516	51	80
28.	ZnS	1200	1	AgNO ₃ +CuCl ₂ (3.7 + 5.1)	NaCl (6.6)	513	10	24
29.	ZnS	1200	1	AgNO ₃ +CuCl ₂ (0.8 + 5.1)	NaCl (6.6)	513	48	7
30.	ZnS	1200	1	AgNO ₃ +CuCl ₂ (0.4 + 2.55)	NaCl (6.6)	513	76	118
31.	ZnS	1250	1	AgNO ₃ +CuCl ₂ (0.4 + 2.55)	NaCl (6.6)	513	61	90
32	ZnS	1300	1	AgNO ₃ +CuCl ₂ (0.4 + 2.55)	NaCl (6.6)	513	48	84
33	ZnS(48)CdS(52):Ag	940	1	AgNO ₃ (0.44)	NaCl (6.6)	537	81	175
34	ZnS(86)CdS(14):Cu	1250	1	CuCl ₂ (2.55)	NaCl (6.6)	560	55	101

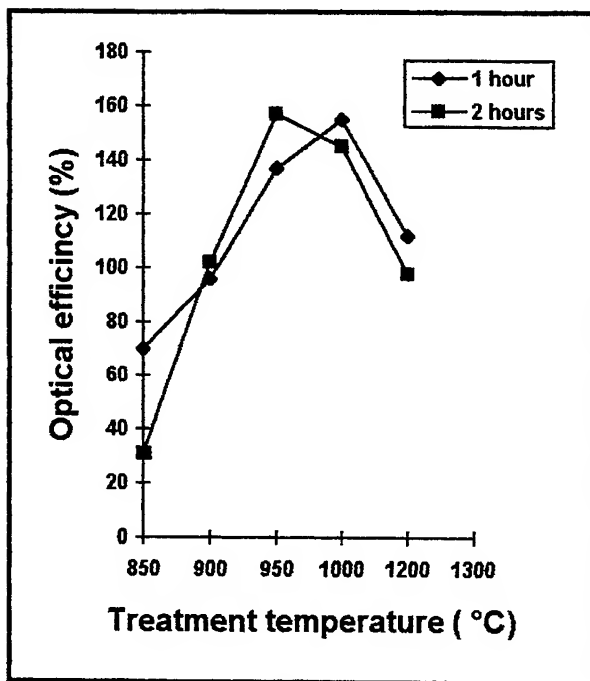


Fig.1. Evolution of optical efficiency of ZnS:Cu,Na phosphor function treatment time and treatment temperature

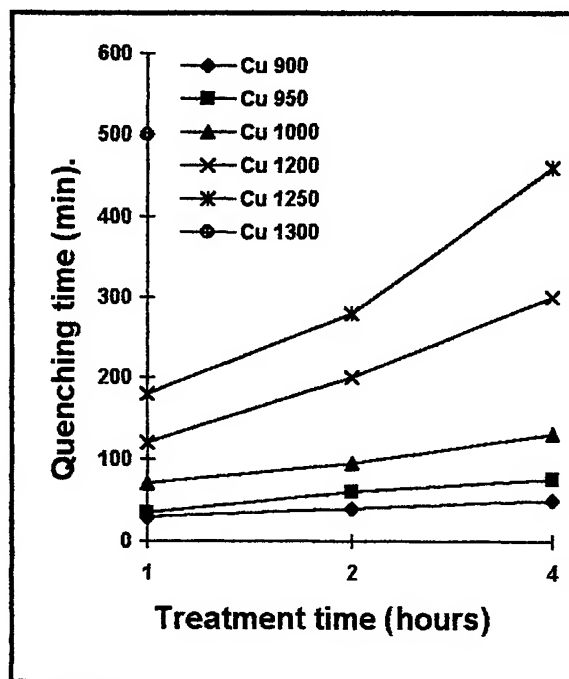


Fig.2. Variation of lightening time of ZnS: Cu, Na function of treatment time and temperature (900, 950, 1000, 1200, 1250, 1300 °C)

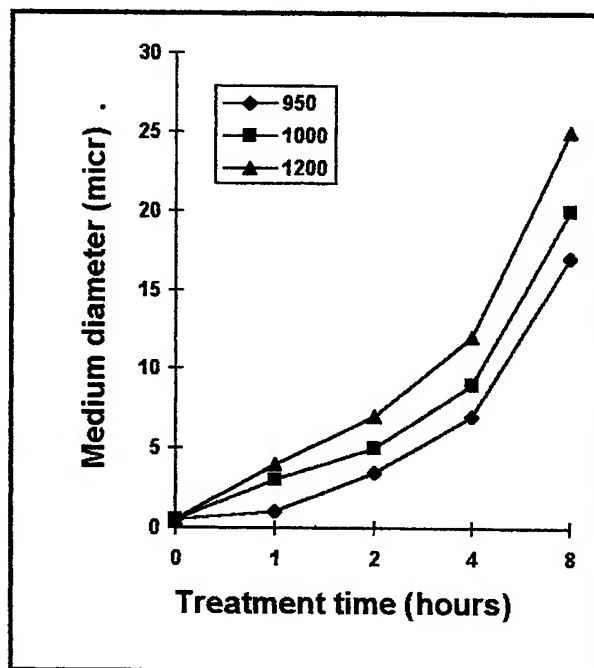


Fig. 3. Evolution of medium diameter of phosphor function of treatment temperature and time starting from powder with 0.5 µm medium diameter

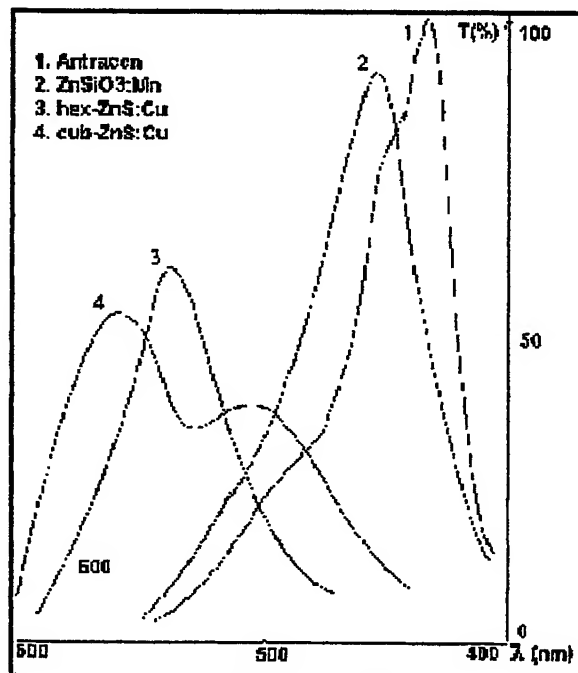


Fig.4. The luminescence of different samples obtained in MATPUR

The influence of processing conditions of zinc sulphide phosphor was studied. A study regarding grain growing of phosphor function of treatment time and temperature was made. Also the phosphors was characterised by:

- a. position of maximum of emission curves;
- b. brightness
- c. optical efficiency;
- d. particle size distribution;
- e. quenching time

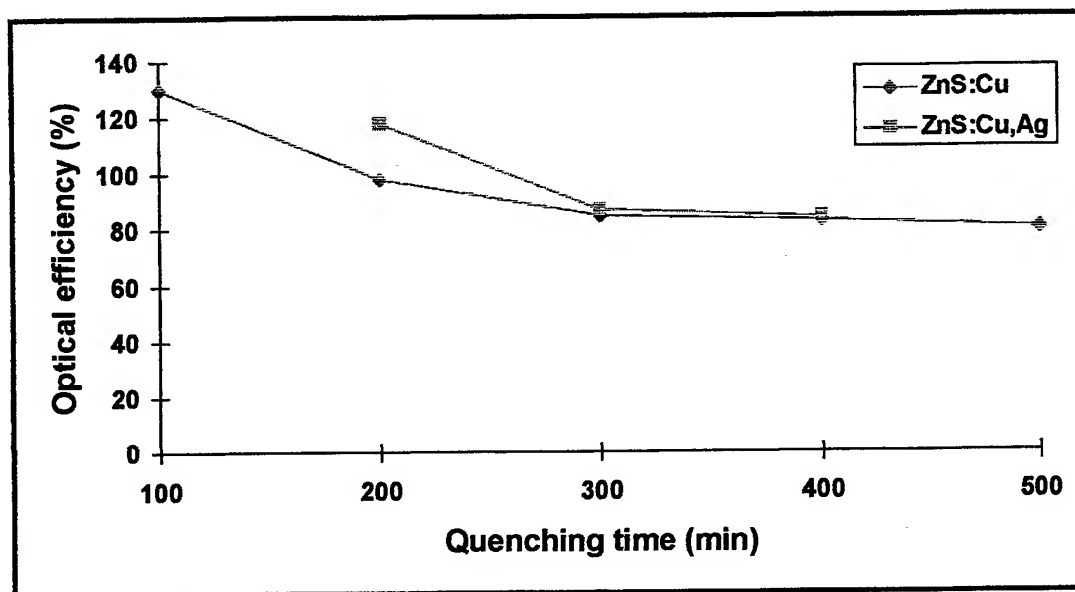


Fig.4. Optical parameters correlation (optical efficiency, quenching time) of zinc sulphide phosphors doped with copper and silver.

The optical properties of phosphors were correlated with processing conditions and their influences upon phosphors ZnS:Cu, ZnS:Cu,Ag, $(Zn_xCd_{1-x})S:Ag$ si $(Zn_xCd_{1-x})S:Cu$.

REFERENCES

1. M.I. Tombak and A.A.Bundel, "Researches regarding obtaining method of zinc sulphide phosphor by reaction between sodium tiosulphate and zinc sulphate.", *J.Neorg.Chim.*, 4, pp.1568-1576, 1959.
2. C.Onose, M. Ionescu, D. Vasiliu, "Synthesis of High Purity Zinc Sulphide of Luminophore Grade and Optical Use", *National Congress of Chemistry*, Bucharest, 1988.
3. Takemura Kenzo, Yoshida Takeshi, Yamazaki Akio, Fukutomi Naoki (Hitachi Chemical Co.Ltd.), "Zinc Sulphide Target for Manufacture of Active Layer in Thin Film Electroluminescent Device", *Jpn. Kokai Tokkyo Koho*, JP 03 110 787, 1991.
4. Sukharaev Yu.G., Antonov S.Yu., Odesa Politechnic Institute SSSR "Method for Controlling the Color of Emitted Light from Sublimed Zinc Sulphide Phosphors in Thin Film Electroluminescent Displays", *SU 1 700 047*, 1991.

Transparent ferroelectric ceramic from chemical synthesized powders

S.Jinga*, C.Onose

MATPUR S.A. Sos.Garii Catelu nr.5, 73611 Bucharest, ROMANIA

ABSTRACT

Chemical synthesis by concomitant precipitation of metallic ions for obtaining a PLZT 10/65/35 composition starting from hydroxides and oxalates was made. Another task was the sintering of oxide powders obtained by thermal decomposition of synthesised precipitates using hot pressing method followed of heat treatment in oxygen stream.

Keywords: coprecipitation, synthesis, PLZT, transparent ferroelectric ceramic.

1. INTRODUCTION

An electrooptic ceramic is a transparent aggregate of ferroelectric single crystal grains, grain size can be varied over a wide range of values (0.5 μ m to 50 μ m) depending on chemical composition and method of fabrication, and optical transmittance in visible and near infrared. Although individual grains are anisotropic, the material is isotropic at a macroscopic scale, since crystallographic axes are oriented at random and anisotropy is averaged out. Electrooptic ceramics have a number of advantages over single crystals. These advantages are: 1.less expensive fabrication procedures; 2.possibility of preparing a wide range of sizes and shapes; 3.controlled orientation of optic axis; 4.design of optical and electrooptical properties by properly adjusting composition and fabrication parameters. The formula for PLZT ceramic is $Pb_{1-x}La_x(Zr_yTi_{1-y})O_3$ and the structure is that of the perovskite ABO_3 , where Pb^{2+} and La^{3+} occupy A sites and Zr^{4+} and Ti^{4+} the B sites octahedrally coordinated to O.^{1,2} As a general, the preparation of transparent ceramics is a difficult task, requiring very careful synthesis and fabrication procedures.

2. EXPERIMENTS

The purpose of our study was chemical synthesis by concomitant precipitation of metallic ions for obtaining a PLZT 10/65/35 composition starting from hydroxides and oxalates^{3,4,5}. Another task was the sintering of oxide powders obtained by thermal decomposition of synthesised precipitates using hot pressing method followed of heat treatment in oxygen stream. Consequently, steps are: chemical synthesis of every hydroxide and oxalate, thermal decomposition of these precipitates, concomitant precipitation of hydroxides and oxalates, thermal decomposition of complex precipitates, hot pressing of synthesised oxide powders, heat treatment in oxygen stream of ceramic for improved the optical and electrical properties.

Sintering conditions concerning both types of oxide powders obtained by common route starting from oxides, or precursor decomposition are presented in the following tables.

Tab. 1 Processing conditions of transparent ferroelectric ceramic obtained by hot pressing in reducing atmosphere

	Could press [kgf]	Intermediate temperature [min/°C]	Temperature [°C]	Time [min]	Force [kgf]	Diameter die [mm]	Atm
1	300	30/700	1200	60	1900	20	argon
2	400	30/600 and 30/920	1200	60	1900	20	argon
3	400	30/600	1000	35	1900	20	argon
4	400	30/600	800	30	1900	20	argon
5	1000	120/600	900	30	1900	20	argon

*Correspondence: Email: sjinga@matpur.ro; Telephone: (401) 255 69 00/188, Fax: (401)255 01 48

Tab. 2. Sintering conditions and stoichiometric correction of electrooptic ceramic

	Intermediate temperature min/°C	Temperature [°C]	Time [min]	Pressure [kgf/mm ²]	Thermal treatment of sintered ceramic in oxygen stream			
					T [°C]	Time [hours]	Flow [l/h]	Support
1	30/600	800	10	5	1200	2	30	alumina
2	30/600	1000	15	5	1200	2	30	alumina
3	140/600	900	75	5	1200	2	35	alumina
4	60/600	900	60	7	1200	2	35	alumina
5	60/600	1000	15	7	1200	2	35	alumina
6	30/600	1000	25	7	1200	1	40	platinum
7	-	-	-	-	1200	1	40	platinum
8	120/600	900	15	7	1200	1	40	platinum

Tab. 3. Processing conditions of electrooptic ceramic obtained by hot pressing from oxide powders as result of inorganic precursors decomposition

Precursors	Temperature [°C]	Time [min]	Pressure [kgf/mm ²]	Thermal treatment of sintered ceramic in oxygen stream			
				T [°C]	Time [h]	Flow [l/h]	Support
1-hydroxides and oxalates	1150	20	7	1200	2	40	platinum
2- hydroxides and oxalates	900	20	7	1200	2	40	platinum
3-oxalates mixture	900	30	6	1200	2	40	platinum
4- oxalate mixture	750	30	6	1200	2	40	platinum
5-hydroxides mixture	750	30	6	1200	2	40	platinum

3. RESULTS

The optimal values obtained for the processing parameters are:

- chemical synthesis of every hydroxide and oxalate - basic pH > 9.5;
- thermal decomposition of these precipitates - 300-700 °C depending on precipitate;
- concomitant precipitation of hydroxides and oxalates - pH=9;
- thermal decomposition of complex precipitates - temperature: 500 °C;
- hot pressing of synthesised oxide powders:
 - temperature range: 1000-1200 °C;
 - pressing time: 1-3 hours;
 - pressure: 7 kgf/mm²;
- heat treatment in oxygen stream of ceramic for improved the optical and electrical properties - treatment time: 2-24 hours; treatment temperature: 1200 °C.

In the following figures and Table 4 are presented thermal conditions of precursor decomposition , TG, DTG, and DTA curves, and endothermic and exothermic effects during thermal analysis.

Tab. 4. Behaviour of complex composition of PLZT at heating.

Sample	Temperature (°C)	Weight loss (%)	Thermal effect
hydroxides and oxalates	25-1000	34.27	
	25-290	5.71	endothermic
	290-430	3.81	endothermic
	430-585	15.36	
	585-950	9.65	
oxalates	25-1000	39.14	
	25-220	6.2	endothermic
	220-370	17.86	exothermic (max.350°C)
	370-510	7.3	exothermic (max.392°C)
	510-800	7.78	
	>900		beginning of exothermic effect

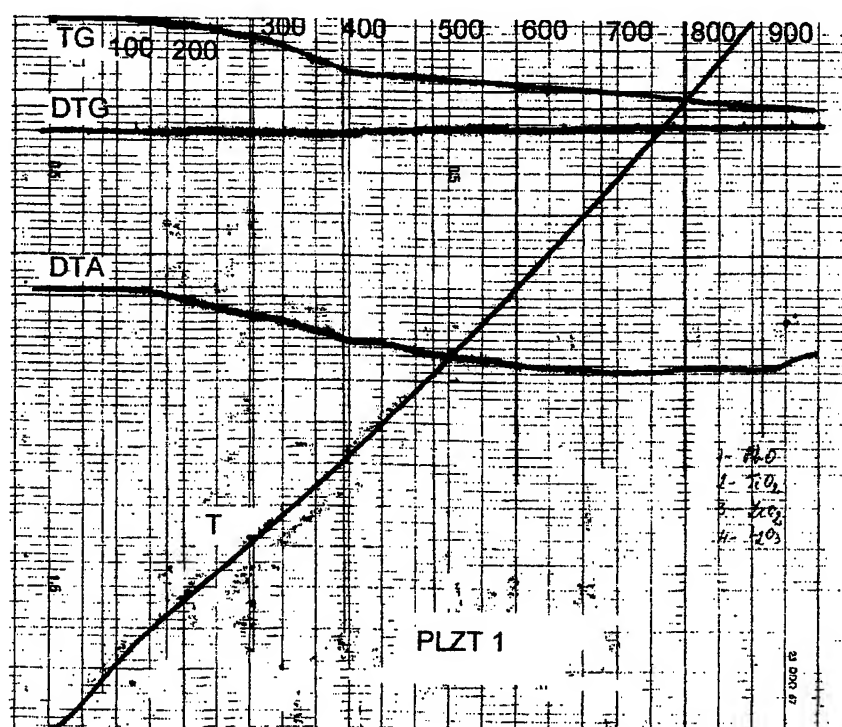


Fig. 1 TG, DTG and DTA curves of PLZT 10/65/35 from oxides

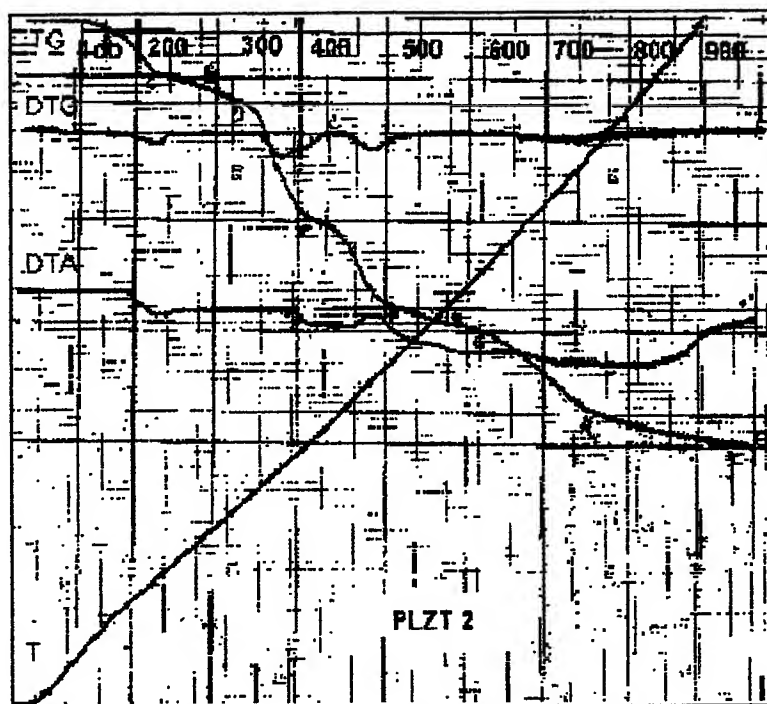


Fig. 2 TG,DTG and DTA curves of PLZT 10/65/35 from hydroxides and oxalates mixture

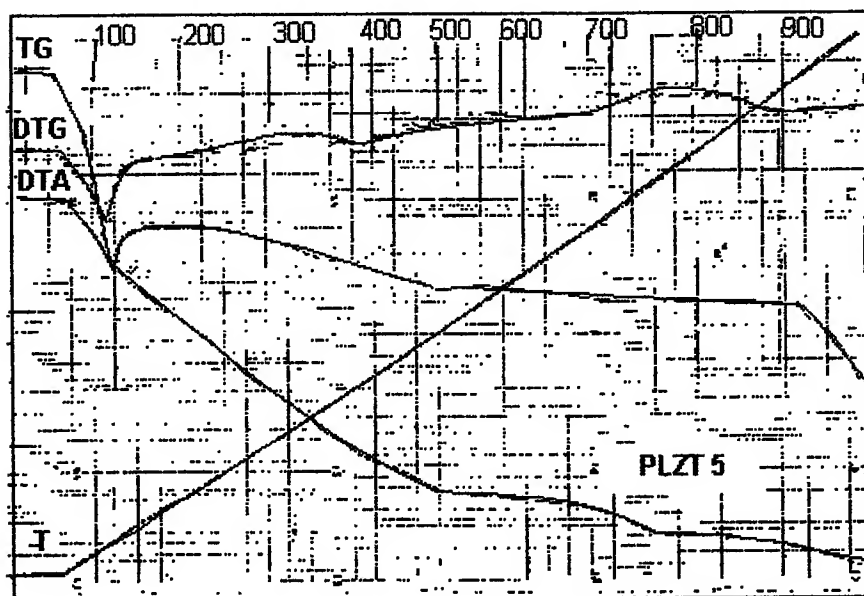


Fig. 3 TG, DTG and DTA curves of PLZT 10/65/35 from hydroxides

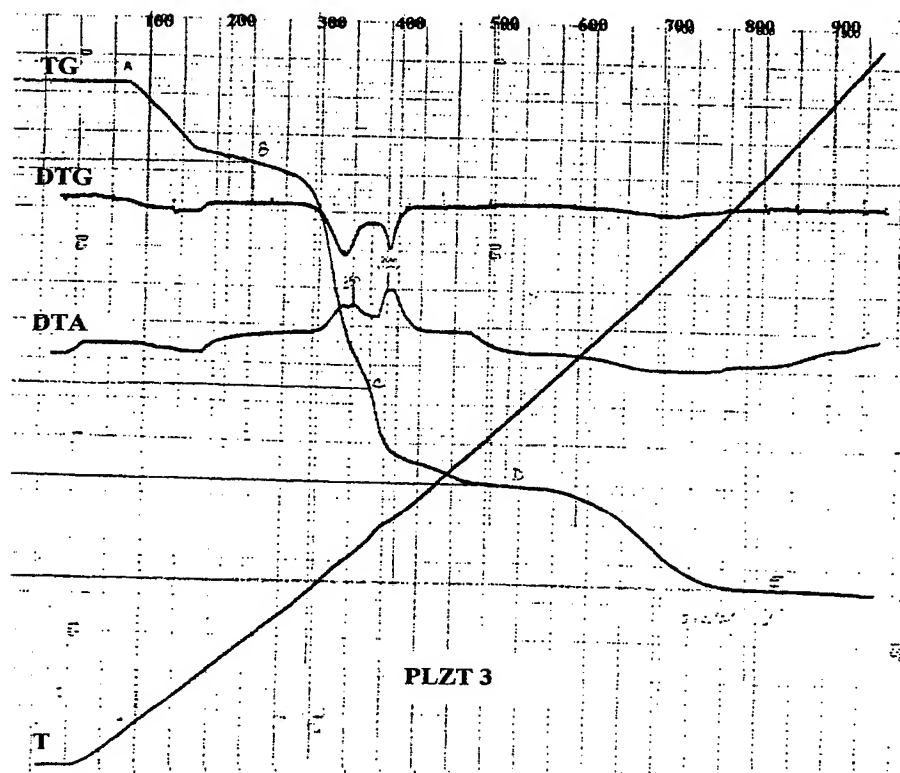


Fig. 4 TG, DTG and DTA curves of PLZT 10/65/35 from oxalates

After Ag electrodes deposition, the electrical characteristics of the sintered body were measured. The values of relative permittivity of hot pressed sintered PLZT ceramics and bulk density are presented in Table 5.

Tab. 5. Electrical measurements and bulk density of PLZT-10/65/35 electrooptic ceramic

Sample	Equivalent circuit	Capacity C_p [nF]	Loss $\text{tg } \delta$ [10^{-3}]	Resonance frequency (R) (Fr/ReZ) [MHz/ Ω]	Antiresonance frequency (Fr/ReZ) [MHz/ Ω]	Density ρ [g/cm^3]	ϵ'	ϵ''
1A	parallel	2,17	40	1,69/32	1,78/36	7,46	3299	122
1B	parallel	4,08	37	1,45/46	1,54/49	7,47	2697	102
1D	parallel	3,18	38	1,82/36	1,95/43	7,39	2824	113

4. CONCLUSIONS

The stoichiometric PLZT 10/65/35 oxide powders of high purity starting from different precursors such as oxalates, hydroxides and hydroxides-oxalates mixture at low temperatures was obtained. From these powders dense fine grained microstructure ceramics was sintered. The results obtained by this way (chemical synthesis - hot pressing - oxygen treatment) were better than that obtained with common technology.

REFERENCES

1. M.Quillec, *Materials for Optoelectronics*, 1996, Kluwer Academic Publishers, Boston/Dordrecht/London
2. A. Sternberg, "Transparent ferroelectric ceramics:properties and applications", *Ferroelectrics*, **91**, pp 53-67, 1989
3. Kanhaiya Lal Yadav, and R.N.P. Choudhary, "Synthesis and characterisation of PLZT (10/65/35)" *J. Mater. Sci.*, **28**, pp 769-772, 1993
4. M.Awano, and H.Takagi, "Synthesis of PLZT ceramics by coprecipitation method and the effects of grinding on synthesis and sintering behaviour of powders" *J.Ceram.Soc.Japan*; **101**, pp 124-128 1993
5. J. Thomson, "Chemical preparation of PLZT powders from aqueous nitrate solutions", *Ceramic Bulletin*, **5**, pp 421-433, 1974

A study of indium antimonide semiconductor material preparation for thermoelectric applications

Mariana Simion^{*a}, Anca Stanculescu^a, Maria Tilica^b, Mihaela Vasilescu^b

^aMATPUR S.A. Bucharest, ROMANIA

^bBIOTEHNOS S.A. - Bucharest

ABSTRACT

Some of the III - V compounds such as InSb, InAs, In As_{1-x}P_x, have high thermal conductivity very high mobility of electrons and low effective masses. Their figures of merit being high enough they are useful materials. For thermoelectric materials, the high mobility of electrons is a very important factor.

Another most important property of a material for thermoelectric applications is its figure of merit, defined as:

$z = \alpha^2 / \rho k$, where, α is the Seebeck coefficient, ρ is the electrical resistivity and k is the thermal conductivity.

The Seebeck coefficient α is given by the equation: $\alpha = -(K/e) \cdot (\delta - \zeta)$, where, K is the Boltzmann constant e is the magnitude of the electron charge and ζ is the reduced Fermi energy.

The most important applications of thermoelectric devices are in medical and bio-technological laboratories and measure apparatus.

This paper presents the scheme of the principle of preparation of n-InSb semiconductor material: direct combination of high purity In and Sb, zone refining process in high purity hydrogen medium and horizontal Bridgman technique of crystal growth.

The material is characterized by chemical stoichiometric determinations and analysis of impurities content as well as by physical analysis: determination of resistivity, band gap, Hall mobility and determination of IR spectra.

Keywords: semiconductor, InSb, thermoelectric devices, Seebeck coefficient, band gap, mobility, carrier concentration, electrical resistivity.

1. INTRODUCTION

InSb semiconductor material has the melting point about 525 ± 0.3 °C¹. The thermal conductivity is 0.04 cal./cm.sec. at 40 °C and 0.02 cal/cm.sec.at 425 °C. The energy gaps at 300 K and 0 K are usually taken to the about 0.17 and 0.23 eV.

The carrier concentration at 77 K is $\approx 1.10^{14}$ cm⁻³. The electron and hole mobilities in the highest purity material are respectively about 7.10^4 and 7.10^2 cm²/V.sec. at 300 K and about 6.10^5 and 1.10^4 cm²/V.sec. at 77 K. The latent heat of fusion is 11.2 ± 0.4 kcal/mole.

One the most important properties of a material for thermoelectric applications is the figure of merit z . The performance of a thermoelectric generator or refrigerator is determined primarily by the figure of merit of the materials, the performance improving with an increase in the figure of merit⁴.

The figure of merit is defined as:

$$z = \alpha^2 / \rho k \quad (1)$$

^{*}Correspondence: E-mail: simion@prima.matpur.ro, Fax: (401)255 01 48; Telephone: (401) 255 69 00/188

where α is the Seebeck coefficient, ρ is the electrical resistivity and k is the thermal conductivity.

The Seebeck coefficient α is defined by relation:

$$\alpha = -(k/e) \cdot (\delta - \zeta) \quad (2)$$

where, k is the Boltzmann constant, e is the magnitude of the electron charge, ζ is the reduced Fermi energy.

$$\zeta = E_F/kT \quad (3)$$

where, E_F is Fermi energy measured from the edge of the band, T is absolute temperature δkT is the average energy of the transported electrons relative to the band edge. It depends on the scattering mechanism and the reduced Fermi energy.

The thermal conductivity is the sum of electronic conductivity k_e and the lattice conductivity k_L . Relation gives the electronic conductivity:

$$k_e = \gamma (k/e)^2 \cdot (T/\rho) \quad (4)$$

where γ is a constant, which depends on the electron scattering mechanism and on the reduced Fermi energy. The electrical resistivity ρ is defined in relation with the electron mobility μ :

$$\rho = (ne\mu)^{-1} \quad (5)$$

And the carrier density is usually determined from the Hall coefficient R by the relation:

$$R = Br(nec)^{-1} \quad (6)$$

where, c is the velocity of light, r is the correction factor which depends on the scattering mechanism and the degree of degeneracy and generally is $1 \div 2$ and B is the correction factor which is normally 1.

The Seebeck coefficient at optimum carrier concentration is about $200 \mu V/^\circ C$ for the materials having figure of merit presented in Fig. 1.

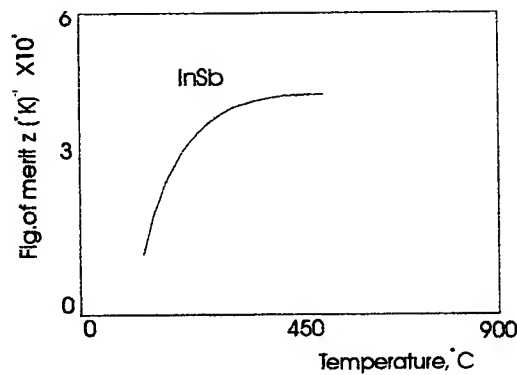


Fig.1. The figure of merit of InSb function of temperature.

The Fig.1 shows the figure of merit of InSb semiconductor compound function of temperature.

2. EXPERIMENTS

In order to obtain semiconductor InSb high grade purity In and Sb have been used ^{2,3}. The high reactivity of melted In and Sb is well known, and that is why the material from which the vessel is made of directly affects the purity grade of the obtained InSb. According to literature indications, quartz seems to be the most recommendable material .

The intermetallic compound has the molecular ratio of 1:1, corresponding to the weight composition of 49.52 % In and 51.48 % Sb. Above 100 °C In and Sb react with O₂ and, when melted, the oxidizing velocity increases notably, changing the stoichiometry of the product. In order to avoid this phenomenon, the synthesis at 700 – 720 °C directly from elements must be lead in reducing atmosphere. The two metals were mixed mechanically.

The reaction time was 3 hours. The product was suddenly cooled, so it detached with noise from the vessel walls. The reaction product has metallic glance, light gray color and its melting point is at 525 °C.

Melting zone refining in reducing atmosphere purified InSb obtained as above. The length of the melted zone was 10 – 12 mm. As a result, a polycrystalline InSb is obtained.

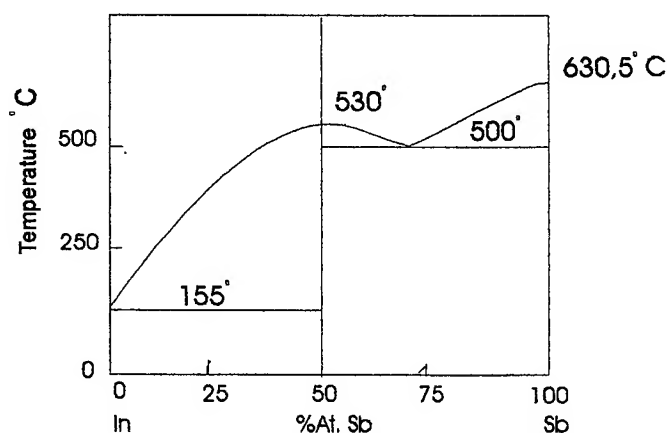


Fig.2. The In-Sb phase diagram.

The Fig.2 presents the In - Sb phase diagram. It shows the composition of stable compound InSb.

In order to transform it into monocrystal, it was sealed in vacuum and Bridgman technique was utilized ¹. No InSb germs have been used to obtain monocrystal. The pression in boat is $1 \cdot 10^{-5}$ mm Hg and the pull rate is 5 - 10mm/hr.

The maximum temperature of the process is 550°C. We obtained ingots with very large grains structure.

3. RESULTS AND DISCUSSIONS

Semiconductor compounds pose problems for more complex than those associated with elemental semiconductors, not only from the standpoint of physics and electronics but also from the metalurgical point of view. For thermoelectric materials, the high mobility of electrons is a very important factor.

Purification becomes more difficult, since zone refining is not applicable to all materials and for all impurities. Furthermore, the reactivity or refractory nature of some of the new materials makes the problem of containers or crucible a very difficult one.

The content of impurities determined in InSb material is presented in table 1. Quantitative analysis was performed using an emission spectroscopy. In the antimony and in its compounds, a most undesirable impurity is the arsine. The arsine content was almost the determination limit.

Table 1. The content of impurities determined in InSb samples.

Elem. Sample	Pb %	As %	Sn %	Fe %	Bi %	Al %	Cu %	Ag %	Zn %
InSb 1	$<1.10^{-3}$	1.10^{-2}	$<10^{-3}$	$<10^{-3}$	$<1.10^{-3}$	1.10^{-3}	1.10^{-4}	$<1.10^{-4}$	$<1.10^{-2}$
InSb 2	$<1.10^{-3}$	1.10^{-2}	$<10^{-3}$	$<10^{-3}$	$<1.10^{-3}$	1.10^{-3}	$<1.10^{-4}$	$<1.10^{-4}$	$<1.10^{-2}$
InSb 3	$<1.10^{-3}$	1.10^{-2}	$<10^{-3}$	$<10^{-3}$	$<1.10^{-3}$	1.10^{-3}	$<1.10^{-4}$	$<1.10^{-4}$	$<1.10^{-2}$

Small deviations from stoichiometry, which ordinarily are of no consequence, become of primary importance when semiconducting properties are considered. In III - V intermetallic compound, an undetectable excess of the group III element can lead to p-conduction, whereas an excess of the group V elements leads to n-type conduction.

Table 2. The relative deviation from stoichiometry for the InSb samples.

InSb	In %	Sb %	Relative deviation %
1	49,1	50,9	1,1
2	48,8	51,2	0,54
3	48,6	51,4	0,15

On wafers 1-mm thickness sliced from InSb ingots, mechanically lapped with an alumina powder and chemical polished by etching in a CP_4 solution, we have measured the Hall effect, the resistivity and the carrier concentration. The band gap energy determined for the InSb is 0.17 eV^3 .

Table 3. The physics characteristics determined for the InSb wafers.

Sample	Thickness W μm	Type of conductb.	Resistivity ρ ($\text{m}\Omega\text{cm}$)	Carrier conc. n (cm^{-3})	Mobility μ ($\text{cm}^2/\text{V}\cdot\text{sec}$)
P 2/1	320	n	4.01	1.01×10^{17}	0.98×10^4
P 2/2	390	n	4.00	1.03×10^{17}	1.01×10^4
P 3/2	605	n	11.34	1.46×10^{17}	0.40×10^4
P 3/8	975	n	9.24	1.15×10^{17}	0.59×10^4
P 4/4	610	n	4.07	7.15×10^{17}	0.22×10^4
P 4/17	505	n	4.02	4.10×10^{17}	3.75×10^4

The samples of InSb were prepared for I.R. spectroscopy. Its absorption spectra were drawn and its absorption peaks were calculated.

We have presented the N.I.R. absorption spectra for the InSb semiconductor at room temperature. InSb monocrystal is used for infrared detection ⁴.

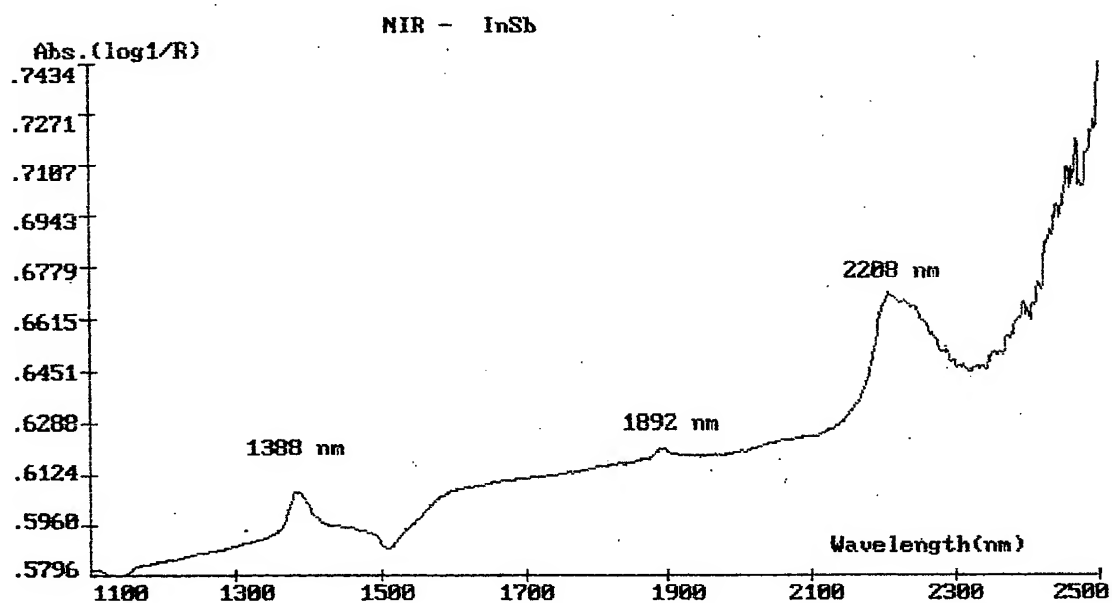


Fig.3. The near I.R.absorption spectrum of InSb polycrystal at room temperature.

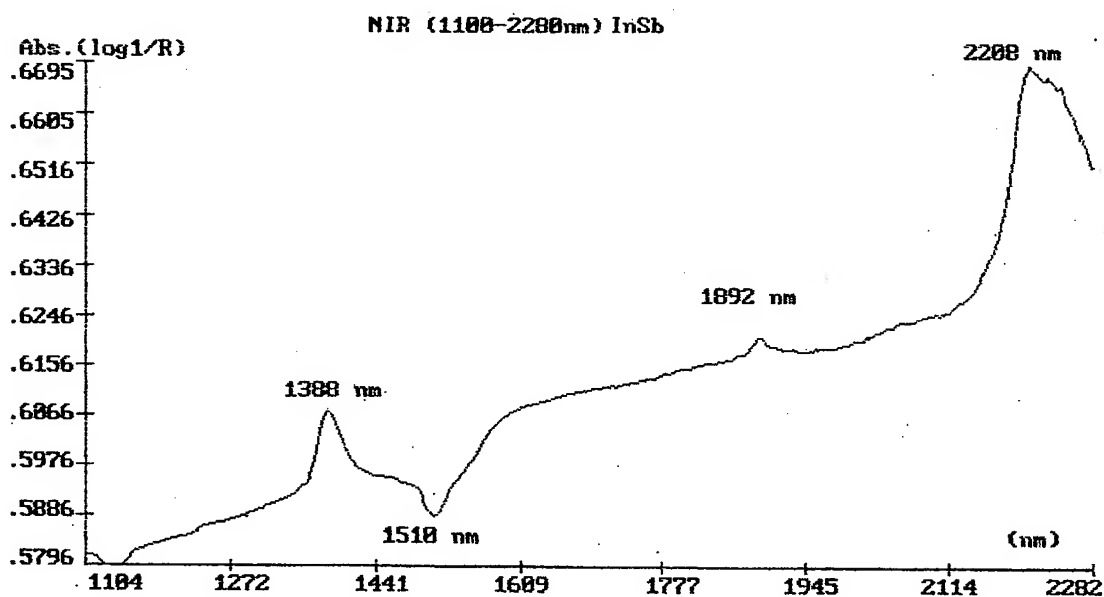


Fig.4. The near I.R.absorption spectrum of n-InSb semiconductor at room temperature.

The Fig. 3 presents the I.R. absorption spectrum of InSb polycrystal material at the normal temperature in the range of wavelength 1100 - 2300 nm.

The Fig. 4 shows the near I.R. absorption spectrum of n-InSb crystalline material at room temperature. It is presented the absorption peaks of InSb semiconductor material.

4. CONCLUSIONS

We have presented the scheme of the principle of preparation of n-InSb semiconductor material: direct combination of high purity In and Sb, zone refining process in high purity hydrogen medium and horizontal Bridgman technique of crystal growth.

Chemical stoichiometric determinations and analysis of impurities content as well as by physical analysis characterize InSb: determination of resistivity, band gap, Hall mobility and determination of IR spectra.

We have presented the In-Sb phase - diagram the figure of merit and the N.I.R. absorption spectra of InSb.

REFERENCES

1. Matsutomo, Toshio; Shimodo, and Takashi, Manufacture of compound semiconductor crystal by Bridgman method, Jpn.Kokai Tokkyo Koho Jp. 62,182, 185(87,182,185) Cl C30B/11/00, 10 aug.1987, Appl.86/22, 612, 4 Feb. 1986, 5pp.
2. Dryburgh, P.M., The estimation of minimum growth temperature for crystals growth for the gas phase, *Journal of Crystal Growth*, 1988, **87**(4), 397 - 407.
3. M.Simion, A.Stanculescu, S.Ionescu, Studiul obtinerii plachetelor de InSb si caracterizarea lor, *Zilele Academiei Timisene*, Proceeding, pp.135-138, 1997.
4. Metallurgical Society Conference, vol.5, *Properties of elemental and compound semiconductors*, edited by Harry C.Gatos, Boston, 1959

Aluminophosphate – doped glasses with rare - earth ions

Rodica Rogojan^{*a}, Paul E. Sterian^b and Mihai Elisa^a

^aMATPUR S.A. Sos.Garii Catelu nr.5, 73611 Bucharest, ROMANIA

^bPhysics Department, University "Politehnica" Bucharest, Splaiul Independentei 313, 77206

ABSTRACT

Aluminophosphate glasses doped with rare-earth ions have recently attracted a large interest owing to their relevant non-linear optical properties. Until now, all studies were done over the glasses doped with rare - earth ions, in which the rare - earth ions were into a vitreous silica matrix. Our study was made as for rare - earth ions (Sm^{3+} , Dy^{3+} , Ce^{3+} or Ce^{4+} and Eu^{3+}) into a vitreous aluminophosphate matrix. In the first step, the samples of rare - earth doped glasses were obtained by melting the raw materials batch and then by adding rare - earth oxides (Dy_2O_3 , Sm_2O_3 , Eu_2O_3). In the second step, the resulted glass was annealed. By mean of a spectrophotometer (SPECORD M-42), were drawn absorption and transmission spectra, in ultraviolet - visible (UV-VIS) domain. For infrared (IR) domain we used a SHIMADZU - FTIR - 8001PC spectrophotometer.

Keywords: optical nonlinear materials, aluminophosphate glass, semiconductor-doped glasses.

1. INTRODUCTION

Glasses containing small quantities of lanthanide ions have important technological applications which utilise transitions electronic energy states, for example, the neodymium glass laser.¹ Many lanthanide ions have an incomplete 4f level that gives rise to the electronically forbidden f - f spectra in the near - infrared/visible/ultraviolet region. The spectra of lanthanide ions also contain bands of much greater intensity owing to charge transfer processes. Intense bands also arise owing to (allowed) interlevel, 4f - 5d, "Rydberg" transitions and for some lanthanide ions these bands are accessible to study since the electronic transitions occur at lower energies than for charge transfer. On dissolution in glass, the majority of rare earth ions introduce very sharp and distinctive absorption bands into the spectral transmission curve. The absorption spectra are due to electronic transitions between energy levels in the 4f shell. Their sharpness is due to the fact that the inner electronic shell is largely shielded from the effects of the ligand field by the outer 5s and 5p electrons. The ligand field is, basically, a perturbation on the energy levels, introducing fine structure to the absorption spectra. In contrast the ligand field for transition metal ions in glass is a factor of hundred stronger and the absorption spectra are due to the transitions between levels produced directly by the field.

Though sharp, the intensities of the absorption bands are relatively weak, the optical absorption coefficients being a factor of ten lower than for the transition ions. Judd² has accounted for such intensities by assuming that transitions of electric dipole character originate from the admixture of terms of opposite parity with the 4f wave functions.

The complexity of the glass absorption spectra depends on the number of unpaired electrons in the 4f shell. The spectra of cerium, europium (2+) are relatively simple, reflecting the stability of the empty, half full and filled 4f electronic shell. In contrast dysprosium impart an array of sharp absorption bands, extending from the near infrared through to the ultraviolet region.

The detailed presentation of the absorption spectra of rare earth ions in glass was given by Herring, Dean and Drobnick². A less detailed presentation in terms of actual spectra, but one providing more theoretical interpretation, was that by Smith and Cohen².

^{*}Correspondence: E-mail: rodica@prima.matpur.ro, Fax: (401)255 01 48; Telephone: (401) 255 69 00/188

In the present paper we present our studies directed on the aluminophosphate vitreous matrix doped with rare earth oxides (Dy_2O_3 , Sm_2O_3 , Eu_2O_3 , CeO_2).

2. EXPERIMENTAL PROCEDURE

A brief description of the technological process will be presented below. The weighing of raw materials according to the glass molecular formula, damp homogenization while chemical reactions of lithium, barium and aluminium phosphate obtaining take place, processes which occur simultaneously at about 200°C .

Then, the drying process and the preliminary heat treatment occur among $100 - 800^\circ\text{C}$, in order to obtain homogeneous phosphates. Melting process takes place at about 1200°C followed by the cleaning up of the molten glass during several hours, process that has the goal of obtaining a homogeneous glass lacked of defects (gases and fibrous inclusions, etc.). After the casting process the colourless and transparent glass samples are annealed at 425°C .

The glass compositions were experimented:

- $\text{Li}_2\text{O} - \text{P}_2\text{O}_5 - \text{Al}_2\text{O}_3 - \text{BaO} - \text{La}_2\text{O}_3$, doped with 1 % (mol percent) or 2 % (mol percent) of $\text{CeO}_2 + \text{Eu}_2\text{O}_3$, Sm_2O_3 or Dy_2O_3 .

3. TRANSMISSION AND ABSORPTION SPECTRA

3.1. Glasses with cerium and europium

Neither of the two possible valency states of cerium, ceric (Ce^{4+}) or cerous (Ce^{3+}), has absorption bands in the visible spectral region. It is, however, possible to form the cerates of tetravalent metals in glass, such as with the titanium or lead.

The optical absorption of both states of cerium is in the ultraviolet region. That of ceric is centred at a wavelength of 240 nm and cerous at 314 nm .

Europium can be present in glass in either the divalent or trivalent state. The absorption spectra of divalent and trivalent europium are similar to those for cerous and ceric ions respectively. This is to be expected since the difference is exactly a half-filled $4f$ shell. Divalent europium has a single band at approximately 340 nm . The primary absorption of trivalent europium is at wavelengths 392 nm and 462 nm .

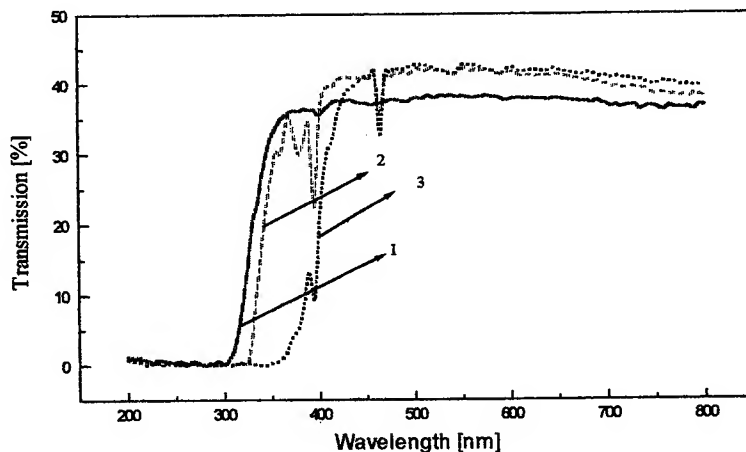


Fig 1. UV-VIS transmission spectra of aluminophosphate glass doped with Europium - Cerium

1. aluminophosphate glass sample; 2. aluminophosphate glass with Eu 1% mole and Ce 1% mole
3. aluminophosphate glass with Eu 2% mole and Ce 2% mole

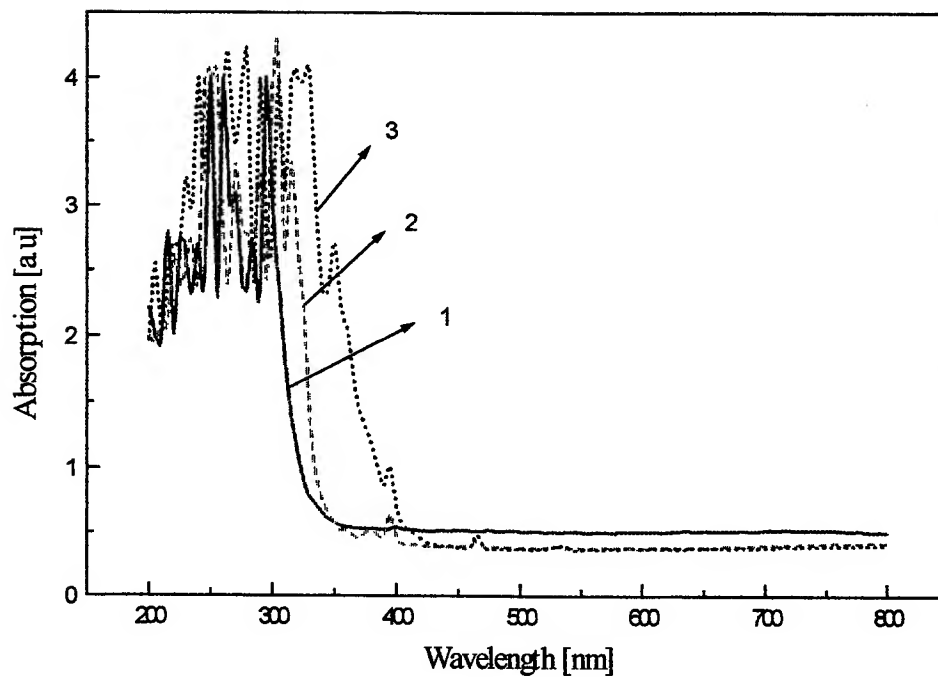


Fig 2. UV-VIS absorption spectra of aluminophosphate glass doped with Europium - Cerium
 1. aluminophosphate glass sample; 2. aluminophosphate glass with Eu 1 % mole and Ce 1% mole
 3. aluminophosphate glass with Eu 2 % mole and Ce 2% mole

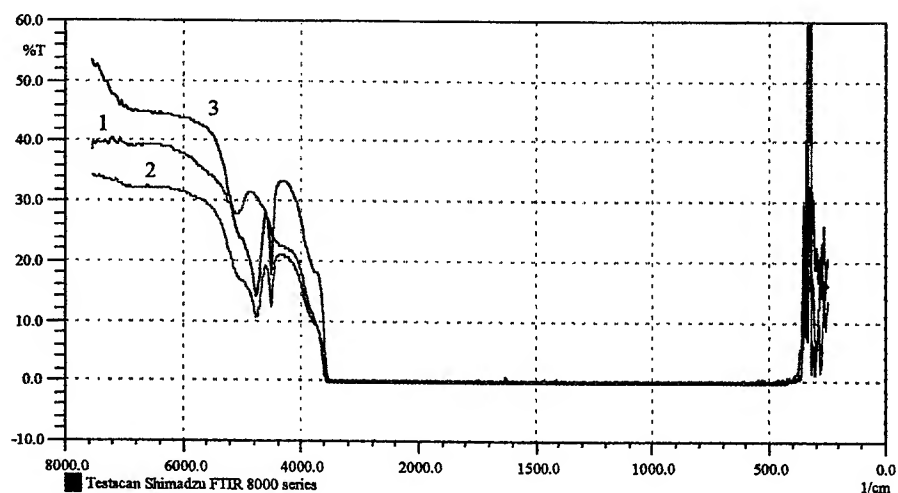


Fig 3. IR transmission spectra of aluminophosphate glass doped with Europium - Cerium
 1. aluminophosphate glass sample; 2. aluminophosphate glass with Eu 1 % mole and Ce 1% mole
 3. aluminophosphate glass with Eu 2 % mole and Ce 2% mole

The Fig. 1 and Fig.2 show the behaviour of the absorption and transmission in the ultraviolet - visible (UV-VIS) range. The optical absorption for the aluminophosphate glass doped with cerium - europium ion has four absorption bands: 310 nm for cerous ions, 360 nm for divalent europium ions, 390 nm and 460 nm for trivalent ions.

The Fig. 3 shows transmission in the infrared range (IR). The aluminophosphate glass doped with cerium - europium ion has two absorption bands: at 4800 and 4600 cm^{-1} .

3.2. Glasses with samarium

Samarium can be present in glass in either the divalent or trivalent state. However, divalent samarium cannot be produced by chemical reduction. It has been formed by X - irradiation by Smith and Cohen².

The absorption spectra associated with trivalent samarium are sharp and well defined in wavelength position in soda - lime - silica glass is 370 nm, 402 nm and 374 nm.

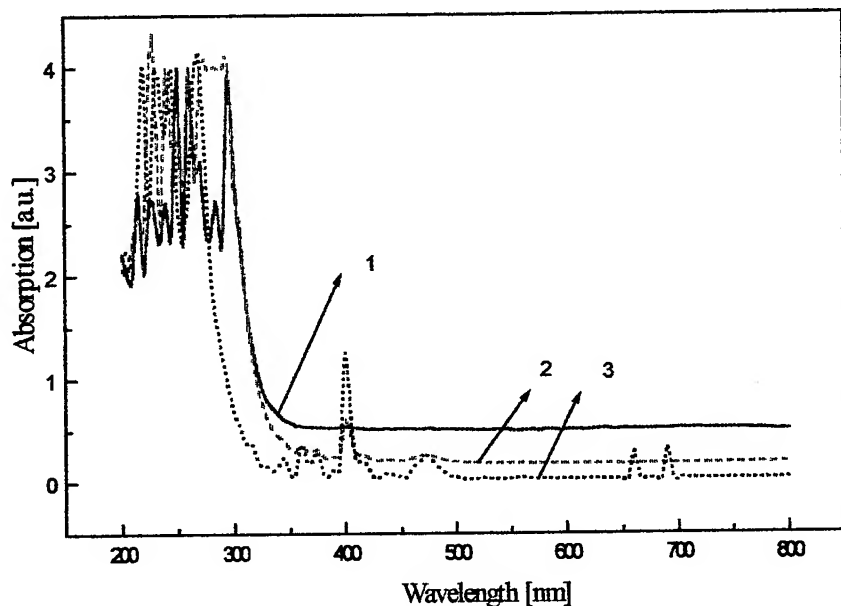


Fig 4. UV-VIS absorption spectra of aluminophosphate glass doped with samarium
 1. aluminophosphate glass sample; 2. aluminophosphate glass with Sm 1% mole
 3. aluminophosphate glass with Sm 2%

The Fig. 4 and Fig.5 show the behaviour of the absorption and transmission in the ultraviolet - visible (UV-VIS) range. The optical absorption for the aluminophosphate glass doped with samarium ion has three absorption sharp and well defined bands: 360 nm, 380 nm and 400 nm for trivalent samarium ions.

The Fig 6 shows transmission in the infrared range (IR). The aluminophosphate glass doped with samarium ions has four absorption bands: at 7200, 7100, 6700 and 6000 cm^{-1} .

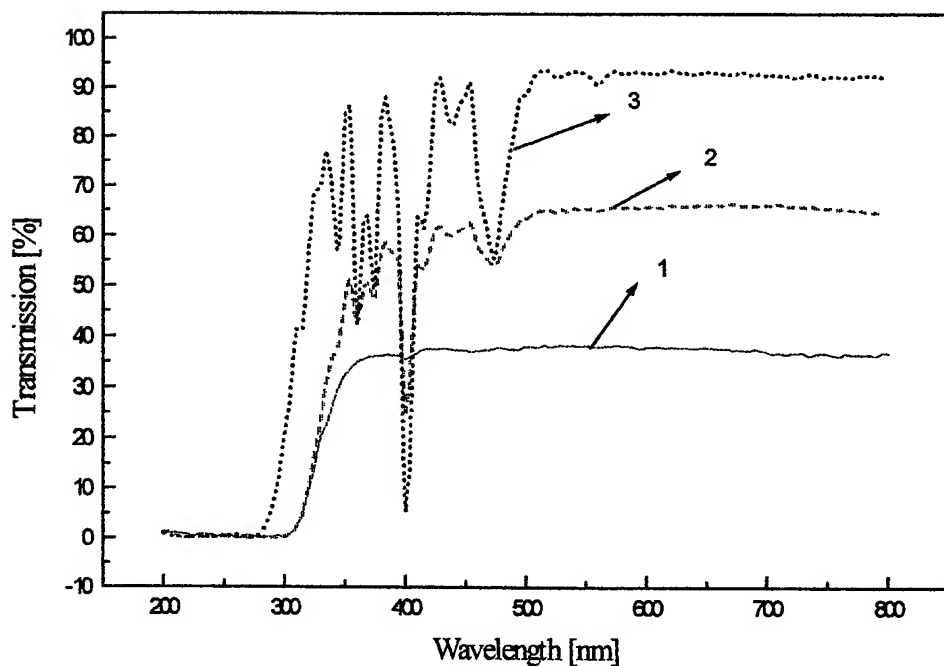


Fig. 5. UV-VIS transmission spectra of aluminophosphate glass doped with samarium
 1. aluminophosphate glass sample; 2. aluminophosphate glass with Sm 1% mole
 3. aluminophosphate glass with Sm 2%

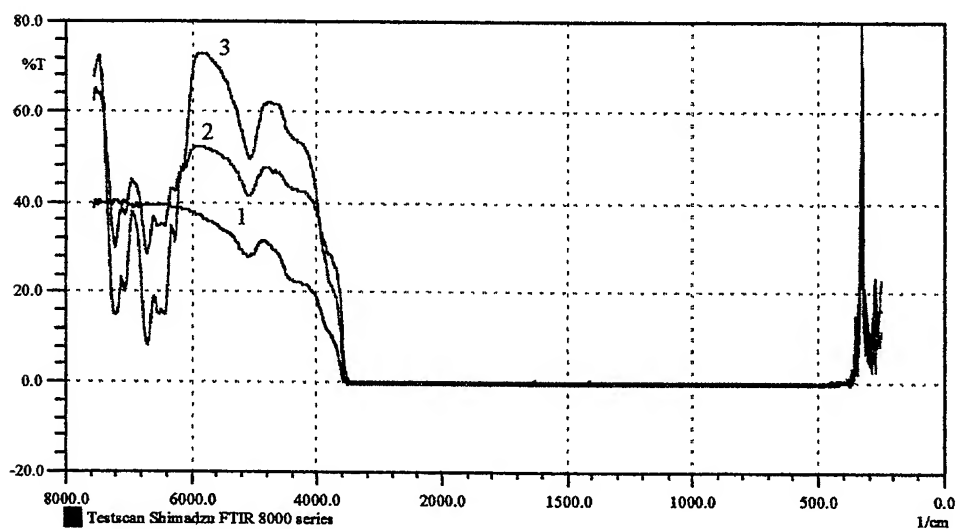


Fig. 6. IR absorption spectra of aluminophosphate glass doped with samarium
 1. aluminophosphate glass sample; 2. aluminophosphate glass with Sm 1% mole
 3. aluminophosphate glass with Sm 2%

3.3. Glasses with dysprosium

This element has a single valency state (tripositive) and has sharp absorption bands to a glass spectral transmission curve. Their main visible and ultraviolet band positions are: 345 nm, 380 nm and 452 nm for a soda - lime silica base glass. Dysprosium has such weak absorption bands that it can hardly be classified as colorants.

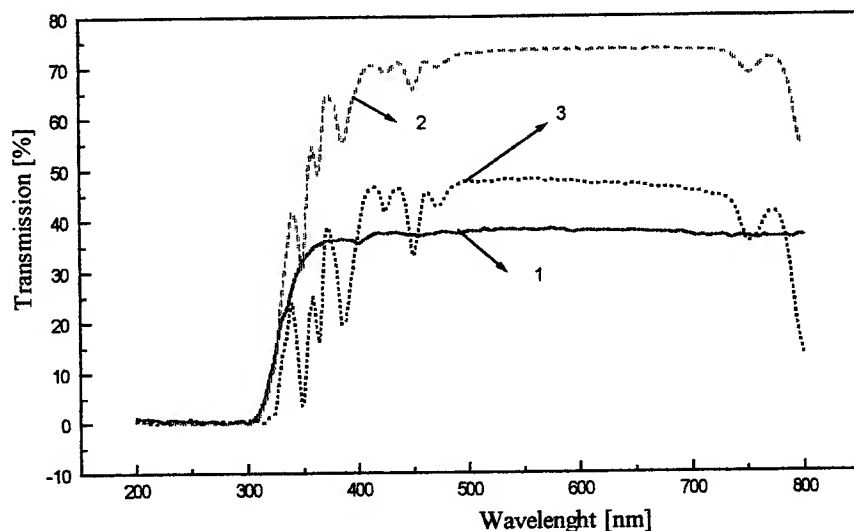


Fig. 7. UV-VIS transmission spectra of aluminophosphate glass doped with dysprosium
1. aluminophosphate glass sample; 2. aluminophosphate glass with Dy 1% mole
3. aluminophosphate glass with Dy 2%

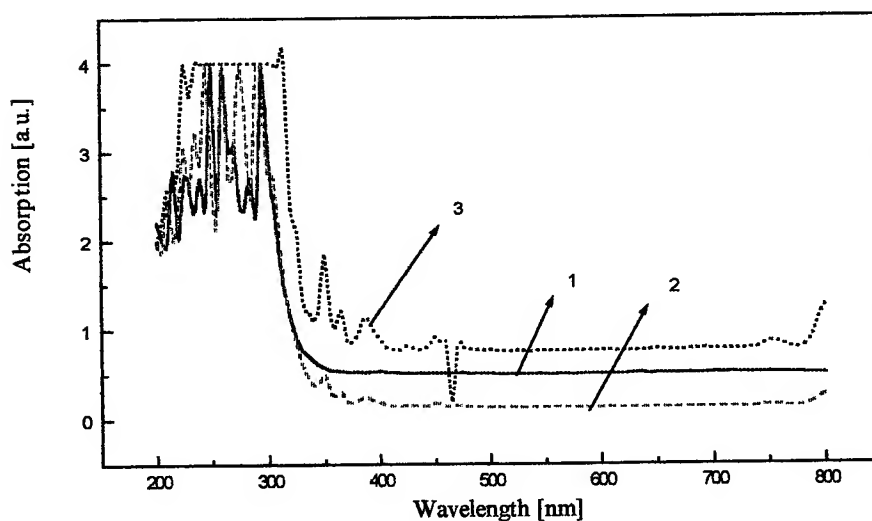


Fig. 8. UV-VIS absorption spectra of aluminophosphate glass doped with dysprosium
1. aluminophosphate glass sample; 2. aluminophosphate glass with Dy 1% mole
3. aluminophosphate glass with Dy 2%

The Fig. 7 and Fig.8 show the behaviour of the absorption and transmission in the ultraviolet - visible (UV-VIS) range. The optical absorption for the aluminophosphate glass doped with dysprosium ions has four absorption bands: 340 nm, 360 nm, 380 nm and 450 nm for trivalent ions.

The Fig. 9 shows transmission in the infrared range (IR). The aluminophosphate glass doped with dysprosium ions has an absorption band: at 5950 cm^{-1} .

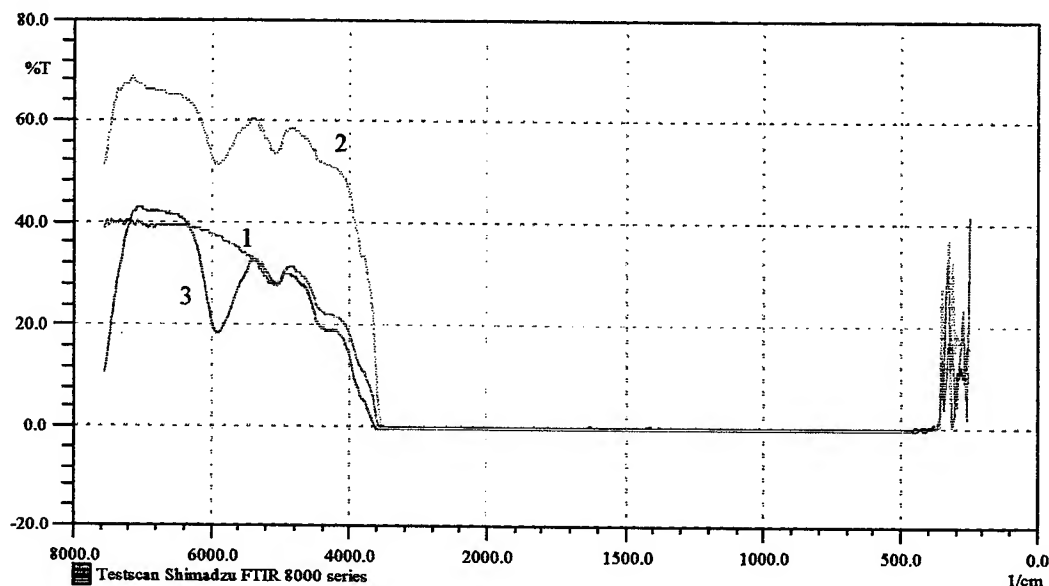


Fig. 9. IR transmission spectra of aluminophosphate glass doped with dysprosium
 1. aluminophosphate glass sample; 2. aluminophosphate glass with Dy 1% mole
 3. aluminophosphate glass with Dy 2%

4. CONCLUSIONS

Our spectroscopic results show in the glass under investigation that the bands of absorption present a shift which depends on the matrix glass composition. It would be a great interest to establish a correlation between the concentration of the rare earth elements and several parameters as: the high of the absorption band, vitreous matrix nature etc.

The possible application as scintillating materials³ suitable for the detection of low rate events has not been investigated. We are planning experiments in order to confirm this possibility.

In the next future, it will be necessary to make some experiments in order to emphasize the non-linear optical properties of these glasses and to estimate their behaviour under laser excitation.

REFERENCES

1. K. Patek, *Glass Lasers*, Butherworkhs, London, 1970.
2. J.Wong, C.A.Angell, *Glass Science by Spectroscopy*, New York, 1976
3. M. Bettinelli, G. Ingletto, P. Polato, G. Pozza, G. Zanella and R. Zannoni, "Optical spectroscopy of Ce^{3+} , Tb^{3+} and Eu^{3+} in new scintillating glasses", *Phys. Chem. Glasses*, **37**(1), pp.4-, 1996.

The influence of the growth conditions on the physical properties of an organic crystalline material for optical application

Anca Stanculescu* and F. Stanculescu

MATPUR, Sos.Garii Catelu nr.5, 73611 Bucharest, Romania

ABSTRACT

We present some investigations on the correlation between the crystalline quality controlled by the physical defects induced by the growth conditions (configurational set-up, thermal gradient at the growing interface, moving speed of the ampoule, geometry of the crucible) and the optical and electrical properties of a benzene disubstituted derivate.

Keywords: organic nonlinear crystal growth, optical properties, electrical properties

1. INTRODUCTION

The most important applications of the optical nonlinear crystals are:

- in telecommunication by optical fiber;
- in optoelectronics for the processing of optical signals;
- in spectroscopy to create coherent, tunable light sources for air and water pollutants identification.

Organic compounds can be used in nonlinear optics as bulk crystal or as thin films.

The advantages of the crystalline organic compounds with optical nonlinear properties in comparison with the classical inorganic materials (LiNbO_3), are:

- strong nonlinear effects characterized by extremely large values for second order susceptibilities;
- very large damage thresholds in laser beams used for nonlinear effect generation, handling power densities $>10^8 \text{ W/cm}^2$;
- large birefringence assuring optimum conditions for the phase-matching process, to increase the conversion efficiency and to induce a strong intensity second harmonic;
- chemical design of organic crystals by "molecular engineering" and conformational analysis for application in the field of nonlinear optics.

Most of the molecules for nonlinear optics derive from an aromatic nucleus with electronic cloud symmetry disturbed by a substituent group, nonlinear susceptibility usually being measured by the average dipole moment interaction between substituent group and electronic cloud. The generation and manifestation of nonlinear optical properties are affected by diffraction phenomena. Organic crystal deterioration is mainly due to some mechanisms also valid for classic nonlinear inorganic crystals: multiphoton absorption; absorption on inclusions; electronic avalanche; autofocusing.

Homogeneity of the bulk optical material is a very important requirement in all virtual applications. For optical devices the homogeneity is necessary to assure high conversion efficiency and lower radiation scattering level, determining phase-matching conditions stability. A benzene di-substituted derivate is a promising material for optical nonlinear applications because it is characterized by a low melting point, transparency in UV-VIS and large values for second order susceptibility and crystallize in a noncentrosymmetric structure.

The most important problems are correlated with the preparation of a bulk material having adequate dimensions and optical quality. To improve the crystalline quality as a consequence of the growth process, it is obvious essential to explain the growth parameters induced defects.

This paper presents some aspects concerning the correlation between the crystalline quality determined by the material purity and the growth conditions and the optical and electrical properties of meta-dinitrobenzene.

Correspondence: Email: anca@matpur.ro

2. EXPERIMENTAL RESULTS

Meta-dinitrobenzene was synthesized in our laboratory using a nitration reaction of the aromatic compound, starting with high purity reagents. Because of the purity requirements in crystal growth, this material has been purified using the following methods:

- a chemical purification (with Na_2SO_3) to remove the ortho and para isomers;
- a slow vacuum distillation under a dynamic vacuum (10^{-4} torr);
- a two stages directional freezing (a length of the molten zone of 3 cm and a traveling speed of 2.5-3 cm/h).

More details concerning the purification processes are indicated in the paper of A. Stanculescu and col.¹

We have chosen the growth from the melt method because of a higher growth rate and of a lack of solvent inclusions in the growing material, this method leading to more pure crystals.

The most important experimental conditions varied to define the crystallization process are:

1. configurational set-up imposed by the chosen crystallization method: horizontal directional solidification or vertical Bridgman-Stockbarger modified method;
2. definition of the interest parameters for a given configuration:
 - the thermal regime characterized by a high thermal gradient across the growing zone;
 - the geometry and the material (Teflon, quartz), of the growing chamber affected by the anisotropy of the growing speed and the adhesion to the wall;
 - the moving regime asking for a small lowering speed of the ampoule in the thermal gradient to remove the solidification heat from the solid-liquid interface.

The first experiment was a directional solidification in horizontal configuration in the below conditions:

- molten zone temperature: 100-120 °C;
- molten zone length: 2 cm;
- molten zone moving speed: 2.5 cm/h.

In the next experiments we have used a Bridgman-Stockbarger growth method². Crystal growth equipment characteristics and improvements are detailed in the paper of A. Stanculescu and col.¹.

We underline that a good growth technique must exceed the following difficulties³:

- a high temperature gradient across the growing zone;
- a thermal and mechanical stress in crystal created by the contact with the growth chamber;
- the anisotropy of the growth speed requiring special geometry for the growing ampoule.

We have studied the Bridgman-Stockbarger crystallization of our organic compound, meta-dinitrobenzene, in different experimental conditions:

- furnace maximum temperature (the hot zone):
 - 1) 114 °C;
 - 2) 110 °C;
- thermostat- bath temperature (the cold zone):
 - 1) 50 °C;
 - 2) 50 °C;
- the thermal gradient at the melt-solid interface:
 - 1) 2-3 °C;
 - 2) 5-7 °C;
- the ampoule moving speed in the furnace:
 - 1) 6-8 mm/h;
 - 2) 0.7-1.5 mm/h.

The high thermal gradient between the hot and the cold zones counteracts the supercooling tendency. Very slow moving speed is imposed by the low thermal conductivity and so can be avoid the twins, additional nucleation and inclusions generation. The importance of growth ampoule geometry and material was discussed in the paper of A. Stanculescu and col.¹.

As-grown ingots have been sliced in wafers polished with a mixture of ethylenglycol - alumina powder of different size (5 μm and then 0.5 μm) and optically characterized by bulk transparency and fluorescence measurements, using a SPECORD M 42. Wafers' thickness is between 0.8 mm and 1 mm.

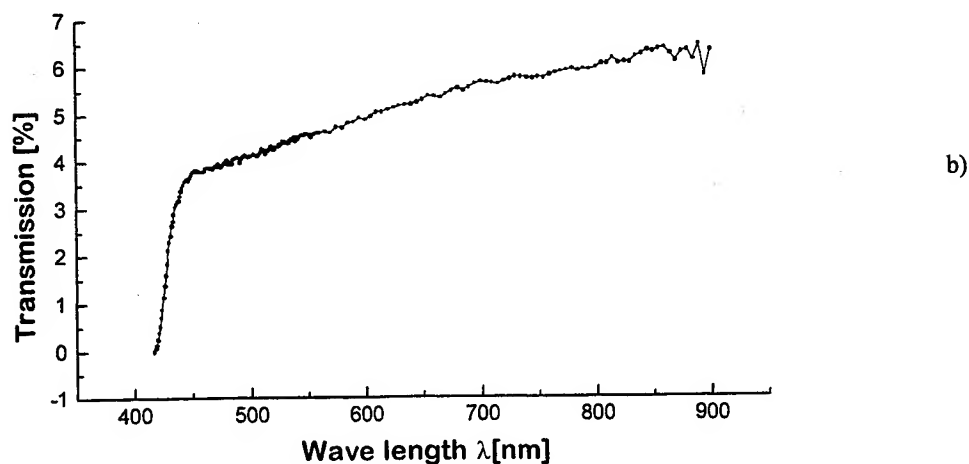
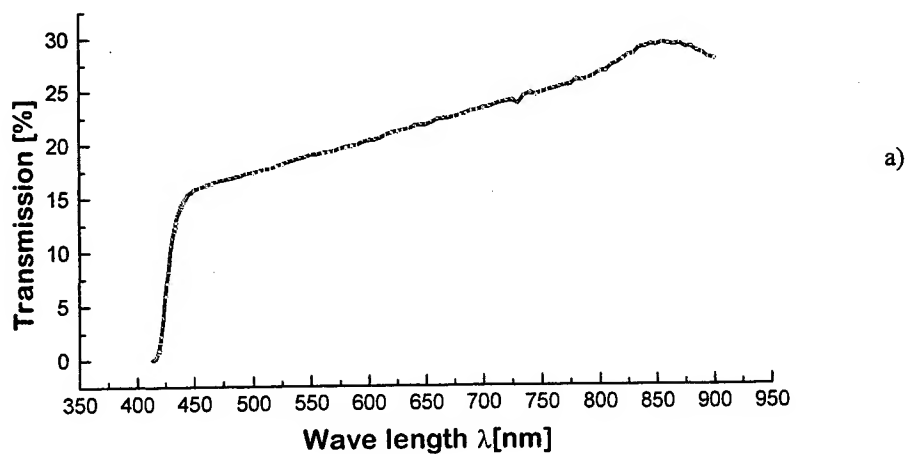
Electrical properties of meta-dinitrobenzene crystalline material have been investigated on films 10-20 μm thick obtained using crystalline fragments from the melt grown ingots. These films were grown between two silicon wafers in a rapid thermal solidification process, in the conditions of a dendritic growth.

The I-V characteristics have been measured on sandwich type structure, semiconductor-insulator-semiconductor (SIS) where the insulator is the organic film and the semiconductor was silicon.

3. DISCUSSIONS

The variations in experimental conditions are reflected in the structural and the compositional quality of our material. The different growth conditions are reflected in changes in structural quality offering the possibility of growth process control. Organic crystal ingot properties are strongly depending on growth conditions. They present twins and cracks.

The highest bulk transmission (~25-30%) has been obtained on wafers cutted from Bridgman-Stockbarger (Fig. 1.c) recrystallized ingot in a Teflon crucible with a steep thermal gradient at the growing interface (5-7 °C) and a slow moving speed (0.7-1 mm/h). These ingots are more homogenous than those grown in other experimental conditions: small interface gradient, fast moving speed (Fig. 1.b). The same shape for the transmission spectrum has been obtain too on wafers cutted from directional solidified ingot in horizontal configuration (Fig. 1.a), but these samples have shown lower mechanical properties and higher fragility creating handling and processing problems.



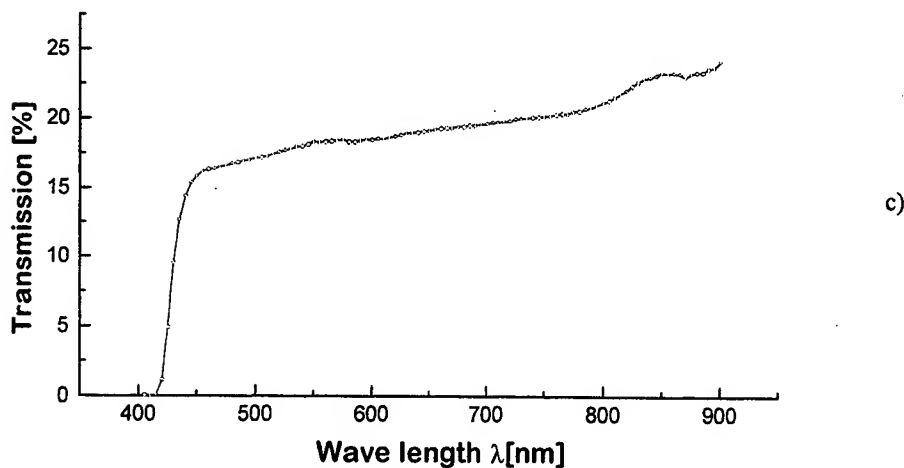
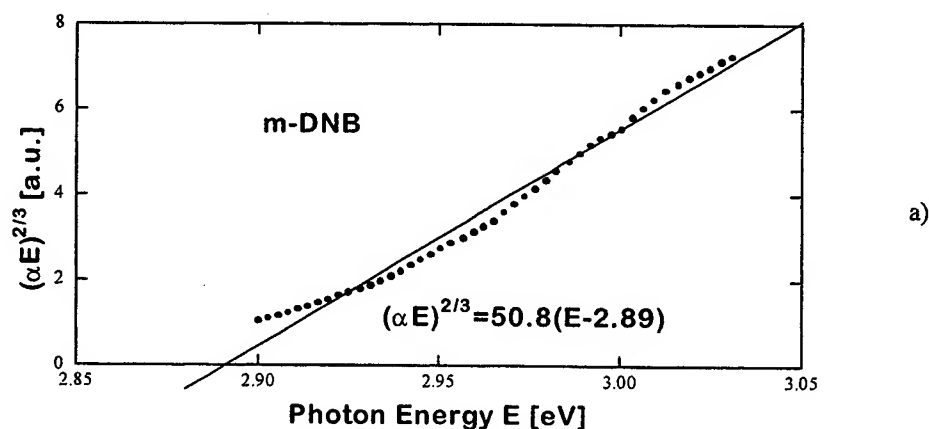


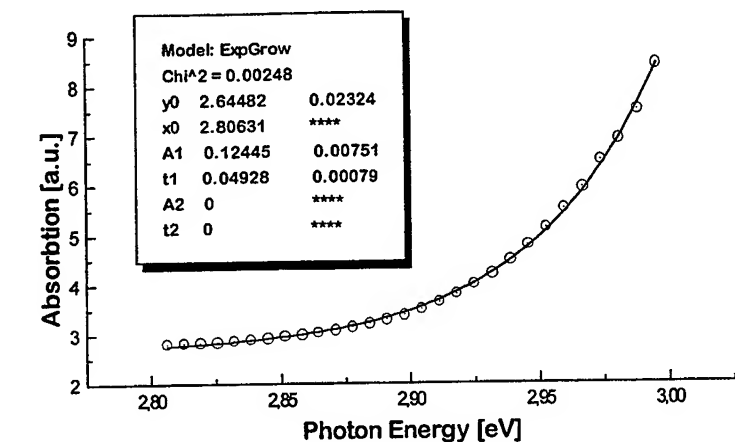
Fig. 1. Transmission spectra on meta-dinitrobenzene wafers:

- a) directional solidified ingot;
- b) Bridgman-Stockbatger ingot grown with small gradient at the interface and fast moving speed of the ampoule;
- c) Bridgman-Stockbatger ingot grown with steep gradient at the interface and slow moving speed of the ampoule.

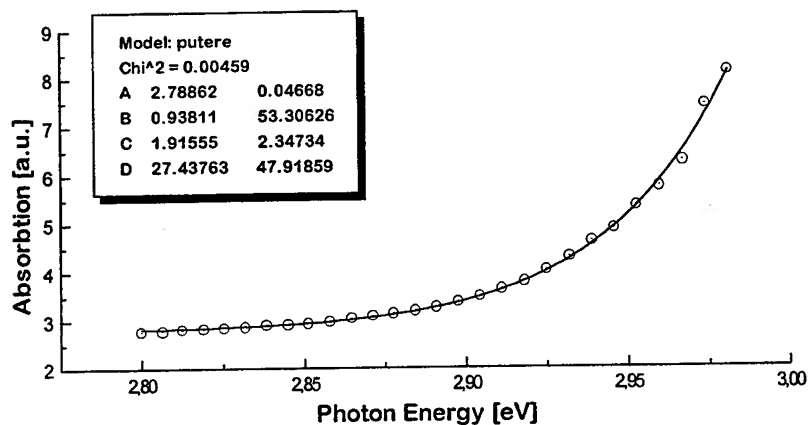
The nonhomogeneities of these ingots have been indicated by the alternation of transparent and opaque zones. Light scattering on material nonhomogeneities has a powerful influence on optical properties (transmission, absorption mechanism) and, as a consequence, on nonlinear phenomena generation.

The processing of experimental transmission data for our organic compound has indicated a clear wide band gap (~ 3 eV) semiconductor and a fundamental absorption edge near $420 \mu\text{m}$ but the results on the absorption mechanism are not consistent and reproducible. For some samples we have obtained a power coefficient $3/2$ suggesting a direct forbidden band to band transition (Fig. 2.a). This intrinsic absorption mechanism, can be "masked" by a strong bulk absorption near the fundamental absorption edge, taking place in thick (bulk) samples. For other samples, a better experimental data fitting implies an exponential function (Fig. 2.b) or a power function (Fig. 2.c), with an exponent that can not be associated to any elementary known intrinsic band to band absorption mechanism. The exponential edge of the absorption can be explained by transition between tails of bands.





b)



c)

Fig. 2. All plots represent absorption coefficient dependence on energy for absorption mechanism identification on different samples from the same directional solidified ingot. The sample purity decreases in the following succession: P3: plot a) > P2plot b) > P1plot c)

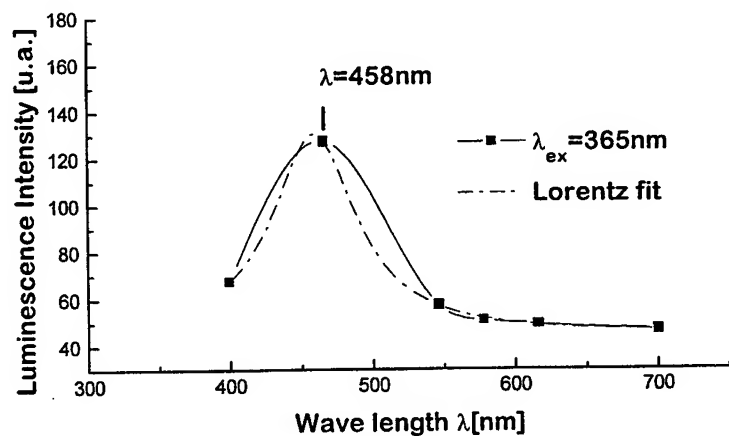
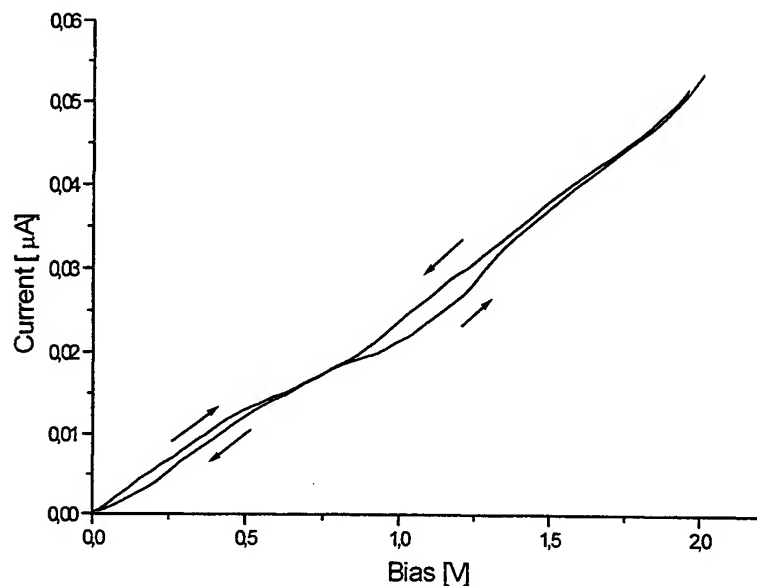


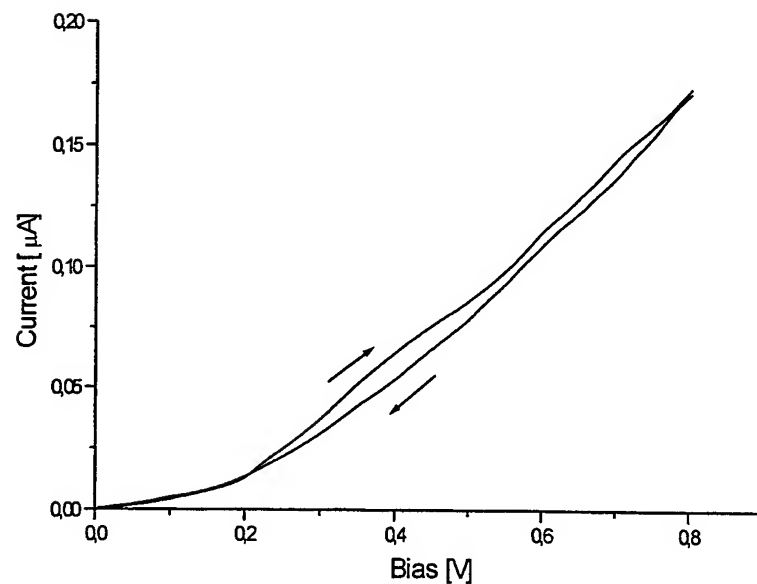
Fig. 3. Fluorescence spectrum on meta-dinitrobenzene wafer grown by Bridgman-Stockbarger process with a steep gradient at the interface and slow moving speed of the ampoule..

The peak of fluorescence spectrum around 458 μm (Fig. 3) has suggested the implication in the light absorption mechanism of same states situated in the band gap, characteristic for an extrinsic absorption. These states can be associated with defects as impurities, lattice defects, or excitons presence.

I-V characteristics are strongly depending on the purification grade. (Fig. 4).



a)



b)

Fig. 4. I-V Characteristics for Silicon-Organic-Silicon SIS structures:

- a) synthesized m-DNB;
- b) directional frozen m-DNB.

4. CONCLUSIONS

We have studied the conditions of an organic compound crystallization, analyzing the influence of experimental parameters on the optical properties of this material. The most homogeneous ingot has been grown in a Bridgman-Stockbarger configuration with a steep thermal gradient and a slow moving speed. Optical absorption characteristics in meta-dinitrobenzene seem to indicate the presence of same energy states in the band gap correlated with the generation of defects and excitons. The I-V characteristics were plotted for some silicon-organic-silicon SIS structures.

REFERENCES

1. Stanculescu and A. Popina, "m-Dinitrobenzene optical nonlinear organic crystal growth for optoelectronics", *SPIE's International Symposium Proceedings, OE-LASE'96*, January - February, San Jose, 2700, pp. 93-99, 1996.
2. Perigaud, "Cristallogénèse de certains dérivés métadisubstitués du benzène", *Bull. Soc. Sci. Bretagne*, 48 (Hors serie), pp. 57-70, 1973.
3. Fox, M. M. Labes and A. Weissberger, *Physics and Chemistry of the Organic Solid State*, 1, Interscience, New York, 1963.

Electric field effect on the electronic states in a GaAs spherical quantum dot

Ecaterina C. Niculescu^a, Edit Lengyel^b, M. Cristea^a

^a"Politehnica" University of Bucharest, Physics Department, Splaiul Independentei 313, 77206
Bucuresti, ^bRomanian National Institute of Material Physics, Bucharest, Romania

ABSTRACT

Using a variational procedure, we have calculated the energy levels in a GaAs spherical quantum dot under the action of an external electric field, assuming an infinite confinement potential. Our results show that the electronic states depend strongly not only the applied electric field, but also on the quantum confinement. Because the field-induced spatial separation of conduction (donor) and valence electrons in GaAs quantum dot decreases the overlap between their associated wave functions, in the presence of the electric field it is expected a reduction of the luminescence. We obtained the dependence of the recombination rate between conduction (donor) and valence electrons as a function of the applied field for different dot radii. We have found that large polarizations are expected for GaAs quantum dot with a radius $R \geq 100$ Å. These aspects must be taken into account in the interpretation of optical phenomena related to shallow impurities in which the effect of an applied electric field competes with the quantum confinement.

Keywords: Quantum dot, electronic states, donor impurity, Stark shift

1. INTRODUCTION

With the development of several experimental techniques, such as molecular beam epitaxy, metal-organic chemical-vapor deposition, and electron beam lithography combined with reverse mesa etching, there has been a lot of work devoted to the understanding of hydrogenic-impurity states in low-dimensional semiconductor heterostructures such as quantum wells, quantum-well wires, and quantum dots. In recent years, there has been great interest in investigating quantum dots (QD) both theoretically and experimentally. Due to the small structure of QD's, some physical properties such as optical and electron transport characteristics are quite different from those of the bulk materials^{1,2}. Recently, Ribeiro *et al.*³ and Yang *et al.*⁴ made have calculated the binding energy of the hydrogen-like impurity in a spherical QD. As expected, they found that the strong electronic confinement leads to a much higher impurity binding energy. However, in their investigation, the influence of the applied electric field on the energy levels is not considered. It has been showed that the presence of the electric field in low-dimensional semiconductor heterostructures gives rise to a polarization of the carrier distribution and to an energy shift of the quantum states^{5,6}. Such effects introduce considerable changes in the energy spectrum of the carriers, which may be used to control and modulate the intensity output of optoelectronic devices. We report in this paper variational calculation of the effect of an external electric field on the electronic states in a spherical GaAs QD. The results are relevant to any optical process, such as emission and absorption in these structures. In this regard, they could be useful in the understanding of the quantum dot lasers. In this calculation we work within the effective-mass approximation and adopt a variational envelope-wave function for donor electron.

In Sec. 2 we consider the effect of an electric field on the eigenstates of an spherical QD, assuming an infinite-confinement potential. The Stark shift in energy position of the photoluminescence impurity peak is discussed in Sec. 3, and our conclusions are given in Sec. 4.

2. EIGENSTATES OF SPHERICAL QUANTUM DOT

Let us consider a particle, with charge e and effective mass m^* in a spherical QD of radius R in the presence of an electric field F along the z axis. We assume that the electron (hole) are completely confined in the microcrystal by an infinite potential barrier. The Hamiltonian of the problem is therefore

* Correspondence: Email: nusa@physics.pub.ro

$$H_s = H_0 + |e|Fz \quad (1)$$

where H_0 is the zero-field quantum dot Hamiltonian

$$H_0 = -\frac{\hbar^2}{2m^*} \nabla^2 + V \quad (2)$$

In GaAs, $m^* = 0.067m_0$ for conduction band, and $m^* = 0.30m_0$ for valence band, where m_0 is the free-electron mass. In the infinite-model approximation the confinement potential is defined as:

$$V = \begin{cases} 0 & \text{if } r < R \\ \infty & \text{if } r \geq R \end{cases} \quad (3)$$

The validity of this approximation depends on the conduction- and valence-band offsets as well as on the radius R . In the case of the semiconductor microcrystals embedded in a glass matrix, we can assume very large band offsets, so that this approximation is justified for all nonzero R values. In the case of finite band offsets, which corresponds to the case of microcrystals surrounded by another semiconductor, the approximation is justified only in the case of intermediate to small quantum confinement ($R \geq 10 \text{ nm}$). Nevertheless, it must be stressed that for very low values ($R \leq 1-5 \text{ nm}$), the effective mass approximation becomes unjustified. Moreover, in the GaAs-Ga_{1-x}Al_xAs system, for the usual Al concentrations the height of the potential barrier is high enough in comparison with the energy level of the ground state. So, it seems to us that the use of the infinite confinement potential approximation, which is consistent to the effective mass approximation, and which is expected to lead to reasonable energy values in the case of practical R values, appear to be a good compromise between accuracy and computer time.

The ground electronic wave function of the Hamiltonian H_0 is

$$\Phi_0(r) = \begin{cases} \frac{\sin(kr)}{r} & \text{if } r < R \\ 0 & \text{if } r \geq R \end{cases} \quad (4)$$

where $k = \pi/R$. In the presence of the electric field, the particle is pushed against (for the electron) or along (for the hole) the direction of the field. This physical situation can be well described if we use a variational function⁵ given by

$$\Phi(\vec{r}) = \exp(-\lambda z) \Phi_0(r) \quad (5)$$

The lowest subband energy is determined by minimizing the expression

$$E(\lambda) = \frac{\langle \Phi(\vec{r}) | H_s | \Phi(\vec{r}) \rangle}{\langle \Phi(\vec{r}) | \Phi(\vec{r}) \rangle} \quad (6)$$

with respect to λ . On the basis of the above equation the electron (hole) energy can be evaluated as function of the applied electric field, and the dimension of the quantum dot. We would like to emphasize that this variational procedure proved to be very successful in explaining experimental data on low-dimensional semiconducting heterostructures.⁵

Fig. 1 shows the variation of the ground state of the conduction (1e) and the valence-band (1h) as functions of the dot size, in spherical GaAs QD structure, in various electric fields. We observe that the energy decreases as the dot radius or the electric field increase. As expected, as in the quantum well case⁵, because the valence-band effective mass is heavy, the valence shift under an electric field is much larger than conduction shift. This 'negative' shift (Stark shift) is more pronounced for large values of R . As a consequence of the Stark shift, the interband absorption edge and the photoluminescence (PL) peak position in the quantum dot shifts downwards in energy.

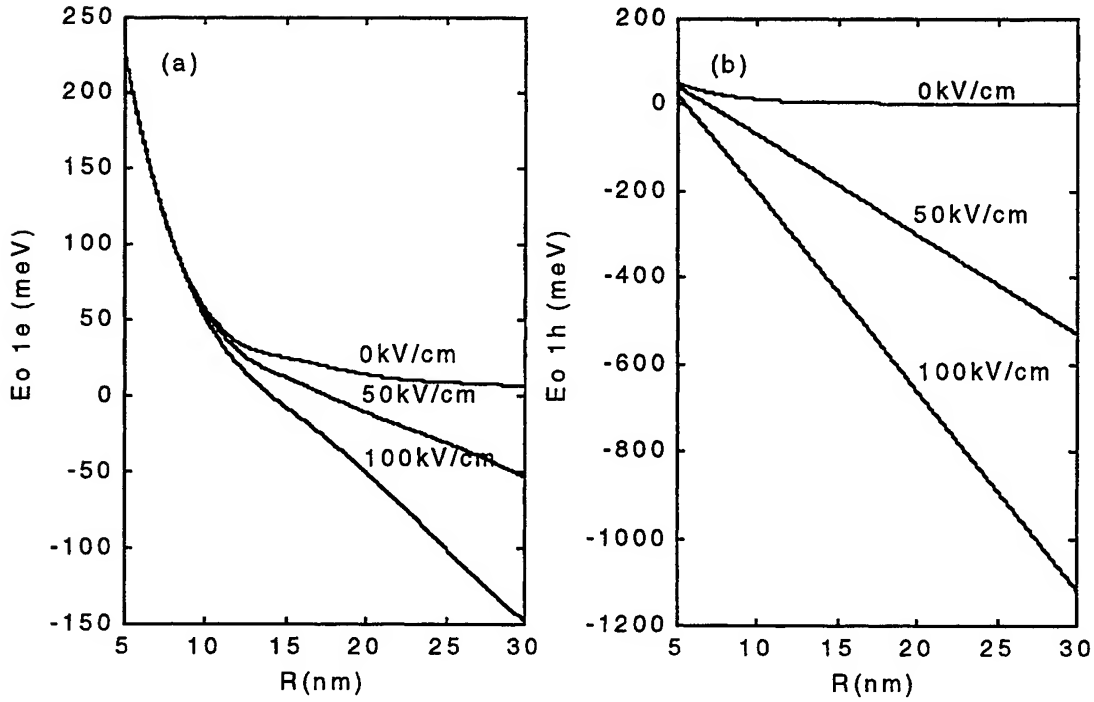


Fig. 1. Energy of the ground state of a GaAs spherical QD as a function of the dot radius for different values of the applied electric field. (a) Conduction electron ($1e$ state), (b) Valence electron ($1h$ state)

Fig. 2 shows the calculated energy position of the PL peak, corresponding to $1e-1h$ transition, versus the electric field strength in a GaAs QD of radius 5 nm and 10 nm, respectively. For small dot sizes, the value of the $1e-1h$ transition is weakly affected by the presence of the electric field. The electron (hole) wave function is significantly modified by the applied electric field for larger radii QD. This is illustrated in Fig. 3, which shows the expectation value of the electron (hole) position along the z -axis, $\langle z \rangle$, as a function of the electric field for $R=5$ nm and $R=10$ nm.

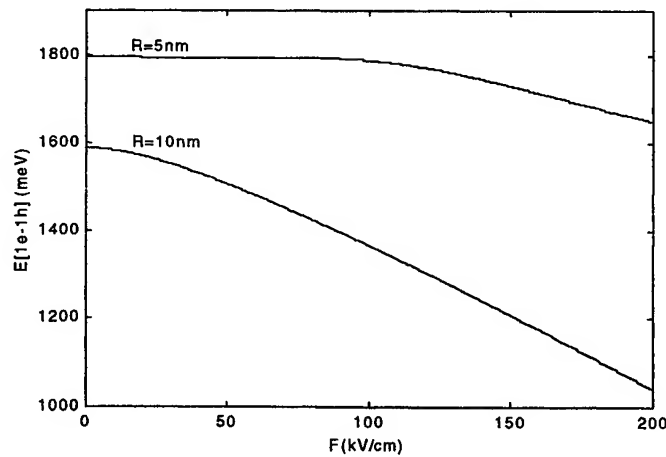


Fig. 2. Transition energy $1e-1h$ as a function of electric field for two dot radius.

We observe that the polarization effect is more pronounced in the valence wave function case, where $\langle z \rangle$ peaks near the dot edge. This spatial separation of carriers strongly affects the overlap integral S_{eh} , defined as $\langle \Phi_e(\vec{r}) | \Phi_h(\vec{r}) \rangle$.

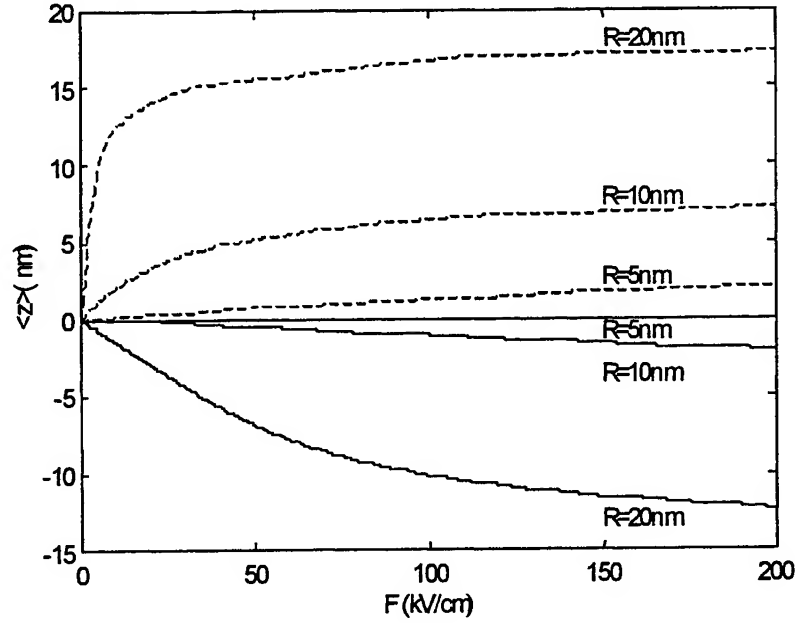


Fig. 3. Expectation value of the conduction (solid line) and valence (dashed line) electron position along the z -axis vs. the applied electric field for different dot sizes.

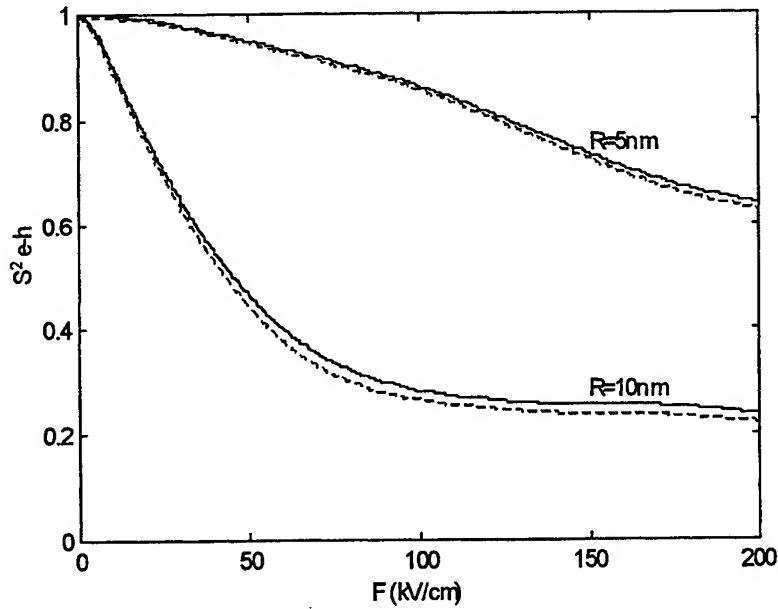


Fig. 4. Square of the overlap integral between electron and hole as a function of the electric field for a QD of $R=5\text{nm}$ and $R=10\text{nm}$. Conduction electron (1e state)-solid line. Donor electron (1s state)-dashed line.

The recombination rate between electron and hole is proportional to S_{eh}^2 , so that this quantity, plotted in Fig. 4 versus the electric field, is significant in PL experiments. Our results showed a shift to smaller values of the PL peak position (Fig. 2) and a strong decrease of PL signal (Fig. 4) as the electric field increases.

3. DONOR IMPURITY IN A GaAs QUANTUM DOT

In the effective-mass approximation, the Hamiltonian of a hydrogenic donor impurity located at the center of a spherical QD in the presence of an electric field F , can be written as

$$H = H_s - \frac{e^2}{4\pi\epsilon r} \quad (7)$$

where $\epsilon = 13.\epsilon_0$ is the dielectric constant of the dot material, with ϵ_0 the vacuum static dielectric constant.

In order to calculate the ground state of the impurity binding energy, the variational technique is used, and for this the trial wave function is taken as

$$\Psi_{1s}(\vec{r}) = \Phi(\vec{r}) \exp(-r/a) \quad (8)$$

where a is the variational parameter.

The ground state energy of a donor impurity in a GaAs QD with an applied electric field is given by

$$E(a) = \frac{\langle \Psi_{1s} | H | \Psi_{1s} \rangle}{\langle \Psi_{1s} | \Psi_{1s} \rangle} \quad (9)$$

and the binding energy is defined as

$$E_b = E_0 - \min_a E(a) \quad (10)$$

With above equations we calculate the binding energy for the ground state of a donor impurity in a spherical GaAs quantum dot, as a function of the dot size, and applied electric field.

In Fig. 5 we present E_b versus radius dot, for different values of the electric field. It is apparent that as the quantum confinement is increased the binding energy is enhanced in the $1s$ -like state. Also, notice that, for strong electric fields, the binding energy reaches a constant value as R is greater than 20 nm; for large value of R the limiting value for the binding energy depends on the value of the electric field (being smaller for higher values of F). One observes that for increasing values of the electric field, the impurity binding energy decreases because the electronic probability density is displaced toward one edge of the dot. Due to the polarization effect is expected a shift in donor electron to valence electron luminescence energy to smaller values with increasing electric field.

In Fig. 6 we display the Stark shift of the $1s$ - $1h$ transition energy as a function of F for two values of the radius dot. Notice that the effect of the electric field is appreciable for large R . The reason of this behavior is that as R increases the quantum confinement become negligible and the carrier motion along the z -axis is essentially dominated by the electric field.

In Fig. 4 we have also shown the square of the overlap integral between the donor wave function Ψ_{1s} and heavy hole wave function Φ_h versus F for a GaAs QD of 5 or 10 nm radius. Due to the electrostatic interaction between the electron and the impurity there exists a greater confinement of the electronic wave function and, therefore, the overlap integral $\langle 1s/1h \rangle$ is slightly reduced in comparison with $\langle 1e/1h \rangle$ integral. It is apparent in Fig. 4 that, although the Coulomb term contributes to the enhancement of the electronic probability density at the center, it does not lead to significant quantitative differences.

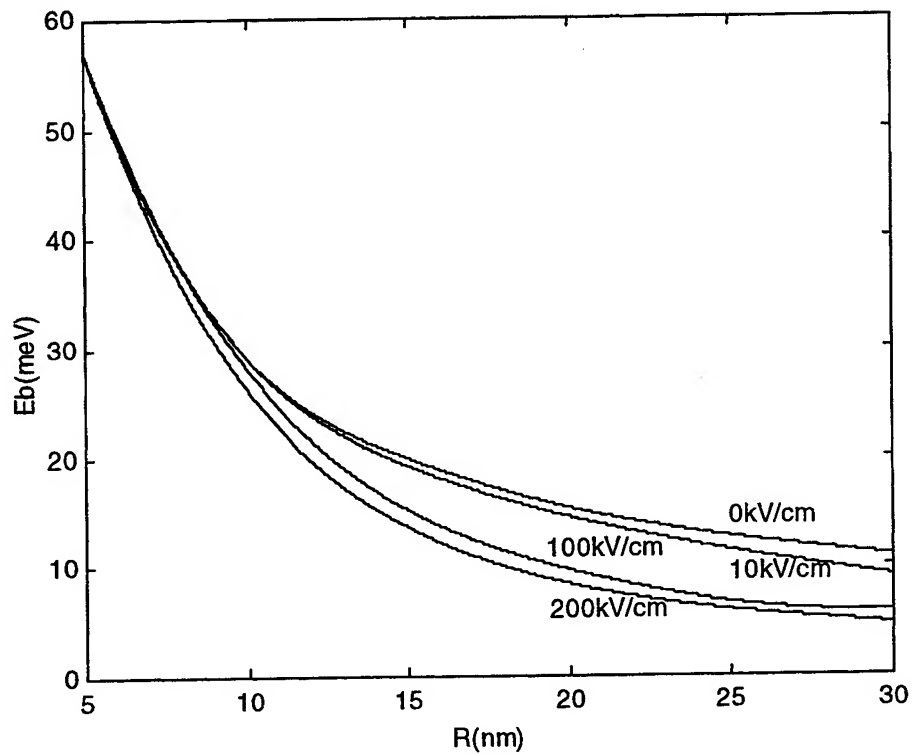


Fig. 5. Variation of impurity binding energy with the radius of the GaAs QD for different values of the applied electric field.

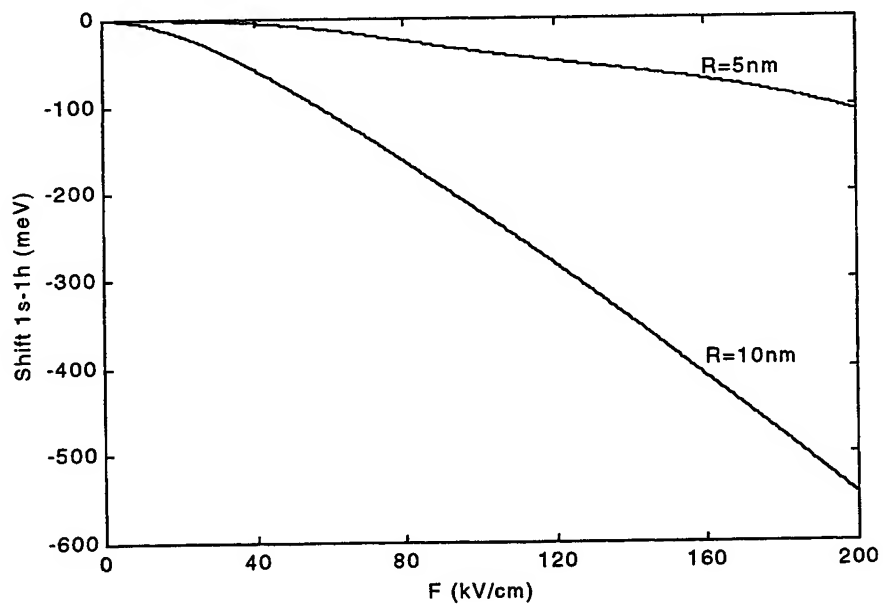


Fig. 6. Shift of the $1s-1h$ transition energy vs. electric field in a GaAs QD for two dot radius

4. CONCLUSIONS

We have studied the influence of the electric field on the electronic states in a spherical GaAs quantum dot, considering an infinite confining potential. Using the effective-mass approximation within a variational scheme we have calculated the energy of the subband states as well as of the *1s*-like state of the donor impurity as a function of the geometry, and applied electric field. We have found that the energies of the electronic states strongly depend, not only on the quantum confinement, but also on the applied electric field.

Our results show that the large polarization is expected for the GaAs QD's with a radius $R > 10\text{nm}$. As in QWs case⁵, the induced spatial separation of conduction and valence electrons should decrease the interband absorption or the radiative emission rate. Also, in the *n*-doped QD's appears a shift in the donor-valence band luminescence energy to lower values with increasing electric field and a reduction of the recombination of carriers.

To our knowledge, this is the first theoretical calculation of the electronic levels in the spherical quantum dot under the electric field. We estimate that the future interpretations of optical phenomena related to electronic states in GaAs QDs, in which the effect of an applied electric field competes with the quantum confinement, must take into consideration these results.

REFERENCES

1. B. Stébé, E. Assaid, F. Dujardin, and S. Le Goff, "Exciton bound to an ionized donor impurity in semiconductor spherical quantum dots", *Phys. Rev. B* **54** (24), pp. 17785-17793, 1996.
2. H. J. Xie and C. Y. Chen, "A bound polaron in a spherical quantum dot", *Eur. Phys. J. B* **5**, pp. 215-218, 1998.
3. F. J. Ribeiro and A. Latge, "Impurities in a quantum dot: A comparative study", *Phys. Rev. B* **50** (7), pp. 4913-4916, 1994.
4. C.C. Yang, L. C. Liu and S. H. Chang, "Eigenstates and fine structure of a hydrogenic impurity in a spherical quantum dot" *Phys. Rev. B* **58** (4), pp. 1954-1961, 1998.
5. G. Bastard, E. E. Mendez, L.L. Chang, and L. Esaki, "Variational calculations on a quantum well in an electric field", *Phys. Rev. B* **28** (6), pp. 3241-3245, 1983.
6. C. A. Duque, A. L. Morales, A. Montes, and N. Porras-Montenegro, "Effects of applied electric fields on the infrared transitions between hydrogenic states in GaAs low-dimensional systems", *Phys. Rev. B* **55** (16), pp. 10721-10728, 1997.

Synthesis of luminescent strontium-magnesium orthophosphate activated with cerium and manganese

Maria Vadan^a, Elisabeth Jeanne Popovici^{*a}, Laura Ungur^a, Marilena Vasilescu^b,
D. Macarovici^a

^a"Raluca Ripan" Institute of Chemistry, Fantanele 30, 3400-Cluj-Napoca,

^b"I.G.Murgulescu" Institute of Physical Chemistry of the Romanian Academy,
Independentei 202, Bucuresti, Romania

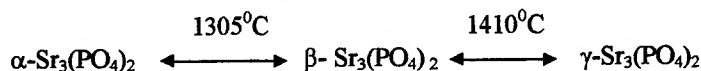
ABSTRACT

Cerium activated strontium-magnesium orthophosphate phosphor exhibits strong UV luminescence (emission maximum at 370-380 nm) whereas cerium - manganese activated phosphor shows pink luminescence (emission maxima at 370-380 nm and 605-610 nm). These phosphors could be used for the manufacture of eritemal or copy machine lamps and for fluorescent lamps for luminous signs, respectively. Samples of $(\text{Sr}_{1-x}\text{Mg}_x)_3(\text{PO}_4)_2:\text{Ce}$ and $(\text{Sr}_{1-x}\text{Mg}_x)_3(\text{PO}_4)_2:\text{Ce,Mn}$ phosphors with variable compositions were synthesised and characterized. Crystalline structure (XRD patterns) and luminescence properties (emission and excitation spectra) were determined and discussed in order to establish the optimum synthesis conditions for phosphor preparation.

Keywords: phosphors, luminescence, phosphates

1. INTRODUCTION

Alkaline earth orthophosphates present polymorphic crystalline structures depending on temperature. Sometimes, the high temperature (HT) structures are good host lattice for phosphors. By the partial substitution of the host lattice cations with other metallic cations with relatively small ionic radius, the HT structures could be also stabilised at normal temperatures. Three polymorphic structures for strontium orthophosphate are known, depending on the temperature^{1,2}.



Sr^{2+} ions can be replaced by other ions, such as Mg^{2+} , Ca^{2+} , Cd^{2+} that form isomorphic structure with that of $\beta\text{-SOP}$ (HT form). This structure is a proper host lattice for phosphors preparation^{3,4}. For the $\text{Sr}_3(\text{PO}_4)_2\text{-Mg}_3(\text{PO}_4)_2$ system, a solid solution possessing $\beta\text{-SOP}$ structure, occurs in the concentration region of 10-35 mole per cent (mole %) Mg.

The present paper presents the results concerning the synthesis of such a host lattice possessing $\beta\text{-SOP}$ structure that could generate appropriate phosphor.

2. EXPERIMENTAL PART

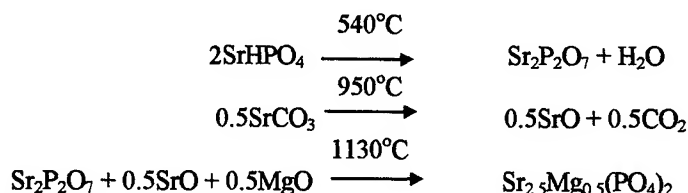
Samples were prepared by thermal synthesis from homogeneous mixtures consisting of SrHPO_4 , SrCO_3 , MgO , $\text{MnNH}_4\text{PO}_4\cdot\text{H}_2\text{O}$ and $\text{Ce}(\text{NO}_3)_3\cdot 6\text{H}_2\text{O}$. All material (with the exception of Ce-compound) were luminescent grade and were prepared in our laboratory by original procedures. For the study referring to the host matrix synthesis, the mixtures were calcinated for 1 h at 1000, 1100, 1200 °C in air. As for the phosphors synthesis, the mixtures were calcinated one hour in N_2 -atmosphere, at 1120 °C. After the thermal synthesis is over, phosphor samples were quickly cooled in N_2 -flow.

* Correspondence: E mail phoratiu@codec.ro; Telephone: +40-64-180165; Fax: +40-64-420441

The samples were characterised by X-Ray diffraction (XRD) method (PW1050 Philips Diffractometer), thermogravimetric analysis (Pauling Erdely OD-102 Derivatograph), IR spectroscopy (75 IR Spectrophotometer, Zeiss-Jena) and fluorescence spectroscopy. Excitation and emission spectra were registered at room temperature (Perkin Elmer 204 Spectrofluorimeter).

3. RESULTS AND DISCUSSION

Strontium-magnesium orthophosphate (SMOP) was prepared by the solid state reaction of SrHPO_4 , SrCO_3 and MgO . The following reactions take place:



The thermal analysis of the mixture reveals that the reagents decomposition reactions proceed at lower temperature than that of the individual compounds (Fig. 1) One can also suppose that the host lattice formation begins at the same time as reagents decomposition but the complete structure is realised only at 1130 °C. This supposition is sustained by the exothermic effect observed on the DTA curve.

The formation of host lattice could be investigated by XRD spectroscopy. In this purpose, the same synthesis mixture with well defined chemical composition, is fired at various temperatures: 1000 °C (6a sample); 1100 °C (6b sample) and 1200 °C (6c sample). The reaction products are investigated by XRD analysis. XRD patterns show that at 1000 °C, the β -SOP structure is already formed. Beside the reflections of this structure some characteristic reflections of the starting substances or secondary products could be observed (Tab. 1). The further temperature increase determines the completion of the solid state reaction. The sample prepared at 1200 °C (6c sample) exhibits the characteristic β -SOP reflections.

Tab. 1 XRD patterns for SMOP-samples prepared at 1000, 1100 and 1200 °C

6a - sample		6b - sample		6c - sample		Structures assigning
d (Å)	I / I ₀	d (Å)	I / I ₀	d (Å)	I / I ₀	
4.45	9.0	4.45	6.0	4.45	23.0	β -SOP
4.34	6.0	4.35	3.0	4.33	24.0	β -SOP
4.22	5.2	-	-	-	-	SrCO_3
3.60	33.0	3.60	13.0	3.62	29.0	β -SOP
3.52	6.2	-	-	-	-	SrCO_3
3.42	54.0	-	-	-	-	$\text{Sr}_2\text{P}_2\text{O}_7$
3.40	94.0	3.36	11.0	-	-	$\text{Sr}_2\text{P}_2\text{O}_7$
3.36	27.0	3.31	6.0	3.35	31.0	β -SOP
3.26	22.0	3.25	30.0	3.26	32.0	β -SOP
3.17	14.0	3.17	3.0	-	-	$\text{Sr}_2\text{P}_2\text{O}_7$
3.04	12.0	3.04	16.0	-	-	$\text{Sr}_2\text{P}_2\text{O}_7$
3.0	100	3.00	100	3.00	100	β -SOP

** Tab. 1 presents only the first part of the XRD spectrum

In the case of phosphor samples 6a and 6b, the IR absorption spectra confirm the presence of un-reacted phase (Fig. 2). For instance, the IR spectra contain some specific bands at 1100-1000 cm^{-1} and at about 720 cm^{-1} that could be correspondingly correlated with the vibrations of P-O and P-O-P bonds from metallic orthophosphates. In the case of phosphor sample 6c, the second band disappears. One can assume that, at temperature higher than 1100 °C, the SMOP lattice is well formed. In this type of crystalline lattice, only a minimal vibration coupling is allowed between the host matrix and the activator ion. As a result, the non-radiative relaxation probability decreases, fact that minimise the luminescent emission attenuation⁵.

By incorporation of cerium ions into the SMOP lattice, three luminescent samples corresponding to 6a, 6b and 6c compositions could be prepared. The excitation spectra of these phosphor samples (Fig. 3a) show two characteristic bands with maxima at about 270 nm and 320 nm, the longer wavelength band being the stronger. The luminescent emission spectra (Fig. 3b) show a single large band in the UV region, with maxima at about 370 nm. The excitability and the emission intensity of these phosphors increase simultaneously with host matrix definitization. The incorporation of a second activator ion (Mn^{2+}), produces an additional emission so that the apparent luminescent emission extends towards the red domain. The synthesised phosphors correspond to a general formula $(\text{Sr},\text{Mg})_3(\text{PO}_4)_2:\text{Ce}, \text{Mn}$ and belong to the category of double -activated or "sensitised phosphors".

The emission spectrum of phosphor containing manganese ions as activator and cerium ions as sensitiser, consists of the Ce^{3+} and Mn^{2+} emission bands centred at about 375 nm and 610 nm, respectively. The relative intensities of the two emission bands depend both on the activator content and the efficiency of the sensitisation process that imply the $\text{Ce}^{3+} \rightarrow \text{Mn}^{2+}$ energy transfer⁶. The efficiency of the energy transfer process is influenced by the relative position of the two activator ions into the host matrix. In this way, the host matrix (with all energetic and spatial characteristics) shows an important contribution to the sensitised luminescence phenomena.

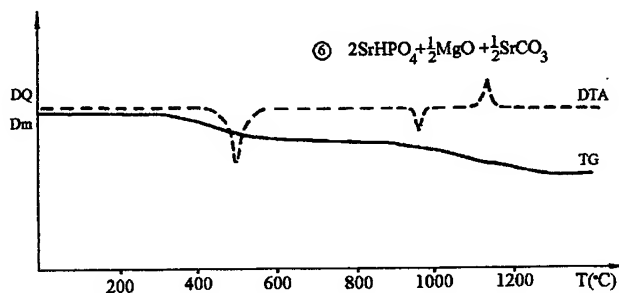


Fig. 1 Thermogravimetric study of the host lattice formation

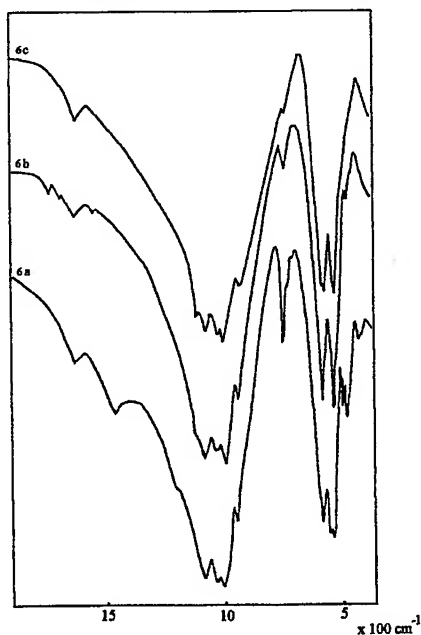


Fig. 2 IR spectra of 6a, 6b and 6c phosphor sample

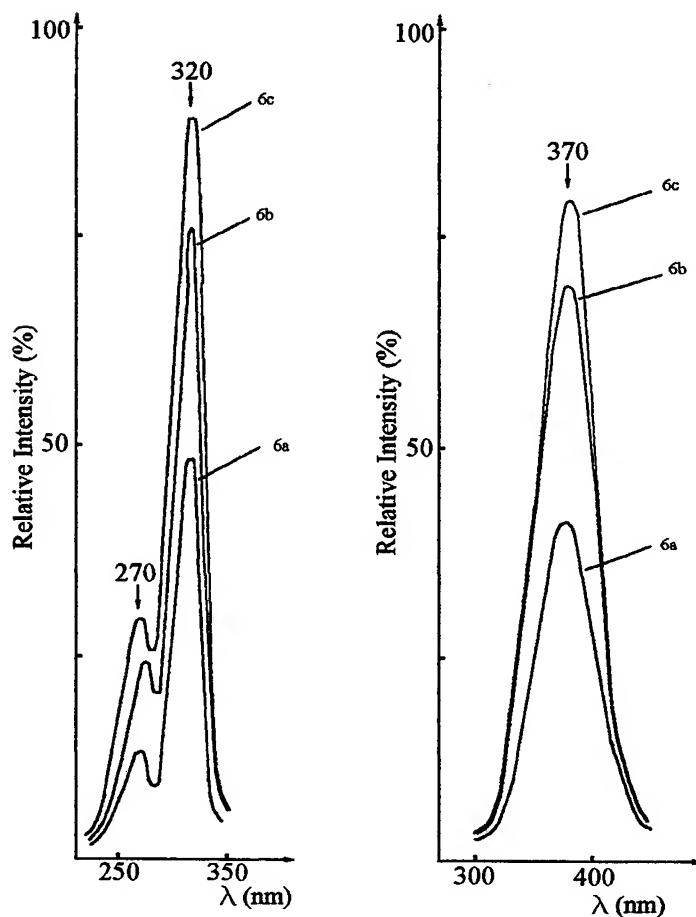


Fig. 3 Fluorescence spectra of $\text{Sr}_{2.5}\text{Mg}_{0.5}(\text{PO}_4)_2:\text{Ce}$ samples fired at different temperatures: 1000 °C (6a); 1100 °C (6b) and 1200 °C (6c): (a) excitation spectra; $\lambda_{\text{em}}=370$ nm; (b) emission spectra; $\lambda_{\text{ex}}=275$ nm;

In order to establish the optimum synthesis conditions for phosphor based on SMOP matrix, the appropriate concentration of cerium has to be established. In this purpose, two series of phosphor samples with different composition were prepared namely: (1) $\text{Sr}_{2.58-x}\text{Mg}_{0.38}\text{Ce}_x(\text{PO}_4)_2$ and (2) $\text{Sr}_{2.50}\text{Mg}_{0.49-x}\text{Ce}_x(\text{PO}_4)_2$ (where $x = 0 \div 0.20$). Fig. 4 illustrates the variation of UV emission intensity with cerium content for the two sample series. The increase of cerium content in parallel with the decrease of magnesium concentration brings about the enhancement of UV luminescence intensity. Inside the β -SOP structure domain, the variation of Sr/Mg cationic ratio, shows no influence on the host matrix, structural purity, but modifies the luminescence intensity.

The optimum manganese concentration was defined by preparing another phosphor series with the general formula $\text{Sr}_{2.46-x}\text{Mg}_{0.35}\text{Ce}_{0.10}\text{Mn}_x(\text{PO}_4)_2$, (where $x=0.04 \div 0.20$). These phosphors were activated with the appropriate cerium concentration (0.10 mole Ce/mole phosphor) and with different manganese amounts. The emission spectra consist in one strong UV emission band and another relatively weak red emission characteristic to cerium and manganese ions, respectively. For phosphor activated with Ce and Mn, the UV emission is less intense than the corresponding one of the phosphor activated only with Ce as activating ion. The maximum Ce→Mn energy transfer is reached at 0.04 mole Mn/mole phosphor (Fig. 5).

Our studies proved that the visible emission of SMOP:Ce,Mn could be realised by creating a cationic deficit into the phosphatic matrix. Fig. 6 presents the variation of ultraviolet and visible emission with the cationic deficit in phosphor series with general formula: $\text{Sr}_{2.46}\text{Mg}_{0.40-x}\square_x\text{Ce}_{0.10}\text{Mn}_{0.04}(\text{PO}_4)_2$ (where $x=0\div0.05$).

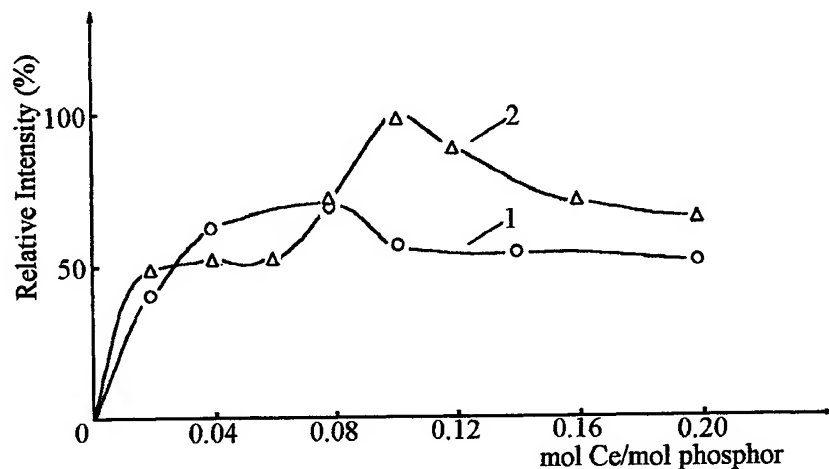


Fig. 4 Variation of I_{UV} with cerium concentration for phosphors:
1) $\text{Sr}_{(2.58-x)}\text{Mg}_{0.38}\text{Ce}_x(\text{PO}_4)_2$, where $x = 0.04\div0.20$;
2) $\text{Sr}_{2.5}\text{Mg}_{(0.49-x)}\text{Ce}_x(\text{PO}_4)_2$, where $x = 0.01\div0.20$.

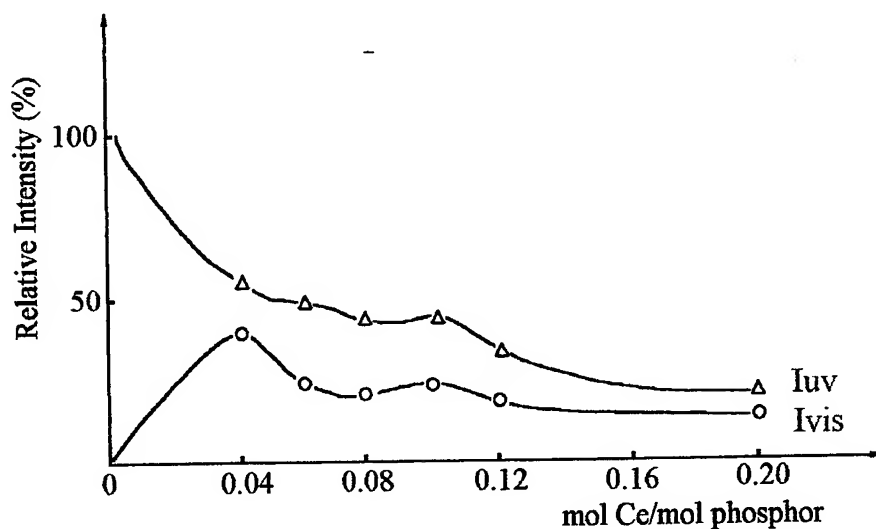


Fig. 5 Variation of I_{UV} and I_{Vis} with manganese concentration for phosphor
 $\text{Sr}_{(2.46-x)}\text{Mg}_{0.35}\text{Ce}_{0.10}\text{Mn}_x(\text{PO}_4)_2$, where $x = 0.04\div0.20$

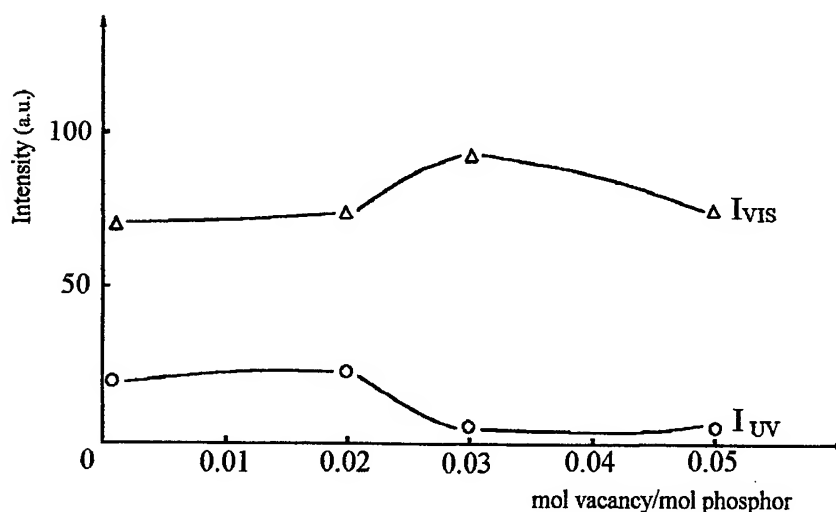


Fig. 6 Variation of I_{UV} and I_{VIS} with cationic deficit for phosphor: $Sr_{2.4x}Mg_{(0.40-x)}\square_xCe_{0.10}Mn_{0.04}(PO_4)_2$, where $x = 0 \div 0.05$

One observes that, for phosphor with 0.03 mole/mole cationic deficit, the visible luminescent intensity (I_{vis}) is considerable increased as compared with the starting phosphor sample. In this case, the Ce→Mn energy transfer is more efficient.

4. CONCLUSIONS

The cationic deficit in phosphatic matrix ensures a better incorporation of activator ions, a good protection of activators against oxidation during the thermal treatment and a good Ce→Mn energy transfer. A too large increase of the cationic deficit could create crystalline lattice distortions and could generate the formation of some undesirable secondary phases.

The SMOP:Ce phosphors show strong ultraviolet luminescence ($I_{max} = 380nm$) under short UV excitation and could be used in eritemal lamps and for the manufacture of copying machine lamps. As for the cerium and manganese activated phosphors, they show UV luminescence, that is characteristic to Ce^{3+} and pink fluorescence, characteristic to Mn^{2+} . This phosphor could be used in fluorescent lamps for light advertising or luminous signs.

REFERENCES

1. R.W. Mooney and M.A. Aia, "Alkaline Earth Phosphates", *Chem.Rev.*, **5**, pp. 433-438, 1961.
2. Z.A. Konstant and A.P. Dindune, *Fosfati Dvuhvalentnih Metalov*, Riga, 1987.
3. J.F. Sarver, M.V. Hoffman and F.A. Hummel, "Phase Equilibria and Tin - Activated Luminescence in Strontium orthophosphate Systems", *J.Electrochem.Soc.*, **108**, 18, pp. 1103-1110, 1961
4. H. Donker, W.M.A. Smit and G. Blasse, "On the Luminescence of Some Tin- Activated Alkaline - Earth Orthophosphates", *J.Electrochem.Soc.*, **136**, pp. 3130-35, 1989.
5. R.K. Ropp, *Luminescence and the Solid State*, Elsevier, New-York, 1991.
6. M. Vadan, E.J. Popovici, L. Pacurar and D. Macarovici, "Study on the Energy Transfer Between Ce^{3+} and Mn^{2+} Ions in some Orthophosphates with Whitlockite Structures", *Romanian J. of Optoelectronics*, **7**, pp. 47-50, 1999.

Studies on thin films CdTe/CdS structures

Ligia Pascu^a, Elisabeth Jeanne Popovici^{a*}, Emil Indrea^b, Rodica Grecu^a, Lucia Păcurar^a

^a"Raluca Ripan" Institute of Chemistry, 30 Fântânele, 3400-Cluj-Napoca, Romania

^bNational Institute of Research and Development of Isotopic and Molecular Technology, 65-103 Donath, P.O.Box 700, 3400 Cluj-Napoca, Romania

ABSTRACT

CdS-CdTe heterojunctions are valuable candidates for photovoltaic conversion of solar energy. In this work, thermal vacuum evaporation has been used to grow CdTe films on glass supported CdS substrate. Cadmium sulphide thin layers have been grown by chemical bath deposition. The influence of different preparation conditions on thin film quality has been studied. The optical homogeneity and film thickness was used as criteria to select the best substrate for the subsequent CdTe deposition. Some structural and optical characteristics of CdS/glass and CdTe/CdS/glass structures have been determined.

Keywords: thin films, cadmium sulphide, cadmium telluride, CdTe /CdS heterostructures

1. INTRODUCTION

CdTe/ CdS heterojunctions are valuable candidates for photovoltaic conversion of solar energy and, generally, thin films of cadmium sulphide have major applications in optoelectronic devices. Cadmium sulphide films could be prepared by various techniques such as: chemical bath deposition (CBD), evaporation, hotwall epitaxy, spray -pyrolysis, close-spaced vapour transport and chemical vapour deposition in different configurations¹. The present work is in response to the renewed interest in chemically deposited cadmium sulphide thin films. In this respect, the actual efforts are concentrated to optimise the CdS thickness in order to increase CdTe/CdS junction solar cell photocurrent performance²⁻⁴.

The paper presents some preliminary tests concerning the preparation of multilayer CdTe/CdS thin film structures where cadmium sulphide and cadmium telluride thin layers are grown by chemical bath deposition and, correspondingly, thermal vacuum evaporation. The aim of this work is to study the influence of different preparation conditions on thin film quality and, consequently, on some of the structural and optical characteristics of CdS/glass and CdTe/CdS/glass structures.

2. EXPERIMENTAL PART

2.1. Samples preparation

The deposition of multilayer CdTe/CdS structures was performed onto optical glass platelets of about 25x40x1 mm³. The substrate was detergent degreased, acid cleaned (in hot K₂Cr₂O₇ / H₂SO₄ mixture) and water washed. The as cleaned glass platelets were kept in distilled water before their utilisation as deposition supports.

Cadmium sulphide thin films were prepared from thiourea and cadmium acetate, in alkaline medium and in the presence of sodium citrate. The chemical bath was prepared from analytical-grade reagents, i.e., Cd (CH₃COO)₂ x 2H₂O, CS (NH₂)₂, Na₃C₆H₅O₇ x 5.5 H₂O and 25 % NH₃ aqueous solution. Thus, 30 ml 0.1M cadmium acetate solution, 120 ml 1M sodium citrate, 200 ml 1.5M NH₃ aqueous solution and 600 ml distilled water were mixed at room temperature. The wet cleaned glass substrates were immersed into the reaction mixture that was introduced into a large beaker, placed in a thermostat. The glass platelets were vertically suspended around the stirrer. The deposition bath was continuously stirred and heated to the required deposition temperature. After the thermal equilibrium was reached, 50 ml 1 M thiourea solution was added under stirring. After a certain deposition time, between 0.5 and 2.0 hrs, the glass platelets were taken out, carefully washed and dried on P₂O₅. The medium pH was controlled with a digital pH-meter and was adjusted with concentrated ammoniac or NaOH solutions.

*Correspondence: E-mail: phoratiu@codec.ro; Telephone. +40- 64-180165; Fax: +40-64-420441

Cadmium telluride thin films were obtained by a thermal vacuum evaporation technique, from 99.999 % CdTe grains (Balzers, Switzerland). The film deposition was performed in high vacuum (10^{-6} Torr pressure) on the CdS deposited glass support heated at 230 °C. The deposition time was between 5 sec. and 1 min

2.2 Samples characterisation

Cadmium sulphide and cadmium telluride films were characterised by thickness, crystalline structure and UV-Vis transmittance or reflectance measurements.

The film thickness was determined by microgravimetric method. The thickness (h) was calculated with the formula $h = \Delta m / 2 \times S \times \rho$ or $h = \Delta m / S \times \rho$ for films deposited either on both sides of the substrate or, respectively, on only one side; the notation meanings are: Δm = amount of CdS or CdTe deposited on substrate, ρ = substance density and S = film surface. The calculation were made with the density values $\rho_{\text{CdS}} = 4.82 \text{ g/cm}^3$ and $\rho_{\text{CdTe}} = 6.20 \text{ g/cm}^3$.

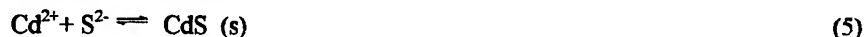
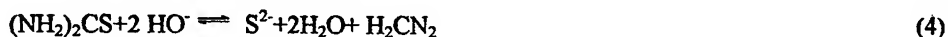
The X-ray diffraction patterns were obtained by means of a standard DRON-3M powder diffractometer, working at 45 kV and 30 mA and equipped with scintillation counter with single channel pulse height discriminator counting circuitry. The $\text{Co K}\alpha$ radiation, Fe filtered, was collimated with Soller slits. The data of the (111) CdTe profile were collected in a step-scanning mode with $\Delta 2\theta = 0.025^\circ$ steps and then transferred to a PC for processing. From the line broadening, the microstructural parameters were calculated.

The optical investigations were made in UV-Vis transmittance measurements, with UNICAM Spectrometer UV4. Some reflectance measurements were made with RSA-UC-40 integrative sphere accessory.

3. RESULTS AND DISCUSSION

3.1. Cadmium sulphide and cadmium telluride films formation

Cadmium sulphide films have been deposited on thoroughly cleaned glass substrates, by the reaction between cadmium acetate and thiourea (TU). The first experiments (A1-A3) were performed in warm deposition baths containing ammoniac aqueous solution. The following reactions are involved⁵:

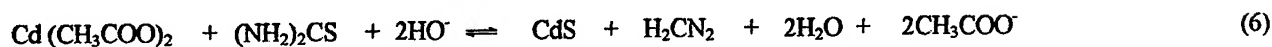


Ammoniac aqueous solution serves at pH adjustment of the deposition medium, before the TU addition. The ammoniac amount is sufficient to convert all cadmium ions into $[\text{Cd}(\text{NH}_3)_4]^{2+}$ form. The rate of CdS formation (reaction 4) is determined by the concentration of Cd^{2+} species provided by $[\text{Cd}(\text{NH}_3)_4]^{2+}$ and the concentration of S^{2-} from the thiourea hydrolysis. The hydrolysis rate depends on the pH and temperature of the solution. High deposition temperature and pH values are in the favour of S^{2-} generation and cadmium sulphide formation.

Cadmium sulphide films prepared in the above-described conditions showed low uniformity and adherence to the substrate. In order to improve the film quality, an additional complexing agent was used, namely sodium citrate. Although the NH_3 itself serves as complexing /chelating agent for Cd^{2+} , the citrate was found to be important to film adherence by further chelating and slowly releasing free Cd^{2+} that combine with free S^{2-} species generated by the thiourea hydrolysis⁶.

Three experiments (A4 - A6) were performed in deposition baths with the same composition, i.e. $[\text{Cd}(\text{CH}_3\text{COO})_2] = 3.0 \times 10^{-3} \text{ mole/L}$; $[\text{Na}_3\text{C}_6\text{H}_5\text{O}_7] = 1.2 \times 10^{-1} \text{ mole/L}$; $[\text{NH}_3] = 3.0 \times 10^{-1} \text{ mole/L}$ and $[\text{TU}] = 5.0 \times 10^{-2} \text{ mole/L}$. The deposition temperature was kept constant at about 70°C and the initial reagents molar ratio was $[\text{Cd}^{2+}]:[\text{TU}] = 1:16,6$ and $[\text{Cd}^{2+}]:[\text{NH}_3] = 1:100$.

The generation of CdS film from cadmium acetate and thiourea could be described by the general equation:



The deposition time was between 0.5 and 2.0 hrs and the pH of the deposition medium was strictly controlled. For A4 samples preparation, the medium pH was adjusted at about 9 by addition of concentrated NH_3 aqueous solution. During the A5 experiment, the pH was kept relatively at high-level ($10.0 \div 11.0$) by adding 1M NaOH solution. No pH adjustment was made during the A6 experiment. In this case, the pH decreased continuously from 10.3 to 8.7.

In our experimental conditions, two yellow-orange CdS deposits were formed on both sides of the glass support. The two equally adherent and homogeneous films were of about 1000 mm^2 surface each. They were specularly reflective and devoid of powdery matter at the surface.

The quality of CdS films could be estimated on the basis of UV - Vis transmittance spectra registered for different portions and positions of the glass substrate. From the optical homogeneity point of view, CdS films are considered good (+), poor (-) and acceptable (\pm) when, for different portions of the film, the absorbencies at 530 nm are comparable in values. In addition, CdS thin films thickness was determined by microgravimetric method. In order to diminish the measurement errors, the film thickness and homogeneity were deduced from the corresponding values for the entire CdS/glass/CdS assembly. Depending on preparative conditions, CdS films with different qualities was prepared, film thickness being between about 0.065 and $0.348 \mu\text{m}$ (Tab. 1).

Tab. 1 Samples code, layer sequence, some CdS films preparative parameters, films thickness (indicated according to layers sequence) and optical homogeneity

Samples Code	Layers sequence	CdS film preparative details			Films thickness (μm)	Optical homogeneity
		pH	Temp ($^\circ\text{C}$)	Time (hrs)		
A41	CdS/glass/CdS	$9.0 \div 9.1$	66	0.50	0.120/glass/0.120	\pm
A42	CdS/glass/CdS	$9.0 \div 9.1$	66	1.00	0.087/glass/0.087	--
A51	CdS/glass/CdS	$10.0 \div 11.0$	72	0.75	0.270/glass/0.270	+
A52	CdS/glass/CdS	$10.0 \div 11.0$	72	2.00	0.338/glass/0.338	\pm
A61	CdS/glass/CdS	$10.3 \div 8.7$	70	0.50	0.105/glass/0.105	--
A62	CdS/glass/CdS	$10.3 \div 8.7$	70	1.00	0.105/glass/0.105	+
A63	CdS/glass/CdS	$10.3 \div 8.7$	70	1.50	0.097/glass/0.097	+
A64	CdS/glass/CdS	$10.3 \div 8.7$	70	2.00	0.076/glass/0.076	+
A65	CdS/glass/CdS	$10.3 \div 8.7$	70	2.00	0.071/glass/0.071	\pm
A66	CdS/glass/CdS	$10.3 \div 8.7$	70	1.50	0.101/glass/0.101	--
A67	CdS/glass/CdS	$10.3 \div 8.7$	70	0.50	0.082/glass/0.082	+
A621	CdTe/CdS/glass/CdS	$10.3 \div 8.7$	70	1.00	0.274/0.105/glass/0.105	+
A641	CdTe/CdS/glass/CdS	$10.3 \div 8.7$	70	2.00	0.198/0.076/glass/0.076	+
A651	CdTe/CdS/glass/CdS	$10.3 \div 8.7$	70	0.70	0.165/0.071/glass/0.071	\pm
A612	CdTe/CdS/glass	$10.3 \div 8.7$	70	0.50	0.208/0.121/glass	--
A671	CdS/glass	$10.3 \div 8.7$	70	0.50	0.065/glass	+
A672	CdTe/CdS/glass	$10.3 \div 8.7$	70	0.50	0.115/0.065/glass	+

The best CdS/glass/CdS structures were selected as support for CdTe deposition. Cadmium telluride films were obtained through sublimation of CdTe grains and deposition onto heated substrates, under vacuum. The CdTe films were deposited on one side of the CdS/glass/CdS structure and measured about 625 mm^2 in surface (A621, A641, A651 samples). Depending on the deposition time, the CdTe film colour was light-to-dark brown and the thickness was variable between about 0.10 and $0.30 \mu\text{m}$. In order to obtain CdTe/CdS/glass assembly (A672 sample), some of the CdS/glass/CdS structures were partially cleaned with HCl solution, resulting in CdS/glass structures (A671).

CdS films with comparable thickness of about $0.10 \mu\text{m}$ were formed in deposition baths with pH below 10 value (A4 and A6 series). One notes that, CdS films prepared in 2 hours deposition were only 0.07 - $0.08 \mu\text{m}$ in thickness (A64 and A65). It is possible that, the prolonged deposition treatment produces the detachment of some small CdS film pieces from the

platelet. It is worth reminding that the film thickness was microgravimetric determined. This method gives the mean thickness value, for both side of the substrate. Moreover, because of the deposition technique (one way stirring), films with unequal thickness could be formed on the two sides of the substrate. This could explain the different thickness values observed for A67 samples and the corresponding A671 prepared by its partially acid cleaning.

The thickest CdS films were deposited at pH values higher than 10. In these conditions, the rate of thiourea hydrolysis is relatively high, thus resulting in an increased supply of free S^{2-} ions to combine, on the nucleation sites at the substrate surface with the Cd^{2+} ions released by dissociation of cadmium chelates.

The surface estate of the glass substrate could also influence the CdS film quality. This fact is illustrated by the different thickness of A61 and A67 films whose deposition time was equal, i.e. 0.5 hrs. Cadmium sulphide films were grown on slightly differently treated substrate. In the moment of immersion into the deposition bath, the glass support for A67 sample was dry. This resulted in the formation of a relatively less thick CdS film as compared with A61 sample prepared with wet glass substrate. Apparently, the CdS film-growing rate was higher in the later case.

3.2. Optical characterisation of cadmium sulphide and cadmium telluride films

Most of the CdS film samples exhibits optical homogeneity and high transparency and shows specular reflectance. Fig. 1 presents the transmittance spectra of some of the CdS films. The optical analysis shows that most of the CdS films exhibits good optical properties with high transmittance for wavelengths greater than the absorption edge at about 510 nm. For optical homogeneous films such as A62, A63 and A67, the transmittance at wavelengths longer than the absorption edge is higher as the film thickness is increased. In spite of the fact that A65 is the thinnest CdS film, its optical transparency is the smallest, thus suggesting the optical non-uniformity of the as prepared CdS films.

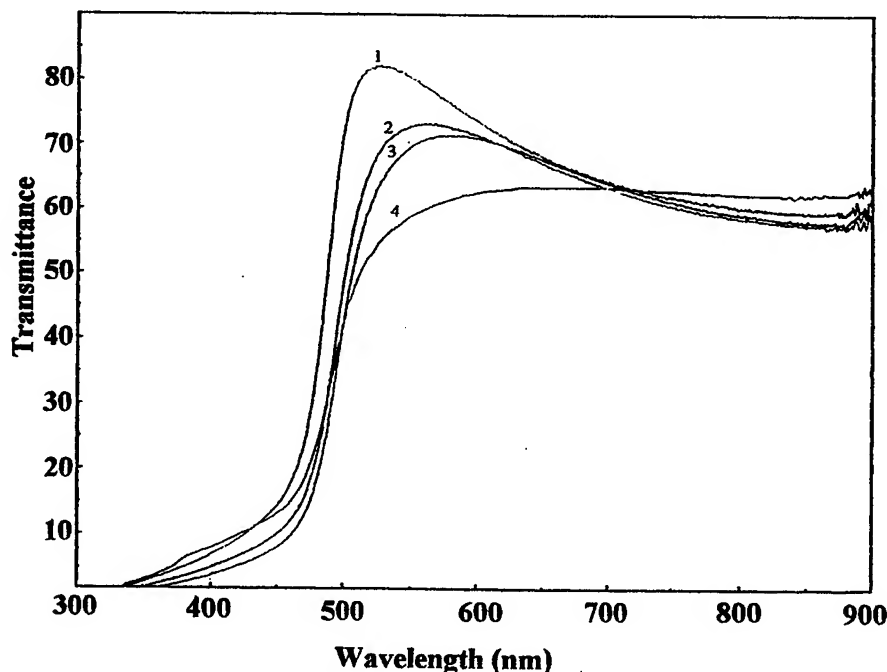


Fig. 1 Optical transmittance spectra of some CdS/ glass/ CdS structures
1) A- 67 sample; 2) A 63- sample; 3) A 62-sample; 4) A 65- sample

The UV - Vis transmittance spectra of some of the heterostructures were measured. The corresponding absorbance spectra of A671 and A672 samples are depicted in Fig. 2. The optical glass support shows a strong absorption under 300 nm that is well-evidenced in curve 2 corresponding to A671 sample. The absorbance spectrum of this sample is characteristic for the homogeneous and well-grown CdS films. The absorbance of CdTe/CdS/glass structure is very high, so that the absorption

spectrum is irrelevant for this case. In fact, the absorption of cadmium telluride film is so intense at above band-gap energies (below about 820 nm) that transmission measurements are impracticable⁷. The optical analysis of CdTe/CdS/glass heterostructure could be performed only on very thin films (in fact, A672 sample was the thinnest heterostructure prepared at very small deposition times for both techniques). The UV - Vis absorbance spectrum of CdTe film could be put in evidence by subtracting the CdS/glass spectrum from that corresponding to CdTe/CdS/glass structure. The characteristic CdTe absorption peak at about 318 nm could be observed; some possible additional absorption peaks at about 500 nm and 720 nm are also suggested. In our experimental conditions, the inflexion corresponding to absorption edge of CdTe is much less abrupt than that of CdS film so that it is rather difficult to be observed.

For CdTe/CdS/glass structure, additional information could be obtained in 0° specular excluded reflectance measurements. Fig. 3 displays plots of the optical absorbance versus wavelengths for CdS/glass, CdTe/CdS/glass and CdTe/glass structures. In these measurements, the light incidence could take place on either glass or film side of the structures. In this respect, the optical absorption spectra are different for the same investigated structure. When the light incidence takes place on the glass side, more structured film spectra could be obtained. These spectra contain the well-defined absorption band of the glass, at about 310 nm, and are situated at higher optical absorption values.

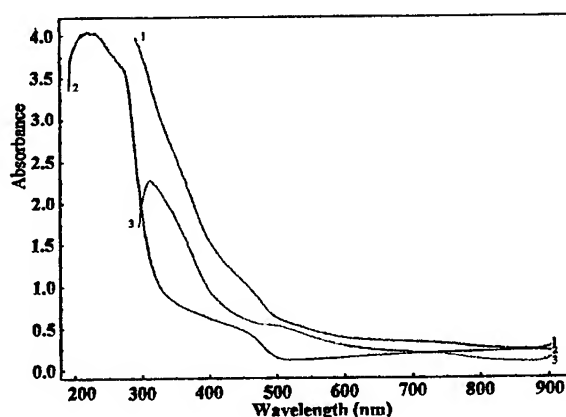


Fig. 2 UV- Vis absorbance spectra of some heterostructures

- 1) A 672-sample with CdTe / CdS / glass structure; 2) A 671- sample with CdS / glass structure; 3) subtraction spectrum (A 672-A 671) representing the CdTe spectrum. (Spectra were registered in transmittance measurement)

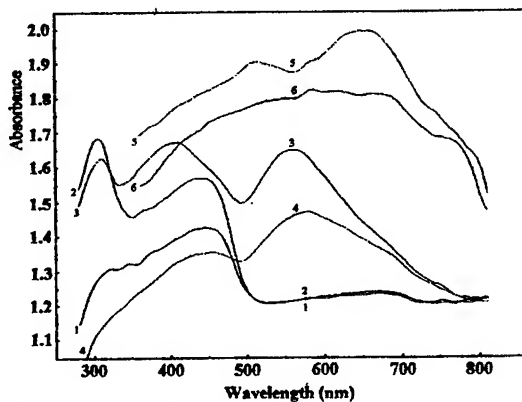


Fig. 3 UV- Vis absorbance spectra of some heterostructures

- 1) A 671 -sample with CdS / glass structure; film side incidence; 2) A 671 - sample with CdS / glass structure; glass side incidence; 3) A 672 -sample; CdTe / CdS/ glass structure; glass side incidence; 4) A 672 - sample; CdTe / CdS/ glass structure; films side incidence; 5) A 7 -sample; CdTe / glass structure; glass side incidence; 6) A 7 -sample; CdTe/ glass structure; film side incidence. (Spectra were registered in 0° specular excluded reflectance measurement)

By comparing the spectra of different film structures, registered in identical conditions, one can note that the strongest absorption bands of CdS and CdTe individual films are slightly shifted toward shorter wavelengths in the CdTe/CdS heterostructure (curves 2, 3 and 5).

3.3. Structural characterisation of cadmium sulphide and cadmium telluride films

Crystalline structure of cadmium sulphide and cadmium telluride films from the CdTe/CdS/glass structure (A672 sample) as well as that of the cadmium telluride film from the CdTe/glass structure (A7 sample) were determined by X-ray diffraction (XRD).

Cadmium sulphide film possesses hexagonal structure (wurtzite-type) and their preferential growing planes are (101) and (002). One can note that CdS was chemical bath deposited on glass and the so formed assembly, was practically annealed at 230 °C, during the vacuum thermal deposition of CdTe film. This treatment assures the hexagonal structure consolidation.

Cadmium telluride film possesses cubic structure (zinc blende type). The strong (111) reflection indicates a highly textured film deposited on CdS or glass surface. This single (111) cadmium telluride XRD line was analysed in order to determine the microstructural parameters of CdTe films deposited on either glass (CdS/glass structure) or CdS support (CdTe/CdS/glass structure).

It is well known that the XRD line broadening is caused by the small size of the crystallites, the lattice strains and faults, and the experimental diffraction geometry⁸. The crystallite size distribution function was determined from the second derivative of the strain-corrected Fourier coefficients by a method developed by Aldea and Indrea by a XRLINE computer program. The structural information obtained by single X-ray profile Fourier analysis of polycrystalline CdTe films were: the effective crystallite mean size (D_m), the root mean square of the microstrains averaged along [hkl] direction, and the stacking fault probability⁹.

Figs. 4 and 5 illustrate the distribution function of the crystallite size and the distribution of the crystalline lattice strains of cadmium telluride films from CdTe/glass and CdTe/ CdS/ glass structures.

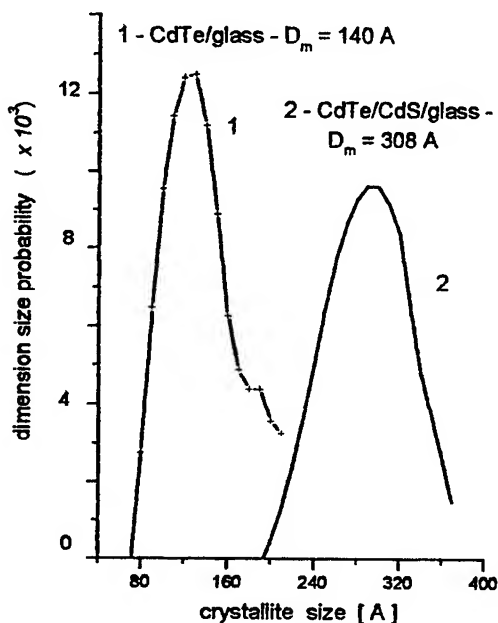


Fig. 4 The crystallite size distribution function of CdTe films
1- CdTe/glass structure; 2- CdTe/CdS/glass structure

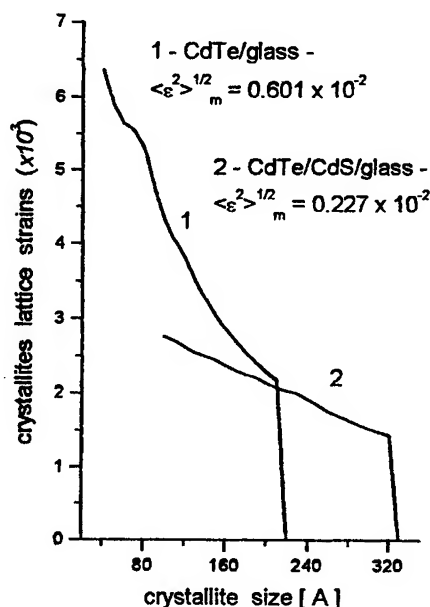


Fig. 5 The crystalline lattice strains distribution of CdTe films
1- CdTe/glass structure; 2- CdTe/CdS/glass structure

One notes that crystallite sizes of cadmium telluride are relatively small when the vacuum deposition is performed on glass substrate. About two times larger crystallite are grown on cadmium sulphide film. As for the crystalline lattice, this is more strained in the case of CdTe film deposited on glass. Table 2 summarises the microstructural parameters of CdTe films, i.e. the effective crystallite size along the perpendicular direction to the (111) planes [D_m], the root mean square of the microstrains averaged along the [111] direction [$(\epsilon^2)_{111}^{1/2}$] and the stacking fault probability [α].

Tab. 2 Microstructural parameters for the CdTe/glass and CdTe/CdS/glass structures.

Samples Code	Layer structure	D_m (Å)	$(\epsilon^2)_{111}^{1/2} \times 10^3$	α
A672	CdTe/CdS/glass	308	2.27	0.028
A7	CdTe/glass	140	6.01	0.074

The crystalline lattice of CdTe film grown on glass supported CdS layer is about three times more rich in stacking faults, and is constituted from larger crystallites than the corresponding film directly grown on the glass substrate.

4. CONCLUSIONS

Cadmium sulphide films were glass deposited from cadmium acetate and thiourea, in the presence of ammoniac and sodium citrate as chelating agent. The CBD conditions assure the formation of CdS films with good optical homogeneity and adherence, with thickness between 0.065 and 0.338 μm , depending on the deposition time and bath alkalinity. Films are specularly reflective and devoid of powdery matter at surface. In vacuum deposition technique, CdTe/CdS/glass structures were obtained, the CdTe films being between 0.115 and 0.274 μm thickness, depending on deposition time.

CdS/glass structures are well characterised by UV-Vis transmittance method that evidences the characteristic CdS absorption bands. CdTe/CdS/glass heterostructures are best characterised by 0° specular excluded reflectance measurements, especially for the light incidence on the glass side of the structure. The strongest absorption bands of CdS and CdTe individual films are slightly shifted toward shorter wavelengths in the CdTe/CdS heterostructure.

XRD patterns show that cubic cadmium telluride film was grown on CdS layer that presents hexagonal crystalline structure. The microstructural investigations illustrate that the cadmium sulphide substrate is favourable to the growth of polycrystalline CdTe films with relatively large crystallite size and low concentration of crystalline imperfections (in comparison with the glass substrate).

REFERENCES

1. Kaur, D.K. Pandya and K.L. Chopra; "Growth Kinetics and Polymorphism of Chemically Deposited CdS Films", *J. Electrochemical Soc.* **127** (4), pp. 943-948, 1980.
2. J. Granata, J. Sites and G. Contreras-Puente, "Effect of CdS thickness on CdS/CdTe quantum efficiency", *Conf. Rec. IEEE Photovoltaic Spec. Conf. 25th*, pp. 853-856, 1996.
3. S. Kumazawa, S. Shibutani and T. Nishio. "15,1% Highly efficient thin film CdS/CdTe solar cell", *Sol. Energy Mater. Sol. Cells*, **49** (1-4), pp. 205-212, 1997.
4. K. Li, A. Wee, J. Lin and L. Tan, "A microstructural study on the surface and interface of CdTe/CdS solar cells"; *J. Mater. Sci.: Mater. Electron.* **8**(3), pp. 125-132, 1997.
5. T.L. Chu, S.S. Chu and N. Schultz, "Solution-Grown Cadmium Sulphide Films for Photovoltaic Devices", *J. Electrochemical Soc.*, **139** (9), pp. 2443-2446, 1992.
6. R. Engelken, S. Ali and L. N. Chang, "Study and development of a generic electrochemical ion-exchange process to form M_xS optoelectronic materials from ZnS precursor films formed by chemical-precipitation solution deposition", *Mater. Lett.*, **10** (6), pp. 264-274, 1990.
7. A.J. Strauss, "The physical properties of cadmium telluride", *Rev. Phys. Appl.*, **5**(3S), pp. 167-184, 1990.
8. E. Indrea and N. Aldea, "XRLINE, a program to evaluate crystallite size of supported metal catalysts", *Comput. Phys. Commun.*, **60**, pp. 155-159, 1990.
9. E. Indrea and A. Barbu, "Indirect photon interaction in PbS photodetectors", *Appl. Surf. Sci.*, **106**, pp. 498-501, 1996.

Calcium tungstate phosphors with well defined particle sizes

Flavia Forgaciu^a, Elisabeth-Jeanne Popovici^{*a}, Cristina Ciocan^a, Laura Ungur^a, Maia Vădan^a

^a“Raluca Ripan” Institute of Chemistry, Fantanele 30, 3400-Cluj-Napoca; Romania

ABSTRACT

Under short UV or roentgen radiation, the self-activated calcium tungstate phosphors ($\text{CaWO}_4:\text{W}$) exhibit blue luminescence and could be used as luminescent pigments for the manufacture of X-ray intensifying screens and fluorescent lamps for luminous signs. As luminescent pigments, $\text{CaWO}_4:\text{W}$ phosphor has to possess high luminescence characteristics and well defined particle sizes. This study presents the influence of synthesis conditions on morphostructural and luminescent characteristics of $\text{CaWO}_4:\text{W}$ phosphors. Phosphors were prepared by thermal synthesis from mixtures consisting of precipitated CaWO_4 and CaCl_2 as flux; both reagents were luminescent grade. Calcination was performed at 600-1000 °C for 0.5-2.0 h, in air. The crystalline structure (XRD-patterns), particle size distribution and luminescent characteristics (emission and excitation spectra) of phosphors were determined and interpreted.

Keywords: phosphors, calcium tungstate, luminescent substances

1. INTRODUCTION

The self-activated calcium tungstate phosphor ($\text{CaWO}_4:\text{W}$), excited by short wavelength ultraviolet radiation, X-rays, or cathode-ray exhibits blue fluorescence and could be used as luminescent pigments for luminous signs or various optoelectronic devices. The luminescent emission is correlated with certain electronic transitions which take place inside of some native defects that are uniformly distributed into the well-formed crystalline structure of calcium tungstate. The nature of the self-activated luminescence centres and the luminescence process have not been entirely elucidated yet, so that tungstate phosphors still arise a lot of interest^{1,2}.

In order to be used as luminescent pigment, $\text{CaWO}_4:\text{W}$ phosphor has to possess the following characteristics: good absorption for the exciting radiation and a high conversion efficiency of the exciting energy visible light; stable luminescent properties; well defined particle sizes, in agreement with the requests of application domain³.

The phosphor synthesis implies both the preparation of the host crystalline substance (i.e. tetr- CaWO_4) and the formation of luminescence centres (i.e. some imperfect tetrahedral WO_4^{2-} groups). Generally, the self-activated phosphor could be obtained by the firing of the CaWO_4 - precipitate. The earlier literature presents rather incomplete information on phosphor preparation. Usually, calcium tungstate is precipitated from calcium chloride and ammonium or sodium tungstate and, in order to create luminescence centres, CaWO_4 - precursor is thermally treated at 700-1000°C⁴. The thermal synthesis is frequently performed in the presence of the mineralising agent that contributes to both the adjustment of phosphor particle size distribution and the crystalline lattice arrangement and the subsequent luminescent centres formation⁵. During this thermal treatment, there could be also created some other lattice defects that show unfavourable effect on the luminescence properties. For this reason, the self-activated calcium tungstate phosphor is very sensitive even to small variations of the synthesis parameters influencing the concentration of native lattice defects.

Calcium tungstate phosphors properties are strongly influenced by the quality of CaWO_4 precursor and conditions of thermal synthesis. Our earlier studies enabled us to establish the correlation between precipitation conditions, morphostructural characteristics of CaWO_4 precursor and luminescent properties generated thereof^{6,7}. The literature data offer few information concerning the consequences of the thermal treatment on phosphor characteristics. There is no correlation between luminescence intensity and firing conditions, or between the particle size distribution and the luminescent properties of self-activated calcium tungstate powders. The objective of this paper is to study the influence of the thermal synthesis conditions on morphostructural and luminescent characteristics of $\text{CaWO}_4:\text{W}$ phosphor. Actually, this

*Correspondence: Email phoratiu@codec.ro; Telephone. +40- 64-180165; Fax: +40-64-420441

study could permit us to precise the optimum thermal treatment for the synthesis of CaWO_4 phosphor utilisable as luminescent pigment.

2. EXPERIMENTAL PART

2.1. Preparation of precursor and phosphor samples

Luminescent grade calcium tungstate (l.g. CaWO_4) is prepared from highly purified solutions of CaCl_2 and Na_2WO_4 . Equal volumes of reagent solutions with equal concentrations were simultaneously added to a bottom solution containing a small Na_2WO_4 amount. The precipitation pH was adjusted to 8.0 ± 0.2 by using small quantities of diluted NaOH solution. The precipitation was conducted at 20°C and was followed by a maturation stage (1hr) taking place at 20°C . The precipitate batches were filtered, well washed and dried at 105°C .

In order to synthesise the corresponding phosphor samples, all CaWO_4 precipitate batches were calcinated at $600\text{--}1000^\circ\text{C}$, in air (in covered crucibles), for 0,5-2,0 hrs. After the thermal treatment is over, the sample are quickly cooled and then they are water dispersed, washed and dried.

2.2. Characterisation of CaWO_4 precursor and phosphors

The CaWO_4 precursor samples were characterised by Atomic Absorption Spectroscopy, thermal analysis, X-ray diffraction and particle size analysis (Coulter Counter method). As for the phosphor samples, they were characterised by particle size distribution (Coulter Counter method) and luminescent properties. The luminescent emission was estimated on the basis of fluorescence spectra that were registered at room temperature on a 204 Perkin Elmer Spectrofluorimeter, with a 254 nm UV excitation, in comparison with standard ($\text{CaWO}_4\text{:W}$ phosphor, N61 type, Bad Liebenstein).

3. RESULTS AND DISCUSSION

Our earlier studies showed that the quality of CaWO_4 - precipitate strongly influences the luminescent properties and morphostructural characteristics of $\text{CaWO}_4\text{:W}$ phosphors. In order to obtain reproducible results, care had to be taken to prepare a large and homogeneous batch of calcium tungstate precipitate with well defined characteristics. Calcium tungstate precursor was prepared at room temperature, by simultaneous addition of CaCl_2 and Na_2WO_4 reagents, in a pH stabilised precipitation medium

The selected precipitation conditions assure the formation of an homogeneous CaWO_4 precipitate with luminescent grade quality. The main precursor characteristics are: low level of metallic impurities content (heavy metal ions amount is less than $1 \times 10^{-4}\%$), small thermal weight loss (Δw is less than 2.5 %), high luminescence ability and uniform particle size distribution with a median diameter of $16 \mu\text{m}^6$.

In order to study the influence of thermal synthesis conditions on phosphor characteristics, various $\text{CaWO}_4\text{:W}$ samples were prepared with or without mineralising agent (flux) at different firing temperatures and for different firing periods.

3.1. Influence of the firing temperature and mineralizing agent on phosphors characteristics

For the beginning, we have in view the influence of firing temperature on the luminescent properties and particles size distribution of $\text{CaWO}_4\text{:W}$ samples. In this respect, two series of self-activated $\text{CaWO}_4\text{:W}$ samples were prepared in different synthesis conditions as follows:

- *Series A*: synthesis mixture without flux; firing temperature $600\text{--}1000^\circ\text{C}$, firing time: 1 hr;
- *Series B*: synthesis mixture with 10 wt. % CaCl_2 ; firing temperature $600\text{--}1000^\circ\text{C}$, firing time: 1 hr;

The luminescence properties of phosphor samples were appreciated on the basis of the fluorescence spectra. All spectra consist of one large emission band centred at about 400 nm, the peak intensity being variable depending on thermal synthesis regime. Fig. 1 shows the variation of the relative intensity with the firing temperature and illustrate the mineralising action of CaCl_2 . The depicted curves show that, for $\text{CaWO}_4\text{:W}$ phosphor samples prepared with or without CaCl_2 , the rise of firing temperature determines a continuous increasing of luminescence intensity. This could be explained by the intensification of intra-grain recrystallisation process and the subsequent formation of both a higher concentration of luminescent centres and a lower concentration of quenching centres.

For *Series A* of samples, fired with no flux addition, the maximum luminescence intensity, is obtained at 900°C and represents only 95 % of the standard corresponding value. The emission intensity of *Series B* of samples, fired with flux

(10 wt % CaCl_2) is with 10-30 % higher than the corresponding values of A phosphor series. This behaviour illustrates the favourable role of both the mineralising agent and firing temperature in the phosphor synthesis. Calcium chloride acts in the favour of lattice defects formation. As a result, an optimum concentration of luminescent centres could be realised and the enhancement of the blue luminescence becomes possible.

In the case of *Series B* of samples, the emission intensity values are situated above 100 %; the maximum value is realised at 900 °C ($I_{\text{rel}} = 106$ %). Above this firing temperature, the luminescence intensity slowly decreases. This could be explained either by a partial thermal dissociation of CaWO_4 determining the formation of non luminescent phases on phosphor grain surface, or by a slight synerisation conducting to the partial annihilation of lattice defects responsible for luminescence.

The mineralising agent acts both in the inter-grain and intra-grain recrystallisation processes whose developing rate depends on firing temperature. Taking into account that inter-grain recrystallisation could influence the grains dimensions of luminescent powders, the particle size distribution of $\text{CaWO}_4\text{:W}$ phosphor samples was determined. From particle size distribution integral curves (registered with Coulter Counter method), the particle median diameter ($d_{50\%}$) is calculated. Fig. 2 presents the variation of the median diameter with the firing temperature and with the flux presence. One observes that, for phosphor prepared without flux addition (sample *Series A*), the median diameter of phosphor grains decreases slowly with the increase of the firing temperature. This could be explained by the fact that, during the thermal treatment, as the firing temperature is rising, the initial grains of CaWO_4 -precursor are gradually disintegrated. The process is complete only at temperature higher than 1000 °C.

In the case of samples prepared with CaCl_2 as mineralising agent (sample *Series B*), the variation of median diameter is quite different. In the beginning, between 600-700°C, the median diameter gradually decreases due to the precursor dispersion. At higher temperatures, the median diameter starts to increase, fact that illustrates the development of inter-grain recrystallisation process. For this phosphor series, the smallest phosphor grains are obtained at 700 °C ($d_{50\%} = 8.0$ μm), in presence of mineralising agent CaCl_2 .

3.2. Influence of the firing time on phosphor characteristics

In order to evaluate the optimum firing time, five phosphor *Series C-G* were prepared in different thermal conditions. Phosphor samples were characterised by particle size distribution and emission spectra so that the median diameter and relative emission intensity could be calculated (Tab. 1).

Tab. 1 Luminescent and granulometric characteristics for $\text{CaWO}_4\text{:W}$ phosphor samples prepared in different thermal conditions (with 10 wt % CaCl_2)

No	Phosphor series	Firing temperature (°C)	Firing time (h)	I_{rel} (%)	$d_{50\%}$ (μm)
1	C	600	0.5	78.5	28.0
2	C	600	1.0	88.0	25.8
3	C	600	1.5	82.5	-
4	C	600	2.0	100.0	12.8
5	D	700	0.5	98.5	9.40
6	D	700	1.0	103.5	9.40
7	D	700	1.5	100.0	-
8	D	700	2.0	103.5	7.80
9	E	800	0.5	102.0	8.0
10	E	800	1.0	104.0	8.0
11	E	800	1.5	104.0	-
12	E	800	2.0	105.5	9.0
13	F	900	0.5	105.0	8.5
14	F	900	1.0	106.0	9.5
15	F	900	1.5	104.5	-
16	F	900	2.0	105.0	11.3
17	G	1000	0.5	106.5	9.2
18	G	1000	1.0	104.0	10.4
19	G	1000	1.5	103.5	-
20	G	1000	2.0	97.5	9.5

Figs. 3 and 4 illustrate the influence of the firing time on luminescent and granulometric properties of *C - G* phosphor samples

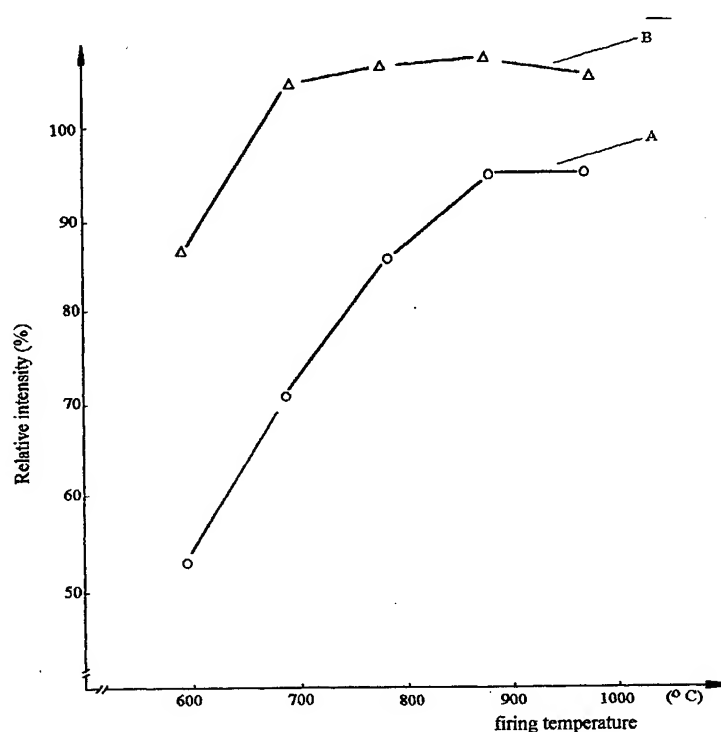


Fig. 1 The variation of relative emission intensity *versus* firing temperatures for $\text{CaWO}_4:\text{W}$ phosphors prepared without CaCl_2 (series A) and with CaCl_2 (series B)

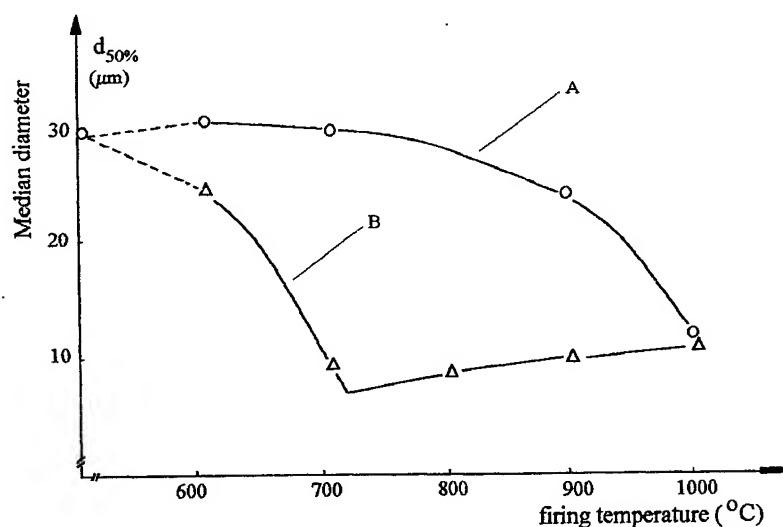


Fig. 2 The variation of the median diameter *versus* firing temperatures for $\text{CaWO}_4:\text{W}$ phosphor samples prepared without CaCl_2 (series A) and with CaCl_2 (series B)

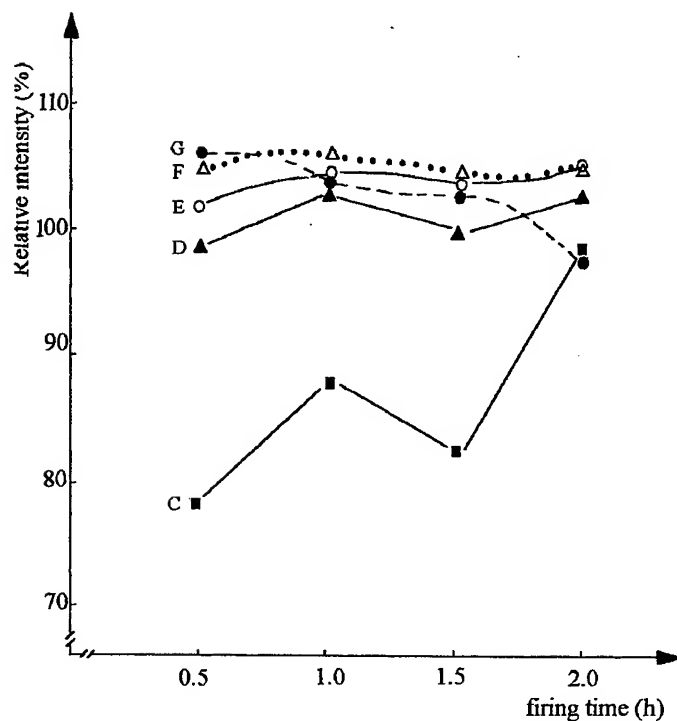


Fig. 3 The variation of relative emission intensity *versus* firing time for $\text{CaWO}_4:\text{W}$ phosphors prepared at different temperatures, with CaCl_2 (series C-G)

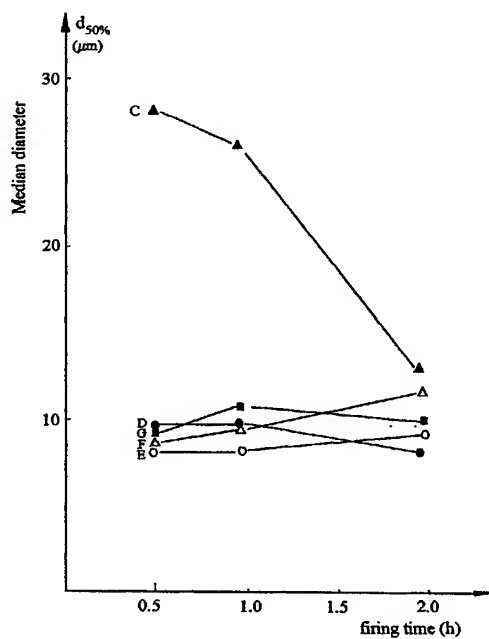


Fig. 4 The variation of median diameter *versus* firing time for $\text{CaWO}_4:\text{W}$ phosphor samples prepared at different temperatures, with CaCl_2 (series C-G)

Fig. 3 illustrates the dependence of relative intensity with the firing time, for temperatures between 600 and 1000 °C. One can note that the luminescence intensity tends to increase with the firing time. For samples prepared at 600, 700 and 800 °C (C, D and E phosphor Series), an irregular variation of emission intensity could be observed. The variation curve of luminescence intensity presents a small maximum corresponding to one hr calcination at about 900 °C. As for the sample Series G synthesised at 1000°C, the relative intensity decreases continuously as the firing time increases.

From the point of view of the modification of particle sizes with firing time and temperatures, two opposite tendencies could be observed: during the thermal synthesis, i.e. the diminution of powder grains that is related to the precursor particles dispersion and the increase of the particle dimensions as a result of inter-grain recrystallisation acceleration. Fig. 4 illustrates the variation of the median diameter with the phosphor firing time. The firing of phosphor samples at 600 °C determines the decrease of the average particles diameter as a result of the precursor grains dispersal. The prolongation of the firing time intensifies this dispersion process. In the case of phosphor samples fired at 700 °C, the same decrease of the particles average diameter could be noticed. A firing period of 2 hrs assures the total dispersion of CaWO_4 -precipitate grains. At firing temperature much higher than that, the prolongation of the firing time acts in the favour of the phosphor grains growth. This indicates that the inter-grain recrystallisation process are intensified during the thermal synthesis stage. The presence of CaCl_2 as a mineralising agent contributes to the enhancement of all these recrystallisation processes.

4. CONCLUSIONS

The thermal treatment conditions influence the morphostructural and luminescent properties of CaWO_4 :W phosphors:

1. The firing temperature influences the particle size distribution of CaWO_4 :W phosphors. A median diameter of about 8.0 μm could be reached by firing the synthesis mixture for 1 hour at 800 °C. Higher dimensions i.e. a median diameter of about 9.5 - 10.0 μm could be obtained with one hour treatment at 900 °C.
2. The firing temperature influences also the luminescent properties of CaWO_4 :W phosphor samples. In the presence of mineralising agent (CaCl_2), the optimum temperature domain is 700 – 900 °C. Below this temperature, the concentration of luminescent centres is smaller then their optimum value and at firing temperature higher then 900 °C, the thermal decomposition could appear so that some non-luminescent local phases could be formatted.
3. The firing time affects especially the particle size distribution of CaWO_4 :W phosphor grains. For phosphor samples prepared at 800 – 900 °C the optimum period for the thermal treatment is 1 hour. The prolongation of the firing time acts in the favour of the phosphor grains increasing.

As a result of this study, the optimum synthesis conditions of the self - activated calcium tungstate phosphor could be established. The material produced by a thermal treatment of one hour firing at 900 °C, shows a relatively strong blue emission and could be used as luminescent pigment.

REFERENCES

1. R. Grasser and A. Scharmann, "The Optical Properties of Extrinsic Anionic Oxo-Complexes in Tungstates", *Phys. Status Sol.*, (a) **130**, pp. K99-K105, 1990.
2. G. Blasse, "Luminescent centres in insulators" in *Solid State Luminescence-Theory, Materials and Devices*, (ed. A. K. Kitai), p.48, Chapman Hall, London, 1993.
3. R.C. Ropp, "Design of Phosphors", *Luminescence and Solid State*, p. 283, Elsevier, Amsterdam -Tokyo, 1991.
4. A.M. Gurvich, "Vvedenie v fizicheskuyu himiyu kristallofosforov", p. 119, Moskva, ed.2, Vyshaia Schola, 1982.
5. A.M. Gurvich, "Vliyaniye uslovii osazhdeniya na dispersnati sulfidov i volframatoov i na svoystva polyaremyh uz nih lyuminoforov", *Sb.Nauch.Tr.VNII.Lyuminoforov I Osobo Chist.Veshchestv.*, Stavropol, **5**, pp.133-143, 1971.
6. F. Forgaciu, M. Nemes, E.J. Popovici, V. Ursu and D. Macarovici, "The influence of precipitation conditions on the quality of CaWO_4 used in phosphor synthesis", *Studia Universitatis Babes-Bolyai, Chemia*, **XL**, pp. 47-54, 1995
7. E.J. Popovici, F. Forgaciu, M. Nemes, V. Ursu and D. Macarovici, "Attempts on the synthesis of some activated calcium tungstate phosphors", *Rom. Journal of Optoelectronics*, **5**, pp. 85-88, 1997.

Synthesis of copper activated zinc sulphide phosphors sensitive to β -radiation

Elisabeth-Jeanne Popovici^a, Flavia Forgaciu^a, Cristina Ciocan^a, Ligia Pascu^a,
D. Angelescu^b, C. Postolache^c

^a"Raluca Ripan" Institute of Chemistry, Fantanele 30, 3400-Cluj-Napoca, Romania

^b"I.G. Murgulescu" Institute of Physical Chemistry of the Romanian Academy,
Independentei 202, Bucharest, Romania

^cInstitute of Physics and Nuclear Engineering, Magurele, Bucharest, Romania

ABSTRACT

Attempts were made to synthesise copper activated zinc sulphide phosphors sensitive to β -radiation. In this purpose, homogeneous synthesis mixtures were prepared from luminescent grade zinc sulphide - *thiosulfate route* -, copper nitrate and alkaline and/or alkaline-earth chloride and were fired at 800-900 °C, in nitrogen atmosphere. ZnS:Cu,Cl phosphors prepared in various synthesis conditions were characterised by crystalline structure, particle size distribution and luminescent properties under UV excitation. Some ZnS:Cu,Cl sample phosphors were used to manufacture radioluminescent sources and their sensitivity to β radiation was estimated. The optimum synthesis conditions were established.

Keywords: phosphors, zinc sulphide, luminescence, radioluminescent substances

1. INTRODUCTION

The simultaneous incorporation of copper ions - *activators* - and halogenide ions - *coactivators* - into the crystalline lattice of zinc sulphide - *host lattice* - generates phosphors that show intensive green luminescence when excited by UV radiation, X-rays, electron beam, α or β radiation etc^{1,2}. There are three most important categories of ZnS:Cu phosphors with different characteristics and applicability:

- powders with small size particles (the particles median diameter d is less than 10 μm), cubic structure and short persistent luminescence \Leftrightarrow luminescent pigments for image intensifiers, β -particles detectors, radioluminescent paints and sources;
- powders with medium size particles ($d = 10 \div 20 \mu\text{m}$), cubic structure and short/medium persistent luminescence \Leftrightarrow luminescent pigments for CRT screens, oscilloscopes;
- powders with large particles (d higher than 20 μm), hexagonal structure and medium/long persistent luminescence \Leftrightarrow luminescent pigments for scintillators, phosphorescent paints.

ZnS-type phosphors are prepared by thermal synthesis from mixtures containing luminescent grade zinc sulphide (i.g. ZnS), alkaline or/and alkaline earth halides (flux) and copper/silver salts (activator source). Luminescent properties, crystalline structure and particle size distribution of ZnS-type phosphors strongly depend on flux nature and concentration, activator type and amount and thermal synthesis conditions. In our previous works we showed that the quality of luminescent grade zinc sulphide used as starting material could influence also the properties of this phosphor type³⁻⁵.

Zinc sulphide used as starting material in phosphor synthesis is usually prepared by H₂S or thiourea methods. Thiosulfate route could be used to produce zinc sulphide with well defined characteristics that could be successfully converted into silver or copper activated phosphors, as shown by our previous papers^{6,7}. The aim of the present study is to report some of our results concerning the conversion of the same ZnS-type into copper activated phosphors with well formed crystalline structure and small powder particles sensitive to β -radiation. Moreover, some of the optimum synthesis conditions could be specified.

*Correspondence: Email phoratiu@codec.ro; Telephone. +40- 64-180165; Fax: +40-64-420441

2. EXPERIMENTAL PART

2.1. Samples preparation

Several luminescent grade zinc sulphide batches were prepared by thiosulfate method from highly purified ZnSO_4 and $\text{Na}_2\text{S}_2\text{O}_3$ solutions. The preparation procedure, that is largely described in our previous work^{3,8}, consists in two stages namely precipitation and pre-calcination. The *precipitation* parameters are as follows: reagents initial concentrations equal to 0,55 mole/L ZnSO_4 and 1,10 mole/L $\text{Na}_2\text{S}_2\text{O}_3$; buffer reagent (sodium acetate) concentration equal to 0.11 mole/L; precipitation time and temperature equal to 2 hrs and 100 °C, respectively; variable maturation period in the range of 24 to 96 hrs. After the maturation period is terminated, the wet sulphide deposit is passed through a plastic sieve with medium sized meshes so that the free sulphur is partially removed. The so obtained precipitate, containing ZnS and free sulphur, is filtered, well washed with demineralized water and dried at 120 °C. The *pre-calcination* of the dry raw sulphide takes place in a preheated furnace at 900 °C, in nitrogen flow; special quartz ampoules are used in this purpose. After one hour of thermal treatment, sulphide samples are quickly cooled to room temperature. In order to control the zinc sulphide particle surface and size, most of the raw sulphide batches were mixed with ammonium chloride before the pre-calcination stage. NH_4Cl addition is calculated to correspond to 5 g/100 g ZnS final product.

ZnS:Cu,Cl samples were prepared in the usual manner of phosphor synthesis. Homogeneous mixtures consisting in 1.g. ZnS, 2% NH_4Cl or NaCl or MgCl_2 or BaCl_2 and $\text{Cu}(\text{NO}_3)_2$ equivalent to 0.01 g Cu/100 g ZnS are prepared. Phosphor samples were synthesised in quartz ampoules, at 800 or 900 °C, in a protective N_2 -atmosphere. The samples cooling was rapidly performed in specially designed device with protective atmosphere. Phosphor samples were water-washed, to remove the remnant flux, and, finally, they were dried and sieved. Mention must be made that all substances used for phosphors synthesis as well as for zinc sulphide preparation are luminescent grade quality and are prepared in our laboratory, by original procedures.

2.2. Samples characterisation

Sulphide and phosphor samples were characterised by crystalline structure, particle size distribution and luminescent properties under UV excitation. XRD patterns were registered on PW 1050 Philips Diffractometer (CuK_α). Particles size distribution was determined with Coulter-Counter method. Emission spectra were registered at room temperature, on a PC coupled 204 Perkin Elmer Spectrofluorimeter; excitation was performed with 365 nm radiation and UG1 optical filter was used to select the exciting radiation. Phosphors luminescent characteristics were compared with those of a ZnS:Cu phosphor sensitive to electron beam. Cathodoluminescent pigment Lumilux B₃₁₋₁₀ (Riedel-de-Haen) was used as standard. The sensitivity to β -radiation of some ZnS:Cu,Cl samples was checked out by using them to manufacture radioluminescent paints or sources (Betaligns) of standard type.

3. RESULTS AND DISCUSSION

Luminescent properties and particle size distribution are the main characteristics determining the use of ZnS-type phosphors as luminescent pigments. These properties depend in a great extent on the zinc sulphide quality and thermal synthesis conditions.

For the preparation of luminescent grade zinc sulphide *via* thiosulfate, method we finalised a procedure consisting of two stages namely precipitation and pre-calcination. During the precipitation stage, as a result of ZnSO_4 and $\text{Na}_2\text{S}_2\text{O}_3$ interaction many secondary products are formed⁹. The separated solid reaction product - called raw sulphide- includes zinc sulphide and a controlled amount of free sulphur. The pre-calcination stage assures the sulphur volatilisation and the thermal recrystallisation of the remaining zinc sulphide. The quality of zinc sulphide prepared by *thiosulfate route* is influenced by many preparative parameters such as: reagent concentration, acidity of precipitation medium, precipitate maturation period, amount of free sulphur in the raw sulphide, presence of some additives in the raw sulphide, pre-calcination regime (firing temperature and time, sample cooling rate, firing atmosphere) etc.

The zinc sulphide prepared *via* thiosulfate method that we usually use in phosphor manufacture is a high purity material, with less than 5×10^{-5} % heavy metal ions concentration, possesses mixed crystalline structure with about 90% cubic modification content, shows uniform particle size distribution with a median diameter of about 6 μm and exhibits good luminescence ability as shown by our previous paper⁵.

For the present study we try to propose another preparation procedure for l.g. ZnS so that the purity state of the grain surface in rapport with oxygenated compounds to become higher. For this reason we try to buffer the precipitation medium so that the pH of precipitation bath to do not decrease under 2 value. The buffer substance is sodium acetate and its addition is made in a special manner. Supplementary we try to assure a complete deoxydization of the sulphide surface by adding ammonium chloride to the raw sulphide before the pre-calcination stage. The simultaneous volatilisation of ammonium chloride and sulphur from the raw sulphide assure a good sulphide deoxydization.

3.1. Influence of synthesis conditions on zinc sulphide and phosphors particle size distribution

Four raw sulphide batches differing by their variable maturation period were prepared in the described conditions and pre-calcinated to give the *A-to-D ZnS-types*. For comparison, an additional *ZnS-E* type, corresponding to *ZnS C* type, was also prepared with no NH_4Cl addition. Tab. 1 presents the particle size characteristics determined from the distribution curves of *ZnS-A type*, *ZnS-B type*, *ZnS-C type*, *ZnS-D type* and *E ZnS-type*. One observes that, the most uniform particle size distribution, i.e. the smallest Δ value, and the lowest median diameter is obtained for *ZnS C-type* prepared with a maturation period of 72 hrs. Moreover, the variation of particle size with the maturation period do not take place as monotonously as we expected. This illustrates also the existence of two opposite processes of agglomeration and dissipation during the pre-calcination process. One can also note that the ammonium chloride addition is in the favour of both particle growth and particle size uniformity increase. (*ZnS C-type* and *ZnS E-type*).

Tab.1. Particle size distribution of some ZnS - types used as starting material in phosphor synthesis

	Preparation conditions		Particle size distribution (μm)			
	Maturation period	Pre-calcination	$d_{80\%}$	$d_{50\%}$	$d_{20\%}$	Δ
<i>ZnS-A type</i>	24 hrs	$\text{NH}_4\text{Cl} / 900^\circ\text{C}$	7.10	9.37	11.86	4.76
<i>ZnS-B type</i>	48 hrs	$\text{NH}_4\text{Cl} / 900^\circ\text{C}$	5.18	9.53	11.58	6.40
<i>ZnS-C type</i>	72 hrs	$\text{NH}_4\text{Cl} / 900^\circ\text{C}$	6.06	9.33	10.71	4.65
<i>ZnS-D type</i>	96 hrs	$\text{NH}_4\text{Cl} / 900^\circ\text{C}$	7.71	10.34	13.04	5.36
<i>ZnS-E type</i>	72 hrs	no additive / 900°C	6.59	9.19	12.33	5.74

$$\text{where } \Delta = d_{20\%} - d_{80\%}$$

In order to study the influence of synthesis conditions on particle size distribution and luminescent properties of zinc sulphide phosphors, four different sample series were prepared:

- *Series A* - $\text{ZnS}:\text{Cu},\text{Cl}$ samples $T_1; T_2; T_3; T_4$ were prepared in the following synthesis conditions: *ZnS A-type* as starting sulphide; $\text{NH}_4\text{Cl}; \text{MgCl}_2; \text{BaCl}_2; \text{NaCl}$ as flux; 800°C as firing temperature;
- *Series B* - $\text{ZnS}:\text{Cu},\text{Cl}$ samples $T_5; T_6; T_7; T_8$ were prepared in the following synthesis conditions: *ZnS A-type* as starting sulphide; $\text{NH}_4\text{Cl}; \text{MgCl}_2; \text{BaCl}_2; \text{NaCl}$ as flux; 900°C as firing temperature;
- *Series C* - $\text{ZnS}:\text{Cu},\text{Cl}$ samples $T_9; T_{10}; T_{11}; T_{12}$ were prepared in the following synthesis conditions: *ZnS B-type* as starting sulphide; $\text{NH}_4\text{Cl}; \text{MgCl}_2; \text{BaCl}_2; \text{NaCl}$ as flux; 800°C as firing temperature;
- *Series D* - $\text{ZnS}:\text{Cu},\text{Cl}$ samples $T_{13}; T_{14}; T_{15}; T_{16}$ were prepared in the following synthesis conditions: *ZnS B-type* as starting sulphide; $\text{NH}_4\text{Cl}; \text{MgCl}_2; \text{BaCl}_2; \text{NaCl}$ as flux; 900°C as firing temperature;

The particle size distribution of some of the phosphor samples were registered. The particle size characteristics are given in Tab. 2 and compared with the corresponding data of the starting sulphide namely the *ZnS A-type*.

Tab.2. Particle size distribution of *ZnS A-type* and the corresponding $\text{ZnS}:\text{Cu},\text{Cl}$ phosphors samples

Phosphor code	Synthesis conditions		Particle size distribution (μm)				
	Flux	Temperature	$d_{20\%}$	$d_{50\%}$	$d_{80\%}$	Δ	R
<i>ZnS A-type</i>	-	-	7.10	9.37	11.86	4.76	0
T_1	NH_4Cl	800°C	6.21	8.63	11.63	5.42	-7.9 %
T_2	MgCl_2	800°C	9.94	13.07	16.54	6.60	+39.5 %
T_3	BaCl_2	800°C	6.56	9.19	11.86	5.30	-1.9 %
T_4	NaCl	800°C	6.21	8.66	11.18	4.97	-7.6 %
T_{10}	MgCl_2	900°C	9.56	13.07	17.19	7.63	+39.5 %

$$\text{where: } \Delta = d_{20\%} - d_{80\%} \quad \text{and} \quad R = \frac{d_{50\%}(\text{Ph}) - d_{50\%}(\text{ZnS})}{d_{50\%}(\text{ZnS})} \times 100$$

One observes that, depending on the chloride nature used as flux, the diameter of phosphor particles is different. With the exception of T_2 and T_{10} phosphors prepared with magnesium chloride, the other phosphor powders possess smaller particle sizes than the starting sulphide itself. All chlorides used as flux in this study produce the particle size diminution with 1,9 to 7,9 % as compared with the starting sulphide. This behaviour illustrates the fact that, the starting sulphide grains are dissipating during the phosphor firing process, conducting to smaller particles than the initial ones.

As for magnesium chloride as flux, a considerable particles growth could be put in evidence; phosphor grains are with 39.5 % larger than the sulphide ones.

3.2. Influence of synthesis conditions on phosphor luminescent properties

The emission spectra of phosphor series A, B, C and D are presented in Fig. 1, in comparison with the spectrum of the standard phosphor. All spectra consist of two large bands in bleu and green region whose intensity differently contribute to the apparent luminescence. The blue-to-green ratio is variable for different phosphor samples and the green emission colour is purer for lower ratios.

On the basis of emission spectra, the luminescence characteristics of phosphor samples are estimated. The main luminescence characteristics namely the relative luminescence intensity and the position of the main emission peak are presented in Tab.3. The green emission band of A-D phosphor series is centred in the range of 515,0 to 518,9 nm. As for the relative intensity, most of the phosphors exhibit less intense luminescence as compared with standard phosphor. Only ZnS:Cu,Cl phosphor prepared with $MgCl_2$ as flux show green luminescence stronger than the standard one. Moreover, for these categories of samples, i.e. T_3 , T_7 , T_{11} and T_{15} , the difference between the green emission band positions and intensities is hardly noticeable. More than that, phosphor prepared with $BaCl_2$ as flux seems to be most sensitive to thermal synthesis conditions. In this particular case, the peak position vary between 515,3 and 518,6 nm whereas the luminescence intensity oscillate between 77.1 and 81.4 %.

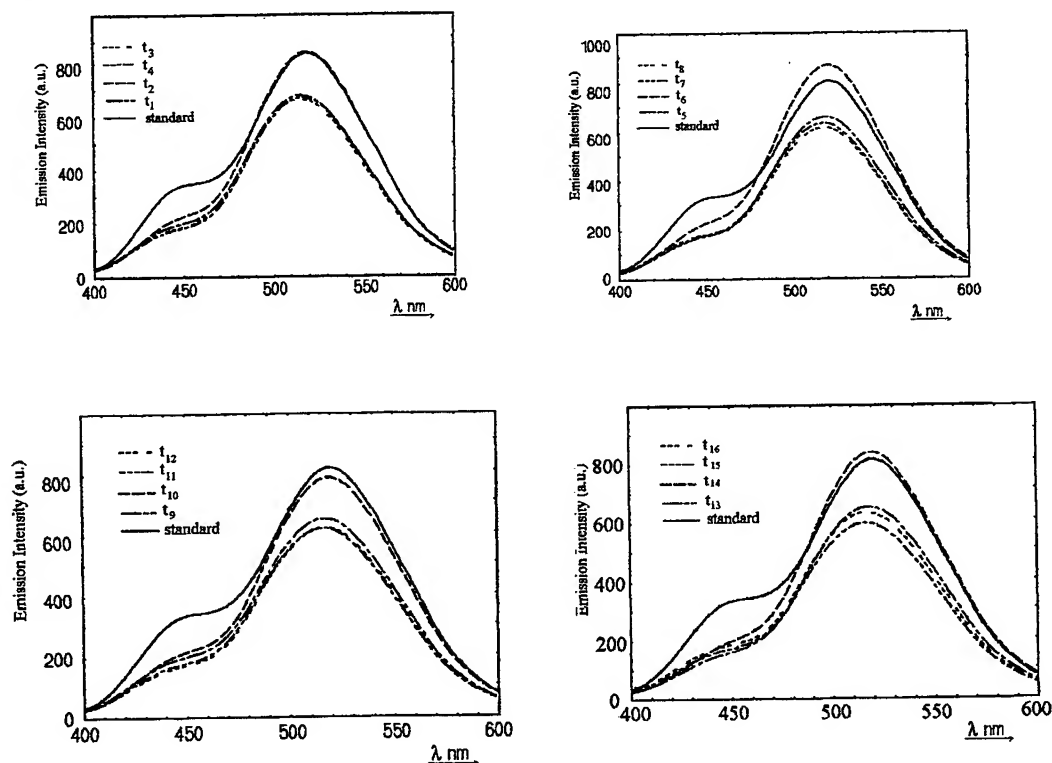


Fig. 1 Emission spectra of ZnS:Cu,Cl samples prepared in various synthesis conditions
Excitation: 365 nm ; Optical filter: UG1

Tab.3. Relative intensity and peak position of the main emission band of ZnS:Cu,Cl samples prepared from different ZnS-type, with various mineralising agents and fired at different temperatures.

	Firing temperature 800 °C		Firing temperature 900 °C	
	ZnS-A type	ZnS-B type	ZnS-A type	ZnS-B type
<i>NH₄Cl - flux</i>	82.3 %; 515.0 nm	80.7 %; 517.5 nm	83.0 %; 516.6 nm	81.4 %; 516.2 nm
<i>MgCl₂ - flux</i>	102.0 %; 518.8 nm	97.4 %; 518.6 nm	109.6 %; 518.9 nm	104.3 %; 518.8 nm
<i>BaCl₂ - flux</i>	80.6 %; 515.8 nm	76.9 %; 518.6 nm	79.8 %; 516.4 nm	74.6 %; 515.3 nm
<i>NaCl - flux</i>	81.4 %; 516.0 nm	77.1 %; 517.0 nm	77.6 %; 516.0 nm	79.08 %; 516.2 nm

On the basis of luminescence spectra, the ratio between the blue and green emission bands was also calculated. The lowest I_{445}/I_{520} values, i.e. 0.229 and 0.214, are observed for T_{13} and T_{14} phosphors prepared at 900 °C, with NH_4Cl and $MgCl_2$ as flux. The highest values, i.e. 0.279 and 0.285, are noted for T_1 and T_5 phosphors prepared at 800 °C, with NH_4Cl as flux, respectively. *ZnS-B type* is most favourable to green emission centres formation whereas *ZnS-A type* facilitates blue centres formation.

Luminescence spectra of ZnS-type phosphors consist of two or more wide emission bands with various intensities, halfwidths and peak positions. In order to obtain additional information about the luminescence of ZnS:Cu,Cl phosphors differently prepared, the luminescence spectra were mathematically decomposed into two Gauss-type curves. Fig. 2 presents the spectrum of T_3 samples, i.e. ZnS:Cu,Cl prepared at 800 °C from *ZnS-A-type* as starting sulphide, with $BaCl_2$ as flux. One can see that with 2 curves, an acceptable Gauss-fitting could be obtained. Gauss parameters of T_1 – T_{16} phosphor spectra are presented in Tab. 4.

The peak position, halfwidths and amplitude values for spectra of phosphors prepared with the same flux show that there are only small differences between samples prepared from different ZnS-types and fired at different temperature. The differences observed between the apparent luminescence emission are the result of variable contribution of these components. This mathematical approach confirms that the same emission centres are implied into the luminescence process, the only difference being their concentration and though their contribution to the apparent luminescence. Their relative ratio of the two Gauss components could explain the slight variation of the peak positions (see also Tab. 3).

Sensitivity to β radiation could be tested by using ZnS:Cu,Cl samples in the manufacture of radioluminescent (RL) sources. In this purpose, T_1 phosphor was used in closed sources (Betaligns) as well as in open ones (radioluminescent paints). In the first case, the phosphor is deposited on the inside wall of a small glass tube filled with tritium gas. In the second, the phosphor is "dispersed" into a tritiated polymer. For Betaligns, a brightness of 1 $\mu La/cm^2$ could be achieved with an activity of 44.4 MBq (1.2 Ci); the tritium β radiation is completely utilised. For radioluminescent paints, a brightness of 1 $\mu La/cm^2$ could be obtained with 55.5 MBq (1.5 mCi); due to a self absorption process, the tritium β radiation is only 80 % used. The sensitivity to β radiation could be increased either by performing particle selection or by trying to synthesise ZnS:Cu phosphors with even smaller particle sizes but with adequate luminescent properties.

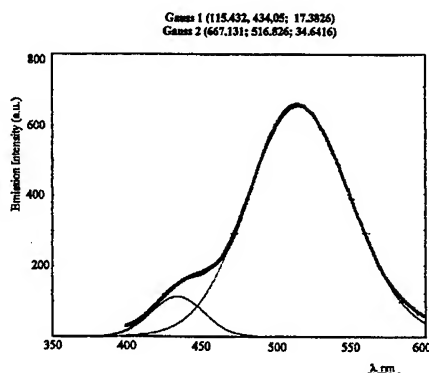


Fig. 2 Gaussian fitting of the emission spectra of -T3 phosphor (*ZnS-A type*, $BaCl_2$ as flux, 800 °C)

Tab.4 Peak positions, halfwidths and amplitudes of the two Gauss components (G1 and G2) of emission spectra of phosphors prepared in different conditions

		Firing temperature 800 °C		Firing temperature 900 °C	
		ZnS-A type	ZnS- B type	ZnS- A type	ZnS- B type
NH ₄ Cl -flux	G1	517.2 nm; 34.9 nm 681.5	517.5 nm; 35.5 nm 669.7	518.5 nm; 34.7 nm 687.7	518.9 nm; 34.7 nm 674.8
	G2	434.8 nm; 17.6 nm 123.5	435.9 nm; 18.0 nm 126.1	434.8 nm; 17.1 nm 110.6	434.5 nm; 16.8 nm 95.6
MgCl ₂ -flux	G1	520.0 nm; 34.4 nm 841.1	520.0 nm; 34.4 nm 804.3	520.0 nm; 34.4 nm 903.9	520.3. nm; 34.5 nm 858.4
	G2	437.9 nm; 17.6 nm 141.5	438.1 nm; 17.5 nm 138.7	438.6 nm; 17.2 nm 142.0	437.3 nm; 16.8 nm 114.2
BaCl ₂ -flux	G1	516.8 nm; 34.6 nm 667.1	517.1 nm; 34.9 nm 638.1	517.8 nm; 34.7 nm 661.2	517.0 nm; 34.9 nm 619.5
	G2	434.0 nm; 17.4 nm 115.4	434.5 nm; 17.5 nm 110.8	434.3 nm; 17.5 nm 112.9	434.2 nm; 17.4 nm 108.9
NaCl -flux	G1	517.8 nm; 34.6 nm 673.2	517.8 nm; 34.8 nm 640.0	517.7 nm; 34.6 nm 644.4	517.4 nm; 34.9 nm 656.8
	G2	433.9 nm; 17.6 nm 115.0	434.4 nm; 17.4 nm 107.1	434.8 nm; 17.6 nm 121.8	434.4 nm; 17.4 nm 120.0

4. CONCLUSIONS

Zinc sulphide prepared by thiosulfate method could be converted into ZnS:Cu,Cl phosphors with small particles sizes and sensitive to β radiation. A high degree of surface grain oxidation could be assured by using sodium acetate and ammonium chloride during the precipitation and pre-calcination stages, respectively. The thermal synthesis could be performed at 800 °C. In spite of the fact that magnesium chloride is favourable to luminescence centres formation, the recommended flux for β sensitive phosphors is NH₄Cl that produces the smallest phosphor particles and generates an acceptable luminescence.

The mathematical approach for emission spectra shows that NaCl, MgCl₂, BaCl₂ and NH₄Cl contribute to the formation of different concentration of the same type of emission centres. These chlorides influence differently the particle growth during the thermal synthesis stage. Magnesium chloride increases the phosphor particle size, being the most effective mineralising agent, whereas the other chlorides produce the grains diminution by dissipating the starting zinc sulphide

REFERENCES

1. I.O. N. Kazankin, L. Ya. Markovskii, I. A. Mironov, F. M. Nekerman and L. N. Netoshina, *Neorganicheskie lyuminoforesy*, Izd. Himya, Leningrad, 1975.
2. M. Gurvich, *Vvedenie v fizicheskuyu himiyu kristallophosphorof*, Vysch. Scola, Moskva, 1982.
3. E.J. Popovici, V. Ursu and D. Macarovici, "Luminescent-grade zinc sulphide prepared by thiosulfate method. II Some physical properties of different ZnS-types", *Roum. Chem. Quart. Review*, 1(3), pp. 239-244, 1993.
4. E.J. Popovici, M. Aneculaese and D. Macarovici, "Luminescent-grade zinc sulphide prepared by thiosulfate method. IV The effect of thermal treatment on some properties of ZnS-types", *Rev. Roum. Chimie*, 41(7-8), pp. 551-557, 1996.
5. E.J. Popovici, M. Aneculaese, V. Ursu and D. Macarovici, "Synthesis of zinc sulphide type phosphors with well defined characteristics", *Rom. J. Optoelectronics*, 5(1), pp. 81-84, 1997.
6. E.J. Popovici, M. Aneculaese, M. Vasilescu and D. Angelescu, "Synthesis of silver activated zinc sulphide phosphors for alfa-ray detectors", *Rom. J. Optoelectronics*, 7(1), pp. 39-42, 1999.
7. E.J. Popovici, M. Aneculaese, and V. Ursu "Luminescence properties of some double activated zinc sulphide type phosphor", *SPIE Proceedings Series*, Bellingham, USA, 3405, pp. 636-640, 1998.
8. E.J. Popovici, M. Aneculaese and D. Macarovici, *Rom. Pat.*, 103769, 1991.
9. M.I. Tombak, A.V. Popova, O.F. Komarand and A.A. Bundel, "O progodonosti tioulsulfatogo metoda v poluchenia sulfida tzinka dlya sinteza lyuminoforov, *Izv. A. N. S. S. S. R, Ser. Fiz.*, XXIII(11), pp. 1363-1369, 1959.

Macroscopic model of PZT ceramics - linear piezoelectric equations

Marian Lazar*

Dept. of I.R., X-Rays, Ultrasounds and Piezo-Ceramics Materials,
Institute of Optoelectronics S.A., Bucuresti-Magurele

ABSTRACT

In $\text{Pb}(\text{Zr}_{1-x}\text{Ti}_x)\text{O}_3$, experiments have shown that conductivity is p-type (Jaffe & Co., 1970). The excess of cation over oxygen vacancies causes a superoxidation of many simple oxides, including ZrO_2 (Rudolph, 1959). These A position vacancies attract electrons to complete the electron shells of surrounding oxygens: they act as acceptors causing the presence of holes in the lattice. The new revised theoretical model presents the basic steps in the solid plasma linear analysis of any acousto-electric problem.

Keywords: PZT-ceramic, macroscopic model, linear equation, dispersion equation, linear mode

1. INTRODUCTION

The piezoelectric effect in the first piezoelectric ceramic with perovskite structure, BaTiO_3 , was discovered in 1947 by Roberts. As a more thorough understanding of the solid solutions of BaTiO_3 -series was being developed, many other ABO_3 -type ferroelectrics and antiferroelectrics with oxygen-octahedron structure, such as PbTiO_3 , KbO_3 , KtaO_3 , NaNbO_3 , NaTaO_3 , PbZrO_3 , PbHfO_3 , LiNbO_3 and LiTaO_3 , were discovered one after the other. Among them, PbZrO_3 (lead zirconate) and PbTiO_3 (lead titanate) were important ceramics with the perovskite structure. In 1950, the anomalous dielectric properties of PbZrO_3 were reported and its antiferroelectricity was confirmed. The phase diagram of the solid solution of PbZrO_3 and PbTiO_3 was published by Sawaguchi in 1953, but no mention of the piezoelectric properties of this solid solution.

Lead titanate (PbTiO_3) is a ferroelectric with a high Curie temperature (490°C) at which the phase transition from the cubic paraelectric phase (above the Curie temperature) to the tetragonal ferroelectric phase (below Curie temperature) occurs.

In 1954, Jaffe et al. reported the discovery of the piezoelectric ceramic $\text{Pb}(\text{Zr}_x\text{Ti}_{1-x})\text{O}_3$ (PZT). In the following ten years, PZT became the main industrial product in piezoelectric ceramic materials.

When Ti^{+4} ions in PbTiO_3 are partially replaced by Zr^{+4} with a molar ratio x , a solid solution of $x\text{PbZrO}_3 - (1-x)\text{PbTiO}_3$ ($0 < x < 100\%$) binary system is formed. This solid solution is called lead zirconate titanate (PZT), and its chemical formula is $\text{Pb}(\text{Zr}_x\text{Ti}_{1-x})\text{O}_3$. PZT has the perovskite structure with Ti^{+4} and Zr^{+4} ions occupying B-sites at random.

2. EXPLANATION OF CONDUCTION PROCESSES IN PZT CERAMICS

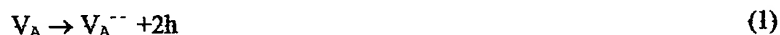
The importance of an understanding of conductive processes cannot be overestimated. Besides the obvious application to thermistors and barrier layer capacitors, the ability to control conductivity, and usually to keep it very low, is highly important to the piezoelectric uses of ceramics. Compositions which are too conductive are difficult to pole, tend to overheat in high power applications, and generally have undesirably high dielectric loss which limits efficiency.

In the following discussion the usual terminology of donor (contributing extra electrons) and acceptor (deficient in electrons, or contributing "holes") will be followed. A positive ion replacing a higher valency ion such as K^{+1} for Ba^{+2} acts as an acceptor in an otherwise unchanged lattice. It contributes fewer electrons than the ion it replaces, thus creating "holes". In contrast, a positive ion replacing another of lower valency such as La^{+3} for Ba^{+2} contributes extra electrons to the structure and is thus a donor. For negative ions the reverse is true: a negative ion replacing another of higher valency such as F^{-1} for O^{-2} needs one less electron and thus acts as a donor, while a negative ion replacing a lower valency ion becomes an acceptor.

*Correspondence: E-mail: marianlazar@yahoo.com

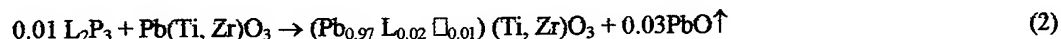
Piezoelectric lead-zirconate-titanate ceramic have perovskite structure $A^{+2} B^{+4} O_3$, A represents a cation with a larger ion radius and B a cation with a smaller ionic radius. In perovskites, because of the density of packing, the presence of interstitial ions appears unlikely (with the possible exception of a very small ions, such as Be^{+2} and B^{+3}). It is known, however, that substantial concentrations of vacancies can be tolerated. The $NaWO_3-WO_3$ solid solution series, the familiar sodium-tungsten bronze, shows that vacancies in the A position can be large in number. Numerous studies on perovskites of formula type $BaFeO_{3-x}$, $SrCoO_{3-x}$, etc., have demonstrated that in some circumstances the perovskites lattice will tolerate a moderate concentration of O position vacancies. There is at present no concrete evidence of the existence of any significant concentration of vacancies in the B position of any perovskite. Compositions with stoichiometry that might yield a perovskite with B position vacancies crystallize instead as a mixture of perovskite and non-perovskite phases. Therefore, all cation vacancies are assumed to occur in the A position.

In $Pb(Zr_{1-x} Ti_x)O_3$, experiments have shown that conductivity is p-type (Jaffe & Co., 1970). This is presumably due to superoxidation, that is excess of cation over oxygen vacancies, (many simple oxides, including ZrO_2 , as found by Rudolph, 1959). These A-position vacancies attract electrons to complete the electron shells of the surrounding oxygens: they act as acceptors causing the presence of holes (electrons defects) in the lattice according to



Substitution of La^{+3} for Pb^{+2} or of Nb^{+5} for $(Ti, Zr)^{+4}$ contributes electrons, and thus reduces the hole conductivity according to the mass action law which requires that the product of electron and hole concentration remain constant, just as the product of H^+ and $(OH)^-$ ions in an aqueous solution is constant. The conductivity is reduced typically by about three-orders of magnitude for amounts of about 1 atom %. It may be seen in Jaffe & Co., 1970, that increases in the amount of additive over 1 atom % do not further affect the resistivity significantly. The lower limits for complete compensation has not been investigated.

One might expect that an increase in concentration of higher valent substituents should cause an excess of electrons over holes and hence substantial n-type conductivity. This is indeed the case with barium titanate but not with lead titanate zirconate. Here the conductivity reaches a low "intrinsic" value with donor doping levels of a few tenths of 1% and does not show further increase or decrease with higher doping. The reason for this is believed to be the formation of Pb-site vacancies as in the reaction (here with La doping):



taking place during the firing process. The high volatility of lead oxide is an essential factor. The additional A-position vacancies caused by this reaction explain the effect of these additives on domain switching phenomena and in particular on the easy relaxation of inter-domain stresses in polarized ceramics.

2.1. Linear model principles

The model assumptions are:

1. The free carriers in PZT - holes, can be treated in the same way as the free positive ions in vacuum. The effect of the environment has been taken into account by introducing new masses for the holes - effective mass approximation.
2. In the processes in which we shall be interested, energy and momentum changes per particle will usually be small, so that we shall not consider band-to-band transitions.
3. Interactions of holes with lattice vibrations are taken into account by introducing constant collision frequencies, $\nu_h = 1/\tau_h$.
4. We neglect at first, the effect of distribution in velocity (or momentum) space and assume constant drift velocities for holes $v_h = v_{oh}$. However, in some cases we take the first-order effects of the distribution into account by introducing a diffusion term in the equation of motion for the carriers.
5. In order to take into account the changes in the numbers of carriers due to recombination or generation, we introduce source or sink terms (into the equation of continuity) proportional to the generation or recombination frequencies ν_{gr} (ν_r -ionization, ν_a -attachement, in general $\nu_g - \nu_r = \nu_i - \nu_a - \nu_r \approx 0$).
6. We further assume that the wavelength of any disturbance is much longer than the Debye length λ_D so that we may treat the hole stream hydrodynamically.

And the analysis basic steps are:

a) If there are mobile holes in the PZT ceramics, they will produce a current when subjected to electric fields: $j_i = \sigma_{ij} E_j$, where σ_{ij} is the conductivity tensor, which has to be calculated in terms of ω_p , v , ω , ω_c , k , Note that σ_{ij} is not an explicit function of the sound parameters.

b) The acoustic portion of the problem is completely described by the displacement u , which is a function of ρ , $//C//$, ω , k , $//e//$ and E (ρ - density of the medium, $//C//$ - fourth-rank elastic tensor, $//e//$ - piezoelectric tensor). It is the dependence on E that is important here since it furnishes the coupling back to the hole motion through $j_i = \sigma_{ij} E_j$. The linear equations used to calculate u are:

$$\rho (\partial^2 u_i / \partial t^2) = \partial T_{ij} / \partial x_j, \quad T_{kl} = C_{ijkl} S_{ij} - e_{mkl} E_m, \quad D_n = \epsilon_{mn} E_m + e_{nij} S_{ij},$$

where T_{ij} - the components of the second-rank stress tensor, S_{ij} - the components of the second-rank strain tensor, D - the electric displacement of anisotropic media.

c) The coupling between the hole motion and the sound is calculated with the help of Maxwell's equations. This leads to a triplet of equations relating the components of the self-consistent field,

$\sum_{j=1,3} a_{ij} E_j = 0$, where a_{ij} contains both hole and sound parameters.

d) The determinant of the three equations yields the dispersion relation: $D(\omega, k) = \text{Det}(a_{ij}) = 0$.

e) The solutions of $D(\omega, k) = 0$, give the allowed modes of the composite system and also show if any instabilities can exist.

3. INTERACTION OF ELECTROKINETIC MODES WITH SOUND WAVES

The spectrum of frequencies and wavelengths of mechanical vibrations that may be permitted in a given solid depends on the detailed nature of the lattice and binding forces. The coherent vibrations of the lattice are called sound waves (coherent phonons).

If the solid either is piezoelectric or has a finite deformation potential, some of the mechanical energy of the vibration is converted to electrical energy; the sound wave is then accompanied by an electromagnetic wave. Hence we may expect strong coupling between the sound waves and the electrokinetic waves in piezo-ceramics.

3.1. Quasi particles and collective modes in PZT-ceramic solid solution

It is possible to view much of the solid state physics in terms of certain elementary excitations that interact only weakly with one another. This view has proved to be very useful both experimentally and theoretically. Its starting point is from the state of the crystalline solid at very low temperature as the ground state; that is, even though the crystalline solid consists of strongly interacting particles, its behavior at finite temperatures and its response to small external disturbances (electrical, mechanical, etc) may be described in terms of weakly interacting quasi particles, which are the lower excited states of the many body system relative to the ground state. Consider for instance, the case of the PZT-ceramic solid solution, in which most of the physical characteristics are determined by the low excited states. We speak of these states as having a few mobile charge carriers (electrons and holes, $p \gg n$) determining the electrical characteristics, or as having a small number of lattice waves - phonons, determining the elastic and thermal characteristics, or as having a small number of spin waves - magnons, determining the magnetic characteristics of the solid.

The quasi-particles in solids with which we shall be mainly concerned in this paper are then holes, electrons and plasmons.

3.1.1. Quasi-particle energy, lifetime and distribution

We describe the conditions that permit us to consider a solid as a collection of essentially independent elementary excitations.

For an excitation of a many-body system to be classified as a quasi-particle, it must have a reasonably well-defined energy.

The energy of a given excitation of momentum p is, in general, complex and represented as $E_p = E_{pr} - iE_{pi}$, where E_{pi} , the imaginary part of the energy, is inversely proportional to the lifetime of the excitation. If the $E_{pr} \gg E_{pi}$, the excitation is long-lived and distinguishable.

In thermal equilibrium, the long-lived excitation may be characterized by a distribution function,

$$f_p(T) = 1 / (e^{\beta(E_{pr} - \mu)} \pm 1) \quad (3)$$

where $\beta = 1/K_B T$ and μ is a normalizing factor ($\mu = E_F$ for fermions) which depend on the number of carriers and the temperature. The plus sign applies if the excitation obeys Fermi-Dirac statistics, the minus sign for Bose-Einstein statistics. Electrons and holes obey Fermi-Dirac statistics, whereas plasmons, helicons, phonons and magnons obey Bose-Einstein statistics.

3.1.2. Electrons

The free electrons in solids are usually quasi electrons. They are either excited from the Fermi sea of electrons as in metals or from the valence band or impurity states as in the semiconductors.

The quasi electron is characterized by an effective mass m_e , which may be considerably different from the free electron mass m_0 . The introduction of the effective mass concept is a simple case of mass renormalization, and it is one method of treating the many-body problem, that is, the interaction of the particle with all the other particles (the background). The effective mass is related to the curvature of the energy surface in the momentum space and is, in general, a tensor quantity:

$$1 / m_{ij} = (1 / 4\pi^2 \hbar^2) (\partial^2 E / \partial k_i \partial k_j) \quad (4)$$

Depending on the nature of the structure of the conduction band, it is possible to excite quasi electrons of different effective masses.

3.1.3. Holes

Holes are characterized as the absence of a quasi electron in an energy state normally occupied by a quasi electron. If a quasi electron is created by being raised out of Fermi sea or out of the valence band into the conduction band, a hole is left behind. The holes are again characterized by an effective mass or an effective mass tensor, and depending on the structure of the valence band, it is possible to excite holes of different effective masses, such as the heavy holes in PZT-ceramics.

3.1.4. Plasmons

A possible elementary excitation of a many-electron system (such as conduction electrons in metals and semiconductors or holes in PZT-ceramics and semiconductors) due to Coulomb interaction is a collective oscillation of the electron or hole particle density, the plasma oscillation. In the limit of long wavelengths, the frequency of the oscillation is given by the plasma frequency, for electrons and holes respectively:

$$\omega_{p-} = (ne^2 / m_e \epsilon)^{1/2}, \quad \omega_{p+} = (pe^2 / m_h \epsilon) \quad (5)$$

where n (negative) is the electron density and p (positive) is the hole density.

The quantum of plasma oscillation is the plasmon. Plasmons are bosons. The plasmon energy is given by $\hbar\omega_p/2\pi$, consequently plasmon energies range from about 5 to 30 eV for electron system of metallic densities and 10^{-5} eV to several electron volts for electron systems realizable in semiconductors.

4. MACROSCOPIC MODEL OF PIEZOELECTRIC MEDIA

An elastic solid subjected to a stress produces displacements of the lattice. The vector \mathbf{u} is taken as the displacement of a particular lattice point. From Newton's equations \mathbf{u} is related to the stress tensor \mathbf{T} by relations:

$$\rho (\partial^2 u_i / \partial t^2) = \partial T_{ij} / \partial x_j \quad (6)$$

where ρ is the density of the medium and T_{ij} are the components of the second-rank stress tensor. In the absence of piezoelectricity \mathbf{T} is related to the second-rank strain tensor \mathbf{S} through the fourth-rank elastic tensor \mathbf{C} , or

$$T_{kl} = C_{ijkl} S_{ij} \quad (7)$$

Equation (4) is the generalized Hooke's law relating stress and strain. Of the nine components T_{kl} or S_{ij} only six are independent, so that in the most anisotropic crystal there are thirty-six independent coefficients C_{ijkl} of the elastic tensor. For isotropic substances most of these coefficients are zero or related to one another. In fact, for an isotropic solid with no crystalline structure there are only two independent constants; all other elastic coefficients such as Young's modulus and the compressibility or the velocity of sound can be expressed in terms of those two constants. We shall deal later with particular crystal lattices in the discussion of piezoelectricity.

There is a variety of shorthand methods for reducing the number of indices in the tensors $//T//$, $//S//$ and $//C//$.

The linear strains, corresponding to the diagonal elements of $//S//$, are defined as:

$$S_{ii} = \partial u_i / \partial x_i \quad (8)$$

The shearing strains (off-diagonal elements) are:

$$S_{ij} = 1/2 (\partial u_i / \partial x_j + \partial u_j / \partial x_i) \quad (9)$$

With this convention $//S//$ is a symmetric tensor. It can be shown that $//T//$ is also a symmetric tensor.

If the unit cell of a crystal contains at least two different atoms, that crystal can exhibit piezoelectricity. In such material, stress can produce electricity, or, vice versa, applying a voltage can produce stress. The relations between the elastic and electrical variables requires the introduction of the piezoelectric tensor $//e//$ which is a third-rank tensor. There are many ways of expressing the connection between $//T//$, $//S//$, \mathbf{D} and \mathbf{E} . We choose the designation usually employed in the literature of acoustoelectric effects.

The pertinent *linear* relations are:

$$T_{kl} = C_{ijkl} S_{ij} - e_{mkl} E_m \quad (10)$$

$$D_n = \epsilon_{mn} E_m + e_{nij} S_{ij} \quad (11)$$

where ϵ_{mn} is the lattice dielectric tensor. If there is no piezoelectricity, that is, $//e//=0$, eq. (10) gives us the usual Hooke's law relating stress and strain, while eq. (11) gives the well-known relation between the electric displacement \mathbf{D} of anisotropic media in terms of the electric field \mathbf{E} .

The new revised theoretical model presents the basic steps in the *solid plasma* analysis of any acousto-electric problem.

Plasma and cyclotron frequencies: the large range of densities and low masses have important consequences in the frequency of oscillation of the carriers when subjected to electromagnetic fields. the plasma frequency ω_p and the cyclotron frequency ω_c are the most important of the oscillations. For typical semiconductors, $\omega_p \approx 10^{12} \text{ s}^{-1}$ (in the millimeter wave region), while for metals, $\omega_p \approx 10^{15} \text{ s}^{-1}$ (in the visible region of spectrum). Cyclotron frequencies in magnetic field of 1000 G range from 10^{10} s^{-1} for metals to 10^{12} s^{-1} for semiconductors whose carriers have small m_e values.

The model framework consists of followings assumptions:

1. The free carriers in PZT - holes, can be treated in the same way as the free positive ions in vacuum. The effect of the environment has been taken into account by introducing new masses for the holes - *effective mass approximation*. Because of periodic potential of the crystal lattice the effective mass of the mobile carriers is generally lower than the free electron mass (m_0). For electrons, the values of m_e/m_0 (the effective mass m_e , is often designated as m^* in the literature) range from 10^{-2} in such solids as Bi and InSb to 1 in most metals (for example, Cu, Na). *The holes also have effective masses that cover such a range.* However, in a given solid, electrons generally have lower effective masses than holes.
2. In the processes in which we shall be interested, energy and momentum changes per particle will usually be small, so that we shall not consider band-to-band transitions.
3. Interactions of holes with lattice vibrations are taken into account by introducing constant collision frequencies, $\nu_h = 1/\tau_h$.

One of the most important differences between gaseous and solid state plasmas is the scattering frequency ν . For gases, ν is often neglected compared to other frequencies since it can be very low for the usual plasma. In solids because of the ever-present thermal vibrations of the lattice, scattering is a very important part of any problem.

A side from phonon scattering of the carriers, there are scattering effects from ionized impurities (Rutherford scattering) and neutral impurities. For dense semiconductor electron-hole plasma ($n \geq 10^{22} \text{ m}^{-3}$) we also have to take into account electron-hole scattering (a special case of Rutherford scattering).

For solids, the value of ν ranges from about 10^{10} to 10^{13} s^{-1} as the temperature increases from liquid helium (4.2 K) to room temperature (300 K). In most of the problem that we shall consider, ν will be a significant parameter. The ratio ω_c / ν will often enter the analyses of the wave interactions to be discussed later. This ratio is about 1 : 10 for the usual laboratory magnetic fields at liquid nitrogen temperatures (77 K).

Lattice dielectric constant: since the crystal lattice that contains the solid state plasma is itself polarizable, it contributes to the dielectric constant ϵ of the entire system. In most semiconductors the relative dielectric constant of the lattice $\epsilon_L = \epsilon / \epsilon_0$ is between 10 and 20. For semimetals, like bismuth, it can have values up to 100.

4. We neglect at first, the effect of distribution in velocity (or momentum) space and assume constant drift velocities for holes $v_h = v_{0h}$. However, in some cases we take the first-order effects of the distribution into account by introducing a diffusion term in the equation of motion for the carriers.

Diffusion effects: With both finite temperature and scattering in the solid, there are diffusion effects whenever the carrier are bunched. Since most of the interesting interactions involve such bunching, diffusion can play a critical role. Diffusion is characterised by the constant D , defined as:

$$D = k_B T / m \nu = v_0^2 / 2 \nu \quad (12)$$

where v_0 is the average thermal velocity of the carriers for the particular distribution function involved. For most solids, under the conditions of interest, $v_0 \approx 10^6 \text{ m/s}$ and $\nu = 10^{13} \text{ s}^{-1}$, so that $D \approx 10^{-1} \text{ m}^2/\text{s}$.

5. In order to take into account the changes in the numbers of carriers due to recombination or generation, we introduce source or sink terms (into the equation of continuity) proportional to the generation or recombination frequencies ν_{gr} (ν_i -ionization, ν_a -attachement, in general $\nu_g - \nu_r = \nu_i - \nu_a - \nu_r \approx 0$).

6. We further assume that the wavelength of any disturbance is much longer than the Debye length λ_D so that we may treat the hole stream hydrodynamically.

When the plasma have has a finite temperature, another important parameter is λ_D , the Debye length. It is defined by the relation:

$$\lambda_D = 2 \pi v_0 / \omega_p, \quad (13)$$

where v_0 is the average thermal velocity of the carriers for the particular distribution function involved. For metals, $\lambda_D \approx 10^{-9} \text{ m}$, while for semiconductors, it is $\lambda_D \approx 10^{-6} \text{ m}$. These values dictate the minimum linear dimensions that the solid can have in order that the plasma exhibit collective effects.

The analysis basic steps are:

a) If there are mobile holes in the PZT ceramics, they will produce a current when subjected to electric fields: $j_i = \sigma_{ij} E_j$, where σ_{ij} is the conductivity tensor, which has to be calculated in terms of ω_p , ν , ω , ω_c , k , Note that σ_{ij} is not an explicit function of the sound parameters.

In the proceeding of the holes motion we will take into account scattering and diffusion and we will use the hydrodynamic equations - in the quasistatic limit: equation of continuity, equation of motion for representative particle of holes and higher orders of distribution function momentum.

b) The acoustic portion of the problem is completely described by the displacement u , which is a function of ρ , $//C//$, ω , k ,

//e// and E (ρ - density of the medium, //C// - fourth-rank elastic tensor, //e// - piezoelectric tensor). It is the dependence on E that is important here since it furnishes the coupling back to the hole motion through $j_i = \sigma_{ij} E_j$. The linear equations used to calculate u are the (6), (10) and (11), in which we establish the type of lattice wave (phonon), longitudinal or transversal, and also we must know the complete set of elastic, piezoelectric and dielectric coefficients.

From the particularized (6) and (10) equations, longitudinal, shear or another modes, we find the particularized equation of lattice motion.

For the wave, we assume all variables to be of the form $\exp(i\omega t - kz)$. When piezoelectric tensor //e// $\neq 0$, the sound is coupled to the electron motion through the electric field.

c) The coupling between the hole motion and the sound is calculated with the help of Maxwell's equations, of particularized (8) and (9), (12) and lattice motion equations. These lead to a triplet of equations relating the components of the self-consistent field,

$$\sum_{j=1-3} a_{ij} E_j = 0 \quad (17)$$

where a_{ij} contains both hole and sound parameters.

d) The determinant of the three equations yields the dispersion relation:

$$D(\omega, k) = \text{Det}(a_{ij}) = 0 \quad (18)$$

e) The solutions of $D(\omega, k) = 0$, give the allowed modes of the composite system and also show if any instabilities can exist.

ACKNOWLEDGMENTS

I am grateful to Professor C. Ciubotariu, Technical University - "Gh. Asachi" of Iasi, and to Professor I. Gotlieb, "Al. I. Cuza" University of Iasi, for helpful discussions.

REFERENCES

1. B. Jaffe, W.R. Cook Jr. and H. Jaffe, *Piezoelectric Ceramics*, Academic Press, New York, 1971.
2. M.C. Steele and B. Vural, *Wave Interactions in Solid State Plasmas*, McGraw-Hill, New York, 1969.
3. Yuhuan Xu, *Ferroelectric Materials and Their Applications*, North-Holland, 1990.
4. P.M. Platzman and P.A. Wolff, *Waves and Interactions in Solid State Plasmas*, Academic Press, New York, 1973.
5. L. Eyraud, *La ceramique piezoelectrique et ses applications electroacoustiques*, INSA-Departement de Genie Electrique, Lyon, France, 1995.
6. L. Bellaiche, J. Padilla and D. Vanderbilt, *Ferroelectric effects in PZT*, Cond. Mat./9802209, 19 Feb. 1998.

Negative magnetoresistance of granular Co-Cu films prepared by electrochemical deposition

Vladimir M. Hutanu^a, Voicu Dolocan^b

^a Institute of Optoelectronics IOEL-SA, PO BOX MG-22, 76900,
Bucharest-Magurele, Romania

^b University of Bucharest, Faculty of Physics, PO BOX MG-11, 76900
Bucharest-Magurele, Romania

ABSTRACT

We have investigated the magnetoresistance and structure of binary metallic systems formed by Cu and Co. The samples were prepared by electrochemical deposition from a single electrolyte acid solution on copper coated glass substrate. The structure of the alloy films before and after annealing has been determined by X-Ray diffraction. Two cubic phases have been revealed in both cases: the Cu-rich (f.c.c.) and another probably Co-rich cubic phase which could not be precisely identified. Field dependence of the magnetoresistance were measured for different field orientations. Isotropic negative magnetoresistance effect of 2 % at room temperature for Cu-Co structures before annealing and of 0.9 % after annealing was found. The temperature dependence of resistivity was measured.

Keywords: Electrochemical deposition, nanometric granular structures, giant magnetoresistance

1. INTRODUCTION

The magnetic granular structures with the nanometric size of ferromagnetic granules imbedded in nonmagnetic metal matrices are of a considerable interest due to their electrical and magnetic properties. As the short-period metal/metal superlattices these granular structures manifest some new phenomena that differ significantly from those of bulk materials.

One of these phenomena is the GMR (giant magnetoresistance)^{1,2} whose continue to be the subject of a large scientific effort both at a fundamental level and at the level of its technological applications to magnetic recording technology. The most of the samples which exhibit high negative MR values have been prepared by sputtering, molecular beam epitaxy (MBE), or other vacuum based techniques³. Some authors⁴⁻⁸ have been reported giant magnetoresistance in magnetic multilayers grown by electrodeposition in a single electrolyte. In the present work we obtain the magnetic inhomogeneous alloy films by electrodeposition. All the deposition were made in the potentiostatic controlled three electrode electrochemical cell. Electrodeposition has some obvious advantages over trivial techniques, since the experimental apparatus required is considerably simpler (and cheaper) than those for techniques which require high or ultrahigh vacuum. The deposited structures has been composition and thickness measured by X-ray fluorescence, their structure was determined by X-ray diffraction and magnetoresistance measurements in the Van der Pauw geometry were performed in all three directions of external magnetic field orientations: longitudinal, transversal (in film plane) and perpendicular to film plane field. The negative magnetoresistance for all field orientations was found. The dependence of resistivity from temperature was measured. The increasing of magnetoresistance with temperature decreasing was found. This work is our first step made to realize magnetic granular alloys by electroplating and to study structure of these materials.

2. EXPERIMENTAL

The Co-Cu inhomogeneous alloy samples were grown from a single electrolytic solution. Electrodeposition of a metal takes place by reduction of its ions at the cathode of an electrochemical cell. Since different metals have different reduction

* Correspondence: Email: vhutanu@mailcity.com

potentials, it is necessary for the alloy deposited from an electrolyte containing more than one ion species to apply the cathode potential of reduction of the less noble metal in solution (Co in our case) then Co and Cu will be deposited with rates governed by the kinetics of the deposition process and concentrations rates in solution.

All the depositions were carried with potentiostatic control in standard 3 - electrodes geometry. A potentiostat (Taquselle model PR-20X) maintains the potential of the film substrate (the cathode) at the desired value relative to the standard calomel saturated reference electrode (SCE) by varying the potential between the film substrate and a platinum auxiliary electrode.

The thickness of the deposited films depends direct on the length of the time impulse which is controlled by a time adjustable relay (TR). Were prepared samples of 1-10 μm thick. The electrolyte for Cu-Co samples has been agitated during the deposition using magnetic agitators.

Each sample was grown on the Cu vacuum evaporated on glass substrates with the thickness of the Cu layer of 1 μm . The part of the Cu substrate including its boundaries and electric contact is covered with an electrical insulator lacquer.

The electrolyte solution for alloy deposition contains 250 g/l $\text{CoSO}_4 \cdot 7\text{H}_2\text{O}$, 50 g/l $\text{CoCl}_2 \cdot 5\text{H}_2\text{O}$, 15g/l $\text{CuSO}_4 \cdot 5\text{H}_2\text{O}$, and Boric acid $\text{B}(\text{HO})_3$ - 35 g/l and has a pH = 2.5...3. All chemicals were p.a. grade with the balance of the solution being distilled water. The depositions were carried at temperature of solution $T = 40^\circ\text{C}$. We deposited our films using cathode potential of - 1.320 V versus SCE.

3. RESULTS AND DISCUSSION

The structure of magnetoresistive films has been determined by X-ray diffraction. In Fig. 1, it is presented o part of diffraction pattern for one of obtained samples.

From the binary alloys diagram, it is well known that the Cu and Co are almost insoluble one in another and they do not create solid solutions or stable alloys with a stabile crystalline grate because in normal state Cu has a cubic face centered grate and Co has hexagonal compact grate. Cien et al. presented the obtaining of some $\text{Co}_x\text{Cu}_{100-x}$ alloys by magnetron sputtering method with substrate cooled at liquid nitrogen temperature where Co is found as f.c.c. grate.

The diagram presented in Fig. 1 shows that in our electrochemical prepared film two phases have been revealed: copper (f.c.c.) with large crystallite size and cobalt (f.c.c.) with fine crystallite size. It is important that in studied structures prepared by electrodeposition, Co appears only in cubic grate and the attempts to find hexagonal Co failed.

In Fig.2, it is presented the Bragg (220) peaks obtained for the same sample with a doubled exposition time and the radiation intensity increased. From profile, the height and the width of the diffraction peaks were found that the concentration of the f.c.c. cobalt phase in the copper matrix is 64 % and the mean crystallite size of cubical cobalt grains is 22.5 nm. The nanometric size of the cobalt particles ensures the appearance of the negative magnetoresistive effects and warrants the development of giant magnetoresistance.

In Fig.3, it is shown a diffraction diagram for another sample. X-Ray diffraction spectrum of as-prepared and anealed samples indicate two separate cubic phases in both cases. One of them is dominant structure Cu -reech (Co-loss 5 %) f.c.c. phase with the lattice constant of 3.612 Å and graine size in direction (220) of 35.5 nm for nonanealing samples and 38 nm for anealing samples. The loss increasing of the grain size due to the anealing were observed, but there are no major modifications of the structure due to the termic treatment were produced. Second phase is minore and could not been identifiacted but probably of all is Co- composite. Its intensity increase with the anealing which attest the Co-origin of them. In this case, the Co concentration is lower than the sensibility threshold of X-ray diffraction method (at about 5 % and from this reason the concentration is determined by XRF X-ray fluorescence. The fluorescence measurements show the presence of Co in alloy in the following concentration $\text{Cu}_{96}\text{Co}_4$ that is under the diffraction detection limit. For this sample the magnetoresistance measurements have been performed.

The electrical resistance was measured in Wan-der-Pauw geometry, using 4 contact points situated in quarter. Magnetoresistance is defined with expression:

$$MR^i = \frac{R_{VDP}^i(H) - R_{VDP}^i(H = 2T)}{R_{VDP}^i(H = 2T)} \cdot 100\% \quad (1)$$

Where index *i* characterizes geometry in which magnetoresistance is measured and can be *t* – transversal when the current is perpendicular on magnetic field. In this case, the current flows between contacts 1 and 4 and tension is measured between contacts 2 and 3. Thus, the transversal resistance Van-der-Pauw is:

$$R_{VDP}^t = \frac{U_{2,3}}{I_{1,4}}, \quad (2)$$

or, *l* – longitudinal – when the electric power is parallel with the field. In this case, the current flows between contacts 1 and 2 and tension is measured between contacts 3 and 4. So, the longitudinal resistance Van der-Pauw is:

$$R_{VDP}^l = \frac{U_{3,4}}{I_{1,2}}. \quad (3)$$

In both cases, the field is applied in film plane. When the field is orientated perpendicular to the film plane the perpendicular magnetoresistance was measured.

In Fig. 4 it is shown MR to a $\text{Cu}_{96}\text{Co}_4$ sample and measured at room's temperature. The curve a shows MR longitudinal and curve b presents the transversal one. It is easy to observe that both are negative and have values more than 2 % at 2 T field.

In Fig. 5 it is shown MR longitudinal, measured at room's temperature for the same $\text{Cu}_{96}\text{Co}_4$ test, after a thermal treatment during 15 minutes at 300 °C temperature in nitrogen atmosphere. By means of arrows it is shown the change direction (variation) of magnetic field: first, the field increasing up to 2 T value (possible maximum of the used electromagnet) and then the lowering till 300 G value (which represents the remnant magnetization of used magnet poles). One can observe that after thermal treatment, the MR value significantly decreased and reaches only 0.7 – 0.9 % values.

In Fig. 6 it is presented the transversal Van-der-Pauw electrical resistance dependence on the measured temperature for the same test, thermal treated, as in precedent figure. The cooling from the room's temperature till – 80 °C has been made in maximum external magnetic field presence $H = 2$ T and at the reaching of this temperature, the magnetic field has been uncoupled. An electrical resistance jump of 4.7 % in relative value, is observed. Then, at warming, the resistance function of temperature in magnetic field absence, has been measured. The distance between the two curves is due to magnetoresistance and it is obvious that the last one is negative and grows at the same time with temperature lowering.

This increasing of MR with the observed temperature coincide in this case with the obtained results by other authors for all kind of tests that demonstrate GMR (giant magnetoresistance).

The thermal treatment influence on magnetoresistance in Co-Cu alloys obtained by electrolytic deposition is similarly with those observed for Ag-Fe alloys obtained by spattering,⁹ that means that the thermal treatment conducts to magnetoreistance decreasing.

4. CONCLUSIONS

The electrochemical deposition method was used to prepare binary metallic granular sistems from single solution. The structure of the layers were investigated by X-ray diffraction. Two separate cubic phases was found. The structure of the probe not changes due to the annealing at the 300 °C. Magnetoresistance measurements for different field orientation show izotropic negative MR about 2 % at room temperature for nonannealing samples and decries MR to 0.7-0.9 % for annealing samples which probably is due to increasing of Co reeach phase. Increasing of negative magnetoresistance to 4.7 % was observed at decreasing temperature measurements (about –80 °C).

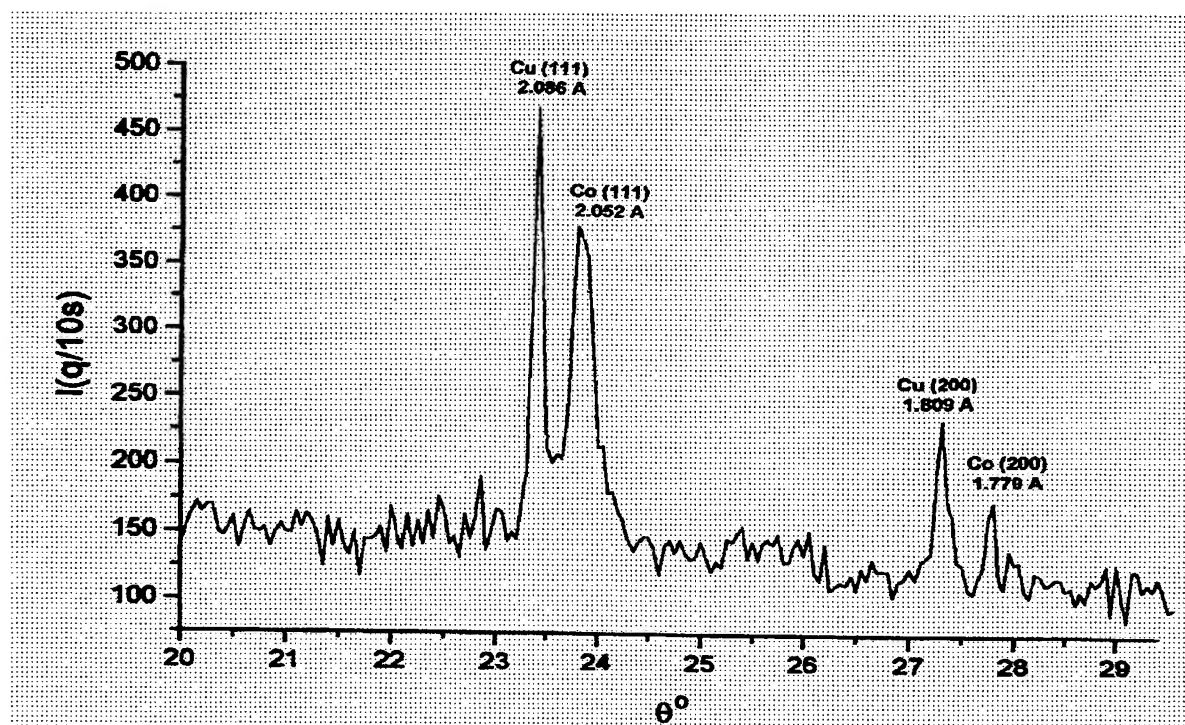


Fig. 1 The part of XRD pattern for $\text{Co}_{60}\text{Cu}_{40}$ electrodeposited sample

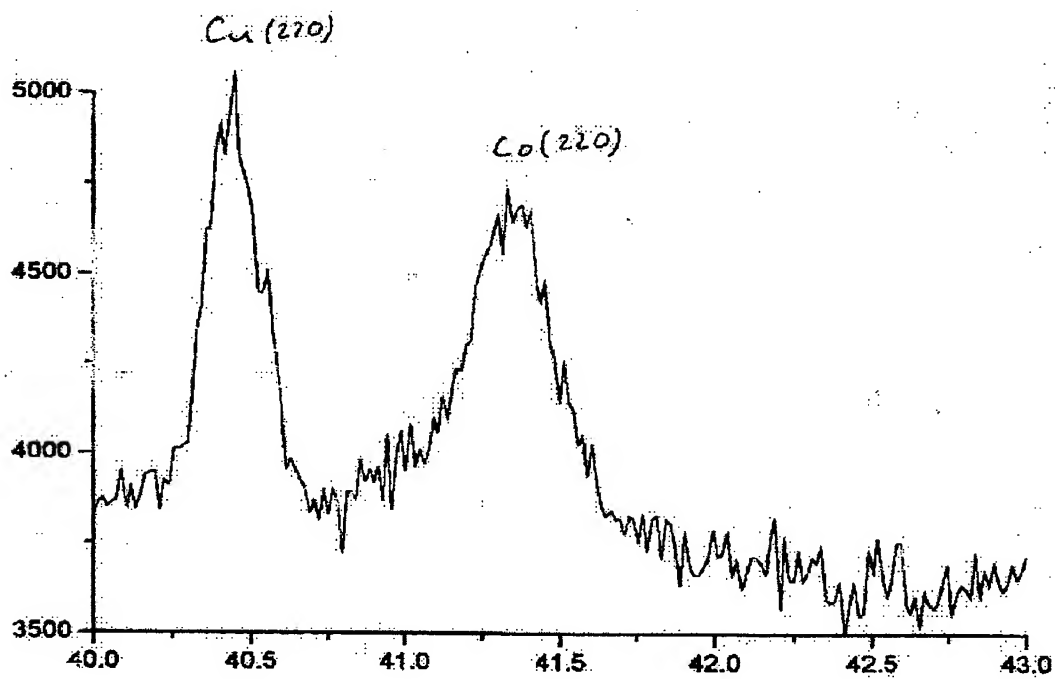


Fig. 2 Main peaks of XRD pattern for $\text{Co}_{60}\text{Cu}_{40}$ grain size determination

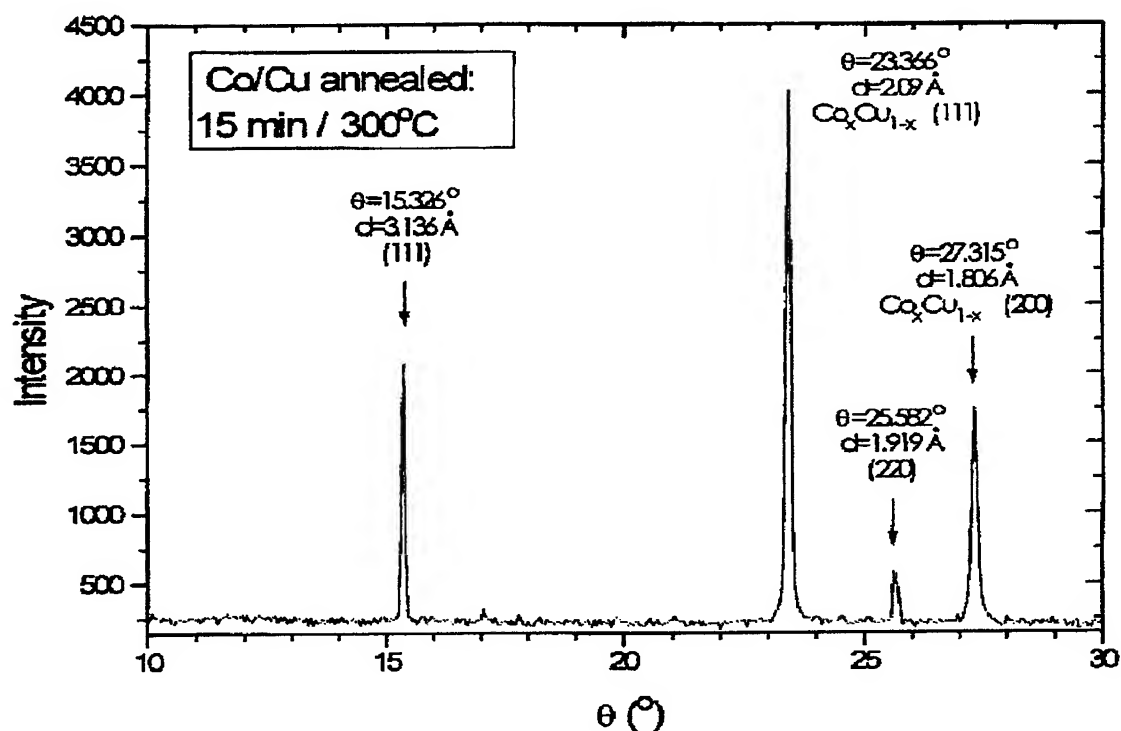


Fig. 3 XRD pattern for $\text{Cu}_{96}\text{Co}_4$ electrodeposited sample

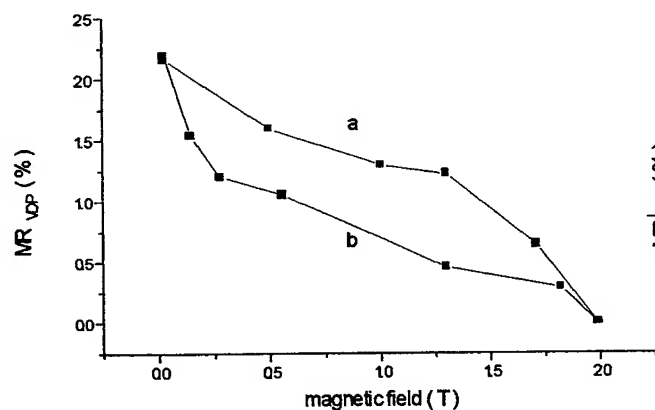


Fig. 4 MR of $\text{Cu}_{96}\text{Co}_4$ sample measured at room's temperature, a) longitudinal MR and b) transversal MR

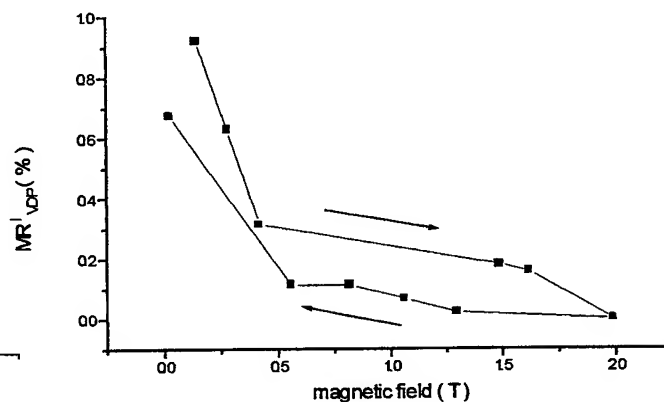


Fig. 5 The longitudinal magnetoresistance of $\text{Cu}_{96}\text{Co}_4$ electrodeposited film after, 15 min annealing at 300°C

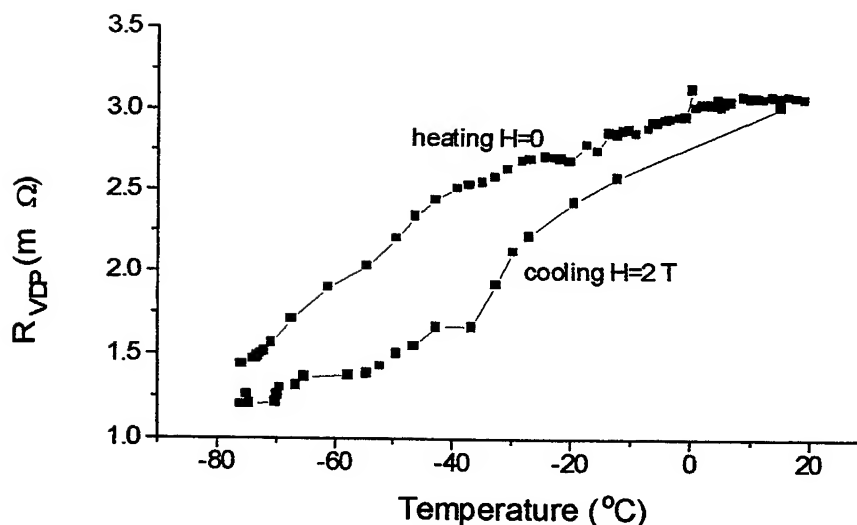


Fig. 6 Transversal Van-der-Pauw electrical resistance of the $\text{Cu}_{96}\text{Co}_4$ electrodeposited film as function of temperature

ACKNOWLEDGMENTS

We are thanking to Dr. I. H. Plonski for letting us to use her experimental equipment to prepare our samples, to Dr. M. Popescu for X-Ray diffraction structure investigations and to N. Marginean for X-Ray fluorescence measurements.

REFERENCES

1. M. N. Baibich, J. M. Broto, A. Fert, F. Nguyen Van Dau, F. Petroff, P. Eitenne, G. Creuzet, A. Friederich, and J. Chazelas, "Giant magnetoresistance of (001)Fe/(001)Cr magnetic superlattices", *Phys. Rev. Lett.* **61**, pp. 2472-2475, 1988.
2. S. S. P. Parkin, R. Bhandra, and K. P. Roche, "Oscillatory magnetic exchange coupling through thin copper layers", *Phys. Rev. Lett.* **66**, pp. 2152-2155, 1991.
3. J. A. C. Bland, and B. Heinrich, eds. "Ultrathin Magnetic Structures I and II," Springer, Berlin-Heidelberg, 1994.
4. M. Alper, K. Attenborough, V. Baryshev, R. Hart, D. S. Lashmore, and W. Schwarzacher, "Giant magnetoresistance in electrodeposited Co-Ni-Cu/Cu multilayers", *J. Appl. Phys.* **75**, pp. 6543-6545, 1994.
5. M. Alper, K. Attenborough, R. Hart, S. J. Lane, D. S. Lashmore, C. Younes and W. Schwarzacher, "Giant magnetoresistance in electrodeposited superlattices", *Appl. Phys. Lett.* **63**, pp. 2144-2146, 1993.
6. S. Z. Hua, D. S. Lashmore, L. Salamanca-Riba, W. Schwarzacher, L. J. Swartzendruber, R. D. McMichael, L. H. Bennet, and R. Hart, "Giant magnetoresistance peaks in CoNiCu/Cu multilayers grown by electrodeposition", *J. Appl. Phys.* **76**, pp. 6519-6521, 1994.
7. S. K. J. Lenczowski, C. Schönenberger, M.A.M. Gijs, and W.J.M. de Jonge, "Giant magnetoresistance of electrodeposited Co/Cu multilayers", *J. Magn. Mater.* **148**, pp. 455-465, 1995.
8. K. Attenborough, R. Hart, S. J. Lane, M. Alper, and W. Schwarzacher, "Magnetoresistance in electrodeposited Ni-Fe-Cu/Cu multilayers", *J. Magn. Mater.* **148**, pp. 335-336, 1995.
9. J.Q. Wang, G. Xiao, "Transition-metal granular solids: Microstructure, magnetic properties, and giant magnetoresistance", *Phys. Rev. B* **49**, pp. 3982-96, 1994.

Preparation and magnetotransport properties of Ni-Bi and Ni-Cu magnetic multilayers

Vladimir M. Hutanu^{*a}, Voicu Dolocan^b

^aInstitute of Optoelectronics IOEL-SA, Atomistilor str. Nr.111, PO BOX MG-22,
76900, Bucharest, Romania

^bUniversity of Bucharest, Faculty of Physics, PO BOX MG-11, 76900, Bucharest, Romania

ABSTRACT

We have investigated the magnetotransport properties of binary metallic systems formed by Ni-Bi and Cu-Ni multilayers. The samples were prepared by electrochemical deposition. Ni-Bi systems were obtained from two separate solutions and Cu-Ni systems from a single electrolyte. The films have been characterized using spectro-ellipsometry. Field dependence of the Hall resistivity and magnetoresistance for both the multilayer deposited structures were measured. Anisotropic magnetoresistance for Cu-Ni structures was found.

Keywords: Electrodeposition, thin films, multilayers, magnetoresistance, spectro-ellipsometry, Hall resistivity

1. INTRODUCTION

The magnetic granular structures with the nanometric size of ferromagnetic granules imbedded in nonmagnetic metal matrices are of a considerable interest due to their electrical and magnetic properties. As the short-period metal/metal superlattices these granular structures manifest some new phenomena that differ significantly from those of bulk materials.

One of these phenomena is the GMR (giant magnetoresistance)^{1,2} whose continue to be the subject of a large scientific effort both at a fundamental level and at the level of its technological applications to magnetic recording technology. For GMR to be observed a fair control over the deposition parameters is needed, since rough interfaces between subsequent layers can influence the effect. That is why most of the samples which exhibit large coupling strengths and high MR values have been prepared by sputtering, molecular beam epitaxy (MBE), or other vacuum based techniques.³ Recently, Alper et al.^{4,5} and Hua et al.⁶ have reported giant magnetoresistance in Co-Ni/Cu multilayers grown by electrodeposition in a single electrolyte. Lenczowski et al.⁷ report the GMR effect in Co/Cu electrodeposited multilayers and Attenborough et al.⁸ report this for Ni-Fe-Cu/Cu multilayers. Electrodeposition has some obvious advantages over trivial techniques, since the experimental apparatus required is considerably simpler (and cheaper) than those for techniques which require high or ultrahigh vacuum.

2. EXPERIMENTAL

The multilayer samples were grown by two methods of electrodeposition. Bi-Ni structures have been prepared from two separate electrolytic solutions, the first used for Bi deposition and the second for Ni deposition. Cu-Ni samples were grown from a single bath.

Electrodeposition of a metal takes place by reduction of its ions at the cathode of an electrochemical cell. Since different metals have different reduction potentials, it is possible to alter the composition of the alloy deposited from an electrolyte containing more than one ion species by altering the cathode potential. Hence, it is possible to electrodeposit a two-component metal/metal superlattice simply by switching between two cathode potentials and using coulometric control⁹.

All the depositions were carried with potentiostatic control in standard 3-electrodes geometry shown in Fig.1. A potentiostat (Taquselle model PR-20X) maintains the potential of the film substrate (the cathode) at the desired value

^{*} Correspondence: Email: vhutanu@mailcity.com

relative to the standard calomel saturated reference electrode by varying the potential between the film substrate and a platinum auxiliary electrode.

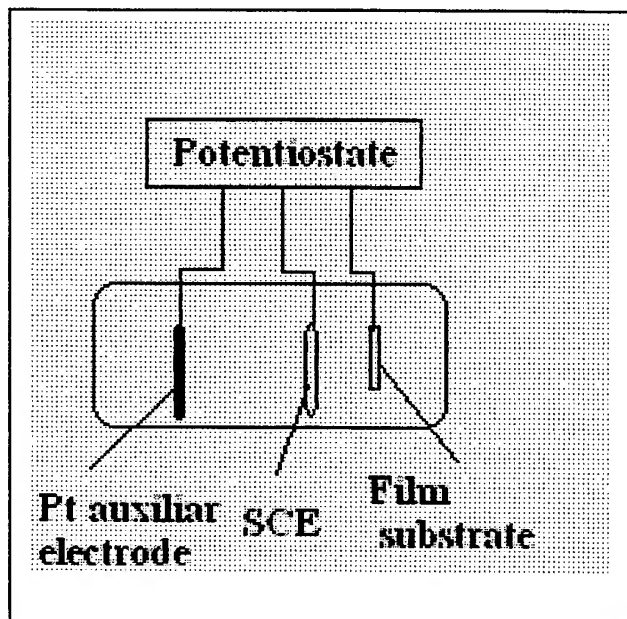


Fig. 1 Schematic diagram of electrolytic cell for multilayer samples preparation, SCE - saturated calomel reference electrode

Each sample was grown on one side of a Cu polycrystalline foil, 0.15 mm thick, that was polished first mechanically and then electrochemically using H_3PO_4 $d = 1.4$, and washed carefully before starting deposition. The other side of the Cu substrate including its boundaries is covered with a lacquer which plays a double role as an electrical insulator and an etch-resistant layer. The electrolyte solution for Bi deposition contains 40 g/l Bi_2O_3 , 104 g/l HClO_4 , 0.03 % glue, 0.08 % β -naftol and has a pH = 1.5. Ni deposition electrolyte solution contains Nickel sulfate $\text{NiSO}_4 \cdot 7\text{H}_2\text{O}$ - 150 g/l, Boric acid $\text{B}(\text{HO})_3$ - 10 g/l and has a pH = 5.5. For Cu-Ni probe the composition of electrolyte was 31 g/l Ni as metal (Ni-sulfate), 2 g/l Cu as metal (Copper-sulfate), 30 g/l Boric acid and 0.1g/l thiourea, pH = 3. All chemicals were p.a. grade with the balance of the solution being distilled water. All the depositions were carried at room temperature.

We deposited our films using cathode potentials of - 0.292 V for Bi, - 1.320 V for Ni in a single solution and - 0.48 V for Cu, - 1.365 V for Ni from the double solution, measured relative to a saturated calomel electrode (SCE). When the cathode potential is - 0.48 V versus SCE we expect that only Cu (the more noble of metals present in the electrolyte) will be deposited, while when the cathode potential is -1.360 V versus SCE, Ni and Cu will be deposited with rates governed by the kinetics of the deposition process and concentrations rates in solution. The electrolyte for Cu-Ni samples has been agitated during the deposition using magnetic agitators.

The thickness of the deposited films depends direct on the length of the time impulse which is controlled by a time adjustable relay (TR). This TR permits to adjust different deposition times for each substance deposition. For example the Cu time deposition is more than ten times longer than the Ni time deposition for equal thick layers.

After growth, the films with their Cu-substrates were mounted on glass using cianoacrilate glue, and Cu substrates were chemically dissolved first using an azotic acid solution and finishing with an ammoniac solution, because otherwise the highly conducting Cu substrate would have the superlattice short circuited during transport measurements.

3. RESULTS AND DISCUSSION

In order to calculate the real thickness of each layer from the measurement of the passed charge during electrodeposition, it is necessary to know the effective current efficiency. This was defined by us as the ratio of the real thickness of an electrodeposited film to its nominal thickness (the thickness calculated assuming bulk densities and 100 % current efficiency). The weighting of the thick layers prepared from the same solution and in the same conditions shows a high current efficiency. In this experiment, the effective current efficiency for Cu deposition was assumed to be 100 % because we do not expect significant hydrogen release at the Cu deposition potential. On the other hand, to compare the real thickness of deposited Bi and Ni layers with the nominal values computed from the Faraday law, spectro-ellipsometry was used. Table 1 displays the results of this comparison. The samples for spectroellipsometry were prepared on two types of

substrates using the same electrolyte. An ITO (InSnO_2) layer of 2000 Å dc sputtered on glass was used as a substrate for electrodeposition because due to its low conductance the necessity of dissolving the substrate vanishes and because of its perfect optical surface favorable for ellipsometry. The second type of substrate used is a Cu vacuum evaporated 9800 Å thick on glass. Results presented in Table 1 show a 90 % current efficiency for Ni deposition but a very low efficiency of about 40 % for Bi deposition. This is due to the growth mechanism of Bi layer. For example we could not obtain the compact Bi layer on the ITO substrate from this electrolyte solution

Tab. 1 Results obtained from comparison between the real layer thickness ellipsometric measured and the nominal ones computed from the Faraday law

Sample	Substrate	Real thick ellipsometric measured, Å	Nominal thick calculated, Å	Current efficiency %
Ni 1	ITO	784	830	94.45
Ni 2	ITO	276	300	92
Ni 3	ITO	290	310	93.5
Ni 4	Cu	285 (without CuO) 213+67(CuO)	275	100
Ni 5	Cu	404 (without CuO) 310+128 (CuO)	450	90 97.3
Ni + Bi	Cu	303 + 880	290+2000	44
Bi + Ni	Cu	1020+ 340	3100+1080	33

For magnetotransport measurements such as Hall effect and magnetoresistance, samples having different geometry have been prepared. A five contacts geometry presented in Fig. 2, was used to measure both Hall resistivity and magnetoresistance on Bi-Ni samples. This permitted to adjust a zero tension at the zero magnetic field by introducing a potentiometer between the contacts 2 and 3 and to calculate the resistivity as a field function by measuring potential differences between contacts 2 and 3. Small indium contacts were used. For the Cu- Ni probe, transport measurements were carried out with point-like pressure contacts like in Fig. 3 (van der Pauw geometry) while the magnetic field, applied in the plane of the superlattice, was stepped in the range - 0.8 to 0.8 T (the maximum field achievable with our electromagnet). The resistance $R_{1,2,3,4}$ is defined as the potential difference $V_4 - V_3$ between contact 4 and contact 3 per unit current flowing from contact 1 to contact 2, while - $R_{2,3,4,1}$ is defined the same way. $R_{1,2,3,4}$ is predominantly a measure of the longitudinal magnetoresistance (current parallel to field) while $R_{2,3,4,1}$ is predominantly a measure of the transversal magnetoresistance (current perpendicular to field). Measurements of Hall resistivity ρ_{xy} were executed using the geometry presented Fig. 2. All measurements were carried out at room temperature. Fig. 4 a and b shows the Hall resistivity ρ_{xy} values for a Ni -Bi (30 nm/200 nm)x6 sample and a pure Bi sample (14 µm) deposited from same solution. The Hall resistivity of Ni-Bi sample is two order of magnitude larger than that of the pure Ni and is dominated by the value of the thick Bi layers Hall resistivity. Hence the field dependence is linearly and its value is close to Bi pure. Fig. 5 presents the Hall resistivity ρ_{xy} for a Cu-Ni (4 nm/ 8 nm)x51 sample. The value of ρ_{xy} is about one order of magnitude less than the value of pure Ni. The shape of the field dependence curves begin at 0.7 T to have another slope. The extraordinary Hall coefficient for ferromagnetic materials R_s is determined as:

$$R_s = a\rho + b\rho^2 \quad (1)$$

where ρ is resistivity, a and b represent the magnitudes of the skew-scattering and the side-jump components, respectively^{10,11}.

There is an obvious Ni layer influence on the magnetic properties of the whole structure and on the conduction electron scattering mechanism. At low magnetic fields ($B < 1 \text{ T}$)¹² the scattering in magnetic multilayered systems is accompanied by a large left-right asymmetry which is described in terms of side-jump and skew -scattering components. These are characteristic of the used sample and depend strongly on the layer thickness.

The magnetoresistance is defined as:

$$MR = \frac{R(H) - R(H = 0)}{R(H = 0)} \cdot 100\% \quad (2)$$

and was measured for Ni-Bi samples using the geometry presented in Fig. 2, with the magnetic field in the plane of and perpendicular to the sample. The perpendicular MR for each Ni-Bi sample was 0.4 % at $B = 0.63 \text{ T}$ and the parallel MR was 0.1 % at a same field. The values of magnetoresistance for Cu-Ni (4 nm/6 nm)x60 and (4 nm/8 nm)x51 were measured using the geometry presented in Fig. 3 (van der Pauw). The field dependence of van der Pauw magnetoresistance is shown in Fig. 6. The anisotropic MR is present: longitudinal VDP MR is positive (curve a) and transversal VDP MR is negative (curve b). The longitudinal MR do not achieve saturation at our field (0.8 T) and the transversal MR shows a maximum at a field around 0.7 T which dovetail with Hall resistivity slope change (Fig.5). This behaviors is a feature of ferromagnetic and is due to the presence of the Ni in structure.

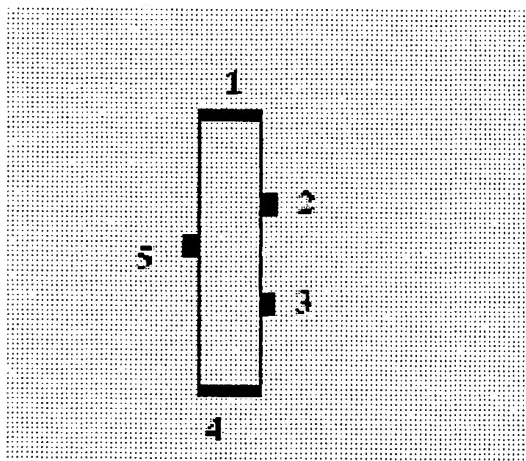


Fig. 2 The geometry of Bi-Ni multilayer samples

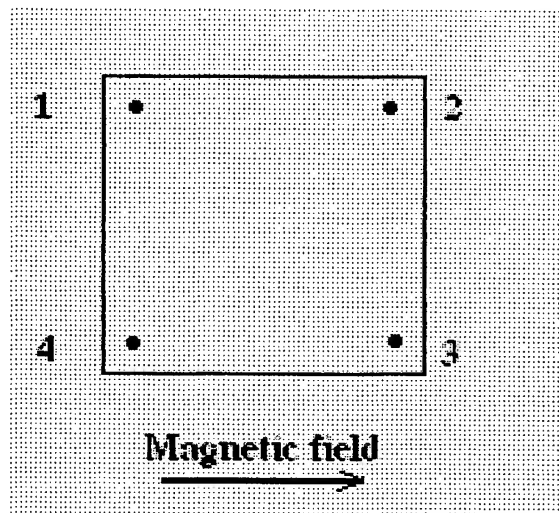


Fig. 3 Experimental geometry used for magnetoresistance measurements in Ni-Cu multilayers

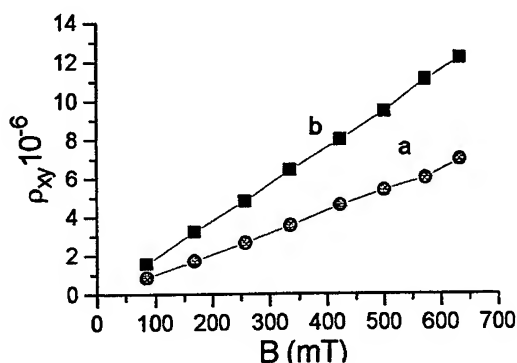


Fig. 4 The field dependence of the Hall resistivity for a) Bi-Ni multilayers and b) Bi pure (14 μ m) thickness film.

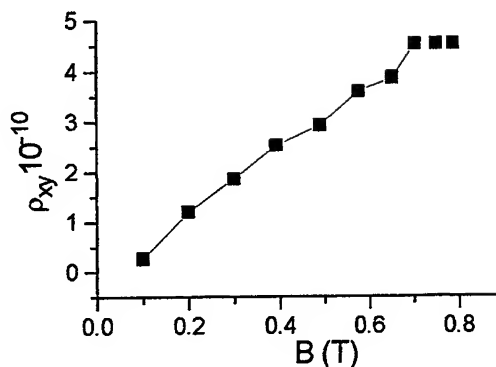


Fig. 5 The field dependence of the Hall resistivity for Cu-Ni (4 nm/8 nm) x51 sample

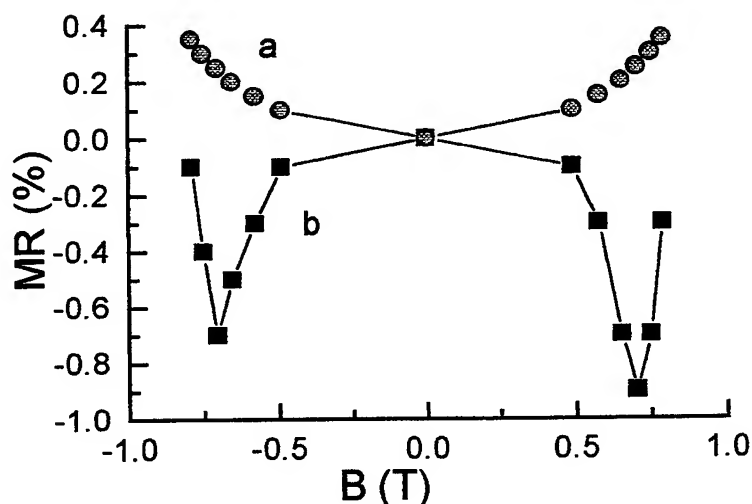


Fig. 6 Van der Pauw magnetoresistance curve for Cu-Ni (4 nm/8 nm) x51 sample: a) longitudinal MR; b) transversal MR

4. CONCLUSIONS

The electrochemical deposition method was used to prepare binary metallic multilayer systems. Two separate electrolytes were used to obtain Bi-Ni samples and single electrolyt bath method was used to prepare Ni-Cu samples. The thickness of the layers were investigated by spectro-ellipsometry which shows a good agreement with nominal (calculated) values for Ni deposition. The magnetotransport measurements such as Hall resistivity and magnetoresistance were carried for each sample. The Bi-Ni samples display behaviors close to pure Bi and Cu-Ni samples have the anisotropic magnetoresistance which is a feature of ferromagnetics.

ACKNOWLEDGMENTS

We are thanking to Dr. I. H. Plonski for letting us to use her experimental equipment to prepare our samples and Dr. M. Gartner for the spectroelipsometry measurements.

REFERENCES

1. M. N. Baibich, J. M. Broto, A. Fert, F. Nguyen Van Dau, F. Petroff, P. Eitenne, G. Creuzet, A. Friederich, and J. Chazelas, "Giant magnetoresistance of (001)Fe/(001)Cr magnetic superlattices", *Phys. Rev. Lett.* **61**, pp. 2472-2475, 1988.
2. S. S. P. Parkin, R. Bhandra, and K. P. Roche, "Oscillatory magnetic exchange coupling through thin copper layers", *Phys. Rev. Lett.* **66**, pp. 2152-2155, 1991.
3. J. A. C. Bland, and B. Heinrich, eds. "Ultrathin Magnetic Structures I and II," Springer, Berlin-Heidelberg, 1994.
4. M. Alper, K. Attenborough, V. Baryshev, R. Hart, D. S. Lashmore, and W. Schwarzacher, "Giant magnetoresistance in electrodeposited Co-Ni-Cu/Cu multilayers", *J. Appl. Phys.* **75**, pp. 6543-6545, 1994.
5. M. Alper, K. Attenborough, R. Hart, S. J. Lane, D. S. Lashmore, C. Younes and W. Schwarzacher, "Giant magnetoresistance in electrodeposited superlattices," *Appl. Phys. Lett.* **63** pp. 2144-2146, 1993.
6. S. Z. Hua, D. S. Lashmore, L. Salamanca-Riba, W. Schwarzacher, L. J. Swartzendruber, R. D. McMichael, L. H. Bennet, and R. Hart, "Giant magnetoresistance peaks in CoNiCu/Cu multilayers grown by electrodeposition," *J. Appl. Phys.* **76**, pp. 6519-6521, 1994.
7. S. K. J. Lenczowski, C. Schönenberger, M.A.M. Gijs, and W.J.M. de Jonge, "Giant magnetoresistance of electrodeposited Co/Cu multilayers," *J. Magn. Mater.* **148**, 455-465, 1995.
8. K. Attenborough, R. Hart, S. J. Lane, M. Alper, and W. Schwarzacher, "Magnetoresistance in electrodeposited Ni-Fe-Cu/Cu multilayers," *J. Magn. Mater.* **148** 335-336, 1995.
9. M. Alper, P. S. Alpin, K. Attenborough, D.J. Dingley, R. Hart, S. J. Lane, D. S. Lashmore, and W. Schwarzacher, "Growth and characterization of electrodeposited Cu/Cu-Ni-Co alloy superlattices," *J. Magn. Mater.* **126** pp. 8-11, 1993.
10. L. Berger, and G. Bergman, "The Hall Effect and Its Applications," eds. C. L. Chien, and C. R. Westgate, Plenum Press, New York, p.57, 1980.
11. C. M. Hurd, "The Hall Effect in Metals and Alloys," Plenum Press, New York, 1972.
12. Y. Aoki, H. Sato, Y. Kobayashi, K. Honda, T. Kumano, S. Hashimoto, T. Yokoyama, T. Hanyu, T. Kaneko, and R. Yamamoto, *J. Magn. Mater.* **126**, p. 448, 1993.

SESSION II

Lasers and Applications

Upconversion violet emission in diluted Er: YAG crystals

S. Georgescu^{*a}, V. Lupei^a, A. Petraru^a, C. Hapenciuc^a, C. Florea^b, C. Naud^c and C. Porte^c

^aInstitute of Atomic Physics, National Institute for Lasers, Plasma, and Radiation Physics, Bucharest, R-76900, P. O. Box MG-36, Romania

^bEcole Supérieure d'Ingénieurs en Electrotechnique et Electronique, BP 99, 2 bd Blaise Pascal, F-93162 Noisy-Le-Grand cedex, France

^cLaboratoire d'Optique des Solides, UMR 7601, Université Paris VI, Pierre et Marie Curie, 4 Place Jussieu, F-75252 Paris cedex 05, France

ABSTRACT

In this paper we discuss the upconversion processes responsible for violet luminescence (in the domain $0.39 \div 0.42 \mu\text{m}$) from the Erbium levels $^2P_{3/2}$ (transition $^2P_{3/2} \rightarrow ^4I_{13/2}$) and $^2H_{9/2}$ ($^2H_{9/2} \rightarrow ^4I_{15/2}$) in diluted Er: YAG crystals, excited with pulsed (532 nm) as well with cw (at 488 nm and 784 nm) lasers. Besides the general need for new spectroscopic data concerning laser materials, the interest for this study is generated by the fact that energy levels of very different quantum efficiencies (~ 0.3 for $^2P_{3/2}$ and ~ 0.0004 for $^2H_{9/2}$) can produce, function of the pumping conditions, fluorescence spectra of comparable intensities or even with reversed intensity ratio. Thus, though for 532 nm pulse excitation (pump transition $^4I_{15/2} \rightarrow ^4S_{3/2}$, the intensity of the lines originating from $^2P_{3/2}$ is much stronger than the intensity of the lines starting from $^2H_{9/2}$, in accord with the corresponding quantum efficiencies, for cw pumping, the excitation at 488 nm (pump transition $^4I_{15/2} \rightarrow ^4F_{7/2}$) produces luminescence spectra of comparable intensities, while for 784 nm ($^4I_{15/2} \rightarrow ^4I_{9/2}$) pumping, the lines originating from $^2H_{9/2}$ level are more intense. Various two- or three-step upconversion mechanisms (ESA at low Erbium concentrations) were proposed to explain the observed luminescence spectra. We found that a rather good description of the intensity ratio of the luminescence spectra, obtained in various experimental conditions, could be obtained in the frame of the Judd-Ofelt model, if a quantitative analysis of the resonance of the ESA transitions with the pumping quanta is performed.

Keywords: Upconversion, Er^{3+} , YAG.

1. INTRODUCTION

The energy level schema of Er^{3+} with many energetic resonances and with important absorption bands in the emission domain of the laser diodes, recommend the Erbium doped crystals as very convenient systems for upconversion lasers. The green luminescence (transition $^4S_{3/2} \rightarrow ^4I_{15/2}$), excited in infrared by upconversion, was extensively studied, due to the possibility of efficient generation at room temperature¹⁻¹². Nevertheless, relatively few papers were devoted to the study of upconversion excited luminescence of the higher Erbium levels¹³⁻¹⁷, though visible laser emission at low temperature from the high energy levels such as $^2P_{3/2}$ and $^2H_{9/2}$, in low phonons crystals, was obtained. Thus, in¹³ blue (on the transition $^2P_{3/2} \rightarrow ^4I_{11/2}$ at 469.7 nm) and green (on the transition $^2H_{9/2} \rightarrow ^4I_{13/2}$ at 560 nm) laser emission in YLiF_4 were reported. Red generation on the transition $^2H_{9/2} \rightarrow ^4I_{11/2}$ (703.7 nm) was also obtained¹⁴. Surprisingly, no paper (in our knowledge) was dedicated to the systematic study of the upconversion luminescence of the $^2P_{3/2}$ level, though the large energy gap ($\sim 3000 \text{ cm}^{-1}$) between this level and $^2G_{7/2}$ assures, even in oxides, a quite large quantum efficiency.

Function of the dopant concentration and pumping characteristics (pumping wavelength, pulsed or cw excitation), various schemes for population of the Erbium levels could be realized. At low dopant concentrations, excited state absorption (ESA) is the main upconversion mechanism, while for higher concentrations cooperative upconversion becomes very active.

For low concentration crystals and short pumping pulses, ESA can take place only from the energy levels which can reach a significant population during the pumping pulse, regardless their lifetime. On the contrary, for cw pumping, when the level populations are practically proportional with their lifetimes, ESA from the long-lived levels could be dominant. For both situations the first and the second (or higher) steps must be resonant (or quasi-resonant) with the pumping quanta. For

E-mail: joe@pluto.infim.ro

higher dopant concentrations, once a metastable level is populated, a cooperative upconversion process could be fed from this population, regardless the pumping quanta.

In this paper we study the upconversion processes responsible for the violet luminescence (in the domain $0.39 \div 0.42 \mu\text{m}$) of the Erbium levels $^2P_{3/2}$ (transition $^2P_{3/2} \rightarrow ^4I_{13/2}$) and $^2H_{9/2}$ (transition $^2H_{9/2} \rightarrow ^4I_{15/2}$) in diluted Er: YAG crystals, excited with pulsed (at 532 nm) as well with cw (at 488 nm and 784 nm) lasers. A forthcoming paper will be dedicated to the higher concentrated Er: YAG crystals.

The fluorescent levels $^2P_{3/2}$ and $^2H_{9/2}$ in YAG are separated from the next lower ones by quite different energy gaps: 3314 cm^{-1} and, respectively, 1757 cm^{-1} (Ref. 18). Since the YAG crystals are characterized by high-energy phonons, very different multiphonon rates, and consequently, very different quantum efficiencies of these levels are expected. On the other hand, the efficiency of the various upconversion mechanisms could be also very different. Such a situation is encountered for the upconversion violet spectra of Erbium in YAG (corresponding to $^2P_{3/2} \rightarrow ^4I_{13/2}$ and $^2H_{9/2} \rightarrow ^4I_{15/2}$ transitions). The aim of this paper is to find out the upconversion mechanisms responsible for violet emission of $^2P_{3/2}$ and $^2H_{9/2}$ levels and, by analyzing the energetic resonance degree between the involved ESA processes and the pumping quanta, to try a quantitative explanation for the observed intensity ratio of luminescence associated with the two transitions, in various pumping conditions.

In this paper, we use the Russell-Saunders limit for the spectroscopic notations. Therefore, some of our notations differ from the notations adopted in¹⁸.

2. EXPERIMENT

The experiments were performed at room temperature on low concentrated Er: YAG samples. The violet luminescence of Er: YAG was excited either with pulsed or cw lasers. The experimental set-up for pulse excitation consisted of a pump (~ 15 ns pulse duration) laser and a GDM 1000 monochromator equipped with an S-20 photomultiplier in photon counting configuration. The fluorescence spectra were obtained with a TURBO MCS scaler. The pulsed excitation was in green (532 nm) using the second harmonic of the Nd: YAG laser Quanta Ray DCR2. For cw pumping, the 488 nm emission line of a Coherent INNOVA 300 Argon laser or the 784 nm emission of a COHERENT Titan Sapphire laser Model 890 was selected and the luminescence was analyzed with an HRS2 Jobin Yvon monochromator, equipped with a cooled S-20 photomultiplier, and a picoammeter on line with a PC. Except for the Titan Sapphire excitation, were due to experimental reasons, the Erbium concentration in the YAG sample was 3 %, the measurements were performed on an Er (0.3 %): YAG sample. The third harmonic (355 nm) of the Nd: YAG pulsed laser was used to measure the fluorescent lifetime of the $^2H_{9/2}$ level.

3. THEORETICAL CONSIDERATIONS

The majority of the observed optical transitions in lanthanide ions are induced electric-dipole transitions. In 1962, independently, Judd¹⁹ and Ofelt²⁰ worked out the theoretical background for the calculation of the induced electric-dipole matrix elements. In the frame of the Judd-Ofelt (JO) model, the line strength for an electric-dipole $f \rightarrow f$ transition between the initial state $|\psi SLJ\rangle$ and the final state $|\psi' S'L'J'\rangle$ is given by

$$S^{ed}(|\psi SLJ\rangle, |\psi' S'L'J'\rangle) = e^2 \sum_{k=2,4,6} \Omega_k \left| \langle |\psi SLJ\rangle U^{(k)} || |\psi' S'L'J'\rangle \right|^2 \quad (1)$$

where Ω_k are the three JO parameters and $\left| \langle |\psi SLJ\rangle U^{(k)} || |\psi' S'L'J'\rangle \right|^2$ are the squares of the reduced matrix elements of the unitary operators $U^{(k)}$ ²¹, in intermediary coupling. The line strength for the magnetic-dipole is given by

$$S^{md}(|\psi SLJ\rangle, |\psi' S'L'J'\rangle) = \frac{e^2 \hbar^2}{4m^2 c^2} \left| \langle |\psi SLJ\rangle \hat{L} + 2\hat{S} || |\psi' S'L'J'\rangle \right|^2 \quad (2)$$

where e , \hbar , c have the usual signification and m is the electron rest mass. \hat{L} and \hat{S} are total orbital and spin angular momentum operators. The dominant terms for intermediary coupling are denoted usually by square parentheses in the definition of the initial and final states.

Denoting here by i and f the initial and final states, the relation between the absorption cross-section for the $i \rightarrow f$ transition, at the pump laser wavenumber E_i and the line strengths for the electric- and magnetic-dipole transition is²²

$$\sigma_{if}(E_i) = \frac{4\pi^2 \tilde{E}}{3c\hbar(2J+1)} \left[\frac{(n^2+2)^2}{9n} S_{if}^{ed} + n S_{if}^{md} \right] \mathfrak{A}(E_i) \quad (3)$$

The factors multiplying the electric- and magnetic-dipole line strengths in the square parenthesis in Eq. (3) are the crystal field corrections, expressed in terms of refractive index n ²³. $\mathfrak{A}(E_i)$ is the value of the overlap integral, calculated for the wavenumber E_i . In Eq. (3) \tilde{E} represents an average on the absorption spectrum. The overlap integral is given by

$$\mathfrak{A}(E_i) = \int f_i(E) \beta(E, T) f_f(E + E_i) dE \quad (4)$$

where $f_i(E)$ and $f_f(E)$ are the shape-functions for the initial and final states and $\beta(E, T)$ takes into account the thermal distribution in the initial state. Varying E_i , the expression (3) simulates the ESA spectrum, if the shape-functions $f_i(E)$ and $f_f(E)$ are known.

The pumping rate in stationary conditions, from the initial state i (0 for the ground state) to the final state f , for the GSA and ESA, in stationary transition are:

$$R_{0f}^{GSA} = \sigma_{0f}^{GSA} \phi, R_{0f}^{ESA} = \sigma_{0f}^{ESA} \phi \quad (5)$$

where σ_{0f}^{GSA} is the ground state absorption cross-section, σ_{0f}^{ESA} is the total ESA cross-section and ϕ is the laser photon flux incident on the crystal. Various sets of JO parameters are found in literature, which differ significantly one of another. In Table 1, we present seven sets of JO parameters used in this paper. The measured fluorescent lifetimes T_k as well as the

Table 1. JO parameters for Er: YAG. (The labels (a) – (g) will be preserved along this paper)

$\Omega_2 (10^{-20} \text{ cm}^2)$	$\Omega_4 (10^{-20} \text{ cm}^2)$	$\Omega_6 (10^{-20} \text{ cm}^2)$	JO set / reference
0.28	1.23	0.78	(a) / Ref. 24
0.19	1.68	0.62	(b) / Ref. 25
0.32	1.19	0.80	(c) / Ref. 26
0.40	0.65	0.75	(d) / Ref. 26
0.45	0.98	0.62	(e) / Ref. 27
1.07	1.61	1.14	(f) / Ref. 26
0.24	1.05	0.56	(g) / Ref. 28

calculated radiative lifetimes T_k^{rad} are shown in Table 2. The significance of the subscript k is given in the left side of the energy level scheme, given in Fig. 2.

4. RESULTS AND DISCUSSION

In the spectral domain spanning the luminescence associated ${}^2\text{H}_{29/2} \rightarrow {}^4\text{I}_{15/2}$ and ${}^2\text{P}_{3/2} \rightarrow {}^4\text{I}_{13/2}$ transitions, two other transitions, namely ${}^4\text{G}_{7/2} \rightarrow {}^4\text{I}_{11/2}$ and ${}^4\text{G}_{9/2} \rightarrow {}^4\text{I}_{9/2}$, could, in principle, give a contribution but, due to the very low quantum efficiency expected for the ${}^4\text{G}_{7/2}$ and ${}^4\text{G}_{9/2}$ levels in YAG (energy gaps of 545 and, respectively, 1425 cm^{-1}), the fluorescence lines corresponding to these transitions were not put clearly into evidence.

Table 2. Measured fluorescence lifetimes T_k and calculated radiative lifetimes T_k^{rad}

JO set →		(a)	(b)	©	(d)	(e)	(f)	(g)
Level	T_k (μs)	T_k^{rad} (μs)						
$^2P_{3/2}$	50	189	184	193	237	232	132	171
$^2H_{9/2}$	0.15	360	374	349	413	436	242	374
$^4S_{3/2}$	16	606	754	591	635	762	415	827
$^4F_{9/2}$	1.5	638	554	645	922	799	467	486
$^4I_{9/2}$	0.05	4635	3744	4727	7394	5809	3458	3188
$^4I_{11/2}$	100	7274	8792	7074	7509	9715	4934	9426
$^4I_{13/2}$	6400	6398	7030	6319	6770	7369	4957	7195

In Fig. 1 we present the room temperature fluorescence spectra in the $23750 \div 25250 \text{ cm}^{-1}$ domain of low concentrated Er: YAG samples, for various excitation conditions: pulse excitation at 532 nm (Fig. 1 a), pulsed excitation at 355 nm (Fig. 1 b), and cw excitation at 488 nm (Fig. 1 c) for an Er (0.3 %): YAG sample, as well as the fluorescence spectrum of an Er (3 %): YAG sample excited at 784 nm, cw (Fig. 1 d). As pointed before, in this spectral domain, the observed fluorescence lines belong to two transitions: $^2P_{3/2} \rightarrow ^4I_{13/2}$ (for $E > 24590 \text{ cm}^{-1}$) and $^2H_{9/2} \rightarrow ^4I_{15/2}$. Due to the weak luminescence for 784 nm excitation, we used a more concentrated sample (3 % instead 0.3 %) and the spectra were obtained with a lower resolution. We consider this concentration still to low to interfere significantly the cooperative upconversion mechanisms. Function of the pumping conditions the relative intensities of the two spectra change dramatically. Thus, for 532 nm pumping, the lines corresponding to the $^2P_{3/2} \rightarrow ^4I_{13/2}$ transition are much more intense than the lines belonging to $^2H_{9/2} \rightarrow ^4I_{15/2}$ transition, while for cw pumping at 488 nm the intensities of the two spectra are comparable. For pumping at 784 nm the transition $^2H_{9/2} \rightarrow ^4I_{15/2}$ gives more intense fluorescence lines.

Since, in the conditions of Figs. 1 a to d, the fluorescence wavelengths are shorter than the pumping ones, the levels $^2P_{3/2}$ and $^2H_{9/2}$ are populated by upconversion processes, except for the case of 355 nm pumping where the $^2H_{9/2}$ level is pumped directly (Fig. 1 b). In this case, the relative intensities of the two spectra can be changed, function of the pump intensity. The pulsed 355 nm excitation allows the direct measurement of the fluorescence lifetime of $^2H_{9/2}$.

Besides the lines associated with $^2H_{9/2} \rightarrow ^4I_{15/2}$ and $^2P_{3/2} \rightarrow ^4I_{13/2}$, in Figs. 1 a, b, another group of lines, marked with arrows, is observed. The possible origin of this group of lines will be discussed at the end of this Section.

The fluorescent levels $^2P_{3/2}$ and $^2H_{9/2}$ have very different quantum efficiencies. The quantum efficiencies $\eta(^2P_{3/2}) = T_7 / T_7^{rad}$ and $\eta(^2H_{9/2}) = T_6 / T_6^{rad}$, as well as the branching ratios β_{71} (transition $^2P_{3/2} \rightarrow ^4I_{13/2}$) and β_{60} (transition $^2H_{9/2} \rightarrow ^4I_{15/2}$), calculated for the seven JO sets, are given in Table 3. The fluorescent transitions are denoted by dashed arrows in Fig. 2.

At low Erbium concentration, only ESA processes can be taken into account. In the following, we will discuss separately the pulsed and the cw experiments.

4.1. Pulsed excitation

4.1.1. Pumping at 532 nm

For short pulse excitation only the pump level (or, for very strong multiphonon transitions, the nearest lower level) succeeds to accumulate a significant population during the laser pulse. For pumping at 532 nm, ESA from $^4S_{3/2}$ (and, possibly, from $^4F_{9/2}$) excites levels placed at higher energies than $^2P_{3/2}$ (Fig. 2). From these levels, via efficient multiphonon transitions, the excitation reaches $^2P_{3/2}$, building a population N_7 . A fraction of 21 to 37 % (as estimated function of the used JO set) from this population is spent in radiative transitions terminating on levels with lower energy than $^2H_{9/2}$, but (63 ÷ 79) % from

N_7 reaches $^2H_{9/2}$ by multiphonon relaxation. Therefore, we can estimate the ratio of the luminescence intensities of the two fluorescence spectra as:

$$\frac{I_f(^2H_{9/2})}{I_f(^2P_{3/2})} = \left[\frac{(a_{76} + w_{76}) / \left(w_{76} + \sum_{j=0}^6 a_{7j} \right)}{\eta(^2H_{9/2}) \beta_{60} N_7} \right] \frac{\eta(^2H_{9/2}) \beta_{60} N_7}{\eta(^2P_{3/2}) \beta_{71} N_7} \quad (6)$$

where a_{ij} and w_{ij} are, respectively, the radiative and multiphonon transition probabilities.

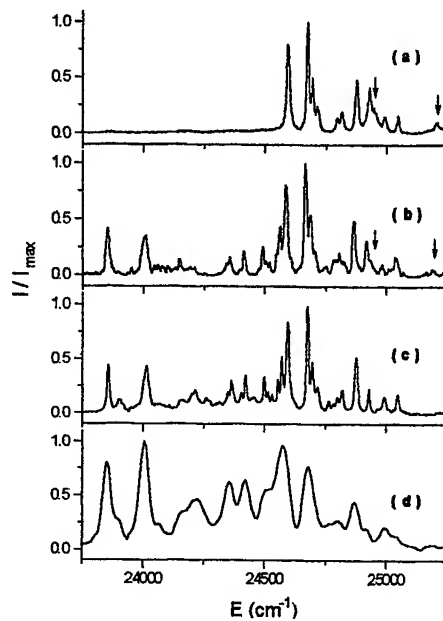


Figure 1. Fluorescence spectra corresponding to $^2P_{3/2} \rightarrow ^4I_{13/2}$ (for $E > 24590 \text{ cm}^{-1}$) and $^2H_{9/2} \rightarrow ^4I_{15/2}$ transitions for an Er (0.3 %): YAG sample (a - c) and for an Er (3 %): YAG sample (d), obtained in various excitation conditions: (a) 15 ns pulses at 532 nm, (b) 15 ns pulses at 355 nm, (c) 488 nm, cw, and (d) 784 nm, cw. Due to the experimental conditions, the spectrum (d) was obtained with a lower resolution.

The ratio of the luminescence intensities is very low, $(1.3 \div 1.6) \times 10^{-3}$ function of the JO set, thus explaining the very reduced intensity of the $^2H_{9/2} \rightarrow ^4I_{15/2}$ spectrum for pulse excitation in $^4S_{3/2}$, when the level $^2H_{9/2}$ is fed mainly via $^2P_{3/2}$.

Table 3. Quantum efficiencies and branching ratios involved in the luminescence of $^2P_{3/2}$ and $^2H_{9/2}$ levels.

JO set →	(a)	(b)	(c)	(d)	(e)	(f)	(g)
$\eta(^2P_{3/2})$	0.265	0.272	0.260	0.211	0.216	0.379	0.292
$\eta(^2H_{9/2})$	0.000417	0.000401	0.00043	0.000363	0.000344	0.00062	0.000401
β_{71}	0.384	0.297	0.390	0.462	0.373	0.391	0.249
β_{60}	0.464	0.417	0.466	0.485	0.447	0.450	0.402

4.1.2. Pumping at 355 nm

As we mentioned before, in this case, the level $^2H_{9/2}$ is pumped directly, while the level $^2P_{3/2}$ is pumped by a two-step ESA (Fig. 2). Nevertheless, due to the large difference in the quantum efficiencies, the intensities of the fluorescence spectra are still comparable (Fig. 1 c). We used 355 nm pumping to measure the lifetime of the $^2H_{9/2}$ level (Table 2).

4.2. CW excitation

4.2.1. Pumping at 488 nm

An inspection of the energy level scheme of Er^{3+} in YAG¹⁸ shows that for 488 nm pumping there are three resonant (or quasi-resonant) excited state absorption: (i) $^4\text{I}_{13/2} \rightarrow ^2\text{K}_{15/2}, ^4\text{G}_{9/2}$, (ii) $^4\text{S}_{3/2} \rightarrow ^4\text{D}_{5/2}, ^4\text{D}_{7/2}$ (Fig. 2), and (iii) $^4\text{I}_{9/2} \rightarrow ^2\text{K}_{13/2}, ^4\text{G}_{5/2}$. The transition (iii) can be eliminated from discussion due to the very low value of the stationary population of $^4\text{I}_{9/2}$ in YAG (the fluorescent lifetime of $^4\text{I}_{9/2}$ is 0.05 μs , compared with 6400 μs , the lifetime of $^4\text{I}_{13/2}$ - see Table 2).

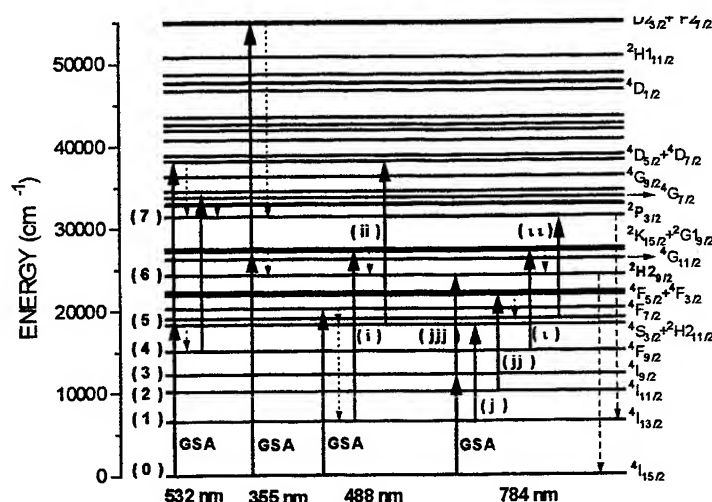


Figure 2. Energy level scheme of Er^{3+} in YAG and the main ESA processes (solid arrows) considered to explain the upconversion spectra from Fig. 1. The multiphonon transitions are represented by dotted lines while the fluorescence ones by dashed lines. The excitation wavelengths are indicated. GSA represents the ground state absorption while (i), (ii), (j), (jj), (i), and (u) are ESA transitions. The spectroscopic notations are in the Russell-Saunders limit.

For stationary pumping at 488 nm the GSA transition $^4\text{I}_{15/2} \rightarrow ^4\text{F}_{7/2}$ is followed by rapid multiphonon transitions to $^4\text{S}_{3/2}$. A rather good approximation for the rate equations describing the populations of the levels $^4\text{I}_{13/2}$ up to $^2\text{P}_{3/2}$ can be obtained if

we take into account the inequality $w_{i,i-1} \gg \sum_{j=0}^{i-1} a_{ij}$ (except for $w_{10} \ll a_{10}$) and that multiphonon transitions connect successive levels

$$\begin{aligned} (1 + \sigma_i^{ESA} T_1 \phi) \frac{N_1}{T_1} &= \frac{N_2}{T_2} = \frac{N_3}{T_3} = \frac{N_4}{T_4} = \frac{N_5}{T_5} \\ (1 + \sigma_{ii}^{ESA} T_5 \phi) \frac{N_5}{T_5} &= \frac{N_6}{T_6} + \sigma^{GSA} \phi N_0 \\ \frac{N_6}{T_6} &= \sigma_i^{ESA} \phi N_1 + \frac{N_7}{T_7} \\ \frac{N_7}{T_7} &= \sigma_{ii}^{ESA} \phi N_5 \end{aligned} \quad (7)$$

where σ_i^{ESA} is the cross-section for the ESA process (i), while σ_{ii}^{ESA} is related to the ESA transition (ii), and σ^{GSA} is the cross-section for the ground state absorption ($^4\text{I}_{15/2} \rightarrow ^4\text{F}_{7/2}$).

For low pump densities (i. e. when both $\sigma_i^{ESA} T_1 \phi$, $\sigma_{ii}^{ESA} T_5 \phi \ll 1$) a simple expression for the ratio of the luminescence intensities can be obtained:

$$\frac{I_{\beta}({}^2H_{29/2})}{I_{\beta}({}^2P_{3/2})} = \frac{N_6}{N_7} \frac{\eta({}^2H_{29/2})\beta_{60}}{\eta({}^2P_{3/2})\beta_{71}} \approx \frac{T_6(T_1x + T_5)}{T_5T_7} \frac{\eta({}^2H_{29/2})\beta_{60}}{\eta({}^2P_{3/2})\beta_{71}} \quad (8)$$

where $x = \sigma_i^{ESA} / \sigma_{ii}^{ESA}$ is the cross-section ratio. According to energy level scheme of Er^{3+} in YAG^{18} , the process (i) is close to resonance, but the process (ii) is not. This resonant / non-resonant relation must be reflected in the ratio of the ESA cross-sections x . From the experiment (Fig. 1 c) $I_{\beta}({}^2H_{29/2}) / I_{\beta}({}^2P_{3/2}) \approx 1$. Function of the selected JO set, the values of x varies from 380 (JO set (b)) up to 460 (JO set (d)). Taking into account the expression (3), this leads to a ratio of the overlap integrals $\mathfrak{I}_i / \mathfrak{I}_{ii}$ from 150 (JO set (g)) up to 280 (JO sets (d) and (f)).

Due to the lack of accurate and detailed experimental data regarding ESA transitions, especially for the spectral range far from the absorption peaks, in order to have an estimation of the ratio of the overlap integrals, we have used the simplest model for the shape functions entering Eq. (4), where both initial and final states are approximated by sums of Lorentzian functions of the same width w , centered on the Stark sublevels E_{ij} . The thermal distribution in the initial state is introduced as

$$f_i(E)\beta(E, T) = \sum_j \left[\frac{2w}{\pi} \frac{1}{w^2 + (E - E_{ij})^2} \frac{\exp\left(-\frac{E_{ij} - E_{i1}}{kT}\right)}{Z} \right] \quad (9)$$

with $Z = \sum_j \exp\left(-\frac{E_{ij} - E_{i1}}{kT}\right)$, where E_{i1} is the lowest Stark sublevel of the multiplet i . The discrete form of the thermal distribution in Eq. (9) is justified by a Lorentzian width $w \ll \Delta E_{k, k+1}$, where $\Delta E_{k, k+1}$ is the energy difference between two successive Stark sublevels. Recently, a simulation of an absorption spectrum using shape functions of adjustable width was performed in order to check the reliability of the JO model in trivalent rare earth ions doped glasses²⁹.

In this simplified model, the ratio $\mathfrak{I}_i / \mathfrak{I}_{ii}$ depends on only one parameter, w . Our calculations have shown that for $w = 1.5 \text{ cm}^{-1}$ the ratio $\mathfrak{I}_i / \mathfrak{I}_{ii} \approx 130$, close to the experimental value obtained with the JO set (g).

An analysis of the experimental GSA and fluorescence spectra shows that the observed spectral lines are close to Lorentzian and usual values for the experimental width w could be found in the interval $2.8 \div 7 \text{ cm}^{-1}$. Noting that the resulting spectral widths are sums of the initial and final widths, a value $w = 1.5 \text{ cm}^{-1}$, used to describe both initial and final states, could be a reasonable one.

For $w = 1.5 \text{ cm}^{-1}$ we calculate $\mathfrak{I}_i(488\text{nm}) = 1.3 \times 10^{-2}$ and $\mathfrak{I}_{ii}(488\text{nm}) = 1 \times 10^{-4}$. In this case, Eq. (3) gives for ESA cross-sections $\sigma_i^{ESA} = 3.3 \times 10^{-20} \text{ cm}^2$ and, respectively, $\sigma_{ii}^{ESA} = 2.6 \times 10^{-22} \text{ cm}^2$ (JO set (g)). With these values for the ESA cross-sections we can evaluate the low pumping flux condition, i. e. $\phi \ll 1 / (\sigma_i^{ESA} T_1) \approx 5 \times 10^{21} \text{ cm}^2 \text{ s}^{-1}$, which corresponds to approximately 20 W mm^{-2} . In our experiments the typical power of the Argon laser was 1 W with an irradiated area of $\sim 0.4 \div 0.5 \text{ W mm}^{-2}$, giving, thus, $2 \div 2.5 \text{ W mm}^{-2}$. It results that, in usual experimental conditions, Eq. (8) is valid.

4.2.2. Pumping at 784 nm

The pumping transition is ${}^4I_{15/2} \rightarrow {}^4I_{9/2}$ (Fig. 2). The Titan Sapphire laser was tuned to maximize both green ${}^4S_{3/2} \rightarrow {}^4I_{15/2}$ and violet ${}^2H_{29/2} \rightarrow {}^4I_{15/2}$ emission.

An inspection of the energy level scheme shows that the ${}^2P_{3/2}$ level can not be populated by two-step mechanisms but by the three-step process (GSA + (j and / or jj) + ν) (see Fig. 2 for notations). The level ${}^2H_{29/2}$ can be populated either by a two-step process (GSA + jjj) or by a three-step one (GSA + (j and / or jj) + ν). Due to the very low stationary population of the ${}^4I_{9/2}$ level in YAG, the reduced line strength for the ${}^4I_{9/2} \rightarrow {}^2H_{29/2}$ transition, and the off-resonance of this transition for the 784 nm pump quanta, the two-step upconversion mechanism can be neglected. This situation is in contrast with the case of low phonon crystals, such as chlorides¹⁵, where the level ${}^2H_{29/2}$ is populated by the two-step process GSA + jjj.

For low and moderate flux densities ($\sigma^{ESA} T \phi \ll 1$) the stationary values of the ${}^2H_{29/2}$ and ${}^2P_{3/2}$ levels are:

$$N_6 \approx \sigma_j^{GSA} \sigma_j^{ESA} T_1 T_6 (\sigma_i^{ESA} T_4 + \sigma_u^{ESA} T_5) N_0 \phi^3$$

$$N_7 \approx \sigma_j^{GSA} \sigma_j^{ESA} \sigma_u^{ESA} T_1 T_3 T_7 N_0 \phi^3 \quad (10)$$

and the ratio of the luminescence intensity of the fluorescent levels $^2H_{9/2}$ and $^2P_{3/2}$ is

$$\frac{I_f(^2H_{9/2})}{I_f(^2P_{3/2})} \approx \frac{\eta(^2H_{9/2})\beta_{60}}{\eta(^2P_{3/2})\beta_{71}} \frac{T_6(\sigma_i^{ESA}T_4 + \sigma_u^{ESA}T_5)}{T_5T_7\sigma_u^{ESA}} = \frac{\eta(^2H_{9/2})\beta_{60}}{\eta(^2P_{3/2})\beta_{71}} \frac{T_6(T_4\gamma + T_5)}{T_5T_7} \quad (11)$$

where $\gamma = \sigma_i^{ESA} / \sigma_u^{ESA}$. An inspection of Fig. 1 d shows that for 784 nm pumping $I_f(^2H_{9/2}) / I_f(^2P_{3/2}) \approx 2$. An analysis, similar to that performed for 488 nm pumping, gives, in this case, values for γ between 3.2×10^6 (JO set (g)) and 4.3×10^6 (JO set (d)). Again, making appeal to Eq. (3), it results a ratio of the overlap integrals $\mathfrak{I}_i / \mathfrak{I}_u$ between 1.8×10^5 (JO set (g)) and 6.7×10^5 (JO set (f)), two order of magnitude larger than for 488 nm pumping. We must note that, due to experimental reasons, (very weak violet fluorescence for infrared pumping) we used a more concentrated sample (3 % instead of 0.3 %). If, in a first approximation, we could still neglect the cooperative upconversion effects, the cross-relaxation processes, affecting the kinetics of the $^4S_{3/2}$ and $^2P_{3/2}$ levels must be taken into account. While the concentration quenching of the $^4S_{3/2}$ level was extensively studied³⁰, no data concerning the concentration quenching of $^2P_{3/2}$ was published. An inspection of the energy level scheme of Erbium in YAG shows that two cross-relaxation mechanisms could be taken into account: ($^2P_{3/2} \rightarrow ^4S_{3/2}$) + ($^4I_{15/2} \rightarrow ^4I_{9/2}$) and ($^2P_{3/2} \rightarrow ^2H_{9/2}$) + ($^4I_{15/2} \rightarrow ^4I_{13/2}$) (Fig. 3 a). We note that, due to relative reduced population of the $^2P_{3/2}$, in the low pumping limit, our calculations shows that the effect of both cross relaxation mechanisms, affecting the $^2P_{3/2}$, on the luminescence ratio, is the same.

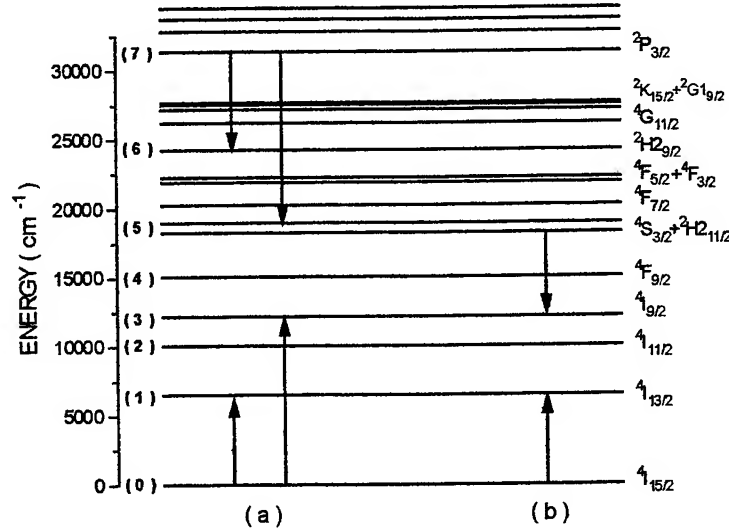


Figure 3. Cross-relaxation processes affecting the kinetics of $^2P_{3/2}$ (a) and $^4S_{3/2}$ (b) levels.

Only the concentration quenching of $^2P_{3/2}$ could affect the luminescence ratio. The concentration quenching of $^4S_{3/2}$ (Fig. 3 b) lowering the population N_5 (and, consequently, N_4), reduces equally the efficiency of both ESA processes (i) and (ii). By comparing the fluorescence kinetics of the $^2P_{3/2}$ level in the 0.3 % and in the 3 % sample, we estimated a reduction of the fluorescent lifetime 2.5 times. As a consequence, since the reduction of the fluorescent lifetime of $^2P_{3/2}$ results in a reduction of the quantum efficiency $\eta(^2P_{3/2})$, the increase of the Erbium concentration from 0.3 % to 3 %, reduces the value of γ , (and the ratio $\mathfrak{I}_i / \mathfrak{I}_u$), with a factor of $2.5^2 = 6.25$. Function of the selected set of JO parameters, the ratio $\mathfrak{I}_i / \mathfrak{I}_u$ varies now from 2.8×10^4 (JO sets (b) and (g)) up to 1×10^5 (JO set (f)). Using the same simplified model for the overlap integrals as for 488 nm pumping (Eq. 9)) and the same width of the Lorentzian functions ($w = 1.5 \text{ cm}^{-1}$), we obtain for the calculated value $\mathfrak{I}_i / \mathfrak{I}_u \approx 1.3 \times 10^4$, approximately half of the experimental value (corresponding to the JO sets (b) and (g)).

Despite the inherent approximations and simplifications, our model gives a rather good explanation of the experiment. The JO model is used three times: first, in the calculation of the line strengths entering the ESA cross-sections (3); second, in the estimation of the radiative lifetimes determining the quantum efficiencies, and third, in the branching ratios. In this case, the errors of the JO model could accumulate. Also, the large spread of the published JO sets²⁴⁻²⁸, concerning the Er: YAG crystal reflects the experimental difficulties in obtaining correct values for JO parameters. For example, replacing the JO set (f) with (b) or (g), the estimated $\mathfrak{S}_i / \mathfrak{S}_u$ ratio changes more than three times. Nevertheless, the most difficult task was to give a quantitative explanation of the "contrast" between the resonant and non-resonant ESA transitions, as estimated from luminescence experiments. We tried to answer this question assuming for the shape functions in the overlap integrals the simplest model: both initial and final states are expressed as sums of Lorentzian functions of the same width. Surprisingly, this one parameter (Lorentzian function width w) model succeeds to support the very large difference in the quantum efficiencies of the fluorescent levels $^2\text{H}_{29/2}$ and $^2\text{P}_{3/2}$, requiring a reasonable value $w = 1.5 \text{ cm}^{-1}$. The fluorescence lines marked with arrows in Fig. 1 a (pumping transition $^4\text{I}_{15/2} \rightarrow ^4\text{S}_{3/2}$) and in Fig. 2 b (pumping transition $^4\text{I}_{15/2} \rightarrow ^2\text{K}_{15/2}$, $^4\text{G}_{9/2}$ do not belong to $^2\text{P}_{3/2} \rightarrow ^4\text{I}_{13/2}$ transition. For pumping at 532 nm, our measurements have shown a cubic dependence of their fluorescence intensity function of the pumping intensity, suggesting a three-step excitation mechanism. The same lines show a quadratic dependence for 355 nm pumping. Therefore, the emitting level must be situated between 37594 cm^{-1} (two 532 nm quanta) and 56391 cm^{-1} (three 532 nm quanta or two 355 nm quanta). The measured fluorescence lifetime of these lines is 4 μs . Because the YAG crystal is characterized by strong phonons, a 4 μs lifetime requires energy gap of $\sim 2500 \text{ cm}^{-1}$. For comparison, the level $^4\text{S}_{3/2}$, characterized by a fluorescent lifetime of 16 μs , is separated from $^4\text{F}_{9/2}$ by a gap of 2876 cm^{-1} (Ref. 18), while $^4\text{F}_{9/2}$, separated from $^4\text{I}_{9/2}$ by a gap of 2529 cm^{-1} , has a lifetime of 1.5 μs . An energy gap of 2500 cm^{-1} , situated at energy higher than 37594 cm^{-1} , is not present in the energy level schema of Er^{3+} , measured in YAG in the transparency domain of the crystal¹⁸, but our simulations of the free ion energy levels suggests that such a gap could exist for energies higher than 45000 cm^{-1} . For example, using a simple model for the free ion (including only electrostatic, spin-orbit and configuration interactions), we found that large enough energy gaps could exist between $^4\text{D}_{3/2}$ and $^2\text{I}_{13/2}$ and between $^2\text{D}_{3/2} + ^2\text{F}_{7/2}$ and $^2\text{H}_{11/2}$ Fig. 2). The experimental work dedicated to the identification of the origin of 4 μs lines is in progress.

5. CONCLUSIONS

This study has shown that for upconversion luminescence, besides the quantum efficiency of the emitting levels, the excitation mechanisms themselves could have an essential influence on the emission intensity. As an example, we have chosen two luminescent levels of Er^{3+} in low concentrated YAG crystals, $^2\text{P}_{3/2}$ and $^2\text{H}_{29/2}$, whose quantum efficiencies differ with about three orders of magnitude. Despite of this, function of the pumping conditions, the luminescence generated by the level with low quantum efficiency could be more intense. The efficiency of the upconversion processes in low concentrated crystals depends on the quantum efficiency of the emitting levels, population of the intermediate metastable levels, energetic resonance with the pump quanta, and the probability of the ESA transitions. The Judd-Ofelt model was used in the estimation of the strength of ESA transitions, quantum efficiencies, and branching ratios. The most difficult problem was to give a quantitative estimation of the energetic resonance of an ESA process with pump quanta. Though very idealized, the description of both initial and final states with sums of Lorentzian functions of the same width, could furnish a basis for the interpretation of the experimental data. Taking into account the accumulated approximations of the Judd-Ofelt model, the spread of the available JO sets, the variety of the pumping conditions, and the complexity of the upconversion processes in high phonon crystals such as Er: YAG, we could consider that the proposed upconversion models are in rather good agreement with the experiment.

ACKNOWLEDGMENTS

This work was supported in part by the Research Grant No. 4093 / 1998 (B1) of the Romanian National Agency of Science, Technology, and Innovation. The authors express their gratitude to Prof. Bernard Clerjaud from the Laboratoire d'Optique des Solides of the University Paris VI "Pierre et Marie Curie" for the encouraging discussions and to Prof. Yves Quéré from Institut de France - Académie des Sciences. One of the authors (SG) thanks Dr. L. Anton from the N. I. L. P. R. P. Bucharest for very valuable discussions.

REFERENCES

1. W. Lenth, R. M. Macfarlane, A. J. Silversmith, International Laser Science Meeting, Atlantic City, NJ, Nov. 1987, in *Laser Focus / Electro-optics*, Dec. 1987, pp. 28.
2. F. Tong, W. P. Risk, R. M. Macfarlane, and W. Lenth, *Electronics Lett.*, **25**, 1389 (1989).

3. T. Hebert, R. M. Macfarlane, and W. Lenth, Proc. of the Internat. Conf. Lasers '90, pp. 386-393.
4. T. Hebert, R. Wannemacher, W. Lenth, and R. M. Macfarlane, *Appl. Phys. Lett.*, **57**, 1727 (1990).
5. P. Xie, S. C. Rand, *Optics Lett.*, **17**(17), 1198-1200 (1992).
6. R. Brede, T. Danger, E. Heumann, G. Huber, and B. Chai, *Appl. Phys. Lett.*, **63**, 729 (1993).
7. T. Danger, J. Koetke, R. Brede, E. Heumann, G. Huber, *J. Appl. Phys.*, **76**, 1413 (1994).
8. F. Heine, E. Heumann, T. Danger, T. Schweitzer, G. Huber, B. Chai, *Appl. Phys. Lett.*, **65**, 383 (1994).
9. M. Pollnau, E. Heumann, G. Huber, *J. Lumin.* **60/61**, 842 (1994).
10. F. Heine, E. Heumann, T. Danger, T. Schweizer, J. Koetke, G. Huber, and B. Chai, OSA Proceedings on Advanced Solid-State Lasers, Tso Yee Fan and Bruce H. T. Chai, eds (Optical Society of America, Washington, DC 1994), Vol. 20, pp. 344-347.
11. F. Heine, E. Heumann, T. Danger, T. Schweizer, J. Koetke, G. Huber, and B. Chai, in Conference on Lasers and Electro-Optics Europe Technical Digest, Amsterdam 1994, paper CMA6, pp. 3-4.
12. F. Heine, E. Heumann, P. Möbert, G. Huber, and B. H. T. Chai, in Advanced Solid-State Lasers, OSA Technical Digest (Optical Society of America, Washington, D. C., 1995), pp. 267-269.
13. T. Herbert, R. Wannemacher, W. Lenth, and R. M. Macfarlane, *Appl. Phys. Lett.*, **57**, 474 (1972).
14. L. F. Johnson and H. J. Guggenheim, *Appl. Phys. Lett.*, **20**, 1727 (1972).
15. T. Riedener, P. Egger, J. Hulliger, and H. U. Güdel, *Phys. Rev. B*, **56**, 1800 (1997).
16. Z. Hasan, L. Biyikli, M. J. Sellars, G. A. Khondaparast, F. S. Richardson, and J. R. Quagliano, *Phys. Rev. B*, **56**, 4518 (1997).
17. D. N. Patel, R. B. Reddy, and S. K. Nash-Stevenson, *Appl. Opt.*, **33**, 7805 (1998).
18. J. B. Gruber, J. R. Quagliano, M. F. Reid, F. S. Richardson, M. E. Hills, M. D. Seltzer, S. B. Stevens, C. A. Morrison, and T. H. Allik, *Phys. Rev. B*, **48**, 15561 (1993).
19. B. R. Judd, *Phys. Rev.*, **127**, 750 (1962).
20. G. S. Ofelt, *J. Chem. Phys.*, **37**, 511 (1962).
21. C. W. Nielson, G. F. Koster, *Spectroscopic coefficients for p^n , d^n , and f^n configurations*, M. I. T. Press, Cambridge, Mass., 1964.
22. D. L. Dexter, in Solid State Physics, eds. F. Seitz and D. Turnbull, Academic Press, 1958, p. 353.
23. C. Görller-Warland and K. Binnemans, in K. A. Gschneider, Jr., L. Eyring, (Eds.), *Handbook on the Physics and Chemistry of Rare Earths*, Vol. 25, ch. 167, North-Holland Publishing, Amsterdam, 1998, p. 101.
24. S. Georgescu, C. Ionescu, I. Voicu, and V. I. Zhekov, *Rev. Roum. Phys.*, **30**, 265 (1985).
25. Q. Wang, S. Y. Zhang, S. Wu, Y. Ren, and X. Dong, *Acta Opt. Sinica*, 307 (1986).
26. Q. Y. Wang, S. Y. Zhang, and Y. Q. Jia, *J. Alloys & Compounds*, **202**, 1 (1993).
27. A. A. Kaminskii, A. G. Petrosyan, G. A. Denisenko, T. I. Butaeva, V. A. Fedorov, S. E. Sarkisov, *Phys. Stat. Sol. A*, **71**, 291 (1982).
28. V. I. Zhekov, Ph. D. Dissertation, Institute of General Physics of the Academy of Sciences of the USSR, Moscow, 1977.
29. K. Binnemans, H. De Leebeek, C. Görller-Warland, and J. L. Adam, *Chem. Phys. Lett.*, **303**, 76 (1999).
30. A. Lupei, V. Lupei, S. Georgescu, I. Ursu, V. I. Zhekov, T. M. Murina, and A. M. Prokhorov, *Phys. Rev. B*, **41**, 10923 (1990).

Resonant photodetection with long wavelength double fused InGaAsP/AlGaAs vertical cavity lasers

V. Iakovlev*, A. Syrbu, C.-A. Berseth, A. Rudra, G. Suruceanu^a, E. Kapon

Department of Physics, Swiss Federal Institute of Technology Lausanne, CH-1015 Lausanne EPFL

^aOn leave from the Technical University of Moldova, Chisinau, Moldova

ABSTRACT

We have evaluated the resonant photodetection characteristics of long wavelength double fused InGaAsP/AlGaAs vertical cavity lasers. Using VCSEL structures fabricated by the localized fusion technique for laser generation, light detection is also possible in open circuit, short circuit and forward biased (FB) regimes. The wavelength selectivity of the detection increases with driving current in FB regime. Detection spectrum with FWHM as low as 0.02 nm is demonstrated in the FB regime at currents above threshold. Investigated structures emit and detect light with high spectral selectivity and may be very useful as multifunctional elements for signal generation and detection in wavelength division multiplexing (WDM) systems.

INTRODUCTION

With the advent of fiber optics components and systems, there is an increasing demand for high-performance photonic devices in modern optical communication networks. Nowadays, crystal-growth techniques provide researchers with the capability of producing epitaxial multilayer structures within exact specifications allowing realization of devices with vertical optical microcavities – vertical cavity surface emitting lasers (VCSELs) and resonant cavity enhanced (RCE) photodetectors. It is becoming of interest to investigate vertical cavity microresonators as multifunctional devices¹⁻⁴ as the main design criteria for emitters (LEDs and VCSELs) and RCE photodetectors are essentially the same. Recently, modified vertical cavity surface emitting lasers were demonstrated to function both as light sources and as avalanche photodetectors². Amplification of an external beam in a vertical-cavity surface emitting laser structure has been already demonstrated experimentally in the near infrared spectral region⁴. To the best of our knowledge, the first experimental realization of a multifunctional long wavelength ($\lambda=1.5\ \mu\text{m}$) InGaAsP MQW vertical cavity laser amplifier-photodetector was demonstrated in ref.3.

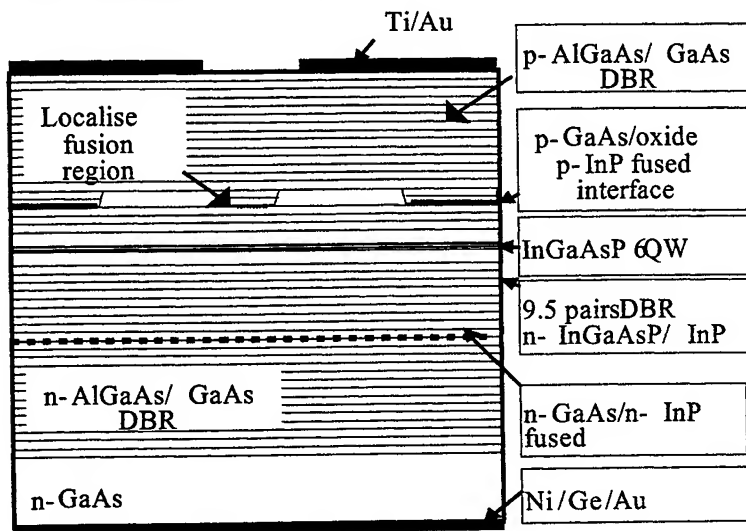
While in VCSELs the resonance is essential for device operation, in an emerging family of optoelectronic devices the performance is enhanced by placing the active device structure inside a Fabry-Perot resonant microcavity¹. The main benefit comes from the wavelength selectivity and a considerable enhancement of the resonant optical field intensity in the cavity. This enhanced optical field allows RCE photodetector structures to be thinner and therefore faster while simultaneously increasing the quantum efficiency at the resonant wavelengths. Off-resonance wavelengths are rejected by the cavity, which makes RCE photodetectors promising for low crosstalk WDM applications. 1530-1565 nm wavelength band is very well suited for fibre communication systems because of the availability of low loss optical fibers and high performance Er-doped amplifiers in this spectral region. So far, successful demonstrations of 1.5 μm vertical cavity surface emitting lasers (VCSELs) were based on structures having at least one AlGaAs/GaAs distributed Bragg reflector (DBR) fused to the InP-based cavity material⁵. To obtain lateral current confinement, the common approach consists in etching mesas on fused structures. In more recent devices, mesa etching is combined with lateral AlAs oxidation. In our alternative approach to the fused long wavelength InGaAsP/AlGaAs VCSELs fabrication⁶ lateral current confinement is obtained by localized fusion. There are several advantages of the localized fusion in VCSELs fabrication as compared with the common mesa etching, lateral oxidation or proton implantation: (i) the possibility of *in situ* built-in current and optical field confinement; (ii) lower series resistance for the same DBR parameters as compared with etched post or proton implanted VCSELs, (iii) easier testing and packaging due to larger area of contacts (as compared with etched posts); (iv) improved thermal properties due to the large dimensions of DBRs on both sides of the active layer.

Correspondence: Email: yakovlev@dpmail.epfl.ch

In this paper we will present the evaluation of the detection characteristics of these novel long wavelength double fused InGaAsP/AlGaAs vertical cavity lasers with a locally fused p-p junction. We will present some details on device design and fabrication. A short description of the experimental set-up for characterization of the VCSEL detection properties will be followed by presentation of the experimental results and discussion.

DESIGN AND FABRICATION

A schematic representation of our VCSEL structure is shown in Fig. 1. This device is assembled using a double fusion technique from three separately grown epitaxial structures, namely n- and p- AlGaAs/GaAs DBRs and InGaAsP/InP active cavity structure. We have used a 30 period p-AlGaAs/GaAs DBR with graded AlGaAs/GaAs interfaces for top mirror and a 35 period n-AlGaAs/GaAs DBR for the bottom mirror. Both n- and p-type GaAs- based epiwafers are grown by metal organic vapor phase epitaxy (MOCVD).



The InP-based active cavity structure is grown by Gas Source MBE and consists of a 9.5 period n-InGaAsP/InP DBR, 6 compressively strained InGaAsP quantum wells sandwiched between two InP spacers forming a 3/2 wavelength cavity, and a 1.5 period p-InGaAsP/InP DBR. The peak of the photoluminescence spectrum of as-grown InGaAsP/InP active structure was at 1550 nm in the wafer center.

Absorption values of 34 cm^{-1} and 7 cm^{-1} for the p and n GaAs/AlGaAs mirrors, respectively, were determined using high accuracy reflectivity measurements^{7,8}. Vertical resistance value of $2.5 \cdot 10^{-3} \Omega \cdot \text{cm}^2$ was measured for the p-mirror.

After structuring the surface of the top DBR wafer by selective chemical etching and fusing it to the InGaAsP/InP wafer we obtain locally

Fig. 1. Schematic representation of the VCSEL structure.

fused regions with an air gap between them. The size of the square-shaped mesa in the central part is $10 \times 10 \mu\text{m}^2$. At the periphery of this structure there is a native oxide layer at the fused interface, which serves to block the current flow.

After selectively etching the InP substrate, a 35 period n-AlGaAs/GaAs DBR is fused to the n-InGaAsP/InP DBR. After this second fusion, p-GaAs substrate is selectively etched, then Ti-Au p-contact on the exposed p-AlGaAs/GaAs DBR as well as Ni-Ge-Au n-contact on the n-GaAs substrate are deposited.

The fusion was carried out using a stainless pneumatic press in a nitrogen environment. This technique allows us to change the pressure during the heating cycle, which is very important in the case of localized fusion. Use of nitrogen instead of hydrogen is reducing considerably all the safety problems and does not seem to affect the quality of fusion. This technique allows us to obtain fused p-GaAs/p-InP structures with a low voltage drop across the junction⁹ and high crystallographic quality fused interfaces.

Cavity mode wavelength (1523.8nm) of the double fused structure (Fig.2) is clearly shorter than the peak reflectivity of the mirrors and is shifted by 30 nm from

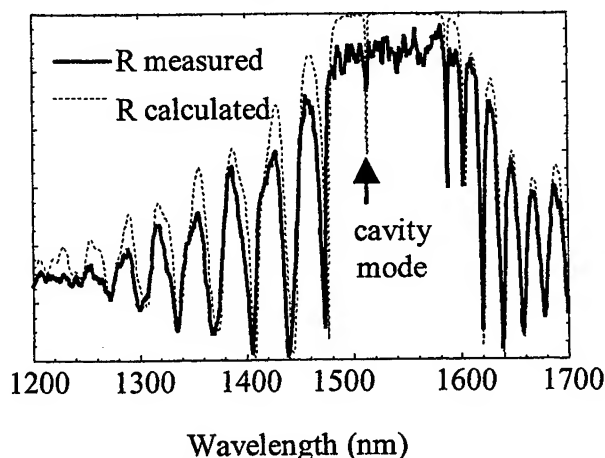


Fig. 2. Reflectivity spectrum in the vicinity of the fused mesa.

the PL peak of the active layer. This shift is the reason why these devices operate RT cw only up to 30 °C, as it was shown in ref.6. At the same time, this shift is beneficial for detection characteristics of the VCSEL structure because cavity mode wavelength is in the spectral range of high absorption of the cavity quantum wells. At room temperature, the VCSEL threshold currents are about 5 mA at 4 V. This relatively high value of the operating voltage is most probably due to nonoptimized doping at the fused p-p junction. Emitting power is in the range of 10 μ W at currents of 5-10 mA. This rather low output power level is caused by the absorption in the top p-AlGaAs/GaAs DBR. Spectral distribution of CW emission consists of a dominant mode with a side-mode suppression ratio of 30 dB. Emission is polarized along one of the [110] axes. The full width at half maximum (FWHM) is less than 0.1 nm, which is the highest resolution of our optical spectrum analyzer. Far field pattern of the VCSEL is circularly symmetric, with 5° FWHM value. Near field pattern below threshold current is nearly 10x10- μ m² in size and square shaped, indicating a good current confinement through the locally fused mesa. Above threshold current near field is almost circular with less than 5 μ m diameter. This is an indication that there is a current channeling mechanism through the central part of the fused mesa. This current funneling through the central part of the mesa leads to enhanced current density followed by lasing. We believe that the current funneling is most probably due to thermally induced switching mechanism at the fused p-p interface.

DETECTION CHARACTERISTICS

A schematic of experimental set-up for characterization of VCSEL detection properties is shown in Fig.3. A standard lock-in technique was used to detect the voltage variation ΔU on the device contacts (a and b in Fig.3) as a result of external illumination. VCSEL is fixed on a probe station and its temperature is stabilized with 0.05°C accuracy. For evaluation of detection characteristics a tunable laser diode with a linewidth of $8 \cdot 10^{-7}$ nm (100 kHz), tunability range 1470-1560 nm and output power of 0.1-1 mW is used. Most of the measurements reported in this paper are performed using 0.1 mW output power of this tunable laser. In order to estimate the response spectrum of the active layer, the cleaved VCSEL structure is measured in the same set-up by illuminating a cleaved facet of the device.

The spectral response of the active layer was found to be constant within 10% in the wavelength range of 1515-1530 nm, therefore we assumed it as constant in the interpretation of the detection spectra. Open circuit (OC) and short circuit (SC) regimes were investigated (with open or closed switchers S_1 and S_2 , respectively, Fig.3). To study the forward biased (FB) regime, S_1 should be open and S_2 -closed. As one can see from the data on Fig.4, measurements of the detection spectra give the value of the cavity mode. (Cavity mode wavelength can be of course determined from measurements of the emission spectra.)

In this experimental set-up we were able to determine the cavity mode wavelength of double fused structures with very low light emission efficiency, with which emission spectra were difficult to measure. We should note that emission spectra peaks always correspond to the wavelength value of the peaks in the detection spectra. This photocurrent spectroscopy of fused VCSEL structures can be used as a non-destructive on-wafer testing method in device fabrication in the same way it is used for short-wavelength VCSELs¹⁰. Full width at half magnitude (FWHM) of response spectra decreases with increasing direct current. FWHM becomes as small as 1 nm at 3mA (Fig. 4d.) and spectral position of the peak shifts to shorter wavelength values with increasing current.

Typically, spectral response on VCSEL structures from this batch is unstable and noisy at current values near threshold (3.5-4.5 mA). At currents well above threshold the spectral response to the external illumination is again stable and can be easily measured but the

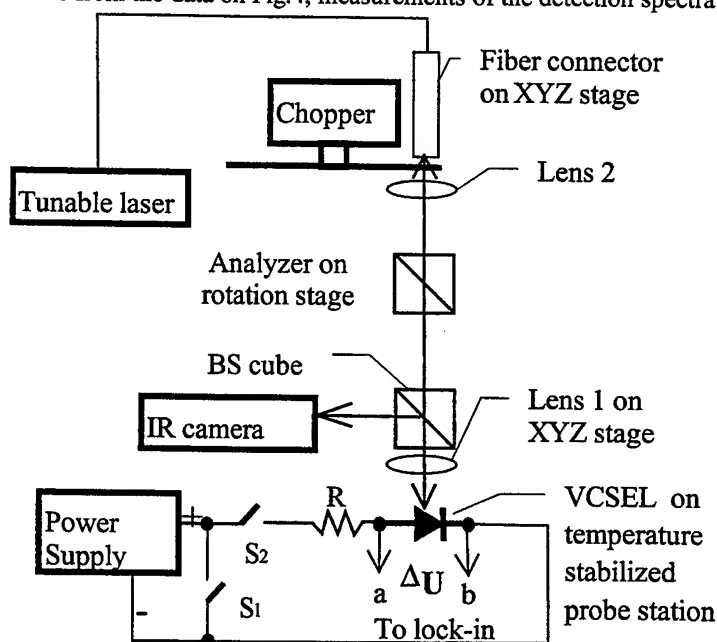


Fig.3. Schematic of the set-up used for detection characteristic measurements. Switchers S_1 and S_2 allow changing the electrical state of the VCSEL structure. For all spectral measurements the value of the resistor R is 1000 Ohms.

polarity is opposite to that at current below 3 mA. More precisely, in OC, SC and FB regimes, at currents below threshold, the voltage at the device contacts decreases, while at current values above lasing threshold the voltage at the VCSEL contacts increases under illumination. Cavity mode at 3 mA is blue-shifted as compared to cavity mode at 1 mA (Fig. 4,d) and with increasing current above 3 mA the cavity mode shifts to longer wavelengths due to self heating.

In Fig.5 we show a photosensitivity spectrum measured at a fixed wavelength of 1527.53 nm of the tunable laser and 1.2I_{th} driving current in the VCSEL structure. The cavity wavelength was tuned by increasing stage temperature with a 0.05°C step. Cavity mode shifts with temperature at a rate of 0.12 nm/°C. Photosensitivity spectrum has a FWHM value of 0.02 nm in this forward biased regime.

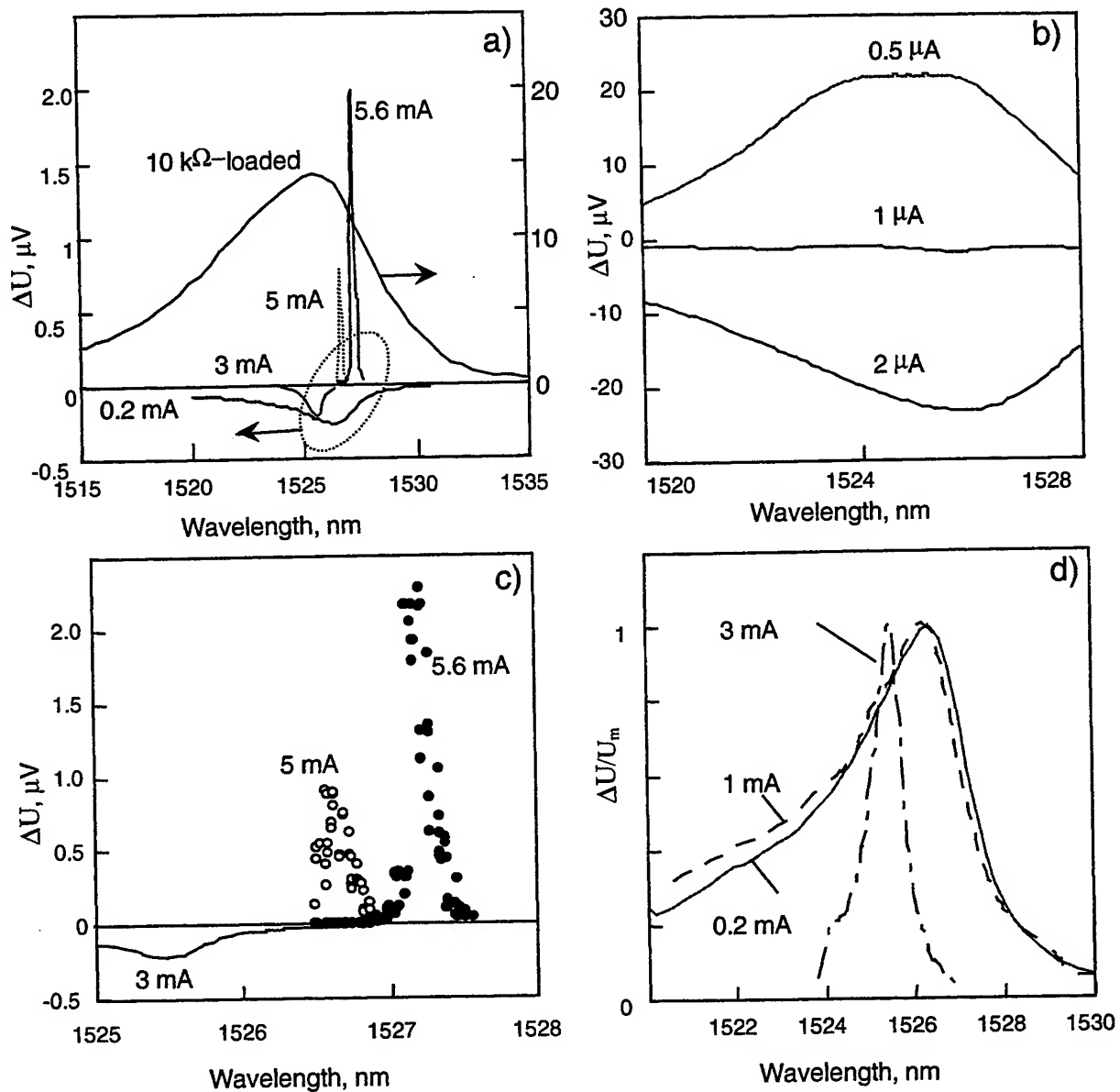
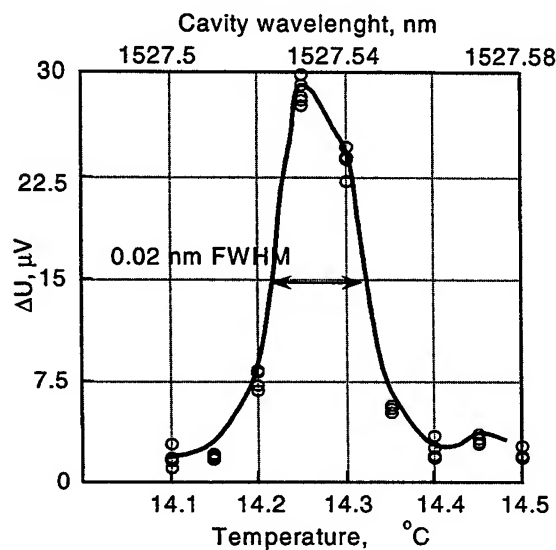


Fig. 4. Response spectra of the VCSEL structure. a) in short circuit (10 kΩ loaded) and forward biased regime at 4 current values. b) in forward biased regime at 3 μA-range current values. c) in forward biased regime at mA-range current values. d) normalized response spectra in 0.2-3 mA current range.

DISCUSSION

VCSEL structures represent in fact a microcavity optical filter. Moreover, this filter has an internal photo-detector p-n junction. For a Fabry-Perot cavity with "hard" mirrors, the FWHM of its transmission spectrum is related to the finesse F and cavity length L as: $\text{FWHM} = c/(2nLF)$, where c is the speed of light in vacuum and n is the effective refractive index of the cavity. Finesse increases with mirror reflectivity r as follows: $F = \pi^*(r)^{1/2}/(1-r)$. If there are absorbing layers in the cavity, the effective value of the reflectivity will be lower, hence FWHM will be higher. Finesse of microcavities with multi-quantum wells active structures sandwiched between multilayer semiconductor DBRs can be drastically improved



eFig. 5. Photosensitivity spectrum of the VCSEL measured at fixed 1527.53 nm wavelength of the tunable laser and 6 mA drive current in VCSEL.

when introducing gain in QWs. Calculation of the F and FWHM for such structures is no more possible to perform with a simple formula, but only numerically, using the transverse matrix method. We performed such calculations for the VCSEL structures experimentally investigated in this paper. It is obvious, that FWHM of the transmission spectra will decrease with the gain value in the InGaAsP QWs as a result of increased finesse of the microresonator. From the calculations we find out that this is a linear dependence: at 0 gain value in QW calculations give $\text{FWHM} = 0.45$ nm. At a gain value of 1500 cm^{-1} calculations give $\text{FWHM} = 0$, which is the threshold condition. The fact that the FWHM values of the spectra from Fig. 4d are 4 times higher than simulated ones may be due to the uncertainty in absorption values of the active layers after fusion, as well as the experimental errors in our set-up in which we used high numerical aperture (0.5) lenses. As one can see in Fig. 4d, the responsivity spectrum at 1 mA current is the convolution of two peaks. The FWHM of the long-wavelength peak is about 2 nm, whereas at 3 mA FWHM of full spectrum is 1 nm. Extrapolation to the 0 value of FWHM (threshold condition) gives a threshold current I_{th} of 5 mA which is in good agreement with the measured value.

The fact that VCSEL structures can be used to detect light even in the forward biased regime is quite easy to understand.

As long as the current density through the active layers is lower than lasing threshold, external light will be absorbed and the total number of the carriers in the cavity will increase. At the current densities above threshold, external light will induce recombination, hence carrier concentration will decrease. In both cases the modulation of the external light will modulate the voltage at VCSEL contacts which is easy to detect with lock-in technique.

The blue shift of the detection spectra (see Fig. 4a) is a result of cavity optical wavelength tuning with driving current. Cavity mode wavelength in vertical cavity microresonators depends on layer thickness and refractive index. As the refractive index value decreases with increasing carrier concentration and increases with increasing temperature, the blue shift in the forward biased regime means that carrier concentration in the cavity increases at lower current densities without significant heating. As carrier concentration is clamped at current densities above the threshold value, self-heating of the cavity will shift the cavity mode to longer wavelengths. Assuming that the active layer refractive index decreases by 0.02 from its value at 10^{16} cm^{-3} , which is carrier concentration of the undoped cavity material, to that at $8 \cdot 10^{18} \text{ cm}^{-3}$ (under injection), the calculated cavity mode shift of 2.5 nm is obtained, which is in good agreement with the measured value of 2 nm.

SUMMARY

The long wavelength double fused InGaAsP/AlGaAs vertical cavity laser structures investigated here emit and detect light with a high spectral selectivity and may be very useful as multifunctional elements for signal generation and detection in WDM systems. VCSEL structures fabricated by localized fusion can detect light in open circuit, short circuit and forward

biased (FB) regimes. The wavelength selectivity of the detection increases with increasing driving current in FB regime. Detection spectra with FWHM as low as 0.02 nm were demonstrated in FB regime at current value above threshold. Wavelength tuning of the VCSEL structure as a detector with driving current was observed. A 2 nm blue shift of cavity mode at low current level was measured and is a result of cavity fill-up with carriers. At higher current densities, close to threshold and above it, cavity mode red shifts due to self-heating. Photocurrent spectroscopy of fused VCSEL structures can be used as a non-destructive on-wafer testing method in device fabrication.

ACKNOWLEDGEMENT

This work is part of the European ACTS VERTICAL project, and is supported by the *Office Fédéral pour l'Education et la Science* of the Swiss Government.

REFERENCES

1. M. Selim Ünlü and Samuel Strite. "Resonant cavity enhanced photonic devices", *Journal of Appl. Phys.*, **78** (2), pp. 607-39, (1995)
2. M Dragas; I.H. White, R.V. Penty, P.J Heard, G. Parry, "Dual Purpose Vertical Cavity Surface Emitting Lasers for Datacommunications Applications". Conference Digest. ISLC 1998 NARA. pp. 107-8. (1998).
3. R. Lewen, K. Streubel, A. Karlsson, S. Rapp. "Experimental demonstration of a multifunctional long-wavelength vertical-cavity laser amplifier-detector". *IEEE-Photon. Technol. Lett.*, **10**, (8), pp.1067-9, (1998)
4. D. Wiedenmann, B. Moeller, R. Michalzik, K.J. Ebeling. "Performance characteristics of vertical-cavity semiconductor laser amplifiers". *Electron. Lett.*, **32**, (4), pp. 342-3, (1996).
5. K. Streubel, M. Hammar, F. Salomonsson, J. Bentell, S. Mogg, S. Rapp, J. Jacquet, J. Boucard, C. Starck, A. Plais, F. Gaborit, E. Derouin, N. Bouché, A. Rudra, A.V. Syrbu, V.P. Iakovlev, C.-A. Berseth, O. Dehaese and E. Kapon, "Long wavelength vertical cavity lasers", Invited paper at Photonic West Conference, January 1999, Proceedings of the SPIE - The international Society for Optical Engineering Vol. 3625.
6. A.V. Syrbu et al., PHOTONICS-98, invited paper, New Delhi, India. Vol.1, pp. 127-133 (1998).
7. C.A. Berseth, A. Schoenberg, O. Dehaese, A. Rudra, , and E. Kapon, "Experimental Method for High Accuracy Reflectivity Spectrum Measurements", *Appl. Optics.*, **37**, pp.6671-6, (1998)
8. C.A. Berseth, A.V. Syrbu, V.P. Iakovlev, O. Dehaese, A. Rudra, E. Kapon. "Highly accurate measurement of reflectivity and optical absorption in distributed Bragg reflectors using wafer fused resonator" *Electron Lett.*, **34**, (18), pp. 1666-7, (1998).
9. L. Sagalowicz, A. Rudra, A. Syrbu, J. Behrend, F. Salomonsson, K. Streubel, M. Hammar, J. Bentell. "Structure of the wafer fused InP (100)-GaAs (100) interface". *Philosophical Magazine Letters*, **76**, pp. 445-52, (1997).
10. Laurent Georjon and Yann Boucher. "Photocurrent and electroluminescence in vertical-cavity surface-emitting lasers" *Journal of App. Phys.* **85**, pp. 3019-22, (1999)

High precision towers for support an optoelectronic detector

Brindus Comanescu^{a*}, Adelina Ighigeanu^a, Daniel Oancea^a, Mihai Petcu^a, Bogdan Tatulea^a
Gueorgui Chelkov^b, Dmitri Dedovich^b, Petr Evtoukhovitch^b, Alexi Gongadze^b, Serguei Podkladkin^b,
Edisher Tskhadadze^b

^aInstitute of Optoelectronics, 111 Atomistilor St, PO Box MG 22, Bucharest, Romania

^bJoint Institute for Nuclear Research, 141980 Dubna, Russia

ABSTRACT

This paper describes the construction of an high precision towers for support an optoelectronic detector during fabrication. For fabrication of an optoelectronic detector is necessary a special room with a special environment. After assembling the frame of detector must be in plane, in range of $\pm 10 \mu\text{m}$. In this condition, we are need special condition for measurement the mechanical pieces and the assemblies. Special construction of detector request that the towers must be very precise, mechanical assemblies that can be replaced very easy will compose them. With this restriction the towers are builds from three parts: inferior, intermediary and superior.

Keywords: high precision tower, precision tools for support

1. INTRODUCTION

Monitoring drift tube (MDT) chambers are main parts of Muon detector of Atlas-collaboration on LHC at CERN. For these chambers assembling special tools with high precision are necessary. The important parts of chamber assembling system are precision towers¹.

The scope of high precision tower during fabrication is to support the frame of future optoelectronic detector for obtain a precision of $\pm 10 \mu\text{m}$.

Technical condition of detector asks for the fabrication special condition of environment and technology. This is the reason for that the tower was design and tests very carefully. In this way we have a chamber with special condition of environment where we put all the tools on a precise granite table during the procedure of assembling (see on Fig. 1a, b, c, d). Scientifically and technical cooperation between Joint Institute of Nuclear Research - Dubna - Russia and Institute of Optoelectronics consist in design and manufacture this tower with very high precision.

1.1. Description

They are six high precision towers as is shown in Figs. 2a, b, c, d, e, f, three fixed on the end of cross plate and three positioned on the granite table (see on Fig. 1). On the reference side of the precision jig, the sphere block pairs constrain all three coordinates (XYZ), one or two coordinates (YZ or Y) and two coordinates (YZ), respectively. On the other side all three sphere block pairs constrain the Y coordinates only. This complies with the rigidity of the MDT chamber during fabrication: after the addition of a first layer of drift tubes the Z location of the middle cross plate can not be adjusted separately, which explain the change from a YZ constraint to a Y constraint for the corresponding sphere block pair.

The Y and Z positions of the precision blocks with respect to the granite table can be adjusted to generate the Y and Z offsets between the various drift tube layers. These offsets apply to all tubes in a layer and therefore deviations from the design values lead to a systematic shift of a complete layer. Therefore the absolute Y and Z location of all spheres will be monitored during chamber fabrication.

For design the components we used the modern technique of conception fabrication and tests.

* Correspondence: E-mail: brindus_comanescu@yahoo.com; Telephone: 00401.780.66.40; Fax: 00401.423.25.32

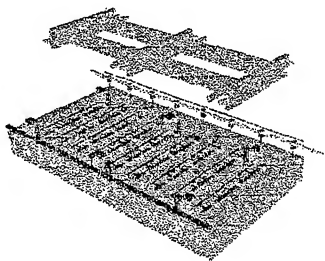


Fig. 1 a) View of all tools on the granite table



Fig. 1 b) Side blocks layer 1



Fig. 1 c) Side blocks layer 2

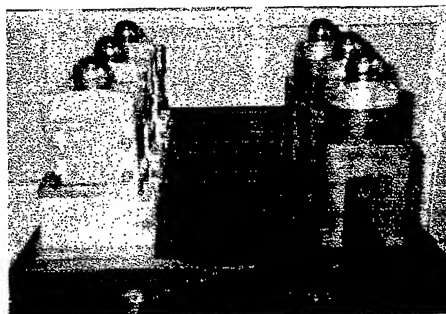


Fig. 1 d) Side blocks layer 3

2. CONSTRUCTION OF HIGH PRECISION TOWER

The optoelectronic detector is composed by a frame and two multilayers of Al tubes glued on the both side of the frame. Three layers of Al tubes compose each multilayer. Because the intermediary assembly gave the high to precision tower we use three different intermediary assembly, one assembly for each layer².

By a simply operation of screwing and unscrewing we can replace the intermediary assembly with another intermediary assembly and we modify very easy the high of the tower. After this operation the tolerances must remain in range $\pm 10 \mu\text{m}$ and we obtain three different type of high precision tower.

The high precision towers are composed by:

1. Inferior Assembly;
2. Intermediary Assembly;
3. Superior Assembly;

The pieces of inferior assembly are made from stainless steel and hard aluminum. The inferior assembly is composed by:

1. Base Plate
2. Base Body
3. Superior Base
4. Lateral Support.

Tolerance for this assembly is $\pm 5 \mu\text{m}$.

As we write in the top of paper we use three type of intermediary assembly. During the process of fabrication we can replace very easy one type of intermediary assembly with another type for obtain a new type of precision tower.

Intermediary assembly is composed by:

1. Intermediary Support
2. Shaft.

In intermediary support we insert the shaft. This is one of the very precise parts of the tower. Is made from stainless steel. The tolerances for distance between holes are $\pm 5 \mu\text{m}$.

Superior assembly is composed by:

1. Support
2. Cover 1
3. Cover 2
4. Sphere Support
5. Distanced 1
6. Distanced 2
7. Balls $\phi 20$.

All the pieces of superior assembly except cover 1 and cover 2 are made by stainless steel. Cover 1 and cover 2 are made from hard aluminum. Sphere support can be moved in 2 direction.

We have two type of high precision tower. For one type of tower, positioned on left side of the granite table, the central part can be moved and blocked with two screw and nuts. For the other type of tower the central part is free and it's find himself the right position.

They are two types of towers, because we put all the tools on the granite table, as is show in Fig. 1 and we use the same tools for fabrication of five type of optoelectronic detectors. In this case, the towers touch the tools on the granite table during fabrication and for this particular reason we design two type of tower.

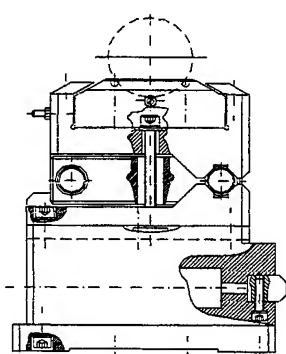


Fig. 2 a) High precision tower left side for first layer

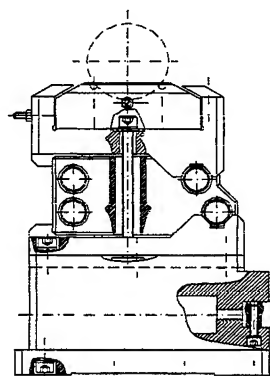


Fig. 2 b) High precision tower left side for second layer

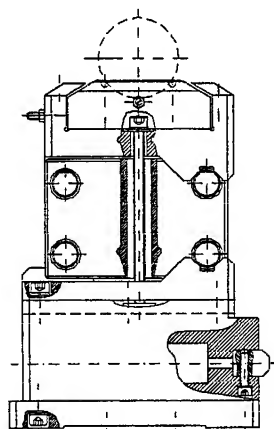


Fig. 2 c) High precision tower left side for third layer

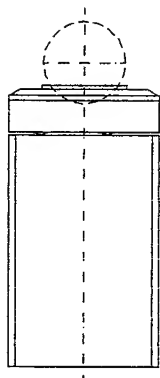


Fig. 2 d) High precision tower left side for first layer

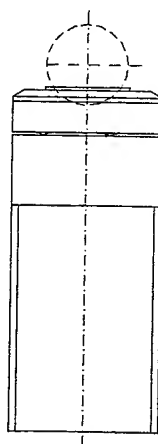


Fig. 2 e) High precision tower left side for second layer

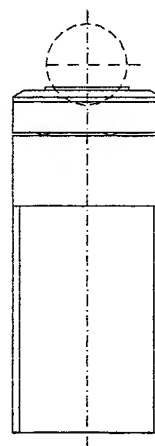


Fig. 2 f) High precision tower left side for third layer

3. CONDITION FOR MEASUREMENT OF THE HIGH PRECISION TOWER

During the research regarding the fabrication of the detector was find that for obtain the technical characteristics for of the detector the special conditions for environment:

- Work temperature: $20^{\circ}\text{C} \pm 1^{\circ}\text{C}$;

- Humidity $45 \pm 5\%$;
- Purity class – 100000.

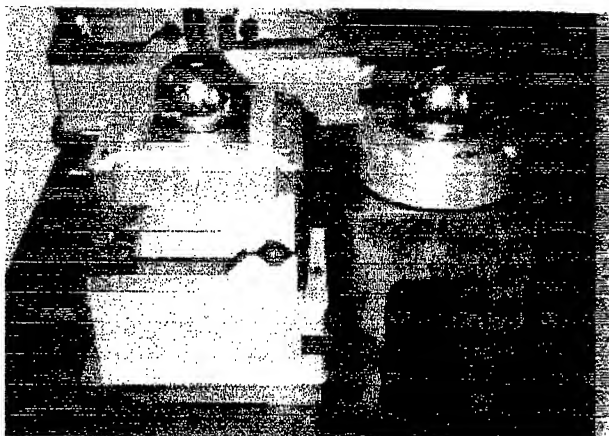


Fig. 3 a) High precision towers for first layer

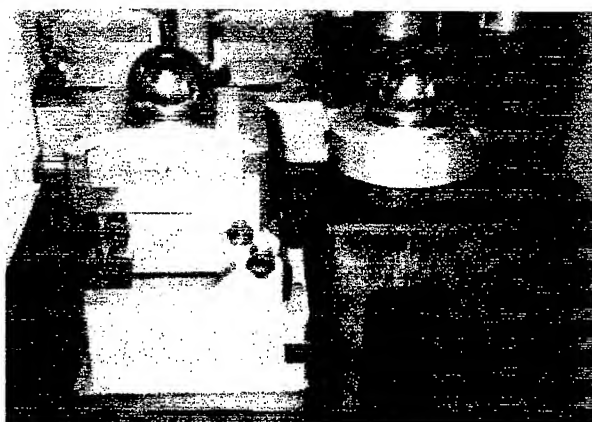


Fig. 3 b) High precision towers for second layer

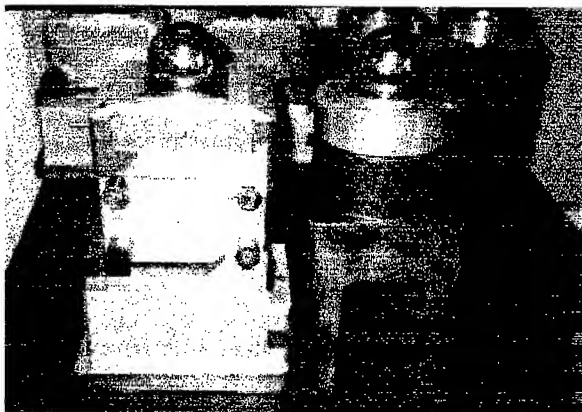


Fig.3 c) High precision towers for third layer

Only in this condition the granite table is stabile and his surface is a plane. Also for measurement and manufacturing we must use special condition for obtain a stabilized tolerances of the mechanical pieces for long time.

After the manufacturing of all assembly we put the entire high precision tower in a clean chamber for 1 day. After 1 day is possible to measure the assembly (Fig 3 a, b, c). If the dimension and the tolerances are not in range we must manufacturing once the sphere support.

For both type of high precision tower we have the same procedure. Measurement of towers we can do using a 3D measurement machine.

4. CONCLUSIONS

A high precision tower was designed using modern techniques of designed assisted by computer. Also, for manufacturing was used equipment controlled by computer (N.C.).

The towers are very easy to maintenance, and very easy to use, to modify the dimensions.

ACKNOWLEDGMENTS

We would like to thank Atlas-muon group members of LNF INFN (Frascati, Italy) for the very useful discussions on the engineering aspects for the tower design.

REFERENCES

1. ***, *Atlas Technical Design Reports and Proposal*, 1997.
2. C. Capoccia, S. Cerioni, M. Curatolo, B. Esposito, M.L.Ferrer, G. Maccarrone, *BML Assembly Manual*, 1999.

Launch of the LP₀₁ mode on an optical fibre (model based on gaussian beam notion)

Carmen Liliana Schiopu , Paul Schiopu*

University "Politehnica", Department of Electronic Engineering , Bucharest, România

ABSTRACT

In this paper, the authors use the launch model of guided modes on a multimode optical fibre, obtaining with computer help - important numerical results , which refer to efficiency of exciting a desired (linearly polarised) LP₀₁ mode. All the theoretical considerations are based on the gaussian beam approximation.

Keywords : launch of the LP₀₁ mode on a multimode fiber optic, gaussian fascicle model, coupling efficiency

1. INTRODUCTION

The efficiency of the injection of an electromagnetic radiation, emitted by a source (laser diode or electroluminescent diode) , in an optical fibre, represents one of the main problems of the telecommunication optical systems^{1,2,3,6,8,11} ; the coupling is determined by the fact that the optical fibre accept any type of radiation and a discrete number of modes (corresponding on certain frequencies), propagation constants and types of polarisation^{12,14,15}. In the same time, the differences between magnitudes of the diameter of the incident fascicle and the fiber diameter, radial shift between the two optical axes, distances between the optical source and the input of the optical fibre, relative orientation of the incident fascicle with respect to the optical fibre axis, can affect substantially the coupling efficiency^{2,5}.

2. THE EXCITATION OF A LP₀₁ MODE BY A FUNDAMENTAL GAUSSIAN FASCICLE

We look over the experimental results (computer modelation) in the case which we consider :

$$E(r) \approx E_0 \cdot \exp\left[-(r/w_G)^2\right] \quad (1)$$

where w_G is the spot radius, corresponding to the fundamental mode.

For many optical fibers, with variable profile of the refractive index, w_G is a little bit higher than the core radius, its magnitude being dependent on the manner in which $n=f(r)$. It varies - also - function of the normalised frequency, so the $w_G \cdot V$ product is maintained constant.

Unlike the gaussian fascicle case, once established w_G value in the transversal section of the fibre optic input, this value remains constant along Oz axis (which means the propagation direction). Therefore, in Figure 1 is shown the variation manner of the coupling coefficient, calculated with the following relation :

$$\eta = \frac{\left| \int_{A_\infty} (\vec{E}_i \times \vec{H}_{lm}^*) d\vec{A} \right|^2}{\operatorname{Re} \left[\int_{A_\infty} (\vec{E}_i \times \vec{H}_i^*) d\vec{A} \right] \cdot \int_{A_\infty} (\vec{E}_{lm} \times \vec{H}_{lm}^*) d\vec{A}} \quad (2)$$

* Correspondence : Email : opto@joe.tehfi.pub.ro ; Telephone : +40.1 410 54 00 / 171 ; Fax : +40.1 410 78 45

presented in references^{11,14,15}; there were taken into account the concrete expressions, similar to the gaussian dependencies of the \vec{E}_{it} si \vec{E}_{01t} components.

The relation (2) depends on the spot radius of the gaussian fascicle, which source is places at the entrance of the fiber. We must recall the fact that w_0 is the minimum radius of the gaussian fascicle spot, in the source origin. With "a" is denoted the radius of the optical fibre core.

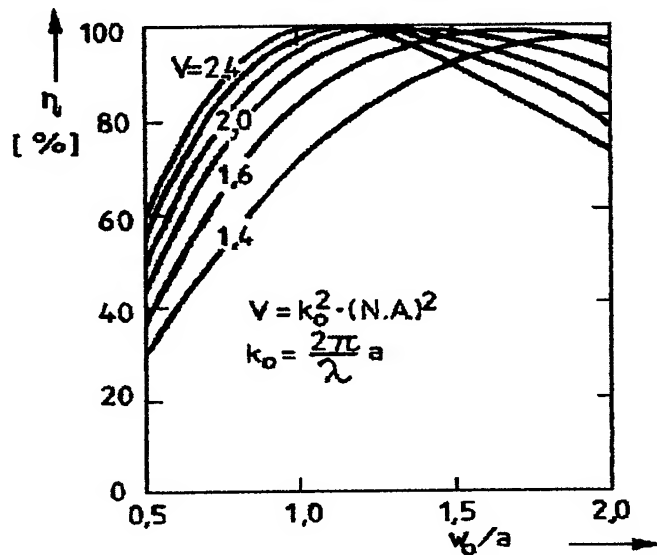


Fig. 1. Launching efficiency η as a function of the spot size w_0 , for different values of the normalized frequency V

The graph¹¹ corresponds to the case of a constant refractive index in the transversal section of the fiber core.

We can observe from Figure 1, that an 100% efficiency can be obtained when the normalised working frequency is very closed to the frequency corresponding to the next (LP_{11}) mode. In other words, we must work far from the cut-off fundamental mode frequency; also, the radius of the gaussian spot must be very close - in value - to the optical fibre radius.

We can say that - in a way - the problem is put from the source point of view : the working frequency and the emitted spot magnitude.

Figure 2 suggests a similar estimation¹¹, but from the fiber optic point of view. The w_G/a rapport is - in this case - a relative measure of the gaussian spot size, which is equivalent to the fundamental mode; this rapport is dependent on the normalised frequency - as shown also on the graph.

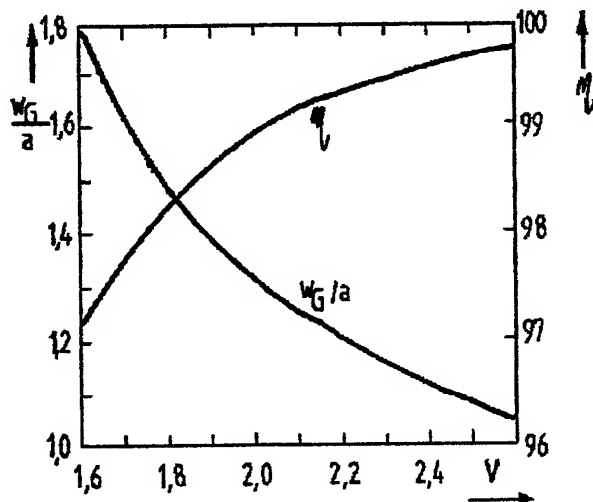


Fig. 2. The launching efficiency and the relative spot size w_G/a as functions of the normalized frequency V

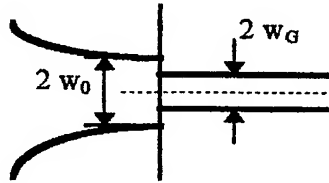
It can be observed that for $V = 2,4$ the coupling efficiency is bigger than 99,7 %.

Along with the normalised frequency decrease, the coupling efficiency decreases too, especially because of the fact that the gaussian approximation is getting farther from the real structure of the interior field. Even so, for $V = 1,6$, η is bigger than 97%.

IMPORTANT OBSERVATION. The coupling coefficient is maximum when the incident wave is identically with the wanted-mode one. Any deviation from this condition decreases the coupling efficiency. The power which is not in wanted modes, will flow to unwanted modes, guided or radiative. This phenomena represents, in fact, a loss of power.

Three big sources of errors appear in the case of this model ; they were nominated in introduction and are : *an axial shift*, denoted in our case " z_w " (because it influences the spot size of the gaussian fascicle emitted by the source and "seen" at the fiber input) , *a radial shift* (between the two optical axes : fascicle and fibre) , denoted with " d " and *an faulty angle* between the two optical axes (denoted with " θ "). It appears - also - the corresponding case to the situation when the sizes of the two spots (w_G and w_0) do not coincide.

2.1. The case $w_0 \neq w_G$ ("unmatching" between the two spots sizes)



This case corresponds to an "amplitude unmatchings" , and appears when the incident wave and the excited one have different amplitudes in the transversal contact section : optical fibre - source ; see Figure 3.

Fig. 3. The geometry of the problem

Figures 4.a. and 4.b. represents the coupling coefficient value :

$$\eta = \left(\frac{2w_0 w_G}{w_0^2 + w_G^2} \right)^2 \quad (3)$$

function of the magnitude rapport between the two spots.

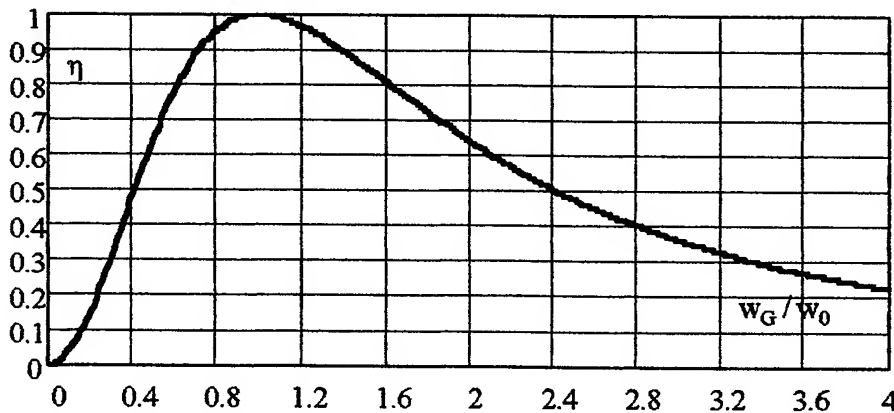


Fig. 4.a. The general dependency of the coupling coefficient as function of the two spots sizes.

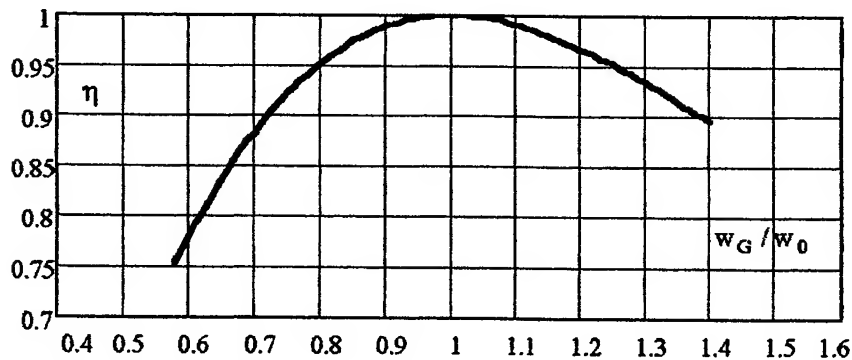


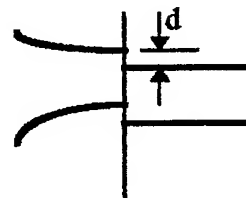
Fig. 4.b. The dependency of the coupling coefficient as function of the two spots sizes (detail).

We can see, from Figures 4.a. and 4.b. that , if the sizes of the two spots are equal, then the coupling efficiency is 100%. A 15% percent "unmatching" between the two radii leads to a 0,1 dB approximate loss.

2.2. The case of a radial shift between the two optical axes ($\exists d \neq 0$)

The treatment of this error source uses, as a primary hypothesis, the condition that all the others ideal conditions are fulfilled. It must be mentioned that – also – this case corresponds to an “amplitude unmatchings” (see Figure 5).

Fig. 5. The geometry of this case



When between the two optical axes there is a radial shift, we can compute the coupling coefficient / the launching loss in decibels, using the formula^{6, 9, 10}:

$$\eta = \exp\left[-(d/w_G)^2\right] \quad \text{or} \quad a = -10 \cdot \log \eta = 4,32 \cdot (d/w_G)^2 \quad (4)$$

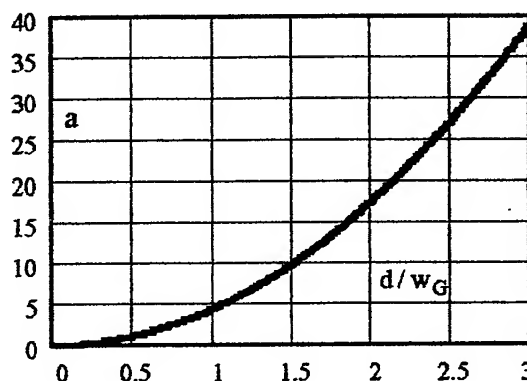
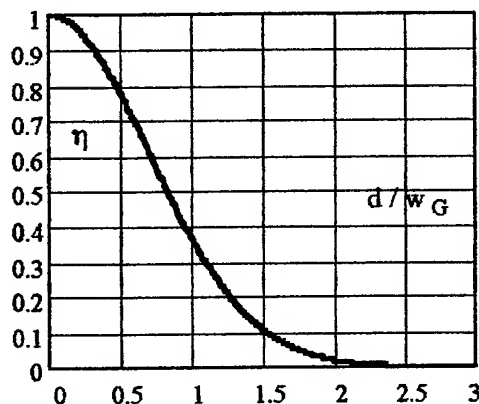


Fig. 6. The efficiency of launching for a transversal offset equal with “d”

It can be observed – from Figure 6 – that for a radial shift equal to the magnitude of the optical fiber own spot (w_G), the coupling efficiency decreases at 37%, which leads to 4,34 dB coupling losses.

For losses smaller than 0,1 dB it is necessary that $d \leq 0,15 w_G$, which is a condition hard to fulfil ($w_G = 5 \mu\text{m}$ implies $d < 0,8 \mu\text{m}$).

2.3. Axial shift case ($\exists z_w \neq 0$)

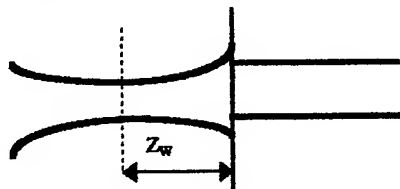
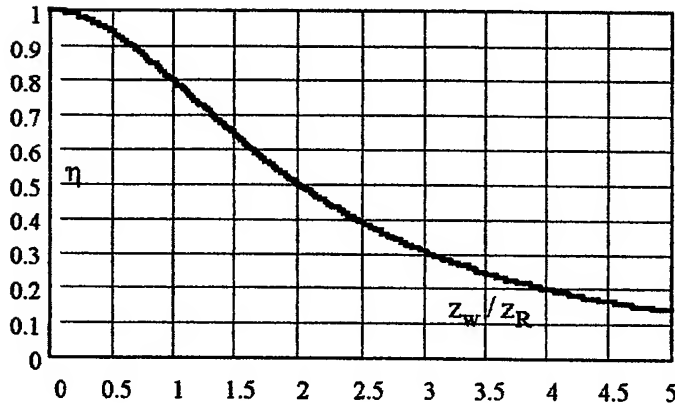


Fig. 7. The geometry of the problem

In this case (also an “amplitude unmatching”), the minimum size of the source spot (w_0) corresponds to a $z = -z_w$ co-ordinate; so, between the source and the fiber entrance it must be the respective distance. Due to the

fascicle divergence phenomenon, it appears – at the same time with the spot size modification – a curvature of the wave surfaces. Also, it appears – like an influence element – The Rayleigh spreading distance¹⁵, so the relation which expresses the coupling efficiency becomes :



$$\eta = \frac{1}{1 + \left(0.5 \cdot \frac{z_w}{z_R}\right)^2} \quad (5)$$

Fig. 8. Launching efficiency for a longitudinal offset " z_w "

From Figure 8 we can easily see that, if $z_w = z_R$, the coupling losses reach 1 dB. For losses smaller than 0.1 dB it is necessary that: $z_w < 0.3 \cdot z_R$

A numerical example shows that, for $\lambda = 1.3 \mu\text{m}$, $w_G = 5 \mu\text{m}$ and $z_R = 60 \mu\text{m}$ results $z_w < 18 \mu\text{m}$, which is a reasonable value, easy to fulfil.

2.4. The case of the faulty angle between the two optical axes ($\exists \theta \neq 0$)

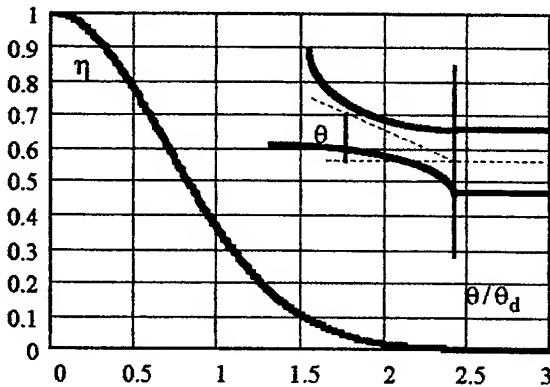


Fig. 9. Launching efficiency for an angular offset " θ "

The corresponding coupling efficiency is, in this situation:

$$\eta = \exp\left[-(\theta/\theta_d)^2\right] \quad \text{or} \quad a = -10 \cdot \log \eta = 4.34 \cdot (\theta/\theta_d)^2 \quad (6)$$

where θ_d is the divergence angle, defined by the corresponding relation from reference¹⁵.

The graph dependence for this last case of an "amplitude unmatched" is shown in Figure 9. We can observe that, to ensure losses smaller than 0.1 dB, it is necessary that the faulty angle be smaller than $0.15 \cdot \theta_d$.

A numerical case shows us that, if $\lambda = 1.3 \mu\text{m}$, the divergence angle is $\theta_d = 4.7^\circ$; it results that θ must be smaller than 0.7° , which is a difficult condition.

3. CONCLUSIONS

The simultaneous attendance of all these error sources is treated in this way - in specialised literature - only in the case of the coupling between two optical fibers.

The corresponding model of this coupling type retakes and uses a big part of the notions included in the reference¹⁵ - especially the elements which are related to the gaussian fascicle type of approximation. It also develops them.

Besides, this is the main reason for which the input coupling was studied in detail, using all the models present in the specialised literature. All the fundamental theoretical notions - which helped us studying also other possible types of

couplings (optical fibre - optical detector or optical fibre - optical fibre) - are found when making an analyse like the one made in this paper.

Also, it is important to mention other sources of input errors, unstudied in this article. These sources can be :

- "phase unmatchings" , when the phase distribution is different- on some elementary areas -which drives us to the conclusion that the scalar product can be smaller than the one in the ideal case (even zero) ;
- "polarisation unmatchings", when the directions of the vectors of the electric fields (incident and corresponding to the wanted mode) are not the same.

SELECTIVE REFERENCES

1. M.J. Adams, *An Introduction to Optical Waveguides*, Wiley & Sons, Chichester, New York, 1981
2. A. Ankiewicz and G.D. Peng, "Generalized Gaussian Approximation For Single-Mode Fibers", *J Lightwave Tech.*, **10**, pp. 22 - 27, 1992
3. M.K. Barnoski (ed.), *Fundamentals of Optical Fiber Communications*, 2-nd ed., Academic Press, New York, 1981
4. G. Cancellieri and A. Orfei, "Discussion on the effective cut-off wavelength of the LP₁₁ - mode in single-mode optical fibers", *Opt. Commun.*, **55**, pp. 311-315, 1985
5. P.K. Cheo, *Fiber Optics and Optoelectronics*, 2nd ed., Prentice Hall, London, 1990
6. R.G. Hunsperger, *Integrated Optics : Theory and Technology*, 2nd ed., Springer Series in Optical Sciences, **33**, Berlin, 1984
7. G. Kennedy and B. Davis, *Electronic Communication Systems* , 4-th ed., Macmillan/Mc Graw-Hill, Lake Forest, 1993
8. R.L. Lachance and P.A. Bélanger, "Modes in Divergent Parabolic Graded-Index Optical Fibers", *J. Lightwave Tech.*, **9**, no.11, pp. 1425 - 1430, 1991
9. S.E. Miller , A.G. Chynoweth, *Optical fiber telecommunications*, Academic Press, New York, 1979
10. J.E. Midwinter, *Optical fibers for transmission*, John Wiley & Sons, New York, 1979
11. D. Marcuse, *Light Transmission Optics*, 2nd ed., Van Reinhold, New York, 1982
12. A.W. Snyder, "Weakly guiding optical fibers", *J. Opt. Soc. Am.*, **70**, pp. 405 - 411, 1980
13. A. Sharma , S.J. Halme and M.M. Butusov, *Optical Fiber Systems and Their Components*, Springer, Berlin, 1981
14. C.L. Schiopu, "Eficienta cuplajului sursa - fibra optica. Model clasic-optica geometrica", Poster la Conferinta Internationala de Semiconductoare (C.A.S.), Sinaia, octombrie 1995, 1995
15. C.L. Schiopu and P. Schiopu, "The Launch of the Guided Modes on an Optical Fibre - A Model Based on Gaussian Fascicle Notion", 1999
16. T. Tamir (ed), "Integrated Optics", Topics in *Applied Physics*, **7**, Springer, Berlin, 1975

Launch of the guided modes on an optical fibre - A model based on gaussian beam notion

Carmen Liliana Schiopu , Paul Schiopu*

University "Politehnica", Department of Electronic Engineering , Bucharest, România

ABSTRACT

In this paper, the authors intend to present and analyse the gaussian model, frequently used when we want to control the coupling between an optical source and a multimode fiber optic. Based on this model, is determined the coupling coefficient in case of injecting radiation coming from a coherent source, analysing the effect of different factors over the efficiency of this coupling.

Keywords : launch of modes on a multimode optical fiber , gaussian beam model, coupling efficiency

1. INTRODUCTION

The gaussian beams are - mathematically speaking - approximate solutions of Maxwell's equations, valid when the beam diameter at the origin (in the point where the source is placed) is bigger then the emitted radiation wavelength (so the idea of a punctiform source is no longer valid).

Observation : The fundamental gaussian beam is similar with what is emitted on the other side of the optical fibre which works on fundamental mode (LP₀₁).

2. CHARACTERISTICS OF A GAUSSIAN BEAM

The gaussian beam model corresponds to the electric field intensity expression :

$$\underline{E}_x(r,z) = \underline{E}_x(0,0) \frac{w_0}{w(z)} e^{-\frac{r^2}{w^2(z)}} \cdot e^{-jkz + j\theta(z) - jk\frac{r^2}{2R(z)}} \quad (1)$$

where $k = k_0 n$. $\underline{E}_x(0,0) = E_0$ can be real, choosing a convenient reference on the time scale.

$$\Rightarrow E_0 \frac{w_0}{w(z)} e^{-\frac{r^2}{w^2(z)}} \text{ is a real value, which expresses the spatial dependency of the beam amplitude;}$$

$$\Rightarrow -kz + \theta(z) - k\frac{r^2}{2R(z)} \text{ is the beam phase.}$$

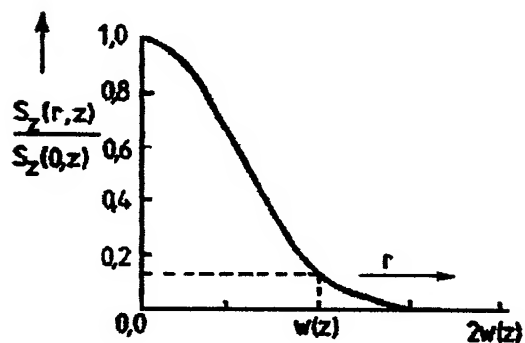


Fig. 1. Distribution of the normalised beam intensity in transversal plane.

The function $w(z)$ represents a way to measure the beam dimension in transversal section. It allows us to estimate the spot size, the diameter being $2w(z)$ (because of the symmetry towards the Oz axes).

Due to the fact that *while the beam is propagated, it will also spread*, the spot size (visualised transversally) depends on z point from the propagation axis.

* Correspondence : Email : opto@joe.tehfi.pub.ro ; Telephone : +40.1 410 54 00 / 171 ; Fax : +40.1 410 78 45

The relation, function of the radius, has the form :

$$w(z) = w_0 \sqrt{1 + \left(\frac{z}{z_R}\right)^2} \quad (2)$$

where w_0 represents the minimum radius of the spot in origin (in $z=0$ plane).

The Rayleigh (scattering) distance is $z_R = \pi w_0^2 / \lambda$.

λ is the wavelength of a plane wave, which has the same frequency as the beam's (emitted by a gaussian source).

At z_R (beam radius) distance, $w(z_R)$ is $\sqrt{2}$ times bigger than the origin radius w_0 . When the distance to source is much bigger than Rayleigh distance, we use the following relation :

$$w(z) = \frac{w_0 |z|}{z_R} = \frac{|z| \lambda}{\pi n w_0} \quad (3)$$

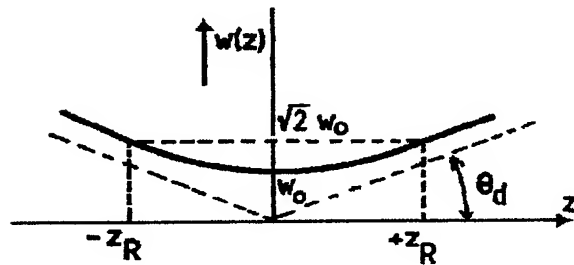


Fig. 2. The variation of the spot size, function of z .

In the specialised literature^{1,4}, when the discussion takes place in a point of co-ordinates $z \leq z_R$, the used term is "near field"; for $z \gg z_R$ we are in the situation of "far field". We observe, from Figure 2, the fact that we can define a divergence angle of the beam, expressed by :

$$\text{tg} \theta_d = \frac{w(z)}{|z|} = \frac{\lambda}{\pi n w_0} \quad (4)$$

From this relation we observe that the spot divergence is proportionally reverse with its radius to source. In other words, when the spot size at the origin (to source) is much bigger than the wavelength, the beam divergence is reduced : $\text{tg} \theta_d \approx \theta_d$ (Figure 3); when the spot size in $z=0$ plane is low, the beam divergence is more emphasised (Figure 4).

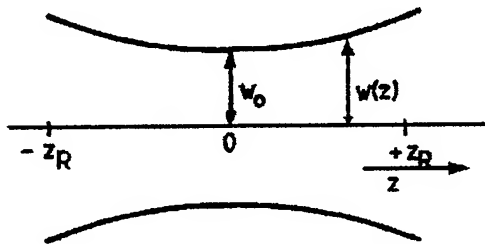


Fig. 3. Beam with a reduced divergence

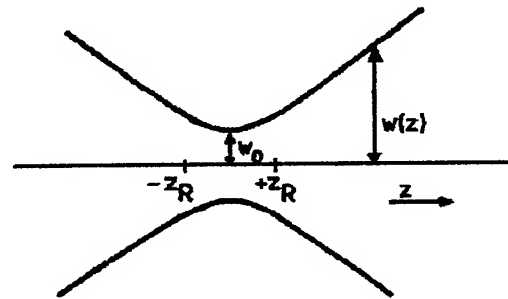


Fig. 4. Beam with big divergence

We underline the important fact that all the gaussian beam theory doesn't regard the case from Figure 4 (so it is not applied to beams with big divergence).

The relations shown before can be used to estimate also other aspects, related to the spatial dependency of the gaussian beam amplitude and phase.

Regarding the amplitude, because :

$$E_x(r, z) = E_0 \frac{w_0}{w(z)} e^{-\frac{r^2}{w^2(z)}} \Rightarrow E_x(0, z) = E_0 \frac{w_0}{w(z)} = E_0 \left[1 + \left(\frac{z}{z_R}\right)^2 \right]^{-1/2} \quad (5)$$

we are able to say that E_0 is the x - component amplitude of the electric field in the plane of origins, when the distance (with respect) to Oz axis is zero ($r=0$). Because it is supposed that the ambience is without losses, the power which comes from the source will not be modified. It appears an "increase / extension" of the spot which leads to the conclusion that E_0 represents - in fact - the biggest amplitude of E_x field component ; while the beam is propagated, the amplitude of its field (related to $r=0$ transversal co-ordinate) will decrease.

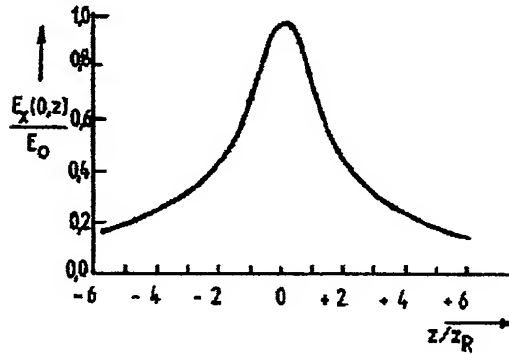


Fig. 5. The amplitude field decreasing.

The Figure 5 shows the way in which this decreasing is produced. At Rayleigh distance from the source, the electric field component's amplitude will represent 0,707 from the entire value in origin. At big z distances from the source , the amplitude becomes proportionally reversed with z , and the intensity decreases proportionally reversed with z^2 (these approximations are the conditions in which we discuss the properties of the field when it is emitted to a big distance from antennas).

The spatial dependency of the phase is :

$$\phi_x(r, z) = -kz + \theta(z) - k \frac{r^2}{2R(z)} \Rightarrow \quad (6.a)$$

$$\phi_x(0, z) = -kz + \theta(z), \quad k = \omega n \sqrt{\epsilon_0 \mu_0} = n \frac{\omega}{c} \quad (6.b)$$

where $\theta(z)$ is interpreted as being the phase difference between the gaussian beam and a uniform plane wave, encoming from the same source. It is used the approximation :

$$\theta(z) = \left[\operatorname{tg} \frac{z}{z_R} \right]^{-1} \quad (7) \quad \Rightarrow \quad \begin{aligned} z < 0, z \gg z_R &\Rightarrow \theta(z) \cong -\frac{\pi}{2}; \\ z > 0, z \gg z_R &\Rightarrow \theta(z) \cong \frac{\pi}{2}; \\ z = 0 &\Rightarrow \theta(z) = 0; \\ z = z_R &\Rightarrow \theta(z_R) = \frac{\pi}{4} \end{aligned}$$

From the relation :

$$\phi_x(r, z) = -kz + \theta(z) - k \frac{r^2}{2R(z)} \quad (8)$$

results that for $z = ct$ (in transversal section) the phase decreases reverse proportionaly with the square of the r distance from Oz axis. So, the wave front is a spherical surface with the curvature radius given by $R(z)$ function, from the last denominator term.

It is shown (in references^{1,5,6,7}) that in origin the curvature is zero, which means that the wave front is plane. For positive values of $R(z)$, the curvature centre is behind the wave front, which means that the beam is spreaded. For negative values of $R(z)$, the curvature centre is placed before the wave front and the beam becomes tighter (this behaviour of gaussian beam is applied specially to lenses). Figure 6 shows the general aspect of a gaussian field in longitudinal section (without many details).

Observation. Because the wavelength is defined as the distance between two surfaces of the same phase and, in case of gaussian beam, the distance between these surfaces of phase is variable from point to point, results that the wavelength has different values, being a local (punctual) dimension.

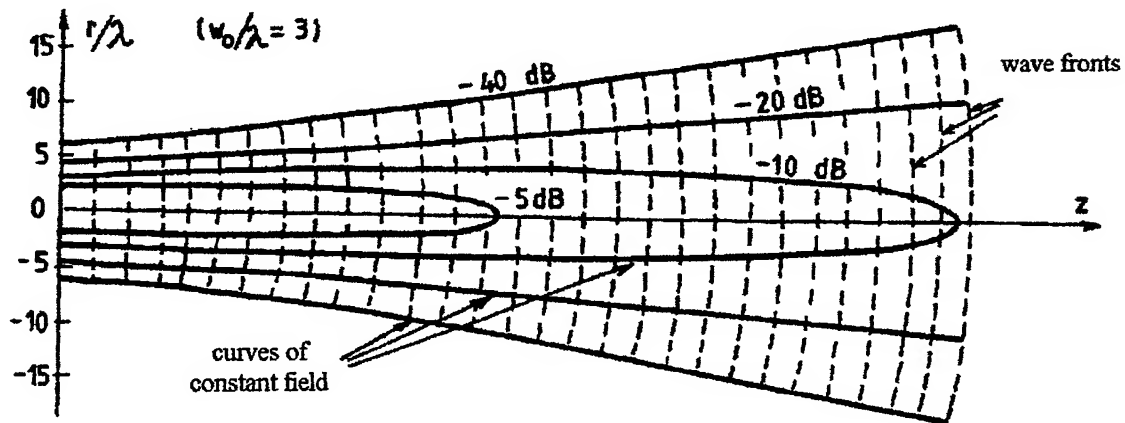


Fig. 6. The general aspect of a gaussian field in longitudinal section.

Between the electric and magnetic field components is the relation :

$$\underline{H}_y(r, z) = n \frac{\underline{E}_x(r, z)}{Z_0} \quad (9)$$

where $Z_0 = \sqrt{\mu_0 / \epsilon_0} = 377 \Omega$ is the free space impedance.

So, we can compute the longitudinal component of Poynting vector (for which all that matters is the product between electrical and magnetical transversal components of the field) :

$$S_z(r, z) = \frac{\pi n w_0^2 E_0^2}{2 w^2(z) Z_0} e^{-\frac{2r^2}{w^2(z)}} \quad (10)$$

The power emitted from the source (as gaussian beam) is obtained if we integrate the power density (in $z = ct$ plane) on transversal section :

$$P = \frac{\pi n E_0^2 w_0^2}{4 Z_0} = \frac{1}{2} S_z(0, z) \cdot A_b(z) \quad (11)$$

where, as we see :

$S_z(0, z)$ is the intensity of the beam in transverse section, for $r = 0$ (on Oz symmetry axis)
 $A_b(z) = \pi w^2(z)$ is the area of the beam in transverse section.

The power transmitted is half of the multiplication between the beam intensity on the propagating axis and the spot area in that point. We can observe that this manner of defining has a general characteristic (is not dependent on z co-ordinate). If we integrate the power density expressed by the longitudinal component of Poynting vector on a circular area of r radius, we obtain the specific power :

$$P(r) = P \cdot \left[1 - e^{-\frac{2r^2}{w^2(z)}} \right] \Rightarrow r = w(z) \text{ implies } P(r) = 0,86 \cdot P \quad (12)$$

which means that on the circular surface of $[2w(z)]$ spot is concentrated 0,86 % from the total power.

3. THE SELECTIVE LAUNCH OF GUIDED MODES AND THE CALCULATION OF THE COUPLING COEFFICIENT (GAUSSIAN MODEL)

Especially on monomode fibres for which the radius (the diameter) has very small values, and for which - to enlarge the frequency band - is imposed the supplementary request that the difference between the two refraction indexes [in fact $NA = \sqrt{n_1^2 - n_2^2}$] be very small, the problem related to optical flux injection doesn't obey anymore (and do not allow) the modelation given by the geometric optics.

The model used comes from the recognition of these initial conditions¹ :

- is considered that the optical beam used to inject the wanted mode (/s) is a gaussian beam (its properties were discussed in the previous paragraph) ;
- $n_1 \cong n_2$ ($NA \rightarrow 0$) is admitted ;
- in a first stage, the losses made by Fresnel reflections at optical fibre input are neglected ;
- we look for preferential excitation of LP_{01} mode (HE_{11} respectively), eventually for LP_{11} mode ($TE_{01}, TM_{01}, TE_{21}$, which simultaneous presence produce a field resultant with a linear polarisation) ;
- the coupling efficiency between the source and optical fibre is discussed for coherent and also for noncoherent sources.

It is accepted - as a first observation - the fact that in an optical wave dielectric guide, it doesn't appear (theoretically) coupling between modes. Therefore, if on an ideal optical fibre which can support - dependent on the frequency of the incident radiation - LP_{01} and LP_{11} mode, we need to excite only the fundamental mode, we assume that the power won't pass from this mode to other modes. In reality, because of the working conditions (fibre curvature) and because of technologies (impurities, discontinuities) there always will exist unwanted couplings in optical fibre guided modes.

Calculating the coupling efficiency, one must use the property of the orthogonality of modes. It is proved that **all the modes (guided or radiative) are orthogonal**. Because of this orthogonality, the total transmitted power through an optical fibre is always the summation of transmitted power on each mode.

In the particular case of injecting a radiation encoming from a coherent source, the problem is solved in Figure 7.

We admit the hypothesis that the middle of optical fibre is covered with a protective material which tends to infinite, having the refraction index equal with the ambience medium refraction index ($n=1$).

The gaussian beam is incident on transversal (marginal) section of optical fibre in $z=0$ co-ordinate point.

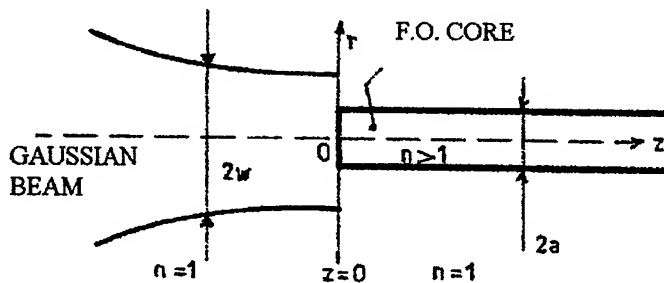


Fig. 7. The geometrical configuration of a gaussian beam injection , in an optical fiber.

It is set the problem of LP_{01} or LP_{11} mode excitation in an optical fiber.

The incident wave is given by the field complex vectors \vec{E}_i and \vec{H}_i .

The electromagnetic field produced in fibre is individualised through \vec{E}_{lm} and \vec{H}_{lm} components (of LP_{lm} guided mode ; in that particular case $l=0, 1$ and $m=1$) ; also, it appears simultaneously unwanted / residual field components, corresponding to radiative or other guided modes.

If it is desirable that the fibre works on LP_{lm} mode, then the coupling efficiency is given by :

$$\eta = \frac{P_{lm}}{P_i} \quad (a = -10 \log \eta) \quad (13)$$

where P_{lm} is the wanted power mode, and P_i is the total power of the incident wave.

The total field on the fibre input can be expressed as a vectorial sum of all the corresponding wanted modes and of all residual fields (amplitude coefficients, respectively each contribution of the vectorial component having unknown values). Mathematically speaking, the initial field is expressed in corresponding terms of guided and unguided modes, which form a set of orthogonal functions.

Then, from Electromagnetics, it is retained and applied the condition of continuity for the field components at the surface of separation between the two mediums, which allows us to specify the values for some of unknown amplitude coefficients, corresponding of guided modes.

For radiative modes we apply the continuity condition and - also - the observation regarding the orthogonality of modes (we don't take into account their nature).

OBSERVATION. The mathematical procedure consists - in fact - in determining the coefficients of the Fourier series, using the "sine" and "cosine" orthogonality property of these functions.

After we have found the amplitudes of the vectorial field components, corresponding to LP_{01} (LP_{11}) wanted mode, we can compute the coupling coefficient given by the relation (1), using the next formula :

$$\eta = \frac{\left| \int_{A_\infty} (\bar{E}_i \times \bar{H}_{lm}^*) d\bar{A} \right|^2}{\text{Re} \left[\int_{A_\infty} (\bar{E}_i \times \bar{H}_i^*) d\bar{A} \right] \cdot \int_{A_\infty} (\bar{E}_{lm} \times \bar{H}_{lm}^*) d\bar{A}} \quad (14)$$

where :

$$\text{Re} \left[\int_{A_\infty} (\bar{E}_i \times \bar{H}_i^*) d\bar{A} \right] \text{ is the power of the incident wave;} \quad (15.a)$$

$$\int_{A_\infty} (\bar{E}_{lm} \times \bar{H}_{lm}^*) d\bar{A} \text{ is the power of the guided wave;} \quad (15.b)$$

because \bar{E}_{lm} and \bar{H}_{lm}^* are in phase, is no longer necessary to specify the fact that it is considered only the real part of the mixt product.

In the integral $\int_{A_\infty} (\bar{E}_i \times \bar{H}_{lm}^*) d\bar{A}$ from nominator, \bar{E}_i represents the local value of the incident field and \bar{H}_{lm}^* corresponds to the excited wave in $z = 0$ coupling plane.

From the law of the energy conservation results that the power which corresponds to excited mode cannot exceed the value of the power transmitted by incident wave.

The maximum value of the coupling coefficient is $\eta = 1$. This value (which corresponds to the optimum coupling) leads, as we saw in the previous relation, to conditions :

$$\bar{E}_i = \bar{E}_{lm} \quad ; \quad \bar{H}_i = \bar{H}_{lm} \quad (16)$$

Therefore, we can assure an optimum coupling only when the incident wave is identical (in totality : as amplitude, phase, polarisation state) with the one corresponding to the wanted mode.

Relation (14) can be written in a simpler form, if :

- the arbitrary amplitudes of the incident wave and of the guided wave are chosen in such a way that the two integrals - from the denominator of the relation (14) - are equal with the unity. The field distributions of the waves are considered to be normalised ;
- in the integral from nominator we take into account only the projections of the field components in a transversal plane [property of the scalar product $(\vec{E}_i \times \vec{H}_{lm}^*) \cdot d\vec{A}$] : that means \vec{E}_{it} , \vec{H}_{it} , \vec{E}_{lmt} , \vec{H}_{lmt} (parallel with $z=0$ plane) . More than that, it is taken into account the fact that between the electric and the magnetic field there are passing relations, depending on the wave impedance of the medium.

4. CONCLUSIONS

The simplified result for coupling coefficient is :

$$\eta = \left| \frac{n_1}{Z_0} \cdot \int_{A_\infty} \vec{E}_{it} \cdot \vec{E}_{lmt}^* dA \right|^2 \quad (17)$$

This expression has the meaning : each element of "dA" area from the transversal surface of the optical fibre generates an elementary magnetic flux, proportional with the scalar product : $\vec{E}_{it} \cdot \vec{E}_{lmt}^*$. The total amplitude is the sum of the complex contributions of all the elementary areas ; in these conditions, the coupling coefficient is proportional with square of the total amplitude module.

As it was shown before, the coupling coefficient is maximum when the incident wave is identically with the wanted-mode one. Any deviation from this condition decreases the coupling efficiency. The power which is not in wanted modes, will flow to unwanted modes, guided or radiative. This phenomena represents, in fact, a loss of power.

OBSERVATION. Also, passing from the ideal case (without Fresnel reflections at the surface of separation between the two mediums) to the real case, we must have in mind the relation - with general character - $\eta_{exp} = (1-T) \cdot \eta$, where T is the reflection coefficient.

REFERENCES

1. A. Ankiewicz and G.D. Peng, "Generalized Gaussian Approximation For Single-Mode Fibers", *J Lightwave Tech.*, **10**, pp. 22 - 27, 1992
2. P.K. Cheo, *Fiber Optics and Optoelectronics*, 2nd ed., Prentice Hall, London, 1990
3. R.G. Hunsperger, *Integrated Optics : Theory and Technology*, 2nd ed., Springer Series in Optical Sciences, **33**, Berlin, 1984
4. G. Kennedy and B. Davis, *Electronic Communication Systems*, 4-th ed., Macmillan/Mc Graw-Hill, Lake Forest, 1993
5. A. Sharma, S.J. Halme and M.M. Butusov, *Optical Fiber Systems and Their Components*, Springer, Berlin, 1981
6. C.L. Schiopu, "Aspecte ale propagarii undelor electromagnetice în fibrele optice", Referat de doctorat, Universitatea "Politehnica" Bucuresti, 1994
7. C.L. Schiopu, "Eficienta cuplajului sursa - fibra optica. Model clasic-optica geometrica", Poster la Conferinta Internationala de Semiconductoare (C.A.S.), Sinaia, octombrie 1995

Power-related frequency shift determinations of an Iodine-stabilized He-Ne laser at 633 nm wavelength by using a master-slave laser system

Gheorghe Popescu*

National Institute for Lasers, Plasma and Radiation Physics, Lasers Dept.,
P.O.Box MG - 36, Bucharest-Magurele, R 76900, Romania

ABSTRACT

The experimental results of the power-related frequency shift of an iodine-stabilized He-Ne laser with two methods of power variation: misalignment of the laser cavity and change of the polarization orientation between iodine cell and gain tube are reported. A small-power internal-mirror He-Ne laser PLL offset-locked to an iodine-stabilized He-Ne laser was used as the reference laser. The data were processed following three methods: the *standard* matrix method, the *diagonal* (line-by-line) method and the *reference line* method. All three methods gave *compatible results*, but the diagonal method is taking advantage of collecting fewer data and being faster. Significant differences appeared among values of power-related frequency shifts, if the method of power variation was different, no matter the group of hfs components or method of data processing under consideration. For the same group of hfs components, deviations of *less than 1 kHz* may exist between frequency shifts computed by using the above mentioned methods of data processing, while the deviations between the frequency shifts calculated at the same power level do not exceed 2 kHz. This is regardless of groups of hfs components. By contrary, differences up to about 14 kHz for a given group of hfs components were observed if the method used to get the power variation was different (no matter the method used for data processing).

Keywords: He-Ne lasers, frequency stabilization, frequency comparison, length primary etalon, metrology

1. INTRODUCTION

In 1992, the Comite International des Poids et Mesures (CIPM) adopted a revision of the 1983 *mise en pratique* of the definition of the meter, the main change being a decrease of about one order of magnitude in the standard uncertainties associated with the frequencies of the recommended wavelengths and a new list of recommended radiations was released¹. The consistency of these new decisions were verified through a series of laser comparisons throughout the world (see for example those carried out during three consecutive years - from 1993 to 1995 - with participation of the BIPM lasers²).

Among the radiations included in the new list for the practical realization of the metre - known as *Recommendation 3* (CI-92), the most popular is that corresponding to a He-Ne laser stabilized by saturated absorption in an intracavity cell filled with $^{127}\text{I}_2$, using third derivative detection technique^{3,4} at wavelength 633 nm. The reproducibility of these devices is usually much better than 2.5 parts in 10^{11} , if operating conditions tighter than those presently recommended are used (we refer to the nominal values of the modulation amplitude, the iodine cold finger and cell wall temperature and the one-way intracavity laser power).

One aim of this experimental work was to prove that using different methods to process the experimental data gives compatible results and, taking into account this conclusion, to promote the idea of direct line-by-line determinations. Another aim was to compare the values of the power coefficient resulting from a linear fit on the experimental data in case of different groups of components and methods of data processing in an attempt to explain the deviations of the frequency difference determinations appearing when different groups of components are used for computations.

* Correspondence: Email: gpopescu@ifin.nipne.ro, fax: (+40) 1 423 17 91.

2. EXPERIMENTAL WORK

The frequency shift due to the intracavity power variation of the laser under study was regarded as an essential determination while the other operation parameters mentioned above were kept at nominal values. The variation of the output power was realized by two methods: rotation of the relative polarization orientation between the gain tube and iodine absorption cell or by tilting the front mirror of the laser cavity. Three different methods for data reduction were used in order to compute the frequency differences: standard matrix measurement, direct line-by-line or diagonal measurement and complete matrix measurement. The experimental work was carried out at the National Research Laboratory of Metrology (NRLM), Tsukuba, Japan during Oct.-Dec., 1997.

2.1 The experimental setup

All measurements regarding the frequency comparison were made by beat-frequency technique which provides a very sensitive means of checking the behaviour of the stabilized lasers. The radiation coming from a small-power internal-mirror He-Ne laser NRLM/FO1 (the reference laser) that was PLL offset locked to the iodine-stabilized He-Ne laser NRLM/P1 (the master laser)⁵ and the radiation coming from an iodine-stabilized He-Ne laser NRLM/N4 (the laser under study)⁶ were optically mixed on the surface of an avalanche photodiode after being mixed on the surface of a beam divider (see the experimental setup presented in Figure 1). Different optical components (plane mirrors, beam dividers, neutral variable filters, quarter-wave plates) were used to get the optical beats.

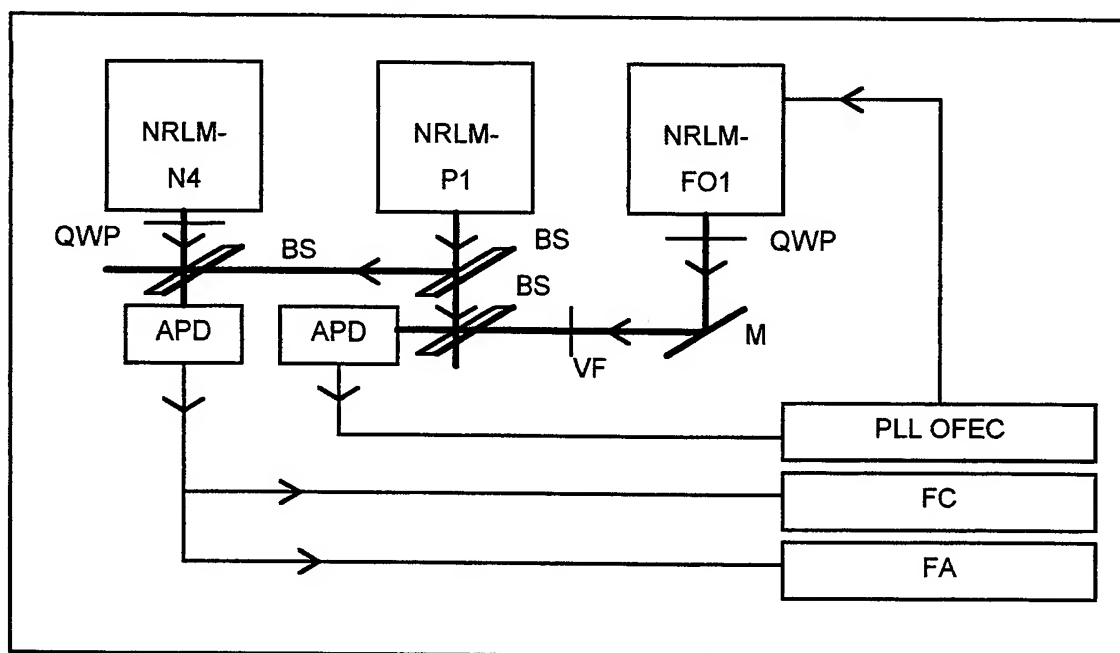


Fig. 1. The set-up used for frequency difference measurements. APD - avalanche photodiode; BS - beam divider; QWP - quarter-wave plate; VF - neutral variable filter; M - mirror; PLL OFEC - PLL offset frequency electronic controller; FC - frequency counter; FA - frequency analyser.

For the best frequency reproducibility, the modulation amplitude and the iodine temperature were strictly checked on both He-Ne/iodine stabilized lasers as to be at the nominal values specified by the CIPM: frequency modulation width 6 MHz and cold-finger temperature 15 °C. For reliable measurements, a signal-to-noise ratio of at least +40 dB was taken to be the threshold for the electrical signal reaching the input of the frequency counter.

During the experimental work both iodine-stabilized He-Ne lasers were successively locked to the saturated absorption hyperfine components of the $^{127}\text{I}_2$ intracavity systems³ from d to j, while between the master and the slave lasers has been continuously monitored a frequency offset of 350 MHz (the frequency of the slave laser NRLM/FO1 was higher than

that of the master laser NRLM/P1). The output power of the laser NRLM/N4 was adjusted as to cover the limits set for the one way intracavity power mentioned in the reference¹, e.g. (10 ± 5) mW. More detailed information on the lasers involved in comparison regarding principal geometrical parameters, operation principles and performances are given elsewhere^{5, 6}.

The operation of iodine-stabilized He-Ne lasers at 633 nm wavelength under conditions specified in Recommendation 3(CI-92) is a sufficient condition to ensure that their absolute frequencies lie inside the given uncertainty of 2.5 parts in 10^{11} . However, the laser frequency comparisons are necessary to test the performances from time-to-time or to determine the sharpness of the traceability⁷. The most important reason of performing this experimental work was to find and prove the existence of an easier and faster way to perform frequency difference measurements. For ensuring the continuity in that field of determinations, it is very important to compare results coming from standard and new proposed methods.

3.1. Methods for data processing

The master-slave laser system proved a fast frequency response and a contribution of less than 15 Hz is supposed to be supplementary added as incertitude on the measured frequency differences. By using the set-up presented in Figure 1, we mixed the light beams coming from the master laser NRLM/P1 and the slave laser NRLM/FO1. A frequency discrepancy σ between the master and the slave lasers smaller than 2 parts in 10^{14} or less than 3 parts in 10^{14} if a 100-s or, respectively, 10-s gate time resulted from the Allan variance stability measurements⁸ (see the graph presented in Figure 2). Under these circumstances, one could assume the performances are very precisely transferred from the master laser to the slave laser. Therefore, we may assume that in fact we were measuring the frequency differences between the lasers NRLM/N4 and NRLM/P1 while counting in fact the frequency beats resulting from mixing light beams coming from the laser NRLM/N4 and from the laser NRLM/FO1.

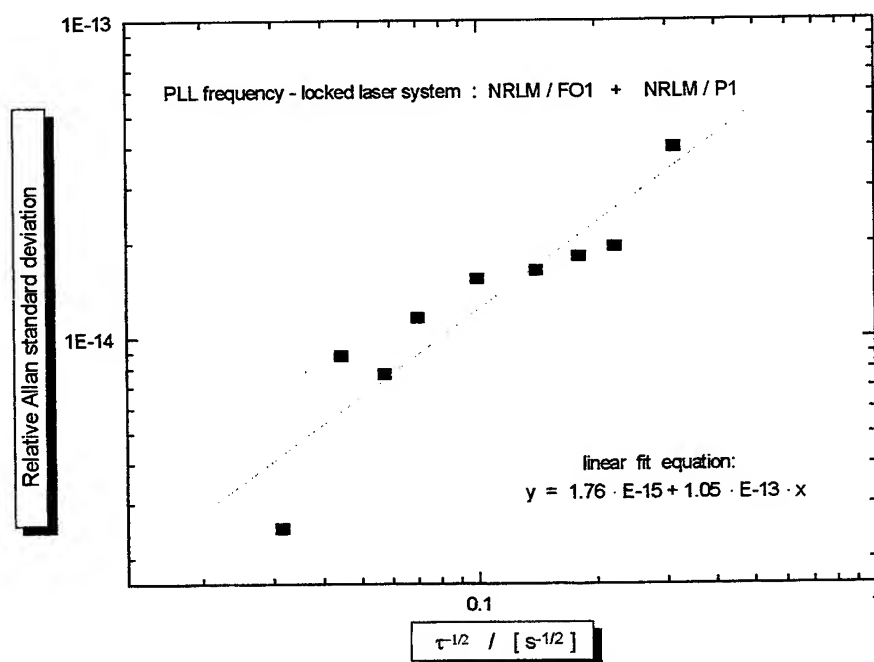


Fig. 2. Relative Allan standard deviation versus inverse of the square root of the averaging time interval. The laser NRLM/FO1 was PLL offset-frequency locked to the laser NRLM/P1.

We remind that in case the *standard matrix method*⁹ would be used for data processing, each frequency difference measurement is provided from a square matrix whose elements were the frequency differences (as a mean of more than

three measurements with an integration time of 10 s) obtained by successively locking the two iodine-stabilized He-Ne lasers NRLM/N4 and NRLM/P1 to all possible combinations of hyperfine components of an available group except those for which both lasers would have been stabilized to the same component. The average of all differences between pairs of frequency difference measurements is taken as the frequency difference between compared lasers when that group of components are considered. (The exception regarding the diagonal elements of a matrix is right because from the beat signal is not resulting which laser frequency is higher).

Following the above definition, in case the *direct line-by-line or diagonal method* would be used for the data processing, the average of all frequency differences (as a mean of more than three measurements with an integration time of 10 s) obtained by successively locking the two compared lasers on the same component of a group could be taken as the frequency difference between compared lasers for that group of components. In order to perform such frequency measurements a frequency offset larger than the frequency intervals between compared components has to be set and then precisely controlled. Frequency offsets continuously adjustable from 100,000.00 to 400,000.00 MHz were easily available by using an improved PLL offset-locking system.

The third method results from considering a square matrix whose elements were the frequency differences obtained by successively locking the two iodine-stabilized He-Ne lasers to all possible combinations of hyperfine components of an available group. We proposed that the average of all differences between pairs of frequency difference measurements representing different components to which are added those representing diagonal elements of the matrix to be taken as the frequency difference between compared lasers in case that a *complete matrix method* for data processing had to be considered.

3.3 Comparative results

All three participating lasers were switched on during the first day of the measurement and remained in operation throughout the comparison in order to obtain a good thermal equilibrium in both mechanics and electronics. All operating parameters for the lasers N4 and P1 were checked and adjusted to be at the nominal value just before starting a new set of measurements. The only exception was the laser intracavity power which remained as a variable parameter. In order to measure and monitor the above mentioned parameters, a RF spectrum analyser, a calibrated thermocouple and power meter were used (first, the output power was measured and, then converted to one-way intracavity power by considering the value of the output mirror transmission coefficient 0.5 %).

The following components available on both lasers (NRLM/N4 and NRLM/P1) were successively considered in the frequency difference determinations: (d, e, f, g), (h, i, j), (d, e, f, g, h, i, j) and the following indexes are used to specify the method used to process the experimental data: M - for the matrix determinations, D - for direct line-by-line or diagonal measurements and C - for complete matrix determinations. In figure 3 are presented the experimental points and as vertical lines the standard deviation. It is shown also a linear fit on the experimental data.

The frequency differences computed when the experimental data shown in Figure 3 were fitted by a linear curve are shown in Table1. An intracavity power of 10 mW was used for these computations, e.g. the nominal value recommended for one way intracavity power. Small differences between the values representing frequency determinations when all three methods of data processing were used for a group of components were noticed

Table 1. The expected frequency differences between the laser NRLM/N4 and the laser NRLM/P1, resulting from a linear fit on the experimental data processed by using different methods for data processing (see text for symbols).

One-way intracavity power [mW]	Method for data Processing	Computed frequency difference for the group: / [kHz]		
		(d, e, f, g)	(h, i, j)	(d, e, f, g, h, i, j)
10	M	-11.70	-7.14	-9.56
	D	-11.31	-7.38	-9.35
	C	-11.54	-7.13	-9.51

In Table 2 one can equally note the values representing the power coefficients calculated for different groups of components, if all three methods for data processing are used. In Figure 4 we present the deviations one can obtain if the frequency difference determinations obtained following the matrix determinations (M) are subtracted from those determinations obtained following the diagonal (M-D) or complete matrix (D-MD) methods.

Table 2. Power coefficients for the laser NRLM/N4, resulting from a linear fit on the experimental data processed by using different methods for data processing (see text for symbols).

Method for data processing	Power coefficient [kHz/mW]		
	(d, e, f, g)	(h, i, j)	(d, e, f, g, h, i, j)
M	1.93	1.49	1.72
D	1.91	1.47	1.68
MD	1.92	1.52	1.71

It is important to know the deviations of the frequency differences obtained when diagonal or complete matrix method were used taking as reference the frequency differences calculated by using the matrix method. at different power levels.

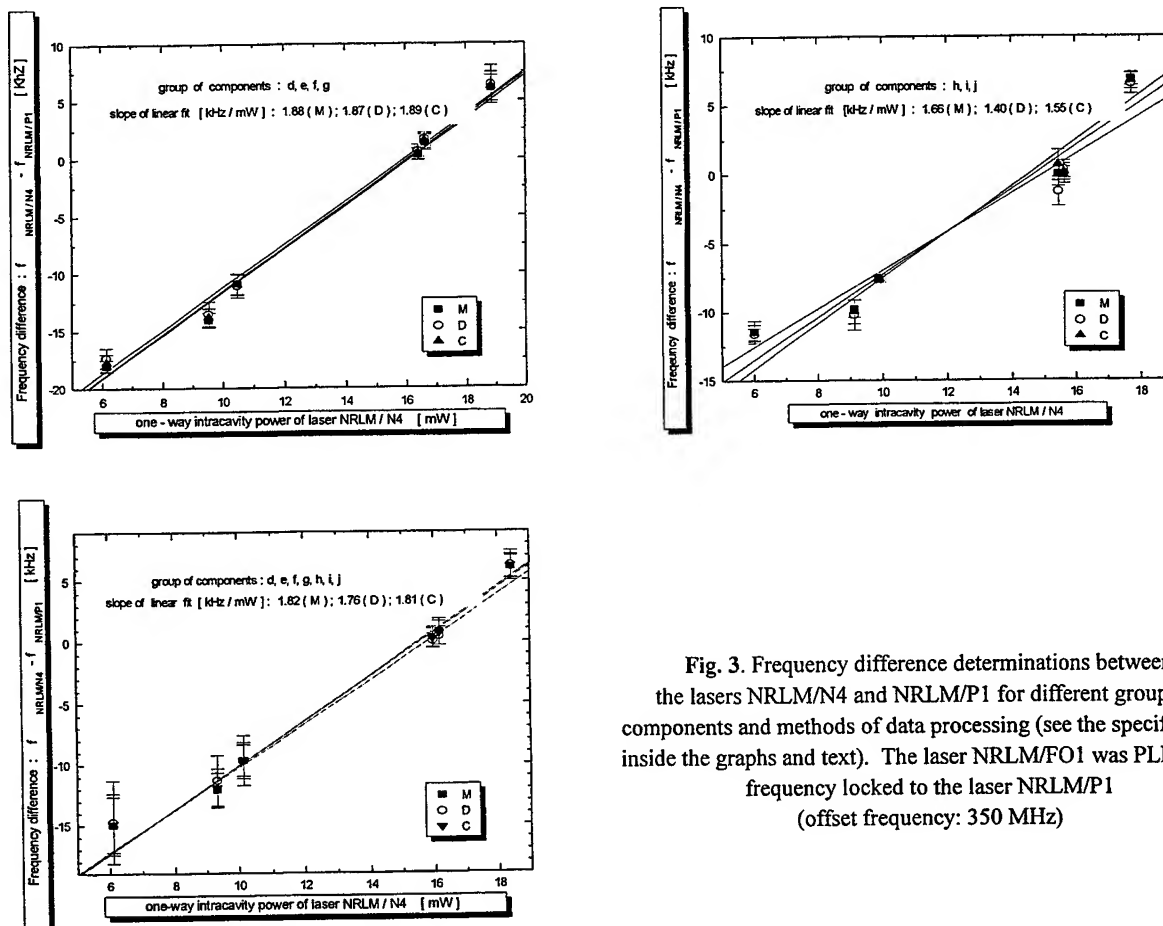


Fig. 3. Frequency difference determinations between the lasers NRLM/N4 and NRLM/P1 for different groups of components and methods of data processing (see the specifications inside the graphs and text). The laser NRLM/FO1 was PLL offset-frequency locked to the laser NRLM/P1 (offset frequency: 350 MHz)

The values of the deviations are presented in Figure 4 as a graph. It is important to note the limits of these values (less than 1.5 kHz) and from far smaller values at the nominal value (10 mW) of the one-way intracavity power.

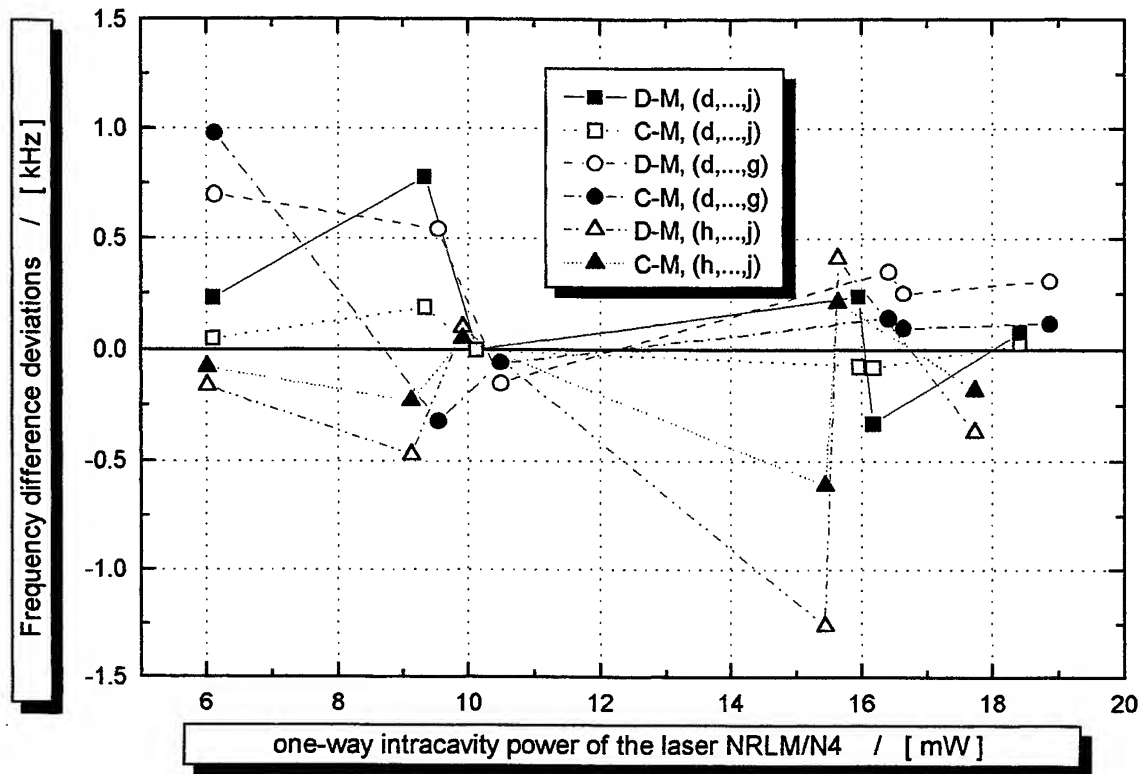


Fig. 4. Deviations of the frequency differences calculated by diagonal (D-M) and complete matrix (C-M) methods when compared with the frequency differences measured by standard matrix method for different groups of components: d, e, f, g, h, i, j; d, e, f, g, h, i, j.

4. CONCLUSIONS

The frequency difference between two iodine-stabilized He-Ne lasers is usually measured by standard matrix method⁹, but the diagonal elements of the matrix – resulting from locking the two lasers to the same component – are not used because there is no information about which laser frequency is higher. By using a master-slave laser system, where the slave laser was frequency offset-locked on the frequency of the master, the above mentioned limitations are easily passed. Frequency discrepancy between the slave laser NRLM/FO1 and the master laser NRLM/P1 smaller than 15 Hz resulted from Allan variance stability measurements for 10-s gate time, so that one can assume that all performances regarding frequency stability and repeatability of the master laser are transferred to and well preserved by the slave laser.

Frequency beats resulting from locking the two iodine-stabilized He-Ne lasers to the same component from d to j were measured and the frequency difference calculated by using three methods: standard matrix, diagonal and complete matrix. A frequency offset continuously adjustable from 100 to 400 MHz was available by using an improved PLL offset-locking system. Deviations smaller than 1.5 kHz resulted when frequency differences computed by using the standard matrix method and the complete matrix method were compared with those obtained when the diagonal method was used. It was proved that relatively small deviations are expected if different methods of data processing are used (one may note that 1.5 kHz represents a relative frequency difference of 3 parts in 10^{12} which is from far smaller than 2.5 parts in 10^{11} which represents the estimated relative standard uncertainty of this type of laser¹).

Taking into account these results, some advantages of using the diagonal method - as a short time for performing the measurements and a quick answer for line-by-line frequency difference measurements - could promote it. Also, it gives the opportunity to study the influence of laser operation parameters on the frequency difference between two lasers locked on the same component with no any influence of the other neighbouring lines.

By using the methods mentioned in Chapter 3.1 for data processing we note very small differences appearing among values of the power coefficients for a given group of components if different methods of data processing were used, while significant differences were noticed when considering the values corresponding at different groups of components. In fact this could explain at some extent the significant differences appearing between frequency difference measurements computed when different groups of components are considered¹⁰.

5. ACKNOWLEDGEMENTS

The author likes to thank to the Japan Society for the Promotion of Sciences (JSPS) for providing funds and to the staff from the National Research Laboratory for making possible this experimental work. Special thanks are addressed to J. Ishikawa for the help in preparing the experiment.

6. REFERENCES

1. T. J. Quinn, "Mise en Pratique of the Definition of the Metre (1992)", *Metrologia*, **30**, pp. 523-541, 1993/1994.
2. T. J. Quinn, *Metrologia*, "Results of recent international comparisons of national measurement standards carried out by the BIPM, 1996", *Metrologia* **33**, pp. 271-287, 1996.
3. G. R. Hanes, C. H. Dahlstron, "Iodine hyperfine structure observed in saturated absorption at 633 nm", *Appl. Phys. Lett.* **14**, pp. 362-364, 1969.
4. A. J. Wallard, "Frequency stabilization of the helium-neon laser by saturation absorption in iodine vapour", *J. Phys. E: Sci. Instrum.* **5**, pp. 926-930, 1972.
5. J. Ishikawa, "A small power He-Ne laser PLL frequency-locked to an iodine-stabilized He-Ne laser", *Appl. Opt.* **34**, pp. 6095-609, 1995.
6. J. Ishikawa, Y. -C. Lee, O. Takano, "A compact iodine stabilized He-Ne laser for intercomparisons", *Proc. of the CPEM*, Braunschweig, Germany, June 17-20, p. 86, 1996.
7. F. Petru, J. Lazar, O. Cip, G. Popescu, J. -M. Chartier, "Frequency comparison of He-Ne/iodine lasers at $\lambda = 633$ nm between the NILPRP and the ISI, and traceability through the BIPM", *Metrologia* **34**, pp. 515-518, 1997.
8. W. D. Allan, "Statistics of atomic frequency standards", *Proc. IEEE* **54**, pp. 221-231, 1966.
9. F. Bayer-Helms, J. -M. Chartier, A. J. Wallard, "Evaluation of the international intercomparison measurements (March 1976) with $^{127}\text{I}_2$ - stabilized He-Ne lasers: spacings of the hyperfine structure components", *PTB-Bericht PTB-ME 17*, pp. 139-146, 1977.
10. J. de Vicente, A. M Sanchez-Perez, F. Bertinetto, "Comparison of He-Ne lasers from the LMM and the IMGC stabilized on $^{127}\text{I}_2$ at 633 nm", *Metrologia* **30**, pp. 503-506, 1993.

The evaluation method for the dynamics of an erbium-doped fiber laser

Florentin I. Vasile^{*a}, Paul Schiopu^b

^aSiemens Company, Bucharest, Romania

^bDept. of Electronics, Univ. "Politehnica" of Bucharest, Romania

ABSTRACT

We propose a simple method for integration by numerical computations of the atomic rate equations for three-level systems and the laser amplifier equations. We calculate the gain coefficient in erbium-doped fiber considering the effects of pump on the system dynamics. Described the atomic rate equations for three-level systems and the dynamics Maxwell-Bloch equations for erbium-doped fiber laser amplifier is presented.

Keywords: EDFA, runge-kutta, maxwell-bloch, dynamic, coherence term, gain coefficient, atomic rate equations

1. INTRODUCTION

The use of erbium-doped fiber amplifiers (EDFA) in optical communication system has virtually eliminated loss as a limitation, and thereby, has enabled optical transmission over trans-oceanic distances without regeneration. The capacity of these long systems is now constrained by fiber dispersion, fiber nonlinearities, and amplifier noise. An evaluation method for dynamics Maxwell-Bloch equations for erbium-doped fiber laser amplifier and the atomic rate equations for three-level systems is presented. The systems are coupled differential equations can only be solved by numerical computations. We used for integration the Runge-Kutta method (4th order). With results investigate principally the effect of the two-photon coherence and gain coefficient. The method by evaluation of signal gain coefficient for erbium-doped fiber amplifier is using for the effects of pump and doped with erbium and the method by evaluation of coherence term is using in atomic coherence.

2. DESCRIPTION OF THE SYSTEM

In this paper, we report an evaluation method for the dynamics of an erbium-doped fiber laser as a function of time. First we proposed a simple method for integration by numerical computations of the atomic rate equations for three-level systems.

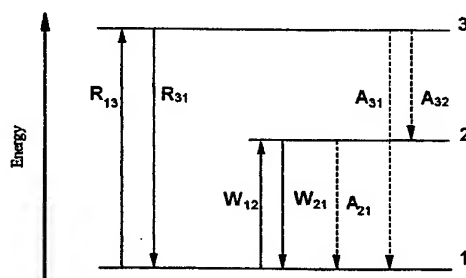


Fig. 1 Energy level diagram corresponding to a basic three-level laser system, where the laser transition occurs between levels 1 (ground) and 2 (metastable)

^{*}Correspondence: Email: Vasile.Florentin@wan.oen.siemens.de; Telephone: +401 4232530; Fax: +401 4234172

The symbols R , W , and A correspond to pumping rates, stimulated emission rates, and spontaneous decay rates between related levels. This system is ¹:

$$\frac{dN_1}{dt} = -R_{13}N_1 + R_{31}N_3 - W_{12}N_1 + W_{21}N_2 + A_{21}N_2 \quad (1)$$

$$\frac{dN_2}{dt} = W_{12}N_1 - W_{21}N_2 - A_{21}N_2 + A_{32}N_3 \quad (2)$$

$$\frac{dN_3}{dt} = R_{13}N_1 - R_{31}N_3 - A_{32}N_3 \quad (3)$$

where N_i are the atomic populations in the energy states 1, 2 and 3 respectively with $i = 1, 2, 3$. The pumping rate from levels 1 and 3 is R_{13} and the stimulated emission rate between levels 3 and 1 is R_{31} . The stimulated absorption and emission rates between levels 1 and 2 are W_{12} and W_{21} , respectively and the spontaneous decay from levels 3 and 2 are A_{32} . A_{21} is spontaneous decay from levels 2 and 1 (see Fig.1). Let ρ be the laser ion density and N_1 , N_2 and N_3 the fractional densities, or populations of atoms in the energy states 1, 2 and 3, respectively. From the excited state corresponding to level 3, there are two possibilities of decay, i.e., radiative and nonradiative. The laser ions density is:

$$\rho = N_1 + N_2 + N_3 \quad (4)$$

and initial conditions is:

$$N_{i0} = \rho \exp(-E_i / K_B T) \quad (5)$$

where $i = 1, 2, 3$. K_B is the Boltzmann constant, T is the temperature for measuring, E_i is the energy levels of erbium. These energy levels are known from energy level diagram of erbium¹ (see Fig. 2). The system of atomic rate equations for three-level is one system of coupled differential equations can only be solved by numerical computations.

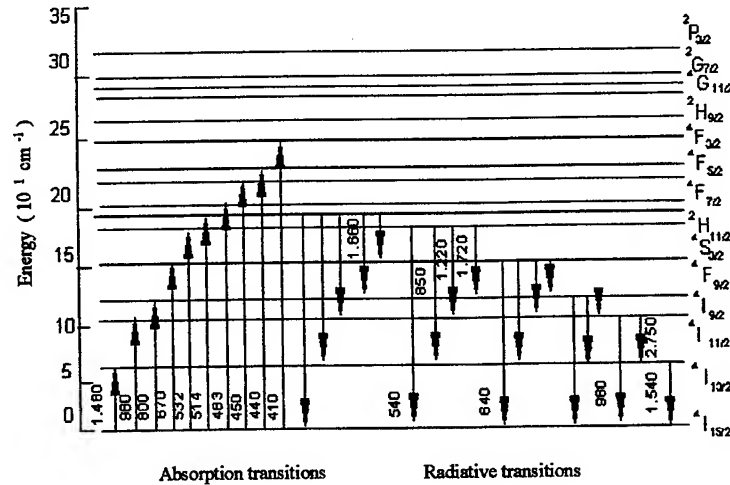


Fig. 2 Energy level diagram of erbium: glass showing absorption and radiative transitions. The transition wavelengths, given in nanometers, are indicated only for transitions experimentally observed in silicate and fluorozirconate erbium-doped fibers

3. STEADY STATE REGIME¹

In the steady state regime for atomic rate equations¹, the populations are time invariant. i.e.:

$$\frac{dN_i}{dt} = 0 \quad (6)$$

where $i = 1, 2, 3$. Let

$$a = R_{31} + A_{32} \quad (7)$$

and

$$b = W_{21} + A_{21} \quad (8)$$

We obtain from Eqs. (2) - (3):

$$W_{12}N_1 - bN_2 + A_{32}N_3 = 0 \quad (9)$$

$$R_{13}N_1 - aN_3 = 0 \quad (10)$$

Replacing

$$N_3 = \rho - N_1 - N_2 \quad (11)$$

in the above and solving for N_1, N_2 yields:

$$N_1 = \rho \frac{ab}{b(a + R_{13}) + a W_{12} + R_{13} A_{32}} \quad (12)$$

$$N_2 = \rho \frac{R_{13} A_{32} + a W_{12}}{b(a + R_{13}) + a W_{12} + R_{13} A_{32}} \quad (13)$$

We replace then the definitions of a and b and factorise the term $A_{21}A_{32}$ in Eqs. (12) - (13) to obtain:

$$N_1 = \rho \frac{(1 + W_{21}\tau)(1 + \frac{R_{13}}{A_{32}})}{(1 + W_{21}\tau)(1 + \frac{R_{13} + R_{31}}{A_{32}}) + W_{12}\tau(1 + \frac{R_{31}}{A_{32}}) + R_{13}\tau} \quad (14)$$

$$N_2 = \rho \frac{R_{13}\tau + W_{12}\tau(1 + \frac{R_{13}}{A_{32}})}{(1 + W_{21}\tau)(1 + \frac{R_{13} + R_{31}}{A_{32}}) + W_{12}\tau(1 + \frac{R_{31}}{A_{32}}) + R_{13}\tau} \quad (15)$$

We assume now that the nonradiative decay rate A_{32} dominates over pumping rates $R_{13,31}$, i.e., $A_{32} \gg R_{13,31}$ and Eqs. (14) - (15) yield:

$$N_1 = \rho \frac{1 + W_{21}\tau}{1 + R\tau + W_{12}\tau + W_{21}\tau} \quad (16)$$

$$N_2 = \rho \frac{R\tau + W_{12}\tau}{1 + R\tau + W_{12}\tau + W_{21}\tau} \quad (17)$$

with

$$R = R_{13}. \quad (18)$$

With the above result, we find that $N_3 = \rho - N_1 - N_2 = 0$, i.e., the pump level population is negligible due to the predominant nonradiative decay (A_{32}) toward the metastable level 2. The steady state populations described by Eqs. (16) - (17) are central to the calculation of gain coefficient in erbium-doped fibers.

4. DYNAMICS MAXWELL-BLOCH

Second we proposed a simple method for integration by numerical computations of the laser amplifier equations or dynamics Maxwell-Bloch equations for erbium-doped fiber laser amplifier as a function of time². The system is:

$$dE_1/dt = -k (E_1 - P_1) \quad (19)$$

$$dP_1/dt = -\gamma_{\perp} (P_1 - D_1 E_1 - C_{32}) \quad (20)$$

$$dD_1/dt = -A_{21} (D_1 + N_{\text{tot}}) - \omega_p (P_1 E_1 + P_p) \quad (21)$$

$$dP_p/dt = -\gamma_{\perp} [P_p - (D_1 - N_{\text{tot}}) - E_1 C_{32}] \quad (22)$$

$$dC_{32}/dt = -\gamma_c C_{32} - \omega_p (2 P_1 + E_1 P_p)/4 \quad (23)$$

where: E , P represent, respectively, the electrical field, the polarisation of the medium and k , γ_{\perp} their respective relaxation constants, while D_1 and A_{21} represent, respectively, the population inversion and the spontaneous transition probability between the level (1) and (2), ω_p is the absorption probability of a pump photon, C_{32} is the coherence term, N_{tot} is the total population of our atomic system, γ_c is the relaxation constant relative and the subscript p indicates the pump transitions between the levels (1) and (3), while the subscript 1 is for the laser transitions between the levels (2) and (1).

5. MODELING WITH RUNGE-KUTTA METHOD

In this section, we are studding the atomic rate equations for three-level laser and two coupled lasers coherently pumped systems. Modeling is made with the help of the computer, using Runge-Kutta method for solving the system of coupling differential equations. First, we are solving the atomic rate equations for three-level laser system. For the Eqs. (1) - (3) from the atomic populations N_1 , N_2 , N_3 in the energy states 1, 2 and 3 respectively, using Eq. (4), we are introducing the following definitions:

$$g_1 = -R_{13} - R_{31} - W_{12} \quad (24)$$

$$g_2 = -R_{31} + A_{21} + W_{21} \quad (25)$$

$$g_3 = R_{31} \rho \quad (26)$$

$$g_4 = W_{12} - A_{32} \quad (27)$$

$$g_5 = -W_{21} - A_{21} - A_{32} \quad (28)$$

$$g_6 = A_{32} \rho \quad (29)$$

In the following, we will use the Eq. (11) and we obtain one quickly solving for the system of coupling equations. With those definitions, Eq. (1) - (3) are given by:

$$dN_1/dt = g_1 N_1 + g_2 N_2 + g_3 \quad (30)$$

$$dN_2/dt = g_4 N_1 + g_5 N_2 + g_6 \quad (31)$$

and

$$N_3 = \rho - (N_1 + N_2) \quad (32)$$

respectively from Eq. (11).

Therefore, the system (1) - (3) can be further simplified by using definitions (24) - (29), and we obtain one new differential equations system. New system (30) - (31) with the link relation (32), is easy to solve in comparison with the system for the Eq. (1) - (3). With numerical computations for the system of Eq. (30) - (31), we find the atomic populations N_1 and N_2 for the different period of the time and the initial conditions. After, using the link relation (32), we obtain the atomic populations N_3 .

The system (30) - (31) is one elementary Cauchy problem, that is one differential equations system by first order linear and coupling for the atomic rate equations in the energetic steady 1, 2 and 3 respectively with the solution to spread between two neighbour points of the network. Using a Runge - Kutta method with a variable integration step h , we have numerically solved the two coupled differential equations (30) - (31).

First, we will solve the system (24) - (29). Using following functions in the Eq. (30) - (31):

$$f_1(N_1, N_2, t) = g_1 N_1 + g_2 N_2 + g_3 = dN_1/dt = N_1' \quad (33)$$

and

$$f_2(N_1, N_2, t) = g_4 N_1 + g_5 N_2 + g_6 = dN_2/dt = N_2' \quad (34)$$

we compute with Runge - Kutta method, the vector component part for k_1, k_2, k_3, k_4 from the function $f_1(N_1, N_2, t)$ and l_1, l_2, l_3, l_4 from the function $f_2(N_1, N_2, t)$ respectively. With:

$$k_1 = h f_1(N_1, N_2, t) \quad (35)$$

$$k_2 = h f_1(N_1 + k_1/2, N_2 + l_1/2, t) \quad (36)$$

$$k_3 = h f_1(N_1 + k_2/2, N_2 + l_2/2, t) \quad (37)$$

$$k_4 = h f_1(N_1 + k_3, N_2 + l_3, t) \quad (38)$$

for the Eq. (31) and:

$$l_1 = h f_2(N_1, N_2, t) \quad (39)$$

$$l_2 = h f_2(N_1 + k_1/2, N_2 + l_1/2, t) \quad (40)$$

$$l_3 = h f_2(N_1 + k_2/2, N_2 + l_2/2, t) \quad (41)$$

$$l_4 = h f_2(N_1 + k_3, N_2 + l_3, t) \quad (42)$$

for the Eq. (31).

With these definitions, we can implement for the Eq. (30) - (31), one program for computing in the language for programming. Resulting:

$$N_{1m+1} := N_{1m} + \frac{k_1 + 2k_2 + 2k_3 + k_4}{6} \quad (43)$$

$$N_{2m+1} := N_{2m} + \frac{l_1 + 2l_2 + 2l_3 + l_4}{6} \quad (44)$$

With the conditions that the following relations

$$\left| \frac{k_2 - k_3}{k_1 - k_4} \right| \quad \text{and} \quad \left| \frac{l_2 - l_3}{l_1 - l_4} \right| \quad (45)$$

must be smaller than some per cents, step h must be decreased. We obtain good solutions if step h for integration is small or the period of time is longer with condition (45). For long period of time, we obtain solutions for the steady state regime. For solving Eq. (30) - (31), we need initial conditions (5).

With the Runge - Kutta method, we can solve the Eq. (19) - (23) for two coupled lasers coherently pumped systems.

Modelling is the same with the first part. Using same method for the first system (1) - (3) to the system (19) - (23), we can be computing E_1 , D_1 , P_1 , P_p and C_{32} .

We can solve the system (19) - (23) with the following functions:

$$s_1(E_1, P_1, D_1, P_p, C_{32}, t) = -k(E_1 - P_1) = dE_1/dt = E_1' \quad (46)$$

$$s_2(E_1, P_1, D_1, P_p, C_{32}, t) = -\gamma_L(P_1 - D_1E_1 - C_{32}) = dP_1/dt = P_1' \quad (47)$$

$$s_3(E_1, P_1, D_1, P_p, C_{32}, t) = -A_{21}(D_1 + N_{tot}) - \omega_p(P_1E_1 + P_p) = dD_1/dt = D_1' \quad (48)$$

$$s_4(E_1, P_1, D_1, P_p, C_{32}, t) = -\gamma_L[P_p - (D_1 - N_{tot}) - E_1C_{32}] = dP_p/dt = P_p' \quad (49)$$

$$s_5(E_1, P_1, D_1, P_p, C_{32}, t) = -\gamma_C C_{32} - \omega_p(2P_1 + E_1P_p)/4 = dC_{32}/dt = C_{32}' \quad (50)$$

Now, we compute with Runge - Kutta method, the vector component parts for n_i , o_i , r_i , q_i , z_i from the functions s_1 , s_2 , s_3 , s_4 , and s_5 respectively:

$$n_1 = h s_1(E_1, P_1, D_1, P_p, C_{32}, t) \quad (51)$$

$$n_2 = h s_1(E_1 + n_1/2, P_1 + o_1/2, D_1 + r_1/2, P_p + q_1/2, C_{32} + z_1/2, t) \quad (52)$$

$$n_3 = h s_1(E_1 + n_2/2, P_1 + o_2/2, D_1 + r_2/2, P_p + q_2/2, C_{32} + z_2/2, t) \quad (53)$$

$$n_4 = h s_1(E_1 + n_3, P_1 + o_3, D_1 + r_3, P_p + q_3, C_{32} + z_3, t) \quad (54)$$

$$o_1 = h s_2(E_1, P_1, D_1, P_p, C_{32}, t) \quad (55)$$

$$o_2 = h s_2(E_1 + n_1/2, P_1 + o_1/2, D_1 + r_1/2, P_p + q_1/2, C_{32} + z_1/2, t) \quad (56)$$

$$o_3 = h s_2(E_1 + n_2/2, P_1 + o_2/2, D_1 + r_2/2, P_p + q_2/2, C_{32} + z_2/2, t) \quad (57)$$

$$o_4 = h s_2(E_1 + n_3, P_1 + o_3, D_1 + r_3, P_p + q_3, C_{32} + z_3, t) \quad (58)$$

$$r_1 = h s_3(E_1, P_1, D_1, P_p, C_{32}, t) \quad (59)$$

$$r_2 = h s_3(E_1 + n_1/2, P_1 + o_1/2, D_1 + r_1/2, P_p + q_1/2, C_{32} + z_1/2, t) \quad (60)$$

$$r_3 = h s_3(E_1 + n_2/2, P_1 + o_2/2, D_1 + r_2/2, P_p + q_2/2, C_{32} + z_2/2, t) \quad (61)$$

$$r_4 = h s_3(E_1 + n_3, P_1 + o_3, D_1 + r_3, P_p + q_3, C_{32} + z_3, t) \quad (62)$$

$$q_1 = h s_4(E_1, P_1, D_1, P_p, C_{32}, t) \quad (63)$$

$$q_2 = h s_4(E_1 + n_1/2, P_1 + o_1/2, D_1 + r_1/2, P_p + q_1/2, C_{32} + z_1/2, t) \quad (64)$$

$$q_3 = h s_4(E_1 + n_2/2, P_1 + o_2/2, D_1 + r_2/2, P_p + q_2/2, C_{32} + z_2/2, t) \quad (65)$$

$$q_4 = h s_4(E_1 + n_3, P_1 + o_3, D_1 + r_3, P_p + q_3, C_{32} + z_3, t) \quad (66)$$

$$z_1 = h s_5(E_1, P_1, D_1, P_p, C_{32}, t) \quad (67)$$

$$z_2 = h s_5(E_1 + n_1/2, P_1 + o_1/2, D_1 + r_1/2, P_p + q_1/2, C_{32} + z_1/2, t) \quad (68)$$

$$z_3 = h s_5(E_1 + n_2/2, P_1 + o_2/2, D_1 + r_2/2, P_p + q_2/2, C_{32} + z_2/2, t) \quad (69)$$

$$z_4 = h s_5(E_1 + n_3, P_1 + o_3, D_1 + r_3, P_p + q_3, C_{32} + z_3, t) \quad (70)$$

With these definitions, we can implement for the Eq. (19) - (23), one program for computing in the language for programming. Resulting:

$$E_{1m+1} := E_{1m} + \frac{n_1 + 2n_2 + 2n_3 + n_4}{6} \quad (71)$$

$$P_{1m+1} := P_{1m} + \frac{o_1 + 2o_2 + 2o_3 + o_4}{6} \quad (72)$$

$$D_{1m+1} := D_{1m} + \frac{r_1 + 2r_2 + 2r_3 + r_4}{6} \quad (73)$$

$$P_{pm+1} := P_{pm} + \frac{q_1 + 2q_2 + 2q_3 + q_4}{6} \quad (74)$$

$$C_{32m+1} := C_{32m} + \frac{z_1 + 2z_2 + 2z_3 + z_4}{6} \quad (75)$$

with the conditions:

$$\left| \frac{n_2 - n_3}{n_1 - n_4} \right|, \left| \frac{o_2 - o_3}{o_1 - o_4} \right|, \left| \frac{r_2 - r_3}{r_1 - r_4} \right|, \left| \frac{q_2 - q_3}{q_1 - q_4} \right|, \text{ and } \left| \frac{z_2 - z_3}{z_1 - z_4} \right| \quad (76)$$

must be smaller than some per cents, step h must be decreased. We obtain good solutions if step h for integration is small or the period of time is longer with condition (76). We used for integration the Runge-Kutta method (4th order). This method gives best results for that type of problems. The Runge-Kutta method uses the step integration in concordance with

error choice. The advantage for using Runge-Kutta method is possibility to autostart, because is step by step type method and the evaluation implies only the function no the derivatives.

6. RESULTS

We calculated the gain coefficient in erbium-doped fiber considering the effects of pump on the system dynamics¹. The signal gain coefficient is:

$$g = \sigma_a(\lambda_s) \{ \eta(\lambda_s) N_2 - N_1 \} \quad (77)$$

with

$$\eta(\lambda_s) = \sigma_e(\lambda_s) / \sigma_a(\lambda_s) \quad (78)$$

Parameter η is of central importance in the modelling of erbium-doped fiber amplifier. The method by evaluation of signal gain coefficient for erbium-doped fiber amplifier is using for the effects of pump and doped with erbium.

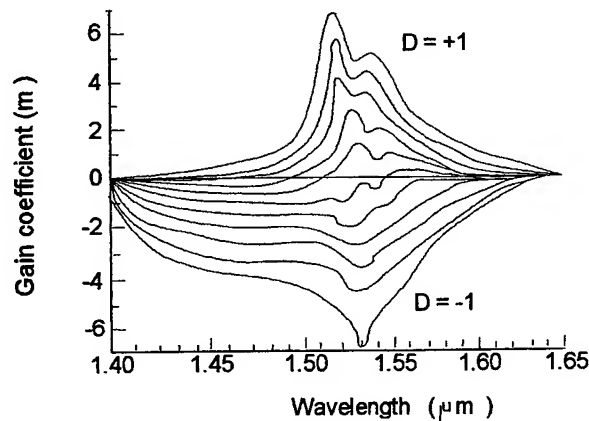


Fig. 3 Signal gain coefficient^{1. and 4.} as a function of wavelength for different relative medium inversion D:

$$D = (N_2 - N_1) / \rho = (2N_2 - \rho) / \rho \quad (79)$$

with $D = -1$ when all ions are in the ground state and gain coefficient is negative. For a spectral region near the long wavelength side of the transitions is characterised by a positive gain coefficient. When $D = +1$, the region of positive gain coefficient widens to spread eventually over the whole spectral region, and they are all in the excited state. That is modelling gain coefficient with homogeneous broadening, for modelling gain coefficient with inhomogeneous broadening using only the results associated with the homogeneous broadening approximation³, but modelling is different. The coherence term C_{32} is very important, because is usual in the atomic coherence and to investigate principally the effect of the two-photon coherence.

7. CONCLUSION

The best solution for atomic rate equations for three-level systems is give if step by integration is small in function with error choice. For great times the solutions coincide to stationary case. The method by evaluation of signal gain coefficient for erbium-doped fiber amplifier is using for the effects of pump and doped with erbium.

ACKNOWLEDGMENTS

Florentin V. acknowledges the support from Dept. of Electronics, Univ. "Politehnica" of Bucharest. This work has been partially supported by the Siemens Company.

REFERENCES

1. E. Desurvire, *Erbium-doped fiber amplifiers*, John Wiley&Sons, New York, 1992.
2. E. Lacot, F. Stoeckel, and M. Chenevier, Dynamics of an erbium-doped fiber laser, *Phys. Rev. A* **49**, no. 5, 1994.
3. C. R. Giles and E. Desurvire, "Modelling erbium-doped fiber amplifiers with fiber background loss", *IEEE Photonics Technol. Lett.*, **3**, p. 625, 1991.
4. F. F. Ruhl, "Accurate analytical formula for gain-optimised EDFAs", *Electron Lett.*, **28**, p. 312, 1992.

Influence of cross-relaxation parameter on the sensitized photon avalanche

E. Osiac, V. Lupei

Institute of Atomic Physics, Bucharest, R-76900, Romania

ABSTRACT

The paper discusses the influence of cross-relaxation parameter on the characteristics of the sensitized photon avalanche.¹ A system Pr^{3+} as activator ion and Yb^{3+} as sensitizer ion were considered for the avalanche process. By numerical modelling of a system of rate equations, time dependencies and pump rate dependencies of populations of energy levels were calculated for three different values of cross-relaxation rate. Correlation between cross-relaxation rate and threshold value of pump intensity was established.

Keywords: sensitized photon avalanche, cross-relaxation process

1. INTRODUCTION

Due to the increasing area of applications of solid state laser, search for new mechanism and materials being able to generate laser emission, is in continuous extension. The existence of efficient and narrow spectral range pumping sources in near infrared (laser diodes), makes the search for processes which could upconvert a infrared pumping light into a visible u.v emission, of great interest. Photon avalanche effect is such a process, and is based on an excited state absorption (ESA) from a metastable state, followed by a cross-relaxation process between an excited ion and a ground state ion, that feeds two excitation in the energy level on which originates ESA (called reservoir). Unfortunately, such a process requires a large concentration of dopant ion, which is not always possible due to technological reasons, and/or because it could generate parasitic de-excitation which may stop the avalanche process. In order to overcome this inconvenient we may codope the crystal host with another species of ion (sensitizer). The sensitizer has to fulfill some conditions: to cross-relax with the activator, to transfer back the excitation to the activator ion and to enter into the crystalline host in a large concentration. If the choice of activator and sensitizer is suitable, we may obtain sensitized avalanche by pumping resonantly from reservoir level of the activator, followed by a cross-relaxed process between an excited activator ion (on the emitting level) and a sensitized ground state ion. The excited level of sensitizer is also feed by a weak, nonresonant pump. At the same time the sensitizer must transfer back the excitation to an activator ion being into ground state, exciting it to the reservoir level. It is possible to obtain in this manner an avalanche like population of the reservoir level which induces, due to resonant efficient ESA between reservoir and emitting level, an avalanche population of the emitting level¹.

However, the avalanche process requires threshold value for some of the parameters². One of the most important parameters is the cross-relaxation rate. This process is in strong competition with all de-excitation processes (radiative and nonradiative) of the reservoir level, and consequently it has to fulfill particular conditions in order to make the avalanche process possible.

This paper presents the influence of cross relaxation parameters on the characteristics of the sensitized photon avalanche process and on the other parameters of the system.

e-mail: eugen@pluto.infim.ro

2. RESULTS

The scheme of sensitized photon avalanche is presented in Figure 1, where A denotes the activator ion and S denote the sensitizer ion. W_{22} and W_{23} are the de-excitation rates for the reservoir and the emitting level and W_{12} is the de-excitation rate for the sensitizer excited level and r is the back transfer rate. Cross-relaxation rate is denoted by s , while u and t represent the rates for the three ion processes, and p and q are the rates for cross-relaxation process between activator ions and the second step of the back transfer from S to A.

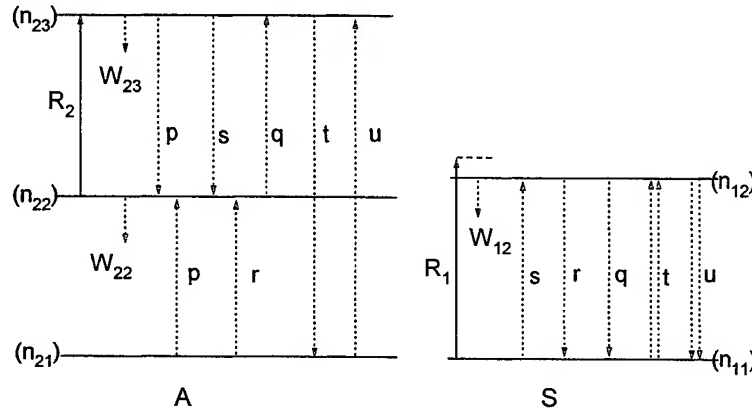


Figure 1 The sensitized avalanche scheme

The sensitized avalanche process can be described by a system of rate equations (1). This system admits an analytical solution only in particular case (stationary regime, low depletion of the ground states and in absence of three ion processes). By taking into account this solution, one can predict the threshold values and conditions for avalanche parameters³.

In order to solve numerically the system (1) we take into account the concrete parameters by consider the pair Pr^{3+} as activator and Yb^{3+} as sensitizer^{4,5}. The levels involved are $^3\text{P}_0$ (n_{23}), $^1\text{G}_4$ (n_{22}), $^3\text{H}_4$ (n_{21}) as emitting, reservoir and ground state energy level and in case of sensitizer $^2\text{F}_{7/2}$, (n_{11}), $^2\text{F}_{5/2}$ (n_{12}), as excited and ground state level.

$$\begin{aligned}
 \frac{dn_{11}}{dt} &= -sn_{11}n_{23} + rn_{12}n_{21} + W_{12}n_{12} + qn_{12}n_{22} - 2tn_{11}^2n_{23} + 2un_{12}^2n_{21} - R_1n_{11} \\
 \frac{dn_{12}}{dt} &= sn_{11}n_{23} - rn_{12}n_{21} - W_{12}n_{12} - qn_{12}n_{22} + 2tn_{11}^2n_{23} - 2un_{12}^2n_{21} + R_1n_{11} \\
 n_{11} + n_{12} &= n_{10} \\
 \frac{dn_{21}}{dt} &= W_{22}n_{22} + bW_{23}n_{23} - rn_{21}n_{12} - pn_{21}n_{23} + tn_{23}n_{11}^2 - un_{12}^2n_{21} \\
 \frac{dn_{22}}{dt} &= -R_2n_{22} - W_{22}n_{22} + sn_{23}n_{11} + rn_{12}n_{21} + (1-b)W_{23}n_{23} + 2pn_{21}n_{23} - qn_{22}n_{12} \\
 \frac{dn_{23}}{dt} &= R_2n_{22} - W_{23}n_{23} - sn_{23}n_{11} - pn_{23}n_{21} + qn_{22}n_{21} - tn_{23}n_{11}^2 + un_{21}n_{12}^2 \\
 n_{21} + n_{22} + n_{23} &= n_{20}
 \end{aligned} \tag{1}$$

The analytical solution of the threshold value of ESA can be obtain in the conditions specified above and is given by

$$R_{2\text{lim}} = \frac{(sn_{10} + W_{23})[W_{22}(rn_{20} + W_{12}) + R_1(W_{22} + rn_{20})]}{srn_{10}n_{20} - b(rn_{20} + W_{12})W_{23} - R_1(rn_{10} + bW_{23})} \quad (2)$$

The conditions of a positive value for $R_{2\text{lim}}$ imposes a threshold value for the cross-relaxation

$$sn_{10} > bW_{23} + \frac{r_{10}}{n_{20}} R_1 \quad (3)$$

The dependence of $R_{2\text{lim}}$ on the cross-relaxation parameters, by taking for the other parameters values characteristic for Pr^{3+} (as activator) and Yb^{3+} (as sensitizer) predicted by equation (2) is represented in figure 2. A saturation like dependence of $R_{2\text{lim}}$ on s is observed.

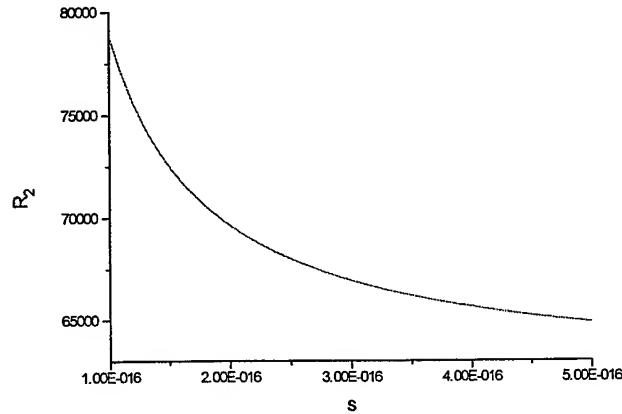


Figure 2 Dependencies of threshold pumping rate on cross-relaxation rate

The numerical modelling was made for three different values for cross-relaxation rate s , in ratios of 1 : 2.5 : 5, starting with $s=1 \cdot 10^{-16} \text{ cm}^3 \text{ s}^{-1}$. For each of these values both the temporal evolution of populations of the levels, which show that after a particular time t_p a stationary regime is reached, and the stationary values of steady state populations versus pump rate R_2 were calculated. The stationary population of the emitting level is quite particular for the avalanche process and it could be seen that three distinct zone exist: under the threshold value $R_{2\text{lim}}$ of the pumping rate a weak quadratic dependence on the pump intensity is observed, immediately above $R_{2\text{lim}}$ a dramatically increase of the populations of the emitting level with small increase of the pumping rate takes place, and this is followed by a saturation-like behavior.

Figures 3 and 4 represent the dependencies of steady state populations of emitting and reservoir level on the pumping rate, for the three different values of the cross-relaxation parameters and several important conclusions can be drawn from these figures:

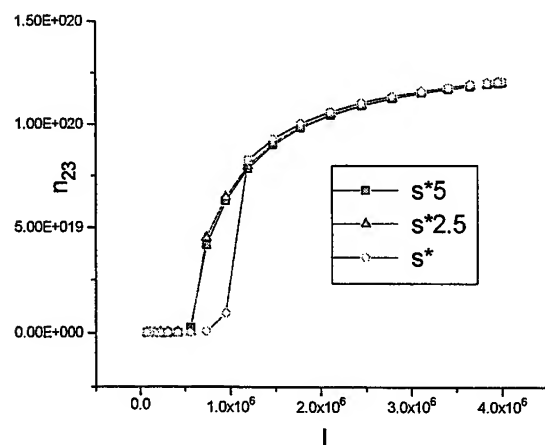


Figure 3 Dependencies of steady state value of emitting level's populations from pump intensities

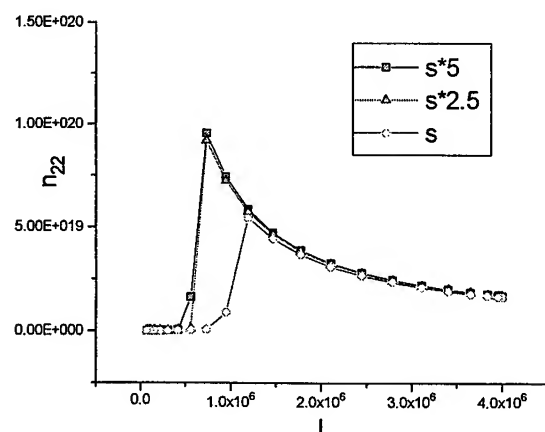


Figure 4 Dependencies of steady state value of reservoir level's populations from pump intensities

-in the saturation zone the values of steady state populations of the emitting level are almost the same for all three cases

-the threshold value of the pumping rate is almost the same for the cases $s=2.5 \cdot 10^{-16} \text{ cm}^3 \text{ s}^{-1}$ and $s=5 \cdot 10^{-16} \text{ cm}^3 \text{ s}^{-1}$ and bigger for $s=1 \cdot 10^{-16} \text{ cm}^3 \text{ s}^{-1}$

-the value of threshold pumping rate is in good agreement with theoretical dependencies of figure 2

-in the case of reservoir level, the shape of steady state populations dependence on pumping rate has a peak, which in the cases of $s=2.5 \cdot 10^{-16} \text{ cm}^3 \text{ s}^{-1}$ and $s=5 \cdot 10^{-16} \text{ cm}^3 \text{ s}^{-1}$ has the same value and is located almost on the same value of pumping rate, but for the case $s=1 \cdot 10^{-16} \text{ cm}^3 \text{ s}^{-1}$ is smaller and located to a high value of pumping rate

-on higher values of pump intensities the steady state value of reservoir level are almost equal for the all three cases

We may conclude from this that a saturation-like behavior of the threshold of the sensitized avalanche takes place with the increase of value of cross-relaxation parameter for the activator ion.

For the case of sensitizer ion, figure.5 shows the steady state populations of the excited level dependencies on the pumping rate. We may observe that in this case semnificative differences between all three cases do exist, not only in the threshold value for pump intensity but also in the intensity dependence of the population and in the maximal value. This difference between the activator and sensitizer could be explain by bottle neck of the back transfer process which means that the

depopulation of the excited level of the sensitizer is lesser on high value of emitting and reservoir level populations, due to the almost complete depletion of ground state level of activator, and consequently the dependence of populations of excited level of sensitizer depends stronger on the value of cross-relaxation rate.

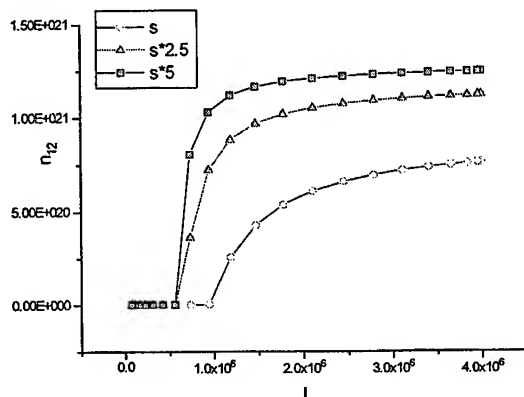


Figure 5 Dependencies of steady state value of sensitizer excited level's populations on pump intensities

The figure 6 shows the temporal evolution of populations for the emitting level n_{23} for all three cases taken into consideration, for the same pumping rate, above the threshold value. We may observe that, the time necessary to reach the steady populations is increasing by lowering the value of cross-relaxation parameter. Also, a change in shape of temporal dependence can be observed on the rise part. The small spike is located on high value of time and populations for the $s=1 \cdot 10^{-16} \text{ cm}^3 \text{ s}^{-1}$ value of cross-relaxation parameters, but for the value of $s=2.5 \cdot 10^{-16} \text{ cm}^3 \text{ s}^{-1}$ and $s=5 \cdot 10^{-16} \text{ cm}^3 \text{ s}^{-1}$ which are almost the same. The differences between these cases are more relevant if we take into consideration the time dependencies of the reservoir level (fig 7). We may observe in this case that both the position and the value of the peak are depending on the value of cross relaxation parameter. We have a faster reach of a higher peak corresponding to a larger value of s , but the decrease to a stationary value is also more radical for this value of s . It could be observe that the stationary value of reservoir populations are the same for all three cases. For the sensitizer ion we have in figure 8, all the three time dependencies. It could be observed that the differences are in the time necessary to reach the saturation region and, in the stationary values of the populations.

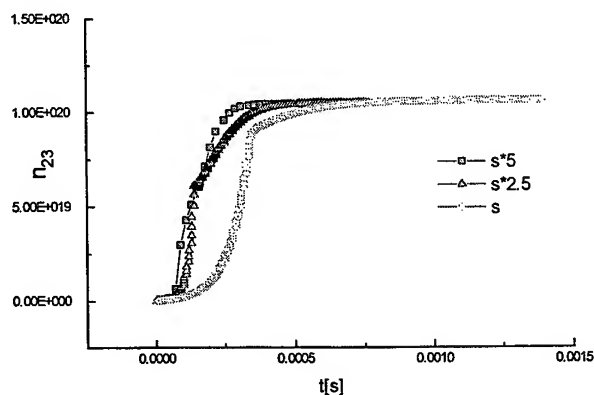


Figure 6 Temporal dependencies of the populations of the emitting level

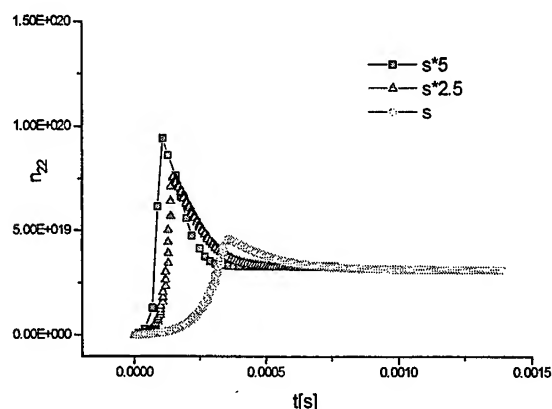


Figure 7 Temporal dependencies of the populations of the reservoir level

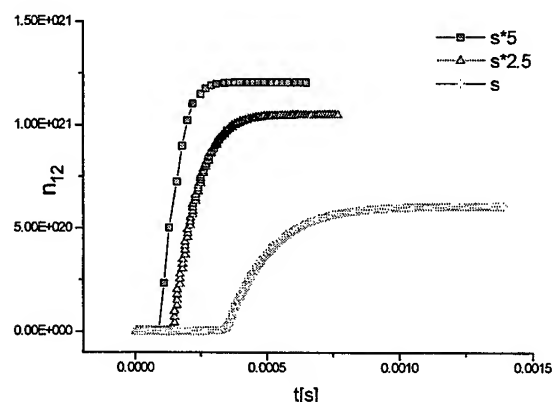


Figure 8 Temporal dependencies of the populations of the sensitizer exciting level

3.CONCLUSION

The value of cross-relaxation rate is determinant for the existence of sensitized photon avalanche, because under some particular value this regime could not be established. The influence on the main characteristics is major, the threshold value of pumping rate, the time necessary to reach the stationary regime, the value of populations under a certain intensity of pump, being under a strong correlation with the cross-relaxation parameter. However, a saturation behavior is taking place in dependencies of values of steady state populations and threshold value of pumping rate, on the cross-relaxation parameter, but for the temporal dynamics of level's populations still remain more significant differences. Differences between dependencies of the activator and sensitizer ion on the cross-relaxation rate shows that for an efficient avalanche process the dynamic of sensitizer population must be taken into consideration.

REFERENCES

1. V. Lupei, *Spectrochim. Acta A* **54**, 1615 (1998)
2. M. F. Joubert, S. Guy, B. Jacquier, *Phys. Rev. B* **48**, 10031 (1993)
3. V. Lupei, E. Osiac, T. Sandrock, E. Heumann, G. Huber; *J. Electrochem. Soc. Luminescent Mat.* **vol.97-29** (1998)
4. T. Sandrock, E. Heumann, G. Huber, B. H. T. Chai, in *OSA Proc. On Advanced Solid State Lasers*, vol. I, Washington DC p. 550, 1996,
5. V. Lupei, E. Osiac, G. Huber, E. Heumann, T. Sandrock, *J. Lumin.* **76/77**, 441 (1998):

The characterization of coated optical components by laser calorimetry

T. Visan, D.G. Sporea*

National Institute for Lasers, Plasma and Radiation Physics, Magurele,
Atomistilor St. 111, RO-76900, Romania

ABSTRACT

This paper presents a new computing procedure for measuring the bulk absorption coefficient of the laser optical components that present a layered structure as the coated optical components. Previously, this measurement has been conducted usually by laser calorimetry with the procedures provided by ISO 11551. However these methods assume the probes to be homogenous and for the inhomogeneous samples this assumption may introduce significant errors in the value of the absorption coefficient. The method is based upon the general solution of the heat diffusion equation calculated for an optical component irradiated by a laser beam with all parameters known. Because the optical component has a layered structure, in order to obtain the solution of the mentioned equation in each layer, a system of heat equations has to be solved. The solutions of this system correspond to the heat diffusion in each layer and they strongly depend upon the absorption coefficient of each layer. Due to the fact that the values for absorption coefficient are small for the studied samples, these solutions are developed in Taylor series with respect to the absorption coefficient. This development leads to a set of algebrical equations that provides the absorption coefficient value of each layer if the temperature in one point of that layer is known. This method has been experimentally tested by evaluating the absorption coefficient of a ZnSe sample with an AR coating of BaF₂ and the results proved to be in agreement with the results obtained by numerically simulating this process.

Keywords: laser calorimetry, heat diffusion, integral operators

1. INTRODUCTION

Optical components for high power/energy lasers have to satisfy rigorous requirements to minimize losses caused by absorption, diffusion, scattering, etc. Hence the measurement of the absorption coefficient is necessary in designing and manufacturing high quality optical components.

There are many methods for evaluating the absorption coefficient value and mostly used is the laser calorimetry¹⁻³ with the standardized versions: gradient method and pulse method. These methods are based on the assumption that the optical component is considered homogenous. These assumptions are no longer valid as many optical components are covered with multi-layer AR thin films. However the methods are a good approximation as long as the thin film thermal properties (thermal conductivity, heat capacity, etc.) are close to the thermal properties of the substrate.

Therefore the aim of this study is to develop a calculus method for evaluating the adsorption coefficient in the case of the composite systems presenting a layered structure. In order to solve this problem the heat equation is solved for each layer of the optical component. Afterwards the function that describes the temperature value in each layer is developed in Taylor series with respect to the absorption coefficient taking into account that its value is very small. In this way for each layer is obtained an algebrical equation with the absorption coefficient as the unknown value. These equations are solved and the absorption coefficient for each layer is obtained.

* Correspondence: Email: sporea@ifin.nipne.ro; Telephone: +40-1-7805385 / 1817; Fax: +40-1-4231791

2. CALCULUS METHOD

In this section is presented the solving procedure of the heat diffusion in a layered structure. Also the probe is assumed to be cylindrical and irradiated with a TEM₀₀ laser beam. For the simplicity of the presentation the probe is considered to be double-layered but in the same manner the method can be applied for systems with more than two layers. The width of each layer of the optical component is equal to a and b and the radius is equal to R.

The equation for the heat diffusion process inside a cylindrical double layered optical component irradiated by the laser beam centered to the probe is:

$$\begin{aligned} \frac{\partial^2 T_1}{\partial^2 r} + \frac{1}{r} \frac{\partial T_1}{\partial r} + \frac{\partial^2 T_1}{\partial^2 z} - \frac{1}{\gamma_1^2} \frac{\partial T_1}{\partial t} &= -\frac{\alpha_1}{k_1} I_0 e^{-\alpha_1 z} e^{-\frac{2r^2}{\omega_0^2}} (h(t) - h(t - t_0)) \\ \frac{\partial^2 T_2}{\partial^2 r} + \frac{1}{r} \frac{\partial T_2}{\partial r} + \frac{\partial^2 T_2}{\partial^2 z} - \frac{1}{\gamma_2^2} \frac{\partial T_2}{\partial t} &= -\frac{\alpha_2}{k_2} I_0 e^{-\alpha_1 a} e^{-\alpha_2 z} e^{-\frac{2r^2}{\omega_0^2}} (h(t) - h(t - t_0)) \end{aligned} \quad (1)$$

The significance of the terms involved in relation (1) are as follows:

$\alpha_{1,2}$ = the absorption coefficient value

$\gamma = \frac{k}{c\rho}$; c = heat capacity; ρ = density

ω_0 = radius of the laser beam

I_0 = intensity of the laser beam

t_0 = the time of exposure to the laser beam

$h(t)$ is the step function of Heaviside

The boundary condition corresponding to the equation (1) are as follows:

$$\begin{aligned} \left. \frac{\partial T_1(r, z, t)}{\partial z} \right|_{z=0} - ET_1(r, 0, t) &= 0 \quad \left. \frac{\partial T_2(r, z, t)}{\partial z} \right|_{z=a+b} + ET_2(r, 0, t) = 0 \\ T_1(r, a, t) &= T_2(r, a, t) \\ k_1 \left. \frac{\partial T_1(r, z, t)}{\partial z} \right|_{z=a} &= k_2 \left. \frac{\partial T_2(r, z, t)}{\partial z} \right|_{z=a} \\ \left. \frac{\partial T_{1,2}(r, z, t)}{\partial r} \right|_{r=R} - ET_{1,2}(R, z, t) &= 0 \\ T_{1,2}(R, z, 0) = T_{\text{initial}} \quad T_{1,2}(r, z, t) \Big|_{r \rightarrow \infty} &= 0 \end{aligned} \quad (2)$$

where E is the emissivity of the outer surface of the optical component and $k_{1,2}$ is the thermal conductivity of each layer.

The boundary conditions (2) correspond to a cylindrical optical component that radiates heat through its outer surface with emissivity equal to E. Also we have written the continuity and energy conservation relations to the interface between layers ($z=a$).

In order to solve the system of parabolic partial differential equations (1) an integral operator is applied to each equation of the system. This integral operator corresponds to the partial differential equation (3).

$$\frac{\partial^2 K_{1,2}}{\partial r^2} + \frac{1}{r} \frac{\partial K_{1,2}}{\partial r} + \lambda_{1,2}^2 K_{1,2} = 0 \quad (3)$$

$\lambda_{1,2}$ = the eigenvalue for the differential operator $\frac{\partial^2}{\partial r^2} + \frac{1}{r} \frac{\partial}{\partial r}$. The expression of this integral operator is given by the solution of equation (3) and is equal to: $K_{1,2} = J_0(\lambda_{1,2} r)$ where J_0 is the Bessel function.

By applying this integral operator the system (1) becomes:

$$\begin{aligned} -\lambda_{1i}^2 \bar{T}_1 + \frac{\partial^2 \bar{T}_1}{\partial z^2} - \frac{1}{\gamma_1^2} \frac{\partial \bar{T}_1}{\partial t} &= -\bar{f}_1(\lambda_{1i}, z, t) \\ -\lambda_{2i}^2 \bar{T}_2 + \frac{\partial^2 \bar{T}_2}{\partial z^2} - \frac{1}{\gamma_2^2} \frac{\partial \bar{T}_2}{\partial t} &= -\bar{f}_2(\lambda_{2i}, z, t) \end{aligned} \quad (4)$$

where:

$$\begin{aligned} \bar{T}_{1,2} &= \frac{1}{C_{1,2}} \int_0^R T_{1,2}(r, z, t) K_{1,2}(r, \lambda_{1,2}) dr \\ \bar{f}_1(\lambda_1, z, t) &= I_0 \frac{h(t) - h(t - t_0)}{C_1} \int_0^R \frac{\alpha_1}{k_1} e^{-\alpha_1 z} e^{-\frac{2r^2}{\omega_0^2}} K_1(r, \lambda_1) dr \\ \bar{f}_2(\lambda_2, z, t) &= I_0 e^{-\alpha_1 z} \frac{h(t) - h(t - t_0)}{C_2} \int_0^R \frac{\alpha_2}{k_2} e^{-\alpha_2 z} e^{-\frac{2r^2}{\omega_0^2}} K_2(r, \lambda_2) dr \end{aligned}$$

The parameters $C_{1,2}$ are the normalizing factors for the applied integral operator and are given by the expression:

$$C_{1,2} = \int_0^R r K_{1,2}^2(r, \lambda_{1,2}) dr$$

At this point is important to establish a relationship for calculating the eigenvalues $\lambda_{1,2}$. This relation is given in expression of the boundary condition at $r = R$ (2).

$$E J_0(\lambda_{1,2} R) - \lambda_{1,2} J_1(\lambda_{1,2} R) = 0 \quad (5)$$

From (5) one can observe that $\lambda_1 = \lambda_2 = \lambda$.

To the system (4) the Laplace transform L is applied and the result is the system (6).

$$\begin{aligned}
& -\lambda_i^2 \tilde{T}_1(\lambda_i, z, s) + \frac{\partial^2 \tilde{T}_1(\lambda_i, z, s)}{\partial z^2} - \frac{s}{\gamma_1^2} \tilde{T}_1(\lambda_i, z, s) = -\left(\frac{1}{s} - \frac{e^{-st_0}}{s}\right) \tilde{f}_1(\lambda_i, z) \\
& -\lambda_i^2 \tilde{T}_2(\lambda_i, z, s) + \frac{\partial^2 \tilde{T}_2(\lambda_i, z, s)}{\partial z^2} - \frac{s}{\gamma_2^2} \tilde{T}_2(\lambda_i, z, s) = -\left(\frac{1}{s} - \frac{e^{-st_0}}{s}\right) \tilde{f}_2(\lambda_i, z) \\
& \tilde{T}_{1,2}(\lambda_i, z, s) = L\left\{\tilde{T}_{1,2}(\lambda_i, z, t)\right\}; \tilde{f}_{1,2}(\lambda_i, z, s) = L\left\{\tilde{f}_{1,2}(\lambda_i, z, t)\right\}
\end{aligned} \tag{6}$$

The solution for the equations (6) is (7):

$$\begin{aligned}
\tilde{T}_1(\lambda_i, z, s) &= M_1 e^{-A_1 z} + N_1 e^{A_1 z} - \frac{1}{A_1 + \alpha_1^2} \frac{e^{-st_0}}{s} \tilde{f}_1(\lambda_i) e^{-\alpha_1 z}; A_1 = \left(-\lambda_i^2 - \frac{s}{\gamma_1^2}\right)^{\frac{1}{2}} \\
\tilde{T}_2(\lambda_i, z, s) &= M_2 e^{-A_2 z} + N_2 e^{A_2 z} - \frac{1}{A_2 + \alpha_2^2} \frac{e^{-st_0}}{s} \tilde{f}_2(\lambda_i) e^{-\alpha_2 z}; A_2 = \left(-\lambda_i^2 - \frac{s}{\gamma_2^2}\right)^{\frac{1}{2}}
\end{aligned} \tag{7}$$

The constants $M_{1,2}$ and $N_{1,2}$ are obtained from the condition of continuity and energy conservation at interface $z = a$.

$$\begin{aligned}
& \tilde{T}_1(\lambda_i, a, s) = \tilde{T}_2(\lambda_i, a, s) \\
& k_1 \left. \frac{\partial \tilde{T}_1(\lambda_i, z, s)}{\partial z} \right|_{z=a} = k_2 \left. \frac{\partial \tilde{T}_2(\lambda_i, z, s)}{\partial z} \right|_{z=a}
\end{aligned}$$

The solutions in Laplace space are: $\tilde{T}_{1,2}(r, z, s) = \sum_{i=1}^{\infty} J_0(\lambda_i r) \tilde{T}_{1,2}(\lambda_i, z, s)$ and the general solution for the system (1) is: $T_{1,2}(r, z, t) = L^{-1}\left\{\tilde{T}_{1,2}(r, z, t)\right\}$

The calculated solution for temperature field distribution corresponding to a double-layered cylindrical probe is presented in Fig. 1. The first layer correspond to a thin film layer of BaF_2 of width equal to 3 μm .

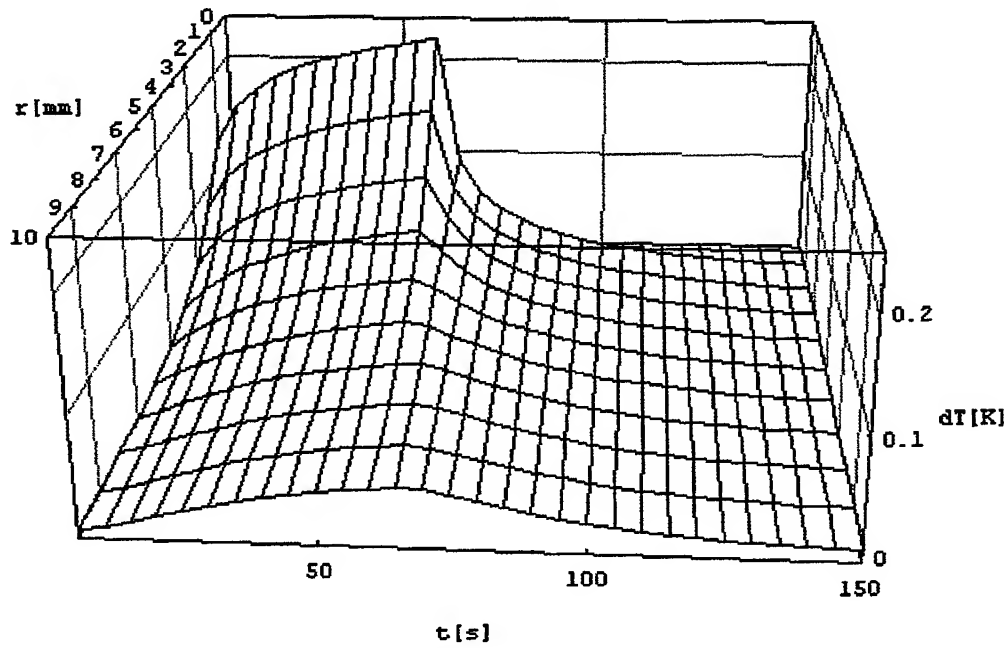


Fig. 1 Calculated temperature field distribution into a ZnSe probe exposed to a 10 W CO₂ laser beam for 60 s

To establish an expression for the absorption coefficient values first the exponential $e^{-\alpha_{1,2}z}$ are developed in Taylor series:

$$e^{-\alpha_{1,2}z} \approx 1 - \alpha_{1,2}z \quad (8)$$

Rewriting the equation (6) in Laplace space and using the relation (8) an algebrical equation is obtained and the solution for $\alpha_{1,2}$ are:

$$\alpha_{1,2} = \frac{-S_{1,2A} + \sqrt{S_{1,2A}^2 - 4S_B C_{1,2}}}{2S_{1,2B}} \quad (9)$$

where:

$$S_{1,2A} = \sum_{i=1}^{\infty} \tilde{T}_{1,2}(\lambda_i, z, s) - M e^{-A_{1,2}z} - N e^{-A_{1,2}z}$$

$$S_B = \left(\frac{1}{s} - \frac{e^{-st_0}}{s} \right) z$$

$$C = \frac{S_B}{z}$$

The relation (9) provides the values of absorption coefficient of each layer if case that the terms S_A , S_B and C can be calculated. These terms can be calculated if the temperature for one point of each layer is known.

3. CONCLUSIONS

This paper presents a simple method to calculate the absorption coefficients for a multi-layer system based on measuring the temperature in a single point of each layer at one moment. We have rigorously described the mathematical method for solving the heat diffusion equation for such systems and derived a formula (9) for calculating the absorption coefficient of each layer.

In the calorimetric procedure for measuring the absorption coefficient the temperature is supposed to be measured in a single point of the probe over a period of time determined by the exposure time. The advantage of this method is that requires only two points for temperature measurement made at a single moment.

The value of absorption coefficient determined by calorimetry is a mean value for probe absorption. The proposed method provides the absorption coefficient of each layer of the composed probe. Therefore the method could be employed to measure the absorption of the thin films deposited on a substrate. The fact that the proposed procedure requires only a single value of the temperature $T(r,z,t)$ makes it sensible to the errors determined by the measuring process. The question to answer at this point is what are the most favorable conditions for temperature measurement. Some studies were conducted on this subject and the measuring point should be as far as possible from the irradiating laser beam.

Regarding the moment of the temperature measurement this should be when the probe is heated enough to have a temperature measured by the thermal sensors significant regarding to their tolerance. The moment should be also situated in a point of minimum slope of the function describing the temperature versus time in order to reduce the errors induced by the inertia of the thermistors.

From the experimental point of view there is no difference between the proposed method and the laser calorimetry method, only the calculus method making the difference between them.

In order to reduce the errors⁴ the exposure time should be no longer than 30 s and the radius of the laser beam should not exceeds 10 % from the radius of the probe.

Looking at the expressions corresponding to the absorption coefficients one may consider that they require a significant computing power in order to reach an acceptable convergence. Some calculations were conducted and the sums involved in the mentioned expression converge very fast and for our calculation after 10 iterations the precision has reached a value of 10^{-1} . The only problem difficult to overcome could by the calculation of the eigenvalues required for absorption coefficient values. The equations that provide these eigenvalues are solved numerically, but once two consecutive eigenvalues are determined the others are determined very quickly as they presents a cuasi-periodicity.

These expressions of the absorption coefficients are calculated numerically like the eigenvalues they contain but most of the mathematical software packages provides procedures for a very fast numerical evaluation of such expression and also very fast procedures for numerically calculation of the roots of equations. Therefore we recommend the implementation of the mathematical model described in this paper using such a mathematical software package.

REFERENCES

1. ***, ISO/TC172/ SC9, Test Method for absorptance of optical laser components, ISO/DIS 11551, 1994.
2. B. Steiger, U. Pfeifer, P. Meja, U. Broulik and V. Neumann, "Practicability of absorption measurements according to ISO/DIS 11551", *Proc. SPIE*, **2870**, pp. 495-501, 1996.
3. A.P. Kubyshev, M.P. Matrosov and A.A. Karabutov, "Photothermal measurements of bulk and surface absorption of transparent infrared optical elements", *Opt. Eng.*, **35**, pp. 3214-3218, 1996.
4. T. Visan, D. Sporea and G. Dumitru, "Computing method for evaluating the absorption coefficient of infrared optical elements", *Infrared Physics and Technology*, **39**, pp. 335-346, 1998.

Studies upon the execution of the materials puncture inlet opening chemical metallizing

Emil Petrescu^{a*}, Paul Penciu^b, Camelia Petrescu^b, Marinela Catrinciuc^b

^a University "Politehnica" Bucharest, Splaiul Independentei 313, Romania

^b Research and Development Institute for Electrical Engineering Bucharest, Splaiul Unirii 313, Bucharest, Romania

ABSTRACT

The short presentation of the YAG: Nd laser's parameters is followed by phenomena that take place at the intersection of the laser radiation with the material to be processed. The laser induced temperature distribution, the parameters that condition the laser process use, the factors that influence the precision of the laser operation, and the technological particularities on the puncture, are problems dealt with before the experimental research's results. The abstract presents a method of selective chemical metallizing of the puncture made in ceramics, as well as application areas and advantages of the laser puncture.

Keywords: laser, chemical metallizing, ceramic

1. INTRODUCTION

The laser is one of the few scientific achievements that found themselves large and varied applications in all the scientific and technical areas in a very short period of time.

It is necessary to know the conditions which the process could be done within, the interactions between the laser radiation and the material to be processed, the energetic parameters and the beam control parameters, the possibilities of quality assurance, the precision and the technical-economical efficiency of the process.

The laser beams are stimulated radiation with specific properties, different from the radiation emitted by the classical sources. Among these properties we mention: the radiation's coherence, the direction, the monochromatism, the radiation's intensity, the low divergence of the beam and the very high power density.

The YAG: Nd laser (the YAG-Y₃Al₅O₁₂ laser doped with neodymium ions) is part of the laser series with solid active mediums that has the following parameters:

- * wave length: 1.064 λ ;
- * photon's energy: 1.86×10^{-19} J;
- * doping density: 2.83×10^{20} cm⁻³;
- * radiation's typical angular divergence: 4.5-5 mrad;
- * maximum output: 2×10^7 W;
- * impulse's maximum energy: 0.005 J;
- * impulse's duration: 1.5×10^{-8} s.

2. PHENOMENA THAT TAKE PLACE AT THE INTERSECTION BETWEEN THE LASER RADIATION AND THE MATERIAL TO BE PROCESSED

For a correct evaluation of the possibilities and limitations of the laser process' technologies, it is important to know all the phenomena that occur at the intersection between the laser radiation and the material to be processed. The analysis of the

radiation's effects has to take into account the absorbed part of the incident flux, the energy's maximum density, the laser's duration, the energy's spectral distribution, focusing conditions, and the radiation's wave length.

The working parameters in the laser process' technologies are determined, on the one hand, by the installation's type, and on the other hand, by the physical-chemical characteristics, temperature and the status of the material surface.

The change of the laser radiation energy into the caloric energy takes place because of the absorption phenomenon from the I_0 intensity flux, that falls on the piece - part of it, RI_0 , is reflected by the material's surface, and another part, $(I-R)I_0$, goes into the material.

The radiation's intensity that penetrates the material will lower exponentially, according to the absorption law:

$$I(z) = I_0(I-R)e^{-\alpha z}$$

where:

R = reflecting coefficient

α = absorption coefficient

Both terms depend on the optical and physical characteristics of the material, on the status of its surface, and on the radiation's wavelength. At the majority of metals, the reflection degree grows with the size of the radiation's wave length.

Another factor that has to be taken into account, because it influences the laser, radiation absorption, is the roughness of the piece's surface that will be processed. It is recommended that the R_z roughness should be greater than the wave length of the incidental laser radiation. The absorption's variation grows according to the temperature of the piece's surface, as this law states:

$$A \approx A_0 \sqrt{1 + \alpha (T_i - T_0)}$$

where:

A_0 = the absorption capacity at the reference temperature

α = constant that depends on the piece's material

T_i = the heating temperature of the piece

3. THE LASER INDUCED TEMPERATURE DISTRIBUTION

At the laser beam impact with the piece's material, the radiation energy changes into caloric one, that travels into the material and modifies its thermal status.

The graphical representation of the laser radiation's action, on the material to be processed, is shown in Fig 1.

The thermal flux propagation within the piece depends on the penetration depth in the material, on the reflectivity changes with the temperature, on time and other factors.

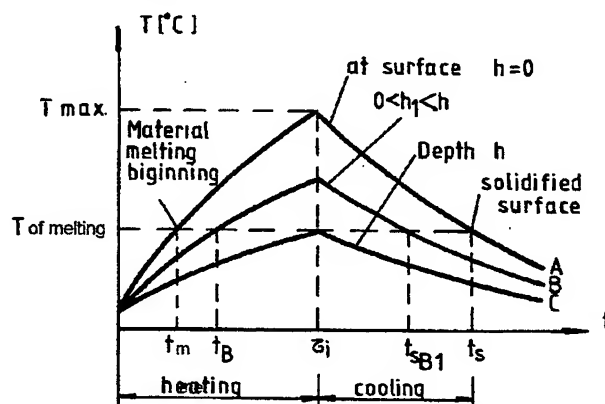


Fig. 1 The graphical representation of the laser radiation's action on the material to be processed

Fig. 2 shows the temperature changes in the material for certain action spans of time of the laser.

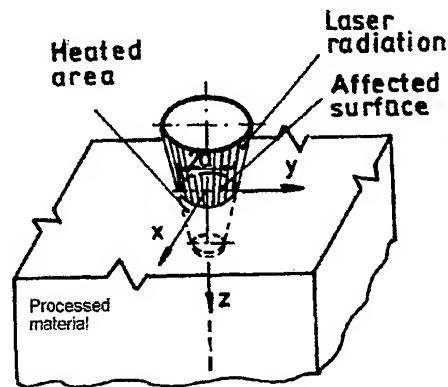


Fig. 2 The temperature variation depending on the penetration depth

4. THE PARAMETERS THAT CONDITION THE LASER PROCESS USE

One of the most important parameters that determine the process type that can be done by laser is the radiation's power density. If the temperature field distribution is known, the critical density of the radiation power q_c , that produces a certain temperature T_m on a surface or in a volume of material, for a laser action duration τ_i (or a moving speed V_p of the piece in front of the beam) can be determined.

$$q_c = 0.885 \lambda T_m / \sqrt{d \tau_i}$$

The dependence between the power density and the laser's action duration is shown in Fig. 3.

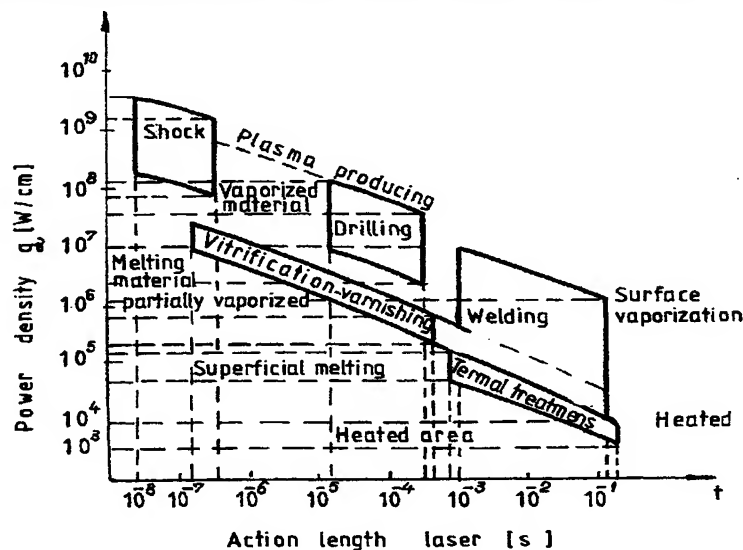


Fig. 3 The laser process possibilities depending on the power density level and the laser action duration

5. THE FACTORS THAT INFLUENCE THE LASER OPERATION'S PRECISION

Using high concentrated radiation, the processing's sizes are relatively small. Thus, the study of the factors that affect the execution precision becomes very important.

The laser process' precision may be treated in two ways: macro- and micro-geometrically.

The execution precision is determined, macro-geometrically by:

- * laser radiation's parameters:
 - * the beam power;
 - * the laser action duration;
 - * the material's spot size.
- * the way the piece is positioned in relation with the radiation's focusing point in the xOy plan and on the Oz axis, respectively with the size and direction of the non-focusing.

From the micro-geometrically point of view, the laser process precision depends on:

- * the way the laser radiation is generated;
- * the spatial and temporal distribution of the beam's energy;
- * the generator's optical systems' imperfections;
- * the temporal and spatial stability of the radiation's parameters.

Other factors that affect a lot the time stability of the laser radiation's parameters, respectively the execution precision of the process, depend on both the wear and using time of the resonant cavities' mirrors and of the pumping cavity of the reflecting surfaces, and on the optical systems' elements of the laser generator.

6. THE TECHNOLOGICAL PARTICULARITIES AT THE PUNCTURE EXECUTION

Similarly with the other laser process procedures, the puncture is based also on the thermal effect of the radiation over the materials.

The use of the laser radiation for the making of the inlet openings in vary materials was the laser's first technological application.

Very fine inlet openings can be done, having the diameter equivalent with the wavelength's size of the radiation, but the inlet openings' sizes are limited to maximal thickness of the material of 12-14 mm and diameter of 0.015-1.5 mm.

At the establishing of the parameters of the puncture process, aside from the correlation of the radiation power density with the laser action power and with the properties of the material to be processed, it is necessary to take into account the radiation absorption degree by the material, because a greater part of the E laser energy might be lost through reflection, from the surface of the piece.

$$E_a = (16R)E$$

where:

R = the material's reflection factor

7. EXPERIMENTAL RESEARCH'S RESULTS

The laser puncture process occurs almost instantaneous. The removal of the material through the radiation's action takes place step by step, starting with a quasi-static phase of heating and overheating of the material, that goes fast into another dynamic melting phase, vaporisation and exhaustion of the gaseous, solid, and liquid products, that are being obtained.

In Fig. 4, the absorption degree of some non-metallic materials is shown; these materials are much used in the making of some laser-punctured pieces, according to the radiation's wavelength. Inlet openings of vary shapes (cylindrical, conic, bulb-shape) can be obtained through the correct control of those elements because the final profile of the formed cavity after the material vaporisation is determined mainly by the radiation focusing mode and the laser impulse's shape.

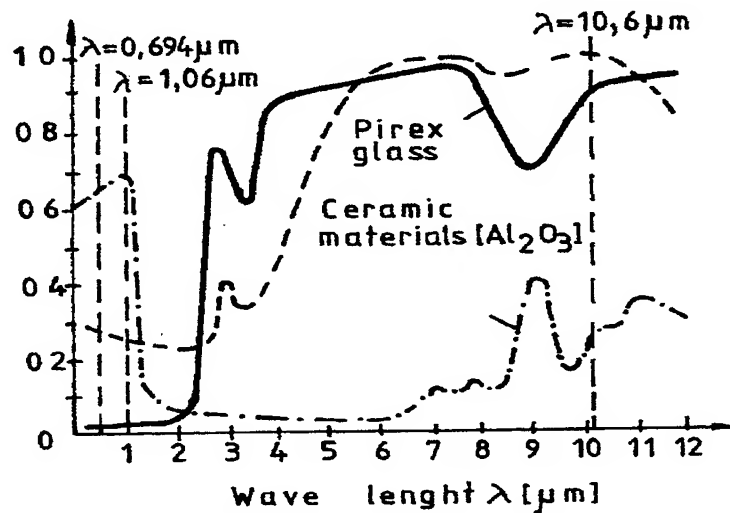


Fig. 4 The absorption; degree of some non-metallic materials

The appreciation of the v_c speed, that heat penetrates into the material with, is done knowing the t time $t = \tau_i$ (the span of time of a laser impulse)

$$v_c = z_c / t_i = 2K / t_i$$

where:

$z_c - 2Kt_i$ = the penetration; depth of the heat in the material
 K = the thermal conductivity of the material
 t = the laser action span of time

If the luminous energy flux $I(t)$ absorbed by the material at the time t , then:

ρ = the specific mass of the material
 T_v = the vaporisation temperature
 L_v = the vaporisation latent heat of the material to be processed

Based on the energy preservation principle, the speed of heading of the vaporisation's front of the material can be determined.

$$V_v(t) = I(t) / \rho(L_v + cT_v)$$

where:

c = the specific heat of the material

The puncture process has the following stages:

- * Following the laser radiation absorption at the material's surface, an increase of the internal energy in the affected micro-zone takes place, much above the equilibrium values;
- * Local vaporisation of some thin layers are produced (5 nm up to 50 nm);
- * The rapid increase of the temperature, with the heating of some material particles adjacent to the radiation focusing point. During a laser impulse (of T_i span of time), aside from the increase of the inlet opening depth, a much increase of the diameter appears, because between the penetration depth h and the diameter of the inlet opening d , there is a non-linear energetic dependence. Another controlled parameter that influences the evolution of the vaporisation process of the material to be processed, and thus the puncture parameters, is the laser action duration, respectively the duration and the number of the overlapping laser impulses.

Fig. 5 shows the variant of the penetration depth h , the diameter d , and the h/d rapport, according to the laser impulse duration.

In the first part of the laser impulse, a rapid increase of the depth and diameter of the inlet opening can be noticed. Actually, 70 % of the depth and 90 % of the diameter are achieved in the first half of the laser impulse duration; after that, a diminishing of the puncture process evolution takes place, determined by the unwanted phenomena that appear in the working zone (shielding, thermal conduction).

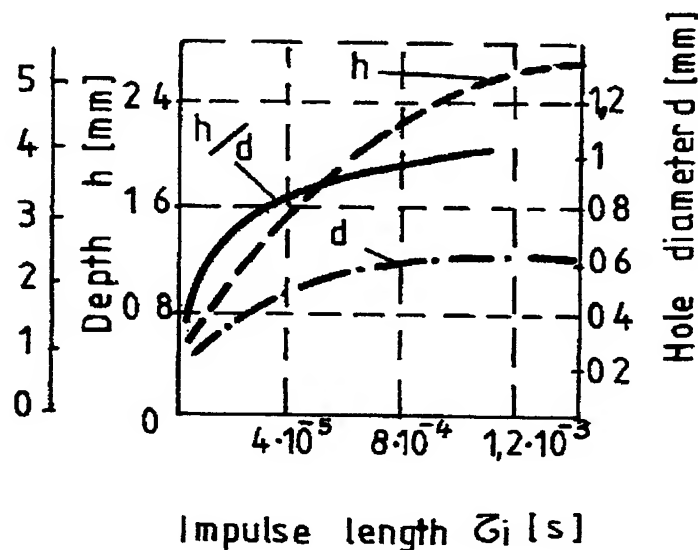


Fig. 5 The inlet opening parameters' variation (d , h , h/d) depending on the laser impulses duration

8. THE SELECTIVE CHEMICAL METALLIZING OF THE PUNCTURE DONE IN THE CERAMIC

Once the ceramic laser puncture is done, the possibility of metallizing these inlet openings through a selective chemical layering appears.

This operation - through a technology that uses the low pressure (evaporation, sputtering, etc.) - leads to lower results, because shading effects appear (unmetallized parts); this happens because the inlet opening direction is almost parallel with the evaporated metallic atoms direction.

After the ceramic puncture is done, its cleaning follows - through immersion in liquid NaOH for 5 minutes, followed by washing in distilled water jet.

After the drying process, over the opening done in the ceramic, a drop of activator paste based on palladium acetate acetyl (PAC 1000 made in ICPE) is being applied. It is treated for 5 minutes at 450°C . The following reaction takes place, reaction verified through differential thermal analysis.

After the activation is done, the inlet openings have been chemically copper-plated. The electrical resistance of the copper path in the puncture, measured between the two faces of the ceramic, was 0.1 ohm.

Ceramic based on Al_2O_3 , AlN , and Si_3N_4 has been metallized.

9. APPLICATION FIELD AND LASER PUNCTURE ADVANTAGES

The laser puncture covers the field of the low dimensions inlet opening making in hard fuse materials having high hardness, with dielectric properties or being good electric conductors, because of the particularities of the material removal process.

The crystals puncture process has been introduced into the current industrial production, in order to obtain small dimensions bearings and screw plates for wire drawing of yarns and micro-yarns. Also, the laser is used successfully for the making of the screw plates' inlet openings for the obtaining of glass yarns, of some micro-inlet openings networks into the ferrite plates for memories, and for the process of some micro-filters from super-alloys.

The laser's using for puncture operations presents a series of advantages, comparing with similar procedures (ultrasounds, electron beam, plasma, electro-erosion):

- * there is no physical contact with the pieces to be processed, the internal tension, the strains and the piece's wear being lowered or even eliminated;
- * any metal could be processed, regarding its properties and characteristics;
- * high precision positioning and processing could be done;
- * the influential thermal zone, adjacent to the inlet opening is reduced to a minimum, because of a very low span of time of the procedure;
- * inlet openings having very high h/d can be done;
- * the laser puncture process allows a complete automatization and the implementation of the numerical control;
- * the considerable shortening of the processing time, the process taking place almost instantaneously.

Thus, the laser process has a wide spectrum of industrial application for: the surface operation of the metallic pieces, the making of the welding assemblies for lamina, micro-contacts and yarns, for punctures, for cuts, trimmings, markings, engravings, static and dynamic balancing, etc.

REFERENCES

1. * * * Laser Handbook, North-Holland Publishing Company, Amsterdam, 1972.
2. Octavian Dontu, Tehnologii de prelucrare cu laser, Editura Tehnica, Bucuresti, 1985.

Plasma Analysis in the Process of Pulsed Laser Deposition of Aluminium Nitride and Titan Nitride Thin Films

C. Grigoriu, Ileana Apostol, *Roxana Rizea, A. Marcu, D. Dragulinescu

Gas Pulsed Lasers Laboratory, National Institute of Lasers, Plasma and Radiation Physics,
P.O. Box M.G. 36, Bucharest, Romania

ABSTRACT

Reactive pulsed laser ablation deposition of thin films is a technique which has already given good results for the formation of metal and semiconductor oxide and nitride films. To improve the quality of the deposited films it is important to understand the ablation process and the materials transport phenomena from the target to the collecting substrate. Optical emission spectroscopy of the plasma plume, formed by the interaction of the laser pulse (KrF laser) with the target (AlN or TiN), is generally used to try to understand the reaction mechanisms during the transport process. A high speed camera was also used to determine plasma plume expansion velocity and the total duration of luminous emission of the plume. The effect of ambient pressure in the ablation chamber on the plasma composition was observed.

Keywords: pulsed laser deposition, optical emission spectroscopy, plasma expansion

1. INTRODUCTION

Pulsed laser deposition (PLD) has been largely applied to obtain thin films of a variety of materials. This technique has been successfully used for dielectric, semiconductor and high-temperature superconducting thin films deposition. Nitrides are very valuable materials, which have found numerous applications ranging from corrosion, radiation-resistant coatings to integrated circuit devices. Aluminium nitride (AlN) is a wide band gap III-IV compound with desirable thermal conductivity, electrical resistivity and acoustic properties. AlN thin films can be a promising material for applications in microelectronics and optoelectronics devices such as passivation and dielectrics layers in integrated circuits, short wavelength emitter and acoustic devices^{1,2}. Titan nitride (TiN) has been extensively studied for the diffusion barrier in advanced integrated-circuit devices.

Problems concerning the nature of species involved in the mass transfer from the target to the substrate, the collision kinetics, the chemistry with the background gas and the correlation between the properties of the deposited films and the characteristics of the plasma induced by the laser are of large interest. It is also highly imperative to control the plasma parameters, like velocity, temperature and electron and ion density, in order to regulate the ablation process³.

Laser ablation, generally, induces the formation of a luminous plasma plume in front of the target that allows one to perform in situ process monitoring. It is supposed that chemical reactions of precursor radicals in the plasma plume strongly affect the film properties and that time and space resolved plasma analysis can contribute to the understanding of the deposition process. There are several techniques for laser-induced plasma diagnostic, including optical emission spectroscopy. Optical emission spectroscopy is a useful tool for in situ plasma characterization during reactive PLD when the presence of an ambient gas makes mass spectroscopy impossible (mass spectroscopy cannot be used at pressures higher than 10^{-4} mbar)⁴.

In attempt to provide more information on the ablation process in general and to assess the performance of nitride systems in particular we have studied the plume species-specific gas dynamics during pulsed laser deposition of AlN and TiN. The dynamics of the flow and composition of the material ejected from AlN and TiN targets have been monitored in real time by optical emission diagnostics. The plume expansion has been examined as a function of time and space in N_2 ambient and in vacuum.

*Corresponding author: Fax: +40 1 423 14 70; Email: roxanar@ifin.nipne.ro

Laser ablation of nitride targets in vacuum leads to deposition of films with a low content of nitrogen. In most cases, during preparation it is necessary to have a supplemental supply of reactive nitrogen for the loss one, that occurs at the stage of ablation, transport and deposition⁵.

This paper presents an emissive spectroscopic study of the emissive plume obtained by irradiation of aluminium nitride (AlN) and titanium nitride (TiN) targets with a Nd: YAG laser, in nitrogen (N₂) atmosphere and in vacuum. This study is very useful, considering our interest in obtaining thin films and nanosize powders of AlN and TiN by laser ablation.

The purposes of this study are to find the emissive elements in visible and ultraviolet domain, which are into this plume, to determine the ablation process efficiency and to study plasma plume expansion in nitrogen atmosphere. We studied changes that occurred in emissive spectra obtained at different nitrogen pressures and in vacuum.

2. EXPERIMENTAL APPARATUS

The diagram of the experimental apparatus used in this study is shown in Fig. 1.

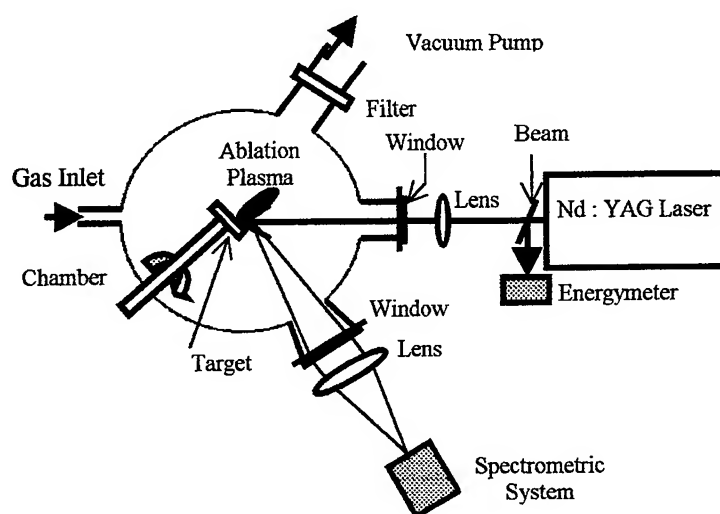


Fig. 1 Experimental set-up

A Nd: YAG, B.M. Industries model 5011-D. NS 10 laser was used as the energy source in these experiments. This laser produced, at $\lambda = 355$ nm, monomod pulses of 7ns, frequency 10 Hz. The pulse energy, which was measured with a power calorimeter (COHERENT LabMaster Ultima), was 50 mJ and fluence 2 J/cm². The laser was focused with a quartz U.V. grade fused silica, antireflex lens, with focal length, $f = 378$ mm. The ablation chamber pressure up to 5×10^{-7} Torr, was realised using an preliminary vacuum pump ULVAC D-650 K and a turbomolecular vacuum pump ULVAC UTM 150.

We have used a Czerny-Tuner, type MC - 25 NP spectrometer, with resolution of 0.08 nm. We have also used aluminium nitrate and titanium nitrate (purity 99.5 %) targets. In order to have a constant removal rate the target was permanently moved by an electric motor, during each experiment.

The experimental parameter varied in this study was nitrogen (purity 99.9999 %) pressure in the ablation chamber. We worked at 100 mTorr, 200 mTorr and in vacuum.

3. RESULTS AND DISCUSSION

Laser ablation of nitride targets in vacuum or inert gas atmosphere leads to deposition of thin films with a low nitrogen content. So, the problem of this kind of deposition is to assure a proper nitrogen content for the material we want to obtain. In most of the cases it is necessary to use a reactive nitrogen atmosphere in order to supply the losses that occur during deposition process. In order to obtain more informations about the laser ablation process, in general, and to improve the nitrogen content in the collected material we have analysed the obtained plasma plume composition.

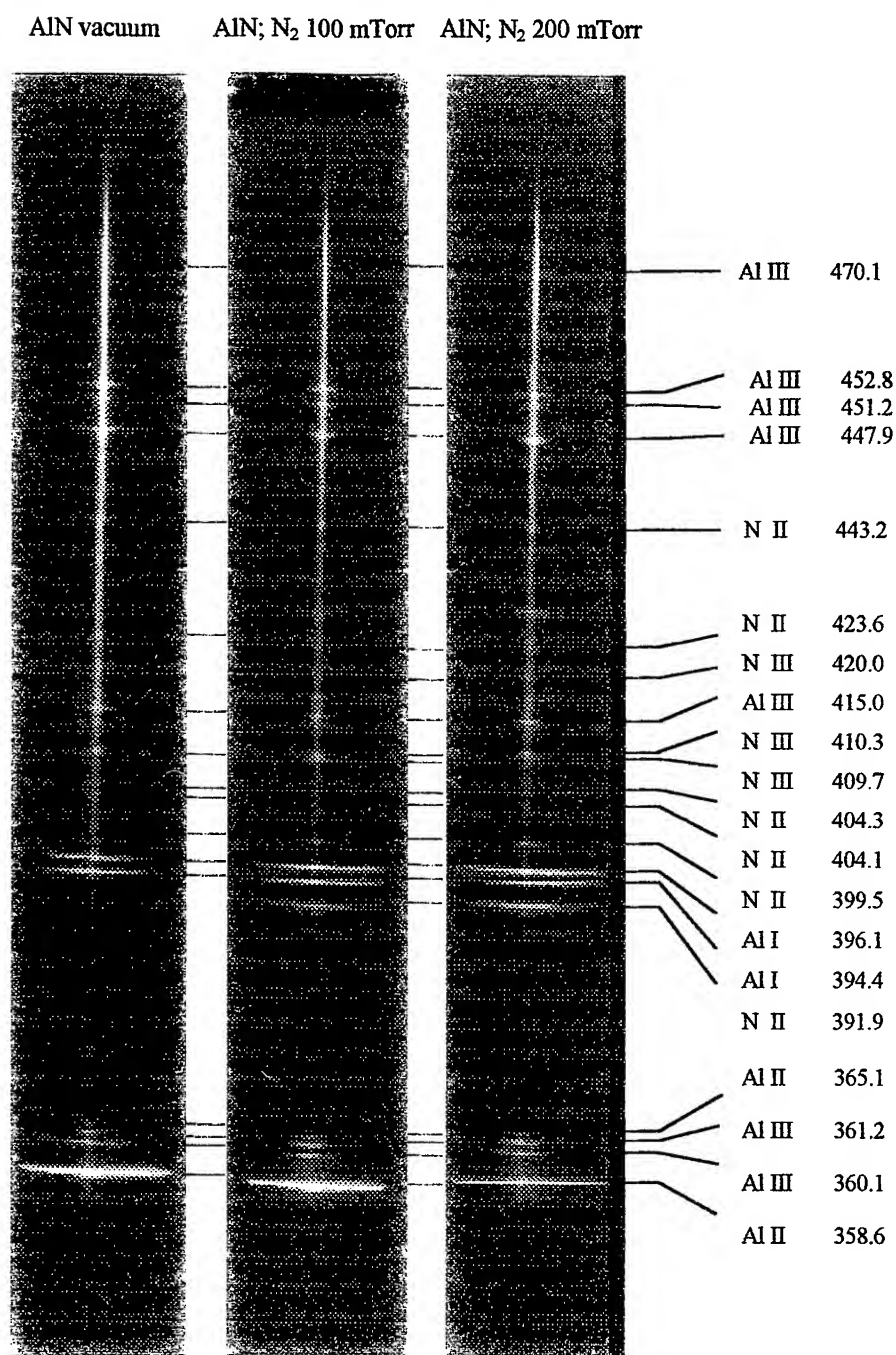


Fig. 2 Emission spectra for AlN target, in vacuum and N₂ atmosphere

The spectra obtained by irradiation of aluminium nitride target in nitrogen atmosphere (pressure of 100 mTorr and 200 mTorr) and in vacuum are shown in Fig. 2. We noticed that there are no remarkable differences between the spectrum obtained at N₂ pressure of 100 mTorr and the one obtained at N₂ pressure of 200 mTorr. Lines Al II 358.6, Al I 394.4, Al I 396.1 stand out, as a very powerful one, in the spectrum obtained at N₂ pressure of 100 mTorr. Analysing the spectrum

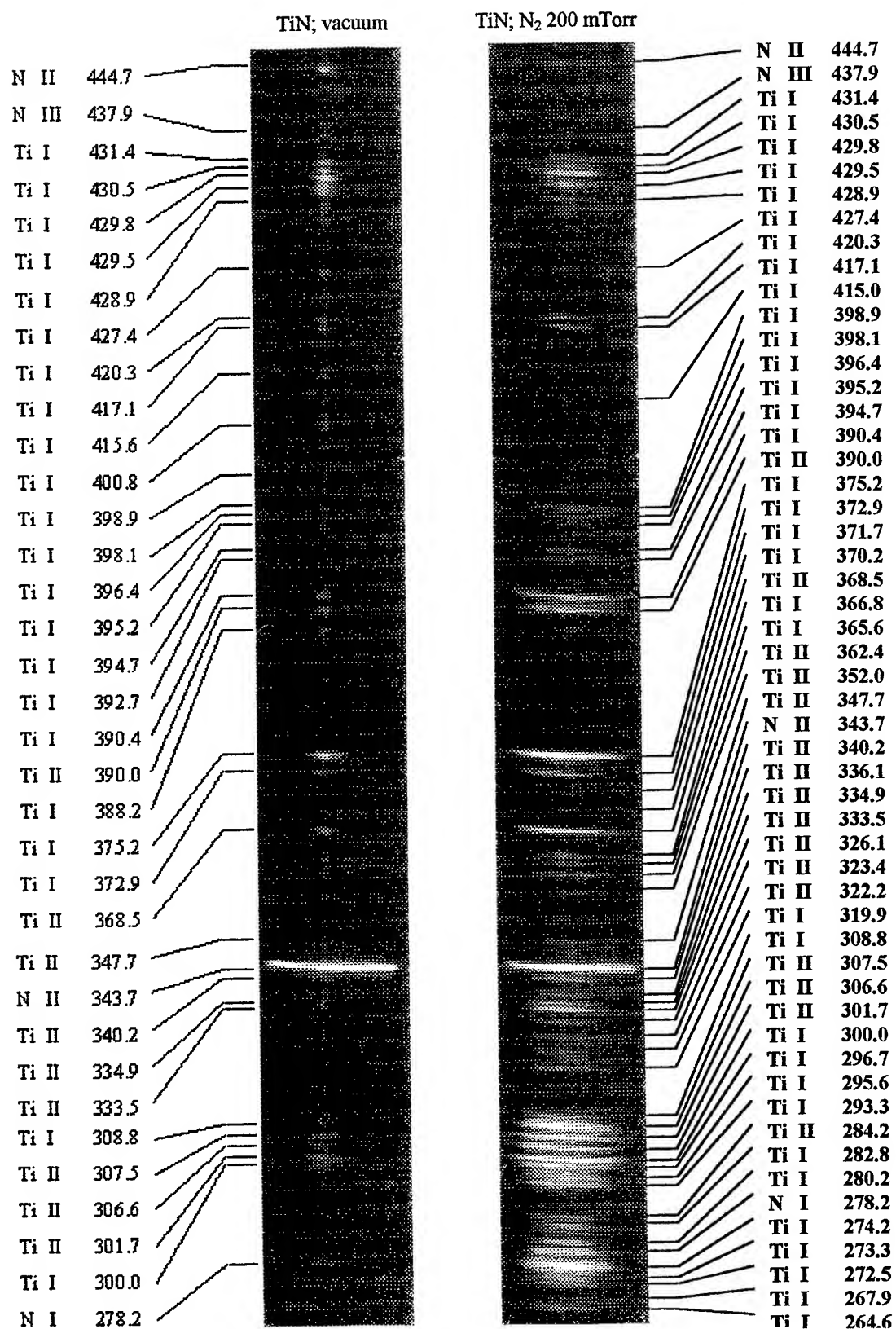
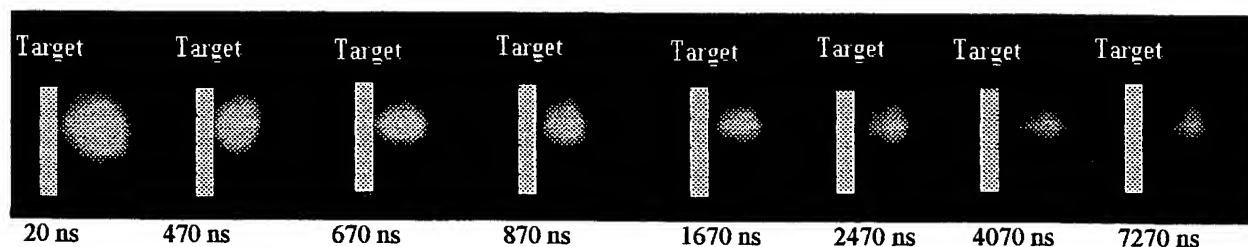


Fig. 3 Emission spectra for TiN target, in vacuum and N₂ atmosphere

obtained in vacuum, comparing with the one obtained in nitrogen atmosphere, one can notice that three of the nitrogen lines have despaired, Al III 415.0 line grows in intensity; lines Al I 394.4 and Al I 396.1 have a lower intensity.

Fig. 3 shows emission spectra of the plume obtained by irradiation of a titanium nitride target into nitrogen atmosphere (pressure of 100 mTorr) and, respectively, into vacuum. There are no important differences between the spectrum obtained at N₂ pressure of 100 mTorr and the one obtained at N₂ pressure of 200 mTorr, as well as in the case of aluminium nitride. The most intense lines, that can be seen in the spectrum obtained at nitrogen pressure of 100 mTorr, differences between the spectrum obtained at N₂ pressure of 100 mTorr and the one obtained at N₂ pressure of 200 mTorr, as well as in the case of aluminium nitride. The most intense lines, that can be seen in the spectrum obtained at nitrogen pressure of 100 mTorr, are: Ti I 390.4, Ti II 390.0, Ti I 375.2, Ti I 372.9, Ti II 368.5, Ti II 347.7, N II 343.7, Ti II 336.1, and the one present into the intervals (293.3, 308.8) and (274.2, 284.2). Analysing the spectrum obtained in vacuum, comparing with the one obtained in nitrogen atmosphere, one notice that an important number of Al and N₂ lines are missing. Also, the spectral lines obtained in vacuum have a much lower intensity that the one obtained into N₂ atmosphere. The only spectral line, very powerful, witch has the same intensity, both in nitrogen atmosphere and in vacuum is N II 343.7.

Therefore, analysing the time integrated emission spectra of ablation plume, we observed that some nitrogen emission lines appear only in the spectra obtained in nitrogen atmosphere, and not in those obtained in vacuum conditions. This fact indicates a higher content of nitrogen in plasma plume, which explains the better quality of the films obtained in nitrogen atmosphere.



Expansion velocity variation

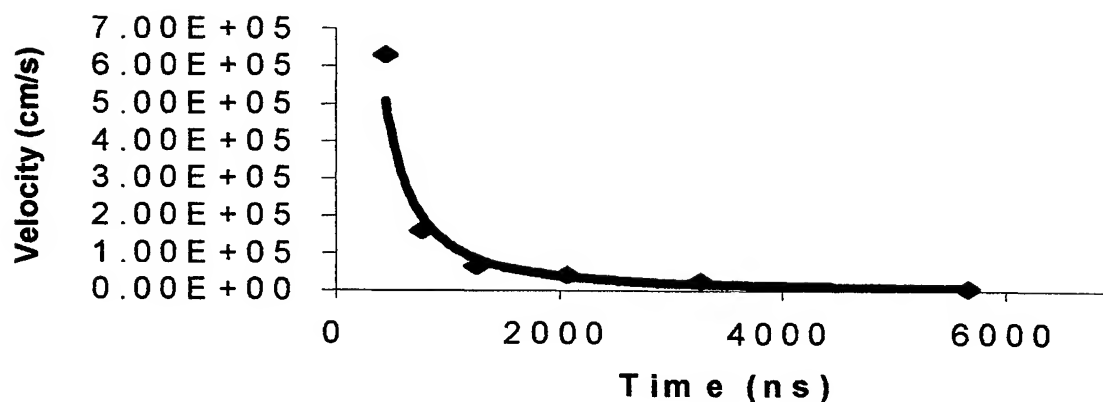


Fig. 4 Plasma plume expansion

To study spatial and temporal evolution of the plasma a high-speed camera was used. Plasma plume photoimages at different moments of time analyses evidence that the longitudinal plume expansion velocity was about 10^6 cm/s and the transversal expansion velocity was about 10^5 cm/s (Fig. 4). The duration of the plasma plume emission in 200 mTorr ambient atmosphere was about 7 μ s.

We have also determined the ablation rate (quantity of material expelled from the target under the action of one laser pulse) in order to establish the efficiency of ablation process. We obtained a rate of 5 mg/pulse at a laser fluence of 10 J/cm².

3. CONCLUSIONS

We realised an emission spectroscopy study of the plasma plume obtained under the irradiation of aluminium nitride or titanium nitride targets with a Nd: YAG laser, in nitrogen atmosphere and in vacuum.

There are no important differences between the spectra obtained at N₂ pressure of 100 mTorr and those obtained at N₂ pressure of 200 mTorr, in case of AlN, as well as in the case of TiN. The spectral lines obtained in vacuum have a lower intensity than the one obtained into N₂ atmosphere. Analyses of the spectra obtained in vacuum, comparing with those obtained in nitrogen atmosphere, evidences that some nitrogen lines are missing in spectra obtained in vacuum, both for AlN and TiN targets. This fact indicates a higher content of nitrogen in plasma plume in case of nitrogen environment, which explains the higher quality of the thin films obtained in nitrogen atmosphere.

The longitudinal plume expansion velocity was about 10^6 cm/s and the transversal expansion velocity about 10^5 cm/s. The duration of the plasma plume emission in 200 mTorr ambient atmosphere was about 7 μ s.

The ablation rate was 5 mg/pulse at a laser fluence of 10 J/cm².

REFERENCES

1. A. Kumar, H. L. Chan and R. Alexandrescu, "The Synthesis, Characterization and Mechanical Properties of Carbides and Nitrides Films Prepared by Pulsed Laser Deposition Method", *Proceedings of SPIE* **3405**, part I, pp. 122-129, 1997.
2. R. D. Vispute, V. Talyansky, R. P. Sharma, S. Choopun, M. Downes, T. Venkatesan, Y. X. Li, L. G. Salamanca-Riba, A. A. Iliadis, K. A. Jones, J. McGarrity, "Advances in Pulsed Laser Deposition of Nitrides and Their Integration with Oxides", *Applied Surface Science* **127/128**, pp. 431-439, 1998.
3. A. Neogi and R. K. Thareja, "Laser-produced Carbon Plasma Expanding in Vacuum, Low Pressure Ambient Gas and Nonuniform Magnetic Field", *Physics of Plasma* **6**, pp. 365-371, 1999.
4. S. Acquaviva, A. P. Caricato, M. L. De Giorgi, A. Luches and A. Perrone, "Spectroscopic Studies During Pulsed Laser Ablation of C-N Films", *Applied Surface Science* **109/110**, pp 408-412, 1997.
5. T. M. Di Palma, S. Orlando, A. Giardini-Guidoni, A. J. Paul, J. W. Hastie, A. Mele, "Composition and Gas Dynamics of Laser Ablated AlN Plumes", *Applied Surface Science* **86**, pp. 68-73, 1995

OPTICAL PHONONS EFFECTS ON LINEWIDTH OF SEVERAL LASER ACTIVE IONS IN YAG

A. Lupei*, V. Lupei, T. G. Sorop, E. Osiac, A. Petraru

National Institute for Lasers, Plasma and Radiation Physics,
R- 76900, P.O.Box MG-36, tel: 423 12 28, fax: 423 17 91 Bucharest, Romania

ABSTRACT

An analysis of low temperature lineshapes (broadenings, asymmetries, splittings) for various absorption lines of several RE^{3+} ions from the beginning Nd^{3+} ($4f^3$) and end of lanthanide series Er^{3+} ($4f^{11}$), Tm^{3+} ($4f^{12}$) embedded in the same crystal, $(\text{Y}_3\text{Al}_5\text{O}_{12})$ - YAG, known as important laser systems for $1\text{-}3\mu\text{m}$ emission is presented. New aspects of the dependence of electron - phonon coupling on RE^{3+} ion and matrix are observed from the analysis of many transitions of these ions at low temperature. These data show that the electron - phonon coupling presents a symmetric behavior in the lanthanide series, larger toward beginning and end. With only very few exceptions, less than 2%, the broadenings or splittings of zero-phonon lines could be connected to optical Raman phonons of undoped lattice. That means that the parity of $4f^n$ states could still be considered a good parent quantum number, even if the local symmetry has no inversion, and the near resonant coupling involves the even part of the electron-phonon coupling operator. Besides, the one phonon relaxation involve the undoped lattice phonons. For ions with small spin - orbit coupling, the vibronic contribution to the line intensity given by i.r. phonons through a Van Vleck mechanism could be important for spin forbidden transitions.

Keywords: linewidth, rare-earth, YAG

1. INTRODUCTION

The electron - phonon interaction effects for rare earths (RE^{3+}) ions in laser crystals are: multiphonon relaxation, vibronic transitions, line broadening, temperature dependence of the line position and width and phonon assisted energy transfer. These processes are important mechanisms governing the laser emission efficiency or thermal effects of RE^{3+} doped laser crystals. The electron - phonon coupling depends on the free ion characteristics and on the host crystal.

No clear explanation of the dependence of electron phonon coupling on the particular rare earth ion is given up to now, although it was investigated in many papers (for references see¹⁻⁴). A symmetric behavior in the lanthanide series (strong in the beginning and end, and weak in the middle) was reported in several papers¹⁻³ with a qualitative explanation given recently.² The coupling parameters of the electron-phonon interaction are often determined from the temperature dependence of the linewidths by using formulas for two phonon Raman processes^{5,6} and a Debye model for phonon density of states. The validity of this model, based on acoustical phonons, should be considered with caution and there are many papers that show the prevailing role of optical phonons in the temperature line broadening and shift (see the references from⁷). The Raman processes are unable to explain the blue shift of some lines, and the model proposed in⁶ is put under question in recent papers connected with Nd^{3+} lines in several laser crystals⁸⁻¹⁰. The dependence on RE^{3+} ion characteristics of the multiphonon relaxation rates was also reported recently.^{11,12}

In this paper an analysis of low temperature lineshapes (broadenings, asymmetries, splittings) for various absorption lines of several RE^{3+} ions from the beginning Nd^{3+} ($4f^3$) and end of lanthanide series Er^{3+} ($4f^{11}$), Tm^{3+} ($4f^{12}$) embedded in the same crystal, $(\text{Y}_3\text{Al}_5\text{O}_{12})$ - YAG, known as important laser systems for $1\text{-}3\mu\text{m}$ emission is presented. The study of linewidth of absorption lines is of theoretical importance for the understanding of electron-phonon mechanisms and of practical importance since the development of diode pumping of RE^{3+} solid state lasers. Attention is paid to near resonant effects¹³⁻¹⁶ involving optical phonons, a theory that can explain the linewidth and temperature dependence of spectral lines, including the blue shift. The possibility of preserving some of the free ion selection rules,¹⁷ helpful for the understanding of the electron - phonon coupling mechanisms is also discussed.

*Correspondence: E-mail: a.lupei@pluto.infim.ro

Another problem of study is if the doping with RE³⁺ ions changes the dynamics of the ideal lattice and how this affects the linewidths. The possibility of the enhancement of the emission or absorption cross sections as proposed for Nd³⁺ in YAG¹⁸ in the case of near resonant electron - phonon effects, that can influence spectroscopic determination of quantum efficiency, is also analyzed.

2. THEORETICAL BASIS

Inhomogeneous and homogeneous linewidths are the two components of the optical spectral linewidths. The inhomogeneous line broadening determines a finite and temperature - independent linewidth. The homogeneous broadening increases with the temperature and is mainly due to interactions between ions and lattice. Homogeneous linebroadening is determined by direct (one-phonon), Raman two phonon scattering and multiphonon processes. For optical absorption of RE³⁺ ions in YAG, at low temperatures, the multiphonon⁵ and Raman processes^{8,19} have a small contribution and the dominant effect is expected from one - phonon near resonant mechanism involving optical phonons.^{7,13} The contribution to the broadening comes from both levels involved in a transition. From the reasons that shall be discussed bellow we shall neglect in the low temperature absorption data the broadening of the lowest level. In this case the lineshape of a transition induced by light of frequency Ω from an initial pure electronic isolated state $|i\rangle$ to final states $|f\rangle$, close to other electronic levels $|r\rangle$ with $\Delta_{f,r} = E_f - E_r > 0$ and such that $\Delta_{f,r}$ is nearly equal to ω_k , a peak in the phonon spectrum, calculated by taking into account the near resonant electron - phonon interaction, is given by²⁰

$$F(\Omega) = \frac{1}{\pi} \sum_f |\langle i|d|f\rangle|^2 \frac{\gamma + \Gamma_f(\Omega)}{[\Omega - \Omega_{f,i} - \Sigma_f(\Omega)]^2 + [\gamma + \Gamma_f(\Omega)]^2} \quad (1)$$

where $|\langle i|d|f\rangle|^2$ is proportional to the intensity of zero-phonon line in the absence of near resonant electron - phonon interaction, d is the effective operator of the optical transition, γ is the linewidth due to radiative relaxation and statistical strain, $\Omega_{f,i}$ is the electronic transition energy in absence of electron - phonon coupling characterized by the Hamiltonian $H = \sum_k V_k Q_k$ with the sum on the phonon modes. At low temperature, only phonon emission is active and the analytical expressions for width $\Gamma_f(\Omega)$ and shift $\Sigma_f(\Omega)$ are given by

$$\Gamma_f(\Omega) = \frac{\pi}{\hbar^2} \sum_r \int_0^\infty A_r(\omega) \rho(\omega) \{ [n(\omega) + 1] \delta(\Omega - \Omega_{f,i} + \Delta_{f,r} - \omega) \} d\omega \quad (2)$$

$$\Sigma_f(\Omega) = \frac{1}{\hbar^2} \sum_r P \int_0^\infty A_r(\omega) \rho(\omega) \left[\frac{n(\omega) + 1}{\Omega - \Omega_{f,i} + \Delta_{f,r} - \omega} \right] d\omega \quad (3)$$

The matrix elements of electron - phonon coupling operator V_k are contained in $A_r \sim |\langle f|V_k|r\rangle|^2$, $\rho(\omega)$ is the phonon density, $n(\omega)$ - is the phonon occupation number, and P signifies the principal value of the integral. If the transition is of induced electric dipole type by odd part of the static crystal field operator H_{cr}^u , d could mean an even effective transition operator¹⁷ acting in the $4f^n$ basis. In this case only the even V_k^g part of the dynamic coupling operator V_k contributes to A_r . The magnetic dipole transitions could have also nonzero matrix elements, as well as the dynamic coupling dipole operator.¹⁶

If the near - resonant coupling is sufficiently strong asymmetries or splittings of the spectral lines are observed in optical absorption spectra. As shown in^{14,15,20} these effects are obtained from relation (1) with $\Omega - \Omega_{f,i} - \Sigma_f(\Omega) = 0$, an equation that has more solutions. For a single phonon emission such as $\Delta_{f,r} \sim \omega_0$, the line is splitted into two Lorentz components, whose intensities and positions depend on the electron - phonon coupling strength and the resonance degree $\varepsilon = |\Delta_{f,r} - \omega_0|$. A quantitative estimation of the coupling strength implies the knowledge of phonon density around the peak, which in the simplest form could be taken as in¹⁴ $\rho(\omega) = a\delta(\omega - \omega_0) + \rho'(\omega)$, that includes a small deviation $\rho'(\omega)$ from a δ function. In this model the intensity of the "zero - phonon" line $i \rightarrow f$ is redistributed between the two components function on the ratio $\frac{\varepsilon}{B^{1/2}}$ with $B = \frac{aA(\omega_0)}{\hbar^2}$. The maximum splitting and intensity redistribution is obtained for $\frac{\varepsilon}{B^{1/2}} \ll 1$, i.e. very good resonance ($\varepsilon \approx 0$) and strong coupling. In the case of $\frac{\varepsilon}{B^{1/2}} \gg 1$ the process is completely out of resonance and the intensity borrowing from zero phonon

line drastically decreases. For a weak coupling and a good resonance the splitting of the line is very small, it takes a Lorentzian form and the expression of $\Gamma_f(\Omega_{f,i})$ gives the probability of one phonon nonradiative emission or the contribution to the broadening of this phonon emission. In case of strong coupling, from experimental data, the positions and intensities of these peaks, one can estimate: the phonon energy, the position of the electronic level f and the coupling strength $B^{1/2}$ that includes the phonon peak intensity. The phonon density around a peak could be taken as having a Lorentz shape.¹⁴ If one have near - resonance with more phonons, a multicomponent line is obtained and the problem could be solved numerically, but many adjustable parameters should be introduced. For the investigated ions, at low temperatures, the ground state could be considered isolated since the Stark structure of the lowest multiplets for Nd^{3+} , Er^{3+} , Tm^{3+} excludes the one - phonon optical effects for the ground levels.

The phonon density of YAG crystal presents sharp peaks, extends up to $\sim 900 \text{ cm}^{-1}$, but all the attempts to give an analytical form for it, in absence of a theoretical calculation are discutable. Information on phonon density was obtained from Raman²¹⁻²³ i.r. spectra,^{24,25} neutron diffraction²⁶ or phonon sidebands.²⁷ In Ia3d spatial group of YAG the optically active phonons ($k \sim 0$) are separated in even - Raman and odd- i.r. Assignments of YAG optical phonons have been tried²³⁻²⁵; some of the peaks up to $\sim 250 \text{ cm}^{-1}$ were connected with the translation vibration of dodecahedral cations, while higher frequency phonons mainly with the vibrations of the tetrahedral group^{23-25,27}. A problem to be taken into account is the influence of the impurity ions on the vibration modes of the ideal lattice. The models of determining the phonon density from the vibronic sidebands⁷ should be also considered with attention since more mechanisms could contribute to vibronic intensities, especially in the case of non-centrosymmetric systems²⁸ and selection rules can work in some cases. Since the RE^{3+} ions enter in YAG in dodecahedral sites of D_2 local symmetry, the wavefunctions of the static crystal field are characterized by irreducible representations of this group and the electron - phonon interaction operator should be written in terms of local symmetry group. For our purpose we shall simplify the problem and separate the electron - phonon coupling operator V_k only in even and odd parts.¹⁷

3. EXPERIMENTAL RESULTS

Low temperature ($T = 10 \text{ K}$) optical spectra in near infrared and visible region were measured on YAG samples grown by Czochralski technique and doped with Nd^{3+} , Er^{3+} , Tm^{3+} with concentrations up to 1-2at. %. The experimental set-up consists of a lamp for pumping and a set-up including a computer - controlled one - meter GDM monochromator with resolution of $\sim 0.5 \text{ cm}^{-1}$, a S20 photomultiplier and a multichannel MCS analyzer.

In D_2 local symmetry of YAG, the Stark levels are either Kramers doublets for Nd^{3+} and Er^{3+} or singlets for nonKramers ion Tm^{3+} and the above theory is therefore applicable. The experimental data at $\sim 10\text{K}$ contain hot bands for Er^{3+} or Tm^{3+} , and some lines present satellite structure or inhomogeneous broadening due to RE^{3+} pairs or nonstoichiometric defects that make also difficulties in the evaluation of the width.

3.1. Analysis of Nd^{3+} spectra in YAG

The absorption data at 10 K of Nd^{3+} ($4f^3$) in YAG in the $10000\text{-}26000 \text{ cm}^{-1}$ range have been analyzed. The electron - phonon is manifested by broadening and asymmetry of some lines. The Nd^{3+} broadened lines are either of one peak Lorentz shape (31 from 70 investigated lines) with the widths up to $\sim 10 \text{ cm}^{-1}$ or of anomalous shapes and much larger linewidths ($10\text{-}50 \text{ cm}^{-1}$) (23 from 70). The widths of the other lines are under $\sim 1 \text{ cm}^{-1}$. A comparison between Stark levels splittings (with a certain error) and Raman²¹⁻²³ or i.r.^{24,25} phonons (see⁷ Tables 6.3, 6.4) has been performed by a computer program. The Stark levels position for Nd^{3+} in YAG are close to those given in^{7,29} and the ground multiplet $^4\text{I}_{9/2}$ energy levels structure assures, at low temperatures, an "isolated" initial level. The Lorentz broadening could be explained by the theory of near - resonant effects discussed above with Raman phonons emission. In Fig. 1 we present the absorption spectrum corresponding to $^4\text{I}_{9/2} \rightarrow ^4\text{F}_{5/2}$ transition at 10K of a Nd^{3+} sample with $\sim 1\text{at. \%}$. Line (1 in Fig. 1), 12370 cm^{-1} (808 nm) corresponds to absorption band used for diode pumping of Nd^{3+} in YAG. In¹⁸ this transitions is given as an example to support the idea that resonant electron - phonon coupling can determine an additional contribution to line intensity, making possible a difference between the absorption and emission cross sections of the same transition. The broadened line (1 Fig. 1) involve a Raman phonon emission (857 cm^{-1}). Diode pumping was recently³⁰ performed in the second line of $^4\text{I}_{9/2} \rightarrow ^4\text{F}_{3/2}$ transition that is also broadened by one phonon emission of a Raman phonon of $\sim 80 \text{ cm}^{-1}$. The spread of the measured widths of the broadened Lorentz lines are given in Fig. 2, where the linewidth values as function on n , the number of f electrons of RE^{3+} ion are presented.

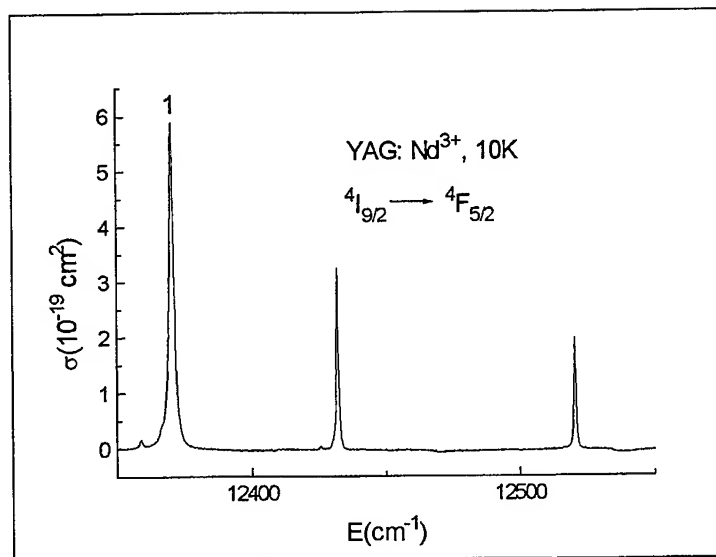


Figure 1. Absorption spectrum of Nd^{3+} in YAG (${}^4I_{9/2} \rightarrow {}^4F_{5/2}$ transition) at 10K.

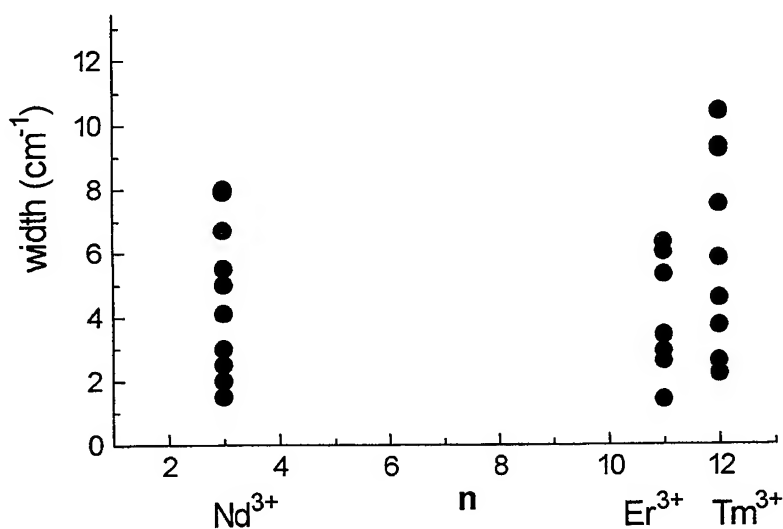


Figure 2. The dependence of linewidth on RE^{3+} ion.

The Nd^{3+} lines that present low intensities and very large linewidths ($10\text{--}50\text{ cm}^{-1}$) are those that correspond to the spin forbidden absorption transitions to the Stark components of levels ${}^2K_{13/2} + {}^2G_{9/2}$ and ${}^2K_{15/2}$.

The intensities of these lines are of about two orders of magnitude smaller than the lines corresponding to spin allowed transitions. The analysis of the data in these regions show many resonances, mainly with i.r., but with Raman phonons too. The broadening of these lines could be connected to an additional contribution given by: induced electric - dipole determined by mixing of excited states by the odd part of the electron - phonon Hamiltonian V_k^u (Van Vleck mechanism¹⁷).

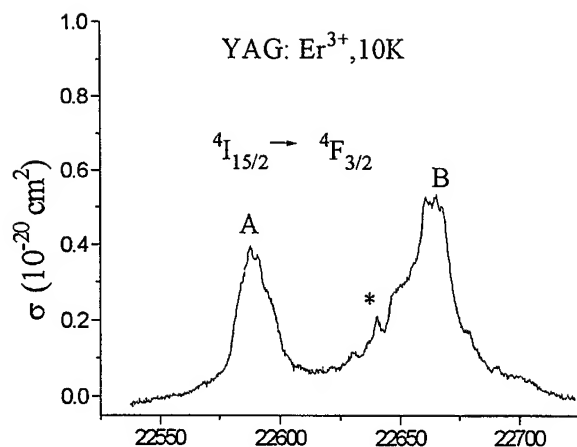


Figure 3. Absorption spectrum of Er^{3+} in YAG ($^4I_{15/2} \rightarrow ^4F_{3/2}$) transition

3.2. Analysis of Er^{3+} spectra in YAG

The absorption lines in the $12000\text{--}25000\text{ cm}^{-1}$ region for Er^{3+} in YAG correspond, with few exceptions, to the levels given in.⁷ The lowest Stark levels of the ground multiplet $^4I_{15/2}$ being $(0, 18, 60, 79\text{ cm}^{-1})$, some hot bands are observed at 10 K. In this case, the single peak Lorentz broadened lines (16 from 31) are connected with Raman phonons emission too and the range of widths is given in Fig. 2. The lines with widths smaller than $\sim 1\text{ cm}^{-1}$ do not involve optical phonons in the broadening. A special lineshape presents two lines corresponding to $^4I_{15/2} \rightarrow ^4F_{3/2}$ transition (Fig. 3), where * denote the hot bands. The lines corresponding to $^4I_{15/2} \rightarrow ^4F_{3/2}$ transition are difficult to analyze since they contain more peaks, but contribution of the hot bands too. However, line A contains two main peaks, while line B is more complex, but with a clear three peak structure. The complex shape can be explained by near resonance splitting processes involving several Raman phonons emission ($296, 371\text{ cm}^{-1}$ for line A and $371, 440$ and 80 cm^{-1} with line B) emission. The resonance degree with 371 and 440 cm^{-1} is very good.

3.3. Analysis of Tm^{3+} spectra in YAG

The "zero-phonon lines" of Tm^{3+} absorption spectra in YAG in the $12000\text{--}22000\text{ cm}^{-1}$ range are analyzed and due to existence of forbidden transitions an accurate energy level diagram is necessary; we used our data.³¹ The linewidth range of one peak broadened Lorentz lines by Raman phonon emission are given in Fig. 2. It is interesting to illustrate the line shapes in the absorption spectrum at 10 K corresponding to $^3H_6 \rightarrow ^1G_4$ Tm^{3+} spin forbidden transition (Fig. 4). Besides the broadened symmetric lines, a clear splitted line (the inserted one) with a distance between peaks of $\sim 8\text{ cm}^{-1}$ is present.. From the resonant splitting and relative intensities of two components, assuming the phonon density around the resonance as a small deviation from a δ function,¹⁴ one get the phonon involved of 145 cm^{-1} , the coupling parameter $B^{1/2} \sim 4\text{ cm}^{-1}$ and the position of the f level (from $\Delta_{f,r}$) at 21533 cm^{-1} as shown by arrow in Fig. 4. In our previous studies, several other resonantly splitted lines in Tm^{3+} spectra in YAG were observed and coupling parameters of $\sim 4\text{--}5\text{ cm}^{-1}$ were estimated.^{32,33} A characteristic of low temperature Tm^{3+} spectra are the rather intense phonon sidebands.

4. DISCUSSION

Three main types of broadened lines have been observed in low temperature absorption spectra of Nd^{3+} , Er^{3+} , Tm^{3+} : (a) single peak homogeneously broadened "zero - phonon lines" of Lorentz shape connected mainly with one phonon emission by the near - resonant electron - phonon coupling; (b) asymmetric lines associated with near resonant splitting and (c) low intensity broad lines. Homogeneously broadened lines of type (a), with the widths

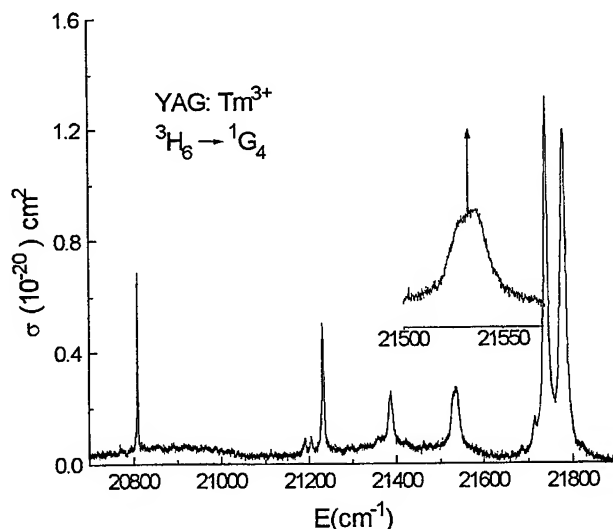


Figure 4. Absorption spectrum of Tm^{3+} in YAG ($^3H_4 \rightarrow ^1G_4$) transition

given in Fig. 2, could be explained by emission of phonons observed in the Raman spectra of undoped crystal, exceptions of this rule do not represent more than $\sim 2\%$. This implies two conclusions: 1) the parity of the $4f^n$ states is still a good quantum number even if the local symmetry (D_2) has no inversion, i.e. the odd static crystal field potential cannot destroy the parity of the $4f^n$ states,¹⁷ and therefore, almost exclusively only the even part of the electron - phonon interaction Hamiltonian gives nonzero matrix elements (near - resonant effects) as suggested in¹⁶ and 2) for these ions, at low concentrations, the coupling involves the phonons of undoped lattice. A possible explanation of the last observation could be that suggested in³⁴ that the relaxation in case of an impurity center with local vibrations can take place by coupling with lattice phonons of close energies.

The estimation of electron - phonon coupling parameters only from linewidth is difficult since in expression (2) both the phonon density and coupling matrix elements are unknown, and the linewidths contain other possible broadening contributions. For these reasons, we consider that a spread of linewidth data obtained for many different transitions of the investigated ions could give a trend of the electron - phonon interaction along the lanthanide series. Indeed the data presented in Fig. 2 show a similar behavior to that obtained in¹⁻⁴ larger at the beginning and end of lanthanide series and could explain the strong coupling observed for Pr^{3+} ³⁵ or Yb^{3+} ³³ in YAG. Some of the lineshapes of Er^{3+} and Tm^{3+} ions (Fig. 3, 4) could be explained by near resonant splittings of "zero-phonon lines".

In¹⁸ it was suggested that vibronic coupling in near resonant condition would lead to enhancement of line intensity and this could explain the difference between absorption and emission cross sections for the same electronic transition. According to the near resonant electron - phonon coupling theory, an intensity redistribution of the zero-phonon line $i \rightarrow f$, due to phonon emission to an intermediate level r (when $\Delta_{fr} \sim \omega_k$) takes place¹⁴⁻¹⁶ either by broadening or splitting of the lines. The difference between absorption and emission cross sections observed for some Nd^{3+} transitions in YAG¹⁸ cannot be explained by such a mechanism. However, other two contributions to the intensity of a line could come from vibronic sidebands: Frank Condon and Van Vleck mechanisms.¹⁷ The Frank Condon contribution connected with diagonal matrix elements of V_k^g is small for RE^{3+} ions and could be neglected in the resonance case. Since in YAG crystal some of the Raman and i.r. phonons have similar energies, the odd part of the electron - phonon interaction Hamiltonian in case of RE^{3+} in noncentrosymmetric sites contain contribution from a Van Vleck mechanism¹⁷ involving i. r. phonons and this could give additional contributions to "zero - phonon lines" intensities. However, this seems unlikely in the case of Nd^{3+} $^4I_{9/2}(1) \rightarrow ^4F_{5/2}(1)$ (808 nm) line since the only phonon that can be emitted is 857 cm^{-1} and in most published works it is assigned as a Raman phonon.

Another type of broadening observed Nd^{3+} spectra could be connected to contribution of electric - dipole induced transitions by odd part of the electron - phonon Hamiltonian - Van Vleck mechanism.¹⁷ In the assumption that the

parity is still a good quantum number, the odd i.r. phonons of YAG could give a contribution too, connected to V_k^u , the odd part of the electron - phonon interaction. This contribution could be important for the transitions whose static crystal field electric - dipole induced probabilities are negligible. Such cases could be those of 19000-22000 cm^{-1} range of Nd^{3+} levels, especially to the Stark levels ${}^2K_{13/2}+{}^2G_{9/2}$ and ${}^2K_{15/2}$. Our estimations, by considering only the free ion parameters, show a negligible J mixing in these cases. The very low intensities of these lines could be qualitatively explained by the relatively small spin - orbit coupling (876cm^{-1} for Nd^{3+}), that determines a small intermediate coupling mixing and in this case the selection rule over S still works. The contribution of the static induced electric - dipole could be small and the line intensities could contain either magnetic dipole contribution and induced electric - dipole determined by mixing of excited states by odd phonons (Van Vleck mechanism). Many resonances between the Stark levels in this region with i.r. and Raman phonons are possible. The Stark splittings allow also for some of these lines a broadening by one phonon resonant processes involving optical phonons observed in Raman spectra, in many lines resonance with more phonons is possible. Such behavior has not been observed for ions with larger spin - orbit parameter such as Er^{3+} (2380 cm^{-1}) and Tm^{3+} (2630 cm^{-1}) where the spin selection rules are relaxed by intermediate coupling.

In conclusion, though for homogeneous line broadening of rare earths ions in solid matrices often the acoustic phonons contribution is considered, the analysis of low temperature spectra of many lines of Nd^{3+} , Er^{3+} , Tm^{3+} in YAG outlines the essential role of optical phonons in the low temperature linebroadening by near resonant electron - phonon coupling, in accord with other recent results.³⁶

REFERENCES

1. A. Ellens, H. Andres, A. Meijerink, and G. Blasse, "Spectral-line-broadening study of trivalent lanthanide-ion series. I. Line broadening as a probe of the electron-phonon coupling strength", *Phys. Rev.* **B55**, pp. 173-179, 1997.
2. A. Ellens, H. Andres, M. L. H. ter Heerdt, R. T. Wegh, A. Meijerink, and G. Blasse, "Spectral-line-broadening study of trivalent lanthanide-ion series. II. The variation of electron-phonon coupling strength through the series" *Phys. Rev.* **B55**, pp. 180-186, 1997.
3. W. F. Krupke, "Optical Absorption and Fluorescence Intensities in Several Rare-Earth-Doped Y_2O_3 and LaF_3 Single Crystals", *Phys. Rev.* **145**, pp. 325-330, 1966.
4. C. Gorller-Walrand, K. Binnemans, *Handbook on the Physics and Chemistry of Rare Earths* **25**, pp. 101-206, Eds. K. A. Gschneieder Jr. and L. Eyring, Elsevier Science Publishers B. V., 1998.
5. W. M. Yen, W. C. Scott, and A. L. Schawlow, "Phonon-Induced Relaxation in Excited Optical States of Trivalent Praseodymium in LaF_3 ", *Phys. Rev.* **136**, pp. A271-A275, 1964.
6. T. Kushida, "Linewidths and Thermal Shifts of Spectral Lines in Neodymium-Doped Yttrium Aluminium Garnet and Calcium Fluorophosphate" *Phys. Rev.* **185**, pp. 500-508, 1969.
7. A. A. Kaminskii, *Laser Crystals*, Springer - Verlag, New York, 1981.
8. X. Chen, and B. Di Bartolo, "Phonon effects on sharp luminescence lines of Nd^{3+} in $\text{Gd}_3\text{Sc}_2\text{Ga}_3\text{O}_{12}$ garnet (GSGG)" *J. of Luminescence* **54**, pp. 309-318, 1993.
9. X. Chen, and B. Di Bartolo, "Temperature dependence of spectral linewidths and lineshifts of Nd^{3+} ions in $\text{CaY}_2\text{Mg}_2\text{Ge}_3\text{O}_{12}$ laser crystal" *J. Appl. Phys.* **75**, pp. 1710-1714, 1994.
10. D. K. Sardar, and S. C. Stubblefield, "Temperature dependencies of linewidths, position, and lineshifts of spectral transition of trivalent neodymium ions in barium magnesium yttrium germanate laser host" *J. Appl. Phys.* **83**, pp. 1195-1199, 1998.
11. Yu. V. Orlovskii, R. J. Reeves, R. C. Powell, T. T. Basiev, and K. K. Pukhov, "Multiple-phonon nonradiative relaxation: Experimental rates in fluoride crystals doped with Er^{3+} and Nd^{3+} ions and a theoretical model", *Phys. Rev.* **B49**, pp. 3821-3830, 1994.
12. T. T. Basiev, Yu. V. Orlovskii, K. K. Pukhov, V. B. Sigachev, M. E. Doroshenko, and I. N. Vorobiev, "Multi-phonon relaxation rates in measurements and theoretical calculations in the frame of non-linear and non-coulomb model of a rare-earth ion-ligand interaction" *J. of Luminescence* **68**, pp. 241-245, 1996.
13. Yu. E. Perlin, A. A. Kaminskii, V. N. Enaki, D. N. Vileghanin, "Electron-phonon resonances in the rare earth ions spectra" *Pisma J. E. T. F.* **30**, pp. 426-429, 1979 (in Russian).
14. Yu. E. Perlin, V. N. Enaki, "Resonances between Stark levels in optical spectra of deep impurities centers", *Physical Processes in Semiconductors*, pp. 3-12, Ed. Stiinta, Chisinau, 1981 (in Russian).

15. V. N. Enaki., " Stark multiphonon resonances in optical spectra of impurity centers" *"Nonequilibrium Processes in Multicomponent Crystals"*, pp. 36-42, Ed. Stiinta, Chisinau, 1988 (in Russian).
16. O. L. Malta, "The Theory of Vibronic Transitions in Rare Earth Compounds" *J. Phys. Chem. Sol.*, **56**, pp.1053-1062, 1995.
17. V. V. Ovsyankin, "Spectroscopy of collective states and cooperative transitions in disordered rare earth activated solids", *Spectroscopy of Solids Containing Rare Earth Ions*, **343**, Eds. A. A. Kaplyanskii, R. M. Macfarlane, Elsevier Science Publishers B.V., pp. 377-391 1987.
18. B. F. Aull and H. P. Jenssen, "Vibronic interactions in Nd: YAG resulting in nonreciprocity of absorption and stimulated emission cross sections" *IEEE J. Quantum Electronics* **QE-18**, pp.925-930, 1980.
19. J. T. Gourley, "Spectral linewidth studies of pr in YAG" *Phys. Rev.* **B5**, pp. 22-30, 1972.
20. V. N. Enaki, A. Lupei, V. Lupei, C. Presura, and V. E. Ciobu, "Effects of resonant electron-phonon interactions for RE³⁺ ions in laser crystals" *Proceedings SPIE*, **3405**, pp. 570-577, 1998.
21. J. A. Koningstein, and O. S. Mortensen, "Laser-Excited Phonon Raman Spectrum of Garnets" *J. Molecular Spectroscopy*, **27**, pp. 343-350, 1968.
22. G. Mace, G. Schaack, N. G. Toaning, and J. A. Koningstein, "Optical Phonons of Terbium-, Dyprosium, and Ytterbium Garnet", *Z. Phys* **230**, pp.391-396, 1970.
23. Yu. V. Voronko, L. M. Ershova, N. A. Eskov, A. B. Kudryavtsev, V. V. Osiko, A. A. Sobol and E. V. Sorokin, "Raman spectra in solid solutions with garnet structure" *Sov. Solid State Physics*, **30**, pp. 512-519, 1988 (in Russian).
24. J. P. Hurrell, S. P. S. Porto, I. F. Chang, S. S. Mitra, and R. P. Bauman, "Optical phonons of yttrium aluminium garnet" *Phys. Rev.* **173**, pp. 851-856, 1968.
25. A. M. Hoffmeister, and K. R. Campbell, "Spectroscopy of yttrium aluminium, yttrium gallium, and yttrium garnets" *J. Appl. Phys.* **72**, pp. 638-646, 1992.
26. S. N. Morozov, S. A. Danilkin, V. V. Zakurkin, S. N. Ivanov, V. V. Medved, S. F. Ahmetov, A. G. Davidcenko., *Sov. Solid State Phys.* **25**, pp. 1135-1142, 1983.
27. V. M. Markushev, V.I. Tsaryuk, V. F. Zolin, "Electron-phonon effects in the excitation spectra of Eu luminescence in YAG" *Optics and Spectr.* **58**, pp. 583-588, 1985 (in Russian).
28. A. Kaminskii, " *Physics and Spectroscopy of Laser Crystals*", Ed.Nauka, Moscow, 1986 (in Russian).
29. G. W. Burdick, C. K. Jayasankar, F. S. Richardson, and M. F. Reid, "Energy-level and line-strenght analyses of optical transitions between Stark levels in Nd³⁺:Y₃Al₅O₁₂", *Phys. Rev.* **B50**, pp. 16309-16325, 1994.
30. R. Lavi, S. Jackel, M. Winik, E. Lebiush, I. Tzuk, M. Katz, "Enhanced Nd:YAG efficincy trough direct ⁴F_{3/2} R₂ sublevel pumping" *Advanced Solid State Lasers* **26**, pp. 17-26, 1999.
31. C. Tiseanu, A. Lupei, V. Lupei, "Energy levels of Tm³⁺ in YAG", *J. Phys.: Condens. Matter* **7**, pp. 8477-8486, 1995.
32. A. Lupei, V. Lupei, "Resonance between electronic and vibronic levels of Tm³⁺ in YAG" *J. Phys.: Condens. Matter* **9**, pp. 2807-2813, 1997.
33. A.Lupei, V. Lupei, V. N. Enaki, C. Presura, and A. Petraru, " Electron-phonon coupling for heavy RE³⁺ ions in crystals" *Spectrochimica Acta Part A* **55**, pp.773-781, 1999
34. V. A. Kremerman, M. Lax, S. G. Demos, D. M. Calistru, and R. R. Alfano, "Non-radiative energy transfer from the impurity ion into the host lattice for Cr⁴⁺ -doped forsterite laser crystal", *Phys. Rev. B* **56**, pp.14391, 1997.
35. P. Caro, " Phonon interferences in the analysis of rare earth 4fⁿ energy levels sequencies" *J. Less Common Metals* **126**, pp. 239-245, 1986.
36. W. Beck, D. Ricard and C. Flytzanis, "Relaxation, homogenous broadening, and frequency shifts: Application to electronic transitions in solids doped with rare-earth ions" *Phys. Rev. B* **15**, pp. 7694-7700, 1997.

On the evaluation of some nonlinear parameters of $\text{Er}^{3+}:\text{Ti:LiNbO}_3$ waveguides from interferometric and near field measurements

N. N. Puscas*

University "Politehnica" of Bucharest, Physics Department, Romania

ABSTRACT

Based on some experimental measurements performed on Er^{3+} -doped Ti:LiNbO_3 optical waveguides, this paper presents some results concerning the evaluation of some nonlinear parameters: third order nonlinearities, the saturation change in refractive index using the low-finesse waveguide Fabry-Pérot resonators.

Keywords: Optical waveguides, $\text{Er}^{3+}:\text{Ti:LiNbO}_3$, losses, attenuation coefficient, third order nonlinearities

1. INTRODUCTION

Several theoretical and experimental papers concerning the characterization of the Er^{3+} -doped Ti:LiNbO_3 optical waveguides using nondestructive methods were reported in the last years^{1,2,3,4,5}. This considerable interest in the field of above mentioned waveguides is related to their potential use in compact and efficient monolithic devices (waveguide lasers, optical amplifiers, optical modulators, switches, filters) combining the rare-earth laser gain and the large range of integrated optical functions already demonstrated.

Using an interferometric technique⁵ the intensity-dependent refractive-index in two-core erbium doped optical fiber has been observed. The theoretical analysis of this effect allowed the determination of some important nonlinear parameters (i. e. third order nonlinearity) for this material. Measuring the contrast of Fabry-Pérot resonances in low-finesse (end-face polished) integrated optical resonators it is possible to determine an upper limit of the waveguide attenuation coefficient².

In this paper we propose a new method for the evaluation of some important nonlinear parameters⁵ (the third order nonlinearity, the saturation change in refractive-index) using the low-finesse waveguide Fabry-Pérot resonators².

2. THE EVALUATION OF THE LOSSES AND THE NONLINEAR PARAMETERS

The transmitted intensity I_T of a symmetrical monomode Fabry-Pérot optical waveguide resonator is:

$$I_T = \frac{T^2 \exp(-\alpha L)}{(1 - \tilde{R})^2 + 4\tilde{R} \sin^2(\Phi/2)} I_0 \eta \quad (1)$$

where I_0 is the incident laser beam intensity, η is the coupling efficiency of the waveguide mode, T the end face mode transmissivity,

$$\tilde{R} = R \exp(-\alpha L) \quad (2)$$

R being the mode reflectivity and α the attenuation coefficient of the optical waveguide having the length L . The internal phase difference at the output ($z = L$) is:

*Correspondence: E-mail: pnt@physics2.physics.pub.ro, Telephone (401) 410.45.85; Fax: (401) 3125365

$$\Phi(L) = \begin{cases} k_0 n_{eff} L, & \text{if } n_{eff} = \text{constant} \\ k_0 \int_0^L n_{eff}(z) dz, & \text{if } n_{eff} = \text{variable} \end{cases} \quad (3)$$

For small contrast K of the Fabry - P  rot resonances

$$K = (I_{\max} - I_{\min}) / (I_{\max} + I_{\min}) \quad (4)$$

where K is independent of I_0 and η , the attenuation coefficient is given by the relation²:

$$\alpha \sim \frac{4.34}{L} (\ln R + \ln 2 - \ln K) \quad (5)$$

If the relative intensities of the longitudinal modes are known (they can be measured with a conventional optical spectrum analyser) and these intensities ratios are stable in time (during the period of measurement), then the response function of the waveguide resonator is a superposition of its response to the single lines alone. In this case (considering that the photodiode is slow enough to integrate the difference frequency terms) Eq. (1) is replaced by a summation of terms which differ only in the internal phases Φ (which are wavelength-dependent.) and intensities I_0 .

Then, measuring the contrast K of the Fabry-P  rot resonances (Eq. 4) it is possible to evaluate the attenuation coefficient of the waveguide using Eq. (5).

In a material characterized by an intensity-dependent refractive-index it is possible to write:

$$n = n_1 + n_2 I(x, y, z) \quad (6)$$

where

$$n_1 = \epsilon_1^{1/2} \quad (7)$$

ϵ_1 being the linear (weak field) dielectric constant, I is the intensity of the electric field, x, y, z define the position in the waveguide (z is the direction of propagation) and

$$n_2 = (\mu_0 / \epsilon_0)^{1/2} \chi / \epsilon \quad (8)$$

represents the third order nonlinearity due to Kerr effect.

Considering that for the optical powers and index changes under consideration, the variations of the refractive-index profile of the waveguide are small it is therefore possible to write a relation similar to (6), but for the effective index in terms of the power in the waveguide (the intensity at any point being proportional to the total power in the waveguide):

$$n_{eff} = n_{eff}(P(z)) = n_{eff}(0) + \Delta n_{eff}(P(z)) \quad (9)$$

and

$$\Delta n_{eff} \approx C \Delta n_{ws} \quad (10)$$

where C is a constant which can be determined by solving the eigenvalue equation for the particular waveguide refractive-index profile and

$$\Delta n_{ws} = n - n_s \quad (11)$$

n_s being the refractive-index of the substrate.

In order to describe the intensity-dependent refractive-index one considered a three-level model for the Er^{3+} -doped Ti:LiNbO_3 optical waveguide (Fig. 1), without taking into account the excited state absorption (ESA)⁵. Also, we have assumed that if all electrons are in the excited state $|2\rangle$, then $n_{eff} = n_{eff2}$ and if all electrons are in the fundamental state $|1\rangle$, then $n_{eff} = n_{eff1}$.

Taking into account that the effective index is in weighted proportion to the concentration of the fundamental state 1:

$$N_1 = N_T / (1 + P / P_S) \quad (12)$$

and excited state 2, respectively:

$$N_2 = N_T / (1 + P_S / P) \quad (13)$$

where $N_T = N_1 + N_2$ and P_S (the transparency power) is the power at which the population is just inverted ($N_2 = N_T / 2$) and then the gain is exactly zero, one obtained:

$$n_{eff}(P(z)) = (n_{eff2} - n_{eff1}) / (1 + P_S / P(z)) \quad (14)$$

Considering no excited state absorption, the power evolution in the waveguide is determined by the attenuation coefficient (at corresponding wavelength) that is $\alpha(0)$ when all the electrons are in the ground state and zero when all the electrons are in the excited state:

$$\alpha(P) = -(1/P)(dP/dz) = (N_1 / N_T)\alpha(0) = \alpha(0) / (1 + P(z) / P_S) \quad (15)$$

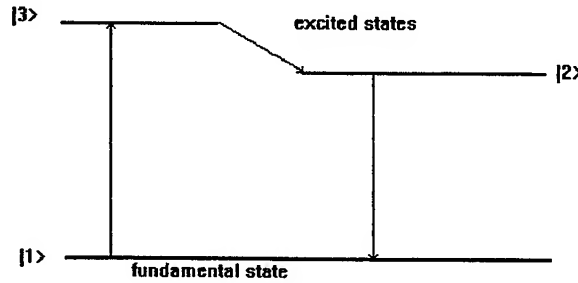


Fig.1 The three-level model for the Er^{3+} -doped Ti:LiNbO_3 optical waveguide

From Eq. (15) one obtained the power as a function of the position in the waveguide:

$$dP(z)/dz = -P(z)\alpha(0)/(1 + P(z)/P_S) \quad (16)$$

Taking into account the excited state absorption

$$\begin{aligned} \alpha(P) &= (N_1 / N_T)\alpha(0) + (N_2 / N_T)\alpha(\infty) \\ &= \alpha(0)/(1 + P(z)/P_S) + \alpha(\infty)/(1 + P_S / P(z)) \end{aligned} \quad (17)$$

where $\alpha(\infty)$ and $\alpha(0)$ are the attenuation coefficients when all the electrons are in the excited state and in the ground state, respectively, Eq. (16) becomes:

$$dP(z)/dz = -P(z)\alpha(0)/(1 + P(z)/P_S) - P(z)\alpha(\infty)/(1 + P_S / P(z)) \quad (18)$$

Solving Eq. (16) (no ESA) or (17) (with ESA) for $P(z)$ one obtains the difference in phase of the light due to the power dependence of the effective index:

$$\Delta\Phi = \Delta\Phi(L) = k_0 \int_0^L \Delta n_{eff}(P(z)) dz = k_0 (n_{eff2} - n_{eff1}) \int_0^L \frac{dz}{1 + P_S / P(z)} \quad (19)$$

For a nonlinear waveguide the third order nonlinearity is:

$$n_2 = dn/dI = (S_{eff} / C\eta)(dn_{eff}/dP) \quad \text{for } P \rightarrow \infty \quad (20)$$

where S_{eff} is the effective pump area of the waveguide and η the fraction of the power in the waveguide.

Taking into account Eq. (14):

$$dn_{eff} / dP = P_S (n_{eff2} - n_{eff1}) / (P + P_S)^2 \rightarrow (n_{eff2} - n_{eff1}) / P_S, \text{ for } P \rightarrow \infty \quad (21)$$

and (20) one obtains:

$$n_2 = (S_{eff} / C\eta)(n_{eff2} - n_{eff1})P_S \quad (22)$$

The difference $(n_{eff2} - n_{eff1})$ can be found by comparing the experimental measurements of $\Delta\Phi$ (with the optical spectrum analyser) for low and high power respectively to predictions from Eq. (16) (no ESA) or (18) (with ESA) and Eq. (20).

Also, it is possible to calculate the saturation change in refractive-index Δn_{sat} using the formula:

$$\Delta n_{sat} = (n_{eff2} - n_{eff1}) / C. \quad (23)$$

The effective pump area is⁶:

$$S_{eff} = \pi W_{p3} (W_{p1} + W_{p2}) / 4 \quad (24)$$

where W_{p1} , W_{p2} and W_{p3} are the three Gaussian parameters which characterize the profiles of the modes intensity (asymmetric and symmetric (fitted) Gaussian distributions, respectively) for depth and width of the waveguide mode (Fig. 2).

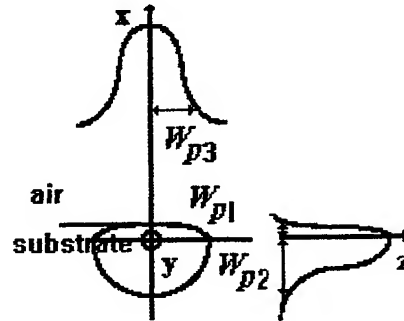


Fig. 2 The waveguide mode's intensity profiles

The fraction of the pump power carried by the active region is:

$$\eta = \int_{\text{active surface}} P_0(x, y) dS \quad (25)$$

where

$$P_0(x, y) = \frac{1}{S_{eff}} \exp(-2y^2 / W_{p3}^2) \begin{cases} \exp(-2x^2 / W_{p1}^2); & x \leq 0 \\ \exp(-2x^2 / W_{p2}^2); & x \geq 0 \end{cases} \quad (26)$$

represents the pump distribution function normalized to unity over surface.

3. THE EXPERIMENTAL ARRANGEMENT

The experimental setup used to measure the attenuation coefficient and the near field of Er^{3+} -doped Ti:LiNbO_3 optical waveguides (W), (prepared by Pirelli-Cavi Laboratories (Milano-Italy) by Ti and Er indiffusion techniques) is presented schematically in Fig. 3. We used a He-Ne laser ($\lambda = 0.63 \mu\text{m}$) for alignment and a laser diode (L. D.) having $\lambda = 1.55 \mu\text{m}$ as light source, coupled together by a 3 dB coupler (C) and focused into the waveguide by the lens (L).

The attenuation coefficient was measured using the resonator method (Fig. 3). The resonator method proves to be especially valuable for characterizing low - finesse waveguide Fabry - Pérot resonators in standard crystal orientation to evaluate the total loss of both polarizations (obtained using the polarizer P).

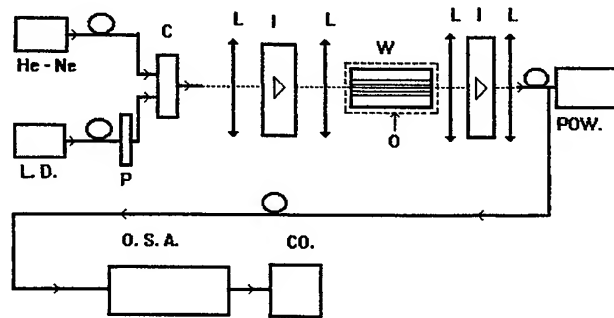


Fig. 3 The schematical experimental arrangement for the measurement of the attenuation coefficient

The spectrum of the laser diode could be measured by an optical spectrum analyser (O. S. A.). Measuring the contrast K (Eq. (4)) of the Fabry-Pérot optical waveguide (placed between two optical insulators (I)) resonances (Fig. 4) it is possible to evaluate a combined loss-reflection factor and thus an upper limit of the attenuation coefficient using Eq. (5) in which the reflectivity $R = 0.142$.

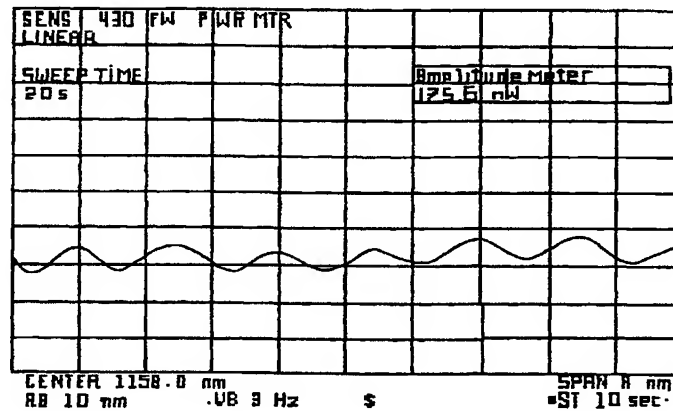


Fig. 4 The transmitted intensity of the waveguide

The transmitted intensity varies periodically with the optical phase difference Φ (Eq. (1)) and can be tuned varying the temperature of the waveguide (using an oven O).

Using a fiber placed near the end of the waveguide we measured the near field and evaluated the Gaussian parameters which characterize the mode intensity profiles in depth and width⁷.

4. DISCUSSION OF THE RESULTS

The attenuation coefficient α was measured using the resonator method presented in Fig. 3 and evaluated using the Eq. (5). In the case of an Er^{3+} -doped Ti:LiNbO_3 optical waveguide having 7.5 μm width and 48 mm length we obtained $\alpha = 1.68 \text{ dB/cm}$.

Solving numerically the equations (16) or (18) and (19) one obtained the values of the third order nonlinearity n_2 (Eq. (22)) and the saturation change in refractive index Δn_{sat} (Eq. (23)), neglecting the ESA and taking into account ESA for several values of the phase difference $\Delta\Phi$ when the incident power P is below and over the transparency power P_S , respectively.

The transparency power may be determined by performing the small-signal measurements and corresponds to the power at which the gain is exactly zero. In all cases the power decreases along the waveguide as can be seen in Fig. 5 for an incident power $P = 4 \text{ mW}$, without taking into account ESA and considering a power transparency $P_S = 10 \text{ mW}$.

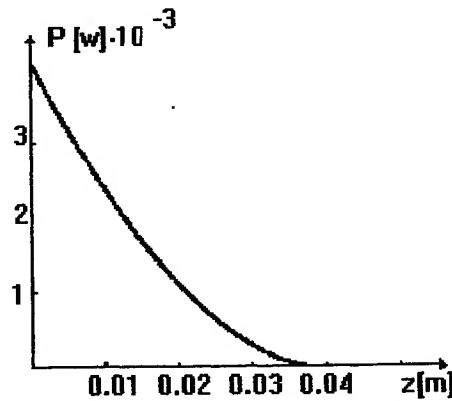


Fig. 5 Theoretical power versus distance, without ESA consideration

Assuming a phase difference $\Delta\Phi = \pi$ and a calculated value $C = 0.14$, we obtained for an Er^{3+} -doped Ti:LiNbO_3 optical waveguide characterized by the Gaussian parameters $W_{p1} = 8.4 \mu\text{m}$, $W_{p2} = 9.9 \mu\text{m}$, $W_{p3} = 7 \mu\text{m}$ and $\eta = 0.5065$ in the conditions above mentioned the following values for the third order nonlinearity and the saturation change in refractive-index, respectively: $n_2 = 8 \times 10^{-13} \text{ m}^2/\text{W}$ and $\Delta n_{\text{sat}} = 1.5 \times 10^{-4}$. Taking into account the ESA, for $\Delta\Phi = \pi$ and an incident power $P = 0.04 \text{ W}$ one obtained: $n_2 = 4 \times 10^{-15} \text{ m}^2/\text{W}$ and $\Delta n_{\text{sat}} = 4 \times 10^{-4}$.

Considering variable the third order nonlinearity, we obtained (without ESA consideration and an incident power $P = 4 \text{ mW}$) versus small lengths of the waveguide, the curves presented in Fig. 6, for several values of the phase difference $\Delta\Phi = 0.1\pi, \pi, 2\pi, 3\pi, 4\pi$.

5. CONCLUSIONS

This paper presents some theoretical and experimental results obtained in the characterization of an Er^{3+} -doped Ti:LiNbO_3 optical waveguide using nondestructive methods.

The attenuation coefficient was measured by the resonator method using the heating of the waveguide in order to obtain the resonances, the obtained results being in good agreement with other published experimental results. Also, in this paper we have proposed a method to evaluate the third order nonlinearity and the saturation change in the refractive-index using the low-finesse waveguide Fabry-Pérot resonator and near field measurements.

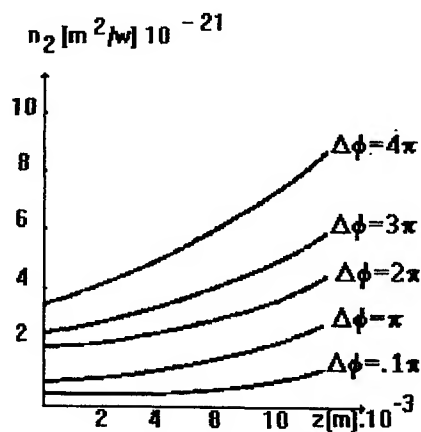


Fig. 6 The third order nonlinearities versus distance

REFERENCES

1. W. Sohler and H. Suche, "Integrated Optics III", *SPIE*, **408**, pp. 163-185, 1988.
2. R. Regener and W. Sohler: "Loss in Low-Finesse Ti: LiNbO₃ Optical Waveguide Resonator", *Appl. Phys. B* **36**, pp. 143-147, 1985.
3. T. Tamir, *Guided-Wave Optoelectronics*, Springer Verlag Berlin, Heidelberg, New-York, London, Paris, Tokio, 1988.
4. R. Brinkmann, W. Sohler and H. Suche: "Absorption, Fluorescence and Stimulated Emission in Ti-Diffused Er:LiNbO₃ Waveguides" in M. Razezghi edition: *Physical Concepts for Novel Optoelectronic Device Applications II*, Proc. Soc. Phot. Industr. Eng. Oct., 1990.
5. R. A. Betts, T. Tiugiarto, Y.L. Xue and P.L. Chu, "Nonlinear Refractive-Index in Erbium Doped Optical Fiber: Theory and Experiment", *IEEE Journ. of Quant. Electron.*, **27**, pp. 908-913, 1991.
6. M. Guidi, I. Montrosset, N. Puscas, L. Balma, R. Corsini and S. Bosso, "Fabrication and Performances Evaluation of Active Er:Ti:LiNbO₃ Waveguide", *SPIE*, **2212**, pp. 586-600, 1994.
7. N. N. Puscas, D. M. Grobncic, I. M. Popescu, M. Guidi, D. Scarano, G. Perrone and I. Montrosset, "Characterization of Er³⁺-doped Ti:LiNbO₃ waveguides: losses, absorption spectra, and near field measurements", *Opt. Eng.*, **1685**, pp. 1311-1318, 1996.

He-Ne laser gain dependence on discharge current and gas pressure from resonant Faraday effect

Alina Gearba*, C. Negutu, Gabriela Cone, I. M. Popescu

Physics Department, "Politehnica" University of Bucharest, Romania

ABSTRACT

It is analyzed the influence of a longitudinal magnetic field on the operating mode of a He - Ne laser, knowing that the magnetic field is used for the suppressing of the λ 3.39 μm , which is amplified in the same time with λ 632.8 nm. It was used the Faraday magneto - optic effect at resonance, so that the λ 632.8 nm He-Ne laser radiation travels through a Ne - Ne mixture, with the pressures ratio $p_{\text{He}}/p_{\text{Ne}} = 5$, in population inversion conditions, placed in a longitudinal magnetic field. It was studied the laser medium amplification coefficient dependence on the parameters: discharge current intensity and total gas pressure.

For the relation between the rotation angle of the polarization plane in a magnetic field and the laser amplification coefficient, in the He - Ne mixture, it was found a linear theoretical dependence. By fitting the experimental data, there are obtained nonlinear dependencies, for $\alpha(p)$ and $\alpha(I)$, which can be explained in the atomic collisions theory.

Keywords: magneto-optical effect, gas laser gain, He-Ne laser.

1. INTRODUCTION

About forty years after Javan¹ constructed the first He-Ne laser $\lambda = 632.8$ nm, the excitation and deexcitation processes for the levels of the atomic gaseous neon, which in a mixture with gaseous helium, can become a laser active medium, are not well-known.

The helium atoms in the gas mixture modifies the electric discharge conditions, the impurity presence reduces the electronic temperature in discharge, reducing the number of electrons with high energy that can excite the $3s_2$ neon upper laser level², the conditions for the change of the absorbing character in one amplifying³. All these induce excitation and deexcitation processes of the neon laser atomic levels. One of the phenomena which offers information about these processes is the Faraday rotation of the radiation polarization plane that propagates through the laser active medium situated in a longitudinal magnetic field. If the radiation emitted by a He-Ne laser with $\lambda = 632.8$ nm propagates through an optical active medium - the He-Ne mixture with controlled concentrations - the absorption and reemission processes of this radiation between neon laser levels are dominant. Similar processes between other levels have so small probabilities, so we can neglect them.

We used the Faraday effect in resonance conditions, in order to obtain the polarization plane rotation of the radiation emitted by a He-Ne laser ($\lambda = 632.8$ nm) in the optical active medium - the electrical discharge in a He-Ne mixture at a low pressure.

2. THEORY

We consider a monochromatic radiation with an angular frequency ω traveling in a gaseous medium along an external magnetic field $\vec{B} \parallel \hat{z}$, where \hat{x}, \hat{y} and \hat{z} define a right-handed coordinate system (the Faraday geometry). The light

* Correspondence: E-mail: alina@physics2.physics.pub.ro. Tel. 410. 45. 42 / 102. Fax: 411.61.71

propagating parallel to \vec{B} is described by two different indices of refraction corresponding to the circular polarization of the positive and negative helicity. As a result, the linearly polarized light traveling through the sample in this geometry will experience a rotation of the polarization plane (Faraday rotation). The polarization of the transmitted light may also show some degree of ellipticity if there is significant circular dichroism induced by the magnetic field. By convention, rotations that are counterclockwise when viewed against the light propagation along the direction of magnetic field are defined as positive.

The Faraday rotation angle Θ_F is given by the well-known expression

$$\Theta_F = \frac{\omega l}{2c} (n_- - n_+) \quad (1)$$

where ω is the photon circular frequency, l the distance in the medium traversed by the light, c the speed of light in vacuum, and n_{\pm} the refractive indices corresponding to the circular polarizations $\hat{\sigma}_{\pm}$. The microscopic origin of the circular birefringence (i.e., the fact that $n_+ \neq n_-$) is related to the electronic transitions experienced by the atoms in the presence of an external magnetic field.

To calculate the difference ($n_+ - n_-$) we must express the electric susceptibility χ_e . For an isolated system in equilibrium, containing weakly interacting particles in energy states $|\mathcal{E}_i\rangle$, and an isotropic medium,

$$\chi_e = \frac{N \sum_i \left(\bar{p}_{ii} \cdot \frac{\vec{E}}{E^2} \right) \exp\left[-\frac{\mathcal{E}_i}{kT}\right]}{\epsilon_0 \sum_i \exp\left[-\frac{\mathcal{E}_i}{kT}\right]} \quad (2)$$

where N is the number of particles per unit volume, \bar{p}_{ii} is the matrix element of the electric dipole moment corresponding to the state $|\mathcal{E}_i\rangle$, and \vec{E} is the applied electric field in the medium. At low pressure, the atomic gases are composed only of atoms, ions and electrons, the dominant polarization mechanism being electronic. In this case the application of an electric field tends to deform the probability distribution of the electron cloud around the nucleus, so that a net induced electric dipole moment is created.

The interaction of an atom with the optical field $\vec{E} \cos \omega t$ is described by the total Hamiltonian $\hat{H} = \hat{H}_0 + \hat{H}_p \cos \omega t$ where \hat{H}_0 is the unperturbed Hamiltonian of the atom (the radiation field is missing) and $\hat{H}_p \cos \omega t$ is the perturbation term. Therefore

$$\hat{H}_p = -\vec{p} \cdot \vec{E} = \sum_k e \vec{r}_k \cdot \vec{E}. \quad (3)$$

All the matrix equations are represented in the vector space of the energy states of \hat{H}_0 . In the resonant case, ω would have a value close to the value of one pair of energy levels \mathcal{E}_m and \mathcal{E}_n (in our case the laser levels). That is,

$$\omega = \frac{\mathcal{E}_m - \mathcal{E}_n}{\hbar} + \Delta\omega \quad (4)$$

with $\Delta\omega \ll \omega$. In an isotropic medium Eq. (2) may be written as⁴:

$$\chi_e = -\frac{1}{\epsilon_0 \hbar} \cdot \frac{N_n - N_m}{\Delta\omega - i\Gamma_{nm}} \left\langle \mathcal{E}_n \left| \sum_k e \vec{r}_k \right| \mathcal{E}_m \right\rangle^2 \quad (5)$$

where N_n and N_m are respectively the number of particles per unit volume in the $|\mathcal{E}_n\rangle$ and $|\mathcal{E}_m\rangle$ states at equilibrium and Γ_{nm} are called the transverse relaxation rates of the off-diagonal matrix elements and are related to the lifetime of the atomic

levels. At equilibrium, $N_n > N_m$ if $\mathcal{E}_m > \mathcal{E}_n$ and an electromagnetic wave is attenuated in the propagating direction. In certain circumstances, if $N_n < N_m$ for $\mathcal{E}_m > \mathcal{E}_n$ (population inversion) the waves are amplified during their propagation through this active medium.

The refractive index depends on the real part of the electric susceptibility:

$$\text{Re } \chi_e = -\frac{\Delta\omega}{\epsilon_0 \hbar} \cdot \frac{N_n - N_m}{(\Delta\omega)^2 + \Gamma_{nm}^2} \left| \langle \mathcal{E}_n | \sum_k e \vec{r}_k | \mathcal{E}_m \rangle \right|^2 \quad (6)$$

Placing the isotropic medium in a dc longitudinal magnetic field \vec{B} , it becomes anisotropic and the difference between the refractive indices is given by:

$$n_+ - n_- = -\frac{1}{n \hbar \epsilon_0} \cdot \frac{(N_n - N_m) \Delta\omega}{(\Delta\omega)^2 + \Gamma_{nm}^2} \left\{ \left| \langle \mathcal{E}_{n, J_n, \mu+1} | \sum_k e \vec{r}_k | \mathcal{E}_{m, J_m, \mu} \rangle \right|^2 - \left| \langle \mathcal{E}_{n, J_n, \mu-1} | \sum_k e \vec{r}_k | \mathcal{E}_{m, J_m, \mu} \rangle \right|^2 \right\} \quad (7)$$

where μ is the magnetic quantum number, $\Delta\omega = \frac{eB}{m_e}$ is the Zeeman splitting, $n = \frac{1}{2}(n_+ + n_-)$ the refraction index for $\vec{B} = 0$, + and - are referred to the radiation emitted for $\Delta\mu = +1$ and $\Delta\mu = -1$, respectively.

If the wave propagates through an anisotropic medium, the initial direction of the polarization is rotated by an angle (from Eqs.(1) and (7)):

$$\Theta_F = -\frac{\omega l e B}{2 n c \hbar m_e \epsilon_0} \cdot \frac{(N_n - N_m)}{\left(\frac{eB}{m_e} \right)^2 + \Gamma_{nm}^2} \left\{ \left| \langle \mathcal{E}_{n, J_n, \mu+1} | \sum_k e \vec{r}_k | \mathcal{E}_{m, J_m, \mu} \rangle \right|^2 - \left| \langle \mathcal{E}_{n, J_n, \mu-1} | \sum_k e \vec{r}_k | \mathcal{E}_{m, J_m, \mu} \rangle \right|^2 \right\} \quad (8)$$

In the case of an absorbing medium $N_n > N_m$ and $\Theta_F < 0$, on the contrary for an active (amplifying) medium $N_n < N_m$ so that $\Theta_F > 0$. We can conclude that the occurrence of the population inversion is emphasized by the change of the sign of the Faraday rotation angle measured in a laser active medium.

The gain of the laser medium depends in the same manner on the population inversion⁵ ($N_m - N_n$) because this is proportional to the imaginary part of the electrical susceptibility χ_e , that is

$$\alpha_{nm} = \frac{4\pi\omega}{\hbar c} \frac{\Gamma_{mn} (N_n g_m - N_m g_n)}{(\Delta\omega)^2 + \Gamma_{mn}^2} \left| \langle \mathcal{E}_n | \sum_i e x_i | \mathcal{E}_m \rangle \right|^2 \quad (9)$$

We can say that in a constant magnetic field, the two quantities Θ_F and α_{nm} are in a direct proportionality. By measuring the Faraday rotation Θ_F as a function of the gas pressures and the discharge current we studied the α_{nm} dependence of these parameters. The Faraday rotation of the polarization plane of the incident laser beam was measured by modulating the incident laser beam with a rotating polarizer⁶. We applied to the optic active medium : a) an electric discharge which populates the excited levels; b) a laser beam linearly polarized in resonance with atomic transition $\mathcal{E}_m \rightarrow \mathcal{E}_n$; c) a static magnetic field parallel to the propagation direction of laser beam and to the discharge electric field.

3. RESULTS AND DISCUSSIONS

In the analysis of the experimental results we made the following hypotheses: a) the laser beam is emitted by an external laser source, independently of the studied atomic medium; b) the atomic levels \mathcal{E}_m and \mathcal{E}_n have a Zeeman structure defined by the angular momentum J_m respectively J_n ; c) the atomic velocities have a Maxwell distribution; d) the discharge is

homogenous in all the volume and constant during the measurements; e) the relaxation mechanisms (collisions, multiple diffusion) are isotropic.

We used as parameters the total pressure of the gaseous mixture and the discharge current intensity. In Figs. 1 and 2 it is represented the laser gain dependence on the total pressure of the gaseous mixture, for two values of the He and Ne pressures ratio, together with a fitting curve of the experimental data and its derivative.

We chose the $p_{\text{He}}/p_{\text{Ne}} = 5$ ratio for which it was demonstrated experimentally⁵ that it appears the optimal oscillation conditions of the He-Ne laser at λ 632.8 nm. We chose another value for the partial pressures ratio to compare the two laser oscillation conditions. For the fitting curve we obtained a function like $\alpha = c_1 p(1 - c_2 p)\exp[-c_3 p]$. In arbitrary units, the values of these empirical constants are $c_1 = 23$, $c_2 = 0.4$, $c_3 = 1.2$ for $p_{\text{He}}/p_{\text{Ne}} = 5$ and $c_1 = 21$, $c_2 = 0.24$, $c_3 = 1.25$ for $p_{\text{He}}/p_{\text{Ne}} = 10$, respectively.

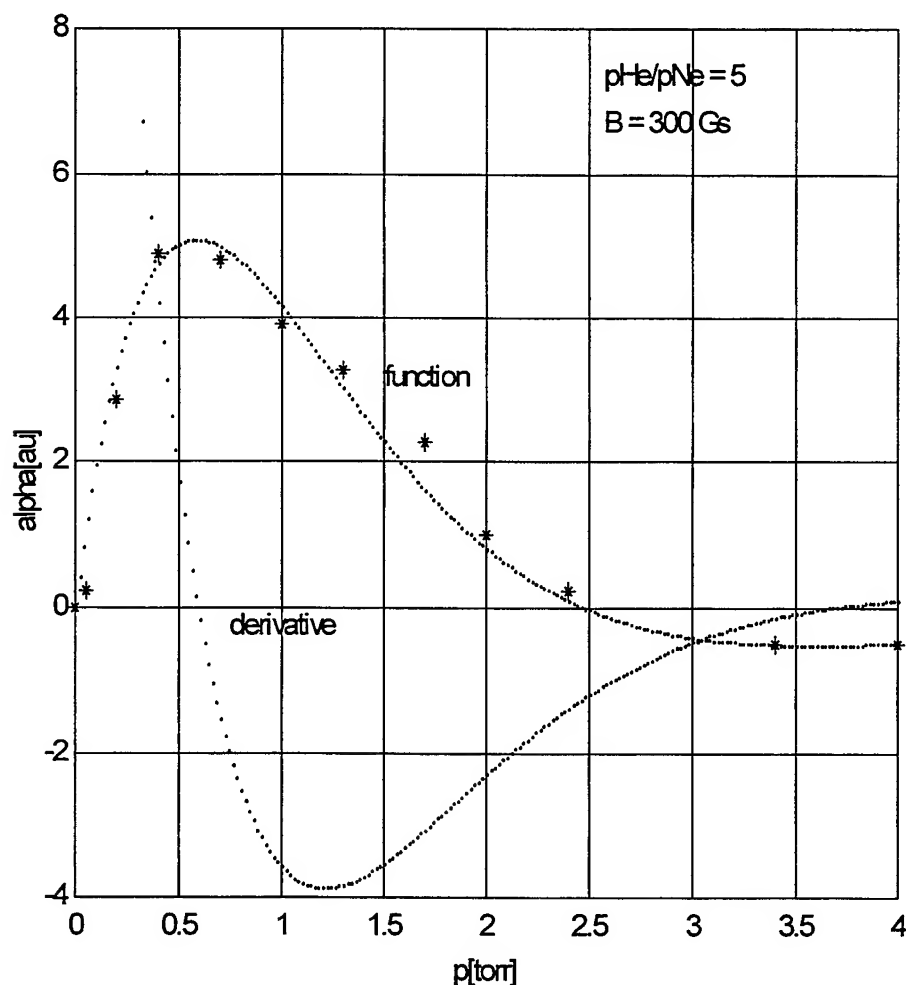


Fig.1. The laser gain dependence on the total pressure of the gaseous mixture for $p_{\text{He}}/p_{\text{Ne}} = 5$;

* - experimental data, - the fitting curve $\alpha = 23p(1 - 0.4p)\exp[-1.2p]$ and its derivative.

In the $p_{\text{He}}/p_{\text{Ne}} = 5$ case (Fig. 1) the maximum value of α (for which the derivative is zero) it is obtained at $p = 0.58$ torr, while for the $p_{\text{He}}/p_{\text{Ne}} = 10$ case (Fig. 2), the maximum value of α appears at $p = 0.66$ torr. Gordon and White⁵ reported that in dc discharge, for $0.6328 \mu\text{m}$ lasers they obtained optimum gains by using $pD = 2.9 \div 3.6 \text{ torr} \cdot \text{mm}$ and $p_{\text{He}} = 5p_{\text{Ne}}$, with $p = p_{\text{He}} + p_{\text{Ne}}$, for laser tubes having a diameter D from 1 to 15 mm. In our case, $D = 6$ mm, so $pD = 3.48 \text{ torr} \cdot \text{mm}$ for $p_{\text{He}}/p_{\text{Ne}} = 5$.

Our result confirms the Gordon and White result. α dependencies on the total pressure, represented in Figs. 1 and 2, confirm the helium role in population of the neon upper laser level.

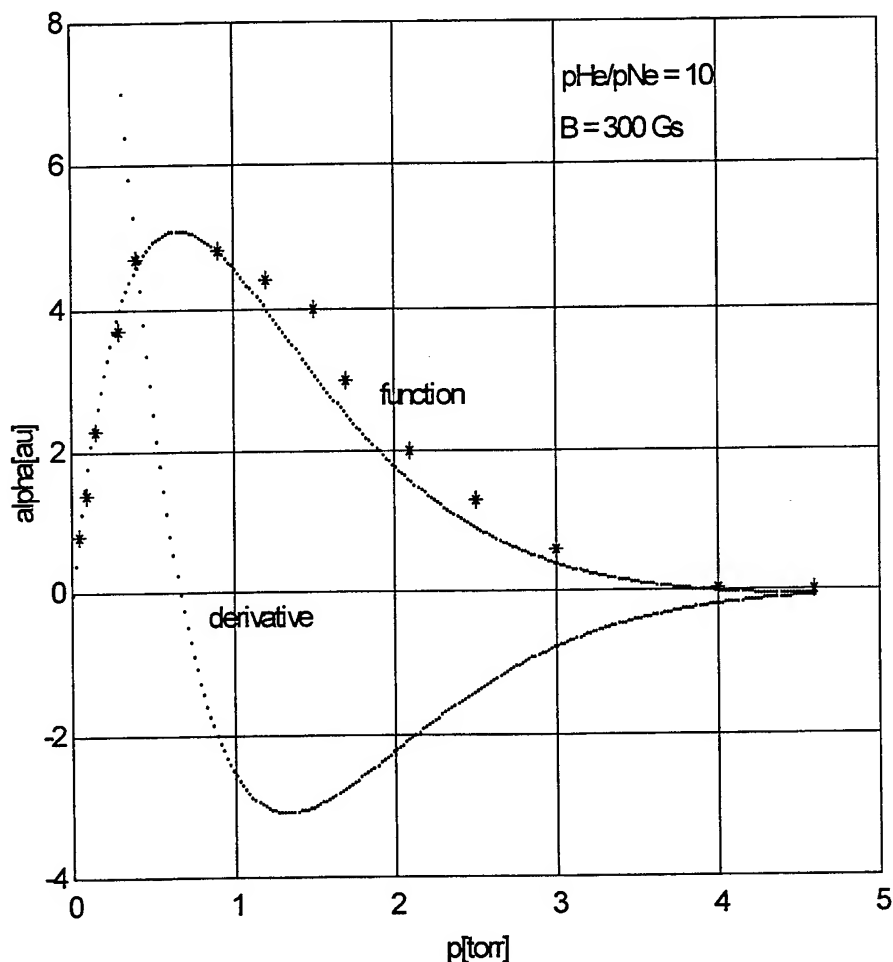


Fig. 2. The laser gain dependence on the total pressure of the gaseous mixture for $p_{\text{He}}/p_{\text{Ne}} = 10$;
* - experimental data, - the fitting curve $\alpha = 21p(1 - 0.24p)\exp[-1.25p]$ and its derivative.

In Figs. 3 and 4 it is represented the gain dependence on the discharge current intensity, together with the fitting curve for two values of the He and Ne pressures ratio. For the fitting curve we obtained an expression like $\alpha = \frac{AI}{1 + BI} - CI$, which is

consistent with the Gordon and White experimental result. They showed that in the case of a gaseous mixture with the partial pressures ratio $p_{\text{He}}/p_{\text{Ne}} = 5$, the population of the upper Ne level, $3s_2$, is related to the discharge current intensity I by

$$n_s = \frac{AI}{1 + BI}, \text{ where } A \text{ and } B \text{ are constants.}$$

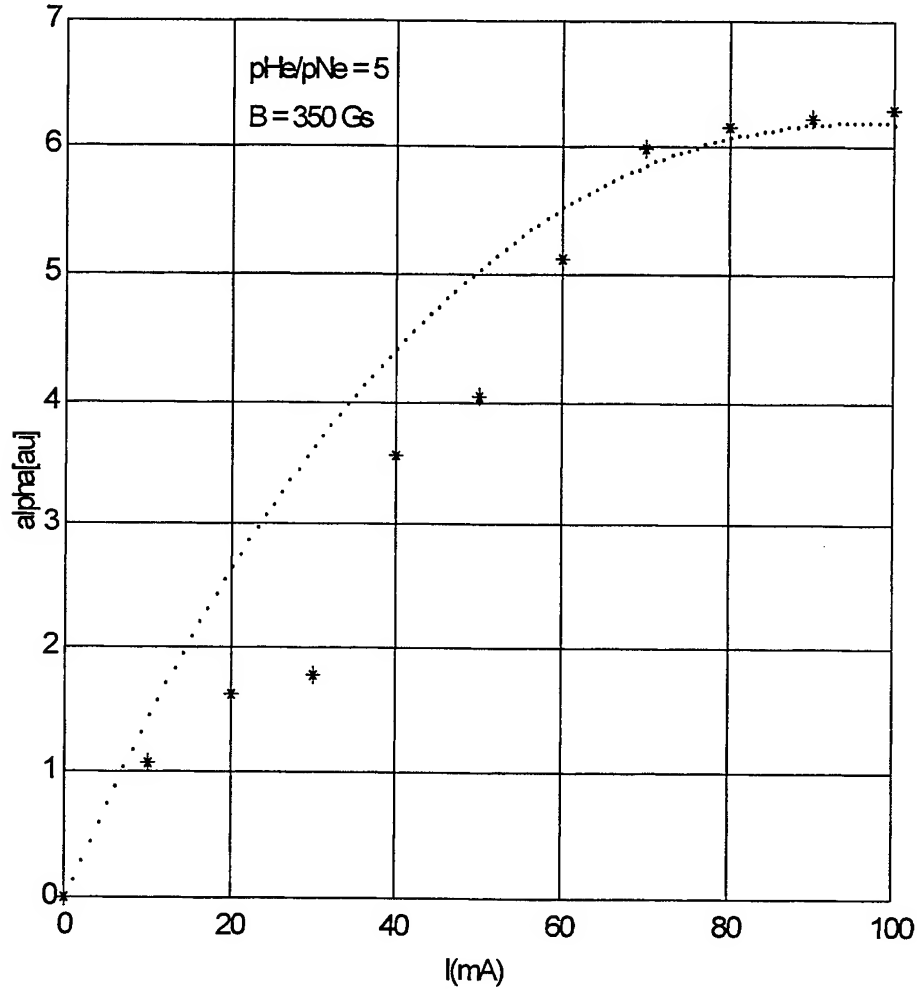


Fig. 3. The laser gain dependence on the discharge current intensity for $p_{\text{He}}/p_{\text{Ne}} = 5$

and $p = 5$ torr; * - experimental data, - the fitting curve $\alpha = \frac{0.293I}{1 + 0.005I} - 0.133I$.

On the other hand, the population of the lower laser level, that is, the $2p_4$ Ne state, was found to be related to the discharge current by $n_p = CI$. In arbitrary units, we obtained for the constants A , B , and C the values $A = 0.293$, $B = 0.005$ and $C = 0.133$ for the $p_{\text{He}}/p_{\text{Ne}} = 5$ case and $A = 1.2465$, $B = 0.0446$ and $C = 0.117$ for the $p_{\text{He}}/p_{\text{Ne}} = 7$ case, respectively. From Figs. 3 and 4 we observe that the gain coefficient arrives at saturation at a smaller value of the current intensity for a smaller total pressure. So, for $p_{\text{He}}/p_{\text{Ne}} = 5$, $I_{\text{sat}} = 80$ mA at $p = 5$ torr, and for $p_{\text{He}}/p_{\text{Ne}} = 7$, $I_{\text{sat}} = 40$ mA at $p = 0.8$ torr. In the literature it is mentioned, as an experimental result, a current saturation value of 30 mA at $p < 1$ torr.

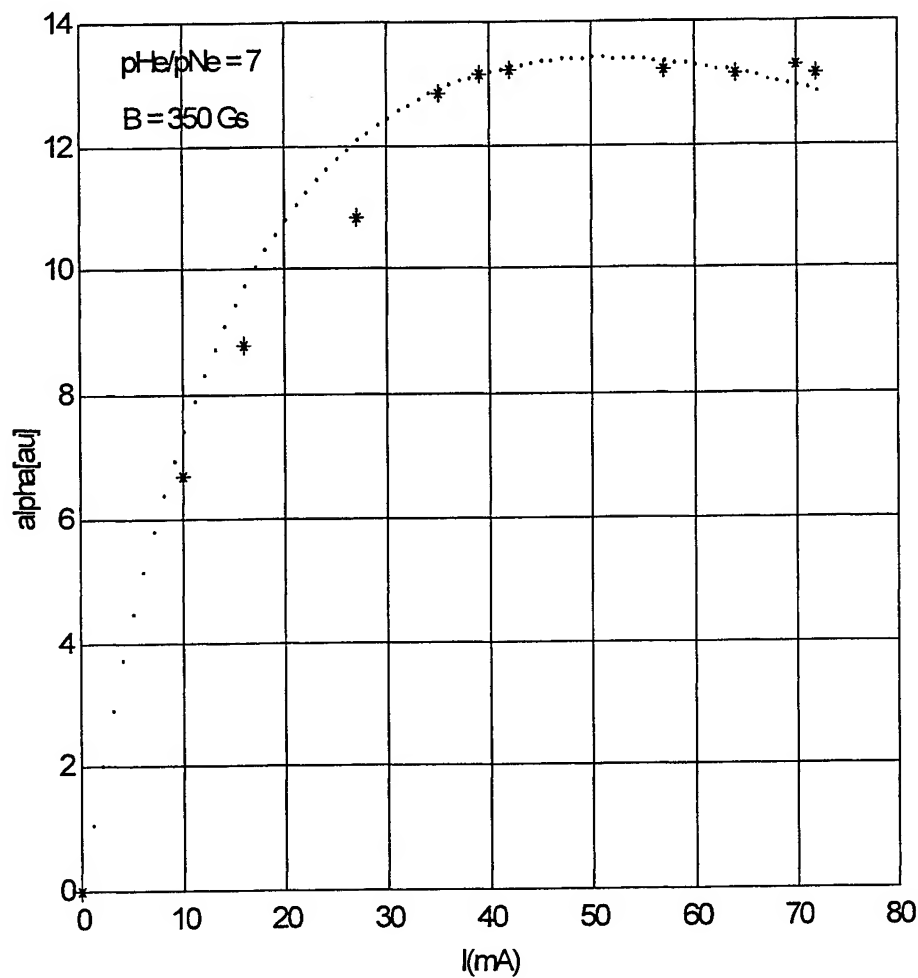


Fig. 4. The laser gain dependence on the discharge current intensity for $p_{\text{He}}/p_{\text{Ne}} = 7$ and $p = 0.8$ torr; * - experimental data, - the fitting curve $\alpha = \frac{0.2465I}{1 + 0.0446I} - 0.117I$.

4. CONCLUSIONS

In conclusion, our results reproduce the conditions for the occurrence of the laser oscillation in a He-Ne gaseous mixture obtained empirically in Refs. 1 and 5. The results may be useful for studying the collision processes among atoms, ions and electrons that are responsible for atomic excitation and deexcitation of energy levels which are involved in laser transition.

REFERENCES

1. A. Javan, "Possibility of production of negative temperature in gas discharge," *Phys. Rev. Lett.*, **3**(2), pp. 38-42, 1966.
2. C. Berenyi, M. Bârlogeanu and V.G. Velculescu, "Influența impurităților asupra liniilor 632.8 nm și 3.39 μm a laserului cu He-Ne," *Stud. Cercet. Fiz.*, **22**(3), pp. 235-241, 1970.

3. A.I. Ciura, M. Ristici and V. Vasiliu, "Spectroscopia de perturbație ca metodă de studiu a caracterului amplificator al unui mediu," *Stud. Cercet. Fiz.*, **29**(9), pp. 969-972, 1977.
4. W.S.C. Chang, *Principles of Quantum Electronics*, Addison Wesley Publ. Comp., Menlo Park, p. 218, 1970.
5. A.D. White and E.I. Gordon, "Excitation mechanisms and current dependence of population inversion in He-Ne lasers," *Appl. Phys. Lett.* **3**, pp. 198-200, 1963.
6. Gabriela Cone, I.M. Popescu, "Population inversion calculus from Faraday rotation in a He-Ne gaseous mixture," *Opt. Eng.*, **35**(5), pp. 1273-1277, 1996.

Global symmetries for the laser radiation

Radu Constantinescu ^a, Carmen Ionescu ^a, Razvan Popa ^a

^a Department of Theoretical Physics,
University of Craiova
13 A.I.Cuza, 1100 Craiova, Romania

ABSTRACT

The paper presents the possibility of analysing the electromagnetic field as a constrained dynamical system. The transversality of the electromagnetic waves leads to difficulties in their covariant description. The longitudinal and the temporal components appear as unphysical degrees of freedom. In order to develop a canonical formalism it is necessary to use a phase space extended with ghost type generators. In this space the gauge symmetry of the field can be replaced by a global BRST symmetry. Our construction will correspond to a generalized symmetry that can be split in many pieces. This decomposition could be very useful in the description of multi-interaction processes.

Keywords: Constrained system, BRST procedure

1. INTRODUCTION

We shall be interested in the covariant description of a laser radiation passing through a dense plasma. The electromagnetic field of the laser light leads to beam generation of many kinds of charged particles: electrons, light ions, and heavy ions. Depending on the light frequency and its intensity, the interactions between the laser radiation and the charged particles could give rise to oscillating confined beam, or could causes the divergence of the beam.

The Maxwell equations for the electric field $\vec{E}(\vec{r}, t)$ and the magnetic field $\vec{B}(\vec{r}, t)$ in vacuo have the form:

$$\begin{cases} \text{div } \vec{E} = \frac{1}{\epsilon} \rho \\ \text{div } \vec{B} = 0 \\ \text{rot } \vec{E} = -\frac{\partial \vec{B}}{\partial t} \\ \text{rot } \vec{B} = \frac{1}{c^2} \vec{j} + \frac{1}{c^2} \frac{\partial \vec{E}}{\partial t} \end{cases} \quad (1)$$

where \vec{j} is the current density, ρ is the charge density, c the light velocity and ϵ is the dielectric constant.

The covariant description of the field could be obtained using the quadripotential $A_\alpha(\vec{r}, t)$ as generalized coordinates and the field tensor

$$F_{\alpha\beta} = \partial_\alpha A_\beta - \partial_\beta A_\alpha \quad (2)$$

In this case the equations (1) became:

$$\begin{cases} \partial_\alpha F^{\alpha\beta} = -\frac{1}{c^2} j^\beta \\ \partial_\alpha F_{\beta\gamma} + \partial_\beta F_{\gamma\alpha} + \partial_\gamma F_{\alpha\beta} = 0 \end{cases} \quad (3)$$

Some problems arise in the regions far from the sources. In this case not all components of the quadripotential $A_\alpha(\vec{r}, t)$ are independent. In the Hamiltonian description, using the Dirac terminology, the electromagnetic field become a constrained dynamical system. It is characterized by two constraints:

-the primary constraint:

$$\pi^0 \equiv F^{00} = 0 \quad (4)$$

-the secondary constraint:

$$\partial_i \pi^i \equiv \partial_i F^{i0} = 0 \quad (5)$$

E-mail address: rconsta@central.ucv.ro

We have used the notation $\pi^\alpha = F^{\alpha 0}$ for the energy-momentum quadrivector..

The constraints (4) and (5) cause difficulties when a quantum description of the system is desired. At the first sight, the canonical structure of the theory can not be established [1].

We shall show in this paper how this problem could be avoided using a special method, known as the BRST technique [2-5]. In essence this technique requires the replacement of the gauge symmetry of the field with a global symmetry, expressed by a differential operator, s^T . This operator could act canonically on the observables of the theory if we consider a special Poisson bracket and a special operator called the BRST charge:

$$s^T * = [* , \Omega^T] \quad (6)$$

The requirement of nilpotency imposes to s^T , requirement specific for any differential, leads on the canonical level to the *master equation*:

$$(s^T)^2 = 0 \Rightarrow [\Omega^T, \Omega^T] = 0 \quad (7)$$

Generally speaking, the relation (7) can not be satisfied in the initial phase space of a constrained system. We have to add new generators and to define an extended phase space. The new generators have not a physical significance, do not appear in the final estimations of the theory, and for this reason they are called *ghosts*.

An interesting feature of the BRST symmetry is the possibility of its extension towards more general ones. Such approaches has been done in [6-10]. We intend to show how this extension work in the case of a laser radiation. We shall analyze the case of a symmetry that could be split in three independent pieces, case known as the $sp(3)$ symmetry. The general frame for this type of symmetry will be presented in the next section, and its application for the electromagnetic field will be done in the third section.

2. THE GENERAL $SP(3)$ BRST THEORY

Let us consider a dynamical system that in the phase space $M_0 = \{q^i, p_i; i = 1, \dots, n\}$ is described by the hamiltonian $H_0(q, p)$ and by the first class constraints $\{G_\alpha(q, p) = 0, \alpha = 1, \dots, m\}$. The first class condition imply the relations:

$$[G_\alpha, G_\beta] = C_{\alpha\beta}^\gamma G_\gamma; [H_0, G_\alpha] = V_\alpha^\beta G_\beta \quad (8)$$

The Poisson brackets are defined so as

$$[q^i, p_j] = \delta_j^i \quad (9)$$

The structure functions $C_{\alpha\beta}^\gamma$ and V_α^β could depend on the canonical variables $\{q^i, p_i\}$ or could be constant as for the case of the Yang-Mills theory.

Because of the gauge invariance, not all the coordinates of M_0 are independent and the canonical quantization is not possible in this space. The BRST method employs an extended phase space that is obtained by adding some ghost variables to the real ones. In this extended space the theory is invariant in relation to a global symmetry, invariance which could be expressed either through the differential operator s^T , or by the BRST charge Ω^T . For an observable A one has:

$$s^T A \equiv [A, \Omega^T] = 0$$

The nilpotency of s^T asks for the validity of the master equation:

$$[\Omega^T, \Omega^T] = 0 \quad (10)$$

In the last two relations the Poisson brackets must be defined on the whole extended phase space M , space that is generated by the coordinates of M_0 and by some canonical pairs of ghosts. The concrete spectrum of ghosts depends on the symmetry we aim to be satisfied. For example in the case of an irreducible gauge theory the Koszul complex of the ghost momenta suitable for defining a $sp(3)$ symmetry would be generated by the variables [11]:

$$P_A \equiv \{P_{\alpha a}, \pi_{\alpha a}, \tau_\alpha; \alpha = 1, \dots, m; a = 1, 2, 3\} \quad (11)$$

The construction of the extended phase space is achieved by adding to each generator from (11) of a canonical conjugated ghost:

$$Q^A \equiv \{Q^{\alpha a}, \lambda^{\alpha a}, \eta^\alpha; \alpha = 1, \dots, m; a = 1, 2, 3\} \quad (12)$$

$$[Q^{\alpha a}, P_{\beta b}] = [\lambda^{\alpha a}, \pi_{\beta b}] = \delta_{\beta}^{\alpha} \delta_b^a; [\eta^{\alpha}, \tau_{\beta}] = \delta_{\beta}^{\alpha} \quad (13)$$

In order to transform the whole extended phase space in a graduate complex, four different degrees will be assigned for each variable, as well as for all the operators acting on this complex. For example, the previous mentioned variables will be characterized by:

* the ghost number (*gh*):

$$\begin{aligned} gh(P_{\alpha a}) &= -gh(Q^{\alpha a}) = -1 \\ gh(\pi_{\alpha a}) &= -gh(\lambda^{\alpha a}) = -2 \\ gh(\tau_{\alpha}) &= -gh(\eta^{\alpha}) = -3 \end{aligned}$$

* the resolution degree (*res*):

$$\begin{aligned} res(P_{\alpha a}, \pi_{\alpha a}, \tau_{\alpha}) &= -gh(P_{\alpha a}, \pi_{\alpha a}, \tau_{\alpha}) \\ res(Q^{\alpha a}, \lambda^{\alpha a}, \eta^{\alpha}) &= 0 \end{aligned}$$

* the level number (*lev*):

$$\begin{aligned} lev(P_{\alpha a}) &= -lev(Q^{\alpha a}) = -a + 1 \\ lev(\pi_{\alpha a}) &= -lev(\lambda^{\alpha a}) = a - 4 \\ lev(\tau_{\alpha}) &= -lev(\eta^{\alpha}) = -3 \end{aligned}$$

Using these graduations, each variable could be written in the form

$$A_{\alpha} \equiv A_{\alpha}^{(gh, lev)}$$

By passing from M_0 to M , the hamiltonian H_0 is to be changed into an extended hamiltonian that must be also a BRST invariant:

$$H_0 \rightarrow H; [H, \Omega^T] = 0 \quad (14)$$

The equations (10) and (14), completed with suitable boundary conditions for Ω^T and for H , define the key problems of the BRST theory. The standard manner in solving these two problems uses the homological perturbation theory. It imposes a decomposition of the BRST charges and of the hamiltonian according the resolution degree:

$$\Omega^T = \sum_{r \geq 0} \Omega^{(r)}; H = \sum_{r \geq 0} H^{(r)}; res \Omega = res H = r \quad (15)$$

The Poisson superbracket defined in the space $M \equiv \{Q^A, P_A\}$ generated by (11) and (12) could be also decomposed according the resolution degree:

$$[A, B] = \sum_{k=0}^3 [A, B]_k; res([A, B]_k) = res(A) + res(B) - k \quad (16)$$

As we are interested now in the implementation of a $sp(3)$ BRST symmetry, we shall aim at a partition of the form:

$$s^T = s_1 + s_2 + s_3 \Leftrightarrow \Omega^T = \Omega_1 + \Omega_2 + \Omega_3 \quad (17)$$

In order to assure the nilpotency of s^T , the operators $s_a, a = 1, 2, 3$ must represent three anticommuting differentials:

$$s_a s_b + s_b s_a = 0 \quad (18)$$

In this case the equation (10) will be equivalent with the set of equations

$$[\Omega_a, \Omega_b] = 0; a, b = 1, 2, 3 \quad (19)$$

The graduation of the three BRST charges will be:

$$gh(\Omega_a) = 1; \text{cop}(\Omega_a) = a; \text{lev}(\Omega_a) = a - 1 \quad (20)$$

Concerning the resolution degree, the decomposition (15) induces similar relations for each $\Omega_a, a = 1, 2, 3$.

$$\Omega_a = \sum_{r \geq 0} \binom{r}{\Omega_a}; \text{res}(\Omega_a) = r \quad (21)$$

Following the line of the homological perturbation theory, the master equations (19) could be projected on different values of the resolution degree. We should obtain a well defined problem and we could determine the charges Ω_a if we should suit (19) with the following boundary conditions:

$$\begin{aligned} \Omega_a^{(0)} &= G_\alpha \delta_{ab} Q^{\alpha b} + \dots \\ \Omega_a^{(1)} &= \epsilon_{abc} \delta^{bd} P_{\alpha d} \lambda^{\alpha c} + \dots \\ \Omega_a^{(2)} &= \pi_{\alpha a} \eta^\alpha + \dots \end{aligned} \quad (22)$$

In the case of the first rank theories, where the functions $C_{\alpha\beta}^\gamma$ and V_α^β are constant, the complete form of Ω_a is [12]:

$$\begin{aligned} \Omega_a &= G_\alpha \delta_{ab} Q^{\alpha b} + \epsilon_{abc} \delta^{bd} P_{\alpha d} \lambda^{\alpha c} + \frac{1}{2} C_{\alpha\beta}^\gamma \delta_{ab} P_{\gamma c} Q^{\beta c} Q^{\alpha b} + \\ &+ \pi_{\alpha a} \eta^\alpha + \frac{1}{2} C_{\alpha\beta}^\gamma \pi_{\gamma c} \lambda^{\beta c} Q^{\alpha b} \delta_{ba} + \frac{1}{12} \epsilon_{cd} C_{\sigma\alpha}^\theta C_{\theta\beta}^\gamma \pi_{\gamma b} Q^{\alpha c} Q^{\beta d} Q^{\sigma m} \delta_{ma} + \\ &+ \frac{1}{2} C_{\beta\alpha}^\gamma \tau_\gamma Q^{\alpha a} \eta^\beta + \frac{1}{12} (C_{\sigma\alpha}^\gamma C_{\gamma\beta}^\theta + C_{\sigma\beta}^\gamma C_{\gamma\alpha}^\theta) \tau_\theta Q^{\sigma a} Q^{\beta n} \lambda^{\alpha n} \end{aligned} \quad (23)$$

The extended hamiltonian could be found out by solving the problem that arises when we extend the requirement from (14) and we ask for the BRST invariances in respect to each individual Ω_a :

$$\begin{cases} [H, \Omega_a] = 0 \\ H|_{P=\pi=\tau=0} = H_0 \end{cases} \quad (24)$$

The solution of this problem, for the first rank theories in the case $\text{sp}(3)$ has the form [12]:

$$H = H_0 + V_\alpha^\beta P_{\beta a} Q^{\alpha a} + V_\alpha^\beta \pi_{\beta a} \lambda^{\alpha a} + V_\alpha^\beta \tau_\beta \eta^\alpha \quad (25)$$

We shall now use these results in order to achieve the $\text{sp}(3)$ quantization of the some close and irreducible models of dynamical systems.

3. THE ELECTROMAGNETIC FIELD

Let us consider first the case of the abelian gauge field, described by the action:

$$S_0[A_\mu] = \int d^4x \left(-\frac{1}{4} F_{\alpha\beta} F^{\alpha\beta} \right) \quad (26)$$

where the field strength is given by $F_{\alpha\beta} = \partial_\alpha A_\beta - \partial_\beta A_\alpha$. The action is invariant under the gauge transformation $\delta_\epsilon A_\mu = \partial_\mu \epsilon$.

The canonical momenta $p_i \equiv F_{i0}$ generate one primary constraint

$$G_1(x) \equiv p_0 = 0 \quad (27)$$

The density of the canonical hamiltonian is:

$$H_c(x) = H_0(x) + A_0(-\partial^i p_i); i = 1, 2, 3 \quad (28)$$

with

$$H_0(x) = \frac{1}{4} F_{ij} F^{ij} + \frac{1}{2} p_i p^i \quad (29)$$

The consistency condition $\dot{G}_1 \equiv [G_1, H_c] \approx 0$ leads to the secondary constraint

$$G_2(x) \equiv -\partial_i p^i \quad (30)$$

There are no more constraints because G_2 and the hamiltonian commutes. The algebra of the systems is defined by the relations:

$$[G_u(x), G_v(y)] = 0; u, v = 1, 2 \quad (31)$$

$$[H_c(x), G_1(y)] = G_2(y) \delta(x - y); [H_c(x), G_2(y)] = 0 \quad (32)$$

By comparison with (8) we could identify:

$$\begin{aligned} C_{\alpha\beta}^\gamma &\equiv 0 \\ V_\alpha^\beta &\equiv \begin{pmatrix} 0 & 1 \\ 0 & 0 \end{pmatrix} \end{aligned} \quad (33)$$

With these identifications, the BRST charges and the extended hamiltonian get the form:

$$\Omega_a = Q^{ub} \delta_{ba} G_u + \epsilon_{amn} P_{um} \lambda^{un} + \pi_{ua} \eta^u; u = 1, 2; a, b, m, n = 1, 2, 3 \quad (34)$$

$$H = H_0 + P_{2a} Q^{1a} + \pi_{2a} \lambda^{1a} + \tau_2 \eta^1; a = 1, 2, 3 \quad (35)$$

A more extended analyze of this theory is presented in [12].

4. CONCLUSIONS

We have analyzed the possibility of the covariant description of the free electromagnetic field corresponding to a laser radiation in the hamiltonian formalism. We concluded that it is possible to implement a very useful generalized global symmetry, called the BRST symmetry, which could replace the gauge symmetry of the original field. The price we have to pay in this implementation is connected with the extension of the phase space of the system by the ghost variables.

The global symmetry is expressed by the BRST charges, and the hamiltonian of the theory have to be replaced by an extended one of the form (35). The remaining problem is connected with the choosing of a gauge fixed hamiltonian, problem which had been tackled in [13].

The important thing we have to retain is that it is possible to construct more than a $sp(2)$ -rank extension of the BRST symmetry. The BRST charges and the extended hamiltonian were minutiously calculated for the $sp(4)$ symmetry in [12], and it had been compared to the standard and $sp(2)$ BRST symmetry. The demonstration relied on the first-rank theories, due to their practical importance and to the fact that their use allows obtaining complete expression for the BRST charges and the hamiltonians. The investigation led us to the statement that it is not trivial to extend the symmetry.

ACKNOWLEDGEMENTS

This work has been partially supported by a grant offered by CNCSIS.

REFERENCES

1. G.t'Hooft - *Renormalizable lagrangians for massive Yang-Mills fields*, Nucl.Phys. **B 35** (1971), 167.
2. C.Becchi,A.Rouet,R.Stora - *The abelian Higgs Kibble model,unitarity of the S-operator*, Phys.Lett. 52 **B**(1974), 344.
3. I.V.Tyutin - *Gauge invariance in field theory and statistical mechanics*, Lebedev Preprint 39/1975.
4. E.S.Fradkin, G.A.Vilkovisky - *Constrained dynamical systems*, Phys.Lett.55**B** (1975), 224.
5. I.A.Batalin, E.S.Fradkin - *Quantization of gauge systems*, Phys.Lett.122**B** (1983), 157.
6. M.Henneaux - *Hamiltonian form of the path integral*, Phys.Reports **126** (1985) 2.
7. I.A.Batalin, P.M.Lavrov, I.V.Tyutin - *Extended BRST quantization of gauge theories*, J.Math.Phys. **31** (1990) 6.
8. I.A.Batalin, P.M.Lavrov, I.V.Tyutin - *An $sp(2)$ -covariant version of generalized canonical quantization*, J.Math.Phys. **31** (1990) 2708.
9. P.Gregoire, M.Henneaux - *Hamiltonian formulation of the anti-BRST transformation*, Phys.Lett. **B227** (1992) 459.
10. P.Gregoire, M.Henneaux - *Quantization of gauge systems*, Preprint ULB-PMIF 92/06.
11. R.Constantinescu - *The generalized Koszul differential in the BRST quantization*, J.Math.Phys. **38** (1997), 2786.
12. A.Babalean, R.Constantinescu, C.Ionescu - *Non-minimal terms for Yang-Mills theory*, J. Phys. A: Math. Gen. **31** (1998) 8653.
13. A.Babalean, R.Constantinescu, C.Ionescu - *The gauge fixing problem in the $sp(3)$ BRST canonical quantization*, J. Phys. A: Math. Gen. **32** (1999) 3005.
14. R.Constantinescu, L.Tatar - *Hamiltonian $sp(3)$ BRST symmetry: existence theorems*, Phys.Lett.**B417** (1998) 269.

Characterization of a resonant photoacoustic cell using the acoustic transmission line model

Simona Cristescu*, Dan C. Dumitras, Doru C. A. Dutu

Department of Lasers, National Institute for Laser, Plasma
and Radiation Physics, P.O. Box MG-36, Bucharest 76 900, Romania

ABSTRACT

The acoustic transmission line model has been used for a quantitative theoretical description of a resonant photoacoustic (PA) cell excited in its first longitudinal mode. Based on this model, the PA cell was divided into a finite number of sequential components represented by analogue electric circuits. Their specific influence to the acoustic behaviour of the cell is presented. The parameters of the cell (the resonance frequency, the cell constant and the quality factor) were determined and the results were compared to predictions from classical theory and to the experimental values. In order to obtain an optimum geometry of the cell, the influence of the buffer radius onto the resonance frequency and the quality factor of the photoacoustic cell was studied for a constant value of the buffer length of 75 mm.

Keywords: photoacoustic cell, acoustic transmission line model

1. INTRODUCTION

Laser photoacoustic spectroscopy represents a recognized method to achieve the spectral signature of molecules. Due to its high sensitivity and resolution, it has been applied in many fields of research like environmental sensing, biology, agriculture and medicine. This technique uses powerful modulated sources of infrared radiation to produce heat and subsequently sound effects in absorbing sample, particularly in gases. The sounds are then detected by sensitive microphones placed inside the PA cell.

During the last years, sensitive PA detectors based on CO₂ and CO lasers have shown their high degree of development¹. The simultaneous detection of several gases at ppb level using one apparatus² and the detection of ethylene concentrations at ppt level³ are only two examples that can prove this.

The detection limits of the PA technique are mainly determined by the laser used as a radiation source and by the photoacoustic cell design. Different resonant cell types were realized depending of the intended application. Their acoustic behavior was studied using the one-dimensional electrical transmission line analogue. The basis of this theory was described by Morse *et al.*⁴ and applied to this field by Kritchman *et al.*⁵. An extended theory with a matrix formalism which permits the quantitative description of the PA signal at any position inside the cell at an arbitrary frequency of modulation was elaborated by Bernegger *et al.*⁶

In this work, we present the acoustic transmission line model applied to a resonant PA cell excited in its first longitudinal mode. The dependence of the cell responsivity on the resonator diameter is demonstrated. The model has been also applied to determine the influence of the buffers radius on the quality factor, resonance frequency and PA background signal. Quantitative results derived from this model are compared to the experimental data. Based on this approach, the geometry of the PA cell can be optimized in order to increase the ratio between the PA signal produced by the gas absorption and the the PA background signal due to the windows absorption⁷.

* Correspondence: Email: simonac@ifin.nipne.ro; Telephone: (401) 423 1470; Fax: (401) 423 1470

2. THEORY

2.1. Energy loss processes

A simple approach to the calculation of the acoustic pressure inside a PA cell and the frequencies of the cell sound resonances can consider a loss-free model. This ideal model yields the first approximation formulae for the resonance frequency⁸ and the cell constant⁹. The practice has proved that the loss effects produce significant deviation from the formulae given by this model.

There are two categories of losses which should be considered¹⁰, the surface losses and the volumetric losses. The surface losses are due to:

- the viscous and thermal dissipation in the boundary layer at the smooth internal surfaces;
- wave scattering at surface obstructions;
- compliance of the chamber walls;
- dissipation at the microphone diaphragm.

The last three effects can be minimized by optimizing the cell design. The first loss mechanism is thus dominant and it should be taken into account. According to Morse⁴, the thermal losses L_{th} and the viscous losses L_v per unit area per second are given by:

$$L_{th} = \frac{(\gamma - 1)\omega}{2\rho c_0^2} d_{th} |p|^2, \quad L_v = \frac{1}{2} \rho \omega d_v |u|^2, \quad (1)$$

where:

$$d_{th} = \sqrt{\frac{2K}{\rho\omega c_p}} \quad \text{and} \quad d_v = \sqrt{\frac{2\eta}{\rho\omega}} \quad (2)$$

are the thermal and viscous boundary layer thicknesses, K is the heat conductivity of the gas, ρ the density of the gas, c_p the heat capacity, η the dynamic viscosity, γ the ratio of the specific heats, ω the angular frequency, p the pressure amplitude, c_0 the sound velocity and u the macroscopic velocity of the gas.

The volumetric losses are due to⁴:

- free space viscous and thermal dissipation ("Stokes-Kirchhoff");
- diffusion effects;
- radiation effects;
- relaxation damping.

In general, these losses are small compared to the surface losses.

2.2. Acoustic transmission line model

The pressure amplitude anywhere inside the PA cell can be described by the one-dimensional electrical transmission line model as long as the acoustic wave is transmitted along the interior of the resonant tube and its wavelength is much larger than the transverse dimensions of the tube^{4, 5, 11}.

Openings and constrictions inside the resonant tube can be expressed as discrete circuit elements per unit length and uniform yielding of the tube walls are considered contribution to the line impedance. According to this theory, the wave pressure amplitude p is the acoustic analogue of the voltage U and the total gas flux Su (with velocity u through the cross section S) is the acoustic analogue of the electrical current I .

The acoustic transmission line model consists of sequential components well described by the analogous elements. In order to derive the general relations between the coupling elements, the transmission line model contains only impedances (Z), admittances (Y) and sources. In this case, their analogue components can be defined using the analogy to the AC circuits theory⁴.

The analogous resistance R per unit length of a tube with cross section S , circumference D and volume V is defined by considering the effects of heat conduction and of viscosity at the tube walls (see eq. 1-2) expressed by the power loss per unit length (i.e. electrical Rl^2),

$$R = \frac{2}{l^2} \cdot (L_{th} + L_v) = \frac{\rho D}{2S^2} \omega [d_v + (\gamma - 1)d_{th}]. \quad (3)$$

The analogous inductance L per unit length of the pipe is given by the kinetic energy in the unity length of the fluid ($W_k = \frac{1}{2} L l^2$),

$$L = \frac{2}{l^2} W_k = \frac{2}{(Su)^2} \cdot \frac{1}{2} S \rho u^2 = \frac{\rho}{S}, \quad (4)$$

where ρ is the density of the gas.

The analogous capacitance C per unit length of the pipe can be defined by the potential energy of the gas molecules ($W_p = \frac{1}{2} C p^2$),

$$C = \frac{2}{p^2} W_p = \frac{2}{(p)^2} \cdot \frac{1}{2} S \kappa_s p^2 = \frac{S}{\rho c_0^2}, \quad (5)$$

where $\kappa_s = \frac{1}{\rho c_0^2}$ is the compressibility factor.

The differential equations for the acoustic wave inside the tube using the electrical transmission line model are given by:

$$\frac{dU(x)}{dx} = -ZI(x), \quad \frac{dI(x)}{dx} = -U(x)Y + I_0, \quad \text{where} \quad \frac{dI_0}{dx} = \frac{(\gamma - 1)P_L \alpha}{\rho c_0^2} \quad (6)$$

with I_0 the acoustic equivalent of an electric current source per unit length of the tube, $Z = R + j\omega L$ and $Y = j\omega C$. Here R , L , C are the analogue acoustic elements defined by the equations (3-5) and P_L is the unmodulated power of the incident laser beam.

The solution of (6) is:

$$U(x) = ZI_0 - Z_c (Ae^{\beta x} - Be^{-\beta x}), \quad (7)$$

where $Z_c = \sqrt{Z/Y}$ is the characteristic impedance of the transmission line and $\beta = \sqrt{ZY}$ the propagation constant. The coefficients A and B can be determined by the boundary conditions.

For the case of sudden changes of the tube cross section, the model of one-dimensional transmission line is only partially valid. As an example, a constriction in the tube (i.e. the change in cross section between the resonator tube and the buffer cavities) produces an increase in viscous energy losses which can be represented in addition by a lumped impedance. To correct the acoustic transmission line model⁴, the additional impedance which should be added is:

$$Z_{ad} = R_{ad} + j\omega L_{ad}, \quad (\text{ad: added lumped circuit element}) \quad (8)$$

where

$$L_{ad} = \frac{\rho}{4D}, \quad R_{ad} = \frac{\sqrt{2\rho\omega\eta}}{8S} \ln \frac{2R}{d_v}. \quad (9)$$

Another element which should be taken into account is the heat produced by the absorption of the radiation into the windows. This process gives rise to a background PA signal mainly due to the thermal expansion and the partially transfer of heat to the medium in contact with the windows. In this case, in the acoustic transmission line model a heat flux must be introduced¹²:

$$I_w = \frac{d_{th} \alpha_w \mu_w^2 P_L}{Tk_w}, \quad (10)$$

where α_w is the absorption coefficient, $\mu_w = \sqrt{\frac{2D_w}{\omega}}$ the diffusion length in the window, D_w the thermal diffusivity, T the ambient temperature and k_w the heat conductivity of the window material.

The acoustic transmission line model allows the sequential arrangements of the electrical elements. Based on this theory, the PA cell can be divided into a finite number of elements n ("subcells") represented by analogue electric circuits. The coupling between these elements is determined by the boundary conditions for the current I (gas flux) and voltage U (pressure),

$$I_i(x_i = 0) = I_{i-1}(x_{i-1} = l_{i-1}) \quad \text{and} \quad U_i(x_i = 0) = U_{i-1}(x_{i-1} = l_{i-1}), \quad (11)$$

where I_i and U_i are the current and the voltage in the subcell " i " of length l_i .

Usually, at the ends of the PA cells used for trace gas detection, the windows are mounted at Brewster angle. In the transmission line model, the windows are represented by impedances Z_w and the boundary conditions at the beginning and at the end of the cell yield two supplementary equations:

$$\begin{aligned} U_1(x_1 = 0) &= Z_{w_1} [I_{w_1} - I_1(x_1 = 0)] \\ U_n(x_n = l_n) &= Z_{w_n} [I_{w_n} + I_n(x_n = l_n)] \end{aligned} \quad (12)$$

with I_{w_1} and I_{w_n} the equivalent currents produced at the windows defined by relation (10).

The influences of the small volumes like microphone hole, gas ports etc. should be taken into account in the acoustic transmission line by considering additional electric elements corresponding to these volumes. For a duct of radius r_d and length l_d the analogue impedance is⁴:

$$Z_d = R_d + i\omega L_d, \quad (13)$$

where

$$R_d = \frac{1}{4S_d} \sqrt{2\rho\omega\eta} \ln \frac{2r_d}{d_v} \quad \text{and} \quad L_d = \frac{\rho l_d}{2r_d}. \quad (14)$$

The input impedance Z_m should be added in the transmission line model, especially in the case of the microphones connecting, together with the current I_m which enter in the microphone space (it is lost from the transmission line) and the voltage U_m at the entrance of the hole (it is equal with that of the line at the connection of the holes with the resonator). The conditions required to attach these elements are:

$$I_i(x=l_i) - I_m = I_{i+1}(x_{i+1}=0), \quad U_i(x=l_i) = U_{i+1}(x_{i+1}=0) = U_m, \quad U_m = Z_m I_m. \quad (15)$$

Based on the relations (3) - (5), the resonance frequency f and the quality factor Q can be calculated. The quality factor Q is defined as the ratio between the energy stored in acoustic wave and the losses per cycle of this wave^{5, 8, 13}. Thus,

$$\omega = 2\pi f = \frac{\pi}{\sqrt{LC}} \Rightarrow f = \frac{1}{2\sqrt{LC}} = \frac{c_0}{2l}, \quad (16)$$

$$Q = \frac{\frac{1}{2} \omega L I^2}{\frac{1}{2} R I^2} \Rightarrow Q = \omega \frac{L}{R}, \quad (17)$$

which for a simple pipe configuration (without buffer volumes) gives the first approximation of the quality factor:

$$Q = \frac{2S}{D[d_v + (\gamma - 1)d_{th}]} \quad (18)$$

It should be also mentioned that the excitation of the PA cell at a longitudinal mode presents the advantage of the resonance frequency and of the quality factor optimisation independently one to each other.

3. RESONANT PHOTOACOUSTIC CELL

An open stainless steel pipe with a small diameter ($\varnothing 6$ mm), introduced coaxially inside a larger cylinder is used as PA resonant cell (Fig. 1). In order to achieve an optimum signal, the length of the resonator was chosen to be 300 mm which corresponds to $\lambda/2$ for a light modulation frequency of 577 Hz. It is excited in the first longitudinal mode¹⁴.

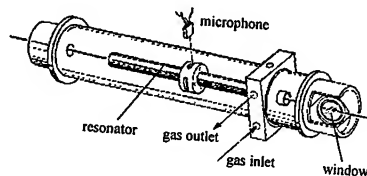


Fig. 1. Schematic view of the resonant PA cell.

The acoustic resonance for the first longitudinal mode of the cell has to coincide with the chopping frequency. In this way, the most efficient coupling between the selected acoustic resonance and the laser beam can be assured. There are many advantages by working at resonance frequency; e.g. the signal levels rise above other noises such as ambient noise or electronic noise, that significantly improves the signal to noise (S/N) ratio.

Two buffer volumes ($\varnothing 57 \times 75$ mm), located at the ends of the resonant tube, suppress other resonance modes and reduce the signal produced by absorption of the cell windows. The acoustic coupling to the resonator is reduced by choosing a large ratio between the buffer diameter and the resonator diameter and the buffer length of 1/4 of the resonator length. Both ends of the outer tube are closed with ZnSe windows (absorption coefficient at room temperature of 0.2 m^{-1}) mounted in aluminium holders at Brewster angle. In this case, the noise due to reflection and absorption of radiation in the windows is minimised. The connection between the buffers and the windows are made by means of small cylinders of minimised length to avoid additional resonances. The resonator tube has polished inner walls and it is centred into the outer tube by a Teflon spacer. At one end there is a massive spacer to prevent the gas of the flowing system to bypass the resonator, while the other end is partially open. The inlet and the outlet of the gas are placed nearby one end of the resonator.

The PA cell is equipped with four sensitive microphones (sensitivity 10 mV/Pa each) connected in series and placed at the antinodes of the standing wave pattern for maximum operating signal. In this way, the gain in sensitivity is due to the fact that the signal increases by 4 times¹⁵ ($4 = \text{number of microphones}$) while the noise increases by 2 times ($\sqrt{4}$) which yields an increase of the signal to noise ratio by a factor of 2. The connecting duct of the microphones to the resonator together with the volume in which the microphone are placed represent a Helmholtz resonator with the resonance frequency and the quality factor given by formulae (16 ÷ 18). The duct has small dimensions and it can be described with an inductance and resistance from relations (3 ÷ 5).

4. RESULTS AND DISCUSSION

For the PA cell described above, the resonance frequency depends on two important factors, the cell geometry and the gas mixture inside the cell. For the first longitudinal mode, the resonance frequency is calculated to be equal to 577 Hz for a sound velocity $c_0 = 346 \text{ m/s}$. To obtain the experimental value of the resonance frequency and also of the quality factor, a mixture of 20 ppm of ethylene (C_2H_4) in nitrogen at a total pressure of 1 atm was used¹⁶. Ethylene gas mixtures are convenient due to its well known absorption strength at CO_2 laser wavelengths. The strongest absorption of C_2H_4 (about 6 times higher than that of other lines) can be observed at the 10P(14) laser line (949.4793 cm^{-1}) due to the overlap between various strong ro-vibrational transitions in C_2H_4 ¹⁷. A weaker absorption was found at the 10P(12) line (951.1922 cm^{-1}) of the CO_2 laser and it was used for background checking.

The PA experiments at the 10P(14) laser line have allowed us to evaluate the resonance frequency $f \cong 560 \text{ Hz}$ and the quality factor $Q_{\text{exp}} = 16.5$, usually defined as the ratio between the resonance frequency and the frequency bandwidth at $1/\sqrt{2}$ of the maximum¹⁸:

$$Q_{\text{exp}} = \frac{f_{\text{res}}}{\Delta f_{1/\sqrt{2}}} \quad (19)$$

For a simple configuration (without buffers) of the cell, the theoretical value of the quality factor, calculated with the first approximation formula⁸, is $Q_{\text{th}} = 22$. The experimentally determined quality factor Q_{exp} is 25 % lower than the theoretical value. To explain this difference additional losses should be taken into account. The acoustic transmission line model allows to evaluate the Q parameter by considering these losses.

As it was mentioned before, the acoustic transmission line model consists of sequential components. In the present study, the following sequences were considered:

- the central component represented by the resonator tube ($\varnothing 6 \times 300$ mm)
- 2 components placed at both ends of the resonator representing the buffer volumes ($\varnothing 57 \times 75$ mm)
- 2 connection elements between the buffers cavities and the windows ($\varnothing 6 \times 12$ mm)
- 2 components of the trace gas ports ($\varnothing 8 \times 30$ mm)
- 4 components corresponding to the microphones connections to the resonator.

To correct the acoustic transmission line model owing to the changes in the cross section between the resonator tube and the buffer cavities, 2 additional lumped impedances (eq. 8 and 9) were included.

It was found that the four sequential components which represent the microphone connections to the resonator can introduce significant modifications to the cell parameters. The microphones are mounted in a Teflon ring pulled over the resonator tube. The acoustic coupling between the resonator and the microphones is made by 4 holes ($\varnothing 1.3 \text{ mm} \times 1 \text{ mm}$). There is no free space between the microphones and the resonator tube which could produce a decrease of the signal and the quality factor. It was found that this possible free space critically influences the Q value.

All the components of the acoustic transmission line model which define these sequences were calculated with the formulae (3 ÷ 10) taking into account the coupling relations (eq. 11 ÷ 15). The numerical values of the characteristics related to the gas properties are listed in Table 1. Based on these considerations, the theoretical value of the quality factor given by the acoustic transmission line model is $Q_{th} = 19.5$ (eq. 17) and shows a 15 % overestimation by comparison with the experiment.

Tab. 1. The characteristic data of nitrogen at room temperature ($T = 295 \text{ K}$) and pressure of 1 atm.

	N ₂
Sound velocity, c_0 [m/s]	346 [19]
Thermal conductivity, K [$\text{W} \cdot \text{m}^{-1} \cdot \text{K}^{-1}$]	25.52×10^{-3} [20]
Dynamic viscosity, η [$\text{Pa} \cdot \text{s}$]	17.6×10^{-6}
Mass density, ρ [kg/m^3]	1.142
Specific heat ratio of the gas, γ	1.4
Heat capacity, c_p [$\text{J} \cdot \text{kg}^{-1} \cdot \text{K}^{-1}$]	1.04×10^3

In order to obtain the experimental value of the cell constant C_{exp} , a calibrated mixture of 1 ppm of C_2H_4 in N_2 at a total pressure of 1 atm was used. The measurements were performed at the 10P(14) CO_2 laser line ($\alpha = 30.4 \text{ atm}^{-1} \text{cm}^{-1}$)²¹. Since the sensitivity of the microphones S_M is constant within the used frequency range, the measured PA signal V is proportional to the cell constant C_{exp} [$\text{Pa} \cdot \text{cm}/\text{W}$],

$$C_{exp} = \frac{V}{\alpha P_L S_M} \quad (20)$$

Here, V is the peak to peak value of the photoacoustic signal [V], c the trace gas concentration [atm], α the gas absorption coefficient at a given wavelength [$\text{cm}^{-1} \text{atm}^{-1}$], P_L the average laser power [W] and S_M the sensitivity of the microphones [mV/Pa].

Experiments have yielded $C_{exp} = 4600 \text{ Pa} \cdot \text{cm}/\text{W}$ which is lower than theoretical value $C_{th} = 12 \times 10^3 \text{ Pa} \cdot \text{cm}/\text{W}$ given by the first approximation formula⁹. Since the pressure amplitude, p , is expressed by the cell constant, the pressure response correction to the peak value, p_{exp} , involves a new evaluation of the cell constant, C'_{exp} , as a function on the experimental quality factor:

$$p = \frac{Q_{th}}{Q_{exp}} \sqrt{2} p_{exp} \Rightarrow C'_{exp} = \frac{Q_{th}}{Q_{exp}} \sqrt{2} C_{exp} \quad (21)$$

The results are shown in Table 2 (the values for the cell constant are multiplied by $\sqrt{2}$).

Tab. 2. The cell constant and the quality factor of the PA cell ($\varnothing 6 \times 300 \text{ mm}$).

Theory			Experiment		Correction
(first approx. formula)	(acoustic transm. line model)				
C_{th}	Q_{th1}	Q_{th}	C_{exp}	Q_{exp}	C'_{exp}
($\text{Pa} \cdot \text{cm}/\text{W}$)			($\text{Pa} \cdot \text{cm}/\text{W}$)		($\text{Pa} \cdot \text{cm}/\text{W}$)
12×10^3	22	19.5	$(6.5 \pm 0.5) \times 10^3$	16.5 ± 0.4	$(7.6 \pm 0.8) \times 10^3$

The cell responsivity R [mV·cm/W] is defined as the magnitude of the electrical signal produced by the microphones for a unit of power absorbed by molecules per unit length,

$$R = C \cdot S_M, \quad (22)$$

with C [Pa·cm/W] the cell constant and S_M [mV/Pa] the sensitivity of the microphones.

The theoretical and experimental values of the cell responsivity (R) as a function of different diameters of the resonator (for a resonator length of 300 mm) are shown in Fig. 2.

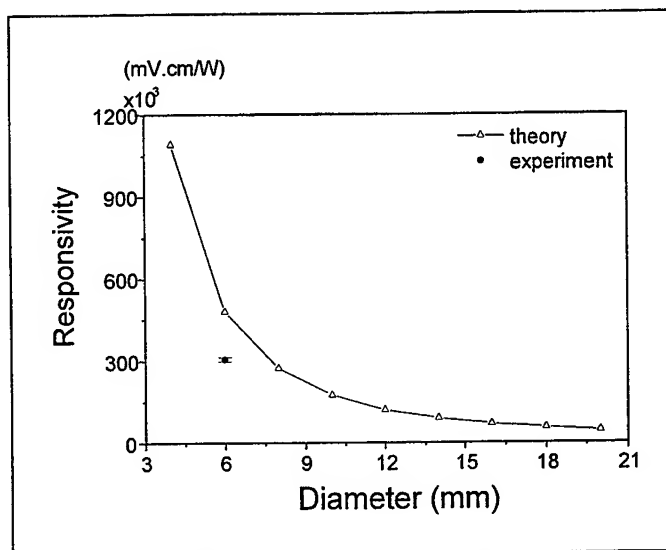


Fig. 2. Cell responsivity versus resonator diameter (resonator \varnothing 6 x 300 mm).

From Figure 2 it can be seen that a small diameter of the resonator is suitable to obtain high values of the cell responsivity. Practically, the resonator diameter is limited by the laser beam profile in order to avoid additional noise caused by the scattered radiation. In this case, the cell responsivity can be improved by using high sensitive microphones. Some external factors, such as the realignment of the set-up or the movement of the PA cell, can influence in time the cell constant value. For this reason, before starting the PA experiments, the cell constant was checked and adjusted after calibration.

As it was mentioned before, the main role of the buffer volumes is to reduce noises produced by absorption of the cell windows. The buffer volumes should be chosen to assure a maximum gas absorption signal with a minimum PA window absorption signal. The influence of the buffer radius on the quality factor and the resonance frequency of the PA cell was studied for a constant value of the buffer length of 75 mm. The results are presented in Fig. 3 and Fig. 4.

The sequential elements described above were introduced gradually in the acoustic transmission line model starting from the central sequential component (the resonator). The corrections were made taking into account the additional lumped impedances (eq. 8, 9). The quantitative influences of the sequential components onto the Q -factor evolution have been estimated. Thus, by adding the gas ports expression in the acoustic transmission line model, an improvement of 1 % in comparison with experiment of the Q_{th} -factor value was observed. Moreover, the microphones expression included in the same model offers an additional improvement of 6 %. As it can be seen from Fig. 3, the quality factor Q was overestimated by both models, the acoustic transmission line model and the corrected acoustic transmission line model, respectively. The corrections introduced did not offer an improvement.

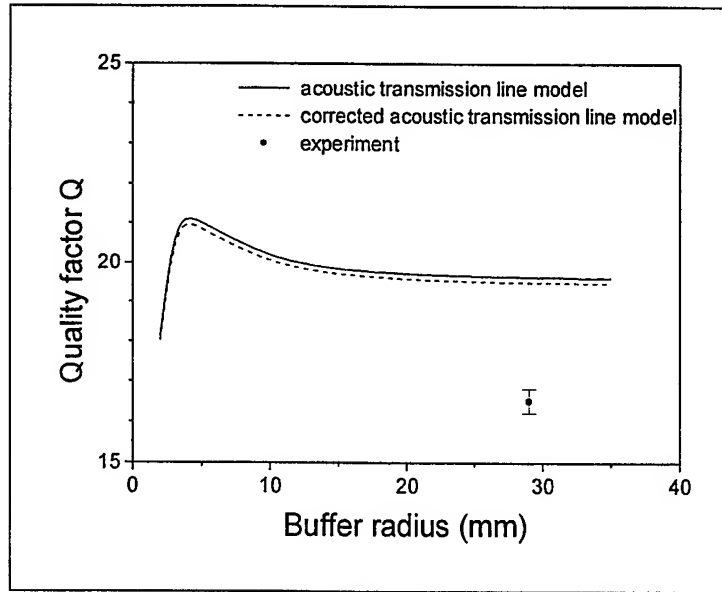


Fig. 3. Experimental and calculated quality factor as a function of the buffer radius (resonator \varnothing 6 x 300 mm, buffer length of 75 mm).

An important improvement is obtained for the resonance frequency calculated with the corrected line model in comparison with experiment (Fig. 4). The acoustic transmission line yields a resonance frequency of 4 % higher than the experiment, while the corrected model overestimates this value by 1 %. The value of the resonance frequency obtained from the first approximation formula⁸ agrees well with the calculation made by the acoustic transmission line model (eq. 16) for large buffer radii.

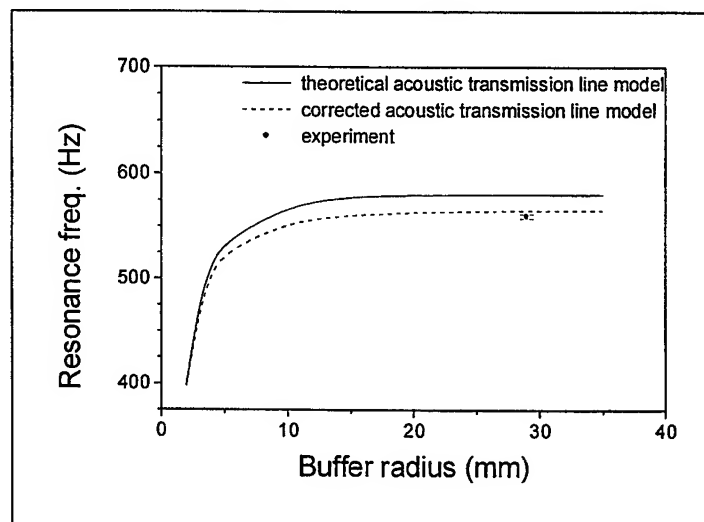


Fig. 4. Experimental and calculated resonance frequency versus the buffer radius (resonator \varnothing 6 x 300 mm and buffer length of 75 mm).

Since the maximum of the Q-factor has been found for small buffer radius, it can be supposed that the volumes with small radii are a good choice for the PA cell buffers. In this case, the coupling between the PA window signal and the resonator increases and the standing wave can not be confined inside the resonator tube, but into the buffers cavities. In Fig. 5, the window absorption signal calculated with the acoustic transmission line model for six different buffer radius is plotted.

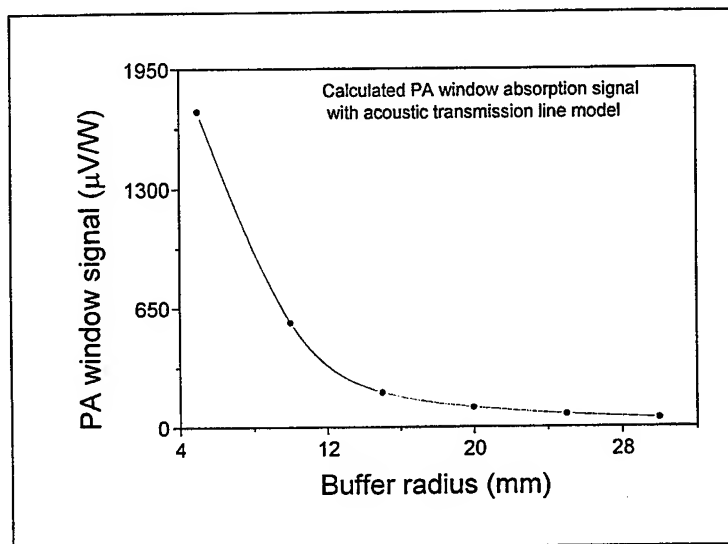


Fig. 5. The calculated window absorption signal (resonator \varnothing 6 x 300 mm, buffer length of 75 mm).

For small buffer radii the window absorption signal becomes stronger. Moreover, at small buffer radii, the resonance frequency and the quality factor drastically decrease (see Fig. 4), which indicated that the standing wave stretches out into the buffer cavities.

5. CONCLUSION

The resonant PA cell was well described by the acoustic transmission line model that includes the surface losses and the volumetric losses. The results given by the model have showed a lower overestimation than the approximate formulae of the classical theory in comparison to the experiment. Significant improvements have been obtained for the quality factor and the resonance frequency. The fairly good agreement with the experimental points confirms the utility of the acoustic transmission line model, especially in the case of the resonance frequency determination. The representation of the PA cell by sequential components of discrete circuit elements allows to investigate the main parameters which are critical for the geometrical optimization of the cell.

REFERENCES

1. F. Harren and J. Reuss, "Spectroscopy, Photoacoustic", in *Encyclopedia of Applied Physics* 19, VCH Publishers, Weinheim, pp. 413-435, 1997.
2. M.W. Sigrist, "Air Monitoring by Spectroscopic Techniques", in *Chemical Analysis Series* 127, Ed. M.W. Sigrist, Wiley, New York, pp. 163-238, 1994.
3. F. Harren, F. Bijnen, J. Reuss, L.A.C.J. Voesenek and C.W.P.M. Blom, "Sensitive intracavity photoacoustic measurements with a CO₂ waveguide laser", *Appl. Phys. B* 50, pp. 137-144, 1990.
4. P.M. Morse and K.U. Ingard, *Theoretical Acoustic*, McGraw-Hill, New York, 1968.
5. E. Kritchman, S. Shtrikman and M. Slatkine, "Resonant optoacoustic cells for trace gas analysis", *J. Opt. Soc. Am* 68, pp. 1257-1271, 1978.
6. S. Bernegger and M.W. Sigrist, "Longitudinal resonant spectrophone for CO-laser photoacoustic spectroscopy", *Appl. Phys. B* 44, pp. 125-132, 1987.

7. F.G.C. Bijnen, J. Reuss and F.J.M. Harren, "Geometrical optimization of a longitudinal resonant photoacoustic cell for fast trace gas detection", *Rev. Sci. Instr.* **67**, pp.2914-2923, 1996.
8. A. Karbach and P. Hess, "High precision acoustic spectroscopy by laser excitation of resonator modes", *J. Chem. Phys.* **83**, pp. 1075-1084, 1985.
9. L. B. Kreuzer, *Optoacoustic Spectroscopy and Detection*, Ed. Y.H. Pao, Academic Press, New York, pp. 1-26, 1977.
10. P. Hess, "Resonant photoacoustic spectroscopy", in *Topics in Current Chemistry*, Vol. III, Ed. F.L. Boschke, Springer, Berlin, Heidelberg, New York, 1983.
11. O. Nordhaus and J. Pelzl, "Frequency dependence of resonant photoacoustic cells: the extended Helmholtz resonator", *Appl. Phys.* **25**, pp.221-223, 1981.
12. A.C. Tam, "Applications of photoacoustic sensing techniques", *Rev. of Mod. Phys.* **58**, pp. 381-431, 1986.
13. R.H. Johnson, R. Gerlach, L.J. Thomas III and N.M. Amer, "Loss mechanism in resonant spectrophones", *Appl. Opt.* **21**, p.81-86, 1982.
14. D.C.A. Dutu, D.C. Dumitras, S. Cristescu and L. Sarcozy, "Evaluation of photoacoustic signal and noises in a sensitive spectrophone irradiated by a CO₂ laser beam", *Rom. Rep. Phys.* **46**, pp. 639-644, 1994.
15. V.P. Zharov and V.S. Letokhov, "Laser Optoacoustic Spectroscopy", *Springer-Verlag Series: Optical Sciences*, Vol. **37**, Springer, Berlin, Heidelberg, pp. 122-124, 1986.
16. D. C. Dumitras, D. C. A. Dutu, S. Cristescu and C. Mujat, "Trace gas analysis using laser photoacoustic spectroscopy methods", *Rom. J. Optoelectr.* **4**, pp. 21-28, 1996.
17. P. Perlmutter, S. Shtrikman and M. Slatkine, "Optoacoustic detection of ethylene in the presence of interfering gases", *Appl. Opt.* **18**, pp. 2267-2274, 1979.
18. R. Gerlach and N.M. Amer, "Brewster window and windowless resonant spectrophones for intracavity operation", *Appl. Phys.* **23**, pp. 319-326, 1980.
19. *Handbook of Chemistry and Physics*, 72nd edn., Ed. D.R. Lide, CRC Press, Boston, 1991-1992.
20. J. Medard *et al.*, *Gas Encyclopedia*, Elsevier, Amsterdam, 1976.
21. R.J. Brewer, C.W. Bruce and J.L. Mater, "Optoacoustic spectroscopy of C₂H₄ at the 9- and 10- μ m C¹²O₂¹⁶ laser wavelengths", *Appl. Opt.* **21**, pp. 4092-4100, 1982.

Accurate method to calculate some periodic integrals occurring in electromagnetic field analysis

C.V. Atanasiu* and I.G. Miron

Institute of Atomic Physics, INFLPR L22, P.O.Box MG 36, Bucharest, Romania

ABSTRACT

In many applications related to the electromagnetic field analysis in a cylindrical coordinates system (r, z, ζ) , the following periodic integrals have to be calculated:

$$\frac{(1 + \alpha)^{1/2}}{4} \int_0^{2\pi} \frac{\cos N u du}{(1 - \alpha \cos u)^\mu},$$

where $\alpha \in [0, 1]$, $\mu = 1/2$ or $\mu = 3/2$, and N is an integer. Usually, the calculation of these integrals is made by recurrence relations. Unfortunately, for $k = \sqrt{2\alpha/(1 + \alpha)}$ less than 0.4 and N greater than 4 the recurrence relations yield incorrect results. We have developed a very accurate method to calculate these integrals as solutions of a hypergeometric differential equation. For any k and N up to 50, these integrals have been computed exactly up to the ninth digit (in double precision). This approach to calculate the periodic integrals has been used for stability analyses in toroidally symmetric tokamak discharges to determine of the vacuum field resulting from the perturbation of a toroidally symmetric plasma.

Keywords: electromagnetic fields, hypergeometric differential equations, tokamak

1. INTRODUCTION

Let us consider an axisymmetrical torus with a arbitrary cross-section, including a singular X point, in a cylindrical coordinate system (r, z, ζ) . By noting with l a contour coordinate in the plane r, z , and with the subscript N the Fourier series development with respect to the azimuthal (toroidal) direction ζ , the normal component of a magnetic field at the torus can be written as

$$B_n(r, z, \zeta) = B_{nN}(r, z)e^{-iN\zeta} = B_{nN}(l)e^{-iN\zeta}. \quad (1)$$

From potential theory^{1,2} it is known that for the normal component of the magnetic field we have the following integral relation

$$2\pi\sigma_N(l) + \oint \sigma_N(l')b_{nN}(l, l')dl' = B_{nN}(l), \quad (2)$$

with

$$b_{nN}(l, l') = n_r(l)b_{rN}(l, l') + n_z(l)b_{zN}(l, l'), \quad (3)$$

where n_r and n_z are the components of the normal vector, while b_{rN} and b_{zN} are the r and z components of the magnetic field given by a unit surface charge σ . The (r, z) coordinates represent the field point, while the (r', z') coordinates represent the source point.

Outside of the torus, the magnetic field is completely described by giving the normal component of the magnetic field at the location of the torus surface. Thus, the normal component of the magnetic field $J\mathbf{B} \cdot \nabla a$ is the required boundary condition for solving for the magnetic field outside the torus. J is the Jacobian of the (a, θ, ζ) coordinates (which can be any set of toroidal coordinates in which the boundary of the torus is defined by $a = \text{const}$). The quantity $J\mathbf{B} \cdot \nabla a$ has units of flux, Volts seconds.

This paper deals with the determination of some periodic integrals arising in the determination of the toroidal harmonics of the magnetic field.

*Correspondence: E-mail: atanasiu@alpha1.inim.ro

2. MAGNETIC FIELD AND SCALAR POTENTIAL CALCULATIONS

For the r and z components of the magnetic field the following relations can be written³

$$b_{rN} = \frac{2r'}{r[(r+r')^2 + (z-z')^2]^{1/2} [r^2 + r'^2 + (z-z')^2]} \times \{ [r^2 - r'^2 - (z-z')^2] D_N + [r^2 + r'^2 + (z-z')^2] C_N \}, \quad (4)$$

$$b_{zN} = \frac{4r'(z-z')}{[(r+r')^2 + (z-z')^2]^{1/2} [r^2 + r'^2 + (z-z')^2]} D_N, \quad (5)$$

where

$$C_N = \frac{(1+\alpha)^{1/2}}{4} \int_0^{2\pi} \frac{\cos N u du}{(1-\alpha \cos u)^{1/2}}, \quad (6)$$

$$D_N = \frac{(1+\alpha)^{1/2}}{4} \int_0^{2\pi} \frac{\cos N u du}{(1-\alpha \cos u)^{3/2}}, \quad (7)$$

and

$$\alpha = \frac{2rr'}{r^2 + r'^2 + (z-z')^2}.$$

The connection with the usual definition of the modulus k of the complete elliptic integrals is given by

$$k^2 = \frac{2\alpha}{1+\alpha} = \frac{4rr'}{(r+r')^2 + (z-z')^2}.$$

Similarly, the scalar magnetic potential can be put in the form

$$\Phi(r, z, \zeta) = \Phi_N(r, z) e^{-iN\zeta}, \quad (8)$$

with

$$\Phi_N(l) = \oint \sigma_N(l') \phi_N(l, l') dl', \quad (9)$$

where

$$\phi_N = - \int_0^{2\pi} \frac{r' \cos N u du}{[r^2 + r'^2 + (z-z')^2 - 2rr' \cos u]^{1/2}} = - \frac{4r}{[r^2 + r'^2 + (z-z')^2]^{1/2}} C_N, \quad (10)$$

is the scalar potential given by a unit charge.

3. CALCULATION OF THE C_N AND D_N INTEGRALS

For the C_N and D_N integrals of Eqs. (6) and (7), we have found the following recurrence relations

$$\begin{aligned} C_0 &= K(k), \\ C_1 &= \frac{[K(k) - (1-\alpha)E(k)]}{\alpha}, \\ C_{N+1} &= \frac{4NC_N/\alpha - (2N-1)C_{N-1}}{2N+1}, \end{aligned} \quad (11)$$

$$D_0 = \frac{E(k)}{1-\alpha},$$

$$D_N = \frac{(2N-1)(\alpha C_{N-1} - C_N)}{1-\alpha^2}, \quad (12)$$

where $K(k)$ and $E(k)$ are the complete elliptic integrals of first and second type, respectively.

A second type of recurrence relation can be deduced by considering the integral

$$G_N(k) = \frac{1}{4} \int_0^{2\pi} \frac{\cos Nu}{(1-k^2 \cos^2 \frac{u}{2})^{3/2}} du = (-1)^N \int_0^{\pi/2} \frac{\cos 2Nu}{(1-k^2 \sin^2 u)^{3/2}} du. \quad (13)$$

We have found that the relation with integral D_N is given by

$$G_N = (1+\alpha)D_N. \quad (14)$$

For the G_N integral, the following recurrence relations has been deduced

$$G_{N+1}(k) = \frac{4N}{2N-1} \frac{2-k^2}{k^2} G_N(k) - \frac{2N+1}{2N-1} G_{N-1}(k), \quad (15)$$

where

$$G_0(k) = \frac{E(k)}{1-k^2},$$

$$G_1(k) = \frac{E(k)}{1-k^2} - 2 \frac{K(k) - E(k)}{k^2}. \quad (16)$$

On the other hand, starting from the definition of integral D_N , the integral C_N can be expressed with the help of integrals D_N by

$$C_N = \frac{\alpha}{4N} (D_{N-1} - D_{N+1}), \quad (17)$$

and thus, a recurrence relation can be written for C_N too.

Even if the second recurrence relation works better than the first one, for $k < 0.4$ and $N > 4$, it yields incorrect results. The explanation is that a three term linear recurrence relation of the form given by Eq. (11) or Eq. (15) has two linearly independent solutions. Only one of these corresponds to the sequence of functions that we are trying to generate. The other one may be exponentially growing in the direction that we want to go, or exponentially damped, or exponentially neutral. If it is exponentially growing, then the recurrence relation is of little or no practical use in that direction. Unfortunately, this is the case we are dealing with.

In the following, the C_N and D_N integrals will be calculated as solutions of a hypergeometric differential equation.

Let us use the following notations:

$$A_N = f(\alpha) \int_0^{2\pi} \frac{\cos Nu}{(1-\alpha \cos u)^{1/2}} du, \quad (18)$$

and

$$B_N = f(\alpha) \int_0^{2\pi} \frac{\cos Nu}{(1-\alpha \cos u)^{3/2}} du, \quad (19)$$

where $f(\alpha)$ is a function of α only and has to be chosen in such a way so as to obtain a differential equation of second order in A_N to "fit" as well as possible with the differential equation satisfied by some known special function.

By using the above definitions , and considering the multiple-angle relation

$$\cos(Nu) = 2 \cos(N-1)u \cos u - \cos(N-2)u,$$

we obtain

$$B_N = -\frac{4}{\alpha}(N-1)A_{N-1} + B_{N-2}.$$

The relations between A_N and B_N are the same as those between C_N and D_N , namely

$$A_N = \frac{\alpha}{4N}(B_{N-1} - B_{N+1}), \quad (20)$$

$$A_N = B_N - \frac{\alpha}{2}(B_{N+1} + B_{N-1}), \quad (21)$$

$$\alpha B_{N+1} - B_N = -(2N+1)A_N, \quad (22)$$

$$B_N - \alpha B_{N-1} = (1-2N)A_N, \quad (23)$$

$$B_N = \frac{2N+1}{\alpha^2-1}(\alpha A_{N+1} - A_N). \quad (24)$$

The derivative of A_N with respect to α is

$$\frac{dA_N}{d\alpha} = \left(\frac{f'}{f} - \frac{1}{2\alpha}\right)A_N + \frac{1}{2\alpha}B_N, \quad (25)$$

where f' is the derivative of f with respect to α . But due to Eq. (24)

$$\begin{aligned} \frac{dA_N}{d\alpha} &= \left(\frac{f'}{f} - \frac{1}{2\alpha}\right)A_N + \frac{1}{2\alpha} \frac{2N+1}{\alpha^2-1}(\alpha A_{N+1} - A_N) \\ &= \left[\frac{f'}{f} - \frac{1}{2\alpha} - \frac{2N+1}{2\alpha(\alpha^2-1)}\right]A_N + \frac{2N+1}{2(\alpha^2-1)}A_{N+1}. \end{aligned} \quad (26)$$

By multiplying Eq. (26) with $2(\alpha^2-1)/(2N+1)$ and differentiating then with respect to α , we obtain

$$\frac{d}{d\alpha} \left[\frac{2(\alpha^2-1)}{2N+1} \frac{dA_N}{d\alpha} \right] = \frac{d}{d\alpha} \left[\frac{2(\alpha^2-1)}{2N+1} \left(\frac{f'}{f} - \frac{1}{2\alpha} - \frac{2N+1}{2\alpha(\alpha^2-1)} \right) A_N \right] + \frac{dA_{N+1}}{d\alpha},$$

therefore

$$\frac{d}{d\alpha} \left[\frac{2(\alpha^2-1)}{2N+1} \frac{dA_N}{d\alpha} \right] = \frac{d}{d\alpha} \left[\left(\frac{2(\alpha^2-1)}{2N+1} \frac{f'}{f} - \frac{\alpha^2-1}{\alpha(2N+1)} - \frac{1}{\alpha} \right) A_N \right] + \frac{dA_{N+1}}{d\alpha}. \quad (27)$$

From Eq. (25) we obtain

$$\frac{dA_{N+1}}{d\alpha} = \left(\frac{f'}{f} - \frac{1}{2\alpha}\right)A_{N+1} + \frac{1}{2\alpha}B_{N+1}.$$

From Eq. (26) we obtain

$$A_{N+1} = \frac{2(\alpha^2-1)}{2N+1} \frac{dA_N}{d\alpha} - \left[\frac{2(\alpha^2-1)}{2N+1} \frac{f'}{f} - \frac{\alpha^2-1}{\alpha(2N+1)} - \frac{1}{\alpha} \right] A_N.$$

Thus

$$\begin{aligned} \frac{dA_{N+1}}{d\alpha} = & \left[\frac{2(\alpha^2 - 1)}{2N + 1} \frac{f'}{f} - \frac{\alpha^2 - 1}{\alpha(2N + 1)} \right] \frac{dA_N}{d\alpha} \\ & - \left[\frac{2(\alpha^2 - 1)}{2N + 1} \left(\frac{f'}{f} \right)^2 - \frac{f'}{\alpha f} - \frac{2(\alpha^2 - 1)}{2N + 1} \frac{f'}{f} + \frac{\alpha^2 - 1}{2\alpha^2(2N + 1)} + \frac{1}{2\alpha^2} \right] A_N \\ & + \frac{1}{2\alpha} B_{N+1}. \end{aligned}$$

We have to find B_{N+1} as a function of A_N . From Eq. (22) we obtain

$$B_{N+1} = \frac{1}{\alpha} [B_N - (2N + 1)A_N].$$

From Eq. (22) and (25) we obtain

$$\begin{aligned} B_{N+1} &= 2 \frac{dA_N}{d\alpha} - 2 \left(\frac{f'}{f} - \frac{1}{2\alpha} \right) A_N - \frac{2N + 1}{\alpha} A_N \\ &= 2 \frac{dA_N}{d\alpha} - 2 \left(\frac{f'}{f} + \frac{N}{\alpha} \right) A_N. \end{aligned}$$

Introducing B_{N+1} in the expression of $dA_{N+1}/d\alpha$, we obtain

$$\begin{aligned} \frac{dA_{N+1}}{d\alpha} = & \left[\frac{2(\alpha^2 - 1)}{2N + 1} \frac{f'}{f} - \frac{\alpha^2 - 1}{\alpha(2N + 1)} + \frac{1}{\alpha} \right] \frac{dA_N}{d\alpha} \\ & - \left[\frac{2(\alpha^2 - 1)}{2N + 1} \left(\frac{f'}{f} \right)^2 - \frac{2\alpha^2 - 1}{\alpha(2N + 1)} \frac{f'}{f} + \frac{\alpha^2 - 1}{2\alpha^2(2N + 1)} + \frac{2N + 1}{2\alpha^2} \right] A_N. \end{aligned} \quad (28)$$

Introducing Eq. (28) in Eq. (27) we obtain

$$\begin{aligned} \frac{2(\alpha^2 - 1)}{2N + 1} A_N'' + & \left[\frac{4\alpha}{2N + 1} - \frac{4(\alpha^2 - 1)}{2N + 1} \frac{f'}{f} + \frac{2(\alpha^2 - 1)}{\alpha(2N + 1)} \right] A_N' \\ & - \left[\frac{2(\alpha^2 - 1)}{2N + 1} \frac{f''}{f} - \frac{4(\alpha^2 - 1)}{2N + 1} \left(\frac{f'}{f} \right)^2 + \frac{4\alpha}{2N + 1} \frac{f'}{f} + \frac{2(\alpha^2 - 1)}{\alpha(2N + 1)} \frac{f'}{f} \right. \\ & \left. - \frac{\alpha^2 - 1}{2\alpha^2(2N + 1)} - \frac{1}{\alpha^2(2N + 1)} - \frac{2N - 1}{2\alpha^2} - \frac{1}{2N + 1} \right] A_N = 0, \end{aligned} \quad (29)$$

and after some simplifications, the differential equation of second order (30) with A_N as unknown is obtained.

$$\begin{aligned} (\alpha^2 - 1)A_N'' + & \left[2\alpha + \frac{\alpha^2 - 1}{\alpha} - 2(\alpha^2 - 1) \frac{f'}{f} \right] A_N' \\ & - \left[(\alpha^2 - 1) \frac{f''}{f} - 2(\alpha^2 - 1) \left(\frac{f'}{f} \right)^2 + 2\alpha \frac{f'}{f} + \frac{\alpha^2 - 1}{\alpha} \frac{f'}{f} - \frac{N^2}{\alpha^2} - \frac{3}{4} \right] A_N = 0. \end{aligned} \quad (30)$$

By choosing $f = C$ (a constant), we obtain

$$\alpha^2(\alpha^2 - 1)A_N'' + \alpha(3\alpha^2 - 1)A_N' + \left(\frac{3\alpha^2}{4} + N^2 \right) A_N = 0. \quad (31)$$

To simplify the solution, we have made the following substitutions

$$x = \alpha^2; A_N(\alpha) = \alpha^N u_N(x), \quad (32)$$

obtaining a differential hypergeometric equation

$$x(1-x)u_N'' + [N+1-(N+2)x]u_N' - \frac{1}{4} \left[N(N+2) + \frac{3}{4} \right] u_N = 0, \quad (33)$$

with the following parameters

$$a \equiv \frac{1}{2} \left(N + \frac{3}{2} \right); b \equiv \frac{1}{2} \left(N + \frac{1}{2} \right); c \equiv N+1; z \equiv \alpha^2.$$

Therefore, one of the solution of the differential equation in A_N is

$$A_N^1 \equiv {}_2F_1 [a, b; c; z] \alpha^N. \quad (34)$$

The second solution of the differential equation has the form

$$\begin{aligned} A_N^2 \equiv & {}_2F_1(a, b; N+1; \alpha^2) \ln(\alpha^2) \alpha^N + \alpha^N \sum_{n=1}^{\infty} \frac{(a)_n (b)_n}{(N+1)_n n!} [\psi(a+n) - \psi(a) \\ & + \psi(b+n) - \psi(b) - \psi(N+1+n) + \psi(N+1) - \psi(n+1) + \psi(1)] \alpha^{2n} \\ & - \alpha^N \sum_{n=1}^N \frac{(n-1)! (-N)_n}{(1-a)_n (1-b)_n} \alpha^{-2n}, \end{aligned} \quad (35)$$

where

$$(\beta)_n = \beta(\beta+1)(\beta+2)\dots(\beta+n-1),$$

and ψ is the logarithmic derivative of the Euler integral of the second kind⁴

$$\psi(z) = \frac{d}{dz} \ln \Gamma(z).$$

Thus, the integral C_N (Eq. (11)), has the expression

$$C_N = \frac{\sqrt{1+\alpha}}{4} [k_1(N) A_N^1(\alpha) + k_2(N) A_N^2(\alpha)], \quad (36)$$

where k_1 and k_2 are function of N only. Considering α infinite, the first term and the infinite sum in the expression of the second solution A_N^2 , vanish, while the finite sum presents terms going to infinity (i.e., they do not cancel reciprocally) for $n > N/2$. But as C_N is the solution of the differential equation for any α , k_2 has to vanish, and C_N becomes

$$C_N = k(N) \frac{\sqrt{1+\alpha}}{4} \alpha^N {}_2F_1 \left[\frac{1}{2} \left(N + \frac{3}{2} \right), \frac{1}{2} \left(N + \frac{1}{2} \right); N+1; \alpha^2 \right]. \quad (37)$$

In the last equation we have replaced the notation $k_1(N)$ by $k(N)$. To obtain the expression of $k(N)$, we will consider in Eq. (18) $f_N(\alpha) \equiv f(\alpha) \neq 1$. Thus, A_N can be written as

$$A_N = k(N) f_N(\alpha) \alpha^N {}_2F_1 \left[\frac{1}{2} \left(N + \frac{3}{2} \right), \frac{1}{2} \left(N + \frac{1}{2} \right); N+1; \alpha^2 \right].$$

The derivative of A_N with respect to α is given then by

$$A_N' = k(N) \left[(f_N + \alpha f_N') \alpha^{N-1} {}_2F_1 + f_N \alpha^{N+1} \frac{1}{2(N+1)} \left(N + \frac{3}{2} \right) \left(N + \frac{1}{2} \right) {}_2F_1^{(1)} \right],$$

where the following notations have been used

$$\begin{aligned} {}_2F_1 &\equiv {}_2F_1 \left[\frac{1}{2} \left(N + \frac{3}{2} \right), \frac{1}{2} \left(N + \frac{1}{2} \right); N+1; \alpha^2 \right], \\ {}_2F_1^{(1)} &\equiv {}_2F_1 \left[\frac{1}{2} \left(N + \frac{7}{2} \right), \frac{1}{2} \left(N + \frac{5}{2} \right); N+2; \alpha^2 \right]. \end{aligned}$$

By introducing the expression giving A_N in Eq. (26) the following equation is obtained

$$k(N) \left\{ \left[N f_N + \frac{1}{2} \left(1 + \frac{2N+1}{\alpha^2-1} \right) \right] {}_2F_1 + f_N \frac{\alpha^2}{2(N+1)} \left(N + \frac{1}{2} \right) \left(N + \frac{3}{2} \right) {}_2F_1^{(1)} \right\} \\ = k(N+1) \frac{\alpha^2}{\alpha^2-1} \left(N + \frac{1}{2} \right) f_{N+1} {}_2F_1^{(2)}, \quad (38)$$

where

$${}_2F_1^{(2)} \equiv {}_2F_1 \left[\frac{1}{2} \left(N + \frac{5}{2} \right), \frac{1}{2} \left(N + \frac{3}{2} \right); N+2; \alpha^2 \right].$$

To obtain information on coefficient $k(N)$ for the $\alpha = 0$ case, equation (38) must be reduced by α^2 . By choosing $f_N(\alpha) = 1$, one obtains

$$k(N) \left[\frac{1}{\alpha^2-1} {}_2F_1 + \frac{1}{2(N+1)} \left(N + \frac{3}{2} \right) {}_2F_1^{(1)} \right] = \frac{1}{\alpha^2-1} k(N+1) {}_2F_1^{(2)}.$$

For $\alpha = 0$, the following recurrence relation is obtained

$$k(N+1) = \frac{1}{2(N+1)} \left(N + \frac{1}{2} \right) k(N). \quad (39)$$

Considering Eq. (37), and taking into account that $C_0 = K(k)$, it follows that $k(0) = 2\pi$. Therefore, Eq. (39) becomes

$$k(N) = \frac{\sqrt{\pi}}{2^{N-1}N!} \Gamma \left(N + \frac{1}{2} \right), \quad (40)$$

while C_N is given by the relation

$$C_N = \frac{\sqrt{\pi(1+\alpha)}}{2N!} \left(\frac{\alpha}{2} \right)^N \Gamma \left(N + \frac{1}{2} \right) {}_2F_1 \left[\frac{1}{2} \left(N + \frac{3}{2} \right), \frac{1}{2} \left(N + \frac{1}{2} \right); N+1; \alpha^2 \right].$$

From relation (24), we obtain the necessary relation for D_N

By using this method, the C_N and D_N integrals have been computed exactly up to the ninth digit (double precision) for any k and for N up to 50.

4. CONCLUSIONS

A reliable accurate numerical method for solving Laplace's equation with Neumann boundary conditions, for a toroidally symmetric configurations with arbitrary torus cross-section, was described.

A new form of the normal component of the magnetic field in a toroidally symmetric configuration has been derived in terms of the solution of a hypergeometric differential equation, which is also appropriate in the large toroidal mode number limit.

The presented approach to calculate the periodic integrals has been used for stability analyses in toroidally symmetric tokamak discharges^{3,5} to determine of the vacuum field resulting from the perturbation of a toroidally symmetric plasma.

REFERENCES

1. E.Martensen, "Über eine Methode zum Räumlichen Neumannschen Problem mit einer Anwendung für torusartige Berandungen", *Acta Mathematica*, **109**, pp. 75-135, 1963.
2. M.A.Jaswon and G.T.Symm, *Integral Equation Method in Potential Theory and Elastostatics*, Academic Press, London, New York, San Francisco, 1977.
3. C.V.Atanasiu, A.H.Boozer, L.E.Zakharov, A.A.Subbotin and I.G.Miron, "Determination of the vacuum field resulting from the perturbation of a toroidally symmetric plasma", *Phys. Plasmas*, **6**, pp. 2781-2790, 1999.
4. A.Erdélyi, *The Bateman Manuscript Project*, McGraw-Hill, New York, 1953, Vol. 1.
5. A.H.Boozer, "Equations for studies of feedback stabilization", *Phys. Plasmas*, **5**, pp. 3350-3357, 1998.

Absorption in a self-heating He-Se laser tube

M.Ristici*, E.Ristici, M.Tivarus, B.Iliescu^a, C.Cotirlan^b

National Institute for Lasers, Plasma and Radiation Physics, Laser Dept., P. O. Box MG-36,
Magurele-Bucharest, 76900, Romania,

^a National Institute for Material Physics, P.O.Box MG-7, Magurele-Bucharest, 76900, Romania

^b Institute of Optoelectronics, P.O.Box MG-22, Magurele-Bucharest, 76900, Romania

ABSTRACT

A self-heating He-Se laser tube has been developed. It was all Pyrex, 60 cm active length, 2 mm ID. The laser beam consisted of seven green lines 28 mW total power. We have examined, by perturbation spectroscopy, the existence of amplification along the laser tube axis. The experimental set-up consisted of: laser tube, two laser mirrors dielectrically deposited for full reflection on 500 ± 50 nm spectral region, a grating monochromator 0.2 nm resolution, a chopper, an EMI 9558QB photomultiplier and a lock-in amplifier. The spontaneously emitted light in the perpendicular direction to the tube axis has been monitored. The laser radiation field that exists in the active medium involves the decreasing of the upper laser level population and thus, the intensity of the corresponded spontaneously emitted line decreases too. Using the chopper, the laser beam is periodically interrupted so that, a modulation of the intensities of the spectral lines appears. The signal sign is opposite for amplification and absorption, respectively. By this technique, we have observed the presence of an absorption region, placed inside the metal reservoir, just where the metal vapors penetrate the discharge. Taking into account the energies of the involved levels, we have proposed a probable reaction.

Keywords: metal vapor laser, gas laser, positive column discharge and emission spectroscopy.

1. INTRODUCTION

The first cw laser action in He-Se mixture was observed and reported by Silfast and Klein^{1,2} on many wavelengths in visible and near infrared region.

The metal vapor laser is not entirely understood. Because of complex design and materials, this kind of laser is very expensive and is not commercial. We believe that a more simple laser tube make this laser more interesting and useful. So, we have studied an all Pyrex He-Se laser tube, and the results were very good.

The Se_2 molecules are normally present in the gas mixture. When the temperature is about 1500 K, the Se_2 molecules become the dominant particles. For the low temperature of 260 °C the vapor pressure of selenium is about 5×10^{-3} Torr³. Such vapors, present in an electric gas discharge, will be broken in selenium atoms by the electron collisions. The same mechanism will develop a high density of positive selenium ions, which, by cataphoresis, penetrate the active region of the discharge moving to cathode.

The energy level diagram of Se^+ shows many levels for electronic configuration $4s^2 4p^2 5p$, whose energies are very close to those of the He^+ ground state⁴. These levels are highly populated. It is known that a charge transfer process between the ground state Se atoms and He^+ ions takes place according to the reaction:



The decay of selenium excited levels is predominantly radiative to levels corresponding to electronic configuration $4s^2 4p^2 5s$. Over 60 laser radiations were generated when a 2 meters active length laser tube had operated. The most powerful emitted radiations are in blue-green region of the spectrum.

*Correspondence: E-mail: ristici@ifin.nipne.ro; Telephone: 7803469/1810; Fax: (401) 4231 791

Using the perturbation spectroscopy, we have discovered a small absorption region in the metal reservoir between the small capillary and the long capillary. This region is thin and it does not affect significantly the parameters of the laser beam.

Also, we have studied the influence of the magnetic field on the spectral line intensities. The magnetic field was placed in the reservoir region. The magnetic field was directed perpendicularly to the tube axis, because only in this case it is effective. The density of selenium ions is higher in the region between the surface of the metal and the tube axis.

In the presence of the magnetic field, the output laser power was higher and also the spontaneous emitted light was increased.

2. EXPERIMENTAL LASER TUBE AND SET-UP

We have developed an original geometry for He-Se laser tube, entirely from Pyrex glass⁵. The metal is heated by the discharge itself, so that a connection between the current value and the vapor pressure is established.

The inner diameter of the capillary is 2 mm. The capillary is firmly welded at one end and has the possibility to dilate to the other. Also, it consists of two pieces: one is long and the other is short and it is placed in the metal reservoir. To decrease the helium losses by diffusion through the capillary at the high operating temperature, a glass mantle surrounds it, so that it remains relatively cold in the operating time.

By heating the spectroscopic pure selenium, the metal vapors are generated. The discharge current heats the capillary and, by radiation, the metal is also heated. In our experiment, the optimum laser operation was obtained when the metal was almost completely melted.

To avoid the melting of the glass capillary, the discharge current is limited to a small value, about 130 mA. As a consequence, the helium pressure must be higher than that reported in literature by other authors². So, for an optimum discharge current value, an adequate helium pressure was 20 Torr. If the helium pressure is higher, the discharge current must be lower and the metal deposition on the capillary appears.

The laser tube has the cut ends at Brewster angle for 500 nm wavelength. Loctite UV 358 has been used to seal the windows of the laser tube. The resonator consists of a pair of the total reflecting dielectric mirrors having curvature radius of 2 m, 100 nm bandwidth centered on 500 nm. Seven Se⁺ lines simultaneously oscillated.

A second anode at the right end of the main capillary was used. Its purpose is to impede the metal vapors to deposit on the right Brewster window of the laser tube.

Fig 1 shows the experimental set-up. On the axis of the resonator there is a chopper, which modulates the laser beam generated inside the resonator. The 90 degree spontaneous emission from three chosen regions was monitored. An optical system consisting in a pair of identical lenses of 250 mm focal distance, focalizes the light on the monochromator slit. The used grating monochromator has a 0.2 nm optical resolution. An EMI 9558 B photomultiplier was used. A synchronous detection block and a recorder were used.

3. RESULTS AND DISCUSSION

Inside the laser tube, three specific regions A, B and C were chosen. The amplification region 'B' is just the active medium (a mixture of helium and selenium atoms and ions); the plasma parameters are about the same as reported elsewhere⁶. The 'C' region is at the end of the long capillary. The 'A' region is placed in the metal reservoir, at the end of the short capillary. In both regions 'A' and 'C', the current density is much lower than in the 'B' region. A blue cloud appears in the 'A' region, between the end of the short capillary and the beginning of the long capillary. This cloud consists in selenium and helium atoms and ions.

Both mirrors are total reflecting. The laser beam is chopped and the lock-in signal is recorded using the experimental set-up described in Fig 1.

For a steady state of the tube operation - a well defined current and metal temperature - a stable plasma region exists in the region "A" of the tube. We have determined, by spectroscopic measurements that the vapour content of that region consists mainly of selenium ions.

Using the set-up presented in Fig. 1, we have obtained a signal that has opposite sign for the amplification and absorption, respectively. We denoted the positive sign for the signal recorded from 'B' region. The discharge current was 130 mA in all cases.

For described tube we have measured the influence of the magnetic field on some selenium spectral lines by spectroscopic method⁷. The magnetic field is effective when it is directed perpendicularly to the tube axis. The density of selenium ions is not uniform around the tube axis, it is higher in the region between the surface of the metal and the tube axis. When they move to enter in the main capillary, the Lorentz force acts on them so that other vapors can lift from the metal surface. In this new steady state the ions are pumped more efficiently in the discharge.

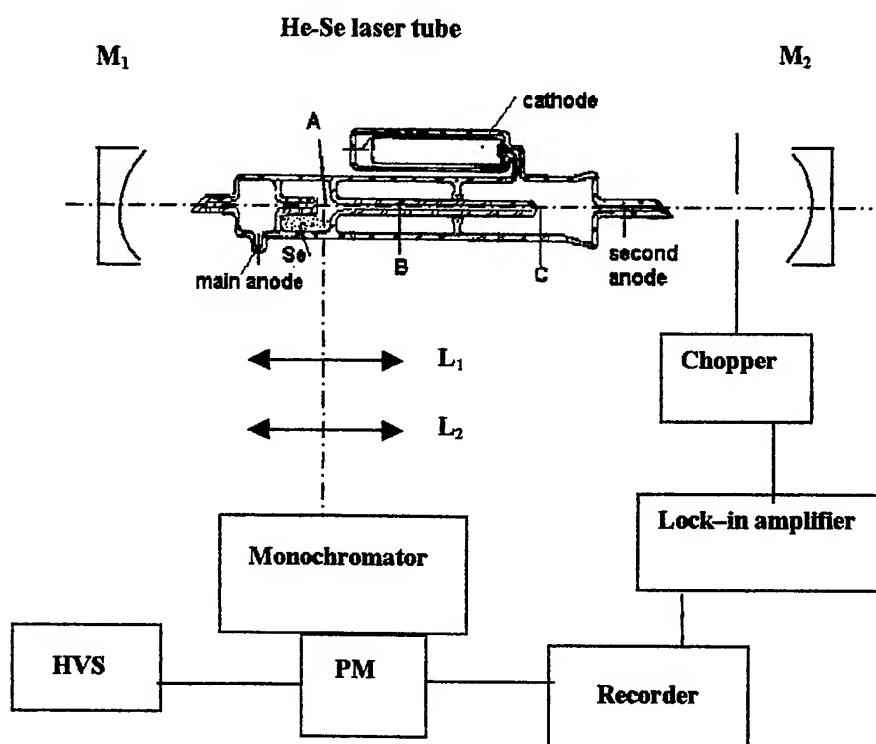


Fig.1 Experimental set-up used in perturbation spectroscopy.
A, B and C – examined regions of the laser tube, M_1 , M_2 – mirrors,
 L_1 , L_2 – optical lenses, HVS – high voltage supply, PM-photomultiplier

Table I presents the spectral lines involved in the laser oscillations. We choose those spectral lines from the visible region of the spectrum, which oscillate inside the resonator that consists of dielectric mirrors with a high reflecting coefficient for all of them.

Using the chopper inside the resonator, we can record the variations of the line intensities from the laser beam. These variations are presented in the Table II.

The spectral scanning records show the presence of signals with opposite phase for 'A' region regarding to those recorded from 'B' and 'C' regions. From Table 2, we can conclude that in the 'A' region the laser radiation is absorbed

for all wavelengths, excepting the 525.36 nm radiation for which this region is perfectly transparent, in opposition with 'B' and 'C' regions, where the radiation is amplified.

The measurements from these regions were made without the presence of a magnetic field "a" and in the presence of a magnetic field "b", respectively. The magnetic field had an influence only if it was placed in the 'A' region.

Tab. I. Spectral lines involved in the laser oscillations

λ (nm)	Upper level	Lower level
497.57	$5p^2D_{3/2}$	$4s4p^4^2P_{3/2}$
499.20	$5p^4P_{3/2}$	$5s^4P_{3/2}$
506.86	$5p^4P_{3/2}$	$5s^4P_{3/2}$
517.60	$5p^4D_{3/2}$	$5s^4P_{3/2}$
522.75	$5p^4D_{7/2}$	$5s^4P_{3/2}$
525.36	$5p^4D_{1/2}$	$5s^4P_{1/2}$
530.53	$5p^2D_{3/2}$	$5s^2P_{1/2}$

Tab. II The variations of the intensities of the spectral lines involved in laser oscillations, in absence of a magnetic field and in its presence.

λ (nm)	497.57	499.20	506.86	517.60	522.75	525.36	530.53	a-without m.f. b-with m.f.
ΔI [u.a]								
ΔI_B [a.u.]	10	38	18	32	75	10	13	a
	23	62	28	50	95	17	20	b
ΔI_A [a.u.]	-15	-26	-11	-25	-60	0	-5	a
	-48	-65	-31	-47	-100	0	-16	b
ΔI_C [a.u.]	7	28	43	35	77	6	13	a
	15	46	20	46	98	10	20	b

Fig. 2 shows the behavior of the 522.75 nm selenium ion laser when the discharge current increases. The curve "a" and "b" are without magnetic field, and with applied magnetic field on the laser tube. For low current region the line intensity increases linearly, but for higher currents the increasing is much abrupt due to the higher vapor density. The magnetic field influence on laser output was also observed⁷.

Fig. 3 presents the absorption of 522.75 laser radiation vs. the distance measured from the end of the small capillary.

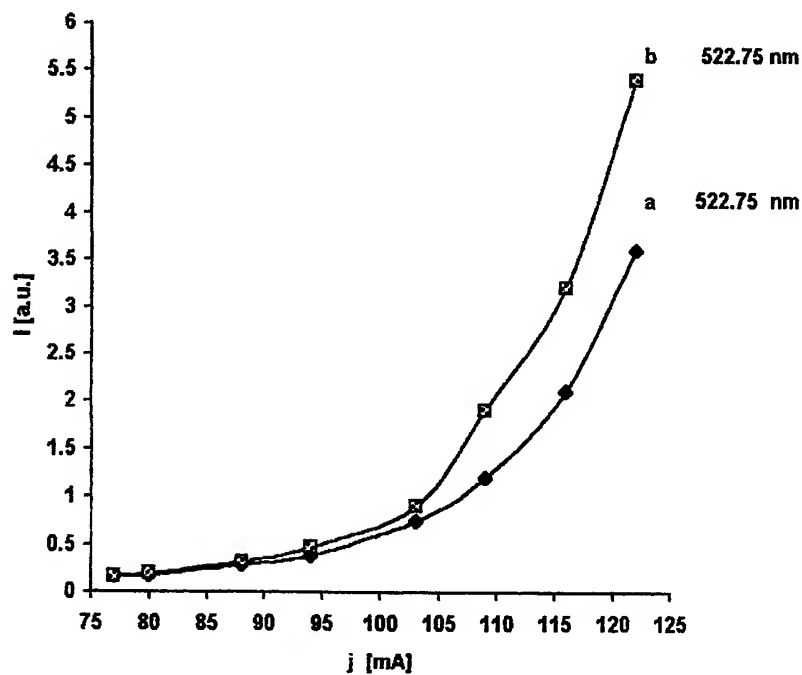


Fig.2 Dependence of the selenium ion line intensity (522.75 nm) on discharge current without (curve "a") and with applied magnetic field (curve "b").

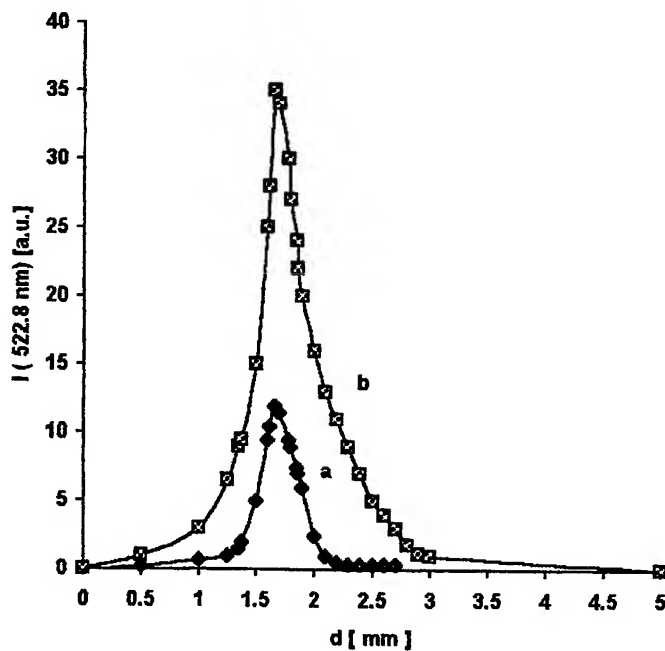
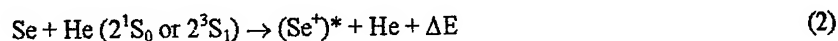


Fig.3 The variations of the intensity of the 522.75 nm spectral line. a - without the magnetic field; b - with the magnetic field applied in the reservoir region.

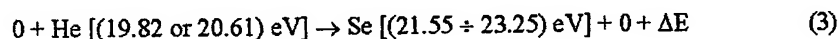
This radiation was preferred for representation because it was the strongest radiation, as we can see from the Table 2. The absorption region was scanned along the tube axis using a 0.5 mm diaphragm. We can observe that the absorption is significant only for one millimeter length in the absence of a magnetic field "a", and two millimeters in the presence of a magnetic field "b", respectively.

The absorption region appears just where the selenium vapor clouds penetrate the discharge region. By electron collisions, the metal molecules are broken in atoms and ions. As a result, the electronic temperature in that region is low so that, the density of helium ions is also low.

As a consequence, the reaction (1) has a low rate and the population inversion does not appear here. The existence of the strong absorption of laser radiation shows that the lower laser levels are highly populated by electronic collisions or, alternatively, by the reaction:



Where $(\text{Se}^+)^*$ levels signify the lower laser levels of the selenium ion. Energetically that corresponds to:



In He-Se positive column, on the tube axis³, $kT \approx 2.5 \text{ eV}$, so that, the supposition of the existence of the reaction (2) seems to be valid.

The presence of such reaction can explain the appearance of the laser radiation absorption in the 'A' region. Evidently, it takes place also in the amplifying region B but with a lower rate, but contributes to a reduction of the population inversion.

4. CONCLUSIONS

An important contribution of helium metastable levels is to generate the selenium ions by electron collisions, but also to populate the lower laser levels.

Using the perturbation spectroscopy method in a home-made self-heating He-Se laser tube, a strong absorption region was detected. The reduction of the emitted laser radiation power is not very important because this region is thin enough.

In our opinion, the reaction presented by eq. (2) is responsible for absorption of the laser beam. The reaction takes place also in the amplification region 'B' but with a lower rate, and contributes to a decreasing of the population inversion.

The presence of the magnetic field involves the increasing of the laser beam power, but also, it influences the absorption of the laser radiation.

We intend to continue this study to find the way for improving the laser operation.

5. REFERENCES

1. W.I. Silfvast and M.B. Klein, "cw Laser action on 24 visible wavelengths in Se II", *Appl. Phys.Lett.* **17**, pp. 400-403, 1970.
2. M.B. Klein, and W.I. Silfvast, "New cw laser transitions in Se II", *Appl. Phys.Lett.* **18**, pp. 482-485, 1971.
3. C.C.Davis and T.A.King, "Advance in Quantum Electronics", edited by D.W. Goodwin (Academic), p.170, 1975.
4. D.C. Martin, "Analysis of the Spectrum of Se II", *Phys.Rev.* **48**, pp. 938-944, 1985.
5. M.Ristici, M.V. Udrea, R. Medianu, and I. Ristici, "A small power He-Se laser", *Proc. SPIE*, **2461**, pp.18-24, 1995.
6. T. Goto, H. Kano and S. Hattori, "Plasma parameters in gas discharges for positive-column He-Se⁺ lasers", *J. Appl. Phys.* **43**, pp. 5064-5067, 1972.
7. M.Ristici, I. Ristici, and R. Medianu, "A medium power cw He-Se laser", *Proc. SPIE* **3405**, pp. 85-88, 1997.

A simple method for characterisation the up-conversion processes governing three-micron generation in concentrated erbium crystals

S. Georgescu* and C. Hapenciuc

Institute of Atomic Physics, National Institute for Lasers, Plasma, and Radiation Physics, Bucharest,
R-76900, P. O. Box MG-36, Romania

ABSTRACT

A simple method that allows the determination of the rates of the two-ion up-conversion processes governing 3- μm laser emission (laser transition $^4\text{I}_{11/2} \rightarrow ^4\text{I}_{13/2}$) in concentrated erbium systems is presented. The method is based on the analysis of the kinetics of the $^4\text{I}_{11/2}$ level, excited with short 532 nm laser pulses, for various pulse intensities.

Keywords: 3- μm laser, Er^{3+} , up-conversion.

1. INTRODUCTION

To understand the efficient 3- μm generation on the self-saturated transition $^4\text{I}_{11/2} \rightarrow ^4\text{I}_{13/2}$ in concentrated erbium systems, at least three energy transfer mechanisms should be taken into account¹⁻¹¹: cross-relaxation from the $^4\text{S}_{3/2}$ level, i. e. ($^4\text{S}_{3/2} \rightarrow ^4\text{I}_{9/2}$) + ($^4\text{I}_{15/2} \rightarrow ^4\text{I}_{13/2}$), up-conversion from the terminal laser level ($^4\text{I}_{13/2} \rightarrow ^4\text{I}_{15/2}$) + ($^4\text{I}_{13/2} \rightarrow ^4\text{I}_{9/2}$), and up-conversion from the initial laser level, ($^4\text{I}_{11/2} \rightarrow ^4\text{I}_{15/2}$) + ($^4\text{I}_{11/2} \rightarrow ^4\text{F}_{7/2}$). Besides, in low phonons crystals (as, for example, fluorides), another cross-relaxation process contributes: ($^4\text{I}_{9/2} \rightarrow ^4\text{I}_{13/2}$) + ($^4\text{I}_{15/2} \rightarrow ^4\text{I}_{9/2}$)^{12,13}. The most fruitful approach for the determination of the up-conversion rates proved to be the analysis of the system response under short pulse excitation¹⁴. In order to separate the effects of the various interactions present in the erbium systems (radiative, multiphonon, cross-relaxation, and up-conversion), a strategy, based on concentration and pump intensity, was adopted¹⁴. Thus, for low pump intensities and low Er concentrations, the behavior of the Er system is linear and the fluorescence lifetimes can be measured and, by evaluating the radiative probabilities with the Judd-Ofelt analysis^{15,16}, the multiphonon transition probabilities can be estimated. Then, for low pump intensities and higher Er concentrations, the comparison of the kinetics of some fluorescent levels with those obtained for low concentrations allows the determination of the cross-relaxation rates. Increasing the pump intensity, the effects of the up-conversion processes on the kinetics of the metastable levels can be well evidenced.

In this paper we present a method based on short pulse excitation at room temperature of the erbium luminescence, with the second harmonic of the Nd: YAG laser. The up-conversion parameters are determined from the analysis of the kinetics of only one level: $^4\text{I}_{11/2}$. The method is then exemplified for Er: YAG crystals.

2. EXPERIMENTAL

The experiments were performed at room temperature on three concentrated Er: YAG samples (erbium concentrations: 40, 50 and 60 %). The luminescence of Er: YAG crystals was excited in green (532 nm) using the second harmonic of the Nd: YAG laser Quanta Ray DCR2 (pulsewidth ~ 15 ns, repetition frequency ~ 20 Hz) and gathered into GDM 1000 monochromator equipped with an S-1 photomultiplier in photon counting configuration. The fluorescence spectra were obtained with a TURBO MCS scaler. The time resolution of the experimental apparatus was 20 ns.

3. RESULTS AND DISCUSSION

3.1. Rate equation model

The usual model describing the kinetics of the metastable levels $^4\text{I}_{13/2}$, $^4\text{I}_{11/2}$, $^4\text{I}_{9/2}$, $^4\text{F}_{9/2}$, and $^4\text{S}_{3/2}$ after a short pump pulse, in the approximation of two-ion energy transfer processes, is based on the following rate equation system:

* Correspondence: e-mail: joe@pluto.infim.ro

$$\begin{aligned}
\frac{dN_4}{dt} &= -(a_{40} + a_{41} + a_{42} + a_{43} + w_{43})N_4 + (a_{54} + w_{54})N_{50} \\
\frac{dN_3}{dt} &= -(a_{30} + a_{31} + a_{32} + w_{32})N_3 + a_{53}N_5 + (a_{43} + w_{43})N_4\omega_{11}N_1^2 - \omega_{30}N_3N_0 + \omega_{50}N_5N_0 \\
\frac{dN_2}{dt} &= -(a_{20} + a_{21} + w_{21} + w_2^{imp})N_2 + a_{52}N_5 + a_{42}N_4 + a_{32}N_3 - 2\omega_{22}N_2^2 \\
\frac{dN_1}{dt} &= -(a_{10} + w_1^{imp})N_1 + a_{51}N_5 + a_{41}N_4 + a_{31}N_3 + (a_{21} + w_{21} + w_2^{imp'})N_2 - 2\omega_{11}N_1^2 + 2\omega_{30}N_3N_0 + \omega_{50}N_0N_5
\end{aligned} \quad (1)$$

where N_0 to N_5 are the populations of $^4I_{15/2}$, $^4I_{13/2}$, $^4I_{11/2}$, $^4I_{9/2}$, $^4F_{9/2}$, and $^4S_{3/2}$ (thermalised, at room temperatures, with $^2H_{11/2}$), respectively. The coefficients a_{ij} are equal with sum of the electric-dipole A_{ij}^{ed} , and magnetic-dipole A_{ij}^{md} transition probabilities (transition $i \rightarrow j$) while w_{ij} are the probabilities of the multiphonon transitions. The energy transfer processes

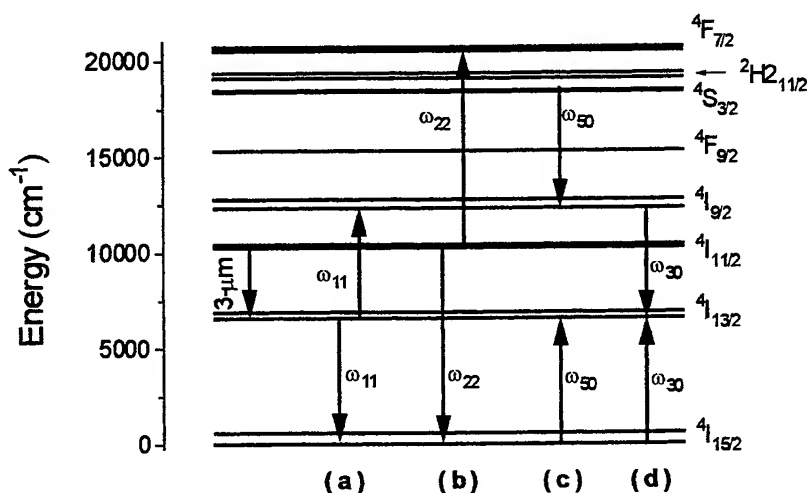


Fig. 1. Energy level scheme of Er^{3+} and the main energy transfer mechanisms: (a) up-conversion from $^4I_{13/2}$, (b) up-conversion from $^4I_{11/2}$, (c) cross-relaxation from $^4S_{3/2}$, and (d) cross-relaxation from $^4I_{9/2}$.

involved in Eqs. (1) are represented by ω_{11} , the rate of the up-conversion from $^4I_{13/2}$ (Fig. 1a), ω_{22} , the rate of the up-conversion from $^4I_{11/2}$ (Fig. 1b); the cross-relaxation processes are represented by ω_{50} (from $^4S_{3/2}$ - Fig. 1c) and ω_{30} (from $^4I_{9/2}$ - Fig. 1d). The initial conditions for Eqs. (1) for pumping in $^4S_{3/2}$ (thermalised with $^2H_{11/2}$) are $N_i(0) = 0$ ($i = 1$ to 4), $N_5(0) = N_{50}$, the population of the $^4S_{3/2}$ ($^2H_{11/2}$) level immediately after the short pumping pulse.

The radiative lifetime of the level i is

$$T_i^{rad} = \left(\sum_j a_{ij} \right)^{-1} \quad (2)$$

while the fluorescent one is given by

$$T_i = \left[w_{i,i-1} + w_i^{imp} + \sum_j a_{ij} \right]^{-1} \quad (3)$$

The parameters w_1^{imp} , w_2^{imp} , and $w_1^{imp'}$ were introduced in (1) and (3) to take into account the presence of the aleatory impurities in the crystal. Due to their long lifetimes, the most affected by the presence of the aleatory impurities are the

levels $^4I_{13/2}$ and $^4I_{11/2}$. According to their role in the de-excitation of the $^4I_{11/2}$ level, we classified the aleatory impurities into two categories^{17, 18}: (i) impurities which merely accelerate the de-excitation of the $^4I_{11/2}$ level and return these excitations to the $^4I_{13/2}$ level; (ii) impurities which take off the excitations from the erbium system. The presence of the first type of impurities implies $w_2^{imp} = w_2^{imp'}$. In the second case, $w_2^{imp} > w_2^{imp'}$. The w_i^{imp} parameters can be obtained from Eqs. (2) and (3), if the fluorescence lifetimes are known.

3.2. The Er: YAG system

For Er: YAG crystals the spectroscopic data entering rate equations (1) are given in Tab.1. The radiative transition probabilities were calculated with a modified Judd-Ofelt analysis¹⁹, which takes into account the peculiar structure of the Er: YAG ground level (two well-separated narrow groups of four Stark sub-levels). The fluorescent lifetimes from Table 1 were measured at low erbium concentrations.

Tab. 1. Spectroscopic data for Er: YAG, at room temperature.

Initial level	Terminal level	A_{ij}^{ed} (s ⁻¹)	A_{ij}^{md} (s ⁻¹)	T_i^{rad} (μs)	T_i (μs)	$w_{i,j-1}$ (s ⁻¹)
$^4S_{3/2}$	$^4F_{9/2}$	0.6	-	619	16	5.56×10^4
	$^4I_{9/2}$	60.5	-			
	$^4I_{11/2}$	31.8	-			
	$^4I_{13/2}$	446.6	-			
	$^4I_{15/2}$	1075.5	-			
$^4F_{9/2}$	$^4I_{9/2}$	0.5	3.9	629	1.5	6.65×10^5
	$^4I_{11/2}$	52.5	10.4			
	$^4I_{13/2}$	63.3	-			
	$^4I_{15/2}$	1485.7	-			
$^4I_{9/2}$	$^4I_{11/2}$	0.6	1.5	4420	0.05	2×10^7
	$^4I_{13/2}$	45.9	-			
	$^4I_{15/2}$	178.3	-			
$^4I_{11/2}$	$^4I_{13/2}$	16.2	12.49	7170	100	9.86×10^3
	$^4I_{15/2}$	110.8	-			
$^4I_{13/2}$	$^4I_{15/2}$	97.9	56.3	6484	6500	~ 0

For medium concentrations, we define the “non-exponential part” of the $^4I_{11/2}$ decay, $f(\tau)$, as the difference between the normalized decays measured at high and low pump energies:

$$f(\tau) = N_2(\tau) / N_{2\max} \Big|_{high} - N_2(\tau) / N_{2\max} \Big|_{low} \quad (4)$$

where $\tau \equiv t / T_2$. The last member of Eq. (4) represents the normalized decay at very low pump energies, when only the linear terms in Eqs. (1) could have a noticeable contribution. We note that the expression (4) represents a generalization of the relation used in^{16, 17}, where, from the normalized decay is extracted an exponential function $\exp(-\tau)$. Obviously, for very high erbium concentrations, the rise-time of the decay can be neglected and $N_2(\tau) / N_{2\max} \Big|_{low} \cong \exp(-\tau)$. Instead, for lower concentrations, due to the lower values of the cross-relaxation rate ω_{50} , the rise-time of the decay should be taken into account. This rise-time is characterized by $\Delta t = (\omega_{50} N_0)^{-1}$. For example, for an Er (40 %): YAG crystal, $\Delta t \approx 5 \mu s$. In Fig. 2, we present the non-exponential part $f(\tau)$ of the $^4I_{11/2}$ experimental decays for an Er³⁺ (60 %): YAG sample. A significant

change of the shape of the function $f(\tau)$ with the pump intensity is observed. For lower pump densities, $f(\tau) > 0$, while for higher pump densities, $f(\tau)$ begins with negative values, this effect increasing with pump energy.

The kinetics of the metastable level $^4I_{11/2}$ was selected in our investigations taking into account the following reasons: (1) this level is the initial level for three-micron laser; (2) an Er^{3+} ion in this state is both "donor" for the up-conversion process ($^4I_{11/2} \rightarrow ^4F_{7/2} + ^4I_{11/2} \rightarrow ^4I_{13/2}$) (Fig. 1 b) and "acceptor" for the up-conversion process ($^4I_{13/2} \rightarrow ^4I_{9/2} + ^4I_{13/2} \rightarrow ^4I_{15/2}$) (Fig. 1 a); (3) the fluorescence wavelength ($\sim 0.97 \mu\text{m}$) allows the use of photomultipliers, which assures a very good linearity, necessary in the analysis of small non-exponentialities.

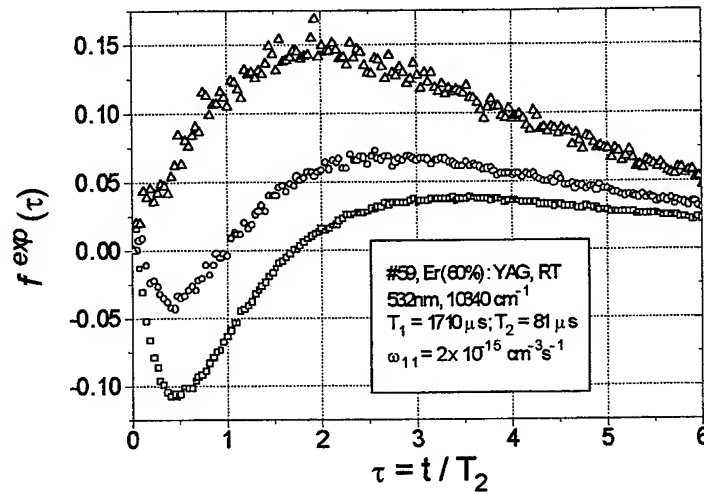


Fig. 2. Experimental non-exponential parts of the $^4I_{11/2}$ decay for various incident energies of the pumping beam (Er (60 %): YAG).

In Fig. 3, we present a family of theoretical curves, generated with the rate equations (1), for the Er (60 %): YAG crystal. For this, we used the spectroscopic data from Table 1 and the facts that for YAG $\omega_{30} = 0$ (Ref. 13).

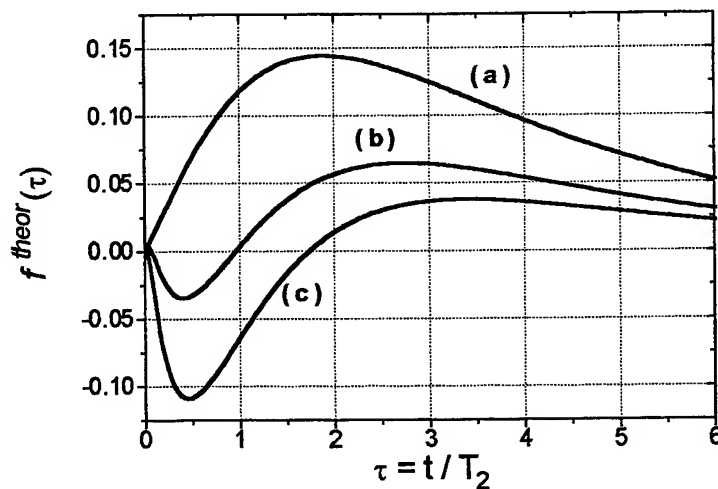


Fig. 3. Theoretical non-exponential parts of the $^4I_{11/2}$ decay in Er (60 %): YAG, obtained with Eqs. (1). The best fit of the experiment was obtained for the following parameters: $\omega_{11} = 2.0 \times 10^{-15} \text{ cm}^3 \text{ s}^{-1}$, $\omega_{22} = 1.8 \times 10^{-15} \text{ cm}^3 \text{ s}^{-1}$, $w_1^{\text{imp}} = 431 \text{ s}^{-1}$, $w_2^{\text{imp}} = w_2^{\text{imp}'} = 2360 \text{ s}^{-1}$, $N_{50} = 9.6 \times 10^{18} \text{ cm}^{-3}$ (curve (a)), $N_{50} = 2.0 \times 10^{19} \text{ cm}^{-3}$ (curve (b)), $N_{50} = 3.0 \times 10^{19} \text{ cm}^{-3}$ (curve (c)), and $w_2^{\text{imp}} = w_2^{\text{imp}'}$.

The other cross-relaxation parameter, namely ω_{30} , varies with the concentration²⁰ (see Tab.2). The best fit of the experimental curves was obtained with the following parameters: $\omega_{11} = 2.0 \times 10^{-15} \text{ cm}^3 \text{ s}^{-1}$, $\omega_{22} = 1.8 \times 10^{-15} \text{ cm}^3 \text{ s}^{-1}$, $\omega_{50} = 1.3 \times 10^{-15} \text{ cm}^3 \text{ s}^{-1}$, $w_1^{imp} = 431 \text{ s}^{-1}$, $w_2^{imp} = w_2^{imp'} = 2360 \text{ s}^{-1}$ (impurities of the first type). The probabilities for transfer to aleatory impurities w_i^{imp} , are calculated with Eq. (2) knowing $T_1 = 1710 \text{ } \mu\text{s}$ and $T_2 = 81 \text{ } \mu\text{s}$. The three theoretical curves differ only by the pump intensities: $N_{50} = 9.6 \times 10^{18} \text{ cm}^{-3}$ (Fig. 3, curve (a)), $N_{50} = 2.0 \times 10^{19} \text{ cm}^{-3}$ (Fig. 3, curve (b)), $N_{50} = 3.0 \times 10^{19} \text{ cm}^{-3}$ (Fig. 3, curve (c)). We note a very good agreement between the experiment (Fig. 2) and theory (Fig. 3). Taking into account the small experimental non-exponentialities (the scale in Fig. 2 is very expanded in the vertical direction), we can consider that the rate equation system (1) offers a very good description of the experiment. Moreover, our analysis shows that the agreement between experiment and theory is very sensitive to the values of the up-conversion rates ω_{11} , ω_{22} , and to the contribution of the aleatory impurities (w_i^{imp}), but less sensitive to the values of the radiative transition probabilities a_{ij} . This can be explained by the inequality $w_{ij} \gg a_{ij}$, characteristic for crystals with very active phonons. Therefore, for Er: YAG crystals, the approximations inherent to Judd-Ofelt theory are not critical.

We measured the kinetics of the $^4I_{11/2}$ decay for three Er: YAG crystals. The resulting energy transfer parameters are presented in Tab.2.

Tab. 2. Energy transfer rates for three Er: YAG crystals

Er concentration (at. %)	40	50	60	Reference
$\omega_{11} (\text{cm}^3 \text{ s}^{-1})$	8.5×10^{-16}	1.3×10^{-15}	2.0×10^{-15}	[6]
$\omega_{22} (\text{cm}^3 \text{ s}^{-1})$	8.5×10^{-16}	1.2×10^{-15}	1.8×10^{-15}	This work
$\omega_{50} (\text{cm}^3 \text{ s}^{-1})$	8.8×10^{-16}	1.1×10^{-16}	1.3×10^{-15}	[20]

Both ω_{11} and ω_{22} increase monotonically with erbium concentration, but a slow decrease of the ratio $\omega_{22} / \omega_{11}$ could be noted. Thus, for the 60 % sample, the ratio $\omega_{22} / \omega_{11} \approx 0.9$, as for ErAG¹⁶. For lower concentrations, this ratio becomes higher: 0.92 for the 50 % sample and 1 for the 40 % one. Nevertheless, a noticeable discrepancy between the ratio of the up-conversion rates $\omega_{22} / \omega_{11}$ obtained in this paper and the value $\omega_{22} / \omega_{11} \sim 3$, obtained previously³, is observed. In order to explain this discrepancy, we note the difference in the pumping conditions. Thus, in the present paper, the pumping was performed in $^4S_{3/2}$, while, in Ref. 3, the pumping took place in $^4F_{9/2}$. Due to the low population of the $^4F_{9/2}$ in the present pumping conditions, when almost all the excitation from the pumping level is transferred by the very effective cross-relaxation ($^4S_{3/2} \rightarrow ^4I_{9/2}$) + ($^4I_{15/2} \rightarrow ^4I_{13/2}$) (Fig. 1 c) to the level $^4I_{9/2}$, the contribution of the energy transfer processes involving the $^4F_{9/2}$ level can be neglected. The situation could be qualitatively different for direct pumping in $^4F_{9/2}$. Besides, the concentration ranges for the Er: YAG crystals pumped in $^4S_{3/2}$ and $^4F_{9/2}$ do not overlap. While a systematic study concerning the concentration dependence of the up-conversion rate ω_{11} in Er: YAG crystals was published some years ago⁶, until now, no such study was devoted to the concentration dependence of ω_{22} . Unfortunately, due to the low absorption cross-section of the Er: YAG crystal at 532 nm (approximately $7 \times 10^{-22} \text{ cm}^2$ – our measurements), in order to put into evidence the up-conversion process ω_{22} , it is very difficult to achieve enough population in $^4S_{3/2}$ for lower erbium concentrations. The simply increase of the pump densities at 532 nm could result in the sample destruction. To overcome this difficulty, a dye laser, tuned on an absorption line belonging to the $^4I_{15/2} \rightarrow ^4S_{3/2}$ ($^2H_{11/2}$) transition should be used.

4. CONCLUSIONS

In this paper we presented a method for determination of the rates of the two-ion up-conversion processes, governing the three-micron emission in concentrated, erbium doped, laser crystals. The luminescence of the erbium levels was excited, at room temperature, with the second harmonic of the Nd: YAG laser. In the frame of this method, the luminescence of only one metastable level, namely $^4I_{11/2}$, was monitored. The change of the kinetics of the $^4I_{11/2}$ level, for various pumping energies, was analyzed. The entire family of decays (the only variable parameter being the pump energy) was described with the same set of material parameters. The possibility to describe an entire family of decays with a single set of material parameters could be considered a criterion for the rate equation model adequacy as well as for the experimental accuracy. The method was successfully applied to three Er: YAG crystals.

REFERENCES

1. V. I. Zhekov, V. A. Lobachev, T. M. Murina, and A. M. Prokhorov, "Efficient cross-relaxation laser emitting at 2.94 μm ," *Kvant. Elektron.*, **10**, pp. 1871-1874, 1983.
2. Kh. S. Bagdasarov, V. I. Zhekov, V. A. Lobachev, A. A. Manenkov, T. M. Murina, and A. M. Prokhorov, "Cross-relaxation YAG: Er laser," *Izv. ANSSSR, Ser. Phys.*, **48**, pp. 1765-1769, 1984.
3. V. I. Zhekov, T. M. Murina, A. M. Prokhorov, M. I. Studenikin, S. Georgescu, V. Lupei, I. Ursu, "Cooperative processes in $\text{Y}_3\text{Al}_5\text{O}_{12}$: Er^{3+} crystals," *Sov. J. Quantum Electron.*, **16**, pp. 274-275, 1986.
4. S. A. Pollack, D. B. Chang, and N. L. Moise, "Continuous wave and Q-switched infrared erbium laser," *Appl. Phys. Lett.*, **49**, pp. 1578-1580, 1986.
5. M. Pollnau, Th. Graf, J. E. Balmer, W. Lüthy, and H. P. Weber, "Explanation of the cw operation of the Er^{3+} 3- μm crystal laser," *Phys. Rev. A*, **49**, pp. 3990-3996, 1994.
6. S. Georgescu, V. Lupei, A. Lupei, V. I. Zhekov, T. M. Murina, and M. I. Studenikin, "Concentration effects on the up-conversion from $^4\text{I}_{11/2}$ level of Er^{3+} in YAG," *Optics Commun.*, **81**, pp. 186-192, 1991.
7. W. Lüthy and H. P. Weber, "The 3 μm erbium laser," *Infrared Phys.*, **32**, pp. 283-290, 1991.
8. J. Breguet, A. F. Umiskov, S. G. Semenov, W. Lüthy, H. P. Weber, and I. A. Shcherbakov, "Comparison of threshold energy of selectively excited YAlO_3 : Er and YAG: Er laser," *IEEE J. Quantum Electron.*, **28**, pp. 2563-2570, 1992.
9. D. J. Simkin, J. A. Konigstein, P. Myslinski, S. A. Boothroyd, and J. Chrostowski, "Upconversion dynamics of Er^{3+} : YAlO_3 ," *J. Appl. Phys.*, **73**, pp. 8046-8049, 1993.
10. M. A. Noginov, S. G. Semenov, V. A. Smirnov, and I. A. Shcherbakov, "Effect of interaction between excited erbium ions on the formation of inverse population on the $^4\text{I}_{11/2} \rightarrow ^4\text{I}_{13/2}$ transition in YSGG: Cr^{3+} , Er^{3+} crystal under stationary excitation," *Optika i Spektrosk.*, **69**, pp. 120-127, 1990.
11. V. Lupei, S. Georgescu, and V. Florea, "On the dynamics of population inversion for 3 μm Er^{3+} lasers," *IEEE J. Quantum Electron.*, **29**, pp. 426-434, 1993.
12. H. Chou and H. P. Jensen, "Upconversion processes in Er-activated solid state laser materials," *Tunable Solid State Lasers, OSA*, **5**, pp. 167-174, 1989.
13. S. Georgescu, T. J. Glynn, R. Sherlock, and V. Lupei, "Concentration quenching of the $^4\text{I}_{9/2}$ level of Er^{3+} in laser crystals," *Optics Commun.*, **106**, pp. 75-78, 1994.
14. S. Georgescu, V. Lupei, T. J. Glynn, and R. Sherlock, "Spectroscopic determination of the figures of merit for 3 μm Er^{3+} lasers," *J. Lumin.*, **60&61**, pp. 241-244, 1994.
15. B. R. Judd, "Optical absorption intensities of rare-earth ions," *Phys. Rev.*, **127**, pp. 750-761, 1962.
16. G. S. Ofelt, "Intensities of crystal spectra of rare-earth ions," *J. Chem. Phys.*, **37**, pp. 511-520, 1962.
17. S. Georgescu, V. Lupei, M. Trifan, T. J. Glynn, and R. Sherlock, "Population dynamics of three-micron emitting level of Er^{3+} in YAlO_3 ," *J. Appl. Phys.*, **80**, pp. 6610-6613, 1996.
18. S. Georgescu, V. Lupei, T. J. Glynn, and R. Sherlock, "Intensity pump effects in the kinetics of $^4\text{I}_{11/2}$ level in ErAG ," *Optics Commun.*, **155**, pp. 61-67, 1998.
19. S. Georgescu, C. Ionescu, I. Voicu, and V. I. Zhekov, "A modified Judd-Ofelt analysis of Er^{3+} in YAG," *Rev. Roum. Phys.*, **30**, pp. 265-276 (1985).
20. V. I. Zhekov, T. M. Murina, A. M. Prokhorov, M. I. Studenikin, S. Georgescu, A. Lupei, and V. Lupei, "Nonradiative transfer of excitation energy in crystals with the interaction of three-optically active centers," *JETP Lett.*, **52**, pp. 670-674, 1990.

1D algorithm for automatic fringe spacing measurement in a straight equispaced parallel fringe pattern

Victor Nascov*, Adrian Dobroiu, Dan Apostol, Victor Damian

National Institute for Laser, Plasma and Radiation Physics

PO Box MG-36, R-76900 Bucharest, Romania

ABSTRACT

Wavelength measurement is a critical topic in many applications. Stationary interferometers, such as Fizeau and Murty, can be successfully used, considering the proportionality between the wavelength and the fringe spacing in the interference pattern. In this work we present a one-dimensional algorithm for the calculation of the fringe spacing and error sources. The final accuracy that can be achieved is also assessed. The experimental data are taken from fringe patterns recorded with a Murty interferometer.

Keywords: Murty interferometer, fringe pattern, wavelength measurements, least squares methods

1. INTRODUCTION

One technique of measuring the wavelength consists in the comparison of the fringe spacings of two intensity recordings, of which one is obtained using a reference wavelength (from a stabilized He-Ne laser for instance) and the other with the unknown light.

Such a technique uses the Murty interferometer^{1,2} (figure 1), which has the advantages of extreme simplicity, mechanical and thermal stability. It consists in a simple plane-parallel glass plate. When illuminated with a spherical wave under an arbitrary angle, two sheared waves are reflected and a pattern of approximately straight equispaced parallel fringes appears. Transmission fringes are visible too, but with much less contrast, as while the amplitudes of the first two interfering waves are nearly equal in reflection, they have very different magnitudes in transmission. If quartz is used instead of glass, the wavelength precision is increased by a better thermal stability.

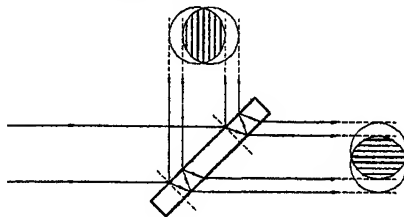


Fig. 1 The Murty interferometer

2. THEORY OF THE MURTY INTERFEROMETER

The lateral shear induced by the Murty interferometer on both transmitted and reflected beams is:

$$s = \frac{e \cdot \sin 2\alpha}{\sqrt{n^2 - \sin^2 \alpha}} \quad (1)$$

where n is the refraction index of the glass plate, e is its thickness and α is the incidence angle of the light beam on the plate.

* Correspondence: E-mail: vnascov@ifin.nipne.ro

Let us analyze the fringe map produced in a plane oriented perpendicularly on the emerging doubled beams. The laser light, emitted in the TEM₀₀ mode is focused on and spatially filtered by a 10-μm pin-hole so that a spherical wavefront is obtained, which is described by the following complex amplitude:

$$u(x, y, z) = A(x, y, z) \cdot e^{i\varphi(x, y, z)}, \quad \varphi(x, y, z) = \frac{2\pi}{\lambda} \cdot \sqrt{x^2 + y^2 + z^2} \quad (2)$$

The coordinate system we used has its origin in the curvature center of the spherical wavefront. The function $A(x, y, z)$ has a slow variation in the region of space where we analyze the interference phenomena, so that we will not detail its explicit form. Only the phase function $\varphi(x, y, z)$ is relevant and we will develop it in a Taylor series, valid at small angles from the propagation axis Oz, where we have $x, y \ll z$:

$$\varphi(x, y, z) = \frac{2\pi}{\lambda} \cdot z \cdot \left[1 + \frac{1}{2} \cdot \frac{x^2 + y^2}{z^2} - \frac{1}{8} \cdot \left(\frac{x^2 + y^2}{z^2} \right)^2 + \dots \right] \quad (3)$$

The first term is constant in a plane (x, y) and hence irrelevant. The second term is the parabolic approximation of the spherical shape of the wavefront, or the paraxial approximation, frequently used in optics. The third term measures the imprecision of the paraxial approximation, and we will take it into account. The following terms are too small to be considered at all.

The two beams obtained by splitting the incoming wavefront have, both in reflection and transmission, the same spherical shape, but different amplitudes. The general expression of the interference fringes in a plane (x, y) is

$$I(x, y) = I_1 + I_2 + 2 \cdot \sqrt{I_1 \cdot I_2} \cdot \cos \Phi(x, y) \quad (4)$$

where I_1 and I_2 are the intensities of the two interfering waves. The function $\Phi(x, y)$ is the phase shift between them:

$$\Phi(x, y) = \varphi_2(x, y) - \varphi_1(x, y) = \varphi(x + s, y) - \varphi(x, y) \quad (5)$$

and it has the following development in Taylor series:

$$\Phi(x, y) = \frac{\pi}{\lambda z} \cdot (2xs + s^2) - \frac{\pi}{4\lambda z^3} \cdot (4x^3s + 6x^2s^2 + 4xs^3 + 4xy^2s + 2y^2s^2 + s^4) + \dots \quad (6)$$

The fringe contrast is considerably better in reflection than in transmission, as the amplitudes of the interfering waves are much closer to each other.

The components of the fringes' spatial frequency along the axes x and y are

$$\nu_x(x, y) = \frac{1}{2\pi} \cdot \frac{\partial \Phi}{\partial x} = \frac{s}{\lambda z} - \frac{s}{2\lambda z^3} \cdot (3x^2 + 3xs + y^2 + s^2), \quad (7)$$

$$\nu_y(x, y) = \frac{1}{2\pi} \cdot \frac{\partial \Phi}{\partial y} = -\frac{s}{2\lambda z^3} \cdot (2xy + ys), \quad (8)$$

In a plane perpendicular to the axis Oz the fringes are parallel and equidistant, oriented normally to the axis Ox, on the condition of limiting ourselves to the paraxial approximation of the spherical wavefronts. In this level of approximation the spatial frequency has only one non-zero component:

$$\nu_x = \frac{s}{\lambda z}, \text{ so that the fringe spacing is } i_x = \frac{1}{\nu_x} = \frac{\lambda z}{s}. \quad (9)$$

We will further consider that the Murty interferometer produces straight parallel and equidistant fringes, but we will remember there is a deviation from this assumption and calculate it, in order to evaluate the accuracy to which the fringe spacing can be taken constant. The deviation of the fringe spacing from the value given by (9) is

$$\delta_x = -\frac{\delta v_x}{v_x^2} = \frac{\lambda}{2sz} \cdot (3x^2 + 3xs + y^2 + s^2). \quad (10)$$

In a small region of the fringe pattern the maximum deviation is negligible relative to the available measurement accuracy of the fringe spacing, as we will see from the numerical results presented in section 4.

3. THE ALGORITHM

The following connection exists between the wavelength and the fringe spacing^{3,5}:

$$\lambda = i_x \cdot \frac{s}{z}, \text{ and compared to the reference wavelength } \lambda = \lambda_0 \cdot \frac{i_x}{i_{x0}}. \quad (11)$$

Our work deals with the process of determining the fringe spacing in a digitally recorded fringe pattern. The accuracy of wavelength measurement is sustained by the accuracy of measuring the fringe spacing.

We already established that the fringes are approximately straight, parallel, and equidistant. Along any direction in the viewing plane, determined by the CCD orientation, the fringe intensity profile is given by:

$$I(x) = I_0 + I_1 \cdot \cos(2\pi vx + \varphi) \quad (12)$$

where I_0 is the background uniform intensity, I_1 is the magnitude of the sinusoidal oscillation, v is the fringe spatial frequency, and φ is the initial phase of this periodic distribution.

The image is recorded digitally and it consists of a map of pixels with quantized intensities having a periodic evolution of the form (12), but also affected by a random noise. In figure 2 we present such an image, acquired with a CCD camera. The function $I(x)$ depends on four parameters (I_0 , I_1 , v , φ) which will be determined by processing an array of pixels using the algorithm described further in the paper. Instead of a two-dimensional image the acquisition of a one-dimensional array of pixels (with a CCD line) is sufficient, as our problem was reduced to the 1D case.

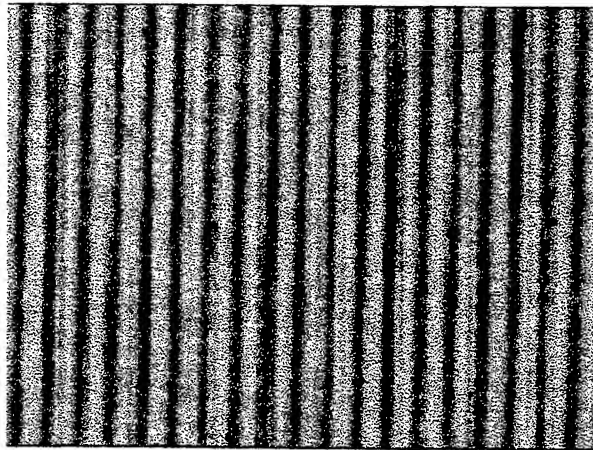


Fig. 2 Fringe pattern obtained with a Murty interferometer

The four parameters are statistical quantities that lead to the specific function $I(x)$ that best approximates the experimental data. The method of maximum plausibility is used, widely applied to processing physical data, with well-known calculation methods adapted to different cases frequently encountered, but given the non-linearity and the harmonicity of the function $I(x)$, the solutions (I_0 , I_1 , v , φ) are determined by using an iterative procedure described in the appendix, which starts with an initial approximation of the parameters.

The first approximation of the parameters (I_0 , I_1 , v , φ) can be obtained by applying a Fourier transform to the experimental data (the fringe pattern) and preserving the first order harmonic term. The Fourier spectrum gives the spatial

frequency ν with a relative accuracy of $1/N_f$, where N_f is the number of fringes in the array. The accuracy of the values in this stage is not vital for the algorithm to work properly.

The approximate values are introduced in the iterative algorithm described in the appendix which has a rapid quadratic convergence, and supplies the final solution with a greatly increased accuracy. At each iteration undergone by the parameters, linear approximations of the function $I(x)$ developed in Taylor series is used around the four parameters obtained in the preceding iteration. The theorem of error propagation allows the calculation of the statistical errors that affect the final results.

4. EXPERIMENTAL RESULTS AND DATA PROCESSING

We obtained the interference pattern using the set-up illustrated in figure 1. The laser source is a frequency stabilized He-Ne laser, at $\lambda = 633$ nm and $P = 0.5$ mW. The glass plate has the thickness $e = 4$ mm and the refraction index $n = 1.5$. When the angle of incidence $\alpha = 45^\circ$ the lateral shear is $s = 3$ mm. The fringe image is acquired at a distance $z = 2$ m with a digital camera having the resolution of 384×288 pixels which uses a CCD array with the dimensions of approximately 4×3 mm. The fringe spacing, calculated with equation (9) is around 0.2 mm. From the formula (10) it can be calculated that over the image area the relative deviation of the fringe spacing is less than 10^{-6} , so that in principle the accuracy of the wavelength measurement is limited to this value.

An array of $N = 384$ pixels is extracted from the image and processed. For this purpose it would be more appropriate to use a CCD line, with considerable more pixels, conveniently oriented, not necessarily on a perpendicular direction relative to the fringes.

The fringe spacing is determined by following these steps:

An initial approximation of the four parameters (I_0 , I_1 , ν , ϕ) is obtained by analyzing the Fourier transform of the intensity profile thus recorded, achieving an accuracy level of $1/N_f$ for the parameter ν (for $N_f = 19$ fringes the relative accuracy is found to be 5% both for the measurement of fringe spacing and the wavelength).

The algorithm then iteratively improves the parameters (I_0 , I_1 , ν , ϕ). Taking advantage of the rapid convergence a number of 5 or 6 iterations is enough for the maximum computation accuracy (in double precision representation) to be reached, largely exceeding the maximum accuracy allowed by the measurement method, so that the computer calculation does not add to the inherent uncertainty.

Figure 3 shows on the same graph the intensities in a 1D-array taken from the image, and the sinusoidal curve that fits these experimental values.

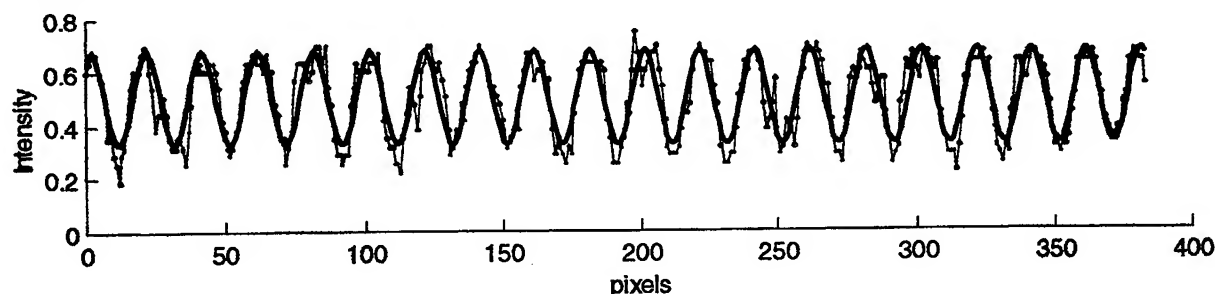


Fig. 3 Intensity profile of the fringe pattern; values taken from the image and fitted.

The algorithm also provides the statistical errors that affect the final results, using the well-known error propagation theorem. The least affected by statistical errors are the parameters ν and ϕ , which are exactly the most important quantities to be measured. The relative error in calculating the fringe spacing and the wavelength is 10^{-4} , but it should be emphasized that better results can be achieved if instead the low resolution CCD matrix one used a CCD line with a few thousand pixels.

5. APPENDIX

Least squares method for linear functions

Let Y be a set of experimental results, measured with mean square deviations σ_Y^2 to which a set of variables X is associated.

Y is an N -element column vector, and X is an N -line \times r -column matrix that contains the values of independent variables, considered unaffected by any measurement errors. A is an r -element column vector, containing the coefficients of the functional relationship between X and Y that have to be determined.

$$Y = \begin{bmatrix} y_1 \\ \vdots \\ y_N \end{bmatrix} \quad X = \begin{bmatrix} x_{11} & \cdots & x_{1r} \\ \vdots & \cdots & \vdots \\ x_{N1} & \cdots & x_{Nr} \end{bmatrix} \quad A = \begin{bmatrix} a_1 \\ \vdots \\ a_r \end{bmatrix} \quad (A1)$$

In a general case σ_Y^2 is the covariation matrix of the values Y , having the dimension $N \times N$ and contains the mean square deviations on the main diagonal while the other elements are the covariations between the various variables y_i . In most practical situations all the values Y are measured with the same accuracy and are independent, so that the quantity σ_Y^2 becomes a scalar. Instead of the quantity σ_Y^2 we will use another quantity, called weight, defined by:

$$P_Y = (\sigma_Y^2)^{-1} \quad (A2)$$

We suppose that there is a linear relationship between the quantities X and Y of the form:

$$Y = X \cdot A \quad (A3)$$

Due to fluctuations of the quantity Y this relationship cannot be exactly fulfilled. Then it becomes necessary that a linear function be found, $f(X) = X \cdot A$, which best approximates the experimental data. Based on the assumption that the fluctuations of the quantity Y are normally distributed, the coefficients A are determined using the least squares fitting method, developed as follows.

We build the scalar function $\chi^2(A)$ which represents the sum of the squared normed deviations of the function $f(X)$ from the experimental data Y :

$$\chi^2(A) = \varepsilon^T \cdot P_Y \cdot \varepsilon \quad \varepsilon = f(X) - Y = X \cdot A - Y \quad (A4)$$

The symbol T represents the operation of matrix transposition. According to the maximum plausibility principle, the function $f(X)$ that best fits the values Y is that for which the function $\chi^2(A)$ reaches its minimum. The values of the parameters A for which the function $\chi^2(A)$ is minimum are obtained by solving an equation system consisting of r linear equations established by equaling to zero the partial derivatives of the function $\chi^2(A)$ relative to each of the parameters A . This is called the "normal equation system":

$$\frac{\partial(\chi^2)}{\partial A} = X^T \cdot (P_Y^T + P_Y) \cdot (X \cdot A - Y) = 0 \Rightarrow [X^T \cdot (P_Y^T + P_Y) \cdot X] \cdot A = [X^T \cdot (P_Y^T + P_Y)] \cdot Y \quad (A5)$$

The solution of this system is:

$$A = B \cdot Y \quad B = [X^T \cdot (P_Y^T + P_Y) \cdot X]^{-1} \cdot [X^T \cdot (P_Y^T + P_Y)] \quad (A6)$$

Using the error propagation theorem we obtain the covariation matrix of these determined parameters, that contains on the main diagonal their square mean deviations:

$$\sigma_A^2 = B \cdot \sigma_Y^2 \cdot B^T \quad (A7)$$

Least squares method for non-linear functions

In this case we search a non-linear dependence between X and Y of the form:

$$Y = f(X, A) \quad (\text{A8})$$

in which the function $f(X, A)$ has a known behavior, but depends on the set of parameters A . It is again obvious that the relationship (A8) will not be exactly fulfilled, but instead we will find the best possible approximation, in the sense of minimizing the function $\chi^2(A)$.

The normal equations for determining the set of parameters A are generally non-linear. They cannot be always solved analytically, and the numerical solving can often prove difficult. The problem can be tackled iteratively, as shown further.

We start from an arbitrary initial approximation A_0 of the parameter set A , obtained by some method or other, with an arbitrary accuracy. The non-linear function $f(X, A)$ is developed as a Taylor series around the values A_0 and the linear term is saved:

$$f(X, A) = f(X, A_0) + D \cdot (A - A_0)$$

$$D = \frac{\partial f(X, A_0)}{\partial A} = \begin{bmatrix} \frac{\partial f(x_{11}, \dots, x_{1r}; A_0)}{\partial a_1} & \dots & \frac{\partial f(x_{11}, \dots, x_{1r}; A_0)}{\partial a_r} \\ \vdots & & \vdots \\ \frac{\partial f(x_{N1}, \dots, x_{Nr}; A_0)}{\partial a_1} & \dots & \frac{\partial f(x_{N1}, \dots, x_{Nr}; A_0)}{\partial a_r} \end{bmatrix} \quad (\text{A9})$$

The N -element vector that contains the deviations of the function $f(X, A)$ from the experimental values Y is

$$\varepsilon = f(X, A) - Y = \varepsilon_0 + D \cdot \varepsilon_A, \quad \varepsilon_0 = f(X, A_0) - Y, \quad \varepsilon_A = A - A_0 \quad (\text{A10})$$

The relationship A(10) is linear, just like equation (A3). For this reason the corrections ε_A of the zero-order approximation A_0 are determined by the same algorithm that was previously described in the case of the linear dependence between X and Y .

Similarly we can define a scalar function $\chi^2(\varepsilon_A)$:

$$\chi^2(\varepsilon_A) = \varepsilon^T \cdot P_Y \cdot \varepsilon = (\varepsilon_0 + D \cdot \varepsilon_A)^T \cdot P_Y \cdot (\varepsilon_0 + D \cdot \varepsilon_A) \quad (\text{A11})$$

and the normal equation system is:

$$\frac{\partial(\chi^2)}{\partial \varepsilon_A} = D^T \cdot (P_Y^T + P_Y) \cdot (\varepsilon_0 + D \cdot \varepsilon_A) = 0 \Rightarrow [D^T \cdot (P_Y^T + P_Y) \cdot D] \cdot \varepsilon_A = -[D^T \cdot (P_Y^T + P_Y)] \cdot \varepsilon_0 \quad (\text{A12})$$

The solution of this system is:

$$\varepsilon_A = B \cdot \varepsilon_0 \quad B = -[D^T \cdot (P_Y^T + P_Y) \cdot D]^{-1} \cdot [D^T \cdot (P_Y^T + P_Y)] \quad A = A_0 + \varepsilon_A \quad (\text{A13})$$

The result A thus obtained is input for a new iteration instead of the zero-order approximation A_0 and the procedure is repeated until the difference between the results of two successive iterations becomes negligible. As a general rule the algorithm has a rapid quadratic convergence, but not necessarily.

After the final result was obtained with sufficient accuracy, its mean square deviations are calculated using the same formula as in the linear case, (A7).

The basic idea of this algorithm consists in the fact that the function χ^2 which depends on the set A of r parameters has an approximately r -dimensional quadratic shape around A_0 (no matter if the function $f(X, A)$ is linear or not) and its minimum can be determined as a solution of a linear equation system. In the non-linear case, the result obtained after each

iteration progressively draws near the solution, except in some inappropriate singularity cases, when the convergence is not attained. It is remarkable that all the operations described for this algorithm are achieved by linear algebra.

REFERENCES

1. K.R.V. Murty, "Use of a single Plane Parallel Plate as a Lateral Shearing Interferometer with a Visible Gas Laser Source", *Applied Optics*, **3**, p. 531, 1964
2. D. Apostol, I. Apostol, and I. N. Mihilescu, "An Infrared Lateral Shearing Interferometer for Plasma Diagnostic and Infrared Optical Components Testing", *Infrared Physics*, **16**, p. 269, 1976
3. D. Apostol and V. Damian, "On a Fizeau refractometer", *St. Cerc. Fiz.* **1**, p. 97, 1989
4. D. W. Robinson, "Automatic fringe analysis with a computer image-processing system", *Applied Optics*, **14**, p. 2169, 1983
5. D. W. Robinson and G. T. Reid, *Interferogram Analysis*, Institute of Physics Publishing, Bristol and Philadelphia, 1993

Study on ultrashort pulse generation and subharmonic bifurcation in directly modulated MQW lasers

M. Guina*, M. Dumitrescu

Optoelectronics Research Centre, Tampere University of Technology,
P.O. Box 692, Tampere, Finland

ABSTRACT

This paper investigates the generation of ultra-short optical pulses from directly modulated multiple-quantum-well (MQW) laser diodes. The ultra-short pulse generation is simulated using the rate equations' model. The effects of the input signal parameters (bias current value and RF current amplitude and frequency) on the duration and magnitude of the pulses are examined from simulations. Particular interest is paid to the influence of spontaneous emission factor on the chaotic laser behavior. The study is focused on improving the understanding of how the phenomenological laser parameters influence the nonlinear dynamics and on establishing the connections between the modulation signal parameters and the nonlinear dynamic behavior. The numerical simulations carried out for different laser structures show good agreement with previously reported results and demonstrate period bifurcation and chaos for some ranges of the bias current and modulation index.

Keywords: semiconductor lasers, large signal modulation, nonlinear behavior, pulse generation, period bifurcation, chaos, simulation.

1. INTRODUCTION

Multiple-quantum-well (MQW) laser diodes are widely used in high-speed optical communication systems due to their superior performances over bulk lasers diodes (higher modulation bandwidth, lower threshold current). Sustained research was aimed at improving the small-signal modulation response of MQW lasers (a bandwidth over 30 GHz was reported¹). Compared with small-signal operation the large-signal direct modulation of semiconductor lasers comes as an important technique for high bit-rate optical fiber communication using ultra-short optical pulses.

Many papers²⁻⁶ indicate that large signal modulation might lead to various irregular behaviors like resonance frequency shift, period doubling, period tripling, period quadrupling and chaos. Despite these indications little work was reported on studying the nonlinear dynamics of MQW. Since directly modulated semiconductor lasers are routinely used for optical communication, it is important to evaluate how the system features might be affected by the possible chaotic behavior. Some previous work on nonlinear effects in semiconductor lasers was focused on lasers with bulk structures but very interesting results have been presented recently⁵ for MQW structures. The main system parameters used in previously nonlinear analysis are the modulation index and the resonance frequency to modulation frequency ratio.

Our work investigates the influence of the drive current (bias + modulation) on pulse generation and related nonlinear phenomena in order to find out the input signal parameters' ranges keeping the laser safe away from undesired nonlinear effects (period bifurcation and chaos). Both the resonance frequency blue-shift with increased bias current and the resonance frequency red-shift with increased RF signal amplitude are considered. After describing the theoretical model used some ultra-short pulse generation numerical simulations are presented. Conditions for period bifurcation and chaos are investigated in certain ranges of bias current, modulation amplitude and spontaneous emission factor.

2. PULSE GENERATION BY LARGE SIGNAL MODULATION

The dynamics of laser diodes may be described in terms of a three-rate equation model ⁷:

$$\frac{dN_c}{dt} = \frac{I}{qV_{act}} - \frac{N_c}{\tau_c} + \frac{N_w}{\tau_{esc}} \quad (1)$$

* Correspondence: Mircea.Guina%ORC@semi.ee.tut.fi

$$\frac{dN_w}{dt} = \frac{N_c}{\tau_c} - \frac{N_w}{\tau_{esc}} - \frac{N_w}{\tau_{nr}} - \frac{N_w}{\tau_n} - v_g g_0 \frac{N_w - N_0}{1 + \epsilon S} S \quad (2)$$

$$\frac{dS}{dt} = \Gamma v_g g_0 \frac{N_w - N_0}{1 + \epsilon S} S - \frac{S}{\tau_p} + \beta_{sp} \frac{N_w}{\tau_n}, \quad (3)$$

where N_w represents carrier density in quantum-well, N_c represents carrier density in confinement region, S is photon density, I is the injected current into the active volume V_{act} , τ_c is the capture time in the QW region, τ_{esc} is the escape time out of QW, τ_{nr} is the non-radiative recombination lifetime in the quantum-well active area, τ_n is the bimolecular recombination lifetime, τ_p is the photon lifetime, v_g is the optical mode velocity, g_0 is differential gain factor, ϵ is the nonlinear gain compression factor, Γ is the confinement factor and β_{sp} is the spontaneous emission feedback factor into the lasing mode. The nonradiative and spontaneous recombination times are given by :

$$\frac{1}{\tau_{nr}} = A + C N_w^2 \quad (4)$$

$$\frac{1}{\tau_n} = B N_w \quad (5)$$

where A, B, C are recombination coefficients depending on material quality and device structure.

Equations (1)-(3) were numerically solved using typical parameters for a MQW DFB laser structure⁵. The values of the parameters involved in model are presented in Table 1.

Tab. 1 Intrinsic MQW laser parameters used in simulation

Parameter	Value
V_{act}	$1 \times 10^{-17} \text{ m}^3$
Γ	0.2
τ_c	$2 \times 10^{-12} \text{ s}$
τ_{esc}	$2 \times 10^{-10} \text{ s}$
τ_p	$1 \times 10^{-12} \text{ s}$
A	10^8 s^{-1}
B	$10^{-16} \text{ m}^3 \text{ s}^{-1}$
C	$3 \times 10^{-41} \text{ m}^6 \text{ s}^{-1}$
$g_0 = dg/dn$	$5 \times 10^{-20} \text{ m}^2$
ϵ	$2 \times 10^{-23} \text{ m}^3$
N_0	$2.41 \times 10^{24} \text{ m}^{-3}$
β_{sp}	5×10^{-5} – varying during simulation

In a direct current semiconductor laser modulation scheme the injection (drive) current consists of a dc bias current I_0 and a modulation current $I_m \sin(2\pi ft)$ where I_m is the modulation amplitude and f is the modulation frequency. The modulation index is defined as the ratio between signal amplitude and bias level: $m = I_m/I_0$.

The simulated optical output variations for different drive signal parameters are used to investigate ultra-short pulse generation.

2.1. Ultrashort pulse generation

For small-signal modulation little harmonic distortion occurs and the steady-state optical output is almost sinusoidal (Fig. 1a). Entering the large signal regime the device behavior becomes strongly nonlinear generating a sequence of pulses with repetition rate equal to the input frequency (Fig. 1b). Increasing further the modulation current amplitude produces ultra-short pulses with about 40 ps duration and increased amplitude.

Pulse bifurcation is another result of large signal modulation. For some modulation depth the output pulse waveforms successively doubles as seen in Fig. 1c and 1d. This is accompanied by a variation in the peak pulse amplitude referred as bifurcation. The period doubling effect can be explained by the following mechanism: as the RF magnitude is increased the resonance frequency (f_r) is shifted to lower frequencies. This resonance frequency shift stops at about half of the modulation frequency when the input power reaches a certain level. Period doubling occurs once f_r reaches half of the modulation frequency. Our simulations demonstrate also the existence of period tripling (three different peak amplitude values) and period quadrupling (four different peak amplitude values).

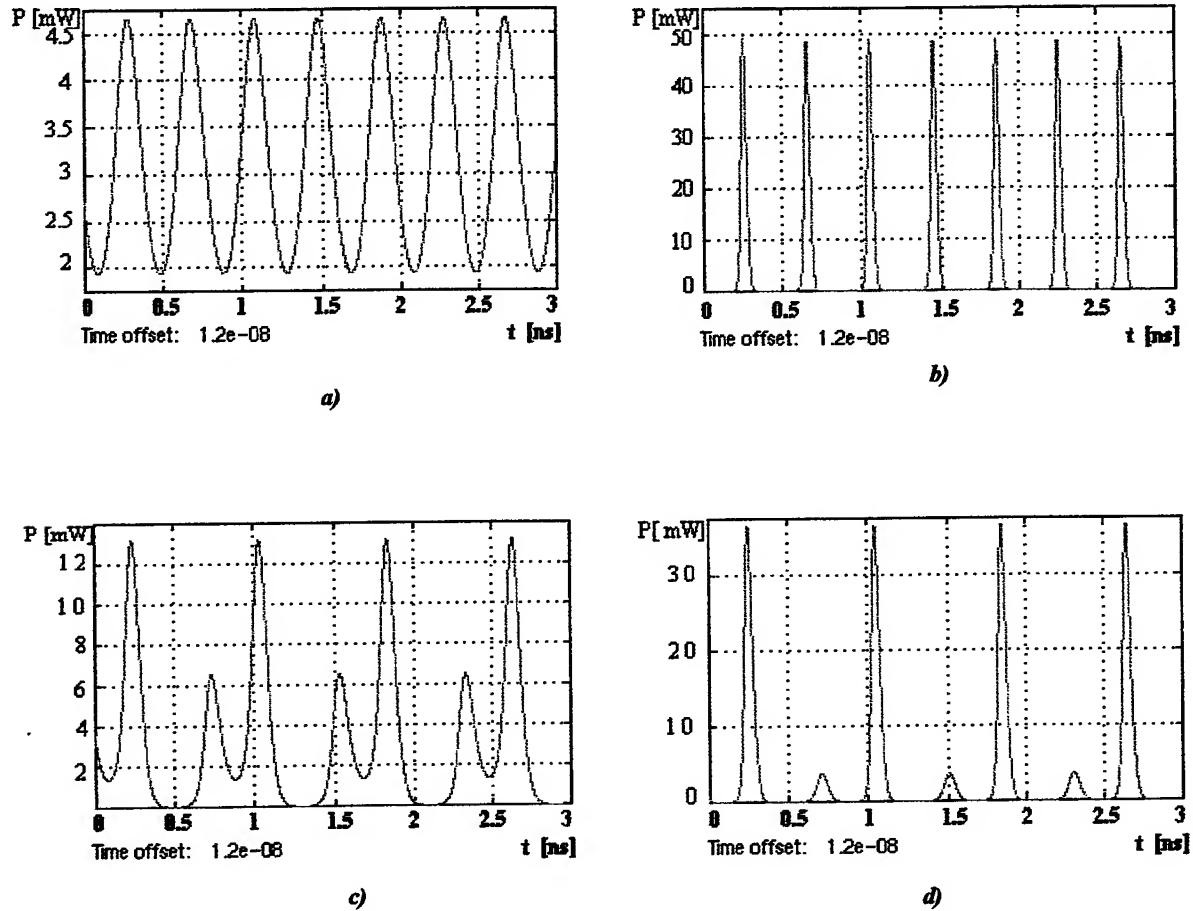


Fig. 1 Waveforms of optical power at various values of modulation index for an MQW laser diode with 6.8 mA threshold current. The bias current is 8 mA and the modulation frequency 2.5 GHz. The modulation current amplitude is : a) $I_{rf} = 0.5$ mA - small signal modulation; b) $I_{rf} = 32$ mA - 40 ps pulse generation at 2.5 GHz rate; c) $I_{rf} = 3$ mA; d) $I_{rf} = 8$ mA - period doubling effect

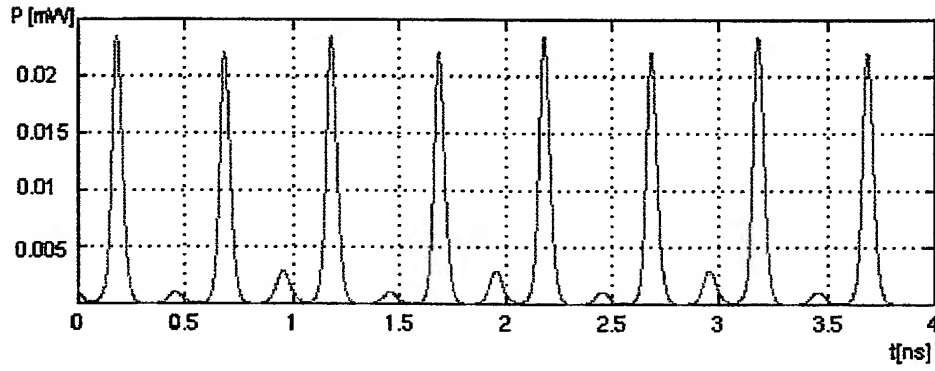


Fig. 2 Period quadrupling for a 8 mA bias current, 12 mA signal magnitude and 4 GHz modulation frequency

2.2. Influences of modulation index on bifurcation diagram

Peak values bifurcation diagram as a function of modulation index (m) is presented for a laser structure biased at 8 mA and modulated at 4 GHz (Fig. 3). The value used for the spontaneous emission factor was 5×10^{-5} . It can be observed that besides period doubling, which appears for a large range of m , period tripling and quadrupling appear for a smaller m domain.

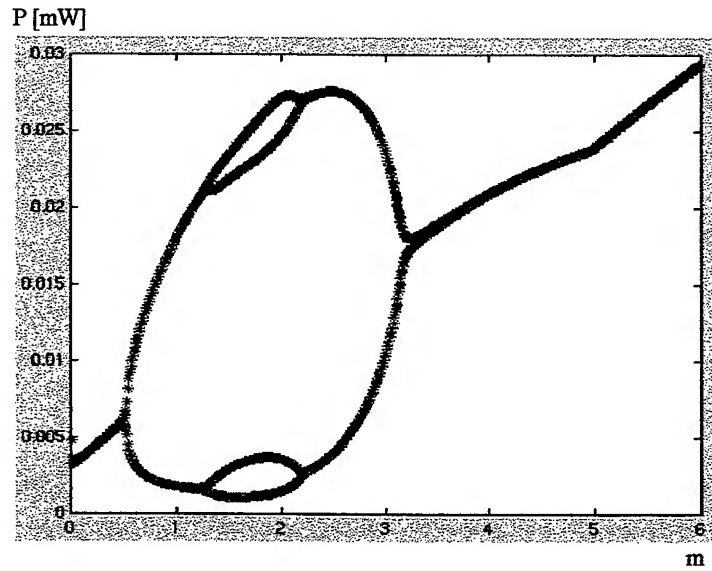


Fig. 3 Bifurcation diagram for 8 mA bias current, 4 GHz modulation frequency and $\beta=5 \times 10^{-5}$

2.3. Bias current influence on bifurcation diagram

In small-signal operation analysis the resonance frequency dependence upon bias current is given by :

$$f_r = \frac{1}{2\pi} \sqrt{\frac{\Gamma g_0 v_g (I - I_{th})}{q V_{act}}} \quad (6)$$

Some of our small-signal modulation simulation results for different values of the bias current are presented in Fig. 4. The resonance frequency shift toward high frequency can be easily observed when the bias current is increased.

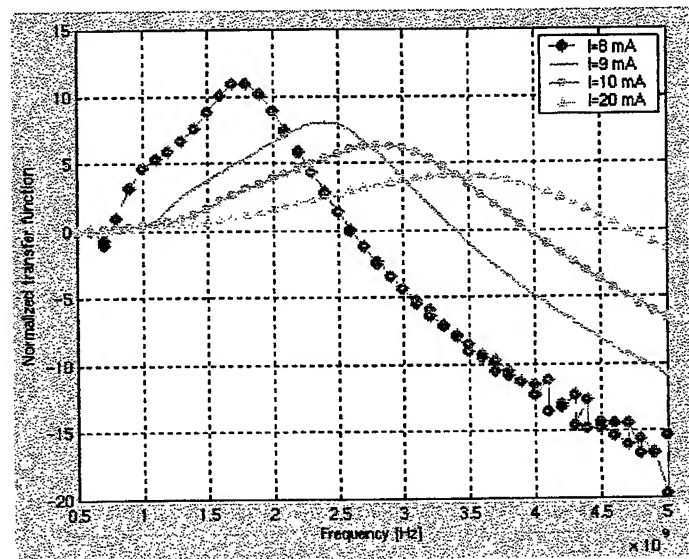


Fig. 4 Small-signal modulation response for different bias current

Due to this effect we are expecting to observe a change of bifurcation diagram (the resonance frequency to modulation frequency ratio is changed). This assumption is confirmed by the results presented in Figs. 5 and 6.

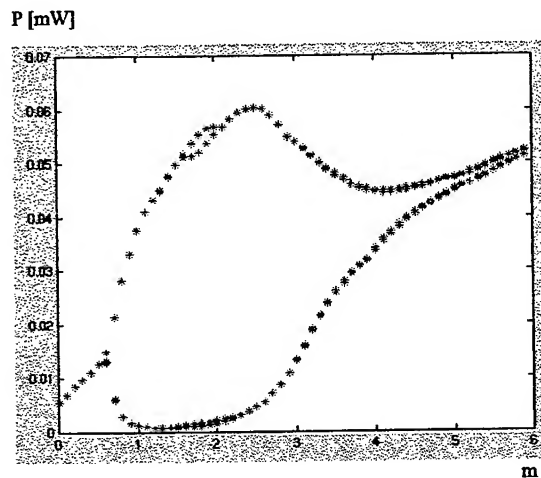


Fig. 5 Bifurcation diagram for 9 mA bias current, 4 GHz modulation frequency and $\beta = 5 \times 10^{-5}$

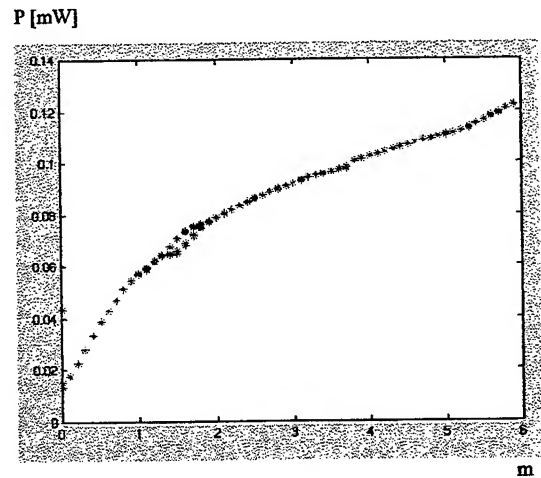


Fig. 6 Bifurcation diagram for 12 mA bias current, 4 GHz modulation frequency and $\beta = 5 \times 10^{-5}$

2.4. Influences of spontaneous emission factor on bifurcation diagram

It is known that the spontaneous emission reaction coupled into the lasing mode plays a large role in determining the nonlinear dynamics of laser diodes^{4,5}. Consequently we have also analyzed the bifurcation diagram for different β values. The simulation results for $\beta = 1 \times 10^{-5}$ (Fig. 7) and $\beta = 1 \times 10^{-4}$ (Fig. 8) shows that for a small spontaneous emission factor just period doubling occurs but for $\beta = 1 \times 10^{-4}$ chaotic behavior appears even at not very high modulation index.

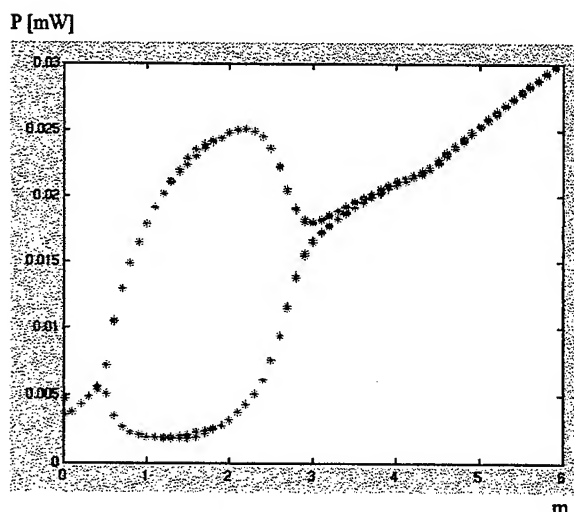


Fig. 7 Bifurcation diagram for 8 mA bias current, 4 GHz modulation frequency and $\beta=1 \times 10^{-5}$

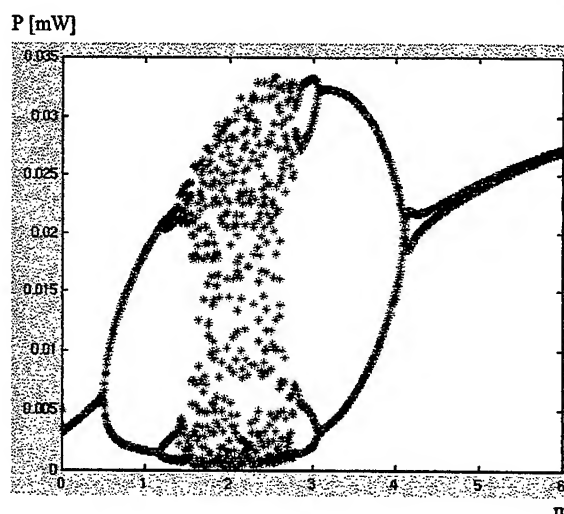


Fig. 8 Bifurcation diagram for 8 mA bias current, 4 GHz modulation frequency and $\beta=1 \times 10^{-4}$

These results make us to conclude that in direct modulation MQW laser systems the chaotic behavior can be avoided through a smaller spontaneous emission factor.

3. CONCLUSION

The generation of picosecond pulses by laser diode large signal direct modulation at microwave frequency has been investigated. The effect of modulation signal parameters (bias current and modulation index) on the pulse generation process has been established. Period doubling, period tripling, period quadrupling and chaos behavior was confirmed for certain values of the modulation signal and spontaneous emission factor. The undesired nonlinear effects can be avoided by choosing the proper values for the modulation parameters (modulation frequency, bias current).

ACKNOWLEDGEMENTS

This work was supported, in part, by a grant from the Centre for International Mobility Finland.

REFERENCES

1. J. D. Ralston, S. Weisser and K. Eisele, "Low-Bias-Current Direct Modulation up to 33 GHz in InGaAs/GaAs/AlGaAs Pseudomorphic MQW Ridge-Waveguide Lasers", *IEEE P.T.L.*, 16, No. 9, pp. 1076-1079, 1994.
2. L. Chang-Hee and Y. Tae-Hoo, "Period doubling and chaos in a directly modulated laser diode", *Appl. Phys. Lett.*, 46, pp. 95-97, 1985.
3. K. Y. H. Kao, "Virtual Hopf Precursor of Period-Doubling Route in Directly Modulated Semiconductor Lasers", *IEEE J. Q.E.*, 29, No. 6, pp. 1617-1623, 1993.
4. S.F. Yu, "Nonlinear Dynamics of Vertical-cavity Surface-Emitting Laser", *IEEE J.Q.E.*, 35, pp. 332-341, 1999.
5. S. Bennett, M. Christopher and S. Iezekiel, "Nonlinear Dynamics in Directly Modulated Multiple-Quantum-Well Laser Diodes", *IEEE J.Q.E.*, 33, No. 11, pp. 2077-2083, 1997.
6. R. Nagarajan, "Effects of Carrier Transport on Injection Efficiency and Wavelength Chirping in Quantum-Well Lasers", *IEEE J.Q.E.*, 29, No. 6, pp. 1601-1608, 1993.
7. H.F. Liu and W.F. Ngai, "Nonlinear Dynamics of Directly Modulated 1.55 μm InGaAsP Distributed Feedback Semiconductor Laser", *IEEE J.Q.E.*, 29, No. 6, pp. 1668-1675, 1993.

Metal grating efficiencies for Smith-Purcell Radiation in relativistic regime

F. Scarlat^{1*}, M. Facina¹, C. D. Dinca¹, V. Manu², A. Karabarbounis³,
C. Trikalinos³, E. Stiliaris³, I. Papadakis³

¹ National Institute for Laser, Plasma and Radiation Physics, Bucharest, 76.900, Romania.

² National Institute for Physics and Nuclear Engineering, Bucharest, 76.900, Romania.

³ University of Athens, Athens, Physics Department, 106.90 Athens, Greece

ABSTRACT

This paper presents the efficiency of Smith-Purcell (SP) radiation generation for lamellar and triangular metal gratings (MG) in H-polarization. The efficiency was calculated by the modal expansion method for lamellar MG and the improved point matching method for triangular MG, respectively. Most important MG parameters involved in the calculation were: the space period, the total number of grooves, the profile and the shape of the groove, and the geometry of the reflecting surface. Calculations were performed for relativistic electron beams (REB) with energies in 1 – 50 MeV domains. The emission angle of coherent SP radiation depending on MG and REB parameters is also presented.

Keywords: Metal grating efficiency, Smith-Purcell radiation

1. INTRODUCTION

An electron moving near a metal grating emits Smith-Purcell radiation. The relation below gives the wavelength of the SP photon:

$$\lambda = \frac{\lambda_g}{|n|} \cdot \left(\frac{1}{\beta} - \sin \eta \right), \quad (1)$$

in which $\beta = v/c$ is the ratio of the velocity v of electrons to the light velocity c in vacuum, λ_g is the metal grating period, n is the spectral order and η is the angle of observation in the (x, z) plane. The schematic layout of the SP effect geometry is presented in Fig. 1.

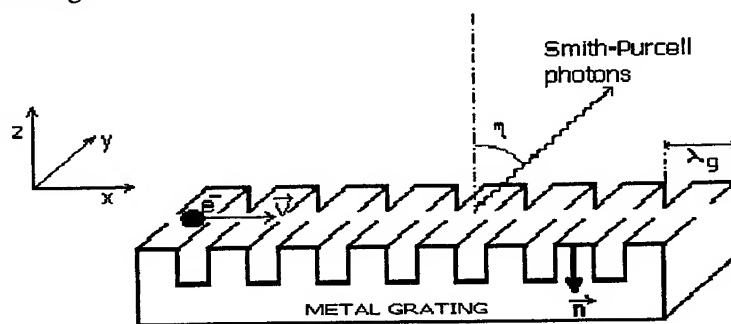


Fig. 1. The geometry of the configuration of Smith-Purcell experiment.

The electron moves in vacuum parallel to the surface of a grating with constant velocity $v = \vec{v} \cdot \vec{i}_x$ along the trajectory $y = 0$

* Correspondence: Email: scarlat@ifin.nipne.ro; Telephone: +40.01.780.42.90; Fax: +40.01.423.17.91

and $z = z_0 = \text{const.}$, where i_x, i_y, i_z are the unit vectors in the x, y, z directions, respectively. The top of the grating is in the (x, y) plane.

A brief review of the basic theory of metal grating coupled radiation and a summary of recent investigations of properties of the radiation produced by a relativistic electron beam is given in reference 1.

This paper presents the two-dimensional SP radiation calculation for metal gratings with rectangular and triangular profile in the H-polarization mode. The method of calculation for SP radiation is based on the Rayleigh expansion of Coulombian field of the electron. The metal grating surface is assumed to be perfect electrically conducting.

2. THE THEORY OF SMITH-PURCELL EFFECT

The electric field of the moving electron is described by a set of evanescent plane waves and the diffraction of these waves produces Smith-Purcell radiation. The total field above the metal grating is $E(x, y, z, t) = E^i + E^r$ and $H(x, y, z, t) = H^i + H^r$, where the index i comes from incident and r comes from reflected. Incident and reflected fields are expanded as Fourier integrals:

$$\begin{aligned} E^i(x, y, z, t) &= (2\pi^2)^{-1} \text{Re} \left[\int_0^\infty d\omega \int_{-\infty}^{+\infty} E^i(x, z; k_{0y}, \omega) \exp(ik_{0y}y - i\omega t) dk_{0y} \right], \\ H^i(x, y, z, t) &= (2\pi^2)^{-1} \text{Re} \left[\int_0^\infty d\omega \int_{-\infty}^{+\infty} H^i(x, z; k_{0y}, \omega) \exp(ik_{0y}y - i\omega t) dk_{0y} \right], \end{aligned} \quad (2)$$

in which $\omega = k_0 \cdot c$, with c the speed of light in vacuum and k_0 the wave vector with components (k_{0x}, k_{0y}, k_{0z}) . In equations (2), E^i and H^i represent the Fourier transforms of the field vectors. The reflected fields are also expanded as Fourier integrals in which the Fourier transforms E^r and H^r satisfy the source-free Maxwell equations:

$$\begin{aligned} (\nabla + ik_{0y}i_y) \times E^r - i\omega\mu_0 H^r &= 0, \\ (\nabla + ik_{0y}i_y) \times H^r + i\omega\epsilon_0 E^r &= 0, \end{aligned} \quad (3)$$

and a boundary condition at the grating surface:

$$\mathbf{n} \times (E^i + E^r) = 0, \quad (4)$$

in which \mathbf{n} is the unit vector normal to the surface, pointing inside the metal grating.

For the H-polarization case, where y components of the Fourier transform of field vectors $H_y \neq 0$ and $E_y = 0$, the Fourier component $H_y^r = H_y - H_y^i$ satisfies the Helmholtz equation:

$$\partial_x^2 H_y^r + \partial_z^2 H_y^r + (k_0^2 - k_{0y}^2) H_y^r = 0, \quad (5)$$

with the boundary condition $\mathbf{n} \cdot \nabla H_y = 0$ on the surface. The reflected field above the grating ($z > 0$) can be represented by a Rayleigh expansion which describes the field in terms of propagating and evanescent waves:

$$\begin{aligned} E_y^r(x, z; k_{0y}, \omega) &= \sum_{n=-\infty}^{+\infty} E_{y,n}^r(k_{0y}, \omega) \exp(ik_{x,n}x + ik_{z,n}z), \\ H_y^r(x, z; k_{0y}, \omega) &= \sum_{n=-\infty}^{+\infty} H_{y,n}^r(k_{0y}, \omega) \exp(ik_{x,n}x + ik_{z,n}z), \end{aligned} \quad (6)$$

in which $k_{x,n} = k_{0x} + 2\pi n / \lambda_g$ and $k_{z,n} = (k_0^2 - k_{0y}^2 - k_{x,n}^2)^{1/2}$.

In order to find the intensity of propagating waves, the coefficients $E_{y,n}^r$ and $H_{y,n}^r$ have to be calculated in the Rayleigh expansions. This problem is referred to as the *grating problem*.

The efficiency of the metal grating, for the H-polarization case, is given by the so-called radiation factors:

$$|R_n(\beta, \eta)|^2 = \frac{4}{e^2} \exp(2|k_{0z}|z_0) \cdot |H_{y,n}^r|^2, \quad (7)$$

in which z_0 is the distance between the top of the metal grating and the electron trajectory. Radiation factors depend upon the experimental setup², the beam parameters and the metal grating.

3. SOLUTIONS OF THE GRATING PROBLEM

For triangular metal gratings, the coefficients of the Rayleigh expansion (6) are found by minimizing the quantity:

$$I_H = \int_L |\mathbf{n} \cdot \nabla (H_y^i + H_y^r)|^2 ds, \quad (8)$$

where L is the length of one period of the grating. This is referred to as Improved Point Matching Method^{3,4}.

The truncated Rayleigh expansion for H_y^r is:

$$H_y^r(x, z; k_{0y}, \omega) = \sum_{n=-N}^{+N} H_{y,n}^r(N; k_{0y}, \omega) \exp(ik_{x,n}x + ik_{z,n}z). \quad (9)$$

When $N \rightarrow \infty$ the set of coefficients $H_{y,n}^r(N; k_{0y}, \omega)$ in (10) converges to the Rayleigh coefficients $H_{y,n}^r$. Minimizing I_H we obtain a system of linear equations which can be expressed in the form of matrix equation $M \times H = V$ ³. For the H-polarization one obtains the following elements of the matrix M and of the vector V :

$$M_{p,n} = \int_L [ik_{x,n}f'(x) - ik_{z,n}] \cdot [ik_{x,p}f'(x) - ik_{z,p}]^* \exp\left[i(n-p)\frac{2p}{\lambda_g}x + i(k_{z,n} - k_{z,p}^*)f(x)\right] \cdot [1 + f'(x)^2]^{1/2} dx, \quad (10)$$

$$V_p = \int_L [ik_{0x}f'(x) + ik_{0z}] \cdot [ik_{x,p}f'(x) - ik_{z,p}]^* \exp\left[i(-p)\frac{2p}{\lambda_g}x + i(-k_{0z} - k_{z,p}^*)f(x)\right] \cdot [1 + f'(x)^2]^{1/2} dx, \quad (11)$$

where $f(x)$ is the function which describes the grating profile for one period and $n, p = -\infty$ to $+\infty$.

This method is generally recommended for continuous functions that describe the grating profile because it doesn't take care of singularity points. In order to make this method suitable for the triangular profile we used a smoothed function by replacing the top of the triangle with a circle arc.

For lamellar gratings we used the Modal Expansion Method⁴. For this case the infinite system of linear equations that have to be solved is:

$$\sum_{n=-\infty}^{+\infty} (k_{z,n}\lambda_g\delta_{k,n} - V_{k,n})H_{y,n}^r = C_k \quad (k = 0, \pm 1, \pm 2, \dots), \quad (12)$$

in which:

$$C_k = \frac{e}{2} \exp(ik_{0z}z_0) \left[k_{0z}\lambda_g\delta_{k,0} + a \sum_{m=0}^{\infty} \varepsilon_m \kappa_m \frac{\Gamma_m - 1}{\Gamma_m + 1} \Psi_{m,k} \Psi_{m,0}^* \right], \quad (13)$$

$$V_{k,n} = a \sum_{m=0}^{\infty} \varepsilon_m \kappa_m \frac{\Gamma_m - 1}{\Gamma_m + 1} \Psi_{m,k} \Psi_{m,n}^*, \quad \Psi_{m,n} = a^{-1} \int_0^a \cos(m\pi x/a) \exp(-ik_{x,n}x) dx \quad (14 a, b)$$

where a is the groove length, $\kappa_m = [k_0^2 - (m\pi/a)^2]^{1/2}$, $\Gamma_m = \exp(2i\kappa_m h)$, $\varepsilon_k = 2 - \delta_{k,0}$, h is the groove height.

The size of the matrix system was increased until the convergence to the desired level of accuracy is obtained.

4. RESULTS AND DISCUSSIONS

Using computer codes we performed calculations involving matrix systems up to 120×120 size. This implies that in the expansion (9) up to $N=60$ harmonics were taken in account. All values have been calculated for the first propagative order $n = -1$, and for an observation plane perpendicular on the grating surface and parallel to the electron trajectory. Results are presented in Fig. 2 - 7.

Fig. 2 presents the calculated radiation factors $|R_{-1}|^2$ versus the angle η for lamellar gratings, for electron energies of 1 MeV and 5 MeV. The data for 5 MeV have been multiplied by a factor of 10^{-1} .

Fig. 3 presents the same results as in Fig. 2, but for other grating parameters and electron energies of 20 and 50 MeV respectively. It can be easily observed that increasing the energy of electrons the radiation factor decreases.

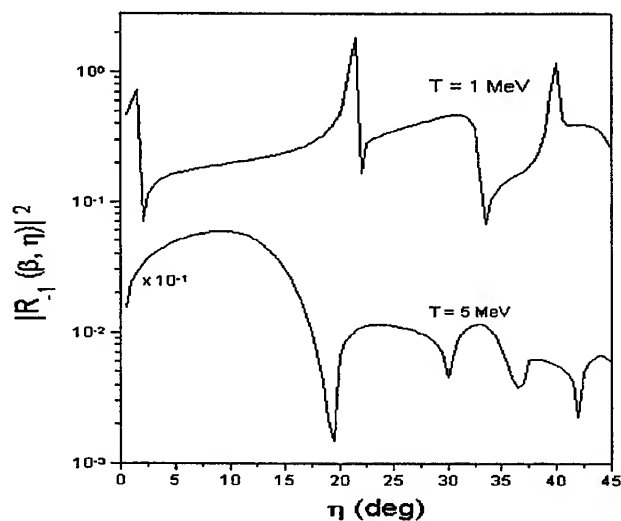


Fig. 2. Radiation factors $|R_{-1}|^2$ versus the angle η for lamellar gratings with $\lambda_g = 1\text{ mm}$, $a = 0.5\text{ mm}$, $h = 0.25\text{ mm}$ and electron energies of 1 MeV and 5 MeV, respectively.

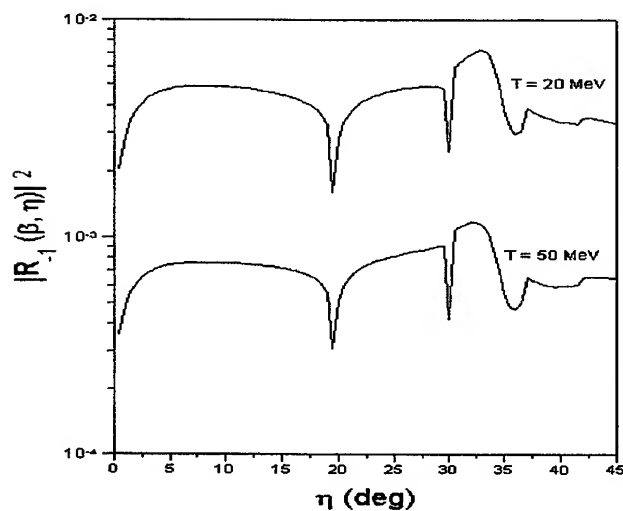


Fig. 3. Radiation factors $|R_{-1}|^2$ versus the angle η for lamellar gratings with $\lambda_g = 2\text{ mm}$, $a = 0.5\text{ mm}$, $h = 0.1\text{ mm}$ and electron energies of 20 MeV and 50 MeV respectively.

Fig. 4 presents the calculated radiation factors $|R_{-1}|^2$ versus the angle η for triangular gratings with angles $\alpha = 30^\circ$ and $\gamma = 23.8^\circ$, $\lambda_g = 2$ mm, $h = 0.5$ mm and electron energy of 10 MeV.

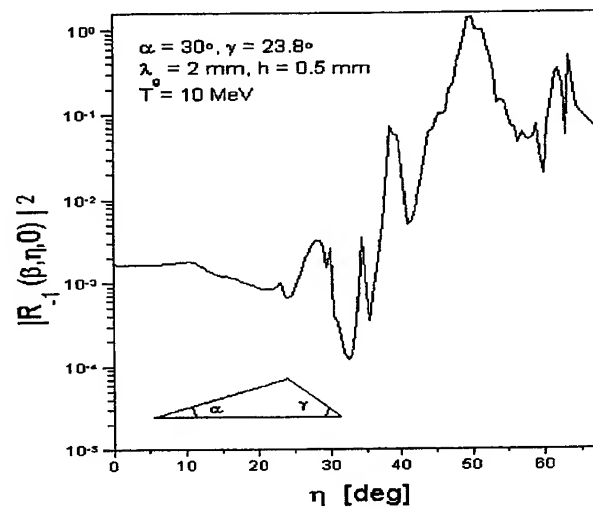


Fig. 4. Radiation factors $|R_{-1}|^2$ versus the angle η for triangular gratings for electron energy of 10 MeV.

Fig. 5 presents a comparison of radiation factors $|R_{-1}|^2$ versus the angle η for triangular gratings with different parameters and electron energy of 1 MeV. The data for the grating with blaze angle $\alpha = 5^\circ$, $\lambda_g = 2$ mm, $h = 0.173$ mm have been multiplied by a factor of 10.

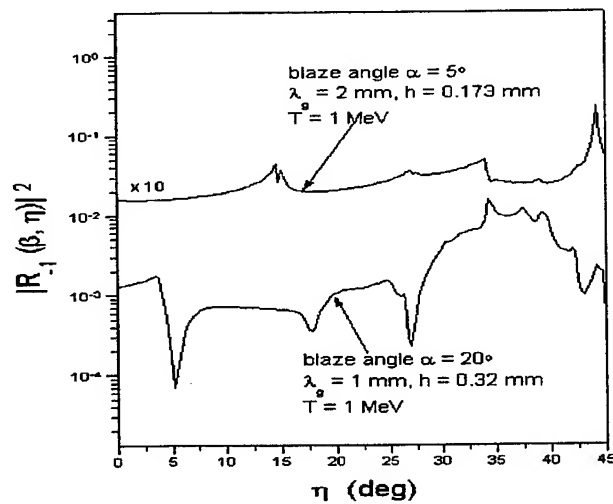


Fig. 5. Radiation factors $|R_{-1}|^2$ versus the angle η for triangular gratings for electron energy of 1 MeV.

Fig. 6 presents a comparison of radiation factors versus the angle η for triangular gratings with blaze angles $\alpha = 10^\circ$ and $\alpha = 15^\circ$, respectively, $\lambda_g = 2$ mm and electron energy of 10 MeV. The data for $\alpha = 10^\circ$ have been multiplied by a factor of 10^{-1} .

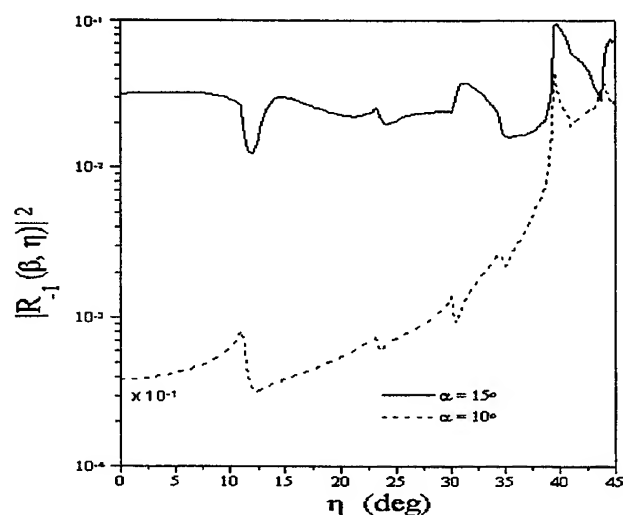


Fig. 6. Radiation factors $|R_{-1}|^2$ versus the angle η for triangular gratings, for electron energy of 10 MeV and blaze angles of 10° and 15° , respectively.

Fig. 7 presents a comparison of radiation factors versus the angle η for triangular gratings with blaze angles $\alpha = 10^\circ$, $\lambda_g = 2$ mm and electron energy of 10 MeV and 30 MeV, respectively. The data for $T = 10$ MeV have been multiplied by a factor of 10^{-1} .

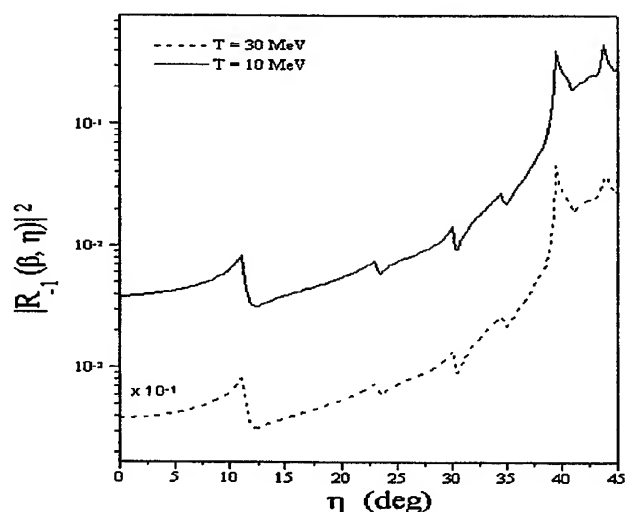


Fig. 7. Radiation factors $|R_{-1}|^2$ versus the angle η for triangular gratings, with blaze angles of 10° and electron energies of 10 MeV and 30 MeV, respectively.

5. CONCLUSIONS

This paper presents the calculated radiation factors $|R_n(\beta, \eta)|^2$ as a measure of the efficiency for Smith-Purcell radiation. For lamellar gratings we used the Modal Expansion Method, and for triangular gratings we used the Improve Point Matching Method. These calculations show that the lamellar gratings are more efficient than the triangular ones with at least one order, for the blaze angles considered. Obviously, an increase in electron energy led to a decrease of the $|R_{-1}|^2$.

We have restricted our calculation for lamellar and triangular gratings with blaze angle to observation angles $\eta < 45^\circ$ where a reliable convergence of the numerical solution of the infinite linear system was obtained. The size of the matrix of the equations system varied between 60×60 and 120×120 .

These calculations allow the choice of the beam and the metal grating parameters in order to perform an experiment for obtaining Smith-Purcell effect. Corrections of these results must be added accounting the experimental data.

REFERENCES

1. J. E. Walsh, "Electron Beam Diffraction Gratings and Radiation", 21st International FEL Conference and 6th FEL Applications Workshop, Invited Paper Mo-O-01, DESY, Hamburg, Germany, August 23 – 28, 1999.
2. O. Haeberlé et al., "Smith-Purcell radiation from electrons moving parallel to a grating at oblique incidence to the rulings", Phys. Rev. E, **55**, 4, pp. 4675 - 4683, 1997.
3. P. M. Van den Berg, "Smith-Purcell radiation from a point charge moving parallel to a reflection grating", J. Opt. Soc. Am., **63**, 12, pp. 1588 - 1597, 1973.
4. R. Petit, *Electromagnetic Theory of Gratings*, Springer - Verlag Berlin, Heidelberg, New York, 1980.

High performance 980 nm emission wavelength InGaAs/AlGaAs/GaAs laser diodes

G.I Suruceanu*, A.N. Caliman, S.F. Vieru, V.P. Iakovlev, A.V. Sarbu, A.Z. Mereuta

Optoelectronics Laboratory, Technical University of Moldova, 168 Stefan cel Mare Ave.,
MD-2004, Chisinau, Moldova

ABSTRACT

This paper presents the fabrication and mirrors passivation process of InGaAs/AlGaAs/GaAs narrow stripe ($w=4\mu\text{m}$) 980 nm emission wavelength laser diodes (LD). After mesa-stripe definition and Au-contact deposition procedures, a procedure of in-vacuum cleaving and in-situ passivation with $\lambda/4$ or $\lambda/2$ -thick ZnSe layers was performed. 960 μm and 500 μm length laser diodes bars was fabricated as a result. Antireflection-high reflectivity (AR-HR) (5 % / 95 %) coating were formed on the bars facets. Laser diodes were soldered p-junction-side down on copper submounts. The room temperature CW threshold current value of 20 mA and CW maximum output power of 440 mW at 760 mA pumping current were obtained. The far-field emission pattern of laser diodes is lateral single mode in large range of output powers (from 10 to 250 mW). These laser diodes were used for laser diode module fabrication. In this module the laser diodes was coupled with tapered single mode $9\mu\text{m}/125\mu\text{m}$ optical fibre with a fused microlens at the end. CW output optical power of 40 mW from the fibre was obtained at 240 mA operating current of the laser diode module.

Keywords: 980 nm laser diode, catastrophic optical damage, mirrors passivation, laser diode module

1. INTRODUCTION

The laser diodes with emission wavelength around 980-nm is the preferred pump source for an erbium-doped fiber amplifier (EDFA) for the next generation of lightwave communication systems because of lower noise, high power conversion efficiency, and low temperature sensivity under operating conditions. An EDFA consists of a short length of an optical fiber whose core has been doped with less than 0.1% Er, an optically rare earth element. Er ions are pumped up to an upper energy level by the absorption of light from the pump source, 980 or 1480 nm. The transition to the ground state emits a photon that may be either spontaneous or stimulated. This devices can be used as a power amplifier to boost transmitter power, an optical repeater to amplify a weak signal, and an optical preamplifier to increase receiver sensitivity¹. The progress in growth and fabrication of 980 nm lasers has been so rapid that the state-of-the-art lasers are now commercially available^{2,3}. Besides InGaAs/GaAs/AlGaAs an "Al- free" InGaAs/InGaAsP/InGaP laser^{3,4}, also grown on GaAs substrates, has emerged as another promising material system for 980 nm pump lasers. All major epitaxial techniques (molecular beam epitaxy (MBE), chemical beam epitaxy (CBE), metallorganic chemical vapour deposition (MOCVD)) have been used to grow high-performance lasers with comparable excellent results. Nevertheless, the problem of catastrophical optical damage (COD) of the mirrors is actual for both laser systems. A various technical solutions were proposed for preventing facet degradation, so as passivation of surface in sulfur or sulfur based compounds ($\text{NH}_4\text{S}_2\text{O}_8$)⁵, cleaning or formation of laser facets in vacuum followed by suitable passivation and coating with dielectric layers (Al_2O_3 , SiO_2 , Zr_2O_3), formation of nonabsorbing mirrors (NAM)⁶.

Here, we report our work aimed in optimising of the mirrors passivation technique to achieve a higher COD level of 980 nm InGaAs/AlGaAs/GaAs lasers and fabrication of laser diode module for pumping of Er^{3+} - doped devices.

2. EXPERIMENTAL

2.1 Basic laser diode structure

The basic laser diode structure was a strained quantum well graded index separate confinement InGaAs/AlGaAs/GaAs heterostructure (GRIN SCH) with central emission wavelength 980 nm and was grown by molecular beam epitaxy

* Correspondence: Phone: (+003732) - 24-71-43, E-mail: optolab@ch.moldpac.md

technique (MBE) on 3° off (100) GaAs substrate⁷. The typical device structure, shown in Fig. 1, is essentially similar to that of an AlGaAs/GaAs quantum-well {QW} laser, except that the GaAs QW's are replaced by InGaAs quantum wells sandwiched between GaAs spacer layers.

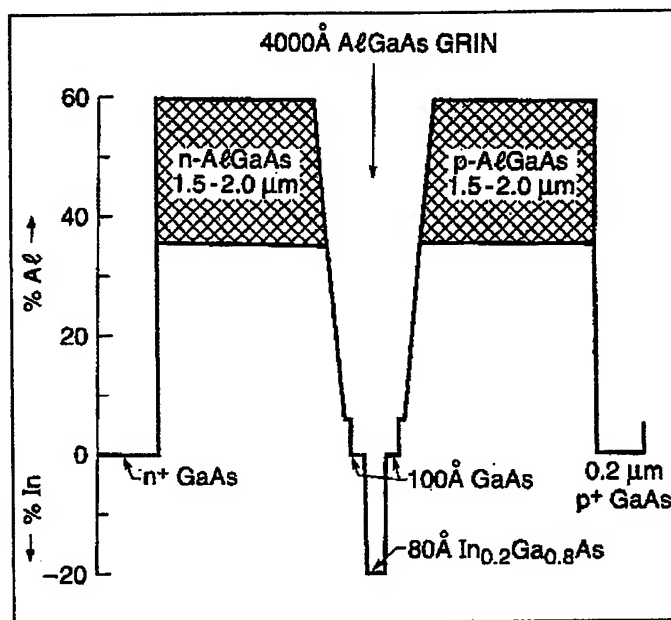


Fig. 1 The schematic representation of $\text{In}_{0.2}\text{Ga}_{0.8}\text{As}/\text{GaAs}$ strained layer GRIN-SCH-QW laser

The structure consist of $0.5\mu\text{m}$ - thick superlattice buffer n^+ GaAs buffer layer, $0.1\mu\text{m}$ -thick superlattice buffer layer of five periods of 10 nm GaAs and 10 nm AlGaAs, a $2.0\mu\text{m}$ thick n - $\text{Al}_{0.6}\text{Ga}_{0.4}\text{As}$ cladding layer, a $0.15\mu\text{m}$ thick linearly graded index layer of n - $\text{Al}_x\text{Ga}_{1-x}\text{As}$ with x and n decreasing from 0.6 to 0.15 and from 5×10^{17} to $1 \times 10^{16}\text{ cm}^{-3}$, respectively, a 60 nm - thick undoped $\text{Al}_{0.15}\text{Ga}_{0.85}\text{As}$ layer, three 8 nm InGaAs/ 10 nm GaAs undoped QW active regions, a 60 nm thick undoped $\text{Al}_{0.15}\text{Ga}_{0.85}\text{As}$ layer, a linearly graded $0.15\mu\text{m}$ thick p - $\text{Al}_x\text{Ga}_{1-x}\text{As}$ layer with x and p increasing from 0.15 to 0.6 and 1×10^{16} to $5 \times 10^{17}\text{ cm}^{-3}$, respectively, a $2.0\mu\text{m}$ thick p - $\text{Al}_{0.6}\text{Ga}_{0.4}\text{As}$ top cladding layer, and a $0.2\mu\text{m}$ thick p^+ GaAs contact layer.

The InGaAs/AlGaAs/GaAs samples were processed into ridge waveguide (RW) lasers. To fabricate these devices a standard photolithographic technique was used to define the $4\text{-}5\mu\text{m}$, and $25\mu\text{m}$ width stripes. The $4\text{-}5\mu\text{m}$ and $25\mu\text{m}$ width stripes oriented in (110) direction were formed by chemical etching of the top layer in $5:\text{NaOH} + 1:\text{H}_2\text{O}_2 + 1:\text{NH}_4\text{OH}$ solution.

The performance of high power laser diode are dramatically affected by degradation processes of Fabry-Perot facets. In this context the mirror facets has to be passivated in order to suppress as much as possible the degradation processes, leading to catastrophic optical damage (COD). From a few numbers of publications there are indications that the COD can be drastically reduced by thin layer of ZnSe⁴ or Si⁸ deposition on the cleaved facet.

The mirror facets in the most semiconductor laser diodes are formed by cleaving in the ambient room air. As a result, the semiconductor surface oxidises and this effect leads in increasing of the surface nonradiative electron-hole recombination and reabsorbed laser emitted light via surface states and cause the excess heating at the laser diode facets and finally to the COD⁹.

During performing this work we have continue to developed the method of the laser diodes mirrors protection simultaneously with cleaving of the epitaxial wafer in vacuum, reported early¹⁰. For this experiments ZnSe and also SiO_2 layers deposited by E-beam evaporation technique were used.

For simultaneously in vacuum cleaving and passivation of LD mirrors bars a mechanical fixture was developed. The fixture consists of two rotatable holders that first cleave and then rotate the epitaxial wafer that the two cleaved facets face the beam of an evaporation source. ZnSe protective films with 100-200 nm thickness ($\sim\lambda/4$ and $\lambda/2$) were deposited to the LD cleaved facets by E-beam evaporation method from the Knudsen cell, in vacuum not worse 10^{-6} mm Hg. The passivation process was made for the LD bars directly cleaved in the stream of evaporated material (in-situ deposited process), and for preliminary cleaved wafer in the ambient room air (ex-situ deposited process).

For surface morphology study of the in-vacuum cleaved facets and for estimation of in-situ ZnSe coated facets status, the atomic force microscopy (AFM) technique and photocurrent spectroscopy (spectral response (SR)) were used as well respectively¹⁰.

The analysis of AFM pictures have shown that for samples in-air cleaved even a short time in air exposed (10 min) is sufficient for growth of an 1,5 nm thick oxide layer on laser diode facets. For in-vacuum cleaved and in-situ coated with 1nm SiO₂ layer samples, the 0,1 nm amplitude of the oxide relief remain constant even after 24 hours to the air exposure, thus proving the excellent passivating properties of 1 nm SiO₂ film.

The SR spectra of InGaAs/AlGaAs/GaAs heterostructures shows the similar results as for AlGaAs/GaAs and "Al-free" laser diodes investigated in¹⁰. The in-situ passivated InGaAs/AlGaAs/GaAs samples had a value of photocurrent signal in short-wave domain higher than for ex-situ passivated and for uncoated laser diodes.

2.2 Laser diodes characteristics

The design of mechanical fixture for in-vacuum cleaving and in-situ passivating allow to cleave laser diode bars with certain cavity length. After standard ohmic contact deposition technique, the epitaxial wafer was in-vacuum cleaved in LD bars with length 500 μ m, 960 μ m (narrow stripe devices ($w=4\mu$ m)) and 750 μ m lengths (broad area devices ($w=25\mu$ m)) and consequently have been passivated with $\lambda/2$ thick ZnSe layers. Laser diode chips was indium soldered p-side down on Cu-Md subcarriers.

In order to estimate the laser diodes performances the light-current and spectral characteristics of InGaAs/AlGaAs/GaAs was performed. The output optical power was measured from AR (5 %) coated facets, using experimental set-up represented in Fig.2.

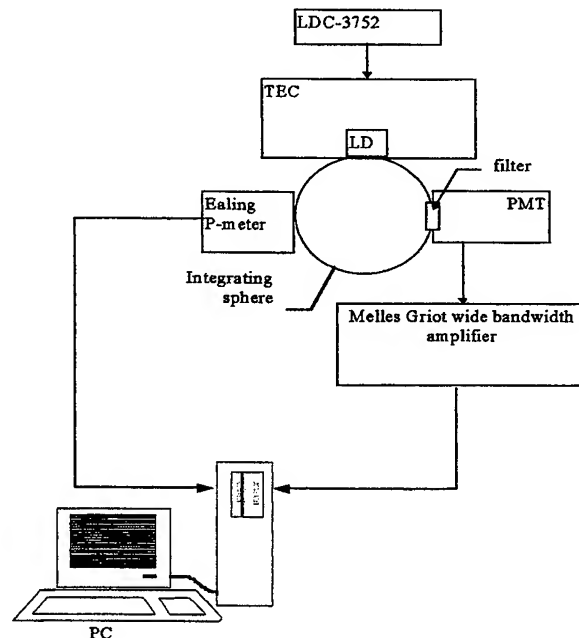


Fig. 2 Experimental set-up for output power measurements of laser diodes

The room temperature continuous wave (CW) threshold current value of 20 mA for narrow stripe ($w=4\text{ }\mu\text{m}$, $L=500\text{ }\mu\text{m}$) and CW maximum output power of 440 mW at 760 mA pumping current were obtained. For broad area ($w=25\text{ }\mu\text{m}$, $L=750\text{ }\mu\text{m}$) LD the CW threshold current 66 mA and CW output power 900 mW at 1.43 A were obtained (Fig. 3). Both devices were $\lambda/2$ ZnSe in-vacuum cleaved, in-situ passivated and AR-HR coated. The emission spectra of narrow stripe LD was longitudinal single-mode with emission wavelength $\lambda=979\text{ }\mu\text{m}$ and bandwidth $\Delta\lambda=0.2\text{ nm}$ ($I=100\text{ mA}$) (Fig. 4 b).

Measured lateral far-field pattern was also single-mode at output levels ranging from 10 to 250 mW (Fig. 4 a).

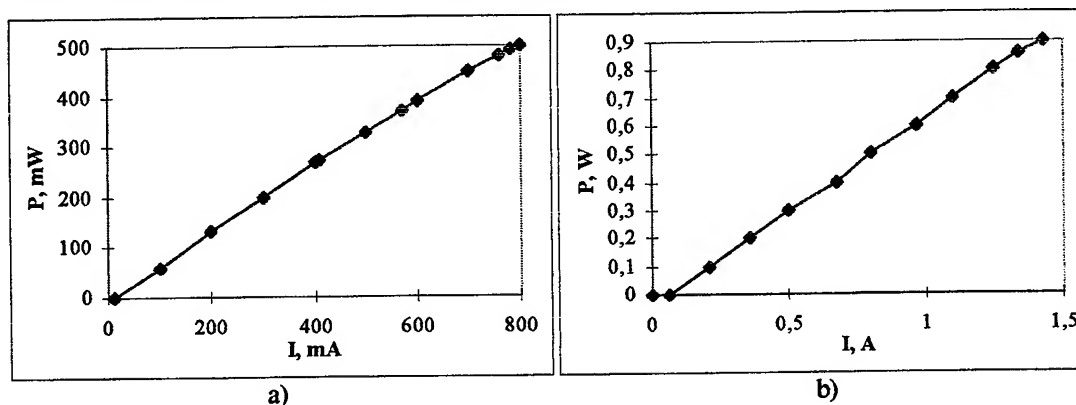


Fig. 3 Light - current characteristics of narrow stripe ($w=4\text{ }\mu\text{m}$) a) and broad area ($w=25\text{ }\mu\text{m}$) b) InGaAs/AlGaAs/GaAs RW laser diodes with ZnSe in-situ passivated mirrors and AR =5 %, HR =95 % coatings

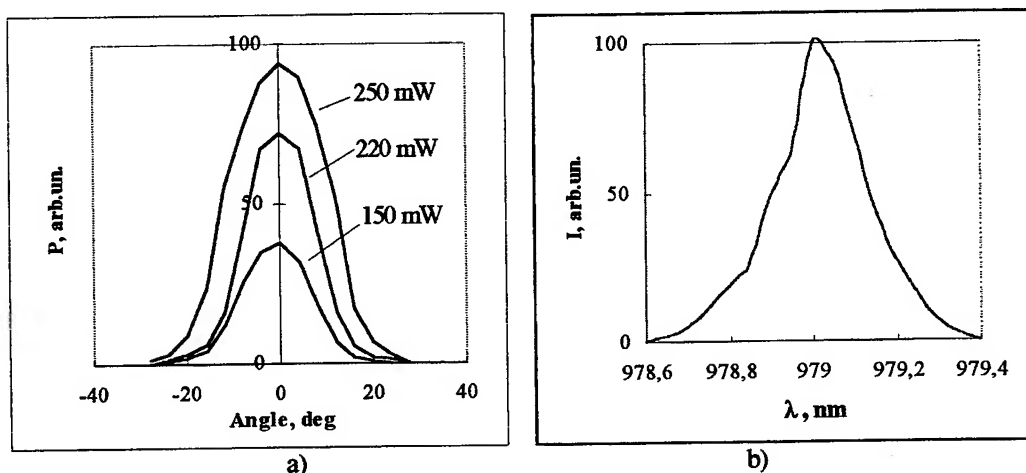


Fig. 4 Far-field pattern (a) and emission spectra (b) of high power 980 nm narrow stripe ($w=4\text{ }\mu\text{m}$) InGaAs/AlGaAs/GaAs laser diode

2.3 Laser diode module fabrication

For laser module fabrication we have used narrow stripe ($w=4\div5\text{ }\mu\text{m}$) InGaAs/AlGaAs/GaAs RW diodes with cavity length $500\text{ }\mu\text{m}$. LD was mounted on AlN/Cu-Md or BeO/Cu-Md subcarriers and the preliminary light-current and far-field distribution characteristics was measured. After this testing procedure the LD was mounted into package (Fig. 5). A special coupling scheme was elaborated in order to achieve efficient coupling of LD emission into single-mode optical fibre. In Fig. 6 is shown a basic layout of laser diode module. The device was temperature controlled using thermoelectric cooler TEMO-5 and thermistor, mounted in nearest vicinity of the LD chip. For optical power monitoring the internal InGaAsP/InP p-i-n photodiodes (home made) were mounted near the rear facet of the laser diode. The end of single-mode

fiber was in vacuum metalised and consequently tapered and microlensed, using electric arc equipment KCC-111. A tapered end of the fibre was installed to the special GaAs-based microsaddle, mounted on the common SiO_2 carrier with two integrated microheater. The positioning of the fibre was performed under continuous control of output power when laser diode operate. As high precision unit for optic fibre positioning a positioner PV-101 was used. In Fig. 7 is shown a optical output power characteristic of LD module SLM-980. CW output optical power of 40 mW from the fibre was obtained at 240 mA operating current of the laser diode module.

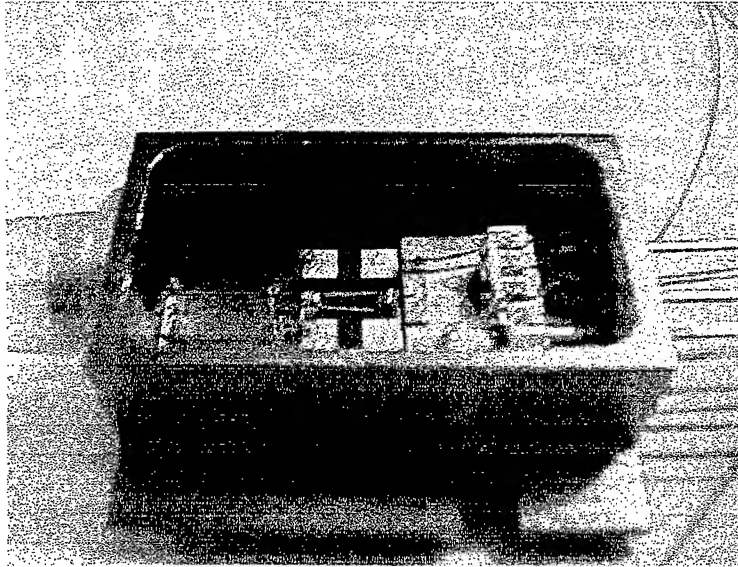


Fig. 5 Picture of the packaged laser diode module SLM-980

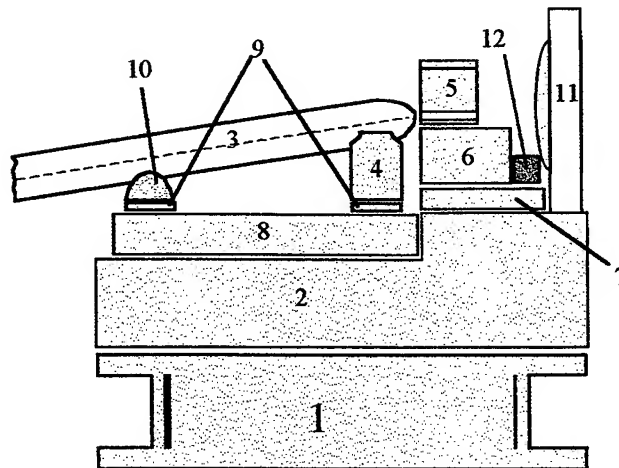


Fig. 6 A basic layout of the laser diode module. 1 - Peltier thermocooler, 2 - Cu carrier, 3 - Single mode fibre optic, 4-Microsaddle, 5 - Laser diode, 6 - AlN or BeO carrier, 7 - Cu-Md carrier, 8 - Quartz carrier with microheater, 9-Microheater, 10 - PbSn alloy, 11 - Monitoring FD, 12 - Thermistor

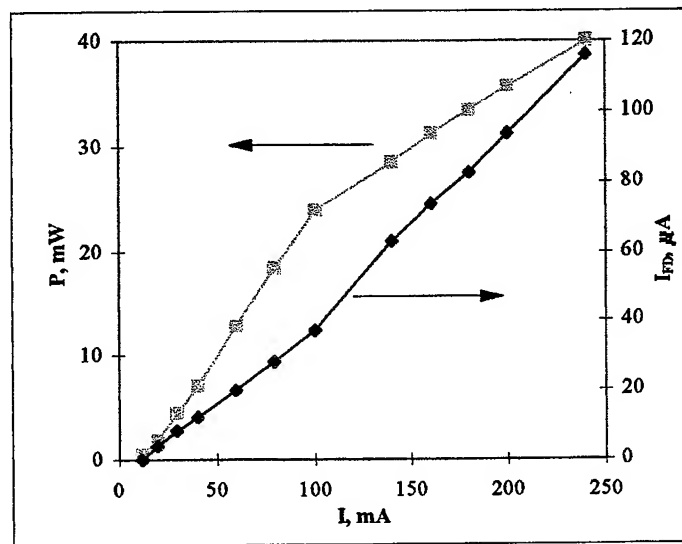


Fig. 7 Light-current characteristics of single mode fibre pigtailed InGaAs/AlGaAs/GaAs LD module

3. SUMMARY

We have realised a scheme for in-vacuum cleaving and in-situ passivating of InGaAs/AlGaAs/GaAs strained quantum well laser diodes. The narrow stripe ($w=4\div5\text{ }\mu\text{m}$) and broad area ($w=25\text{ }\mu\text{m}$) ZnSe-AR-HR coated devices were fabricated. The results of AFM and SR studies allow us to say that the consequence of the in-situ deposited ZnSe or SiO_2 layers on the mirrors facets is the density states reducing in comparison with uncoated or ex-situ passivated samples. This fact is very attractive for increasing of the laser diodes COD level.

The room temperature threshold current of 20 and 66 mA and CW maximum output power of 440 mW ($I_{\text{pumping}}=760\text{ mA}$) and 900 mW ($I_{\text{pumping}}=1.43\text{ A}$) for narrow stripe and broad area LD, respectively, was achieved. Using narrow stripe device a single mode fibre pigtailed LD module was fabricated. CW output optical power of 40 mW from the fibre was obtained at 240 mA operating current of the laser diode module.

ACKNOWLEDGEMENTS

This work was performed with support of the INCO Copernicus Programme: "Novel optical devices and measurement techniques, technology transfer and training" Contract No: IC15-CT96-0820 (DG12MUYS).

REFERENCES

1. J.L.Zyskind, C.R.Giles, R.Simpson and D.J.DiGiovanni, "Erbium-doped fiber amplifiers and the next generation of lightwave systems", *AT T Tech. J.*, **71**, pp 53-62, 1992.
2. M.Okayasu, T. Taceahita, M. Yamada and O. Kogure, "High-power 0.98 μm GaInAs strained quantum well lasers for Er-doped fibre amplifier", *Electron. Lett.*, **25**, pp. 1563-1565, 1989.
3. H.Asonen, A.Ovtchinnikov, G.Zhang, J.Nappi, P.Savolainen, and M.Pessa, "Aluminium-Free 980 nm GaInAs/GaInP pump lasers", *Quantum Electr.*, **30**, pp. 415-423, 1994.
4. A.V. Syrbu, V.P.Yakovlev, G.I.Suruceanu, A.Z.Mereutza, L.J.Mawst, A.Bhattacharya, M. Nesnidal, J.Lopez and D.Botez, "ZnSe-facet-passivated InGaAs/InGaAsP/InGaP diode lasers of high CW power and Wallplug efficiency", *Electron Lett.*, **32**, pp. 352-354, 1996.
5. Beister G., Maeger J., Gutsche D., Erbert G., Sebastian J., Vogel K., Weyers M., Wurfl J. and Daga O.P., "Simple method for examining sulfur passivation of facets in InGaAs/AlGaAs ($\lambda=0.98\text{ }\mu\text{m}$) laser diodes", *Appl. Phys. Lett.*, **68**, N.18, pp. 2467-2468, 1996.

6. Botez D. and Connolly J.C. "Nonabsorbing mirror (NAM) CDH-LOC diode lasers", *Electron. Lett.*, **20**, N.13, pp. 530-532, 1984.
7. N.Chand,N.K.Dutta,S.N.G.Chu,A.V.Sirbu.A.Z.Mereutza, and V.P.Iacovlev,"High performance strained InGaAs/AlGaAs buried heterostructure QW lasers by in-situ etching and regrowth", *Appl.Phys.Lett.*, **62**, pp. 1818-1820, 1993.
8. L.W.Tu, E.F.Shubert, M.Hong and G.J.Zudzik, "In-Vacuum cleaving and coating of semiconductor laser facets using thin silicon and a dielectric", *J. Appl.Phys.* **80**, pp. 6448-6451. 1996.
9. Fukuda M., Okayasu M., Temmyo J. and Nakano J., "Degradation behaviour of 0.98 μm strained quantum well InGaAs/AlGaAs lasers under high power operation", *IEEE J. of Quantum Electronics*, **30**, pp.471-476, 1994.
10. A.N. Caliman, S.F. Vieru, G.I. Suruceanu, O.V. Catughin, V.V. Nantoi, V.P. Iakovlev and A.V.Sarbu "Characterisation of in-vacuum cleaved and in-situ passivated laser diode mirrors" *Proceedings of 5th SIOEL-98*, Bucharest, Romania, p. 39 , 23-25 September 1998

Tunable laser diode sources for 830 nm and 980 nm wavelength range

G.Suruceanu *

Optoelectronics Laboratory, Technical University of Moldova, 168 Stefan cel Mare Ave.,
MD-2004, Chisinau, Moldova

ABSTRACT

This paper describes the fabrication technique and operating characteristics of cleaved-coupled cavity (C3) tunable source with central emission wavelength 835nm and 980 nm. The C3 concept is realised using gain-guided AlGaAs/GaAs single quantum well (SQW) and ridge-waveguide InGaAs/AlGaAs/GaAs multiquantum well (MQW) heterostructures. The tunable wavelength range for these devices was 10 nm and 16 nm respectively. The coupled cavity was formed by cleaving the laser diode (LD) chips in two parts. The cleaved sections held together by the contact metals, were then indium soldered p-side up to a copper heat sink for CW operation. The sections length of the 980 nm C3 laser was 320µm and 440 µm and 240 µm, 260 µm for 835 nm device. The emission spectra of 835 nm and 980 nm C3 laser diodes are presented.

Keywords: tuneable source, cleaved-coupled-cavity laser diode

1. INTRODUCTION

Currently wavelength tunable semiconductor laser diodes has very large application in different field such as wavelength division multiplexing (WDM) telecommunications systems, Raman spectroscopy, frequency doubling, material characterisations, remote sensing ^{1,2}. The distinguished characteristics of this optoelectronics devices and subsequently the main requirement, is a narrow spectral -linewidth and widely wavelength tunable range.

The tuneable laser diodes can be divided in three groups defined by different tuning mechanism ¹:

- 1) Interferometric tuneable lasers like cleaved-coupled cavity C3 and Y lasers.
- 2) Contradirectional filtering tuneable lasers such as distributed feedback (DFB) and distributed Bragg reflectors (DBR) lasers.
- 3) Codirectional filtering structure like vertical cavity filtering structure like the vertical cavity filter (VCF) laser.

Such of devices that represents this classifications has proper advantages and disadvantages that consist in technical performances and fabrication abilities, but one the main requirement is technological simplicity and wide tuneable performances.

Currently the main applications of tuneable laser sources are in WDM telecommunications systems, where the sources with emission wavelength at 1,55 µm and 1,3 µm are needed. A large number of DFB and DBR schemes have been proposed and developed for this applications, but technological procedures of devices fabrication are very sophisticated ¹. On the other hand, there are special applications such as high resolution atomic microscopy, laser cooling of neutral atoms ^{2,3}, new optoelectronics devices testing, where the low- cost tuneable sources, emitting in the 800 - 1000 nm wavelength range are needed. How was mentioned above, one of the scheme for wavelength tuning is a C3 laser diode. This is a simple scheme and is relatively easy to fabricate. The first results about realisation of this device was presented by Tsang for C3 emitting in 1,55 µm wavelength range⁴. In this paper are presented the experimental data of investigations and fabrication procedure of AlGaAs/GaAs single quantum well (SQW) and InGaAs/AlGaAs/GaAs multiquantum well (MQW) C3 laser diodes operating in the 830 - 850 nm and 970 - 980 nm wavelength range.

* Correspondence: Phone: (+003732) - 24-71-43, E-mail: optolab@ch.moldpac.md

2. EXPERIMENTAL

2.1. Basic structures

Two sets of heterostructure were used in this work - AlGaAs/GaAs single quantum well (SQW) and InGaAs/AlGaAs/GaAs multiquantum well (MQW) heterostructures. The AlGaAs/GaAs heterostructure with central emission wavelength 835 nm was grown using low temperature liquid phase epitaxy (LPE) technique in the temperature interval 600- 640 °C⁵ and consists of a 2 μm n-GaAs buffer layer, a 0.9 μm n-Al_{0.64}Ga_{0.36}As cladding, 0.15 μm n-Al_{0.6-0.3}Ga_{0.4-0.7}As graded index (GRIN) waveguiding, 17 nm n - Al_{0.08}Ga_{0.92}As active layer, 0.15 μm n-Al_{0.6-0.3}Ga_{0.4-0.7}As GRIN waveguiding, 0.2 μm n - Al_{0.66}Ga_{0.34}As cladding, 0.4 μm p- Al_{0.66}Ga_{0.34}As cladding and a 0.2 μm p⁺ GaAs cap layer.

The second heterostructure was InGaAs/AlGaAs/GaAs strained multiquantum well (MQW) graded index separate confinement heterostructure (GRIN SCH) with central emission wavelength 980 nm and was grown by molecular beam epitaxy technique (MBE) on 3° off (100) GaAs substrate⁶. The structure consist of 0.5 μm - thick superlattice buffer n⁺ GaAs buffer layer, 0.1 μm -thick superlattice buffer layer of five periods of 10 nm GaAs and 10 nm AlGaAs, a 2.0 μm thick n - Al_{0.6}Ga_{0.4}As cladding layer, a 0.15 μm thick linearly graded index layer of n- Al_{1-x}Ga_xAs with x and n decreasing from 0.6 to 0.15 and from 5×10^{17} to $1 \times 10^{16} \text{ cm}^{-3}$, respectively, a 60 nm- thick undoped Al_{0.15}Ga_{0.85}As layer, three 8 nm InGaAs/10 nm GaAs undoped QW active regions, a 60 nm thick undoped Al_{0.15}Ga_{0.85}As layer, a linearly graded 0.15 μm thick p-Al_xGa_{1-x}As layer with x and p increasing from 0.15 to 0.6 and 1×10^{16} to $5 \times 10^{17} \text{ cm}^{-3}$, respectively, a 2.0 μm thick p- Al_{0.6}Ga_{0.4}As top cladding layer, and a 0.2 μm thick p⁺ GaAs contact layer.

The AlGaAs/GaAs and InGaAs/AlGaAs/GaAs samples were processed into oxide stripe gain-guided (GG) and ridge waveguide (RW) lasers respectively. The reason of choice of such LD design is the longitudinal mode discrimination proprieties. For gain - guided and weakly guided (RW with low depth ridge) the discrimination ratio of longitudinal mode is less then for buried heterostructure (BH) LD, or other strongly index- guided LD⁷. To fabricate oxide stripe GG lasers a standard photolithografic technique was used to define the 6 - 7 μm width stripes. The 4 -5 μm width stripes (RW InGaAs/AlGaAs/GaAs) oriented in [110] direction were formed by chemical etching of the top layer in 5:NaOH+1:H₂O₂ + 1:NH₄OH solution. After standard ohmic contact deposition procedure, the laser diode bars with cavity length 240 μm , 260 μm (AlGaAs/GaAs) and 760 μm (InGaAs/AlGaAs/GaAs) were cleaved from the samples.

For improving of reciprocal cavity coupling ratio of C3 devices, the antireflection coating (AR) of inside facets are needed. In this work the AR coating ($R=0.1$) was deposited only on one facet of the (AlGaAs/GaAs) laser diode (LD) bars, after first $\lambda/2$ ZnSe deposition procedure⁸. So the LD bars with asymmetrical coating ($R_1=0.3$, $R_2=0.1$) were prepared.

The InGaAs/AlGaAs/GaAs 760 μm cavity length samples was subsequently cleaved into discreet laser diodes chips and after then - was cleaved into 2 parts (sections) with length 320 μm and 440 μm length. The cleaved sections, held together by the contact metals, were then indium soldered p- side up to a Cu heatsink.

The AlGaAs/GaAs was also cleaved into discreet LD and was mounted on the common Cu heatsink in order to form a coupled cavity scheme. The AR facets were put inside of the device and after reciprocal adjustment of the stripes the sections were indium soldered as well. The intercavity gap width L_g was for AlGaAs /GaAs about 5 μm and for InGaAs/AlGaAs/GaAs about 1 μm .

2.2. Tuning mechanism and C3 performances

Generally the C3 scheme that have used in present work is named active-active schemes, because both sections can be pumped to provide gain. The devices from this category are also called three-terminal devices, since three electrical contacts are used to pump the two optically coupled but electrically isolated cavity sections. The active-active scheme offers the possibility of electronic shifting since the current of two cavities can be independently controlled. If one of the cavities is operated below threshold, a change in its drive current significantly changes the carrier density inside the active region. Since the refractive index of a semiconductor laser changes along with the carrier density, the longitudinal modes shift with a change in the drive current, and different FP modes of laser cavity can be selected.

In the design of a coupled-cavity lasers, the cavity length L_1 and L_2 are adjustable to some extent. The performances of such lasers depends on the relative optical length $n_1 L_1$ and $n_2 L_2$ of the two cavities, where n_1 and n_2 are the effective refractive indices. Another parameters of C^3 laser is the intercavity gap width L_g between cavities, and of that depend the coupling efficiency. The air gap itself forms a third cavity, and the intercavity coupling is affected by the loss and phase shift experienced by the optical field while traversing the gap. A theoretical analysis of the C^3 lasers shows⁷ that the coupling constant C have a maximal value for $L_g = m\lambda/2$ (m is an integer), but decrease exponentially with increasing of m . Due of this fact, we have fabricated the C^3 with different values of intercavity gap ($1\ \mu\text{m}$ and $5\ \mu\text{m}$), because varying L_g we have vary the coupling constant C as well and so may vary the tuneable performances of devices. In Fig. 1 and Fig. 2 the schematic representation and a picture of C^3 are shown.

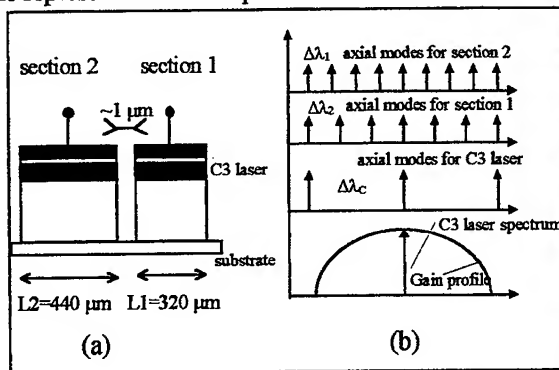


Fig.1 Tuning mechanism of C^3 laser diode

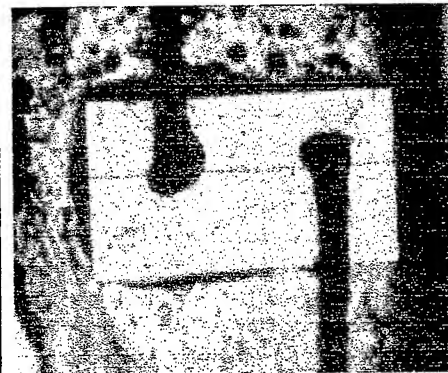


Fig. 2 The picture of the InGaAs/AlGaAs/GaAs C^3 laser diode

For Al GaAs / GaAs C^3 device the length of output cavity, section 1, was $240\ \mu\text{m}$ while the length of the control cavity, section 2, was $260\ \mu\text{m}$. The CW threshold current for laser section 1 was 21 mA with no current applied to the other cavity. For laser section 2 this parameter was 22 mA. For InGaAs/AlGaAs/GaAs C^3 device the lengths of sections 1 and 2 was 320 and 440 respectively. The CW threshold currents of sections 1 and 2 at room temperature was 15 mA and 18 mA respectively. The spectral characteristics of the C^3 lasers were measured under various operating conditions by changing the level of pumping current via sections and also the temperature of devices. In Fig. 3 is shown the experimental set-up that have used for investigations during performing of this work.

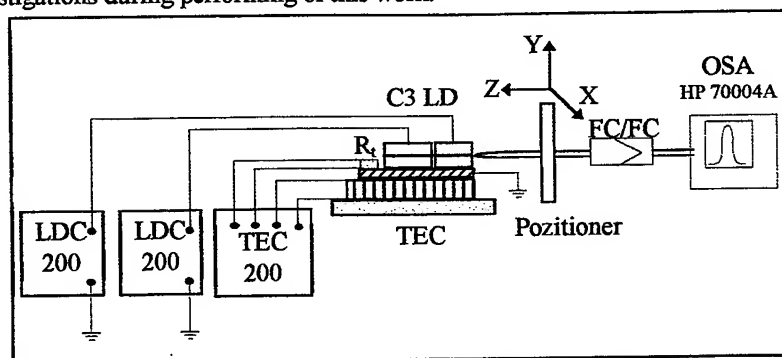
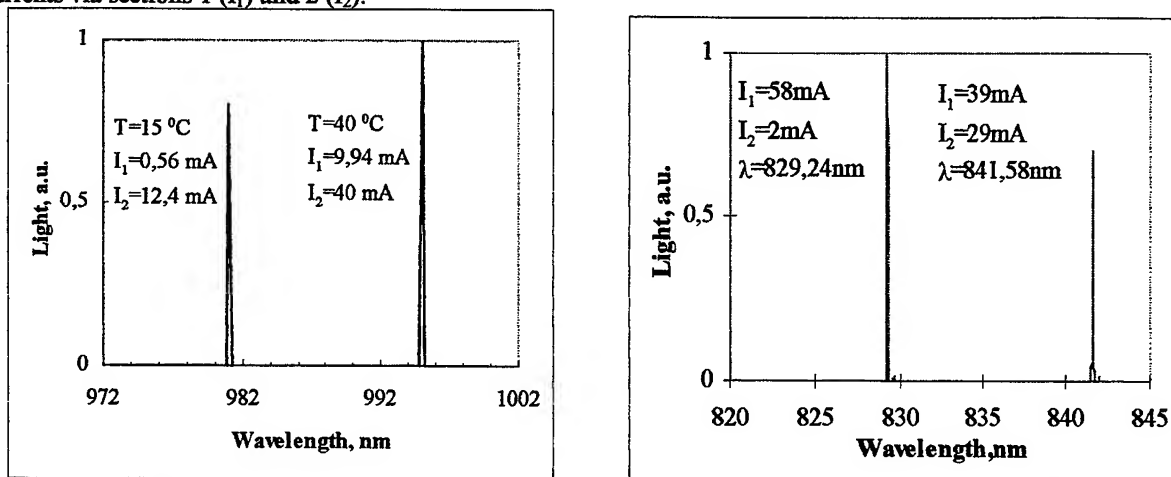


Fig. 3 Experimental set-up for spectral measurements of C^3 devices

The C^3 devices was temperature controlled using the 5,3 W thermoelectric cooler (TEC) Melcor and TEC driver TED 200. The section 1 and 2 was independently pumped using two laser diode controller LDC 200. For coupling of C^3 LD with single mode fibre ($5,5\ \mu\text{m} / 125\ \mu\text{m}$) the hemispherical microlensed fibre and Newport positioner was used. Other end of the fibre was spliced with FC connector. The spectral characteristics of Al GaAs/GaAs and InGaAs/AlGaAs/GaAs C^3 was measured using Hewlett Packard optical spectrum analyser OSA HP 70004A with spectral resolution bandwidth 0.08 nm. Fig.4 shows the optical spectra obtained for different currents applied to section 1 and 2 for InGaAs/AlGaAs/GaAs and AlGaAs/GaAs devices. The wavelength tunability range for Al GaAs/GaAs and InGaAs/AlGaAs/GaAs C^3 was estimated 12.3 nm and 16 nm respectively.

In Tab. 1 are shown the experimental data of measured emission spectra of AlGaAs/GaAs C3 LD for various combinations of currents via sections 1 (I_1) and 2 (I_2).



a) b)
Fig. 4 Emission spectra of 980 nm a) and 835 nm C3 laser b) under various pumping currents

Tab.1

λ , nm	Operation condition		
	I_1 , mA;	I_2 , mA	T , °C
829.24	58	2	15
829.29	60	2	
832.7	48.1	4	15
832.846	40.7	9	
833.93	0	29	23
834.1	2.86	32.5	23
834.96	30.6	19.1	
835.18	14.06	26	23
835.25	18.52	29	
835.86	16.23	32.5	
835.88	16.44	32.5	
835.95	35.6	29.6	
836.93	29.6	40.5	23
837.10	41.8	21.5	23
837.87	27.46	36	
837.98	19.1	29	
838.1	17.2	26	23
838.15	19.18	29	
838.38	42	6	
838.40	16.6	29	
838.43	41.9	32.8	
838.73	17.53	32.5	
838.78	42	36	
839.308	31.9	25.5	23
839.658	31.9	29	
839.96	31.9	32	
840.08	27.66	29	23
841.58	39	29	23

Usually the emission spectra of the C3 devices when operating only one cavity (section 1) is longitudinal multimode, but when applied current to a second section the emission spectra becomes single mode with secondary mode rejection ratio no less than 30 dB. Fig. 5 illustrates the single mode emission spectra for one and another devices when the both sections are pumped. The measured bandwidth of both devices in this case was limited by spectral resolution of optical spectrum analyser OSA HP 70004A (0.08 nm) and was less then 0.08 nm. The highest optical output power obtained in a single longitudinal mode regime was 10 mW for AlGaAs/GaAs and 12 mW for InGaAs/AlGaAs/GaAs.

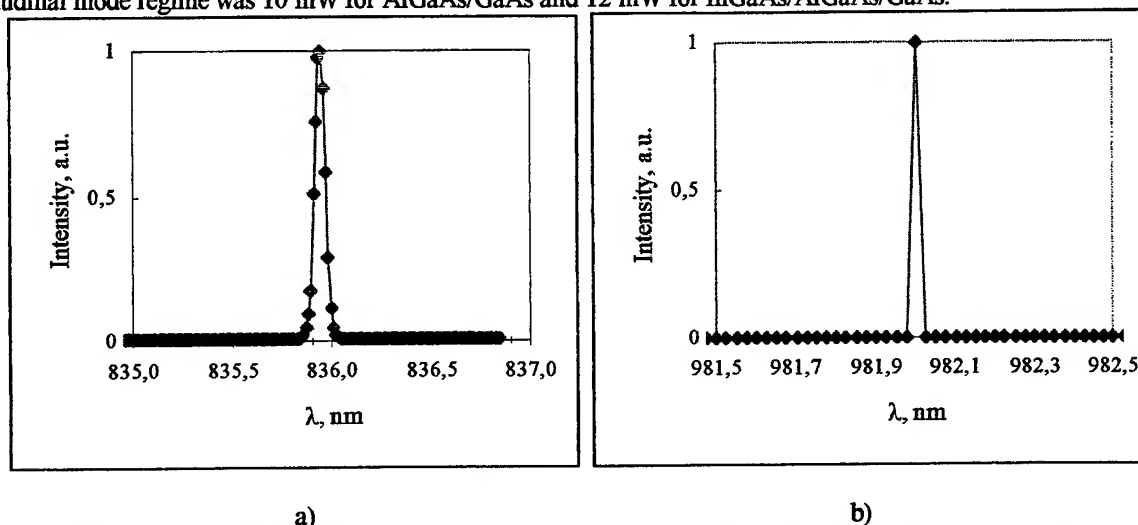


Fig. 5 Emission spectra of 835 nm ($I_1=35.6$ mA, $I_2=29.6$ mA) (a) and 980 nm ($I_1=2.52$ mA, $I_2=12.4$ mA) (b) C3 lasers, $\Delta\lambda < 0.08$ nm

3. SUMMARY

By performing the present work a cleaved coupled cavity laser diode for 830-850nm and 970-980 nm wavelength range was developed. These devices are a simple and nonexpensive wavelength tunable sources. The wavelength of such device may be shifted and adjusted to a fixed value by changing of pumping currents via sections or by changing the device temperature. The tunability range was 12,3 nm for AlGaAs/GaAs gain – guided C3 LD and 16 nm for InGaAs/AlGaAs/GaAs ridge waveguide device. The AlGaAs/GaAs C3 LD was designed with AR coating of inside facets and the intercavity gap $L_g \cong 5\mu$ m, while the InGaAs/AlGaAs/GaAs C3 has uncoated facets and intercavity gap $L_g \cong 1\mu$ m. Nevertheless, the tunability wavelength range was comparable for one and another device. This fact allow to conclude that by using the AR coating device design we may to increase the intercavity gap, while the tunability range is not very strong affected by this fact. The C3 devices can operate in a stable non-hopping single mode regime with spectral bandwidth less than 0,08 nm. These source can be useful in several applications in which the wavelength tunability and concomitantly the relatively narrow bandwidth are needed.

ACKNOWLEDGEMENTS

Author is highly grateful to A. Caliman, S.Vieru, V.Iakovlev, A.Sarbu, A.Mereuta and A.Podoleanu (School of Physical Science, UKC, United Kingdom) for their valuable contributions to work at various form.

This work was performed with support of the INCO Copernicus Programme: "Novel optical devices and measurement techniques; technology transfer and training" Contract No: IC15-CT96-0820 (DG12-MUYS) and partial support of Moldavian Government Research Programme (Grant 108 BS).

REFERENCES

1. F. Delorme " Widely Tunable 1.55 μ m lasers for Wavelength - Division - Multiplexed Optical Fiber Communications ", *IEEE Journal of Quantum Electronics*. 34, No. 9, pp. 1706 - 1716, September 1998.

2. Ming - Vei Pan, George R. Gray, Lee M. Smith, Robert E. Benner, Carl W. Johnson and Daniel D. Knowlton. "Fiber coupled high - power external cavity semiconductor laser for real - time Raman sensing", *Applied Optics*, **37**, No. 24, pp. 5755 - 5759, August 1998.
3. L. Viana, S.S. Vianna, M. Oria, and J.W.R. Tabosa "Diode laser mode selection using long external cavity", *Applied Optics*, **35**, No. 3, pp. 368 - 371, January 1996.
4. W.T. Tsang, N.A. Olsson, R.A. Logan, J.A. Ditzenberger, I.P. Kaminow and J.-S. Ko "Single - longitudinal mode performance characteristics of cleaved - coupled - cavity lasers", *Appl. Phys. Lett.*, **43**, No. 1, pp. 1003 - 1005, December 1983.
5. Zh. I. Alferov, V.M. Andreyev, A.Z. Mereutza, A.V. Syrbu, and V.P. Yakovlev "Extremely low threshold current AlGaAs buried - heterostructure quantum well lasers grown by liquid phase epitaxy", *Appl. Phys. Lett.*, **57**, No. 27, pp. 2873 - 2875, December 1990.
6. Naresh Chand, N.K. Dutta, S.N.G. Chu, A.V. Syrbu, A.Z. Mereutza and V.P. Yakovlev "High performance strained InGaAs buried - heterostructure quantum well lasers fabricated by in situ etching and regrowth", *Appl. Phys. Lett.*, **62**, No. 15, pp. 1818 - 1820, April 1993.
7. Govind P. Agrawal, N. K. Dutta, *Semiconductor lasers* Second Edition. Van Nostrand Reinhold, New York, pp 385-425, 1994
8. A.N. Caliman, S.F. Vieru, G.I. Suruceanu, O.V. Catughin, V.V. Nantoi, V.P. Iakovlev and A.V. Sarbu "Characterisation of in-vacuum cleaved and in-situ passivated laser diode mirrors", *Proceedings of 5th SIOEL-98*, Bucharest, Romania, p. 39, 23-25 September 1998.

SESSION III

Optoelectronic Components: Analysis and Control Methods

Solar cells optimization from spectral response

G.Stoenescu *

University of Craiova, Department of Physics
13 A.I.Cuza, Craiova 1100, Romania

ABSTRACT

We propose a rigorous theoretical simulation of the homojunction solar cell spectral response which allows us to derive the absorption spectra of the given samples and to study the influence of high energy particle beams on the cell performances. Moreover, the computation based on our model provide the values of certain microscopical parameters which are consequently used in solar cells design optimization.

Keywords: solar cells, irradiation, spectral response

1. INTRODUCTION

The action of high energy particle beams (electrons, protons, neutrons, X-quanta) may strongly change the energy spectrum corresponding to the induced crystalline defects in the Si solar cell structure,^{1 2}: one of them implies an increasing in the electron-lattice interaction for the electrons laying in the higher valence states, thus strengthening their localization degree; an other one leads to a decrease in the interaction energy and of the localization degree as well.

One may describe the effects of these phenomena,^{3 4} in terms of the energy gap value and of its variation as a function of the electronic valence states. The energy gap changing is also recognizable in the spectral response of the photocurrent or photovoltage. It is obviously displaced towards smaller wavelengths (larger energy values) in the first analyzed case, while in the second one we measured a displacement in the opposite direction.

A meaningful and rigorous form of the spectral response is given if we use a theoretical model depending on the absorption coefficient $\alpha(\lambda)$, base layer width, top layer width, space-charge width, top and base layer minority-carrier diffusion lengths, top and back -surface minority-carrier recombination velocities, top and base layer minority-carrier diffusion velocities.

We computed these microscopical parameters and their modified values after irradiation showing that the effect on the spectral response is important from the point of view of its displacement towards smaller wavelength values.

2. THE ROLE OF THE PREPARATION TECHNOLOGY AND IRRADIATION PROCESS

We present in this section the technological procedure for the preparation of $\text{Cu}_x\text{Se-CdSe}$ solar cells as well as our studies on the influences of the preparation conditions and irradiation processes on the thin films properties.

The $\text{Cu}_x\text{Se-CdSe}$ solar cells were produced by using: a first electrode obtained by deposition on a glass substrate, after the CdSe thin film has been condensed; a Cu_xSe layer made by dipping in hot CuCl solution (15-40s); an upper grill Au or Au and Cu electrode obtained by thermal evaporation in vacuum.

The CdSe thin films have been obtained by thermal evaporation and condensation in vacuum (10^{-5} torr). The substrate consists of optically flat silica glass heated at 25 up to 370°C temperature. The evaporation temperatures were 700, 760, 780°C . The thickness of the resulted layers was $0.3 - 4.5\mu\text{m}$.

The following parameters were modified during the fabrication procedure: the evaporation chamber pressure ($5 \cdot 10^{-5} - 5 \cdot 10^{-6}$ torr); the evaporation ($700 - 780^\circ\text{C}$) and condensation ($25 - 380^\circ\text{C}$) temperatures; the evaporation duration; the distance between the evaporator and the substrate; the layer thickness; the substrate nature.

The crystalline structure, the size and degree of orientation of the crystallites depend on the experimental conditions during preparation, especially on the substrate temperature during condensation. A clear improvement in this structure was proven to occur when the substrate temperature is increased and the evaporation chamber pressure

Correspondence: Email: gstoen@hotmail.com, Fax: 40 51 415077

is decreased. The electrical resistivity, photoconductivity and optical absorption spectra of the thin films strongly depend on the preparation and further treatments.

The irradiation (3-10 MeV fast electrons) action on the crystalline structure and cells performances was also investigated. Electron diffraction technique was then used in order to study the crystalline structure for various deposition conditions and irradiation parameters.

The structural analysis performed by electron diffraction on CdSe thin films showed a strong dependence on the sample producing technique, specially on the substrate temperature. For low temperatures ($t_s = 25 - 150^\circ\text{C}$), the crystallites have small dimensions ($L \sim 10^{-5}\text{cm}$) and a large number of defects occurs. By contrast, if the temperature is higher ($t_s = 250 - 350^\circ\text{C}$) and the pressure is about 10^{-5} torr, the crystalline structure is clearly improved. In addition, these layers have a better behavior after irradiation, for 7-9 MeV fast electron irradiation, up to $5 \cdot 10^7$ Gy doses.

We used CdSe thin films obtained at various t_s values and then irradiated with fast electrons in order to increase the crystallite dimensions and orientation degree and to decrease the number of non-stoichiometric atoms as well.

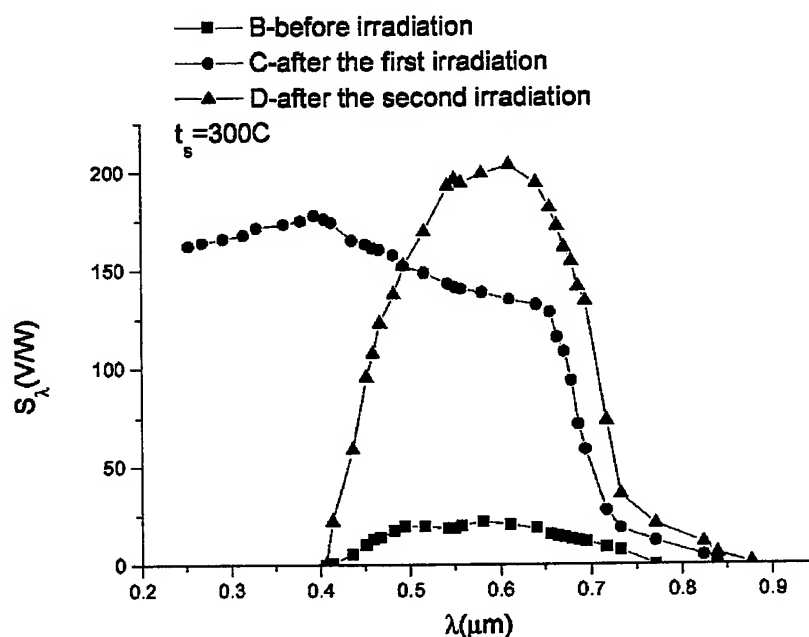


Fig.1 Photoconductivity of the CdSe thin films, for substrate temperature $t = 300^\circ\text{C}$

This effect is based on the mechanism induced by the irradiation process,^{5 6} which, if the dose is large enough, enhances the diffusion of the imperfection atoms (Cd and Se) which in turn may fill the nodal vacancies in the lattice.

The samples were also subjected to a supplementary irradiation having a quite small dose ($1.2 \cdot 10^5$ Gy), in order to avoid the irradiation threshold value corresponding to the maximum in photocurrent values. We show in fig. 1,2 the photoconductivity measurements for two substrate temperatures and unirradiated as well as irradiated samples, proving that an improvement occurs at higher t_s . By contrast, if the original structure of the sample is very poor, the irradiation leads to an increasing of the defects number and even to the appearance of the amorphous phase.

In conclusion, the substrate temperature and the irradiation doses were shown to be the main factors which determine the changing in the cell behavior due to the microscopical modifications.

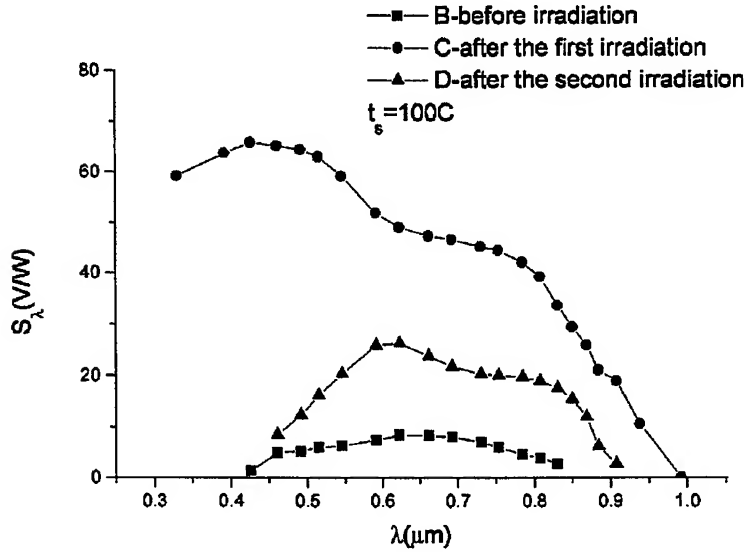


Fig.2 Photoconductivity of the CdSe thin films, for substrate temperature $t = 100^{\circ}\text{C}$

3. CONCLUSIONS AND RESULTS OF THE THEORETICAL SIMULATIONS FOR SOLAR CELLS

Generally, one of the main criteria in selecting the semiconductor materials for preparing solar cells is the stability of their performances under certain variations in the medium conditions and specially under the action of high energy particle beams (electrons, protons, neutrons, X-quanta).

These radiation types may strongly change the energy spectrum corresponding to induced crystalline defects: the one which implies an increasing in the electron-lattice interaction for the electrons laying in the higher valence states, thus strengthening their localization degree; the one which leads to a decrease in the interaction energy and of the localization degree as well.

One may describe the effects of these phenomena in terms of the energy gap value and of its variation as a function of the electronic valence states. The energy gap changing is also recognizable in the spectral response of the photocurrent or photovoltage.

The response is obviously displaced towards smaller wavelengths (larger energy values) in the first analyzed case, while in the second one we measured a displacement in the opposite direction. The experimental results are given in fig. 3, 4. They show a clear dependence of the spectral shift (and of the energy gap as a consequence) on the irradiation doses.

The fitting of the experimental curve is easily obtained by using a double gaussian-like curve:

$$V_{oc}(\lambda) = \sum_{i=1}^2 \frac{A_i}{w_i \sqrt{\pi/2}} \exp \left\{ -\frac{2(\lambda - \lambda_{ci})^2}{w_i^2} \right\} + V_{oo} \quad (1)$$

The effect of the irradiation process on the characteristics of this curve are given by the following values: the position of the first peak is progressively displaced from $0.86 \mu\text{m}$ (the unirradiated cell) down to $0.76 \mu\text{m}$ after the second irradiation while the position of the second peak is displaced from $1.020 \mu\text{m}$ (the unirradiated cell) down to $0.9423 \mu\text{m}$.

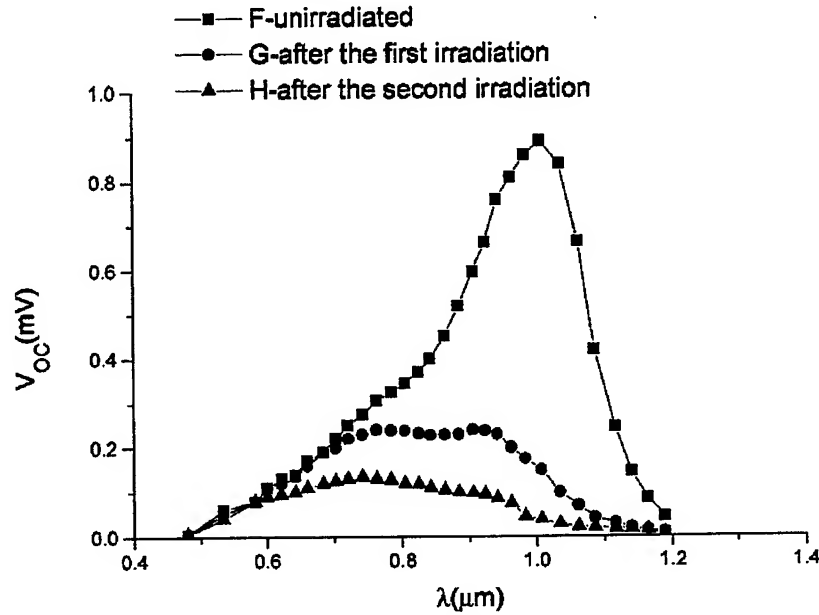


Fig.3 Spectral response of the irradiated and unirradiated samples

One may easily verify that the displacement in the spectral response, which depends on the energy gap value, is determined by the irradiation doses.

A meaningful and rigorous form of $V_{oc}(\lambda)$ is however given if one uses the theoretical model³ described by the following expression:

$$V_{oc} = kT \ln \left(\frac{\phi a_1}{a_2 + a_3 + J_{RB}} \right) \quad (2)$$

where:

$$a_i = f_i(d, \alpha, L_p, L_n, S_p, S_n, D_p, D_n, W) \quad (3)$$

with $i = 1 \div 3$ and the absorption spectra $\alpha(\lambda)$ are known, while the rest of standard denoting refers to the diffusion lengths of the negative and positive charge carriers (L_p, L_n), the widths of the spatial charge domains (S_p, S_n), recombination rates (D_p, D_n), top layer width (W) and barrier width (d).⁷

The explicit expressions of the functions a_i may be written as follows:

$$a_1/e = \left[\frac{\beta_2^2}{\beta_2^2 - \beta_1^2} B_1 - \frac{\beta_2^2 \exp(-\beta_2)}{\beta_2^2 - \beta_1^2} (1 + B_2) \right]_{top} + [(1 - \exp(-\beta_4)) \exp(-\beta_2)]_{barrier} + \left[\frac{\beta_6^2}{\beta_6^2 - \beta_5^2} \exp(-\beta_2) \exp(-\beta_1) (1 + B_3 - B_4) \right]_{base} \quad (4)$$

$$a_2 = \frac{e D_p p_{n0}}{L_p} \left[\frac{\beta_3 \cosh \beta_1 + \sinh \beta_1}{\beta_3 \sinh \beta_1 + \cosh \beta_1} \right]_{top} \quad (5)$$

$$a_3 = \frac{e D_n n_{p0}}{L_n} \left[\frac{\beta_7 \cosh \beta_5 + \sinh \beta_5}{\beta_7 \sinh \beta_5 + \cosh \beta_5} \right]_{base} \quad (6)$$

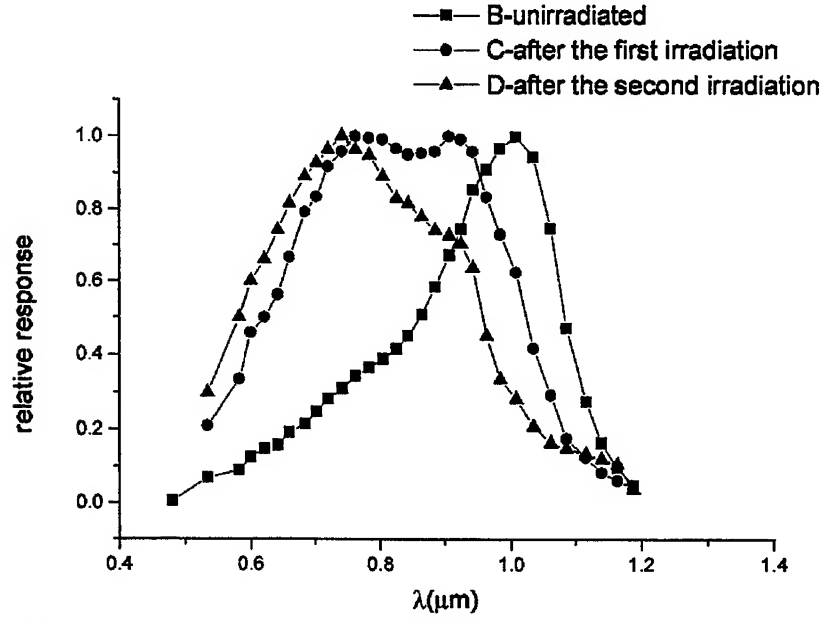


Fig.4 Relative spectral response for irradiated and unirradiated samples

where:

$$B_1 = (\beta_3 \beta_1 / \beta_2 + 1) (\beta_3 \sinh \beta_1 + \cos \beta_1)^{-1} \quad (7)$$

$$B_2 = \frac{\beta_3 \cosh \beta_1 + \sinh \beta_1}{\beta_3 \sinh \beta_1 + \cosh \beta_1} \quad (8)$$

$$B_3 = \frac{(\beta_7 \beta_5 / \beta_6 - 1) \exp(-\beta_6)}{\beta_7 \sinh \beta_5 + \cos \beta_5} \quad (9)$$

$$B_4 = \frac{\beta_5 \beta_7 \cosh \beta_5 + \sinh \beta_5}{\beta_6 \beta_7 \sinh \beta_5 + \cosh \beta_5} \quad (10)$$

and

$$\begin{aligned} \beta_1 &= dL_p; \beta_2 = d\alpha; \beta_3 = L_p S_p D_p; \beta_4 = W\alpha \\ \beta_5 &= LL_n; \beta_6 = L\alpha; \beta_7 = L_n S_n D_n \end{aligned} \quad (11)$$

showing the interplay of the specific combination of cell characteristic lengths and material properties.

The results of the theoretical simulations and experimental measurements are also given in fig. 3, 4 (continuous lines for the theoretical curves), while the specific microscopical parameters are determined by applying the Levenberg-Marquart method for a test function:

$$F = \sum (f_i - f(x_i; z_1, \dots, z_n))^2 \quad (12)$$

where: $f_i = (V_{oc})_i$ are the measured values of the open circuit voltage, $f(\lambda_i; z_1, \dots, z_n)$ are the computed values of the same voltage for the set of wavelengths $\{\lambda_i\}$ and z_1, \dots, z_n are the microscopical parameters to be calculated.

These parameters were computed by minimizing the test function the results being given by the following values:

$$L_n = 8.002, L_p = 7.924; L_p^2/D_p = 25\mu s, L_n^2/D_n = 70\mu s$$

$$\Delta L_n = 0.216, \Delta L_p = 0.114; \Delta (L_n^2/D_n) = 1.005, \Delta (L_p^2/D_p) = 0.973$$

clearly proving that they are modified at irradiation and that the effect on the spectral response is useful from the point of view of the displacement towards smaller wavelength values.

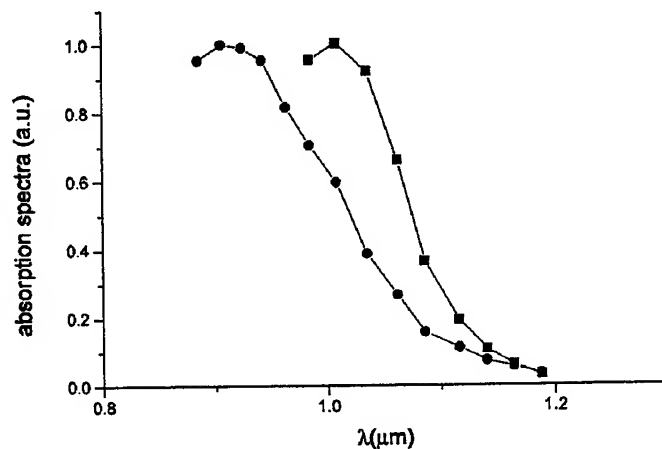


Fig.5 Absorption spectra for unirradiated (squares) and irradiated (circles) samples

One may also have a strong control on their changing when the cells are subjected to high energy particles beams, i.e. in realistic functioning conditions.

Moreover, the dependence $\alpha(\lambda)$, (fig.5, scaled in arbitrary units), may be calculated from the same response spectra, both before and after the irradiation processes, showing the corresponding displacement of the peaks along the wavelength axis. The method we propose in this paper is therefore an appropriate and effective procedure which may be used in the design optimization of the solar cells by taking into account the influence of high energy particle beams on the cell performances.

REFERENCES

1. W.-S. L. J. A. T. Ma, D. Ueda and J. S. H. Jr., "Influence of buffer layer thickness on dc performances of gaas/algaas heterojunction bipolar transistors grown on silicon substrates," *IEEE El. Device Letters* 9, pp. 657-659, 1988.
2. S. J. Fonash, *Solar cell device Physics*, Academic Press, New York, 1981.
3. I. S. P. C. N. B. I. Spanulescu, V. Ruxandra and G. Stoenescu, "The cdse thin films for solar cells," *Anal. Univ. Bucharest* 34, pp. 13-16, 1990.
4. I. S. G. Stoenescu, V. Calian and N. Baltateanu, "Characteristic parameters changes for mos circuits irradiated by fast electrons," *Optoelectronica* 4, pp. 71-74, 1996.
5. C. M. Dozier and D. B. Brown, "Photon energy dependence of radiation effects in mos structures," *IEEE Trans. Nucl. Sci. NS* 27, pp. 1694-1699, 1990.
6. V. Dolocan, *Fizica jonctiunilor semiconductoare*, Edit. Academiei, Bucharest, 1982.
7. I. S. N. B. G. Stoenescu, V. Calian and V. Ruxandra, "The effect of accelerated electron irradiation on electric conductivity of cdse thin films," *Teaching the Science of New Materials proc.*, pp. 314-316, 1995.

Contribution in the study of improved measurement precision through continuous optical focusing on opto-electronic detection devices

Catalin A. Spulber* , Gabriel E. Constantinescu

Research and Design Institute for Optical Industry "Pro Optica S.A."

4, Bucovina St., RO- 74404 Bucharest, Romania

ABSTRACT

This paper reports on minimising measurement errors that are characteristic of small distances of the object plane through continuous focusing of optical systems that concentrate radiation on a typical opto-electronic detection device. One such system is the catoptric objective that uses a focusing system based on the movement of a mobile element inside the objective (e.g. the secondary mirror of a Cassegrain optical system, maintaining a fixed position of the detection device with respect to the primary mirror). Our results show that decreasing the distance between the mobile and fixed element leads to an increase of the focal distance and consequently of the object plane distance. The measurement precision increases with optical amplification, and hence, we studied the way optical amplification changes with a continuous focusing, in two different situations: the detection device is calibrated at the maximum distance and the detection device is calibrated at the minimum distance. Finally, we present different examples of variation of measurement precision for discrete values of properties of some objectives. In order to minimise image-focusing errors for the extreme distances, aberrations optimisation of the optical system for an intermediate position of the object plane was factored in.

Keywords: Opto-electronic detection devices, optics systems, optical focusing.

1. INTRODUCTION

Among the most used opto-electronic devices are those that receive or have an immediate control in image processing in order to display and/or process it, such as those using CCD cameras or those using as a detection element linear or rectangular matrices with IR detectors (IR-CCD).

Many of uses of these devices require minute distances between the object (that is measured) and the opto-electronic device which collects, concentrates and converts radiation emitted by the object, irrespective of the spectral range of these radiation.

Any variation in the distance between the object and the opto-electronic device will change the electric signal strength emitted by the detection elements and ultimately leads to an alteration in image quality¹. Corrections are either through feedback-based (continuous, manual, or automated optical focusing of the optical system on the detection elements plane) or software-based (controlled assurance of the electronic correction of the signal).

The following is a theoretical overview of several manifestations of the errors following this variation of the distance. We chose a catoptric optical system as our example, because it is very simple to correct for the distance by moving one of the two mirrors. The signal degradation was globally evaluated, by analysing the changes in the optical amplification. In order to make things simple, a single detection element is assumed

* Correspondence: E-mail: prooptic@fx.ro

2. PRIMARY CONSIDERATIONS REGARDING OPTICAL AMPLIFICATION

Consider the Cassegrain opto-electronical configuration shown in Fig.1. Optical amplification is defined as a ratio of the illumination in the image plane to that on the object plane. Illumination on the image plane depends on the optical and energetic parameters of the objective: focal length (f_{ob}), diameter of the entrance aperture (D_{ob}), diameter of the detection element (D_d), transverse magnification (β) and the transmission factor (τ_0) on the spectral range.

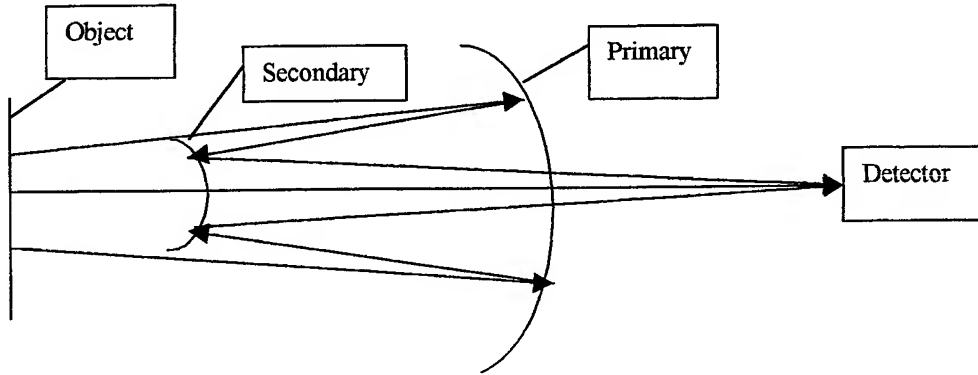


Fig.1 Cassegrain opto-electronical configuration

Optical amplification can be defined as²:

$$A = \tau_0 \omega \frac{D_{ob}^2}{4}$$

$$A = \frac{\tau_0}{4} \frac{D_{ob}^2}{\beta^2 f_{ob}^2} \quad (1)$$

where $\omega = \frac{A_d}{f_{ob}^2}$ is the solid angle covering the measured area on the object plane³, $A_d = \frac{\pi D_d^2}{4}$ and $\beta = \frac{D_d}{D}$. For a catoptric objective in a Cassegrain assembly:

$$\tau = \tau_0 \frac{D_p^2 - D_s^2}{D_p^2}, \quad D_{ob} = D_p \quad (2)$$

where D_p - diameter of the primary mirror, D_s - diameter of the secondary mirror.

Let's consider two different situation of the feedback based correction mechanism: (a) focusing is achieved by moving a mobile element of the optical system, while the detection element is stationary and (b) focusing is achieved by moving the detection element.

2.1 The detection element is stationary – focusing by moving the secondary mirror.

A catoptric objective with the following specifications was considered: $D_p = 50\text{mm}$, $D_s = 22\text{mm}$, $l_s = 11.79 \dots 6.741\text{mm}$, $f_{ob} = 53.40 \dots 90.477\text{ mm}$, $s' = q = 80.18\text{ mm}$. For two given distances: $L=122\text{ mm}$ and $L=512\text{ mm}$, we derived the following values $\beta = -1.186$, $f_{ob} = 53\text{mm}$ and respectively $\beta = -0.226$, $f_{ob} = 90.4\text{mm}$. The ratio of the corresponding

amplifications of the two focal lengths is $\frac{A_{90}}{A_{53}} = \left(\frac{\beta_{53} f_{53}}{\beta_{90} f_{90}} \right)^2 = 9.5$, but the distance ratio is $\frac{514}{122} = 4.2$ only.

Calculations for different values of L and f_{ob} , result in a relation $A=A(f_{ob})$, depicted in Fig.2. One can notice that an increase in the focal length results in an increase in the optical amplification. L and f_{ob} have an inverse relation, and therefore, overall, the optical amplification increases as L decreases.

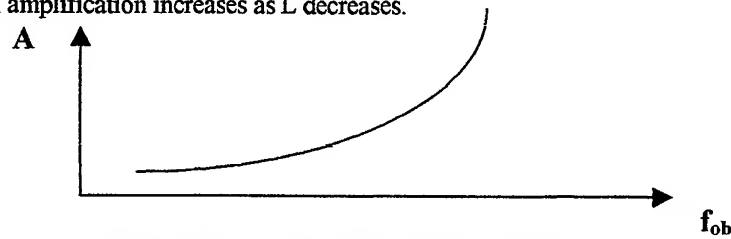


Fig.2 - Aspect of $A(f_{ob})$ function for a given s'

2.2 Focusing is achieved by moving the detection element

In this situation, the following relationship is used²:

$$A = \frac{L_0^2 (L - f_{ob})^2}{L^2 (L_0 - f_{ob})^2} \quad (3)$$

where L_0 – the distance where focusing is performed. Using the same values as in section 2.1, we can derive:

$$\frac{A_{90}}{A_{53}} = \frac{(514 - 90)^2 (L_0 - 53)^2 122^2}{(122 - 53)^2 (L_0 - 90)^2 514^2} = 2.12 \frac{(L_0 - 53)^2}{(L_0 - 90)^2} > 1$$

In order to minimise measurement errors, when continuous focusing is performed on a stationary detection element, for different measuring distances, one needs to minimise the diffusion surface area. A correction must be applied for the size of the diffusion spot for an intermediate object distance, at which the device is calibrated; when the distance is either very large or very small, the size of the spot has minimal variations, in opposite directions. The correction for the diffusion spot is performed by changing the curvatures of the mirrors while keeping the focal length of the objective constant (bending). The size of the spot Tab.1 illustrates various spot sizes when the objective has those particular specifications shown in Tab.3 (optimised case). See also Fig.3...Fig.5.

Tab.1 – Spot sizes for an optimized objective

Size of the diffusion spot = D_{SPOT}		$r_P = -50.779 \text{ mm}$ $r_S = -51.846 \text{ mm}$ $l_S = 11.79...6.741 \text{ mm}$ $f_{ob} = 53.40...90.477 \text{ mm}$ $s' = q = 80.18 \text{ mm}$			$D_P = 50 \text{ mm}$ $D_S = 22 \text{ mm}$ $D_d = 1 \text{ mm}$
L	l_S	β	f_{ob}	D_{SPOT}	
122.72	11.79	-1.186	53.40	+0.5	
155.139	10.21	-0.878	61.25	0	
513.99	6.741	-0.226	90.477	-0.5	



Fig. 3
Aspect of $l_S(L)$ -function for a given s'

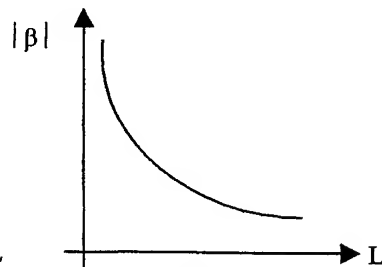


Fig. 4
Aspect of $|\beta|(L)$ - function for a given s'

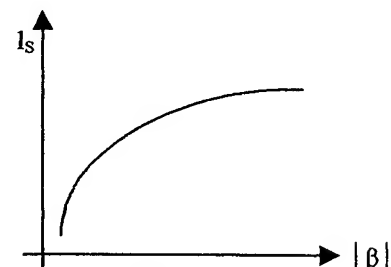


Fig. 5
Aspect of $l_S(\beta)$ - function for a given s'

Conclusion: Optical amplification is larger when focusing is performed by moving the secondary mirror, rather than the situation when the detection element is stationary and the optical system is mobile.

3. EXAMPLES OF CALCULATIONS

3.1 The detection element is stationary, the focusing plane varies depending on the distance from the object plane, and calibration is performed at a finite distance.

Using relationship (3) with the following objective specifications, the data in Tab.2 is obtained (see Fig.6 and Fig.7)

Tab.2 – Values for the optical amplification for an objective with immobile mirrors

Initial objective specifications															$r_p = 105 \text{ mm}$	$D_p = 49 \text{ mm}$
															$r_s = 105 \text{ mm}$	$D_s = 22 \text{ mm}$
															$l_s = 28 \text{ mm}$	
															$f_{ob} = 98 \text{ mm}$	
Calibration performed at $L_0= 70 \text{ mm}$ (see Fig.6)																
$L[\text{mm}]$	70	80	90	100	110	120	130	140	150	160	170	180	190	200		
A_l/A_{70}	1	0.4	0.1	0	0.1	0.4	1	1.8	2.8	4	5.4	7.1	9	11.1		
Calibration performed at $L_0= 200 \text{ mm}$ (see Fig.7)																
$L[\text{mm}]$	70	80	90	100	110	120	130	140	150	160	170	180	190	200		
A_l/A_{200}	0.1	0.016	0.01	0	0.01	0.016	0.1	0.16	0.25	0.36	0.49	0.64	0.81	1		
A_{200}/A_{70}	10	25	10	∞	10	2.5	10	11.2	11.2	11.1	11.1	11.1	11.1	11.1		

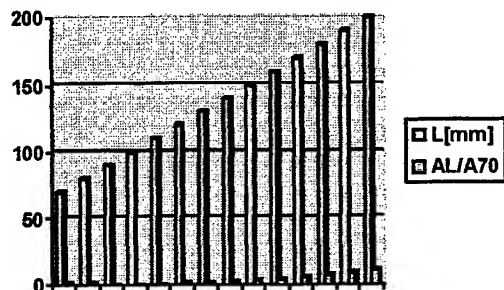


Fig.6 - Modification of amplification with respect to L distance, divided by the amplification for the calibration distance L_0

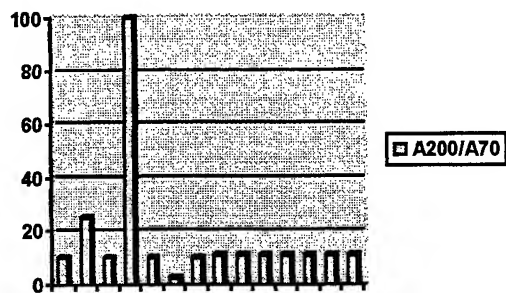


Fig.7 - Ratio of the amplifications for some distances $L=70 \dots 200$ when the calibration distance has the extreme values $L=70$ and $L=200$

3. 2 The detection element is stationary, focusing is independent of the distance from the object plane, focusing is continuous and calibration is performed at a finite distance

In this situation, relationships (1) and (2) are used and the resulting data can be found in Tab.3.

Tab.3 – Values of the optical amplification and the others optical parameters for 4 objectives with mobile secondary mirror

Case 1: Initial objective specifications							$r_p = 32 \text{ mm}$ $D_s = 6.7 \text{ mm}$		$D_p = 15 \text{ mm}$ $l_s = 8.5 \text{ mm}$		$r_s = 32 \text{ mm}$ $f_{ob} = 30 \text{ mm}$			
$L_s [\text{mm}]$	5.1	4.3	3.7	3.2	2.5	2.1	2	1.8	1.7	1.6	1.5	1.4	1.35	1.3
$f_{ob} [\text{mm}]$	50	60	70	80	100	120	130	140	150	160	170	180	190	200
A_f / A_{s0}	1	0.7	0.5	0.4	0.3	0.2	0.2	0.1	0.1	0.1	0.1			
Case 2: Initial objective specifications							$r_p = 32 \text{ mm}$ $D_s = 11 \text{ mm}$		$D_p = 25 \text{ mm}$ $l_s = 9 \text{ mm}$		$r_s = 24.15 \text{ mm}$ $f_{ob} = 38 \text{ mm}$			
$L_s [\text{mm}]$	7.8	7.1	6.7	6.4	5.8	5.5	5.4	5.3	5.2	5.1	5.1	5	4.9	4.9
$f_{ob} [\text{mm}]$	50	60	70	80	100	120	130	140	150	160	170	180	190	200
A_{s0} / A_f	1	1.4	1.9	2.6	3.2	5.7	6.7	7.8	9	10.2	11.5	13	14.4	16
Case 3: Initial objective specifications							$r_p = 105 \text{ mm}$ $r_s = 105 \text{ mm}$ $l_s = 28 \text{ mm}$ $f_{ob} = 98 \text{ mm}$		$D_p = 49 \text{ mm}$ $D_s = 22 \text{ mm}$					
$L_s [\text{mm}]$	39	34	31	28	25	23	21	20	18	17	16	15	14.5	14
$f_{ob} [\text{mm}]$	70	80	90	100	110	120	130	140	150	160	170	180	190	200
A_f / A_{70}	1	0.8	0.6	0.5	0.4	0.3	0.3	0.2	0.2	0.2	0.2	0.15	0.13	0.12
Optimised Case: Initial objective specifications (see Fig.8 and Fig.9)							$r_p = -50.779 \text{ mm}$ $r_s = -51.846 \text{ mm}$ $l_s = 11.79 \dots 6.741 \text{ mm}$ $f_{ob} = 53.40 \dots 90.477 \text{ mm}$ $s' = q = 80.18 \text{ mm}$		$D_p = 50 \text{ mm}$ $D_s = 22 \text{ mm}$					
$L [\text{mm}]$	122.7	130	140	150	160	170	180	190	200	300	400	500		
$F_{ob} [\text{mm}]$	53.40	55.38	57.88	60.16	62.24	64.15	65.92	67.55	69.06	79.76	85.97	90.02		
$l_s [\text{mm}]$	11.79	11.35	10.84	10.41	10.04	9.73	9.45	9.21	9.0	7.72	7.12	6.78		
β	1.186	1.1	1	0.91	0.845	0.785	0.732	0.686	0.646	0.406	0.296	0.233		
A_L / A_{122}	1	1.08	1.19	1.34	1.44	1.58	1.72	1.86	2	3.82	6.18	9.11		
A_L / A_{200}	0.49	0.53	0.59	0.66	0.84	0.78	0.85	0.92	1	1.89	3.07	4.52		
A_{200} / A_{122}	2.01	2.01	2.01	2.01	2.01	2.01	2.01	2.01	2.01	2.01	2.01	2.01		

Note: A_L and A_f are the optical amplifications for current values of the object distance and respectively of the focal length

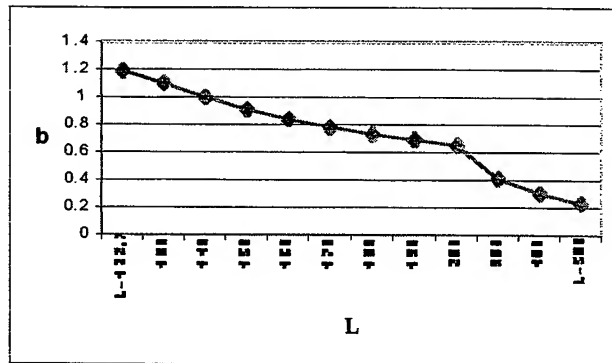


Fig. 8 – Evolution of the magnification β with the change of the L- distance

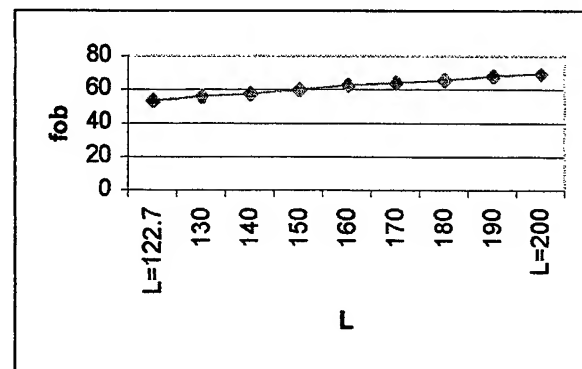


Fig. 9 – Evolution of the focal length f_{ob} with the change of the L- distance

4. CONCLUSIONS

- 1) The main error sources in recording of the radiation by an opto-electronic device are:
 - using a distances between the device and the measuring area that are different than the calibration distance;
 - measuring areas that are smaller than the field of view;
- 2) Image quality can be preserved either by continuous focusing (of the objective) or by moving the entire objective relative to the detection element;
- 3) Using continuous optical focusing results in a decrease in optical amplification as the distance between the two mirrors decreases (catoptric objectives); this decrease is larger for smaller focal lengths, which suggests using larger focal lengths;
- 4) Device calibration at the largest possible distance is an advantage, even if focusing is continuous.

REFERENCES

1. C.Spulber, and O. Spulber, "About the possibility of software optimisation of the measurement precision in radiation pyrometry", *The 4 -th Symposium of Optoelectronics*, Bucharest, pp.23, Sept. 1996.
2. R.G.Driggers and all "Long-range radiometer measurements with a close-range reference", *Applied Optics*, vol. 32, pp. 6072-6076, 1993.
3. C.Spulber, and M. Arion, "On a IR temperature measurement using a radiation ratio pyrometer ", *Revista Romana de Mecanica Fina si Optica* , vol. III, pp. 257-267

Photoconductive frequency-resolved spectrometer

Ioan Burda*, Simion Simon, Gheorghe Cristea, Georgeta Cerbanic,
Lavinia Cociu, Mihai Todica

"Babes-Bolyai" University, Department of Physics, 3400 Cluj-Napoca, Romania

ABSTRACT

The study of recombination lifetimes and kinetics is an essential part of the analysis of recombination mechanisms in semiconductors. The fundamental differences between the experimental techniques, which are used for, frequency-resolved and for time-resolved spectroscopy are present in this paper. A photoconductive frequency-resolved spectrometer (PCFRS) for carrier lifetime determination in semiconductor is described. The PCFRS uses a super-bright light emitting diode, which can be modulated directly and the sample acts as a detector. An embedded system with 68HC11 microcontroller ensures all basic functions of this spectrometer. This PCFRS is designed for a narrow lifetimes range, the operation range is between 0.159 s and 0.159 ms. Typical error is less than 0.5% for the range of lifetimes reported.

Keywords: recombination, lifetime, spectrometer, embedded system, microcontroller

1. INTRODUCTION

The recombination kinetics and lifetimes of a luminescence process often provide evidence crucial to an understanding of its recombination mechanism. Lifetime or decay measurements have been made by many diverse methods, according to the equipment available and time-scale of interest.

The semiconductor materials used for photoresistor can be characterized in a narrow lifetime range, but high resolution in frequency domain is necessary. This is because multi-lifetime or non-exponential dependence is present in these materials. The photoresistor device tested normally has a highly non-linear response, with lifetime dependent on the mean level of excitation. The non-exponential dependence in the low frequency domain contains information about bulk properties¹ of the photoresistor material.

In the archetypal time-resolved spectroscopy (TRS) experiment¹, a δ -function light pulse excites the sample and the luminescence is detected during an infinitely narrow boxcar gate set at some time t_d after the pulse. In principle, only a single excitation pulse is used and the decay curve is obtained from an ensemble of such experiments, each with a different value of t_d .

The simplest form of frequency resolved-spectroscopy (FRS) is the quadrature method in which the excitation is continuous-wave an infinitely small sinusoidal amplitude modulation, and the detection is carries out by using a lock-in amplifier set in quadrature. Thus in FRS the excitation and detection functions are orthogonal δ -functions in frequency space; in TRS they are ideally δ -functions in real time. This is the fundamental difference between the techniques.

In FRS method if the frequency is sweeping the lifetime distribution is generated directly. This is a considerable advantage over TRS where, for non-trivial systems, the lifetime distribution has to be laboriously reconstructed from data from a large number of transient experiments of differing pulse lengths, intensities and periods. A typically photoconductive frequency-resolved spectrometer² (PCFRS) uses a light emitting diode, which can be modulated directly and the sample acts as a detector.

* Correspondence: Email: iburda@phys.ubbcluj.ro; Telephone: +40 064 191315; Fax: +40 064 191906

2. THE SPECTROMETER THEORY

In distant-pairs systems, recombination may be monomolecular over a very wide range of excitation intensity. The probability of recombination between a given electron and some single hole is close to one; the probability of recombination with any other hole is small. First-order kinetics, strictly, should refer to an exponential decay with lifetime independent of carrier density. In a distant-pair system, at low excitation pulse intensities, the kinetics are first-order. This is because the excitation is a small perturbation of the metastable excited state; the carriers injected by the pulse are sparse compared with the metastable carriers and do not interact with each other during their decay.

The experimental system consists of an ensemble of centres with a distribution of lifetime $P(\tau)$. The kinetics is then first-order and monomolecular, although the form of the decay curve is left unspecified. If the excitation is modulated at an angular frequency ω it may be written as

$$G(t) = G_0 + g \sin(\omega t), \quad g < G_0 \quad (1)$$

where G_0 is the excitation rate and g is amplitude of the modulation. For a component of the luminescence with a lifetime τ , we may then write

$$I(\tau, t) = \int_{-\infty}^t \tau^{-1} \exp[-(t-u)/\tau] \{G_0 + g \sin(\omega u)\} du = G_0 + g(1 + \omega^2 \tau^2)^{-1} [\sin(\omega t) - \omega \tau \cos(\omega t)]. \quad (2)$$

The lock-in output is

$$S(\tau) = (2\pi)^{-1} \omega \int_0^{2\pi/\omega} I(t) R(t) dt, \quad (3)$$

and for quadrature the lock-in response function $R(t)$ is given by

$$R(t) = -\cos(\omega t), \quad (4)$$

giving

$$S(\tau) = g / [(\omega \tau)^{-1} + \omega \tau], \quad (5)$$

and the lock-in output from all lifetimes components as the frequency sweep is

$$S(\omega) = \int_0^{\infty} P(\tau) S(\tau) d\tau. \quad (6)$$

The response of the in-phase FRS method, it is merely necessary to replace $R(t)$ above by

$$R(t) = \sin(\omega t), \quad (7)$$

giving

$$S(t) = g / (1 + \omega^2 \tau^2). \quad (8)$$

The in-phase FRS gives the integral of lifetime distribution, between the limits $\tau \sim (\omega)^{-1}$ and ∞ , while the quadrature FRS gives the lifetime distribution directly.

The foregoing analysis assumes that the emission comes from a set of centres whose lifetime distribution is independent of excitation power (or independent by the pump rate G). This condition is not satisfied in two cases: optical saturation of long-lives centres and distant-pair recombination. The effect of optical saturation is to quench the contribution to the FRS signal; if the modulation amplitude g is finite, higher harmonics will be generated.

Distant-pair recombination is no optical saturation of long-lives centres in the usual sense. The density of pairs of very large separation does not depend on G . Pairs of these large separation therefore do not contribute to the FRS signal.

The depth of modulation g/G_0 is typically 10% to 50% in practical FRS experiments; those ensure a signal-to-noise ratio superior in comparison with TRS technique. Because the PCFRS technique uses the sample acts detector the depth of modulation can be fixed up to 20 % with very good discrimination performance. The excitation power is very low because only a super-bright LED also commercially available ensures the light. But all this experimental condition in approximation of this theory can be an advantage. The performance of the signal generator (responsible for light modulation) and lock-in amplifier is very important in PCFRS technique.

The FRS and TRS are complementary methods. But only for single lifetime systems with an exponential decay, and lifetimes less than a microsecond. Where signals are weak, or superimposed on a DC offset, the superior signal-to-noise ratio of FRS and its positive rejection of unmodulated signals are strong advantages.

In Fig. 1 is shown the typically quadrature (D) and in-phase response function (C) of the FRS method. The data plotted in Fig. 1 contain real data collected with PCFRS described in present paper using at sample a commercially photoresistor. The multi-lifetime is present in this sample and non-exponential response is observed.

A good agreement is obtained by comparison¹ with a quadrature FRS obtained from a RC filter, the resonance is obtained for $\omega RC = 1$ or $\omega\tau = 1$. Also, a very close ideated experiment with RC circuit can be making for simulate the classical generation-recombination experiment.

Except the trivial case of a single lifetime, data reduction is carried out by curve fitting or by deconvolution. All this complex data processing can be make with a complex data acquisition system, the parallel data processing is a very fast solution.

2. THE SPECTROMETER

Homewood, Wade and Dunstan² have presented the measurement principles of a PCFRS, using commercial LEDs as the source of light. In this case the modulation (AC component) and DC level can be applied directly by driving the LED from a signal generator. The semiconductor sample response (photoconductivity) to the modulation is measured using quadrature lock-in detection.

The block diagram of PCFRS is shown in Fig. 2. The principal parts of this spectrometer are host systems (an IBM PC), the embedded systems with 68HC11 microcontroller and the analog signal processing part. With a general purpose 68HC11 microcontroller³ the signal generator and data acquisition for

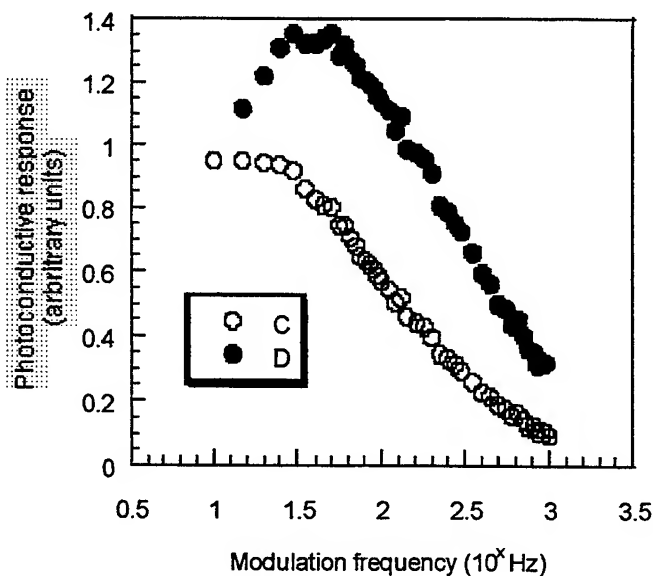


Fig. 1 The quadrature FRS response function (D) and in-phase FRS response function (C).

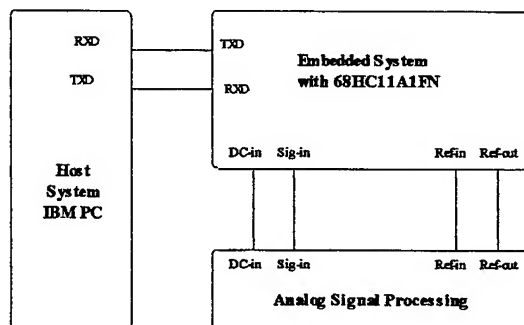


Fig. 2 The block diagram of the photoconductive frequency-resolved

measuring the sample photoconductivity. The output signal of the amplifier is applied at the Sig-in input. For semiconductor samples, the level of the DC component is also measured through the DC-in signal. This external circuitry is sufficient to implement all functions because the internal peripherals of the microcontroller can be adapted by software for this application.

2.2. Software

Very important for this application is the output-compare function (TIMER) which is used for the generated PWM signal with duty cycle specified in a buffer memory (maximal 8192 bites, sine wave). Any waveforms can be obtained with this technique (DDS-Direct Digital Synthesizer)⁵.

The acquisition data and control of PCFRS is performed by the embedded system (with MC68HC11A1FN). The time critical task performed by the embedded system generates the PWM signal (Ref-out), reads the value of the signal response of the semiconductor sample (Sig-in), reads the value of the reference signal (Ref-in) and stores these data in two internal memory buffers.

The PWM signal (OC1 and OC2 is used together to produce one PWM output) with period of 128 μ s and resolution of 500ns is generated with a duty cycle specified ($128/0.5 = 256$ which is the resolution for duty cycle of 0 to 100 percent) in a buffer memory. This task only produces duty cycles of 50 to 100 percent. When a smaller duty cycle is specified, it is automatically changed to 100 percent minus the specified duty cycle, and the polarity of the output is switched. To perform all these functions, only 128 μ s is available; the real performance of the task is 116 μ s. The maximal resolution in frequency in this configuration is less than 1 Hz and can be customized over a large range. An auxiliary square wave signal is available at the OC4/OC1 pin for testing, or eventually, for external chopper synchronization.

The maximum measurement points are 8192 (N) and the same number is available for the PWM buffer memory (limited by RAM memory of the embedded system, 24 K-byte all buffers). The particular situations are important in practice; if the resolution in frequency must be equal to 1 Hz (0.999936 Hz), 7812 measurement points ($1s/128 \mu s = 7812.5$) are necessary. In this situation, the PWM signal with frequency equal to 1 Hz is composed of 7812 samples ($q = 1$). For a PWM signal with frequency equal to 1 kHz for each signal period ~ 8 samples are used ($q = 1000$); in other words, in the wrong case $f_m \approx 8 f_r$. If the frequency resolution can be 10 Hz (10.0096 Hz) only, 782 points of measurement are necessary. In this particular case the measurement is very fast.

Typical error is less than 0.5 percent for the range of frequencies reported. This performance is possible though the mode of synchronization between the signal generator and the measurement and is limited by the 8-bit resolution of the ADC subsystem.

The host system performs the next sequence: initialize the number of point measurements (N), perform and transfer duty cycles for the sine wave to the PWM buffer memory of the embedded system and command the acquisition task. After loading all the data, these are performed in accordance with Fourier analysis⁵ and quadrature lock-in detection.

The nonlinear transfer characteristics of amplifiers and low-pass filters at low and

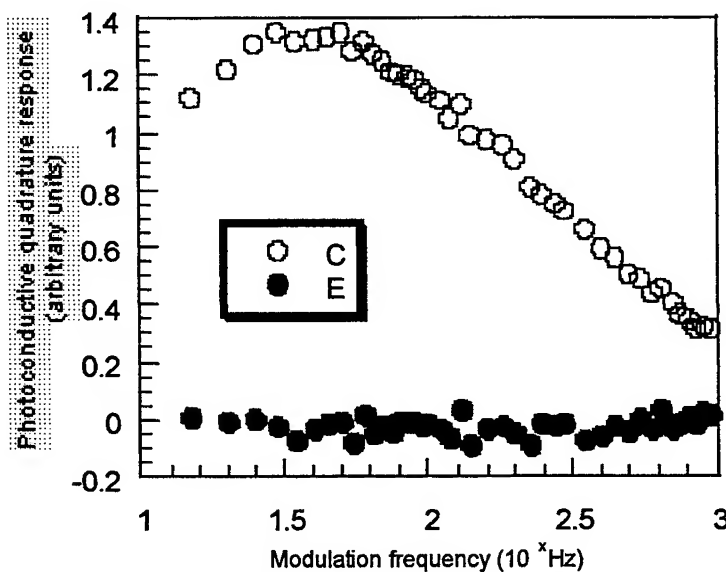


Fig. 4 The noise signal (E) obtained by deconvolution from the quadrature PCFRS response (C)

high frequencies is also corrected through software by the program (written in C language), which is implemented in the host system at the end of the measurement of all frequencies. The program also has tasks of measuring the level of AC and DC components for the output signal, which drives the LED and the DC level of the semiconductor sample. In Fig. 4 (E) is shown the noise signal obtained by deconvolution⁶ from quadrature PCFRS response (C), if the sample is a commercially photoresistor. All this complex data processing demonstrates the power and flexibility of the present spectrometer.

3. CONCLUSIONS

In this paper we present the fundamental differences between the experimental techniques which are used for frequency-resolved and for time-resolved spectroscopy. The FRS technique applied in particular case of PCFRS is capable of superior discrimination and can give better signal-to-noise ratios, enables unambiguous interpretation, free of the problems that arise by the build-up of a metastable background population.

An embedded system with 68HC11 microcontroller ensures all basic functions of this spectrometer. The performance of this PCFRS is the operation range (between 0.159 s and 0.159 ms) at 1 Hz frequency resolution and the typical error is less than 0.5% for the range of lifetimes reported.

ACKNOWLEDGMENTS

It is a pleasure to acknowledge to Motorola literature center for documentation and software support. This material is based upon work supported by the CNCSU under grant No. CNCSIS - 212.

REFERENCES

1. S. P. Depinna and D. J. Dunstan, "Frequency-resolved spectroscopy and its application to the analysis of recombination in semiconductors," *Phil. Mag.* B50, pp. 579-597, 1984.
2. K.P. Homewood, P. G. Wade and D. J. Dunstan, "A simple photoconductive frequency-resolved spectrometer for carrier lifetime determination in semiconductors," *J. Phys. E: Sci. Instrum.* 21, pp. 84-85, 1988.
3. M68HC11RM/AD, *Reference Manual*, Motorola INC., 3, 1991.
4. S. Cova, A. Longoni and I. Freitas, *Sci. Instrum.* 50, p. 296, 1979.
5. Rohde Ulrich, *Digital Frequency Synthesizers, Theory and Design*, Pentice-Hall, 1983.
6. D. Goldfarb and A. Idnani, "A numerically stable dual method for solving quadratic programming," *Math. Programming*, 27, pp. 1-33, 1983.

Improved method for processing Newton's rings fringe patterns

Adrian Dobroiu^{*a}, Adrian Alexandrescu^b, Dan Apostol^a, Victor Nascov^a, Victor Damian^a

^aNational Institute for Laser, Plasma and Radiation Physics, Laser Department,

PO Box MG-36; București-Măgurele, Romania

^bUniversity "Politehnica", București, Romania

ABSTRACT

A new method of processing Newton's rings fringe patterns is presented. After the center of the circular rings is found, a special type of pixel intensity spectrum is calculated, in which the two-dimensional pattern is reduced to a one-dimensional profile showing a periodic structure of fringes. By further processing the parameters of the initial interferogram can be easily extracted. The statistical nature of the method (achieved by taking into account all pixel intensities) leads to a higher accuracy and a better immunity to noise.

Keywords: fringe processing, Newton's rings, interferometry, feature extraction, spherical wavefront, curvature radius

1. INTRODUCTION

Newton's rings fringe patterns are often encountered when dealing with experiments such as interference of spherical wavefronts or piston movement in holographic interferometry. Processing of these patterns must be able to provide useful information about the curvature radii or the amount of movement. Our paper presents a new improved processing method for calculating the parameters that determine the fringe pattern, owing its efficiency to the statistical consideration of all pixel intensities.

2. INTERFEROGRAM DESCRIPTION

In the case of a Fizeau-type interferometer, the intensity of a Newton's rings fringe pattern one obtains is given by the following formula:

$$I(x, y) = E^2 \frac{R_1^2 + R_2^2 - 2R_1R_2 \cos\left(\frac{4\pi}{\lambda} h(x, y)\right)}{1 + R_1^2R_2^2 - 2R_1R_2 \cos\left(\frac{4\pi}{\lambda} h(x, y)\right)}, \quad (1)$$

where E is the amplitude of the incident wave, R_1 and R_2 are the reflectivities of the two surfaces (in terms of amplitude), λ is the wavelength, and $h(x, y)$ is the distance between the two surfaces at position (x, y) , as given below for spherical surfaces:

$$h(x, y) = h_0 + \left(r_2 - \sqrt{r_2^2 - d^2}\right) - \left(r_1 - \sqrt{r_1^2 - d^2}\right) \approx h_0 + \frac{d^2}{2} \left(\frac{1}{r_2} - \frac{1}{r_1}\right), \quad (2)$$

* E-mail: dobad@ifin.nipne.ro

with r_1 and r_2 being the curvature radii of the two surfaces and d is the distance from the current point (x, y) to the point of minimum (or maximum) spacing between surfaces, denoted by h_0 . The parabolic approximation is applicable for most practical situations.

Fringes generated in holographic interferometry by piston movement differ from those described above only in their profile, which is sinusoidal:

$$I(x, y) = 2E^2 \left[1 + \cos \left(\frac{4\pi}{\lambda} h(x, y) \right) \right]. \quad (3)$$

In either case, the interferogram will contain circular concentric rings, whose spacings decrease when going outward from their common center. A simulated interferogram obtained by supposing a Fizeau-type setup is shown in figure 1.

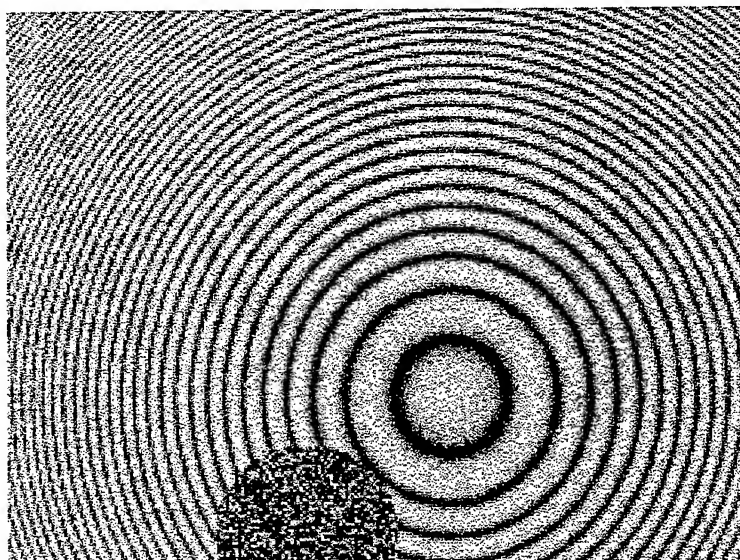


Figure 1. Simulated interferogram. Noise amplitude was taken 25% of the fringe uniform contrast. At the bottom there is a region with no visible fringes used for checking the ability of the method to ignore fringeless zones.

3. PROCESSING METHOD

If the curvature radius of one of the surfaces is known, the other can be calculated by analyzing the fringe structure in the interferogram. Processing of such fringe patterns starts with finding the center of the circular fringes. This can be achieved automatically by applying one of the already developed algorithms.¹⁻³ We developed our own routine, which allows us to find the ring center with an error of around 1 pixel. This paper is only focused on the subsequent steps.

Once the center of the rings has been found, their successive radii must be measured. Then, irrespective to the fringe profile (sinusoidal or not), the unknown surface curvature can be calculated using the formula

$$d_k^2 = \frac{k\lambda - 2h_0}{\frac{1}{r_2} - \frac{1}{r_1}}, \quad (4)$$

where k indexes the consecutive rings, which gives the squared radii of the bright (or dark) rings.

The processing method we propose here consists in building a spectrum of the pixel intensities as a function of the distance to the ring center. The novelty is that the channels of this spectrum are arranged in a parabolic manner, that is, the channels are equidistant in d^2 rather than in d . The idea was suggested by equation (4) itself.

The squared distance from each pixel to the ring center is calculated and its intensity is stored in the corresponding channel. After the whole interferogram was taken into account, every spectrum channel contains the mean intensity of all pixels whose squared distance to the ring center falls within that channel. Such a spectrum is given in figure 2.

The most important effect of this non-linear arrangement is that the fringe profile seen in the spectrum becomes periodic, while a linear spectrum would show widely spaced fringes at lower channels and narrow ones at the other end. Equispaced fringe profiles obviously allow simpler and better further analysis. Hence, a Fourier transform (see figure 3) can be applied to the spectrum in order to determine the fringe spacing, Δd^2 , which is related to the unknown surface curvature through equation (4):

$$\Delta d^2 = \frac{\lambda}{\frac{1}{r_2} - \frac{1}{r_1}}. \quad (5)$$

For instance, if the reference surface is flat, $r_1 = \infty$, and $\Delta d^2 = \lambda r_2$.

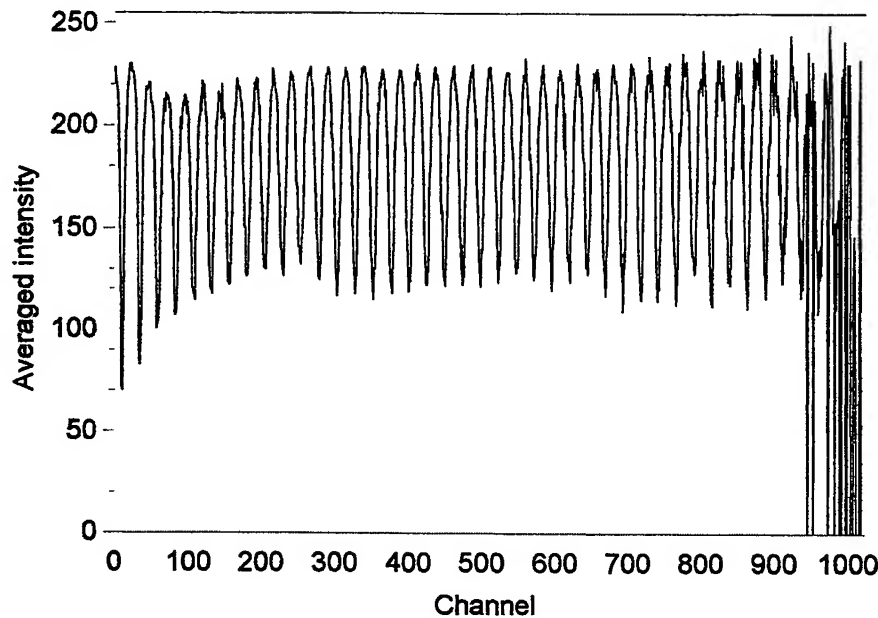


Figure 2. The pixel intensity spectrum versus the squared distance to the ring center, calculated for the interferogram in figure 1. The maximum channel index (1023) corresponds to the largest d^2 in the field. The breaks at the end of the spectrum (starting around channel 940 here) are due to the fact that toward the corners of the interferogram the channel population decreases significantly and there are some channels in which there is no pixel to be taken into account for the average intensity calculation. In these channels the intensity was taken arbitrarily zero.

Using several peaks in the Fourier transform (when the fringe profile is not sinusoidal, as it is the case when working with Fizeau interferometers) increases the accuracy of fringe spacing computation. Also, each of these peaks can be fitted with a continuous curve (such as spline), which allows a better estimation of the peak position than the rough integer index of the maximum value.

A better approach was tested and gave very satisfactory results: After the fast Fourier transform of the spectrum is calculated and the peak corresponding to the spectrum periodicity is found, another Fourier analysis is performed at a number of *intermediate* frequencies, between the left-hand and the right-hand neighbors of the peak frequency. Then the frequency is chosen which leads to the maximum Fourier amplitude. While the simple choice of the peak in the fast Fourier transform array allows a resolution of ± 0.5 fringe, our approach can give results up to 100 times more accurate.

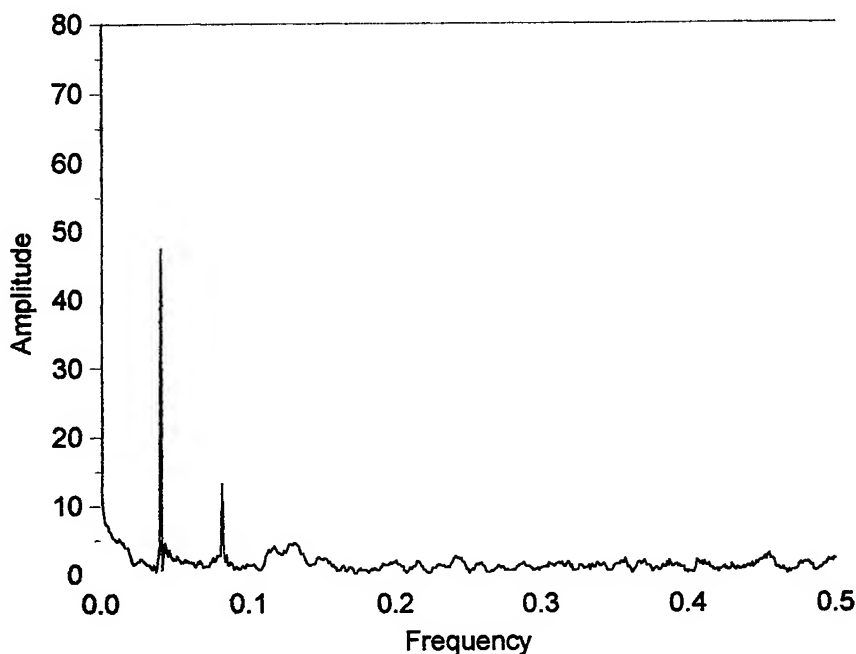


Figure 3. The Fourier transform of the spectrum reveals the periodicity of the fringe profile, thus allowing the calculation of the unknown surface curvature radius.

Another advantage provided by the non-linear choice of the channel arrangement is that all channels are roughly equally populated (about the same number of pixels are taken into account for each channel), for distances less than the closest margin of the interferogram to the ring center. This happens because the number of pixels found at distances falling within a given range grows parabolically when going outward, which is compensated by the parabolic division of the spectrum into channels.

The statistical nature of the spectrum (due to the averaging of pixel intensities within each channel) is yet another advantage as the process produces a noise-suppressed result. Thus, the method we present here has the qualities of a spin filter.⁴ The Fourier analysis of the spectrum continues this feature of equal participation of all pixels.

The spectrum also contains information about the reflectivities of the two surfaces, hidden in the fringe profile. If one surface has a known reflectivity, by further processing one can establish the unknown reflectivity.

4. TESTS

Tests were performed on real and simulated interferograms. Simulations were very useful as a testing tool because they allowed a wide range of situations, hardly attainable experimentally, as well as a direct verification of the results.

In ideal cases, with noise-free uniformly illuminated images, the surface curvature was retrieved with an accuracy much below 1%. In situations closer to real world interferograms (comprising a 25% noise, variable illumination and large areas with invisible fringes) an accuracy of around 1% was obtained. For example, the curvature radius of the simulated test surface that produced the interferogram in figure 1 was found with an error of 0.8%.

Unwanted moiré effects appeared when simulating small curvature radius surfaces and affected the overall accuracy. These effects are greatly reduced if the simulation performs an integration of the calculated intensity at the pixel level (rather than just calculating the intensity in the point at the center of the pixel), much as a real CCD camera would do, which does prolong the computing time, but is workable even on slow machines. Another idea is to calculate the intensity still in one point for each pixel, but locating this point randomly in the square area corresponding to the pixel. This approach dramatically reduces the moiré effect, but when fringes become very narrow (comparable to the pixel size) an intense noise appears instead of the usual uniform gray level that is seen in actual interferograms.

Tests on an experimental spherical mirror showed a sufficiently good accuracy as to match the focal length measurement obtained by means of geometrical optics, despite the fact that the digital camera we used (Sony's Mavica FD7) had an unexpected aspect ratio of about 104:100. Elliptical instead of circular fringes appeared and not only the precision of the ring center retrieval was altered, but also the fringe spacing assessment.

The accuracy of this method depends on the following parameters:

- ◆ the efficiency of retrieving the ring center;
- ◆ the circularity of the fringes, which can be affected both by a non-spherical shape of the surfaces and by an aspect ratio of the camera different from 1:1;
- ◆ the number of channels in the spectrum, if it is so small as to become comparable with the number of rings;
- ◆ the amount of noise present in the interferogram;
- ◆ the knowledge of the wavelength, the pixel size and other geometrical or optical parameters that intervene in the image formation.

Most of the parameters above can be improved. For instance, the aspect ratio of the camera can be changed to become 1:1 by a preliminary stretching of the interferogram on one dimension, which also greatly helps the ring center finding routines. An actual stretching needs not to be performed if the algorithm is implemented with the possibility of specifying non square pixels.

A few details are worth being mentioned about the influence of ring center accuracy on the overall error of the method. Simulations allowed the assessment of this influence by making possible the spectrum computation in two cases: with the exact position of the ring center, and with the position as found by our centering routine (or an intentionally displaced position). If the exact center position is input to the fringe profiling procedure then curvature radius evaluation errors were generally found to be less than 0.2% (in situations close to actual interferograms). If the centering routine is able to find the ring center with an error of about 2 pixels then the curvature radius error increases to as much as 1.5% in some cases.

Generally, the curvature radius estimation error is around 0.5%, and is not much influenced by the noise level. As expectable, this error decreases for larger interferograms. For a given dimension of the interferogram (in pixels) there seems to be an optimum range for the number of fringes in the interferograms that leads to small errors. For example, if the interferograms are recorded in 160×160-pixel matrices, the number of fringes must be between approximately 7 and 50 for the final error to be less than 1%. This range corresponds to a curvature radius range of almost one order of magnitude, in our simulations from 0.35 m to 2.2 m; this range can be shifted using zoom optics. If larger images are used, then the upper limit can be pushed higher because it is only imposed by the insufficient sampling of the fringes. On the other hand the lower limit is fixed due to the fact that with decreasing fringe numbers the Fourier transform becomes unable to discern these numbers exactly, by detecting the peak position.

5. CONCLUSION

A new type of intensity spectrum was introduced to better manipulate the interference data contained in a Newton's rings fringe pattern. Tests showed a good accuracy of the final result (surface curvature) even in difficult conditions. The statistical nature of the method proves once again its superiority over the topological techniques, which are easily disturbed by defects and noise present in the image.

REFERENCES

1. David W. Robinson, "Automatic fringe analysis with a computer image-processing system," *Appl. Opt.* **22**(14), pp. 2169-2176, 1983.
2. Hugo D. Navone and Guillermo H. Kaufmann, "Automatic digital processing in speckle photography: comparison of two algorithms," *Appl. Opt.* **28**(2), pp. 350-353, 1989.
3. Guillermo H. Kaufmann and Gustavo E. Galizzi, "Digital processing of dual-plate speckle photography data," *Appl. Opt.* **31**(10), pp. 1537-1541, 1992.
4. Qifeng Yu, "Spin filtering processes and automatic extraction of fringe centerlines from interferometric patterns," *Appl. Opt.* **27**(18), pp. 3782-3784, 1988.

Computer assisted electropneumatical system to compensate the sag of an optoelectrical detector

Marian Blejan^{a*}, Petrin Drumea^a, Ioana Enache^a, Mihai Marin^a
Brindus Comanescu^b, Daniel Oancea^b

^a Hydraulics and Pneumatics Research Institute, 14 Cutitul de Argint St., code 75212, Bucharest 4, Romania, Ph: 00401.336.39.91 Fax: 00401.337.30.40

^b Institute of Optoelectronics, 111 Atomistilor St, PO Box MG 22, code 76900, Bucharest, Romania

ABSTRACT

This paper present an electropneumatical system computer assisted for compensate the sag of an optoelectrical detector. This system is used for compensate the sag of a frame of an optoelectrical detector during the fabrication. For push-up group we use pneumatically servocylinders which allowed a very precise control of the sag through force. Each servo cylinder includes a proportional pressure regulator for regulating the pressure proportional to a specified electrical nominal value. The system is controlling by a PC with 2 acquisition board, one of them for monitoring the force of the transducer (regulated quantity) and the other board for controlling the pressure of the gas (command quantity) in servo cylinders. The software subsystem for developing the tuning numerical algorithm contents WIN 98 operating system, TestPoint rapid application development platform for data acquisition and graphic user software and Delphi rapid application developing platform for real time control algorithm module.

Keywords: electropneumatical systems, servocylinders, data acquisition systems

1. INTRODUCTION

The experiences clung by the development of the optoelectrical detectors which control the interaction proton-proton make necessary to used some devices by high technology like the computer aided electropneumatical system which assure compensation of deflection of the optoelectrical detector spacer because of the weight force during the fabrication.

This is realized by introduction in detector spacer two long tubes at the each end and two tubes on its middle, which are supported on each end by a servopneumatic system. The pressure inside the servopneumatic cylinders determines the forces, which trough the bars are transmitted to the detector spacer.

During the fabrication six precision blocks sustain the optoelectronic detector; the deformation, due gravitational force, is compensated with pneumatically system by applied force in some calculated points of SAG¹.

2. PNEUMATIC SYSTEM

The pneumatic system showing in Fig 1, is composed by:

- two compressed air prepare units (filter-regulator)
- eight pneumatic servocylinders
- interconnection elements

* Correspondence: E-mail: ihp@fx.ro

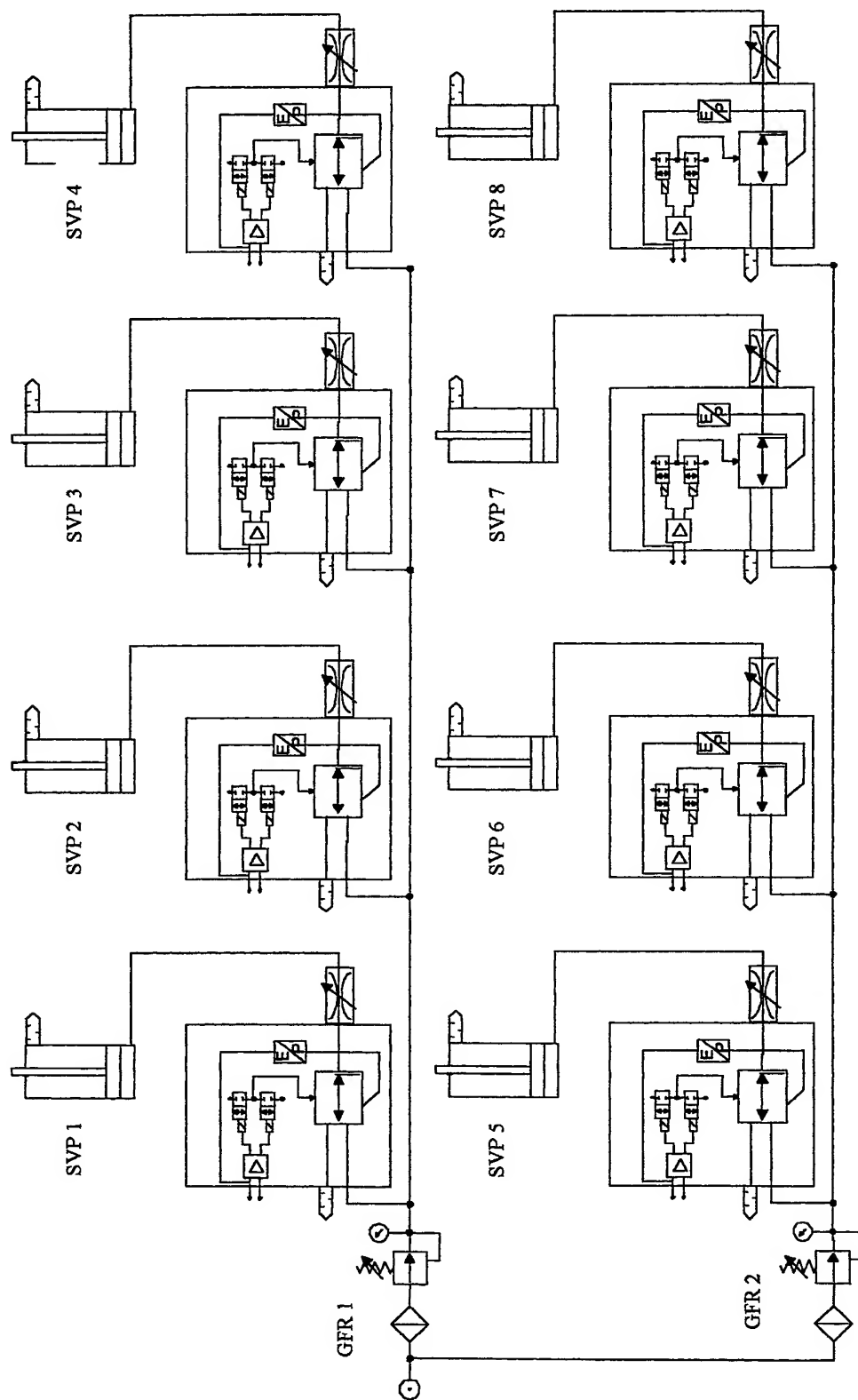


Fig. 1 Sag compensation. Pneumatically diagram

2.1. Compressed air prepare unit

The compressed air prepare unit (filter-regulator), has the role to filtrate the compressed air to input on the system and to according the system pressure to the desired value irrespective of pressure fluctuations in the supply. The filter and regulator are combined into a single unit, which has a manometer, releasing water and automatic purge. The regulated pressure range is 0...12 bar with a nominal flow by 3400 l/min and filter rating 40 μ m. On the input system must be assured a flow by 3000 l/min at a minimal pressure by 6,5 bar.

2.2. Pneumatic servocylinder

The eight pneumatic cylinders have the role to compensate the optoelectronic detector spacer deformation by force developed in the cylinder rod.

They can assure movements with various speeds obtained with throttle valve, which is situate behind pneumatic cylinder and the necessary forces through proportional pressure regulator.

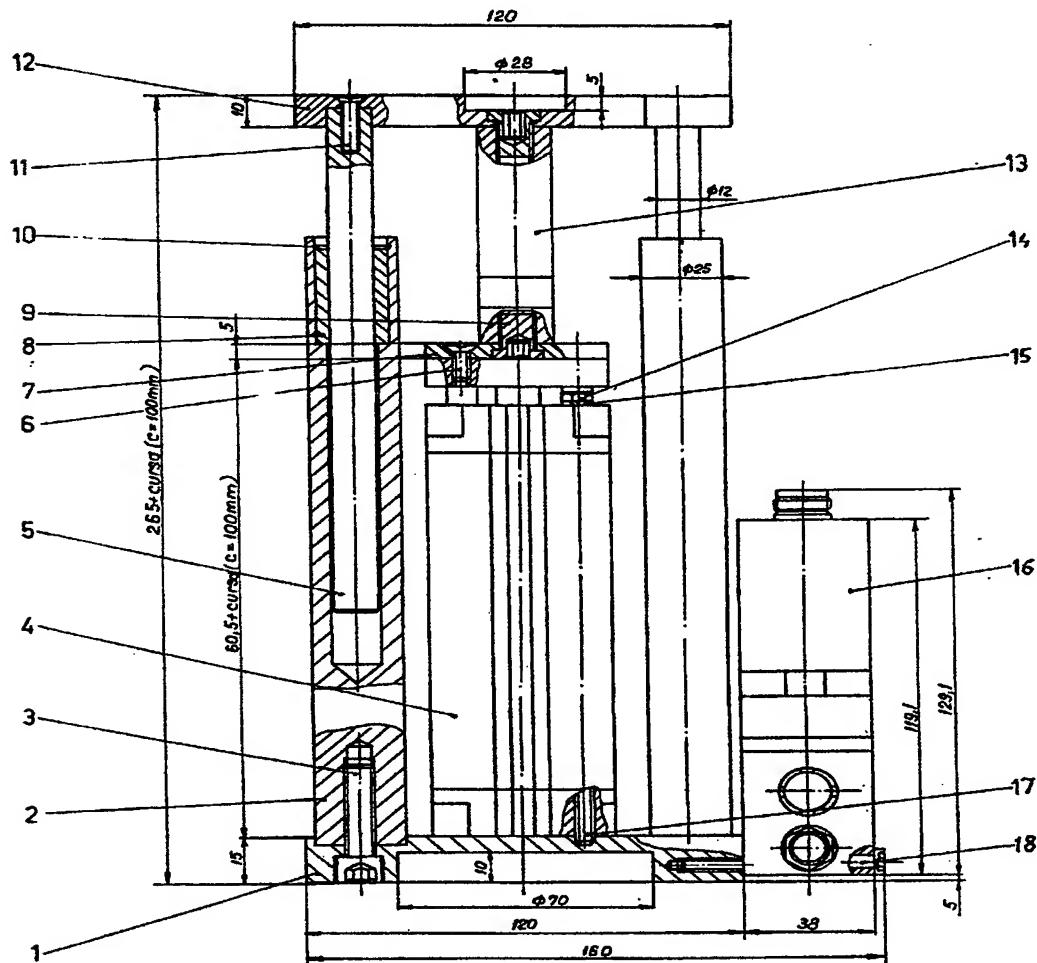


Fig.2 Pneumatical servocylinder – SVP

Each pneumatic servocylinder SVP, as is showing in Fig. 2 is composed by:

- one proportional pressure regulator
- one throttle valve
- one pneumatical cylinder secured against rotations;

- d) one force transducer
- e) one mechanical system for support and guide

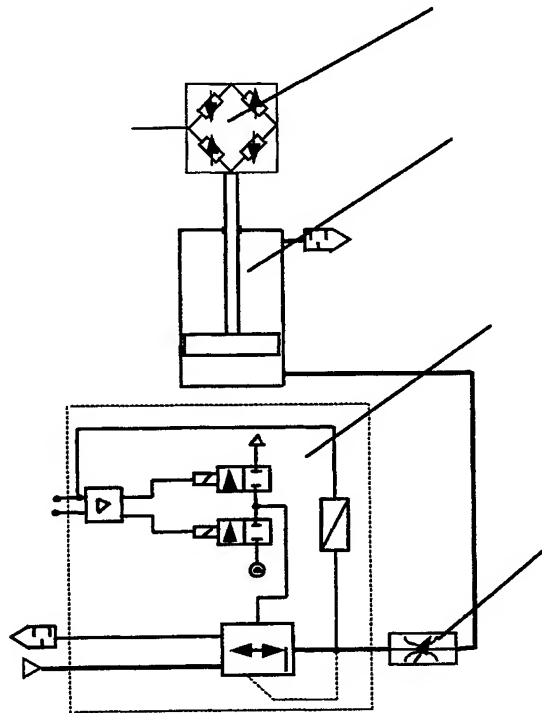


Fig. 3 Pneumatically servocylinder diagram - SVP

The diagram of the pneumatic servocylinder is showing in Fig. 3

- a) The proportional pressure regulator controls the output pressure at the working air connection. The electronic control compares the pressure value with the nominal value. If the nominal and actual values differ, the regulating valve will be actuated until the output pressure is the same as the nominal value. The features of this proportional pressure regulator are:
 - maximum work pressure – 12 bar;
 - pressure range 0...10 bar;
 - medium – compressed air, filtered(40 μ m), lubricated or unlubricated;
 - power consumption – max. 3,6 W
- b) The throttle valve is used to regulate airflow necessary to control piston speed of cylinder. Airflow is approximately equal in both directions and can finely adjusted between 0...350 l/min at pressure between 0...10 bar.
- c) The pneumatically cylinder is non-rotating with yoke plate and guide rods type. It is assembled in vertical position to assure the vertical movement of system at required forces and speeds. The most important parameters of this cylinder are:
 - piston rod diameter - 32 mm;
 - maximum stroke – 100 mm
 - maximum work pressure – 10 bar;
- d) The force transducer is situated at pneumatic cylinder rod end and gets information about push force of optoelectronic detector spacer and sends this information to the data acquisition and control system.

- e) The mechanical system for support and guide is used to sustain the optoelectronic detector spacer and assures an action on the same axis of gravitational force with servocylinder force on the transducer axis.

3. DATA ACQUISITION AND CONTROL SYSTEM

The data acquisition and control system, showing in Fig 4, is developed based on the personal computer with Pentium II – 400 MHz, processor and 64 MB RAM which include two data acquisition boards such as an analog inputs board – DAS 1802 ST and an analog outputs board – DDA 08. The pressure form inside of pneumatic servocylinders is monitoring by a pressure transducer built-in pressure proportional regulator and the regulated force is monitoring by a force transducer. To supply the pressure proportional regulator and load cell the system use a power supply 24Vcc/40W. The software support used to developed this application is Windows '98 operating system, rapid application development software Delphi 3, advanced software operating ASO Win '95 / 32 bit –software support to handling acquisition boards. These elements are use to develop the software which control the system also to develop the communication software between pneumatic sub-system and process monitoring system (high level system).

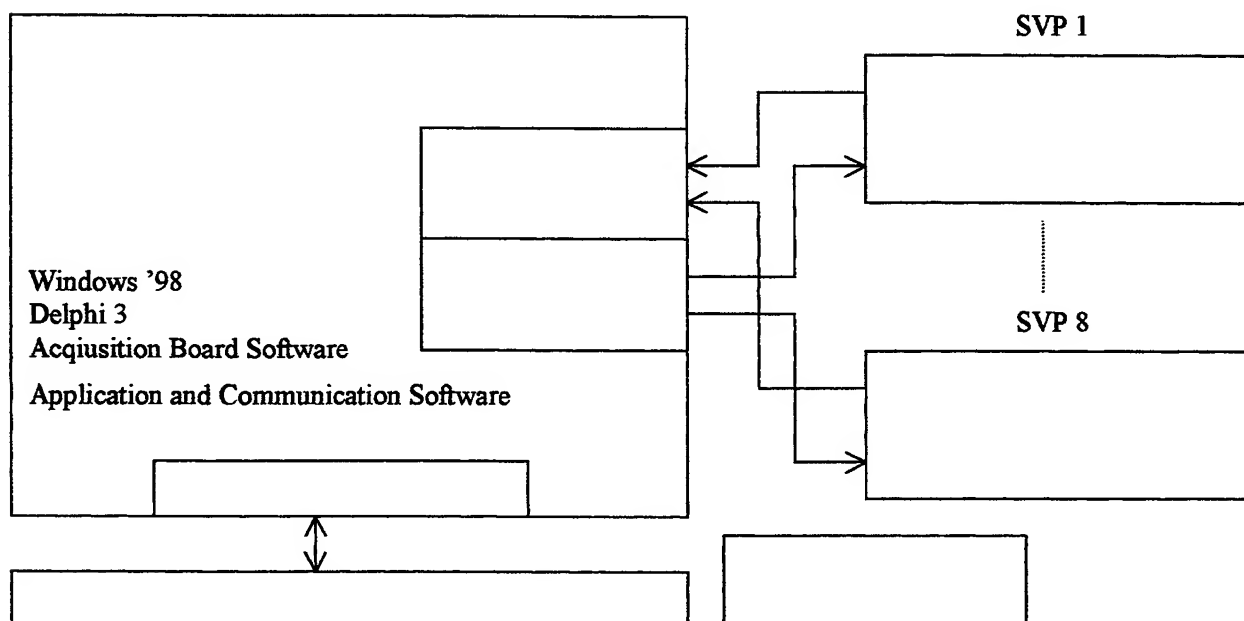


Fig.4 Acquisition and control system diagram

The load cell from the rod of servopneumatical cylinder allows reading of the rod load in 0...100 Kg range with 0.02 % error and converting this regulated quantity to 4-20 mA two wire signal².

The analog inputs board DAS 1802ST monitoring the load cells and the pressure transducers on the servopneumatical cylinder (eight channels for the load and eight channels for the pressure) with an individual gain for each channel, 333,3 KSample/s data trough rate and 12-bit resolution. For high-speed process data this board allow DMA transfer⁵.

The analog output board DDA 08 drives all eight nominal values of proportional pressure regulators in 4- 20mA range with 12-bit resolution⁶.

The proportional pressure regulators and the load cells are supplies by a 24 Vcc/40W stabilized power supply. Also this system includes two connection boxes and wires required binding all devices of pneumatically system.

The purpose of pneumatically system is to control the load of the each pneumatically servocylinders in 0...400 N range with 0.5 N precision respecting load program of each servocylinders. The data acquisition and control system is required for monitoring and control the pneumatically system⁴.

The pneumatically servocylinder consist of a pneumatically cylinder drives by a proportional pressure regulator which allows an easy control of the rod load⁵.

The precisely control of the rod load is obtained with load cell data through software control of the pressure nominal value from proportional pressure regulator.

4. APPLICATION SOFTWARE

The application software is purpose to obtain a precisely driving of rod load and monitoring and transmission of system status to up-level system (process monitoring system).

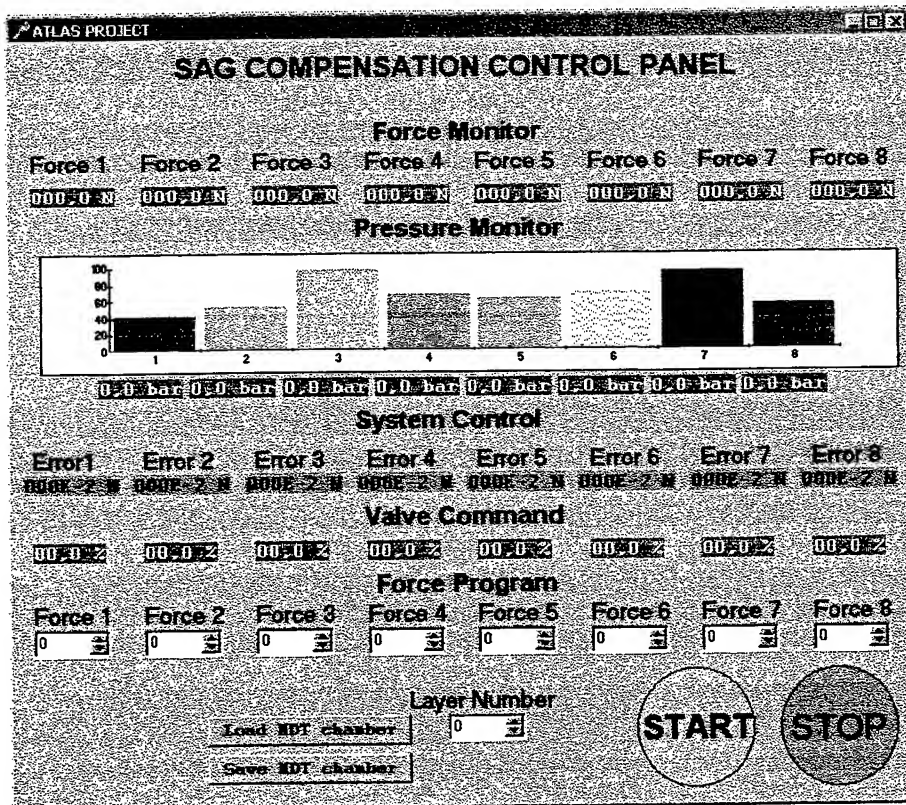


Fig. 5 Application panel

The application panel which is the pneumatically system user interface is showing in Fig. 5. Application panel offers evolution of interest quantities on the system respectively load and pressure on the cylinder rod. Also the panel offers data about regulation process like pressure nominal value, load error value. Other function of this software is reading and writing files which contains load nominal values (on the many instances of the mounting). Starts and stops regulation process is special regime of the nominal load value respectively slow ramp of this; this regime is triggered on the "Start" and "Stop" buttons. Also this software offer the server application for the up-level system which monitoring mounting process.

Software support for run-time is WINDOWS98 operating system, acquisition boards drivers (DLL libraries) and virtual memory driver for shared the memory between application and acquisition boards drivers. For application development is also necessaries acquisition boards configuration software and 32-bit rapid application development software Delphi 3.

5. CONCLUSIONS

- The electropneumatical system for compensate the sag of an optoelectrical detector was designed with modern devices, able to allow all features required.
- The electropneumatical system was designed like a mechatronical system when the electronically and pneumatically devices are functionally combined, directly and locally guided by the information system.
- The system developed by the Institute of Optoelectronics and Hydraulics and Pneumatics Research Institute assure independent control of the load on each cylinder.
- The system was designed, as an open system to allow futures developments if is necessary to update the regulation strategy.
- The system is flexible, easy maintenance and robust control.

REFERENCES

1. C. Capoccia, S Cerioni and B Esposito, *Cross-plate compensation in the assembly of the MDT chambers*, 1998.
2. M. Blejan, P. Drumea, A. Mirea and I. Enache, "Regulatoare numerice destinate automatizarilor electrohidraulice" *Rev. HIDRAULICA*, nr. 1, 1999.
3. M. Blejan, P. Drumea and M. Comes, "Servoamplifier for Proportional Hidraulic Valves Used in Automatization Systems" *2-nd Symposium Microelectronics Tehnologies and Microsystems*, Lviv, June 15-17, 1998.
4. ***, *Pneumatically catalogue Festo*, SMC, Bosch, Parker, 1999.
5. ***, Keithley Metrabyte, *DAS 1802ST and DDA 08 User's guide*, 1999.
6. ***, Keithley Metrabyte, *Function Call Driver User's guide*, 1999.

Optoelectronic systems - products design of world-class

Letitia Tanase^{a*}, Maria Cucu^b

^a Institute of Optoelectronics, Str. Atomistilor nr.1, Bucharest – Magurele, ROMANIA

^b Research and Design Institute for Production Systems, Sos. Oltenitei nr. 107-111, Bucharest, Romania

ABSTRACT

Product designing is one of the phases of the project management. The Quality System's elements, referable to design, are included in the project management. The product definition in accordance with the stated and implied requirements, is the most important phase for the product's quality. Obviously, the sooner the best solution is selected and the deficiencies detected, the better the product quality will be, and at better price. From here, it results the importance of the design and Quality System planning. Design is a creative task which starts with stated needs and existing Knowledge, and ends with definition of a product that satisfy those needs and is industrially feasible. The products must be designed for the client's, not the company's benefit. The products that don't have the right set of features won't be as well saleable those products that have the right set of features. The best design may fail if it's not correctly planned. Quality planning provide a structure that helps a successful project. The emphasis is made on learning the concepts and abilities, on tools and techniques required to build Quality.

"It is not because things are difficult that we do not dare, it is because we do not dare that they are difficult." (Seneca)

Keywords: Quality assurance, quality control, designing, world-class products

1. INTRODUCTION

The optoelectronic systems with image intensifiers have nowadays applications in different areas: military, industrial or scientific. They allow an important increase of acquisition capacity of information from different objects, in low level at light and low signal conditions. A large spectrum at wavelengths, from X-rays to near infrared, can be converted in visible.

The optoelectronic systems, with image intensifier have nowadays an appreciable extension in many applications. They are not limited any at the night vision and they have many industrial and scientific applications. For this last, the optoelectronic systems with image intensifiers are complied with CCD almost in every case. By a good choice of input window and of type of photocathode, the spectrum of frequencies can be also selected for every application. The choice of screen's type for these systems is important concerning the rapidity of system's work.

The variety and complexity of extant systems require a realistic selection of components and a well controlled based a mathematics design, depending a concrete application. Generally speaking, an optoelectronic system with image intensifier can be considered like a "black box", with input and output terminals represented by objective and ocular, which couples the message received from target disposed in object field with the operator's visual receive, in order to analyze and make a decision. The ray modulated by the object arrives at input terminal of system and, after it is transformed by optoelectronic process, an output image is formed. The operator who analyses it and makes a decision views this image. This assembly is presented in Fig. 1¹.

* Correspondence: Phone: (401) 780.66.40; Fax: (401) 423.25.32

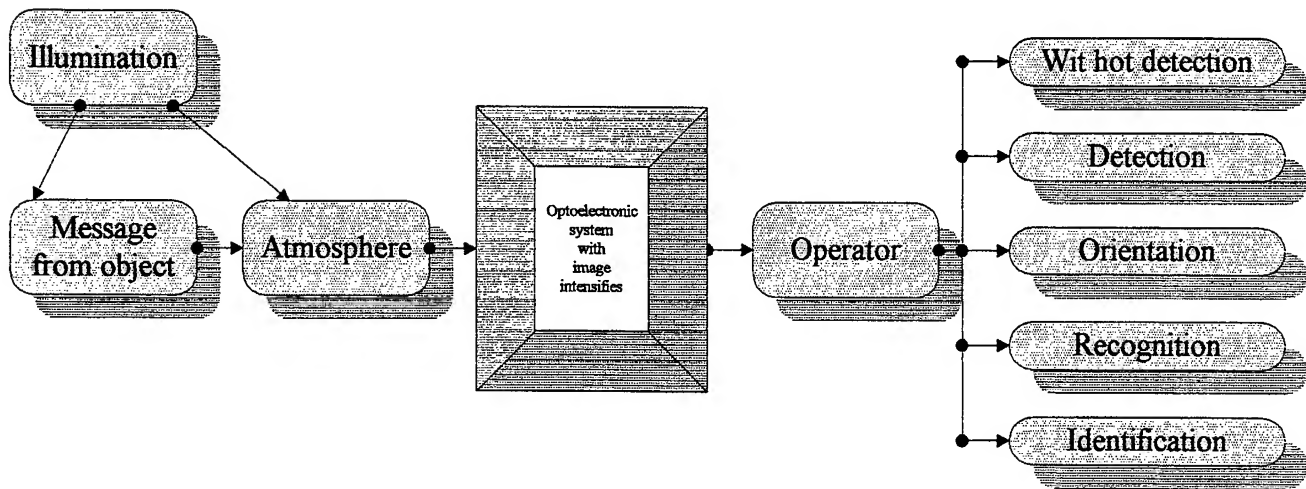


Fig. 1 Proces de formare a imaginii in sisteme optoelectronice cu intensificator de imagine

The design is "a creative activity which, starting from expressed needs and from extant knowledge, finally defines a product which satisfies these needs and it is possible to manufacture".

Products should be designed to benefit the customer. Products should not be designed for the benefit of the company. Products that do not possess the right mix of features and are free from defects will not be as saleable as those products that do. Companies who do not follow these and other quality tenets often suffer from the loss of revenue and the cost of poor quality. Since one of the success factors for our products is its ability to address customer needs, we should look at their influence. A customer is anyone affected by our work. Customers ultimately define quality for our products for us. Knowing our customers is critical to the quality planning process. Identifying our customers and discovering their needs will allow you to design the right mix of product features, which will meet those needs. One of the major obstacles you will be able to avoid is the costly delay that results from continually redesigning products because they do not possess features customers prefer or to overcome defects missed during planning⁴.

The best project can fail when it was not planned properly. Quality planning will provide a structure to help successfully complete any project. The emphasis is placed on learning the concepts, skills, tools, and techniques needed to build quality into your product.

The term quality has evolved to mean different things for different people at different times. A short definition of quality is "Quality means meeting or excelling customer expectations". This short definition incorporates 2 dimensions:

- **Particular characteristics of the product.** In the customers' eyes, higher quality means providing more of the feature or characteristics customers prefer.
- **Freedom from deficiencies.** This is when the product, a particular product feature, as collection of features functions properly as it was design Ned. In the customers' eyes, the fewer the defects, the higher the quality.

Successful quality planning projects address both dimensions identifying the correct features and providing them without deficiency. Having the right mix of customer features that are free from deficiencies increases customer satisfaction and decreases their dissatisfaction. This not only elevates the saleability of the product, but it also reduces the likelihood that customers will defect to purchase a competing product.

Organizations succeed only if the customers are willing to use and pay for the goods and services provided. We attract customers by offering products that match their needs. We retain those customers by continuing to provide products that are free of deficiencies. Research has shown that there are specific practices, which help top companies thrive. These management practices are what is collectively known as Total Quality Management. TQM succeeds because it leads to Delighted customers. Providing product features that meet customer needs attracts customers and promotes customer satisfaction. Continuing to provide products that are free of defects and deficiencies retains customers by reducing customer

dissatisfaction. When deficiencies exist, adding more product features will not overcome customer dissatisfaction unless the deficiencies are also removed^{2,6}.

2. THE JURAN TRILOGY

Managing for quality requires that an organization plan for the quality of its products, improve them at a revolutionary rate, and control its processes to maintain quality. These three interrelated managerial processes are known collectively as The Juran Trilogy^{7,8}.

1. **Quality planning** designs new goods and services that meet customer needs. It ensures that the right set of good or service features is delivered and that deficiencies are kept to a minimum. Quality planning may also be used to redesign existing goods and services or plan new processes such as product development. A process is an "ensemble of independent resources and activities which transforms the input data into output data". In an organization, we can consider that different technical and administrative activities make up an ensemble of processes and that these are a concatenation of activities achieved with human and material means, information and methods or procedures. Each process is characterized by measurable entrance data, an added value, measurable exit data, where corrections, corrective actions or preventive measures, are possible, and thereby, an improvement becomes possible (Fig. 2)⁹.
2. **Quality improvement** deficiencies in existing goods, service, or processes. Reaching a new level of performance is frequently referred to as a breakthrough.
3. **Quality control** ensures that the results of the first two processes are sustained over time¹⁰.

The Juran Trilogy illustrates the three managerial processes of quality and how they fit together. The decision to design these products is based, primarily, on such factors as changes in the technology or the market, benchmarking, and/or strategic business plans.

3. DESIGNING WORLD CLASS PRODUCT

In order to control a design activity, there are *ten elementary steps* in the design process:

1. Establish what the customer's need and expectations are;
2. Convert the customer's need into technical specifications;
3. Prepare a feasibility study, in order to establish if the requirements can be achieved;
4. Plan the necessary activities, in order to achieve the specified requirements;
5. Provide and organize adequate resources;
6. Prepare a study for the project definition in which the optimum solution is selected from several variants;
7. Develop a specification in which all the product's features are detailed;
8. Manufacture a model or prototype of the products;
9. Make additional tests in order to establish if the product meets the requirements and satisfy the customer's needs;
10. Introduce the gathered data into the design process in order to initiate actions aimed at improving quality of product and process.

The design and development plans have to identify the necessary activities, who will make them, when they begin and when they finish. An advantageous skill is to use a network-diagram, which makes the correlations between all activities. It is necessary to elaborate plans for each new project and for each modification of an existing project in order to improve the performance of the product⁷.

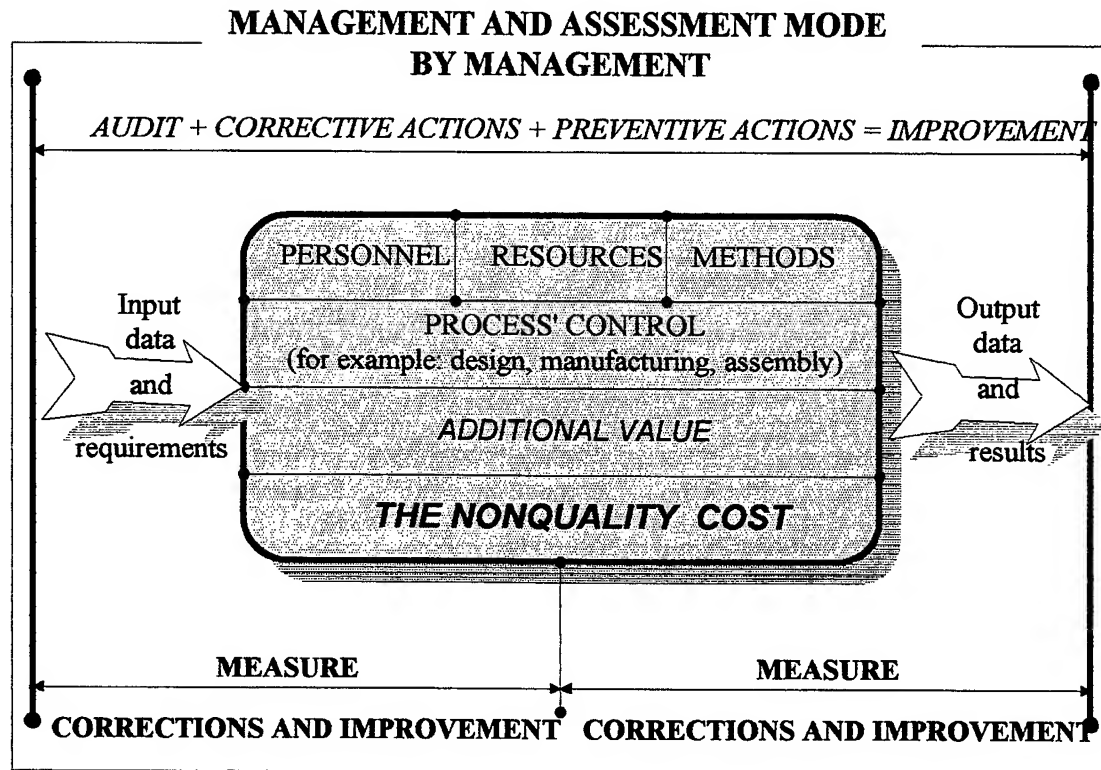


Fig. 2 Tackling the improvement of process

Designing and development aren't complete until it isn't demonstrated that the project meets the specified requirements. That is why the design and development plans must contain the project's test and validation activities too¹¹.

The ten steps mentioned above can be grouped in *four fazes* of the evolution of a product:

- *The feasibility phase;*
- *The project definition phase;*
- *The development phase;*
- *The manufacture phase.*

For that reason, the design and development plans may consist in four separate documents, each for one of the above phases, and each document containing details of the next phase. In order to maintain control over all the activities, it may be necessary to prepare separated plans, to which the general plan may referee. The design process steps are descried in Fig. 3⁸.

The design process represents the phase between the design requirement receiving and the output producing (Fig. 4).

3.1. Design Review

The design review represents a part of the design control process, in which the design performance is measured, the design is compared with the prescribed requirements and the feedback io provided, so that the deficiencies are corrected before the approach of the next phase. Although the design documentation have passed through a verification process, the purpose of the design review is not to evaluate these documents, but to subject the design to assessment of an independent team of experts, in order to establish if the solution selected is the best. The design review must reveal the deficiencies of the designing, before their elimination becomes too expensive. Depending on the design complexity and the risks implied, the following design reviews may be necessary:

- The design requirement review: it establishes if the design requirements may be met and that they reflect the customer needs, before the beginning of the design activity.
- The concept review: it establishes if the concept meets the requirements, before the design is finished.
- The preliminary design review: it establishes if all the risks have been diminished/ removed, and all the development specifications have been prepared for each subelement of the product, before the beginning of the detailed design activity.
- The critical design review: it establishes if the detailed design of each part of the product complies with the development specification and if the product specification has been prepared before the manufacture of the prototype.
- The review in view of the design qualification/ validation: it establishes the design configuration and that the design may be subjected to qualification before the beginning of the demonstration phase.
- The final review: it establishes if the design meets the development specification's requirements, before preparation for manufacturing.

The difference between verification and validation:

- Verification compares design output to input; it is the *producer's* point of view.
- Validation ensures that the product meets user needs and requirements; it is the *customer's* point of view.

3.2 Design Verification

There are 2 types of verification: the verification activities made on the product's components in order to establish the compliance with the specifications; and the verification of the final design in order to establish its performance. The adequate phases of verification follow the review program, but may include additional phases. Design verification must be done when there is a verifiable output. When a system is designed, there are design requirement for each subsystem, equipment, unit, and the like, until the last component and material. The verification may take the form of document review; test and demonstrations; alternative calculations; comparison to other designs, and the like.

3.3 Design Validation

The verification demonstrates that the design is right; the validation demonstrates that it's the right design. Design validation is an evaluation process, which establishes that the design meets all the user's requirements. Validation goes beyond the verification, by the establishment of safety characteristics and performance limits.

Design Validation may take the form of qualification tests, by which the product is tested till and beyond the design limits, in order to collect operational and performance data. Also, the product is subjected to performance tests and maintainability test, in specified functional conditions⁵.

4. QUALITY PLANNING ROADMAP

Quality planning is a structured process designed to create products that meet customer needs and are free from deficiencies. The steps of the process are:

1. Establish Project
2. Identify Customers
3. Discover Customer Needs
4. Develop Product
5. Develop Process
6. Develop Process Controls/ Transfer to Operations

Measurement is crucial at each step of the process. From the very beginning, it is essential to establish ways to measure goals, customers, customer needs, product features, and quality control, and, finally, to measure the effectiveness of the plan to operations. Measurement of the results of activities within each of the six steps and the results of the steps themselves helps to ensure that a quality planning project meets specific quality goals. Measurement usually takes the form of gathering and analyzing data, such as surveying customers, establishing quality goals, establishing the means for measurement, and simulating and testing prototypes against these goals.

<i>Stage</i>	<i>What is required?</i>
Design Planning	<ul style="list-style-type: none"> ➤ Procedures for each activity ➤ Responsibilities identified ➤ Resource adequate; qualified resources ➤ Interfaces between groups defined ➤ Communication between groups established ➤ Plans updated as design evolves
Design Input	<ul style="list-style-type: none"> ➤ Design requirements identified, including: <ul style="list-style-type: none"> ✓ Acceptance criteria ✓ Requirements of regulatory bodies ✓ Proper functioning ✓ Safety characteristics ➤ Reviewed for adequacy ➤ Incomplete, ambiguous or conflicting requirements resolved
Design Output	<ul style="list-style-type: none"> ➤ Technical documents to be used from production through servicing (drawings, specifications, instructions and procedures) that are crucial to safe functioning of the product, including: <ul style="list-style-type: none"> ✓ Operation ✓ Storage ✓ Handling ✓ Maintenance ✓ Disposal ➤ Output documents to be reviewed before release
Design Review	<ul style="list-style-type: none"> ➤ Scheduled reviews of development status with all participating groups ➤ Record of reviews maintained
Design Verification	<ul style="list-style-type: none"> ➤ A plan to verify that output meets input. Techniques may include: <ul style="list-style-type: none"> ✓ Alternative calculations ✓ Comparison to other designs ✓ Tests and demonstrations ✓ Document review
Design Validation	<ul style="list-style-type: none"> ➤ A plan to validate that user needs and requirements are met <ul style="list-style-type: none"> ✓ Follows successful verification ✓ Defined operating conditions ✓ Normally done on final product ✓ May have different validations for specific intended uses
Design Change	<ul style="list-style-type: none"> ➤ A plan to control design changes before implementation <ul style="list-style-type: none"> ✓ Identify ✓ Document ✓ Review ✓ Approve

Fig. 3 Design Stages

4.1 Quality Planning Steps

1. Establish the Project

The six steps of Quality planning can be explained through a series of logical questions that planners need to answer. An organization starts the planning process by first selecting the goods, services, or processes to be designed or redesigned. The Questioning process begins with a series of inputs or known information. Given what we know about markets, customers, technology, the question to be answered is: "What do we want/ need to build?" The answer to this question establishes the kind of product to be built. However, one cannot plan in the abstract. One cannot develop an effective plan unless specific goals have also been established. A more complete answer to the question will provide a greater focus for the team. These specific goals are vital to both the team and the organization because they become indicators of success for the final design. This mission statement is passed on to the team that verifies whether the statement meets the criteria of an effective mission.

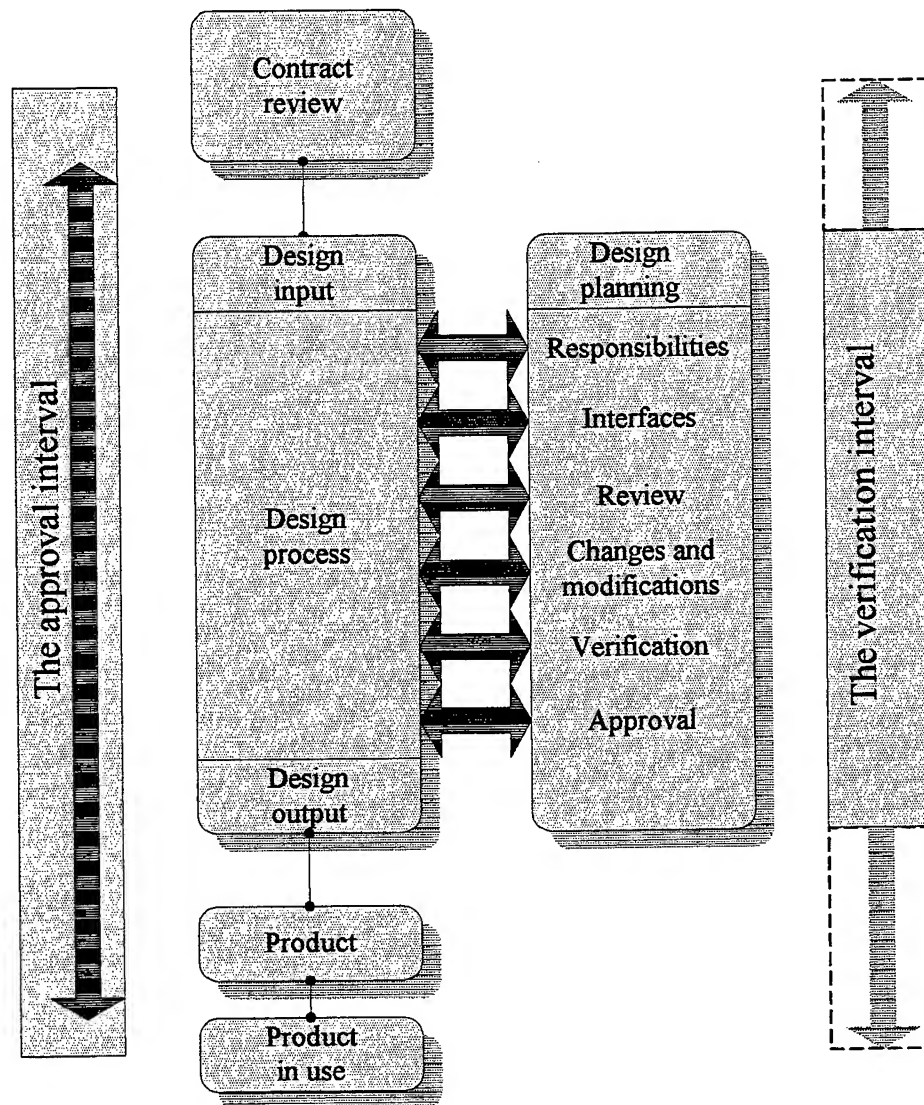


Fig.4 Design Process

2. Identify customers

Once the project has been established and the team knows what they want to create, the next logical question to ask is "For whom are we building this?" The answer to this question will lead the team to identify the most critical or vital few external and vital few internal customers. Many organizations and many planning teams often assume they know their customers are. Although the buyer is certainly important, he or she may represent only a small percentage of individuals affected by the product. Typically, customers include suppliers, end users, new and potential customers, and the media or governmental agencies that are affected when products may fail. Other customers are internal. They include the workers who create the product or deliver the service, sales people who sell the product, customer service representatives who answer customer questions, etc.

3. Discover customer needs

Now that we know the product we want to create and for whom it will be built, the third question to ask is, "What benefit will they want from it?". Answering this question result in a precise list of needs the most critical customers you identified in the previous step.

Customers do not always state their needs in ways teams'can easily understand. Needs are generally expressed in the language of the customer, not of the organization. Some needs will be stated explicitly by the customer; others remain unstated and must be uncovered. Needs can arise from many places, including the perception of customer, cultural factors, or even unintended uses of a product.

4. Develop product

Now that the team knows the product they want to create, for whom it will be built, and the benefit they want from it, the fourth question to ask is "What will create the benefit?". Experience has demonstrated that this step is potentially one of the most innovative and creative phases in the planning process. Answering this question result in the team developing specific product features, which will address customers' needs. Each feature must have a quality goal. The goals are the targets each product feature must be able to meet. Quality feature goals may come from the customer, the organization, benchmarking, regulatory bodies, etc. The team will eventually need to decide which features and goals from all the possible choices will be selected to become part of the final design. Through the use of specialized quality tools, teams will be able to determine the optimum by finding a balance between meeting the needs of customers and suppliers alike, meeting the competition, and minimizing the combined costs of customers and suppliers.

5. Develop process

Now that the team knows the product they want to create, for whom it will be built, the benefit they want from it, and what will create that benefit, the fifth step is to ask, "How do we deliver that product best?". In this step, the team develops the processes which will be able to produce the product features required to meet customers' needs.

Process development creates the means for producing the product and meeting quality goals. These include creating the procedures, methods, instructions, etc., for converting the plan into actions workers will use to build the good or deliver the service. The team selects the various process features and process feature goals that will make up the process design. They also establish that the process is capable of meeting quality goals, thereby minimizing deficiencies. Many of the kinds of analyses used in the previous step to select the final product feature and goals will also be applied to optimize and select those process feature and goals that will make up the final process design.

6. Develop process controls/ transfer to operations

Finally, the team needs to ask, "How do we ensure it works as designed?". The output of step six is the total plan which includes all the means, process specifications, procedures, instruction books, briefings, training, etc., required to meet product and process goals. The plan also incorporated the process control system that is developed in this step to ensure that the process continues to work and meet quality goals over and over again. The final activity in this step is the formal transfer of the plan to operational forces. This activity is crucial since it is important to have a smooth transition from design to implementation of the plan.

4.2 Modern Quality Planning

Today's quality planning model emphasizes customer needs and teamwork. It provides a structure and system of interrelated elements for ensuring customer satisfaction by identifying the best combination of feature and keeping defects to a minimum. Planning for quality also means identifying up-front the resources, activities, procedures, and data required producing a product, which will meet or exceed customer requirements. This approach can achieve first-time results: delighting customers with the right combination of features and deficiencies significantly lower.

Within the boundaries of the project, all departments and functions affected try the product and are involved at each phase of the quality planning process. This team approach ensures that the needs of internal and external customers are considered to design a quality product before being released to operations.

5. MAINTAINING THE CUSTOMER

An organization is developing the customer focus in order to satisfy better its customers. For that, the organization uses the data referring to customer satisfaction, in order to measure its success another important measure of success is the customer retention³.

The customer satisfaction is the critical part of the customer retention, but the two factors are not synonym. A satisfied customer is not all ways a maintained customer. The customer satisfaction is critical, but it's the means to an end, not the end itself. The end is the customer retention. For that the organization must measure its success by using the data referring to the customer retention, rather than the data referring to customer satisfaction. The issue is not if the customer is satisfied with the company's products or services, but if hear she is sufficiently satisfied to be maintained.

In order to maintain customer for a long term, a company must make them it's partners, and must make a proactive research of the input data from the customers, rather than wait for customers to complain and then react to the feedback after the problem occurs.

Many companies make the mistake to react only to the declared complaints of the customers, and don't go further, to find out what has not been said. The record of the complains represents the peak of on iceberg. In order to gather the unrecorded complaints, one may use techniques such as customer surveillance, customer testing, customer interviews, and the sending of sales representative to gather customer data.

REFERENCES

1. M. Marzu and T.Necsoiu, *Metode moderne ale opticii pentru calculul sistemelor optoelectronice de vedere pe timp de noapte*, Ed. Inst. de Optoelectronica, Bucuresti, 1998.
2. V. Antonescu and D. Constantinescu, *Managementul Calitatii Totale*. OID-MICM, 1993.
3. M. Brassard, *The Memory Jogger*. Featuring the Seven Management and Planning Tools, QPC-1989.
4. W. E. Deming, *Quality, Productivity and Competitive Position*, MIT Center For Advanced Engineering Study, Cambridge, USA, 1982.
5. A. V. Feigenbaum, *Total Quality Control*, New York, 3e edition Mac Graw Hill Book Company, 1983.
6. P. Hermel, *Qualite et Management*, Paris, Editions d'Organisation, 1989.
7. J. M. Juran and F. M. Gryna, *Quality Control Handbook*, Mac Graw Hill Co, 4e edition, 1988.
8. J. M. Juran and F. M. Gryna, *Quality Planning and Analysis*, Mac Graw Hill Co, 2e edition, 1979.
9. J. M. Juran, *Planifier la Qualite*, Afnor Gestion, 1989.
10. M. Perigord, *Reussir la Qualite Totale*, Paris, Editions d'Organisatio, Coll. "Management 2000", 1987.
11. M. Perigord and Y. Chaihneau, *Du management de projet a la Qualite Totale*, Paris, Editions d'Organisatio, Coll. "Management 2000", 1990.

Quality control of product/process using non-destructive control and possibilities of robotic investigation

Letitia Tanase^{a*}, Mihai Margaritescu^b

^{a, b}EUROTEST 2000 SRL, Str. Atomistilor nr.1, Bucuresti – Magurele

ABSTRACT

In the paper, the possibilities to improve the quality of products/ processes using modern methods and equipment for non-destructive control are presented. The quality control is represented by the operational techniques and activities used to fulfil the conditions concerning the quality, it is a way to verify the realization of quality and to establish necessary actions to correct the non-conformities. The defectoscopy represents an assembly of methods to examine materials, pieces and joins to discover their defects (flaws, emptiness, inclusions, etc.) by non-destructive control methods. The essential requirements of non-destructive control, in connection with the imperatives of total quality's concept determinate in a short period of time a high attainment of systems' quality. In the second part of the paper, the possibility to achieve non-destructive control with the aid of robotic systems, the appropriate cases in which the robots are useful, the type of robot together with constructive details are presented. The two main directions where the robotics is useful are non-destructive control in technological flux and the control in hostile or unapproachable environment for human operator. In the first case are used robots with proper software, and in the second, remote control robots. Finally, the advantage offered by the robot utilization for non-destructive control in special situations is emphasized.

"Measurement is the first step that leads to control and eventually to improvement. If you can't measure something, you can't understand it. If you can't understand it, you can't control it. If you can't control it, you can't improve it."

(H. James Harrington)

Keywords: non-destructive control, control of product / process, robotics, sensors

1. INTRODUCTION

In the modern conception, the control task is to action and to intervene operatively so that the final product to correspond with required conditions, to fulfil conformity quality, that is all the elements which characterizes the product or the piece to correspond with what is written in specifications or in contract. The control action takes into account all stages of process achievement, in every stage specific methods being utilized³.

Indifferent of the measures nature which applies, the central problem is the correct establishment of the cause that generate defects, so that the most suitable measures can be applied to reduce its effect. The causes cognition supposes a continuous concern of all the factors which participates at a product achievement, supposes the evaluation, the analysis and the quality control (product, process) permanently and systematic⁸.

Processes at which the work refers are the processes which produce results, the processes which implement or reproduce the project, the repeatable processes which generate products. These processes differs of the design process through the fact that they are destine to multiply the product every time at the same standards. The design process is a journey in unknown, meanwhile the production process is a journey on a proved way, with predictable results. The design process requires control to maintain a pre-established standard.

There are two ways to control the product quality:

- controlling the product that traverse the manufacture process;
- controlling the processes through which the product passes.

The product control is based on the production equipment control, meanwhile the product control is based on the product check at the output from different stages of the process¹². In practical activity, the both types of control are applied,

* Correspondence: Phone: (401) 780.66.40; Fax: (401) 423.25.32

according to Fig. 1. If the control is focused only above the process outputs, excluding anything, it will be discovered that in many cases the necessity of the finite product re-manufacturing will appear. If the control is focused above the process, using the results of the product check, then the reprocessing are gradual reduced until all the coming out products from the process have a constant quality.

A simple production process is illustrated in Fig. 2, in which the shadowed boxes indicate the external interference of the production process.

2. THE PROCESS AND PRODUCT CHARRACTERISTICS CONTROL

The quality plan or the quality proceedings must not contain requirements referring to the product, but the check methods, the precautions and the necessary recordings must be provided. The controlled conditions include the monitoring, the inspections and the tests in process. All the controls must have a check stage and a feedback loop. The manufacture of some products can be controlled only through the product inspection^{9,11}.

The process control means that the operators know what results they must obtain, what results were been obtained and they can correct the performance if the obtained results are not what is required. In the process specification the observed parameters and the limits between the process must maintain are defined¹.

2.1. How is it done ?

1. The base for the process/ product control in the quality plan.
2. The critical control points are identified.
3. The factors that affect the key process control are defined: equipment, environment, the dangerous materials control.
4. The following requirements of the product are identified: specifications, perform standards, legal standards and codes.
5. The existent monitoring techniques are analyzed.
6. The control and approval proceedings are developed.
7. The work instructions/ the job descriptions are developed.
8. The control equipment maintenance proceedings are developed.
9. The special processes are identified.
10. The control of the process change is implemented.
11. The proceedings are reexamined/ improved.
12. The reexaminations are estimated.

2.2. Special processes

There are some processes in which the conform product is total dependent of the personnel and equipment capability and the utilized facilities and in which the conformity can not be integral check through the finite product examination in any assembly stage. If anything of these factors is inadequate, the deficiencies may appear long time after the product there is in exploitation. Among these products there are coverings, welding and cling joining, castings, forging, moulding, heat treatments and inspection and testing techniques such as: X-Ray and US examinations, environment tests and mechanical stress tests^{4,5}.

A special attention must be granted to these processes to assure the continuous capability to fulfil the specifications⁸. This may include:

- The process and equipment pre-qualification; all the factors that affect the process are identified (materials, operations, environment, utilities, equipment controls), so that the potential variability that affect the product quality to be controlled.
- The utilization of qualified personnel that fulfils specific training criteria.
- The monitoring and continuous control of the critical characteristics of the process.
- The maintaining and analyzing of the process, equipment and personnel recordings.

2.3. The products / processes quality

The products / processes quality depends in special of:

- The documents quality that define the product.
- The raw materials or base products quality.
- The control of manufacture processes, that begins with their qualification.
- The personnel qualification that perform and inspect.
- The control of the inspection, measurement and testing equipment.
- The "key points" identification, that is the control points of a process that presents a particular importance of the point of view of risk at which the product quality is exposed, the installations and personnel security and the environment protection.

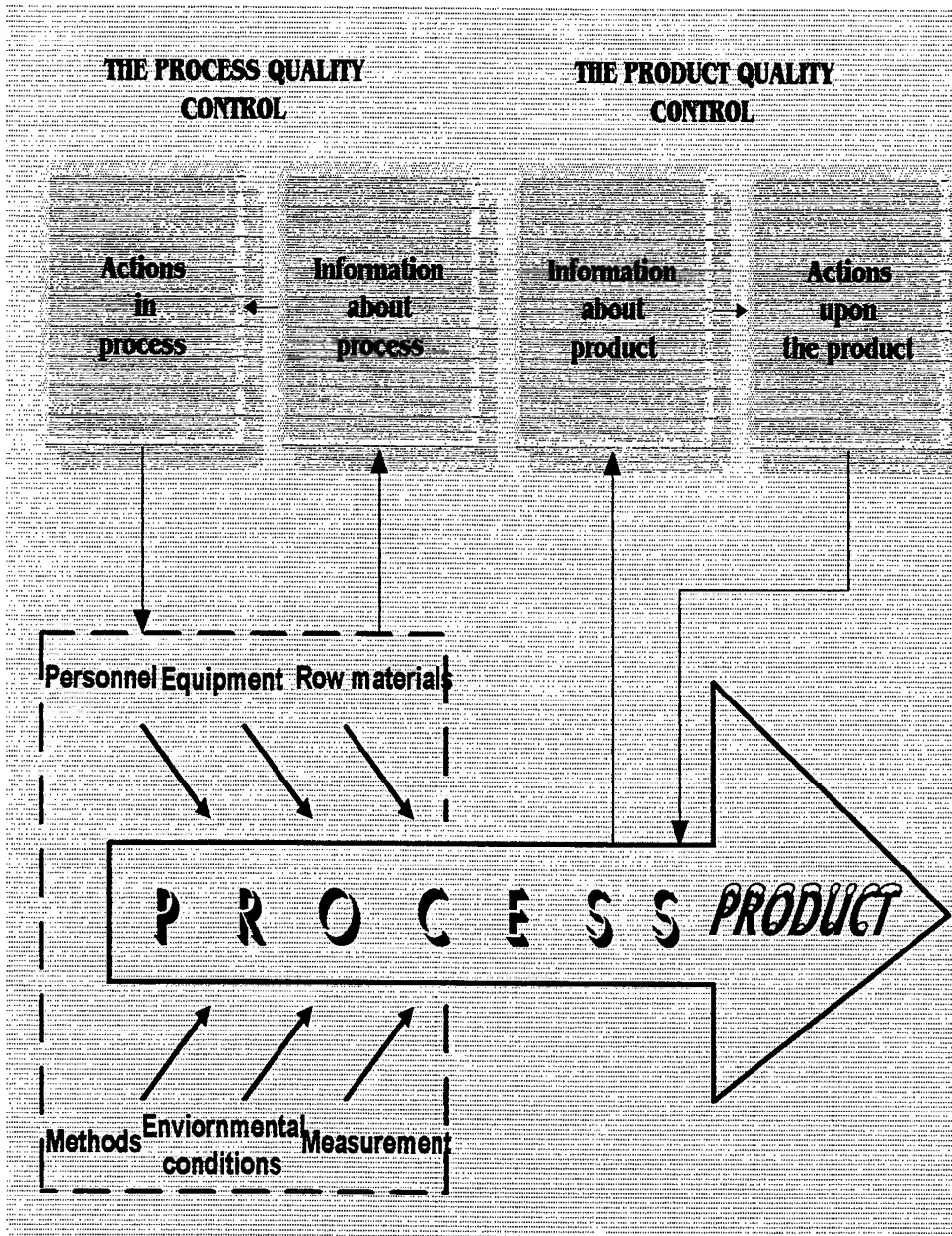


Fig. 1 Model of process control

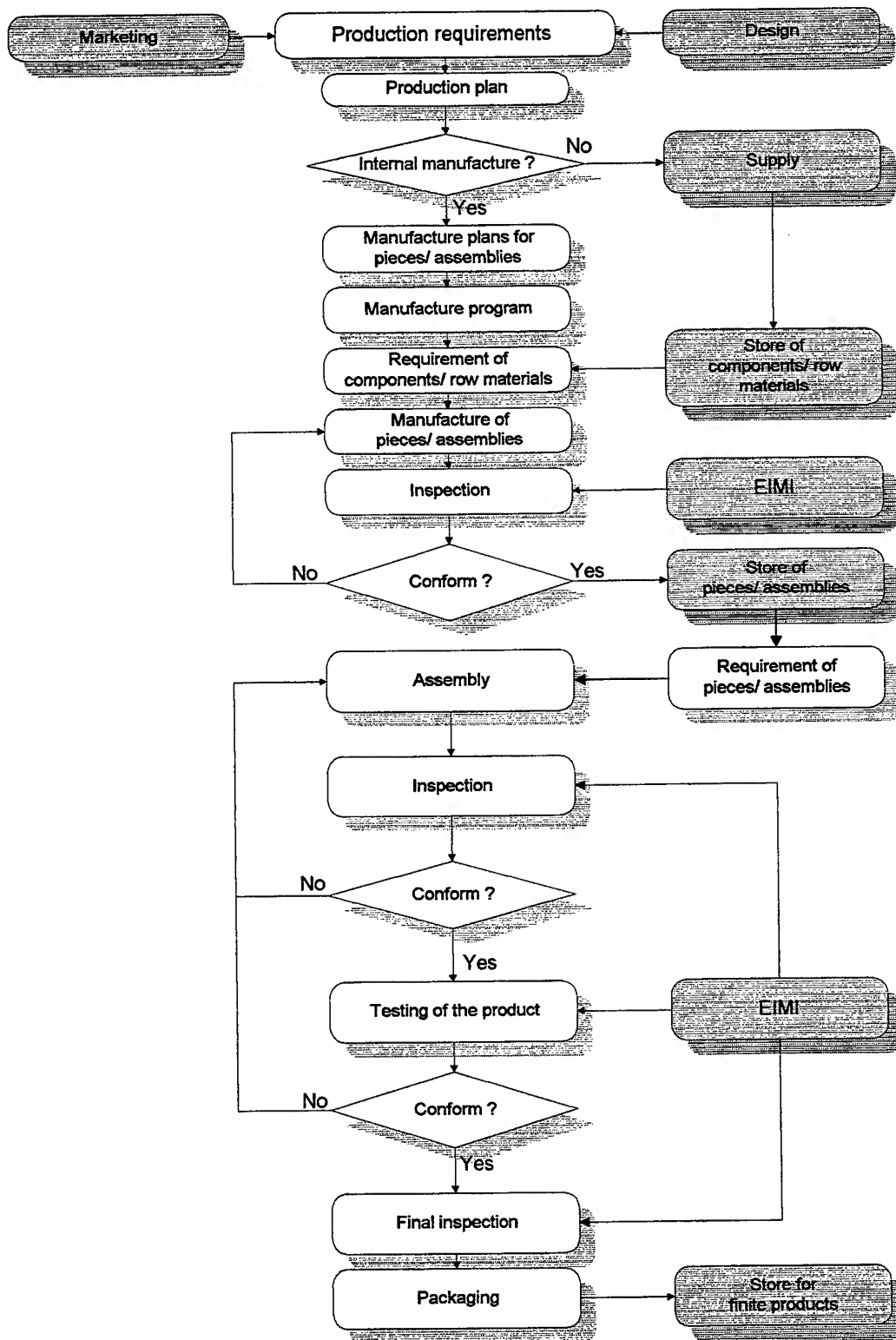


Fig. 2 The manufacture process

The products quality control can be performed through non-destructive examinations. This represents an assembly of proceedings for materials and parts examinations, with the task to put in evidence of their defects (fissures, gaps, inclusions, etc.) through non-destructive control methods¹⁰.

The non-destructive examinations may be applied to all the parts from a series or all the components of an assembly without reduce their functional capacity, because the control does not debase the controlled piece. With the aid of these methods the defects detecting and the measurement of some technical characteristics of the materials, parts or assemblies are possible.

The advantages of the non-destructive examinations are:

- The parts which are or will be in function can be controlled and the conclusions refer at those parts.
- Every part can be controlled, if it is justified from economical point of view.
- The whole part or only some zones can be controlled.
- Different zones can be simultaneous controlled with specific methods for different characteristics.
- The parts can be controlled meantime they work, because the control does not influence the lifetime.
- Repeated controls can be performed upon the same part and it can be established when the part is not capable for work, avoiding its destruction.

The non-destructive examinations have a special importance for technique, due their advantages and due the fact that through the combination of different methods can be put in evidence almost all the types of defects, their estimation being possible. More much, the non-destructive methods can be applied to the metallic materials and to the non-metallic materials too¹⁰.

The wide applicability domain of the non-destructive examinations owes the fact that it is suitable to industrial applications, indifferent of the manufacture series size, that through the combination of different methods a complete control of the products is assured, that it is economical and that due the achieved equipment and apparatus, it can be applied in laboratories, workshops and in building-sites.

3. THE QUALITY CONTROL WITH THE AID OF ROBOTS IN NON-DESTRUCTIVE EXAMINATIONS

How varied are the control methods, methods using ultrasounds, penetrable liquids, magnetic powders, X rays, thermo-vision or holography, so varied are the situations in which these must be applied. In function of the nature of the controlled object, of the number of the same type controlled objects, of the environment particularities and of the most adequate method, it results a wide domain for the non-destructive examinations. In many situations, the control operation has a repeatable character, (obviously in the case of measurement in the technological flux of a great number of identical pieces, in one or more points), or counter, the operation has a singular, non-repeatable character, but it is performed in hostile or even inaccessible operator environment. In the situations mentioned above, the quality control with the aid of the robotic systems represents the solution of these problems, but in the same time can offer a superior level of the quality control.

In the followings, the most frequent met cases in which the robotic aid is useful will be presented, in parallel with the corresponding robot types.

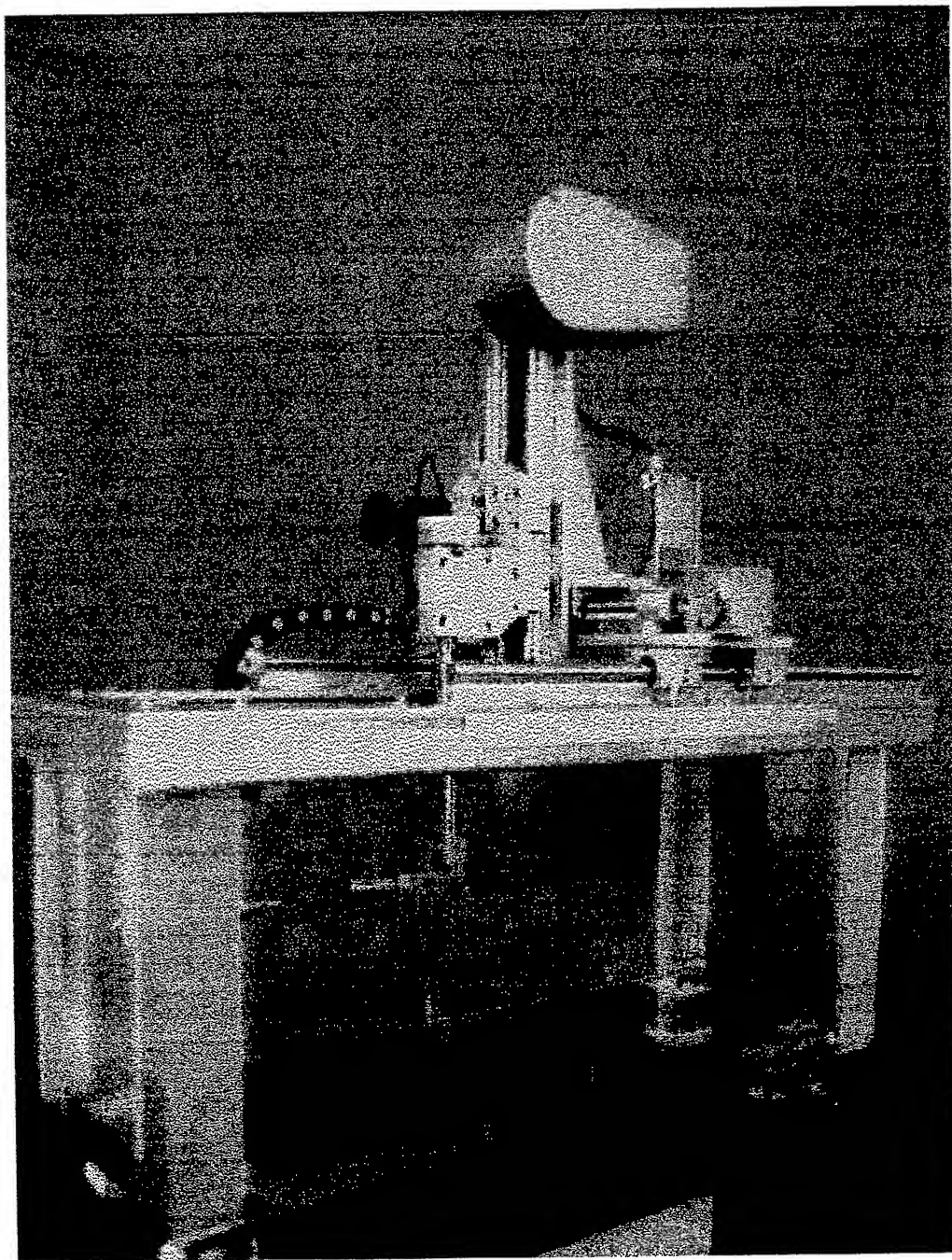
3.1. The quality control in technological flux

It is characterized by the control in one or more points of a great number of identical pieces, that implies achievement in identical mode the sensor movement, bringing this in contact with the piece in the control period, retreat movement, rotation movement of the piece, achievement the measurement in another point.

In the case of US control, the robots are fit by excellency for the sensor movement relative to a fixed coordinate system, assumed for example to be the immersion bath. In the Fig. 3a such a robot is represented, achieved of the firm ISOTEST – Italy², that can bring the sensor in any point of the operation space with the aid of the three degrees of freedom mechanism, more exactly three translations corresponding to x, y, z axes. The orientation movement is manual performed.

The corresponding three cars are translated with the aid of three step-by-step motors, controlled by a computer (PC type), endowed with specific software, working under “Windows”. It is remarkable that the program allows to process the

information transmitted by US transducer through intermedium of an interface, to display on monitor the defects diagrams and to print the analysis certificate. Some robots of this type are endowed with the fourth degree of freedom too, that allows the object rotation movement (Fig. 3b). The displacements and the rotations can be carried out with variable velocities, easily to modify.



a) with three degrees of freedom

Fig. 3 US Control Systems in immersion



b) with four degrees of freedom

Fig. 3 US Control Systems in immersion

The question that appears is: From what number of pieces is it convenient from economical point of view to use such a robot? Without to propose to indicate an exact value, it can be appreciated at some thousands the number of identical objects for which it is justified that an enterprise to purchase a robotic equipment, if it is probably to appear the necessity of the same kind pieces control. If this thing is certain, the mentioned number may be smaller (some hundreds of objects), because the software modification is cheaper.

The positioning and orientation movement upon the measured piece surface can be achieved too with robots having rotational couples. However, the software achievement is more difficult, the expression of the internal coordinates of the robot (the rotation angles from kinematic couples: q_1, q_2, \dots, q_n) in function of its external coordinates (the coordinates x, y, z of the characteristic point of the robot, which is materialized by a point from the transducer surface and three angles α, β, γ that defines the transducer orientation) being necessary:

$$\begin{cases} q_1 = q_1(x, y, z, \alpha, \beta, \gamma) \\ \dots \\ q_n = q_n(x, y, z, \alpha, \beta, \gamma) \end{cases} \quad (1)$$

Solving the system of equation (1) we obtain the solution of the "inverse kinematic problem". In the case in which the robot is redundant, that is it has degrees of freedom in excess and can perform the positioning movement in more modes, this solution is not unique; in this case it has to be introduced supplementary conditions, of path optimization, so that the computer can take a decision⁷. The advantage of these robots is that they look like the human organism as structure and they are "skilful".

3.2. The investigation in hostile environment

It is situated at the opposite pole in comparison with the preceding case, it is characterized through the non-repeatable, sometimes unexpected element of the control action, the use of programmable robots being total inadequate. In this case it is necessary to appeal at *remote controlled robots*, that are driven by a human operator situated at distance. The remote control may be performed by cable or by radio (about ten times more expensive).

It is most suitable for the inspection with camera device or with thermo-vision systems, without exclude another types of transducers, in spaces with constant arisen temperature (40 – 60 °C), in chemical or radioactive contaminated environments. Robots of this kind were used for inspection and manipulation too of dangerous objects at the nuclear power station from Cernobil. Two variants of remote controlled robots for intervention in hostile environments and for dangerous objects manipulation were designed and carried out (Fig. 4 and Fig. 5).

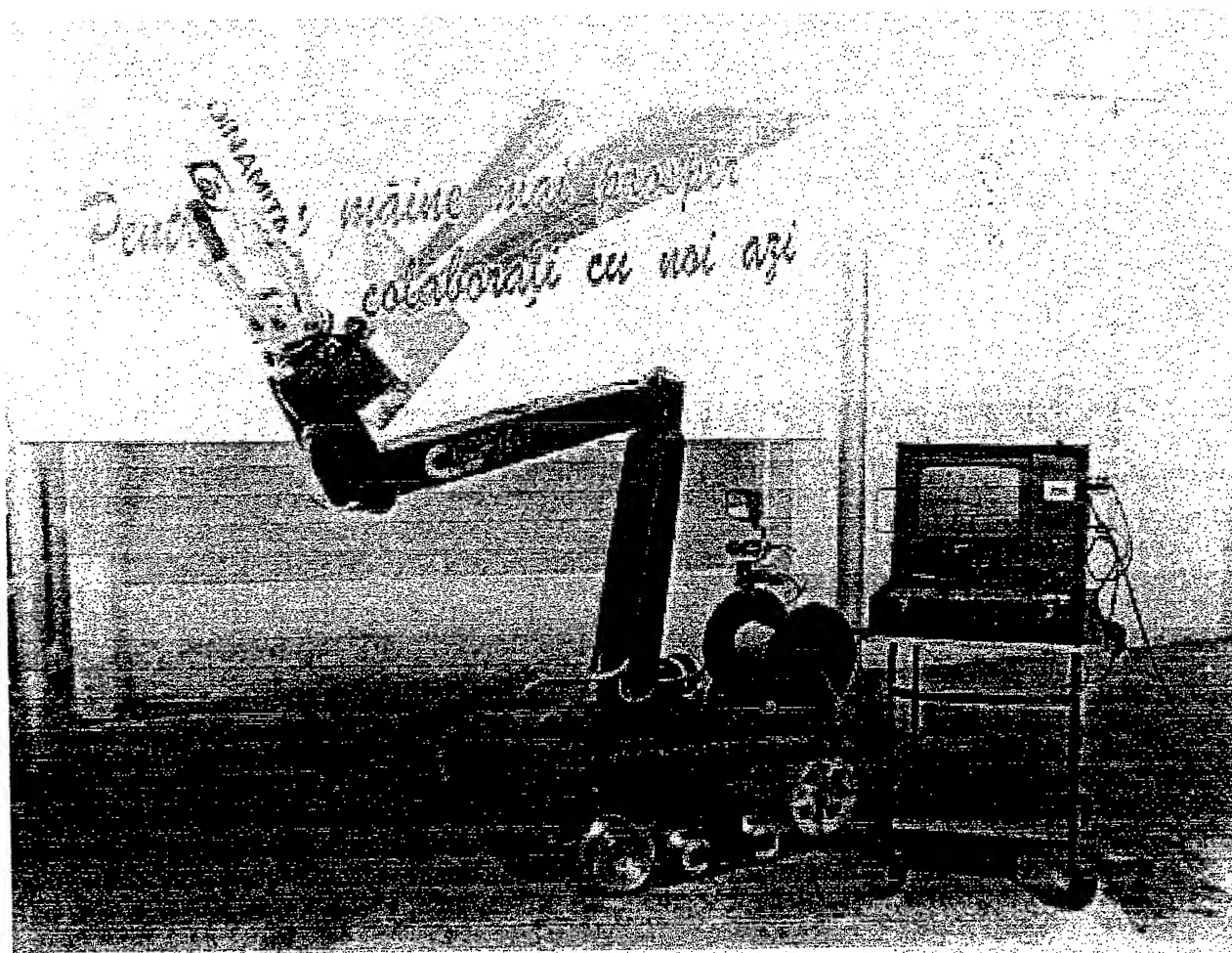


Fig. 4 Remote controlled robot for intervention in hostile environments (the variant with fixed track)

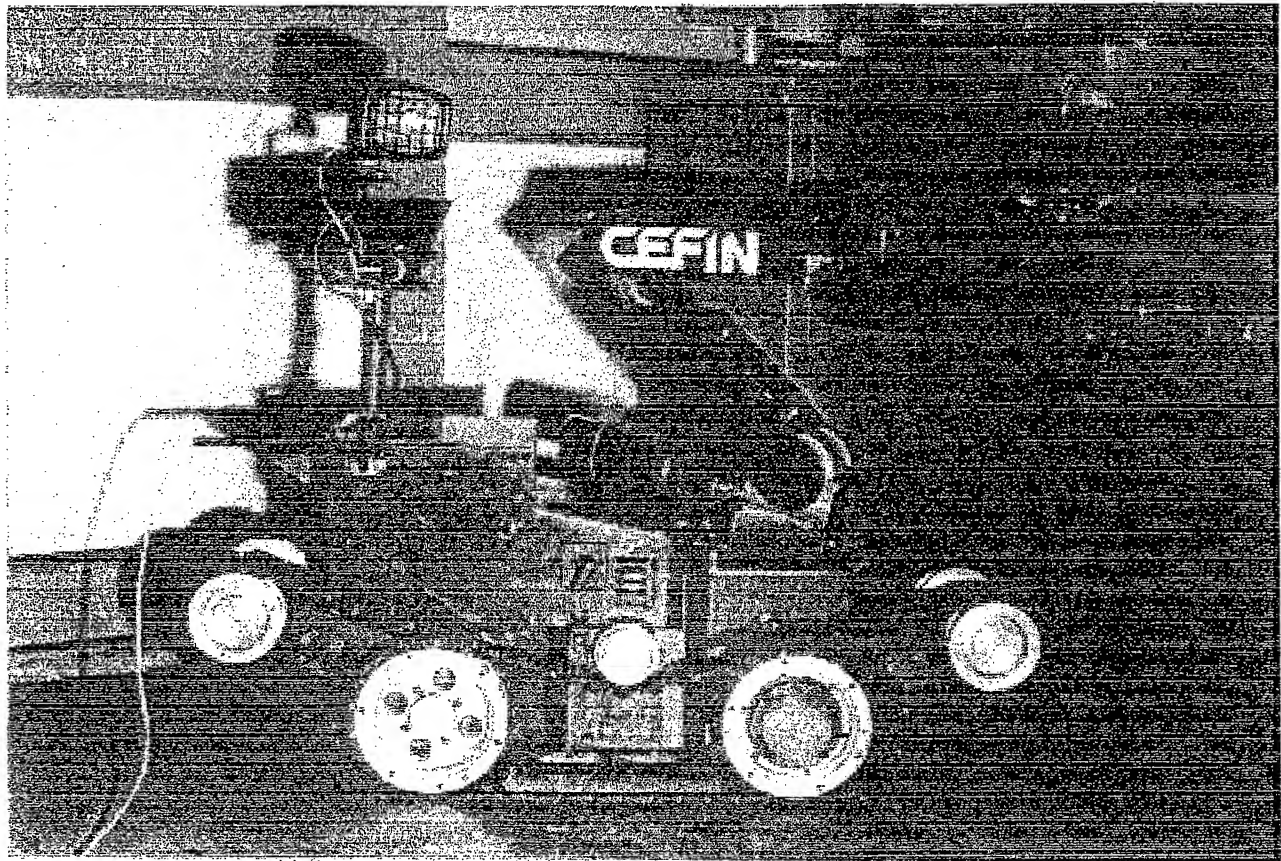


Fig. 5 Remote controlled robot for intervention in hostile environments (the variant with bendable track)

These robots, having similar structure, are made up from a transporter vehicle (that can climb edges, stairways, can pass through an ordinary door) and the positioning and orientation mechanism of the gripper; the robot has five degrees of freedom, exclusive the grip movement, is endowed with two color camera devices, the image being transmitted to a monitor, situated above the control panel. They can be easily adapted for non-destructive examinations through elimination of the grip function and the assembling the desired transducers or equipment.

3.3. The investigation in the interior of the pipes

The net of water pipes (we distinguish here the pipes for supplying with water, canal pipes and district heating pipes) requires an ample volume of effort for maintenance and rehabilitation and important expenses too. The modern rehabilitation methods, named "no dig", bring significant thrifths in comparison with classical methods of pipes replacement and have beneficial consequences above environment. To apply these methods is necessary beforehand to carry out an inspection inside the pipe with the purpose of corrosion degree estimation and local defects detection. After rehabilitation, the final check is carried out with the same equipment. If for the first type of defects the inspection can be achieved with a camera device or a thermo-vision system, for hidden defects detection, the ultra-sounds control is indicated.

The inspection equipment has to fulfil some specific conditions:

- to have the sizes suitable for the diameters of the pipes;
- to be protected against the hostile environment from the damaged pipes;
- to be sufficient of mobile and robust;
- to allow permanently the control of the developed activities with the aid of a surface station.

The inspection equipment is composed by a remote controlled vehicle that passes the pipe, endowed with camera device, illumination system, thermo-vision system or ultra-sounds transducers and the surface part that controls and records the position and the type of every defect.

The camera device may be fixed, in special for pipes of small diameter (Fig. 6), or with possibility of orientation with the aid of a mechanism or may be maintained on the axis of the pipe acting a parallelogram mechanism (Fig. 7). In the case of ultra-sounds control, the sensor must be brought in contact with the wall of the pipe on the whole circumference. This requires a special remote controlled mechanism, capable to bring into position and to establish the correct direction of the sensor, which in fact is a robotic arm with at least three degrees of freedom⁶.

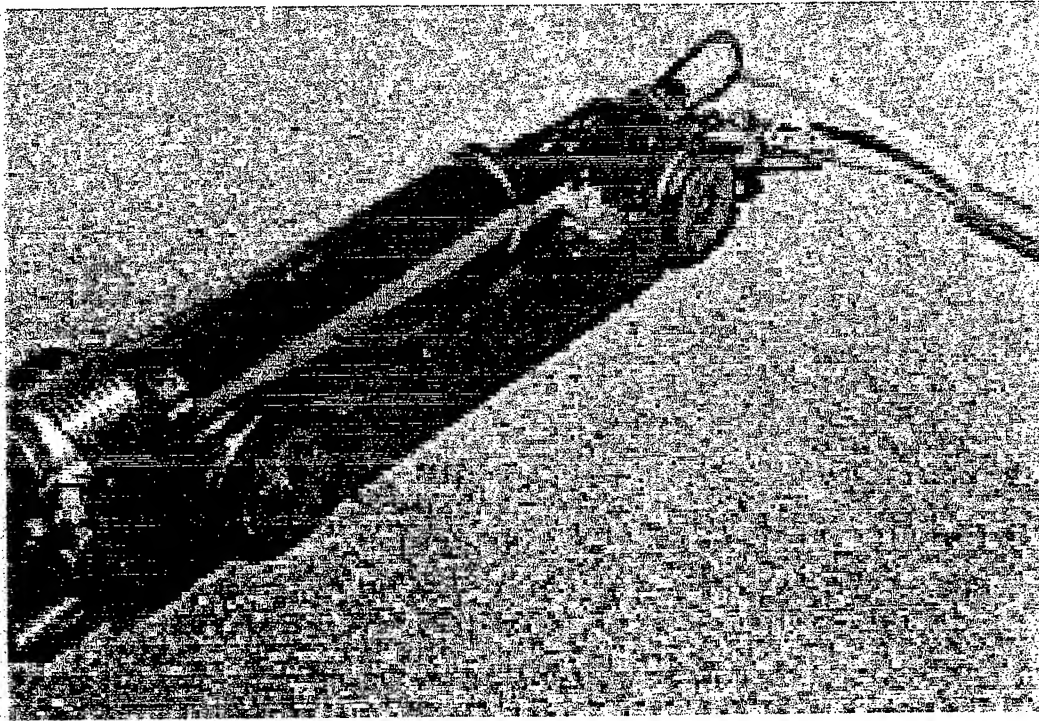


Fig. 6 Inspection system with camera device in pipe of great diameter

Supplementary, it has to be solved the problem of supply with coupling substance; this has the task to assure proper conditions for measurement. Since the interior of the pipe may be irregular, the robotic arm must be provided with compliance. The vehicle must adapt itself to particular conditions, that is it must not overturn or must function in any position; it must not hang up itself of different obstacles; it must have a given autonomy, up to 500 meters. This distance generates some problems in connection with the propulsion mode. In the case of a motor vehicle the motor (and the motors for the action of the robotic arm too) may be of hydraulic or electric type. The supply with energy must be achieved through cables, because the batteries are sizable and have an unsuitable form. The data transmitted of sensors are processed in a computer standing in a laboratory-car. After the measurements are finished, a detailed and complete information about the state of pipes system and a precisely description of defects result.

In conclusion, the robotics is useful for the non-destructive examinations domain in two situations:

- for control in technological flux;
- for control in hostile or dangerous environment.

Equipment of this type are more and more frequent utilized, being important the lifetime, the position accuracy (that is reflected in the quality of the measurement process) and the improvement of the software.

The conception and achievement of robotic systems for non-destructive examinations represents one of the most important concern within the framework of the EUROTTEST 2000 society; the collaborations with institutes or firms which are connected with this field of activity, such as ISOTEST - Italy, The Optoelectronics Institute Bucharest, The National

Research – Development Institute for Fine Mechanics CEFIN Bucharest and others, guarantees products of high performances.



Fig. 7 Inspection system with camera device in pipe of small diameter

REFERENCES

1. Brakhahn W. and Vogt U., *"ISO 9000 pentru servicii-Rapid si sigur spre certificare"*, Ed. Tehnica, Bucuresti, 1998.
2. Cantore C. and Robu M., *"Experimental tests for the characterization of ultrasonic probes utilized for non destructive examinations in the industrial field"*-SIOEL, 1998.
3. Froman B., *"Le manuel qualité. Outil stratégique d'une démarche qualité"*, AFNOR 1995.
4. Ishikawa K., *"La Gestion de la Qualité-outils et applications pratiques"* Ed. Dunod, Paris, 1992.
5. Juran J. M., *"Juran on Leadership for Quality"*, The Free Press, New York, 1988.
6. Lata I., Margaritescu M. and Marin D., *"Starea actuala si perspective privind echipamente moderne de investigare si reabilitare a retelelor subterane de conducte pentru apa canal si gaze naturale"*-Studiu tehnic realizat de INCDMF-CEFIN Bucuresti, 1996.
7. Margaritescu M., *"Determinarea si compensarea erorilor de pozitionare ale robotilor din mecanica fina"*- Teza de doctorat, 1999.
8. Mitonneanu H., *"O noua orientare in managementul calitatii: sapte instrumente noi"*, Ed. Tehnica, Bucuresti, 1998.
9. Périgord M., *"Réussir la qualité totale"*, Les Éditions d'organisation, Paris, 1990.
10. Panaitescu I., Negulescu V., Dascalu E., Vladescu E., Curelea E. and Baltac I., *"Defectoscopie nedistructiva"*, Ed. didactica si pedagogica, Bucuresti
11. Stora G. and Montaigne J., *"La Qualité Totale dans l'entreprise"*, Éditions d'Organisation, Paris, 1990.
12. Zgura Gh., Solomon Gh. and Szuder A., *"Elemente de asigurarea calitatii"*, Ed. Tehnica, Bucuresti, 1998.

Precision improvement in ellipsometric type measurements for the refraction index using numerical code processing

A Belea, M. Bulinski

University of Bucharest, Faculty of Physics, Dept. of Optics,
P.O. Box MG-63, 72996 Bucharest, Romania

ABSTRACT

Using a numerical code assisted data processing we show that the precision in the ellipsometric type measurements can be improved with a sufficient degree of confidence, up to an order of magnitude. Our method is based on fitting the experimental data with a pair of functions of known theoretical behavior. Essentially, we corroborate the results obtained from one strongly nonlinear function to those given by another behaving 'ultra-linearly'. When working with consistent experimental data, this procedure leads to a pair of 'outputs' that enhance one another producing an increased degree of precision. The paper explicitly applies this idea to an ellipsometric type measurement for the refraction index of a glass specimen.

1. INTRODUCTION

Ellipsometric type measurements provide a basic technique to obtain some essential optical information on the properties of a given material^{1,3}. As known, such methods can also be used on thin films and wave guides. No matter the precision offered by the experimental setup, it is possible to improve it by an order of magnitude exploiting numerical assisted data processing.

The basics of our method consists in fitting the available experimental data with a pair of functions of known theoretical behavior. It is important to corroborate one strongly nonlinear function to another behaving 'ultra-linearly'. Our experience revealed that the confidence test (Chi-square) is more easily satisfied when fitting a data base with a nonlinear function than when one uses a very simple dependency. In other words, things happen as if the nonlinear fit would tend to make the experimental data look 'better', even if some low accuracy measurements might be present. On the other hand, the 'ultra-linear' fit makes all errors become more evident. When using consistent experimental data, even if affected by errors, this procedure leads to a paired set of 'outputs' that agree to each other with an increased (by one) degree of accuracy. The paper explicitly applies this idea to an ellipsometric type measurement for the refraction index of glass prism.

The work has the following organization: the second part emphasized on the theoretical background founding the numerical assisted technique. The third part contains the experimental results and their processing. Appendix 1 indicate the possible error sources. Appendix 2 presents the immediate experimental consequences, needed to be taken into consideration on account of the suggestions given by Appendix 1.

2. THE DESCRIPTION OF THE NUMERICAL TECHNIQUE

The theory of reflection of plane waves incident on a plane separation surface between two transparent dielectrics² leads to an expression for the reorientation of the plane of the polarization. This reads

$$\tan(\Delta) = \frac{\cos(i+r)}{\cos(i-r)} \tan(\alpha_p) \quad (1)$$

*Correspondence: Telephone: 780.47.70

where Δ means the orientation of the polarization plane of the reflected beam (taken with respect to the plane of incidence), α_p designate the orientation of the polarization plane of the incident beam, while i and r mean the incidence and transmission angles respectively. If n represents the value of the relative refractive index, then by the law of refraction

$$r = \arcsin(\sin(i)/n) \quad (2)$$

Combining (1) and (2) we get

$$\Delta = \arctan \left[\frac{\cos(i + \arcsin(\frac{\sin i}{n}))}{\cos(i - \arcsin(\frac{\sin i}{n}))} \tan(\alpha_p) \right] \quad (3.a)$$

$$n = \left| \frac{\tan i}{\sin \Delta - \tan \alpha_p \cos \Delta} \right| \sqrt{\sin^2 \Delta + \tan \alpha_p \cos^2 \Delta - \tan \alpha_p \sin 2\Delta \cos 2i} \quad (3.b)$$

We can interpret (3.a) as defining a function $\Delta = \Delta(i, \alpha_p)$, which admits n as parameter. This interpretation ensues from the fact that on a standard ellipsometric setup, the values of i and α_p behave like real variables, while n is to be determined. Once we have a value of the triplet $(\Delta(i, \alpha_p))$, we can compute the corresponding value for n . Obviously, Eq. (3.a) shows that the relation between Δ and its variables is strongly non-linear. Equation (3.b) defines n as a function of (i, α_p, Δ) . However, physical reasons impose that the refractive index is nothing but a constant. When reading Eq. (3.b) such as written, one can interpret it as another highly non-linear equation. Still, because of the physical grounds just mentioned, the complete cast of Eq. (3.b) should read as

$$n = \left| \frac{\tan i}{\sin \Delta - \tan \alpha_p \cos \Delta} \right| \sqrt{\sin^2 \Delta + \tan \alpha_p \cos^2 \Delta - \tan \alpha_p \sin 2\Delta \cos 2i} = ct. \quad (4)$$

wherefrom we infer that any graphical representation of n as a function of i runs as a straight line parallel to one axes of coordinates. Because of this simple character we say that Eq. (3.b) produces an 'ultra-linear' dependency.

To exploit code assisted data processing, we first need a collection of experimental data that when best fitted by Eq. (3.a) will produce one value for n , while when best fitted by Eq. (3.b) will (generally) produce another one. The coincidence of these two values indicates both the consistency of the experimental data base and a value for n , which benefits of an improved level of accuracy. In fact, it is highly improbable that the same data base could be fitted by the same value of n through two so different mathematical functions.

Avoiding all complex mathematical arguments, we simply offer the following remarks: in contrast to linear functions, the pattern of highly non-linear functions is locally characterized by long (eventually infinitely long) Taylor expansions. Taking in view the cut offs related to the use of a numerical algorithms, given a range of values, two nonlinear functions might well substitute in one another, just because they might be similar in the limited number of terms considered in series expansions that feed the numerical algorithm. This is the core of the argument allowing to understand why nonlinear functions can easily fit data bases within a good confidence profile. It easily understood also that when we use a linear functions to fit the data base, all arguments will run in quite the opposite direction.

As discussed in Appendix 1, ellipsometric type measurements involve problems of error elimination which are not easy to circumvent. Appendix 2 presents one option to improve the precision of the data recording (associated to one of the variables) and to acquire a good quality experimental data base. Our standard in appreciating both the consistency of a data base (a premise for the present technique manipulations) and the quality of the overall results will be discussed in the following section.

3. MEASUREMENTS LEADING TO THE EXPERIMENTAL DATA BASE

Presently we will discuss two distinct sets of experimental results. One of them will be invoked as the 'Bad' database, while the other will be called the 'Good' data base. Both sets are processed similarly. The records have been taken using an ellipsometric arrangement. It consists of a mercury lamp, a polarizer, a goniometric table (allowing one to modify the incidence of the beam reaching the probe), and an analyzer followed by photomultiplier. All angular scales are of the same precision class, that is ± 0.5 minutes.

A complete set of experimental data consists of two data bases. As discussed in Appendix 2, the first one is needed in order to get the orientation of the polarization plane of the light incident on the probe (with a very high degree of precision, in order to reduce one source of errors in this experiments). The second set of data, when used in conjunctions Eqs. (3), leads to the refractive index of the sample. Practically, we have gathered the experimental data using a glass prism as a sample. To acquire a comparison value, we have measured the refractive index of our probe (for the green line of the mercury lamp) with a Zeiss Jena optical goniometer obtaining $n=1.5187 \pm 0.0001$.

One collection of data, namely the one that we presented as the 'Bad' data base, was taken to our best accuracy, using the eye as a detector. A second collection of data, that we have called the 'Good' data base was taken in similar conditions but using as photomultiplier as detector. Even more, the measurements on the photomultiplier's scale were taken following Archer's suggestions².

Figs. 1 and 2 present the results obtained from the 'Bad' data base while Figs. 3 and 4 illustrate the results produced by the 'Good' data base.

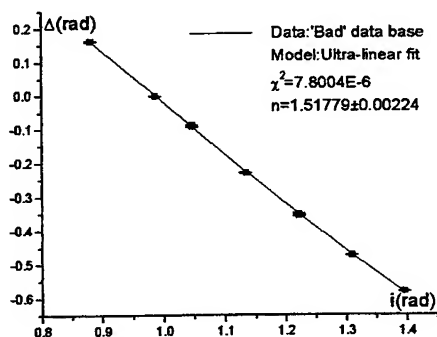


Fig. 1 Experimental data and $\Delta=\Delta(i)$ fit for the 'Bad' data base

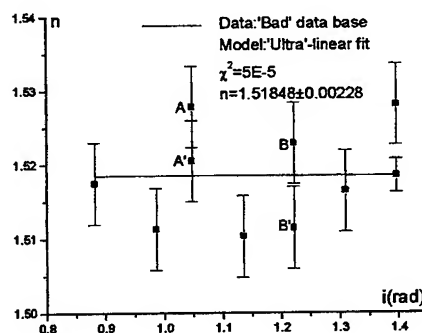


Fig. 2 Computed data and $n=n(i)$ fit for the 'Bad' data base

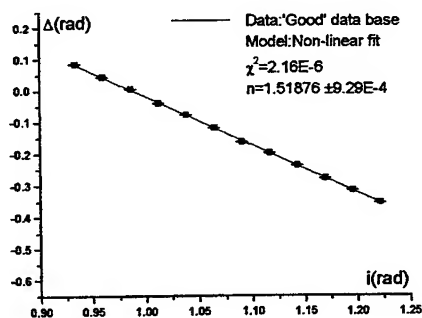


Fig. 3 Experimental data and $\Delta=\Delta(i)$ fit for the 'Good' data base

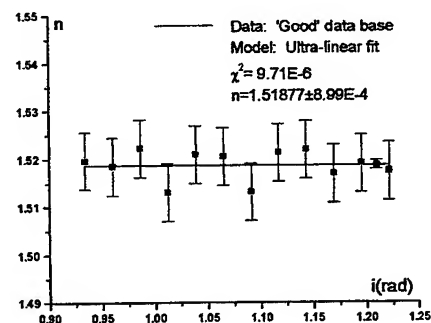


Fig. 4 Computed data and $n=n(i)$ fit for the 'Good' data base

All four figures contain: a) the experimental data and the experimental errors (shown as bars); b) the best fit curves together with an indication of the fitting precision (only for $n=n(i)$); c) the pair of numbers giving the value of the confidence test (χ) and the values obtained for the refractive index.

The experimental errors connected to the margins of reproducibility for several series of data (measured in the same general conditions) are shown in Fig. 2 by the pairs of points (A, A') or (B, B').

A first obvious indication of the poor quality of the data collection shown in Figs. 1, 2 consists in the fact that the fitting curve for $n=n(i)$ does not intercept all error bars. A second (more important) 'bad' characteristic follows from the fact that the two values for the refractive index do coincide only up to the second decimal. In contrast, for the data base shown in Figs. 3, 4 both fitting curves run inside all error bars and the pair of values for the refractive index coincide up to the 4th decimal. For these reasons we have called this collection of data the 'Good' data base. However we can note a third distinction between a 'Good' and 'Bad' data bases as arising from the fact that the values of the confidence figures are comparable only for the 'Good' data base (see Figs. 3,4).

Comparing Fig. 1 and 2 (or Fig. 3 and 4) we can see that the confidence test figures are a smaller (the fit is more credible) in the case of the non-linear function $\Delta=\Delta(i)$.

In the case of the 'Good' data base, we note that not only the values for the refractive index do coincide to the 4th decimal, but even more, that they also agree (to the same precision) with the value obtained using the minimum deviation method. Corroborating the experimental errors bars for the two collections of data with the quality exhibited by the value of the refractive index, we note that in both cases the algorithm proposed in this paper leads to a improvements of the precision by one order of magnitude. However, we insist on the fact that the improvement is much more important if the processed data base is consistent (i.e., it displays a reduced amount of experimental errors).

4. CONCLUSIONS

We have shown that using two very different types of functions (imposed by theoretical grounds), their best fit with respect to the same collection of experimental data ensures a confirmation of the consistency (quality) of the data base. Even more, our results show that the method presented can improve the accuracy in the value of the parameter to be determined by one order of magnitude (in our case the value of the refractive index).

However, as common to all code assisted procedures (eg. phase unwrapping, noisy signal analyze, digital image restoration, etc.) these techniques involve some degree of personal confidence from user's side. Finally, we think that the method presented in this paper can receive specific implementations, allowing its extension to other similar problems.

APPENDIX 1

This part presents an analysis of the different errors sources and their effects upon the results obtained from ellipsometric type data bases. In association with our Eg. (3.b) and using standard procedures, we find the relative error for the refractive index as

$$\frac{\Delta n}{n} = \sqrt{A^2 \Delta_i^2 + B^2 \Delta_\Delta^2 + C^2 \Delta_{\alpha_p}^2} \quad (\text{A.1.1})$$

where

$$A = \frac{1 + \tan^2(\Delta)}{\tan(\Delta)} + \frac{\tan(\alpha_p) \sin(2i) \sin(2\Delta)}{\sin^2(i) + \tan^2(\alpha_p) \cos^2(i) - \tan(\alpha_p) \sin(2i) \cos(2\Delta)} \quad (\text{A.1.2})$$

$$B = \cos(i) + \tan(\alpha_p) \sin(i) + \frac{\sin(i) \cos(i) (1 - \tan^2(\alpha_p)) - \tan(\alpha_p) \cos(2i) \cos(2\Delta)}{\sin^2(i) + \tan^2(\alpha_p) \cos^2(i) - \tan(\alpha_p) \sin(2i) \cos(2\Delta)} \quad (\text{A.1.3})$$

$$C = (1 + \tan^2(\alpha_p)) \left(\cos(i) + \frac{2 \tan(\alpha_p) \cos^2(i) - \sin(2i) \cos(2\Delta)}{2 \sin^2(i) + \tan^2(\alpha_p) \cos^2(i) - \tan(\alpha_p) \sin(2i) \cos(2\Delta)} \right) \quad (\text{A.1.3})$$

Numerical tests show that for the usual experimental range defined by $i \in (0, \pi/2)$, $\Delta \in (-0.5, 0.5)$, and $\alpha_p \in (0, \pi/2)$, we have reasonably $A \sim B \sim C \sim 10$. For this reason the best theoretical precision for n , (in our experimental setup) cannot exceed the second decimal when using the eye as detector, or the third decimal in the case of a photomultiplier.

Because the errors introduced by the three sources (i, α_p, Δ) are comparable and because we dispose of only two physical laws to fit the data, it becomes stringent to eliminate at least one source of errors (or, more reasonably expressed, to make one source of errors negligible in comparison to others). This issue is discussed in Appendix 2.

APPENDIX 2

In order to give an accurate specification for the orientation of the plane of polarization of the incident beam we have followed a three steps procedure. The first step consists in acquiring a collection of data relating the readings of the polarizer's positions to those of the analyzer, readings taken at 'grazing' incidence on the probe (in fact, this operation does not require the probe to be present). The data were collected for extinctions. While theoretically these relation should read

$$\alpha_A = \alpha_p \pm ct. \quad (\text{A.2.1})$$

we have admitted a more general linear relation

$$\alpha_A = a\alpha_p \pm b \quad (\text{A.2.2})$$

The resulting calibration graph is given in Fig. 5.

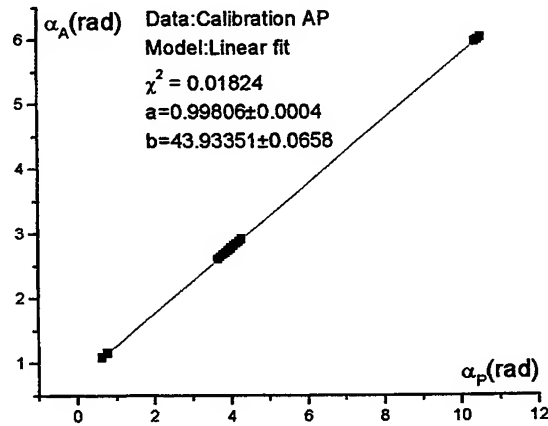


Fig. 5 Linear fit calibration curve for the analyzer's vs. polarizer's angular positions

In the second step we have used only the polarizer and the probe in order to establish the readings on the polarizer's scale giving extinctions at different angles of incidence on the probe. This was meant in order to specify the position of the plane of incidence, α_{p0} , on the polarizer scale. To increase the accuracy of the readings, we have used the method recommended by Archer¹. The results are shown in Fig. 6.

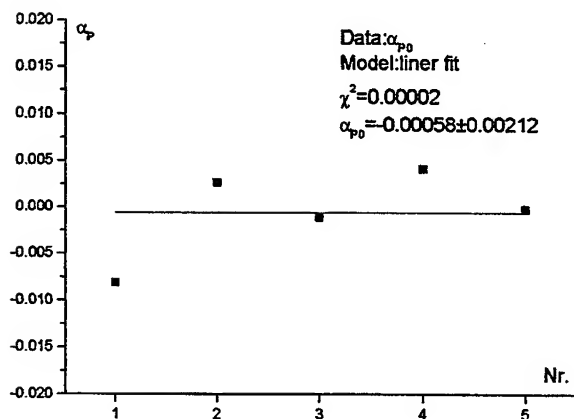


Fig. 6 Angular position of the plane of incidence

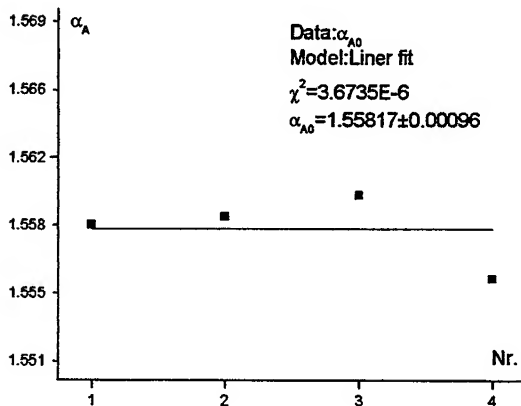


Fig. 7 Improved specification of Δ

The third step consists in giving a refinement to the value of Δ appearing in Eq. (1). This was done by setting a crude value of Δ obtained by simply changing α_{p0} to $\alpha_{p0} + \Delta$. Then we took several readings for the analyzer's scale (at grazing incidence and for extinction) in order to get a fitted value of α_A , as shown in Fig. 7. Finally, we have used this value and the reverse of Eq. (A.2.2) in order to obtain an improved value of Δ .

REFERENCES

1. Archer, R. J., *Ellipsometry*, Gaertner Scientific Corp., Chicago, 1968.
2. Born, M. and E. Wolf, *Principles of Optics*, Pergamon Press, Oxford, London, New York, 1964.
3. Walter G. Driscoll, *Handbook of Optics*, McGraw-Hill Book Company, New York, San Francisco, etc., 1978.

Temperature And Dopant Concentration In Single Mode 5 Micron Diameter Optical Fiber -Cooling Through The Die - Implications For Laguerre Orders In Optical Refractive Synchronization

by

J. R. Palmer

SilkRoad, Inc.
9707 Waples, St. San Diego, CA, 92121
U.S.A.

Abstract

The object of this paper is to evaluate both the temperature distribution and the dopant concentration for a 5 micron diameter single mode SiO₂ fiber optic that is doped with GeO₂. Fundamentally, what drives the need to know this information springs from a theoretical model which suggests that the index of refraction, leading from the center to the edge, follows a parabolic curve. It is the contention of this paper that the index of refraction in an optical fiber follows more of a

Lorentzean curve rather than a truncated parabolic, ^{[1],[2],[3],[4]} i.e., $n(x) = n_f^2 \left(1 - \frac{x^2}{x_0^2}\right)$, or a $\frac{1}{\cosh^2}$ profile,

i.e., $n(x) = n_s^2 + 2n_s \frac{\Delta n}{2} \frac{2x}{h} \cosh$, or an exponential profile, although the exponential more closely follows what is

described in this paper, i.e., $n(x) = n_s^2 + 2n_s \Delta n e^{\left(\frac{-2|x|}{h}\right)}$. In this analysis one will find that the temperature gradient from the center to the edge of the radius is more than substantially steep. Additionally, one finds from the diffusivity of GeO₂ in the liquid SiO₂, that it takes only 0.07 seconds for the temperature to drop to the point where the GeO₂ freezes. Because of the diffusion of the GeO₂ in the SiO₂ one finds a depletion at the center of 28.44% and a continuing diminution

as one proceeds outward to a radius of 1.25(10⁻⁶) meters where the accretion of GeO₂ begins and continues to increase until, at the wall, the outer radius has an accretion of 27.24%.

Introduction

The major undertaking of this paper is to describe the temperature gradient as a function of time when the optical fiber material is pulled through the die and subsequently cools. There are a number of components to this problem and we will take each of them in their turn. After describing each of the components, we will combine them to bring about a comprehensive analysis.

One of the main driving threads that has motivated this paper is the concept that most authors have begun from a basic premise that light passing through the fiber is a standing wave phenomena. This is, fundamentally, not true. As the analysis will demonstrate, the fiber, because of the technique of cooling provides that the fiber is marginally bi-refrigent. As such, the fiber will display some modicum of crystal structure, however small, and will provide a difference in index not only proceeding from center to edge; but, around the circumference at each radial node. More importantly, because the analysis is ideal, and therefore, symmetrical, it violates the most basic of concepts, "... mother nature is never that uniform."

Consequently, the fiber will reflect an ellipsoidal rotary power, i. e., angular momentum, not a standing wave phenomena. [5],[6],[7],[8] Nor does the light lend itself to such an analysis. The fiber must be evaluated as a bi-refrigrant material, or crystal if you will.

Analysis

The first component of the analysis will be to determine a heat transfer coefficient for a heated round element that is horizontal and rotating, giving up heat to forced air cooling at the surrounding environment. One may evaluate the heat transfer coefficient from the following equation for the stagnation boundary [9],[10],[11]

$$h_c = \sqrt{\frac{V_\infty * D_o}{\nu_f}} * \frac{k}{D_o} \quad (1)$$

where;

- V_∞ = Velocity of air impinging on the fiber, $\frac{\text{cm}}{\text{seconds}}$
- D_o = Diameter of the fiber, cm
- ν = The viscosity of the air at the average temperature between the surface of the fiber and the incoming air, $\frac{\text{cm}^2}{\text{sec}}$
- k = Thermal conductivity of air at the average temperature. $\frac{\text{W}}{\text{cm} - ^\circ\text{C}}$
- h_c = Stagnation Point Heat Transfer Coefficient, $\frac{\text{W}}{\text{cm}^2 - ^\circ\text{C}}$

If we use an average temperature of 1350°C between the incoming air and the surface of the SiO₂ at melt we would have,

- D_o = Diameter of the fiber, cm = $5.0(10^{-4})$ cm [10]
- ν = The viscosity of the air at the average temperature between the surface of the fiber and the incoming air, $\frac{\text{cm}^2}{\text{sec}}$ = $3.1493 \frac{\text{cm}^2}{\text{sec}}$ [10]
- k = Thermal conductivity of air at the average temperature. $\frac{\text{W}}{\text{cm} - ^\circ\text{C}}$
= $3.124 (10^{-5}) \frac{\text{W}}{\text{cm} - ^\circ\text{C}}$ [10]

Based on these values at a velocity (V_∞) of 162, $\frac{\text{cm}}{\text{seconds}}$ of air coming in at 21 °C, we would have a heat transfer coefficient of $0.01 \frac{\text{W}}{\text{cm}^2 - ^\circ\text{C}}$. We will assume that the air velocity is rotated around the fiber diameter to insure

that there is an even heat transfer coefficient from the fiber diameter. For the purpose of this analysis, we will assume that there is forced convection cooling over the outside of the fiber glass coming out of the die. For this discussion we will assume that the heat transfer coefficient is on the order of $0.01 \frac{\text{W}}{\text{cm}^2 - ^\circ\text{C}}$. We will, however, also present an evaluation

for a heat transfer coefficient of $0.001 \frac{\text{W}}{\text{cm}^2 - ^\circ\text{C}}$ for a comparison. The next constituent that we need to undertake is the transient heat transfer and subsequent gradient through the optical fiber as a function of time. In order to accomplish this task we will use the following *Palmer Transform*, [12],[13],[14] such that,

(2)

Convolved Transform , for $R_0 \geq R_1 > 0$

For Cooling Of a Temperature Source the Transform would be;

$$\Delta T_R = R_0 * \eta_c * \Delta T^0 * \Delta \tau * \frac{\Gamma}{V} \frac{\Delta T \{ h_c \frac{\Delta T_0 \nabla \sqrt{\psi}}{\sqrt{\kappa}} \} \lambda \sqrt{\phi=0.5}}{\frac{\Delta T^0 \tau \nabla \sqrt{\theta^{1.5}}}{\Gamma \sqrt{\chi^{2.5}}}} \alpha \sqrt{V}$$

The deconvolved Transform will look like,

$$\Delta T = \left(\frac{2 H_c \Delta T_0 \sqrt{\alpha \sqrt{R_1}}}{\sqrt{R_0}} \right) * \sqrt{\tau_0} - \sqrt{\tau_0 - \tau} * \text{ierfc} \left[\frac{R_0 - R_1}{2 * \sqrt{\alpha * \tau}} \right] \\ + \left(\frac{4 H_c \Delta T_0 \alpha \sqrt{R_1}}{\sqrt{R_0}} \right) * \sqrt{\tau_0} - \sqrt{\tau_0 - \tau} * \left[\frac{1.0}{8 * R_0} + \frac{3}{8 * R_1} - H'' \right] * \text{ierfc} \left[\frac{R_0 - R_1}{2 * \sqrt{\alpha * \tau}} \right]$$

where;

$$H_c = \frac{h_c}{k_0}, \frac{1.0}{\text{cm}}$$

$$\alpha = \text{Thermal diffusivity of SiO}_2, 0.0084 \frac{\text{cm}^2}{\text{seconds}} \quad [15]$$

$$k_0 = \text{Thermal conductivity of SiO}_2, 0.0137 \frac{\text{W}}{\text{cm} - ^\circ\text{C}} \quad [15]$$

$$H'' = H_c + \frac{1.0}{R_1}$$

$$\tau_0 = \text{Heating + Cooling time, seconds}$$

$$\tau = \text{Heating time only, seconds}$$

$$\Delta T_0 = \text{Temperature difference for heating, } ^\circ\text{C}$$

$$R_0 = \text{Outside radius of optical component, cm}$$

The next condition that we need to satisfy will be the temperature diminution with time for cooling of the center, [12],[13],[14] such that, i.e., $R_1 = 0$. In order to accomplish this task we will use the following *Palmer Transform*,

(3)

Convolved Transform , for $R_1 = 0$

For Cooling of the Center of a Cylindrical Temperature Source, the Transform would be;

$$\Delta T_{R_0} = R_0^0 * \eta_c^0 * \Delta T^0 * \Delta \tau * \frac{\Gamma}{V} \frac{\Delta T \{ h_c \frac{\Delta T_0 \nabla^{\sqrt{\psi}}}{\sqrt{\kappa}} \} \lambda \sqrt{\phi=0.}}{\frac{\Delta T^0 \tau \nabla^{\sqrt{\theta}} \alpha \sqrt{V}}{\Gamma \sqrt{\chi^0}}}$$

and de-convolved would be,

$$\begin{aligned} \Delta T_{R_0} = & \left\{ \frac{\Delta T_0 * R_0}{\sqrt{\alpha \pi (\tau_0 - \tau)}} \right\} \left\{ 1.0 + \left[\left[\frac{2 \alpha (\sqrt{\tau_0} - \sqrt{\tau_0 - \tau})}{R_0^2} - 1.0 \right] \right. \right. \\ & \times \operatorname{erf} \left[\frac{R_0}{2 \sqrt{\alpha (\sqrt{\tau_0} - \sqrt{\tau_0 - \tau})}} \right] \left. \right\} - \left\{ 2 (\sqrt{\tau_0} - \sqrt{\tau_0 - \tau}) \sqrt{\frac{\alpha}{\pi R_0^2}} \right. \\ & \times e^{-\left(\frac{R_0^2}{4 \alpha (\tau_0 - \tau)} \right)} \left. \right\} \left\{ \operatorname{erfc} \left[\frac{R_0}{2 \sqrt{\alpha \tau}} \right] - \left\{ e^{(H_c^2 \alpha (\tau_0 - \tau) + H_c * R_0)} \right. \right. \\ & \times \operatorname{erfc} \left[\frac{R_0}{2 \sqrt{\alpha \tau}} + H_c \sqrt{\alpha \tau} \right] \left. \right\} \end{aligned}$$

Another technique for finding the temperature at the center of a cylinder is found from, [13],[16],[17]

(4)

$$\begin{aligned} \Delta T_{R_0} = & \Delta T - \left\{ \frac{\Delta T R_0}{\sqrt{\pi \alpha (\tau_0 - \tau)}} \right\} * e^{-\left(\frac{R_0^2}{8 \alpha (\tau_0 - \tau)} \right)} * K \frac{1}{4} \left[\frac{R_0^2}{8 \alpha (\tau_0 - \tau)} \right] \\ & \times \left\{ \operatorname{erfc} \left[\frac{R_0}{2 \sqrt{\alpha \tau}} \right] - \left\{ e^{(H_c^2 \alpha (\tau_0 - \tau) + H_c * R_0)} \right. \right. \\ & \left. \left. \operatorname{erfc} \left[\frac{R_0}{2 \sqrt{\alpha \tau}} + H_c \sqrt{\alpha \tau} \right] \right\} \right\} \end{aligned}$$

In order to assist in this particular calculation, we have tabulated some of the values based on those taken from reference[13] and included some of reference[17].

	$\left(\frac{R_o^2}{8 \alpha (\tau_o - \tau)} \right)$		$K_{\frac{1}{2}}$		$K_{\frac{1}{4}}$
	$11 \cdot (10^{-6})$		$1.2533(10^3)$		940.11
	$11 \cdot (10^{-5})$ [13] lref		396.333		297.289
	$11 \cdot (10^{-4})$		125.333		94.011
	$11 \cdot (10^{-3})$		39.515		29.6399
	$11 \cdot (10^{-2})$		12.4084		9.308
	$l(0.10)$		3.5862		2.69
	$l(0.20)$		2.2945		1.878
	$l(0.30)$ [17] lref		1.6952		1.448
	$l(0.40)$		1.3283		1.1651
	$l(0.50)$		1.0750		0.9603
	$l(0.60)$		0.8879		0.8039
	$l(0.70)$		0.74388		0.6806
	$l(0.80)$ [17] lref		0.62962		0.5809
	$l(0.90)$		0.53712		0.4989
	$l(1.00)$		0.46107		0.4307

Now that we know how to calculate the temperature through the cylindrical fiber, we now need to find the diffusion and motility of the dopant in the SiO₂. The most common dopant that is used in optical fiber is GeO₂ [18],[19]. Murata [18]

gives one the better overview of the various techniques for the manufacture of optical fiber. He basically describes chemistry of the different processes, i.e., MCVD, PCVD, PMCVD, et al., and the deposition of the GeO₂ into the inside of SiO₂ tube where this becomes what is called the preform rod which is subsequently placed into a furnace at 2100°C to 2500

°C in preparation to collapse and drawing [18]. Based upon the descriptions by Murata, one may make a boundary condition that the GeO₂ is uniformly distributed through the core of the fiber as it is passing through the furnace. Under that assumption, one needs to look at the redistribution of the GeO₂ as a function of time and temperature in the fiber as it passes through the furnace and subsequently is cooled and inspected antecedent to spooling on the mandrel.

Using this boundary condition, one can determine the diffusion and motility of the GeO_2 in the furnace and subsequent cooling. We can begin by outlining the basic expression for finding the coefficient of diffusivity of GeO_2 in SiO_2 . In order to facilitate this process we will use the Wilke-Chang [19],[20],[21] correlation coupled with the Sitaraman-Ibrahim-Kuloor [22] empirical correlation such that,

$$D_{12}^{[0]} = 5.4(10^{-8}) * \left\{ \frac{\sqrt{M_2} * \Delta H_{b2}^{0.3333} T}{\mu_L \sqrt{V_1} \Delta H_{b1}^{0.30}} \right\}^{0.93} \quad (5)$$

where;

M_2 = Molecular weight of GeO_2

V_1 = Molecular volume of SiO_2 , $\frac{\text{cm}^3}{\text{gram}}$

ΔH_{b1} = Latent heat evaporation of SiO_2 , $\frac{\text{calories}}{\text{gram}}$
 = $30.3463 \frac{\text{calories}}{\text{gram}}$ [23],[24]

ΔH_{b2} = Latent heat evaporation of GeO_2 , $\frac{\text{calories}}{\text{gram}}$
 = $34.321 \frac{\text{calories}}{\text{gram}}$ [23],[24]

μ_1 = First order viscosity of the SiO_2 , centipoises

T = Temperature under evaluation, $^\circ\text{K}$

The value of μ_1 can be determined using the Chapman-Enskog Theorem inclusive of the Collision Integral [21],[22]

Such that,

$$\mu_1 = 2.669(10^{-3}) * \frac{\sqrt{M_1 T}}{\sigma * \Omega_v} \quad (6)$$

where;

M_1 = Molecular weight of SiO_2
 = 60.06 [23],[24]

M_2 = Molecular weight of GeO_2
 = 104.60 [23],[24]

σ = Hard sphere diameter, \AA
 = $10^{-2} * \left[\left(\frac{V_1 * 3}{2 \pi N_0} \right)^{0.33333} \right]$ or one can use $1.18(10^{-2}) * V_{1b}^{0.333333}$
 = 5.968\AA Note; This value changes with each different V_1 value.

N_0 = $6.02(10^{23})$ Avogadro's Number

$V_{1b} = \frac{60.06 \frac{\text{grams}}{\text{gram mole}}}{2.2 \frac{\text{grams}}{\text{cm}^3}} * \frac{2863^\circ\text{K}}{294.15^\circ\text{K}}$

$$= 268.103 \frac{\text{cm}^3}{\text{gram-mole}}$$

$$T_b = \text{Boiling temperature of SiO}_2 \text{ is } 2590^\circ\text{C or } 2863^\circ\text{K} \quad [23],[24]$$

$$T_m = \text{Melting Temperature of SiO}_2 \text{ is } 1727^\circ\text{C or } 2001^\circ\text{K} \quad [23],[24]$$

$$T_m = \text{Melting Temperature of GeO}_2 \text{ is } 1115^\circ\text{C or } 1388^\circ\text{K} \quad [23],[24]$$

$$T_c = \text{Critical Temperature of SiO}_2 \text{ is } 1.47 * T_b^{1.03} \quad [23],[24]$$

$$= 5343.715^\circ\text{K}$$

$$\text{and } T^* = 1.33 * \left(\frac{T_b}{T_c} \right) \quad [23],[24]$$

$$= 0.7125$$

$$\Omega_v = \frac{1.0}{0.697 * (1.0 + 0.323 * \ln(T^*))} \quad [23],[24]$$

$$= 1.6111$$

From Eq. (6), then, we can find the first component of the final equation, so that,

$$\mu_1 = 2.669(10^{-3}) * \frac{\sqrt{M_1} T}{\sigma * \Omega_v}$$

$$= 1.9369(10^{-2}) \text{ centipoise @ } 2863^\circ\text{K}$$

The viscosity of the Liquid SiO₂ follows from, [25],[26],[27],[28]

$$\mu_L = \mu_1 e^{\left(\frac{\Delta H_{b1}}{T} \right)} \quad @ T = 2863^\circ\text{K}$$

$$= 1.9369(10^{-2}) e^{\left(\frac{30.3463}{2863} \right)}$$

$$= 1.9575(10^{-2}) \text{ centipoise}$$

(7)

and now we can solve Eq. (5), so that,

$$D_{12}^{[0]} = 5.4(10^{-8}) * \left\{ \frac{\sqrt{M_2} * \Delta H_{b2}}{\mu_L \sqrt{V_1} \Delta H_{b1}} \frac{T^{0.3333}}{0.30} \right\}^{0.93}$$

$$D_{12}^{[0]} = 5.4(10^{-8}) * \left\{ \frac{\sqrt{104.6} * 34.321}{1.9575(10^{-2}) \sqrt{268.103} 30.3463} \frac{2863^{0.3333}}{0.30} \right\}^{0.93}$$

$$D_{12}^{[0]} = 2.561(10^{-3}) \frac{\text{cm}^2}{\text{second}} \quad @ 2863^\circ\text{K}$$

To save the reader a lot of work, we have built a second order polynomial that will provide the value of $D_{12}^{[0]}$ as a function of $T^\circ\text{K}$ from 2863.15°K to 1388.15°K.

(8)

$$D_{12}^{[0]} = 6.34007(10^{-4}) + 7.543905(10^{-7}) T - 2.854592(10^{-11}) T^2$$

We must first calculate the temperature gradient as a function of heating and cooling time and then we must discretize the diffusion from each of the radii to the adjoining cooler radii that have not achieved solidus within the range of

the GeO₂ material that is locked into the SiO₂ melt, i.e., temperatures of the SiO₂ greater than 1115 °C. Again, we are assuming that the GeO₂ is uniformly distributed in the preform and subsequent collapse into the fiber when going through the furnace and the concomitant motility of the GeO₂ to the cold wall when cooling, coming out of the furnace.

[16],[25],[26]

The diffusion may follow the equation below, so that,

(9)

$$\Theta_o = \frac{2 \sqrt{D_{12}^{[0]}} (\sqrt{\tau_o} - \sqrt{\tau_o - \tau}) \sqrt{R_1}}{\sqrt{R_o}} \operatorname{ierfc} \left[\left(\frac{R_o - R_1}{2 \sqrt{D_{12}^{[0]}} \tau} \right) \right] + \frac{D_{12}^{[0]} (\sqrt{\tau_o} - \sqrt{\tau_o - \tau}) (R_1 + 3 R_o)}{2 \sqrt{R_1} R_o^{1.5}} \operatorname{ierfc} \left[\left(\frac{R_o - R_1}{2 \sqrt{D_{12}^{[0]}} \tau} \right) \right]$$

and,

(10)

$$C_{1,2,3 \dots} = C_o \frac{1.0}{\Theta_o}$$

where;

C_o = Initial concentration of GeO₂

$C_{1,2,3 \dots}$ = Concentration of GeO₂ along the radius leading from center to the edge.

However, when one is discretizing over a very short distance, it is possible to use Equation (11) without too much fear of inaccuracy, i.e.,

[16],[25],[26]

(11)

$$C_{1,2,3 \dots} = C_o \operatorname{erf} \left[\left(\frac{R_x - R_1}{2 \sqrt{D_{12}^{[0]} (\tau_o - \tau)}} \right) \right]$$

Essentially, then, the chemistry for the inner core of the optical fiber glass is determined by using the inside diameter of a preform as reaction chamber of flowing gas with the appropriate constituents in order to deposit on the inside radius of the preform the required chemistry for the refractive indices that are required. Figures (1), (2) and (3) give an idea of how this process is undertaken. Additionally, Nakahara [18],[29]

suggests that there are some additional chemistries that are often used in the reactor formulation, e. g., P₂O₅ and B₂O₃. B₂O₅ requires a minimum temperature for vaporization of 1773.15 °K [24]

and P₂O₅ melts at 846.15 °K [23]. In the one case, the cooling process will permit a substantial motility with diffusion from the center to the outer radial boundary, something substantially larger than GeO₂. In the second case, the motility with diffusion will be somewhat less than GeO₂.

Based on the equations shown above, we have calculated both the temperature gradient and diffusion gradient for a preform that is reduced to a fiber coming through the furnace and subsequent cooling. Using a film coefficient of 0.01

$\frac{W}{2}$ and the diffusion of the GeO₂ in the SiO₂ we find from Figures (4) and (5) that the radial diffusion cm - °C

concentration from center to edge over a span of time of 0.07 seconds of cooling will provide, from the *Lazor Code*™ the value shown in Table I.

[18],[30]

Using the Sellmeier Equation we can look at the gradient of the optical index for a 3.1-mol% doping, i.e.,

$$n = \sqrt{\left[\frac{a_1 \lambda^2}{(\lambda - b_1)^2} + \frac{a_2 \lambda^2}{(\lambda - b_2)^2} + \frac{a_3 \lambda^3}{(\lambda - b_3)^2} \right] - 1.0}$$

where;

for 3.1%-Mole

$$\begin{aligned}\lambda &= \text{wavelength, } 1.55 \\ a_1 &= (0.7028554 - 0.6961663)*M + 0.6961663 \\ a_2 &= (0.4146307 - 0.4079426)*M + 0.4079426 \\ a_3 &= (0.8974540 - 0.8974994)*M + 0.8974994 \\ b_1 &= (0.00529581 - 0.004679148)*M + 0.004679148 \\ b_2 &= (0.01351206 - 0.01306644)*M + 0.01306644 \\ b_3 &= 97.934\end{aligned}$$

for 7.9%--Mole

$$\begin{aligned}\lambda &= \text{wavelength, } 1.55 \\ a_1 &= (0.7136824 - 0.6961663)*M + 0.6961663 \\ a_2 &= (0.4254807 - 0.4079426)*M + 0.4079426 \\ a_3 &= (0.8964226 - 0.8974994)*M + 0.8974994 \\ b_1 &= (0.003803952 - 0.004679148)*M + 0.004679148 \\ b_2 &= (0.011614969 - 0.01306644)*M + 0.01306644 \\ b_3 &= 97.934 \\ M &= \text{The value shown in the column for each radius as a function of run time.}\end{aligned}$$

Based on this equation, we find that the index of refraction at the center is on the order of 1.443 and at the outer radial wall is 1.4457. We have plotted the gradient in *Figure (6)*. One finds from this plot that the distribution looks more like a Lorentz than a Gaussian distribution. At this point we need to evaluate the commensurate imaginary part of the optical index and the total loss per meter that attends the gradient of the index. The total loss of the fiber per unit distance follows from, [18],[31]

$$\alpha = \frac{A}{\lambda} + B + C(\lambda) + \alpha_{IR}(\lambda) + \alpha_{UV}(\lambda) \quad (12)$$

where;

$$\begin{aligned}A &= \text{Coefficient of Rayleigh scattering loss} \\ B &= \text{Loss due to waveguide imperfection} \\ C(\lambda) &= \text{Loss caused by impurities} \\ \alpha_{IR} &= \text{Loss due to infrared absorption} \\ \alpha_{UV} &= \text{Loss due to ultraviolet absorption} \\ \alpha &= \text{Total loss of the fiber}\end{aligned}$$

It is estimated that the minimum value of A for SiO₂ fiber is on the order of 0.65 [18],[31],[32],[33]. The best values for α is on the order of $\frac{0.157 \text{ dB}}{\text{km}}$. We can convert this to a standard optical loss, such that,

$$\alpha = 10 \quad (13)$$

$$= \frac{1.0368}{\text{km}} \quad \text{or} \quad \frac{1.0368(10^{-3})}{\text{meter}} \quad [34],[35]$$

However, Wooten and others suggest that the value of α should be more on the order of

$$\frac{1.41 (10^{-3})}{\text{meter}} \quad \text{for SiO}_2 \text{ at } 1.55\mu. \text{ In order to be the most conservative we will use the value suggested by Wooten, et. al.}$$

Since the k and α are relative for this analysis the precision is not required. However, as a user of fiber, one would very much

like to have a fiber that had $\frac{0.157 \text{ dB}}{\text{km}}$. At this point, then, we can calculate the imaginary part of the optical index and relate that to the real part of the optical index, i.e., [34],[35]

$$k = \frac{\alpha \lambda}{4 * \pi} \quad (14)$$

and

$$\alpha = \frac{4 * \pi * \sigma}{n * C} \quad (15)$$

where;

$$\sigma = 4.870792(10)^4$$

$$C = 3(10)^8 \frac{\text{meters}}{\text{second}}$$

$$n = \text{Real part of the optical index}$$

We have plotted the values as a function of the diffusion and index gradient relating to the temperature gradient in Figures (7.0) and (8.0), using the values from Table (1).

Conclusion

The foregoing analysis would lead one to believe that the index shape going down the fiber is clearly not a parabola, truncated or otherwise. The shape of the curve clearly outlines a Lorentz type of curve. Additionally, it becomes clear that the fiber is mildly birefringent and, as a consequence, does not allow for a treatment of a standing wave to describe the physics of propagation. Rather, it seems clear that the fiber will be circular polarized and will support a substantial number of Laguerre orders propagating from the modulator under the condition of *Optical Refractive Synchronization*.

References

- 1.0 H. Kogelnik, "Theory Of Dielectric Waveguides," *Integrated Optics*, T. Tamir, ed., Topics In Applied Physics, Vol. 7, 2nd ed., Springer-Verlag, New York, NY, 1985.
- 2.0 D. F. Nelson and J. McKenna, *J. Appl. Physics*, **38**, 4057, 1967.
- 3.0 J. R. Carruthers, I. P. Kaminow, and L. W. Stultz, *Appl. Opt.*, **13**, 2333, 1974.
- 4.0 D. Marcuse, *Light Transmission Optics*, Van Nostrand Reinhold Co., New York, NY, 1972.
- 5.0 E. E. Wahlstrom, *Optical Crystallography*, John Wiley and Sons, New York, 1949.
- 6.0 A. Yariv and P. Yeh, *Optical Waves In Crystals*, John Wiley and Sons, New York, 1984
- 7.0 J. F. Nye, *Physical Properties Of Crystals*, 2nd ed., Oxford University Press, Oxford, England., 1985
- 8.0 E. A. Wood, *Crystals And Light*, 2nd. ed., Dover Publications, Inc., New York, NY, 1977.
- 9.0 H. Wolf, *Heat Transfer*, Harper and Rowe, New York, NY, 1983.
- 10.0 F. Kreith, *Principles of Heat Transfer*, 2 nd. ed., International Textbook Co., Scranton, PA, 1966.

- 11.0 E. R. G. Eckert, and R. M. Drake, *Heat And Mass Transfer*, 2nd. ed., McGraw-Hill Publishing Co., New York, N Y, 1959.
- 12.0 J. R. Palmer, *Transient Heat Transfer In Flat Plates*, Vol. I, Conduction of Heat In Solids, *Pro Se* Publishing, San Diego, CA, 1996 (now available from Amazon.com).
- 13.0 J. R. Palmer, *Transient Heat Transfer In Flat Plates*, Vol. III, Conduction Of Heat In Cylinders And Spheres, *Pro Se* Publishing, Sand Diego, CA, (In Process).
- 14.0 J. R. Palmer, "Destruction Of Optical Fiber Under High Power Laser Flux Density", *Lecture Notes*, St. Petersburg, Russia, 1988.
- 15.0 W. P. Barnes, "Optical Materials - Reflective," *Applied Optics And Optical Engineering*, Vol. VII, R. R. Shannon and J. C. Wyant, eds., Academic Press, New York, NY, 1979.
- 16.0 H. S. Carslaw, and J. C. Jaeger, *Conduction of Heat In Solids*, 2nd ed., Oxford University Press, Oxford, England, 1978.
- 17.0 H. R. F. Carsten and N. W. McKerrow, "The Tabulation Of Some Bessel Functions $K_\nu(x)$ and $K_\nu'(x)$ Of Fractional Order," *Phil. Mag.*, (7) 35, 1944, 812.
18. H. Murata, *Handbook Of Optical Fibers And Cables*, 2nd. ed., Marcel Dekker, Inc., New York, NY, 1996.
- 19.0 L. B. Jeunhomme, *Single-Mode Fiber Optics - Principles And Applications*, 2nd. ed., Marcel Dekker, Inc., New York, NY, 1990.
- 20.0 C. R. Wilke and P. Chang, *AIChE J.*, 1(2):270, 1955.
- 21.0 R. C. Reid and T. K. Sherwood, *The Properties Of Gases And Liquids*, 2nd ed., McGraw-Hill Book Co., New York, NY, 1966.
- 22.0 R. C. Reid, J. M. Prausnitz and B. E. Poling, *The Properties Of Gases And Liquids*, 4th ed., McGraw-Hill Book Co., New York, NY, 1987.
- 23.0 C. D. Hodgman, ed., *Handbook Of Chemistry And Physics*, 34th ed., Chemical Rubber Publishing Co., Cleveland, Ohio, 1952.
- 24.0 D. E. Gray, ed., *American Institute Of Physics Handbook*, 3rd ed., McGraw-Hill Book Co., 1972.
- 25.0 R. B. Bird, "Theory Of Diffusion," *Advances In Chemical Engineering*, Vol. 1, T. B. Drew and J. W. Hoopes, eds., Academic Press, New York, NY, 1956.
- 26.0 J. Crank, *The Mathematics Of Diffusion*, 2nd. ed., Oxford University Press, Oxford, England, 1983.
- 27.0 E. L. Cussler, *Diffusion-Mass Transfer In Fluid Systems*, University Of Cambridge Press, Cambridge, England, 1984.
- 28.0 H. J. V. Tyrrell and K. R. Harris, *Diffusion In Liquids*, Butterworths monographs In Chemistry, Boston, MA, 1984.
- 29.0 M. Nakahara, "Optical Fibre Fabrication Techniques," *Telecommunication Journal*, Vol. 48, 1981, (pp 643-649).
- 30.0 S. Kabayashi, S. Shibata, N. Shibata and T. Izawa, "Refractive Index Dispersion Of Doped Fused Silica," *IOCC'77*, 1977, (pp309-312).

31.0 H. Yokota, G. Tanaka, H. Kanamori, F. Mizutani, H. Suganuma and T. Kanzuka, "Loss Characteristics Of Pure -Silica Core Single - Mode Optical Fiber," *National Conv*, IECE J., 1127:4-251, March, 1985.

32.0 K. Inada, "A New Graphical Method Relating Optical Fiber Attenuation," *Opt. Comm.*, 19 (3), December, 1976, (pp 437-439).

33.0 J. Schroeder, R. Mohr, P. B. Marcedo and C. J. Montrose, "Rayleigh and Brillouin Scattering In K₂O-SiO₂ Glasses," *J. Amer. Ceram. Soc.*, 56 1973, (pp 510-514).

34.0 F. Wooten, *Optical Properties Of Solids*, Academic Press, Inc., New York, NY, 1972.

35.0 E. D. Palik, ed., *Handbook Of Optical Constants OF Solids*, Academic Press, Inc., New York, NY, 1985.

For Further Author Information:

Email: james.palmer@silkroadcorp.com
Telephone: (858) 457-6767
Web Site: <http://www.silkroadcorp.com>
Fax: (858) 457-6757
U.S.A.

Radius (10 ⁻⁷) meters	SECONDS OF COOLING TIME							
	0.01	0.02	0.03	0.04	0.05	0.06		
0	0.8732	0.7916	0.7676	0.7396	0.7276	0.7156		
1.25	0.8732	0.8044	0.7884	0.7724	0.7644	0.7584		
2.5	0.8732	0.8172	0.8092	0.8052	0.8012	0.8012		
3.75	0.8621	0.8201	0.8201	0.8221	0.8261	0.8321		
5	0.851	0.823	0.831	0.839	0.851	0.863		
6.25	0.8653	0.8515	0.8667	0.8667	0.8667	0.8667		
7.5	0.8797	0.84	0.903	0.903	0.903	0.903		
8.75	0.9161	0.93	0.903	0.903	0.903	0.903		
10	0.9525	0.9801	0.9801	0.9801	0.9801	0.9801		
11.25	0.9536	0.9871	0.9871	0.9871	0.9871	0.9871		
12.5	0.9546	1.006	1.006	1.006	1.006	1.006		
13.75	0.9611	1.0304	1.0304	1.0304	1.0304	1.0304		
15	1.0324	1.0548	1.0548	1.0548	1.0548	1.0548		
16.25	1.04865	1.04865	1.04865	1.04865	1.04865	1.04865		
17.5	1.0649	1.0649	1.0649	1.0649	1.0649	1.0649		
18.75	1.0859	1.0859	1.0859	1.0859	1.0859	1.0859		
20	1.1069	1.1069	1.1069	1.1069	1.1069	1.1069		
21.25	1.1262	1.162	1.162	1.162	1.162	1.162		
22.5	1.1454	1.184	1.184	1.184	1.184	1.184		
23.75	1.2089	1.2089	1.2089	1.2089	1.2089	1.2089		
25	1.2724	1.2724	1.2724	1.2724	1.2724	1.2724		

Table I

Run Time - Seconds

GeO₂ In SiO₂ Solvent

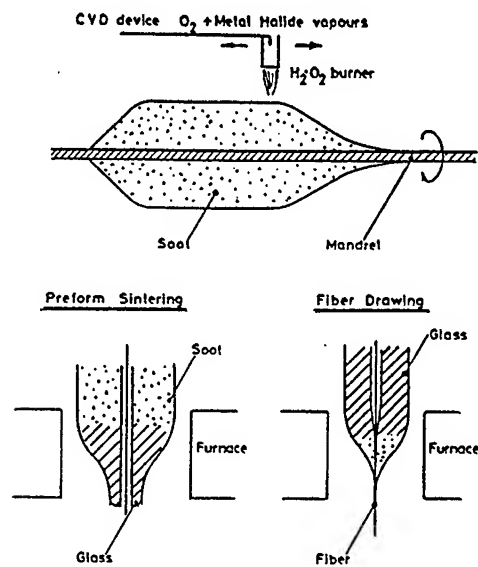


Figure 1.0

OVD Method For Implating Chemistry Reaction And Fiber Forming

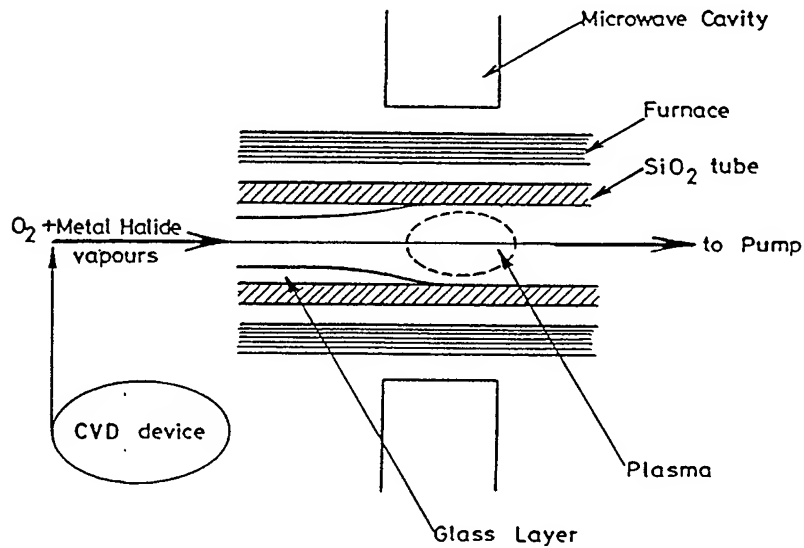


Figure 2.0

PCVD Method For Implating Chemistry Reaction And Fiber Forming

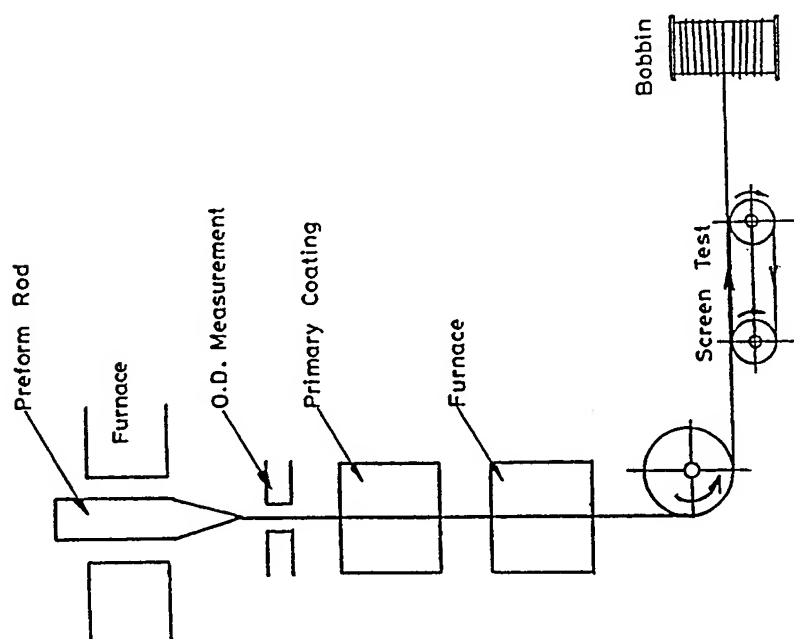


Figure 3.0

Fiber Drawing

Time Temperature History For GeO₂ Doped SiO₂ 5 Micron Diameter Fiber

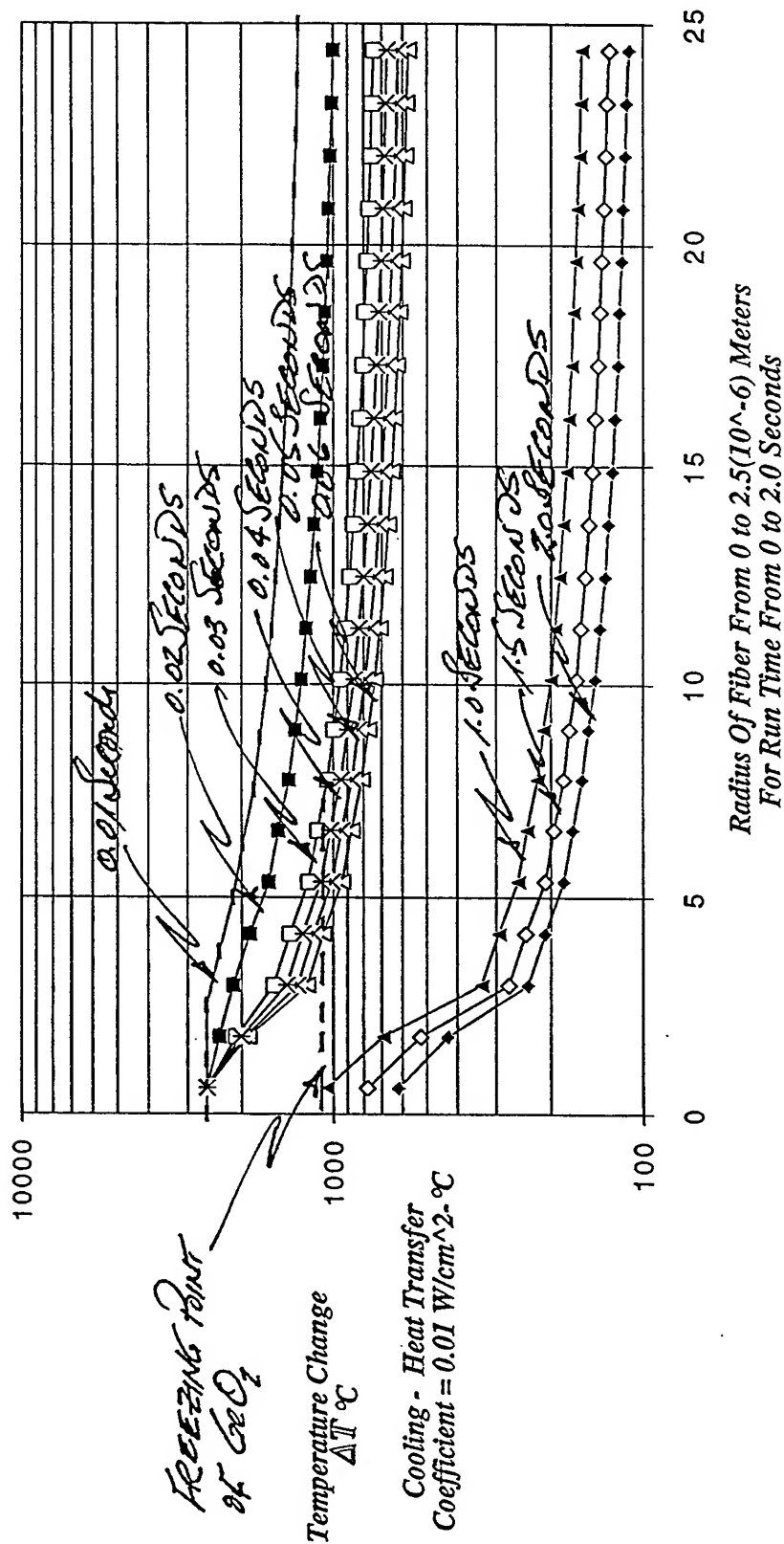


Figure 4.0

Temperature Gradient Along The Cylindrical Radius
As A Function Of Time

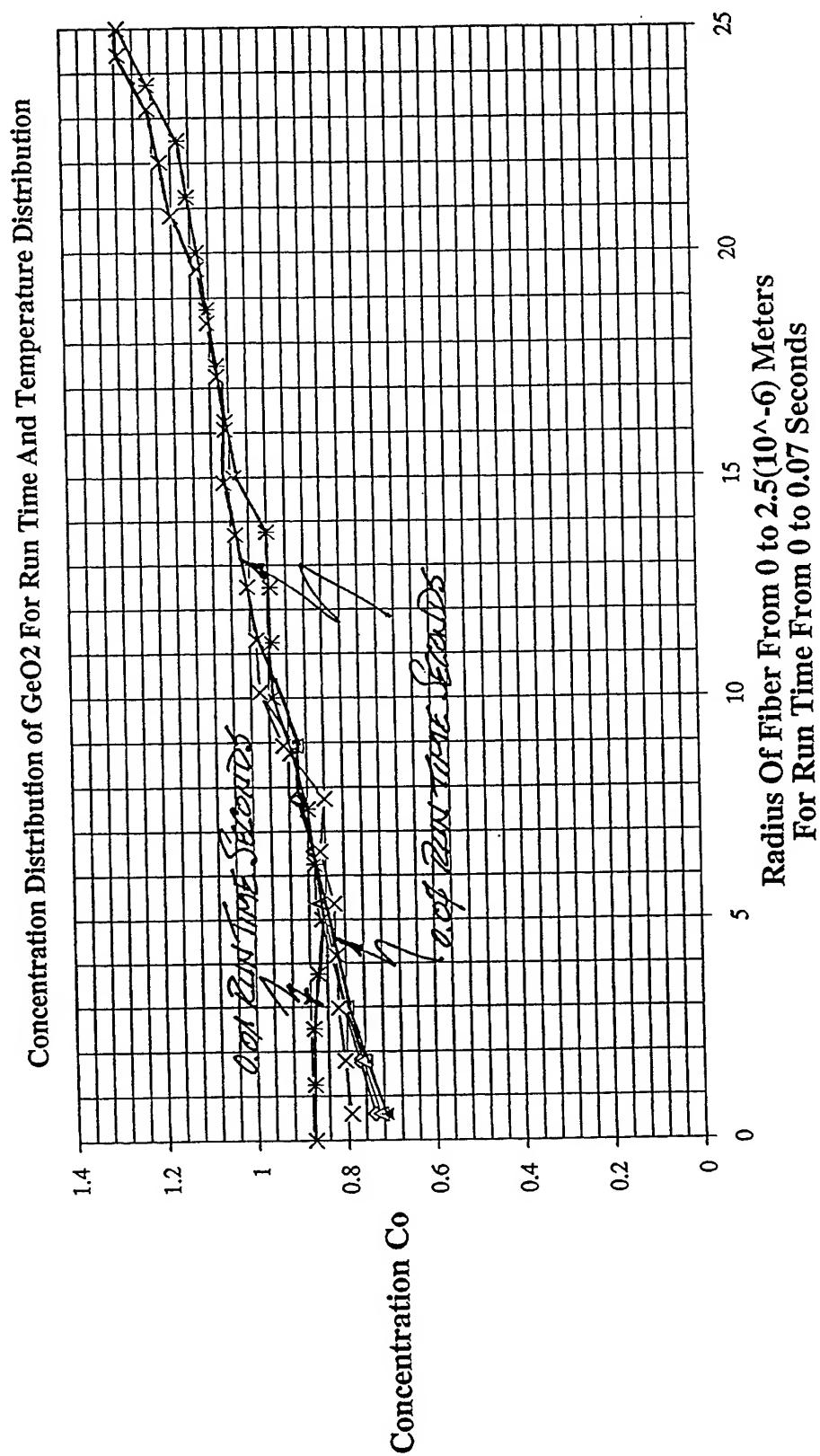


Figure 5.0

Diffusion Gradient As A Function Of Radius And Time

Lorentizan Geometry

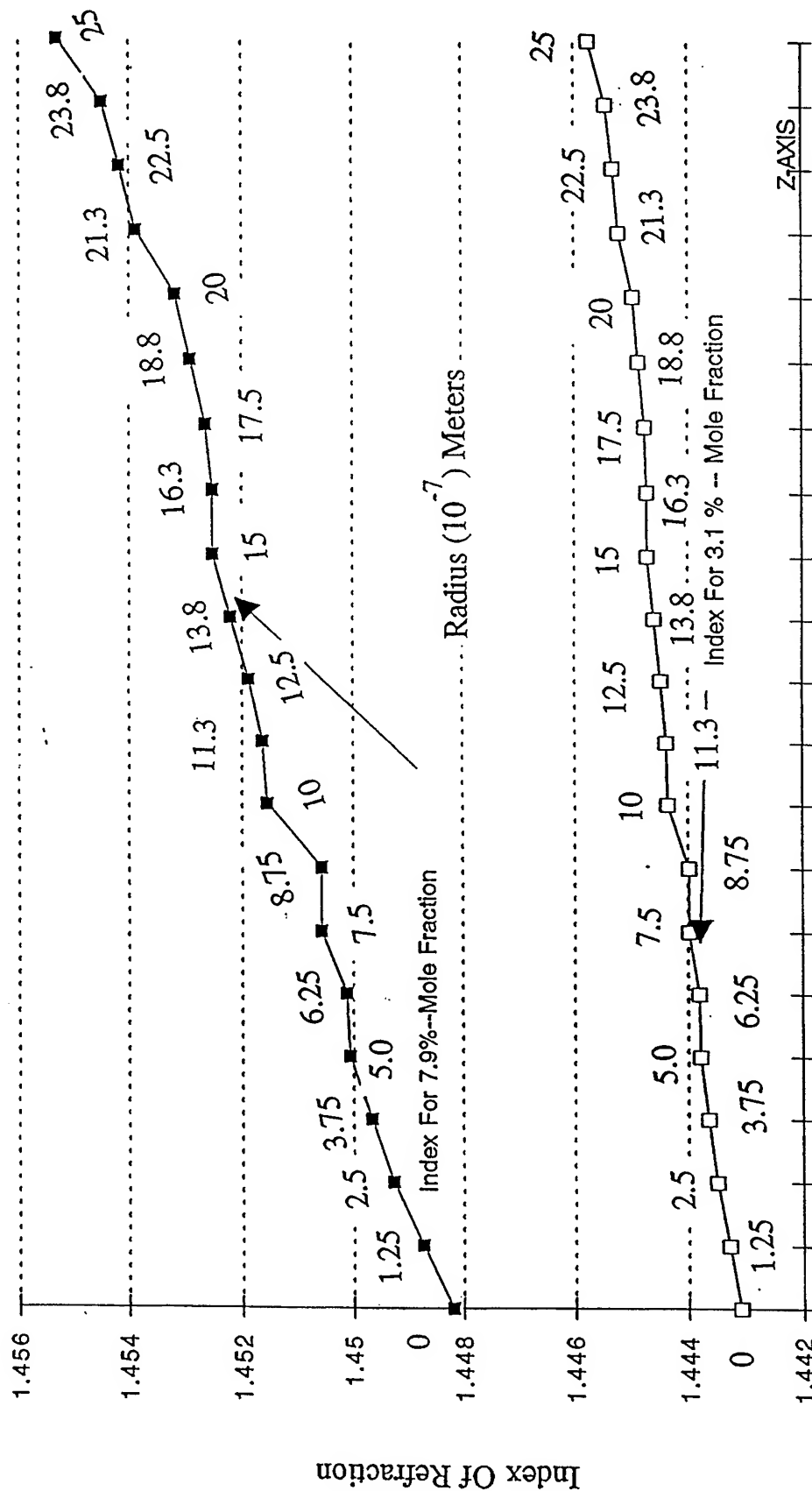


Figure 6.0

Index Gradient As A Function Of Radius - 3.1 % And 7.9% -Mole

Lorentizan Geometry

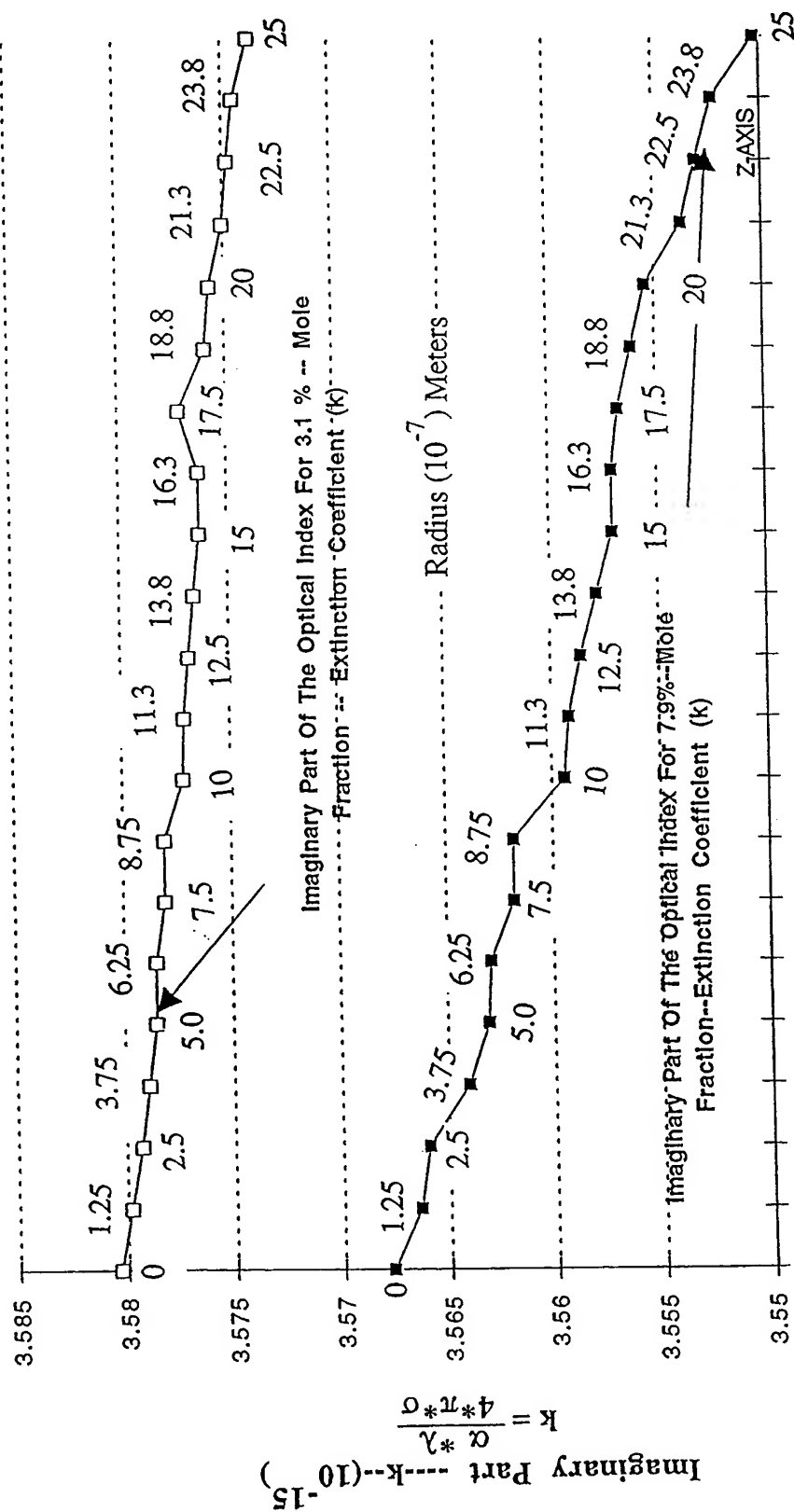


Figure 7.0

Imaginary Part Of The Optical Index
Extinction Coefficient

Lorentizan Geometry

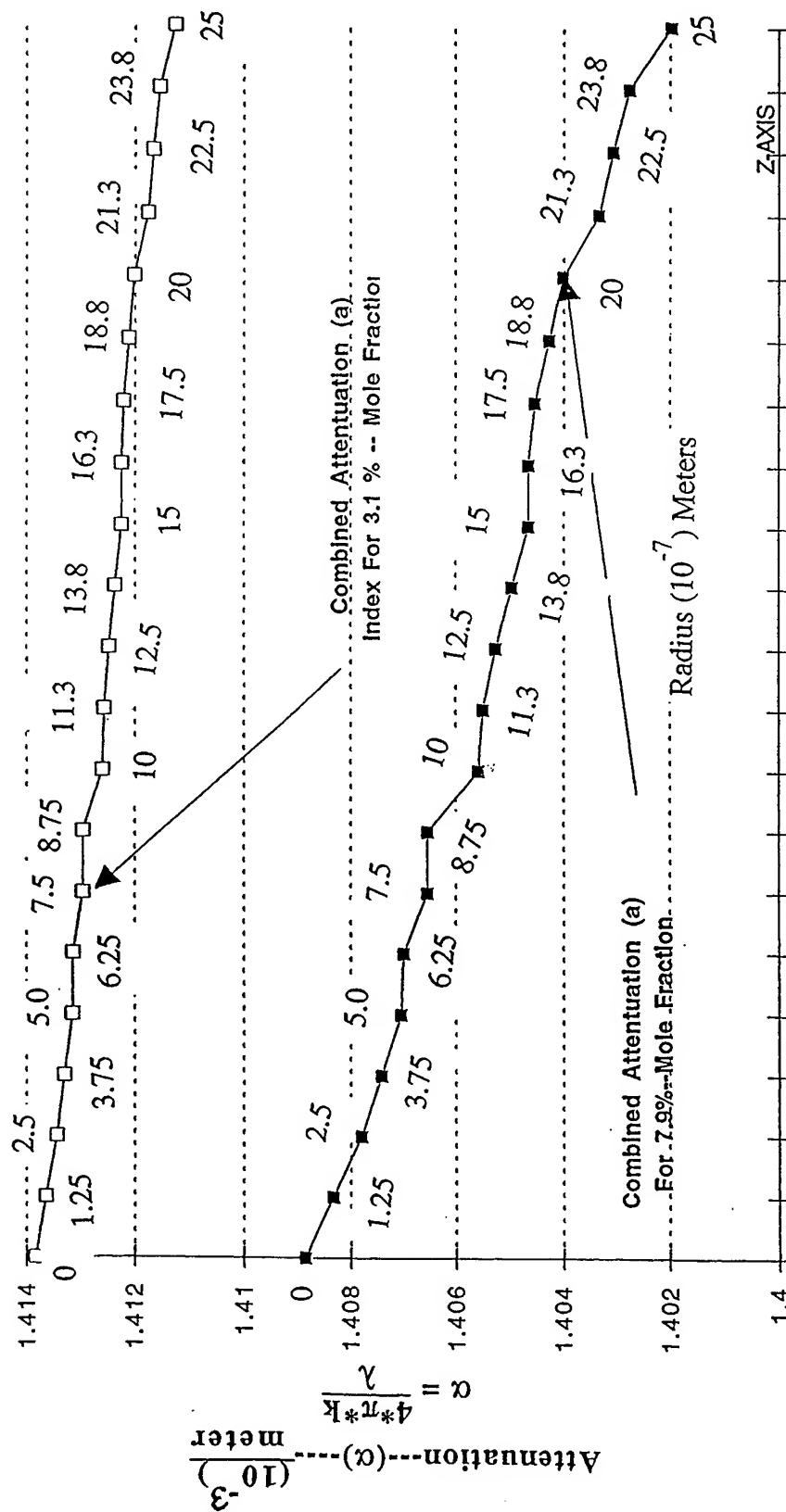


Figure 8.0
Attenuation Coefficient

Considerations on joined optical channels

George Copot*, Rodica Copot
Institute of Optoelectronics, Magurele - Bucharest

ABSTRACT

In many opto-electronical apparatuses it is necessary to overlap two or more optical images on the same image plane. For apparatuses having similar optical scheme, such a problem means different optical path and components for subassemblies with similar function. For each application, there are designed specific optical channels using similar optical elements to project similar objects, which differ in shape and size. Hence such devices have many disadvantages and basically they are not interchangeable. That is why it is very important to find new methods to join optical channels and the paper presents the results of the studies we have made in this direction.

Keywords: optical system, optical channel, night aiming device, aiming graticule, elevation angle

1. INTRODUCTION

It is well-known that the design of the aiming graticule for the night aiming devices implies optical systems that are included into the device construction. These subassemblies inject gradet scales with the proper elevation angles according to the types of munition that are being used and they use more optical paths, one for each projected element. These optical paths are combined by at least two beamsplitters.

There is not an independent module that settles the matter and that could be used for varied types of weapons and munition.

2. PRESENTATION OF THE MODULE

We have had to design a module for the aiming graticules injection for various night aiming devices. We have had to take into consideration the following constituent assemblies:

- aiming graticule – angular scale assembly with afferent acting device;
- objectives assembly;
- beam splitter assembly;
- mobile mirror assembly with afferent acting device;
- fixed mirror assembly;
- general frame of the module provided with a device for placing and centering on the night sight apparatus.

The design is described as it follows according with Figure 1 (isometric projection of the module with sections to emphasize the main assemblies) and Figure 2 (optical scheme of the module containing the illustration of the manner of combination of the optical paths and of the way the image is obtained).¹

The module consists from an aiming graticule – angle scale assembly (1), an objective assembly (2), an optical beam splitter assembly and a fixed mirror assembly (4), all four being positioned inside a frame (6) which is equipped with a cylindrical surface (a) for positioning and centring the module on the aiming device it is attached to as well as with several passing wholes (b) for fixing. On the frame there are also two mechanisms: one for operating the aiming graticule (7) and the other for operating the mobile mirror (8).

*Correspondence: Email:gcopot@k.ro; Telephone: 401 780 6640; Fax: 401 423 2532

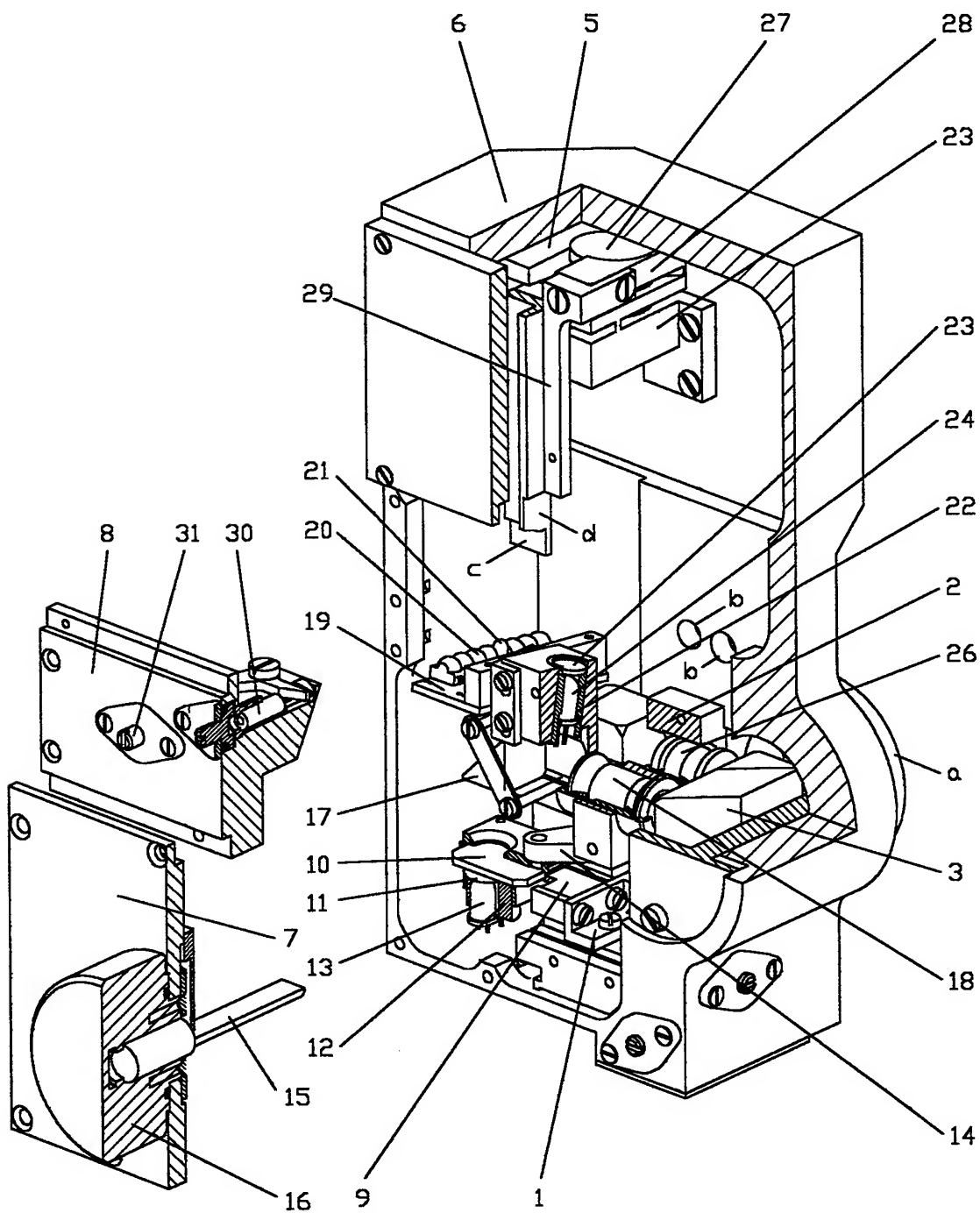


Figure 1



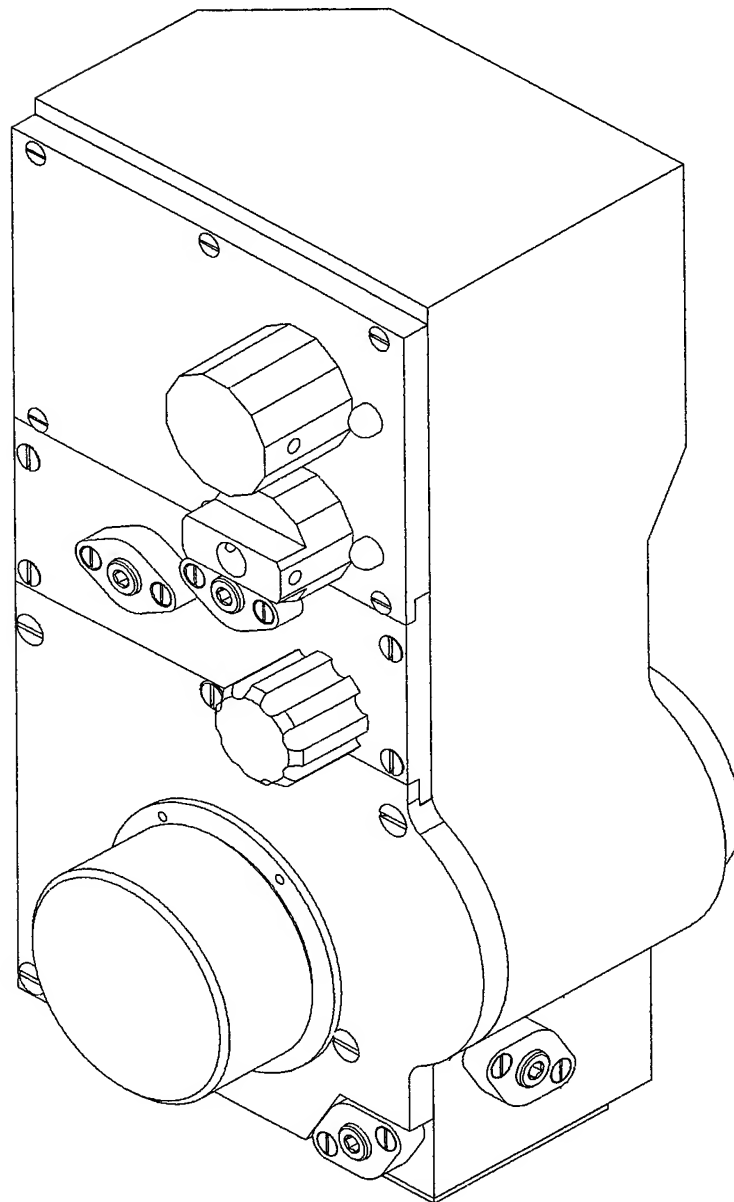


Figure 3

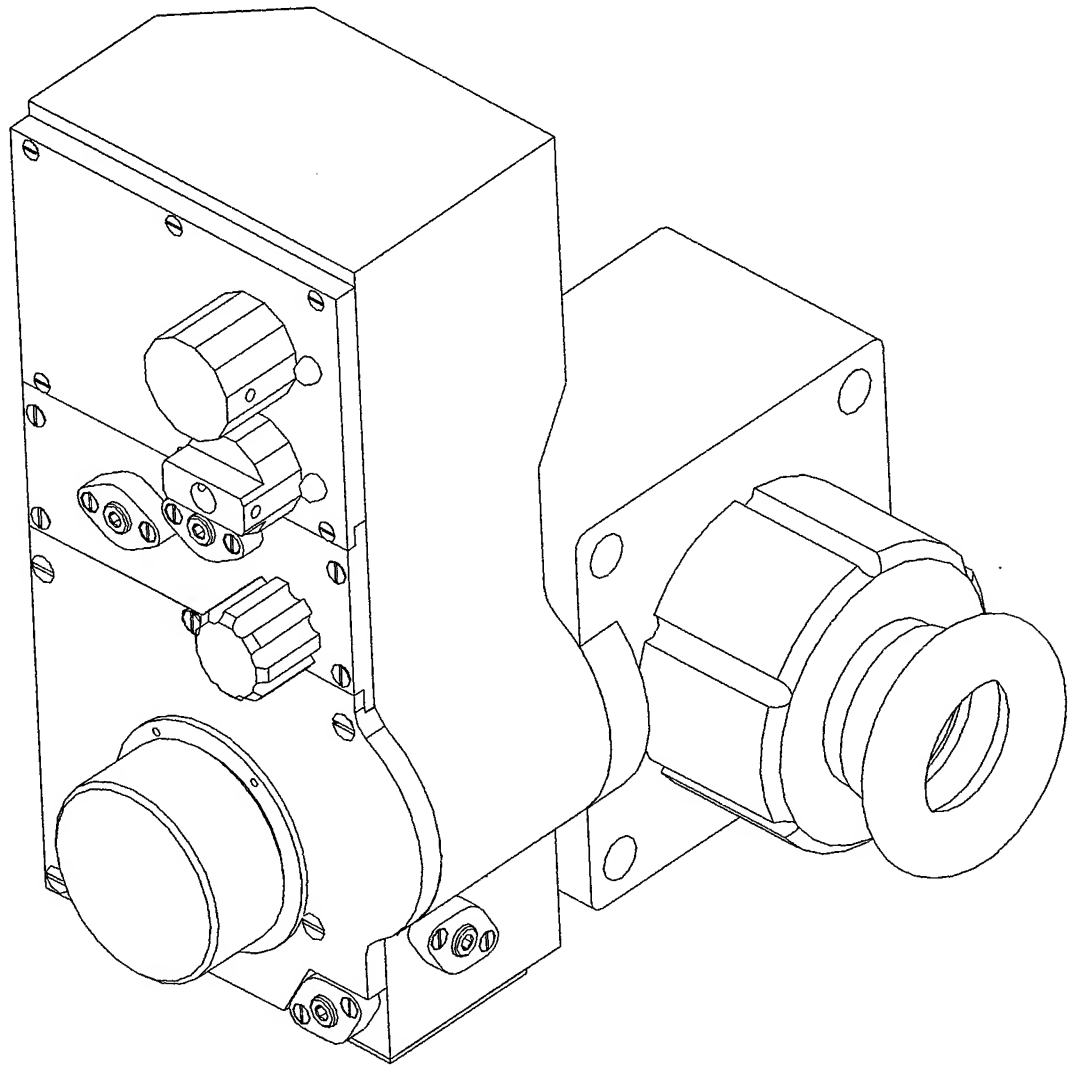


Figure 4

The aiming graticule – angle scale assembly contains the support (9) to which a scale graticule (10) with engraved angle marks is fixed. The assembly also sustains and guides the movement of an aiming graticule (11) which is fixed into a mounting (12) together with the light emitting diodes (13) which ensure the lightening of the marks engraved on the graticules. The position of the aiming graticule towards the scale graticule results from the position of a lever (14) which is operated by a peg (15) that belongs to the aiming graticule operating mechanism and is operated by the shooter using a button (16). The aiming graticule is positioned nearly the scale graticule so that the engraved marks (transparent marks on a dark background) on the two glass plates should overlap in the image plane. A transparent window engraved on the aiming graticule permits the partial display of the angular scale and the change of the place of the aiming graticule when pushing the button (16) permits the display only of the zone belonging to the neighbourhood of the adjusted elevating angle.

The objective assembly contains: a 90°deviation prism (17); an objective (18) for the injection of the aiming graticule and of the angular scale; a subassembly with display elements (19) which consist of two groupes of numeric display boards with 4 digits each and also of a light emitting diode (21); a mark assembly for the laser rangefinder (22) which contains a target positioning graticule (23) and a light emitting diode (24), a 90°deviation prism (25), an objective (26) for the projection of both numeric display boards and the positioning graticule.

The mobile mirror assembly consists of: a mirror (27) fixed to an elastic support (28) so that the mirror can oscillate on two axes, a lever (29) with two surfaces (c) and (d) where two adjusting mechanisms (30) and (31) belonging to the (8) assembly, are operating.

The (32) mirror of the fixed mirror assembly deviates the A beam from the numeric display boards towards the (25) prism. After a new deviation in a perpendicular plane on the first one, the beam is directed to (26) objective. The (27) mobile mirror deviates the B beam from the positioning graticule towards the (25) prism and (26) objective. In this way the first joining up of two beams is obtained without radiant energy losses.

The emergent beams from (26) objective, A' and B', are reflected by the (e) surface of the (33) beamsplitter and are directed towards the image plane.

The C beam is deviated by the (17) prism, then it passes the (18) objective, it is deviated again and it passes the (e) surface and it is directed towards the same image plane, as C' beam.

Adjusting of the relative position of the projected images, their centring in the field of view are achieved by the translation and the rotation of the (3) beam splitter and the rotation of the (27) mobile mirror. Focusing in the same plane of all the images is made by the axial moving of the (18) and (26) objectives and of the mark assembly of the laser rangefinder.

The aiming graticule assembly was carried out in a compact and miniatural construction as it is shown in Figure 3. The overall dimensions of the module are 170 x 95 x 60 mm.

The attachement of this modular configuration at the ocular assembly of a night aiming sight was made with minimum adaptations of the existing device. It was obtained the assembly that is shown in Figure 4.

3. CONCLUSIONS

The module for the injection of aiming graticules has the following advantages:

- it can be attached to already existent aiming devices or included into the construction of new ones;
- it uses a single angular scale of elevation and displays a limited number of marks those in close proximity of the selected angle;
- it permits the simultaneous display of all signs and entire information, but it also allows the selection of the necessary signs and amounts of information according to a previously defined manner of use.

REFERENCES

1. Application for protecting by patent no. C/44 / 1999.01.31 of OSIM, Romania

Thermovision used for determination of thermal losses in thermoelectric plants

Rovena Pascu*, Alexandra Caramizoiu
Institute of Optoelectronics, 76900, 111 Atomistilor Str., Bucharest, Romania

ABSTRACT

Thermographic methods and equipment are very useful in detecting energy losses by heat emission in thermoelectric plants; these methods allow the predictive maintenance of such plants and ensure a diminution of operating costs. Classical methods for determination of warmer spots and areas (into which the heat exchange between the object and environment exceeded the admissible values) are inefficient and sometimes impossible to achieve, especially in the case of large plants. A global analysis of the areas into which can appear heat leakage was carried out using thermography, the method being independent from the complexity and the placing of plants. The method of thermography allows an easy location of these thermal losses and their qualitative estimation. Experiments were carried out using the LORIS thermovision equipment. The thermal images were processed dedicated software, ThermoGRAM for Windows 95. Some relevant thermal images presented in this paper, also.

Keywords: thermovision, thermoelectric and electric plants

1. INTRODUCTION

Every object from the nature emits what is usually called thermal radiation, which mainly consists on electromagnetic radiation emitted during the transmission between rotational and vibration levels and, in particular, on electromagnetic thermal radiation reflected by the object and emitted by other thermal sources.

The image obtained from the information contained in a IR band of the electromagnetic spectrum is generated and contains data about the temperature of the surface of objects. The common action of the temperature and the characteristics of reflection and emission of the surveyed objects from the field of view can be modelled in terms of an equivalent temperature of these objects. At such a temperature the measured density of the emitted radiation in the region of the examined element would be obtain, if the object would be an absolutely blackbody. In the same manner, the density of the emitted radiation, measured by taking into account the atmospheric attenuation, can be modelled in terms of an a apparent temperature. The apparent temperature has a smaller value than the calculated equivalent temperature.

The equipment¹ that can offer information about the field of view under the form of such thermal images (thermal maps) is named thermovision equipment. The principle of obtaining thermal images using a thermovision equipment operation is the following: the optical system focused the infrared radiation emitted by the objects in the field of view, makes its spectral filtration and focused it on the system of detectors (single or multiple detectors or matrix of detectors). The scanning system ensures the coverage of the whole image by the detectors. The output electrical signals of the detectors are then amplified, multiplexed, analog-to-digital converted and reproduced in the form of a TV-compatible image displayed on usual TV or video monitors. The contrast of image and the brightness can be adjusted in order to have a thermal image looking like the corresponding visible image. The thermovision equipment are apparatus that use a high technology; they have high performances in the field of measuring the temperature and emissivities, and are very expensive.

The problem of preventive maintenance and non-destructive control by monitoring in real time the installations and equipment using the thermovision method² is of a great importance for a large number of industrial branches as: metallurgy, chemical industry, machine building industry, energy, transportation of the thermal agents. The identification in due time of critical points of the installations would permit to the companies to prevent the destroy of the installations and of course to save the time and costs required by repairing of such installation.

* Corresponding: Phone: (401) 780.66.40; Fax: (401) 423.25.32

2. EXPERIMENTAL EQUIPMENT AND SET-UP

The type of the system used for measuring in far infrared is Thermoteknix for Microsoft Windows (ThermaGRAM), which used as a thermal sensor the LORIS equipment made by Inframetrics.

2.1. Thermovision equipment

The thermovision system LORIS has a performant telescope in infrared with two compatible fields of view. The thermal sensor and the telescope are integrated into a sealed and secured casting. The video signal furnished by equipment is according TV CCIR 625 standard and the image is according the law of thermal detectors of black-white type. The thermal image is furnished from a four IR detectors group of CdHgTe type; this type of detectors can ensure the operation of the equipment in the 8-12 μm atmospheric window. The detectors are cooled to -196°C (77 K) using a miniatural cooler heaving as a working agent helium in close circuit. The power consumed by this cooler is extremely low (under 3,5 W) and this allows the supply of whole equipment from batteries. One scanner in two axis (the device of tri-dimensional scanning of virtual image) and the electronic blocks that generate the video signal using the output signal of the detectors ensure the obtaining of a high quality signal according the above mentioned TV standard.

A very important facility of this equipment consists on the possibility of direct connection with a PC type endowed with a board of a ThermaGRAM type for acquisition and quick processing of thermal images. The equipment can be remote controlled using a panel. The others characteristics are:

- fields of view: $7^\circ \times 5^\circ$, $2.3^\circ \times 1.2^\circ$ plus the possibility of using the electrooptic zoom and optical zoom (x2, x4)
- detectors: 4 detectors, CdHgTe
- thermal resolution: 0.01°C
- domain of measured object's temperature: -195°C - 100°C without use of a diaphragm to be needed; up to 1500°C with a diaphragm;
- cooling: down to 77 K; miniaturised criogenerator (Stirling cycle with He as a cooling agent)
- controls on the remote control panel; polarity, level of signal, changing the field of view, focusing

2.2. Thermoteknix ThermaGRAM

The Thermoteknix ThermaGRAM consists on³:

2.2.1 Hardware

Thermoteknix GRAM (or ThermaGRAM) is a board for real-time processing (subtract, average, filter, etc) of the thermal images. It has a high-precision analogue-digital converter, a 12-bits input and an electronic digital PLL that ensures video synchronization without a jitter and with a high tolerance to signal variations induced by analogue recording media (VCRs). The use of average is a very important feature for images with analogue input, because it allows reducing the noise level in the signal. The programmable amplification and the control over the offset ensure obtaining precise and real-time measurements of the input video signal.

2.2.2 Software

ThermaGRAM for Windows is a sophisticated software for acquisition and analysis of thermal images. The acquired images can be loaded in files or can be visualised ("live") on the computer's monitor by connecting a video camera or a VCR. The "live" images can be "frozen" and saved on the disk. An "incremental save" command allows to the user to easily successively save the images under some filenames that can suggest the fact that these files represent different moments of the same process, registered by sampling. The modernised GRAM board allows to "live" acquire and save a set of images at two seconds intervals. The successive files obtained using one of these methods can be automatically loaded in a Windows "super-image", in order to be analysed afterwards using some pre-established procedures.

The thermal images loaded in files can be visualised using a large scale of various pseudo-colour palettes; for every palette, the temperature interval can be manually changed or optimised by the computer.

The analysis possibilities are the followings:

- Displaying punctual temperatures (at a pixels level);
- Tracing isothermes for individualising with a specific colour band the portions from the images that have a temperature within a specific interval;
- Tracing contours that can be used afterwards as graphic entities ("objects") for establishing the "intervals dividers" (as means of display the minimum, maximum and median temperature along a line) or for tracing temperature profiles along a line in a distinct graphic window;
- Tracing temperature profiles over the displayed image;
- Tracing rectangular, elliptic and polygonal contours that can be used afterwards as "objects" for displaying the minimum, maximum and mean temperatures in a specific region, using histograms;
- Displaying the differences between temperatures using various other means;
- Using labels for identification of "objects", etc.

2.3 Experimental set-up

Using the LORIS thermovision equipment, experiments were done at CET-Vest Bucharest. The equipment, controlled by the controlling panel, was connected to a VCR and a PC. The thermal images registered using the LORIS equipment (for the 8 - 14 μm) were visualised in real-time on the computer's monitor and saved on the videotape. The images were processed using the dedicated software.

3. EXPERIMENTAL RESULTS

The results are presented in the form of processed thermal black and white images. Using thermovision technique, point or regions of the installations warmer than normal could be identified.



Fig.1 Steam turbine. The standard breakage, corrosion or a poor connection can lead to a modification in thermal radiation emission

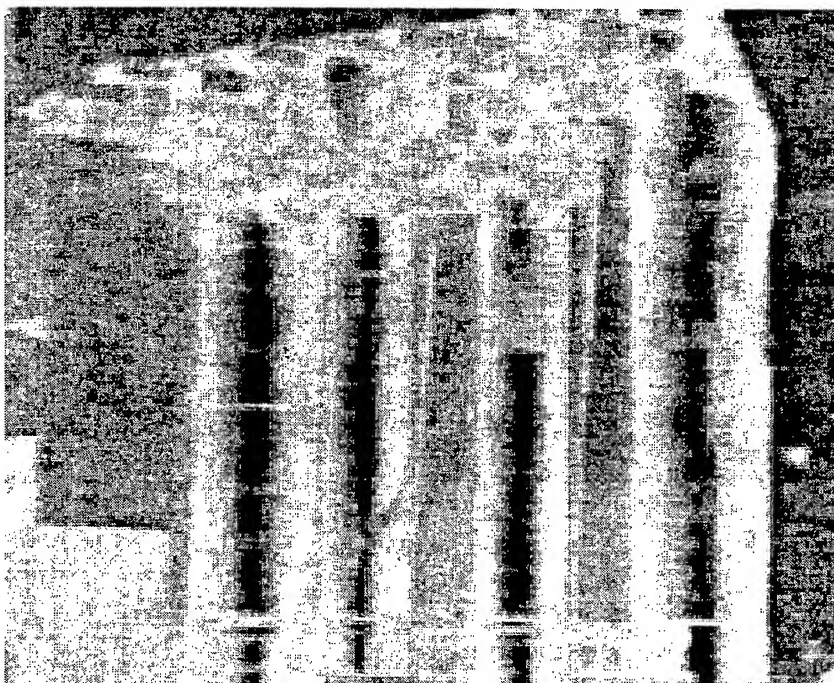


Fig.2 Transport pipes of the thermal agent. The uniformity in heating can be seen in this image



Fig.3 Transport pipes of the thermal agent. The uniformity in heating can be seen in this image (blacker zone)



Fig.4 Steam turbine. The uniformity in heating can be seen in this image (black zone)



Fig. 5 Detail of a steam transport pipe. Differences between its lower and upper parts from a temperature's point of view can be observed, and also a possible future break



Fig.6 Early stage of processing a thermal image of the steam transport pipes

REFERENCES

1. J.M.Lloyd, *'Thermal Imaging Systems'*, Plenum Press, New York, 1975.
2. The Infrared Handbook, The Infrared Information Center - Environmental Research Institute of Michigan, 1989.
3. ThermaGRAM User Manual, Thermoteknix Systems Ltd, issue 1.2, 1995.

Simple effective tests for beam propagation method programs

M. Dumitrescu^a, O. Iancu^b, J.-M. Karam^c

^a Optoelectronics Research Centre, Tampere University of Technology,
P.O. Box 692, FIN-33101, Tampere, Finland.

^b Optoelectronics Research Center, 'Politehnica' University of Bucharest,
Bd. Armata Poporului 1-3, Bucharest, Romania.

^c Institut National Polytechnique de Grenoble, TIMA-CMP,
46 av. Félix Viallet, 38031 Grenoble, France.

ABSTRACT

In view of the increased need of an effective, practical and unified test set to evaluate the modeling capabilities (and ultimately the trustworthiness) of beam propagation method (BPM) based programs, we propose a incipient set of tests to be used for a standard evaluation. The proposed tests have been chosen to be simple, easy to implement and enable a fairly good (although not complete) evaluation without the need of any experiment. Interesting aspects of the tests' results and some straightforward, practical criteria to estimate program capabilities and to tune the simulation parameters are presented. A cross-checking between 'Mode Solver' (MS) based and BPM based programs is also put into discussion. A paraxial error evaluation method is presented and the transverse mesh influence on the paraxial error is analyzed.

1. INTRODUCTION

Besides the commercial software packages using 'Beam Propagation Method' (BPM) variants there are many literature reports presenting improvements on BPM all the time^{1,2,3,4}. While the authors choose their examples to illustrate the advantages of their BPM tools the potential users are almost never able to make a consistent comparison based on the different examples. Furthermore the various criteria for BPM program evaluation are frequently either formal, abstract ones – difficult to connect to a real problem – or impractical – presuming laborious theoretical investigations. In the meantime only a few comparative analysis (mostly for particular devices) for several BPM implementations have been reported^{5,6} and no standard benchmark test has emerged for a unified evaluation. In line of the development of a standard benchmark test for BPM based programs we propose some simple and effective tests : homogenous space propagation, eigenmode propagation in monomode and multimode waveguides and eigenmode selection through propagation of an arbitrary injection. The proposed tests have been chosen because they are simple, easy to implement and enable a fairly good evaluation without the need of any experiment.

2. BEAM PROPAGATION METHOD FORMULATION

The BPM problem formulation approximations must be carefully analyzed since they may significantly affect the BPM variant applicability and the accuracy of the results. The starting point for any BPM variant is the set of rigorous vectorial propagation equations derived from the Maxwell equations :

$$\Delta \vec{E} + \nabla \left\{ \frac{\nabla [\varepsilon_0 \varepsilon(x, y, z)]}{\varepsilon_0 \varepsilon(x, y, z)} \cdot \vec{E} \right\} + k_0^2 \varepsilon(x, y, z) \vec{E} = 0 \quad (1)$$

$$\Delta \vec{H} + \nabla \left\{ \frac{\nabla [\varepsilon_0 \varepsilon(x, y, z)]}{\varepsilon_0 \varepsilon(x, y, z)} \times (\nabla \times \vec{H}) \right\} + k_0^2 \varepsilon(x, y, z) \vec{H} = 0 \quad (2)$$

* Correspondence: Mircea.Guina%ORC@semi.ee.tut.fi

In order to simplify the problem practically every BPM variant uses some approximations. Among the most frequent ones are the paraxial approximation and the weak contrast approximations (weak transverse contrast ($\nabla_t \epsilon \approx 0$), weak longitudinal contrast ($\nabla_z \epsilon \approx 0$ if the generic, axial direction of propagation is taken to be Oz) and weak overall contrast ($\nabla \epsilon \approx 0$)). Also reduction in the problem dimensionality (from 2D to 1D in the transverse section)² and spatial variable change or conformal mappings are frequently employed^{7,8}.

The paraxial approximation (PA) providing equation simplification and a simplified solution form assumes that the energy is propagating only in a narrow solid angle around the generic direction of propagation (Oz). Special care should be taken in using the PA since the associated error (when the energy is propagating in a wider angle around Oz) is not easy to notice and may be neglected in analysis. The weak transverse contrast approximation enables scalar formulation but the simplification is paid by the loss of vectorial information (for example the polarization information cannot be extracted). While some approximations are obvious in problem formulation there are many situations when the approximations are not apparent. The solution form :

$$\Psi(x, y, z) = P(x, y, z) \exp(-j k_0 n_0 z) \quad (3)$$

obviously implies the weak longitudinal contrast (since only the progressive propagation is considered) and the paraxial approximation for a field envelope $P(x, y, z)$ presumed to be slowly varying in the z-direction. On the other hand the weak overall contrast approximation may be introduced in a less visible manner by the implementation of the continuity conditions. Also many times some of the approximations' consequences are presumed without explicitly mentioning the respective approximations in the problem formulation. For example the coupling between transverse and axial components, which is a consequence of the refraction index variation along the axial direction, is frequently ignored even in vectorial formulations although the weak longitudinal contrast approximation is not mentioned.

The application of a certain set of approximations to (1) and (2) leads to the equation to be solved, usually either the scalar Helmholtz equation :

$$\frac{\partial^2 P}{\partial x^2} + \frac{\partial^2 P}{\partial y^2} + \frac{\partial^2 P}{\partial z^2} - 2jk_0 n_0 \frac{\partial P}{\partial z} + k_0^2 (n^2 - n_0^2) P = 0 \quad (4)$$

or the scalar parabolic equation :

$$\frac{\partial^2 P}{\partial x^2} + \frac{\partial^2 P}{\partial y^2} - 2jk_0 n_0 \frac{\partial P}{\partial z} + k_0^2 (n^2 - n_0^2) P = 0 \quad (5)$$

Most frequently finite difference method (FDM), finite element method (FEM) or (Fast) Fourier Transform (FFT) formalisms are employed (usually together with some improvement like the Padé approximation, alternate direction implicit approach, DuFort-Frankel scheme or Douglas scheme^{1,4,9,10,11}) towards the solution. At this stage special attention must be given not only to the operator modifications but also to their application point. For example the application point for the $\partial^2/\partial x^2$ and $\partial^2/\partial y^2$ operators in the FDM formalism delimitates the explicit methods from the Crank-Nicholson ones and affects the transverse sample correlation. Also sensible accuracy improvement may be obtained by properly placing the application point of the phase and spectral correction operators in the split-step FFT BPM.

The FFT formalism enables an interesting insight in the propagation modeling. The spatial spectrum samples obtained by applying the FFT to the transverse field distribution samples correspond to transverse-plane projections of plane waves propagating at different angles with respect to Oz. The angles θ_i for 1D transverse section are given by :

$$\theta_i \cong \arcsin[\lambda_0 / (n_0 T_{x_i})] \quad (6)$$

where T_{xi} is the 1D transverse periodicity associated with the spatial spectrum sample. Since the plane wave propagation angles increase with reduction of the associated transverse periodicity the maximum angle at which the energy propagation is modeled is – for a constant discretization step :

$$\theta_{\max} \cong \arcsin[\lambda_0 / (2n_0 \Delta x)] \quad (7)$$

Therefore in order to avoid that the transverse mesh produces some paraxial error (in the sense that the energy propagation is considered to take place in a solid angle smaller than the real one) the transverse mesh step should be smaller than $\lambda_0 / (2 \cdot \max\{n\} \sin \theta_{r_{\max}})$ - where $\theta_{r_{\max}}$ is the maximum angle at which the energy propagates in the real case. If $\theta_{r_{\max}}$ is not known a more restrictive condition can be imposed $\Delta x \leq \lambda_0 / (2 \cdot \max\{n\})$. In case of variable transverse mesh step the conditions must be fulfilled by the maximum transverse mesh step to assure that local energy propagation is properly modeled. Fortunately even in the most restrictive conditions this limitation imposed on the transverse mesh step can be respected rather easily. It has to be mentioned that these limitations are intrinsic to transverse discretization and are valid for all BPM variants irrespective on whether the spatial spectrum is calculated or not.

The boundary conditions also have a significant influence on the accuracy of the results mostly when simulation uses a small transverse calculus window (TCW) and/or divergent propagation takes place. Various boundary conditions have been proposed - absorbing boundary conditions, transparent boundary conditions, impedance-matched boundary layers^{12,13}. Since there is not possible to assure zero boundary reflectivity for all incident angles and a wide spectral range the boundary conditions may sometimes require adjustment according to the simulation problem – a fact not obvious for the inexperienced user.

In our tests we have used several BPM variants mostly in our own implementation (8 FDM based variants and 4 FFT based variants). Unfortunately, up to the moment of paper publication we could not get the agreement from the commercial BPM program vendors to include a comparative set of results obtained using their programs. However many of our conclusions were derived from tests performed with BPM programs from different sources.

3. HOMOGENOUS SPACE PROPAGATION TEST

Although performing a homogenous space BPM propagation test may seem at least strange there are a lot of interesting conclusions to be drawn. Actually there is no BPM method capable of performing a reasonably accurate homogenous space propagation – mostly if the incident beam diameter is small. The difficulties arise mostly from the increase in maximum divergence angle and in diffraction effects as the incident beam diameter is decreasing. Fig. 1 shows an example result of FFT BPM homogenous space propagation modeling. The transverse section was taken 1D – in order to have a better representation of the modeled propagation (this being valid for all the BPM results presented in the paper) – and the injected beam was taken to have a parabolic distribution – in order to have clearly delimited the region through which the energy is injected.

The first thing that can be analyzed is the shape of the wavefront for a (quasi-) punctual source. The closer the calculated wavefront is to a semi-circle (for 1D transverse section) or to a hemi-sphere (for 2D transverse section) the better is the dispersion equation approximated. The paraxial approximation changes the hemispheric dispersion equation ($k_z = [k_0^2 \cdot n_0^2 - (k_x^2 + k_y^2)]^{1/2}$) into a series expansion approximation that frequently uses only the quadratic term thus leading to a parabolic dispersion equation ($k_z = k_0 \cdot n_0 - k_x^2 / (2 \cdot k_0 \cdot n_0)$). Analyzing the difference between the wavefront of the homogenous space propagation and the envelope of weighted semi-circular / hemispheric wavefronts associated with all the source points in the 1D / 2D transverse section one can easily find out the angle at which the difference becomes unacceptable (θ_{err}). If this θ_{err} angle is greater than the maximum angle at which the energy is propagating in the structure to be modeled - then the respective BPM method will model the divergent energy propagation with acceptable accuracy.

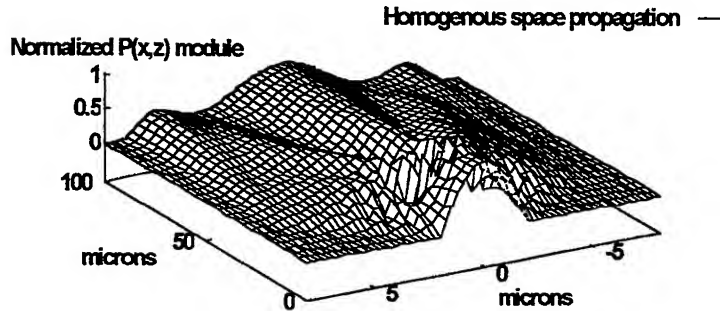


Fig. 1 BPM-modeled homogenous space propagation (1D transverse section)

An interesting modeling phenomenon can sometimes be observed by analyzing the power transfer. Since the time dimension

of the problem is neglected, power transfer through a wavefront is proportional with $\mathfrak{I} = \int_{\text{on wavefront}} [P(x, y, z)]^2 ds$. Fig. 2

shows the computed value of \mathfrak{I} (in arbitrary units) depending on the radial distance to the wavefront along which the integral is computed. The initial wavefront (from which the radial distance is measured) was taken to span up to the diameter of the injected beam and the integral was taken – obviously – only inside the area covered by simulation. While the homogenous medium has no gain or loss one would expect constant \mathfrak{I} up to the point where the wavefront reaches the border of the transverse calculus window (TCW) – or, more correctly, up to the point where the wavefront reaches the boundary condition region. From this point on one would expect a decrease in \mathfrak{I} as the energy leaves the calculus window through the border. The rate at which energy is lost through the border can also be analytically evaluated and compared with the energy loss through the border given by BPM simulation. The difference is a good indicator of the quality of the border conditions used. If the decrease in \mathfrak{I} on the second part of the variation depicted in Fig. 2 is due to energy loss through the border what is the explanation for the first part of the variation? At first we considered it a spurious effect of the numerical method. Afterwards we found, however, a possible physical explanation.

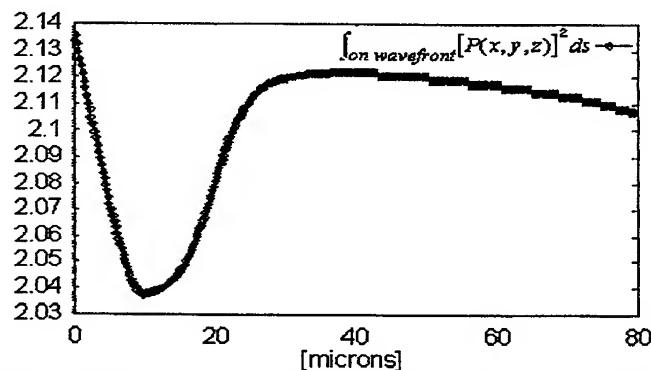


Fig. 2 Variation of the field distribution energy along successive wavefronts in a BPM-modeled homogenous space propagation

The diffraction is a continuous phenomenon and the BPM method is not able to model its effects when they are felt over distances that are smaller than the discretization steps. Therefore at small z_i , where the diffraction phenomenon has effects on a spatial range smaller than the discretization steps, the modeled field distribution has discontinuities. As the propagation continues towards greater z_i the spatial range of the diffraction effects becomes greater than the discretization steps and the BPM method captures more accurately the diffraction effects (the field distribution becomes smoother). It seems that the BPM method accumulates at least some of the field energy from the regions with field distribution discontinuities in higher-frequency spatial-spectrum components. As the spatial extension of diffraction effects becomes comparable and then greater

than the discretization steps the BPM method gradually recovers this energy into lower-frequency spatial spectrum components. We observed the effect in more than one FFT-BPM but the magnitude and the distance over which the 'recovery' took place were different for the same modeling problem. Although the conservation properties of the scalar and polarised FD-BPM have been mentioned in literature⁶, to the best of our knowledge the 'recovery' effect was not systematically analyzed or explained – probably due to the small distance scale over which it takes place. The effect is clearly depending on the method and simulation parameters but it still could be considered a favorable temporary spectral-aliasing effect if the distributions in the 'discontinuity' area are not used in the analysis supported by simulations.

4. EIGENMODE PROPAGATION TEST

Another simple test is to propagate the eigenmode of a monomode guide. At first sight it seems that not many conclusions can be drawn. There are however some interesting observations to be made analyzing the results of such a test. The energy in the spatial TCW must be equal with the energy in the spectral calculus window and both must remain constant with increasing z . The failure to fulfil this condition indicates that either the TCW extension or the TCW discretization step were not properly chosen. Some other conditions to be observed are that the wavefront should be plane for a real-valued refraction index distribution and that the field envelope distribution should remain constant along Oz . However we found out by using this test that many BPM programs do not propagate the eigenmode of the structure but rather a stable transverse distribution which could be considered an eigenvalue of the BPM operator – since for a uniform guide the BPM operator remains constant. Although most of the times the error is rather small the effect can be easily observed. Fig. 3 shows the result of an eigenmode propagation test using a FDM-BPM variant. Since the injected field distribution is exactly the analytic eigenmode of the monomode guide over which the propagation is simulated it can be seen that the propagated stable field distribution is in fact the FDM-BPM operator eigenvalue.

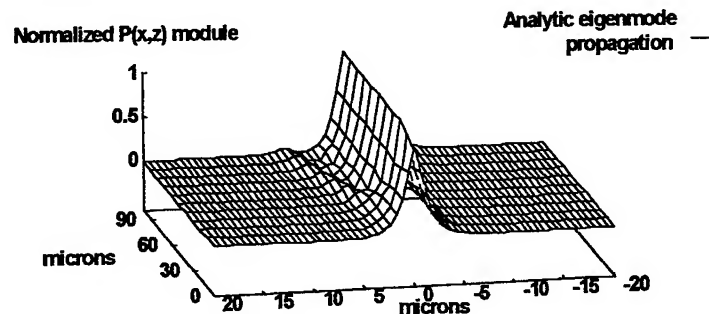


Fig. 3 BPM eigenmode propagation in a monomode guide – showing that the propagated stable transverse distribution is actually a BPM operator eigenvalue

If the guide to be modeled has a refractive index distribution that doesn't enable an analytic solution a crosscheck between a BPM and a Mode Solver (MS) method can be used. If the solution obtained by the MS is propagated by the BPM along the same guide with no significant alteration then the two methods validate each other. If significant difference occurs then both methods should be checked against some propagation problems with analytical solution.

The results of the eigenmode propagation test can also be used to evaluate the effective index of the guided modes. Since the phase correction included in the neglected ($\exp(-j \cdot k_0 \cdot n_0 \cdot \Delta z)$) term is different from the actual spatial phase correction term ($\exp(-j \cdot k_0 \cdot n_{eff} \cdot \Delta z)$), the residual phase correction ($\exp(j \cdot k_0 \cdot (n_{eff} - n_0) \cdot \Delta z)$) is included into $P(x, z_i)$ samples and can be used to evaluate the guided mode effective index. Fig. 4 shows the distribution of the real part of a FFT-BPM propagated eigenmode envelope $P(x, z_i)$. The envelope variation due to the residual phase correction can be easily observed and its period can be used to evaluate the guided mode effective index. Superior results in evaluating the propagation constants can be obtained using the imaginary distance BPM approach¹⁴.

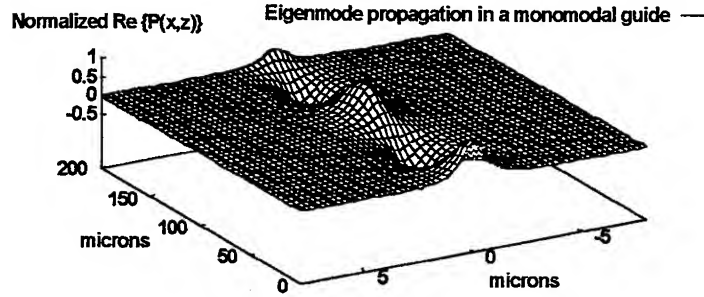


Fig. 4 Normalized real part of a BPM-propagated eigenmode envelope

A more powerful eigenmode propagation test can be realized by simulating the propagation along a monomodal straight guide that is tilted with respect to the generic direction of propagation Oz ⁵. In this case not only the BPM ability to model divergent energy propagation is tested but also the BPM-variant sensitivity to transverse discretization errors. The discretization errors produce an error field consisting of a set of plane waves propagating at different angles with respect to the Oz axis. The error field, although generally weak, can accumulate constructively – and significantly alter the BPM simulation results – if its phase change adds up to $2n\pi$. If the longitudinal discretization step is taken to be smaller than $2\pi/[n_0(k_0 - k_z)]$ then the constructive accumulation of the error field cannot take place. A number of BPM variants have been proposed for dealing with inclined guide sections ^{1,4,5,6}. Although the coordinate changes and the conformal mappings may be very effective in certain situations our point is that their use should be carefully analyzed since they induce significant restrictions on the BPM operators and on the discretization mesh.

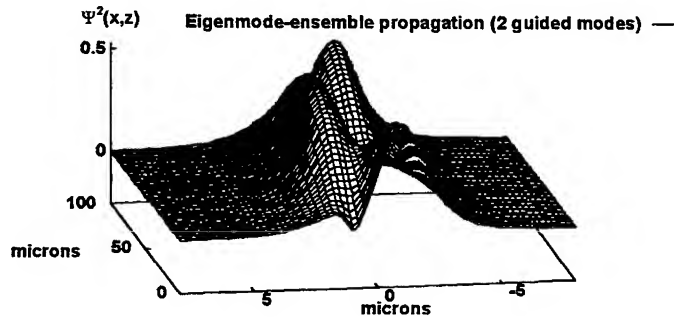


Fig. 5 BPM-modeled propagation of a 2 guided modes ensemble

The propagation of a guided mode ensemble in a multimode guiding structure can also lead to some interesting observations. Fig. 5 shows a FDM-BPM modeled propagation of the 2 guided modes ensemble in a step index profile guide while Fig. 6 shows a FFT-BPM modeled propagation of the 5 guided modes ensemble in a graded index profile guide. The simulations were carried out on a 1D transverse calculus window and the final result was obtained by adding the neglected phase term to the $P(x,z)$ BPM solution : $\Psi(x,z) = P(x,z)\exp(-jk_0 n_0 z)$.

The BPM-simulated eigenmode ensemble propagation should exhibit a periodical Oz distribution. The closer this distribution is to the analytical or MS-derived eigenmode ensemble distribution $\Psi(x,z)$

$$\Psi(x,z) = \sum_{i=0}^{N-1} m_i \Psi_i(x) \exp(-jk_0 n_{eff_i} z) \exp(j\phi_i) \quad (8)$$

(where N is the number of guided modes and Ψ_i , $n_{eff,i}$, m_i , ϕ_i are respectively the guided modes' field distributions, effective indices, weights and initial phase values for a 1D transverse window) the better are the BPM variant capabilities to model not only divergent energy propagation but also reflections from dielectric interfaces. What can also be observed from Fig. 5 and 6 is that as the number of guided modes increases and the problem comes closer to the ray optics approximation, the BPM modeled field distribution presents one or more maximum-field paths that come closer to the geometrical optics ray path(s).

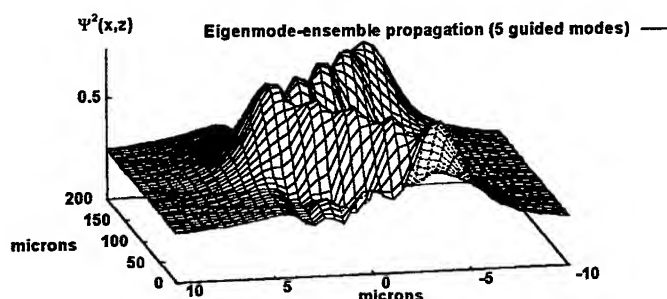


Fig. 6 BPM-modeled propagation of a 5 guided modes ensemble

5. EIGENMODE SELECTION TEST

Simulating the propagation of an arbitrary injection in a z -uniform guiding structure can sometimes lead to more complete conclusions on the BPM variant capabilities than the simulation of eigenmode propagation. Fig. 7 shows the result of propagating a quasi-parabolic field profile injection in a monomode guiding structure. It can be observed that the eigenmode is gradually selected while the injected energy that is not coupled into the eigenmode is eliminated by radiative modes through the cladding. Details of the eigenmode selection process can be observed in Fig. 8 where the quasi-parabolic injection, the eigenmode and the field distribution obtained after a $40\mu\text{m}$ BPM propagation of the quasi-parabolic injection are presented.

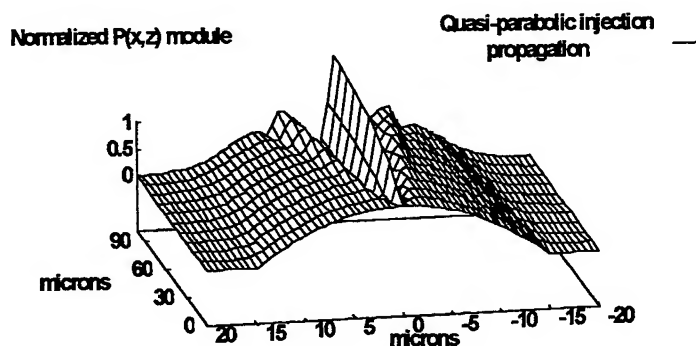


Fig. 7 Eigenmode selection modeling through BPM propagation of an arbitrary injection

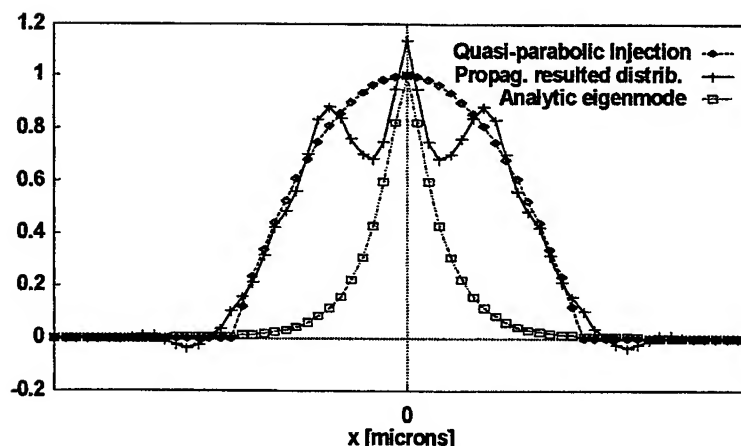


Fig. 8 Comparison of the injected field distribution, eigenmode distribution and field distribution resulted after 40 μ m BPM propagation

All the conclusions of an eigenmode propagation test can be obtained from an arbitrary injection test with the cost of a simulation over a longer propagation distance. The supplementary propagation distance is the distance over which a stable (in the monomode guide case) or periodical (in the multimode guide case) field distribution is obtained. Over this distance the injected field energy that was coupled into radiative modes is eliminated through the cladding and the remaining guided mode(s) produce the stable or periodical field distribution.

Apart from the eigenmode propagation test conclusions the eigenmode selection test enables the evaluation of radiative mode handling by the BPM variant under investigation. Even simpler than comparing the stable or periodical field distribution obtained by BPM simulation with the analytical or MS derived solutions, a comparison of the BPM obtained coupling coefficient(s) (as the ratio of the resulting guided mode(s) energy over the injected field energy) with the analytically obtained ones gives a rapid measure of the BPM variant capability to treat radiative modes. It must be mentioned however that the distance (D) over which the BPM simulation produces a stable or periodical field distribution is also a measure of the BPM variant capability to accurately model radiative mode propagation. In our experience the distance D was the simulation result parameter that varied the most from one BPM variant to another but since some experimental data are needed to evaluate the right D distance no conclusion could be drawn out of this difference. Another observation to be made is that the transverse mesh choice significantly affected the BPM-resulted coupling coefficients while the longitudinal discretization affected more the distance D.

6. OTHER TESTS

Many other tests have been used by different authors for BPM variant evaluation : divergent (Y-coupler) propagation modeling, longitudinally reflective structures modeling, co- and contra-directional coupling, mode conversion and polarization modeling, complex valued refraction index structures modeling, etc. All these tests, although enabling interesting conclusions on a case to case basis, are not general enough to be used in a standard evaluation – mostly when many BPM variants do not aim at all to some modeling capabilities (like for example modeling structures with longitudinal reflections).

From among the tests with lesser generality we frequently used the Y-coupler propagation modeling since it somehow combines the eigenmode propagation in straight parallel to Oz and inclined guides and the eigenmode selection test. The main problem for the Y-coupler test is that there are no accurate solutions – analytical or by other methods – apart from the BPM ones so that a result verification – other than experimental – is difficult. Fig. 9 shows a BPM-modeled propagation in a wide angle Y-coupler. The gradual coupling into the Y-coupler branches can be seen although it is not clear how accurately this phenomenon is modeled. A possible experimental verification of the Y-coupler BPM modeling could be to verify the branch coupling coefficients dependence on the position of the injected field with respect to the axis of the Y-coupler and on the length of the Y-coupler input section (ped).

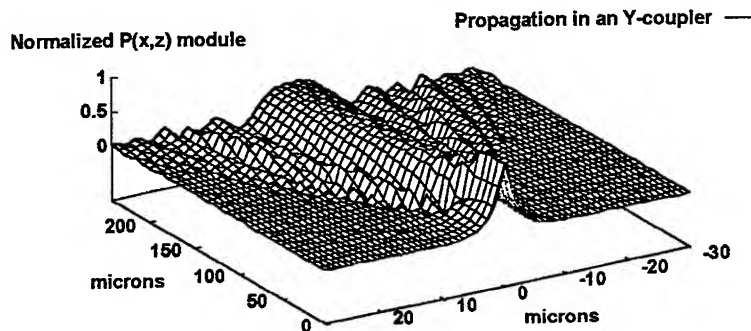


Fig. 9 BPM-modeled propagation in a wide angle Y-coupler

7. CONCLUSIONS

A few simple tests have been proposed for a standard evaluation of BPM variants : homogenous space propagation, eigenmode propagation in monomode and multimode waveguides and eigenmode selection through propagation of an arbitrary injection. We have shown that these tests enable many observations on the BPM variant capabilities and on the choice of simulation parameters. The paraxial approximation and the maximum angle at which the divergent energy propagation is modeled with acceptable accuracy can be estimated. The quality of the border conditions can be evaluated. The proper choice of the transverse calculus window extension and discretization can be analyzed and the maximum angle at which the energy propagation is modeled – for the given transverse mesh – can be determined. The guided modes effective refraction index can be calculated if reasonably accurate modal field distributions are known. Also the accuracy in handling the radiative modes can be estimated.

Furthermore some interesting effects were analyzed. The BPM capability to restore energy temporarily stored in higher spatial frequency components was discussed. The possibility to detect if the stable field distribution propagated by the BPM through a monomode guiding structure is not actually a BPM operator eigenvalue was presented. Some ways to crosscheck the BPM results with Mode Solver method results were proposed. Eigenmode ensemble propagation showed the electromagnetic approximation convergence with the ray approximation for highly multimode structures.

During our tests the spatial spectrum shape and evolution was very useful in analyzing many simulation parameters. Not only that the spectral aliasing could be easily detected – when the higher frequency spectral samples were not negligible – but also the apparition and propagation of discretization errors – with their specific comb shape – and the privileged and forbidden energy propagation directions could be observed.

REFERENCES

1. E. E. Kriezis and A. G. Papagiannakis, "A Three-Dimensional Full Vectorial Beam Propagation Method for z-Dependent Structures", *IEEE J. of Quantum Electronics*, **33**, No. 5, pp. 883-890, 1997.
2. D. A. M. Khalil and T. A. Amer, "Weighted-index beam-propagation method for analysis of three-dimensional optical structures", *IEE Proc.-Optoelectron.* **144** (4), pp. 197-202, 1997.
3. S. Balsamo, F. Sartori and I. Montrosset, "Dynamic Beam Propagation Method for Flared Semiconductor Power Amplifiers", *IEEE J. of Selected Topics in Quantum Electronics*, **2**, No. 2, pp. 378-383, 1996.
4. Y. Tsuji, M. Koshihara and T. Shiraishi, "Finite Element Beam Propagation Method for Three-Dimensional Optical Waveguide Structures", *J. of Lightwave Technology*, **15**, No.9, pp. 1728-1734, 1997.
5. H.-P. Nolting and R. März, "Results of Benchmark Tests for Different Numerical BPM Algorithms", *J. Lightwave Technology*, **13**, pp. 216-224, 1995.
6. J. Haes et al., "A Comparison Between Different Propagative Schemes for the Simulation of Tapered Step Index Slab Waveguides", *J. of Lightwave Technology*, **14**, No.6, pp. 1557-1569, 1996.

7. P. Sewell, T. M. Benson, T. Anada and P. C. Kendall, "Bi-Oblique Propagation Analysis of Symmetric and Asymmetric Y-Junctions", *J. of Lightwave Technology*, **15**, No. 4, pp. 688-696, 1997.
8. P.-L. Fan, M.-L. Wu and C.-T. Lee, "Analysis of Abrupt Bent Waveguides by the Beam Propagation Method and the Conformal Mapping Method", *J. of Lightwave Technology*, **15**, No. 6, pp. 1026-1031, 1997.
9. H. M. Masoudi and J. M. Arnold, "Spurious Modes in the DuFort-Frankel Finite-Difference Beam Propagation Method", *IEEE Photonics Technology Lett.*, **9**, No. 10, pp. 1382-1384, 1997.
10. J. Yamauchi, J. Shibayama, M. Sekiguchi and H. Nakano, "Finite-Difference Beam Propagation Method Based on the Generalized Douglas Scheme for a Nonuniform Grid", *IEEE Photonics Technology Lett.*, **9**, No.1, pp. 67-69, 1997.
11. O. Mitomi, K. Kasaya, "Wide-angle finite-element beam propagation method using Padé approximation", *Electron. Lett.*, **33**, No. 17, pp. 1461-1462, 1997.
12. C. Vassallo and J. Michiel van der Keur, "Comparison of a few Transparent Boundary Conditions for Finite-Difference Optical Mode-Solvers", *J. of Lightwave Technology*, **15**, No. 2, pp. 397-402, 1997.
13. D. Yevick, J. Yu and F. Schmidt, "Analytic Studies of Absorbing and Impedance-Matched Boundary Layers", *IEEE Photonics Technology Lett.*, **9**, No.1, pp. 73-75, 1997.
14. M.M. Spuhler, D. Wiesmann, P. Freuler and M. Diergardt, "Direct computation of higher-order propagation modes using the imaginary-distance beam propagation method", *Optical and quantum Electronics*, **31**, No. 9/10, pp. 751-761, 1999.

Growth and spectral characteristics of Nd^{3+} in calcium lithium niobium gallium garnet (CLNGG) crystals

A. Lupei, V. Lupei, E. Osiac, L. Gheorghe, M. Petrache, C. Stoicescu, A. Petraru

National Institute for Lasers, Plasma and Radiation Physics, Bucharest, Romania
R- 76900, P.O. Box MG-36, tel: 423 12 28, fax: 423 17 91 , e-mail: a.lupei@pluto.infim.ro

ABSTRACT

Laser crystals with disordered structure present a series of advantages for diode pumping or short pulse generation as compared with ordered crystals. Such a system proved to be calcium lithium niobium gallium garnet (CLNGG) doped with Nd^{3+} . The paper presents the growth and X-ray analysis of specially doped CLNGG. Very few spectroscopic data on this system have been previously published. The paper presents low temperature (10K) absorption spectra, site selective excitation and lifetime measurements of Nd^{3+} in CLNGG. At least four distinct nonequivalent centers are observed, the spectral lines for every center presenting a disordered Gaussian shape. Based on structural, spectral static and emission dynamics data an attempt of modeling the structure of these centers is proposed.

Keywords: Laser crystals, Nd^{3+} in calcium lithium niobium gallium garnet, optical spectroscopy

1. INTRODUCTION

Interesting solid state laser materials for diode pumping, or short pulse generation or amplification could be the crystals with disordered type structure. Such systems proved to be calcium niobium gallium garnet (CNGG) and calcium lithium niobium gallium garnet (CLNGG) doped with rare earths ions (RE^{3+}). These crystals present several advantages as compared with ordered garnet crystals such as YAG: low melting point (smaller than 1500°C that makes the growing possible without iridium and therefore a simplified technology), much larger absorption and emission bands and allow large doping level with ions such as Nd^{3+} . These crystals present a better thermal conductivity than glasses. Originally CNGG was synthesized in a polycrystalline form using a solid state phase reaction method¹ with the formula $\text{Ca}_3\text{Nb}_2\text{Ga}_3\text{O}_{12}$. X-ray and Raman data^{1,2} on the melt grown (congruent composition) CNGG single crystals have a different composition, $\text{Ca}_3\text{Nb}_{1.68}\text{Ga}_{3.2}\text{V}_{0.12}\text{O}_{12}$, where V means cationic vacancy. The extra amount of Nb^{5+} in this material relative to stoichiometric structure is compensated by vacancies. By Raman spectroscopy^{4,5} it was shown that V are usually in octahedral (a) and tetrahedral (d) sites of the garnet lattice, and their concentration can be reduced by addition of other cations. Thus, the addition of Li^+ is accompanied by a vacancies concentration decreasing practically to zero⁴; and essentially a new type of crystal, calcium lithium niobium gallium garnet (CLNGG) was obtained⁶. The CNGG and CLNGG structures are disordered due to various possibilities of arrangements of Nb^{5+} , Ga^{3+} , Li^+ or V in octahedral or tetrahedral sites.

Lasing and several spectral characteristics of crystals were investigated, especially Nd^{3+} doped CNGG⁶⁻¹¹, Cr^{3+} and Nd^{3+} :CNGG^{6,7}, or Nd^{3+} : CLNGG⁷⁻¹⁰. The main results of these investigations are that Nd^{3+} presents a multisite structure with at least four centers and with lines of Gaussian shape indicating the disordered structure. An attempt of assignment to connect the four line structure to a structural model for Nd^{3+} : CNGG has been recently proposed¹¹. The lasing characteristics are different for the two (CNGG and CLNGG) crystals. Laser emission in different regimes was obtained: free running, Q-switch, ultrashort pulse (pico or femtoseconds). A comparison of Nd^{3+} emission in CLNGG and CNGG crystals revealed several advantages of the latter, such as: higher damage threshold (twofold), lower divergence and thermal lens effects at high pumping. Though the concentration of Nd^{3+} in the crystals used for laser emission is rather high (larger than 3at.%), the energy transfer processes are practically not investigated and refer mainly to transfer from Cr^{3+} to Nd^{3+} : CNGG^{6,12} and are treated in a very global way.

The spectroscopic properties of Nd^{3+} : CLNGG are less studied and no report on energy transfer processes has been published. The purpose of this paper is the study of growth conditions, X-ray analysis and spectroscopic characteristics of Nd^{3+} in CLNGG single crystals. Low temperature high resolution absorption spectra, selective excited luminescence, luminescence kinetics are analyzed. Based on the composition, spectral and kinetics data an attempt of modeling of the multisite structure is proposed.

2. EXPERIMENT

Single crystals of CLNGG, pure and doped with Nd^{3+} , were grown by Czochralski technique (in a standard radio frequency heating furnace driven by a 100 kW generator) using platinum crucibles. For doping with Nd^{3+} of CLNGG, the stoichiometric neodymium lithium niobium gallium garnet $\text{Nd}_3\text{Li}_x\text{Nb}_x\text{Ga}_{5-2x}\text{O}_{12}$ (NLNGG) was prepared. Good quality samples doped with Nd^{3+} from 0.1 to ~10% have been obtained. The garnet phase identification and determination of the lattice parameter of sintered materials and grown crystals were performed by X-ray diffractometer (TUR M 62) with $\text{Cu K } \alpha_1$ (30 kV, 15 mA). Spectroscopic investigations of Nd^{3+} :CLNGG single crystals were performed at various temperatures by using a Cary spectrometer or an experimental set-up for transmission measurements based on a high resolution monochromator and a photon counting system (Turbo-MCS), and closed cycle refrigeration system. Selective excitation has been done by a Quantel dye laser.

3. RESULTS

3.1 Crystal growth

For Nd^{3+} doping of CLNGG, neodymium lithium niobium gallium garnet (NLNGG) was prepared and since no phase diagram for this compound was reported in the literature, a solid state reaction technique was adopted in order to obtain the garnet phase. The stoichiometric composition of $\text{Nd}_3\text{Li}_x\text{Nb}_x\text{Ga}_{5-2x}\text{O}_{12}$ for our study was chosen corresponding to the optimal composition of Li^+ in CLNGG^{13} , i.e. $x = 0.275$. Thus, the doping can be made simply by mixing the proper amounts of CLNGG ($\text{Ca}_3\text{Li}_{0.275}\text{Nb}_{1.775}\text{Ga}_{2.95}\text{O}_{12}$) and NLNGG ($\text{Nd}_3\text{Li}_{0.275}\text{Nb}_{0.275}\text{Ga}_{4.45}\text{O}_{12}$). The raw material of NLNGG was sintered for about 30 min at 1420°C , resulting ceramic samples. From the X-ray powder diffraction pattern, obtained on these ceramic samples, it was demonstrated that this composition has a garnet structure. Lattice parameter measured on sintered material is $a=12.508\text{\AA}$ at room temperature, a value very close to our determinations of CLNGG lattice parameter (12.51\AA) that is smaller than that reported previously. These results suggest the possibility of larger doping levels of Nd^{3+} in CLNGG by using the mixture of the two garnets. Single crystals of pure CLNGG were grown from a $\text{Ca}_3\text{Li}_{0.275}\text{Nb}_{1.775}\text{Ga}_{2.95}\text{O}_{12}$ melt composition, after sinterization at 1350°C for 3h. The crystals were grown by using an $\langle 111 \rangle$ orientated crystal seed obtained from a preliminary platinum wire grown crystal in air atmosphere. Doping with Nd^{3+} of CLNGG was obtained by mixing and melting in the desired quantities of CLNGG and NLNGG garnets. In this way Nd^{3+} doped (from 0.1 to 10at.%) CLNGG single crystals were successfully grown. The melting temperature in this case was around 1470°C . The lattice parameter of Nd: CLNGG was measured to be $a=12.51\text{\AA}$ at room temperature, similar to the undoped crystals. The grown crystals were transparent and pale yellowish brown in color. After annealing at 1200°C for 1h, Nd^{3+} doped single crystals become pale yellowish.

3.2 Absorption spectra

The low temperature (10K) absorption spectra in various spectral regions have been measured. Since the Nd^{3+} enters in dodecahedral c-sites of symmetry D_2 or lower, the J multiplets are split in Stark doublets. Every line presents a multicomponent structure, observed even at room temperature. At 10K, the structure is well resolved in the spectra corresponding to $^4\text{I}_{9/2} \rightarrow ^2\text{P}_{1/2}$ transition. Since this line (see for example in Fig. 1 the absorption spectra a sample with 7.5at. % Nd in CLNGG) is connected to transition to a single Stark level, the components are due to multisite structure. The line can be rather well described by a sum of four Gaussians with linewidths varying between $6 - 14\text{cm}^{-1}$ and a distance between extreme maxims of about 70cm^{-1} , as shown in Fig. 1. The concentration dependence of the relative intensities of the four components is almost linear, as shown in Fig. 2

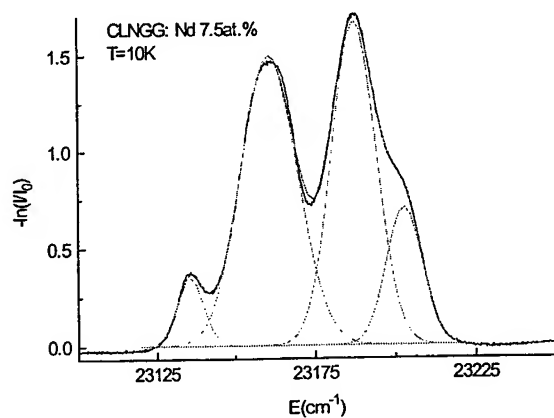


Fig. 1 The absorption spectrum of $\text{Nd}^{3+} \ ^4\text{I}_{9/2} \rightarrow \ ^2\text{P}_{1/2}$ transition in CLNGG

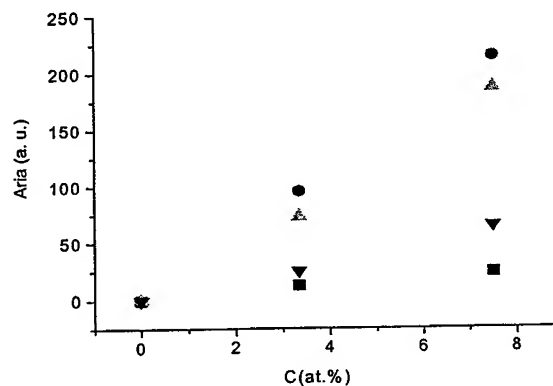


Fig.2 Concentration dependence of line components

If the transition probabilities of the four centers are the same, the relative intensities are proportional to the centers concentration. This is not the case, as the emission kinetics show. The line structure corresponding to the absorption to the $\ ^4\text{F}_{3/2}$ and $\ ^4\text{G}_{5/2}$, the emission and selective pumping levels, is not so well resolved, as shown in Fig. 3.

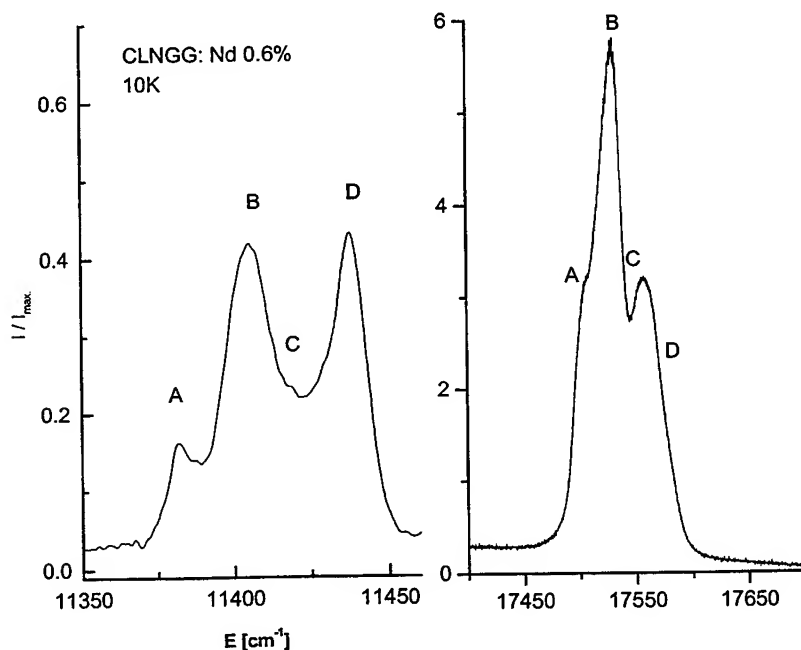


Fig. 3 The absorption spectra corresponding to $\ ^4\text{I}_{9/2} \rightarrow \ ^4\text{F}_{3/2}$ and $\ ^4\text{I}_{9/2} \rightarrow \ ^4\text{G}_{7/2}$ at 10K for a sample with 0.6 at.% Nd.

3.2 Emission kinetics

The analysis of the emission kinetics of Nd^{3+} in CLNGG has not been investigated, to our knowledge, up to now. The overlapping of the excitation and emission components makes difficult the study of the selective emission and kinetics. We managed to solve the emission decays of A, B and D lines corresponding to ${}^4\text{F}_{3/2}(1) \rightarrow {}^4\text{I}_{9/2}(1)$ (Fig. 3a) transition at 10K. The decays at low Nd^{3+} content are exponential with lifetimes varying between $\sim 160\mu\text{sec}$ for center A and $\sim 240\mu\text{sec}$ for center D, 180-190 μsec for center B as compared with the lifetimes range measured¹² for Nd^{3+} in CNGG 170 - 210 μsec . At higher concentrations the decays becomes nonexponential. Every center presents its own concentration dependence of the nonexponentiality. The nonexponentiality of line D can be better analyzed. Without entering into details, we can say that the nonexponentiality is complex, but can be described, at 10K, in terms of static energy transfer with two types of interactions¹⁴, a short range -superexchange and a dipole-dipole for long times. At room temperature the decays are faster and at high concentration migration effects should be taken into account. The measurements on energy transfer are in progress.

4. DISCUSSION

Single crystals of CLNGG single and Nd^{3+} doped have been grown by Czochralski method and using as dopant a new Nd^{3+} garnet (NLNGG). X ray measurements on single crystals present, besides the normal reflections characteristic to garnet structure, intense (222) forbidden transitions that indicate a disordered occupation of octahedral sites. The presence of these transitions on all $\langle 111 \rangle$ directions suggest a disordered structure, but the global crystal could remain with garnet structure. The attempt to demonstrate the existence of a lower symmetry by comparing the i.r. and Raman phonons in CNGG is nonconcludent¹⁵ since phonons of similar energies have been observed in i.r. and Raman spectra of YAG too (see for example Tables 6.3, 6.4 in the book of Kaminskii¹⁶). Thus, is not surprising that no electrooptical effect can be observed in CNGG. Interesting results have been obtained in the analyses of Raman spectra^{3,4} where a multimod behavior of some peaks connected with quasilocalized A_{1g} vibrations of tetrahedral groups $[\text{GaO}_4]$ and $[\text{NbO}_4]$ is observed. The multimod behavior is characteristic to disordered systems. A series of additional satellites are observed Raman spectra of congruent grown crystals, as compared with stoichiometric sintered composition. These satellites were connected with the presence of cationic vacancies in octahedral and tetrahedral sites. The introduction of Li^+ leads to decreasing the intensity of these satellites and the apparition of a new one, a prove that the vacancies are responsible for these peaks. It was concluded that vacancies and Li^+ enter preponderantly in octahedral sites. Another conclusion drawn from Raman spectra is that the dodecahedral sublattice is not perturbed.

A characteristic of Nd^{3+} in CLNGG is smaller Stark splittings of the J multiplets as compared with YAG, a fact that can be due⁵ to the larger lattice constant. An energy level diagram for Nd^{3+} in CLNGG is difficult to perform, since even at room temperature every line presents a multicomponent structure. As the absorption and emission spectra show, the Nd^{3+} in CLNGG present a number of at least four lines, each line presenting a prevailing inhomogeneous (Gaussian) broadening at low temperatures. The structure observed in ${}^4\text{I}_{9/2} \rightarrow {}^4\text{F}_{3/2}$ transition is similar to that previously reported⁹ at 77K. It is interesting to mention that in Nd^{3+} spectra of CNGG we observed at least five nonequivalent centers. Such a structure could be present in CLNGG too but it is less evident.

The absorption spectrum of Nd^{3+} in CLNGG corresponding to ${}^4\text{I}_{9/2} \rightarrow {}^2\text{P}_{1/2}$ transition can be decomposed in at least four Gaussian components as shown in Fig. 1, and the relative intensities do not change essentially with Nd^{3+} content. The relative area of the four components are given in Table 1, and if we consider that the cross sections are the same, the area should be proportional to the relative concentration of the four main Nd^{3+} centers. Nd^{3+} replace easily Ca^{2+} in dodecahedral sites since they have in eightfold coordination almost identical ionic radii¹⁶ (1.12Å). To explain the observed four lines (Fig. 1) structure we consider that the different crystal fields at the Nd^{3+} dodecahedral site are determined by composition of the first cationic tetrahedral and octahedral spheres around it. According to the composition of CLNGG ($\text{Ca}_3\text{Li}_{0.275}\text{Nb}_{1.775}\text{Ga}_{2.95}\text{O}_{12}$), the tetrahedral sites contain almost entirely Ga^{3+} ions, and therefore the observed structure is expected to be connected with the randomly occupation by Li^+ and Nb^{5+} of the first octahedral sphere (four places at 3.5Å). If we assume a random distribution of Nd^{3+} in crystal, the probability to have a complex with n (0-4) Li^+ ions in octahedral vicinity of Nd^{3+} is given by binomial distribution:

$$P_n = \frac{4!}{(4-n)!n!} \beta^n (1-\beta)^{4-n}$$

where β is the relative concentration of Li^+ in octahedral sites. From the structural formula of CLNGG, β is estimated to be 0.1375. If one compare the values of P_n ($n = 0, 1, 2, 3$) with the relative experimental area of absorption spectra (Fig. 1), the best rms. is obtained for $\beta=0.1882$, a slightly larger value than that obtained from the structure. As can be observed (Table 1) the experimental results are in rather good agreement with theoretical estimations of P_n , exception being the most shifted line situated at 23135cm^{-1} . The differences could appear from the fact that the composition of the line is more complex and the assumption that the cross sections are identical for the four centers. Since lifetime of $^4\text{F}_{3/2}$ level are different one could expect different cross sections for various centers. This model could explain rather well the local order, but the Gaussian shape of every line can be connected with the disordered structure of this crystal.

Table 1 The experimental relative normalized area of four centers and calculated probabilities of having 0, 1, 2 or 3 Li^{3+} near neighbors for two values of β the relative concentration of Li^+ in octahedral sites.

Center position in $^4\text{I}_{9/2} \rightarrow ^2\text{P}_{1/2}$ transition (cm^{-1})	Measured normalized area	P_n	
		$\beta=0.1375$	$\beta=0.1882$
23161	0.4317	0.5534	0.4349
23188	0.4070	0.3529	0.4032
23202	0.1228	0.0844	0.1399
23135	0.0384	0.009	0.0217

These estimations suggest a correlated distribution of cations around dodecahedral Nd^{3+} with an enhanced Li^+ content in near neighbor coordination octahedral sphere. An illustration is given in Fig. 4 where Nd^{3+} near neighbors are 2 Ga^{3+} cations in tetrahedral sites and 3 Nb^{5+} and 1 Li^+ cations in octahedral sites.

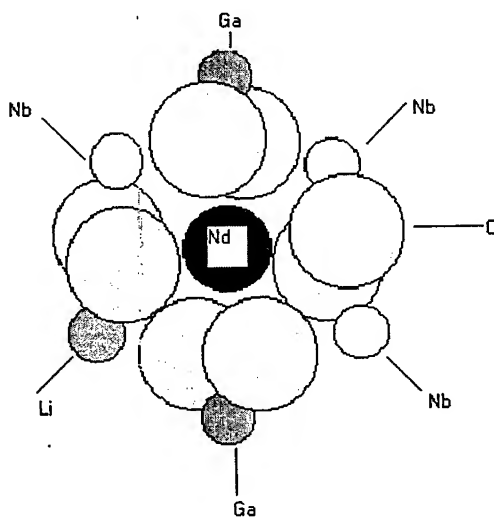


Fig. 4 The proposed model for one of the Nd^{3+} centers in CLNGG: the dodecahedral Nd^{3+} and two nearby tetrahedral sites occupied by Ga^{3+} , and four octahedral sites occupied 3 Nb^{5+} and 1 Li^+ .

One should mention that in case of RE^{3+} doped YAG, grown at high temperature, an octahedral nonstoichiometric defect (Y^{3+} replacing octahedral Al^{3+}) leads to nonequivalent P - centers¹⁷, manifested in optical spectra as satellites around RE^{3+} main lines. It was shown that due to the large difference between Y^{3+} (0.9\AA) and Al^{3+} (0.53\AA) sixfold coordinated ionic radii, one $\text{Y}^{3+}(\text{a})$ determine more satellites of equal intensities and close lifetimes. As shown recently¹⁸ for Er^{3+} in YAG four satellites could be solved and assigned to dependence of $\text{Y}^{3+}(\text{a})$ perturbation on direction. Such an anisotropy could exist in the case of

CLNGG too, but could be lost in linewidths. The difference of ionic radii of Li^+ in sixfold coordination 0.74Å and Ga^{3+} 0.62Å, or Nb^{5+} 0.64Å is much smaller than in previous case and the anisotropy of perturbations could be smaller. In the linewidth are lost also the $\text{Nd}^{3+}(\text{c})$ - $\text{Nd}^{3+}(\text{c})$ pairs, but they are present as the analysis of the decays show.

In conclusion, growth conditions, X-ray and low temperature spectroscopic measurements of Nd^{3+} in disordered laser system CLNGG have been investigated. Based on low temperature high resolution absorption spectra and site selective measurements along with structural data, a modeling of Nd^{3+} multicenter structure in these disordered crystals is proposed. It assumes a different occupation of the first coordination octahedral sphere in the vicinity of dodecahedral Nd^{3+} with: 4 Nb^{5+} , 3 Nb^{5+} - 1 Li^+ , 2 Nb^{5+} - 2 Li^+ and 1 Nb^{5+} - 3 Li^+ . The next cationic coordination spheres contain in an random distribution Ga^{3+} , Nb^{5+} , Li^+ , Ca^{2+} or vacancies, and this leads to Gaussian lineshape of the spectral line for every center. A more detailed analysis of the nature of Nd^{3+} nonequivalent centers in CLNGG and CNGG is under study.

REFERENCES

1. A. A. Schwartz, E. L. Dukhovskiy, and A. I. Agranovskiy, *Sov. Proc. of Acad. Sci. USSR, Series: Inorganic Materials*, Vol. 1, pp. 1617., 1965.
2. A.A. Kaminsky, E. L. Belokoneva, A. V. Butashin, "Crystal structure and spectral and luminescent properties of $\text{Ca}_3(\text{Nb,Ga})_2\text{Ga}_2\text{O}_{12}:\text{Nd}^{3+}$ garnet with cationic deficiencies" *Sov. Proc. of Acad. Sci. USSR, Series: Inorganic Materials*, Vol. 22, pp. 1061-1071, 1986.
3. Yu. K. Voronko, A. B. Kudryavtsov, V. V. Osiko, A.A. Sobol et al., "Raman scattering of light in of solid solutions with garnet structure", *Sov. Acad. Sci. Reports*, Vol. 298, pp. 604-607 1988.
4. Yu. K. Voronko, N. A. B. Eskov, V. V. Osiko, A.A. Sobol, "Raman scattering of light in crystals and melt of calcium-niobium gallium garnet" *Raman Solid State Physics*, Vol. 30, pp. 512-518, 1988.
5. S. E. Sarkisov, A. A. Kaminskii, "Optical Phonon Spectroscopy of Heterovalent Disordered $\text{Ca}_3(\text{Nb,Ga})_2\text{Ga}_2\text{O}_{12}$ Crystals with Garnet Structure", *Phys. Stat. Sol.(a)*, Vol 107, pp. 365 -371, 1988.
6. Yu. K. Voronko, S. B. Gessen, M. A. Eskov, A. A. Sobol et al. "Spectroscopic and lasing properties of calcium-niobium gallium garnet with Cr^{3+} and Nd^{3+} ", *Sov. J. Quantum Electronics*, Vol. 15, pp. 312- 317, 1988.
7. Yu. K. Voronko, S. B. Gessen, M. A. Eskov, A. A. Sobol et al., "Effective laser media utilizing calcium-niobium gallium garnets doped with Nd^{3+} ", *Sov. J. Quantum Electronics*, Vol. 17, pp. 307-310, 1990.
8. T.T. Basiev, Yu. K. Voronko, N. A. Eshov, et al., "Calcium - Niobium - Gallium Garnet with Nd - a New Active Medium For Lasers with Ultrashort Pulse Duration ", *Proc. SPIE*, Vol. 1839, pp. 91-103, 1991
9. Yu. K. Voronko, N. A. Eskov, S. B. Gessen, V. V. Osiko, A. A. Sobol, "Lasing properties of neodymium-doped calcium - niobium - gallium garnet at wavelengths of 1.06 and 1.33 μm ", *Quantum Electronics*, Vol. 23, pp. 494-496, 1993.
10. K. Shimamura, M. Timoshechkin, T. Sasaki, K. Hoshikawa, T. Fukuda, "Growth and characterization of calcium-niobium gallium garnet (CNGG) single crystals for laser application", *J. of Crystal Growth*, Vol. 128, pp. 1021-1024, 1993.
11. A. Brenier, G. Boulon, K. Shimamura, T. Fukuda, "Growth by μ -pulling-down method and spectroscopic investigation of Nd^{3+} -doped of calcium niobium gallium garnet ", *J. of Crystal Growth*, Vol. 204, pp. 145 - 149, 1999.
12. R. Balda, J. Fernandez, M. A. Ilarramendi, "Steady - state and time - resolved laser of Cr^{3+} and Nd^{3+} singly and doubly doped calcium niobium gallium garnet", *Phys. Rev. B*, Vol. 48, pp. 9279 - 9290, 1993.
13. M. Yu, V.I.Chani, K.Shimamura and T.Fukuda, " $\text{Ca}_3(\text{Li, Nb, Ga})_2\text{O}_{12}$ garnet crystal from stoichiometric melts" *Crystal Growth*, Vol. 171, pp. 463-471, 1997.
14. A. Lupei, V. Lupei, E. Osiac, A. Petraru, L. Gheorghe, "Spectral characteristics of Nd^{3+} in calcium lithium niobium gallium garnet (CLNGG) crystals", *International Conf. of Luminescence*, Japan, 1999.
15. K. Shimamura, P. Becker, B. Wyncke, F. Brehat, T. Fukuda, C. Carabatos-Nedelec, "Vibrational spectra of a Ca-Nb-Ga garnet (CNGG) single crystal studied by Raman and infrared reflectivity spectroscopy", *J. Phys. Condens. Matter.*, Vol. 10, pp. 6865-6873, 1998.
16. A. A. Kaminskii, *Laser Crystals*, Springer-Verlag Berlin Heidelberg, 1981.
17. V. V. Osiko, Yu. K. Voronko, A. A. Sobol, "Spectroscopic Investigation of Defect Structures and Structural Transformations in Ionic Crystals", *Crystals 10*, Springer-Verlag Berlin Heidelberg, 1984.
18. A. Lupei, V. Lupei, E. Osiac, J. Phys., "Spectral and dynamical effects of octahedral impurities on RE^{3+} in garnets" *Condens. Matter*, Vol. 10, pp. 9701-9710, 1998.

Numerical algorithm for complex fields reconstruction

M. Bulinski, A Belea

University of Bucharest, Faculty of Physics, Dept. of Optics,
P.O. Box MG-63, 72996 Bucharest, Romania

ABSTRACT

The paper presents a method to retrieve the relative phase of an optical field starting from three digitized intensity records. One record is that of the classical intensity of the field itself, while the second and the third are intensities obtained after some filtering operations performed in the Fourier space of the optical field. The paper also gives several applications of the algorithm to both one-dimensional and two-dimensional cases.

1. INTRODUCTION

As known, experimental techniques such as optical interferometry, tomography and image processing propose some elaborate algorithms to obtain a full reconstruction of an optical field (signal). Apart from requiring some expensive equipment, such techniques are also times consuming. However, one can distinguish a class of applications where optical operations in the Fourier space of the signal can be applied, thus leading to considerable simplifications to the entire problem.

We propose a method to retrieve the relative phase of an electromagnetic complex field distribution starting from the values of this field taken over a discrete grid of points (in fact, a digitized version of the traditional continuous records). The technique is based on three intensity records of the field, of which one is the record of the field's intensity, while the others are obtained by operations performed in the Fourier space of the signal. This work discusses numerical recovery of optical fields from three intensity records. We shall discuss the relevance of our method by applying it to several one-dimensional and two-dimensional cases.

This paper has the following organization: the second part presents the basics of the technique. The third part discusses two significant one-dimensional cases. The fourth part presents a general two-dimensional optical field restoration. The main conclusions of the paper are given in the fifth part.

2. BASIC PRINCIPLES OF THE METHOD

Let $f(\mathbf{x})$ represent a complex function that admits a Fourier transform and depends on the two dimensional vector \mathbf{x} . Let $F(\mathbf{v})$ be the Fourier transform of $f(\mathbf{x})$. We have the following relations²

$$F(\mathbf{v}) = \int_A f(\mathbf{x}) \exp(-j2\pi\mathbf{v}\mathbf{x}) d\mathbf{x} \quad (1)$$

$$f(\mathbf{x}) = \int_B F(\mathbf{v}) \exp(j2\pi\mathbf{v}\mathbf{x}) d\mathbf{v} \quad (2)$$

where \mathbf{v} represents the variable in the spatial frequency domain, while A and B represent two dimensional rectangular domains having the origin as a center of symmetry. Introducing

(3)

*Correspondence: Telephone: 780.47.70

$$f_0 = \frac{1}{\|A\|} \int_A f(\mathbf{x}) d\mathbf{x}$$

we can write

$$f(\mathbf{x}) = f_0 + f'(\mathbf{x}) \quad (3)$$

where f_0 represents the "zero order spatial frequency" term.

Using de Moivre's formula we split our functions as

$$f(\mathbf{x}) = \rho(\mathbf{x}) \exp(\varphi(\mathbf{x})) \quad (4)$$

$$f_0 = \rho_0 \exp(\varphi_0) \quad (5)$$

$$f'(\mathbf{x}) = \rho'(\mathbf{x}) \exp(\varphi'(\mathbf{x})) \quad (6)$$

Introducing

$$I(\mathbf{x}) \equiv |f(\mathbf{x})|^2, \quad I'(\mathbf{x}) \equiv |f'(\mathbf{x})|^2, \quad I_0 \equiv |f_0|^2 \quad (7)$$

and using the following relations³

$$I_0 = \frac{1}{A} \int_A (I(\mathbf{x}) - I'(\mathbf{x})) d\mathbf{x} \quad (8)$$

$$I(\mathbf{x}) = I_0 + I'(\mathbf{x}) + 2\sqrt{I_0 I'(\mathbf{x})} \cos(\varphi'(\mathbf{x}) - \varphi_0) \quad (9)$$

$$I''(\mathbf{x}) \equiv I_0 + I'(\mathbf{x}) + 2\sqrt{I_0 I'(\mathbf{x})} \sin(\varphi'(\mathbf{x}) - \varphi_0) \quad (10)$$

we infer

$$\cos(\varphi(\mathbf{x}) - \varphi_0) = \frac{I(\mathbf{x}) + I_0 - I'(\mathbf{x})}{2\sqrt{I_0 I(\mathbf{x})}} \quad (11)$$

$$\sin(\varphi(\mathbf{x}) - \varphi_0) = \frac{I''(\mathbf{x}) - I_0 - I'(\mathbf{x})}{2\sqrt{I_0 I(\mathbf{x})}} \quad (12)$$

2.1. Phase Recovery

In spite of the fact that the left sides of Eqs. (11, 12) are linked by a fundamental trigonometric identity, the fact that this relation has a nonlinear character makes it necessary to express the sine and cosine functions directly in terms of the experimental data (just as has been done in the above relations). This requirement is imperative if a complete phase recovery (phase unwrapping) must be achieved from the experimental records.

It is worthwhile to mention that the complete phase recovery is possible only through numerical processing. One starts by creating the wrapped version of the phase (that is $(\varphi(x) - \varphi_0(x)) \bmod 2\pi$) from Eqs. (11, 12). Then the unwrapping can follow the algorithm proposed by Ghiglia-Romero⁴. Our preference for this technique (over the classical 'following path' algorithm) is motivated by the advantages offered by this technique when treating noisy signals.

2.2. Intensity Records

The unusual intensities introduced as I_0 , $I'(x)$, $I''(x)$ deserve a special consideration. In fact, these three entities have a specific meaning when related to the Fourier space of the optical field. Thus, I_0 represents the square module of the element $(0,0)$ in the two-dimensional Fourier transform of the signal (i.e., the square module of the zero order spatial harmonic). $I'(x)$ represents the intensity of the reconstruction (the inverse Fourier transform) of the Fourier space of the optical field $f(x)$, when a stop screen eliminates the zero order harmonic. Finally, $I''(x)$ represents the intensity obtained by inverting the Fourier space of $f(x)$ after one has retarded by $\pi/2$ the zero order spatial harmonic.

Practically, the records $I'(x)$, $I''(x)$ can be obtained in two ways. Either by a numerical procedure that handles $f(x)$ in the desired manner (a choice recommended mostly for theoretical investigations) or, by processing the field by some standard optical arrangements. The basic setup needed to operate on the Fourier space of an optical field, essentially consists in a pair of confocal lenses placed light as shown in Fig. 1.

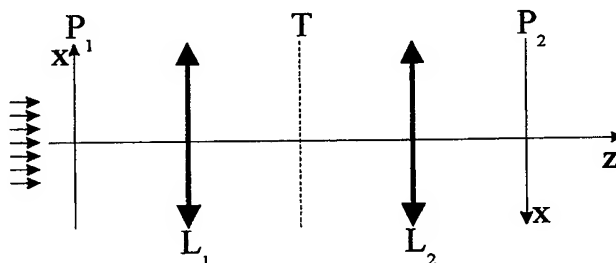


Fig.1 Optical filtering setup

Let planes P_1 and P_2 be both Fourier conjugated to plane T. Then, over plane T one always gets a Fourier transform, $F(\nu)$, of the field covering plane P_1 , say $f(x)$. When nothing in plane T does obstruct the light's propagation, then over plane P_2 we find an exact version of $f(x)$. However, if one places in plane T a stop transparency (screen) that blocks the zero-frequency harmonic, then plane P_2 is covered by the distribution $f'(x)$. Taking two independent records across P_2 with a quadratic detector, one gets the two intensity functions $I(x)$, $I'(x)$. In order to obtain the third distribution $I''(x)$, one must substitute the stop transparency by a suitable dephasing plate and then take a record the intensity over plane P_2 .

3. ONE-DIMENSIONAL EXAMPLES

To give an intuitive test to our numerical approach, we have chosen the simple case of a monochromatic plane wave incident normally on a screen containing a one-dimensional slit. A very simple optical field characterizes this case. Obviously, the amplitude is constant over the slit and nil everywhere else on the screen. Correspondingly, the phase of the wave is constant over the entire plain containing the slit.

This simplicity allows us to 'numerically' propagate the field at different distances away from then screen and then to simulate the three records $I(x)$, $I'(x)$ and $I''(x)$, wherefrom to recover the optical field using Eqs. (11, 12) and phase unwrapping. We have treated explicitly two types of propagation: one very short (close to the screen) and another sufficiently great to give an image of the field distribution that can be compared to the classical diffraction pattern for a slit.

The technique of field propagation is somewhat standard^{2,5} involving three steps. One starts by finding the spatial harmonics (i.e., expressed as a the set of infinite extension plane waves) of the input field (in our case given by a limited cross section plane wave). Then, these harmonics are suitably dephased (in agreement with the propagation distance) and finally recomposed to obtain the new field values in the 'observation' plane.

To simulate the experimental operations leading to $I(x)$, $I'(x)$ and $I''(x)$, one must go through other three steps imitating the optical operations performed by the arrangement shown in Fig. 1

The complete field recovery goes through the two stages explained in Sec.2.1.

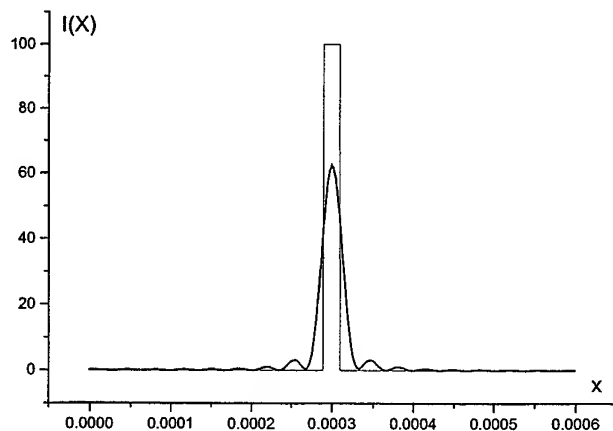


Fig. 2 The input and diffracted intensities far from the slit

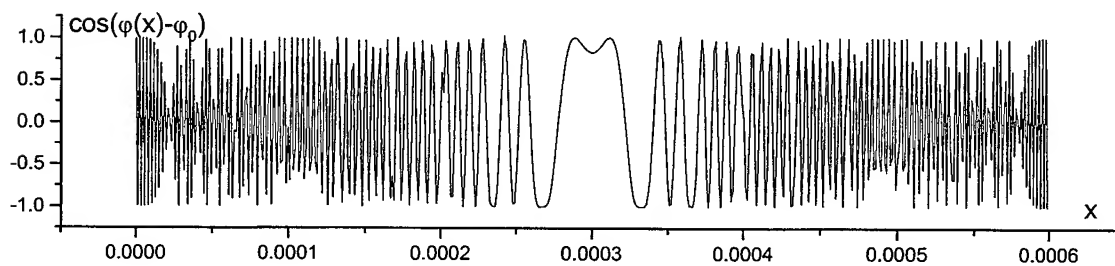


Fig. 3 The graph of $\cos(\varphi(x) - \varphi_0(x))$

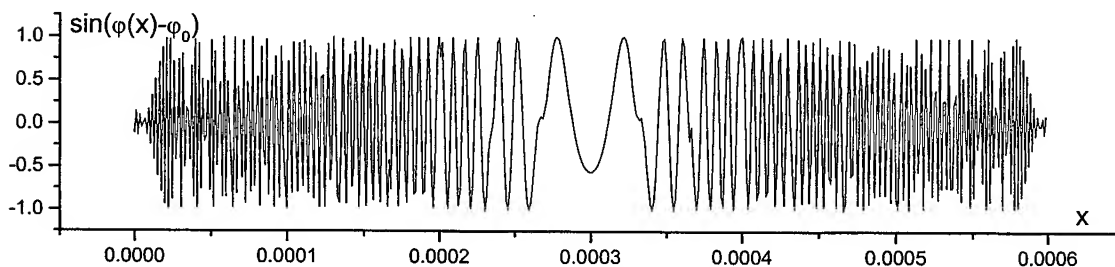


Fig. 4 The graph of $\sin(\varphi(x) - \varphi_0(x))$

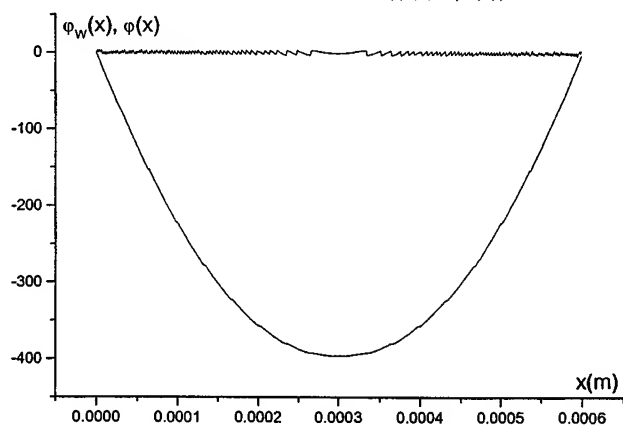


Fig. 5 The wrapped and recovered phase close to the slit

Figs. 2-5 illustrate different stages of the simulated 'slit-to-observation plane' propagation process, followed by 'data recording' and ending by a complete field reconstruction. In this case, the 'observation' plane is 'placed' at a large distance from the slit. As expected, the intensity distribution has the well-known diffraction pattern (see Fig. 2). The recovered phase shown in Fig. 3 indicates that the wave front in the observation plane is quasi-spherical. This is natural if we recall the far field characteristics of a Gaussian beam having the waist coincident with the slit. For the economy of the paper we have left aside the diagrams showing the distributions of $I'(x)$, $I''(x)$ in the 'observation' plane. Still, it is important to note that these distributions were prepared numerically, because we wanted to show that the total field recovery operations can be based on these records.

Figs. 6-7 show in a condensed form the results obtained in a second case where the observation plane is close to the slit. Essentially, we illustrate the observed intensity and the phase recovered. The intensity in the observation plane does not behave in an intuitive manner. However, our results are similar to those of Garcia, Mas and Dorsch⁶. A more intuitive

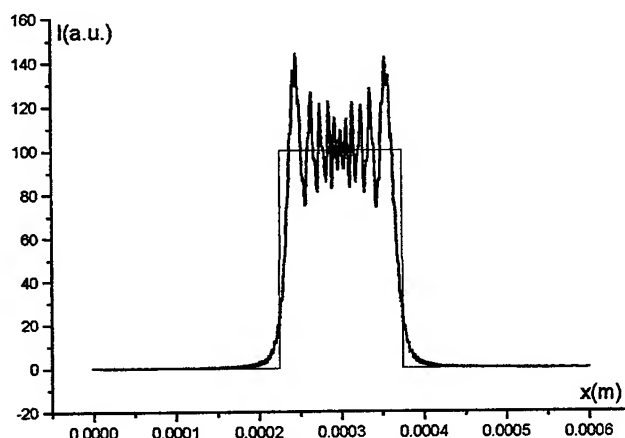


Fig. 6 The input and diffracted intensities close to the slit

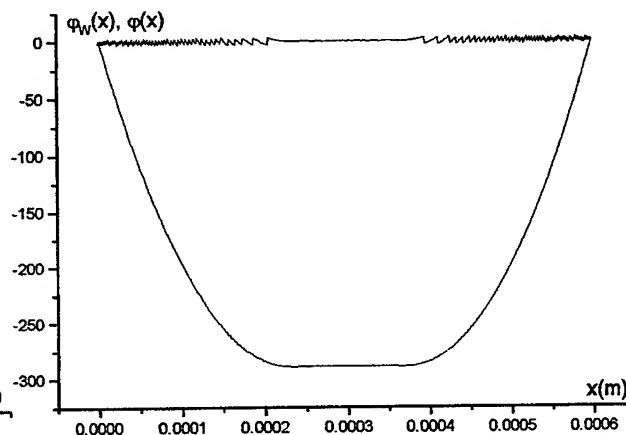


Fig. 7 The wrapped and recovered phase close to the slit

behavior is exhibited by the recovered phase, which shows that close to the slit the field continues to propagate as a quasi-plane wave.

4. A TWO-DIMENSIONAL EXAMPLE

In this section we present one case that can be rated as pertaining to the class of most complex optical fields, essentially because this case is two-dimensional. Mathematically, we have defined a complex field combining three components, all with Gaussian distributions in amplitudes and in phases. The following equations express the proposed combination

$$u(x, y) = \rho \exp j\phi \quad (13)$$

$$\begin{aligned} \rho &= 3 \exp\left(-\frac{(x-2)^2 + (y-2)^2}{6}\right) + 0.5 \exp\left(-\frac{(x+1)^2 + (y+1)^2}{2}\right) + 4 \exp\left(-\frac{(x+5)^2 + (y-4)^2}{20}\right) \\ \phi &= 20 \exp\left(-\frac{x^2 + y^2}{2}\right) - 8 \exp\left(-\frac{(x-5)^2 + (y-5)^2}{2}\right) + 3 \exp\left(-\frac{(x-4)^2 + (y+3)^2}{10}\right) \end{aligned} \quad (14)$$

The graphs of the resulting superposition in $\rho(x, y)$ and $\phi(x, y)$ are given in Figs. 8-9. Because the effects of an eventual propagation cannot bring anything new, in this case we have omitted it preferring to produce directly the simulated experimental records. The results, namely $I'(x, y)$, $I''(x, y)$ are given in Figs. 9-10. Because the graph of $I(x, y)$ is simply the square of $\rho(x, y)$ given in Fig. 8, we have omitted to give it (even if its record has been created).

In Fig. 11 we have shown the wrapped phase as obtained using Eqs. 11-12. Because the unwrapped phase looks similar to $\phi(x, y)$ shown in Fig. 9 (which means that the phase recovery was good enough), we have chosen to illustrate in Fig. 13 the difference between the input phase and unwrapped output phase as a measure of the accuracy of the numerical approach.

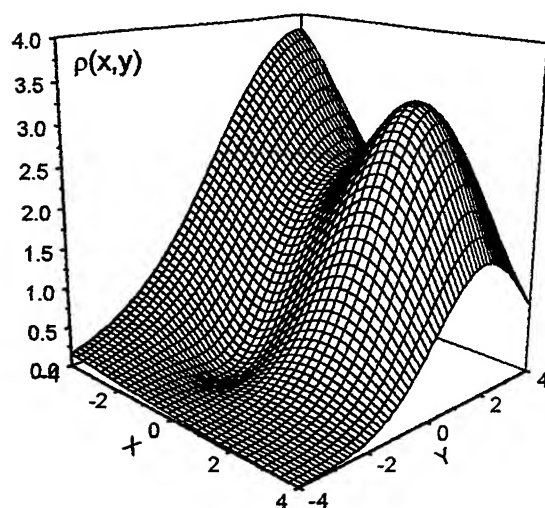


Fig. 8 The input amplitude $\rho(x,y)$

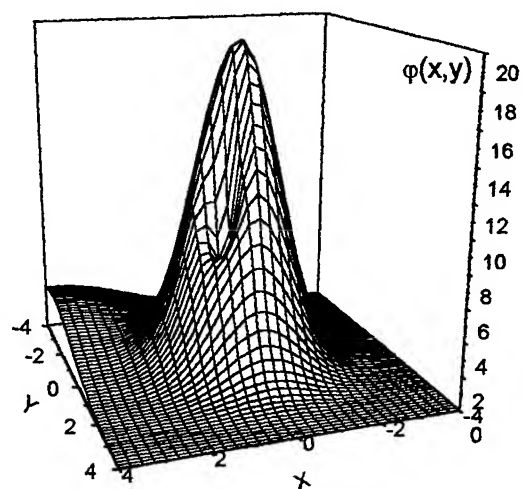


Fig. 9 The input phase $\varphi(x,y)$

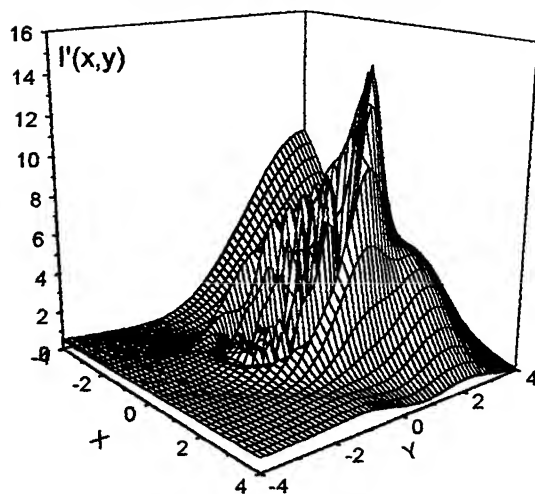


Fig. 10 The distribution $I'(x,y)$

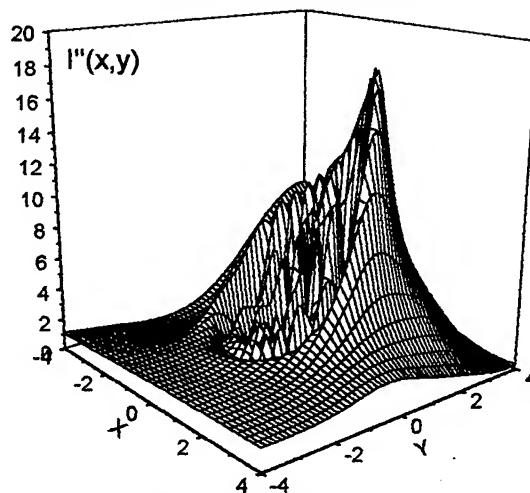


Fig. 11 The distribution $I''(x,y)$

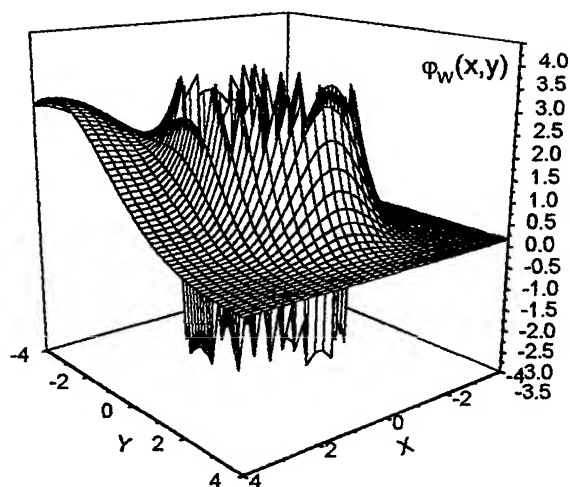


Fig. 12 The wrapped output phase $\varphi_w(x,y)$

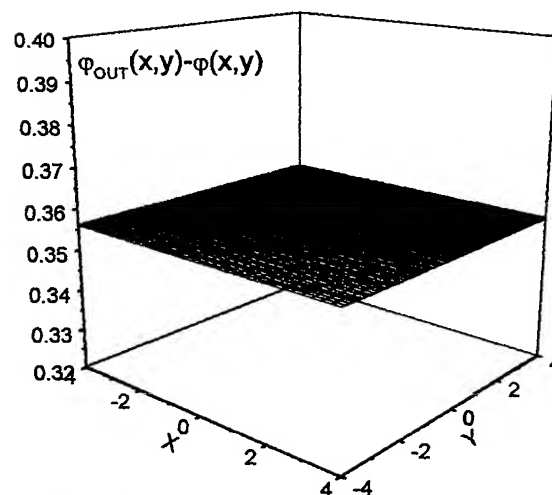


Fig. 13 The accuracy of the phase recovery $\varphi_{OUT}(x,y) - \varphi(x,y)$

5. CONCLUSIONS

The paper shows that three intensity records can be numerically processed to fully recover the optical field distribution. We have also shown that the three intensity records can be obtained practically using a standard optical arrangement allowing optical processing in the Fourier space of the input field. Starting from a simple field and simulating its propagation followed by three distinct intensity records, we have demonstrated the overall consistency of the proposed recovery algorithm.

REFERENCES

1. Y. Sirel, "Design of algorithms for phase measurements by the use of phase-shifting," *Appl. Opt.* **35**, pp. 51-60, 1996.
2. J. W. Goodman, *Introduction to Fourier Optics*, McGraw-Hill, New York, 1968.
3. M. Bulinski, A. Belea, "Retrieving complex field values using intensity records", *Ann. Univ. Buc.* **XLVIII**, 1998.
4. D. C. Ghiglia, L. A. Romero, "Robust two-dimensional weighted and unweighted phase unwrapping that uses fast transforms and iterative methods," *J. Opt Soc Am. A* **11**, pp. 107-117, 1994.
5. T. Tomassi, B. Bianco, "Computer-generated holograms of tilted planes by a spatial frequency approach," *J. Opt Soc Am. A* **10**, pp. 299-305, 1993.
6. J. Garcia, D. Mas, R. G. Dorsch, "Fractional-Fourier-transform calculation through the fast-Fourier-transform algorithm," *Appl. Opt.* **35**, pp. 7013-7018, 1996.

Analysis of the third order harmonic generation process in optical organic waveguides

N. N. Puscas

University "Politehnica" of Bucharest, Physics Department, Bucharest, Romania

ABSTRACT

Based on the coupled amplitude equations model in this paper we present a theoretical analysis of the third order harmonic generation process in optical organic waveguides.

Also, we report the experimental conditions which must be accomplished in order to obtain the best conversion efficiency. The obtained results can be used for the design of the optical organic waveguides in which third harmonic is generated.

Keywords: third order harmonic generation, organic waveguides, poled polymers, amorphous and oriented polymers

1. INTRODUCTION

After the development of the high power lasers in the last twenty years, the electric field intensities ($10^7 \div 10^8$ V/cm) become comparable with the atomic electric field intensities ($3 \cdot 10^8$ V/cm). The interaction between such strong laser fields and matter determines changes of its properties because of the nonlinear effects which appear^{1,2}.

In the case of the optical waveguides even the optical powers available are rather small (~ 1 W), due to their small dimensions (few microns in width and depth, respectively), the local intensities ($I = P/A$, where P represents the incident power laser and A the transversal surface of the waveguide) become appreciable ($\sim 10^6$ W/ μm^2)^{2,3}.

Several poled polymers with large second order nonlinear susceptibility and good optical quality and also amorphous and oriented polymers yielding good optical quality and large third order nonlinear susceptibility were obtained in the last years⁴. In the case of the second order nonlinear optical properties the charge transfer molecules with large fundamental state dipolar moments are used while the polymers are used as matrix for these molecules. For third order effects the most suitable are the conjugated in one dimension polymers because the π electron cloud leads to an enhancement of the molecular hyperpolarizability tensor component in the polymer chain direction.

In order to get oriented (ordered) conjugated polymer thin films several methods were elaborated, like: Langmuir-Blodgett technique, shear technique, stretching technique and epitaxy⁴.

Taking into account that for cubic optics there are no thin film symmetry requirements, from practical point of view the most interesting are either monooriented thin films or completely disordered (amorphous) ones. In the first case one obtains the best conversion efficiencies of the nonlinear processes while in the second one the best optical quality of the thin films.

This paper is organized as follows. In Sect. 2 are presented some theoretical considerations concerning the coupled wave equations for the harmonic amplitudes which describe the third harmonic generation process. Sect. 3 is dedicated to the discussion of the simulation results while Section 4 deals with the conclusions of this paper.

2. COUPLED WAVE EQUATIONS FOR HARMONIC AMPLITUDES

The phenomenological description of the nonlinear effects can be made using the power series development of the nonlinear polarization

*Correspondence: E-mail: pnt@physics2.physics.pub.ro, Telephone (401) 410.45.85, Fax: (401) 3125365

$$\bar{P}^{nl} = \epsilon_0 \chi^{(2)} \bar{E}^2 + \epsilon_0 \chi^{(3)} \bar{E}^3 + \dots \quad (1)$$

where \bar{E} represents the intensity of the electric field and $\chi^{(2)}, \chi^{(3)}, \dots$, are the second and third order nonlinear susceptibilities, respectively.

In the case of three interacting waves having the frequencies

$$\omega_3 = \omega_1 + \omega_2 \quad (2)$$

the second order nonlinear effects can be described using the corresponding nonlinear polarization:

$$P_i^{nl}(\omega_3, \vec{r}) = \frac{1}{2} \chi_{ijk}^{(2)}(-\omega_3; \omega_1, \omega_2) E_j(\omega_1) E_k(\omega_2) \times \exp[i(\vec{k}_1 + \vec{k}_2) \cdot \vec{r} - i(\omega_1 + \omega_2)t] + c.c. \quad (3)$$

where i, j, k correspond to the cartesian co-ordinates. The second order nonlinear polarization acts like a source in the Maxwell's equation:

$$\nabla \times (\nabla \times \bar{E}) + \frac{1}{c^2} \frac{\partial^2 \bar{E}}{\partial t^2} = -\mu_0 \frac{\partial^2 \bar{P}}{\partial t^2} \quad (4)$$

the intensity of the emitting radiation being proportional with $|\chi^{(2)}(\omega_3)|^2$.

If

$$\omega_1 = \omega_2 \quad (5)$$

Eqs. (2) and (3) describe the second order harmonic generation.

For four interacting waves having the frequencies

$$\omega_4 = \omega_1 + \omega_2 + \omega_3 \quad (6)$$

the third order nonlinear polarization is:

$$P_i^{nl}(\omega_4, \vec{r}) = \frac{1}{2} \chi_{ijkl}^{(3)}(-\omega_4; \omega_1, \omega_2, \omega_3) \times E_j(\omega_1) E_k(\omega_2) E_l(\omega_3) \exp[i(\vec{k}_1 + \vec{k}_2 + \vec{k}_3) \cdot \vec{r} - i\omega_4 t] + c.c. \quad (7)$$

the emitted radiation being proportional with $|\chi_{ijkl}^{(3)}(-\omega_4; \omega_1, \omega_2, \omega_3, \omega_4)|^2$.

If

$$\omega_1 = \omega_2 = \omega_3 \quad (8)$$

Eqs. (4) and (7) describe the third harmonic generation.

Based on the theoretical models presented in papers^{5,6,7} one considered that the third harmonic in an organic waveguide yielding second and third order nonlinearities (mixture of poled polymer and oriented (ordered) conjugated polymer) is resulting from two simultaneous processes:

1) the step processes involving the second order nonlinearity:

$$\omega + \omega \rightarrow 2\omega; k_1 + k_1 = k_2 + \Delta k_{12} \quad (9)$$

$$\omega + 2\omega \rightarrow 3\omega; k_1 + k_2 = k_3 + \Delta k_{123} \quad (10)$$

2) the direct process involving the third order nonlinearity:

$$\omega + \omega + \omega \rightarrow 3\omega; k_1 + k_1 + k_1 = k_3 + \Delta k_{13} \quad (11)$$

where:

$$\Delta_{13} = \Delta_{12} + \Delta_{123} \quad (12)$$

In the plane wave approximation

$$E_j = A_j \exp[i(\omega_j t - k_j z)] \quad (13)$$

from Maxwell's Eq. (4) with the polarizabilities expressed by (3) and (7) the following set of differential equations for coupled amplitudes of the interacting waves, in a lossless medium, are obtained in the form ($j \rightarrow 1, 2, 3$)^{5,6}:

$$\frac{dA_1}{dz} = -i\sigma_1 A_1^* A_2 \exp(i\Delta_{12}z) - i\sigma_1' A_2^* A_3 \exp(i\Delta_{123}z) - i\sigma_1'' A_1^{*2} A_3 \exp(i\Delta_{13}z) \quad (14)$$

$$\frac{dA_2}{dz} = -i\sigma_2 A_1^{*2} \exp(i\Delta_{12}z) - i\sigma_2' A_1^* A_3 \exp(-i\Delta_{123}z) \quad (15)$$

$$\frac{dA_3}{dz} = -i\sigma_3 A_1 A_2 \exp(-i\Delta_{123}z) - i\sigma_3' A_1^3 \exp(-i\Delta_{13}z) \quad (16)$$

where

$$\sigma_1 = 4\pi\omega\chi^{(2)} / Fcn_1, \quad \sigma_1' = 6\pi\omega\chi^{(3)} / Fcn_1, \quad \sigma_1'' = 6\pi\omega\chi^{(2)} / Fcn_1 \quad (17)$$

$$\sigma_2 = 4\pi\omega\chi^{(2)} / Fcn_2, \quad \sigma_1' = 6\pi\omega\chi^{(3)} / Fcn_2 \quad (18)$$

$$\sigma_3 = 4\pi\omega\chi^{(2)} / Fcn_3, \quad \sigma_1' = 6\pi\omega\chi^{(3)} / Fcn_3. \quad (19)$$

In Eqs. (14)-(19) $|A_j|^2$ directly measures in Watts the power carried by the j -th modes, n_j is the nonlinear refractive-index and F is the overlap integral.

For the numerical integration of Eqs. (14)-(16) we introduced the real amplitude and phase of the waves

$$A_j(z) = A_j'(z) \exp[i\theta_j(z)] \quad (20)$$

and also the normalized corresponding amplitudes

$$a_j(z) = A_j'(z) / A_1'(0) \quad (21)$$

and normalized distance, respectively

$$\tilde{z} = z\sigma_2 A_1'^2(0). \quad (22)$$

We obtained the following equations for the normalized amplitudes, a_j , and phases, θ_j :

$$\frac{da_1}{d\tilde{z}} = -\sigma_{10} a_1 a_2 \sin \Psi - i\sigma_{10}' a_2 a_3 \sin(\Phi - \Psi) - \sigma_{10}'' a_1^2 a_3 \sin \Phi - \sigma_{10}''' a_1 \quad (23)$$

$$\frac{da_2}{d\tilde{z}} = \sigma_{20} a_1^2 \sin \Psi - \sigma_{20}' a_1 a_3 \sin(\Phi - \Psi) - \sigma_{20}'' a_2 \quad (24)$$

$$\frac{da_3}{d\tilde{z}} = \sigma_{30} a_1^3 \sin \Phi + \sigma_{30}' a_1 a_2 \sin(\Phi - \Psi) - \sigma_{30}'' a_3 \quad (25)$$

$$\frac{d\Psi}{d\tilde{z}} = -\tilde{\Delta}_{12} + \left(\sigma_{20} \frac{a_1^2}{a_2} - 2\sigma_{10} a_2 \right) \cos \Psi - \left(\sigma_{20}' \frac{a_1 a_3}{a_2} - 2\sigma_{10}' \frac{a_2 a_3}{a_1} \right) \cos(\Phi - \Psi) - 2\sigma_{10}'' a_1 a_3 \cos \Phi \quad (26)$$

$$\frac{d\Phi}{d\tilde{z}} = -\tilde{\Delta}_{13} + \left(\sigma_{30} \frac{a_1^3}{a_3} - 3\sigma_{10}'' a_1 a_3 \right) \cos \Phi - \left(\sigma_{30}' \frac{a_1 a_2}{a_3} - 3\sigma_{10}' \frac{a_2 a_3}{a_1} \right) \cos(\Phi - \Psi) - 3\sigma_{10} a_2 \cos \Psi \quad (27)$$

where

$$\Psi = 2\theta_1 - \theta_2 - \tilde{\Delta}_{12} \tilde{z} \quad (28)$$

$$\Phi = 3\theta_1 - \theta_3 - \tilde{\Delta}_{13} \tilde{z} \quad (29)$$

$$\sigma_{10} = \frac{\sigma_1}{\sigma_3 A_1'(0)}, \quad \sigma_{10}' = \frac{\sigma_1'}{\sigma_3 A_1'(0)}, \quad \sigma_{10}'' = \frac{\sigma_1''}{\sigma_3}, \quad \sigma_{10}''' = \frac{\sigma_1'''}{\sigma_3 A_1'^2(0)} \quad (30)$$

$$\sigma_{20} = \frac{1}{A_1'(0)}, \quad \sigma_{20}' = \frac{\sigma_2}{\sigma_3 A_1'(0)}, \quad \sigma_{20}'' = \frac{\alpha_2}{\sigma_3 A_1'^2(0)} \quad (31)$$

$$\sigma_{30} = 1, \quad \sigma_{30}' = \frac{1}{A_1'(0)}, \quad \sigma_{30}'' = \frac{\alpha_3}{\sigma_3 A_1'^2(0)} \quad (32)$$

$$\tilde{\Delta}_{12} = \frac{\Delta_{12}}{\sigma_3 A_1'^2(0)}, \quad \tilde{\Delta}_{13} = \frac{\Delta_{13}}{\sigma_3 A_1'^2(0)}. \quad (33)$$

In Eqs. (30)-(32) α_j characterizes the losses of the j -th modes.

3. DISCUSSION OF THE NUMERICAL RESULTS

For the numerical integration of the coupled amplitude equations (23)-(27) which describe the third order harmonic generation process, the following initial conditions were assumed:

$$a_1(0) = 1, \quad a_3(0) = a_5(0) = 10^{-5}; \quad \Psi(0) = \Phi(0) = 10^{-5}. \quad (34)$$

We considered that the fundamental power density of a Nd:glass laser pumping radiation, ($\lambda = 1.06 \mu\text{m}$), is 10^8 W/cm^2 . The parameters utilised for the integration of the coupled amplitude equations correspond to a mixed structure: polymers (used as matrix)+charged transfer molecules. In the calculation of the nonlinear coefficients (17)-(19) we used the following values for the second and third order nonlinear susceptibilities, respectively: $\chi^{(2)} = 8.2 \times 10^{-15} \text{ m}^2/\text{W}^2$ and $\chi^{(3)} = 1.4 \times 10^{-18} \text{ m}^2/\text{W}^2$. The loss coefficients were estimated to 3 dB/cm both for the fundamental and for the second and third harmonic radiations and the effective area was considered about $F \approx 10 \mu\text{m}^2$.

The best conversion efficiency of the third harmonic generation ($\sim 20\%$) was obtained for a normalized distance $\tilde{z} = 10^3$, (corresponding to a length of the waveguide of about 1 cm), when the normalized wave vector mismatches are $\tilde{\Delta}_{12} = \tilde{\Delta}_{13} = 0$ (phase matching) (Fig. 1).

Taking into account the losses and the effects of the wave vector mismatches (i. e. $\tilde{\Delta}_{12} = -0.012$, $\tilde{\Delta}_{13} = -0.004$ (Fig. 1), $\tilde{\Delta}_{12} = -0.012$, $\tilde{\Delta}_{13} = -0.005$ (Fig. 2), $\tilde{\Delta}_{12} = -0.012$, $\tilde{\Delta}_{13} = -0.04$, $\tilde{\alpha} = 0.01$, (Fig. 3), we obtained much smaller conversion efficiencies.

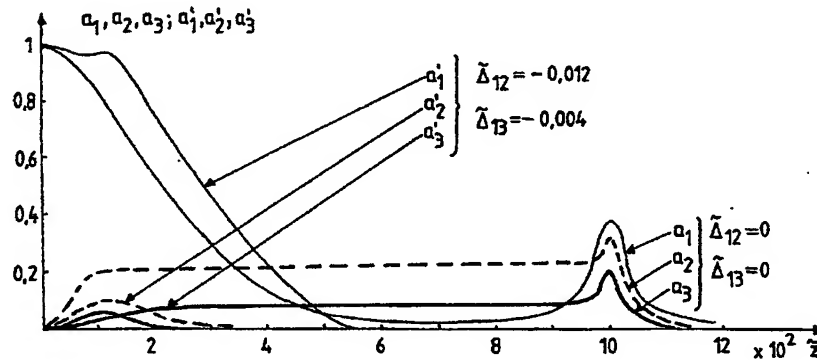


Fig. 1 The dependence of the normalized amplitudes of the fundamental, second and third order harmonics for: $\tilde{\Delta}_{12} = 0$, $\tilde{\Delta}_{13} = 0$ and $\tilde{\Delta}_{12} = -0.012$, $\tilde{\Delta}_{13} = -0.004$.

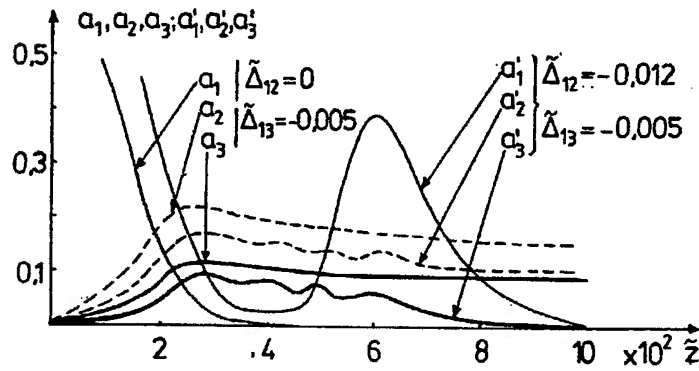


Fig. 2 The dependence of the normalized amplitudes of the fundamental, second and third order harmonics for: $\tilde{\Delta}_{12} = 0$, $\tilde{\Delta}_{13} = -0.005$ and $\tilde{\Delta}_{12} = -0.012$, $\tilde{\Delta}_{13} = -0.005$

Good conversion efficiencies ($\sim 15\%$) corresponding to the third harmonic generation process were obtained even for rather low values of the incident laser intensities (10^6 W/cm^2) when there are no wave vector mismatches ($\tilde{\Delta}_{12} = 0$, $\tilde{\Delta}_{13} = 0$ and $\tilde{\Delta}_{12} = -0.012$, $\tilde{\Delta}_{13} = 0$ (Fig. 4)).

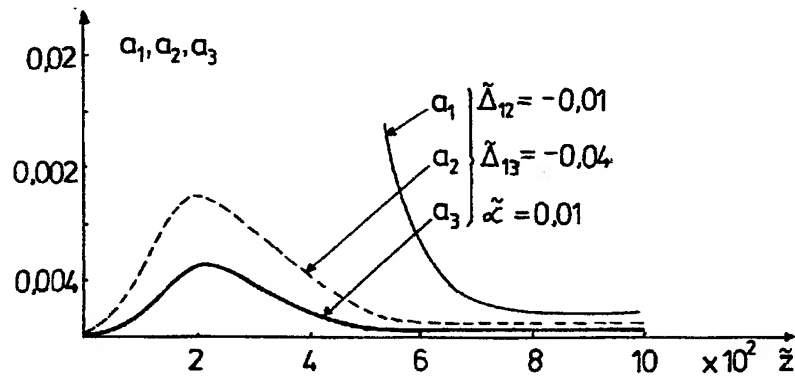


Fig. 3 The dependence of the normalized amplitudes of the fundamental, second and third order harmonics for: $\tilde{\Delta}_{12} = -0.012$, $\tilde{\Delta}_{13} = -0.04$, $\tilde{\alpha} = 0.01$.

4. CONCLUSIONS

In this paper we present a theoretical analysis of the third harmonic generation process in optical organic waveguides. By numerical integration of the coupled amplitude equations we have obtained the conditions which must be accomplished, for normalized wave vector mismatches and for normalized distance in order to obtain the best conversion efficiency.

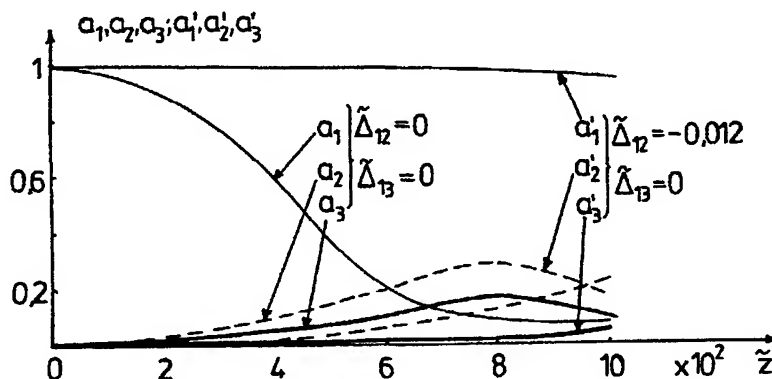


Fig. 4 The dependence of the normalized amplitudes of the fundamental, second and third order harmonics for: $\tilde{\Delta}_{12} = 0$, $\tilde{\Delta}_{13} = 0$ and $\tilde{\Delta}_{12} = -0.012$, $\tilde{\Delta}_{13} = 0$.

The simulation results can be used for the selection of those organic structures (mixture of poled polymer and oriented (ordered) conjugated polymer) and experimental parameters (incident power, waveguide length, wavevector mismatch etc.) which assure the best conversion efficiency in the third order harmonic generation process in optical organic waveguides.

REFERENCES

1. R. W. Boyd, *Nonlinear Optics*, Academic Press Inc. 1991.
2. G. P. Agrawal and R. W. Boyd, *Contemporary Nonlinear Optics*, Academic Press Inc. 1992.
3. D. B. Ostrowsky, R. Reinisch, *Guided Wave Nonlinear Optics*, Kluwer Academic Publishers, Dordrecht, Boston, London, NATO ASI Series, **214**, 1992.
4. F. Kajzar, "Organic molecules for guided wave quadratic and cubic optics", in *Guided Wave Nonlinear Optics*, editors: D. B. Ostrowsky, R. Reinisch, Kluwer Academic Publishers, Dordrecht, Boston, London, NATO ASI Series, **214**, pp. 87-111, 1992.
5. N. Bloembergen, *Nonlinear Optics*, Benjamin W. A. Inc. New York, 1965.
6. N. N. Puscas and I. M. Popescu, "Theoretical analysis of the third order harmonic generation in organic waveguides", *First Annual Meeting of European Optical Society (EOSAM)*, Universidad de Zaragoza, Spain, Abstracts, pp. 47-48, 1993.
7. I. Montrosset, Montrosset, P. Lambkin and G. Perrone, "Modelling of guided devices", *Guided Wave Nonlinear Optics*, ed. D. B. Ostrowsky, R. Reinisch, Kluwer Academic Publishers; Dordrecht, Boston, London; NATO ASI Series, **214**, pp. 113-132, 1992.

Pointing out the structure of double layers through spectroscopic methods

Benedict Opreșcu^{*a}, Mircea Sanduloviciu^b

^aThe Faculty of Science, Univ. of Pitești, Targul din Vale, N° 1, Pitesti, 0300, Romania

^bThe Department of Plasma Physics, Al. I Cuza University, Iasi, 6600, Romania

ABSTRACT

The present paper investigates the dependence of local emissivity, for two spectrum lines of helium, upon the location within a stationary double layer. The experimental results are explained starting from a new phenomenological model, which takes into account the non-elastic interactions between the accelerated electrons and the atoms of the working gas.

Keywords: double layers, local emissivity, non-elastic processes, spectroscopic methods

1. INTRODUCTION

In order to investigate the medium within double layers, the method of (electrostatic or emitting) probes is currently used¹. As double layers are strongly influenced by the properties of the solid bodies that bound the ionised medium these are formed in, the displacement of the probe can determine significant alterations of the double layer parameters. It is for this reason that the results provided by the methods based upon probes, in the field of double layers, must be regarded with reservation.

Unlike the methods using probes, the optical methods have the essential advantage of not significantly perturbing the double layer. Obviously, the method of investigating the double layer structure through the analysis of the radiation emitted by the double layer does not allow the direct emphasising of the local physical parameters which characterise the double layer (the electric potential, electric charge densities, the average energy of the electrons, etc.). That is why the emphasising of the double layer structure through this method is in close connection to the theoretical model used for explaining the appearance of this type of self-organisation of matter. The present paper investigates the dependence of local emissivity, for two spectrum lines of helium, upon the location within a stationary double layer.

2. THE EXPERIMENTAL DEVICE AND THE EXPERIMENTAL RESULTS

2. 1. The experimental device

We started in conceiving and realising the experimental device from the mechanism of producing the double-layer. In keeping with this mechanism, there has to be a source of electrons having as low energy as possible, as well as area for their acceleration. Proceeding from this idea, we made up the experimental device presented in Fig.1.

At the left of this figure can be seen the plasma source. As can be noticed, it includes a hollow cathode which allows for a high value current to be obtained at a low burning tension. This is extremely important because, as is generally known, only the slow electrons are useful in the production of the electric charge structure. In order to facilitate the passing of the cathode electrons towards the acceleration zone, we used a ring electrode as the anode.

At the right of Fig. 1 can be seen the area of electron acceleration. This region is composed of a metal grid and an electron-collecting plate.

^{*}Correspondence: E-mail: chidu2@yahoo.com, fax: 048-216448

As a working gas is used high-purity helium. The working pressure was selected within the interval 0.1-1 torr.

2.2. Experimental results

If the pressure in the discharge tube and the parameters of the plasma source are kept constant, for a certain anode-grid distance, the volt-ampere characteristic of the area of generation of the structure is obtained. Such a characteristic is presented in Fig. 2.

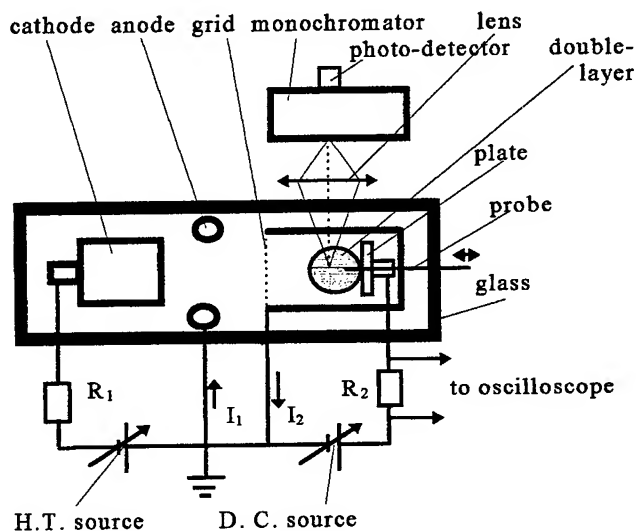


Fig.1 Experimental set-up

In the EF region of the volt-ampere characteristic, a stationary double layer is formed in front of the grid. In these conditions, probe measurements can be made in order to evince the properties of the medium within the structure. By moving, by means of the screw of the micrometer, the probe along the axis of the plate, and thus determining for each point the potential of the place, we could establish its dependence on the distance from the plate bottom. In Fig. 3, such a dependence is shown, when the working point of the installation lies within the DEF region along the volt-ampere characteristic. It is found that, in front of the plate, there is an increase of the potential. In the figure, the potential of the plate is considered as the reference potential. The distances are measured from the bottom of the plate.

The dependence of the intensity of the two spectre lines of helium under investigation along the double layer is presented in Fig. 4. The maximum of the intensity of the spectre line of 501.6 m is found to appear before the 667.8 nm radiation reaches the extreme value.

By studying the radial dependence of the intensity of the light emitted by the structure, we can determine, by means of the formula²:

$$\varepsilon(r) = -\frac{1}{\pi} \int_r^R \frac{\Gamma(x) dx}{\sqrt{x^2 - r^2}}, \quad (1)$$

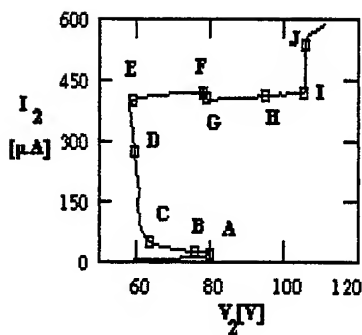


Fig.2 The current-voltage characteristic.

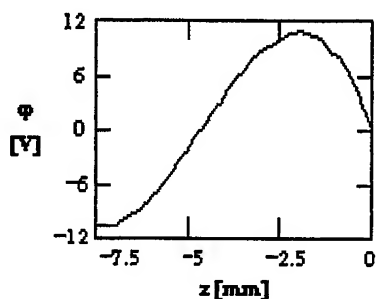


Fig.3 Distribution of potential inside the double-layer.

where $\epsilon(r)$ is the local plasma emissivity at a distance r from the plasma center, $I'(x) = dI(x)/dx$ and $I(x)$ represent a set of

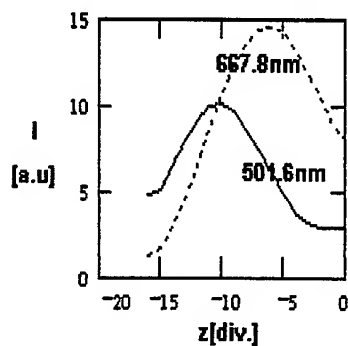


Fig.4 Dependence of spectral lines intensity upon the distance to the plate.

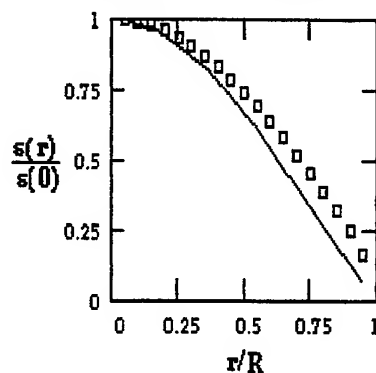


Fig.5 Dependence of relative emissivity upon the distance to the axis of the discharge tube.

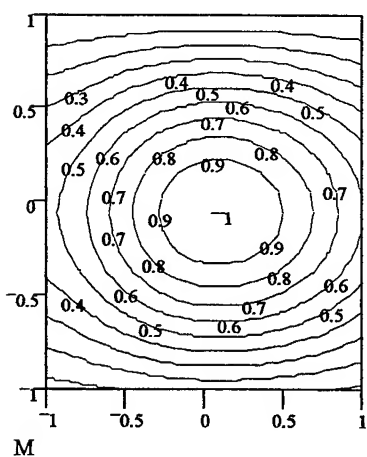


Fig.6 Dependence of local relative emissivity on the location within the double layer, for the 501.6 nm radiation of He

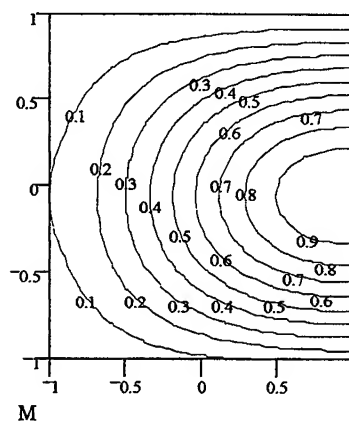


Fig.7 Dependence of local relative emissivity on the location within the double layer, for the 667.8 nm radiation of He

time-integrated values measured at distance x , the dependence of the local emissivity upon the distance to the axis of the discharge tube. In Fig. 5 is presented the dependence of the relative local emissivity upon the distance to the axis of the discharge tube. The continuous line indicates the dependence of the relative electron concentration upon the distance to the axis of the discharge tube, as resulting from Schottky's theory on the positive column.

By combining the axial as well as radial experimental results on the intensity of spectre lines, a fairly suggestive two-dimensional representation can be given of the emissivity of the medium within the structure, for the two spectre lines under investigation. In Figs. 6 and 7 is represented, along the horizontal axis, the normalised z/z_{\max} distance, considering the origin of the axes in the point where the radiation of 501.6 nm has the maximum intensity, and, along the vertical axis, the normalised r/R radius.

3. THE PHENOMENOLOGICAL INTERPRETATION OF THE EXPERIMENTAL RESULTS

In order to be able to account for the experimental results presented in the previous section, we shall have recourse to the phenomenological model presented in³. In what follows, we shall make a new, nut-shell presentation, of this model.

By closing the plate circuit, through the application of an electric field between the grid and the plate, a part of the grid electrons make for the plate.

When the energy of the accelerated electrons in the applied field reaches values corresponding to the excitation potential of the gas atoms, part of them collide with the atoms non-elastically. The electrons having produced atom excitation accumulate in front of the plate in the shape of a stratum of negative electric charge. In case the potential difference between the grid and the plate is greater than the ionization potential of the gas atoms, a part of the electrons which did not lose their energy through excitation collisions may produce ionizations of the atoms near the plate.

In case the number of the ionization processes per time unit becomes significant, the resistance of the gas column comprised between the grid and the plate gets down. Under these conditions, the electric tension falling within the electrons acceleration zone is diminished, thus resulting in a negative slope of the volt-ampere characteristic. This is beginning in the A point along the characteristic.

If the rate of generating ions exceeds a critical value, the processes of diffusion and drift can no longer compensate the accumulation of positive ions. In these conditions, within the region in the neighbourhood of the plate where the cross-section of gas atom ionization has the maximal value, a positive electric charge distribution begins to evolve.

The distribution of positive electric charge interacts with the distribution of negative electric charge (which is positioned around the zone in which the cross-section of gas atoms excitation is maximal), thus generating a double-layer. As a result of the electrostatic interactions, the locations of the negative spatial layer and that of the positive spatial layer change in the opposite direction of the other electric field. Having an effect similar to the forces of superficial tension, the electrostatic forces tend to bring the double-layer to the same form as the area of the minimal surface.

Upon the appearance of the spheric structure, the intensity of the electric current passing through the plate is suddenly increased as a result of the enlargement of the effective area of electron collecting, as well as the increase in the ionization rate. As the average values of the rates of the excitation and ionization processes corresponding to the BC area do not permit maintaining the spheric structure, the latter comes back to the plane shape. This can be accounted for by the fact that the passing to the spheric layer only takes place when the rate of the excitation and ionization processes exceeds a critical value. Because those processes have a statistic character, the moment of the passing from the plane layer to the spheric layer is not well defined, as was experimentally proved.

The ions resulted from the ionization processes near the plate migrate to the grid. A part of them can recombine, on the glass wall, with the electrons, while the other part of them reach the negative electric charge zone near the grid. As a result of the increase in ions concentration near the grid, the slowing down electric field for the electron decreases. This decrease leads to an increase in the electronic current that goes to the plate. The increase of the electrons flux getting to the grid amplifies the rate of the excitation and ionization processes. If the overrate of excitations and ionizations is

significant, the new transition from the plane stratum of negative charge to double-layer is determined by the previous transition. Over a certain value of the intensity of the plate current, the above mentioned mechanism becomes so intense that, the transitions from the negative charge stratum to the electric charge structure become perfectly coherent. This phenomenon can be experimentally observed when it gets over point C on the characteristic.

If the flux of electrons reaching the plate exceeds a certain value, the processes of excitation and ionization allow for the making of a stationary structure, as the oscillations in the plate circuit cease.

The distributions of electric charge that make up the stationary double-layer achieve alterations of the electric potential in front of the plate. In conformity to Poisson's equation, within the space region in which there is a distribution of negative electric charge, the second order derivative of the potential must be positive, and within the region in which the charge distribution is positive, the second order derivative of the potential is negative. Moreover, the electric potential within the positive charge region must be higher than that in the surrounding regions. The experimental results referring to the potential distribution in front of the plate area are in keeping with what was previously said. The fact that, within the region in which the electric potential exhibits a maximum, there is an agglomeration of the positive ions is proved - in a direct manner, too - by the fact that within that region there exists a maximum of the ionic probe current of saturation.

The distributions of the emissivity for the two spectre lines under investigation come as a confirmation of the theoretic model presented in^{3, 4}. In fact, the spectre line of 501.6 nm, with the excitation energy of 23.09 eV appears as a consequence of the excitations through inelastic collisions between the Helium atoms and the electrons. Consequently, in the region where the emissivity for the line of 501.6 nm is maximal, an electron agglomeration is bound to form. The 667.8 nm line appears primarily as a result of the processes of re-combination of the helium ions on superior energy levels, followed by a transition from level $3D^1$ to level $2P^1$. Therefore, in the region where this line is intense, there is an agglomeration of positive ions. Taking as a basis these considerations, we can admit, with a fair approximation, that the surfaces on which the emissivities are constant are also those surfaces on which the concentrations of electrons and ions, respectively, are constant. The fact that the two spectre lines do not have the same position of the intensity maximum proves that the cross-sections of excitation and ionisation reach their maximum values in distinct places, which is essential, in keeping with the previous theory, for the double layer to form.

4. COMMENTS

The diagnose of the spatial electric charge structures can be effected through of the sounding method, and also by means of analysing the light emitted by the structures. Either method presents advantages as well as disadvantages. The main advantages of the sounding method are: simplicity of the experimental device and the direct determination of the local physical parameters of the medium. The main disadvantage is connected with the perturbing of the physical properties of the medium in which the sound is introduced. In the case of the double layers, that perturbation can be essential.

The method based on the analysis of the properties of the radiation emitted by the double layer has the disadvantage of using a more expensive experimental device, as well as the fact that the experimental results do not directly provide the local physical parameters of the medium under investigation. The advantages of the spectre method, unlike the procedure based on the probe method, are determined by the fact that the structure is not perturbed and also the possibility of scanning the whole structure, which is rather difficult to do practically by moving a probe.

REFERENCES

1. M. Sanduloviciu, "Quantum processes as generators of the energy source for ion-cyclotron oscillations", *Romanian Rep. in Physics*, 40, pp. 745-756, 1997;
2. S. Djurovic, "Abel inversion by Jacobi polynomials", *19th SPIG, Contributed Paper*, Editors: N. Konjevic, M. Cuk and I. R. Videnovic, pp. 329-332, Publisher: Faculty of Physics, University of Belgrade, Belgrade, 1998;
3. B. Oprescu and M. Sanduloviciu, "Non-linearity of the current-voltage characteristic in gases and their self-organizing processes", *Rom. Journ. of Optoelectronics*, 6, pp. 27-33, 1998;

4. B. Oprescu and M. Sanduloviciu, "Self-organization phenomena in current carrying plasmas", *19th SPIG, Contributed Paper*, Editors: N. Konjevic, M. Cuk and I. R. Videnovic, pp. 725-728, Publisher: Faculty of Physics, University of Belgrade, Belgrade, 1998;
5. B. Oprescu, M. Sanduloviciu and Gh. Dima, "Means of influencing the producing rate of the double-layers by distribution on energies of the injected electrons in the producing zone", *Balkan Phys. Letters*, **5**, pp. 1367-1370, 1997;
6. E. Lozneau and M. Sanduloviciu, "A new test experiment with relevance for the physical basis of the synergetic science", *19th SPIG, Contributed Paper*, Editors: N. Konjevic, M. Cuk and I. R. Videnovic, pp. 705-708, Publisher: Faculty of Physics, University of Belgrade, Belgrade, 1998;
7. S. J. Talasman, "On the genesis of spatio-temporal selforganized structures in plasma devices", *Rom. Journ. Phys.*, **40**, pp. 193-207, 1995.

MOS Transistors microscopic analysis

G. Stoenescu *, N. Baltateanu

University of Craiova*, Department of Physics

13 A. I. Cuza, Craiova 1100, Romania

Hyperion Institute for Research and Development, Bucharest, Romania

ABSTRACT

Our paper studies the influence of the irradiation by fast electrons on the characteristic properties and microscopic parameters of certain MOSFET transistors with p-induced channel (ROS05). Using the experimental data, an appropriate theoretic model and an optimization method, the following specific parameters were computed for the irradiated and un-irradiated samples: the electron mobility, the Fermi energy value, as well as the saturation voltage and the changing of the drain channel length.

Keywords: MOS transistors, optimization, microscopic parameters, irradiation

1. INTRODUCTION

Our paper studies the influence of the irradiation by fast electrons on the characteristic properties and microscopic parameters of certain MOSFET transistors with p-induced channel (ROS05). The integrated MOS type circuits are widely used in the production of logical circuits with high commutation speed and low energy consume.

Using the experimental data, an appropriate theoretic model and an optimization method, the following specific parameters were computed for the irradiated and un-irradiated samples: the electron mobility, the Fermi energy value, as well as the saturation voltage and the changing of the drain channel length.

Our work thus connects two interesting features of these devices:

the variation of the main characteristics of the MOS transistors after the irradiation with fast electrons;

changing of the microscopic (Fermi energy, electron mobility) and macroscopic (length of the drain channel, saturation voltage) parameters under the same conditions.

2. EXPERIMENTAL METHOD

The transfer and output characteristics of the transistors were traced at constant temperature ($T=30^{\circ}\text{C}$, obtained with a U10 type thermostat) using a KIPP-ZONEN, BD30 X-Y recorder and high precision digital voltmeters of the HP 3480A and KEITHLEY 161 type.

The irradiation was performed using fast electrons (3 MeV), the dose was 10 MRd (10^5 Gy) and the exposing time had a 16 minute value. For the output characteristics recording the V_{GS} voltage was kept constant while modifying V_{DS} .

The transfer characteristics proved to have a strong displacement in the sense of increasing the threshold voltage from 4-5 V up to 20-25 V. The slopes of the characteristics were practically unmodified and this seems to be a result of the accumulation of the positive charge in the oxide layer placed between the "gate" and the substrate of the transistors.

The fast electrons which cross this layer during the irradiation process provoke the ionization of the atoms and a secondary electron emission from the oxide layer which finally leads to the accumulation of the positive charge in the oxide. This positive charge creates an electric field which has a major contribution in the transfer characteristics displacement towards high voltage values.

Correspondence: Email: gstoen@hotmail.com; Fax: 40 51 415077

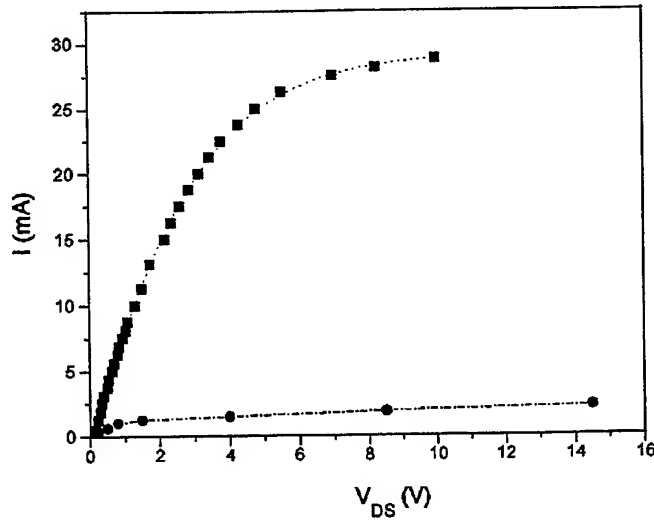


Fig.1 Experimental characteristics of unirradiated (squares) and irradiated (circles) samples

3. THEORETICAL STUDY AND COMPUTER SIMULATIONS

The general form of the model,^{1, 2, 3} we used in the study of the intensity-voltage characteristics is given by:

$$I_D = \sum_{i=0}^2 P_i V_{DS}^i + P_3 (V_{DS} + P_4)^{3/2} \quad (1)$$

If we chose the parameters P_i (for $i = 0, 4$) as:

$$P_0 = -\frac{2}{3} x_1 x_2 x_3^{3/2} \quad (2)$$

$$P_1 = V_{GS} x_1 \quad (3)$$

$$P_2 = -\frac{1}{2} x_1 \quad (4)$$

$$P_3 = -\frac{2}{3} x_2 x_1 \quad (5)$$

$$P_4 = x_3 \quad (6)$$

with:

$$x_1 = \frac{\mu_n \epsilon_d B}{L w_i} \quad (7)$$

$$x_2 = \frac{w_i}{\epsilon_d} \sqrt{2 e \epsilon_s N_a} \quad (8)$$

$$x_3 = 2 \cdot \Phi_F \quad (9)$$

then we obtain the well-known expression of the intensity:

$$I_D = x_1 \cdot \left\{ V_{GS} \cdot V_{DS} - \frac{1}{2} V_{DS}^2 - \frac{2}{3} x_2 \cdot \left[(V_{DS} + x_3)^{3/2} - x_3^{3/2} \right] \right\} \quad (10)$$

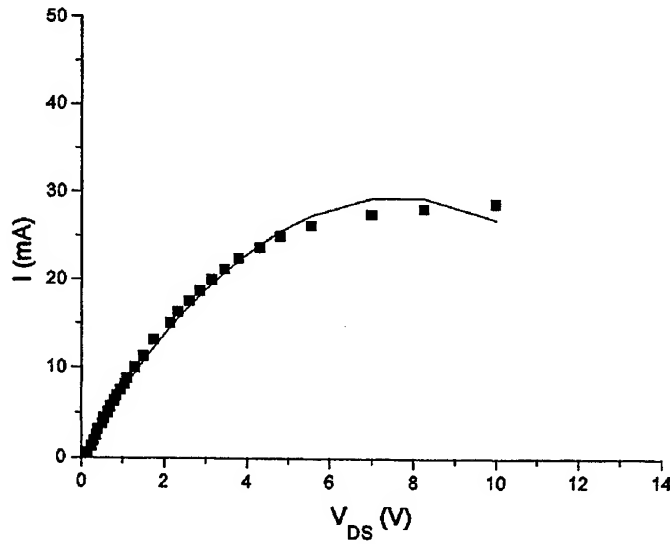


Fig.2 Experimental and theoretical characteristics for unirradiated samples

On the other hand, the results of the simulation (fig. 2, 3) based on (10) for the values of the microscopic parameters,^{2, 4, 3} lead us to the conclusion that for the analyzed MOS transistors the hypothesis: $V_{DS} \ll 2\phi_F$ is verified.

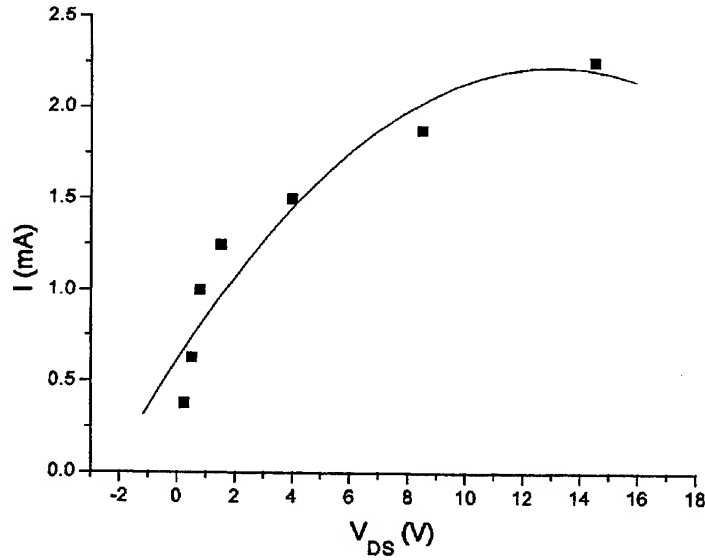


Fig.3 Experimental and theoretical characteristics for irradiated samples

This allows us to use a simpler model of the intensity-voltage characteristics having:

$$P_j = 0 \quad (11)$$

with $j = 3, 4$ and

$$P_1 = x_2 (V_{GS} - x_1) \quad (12)$$

$$P_2 = -\frac{1}{2}x_2 \quad (13)$$

giving:

$$I_D \cong x_2 \cdot \left[(V_{GS} - x_1) V_{DS} - \frac{1}{2} V_{DS}^2 \right] \quad (14)$$

where

$$x_2 = \frac{Z}{L} \mu_n C_0 \quad (15)$$

and

$$x_1 = 2\phi_F + \frac{1}{C_0} [2\epsilon_s q N_a (2\phi_F)]^{1/2} \quad (16)$$

the Fermi potential being measured,^{5, 6, 7} with respect to the middle of the un-allowed energy band.

Here x_1, x_2 depend on,^{8, 9, 10} the acceptors concentration N_a , the electron mobility μ_n , the dielectric constants of the layers, the MOS transistor width, the oxide layer width, the length of the channel between source and drain contact L , the Fermi potential ϕ_F .

The parameters P_i ($i = 1, 4$) were obtained from the comparison of the experimental and theoretical I-U curves, by minimizing the test function:

$$F \equiv \sum_{i=1}^N [I_D(V_{DS}^i) - I_D^i]^2 \quad (17)$$

where I_D^i are the experimental values and the function $I_D(V_{DS})$ is defined by the theoretical models (10) and (14) respectively.

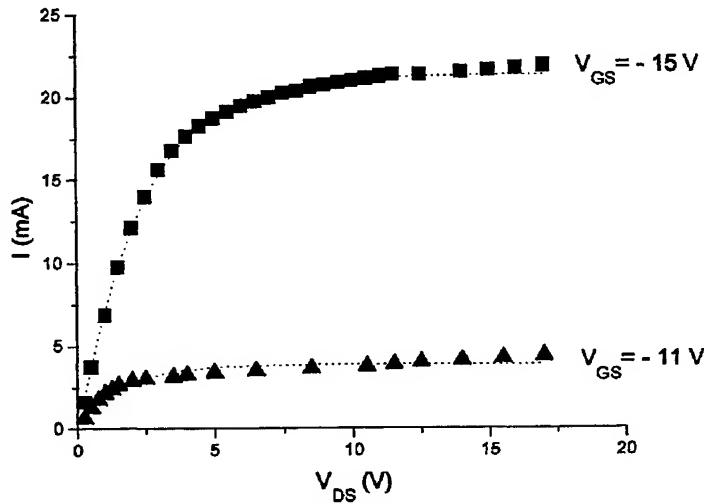


Fig.4 Transfer characteristics at different V_{DS} values for irradiated samples

Consequently, the mobility (μ_n) and the Fermi energy (ϕ_F) were calculated for the given transistors, both before and after the irradiation process and for different values of V_{GS} .

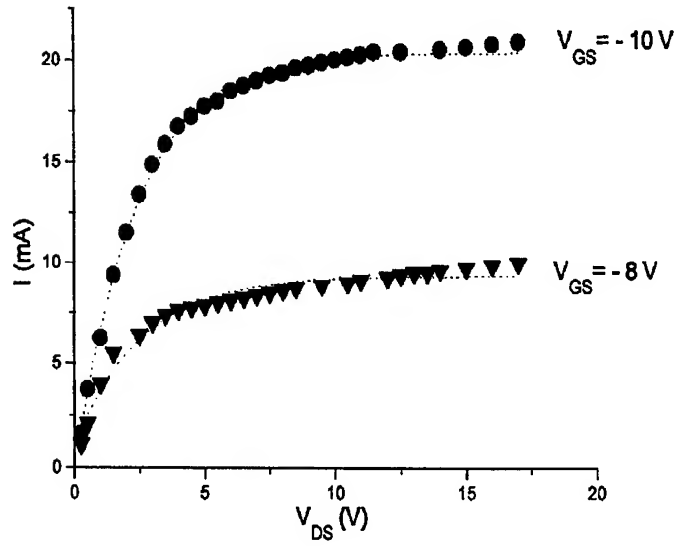


Fig.5 Transfer characteristics at different V_{DS} values for unirradiated samples

Moreover, the saturation voltages (V_{sat}) were calculated, for the experimentally measured saturation currents (I_{sat}), using a dependence of the type [3]:

$$V_D^{sat} \cong \left[\frac{2L}{Z} \cdot \frac{I_D^{sat}}{\mu_n C_0} \right]^{1/2} \quad (18)$$

This made possible to compute the decreasing of the drain channel length

$$\Delta L \cong \left[\frac{1}{qN_a} 2\epsilon_s (V_{DS} - V_{DSat}) \right]^{1/2} \quad (19)$$

due to it's closing for $V_{DS} > V_{DSsat}$ when the width of the spatial charge domain of the drain is increased.

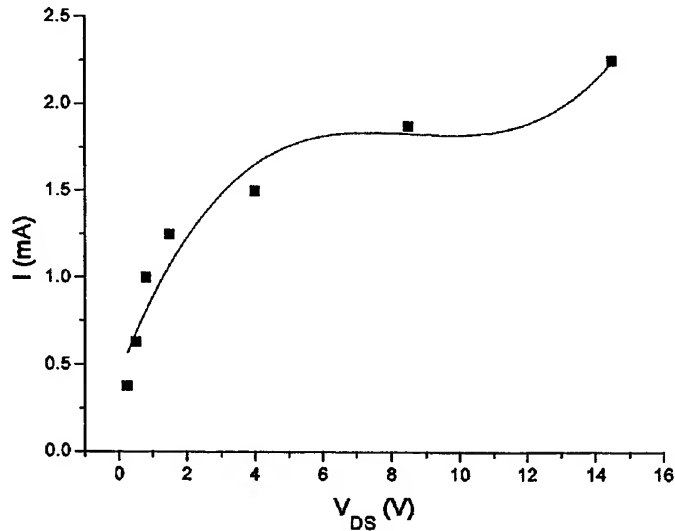


Fig.6 Experimental and theoretical (using the first model) characteristics

4. RESULTS AND CONCLUSIONS

The experimental I-U characteristics and the theoretical curves are presented in fig. 1 - fig. 5, for a ROS05 transistor, $V_{GS} = -12V$, unirradiated and irradiated respectively.

The results of our nonlinear fitting procedure gave us two sets of parameters:

a) using the first model, the following values were computed, for the irradiated and unirradiated samples:

Parameters	unirradiated sample	irradiated sample
P_0/P_2	22.001	21.931
P_0/P_3	207.898	218.076
P_3/P_2	0.102	0.095

b) using the second model, the corresponding values were obtained:

Parameters	unirradiated sample	irradiated sample
P_1	7.6160	0.24605
P_2	-0.49742	-0.00942

The calculated values of the "Fermi potential" (0.021 eV) and of the x_1 parameter in the second model which depends on the acceptors concentration are unchanged under the electron irradiation process.

By contrast, the electrons mobility was proved to be modified as a result of the irradiation process, its value being decreased from : $0.17004 \text{ m}^2/Vs$ down to $0.00322 \text{ m}^2/Vs$ for $V_{GS} = -12V$ while the change of the drain channel length was $\delta\Delta L = 12.014 \text{ \AA}$ therefore showing a good agreement with the experimental and phenomenological analysis.

In conclusion, our results showed a decreasing of the electron mobility after irradiation process while the Fermi energy was not changed, both parameters depending also on the V_{GS} value.

REFERENCES

1. I. S. P. C. N. B. I. Spanulescu, V. Ruxandra and G. Stoenescu, "The cdse thin films for solar cells," *Anal. Univ. Bucharest* **34**, pp. 13-16, 1990.
2. I. S. N. B. G. Stoenescu, V. Calian and V. Ruxandra, "The effect of accelerated electron irradiation on electric conductivity of cdse thin films," *Teaching the Science of New Materials* **proc.**, pp. 314-316, 1995.
3. I. S. G. Stoenescu, V. Calian and N. Baltateanu, "Characteristic parameters changes for mos circuits irradiated by fast electrons," *Optoelectronica* **4**, pp. 71-74, 1996.
4. C. M. Dozier and D. B. Brown, "Photon energy dependence of radiation effects in mos structures," *IEEE Trans. Nucl. Sci. NS* **27**, pp. 1694-1699, 1990.
5. R. I. Baron and L. Higbie, *Computer Architecture*, Addison-Wesley, New York, 1994.
6. S. J. Fonash, *Solar cell device Physics*, Academic Press, New York, 1981.
7. E. H. Nicollian and J. R. Brew, *MOS (Metal Oxide Semiconductor) Physics and Technology*, Wiley, New York, 1982.
8. W.-S. L. J. A. T. Ma, D. Ueda and J. S. H. Jr., "Influence of buffer layer thickness on dc performances of gaas/algaas heterojunction bipolar transistors grown on silicon substrates," *IEEE El. Device Letters* **9**, pp. 657-659, 1988.
9. V. Dolocan, *Fizica jonctiunilor semiconductoare*, Edit. Academiei, Bucharest, 1982.
10. P. E. Gray and C. L. Searle, *Modern Electronics*, World Scientific, New York, 1973.

Temperature dependencies of optical parameters from EBBA channeled spectra

M. Ursache, M. Socaciu *, V. Calian
University of Craiova, Department of Physics
13 A.I.Cuza, Craiova, 1100, Romania

ABSTRACT

Starting from the experimental channeled spectra $I(\lambda, T)$ of the nematic EBBA liquid crystal and using a nonlinear optimization algorithm, we computed the dispersion curves of the ordinary and extraordinary indices, of the birefringence and the band contributions to these dependencies, as functions of the temperature. The theoretical interpretation of the spectra and the data processing technique allowed us to compute the realistic variation of the order parameter S and correction factor g with the same external parameter.

Keywords: EBBA liquid crystals, channeled spectra, dispersion curves, temperature dependence, order parameter.

1. INTRODUCTION

The characteristics of optical liquid crystal devices are determined by the refractive indices of the materials, thus the understanding of the relation between refractive indices and molecular properties is necessary in improving the design of new liquid crystal materials. Knowing the refractive indices dependence on temperature is also important in computing the order parameter dynamics which has the main role in mesophase identification,^{1, 2}

The temperature mesogenic range, dielectric constant, birefringence, photo and chemical stability are the most important physical properties of nematic liquid crystals for electro-optical application. Most liquid crystals are non-absorbent in the visible spectra region and their refractive indices only weakly depend on the light wavelength. The dispersion of the refractive indices is determined by the electronic absorption bands where the refractive index has a strong variation with the wavelength,^{3, 4}

In this paper we derive the ordinary and extraordinary indices dispersion as well as the birefringence dispersion of EBBA nematic liquid crystal at different temperatures. We have also studied the absorption bands contributions to these dispersion curves, the order parameter S and correction factor g as functions of temperature.

The available experimental methods for measuring indices dispersion provide discrete or quasicontinuum spectra, the latter having obvious advantages. We improved the experimental set-up of the Talbot-Rayleigh method⁵ and we propose a rigorous interpretation and data processing technique, in order to increase the accuracy and to reduce the computation time, obtaining the spectra dependence on temperature as an external parameter, in addition.

Moreover, the higher precision optimization method described in this paper eliminates the necessity of the measurements based on the so-called "reference point" and generates all the parameters needed in the calculation of birefringence dispersion, bands contribution and order parameter temperature dependence.

2. EXPERIMENT AND COMPUTER SIMULATIONS

We measured the $I(\lambda)$ spectra of the nematic EBBA liquid crystal at different temperature values, for both crossed and parallel polarizers, by using an experimental set-up of the Talbot-Rayleigh type⁵ with several constructive improvements and a different method of establishing the wavelength - coordinate correlation.

The experimental method consists of recording the channeled interference spectrum in a diffraction order of the white light source, after the initial beam had been split in two components, only one of them passing through the anisotropic sample. The data acquisition is performed by a CCD linear array with short response time appropriate for unstable conditions. Our experimental set-up was improved with respect to the standard Talbot-Rayleigh interferometer,⁵ by the following features.

Correspondence: Email: msocaciu@central.ucv.ro, Fax: 40 51 415077

Firstly, the cell was half filled by capilarity with uniaxial EBBA nematic liquid crystal ((p-etoxybenzylidene)-p-n-butylaniline), using a 180 μm thick glass plate inserted into the cell as a separator and as a reference material, being in contact with the top surface of the liquid crystal. On the other hand, the effect of the reference material was cancelled by introducing a compensatory plate, made from the same glass as the separator and having the same thickness, placed in front of the liquid crystal cell.

An other characteristic of our technique is our solution to eliminate the uncertainty of the usual method in the correlation between the x -coordinates in the output plan and the wavelength values. In this purpose, we measured the x -positions of the diffraction maxima by a CCD linear array for 10 dichroic filters and drew the resulted $x(\lambda)$ curves. The auxiliary measurements ($n_{ref}^{e,o}(T, \lambda)$ and polarized absorption spectra) imposed by the previous methods which were based on the determination of the channel orders in the $I(\lambda)$ spectra⁶ were eliminated due to our modified data interpretation and processing.

In order to obtain the $n_{e,o}(T, \lambda)$ dependencies, we developed a non-linear $I(\lambda)$ curve fitting procedure based on a Levenberg-Marquart minimization algorithm. This aim is in turn accomplished only after the theoretical expression of the intensity is calculated.

The first step of our procedure establishes this function, starting with the amplitude of an arbitrary wave emerging from a point that has an arbitrary x -coordinate, under the diffraction angle θ : taking into account the transmission coefficient of the liquid crystal cell (T_1) and the changing of the light phase after the cell and grating. Calculating the light intensity in the arbitrary point we obtained:

$$I = \frac{N^2 p^2}{4} \left(\frac{\sin \frac{\pi}{\lambda} p \theta}{\frac{\pi}{\lambda} p \theta} \right)^2 \left[\frac{1 + T_1^2}{2T_1} + \cos \left(\frac{2\pi}{\lambda} (n - 1) d + \frac{2\pi}{\lambda} p \theta \right) \right] \quad (1)$$

where p is the diffraction grating constant and $\sin \theta \approx \theta = x/f$, f being the focal length of the lens.

The second step of our method consists of choosing the model for the ordinary and extraordinary indices dependence on the wavelength values. We used the realistic three-band model,^{4,7} which accounts for all electronic transitions from the electronic transition spectrum. There are three bands consisting of one λ_0 -band ($\sigma - \sigma^*$ transition), and two λ_1 - and λ_2 - bands (two $\pi - \pi^*$ transitions).

The model is described, for $\lambda \gg \lambda_0$ by the following relations:

$$n^{e,o}(\lambda) \cong 1 + P_0^{e,o} + P_1^{e,o} \frac{\lambda^2 P_3}{\lambda^2 - P_3} + P_2^{e,o} \frac{\lambda^2 P_4}{\lambda^2 - P_4} \quad (2)$$

where $P_0^{e,o} = g_0^{e,o} \lambda_0^2$, $P_3 = \lambda_1^2$, $P_4 = \lambda_2^2$. The values of $P_i^{e,o}$ determine the external parameter effect on the refractive indices, i.e. the temperature, in our experiment.

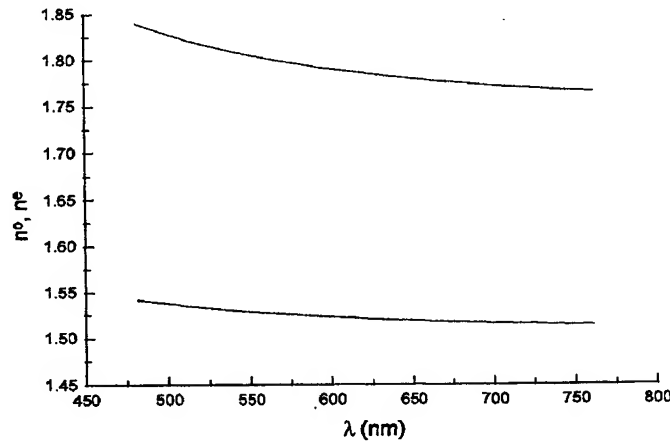


Fig.1 The dispersion curves of n^o, n^e at $T = 74^\circ\text{C}$

This expression (2) was inserted into the formula (1) and we performed the nonlinear fitting of the experimental and theoretical $I(\lambda)$ curves for parallel and crossed polarizers in order to obtain all the parameters necessary in formula (2) for the ordinary and extraordinary indices, at each temperature value. As an example we show these dependencies in fig.1 and fig.2, for $T = 74^\circ C$. The $\lambda_0, \lambda_1, \lambda_2$ values resulted from our simulations are: $\lambda_0 = 123nm$, $\lambda_1 = 203nm$, $\lambda_2 = 304nm$.

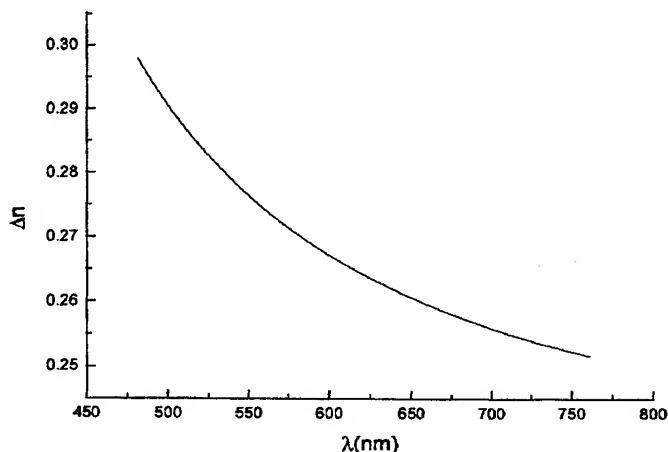


Fig.2 The dispersion curve of Δn at $T = 74^\circ C$

Each band contribution ($C_{\lambda_i}^j$ (%), where $i = 0, 1, 2$ and $j = n^o, n^e, \Delta n$) to the refractive indices and birefringence were calculated by the following formula:

a) λ_i -band contributions ($i = 0, 1, 2$) to both refractive indices:

$$C_{\lambda_i}^j (\%) = \frac{P_j^{e,o} \frac{\lambda^2 \lambda_i^2}{\lambda^2 - \lambda_i^2}}{P_0^{e,o} + P_1^{e,o} \frac{\lambda^2 P_3}{\lambda^2 - P_3} + P_2^{e,o} \frac{\lambda^2 P_4}{\lambda^2 - P_4}} \quad (3)$$

for $j = n^o, n^e$.

b) λ_0 -band contribution to birefringence:

$$C_{\lambda_0}^j (\%) = \frac{n_0^e - n_0^o}{n^e - n^o} \quad (4)$$

for $j = \Delta n$.

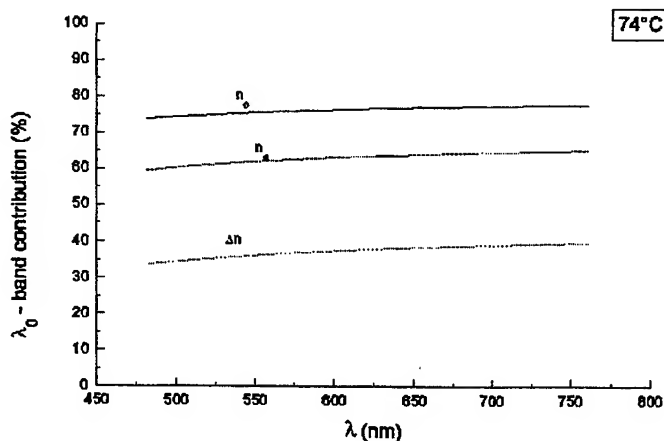


Fig.3 λ_0 band contribution to $n^o, n^e, \Delta n$

c) λ_i -band contributions ($i = 1, 2$) to birefringence:

$$C_{\lambda_i}^j (\%) = \frac{P_i^e \frac{\lambda^2 \lambda_i^2}{\lambda^2 - \lambda_i^2} - P_i^o \frac{\lambda^2 \lambda_i^2}{\lambda^2 - \lambda_i^2}}{R_0 + R_1 \frac{\lambda^2 P_3}{\lambda^2 - P_3} + R_2 \frac{\lambda^2 P_4}{\lambda^2 - P_4}} \quad (5)$$

where $j = \Delta n$ and $R_i = P_i^e - P_i^o, R_0 = P_0^e - P_0^o$.

In fig. 3, 4, 5, we present the graphical representation of the band contributions to $n^o, n^e, \Delta n$ as λ - functions, at $T = 74^\circ C$.

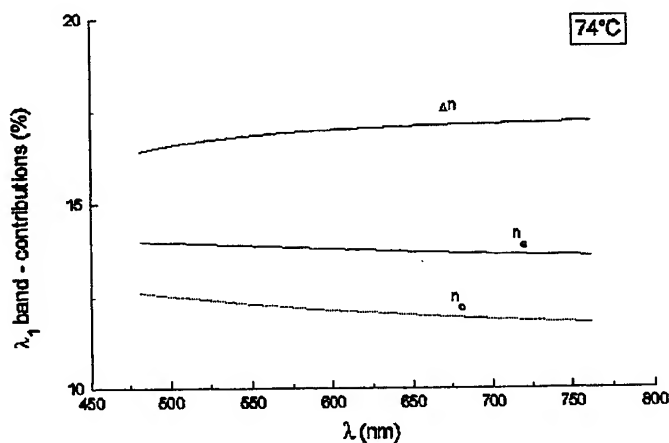


Fig.4 λ_1 band contribution to $n^o, n^e, \Delta n$

It is seen from fig. 3 that the λ_0 - band contributions to refractive indices is much higher than the contribution to birefringence, in the visible region, due to the high optical density of the $\sigma - \sigma^*$ transitions.

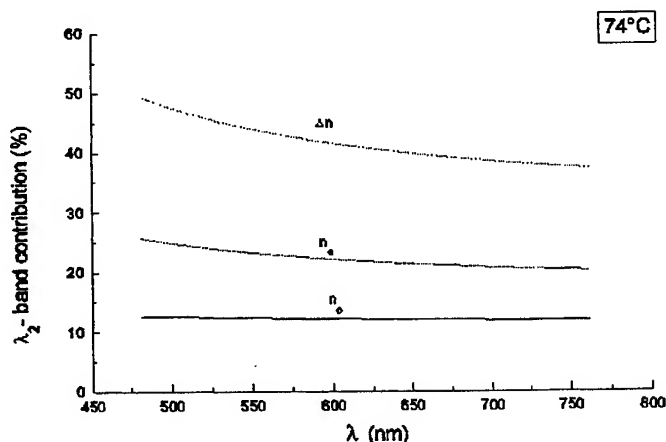


Fig.5 λ_2 band contribution to $n^o, n^e, \Delta n$

We can also conclude from figure 4, 5 that the contributions of the $\pi - \pi^*$ electronic transitions (λ_1, λ_2 - bands) are dominant in the birefringence and lower in the refractive indices.

The computation of the temperature dependencies for the order parameter S and the correction factor g starts with the model proposed by Khoo and Normandin⁷ for the dielectric constants which includes the dielectric anisotropy as a function of temperature in the nematic phase. Knowing that the dielectric constant of the isotropic phase and the dielectric anisotropy are proportional to ρS , we obtained the following relations:

$$C_2 \rho S = (n^e)^2 - (n^o)^2 \quad (6)$$

and

$$C_1 \rho = 1 - \varepsilon_i \quad (7)$$

where

$$\varepsilon_i = \frac{1}{3} (n^e)^2 + \frac{2}{3} (n^o)^2 \quad (8)$$

is the optical dielectric constant of the isotropic phase ($S = 0$), ρ is the density, C_1, C_2 are constants which depend on the liquid crystal structure.

The previous steps of our calculations provide the functions $n^o(\lambda), n^e(\lambda)$ for each temperature value in the measurement domain, allowing us to represent $n^o(T), n^e(T)$ as in fig. 6, for any wavelength λ . A direct consequence is that one may easily derive the $S(T)$ function, up to a constant (C_2/C_1), by dividing the equations (6), (7) and then obtain the temperature dependence of the order parameter by using the border conditions $S_{\max} = 1$ and $S_{\min} = 0$. The resulted $S(T)$ is presented in fig. 7.

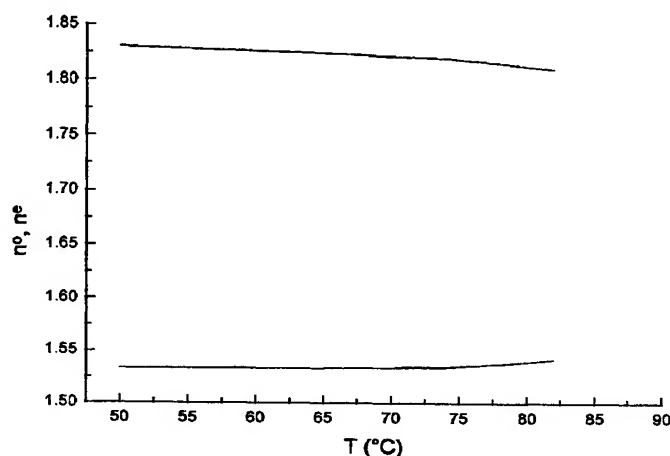


Fig.6 Ordinary and extraordinary indices as functions of temperature, at $\lambda = 514.5m$

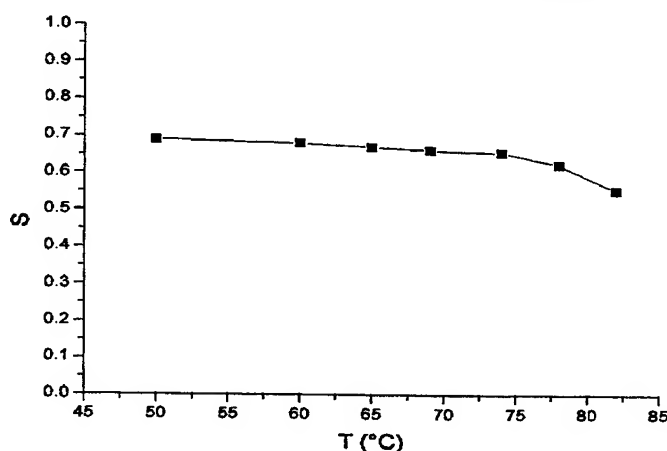


Fig.7 Order parameter S as function of temperature

The internal field has a special significance for anisotropic materials like the liquid crystals, thus the geometrical parameter m of the liquid crystal molecules, determined by their dimensions, may be computed by fitting (fig. 8) the local field correction factor g generated from the experimental dispersion curves with the theoretical one² having the expression:

$$g(T) = \frac{n^e}{n^o} \frac{1 + (L_{\max} - 1/3) S(T) ((n^o)^2 - 1)}{1 - 2/3 - 2(L_{\max} - 1/3) S(T)} \quad (9)$$

Here L is the Lorentz factor of the molecules and $S(T)$ is the realistic function derived from our dispersion curves.

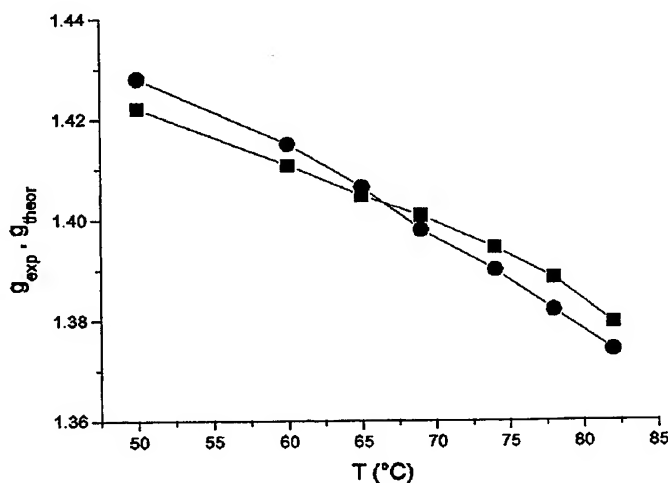


Fig.8 Experimental (squares) and theoretical (circles) correction factor g as function of temperature

The maximal value of L in (9) is expressed in terms of the geometrical ratio m as follows:

$$L_{\max} = \frac{m}{2(m^2 - 1)} \left(m - \frac{1}{2\sqrt{m^2 - 1}} \ln \frac{m + \sqrt{m^2 - 1}}{m - \sqrt{m^2 - 1}} \right) \quad (10)$$

Our simulations (fig. 8) lead us to the values $L_{\max} = 0.46$ and $m = 4$, in good agreement with the experimental value of the ratio m obtained by various methods.

3. CONCLUSIONS

The aim of our procedure is to compute both the dispersion curves and the bands contributions to these dependencies in a fast and accurate way. The absorption wavelengths are also obtained, eliminating the more expensive recording of polarized absorption spectra but in good agreement with the experimental results.

The "dynamics" of the order parameter $S(T)$ and the behavior of the correction factor g are consequently calculated from the experimental data provided by the channeled spectra. This makes possible to compute the geometric ratio m for the EBBA liquid crystal.

In addition, the method can be applied to any anisotropic material, the precision in the quasicontinuum dispersion curves is higher ($5 \cdot 10^{-6}$) than the ones reported until now, the data acquisition and processing being efficiently integrated by the proposed technique. The same analysis may be easily reproduced for a different external parameter (electric field or temperature and electric field), an important aspect in studying material responses and their nonlinear optics applications.

REFERENCES

1. I. Abdulhalim, "Dispersion relations for the refractive indices and the effective birefringence of liquid crystals," *Mol. Cryst. Liq. Cryst.* **197**, pp. 103-108, 1991.
2. I. C. Khoo and S.-T. Wu, *Optics and nonlinear optics of liquid crystals*, World Scientific, New York, 1993.
3. S. T. Wu, "Birefringence dispersions of liquid crystals," *Phys. Rev.* **33**, pp. 1270-1274, 1986.
4. S. T. Wu, "A semiempirical model for liquid crystal refractive index dispersions," *J. Appl. Phys.* **69**, pp. 2080-2087, 1991.
5. M. Boschmans, "Local channeled spectrum analysis as a measure of the local birefringence and molecular orientation in liquid crystals," *Mol. Cryst. Liq. Cryst.* **199**, pp. 267-275, 1991.
6. M. Warrengem and G. Joly, "Liquid crystals refractive indices behavior versus wavelength and temperature," *Molec. Liq. Cryst.* **207**, pp. 205-218, 1991.
7. I. C. Khoo and R. Normandin, "The mechanism and dynamics of transient thermal grating diffraction in nematic liquid crystal," *IEEE J. Quantum Electron.* **QE 21**, pp. 329-335, 1985.

Antisymmetrized Molecular Dynamics simulations for conduction mechanisms in CdSe thin films

V. Calian *, G. Stoenescu
University of Craiova, Department of Physics
13 A.I. Cuza, Craiova 1100, Romania

ABSTRACT

An extended version of the Antisymmetrized Molecular Dynamics (AMD) method is derived in order to study clustering aspects for two conduction regimes defined by the role of intercrystalline barriers and crystallites in CdSe thin films and to compute the related interaction potentials. The influence of the fast electron irradiation on the conduction mechanism is consequently expressed in terms of the changings in microscopical parameters.

Keywords: Antisymmetrized Molecular Dynamics, intercrystalline barriers, clusters, CdSe thin films.

1. INTRODUCTION

Two conduction regimes defined by the role of intercrystalline barriers and crystallites respectively are simulated by extending the Antisymmetrized Molecular Dynamics (AMD) method and by computing the related interaction potentials in CdSe thin films.

The influence of the fast electron irradiation on the conduction mechanism is consequently expressed in terms of microscopical parameters changing. Moreover, the values of the main parameters are calculated by a Levenberg-Marquart optimization method from the experimental data and an appropriate theoretical model of the I-E characteristics. The extended version of the AMD method is derived in order to study "clustering" aspects,^{1, 2} connected both to structural and collisional problems.

The microscopical description of the formation and dissolution of clusters, without starting with the hypothesis of their existence, is a difficult goal which proved to be treatable by the quantum mechanical approach given in AMD framework.

In conclusion, a complete description of the microscopic - macroscopic interplay in the conduction mechanisms and their quantitative evaluation is possible after the interaction potentials are computed, in order to relate it to the crystallites dynamics.

2. LIMITS OF THE AMD METHOD AND OF THE THEORETICAL MODELS

Usually, in order to propose a theoretical interpretation for the experimental results concerning the temperature dependence of the resistivity of the polycrystalline thin films, one uses an expression generated by an ohmic approximation of the current versus electric field characteristic. As a result, the electric resistivity depends on the temperature as follows:

$$\rho = \rho_0 \exp(\Delta\epsilon/kT)$$

where $\Delta\epsilon$ is the activation energy, depending on the charge carriers concentration and their mobility, and k is the Boltzmann constant.

As a consequence, a logarithmic plot will look linear, in contradiction with the experimental results which exhibit a significant displacement from the simple evoked model, specially at low temperatures. The study and a more rigorous interpretation,^{3, 4, 5} of the electric conduction mechanisms in polycrystalline CdSe thin films in intense electric fields will have therefore to take into account the field effect at the intercrystalline barriers and in the crystallites as well.

The model of the polycrystalline thin films we will use consists of a system of similar crystallites, chaotically distributed, separated by intercrystallite barriers. The measurable physical properties of the thin films are obtained

Correspondence: Email: violetaxx@hotmail.com, Fax: 40 51 415077

from the average quantities calculated on a large number of crystallites which establish the connection between the microscopical and macroscopical parameters of the layer. The exponential form of the current-electric field curves is explained by the dominant conduction mechanism⁶ based on the role of intercrystalline barriers.

This mechanism is a characteristic feature of the thin film behavior in intense electric fields as well, but only for low temperature values. The validity of the described model for the case of strong electric fields may be explained by taking into account the presence of "hot" charge carriers in the crystallites.⁷ In this domain, for higher temperatures, the negative differential resistivity appears only at lower values of the electric field.

The dynamical process of the formation and/or dissolution of clusters may be treated by using the so-called Antisymmetrized Molecular Dynamics (AMD) theory, originally proposed for nuclear collision and fragmentation problems.¹ The AMD theory is a quantum mechanical one since it treats the time-development of the system wave function which is exactly antisymmetrized.

If the model is made more complex by a many-particle interaction potential, the approximation which is usually assumed in the AMD description and that allows us to solve the dynamics (1) is no longer valid:

$$i\hbar \sum_{jj'} C_{kk',jj'} \frac{d}{dt} Z_{jj'} = \frac{\partial}{\partial Z_{kk'}} \frac{\langle \phi(\{Z_j\}) | H | \phi(\{Z_j\}) \rangle}{\langle \phi(\{Z_j\}) | \phi(\{Z_j\}) \rangle} \quad (1)$$

where:

$$C_{kk',jj'} = \frac{\partial^2}{\partial Z_{kk'}^* \partial Z_{jj'}} \log \langle \phi(\{Z_j\}) | \phi(\{Z_j\}) \rangle$$

with: $k, j' = x, y, z$.

Solving the additional, more involved problem is however possible if one writes the potential as:

$$V(z_1, \dots, z_N) \equiv V(Z) = \frac{1}{2!} \sum_{i,j \in Z} V(z_i, z_j) + \dots \quad (2)$$

$$+ \frac{1}{N!} \sum_{j_1, \dots, j_N \in Z} V(z_{j_1}, \dots, z_{j_N}) \quad (3)$$

Introducing a set of auxiliary parameters s_i in the potential, such that:

$$V(z_{j_1}, \dots, z_{j_N}) \rightarrow V(z_{j_1}, \dots, z_{j_N}, s_{j_N})$$

a system of differential equations and its solution is obtained, for the boundary conditions imposed at $s_i = 0$ permitting then to compute the intercrystallites barrier potential for different regimes.

We will formulate in this section the AMD theory for collisional processes, starting with the wave function of the analyzed system with A, B components:

$$\phi(\{Z_j\}) = a \{ \psi(A, Z_A) \psi(B, Z_B) \} \quad (4)$$

$$\psi(j, Z_j) = \exp \left(-A_j \nu \left(X_j - \frac{Z_j}{\sqrt{A_j \nu}} \right)^2 \right) \phi(j) \quad (5)$$

with $j = A, B$.

The main advantage and importance of the method lays in the fact that the results are obtained without any model assumption of clustering. However, a few problems may be identified at this point:

p1) the initialization problem, namely the construction of the ground-state wave function of the colliding components;

p2) the incorporation of many-particles collisions;

- p3) the usual approximation on the potential which narrows the applicability of the method;
 p4) the necessity to take into account the multiparticle interaction terms described by a realistic potential of the type:

$$V = \sum V_i + \frac{1}{2!} \sum V_{ij} + \frac{1}{3!} \sum V_{ijk} + \dots \quad (6)$$

3. QUANTUM MONTE-CARLO TECHNIQUE FOR THE INTEGRATION STEP

The Monte-Carlo method may offer the chance to calculate multidimensional integrals which obviously occur while we solve our dynamical problem. If the spatial configuration of the system is described by a $3A$ -dimensional vector (R) and we have to integrate a function of R ($f(R)$), then we need a suitable weight function $W(R)$, real, positive and normalizable, so that it can be used as a probability distribution in order to write:

$$\int F(R) dR = \int \frac{F(R)}{W(R)} W(R) dR \quad (7)$$

The ensemble average is then defined as:

$$\overline{F/W} = \frac{1}{N_c} \sum_{i=1}^{N_c} F(R_i) / W(R_i) \quad (8)$$

such that:

$$\int F(R) dR = \lim_{N_c \rightarrow \infty} \overline{F/W} \int W(R) dR \quad (9)$$

for N_c the number of configurations $[R_i]$ distributed with the weight $W(R)$.

The value of the integral, computed by Monte-Carlo technique where N_c is certainly finite will then be:

$$\int F(R) dR = (\overline{F/W} \pm \delta) \int W(R) dR \quad (10)$$

with:

$$\delta = \sigma / \sqrt{N_c} \quad (11)$$

and

$$\sigma^2 = \frac{1}{N_c} \sum [F(R_i) / W(R_i) - \overline{F/W}]^2 \quad (12)$$

These formula are valid if the $F(R_i) / W(R_i)$ values have a normal distribution. However, if is not the case, block averages must be first performed. In QMC calculations, it is most useful to chose:

$$W(R) = \psi^+(R) \psi(R) \quad (13)$$

with the ψ - wave function.

The expectation value of an operator O is then given by:

$$\begin{aligned} \langle O \rangle &= \frac{\int \psi^+(R) O \psi(R) dR}{\int \psi^+(R) \psi(R) dR} = \\ &= \overline{\psi^+ O \psi / \psi^+ \psi} \pm \delta \end{aligned} \quad (14)$$

The configurations $[R_i]$ are obtained by sampling the weight function $W(R)$ and when this is not a simple function the Metropolis algorithm based on the principle of detailed balance has to be used.

4. EXTENDED AMD

The goal of this section is to propose an extended version of the AMD theory, so that we may solve the problems p1)-p4) mentioned in section 2. The following algorithm was used:

Step 1) design a procedure for computing the expectation value of an operator, based on the QMC with Metropolis sampling. We also compared the results with the available density distribution of states.

Step 2) write the AMD time-dependent equations of motion in canonical form:

$$i\hbar \frac{d}{dt} W_j = \frac{\partial}{\partial W_j^*} \frac{\langle \phi(\{Z_j\}) | H | \phi(\{Z_j\}) \rangle}{\langle \phi(\{Z_j\}) | \phi(\{Z_j\}) \rangle} \quad (15)$$

where the canonical coordinates should satisfy:

$$\begin{aligned} \sum \left(\frac{d}{dt} Z_k^* Z_j - \frac{d}{dt} Z_j^* Z_k \right) \frac{\partial \log \langle \phi(\{Z_j\}) | \phi(\{Z_j\}) \rangle}{\partial Z_j^* Z_j} = \\ \sum \left(\frac{d}{dt} W_j W_j^* - \frac{d}{dt} W_j^* W_j \right) + \frac{dF}{dt} \end{aligned} \quad (16)$$

Step 3) compute the inter-cluster potential (V') after the center of mass coordinate (X) is separated in the wave function $\phi(\{Z_j\})$:

$$\phi(\{Z_j\}) = \exp \left[- (A+B) \nu \left(X - \frac{Z}{\sqrt{(A+B)\nu}} \right)^2 \hat{\phi}(\{Z_j\}) \right] \quad (17)$$

such that:

$$\frac{\langle \phi | H | \phi \rangle}{\langle \phi | \phi \rangle} = \frac{\langle \hat{\phi} | H | \hat{\phi} \rangle}{\langle \hat{\phi} | \hat{\phi} \rangle} = E \quad (18)$$

and:

$$V' = E - \frac{K^2(sol)}{2\mu} \quad (19)$$

is the potential, calculated as a function of the solution of the equation (18). It is obviously very deep when the fragments energy is high.

Step 4) cut the solution V'' of a differential equation given by an auxiliary theory in order to recover the V' value obtained at step 3, allowing us to identify the type of inter-cluster interaction. The solution V'' is found as follows. A set of extra-variables is introduced, creating the auxiliary potential:

$$V'' = \frac{1}{2!} \lambda_2 \sum V_{ij} + \frac{1}{3!} \lambda_3 \sum V_{ijk} + \dots \quad (20)$$

which, for $\lambda \rightarrow \lambda^0$ tends to V' (the full theoretical interaction term).

The following differential equation is then satisfied by the transformed V'' :

$$\sum \frac{d}{d\lambda_i} \overline{V''} = \sum \overline{V'} \quad (21)$$

with the boundary conditions:

$$\overline{V''}(\lambda \rightarrow \lambda^0) = V' \quad (22)$$

and with operator averages in the relations (19-21), providing the correct value of the inter-cluster potential.

5. CONCLUSIONS

The numerical values we obtained for the inter-cluster potentials prove that the proposed method is a good alternative in order to investigate, on a rigorous theoretical basis, the number of terms in the interaction potential, their nature and values, without preliminary hypothesis on its form, for the two regimes under consideration in explaining the conduction mechanisms based on the role of intercrystalline barriers:

a first regime, where the dominant role belongs to the intercrystalline barriers in I-E characteristics, in intense electric fields and low temperatures;

a second regime, where the main role belongs to the crystallites, due to the "hot electrons", valid for even higher electric fields.

The phenomenological considerations and the experimental results are well predicted by our computational method. The two cluster distribution function, for instance, provide additional information on crystallite structure and role.

The two cluster density in configuration space, when two-fragments interaction is considered, is computed from:

$$\rho_{AB}^{A,B,A+B}(r_{AB}) = |\langle A\psi_A\psi_B, r_{AB} | \psi_{A+B} \rangle|^2 \quad (23)$$

where $\psi_{A+B}, \psi_A, \psi_B$ are the functions of the initial cluster and the fragments A, B , while r_{AB} is the distance between the centers of the clusters.

This give us the probability of finding the fragments A and B at distance r_{AB} in the cluster. We illustrate the method described in the previous sections by the behavior of this distribution function (fig. 1) which explains the conduction regime changing.

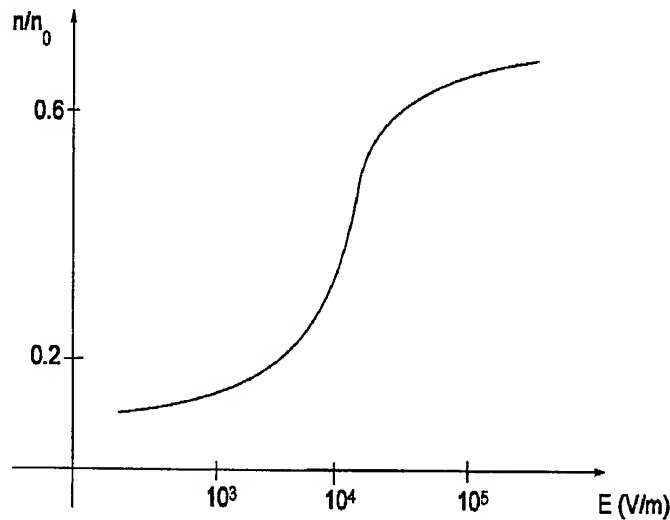


Fig.1. Two-cluster distribution as a function of the electric field regime

This proves that the crystallites role is increased when the values of the electric field become very high. Eventually, one hopes to understand the short range structures and the dynamics of formation and dissolution of crystallites, using more elementary ensembles and evaluating the number of terms in the interaction potential properly.

Applying the procedure developed in order to identify the type of intra-cluster and inter-cluster potential, respectively, we arrived to the conclusion that the series (20) must be cut off at different values of the number of terms (fig. 2) which is connected to the type of the involved mechanism.

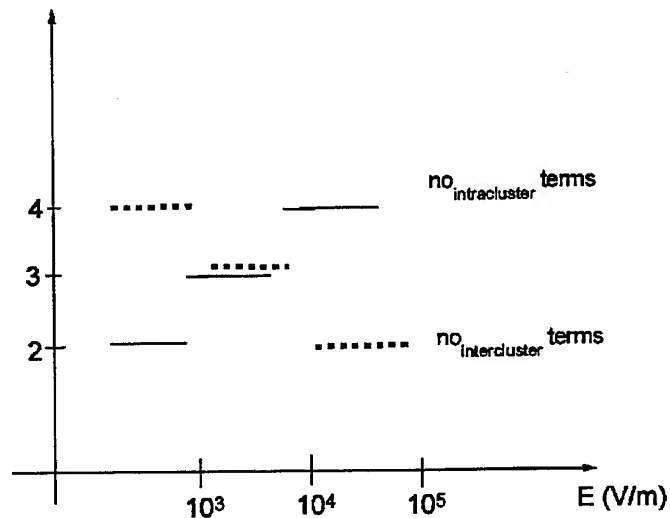


Fig.2 The number of terms in the interaction potential in different regimes

One can see that the correlation inside the crystallites grows at the transition from the first to the second regime while the correlation between the crystallites decreases. In conclusion, for the polycrystalline CdSe thin films, there is a strong correlation between their electric properties and their crystalline structure. This connection is specially manifested by the electric conductivity mechanisms which are mainly influenced by the presence of the intercrystalline barriers.

At high temperatures, the typical exponential form of the current versus electric field characteristics determined by the leading role of the barriers in the conduction mechanism is followed by a clear change in the characteristic shape which proves that the conduction mechanism is modified. In this case, the influence of the "hot" charge carriers becomes important. On the contrary, the second type of conduction mechanism, exhibited in very intense electric fields, is determined by the crystallites.

REFERENCES

1. H. Horiuchi, "Clustering in nuclear structure and collisions," *NATO ASI Series* 359, pp. 29-51, 1997.
2. H. Horiuchi, *Trends in Theoretical Physics*, Addison-Wesley, New York, 1991.
3. I. S. N. B. G. Stoenescu, V. Calian and V. Ruxandra, "The effect of accelerated electron irradiation on electric conductivity of cdse thin films," *Teaching the Science of New Materials proc.*, pp. 314-316, 1995.
4. R. I. Baron and L. Higbie, *Computer Architecture*, Addison-Wesley, New York, 1994.
5. P. E. Gray and C. L. Searle, *Modern Electronics*, World Scientific, New York, 1973.
6. V. Dolocan, *Fizica jonctiunilor semiconductoare*, Edit. Academiei, Bucharest, 1982.
7. I. S. G. Stoenescu, V. Calian and N. Baltateanu, "Characteristic parameters changes for mos circuits irradiated by fast electrons," *Optoelectronica* 4, pp. 71-74, 1996.

Calculations of the near-field enhancement in surface enhanced Raman scattering on periodically structured metallic substrates

M. Palamaru, S. Astilean*

Optics and Spectroscopy Dept., Faculty of Physics, Babes-Bolyai University,
1 Mihail Kogalniceanu St., 3400 Cluj-Napoca, Romania

ABSTRACT

We study from a theoretical point of view the electromagnetic enhancement related to the surface enhanced Raman scattering (SERS) on silver gratings. The local field is obtained by means of numerical calculations based on the rigorous coupled-wave analysis (RCWA). Enhancements of up to 10^6 in the Raman signal of molecules adsorbed on these gratings could be obtained at the excitation wavelength $\lambda=514$ nm.

Keywords: metallic gratings, coupled-wave analysis, surface enhanced Raman scattering

1. INTRODUCTION

When metal nanoparticles are excited by light, they exhibit collective oscillations of their conduction electrons known as surface plasmons. Surface plasmons are trapped electromagnetic waves, which propagate along the metal/dielectric interface and decays exponentially with distance away from the interface. Their resonance energy is strongly dependent on the interparticle distance, the details of the size and shape of nanoparticles, and the dielectric properties of the local environment in which the nanoparticle is embedded. It is now generally recognized that these electromagnetic modes modify spectroscopic properties of an adsorbed molecule in a radical manner by changing the laser field incident on the molecule. Perhaps the most notable effect associated with surface plasmons on rough metal surfaces is the surface enhanced Raman scattering (SERS)^{1,2}. In SERS, enhancements of up to 10^6 in the Raman signal can be obtained from molecules adsorbed on rough metal surfaces. It is generally accepted the electromagnetic mechanism to explain this enhancement.

However, in addition to the electromagnetic mechanism, other effects, such a resonance Raman scattering or chemisorption, can have a multiplicative impact upon the SERS signal^{1,2}.

In order to mediate efficiently the surface plasmon excitation, the SERS requires rough metallic substrates with structures in the nanometer range. It is known that irregularly roughened substrates as colloids, electrochemical roughened surfaces and islands films exhibit generally poor reproducibility and limited durability of the structures. On the contrary, lithographically prepared substrates, as *regular metallic nanostructures* are stable and reproducible structures. Therefore, they have recently attracted interest for using as SERS substrates^{3,4}. In general, electron-beam lithography offers a greater variability in the structural properties of substrates. For instance, sub-wavelength gratings can be fabricated with independently varying period, width and depth of grooves. Furthermore, vertical walls can be generated using appropriate acceleration voltage and exposure doses. The first SERS measurement indicated that such manufactured gratings exhibited stronger SERS signals than the classical metal nanoparticles⁴. In the future, nanoengineered metallic gratings may provide new strategies for other related spectroscopies and biosensing applications. Much of the current interest in SERS should be directed toward developing theoretical tools to design high sensitive nanogratings.

In this paper we study the classical electromagnetic enhancement on sub-wavelength reflection and transmission metallic gratings. Our aim is to optimize the grating structure (period, depth and groove size) in order to get a maximum enhancement at the excitation wavelength $\lambda=514$ nm. As figure of merit we use the absorption peak originated on the surface plasmons excitation⁵. The light - grating interaction is analyzed by means of numerical calculations based on the rigorous coupled-wave analysis (RCWA) of diffraction.

*Correspondence: E-mail: sastil@phys.ubbcluj.ro; Telephone: 64 40 53 00; Fax: 64 19 06

2. NUMERICAL METHOD

There are two kinds of gratings considered here, namely transmission gratings on glass substrate and reflection gratings on silver substrate (see Fig. 1). The width of the groove (air gap between metal ridges), the period and the thickness of the grating are denoted by w , p and d respectively. The grating is situated in the Oxy plane, its periodicity is extended along the Ox direction and its thickness is fixed along the Oz direction between $z=0$ and $z=d$. This periodic structure is illuminated by a plane electromagnetic wave of TM polarization (the magnetic-field vector is parallel to the Oy direction) at the incidence angle θ . The wavelength is denoted by λ (in air).

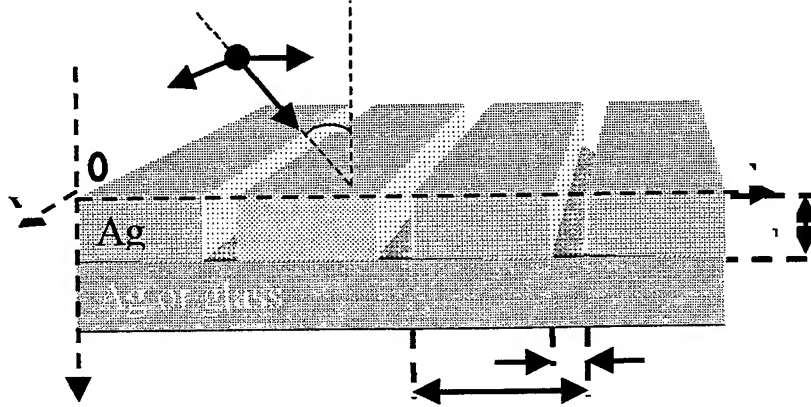


Fig. 1 Silver gratings analyzed in this paper. In the grating region, the relative permittivity is alternatively 1 (vacuum) and ϵ (silver). The refractive index of the incidence medium is equal to unity (vacuum). The refractive index of the substrate is 1.52 (glass) for transmission gratings and ϵ (silver) for reflection gratings

As a response to the incident field, the grating will give rise a diffracted field in the region above and below it and a stationary field pattern inside it. All fields can be computed by using the RCWA. The RCWA is a versatile and efficient tool for modeling the diffraction of electromagnetic waves by periodic structures. A step-by-step formulation of the RCWA for binary gratings is presented in Ref. 6. Recently, the convergence performance in the case of TM polarization and metallic gratings has been substantially improved⁷. In order to calculate the near field pattern we use an efficient extension of that implementation⁸.

The relative permittivity $\epsilon(x)$ in the grating region is a periodic function along the Ox direction and therefore $\epsilon(x)/\epsilon_0$ and $\epsilon_0/\epsilon(x)$ can be expanded in Fourier series, the m -th Fourier coefficients being ϵ_m and a_m respectively. Because of periodicity, the electromagnetic fields inside the grating region ($0 < z < d$) can be also expressed as a Fourier expansion of space-harmonic fields while away from the grating (far-field region) the diffracted fields are taken as a superposition of plane waves (i.e. Rayleigh expansions). By writing down the Maxwell equations inside the grating region, the differential coupled-wave equations are obtained. Once the eigenvalues and eigenvectors of these equations are found, the boundary conditions at the grating interfaces are matched and the Rayleigh and Floquet coefficients are computed, determining the electromagnetic fields in all space.

Although the RCWA naturally provides a description of all electromagnetic field components through their harmonic coefficients, our approach does not use all the Fourier series. Only the field components that are continuous functions of the x coordinate in the grating region are Fourier expanded. In the case of TM polarization, due to their continuous nature at the permittivity discontinuities, the y component H_y of the magnetic field, the x component D_x of the displacement vector and the z component E_z of the electric field are expected to be well approximated by Fourier series.

The equations used for the computation of the y component H_y of the magnetic field vector are:

$$H_y = \sum_m U_m(z) \exp(-ik_m x), \quad (1)$$

$$|U| = W \left\{ \exp(-k_0 Q z) [c^+] + \exp[k_0 Q (z - h)] [c^-] \right\}, \quad (2)$$

where k_{xm} is equal to $2\pi((\sin \theta/\lambda)-(m/p))$ and the vector \mathbf{U} is formed by the normalized amplitudes $U_m(z)$ of the magnetic space harmonic. We denote by \mathbf{Q} the diagonal matrix formed by the square root of the eigenvalues, by \mathbf{W} the eigenvector matrix and by \mathbf{C}^+ and \mathbf{C}^- the vectors formed by the Floquet coefficients.

The x component D_x of the displacement vector and the z component E_z of the electric field are computed from:

$$D_x = \sum_m G_m(z) \exp(-ik_{xm}x), \quad (3)$$

$$|G| = \frac{ik_0}{\omega} \mathbf{WQ} \left\{ \exp(-k_0 Q z) [\mathbf{C}^+] + \exp[k_0 Q (z-h)] [\mathbf{C}^-] \right\}, \quad (4)$$

$$E_z = \sum_m F_m(z) \exp(-ik_{xm}x), \quad (5)$$

$$|F| = \frac{-i}{\omega \epsilon_0} \mathbf{E}^{-1} \mathbf{K}_x |\mathbf{U}|, \quad (6)$$

where \mathbf{E} is Toeplitz matrix formed by the permittivity harmonic coefficients, \mathbf{K}_x is a diagonal matrix with the m , m element being k_{xm} and ω is the angular frequency of the incident wave.

3. RESULTS AND DISCUSSION

Our results are with respect to the above examples of lamellar silver gratings. For the purpose of RCWA calculations, the complex index of refraction for silver $\epsilon(\omega)=[n(\omega)+ik(\omega)]^2$ is interpolated from values tabulated in Ref. 9. In order to interpret published experimental results^{3,4} and taking into account a fabrication purpose, we investigate only silver gratings of fixed period ($p=300$ nm). While the whole visible region of the spectrum (between 350 nm and 750 nm) may be of real interest, we have optimized grating structures only for operation with the available light source of wavelength $\lambda=514$ nm, wavelength which coincides with one of emission lines of our Ar⁺ laser. At this light wavelength and at normal incidence all gratings, both in reflection and transmission, behave as 'zero-order' diffraction gratings. This means that all diffracted orders, other than zero-th forward-transmitted and backward-reflected orders, are evanescent. Losses to metal (absorption) associated with the imaginary part of the refractive index, physically manifested as carrier heating in the metal, can be extracted from RCWA calculations by a relation of type $A=1-\eta_{0,t}-\eta_{0,r}$, where $\eta_{0,t}$ and $\eta_{0,r}$ are the zero-order transmission and reflection efficiencies, respectively. It is understood that for reflection gratings $\eta_{0,t}$ is zero. It is well known that stochastically roughed SERS substrates show strong resonances of their collective plasma oscillations (surface plasmons), leading to spectrally selective absorption spectra. Absorption spectra are also strongly dependent on the particle shape and orientation, as well as on inter-particle coupling, so-called local field effects. Therefore in the first step of our study, we have examined the height and position of the absorption maximum of gratings. As pointed, both gratings have been optimized to get the maximum absorption at the laser line $\lambda=514$ nm and for a fixed grating period $p=300$ nm. We emphasize that this optimization is necessary in order to get the maximum SERS signal or, in other words, the maximum local field enhancement on gratings.

As a result of the optimization process, we have deduced that a more pronounced absorption is obtained for small groove widths. Finally we have chosen a groove width of 43 nm, supposing that such fabrication requirements may be fulfilled by the e-beam lithography. We are interested in deep enough gratings. As regards to the grating depths, the optimum depth is found to be 379 nm for gratings operating in reflection and 250 nm for gratings operating in transmission.

Fig. 2 shows the typical absorption spectra of these gratings in the visible region. In the case of reflection grating, the absorption peak A (Fig. 2a) represents 91% of the incident light while 9 % light is reflected. In the case of transmission grating the absorption peak B (Fig. 2b) represents 81 % of the incident light while 17 % light is reflected and 2% is transmitted. Less prominent absorption peaks are also observed, as for example at $\lambda=410$ nm for reflection grating and a smooth absorption less than 5 % is present for both gratings over the whole spectrum. The resonance observed at the wavelength $\lambda=353$ nm is not a grating specific feature and is assigned to bulk silver plasmons (identical behaviors are obtained for both gratings).

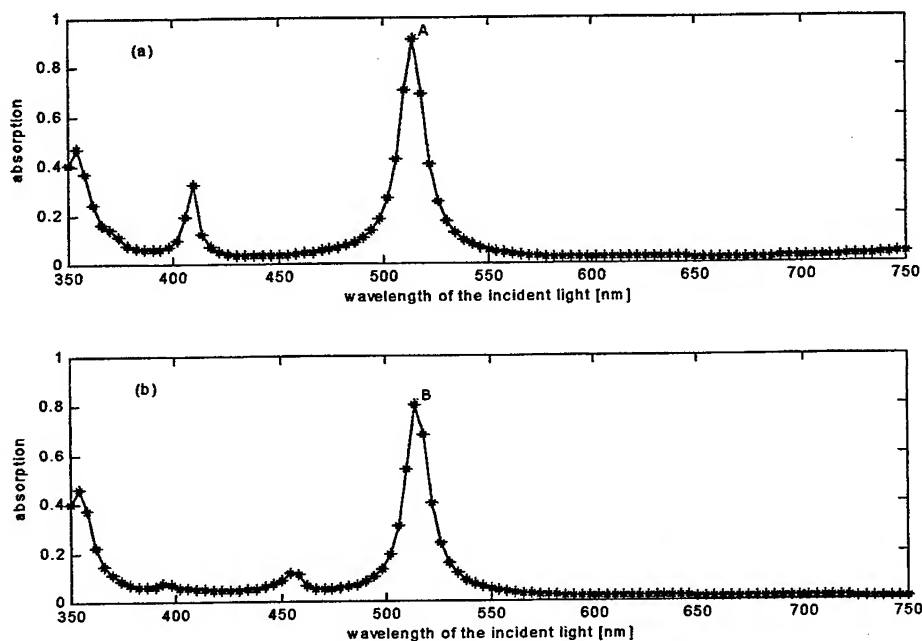


Fig. 2 Absorption spectra of gratings: (a) reflection grating and (b) transmission grating. The grating parameters are: $p=300$ nm, $w=43$ nm, $d=250$ nm for case (a) and $d=379$ nm for case (b).

Such absorption peaks are explained by excitation of surface plasmons. Of a great importance for SERS is whether there is any significant local field enhancement accompanying the absorption spectrum. Up to now almost all theoretical papers devoted to near-field enhancement in metallic gratings are dealing with sinusoidal gratings¹⁰ where surface plasmons propagate along the corrugated surface. It was shown that for deep gratings the electromagnetic field is localized on the top of the groove, contrary to shallow gratings where the absorption leads to field enhancement both on the top and in the bottom of the groove. However, the aim of this paper is to analyze the local field enhancement in binary, metallic gratings of very narrow and deep enough slits or grooves. As far as we know, this is the first paper that presents such results for electromagnetic field distribution near the surface of binary metallic gratings with very deep grooves and slits.

Fig. 3 shows a detailed picture of the field enhancement generated for the case of reflection gratings (Fig. 3a) and transmission gratings (Fig. 3b), respectively. We have evaluated the field at $\lambda=514$ nm, the wavelength of maximum absorption. Clearly, the incident light is exciting plasmons trapped on the vertical walls of the groove (slit). As usual, we have represented the field enhancement as a ratio between local calculated field E_{loc} and the incident field E_0 (normalized to unity). However, we emphasize that the net enhancement of the Raman signal is different from the electromagnetic enhancement shown in Fig. 3. In fact the Raman enhancement occurs due to two sources: (1) the molecule is placed near the surface in a local enhanced field and (2) the dipolar radiation scattered by molecule is capable of coupling to the metal and enhancing the signal. The two sources of enhancement are multiplicative and couple together to give the Raman enhancement:

$$\rho = E(\omega_0)^2_{local} E(\omega_{Raman})^2_{local} \quad (7)$$

where ω_0 is the laser frequency and ω_{Raman} is $(\omega_0 - \Delta\omega_{Raman} \text{ shift})$. Our calculations show that these localized resonant modes are able to produce enhancements as large as $\rho = 10^5$ in the Raman signal of molecules adsorbed inside the gratings. Contrary to the sinusoidal gratings where there is a considerable field enhancement along the entire surface, the field enhancement in deep binary gratings is localized only inside the grating (see Fig. 3). The maps in Fig. 3 show that the electromagnetic field is confined inside the slit and shaped in the form of standing waves. This observation clearly reveals that the electromagnetic field inside the grating is basically governed by the backward and forward propagation of one

single mode. This result gives quantitative support to the idea that SERS is a very local phenomenon occurring at pores and corners of rough surface.

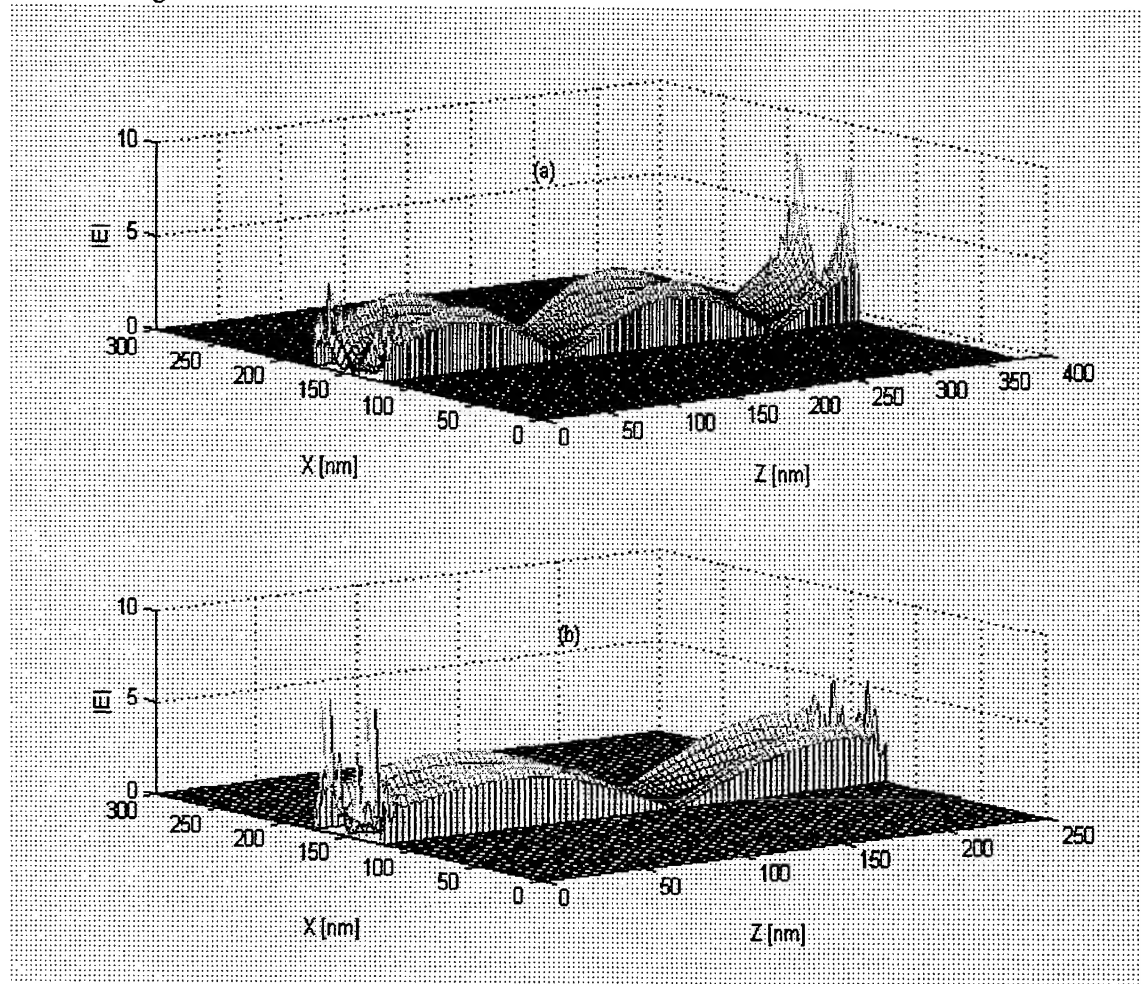


Fig. 3 Distribution of the electric field amplitude inside one grating period: (a) reflection grating and (b) transmission grating. The gratings' parameters are given in the caption of Figure 2. Gratings are normal illuminated by TM-polarized light of wavelength $\lambda=514$ nm from the half plane $z<0$.

Although we have examined two very different metallic structures, i.e. reflection and transmission gratings, they do not present so very different near-field optical responses. From this point of view, our calculations help to explain why rough surface, whose large scale features are quite different present, strong similarities in the strength and frequency dependence of the observed enhancement.

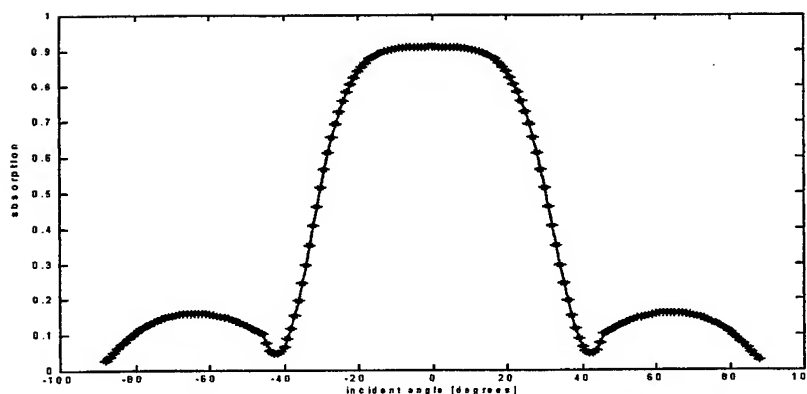


Fig. 4 Absorption versus angle of incidence in the case of reflection grating excited with light of $\lambda=514$ nm. Higher values of absorption are consistent with higher local fields inside the grating structure

The absorption of shallow sinusoidal gratings is, in general, narrow and therefore the divergence of the incident optical beam leads to a significant reduction of the light-plasmons coupling. On the contrary, our calculations show that deeper gratings increase the angular tolerance for light-plasmons coupling without modifying spectral bandwidth. This phenomenon is clearly shown in Fig. 4, where we display the absorption as a function of the angle of incidence for a reflection grating. The angular tolerance of the incident beam exceeds 30° .

CONCLUSION

In this paper we have performed a numerical study of electromagnetic enhancement on metallic gratings with very deep grooves or slits. Our results indicate in a quantitative way that SERS may be produced by excitation of very localized plasmon modes localized in grooves. Enhancements of about 10^5 - 10^6 in the Raman signal are predicted. We have also analyzed the dependence of these enhancements as a function of incidence angle. Our results allow quantitative comparison with experimental results already obtained with metallic gratings^{3,4} synthesized by electron-beam lithography. It is likely that one will be able to use these results in order to design high sensitivity metallic gratings for SERS and other related spectroscopies.

REFERENCES

1. M. Moskovits, "Surface-enhanced spectroscopy", *Mod. Phys.* **57**, pp. 783-826, 1985.
2. A. Otto, I. Mrozek, H. Grabhorn and W. Akemann, "Surface-enhanced Raman scattering", *J. Phys. C* **4**, pp. 1143-1212, 1992.
3. M. Kahl, E. Voges, and W. Hill, "Optimisation of SERS substrates by electron-beam lithography", *Spectroscopy Europe* **10**, pp. 8-13, 1998.
4. M. Kahl, E. Voges, S. Kostreva, C. Viets, and W. Hill, "Periodically structured metallic substrates for SERS", *Sensors and Actuators* **51**, pp. 285-291, 1998.
5. A. Wirgin and T. Lopez-Rios, "Can surface-enhanced Raman scattering be caused by waveguide resonances?", *Optics Comm.* **48**, pp.416-420, 1984.
6. M. G. Moharam, E. B. Grann, D. A. Pommet, and T. K. Gaylord, "Formulation for stable and efficient implementation of the rigorous coupled-wave analysis of binary gratings", *J. Opt. Soc. Am. A* **12**, pp. 1068-1076, 1995.
7. Ph. Lalanne and G. M. Morris, "Highly improved convergence of the coupled-wave method for TM polarization", *J. Opt. Soc. Am. A* **13**, p. 779 (1996).
8. Ph. Lalanne and M. P. Jurek, "Computation of the near-field pattern with the coupled method for transverse magnetic polarization", *Journal of modern optics* **45**, pp. 1357-1374, 1998.
9. P. B. Johnson and R. W. Christy, "Optical constants of noble metals", *Phys. Rev. B* **6**, pp.4370-4379, 1972.
10. E. Popov and L. Tsonev, "Electromagnetic field enhancement in deep metallic gratings", *Optics Comm.*, pp. 193-198, 1989.

Electrical properties of irradiated CdSe thin films

G. Stoenescu *

University of Craiova, Department of Physics
13 A.I. Cuza, Craiova 1100, Romania

ABSTRACT

In this paper we present some experimental results concerning the effect of fast electrons irradiation on the specific conduction mechanisms in semiconducting polycrystalline vacuum evaporated CdSe thin layers, in strong electric field, and we give an interpretation of the non - ohmic electrical conduction in these layers. Two conduction regimes defined by the different roles of the intercrystalline barriers and crystallites respectively are analysed. The changing of some microscopic parameters (barrier lengths and potential barriers height) is calculated from the fitting of the experimental and theoretical I-E characteristics, both for irradiated and unirradiated films.

Keywords: thin films, irradiation, conduction mechanisms, crystallites

1. INTRODUCTION

The thin layers of semiconductor compound of $AIIB^{VI}$ type find important applications in microelectronics, dosimetry, optics, automation, optoelectronics and so on. Among these, the CdSe thin layers present a great interest for obtaining optoelectronic devices. Due to their importance in low - cost solar cell technology with heterojunctions made by thermal evaporation in vacuum, the CdSe semiconducting polycrystalline thin layers have been considered with an increasing interest in the last decade.

The studies on the electrical properties of semiconducting polycrystalline CdSe thin layers in strong electric field point out a non - ohmic behavior of the current - field characteristics,^{1, 2, 3} These studies have revealed the close relationship between the electrical conductivity and the structure of the polycrystalline thin layers consisting of a system of crystallites and intercrystalline barriers.

Our previous experiments showed that the electrophysical and structural properties of CdSe thin layers strongly depend on the substrate temperature during the condensation of the layers.¹

Generally, ionizing radiation has strong effects on the crystalline structure, electrical and optical properties of the semiconductor thin layers. These effects are mainly related to sample preparation and especially to the temperature during the growth process.^{4, 5}

2. EXPERIMENTAL MEASUREMENTS

The CdSe thin layers studied in this paper were obtained by the conventional method of thermal evaporation and condensation in vacuum, similar to the one we had previously described.¹ Optical plates of silica glass were used as substrates to obtain the samples under various experimental conditions.

The temperature of the glass substrates was maintained constant during the process of deposition with values in the range 30 - 380°C. CdSe thin layers have been obtained at various deposition rates with values in the range of 1 - 2.8 nm s⁻¹ and 0.01 - 5.5 nm s⁻¹ respectively.

The pressure within the evaporation enclosure was varied between 10⁻⁵ torr and 5 · 10⁻⁵ torr. The final thickness of the obtained films were approximately contained between 0.3 and 4.0 μm. Gold or silver electrodes were deposited on the layers by thermal evaporation in vacuum.

Several CdSe thin layers thus obtained under various experimental conditions were subjected to irradiation with accelerated electrons (1 - 10 MeV) supplied by a linear accelerator. The irradiation doses were varied between 10⁷ and 2 · 10¹⁰ rad, measured with 5% accuracy.

The structural properties of the thin films of CdSe were investigated (by X - ray and electron diffraction) as well as the optical absorption and electroconductivity, both before and after irradiating the corresponding samples with accelerated electrons.

Correspondence: Email: gstoen@hotmail.com; Fax: 40 51 415077

3. THEORETICAL MODEL AND SIMULATIONS

We must emphasize that the CdSe thin layers present a great interest for obtaining optoelectronic devices,^{6, 7, 8} Due to their applications in low-cost solar cell technology with heterojunctions made by thermal evaporation in vacuum, the CdSe semiconducting polycrystalline thin films have been widely analyzed.

However our study aims to compute some different parameters of these films, which can improve the theoretical interpretation of the physical processes at microscopic scale: the intercrystalline barrier length and the height of the potential barrier in certain polycrystalline CdSe thin films, as well as their changing as a consequence of fast electron irradiation.

The experimental results lead to the conclusion that there is a strong correlation between the electric properties and the polycrystalline structure of the CdSe layers which consists of a system of crystallites and intercrystalline barriers. Some parameters of the I-E characteristics have significant changes due to the structural transformations occurred after the irradiation process. The orientation and the dimension of the crystallites are modified as a result of the fast electrons irradiation (3 MeV) of the thin films. These changing depend on the deposition conditions and on the phase transitions involved.

If the irradiation doses have mean values (around 10^8 rad) and if the crystalline structure of the films is a good one, then the result is an improvement of the structure, an increasing in the crystallite dimension and in their orientation degree. The electrical conductivity (in high electric fields) is mainly determined by the presence of the intercrystalline barriers.

The complete mechanism contains a regime dominated by the presence of the intercrystalline barriers and an other one which is due to the crystallites mediated conduction. Assuming that the intercrystalline barriers have a leading role in the electric conduction mechanism for the CdSe films, the following model was established¹:

$$I = g d A(T) [\exp(B(T) E) - 1] \quad (1)$$

where:

$$A(T) = \frac{q}{4} v_t(T) n(T) \exp(-q\phi/kT) \quad (2)$$

$$B(T) = \frac{ql_b}{kT} \quad (3)$$

$$v_t(T) = \sqrt{\frac{8kT}{\pi m^*}} \quad (4)$$

$$n(T) = 2 \left(\frac{m^* kT}{\hbar^2} \right)^{3/2} \cdot \exp \left\{ -\frac{1}{kT} (E_c - E_F) \right\} \quad (5)$$

while $q\phi$ is the height of the potential barrier with respect to the conduction energy band, E_F is the electron Fermi energy, l_b - the length of the intercrystalline barrier.

The relation (1) is derived starting from the expressions of the electric current densities in the barrier and crystallite, respectively, for the case of high electric field but not over a certain threshold of E . In this case, it is assumed that the potential difference on the barrier is equal to the one corresponding to a barrier-crystallite pair.

The model is appropriate for a wide range of the temperature values and well reproduces the current versus electric field characteristics, even their forms are highly nonohmic,^{9, 10, 11} mainly in intense electric fields. However, when working at very strong electric fields and high temperatures, one can notice that the form of the $I - E$ curves is changed.

This effect may be explained by taking into account the "heating" of the charge carriers in the crystallites,^{12, 13, 14} such that the relation between j and E is more involved:

$$j = q n(T) v(E) \quad (6)$$

where only the mobility of the charge carriers depends on the electric field while the coefficient of $v(E)$ depends on the temperature and on the mechanism responsible for the "hot" electrons scattering.

The overall dependence of j on the electric field is in good agreement with the experimental data if we assume an expression,^{4, 10} of the type:

$$j \sim \Lambda E^{1/2} \quad (7)$$

with a function of temperature $\Lambda(T)$ which may also be theoretically derived at least in the case of an isotropic semiconductor having electron scattering on acoustic phonons.

This hypothesis leads to a different expression of the $I - E$ dependence which in turn may be improved in order to give an interpretation to the negative differential resistivity region occurred at high temperatures, such that:

$$j = \alpha (T_0 + \gamma j E)^2 \exp \left(\frac{\beta E - C}{T_0 + \gamma j E} \right) \quad (8)$$

Here:

$$\gamma = 1/\sigma$$

with σ - a coefficient which depends on the heat exchange and on the sample geometry, T_0 is the medium temperature and

$$j = j(E, T_0)$$

All these regimes are, in conclusion determined specially by the role played by the crystallites and by the intercrystalline barriers in the conduction mechanism, proving again the interplay between the microscopical and macroscopical characteristics.

4. RESULTS AND DISCUSSIONS

Our experiments showed that the crystalline structure and other electrophysical properties of the CdSe thin layers strongly depend on the samples preparation conditions, especially on the substrate temperatures.

The perfect crystalline structure of the CdSe thin layers crystallites, their size and orientation degree depend on the experimental conditions of preparation, especially on the substrate temperature during condensation,^{1, 9, 11} The crystalline structure improves when the substrate temperature increases (above 200°C).

The action of the irradiation proved to be important for the CdSe layers obtained on low temperature substrates ($t_s \sim 100 - 150^\circ C$) containing small oriented crystallites having certain structural imperfections, especially packing defects.

Usually, for the CdSe thin layers obtained on low temperature substrates ($100 - 150^\circ C$) whose structure shows many defects, irradiation with doses of about $10^5 - 10^6$ Gy by electrons accelerated up to kinetic energies of 3 MeV, leads to a deterioration of the crystalline structure and to the appearance of an amorphous phase at least in the surface layers of the sample.

The irradiation with the same dose ($10^5 - 10^6$ Gy) of the thin layers obtained on heated supports ($t_s \sim 250 - 300^\circ C$), containing crystallites preferentially oriented and with a good crystalline structure, led to the increasing of the crystallites orientation degree and to the improvement of their crystalline structure,^{1, 4, 9, 10} Our experience showed that the electrical properties strongly depend on the action of the accelerated electrons irradiation of the CdSe thin layer crystalline structure.

Thus the current versus electric field characteristics of the irradiated samples differs from those obtained before irradiation. The effect of fast electron irradiation occurs in the current vs electric field characteristics especially in high electric fields.

Experimental current versus electric field ($I - E$) characteristics of semiconducting polycrystalline CdSe thin layers, before and after fast electron irradiation were obtained for different temperatures varying between $-150^\circ C$ and $+250^\circ C$.

We analyzed the significant results obtained with CdSe layers of about $0.6 \mu m$ thickness, grown on glass substrates maintained at a temperature of about $100^\circ C$. A family of currents versus electric field ($I - E$) characteristics was obtained. We thus noticed that the diagram corresponding to $3 \cdot 10^5$ V/m for low temperatures (below $0^\circ C$) differs from those of high temperatures.

The diagram for low temperatures are straight lines and therefore the conduction is ohmic. In the high electric field strength range and at temperatures higher than 0° C, these characteristics present a non - ohmic behavior. This non - ohmic behavior for unirradiated thin layers is exhibited starting with the 13° C temperature, while in the case of irradiation this threshold value is 82° C.

In this case, the I-E characteristic presents, at low fields, a portion of ohmic dependence of the current on the applied electrical field,^{15 16} followed by an exponential dependence of the current on the field strength at high fields.

The non-ohmic characteristics can be interpreted using a sample model of thin polycrystalline film consisting of a system of crystallites and intercrystalline barriers of the same type, randomly oriented. Therefore the exponential shape of these I-E characteristics can be explained considering the predominant role of the intercrystalline barriers in the electric conduction of the polycrystalline CdSe layers.

By fitting the theoretical curves given by (1) and the experimental I-E characteristic, the microscopic parameters were calculated and their changing after the irradiation process was analyzed.

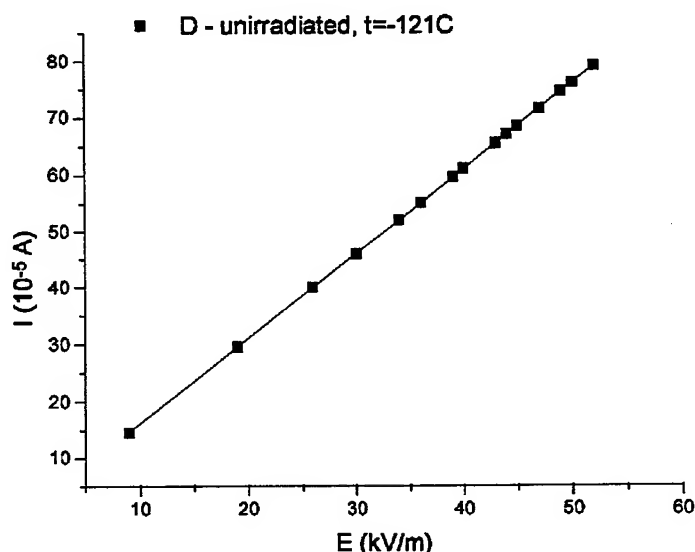


Fig.1 Experimental and theoretical characteristics for unirradiated samples, at $t = -121^{\circ}\text{C}$.

In fig. 1 and fig. 2 the experimental and theoretical curves are showed for the irradiated and unirradiated samples respectively.

We give the results of our computations concerning the parameter changings after the irradiation in what follows:

Coefficient	unirradiated sample	irradiated sample
$gdA(T)$	3708.55511	4707.72432
$\frac{q}{4}v_t n \exp(-q\phi/KT)$	1382.65902	1766.73941
KT/ql_b	2505.04423	5010.54158

The calculation of the parameters used by the proposed theoretical model leaded to the following values : $q(\phi^{unirr} - \phi^{irr}) = 0.12\text{eV}$ and $l_b^{unirr}/l_b^{irrad} = 1.91$ which show the expected changings in the values of the barrier length and of the potential barrier height.

In addition, these values may be verified if one derives on the same lines the theoretical expressions of the electrical resistivity and of the differential resistivity as functions of the mean crystallite dimension:

$$D = \frac{KTg^2d^2\Lambda^2}{qI^2} \left[\ln(1 + I/Agd) - \frac{I}{I + Agd} \right] \quad (9)$$

where: D is the mean length of the crystallites.

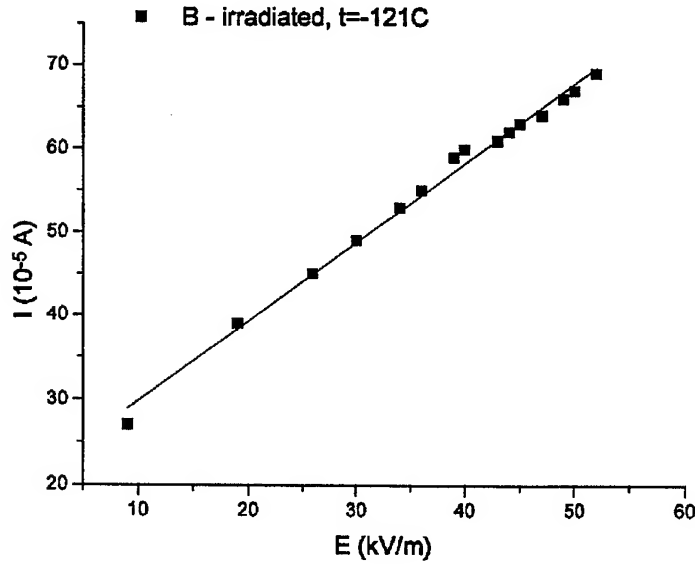


Fig.2 Experimental and theoretical characteristics for irradiated samples, at $t = -121^{\circ}\text{C}$

The two auxiliary functions needed in order to perform a nonlinear fitting of the experimental measurements and theoretical curves are therefore the resistivity:

$$R = \frac{KTL}{qI} \ln \left(1 + \frac{I}{Agd} \right) + LI \frac{1}{(gd\Lambda)^2} \quad (10)$$

and the differential resistivity:

$$R_d = \frac{KTL}{q(I + Agd)} + 2LI \frac{1}{(gd\Lambda)^2} \quad (11)$$

respectively.

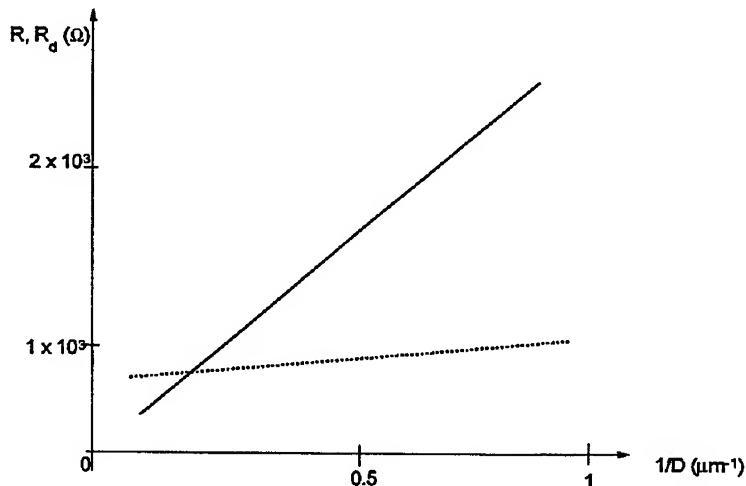


Fig.3 Resistivity and differential resistivity versus the crystallite dimensions

5. CONCLUSIONS

The values of A (2) give us once more the height of the potential barrier $q\phi$. In fig. 3, the results of the nonlinear fitting procedure are presented, the variation of $q\phi$ being in good agreement with the results based on our first method: $q\Delta\phi = 0.11\text{eV}$.

The structural transformation which occurs after the irradiation changes certain parameters of the I-E characteristics of the thin layers, in comparison to the case when no irradiation process is performed.

The irradiated thin layers show ohmic conduction up to the electric field strength values, conduction which is higher than the upper limit for the electric field strength in the condition for the ohmic conduction in the case of unirradiated layers. The linear parts slopes of the unirradiated thin layers characteristics are generally greater than those obtained for the irradiated samples.

Our experimental results show that there is a close correlation between the electrical properties and the structure of the polycrystalline CdSe thin layers consisting of a system of crystallites and intercrystalline barriers. These results have also revealed that the electrical conductivity of the analyzed CdSe thin films within a strong electric field is essentially determined by the presence of the intercrystalline barriers.

REFERENCES

1. I. S. P. C. N. B. I. Spanulescu, V. Ruxandra and G. Stoenescu, "The cdse thin films for solar cells," *Anal. Univ. Bucharest* **34**, pp. 13-16, 1990.
2. I. S. N. B. G. Stoenescu, V. Calian and V. Ruxandra, "The effect of accelerated electron irradiation on electric conductivity of cdse thin films," *Teaching the Science of New Materials proc.*, pp. 314-316, 1995.
3. I. S. G. Stoenescu, V. Calian and N. Baltateanu, "Characteristic parameters changes for mos circuits irradiated by fast electrons," *Optoelectronica* **4**, pp. 71-74, 1996.
4. C. M. Dozier and D. B. Brown, "Photon energy dependence of radiation effects in mos structures," *IEEE Trans. Nucl. Sci. NS* **27**, pp. 1694-1699, 1990.
5. W.-S. L. J. A. T. Ma, D. Ueda and J. S. H. Jr., "Influence of buffer layer thickness on dc performances of gaas/algaas heterojunction bipolar transistors grown on silicon substrates," *IEEE El. Device Letters* **9**, pp. 657-659, 1988.
6. T. U. S. Ohke and Y. Cho, "Optical waveguides using gaas/algaas multiple quantum wells," *Opt. Commun.* **56**, pp. 235-239, 1985.
7. J. Kraus and P. P. Deimel, "Calculation of the propagation constant of the optical modes in multi-quantum-well structure," *IEEE J. Quantum Electron.* **26**, pp. 824-826, 1990.
8. A. P. Zhao and S. R. Cvetkovic, "Finite element analysis of semiconductor laser arrays," *Microwave Opt. Technol. Lett.* **4**, pp. 247-250, 1991.
9. V. Dolocan, *Fizica jonctiunilor semiconductoare*, Edit. Academiei, Bucharest, 1982.
10. P. E. Gray and C. L. Searle, *Modern Electronics*, World Scientific, New York, 1973.
11. R. I. Baron and L. Higbie, *Computer Architecture*, Addison-Wesley, New York, 1994.
12. S. J. Fonash, *Solar cell device Physics*, Academic Press, New York, 1981.
13. E. H. Nicollian and J. R. Brew, *MOS (Metal Oxide Semiconductor) Physics and Technology*, Wiley, New York, 1982.
14. H. Horiuchi, "Clustering in nuclear structure and collisions," *NATO ASI Series* **359**, pp. 29-51, 1997.
15. T. U. S. Ohke and Y. Cho, "Tm-mode propagation and form birefringence in gaas/algaas multiple quantum wells optical waveguide," *Opt. Commun.* **70**, pp. 92-96, 1989.
16. A. P. Zhao and S. R. Cvetkovic, "Finite element solution of nonlinear tm waves in mqw waveguides," *IEEE Photon. Technol. Lett.* **4**, pp. 1231-1234, 1992.

Experimental investigation on multimode quartz fibre phase conjugation using SBS

Anca Mocofanescu*, M. Zamfirescu, C. Fenic, A. Stratan, T. Visan

National Institute for Laser, Plasma and Radiation Physics, Lasers Dept.

P.O. Box MG-36, Bucharest 76900, Romania.

ABSTRACT

The beam quality of solid-state lasers with high average power can be greatly improved using phase conjugators based on stimulated Brillouin scattering (SBS). The common phase conjugators used till now are liquid or gas cells. Using SBS in glass fibres as phase conjugators the field of applications can be expended. The long interaction length and small cross-sections of the fibres result in an appreciable reduction of SBS threshold and avoid optical breakdown which could happen in liquids and gases at high input energies. Other advantages of glass fibre phase conjugators are harmlessness and easy handling. We have experimentally investigated a phase conjugator based on SBS obtained in an undoped quartz fibre with core diameter of 200 μm . The SBS threshold reflectivity and phase conjugation capability were measured with 18 ns pulses at 1.06 μm wave length with different input energies.

Keywords: stimulated Brillouin scattering, optical fibers, phase conjugation, solid-state lasers, beam quality.

1. INTRODUCTION

The power needed to generate SBS in non guide materials is of the order of 10^5 W. This power can be reduced by increasing the interaction length and decreasing the cross-section area of the light beam and these requirements are satisfied by wave guides, among which the fiber seems to be most attractive. SBS in optical fibers is much easier to realize and handle. Since 1972, when SBS was observed in single mode fibers for the first time¹ there have been many investigation of this topic². It should be noted that the research was concentrated principally on single mode fibers, which are not suitable for phase conjugation (PC). Phase conjugation in fibers was obtained for the first time in a multimode fiber in Russia, in the 1980's³. PC can only be achieved in multimode fibers because only these fibers provide the nonuniform pump waves needed.

Recent experiments with multimode fibers were made by Eichler et al.⁴ who developed a new kind of phase conjugators based on SBS in glass fibers (undoped multimode quartz fibers). The used fibers were of a core diameter of 200 μm and different lengths. Using a Nd:YAG laser with a 50 cm coherence length, near diffracted limited and a 17 m length fiber, the SBS threshold was found to be 17kW, the SBS reflectivity up to 50% and SBS fidelity up to 93%. The influence of the coherence length of the input beams was found to be a decisive factor for the limitation of the SBS interaction length in the fiber. The conclusion was: if the linewidth of the single laser mode becomes small compared to the Brillouin linewidth, the interaction length of SBS in the fiber is no longer limited by the coherence of pump beam but only by fiber attenuation. The fiber phase conjugators are harmless to environment and can be handled safely in contrast to dangerous fluid and gaseous SBS media, which are toxic or operated at high pressure. Besides having low reflectivity and needing a long coherence length in the pump laser system, this simple quartz multimode fiber system still has a dynamic range as low as 20 times the threshold energy.

A. Heuer⁵ has demonstrated SBS in a novel optical fiber phase conjugated mirror as a generator - amplifier system using a tapered quartz fiber. In this case the threshold energy was reduced to 15 μJ and the SBS reflectivity was 92%. The fiber was pumped in a dynamic power range of 1:267. The phase conjugation fidelity was measured to be greater than 95%, over the entire pump energy range.

• Correspondence: Email: amocof@ifin.nipne.ro; Telephone: (40) 1 780 53 85; Fax: (40) 1 423 17 91

2. EXPERIMENTAL SET-UP

We investigated the phase conjugation in multimode optical fibers using a typical setup for such experiments (Fig.1).

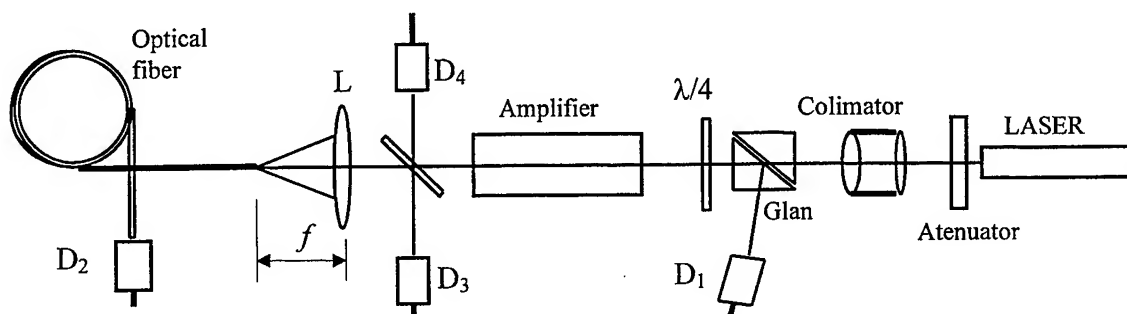


Fig.1. Experimental set-up.

We used a Nd:YAG laser (oscillator-amplifier system) and a quartz fiber of 200 μm core diameter. The laser oscillator was operated in the Q-switched mode with a LiF:F_2 crystal with the initial transmission of 50 %. The oscillator was kept near threshold in order to generate a single pulse. The resonator length was 45 cm. The short resonator, the passive Q-switch and an intracavity Fabry-Perot etalon allowed a radiation with reduced spectral linewidth (coherence length - 30 cm). The duration of the laser pulse was 18 ns and the maximum output energy was 4 mJ in a beam with a near Gaussian transversal distribution. The beam was focused with a lens of focal length 16 cm in a quartz fiber with 200 μm core diameter, 2 m length and 0.2 numerical aperture, having a polished entrance surface. The diameter of the focal waist was 100 μm . The transmission of the fiber was maximum 65 %.

The phase conjugation properties were studied using a CCD camera and a SPIRICON system for analyzing the transversal structure of the beams. The temporal behaviour was measured with a digital oscilloscope Tektronix TDS 350 and a fast photodiode (rise time < 1ns). Piroelectric detectors were used to measure laser beam energies (incident, Stokes and transmitted energy).

3. EXPERIMENTAL RESULTS

To ascertain that PC indeed took place, the spatial distribution pattern of the Stokes wave field was recorded with the CCD camera (placed in the position of detector D1) and compared with the spatial distribution of the pump field (recorded in the position of detector D4). Figure 2a. shows an example of the spatial distribution of the pump wave, and figure 2b shows that of the Stokes wave. The spatial distribution of incident laser field is reproduced in a good way by that of the Stokes field.

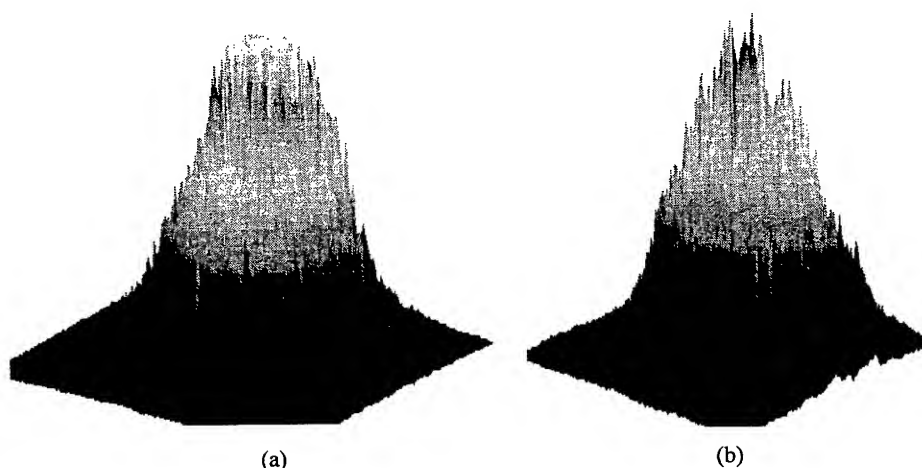


Fig. 2. Transverse beam structure of (a) the input beam, (b) the SBS-reflected beam.

Fig.3 shows the spatial distribution of transmitted beam through the fiber, which exhibits a much distorted distribution. To record this spatial distribution the CCD camera was placed in the position of detector D2.

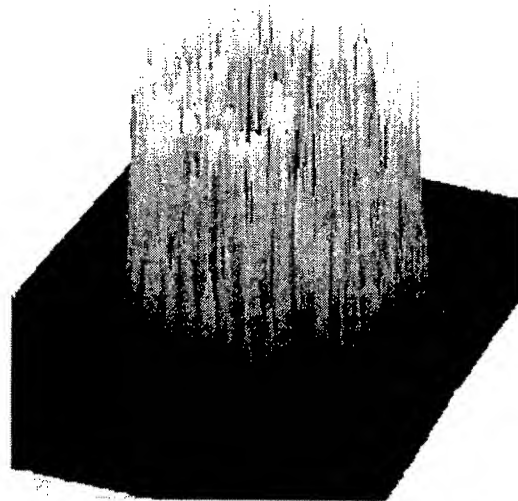


Fig. 3. Transverse beam structure of transmitted beam through the fiber.

The SBS reflectivity was measured using experimental set-up shown in Fig.4.

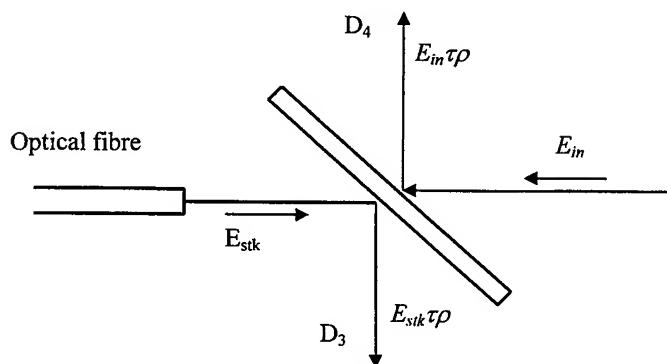


Fig. 4. Experimental set-up for SBS reflectivity measurement.

A glass beam splitter with 8 % reflectivity and two detectors were used to measure the energy incident on the fiber (D4) and the Stokes energy (D3).

The SBS measured reflectivity is defined as the ratio of the Stokes energy and the energy incident on the fiber:

$$R = \frac{E_3}{E_4} = \frac{E_{stk}}{E_{in}} \quad (1)$$

The dependence of the SBS reflectivity against the pumping energy is shown in Fig. 5.

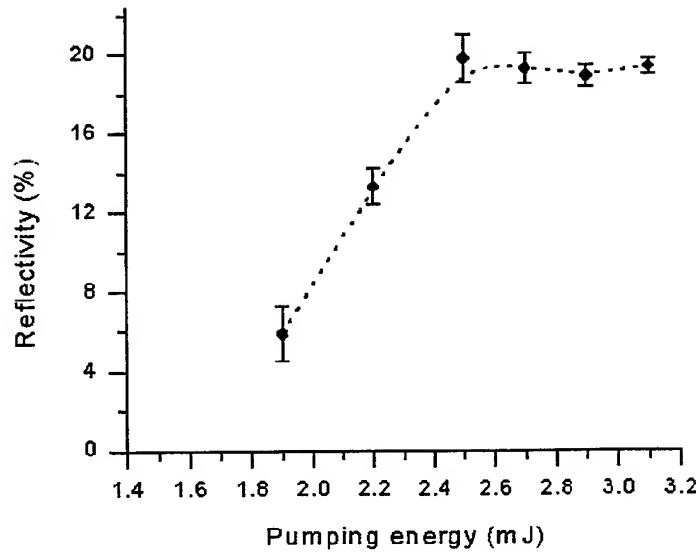


Fig. 5. Reflectivity against pumping energy.

The SBS threshold energy was found 1.6 mJ (88 kW) and the maximum reflectivity was 20 %. The low value of the reflectivity and increased threshold energy in comparison with Eichler's experiment is explained by the worse coherence of our laser and the fact that we did not calibrate the system, and did not take into account the Fresnel losses and the coupling efficiency in the formula for the reflectivity.

The SBS threshold power in a fiber can be estimated ⁴:

$$P_{th} = \frac{21A_{eff}}{g_B L_{eff}} \quad (2)$$

where A_{eff} is the effective core area, g_B – Brillouin gain which is for quartz $2.3 \cdot 10^{-9}$ cm /W and L_{eff} is the effective interaction length in the fiber which depends on the coherence length and the fiber length, according to:

$$\frac{1}{L_{eff}} = \frac{1}{L_{coer}} + \frac{1}{L} \quad (3)$$

From this formula, we deduced the coherence length of our laser to be 35 cm, which is in good agreement with the measurement made with a Michelson interferometer.

Another fact which may contribute to these different values is the duration of our laser pulse (18 ns) which is short in comparison with the phonon lifetime in quartz (5 ns) so SBS occurs at the limit between the steady state regime and the transient regime.

This conclusion is sustained by the time measurements obtained with a fast photodiode with a rise time of 1 ns and a Tektronics TDS 350 digital oscilloscope.

Figure 6 shows the oscilloscope trace of the incident laser of 18 ns duration.

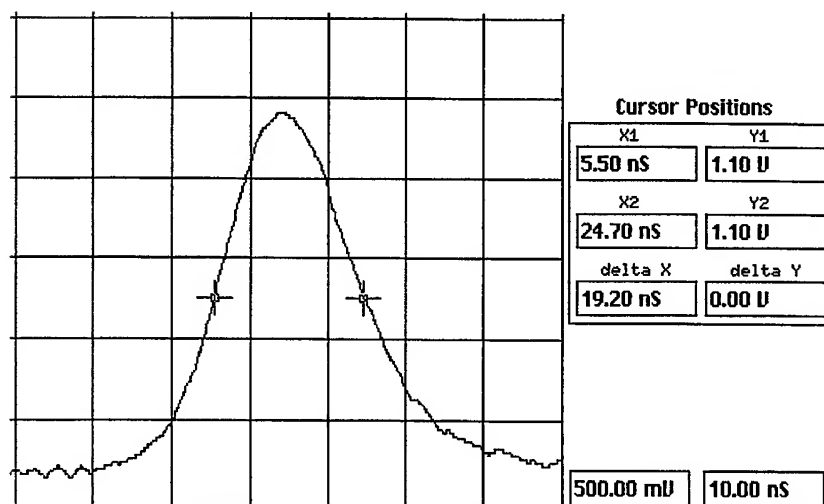


Fig. 6. Oscillator puls duration.

Fig 7a. and b. shows the transmitted pump pulse and the Stokes pulse, respectively, near threshold.

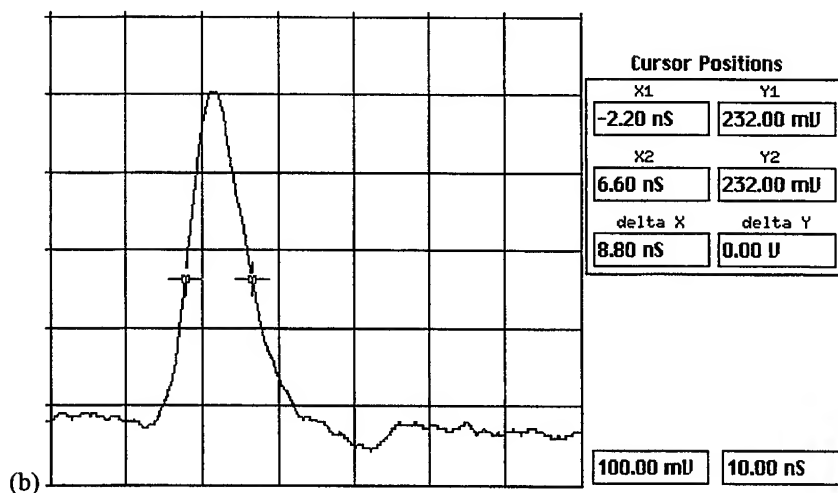
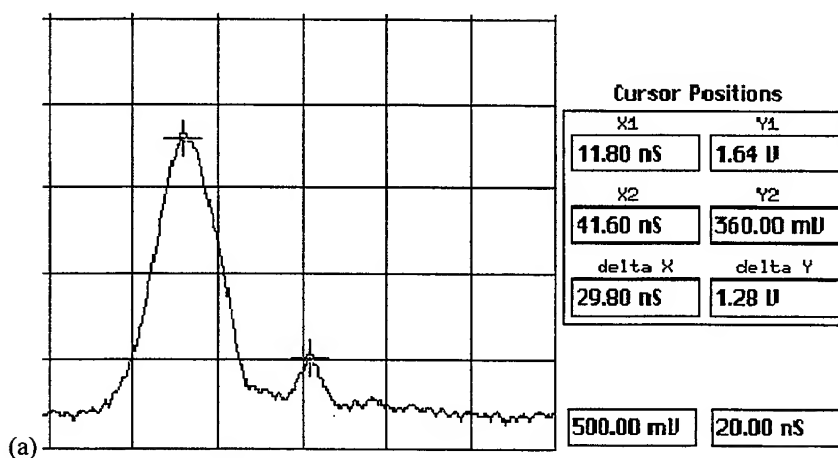


Fig.7. Transmitted pump pulse (a) and the Stokes pulse (b), near threshold.

As one can see that the Stokes pulse is two times reduced in duration so we can say that SBS takes place in transient conditions. Under increased pumping power the transmitted pulse and the Stokes pulse exhibit multiple pulse behaviour (Fig.8a. and b.).

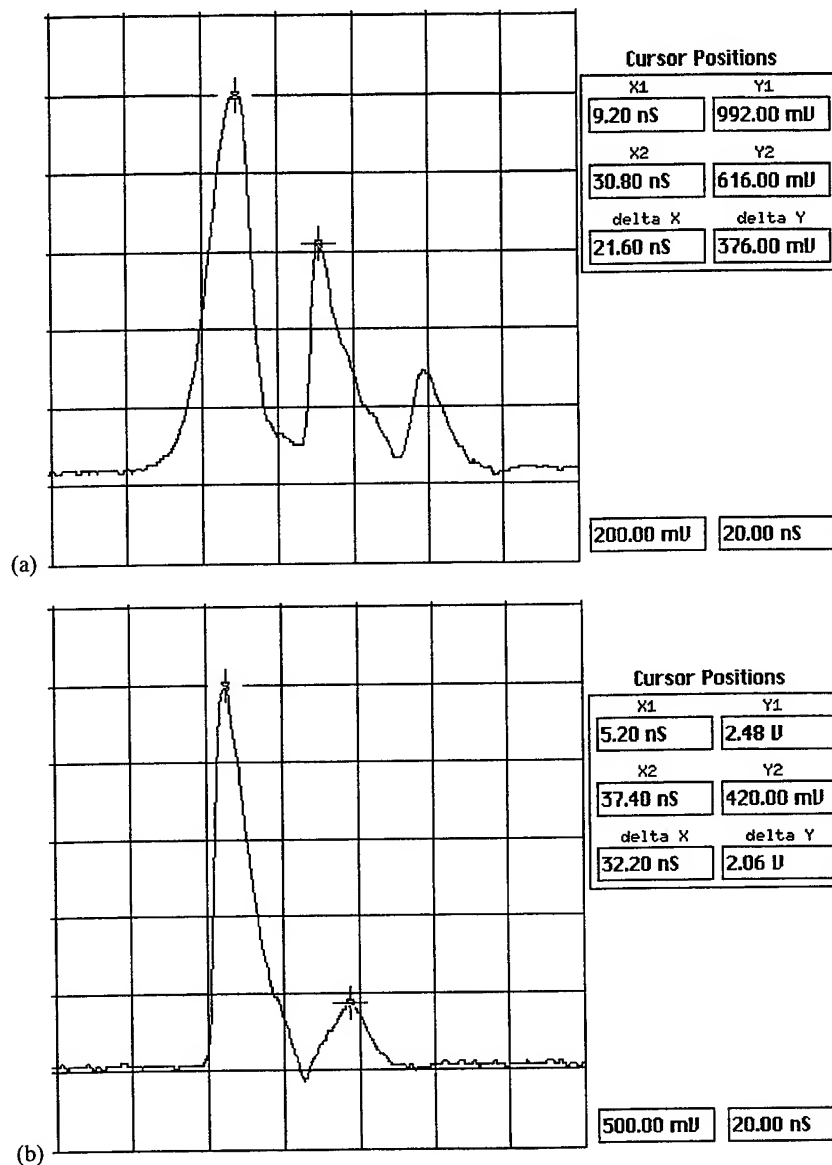


Fig.8. Transmitted pulse (a) and the Stokes pulse (b) for 3 mJ input energy .

This behaviour is specific for the transient regime and was also observed ⁶ in the tapered geometry with liquid SBS media.

This particular time dependence of the Stokes and transmitted pulse can be explained by the interaction between the Stokes pulse and the incident laser pulse, which may exchange back and forth energy, during the pumping pulse duration. The Stokes pulse is generated by the interaction between the incident laser field and the acoustic field so when the Stokes pulse will have a maximum, the transmitted pulse will have a minimum. When the Stokes radiation propagates through the fiber, the leading edge of the Stokes pulse increases in intensity but its tail can continually lose energy back to the laser pulse. The regenerated laser pulse will have the phase shifted with π and can generate a new Stokes pulse in interaction with the acoustic field, if it has enough energy the process repeating until the energy will decrease under the SBS threshold.

4. CONCLUSIONS

We have demonstrated that phase conjugation in multimod quartz fibers can be a good means to correct phase distortions in solid-state lasers with high quality beam.

The SBS threshold energy of the fibers is lower in comparison with other nonlinear media (CS_2) and decreases at small core diameter. The reflectivity and the fidelity are dependent on the coherence length of the pump laser. The power of the input pulse is limited by the damage threshold of the optical fiber (1 GW/cm^2 for the nanosecond laser pulses). Under increased pumping power the transmitted pulse and the Stokes pulse exhibit multiple pulse behaviour.

REFERENCES

1. E.P. Ippen and R.H. Stolen, "Stimulated Brillouin in optical fibers", *Appl. Phys. Lett.* **21**, no.11, pp.539-540, 1972.
2. G.P. Agrawal, *Nonlinear Fiber Optics*, 2nd ed., pp. 370-399, Academic Press, San Diego Calif., 1995.
3. E.A. Kuzin, M.P. Petrov and A.A. Fotiadi in *Optical Phase Conjugation*, pp.74-96, M.Gower, Springer-Verlag, 1994.
4. H. Eichler, J. Kunde and B. Liu, "Quartz fibre phase conjugation with high fidelity and reflectivity", *Optics Comm.* **139**, pp.327-334, 1997.
5. A. Heuer and R. Menzel, "Phase-conjugating stimulated Brillouin scattering mirror for low powers and reflectivities above 90% in an internally tapered optical fiber", *Optics Lett.* **23**, no.11, pp. 834-836, 1998.
6. M.J. Damzen and H. Hutchinson, "Laser Pulse Compression by Stimulated Brillouin Scattering in Tapered Waveguides", *IEEE Journal of Quantum Electronics* **QE-19**, no.1, pp.7-14, 1983.

Numerical method for nonlinear optical devices

Violeta Calian *, Marcela Ursache, Margareta Socaciu
University of Craiova, Department of Physics
13 A.I. Cuza, Craiova 1100, Romania

ABSTRACT

An extension of the "Orthogonal Collocation Method" is proposed in order to treat various realistic problems of nonlinear waveguiding in multiple-layer structures. The simulation results may be an important factor in designing multiple quantum wells structures (MQW) structures which are widely used in optical signal processing devices.

Keywords: nonlinear waveguiding, multiple-layer structure, Orthogonal Collocation method.

1. INTRODUCTION

There is a large number of linear and/or nonlinear optical devices based on the "multiple quantum wells" (MQW) waveguide structures - MQW laser, filters, directional couplers, quantum - confined Stark modulator, self-electro-optic devices, bistable optical devices - which are highly studied experimentally. The characteristics of the linear and nonlinear waveguided propagation in multiple-layer systems are a problem of crucial importance,^{1, 2, 3} due to their potential use in the domain of optical signals processing. This type of optical structures offer advantages that include: suitability for integration of device components, strong nonlinearity, very fast response time.

Our paper presents a new method for the numerical simulation of several realistic problems,^{4, 5} which include the case of linear and/or nonlinear media having an arbitrary refraction index profile and/or nonlinearities caused by various mechanisms (thermal nonlinearities, electronic distortion, molecular orientation), obtaining the TE and TM solutions for this type of MQW waveguiding structures.

The numerical methods used to solve this kind of problems based on the finite-element technique,⁶ the "averaged index" method,² the "beam propagation" method,¹ are well known, as well as their difficulties and limits. An extension of the "Orthogonal Collocation Method" is applied, for the case of coupled differential equations and an infinite range of independent variables. The accuracy and the results are compared to the available ones obtained by using other techniques.

Several specific cases were solved, comparing the results afterwards with the available ones, obtained by using other methods,^{6, 2, 3}: a) linear structures with different layer number and widths; b) nonlinear systems with different nonlinearity mechanisms.

2. THE WAVEGUIDING PROBLEMS

The collocation methods belong to the family of weighted residuals used in solving differential equations,^{7, 8, 9} The solution of a differential equation is written as a linear or polynomial combination or as a linear combination of a set of polynomials or functions. The development coefficients are obtained from the condition that it must verify exactly the given differential equation, for a certain number of points belonging to the axis (or plane) of independent variables. These are the so-called "collocation points". In the initial forms, they were chosen to be equidistant but such a technique implied the occurrence of divergence in results (the phenomenon is known as "Runge divergence"). The solution is to use orthogonal polynomials as basis functions of the development.

The results provided by this method are comparable to the Galerkin ones from the precision point of view, but the implementation is much simpler. The symmetry and the spatial period of the guiding structure are the "key" for the choice of the orthogonal functions basis, in the case of an infinite set of independent variables the most appropriate being the Hermite-Gauss or Laguerre-Gauss functions.

Correspondence: Email: violetaxx@hotmail.com, Fax: 40 51 415077

2.1. TE polarised waves in MQW waveguides

The Maxwell equations imply that the TE polarised waves in MQW waveguides (consisting of M "barrier-well" pairs having t_b and t_g widths) must verify the equation:

$$\frac{d^2 E_x}{dy^2} + (k_0^2 \epsilon'_x - \beta^2) E_x = 0 \quad (1)$$

where: k_0 - wave number for the free space, β - propagation constant for the propagation direction "z",

$$\epsilon'_{i,x} = \epsilon_i + a_i f(E_x)$$

$$a_i = c_0 \epsilon_0 n_{i,x}^2 \cdot n_i'' \quad (2)$$

with c_0 - light speed in vacuum, a_i - nonlinearity coefficient for each medium, n_i'' - optical nonlinearity coefficient ($n'' = 0$ for linear media), n_i - refraction index of each layer, $i = \overline{1, M}$

$$f(E_x) = |E_x|^s$$

where "s" depends on the nonlinearity type ($s = 2$ for the Kerr - like case).

The total optical power for TE waves, per unit length along the "x" axis is then given by:

$$P = \frac{1}{2} \int_{-\infty}^{\infty} E_x H_y^* dy = \frac{c_0 \epsilon_0}{2} \cdot \frac{\beta}{k_0} \cdot \int_{-\infty}^{\infty} |E_x|^2 dy \quad (3)$$

2.2. TM polarised waves in MQW waveguides

For the TM polarised waves and the same guiding structure one obtains:

$$\frac{d}{dy} \left(\frac{1}{\epsilon'_z} \cdot \frac{dH_x}{dy} \right) + \left(k_0^2 - \frac{\beta^2}{\epsilon'_y} \right) H_x = 0 \quad (4)$$

where:

$$\begin{aligned} \epsilon'_{i,y} &= \epsilon_i + a_i f(E_y) + b_i f(E_z) \\ \epsilon'_{i,z} &= \epsilon_i + b_i f(E_y) + a_i f(E_z) \end{aligned} \quad (5)$$

while the b_i values depend,^{10 cite8,11} on the considered mechanism: $b = a$ for thermal nonlinearities, $b = a/3$ for electronic distortions type, $b = -a/2$ for molecular orientation nonlinearities.

For the computation of $\epsilon'_{i,y}$ and $\epsilon'_{i,z}$, the E_y , E_z are involved and they are given by:

$$E_y = -\frac{1}{c_0 \epsilon_0} \cdot \left(\frac{\beta}{k_0} \right) \cdot \frac{1}{\epsilon'_y} \cdot H_x \quad (6)$$

$$E_z = j \frac{1}{c_0 \epsilon_0} \cdot \left(\frac{1}{k_0} \right) \cdot \frac{1}{\epsilon'_z} \cdot \frac{dH_x}{dy} \quad (7)$$

thus the problem imply to solve the coupled equations (4), (5), (6), (7).

The total optical power for the TM case per unit length along the "x" axis is defined by:

$$P = -\frac{1}{2} \int_{-\infty}^{\infty} E_y H_x^* dy = \frac{1}{2c_0 \epsilon_0} \cdot \frac{\beta}{k_0} \cdot \int_{-\infty}^{\infty} \frac{1}{\epsilon'_y} |H_x|^2 dy \quad (8)$$

3. THE EXTENDED "ORTHOGONAL COLLOCATION" METHOD

For the three - dimensional case, the solution of the equations (1) or (4) is written as a double linear combination over sets of appropriate orthogonal functions::

$$\varphi(x, y, z) = \sum_{n=1}^{N1} \sum_{m=1}^{N2} K_{nm}(z) \Phi_n(x) \eta_m(y) \quad (9)$$

where $\Phi_n(x)$, $\eta_m(y)$ are Hermite-Gauss functions:

$$\begin{aligned} \Phi_n(x) &= N_{n-1} H_{n-1}(\alpha x) \exp \left\{ -\frac{1}{2} \alpha^2 x^2 \right\} \\ \eta_m(y) &= M_{m-1} H_{m-1}(\gamma y) \exp \left\{ -\frac{1}{2} \gamma^2 y^2 \right\} \end{aligned} \quad (10)$$

and N_{n-1} , M_{m-1} are the normalisation constants, α and γ - two parameters which can be arbitrarily fixed.

Choosing α , γ and N_1 , N_2 values is a crucial step for the accuracy of the solution. This is certainly increased as a function of the collocation points numbers (N_1 , N_2) while α and γ are established in correlation with the " t_g " and " t_b " values, such that to obtain a sufficiently accurate division of the domain.

The collocation points are calculated from the condition:

$$\begin{aligned} H_{N1}(\alpha x_j) &= 0, \quad j = \overline{1, N1} \\ H_{N2}(\gamma y_l) &= 0, \quad l = \overline{1, N2} \end{aligned} \quad (11)$$

thus from the well-known zeroes of Φ_{N1+1} and η_{N2+1} respectively.

If one writes the TE and TM wave equations for this double set of points, then one obtains a differential equations system of the following type:

$$\frac{d^2 \Psi}{dz^2} + S_0 \Psi + \Psi T^t + R(\Psi) = 0 \quad (12)$$

where Ψ is a $N1 \times N2$ matrix defining the $\varphi(x, y)$ field on a matrix of collocation points

$$[\Psi(z)]_{ij} = [\varphi(x_i, y_j, z)]$$

and

$$S_0 = B A^{-1}$$

with:

$$[B]_{kl} = \frac{\partial^2 \Phi_k}{\partial x^2} \Big|_{x_l} \quad (13)$$

$$[A]_{kl} = \Phi_k(x_l) \quad (14)$$

The matrix T is computed as th matrix S_0 , for $\eta(y)$ and the set of points $\{y_j\}$ with $j = \overline{1, N2}$. The term $R(\Psi)$ is a $N1 \times N2$ matrix whose elements are given by the linear contributions in E_x for the TE case and in H_x for the TM case, respectively, calculated on the points (x_j, y_l) , $j = \overline{1, N1}$, $l = \overline{1, N2}$.

Solving the system (12) is in consequence possible and straightforward by using a typical method such as Runge-Kutta of the forth order, obtaining therefore the electric and magnetic field profiles.

4. LINEAR MQW GUIDES

The method was firstly tested on the cases of TE and TM waves propagation in the linear type MQW structures. In these cases, all the media of the MQW structures are linear, i.e.: $n_i'' \equiv 0$, $i = \overline{1,3}$, such that the equation (2) must be written as: $\epsilon'_{i,x} = \epsilon_i = n_i^2$ for the TE waves and the equation (5) must be: $\epsilon'_{i,x} = \epsilon'_{i,y} = \epsilon_i = n_i^2$ for the TM waves.

Using orthogonal collocation method, a MQW guiding structure was studied for the case of a material system GaAs-GaAlAs having the following linear parameters:

$$n_1^2 = 11.56; n_2^2 = n_3^2 = 11.22; t = t_w = t_b$$

such that to be able to compare the results with the ones obtained by the finite element and averaged index method.⁶

The following results were derived:

A) The number of modes and the propagation constant (β/k_0) are growing while the barriers number increases, if the barrier width is kept constant. There is a very good agreement with the two mentioned methods if the structural period is small enough in comparison with the guiding region width. Otherwise certain differences occur only for the "averaged index" method which can not simulate correctly the given structure anymore.

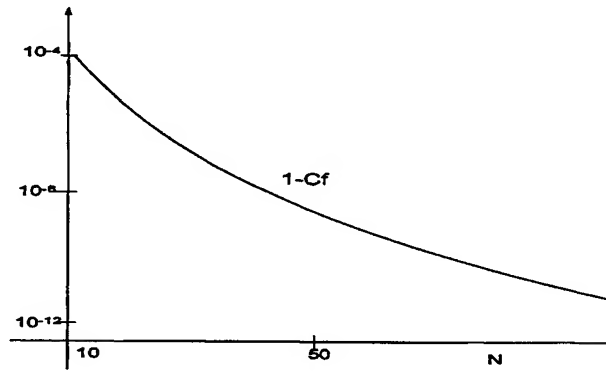


Fig.1 The error in the correlation factor as a function of the number of the collocation points

B) The modal birefringence calculation, for TE_0 and TM_0 , as a function of the well width and for different barrier-well numbers, lead us to the conclusion of having optimum values of $t_g = 26, 8.4, 5.3nm$ for a number of barriers $N = 10, 30, 50$ respectively, in a good agreement with the results given by the finite element method: $t_g = 25, 8.6, 5.2nm$ and for the same N - values.

C) The number of modes and the corresponding propagation constants were computed for several values of the ratio well-to-barrier width ($r = t_g/t_b$). We thus proved the variation of these parameters with r and we calculated the maximum value of the birefringence for $r = 1.12$, if r was tuned between 0.5 and 2. The results in⁶ offered us a value $r = 1.0$. In addition, we can plot the error in the correlation factor as a function of the number of the collocation points (fig.1) and as a function of the propagation distance (fig.2).

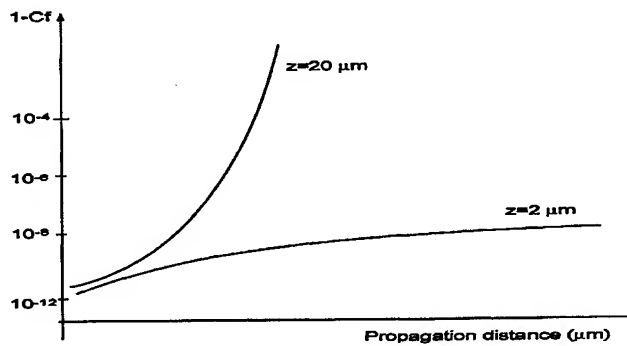


Fig.2 The error in the correlation factor as a function of the propagation distance

5. CONCLUSIONS

The orthogonal collocation method was then applied for a nonlinear MQW guiding structure having the following parameters: $n_1'' = n_3'' = 0$, $n_2'' = a_2(c_0\epsilon_0 n_2^2) = 2 \times 10^{-9} \text{ m}^2/\text{W}$, the total width of the MQW region: $T = 610 \text{ nm}$; $r = 0.5$ and the barriers number $N = 30$.

The structure was chosen as in⁶ such that one is able to compare the results. In order to test the validity of our technique, we studied several problems:

A) The effective refraction index βk_0 convergence as a function of the iterations number, for the following cases:

A1) a nonlinear TE_0 mode for a Kerr - like problem ($s = 2$)

A2) a nonlinear TM_0 mode for the nonlinearity mechanism given by electronic distortions ($b = a/3$ and $s = 2$),

for different values of the total optical power P .

The limiting values of the optical power were calculated starting from the equations (3), (8).

One can notice in the following tables the comparison between the values of the propagation constant, computed for the TE_0 and TM_0 modes, as well as the extremum values of the functions involved in optical power calculation, obtained from two numerical procedures: the orthogonal collocation and the finite element method.

Tab. 1. TE_0 mode values of the propagation constants at different values of the optical power, by two numerical methods

TE_0	$\frac{\beta}{k_0}$ ($P = 200 \text{ W/m}$)	$\frac{\beta}{k_0}$ ($P = 400 \text{ W/m}$)	$\frac{\beta}{k_0}$ ($P = 600 \text{ W/m}$)	$\frac{\beta}{k_0}$ ($P = 800 \text{ W/m}$)
Orthogonal Collocation	4.25613	5.43618	6.43821	7.26223
Finite Element	4.25602	5.43600	6.43809	7.2621

Tab. 2. TM_0 mode values of the propagation constants at different values of the optical power, by two numerical methods

TM_0	$\frac{\beta}{k_0}$ ($P = 200 \text{ W/m}$)	$\frac{\beta}{k_0}$ ($P = 400 \text{ W/m}$)	$\frac{\beta}{k_0}$ ($P = 600 \text{ W/m}$)	$\frac{\beta}{k_0}$ ($P = 800 \text{ W/m}$)
Orthogonal Collocation	3.66810	3.87808	4.02518	4.31220
Finite Element	3.66806	3.87801	4.02510	4.31212

B) Computing the electric field profiles for TE_0 , TM_0 and nonlinear guided modes, as functions of the total optical power P , for different nonlinearity mechanisms:

$$b = a, b = a/3, b = -a/2, r = 0.5$$

when for the TE_0 case we assumed $s = 2$, we were able to compare the maximum values of $\sqrt{\frac{a}{2}}E_x$ and H_x parameters for different values of the optical power, as presented in tab.3.

Tab. 3. The maximum values of $\sqrt{\frac{a}{2}}E_x$ and H_x parameters for different values of the optical power and two numerical methods

Mode	TE_0		TM_0	
Numerical Method	$(\sqrt{\frac{a}{2}}E_x)_{\max}$	$P(W/m)$	$(H_x)_{\max}$	$P(W/m)$
Orthogonal collocation	3.223	200	0.711	400
Finite Element	3.201	200	0.703	400
Orthogonal collocation	6.427	600	1.258	1000
Finite Element	6.413	600	1.250	1000
Orthogonal collocation	8.140	1000	1.621	1500
Finite Element	8.126	1000	1.601	1500

As a consequence, the field distributions dependent on the power P and there is, for the case $b = -a/2$, even a threshold value of the power ($P_{\lim} \cong 1150W/m$, according to the finite element method and $P_{\lim} \cong 1200W/m$ according to the orthogonal collocation method) which may be used in designing power limiting devices. The analysed properties may be of major importance for designing and optimising the devices based on MQW structures.

REFERENCES

1. M. D. Feit and J. Fleck, "Analysis of waveguides and couplers by the propagation beam method," *J. Opt. Soc. Am. A* **7**, pp. 73-79, 1990.
2. J. B. Hock and W. Burns, "Mode dispersion in diffused channel waveguides by the effective index method," *Appl. Opt.* **16**, pp. 113-118, 1977.
3. A. Sharma, "Numerical simulation methods for wave propagation through optical waveguides," *LAMP* **4**, pp. 1-8, 1993.
4. U. T. U. L. M. W. Biehlig, F. Lederer and A. D. Boardman, "Tm-polarized nonlinear guided waves in multilayer systems," *IEEE J. Quantum Electron.* **27**, pp. 238-242, 1991.
5. A. P. Zhao and S. R. Cvetkovic, "Finite element analysis of semiconductor laser arrays," *Microwave Opt. Technol. Lett.* **4**, pp. 247-250, 1991.
6. R. S. Cvetkovic and A. Zhao, "Finite element formalism for linear and nonlinear guided waves in mqw waveguides," *J. Opt. Soc. Am. B* **10**, pp. 1401-1407, 1993.
7. J. Kraus and P. P. Deimel, "Calculation of the propagation constant of the optical modes in multi-quantum-well structure," *IEEE J. Quantum Electron.* **26**, pp. 824-826, 1990.
8. S. Banerjee and A. Sharma, "Propagation characteristics of optical waveguiding structures by direct solution of the helmholtz equation for total fields," *J. Opt. Soc. Am. A* **6**, pp. 1884-1894, 1989.
9. A. S. S. Deb, "Nonlinear pulse propagation through optical fibers: an efficient numerical method," *Optical Engineering* **32**, pp. 695-699, 1993.
10. A. P. Zhao and S. R. Cvetkovic, "Finite element solution of nonlinear tm waves in mqw waveguides," *IEEE Photon. Technol. Lett.* **4**, pp. 1231-1234, 1992.
11. T. U. S. Ohke and Y. Cho, "Tm-mode propagation and form birefringence in gaas/algaas multiple quantum wells optical waveguide," *Opt. Commun.* **70**, pp. 92-96, 1989.

Optoelectronic visualisation and study of heat transfer from metal wires to water by a compact schlieren system

A. Petris^{*a}, D. Popa^b, A. Jianu^a, C. Popa^b and V. I. Vlad^a

^a Institute of Atomic Physics, NILPRP – Dept. of Lasers, Bucharest, Romania

^b University “Politehnica” Bucharest, Dept. of Physics, Romania

ABSTRACT

The aim of this paper is to present some results in the experimental study of heat transfer in fluids by optoelectronic methods. The thermal source was a thin metal wire (TMW) heated by electrical impulses and the propagation medium was the distilled water. We studied the following configurations for the thermal wave propagation and heat transfer:

1. horizontal TMW far from the water tank walls;
2. horizontal TMW in the proximity of a vertical metal wall and at a discontinuity introduced by another metal wire;
3. horizontal TMW with a controlled air bubble flow.

The phase perturbations in the transparent medium (water) were visualised by a compact schlieren system with laser diode illumination and were digitally processed in a PC. These results offer a better understanding of some progressively complex thermohydrodynamic phenomena. Some possible applications are in visualisation of the route to turbulence in these flows and in designing calibrated phase objects.

Keywords: Schlieren technique, heat transfer, multiphase turbulent flow

1. INTRODUCTION

For the majority of heat transfer in fluids and fluid dynamic problems, an analysis of the processes taking place in a flow field is only feasible with the help of flow and heat transfer visualisation. A flow picture provides some global information about the flow field, which is indispensable for a qualitative description of the phenomena. Based on the visualisation, further, more detailed and quantitative measurements may be performed.

The schlieren technique is a simple, noninvasive and real-time procedure for visualising phase non-uniformities in transparent media and their temporal and spatial evolution¹⁻⁴. A schlieren instrument records changes in the refractive index distribution of transparent media i.e the distribution of the refractive index gradient. Areas of equal grey level in the schlieren patterns describe zones of equal deflection angles of the light rays. Fluid flows are purely phase objects since their only effect is to produce a difference in optical path between various regions of the incident wavefront. The distribution of the refractive index gradient can be related to density, temperature, or pressure distributions within the flow.

We present the results in the visualisation of the heat transfer in water and in water with bubble flow, in different conditions, obtained with a compact schlieren system which use a red laser diode as light source.

2. EXPERIMENTAL SET-UP

The phase perturbations in the transparent medium (water) due to the thermal fronts propagation were visualised and recorded by the experimental arrangement shown in Fig. 1. The schlieren system has been setup with a single transverse mode laser diode (SDL 7501) as light source ($P = 15$ mW, $\lambda = 633$ nm) which provides an uniform and intense illumination. We also used a He-Ne laser ($P = 20$ mW, $\lambda = 633$ nm) to compare the quality of the schlieren images.

* Correspondence: Email: petris@ifin.nipne.ro ; Telephone: 40-1-423 1470 ; Fax: 40-1-423 1791

A "knife-edge" filter placed on a micrometric x-y translation stage allows the visualization of the refractive index gradient along any direction by suitable rotation, particularly the vertical or horizontal component of the refractive index gradient. A horizontal wire-type heater, placed perpendicular to the light beam direction, generates thermal fronts in a water tank with optical windows. A thermocouple sensor in contact with the heater measured the difference between heater and water temperatures. The schlieren patterns have been recorded using a CCD video camera connected to a VCR or to a PC with a frame-grabber, for further processing.

To study the influence of the bubble flow on the heat transfer, the experimental set-up was provided with a bubble generator consisting in a battery-supplied micro-pump, connected to a small diameter pipe placed under the heater. This generator allowed us to obtain single air bubbles at controlled time moments, correlated with the thermal fronts evolution.

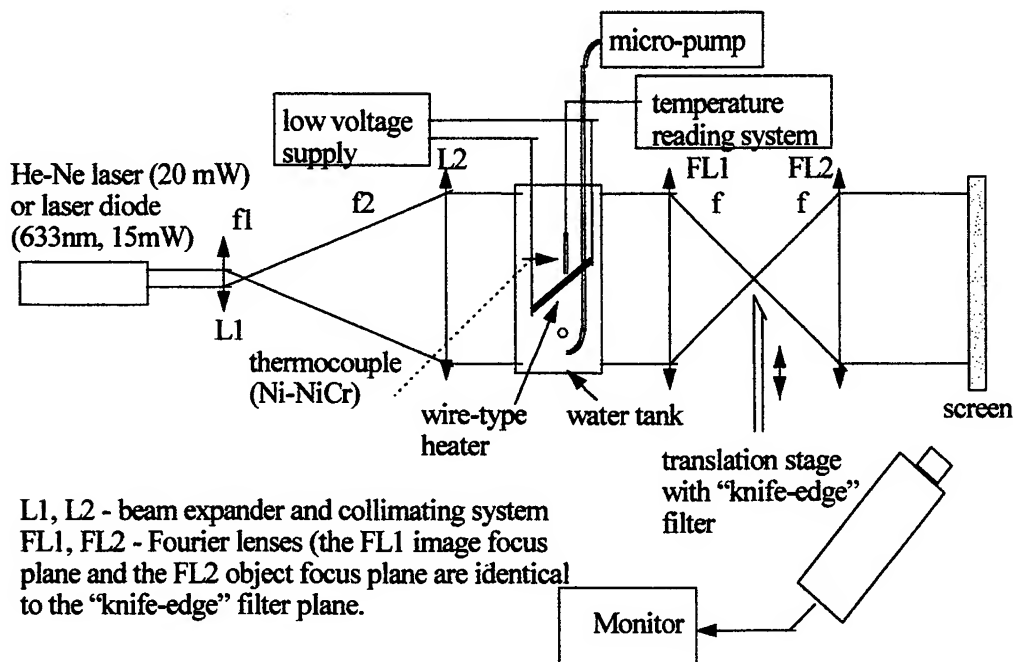


Fig. 1 Schlieren experimental set-up

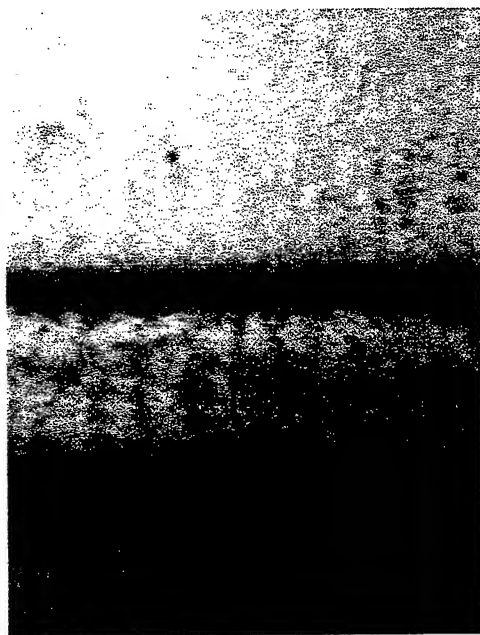
The images obtained in the experiments with the air bubble flow have been recorded using a video camera (Panasonic SVHS 625; recording speed 50 frames/s) with variable shutter time. The following exposure times have been used: 1/120, 1/250, 1/500s. The images recorded on the VCR have been digitised (colour, 24 bits or grey level, 8 bits).

3. EXPERIMENTAL RESULTS AND DISCUSSIONS

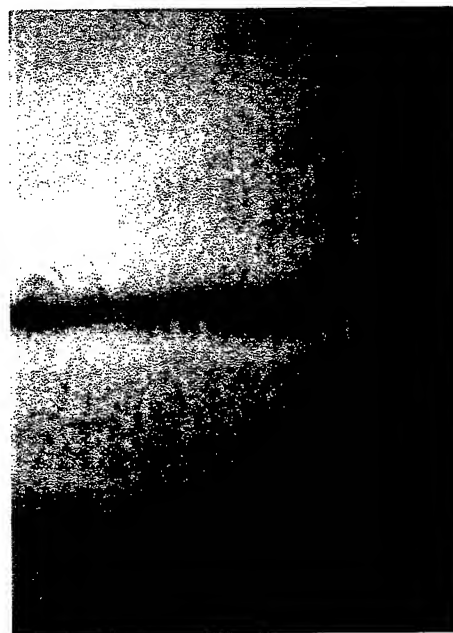
Schlieren technique was used to visualise the propagation of linear thermal fronts in distilled water and their distortions produced by: the presence of a vertical metallic wall; the change of the heater profile and the rising air bubbles.

The heater has been placed close to the bottom of the water tank. The motion of the thermal front has been continuously recorded by a VCR, from the moment it left the heater and until it arrived to the free surface of the water.

In Fig. 2a, b, c are shown snapshots of the rising thermal front. These images have been obtained by short heating (about 5 sec.) of the linear heater, increasing its temperature with approx. 5°C. The thermal front produced by the linear wire heater



(a)



(b)



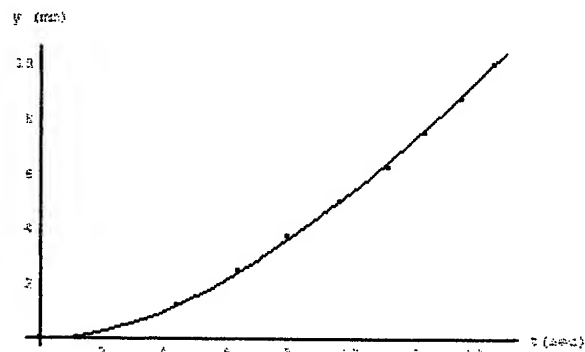
(c)

Fig. 2 Snapshots of the rising thermal front: a) the thermal front produced by the linear wire heater far from the walls of the water tank; b) the thermal front produced by the linear wire heater close to the metallic wall (the wire heater passes horizontal across the water tank and vertical along the metallic wall); c) the distortions of the thermal front produced by a non-uniformity created on the metallic heater.

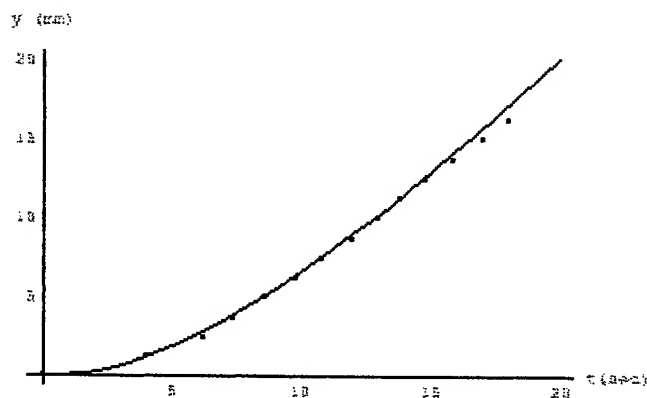
far from the walls of the water tank is shown in Fig. 2a, and close to the metallic wall of the tank, in Fig. 2b (the wire heater passes horizontal across the water tank and vertical along the metallic wall). The thermal fronts are the horizontal black bands in the middle of the image. Fig 2c shows the distortions of the thermal front produced by a non-uniformity created on the metallic heater (both diameter and heat capacity are changed along a region of the wire). The increasing of the heat capacity produce a delay in the building of the thermal front. The diameter of the heater has been changed by wrapping a small diameter metallic wire around the heater.

Experiments shown the influence on the building of the thermal front of both the heating duration and the amount of the heat dissipated in the wire heater. Propagation of the thermal front is strongly influenced by the previous heating cycles which are changing the water temperature as a whole and also its vertical gradient. These affect the Archimedic force and the heat transfer. After several heating cycles the heat accumulated in the top layers of the water produces a vertical temperature and density gradient inside the tank. As the thermal front is rising, the Archimedic force is lowering and the rising speed is going to zero, the thermal front is spread and the convection and diffusion mechanisms become dominant.

From a sequence of images of a rising linear thermal front (like that presented in Fig. 2a), recorded with a VCR and further acquired with a frame grabber, we were able to measure the distance traversed by the thermal front as a function of time.

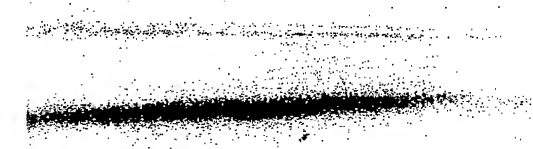


(a)



(b)

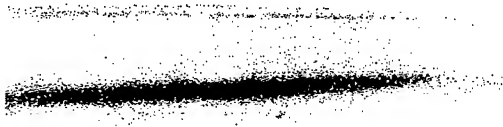
Fig. 3 The distance traversed by the thermal front as a function of time. The experimental data (dots) and the theoretical dependence (continuous line) for two heating temperatures: a) 2°C and b) 6°C).



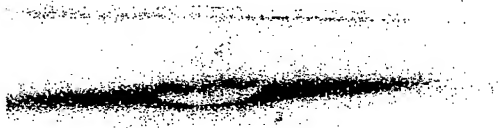
1 ($t=0$) – rising thermal front separated from the wire heater



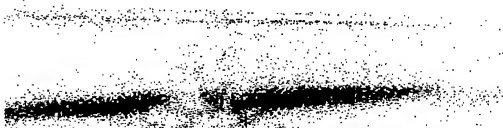
2 ($t=20\text{ms}$) – bubble in the field between the wire heater and the thermal front



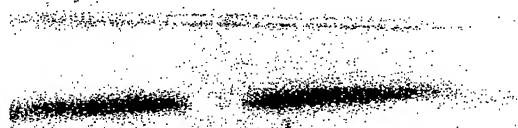
3 ($t=40\text{ms}$)



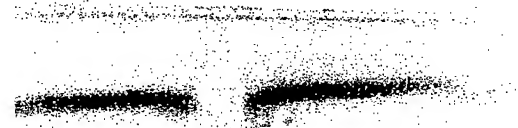
4 ($t=60\text{ms}$)



5 ($t=80\text{ms}$)



6 ($t=100\text{ms}$)



7 ($t=120\text{ms}$)



8 ($t=140\text{ms}$)



9 ($t=160\text{ms}$)



10 ($t=180\text{ms}$)

Fig. 4 Rising thermal front (separated from the wire heater) disturbed by the air bubble (heating temperature $\sim 5^\circ\text{C}$; exposure time = $1/120\text{s}$)

The dependencies obtained for two values of the heating temperatures of the heater (2°C and 6°C) are shown in Fig. 3a,b (dots). The experimental data show that for short times after heating the wire the rising of the thermal front due to the Archimedic force is dominant, so that in the first approximation for this case, thermal convection and diffusion may be neglected. As experiments suggested, we considered a simplified model according to which the heat transfer from the wire to the water layer from its vicinity creates a cylinder of heated water which after leaving the wire keeps for a given time an approximately constant diameter. A further simplification was to consider a constant density (temperature) inside the cylinder. This cylinder is moving accelerated by the Archimedic force up to a constant velocity determined by a resistive force proportional to the velocity. According to this simplified model the space – time function depends on two parameters, a and b :

$$y = (a/b)[\exp(-bt) - 1] + at \quad (1)$$

The best fit of the experimental data with Eq. 1, for $a = 1.45 \text{ mm/s}$, $b = 0.1 \text{ s}^{-1}$, respectively $a = 1.7 \text{ mm/s}$, $b = 0.11 \text{ s}^{-1}$ is shown in Fig. 3a,b (the continuous line).

In Eq. 1 the parameter a represents the asymptotic velocity of the thermal front, corresponding to the maximum slope of the space – time dependence in Fig. 3. As can be seen in Fig. 3b, for longer time intervals the propagation velocity is decreasing. This is due to the fact that thermal convection and diffusion become to play an important role. This fact is also shown by the spreading of the intensity distribution in the schlieren image due to the increasing of the cylinder diameter and the corresponding decreasing of the temperature gradient up to the disappearance of the cylinder (thermal front) image.

The heat transfer in multiphase multicomponent turbulent flows is an important and difficult problem for the safety of the nuclear power plants and chemical reactors. The distortions of the thermal front propagation produced by a single bubble flow were visualised with our schlieren system (Fig. 4). In this figure the vertical axis is reversed. The heating temperature was $\sim 5^\circ\text{C}$.

3. CONCLUSIONS

A compact schlieren system with red laser diode illumination, CCD camera recording and image computer processing was built. This system was used for visualisation of temporal and spatial evolution of the thermal fronts in water, for various experimental conditions. The experiments have shown that the schlieren method is capable of producing good contrast images of the refractive index changes for local heating as small as 1°C in the near vicinity of the heater. The experimental results for the propagation of a linear thermal front are in good agreement with the simple model we proposed. The study of the propagation of linear thermal fronts in liquids allows the investigation of more complex phenomena, like the turbulence appearing in multiphase multicomponent flows.

REFERENCES

1. W. Hauf, U. Grigull, "Optical Methods in Heat Transfer", in J. P. Hartnett, T. F. Irvine, Jr., Eds., *Advances in Heat Transfer*, Academic Press, New York, London, pp. 133 – 366, 1970
2. W. Merzkirch, *Flow Visualisation*, Academic Press, 1974
3. V. I. Vlad, N. Ionescu-Pallas, I. Apostol, "Accurate refractive index measurements using computerised Schlieren and focusing methods", *Proc. SPIE*, 1319, pp. 649 – 654, 1990, and *Rev. Roum. Phys.*, 36, pp. 915 - 922, 1991
4. V. I. Vlad, N. Ionescu – Pallas, I. Apostol, "Quantitative Schlieren method using digital image processing for supersonic flow characterization", *Proc. SPIE*, 1771, pp. 1771 – 1774, 1992

Wavelength assignment algorithms in all-optical networks

Claudiu Bulaceanu

PricewaterhouseCoopers - Management Consultants

ABSTRACT

We consider the problem of wavelength reuse assignment and of routing in all-optical networks. Since the capacity of number of wavelengths of current optical communication devices are restraint, the optical wavelength reuse is the only solution for this issue. The problem is NP-complete and therefore does not have one and only solution. Several algorithms were proposed along the years on this subject. In this work we develop a metric for Wavelength Assignment Algorithms (WAA) in all-optical networks like deBruijn networks for instance. We derive an upper bound of traffic corresponding to connections in such a network. The bound depends on the number of wavelengths, number of nodes and number of edges of the network respectively. We compare the bound with the simple shortest path algorithm to test its validity. The simulation test results show that it is feasible to get several all-optical connections to each node in a large network using a relatively limited number of wavelengths compared with the number of traffic sources.

Keywords: optical communications, algorithm, metric, upper bound of traffic

1. INTRODUCTION

In this work we develop a metric for Wavelength Assignment Algorithms (WAA) in all-optical networks. Compared to conventional optical networks where at each node an optical to electronic conversion and vice versa is made the all optical networks assume that no conversion is made at one node and the optical signal is just re-routed or converted to another wavelength at one node. Another effect is that no buffering is done at the intermediate nodes.

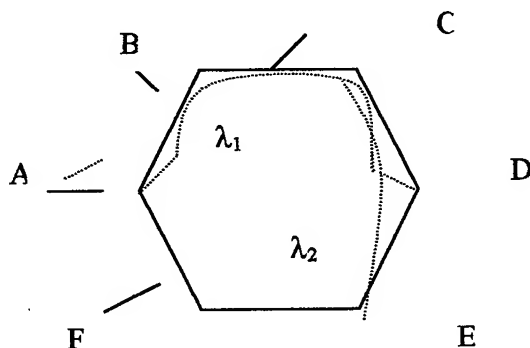


Fig. 1 A WDM all-optical network

In an all-optical network each connection must be assigned a specific path in the network and a wavelength which is the same on every link on the assigned path. Moreover, the wavelengths and paths assigned must be such that no two paths that share an edge are assigned the same wavelength.

The WAA problem has been considered earlier in [1-4]. Several heuristic algorithms have been proposed and their performance has been quantified via simulation.

A similar routing problem arises in circuit-switched telephone networks. Here, one has to route connections by selecting a path for each connection such that there is a circuit available to accommodate the call in every link on the path. In the

* Correspondence: email: claudiu.bulaceanu@ro.pwcglobal.com

optical model we must satisfy not only the constraint specific for switched networks but also the additional constraint that the same wavelength has to be assigned to the connection on every link in the path.

The routing problem in circuit-switched networks has been studied extensively. It is well-known that the routing problem can be formulated as an integer linear problem (ILP). It was shown that an upper bound on the carried traffic can be obtained by relaxing the ILP to a linear program (LP) and moreover that the bound holds for random offered traffic as well. Since the WAA problem in our model is a more constrained version of the routing problem in circuit-switched network, it is clear that this bound will also be an upper bound for the carried traffic in our network model. Our objective in this paper is to derive a better upper-bound.

We will first consider the case when we are given a fixed set of connections to be routed. We formulate the WAA problem as an integer linear program (ILP) where the objective is to maximize the number of connections that are successfully routed. If we relax the integrality constraints in this ILP we get an LP whose value represents an upper bound on the number of connections that can be successfully routed.

2. PROBLEM FORMULATION

The network is represented by an undirected graph G . We assume that all connections to be routed are full duplex, all links are bi-directional and a duplex connection is using a single wavelength λ .

Let N denote the number of source-destination (s-d) pairs in the network, M the number of links and A the number of wavelengths available on each link. For any WAA algorithm let $n_i, i=1, \dots, N$, denote the number of connections carried between source-destination pair i and n the N -vector (n_i) . Let ρ denote the total offered load, $p_i \rho, i=1, \dots, N$ the offered load between source-destination pair i and p the N -vector (p_i) . The offered load for the deterministic case is the number of connections that are available to be routed. In the random case it is expected that the number of connections to be in progress if one could successfully route all call arrivals.

Let P denote the total number of available paths on which connections can be routed. The set of paths will either be given or can be routed. The set of paths could either be given or can be computed given the graph G and the set of source-destination pairs.

Let $A=(a_{ij})$ be the $P \times N$ path s-d pair incidence matrix where

$$a_{ij} = \begin{cases} 1, & \text{if path } i \text{ is between source-destination pair } j \\ 0, & \text{otherwise} \end{cases} \quad (1)$$

Let $B=(b_{ij})$ be the $P \times M$ path-edge incidence matrix, where

$$b_{ij} = \begin{cases} 1, & \text{if link } j \text{ is on path } i \\ 0, & \text{otherwise} \end{cases} \quad (2)$$

A. The straightforward formulation

The operation of every WAA algorithm in an *optical network* can be represented by a $P \times A$ path-wavelength assignment matrix which we denote by $C=(c_{ij})$ where

$$c_{ij} = \begin{cases} 1, & \text{if the WAA algorithm assigns wavelength } j \text{ to path } i \\ 0, & \text{otherwise} \end{cases} \quad (3)$$

The optimal WAA algorithm for the deterministic case is found by solving the following ILP whose value we denote by $C_o(\rho, p)$.

The objective is to maximize the carried traffic

$$C_o(\rho, p) = \max \sum_{i=1}^N m_i \quad (4)$$

subject to

$$\begin{aligned} n_i &\geq 0, \text{ integer}, i=1, \dots, N \\ c_{ij} &\geq 0, \text{ integer}, i=1, \dots, P, j=1, \dots, A \end{aligned} \quad (5)$$

$$C^T B \leq 1_{\Lambda \times M}$$

is the capacity constraint and denotes that only one wavelength is used on a given link.

The traffic demands are

$$\begin{aligned} n &\leq 1_A C^T A \\ n_i &\leq p_i p \quad i=1, \dots, N \end{aligned} \quad (6)$$

where $1_{X \times Y}$ represents an $X \times Y$ matrix all of whose elements are unity and 1_X represents a $1 \times X$ matrix all of whose elements are unity.

The *circuit-switched network* operates as follows.

We represent the operation of any routing algorithm as a vector of path-flows $pf = (pf_i)$ where pf_i denotes the flow on path i . Then the optimal routing algorithm for the deterministic case is found by solving the following ILP whose value we denote by $C_c(\rho, p)$.

The objective is to maximize the carried traffic

$$C_c(\rho, p) = \max \sum_{i=1}^N m_i \quad (7)$$

subject to

$$\begin{aligned} n_i &\geq 0, \text{ integer}, i=1, \dots, N \\ pf_i &\geq 0, \text{ integer}, i=1, \dots, P, j=1, \dots, A \end{aligned} \quad (8)$$

$$fB \leq 1_M \Lambda \quad (9)$$

which denotes that not more than Λ units of flow on any link.

The traffic demands are

$$\begin{aligned} n &\leq 1_A C^T A \\ n_i &\leq p_i p \quad i=1, \dots, N \end{aligned} \quad (10)$$

It is easy to demonstrate that

$$C_o(\rho, p) \leq C_c(\rho, p) \quad (11)$$

As such the optical and circuit-switched traffic have an identical upper-bound.

3. BETTER UPPER-BOUND ALTERNATIVE

We will use a new graph G_a where each node corresponds to a path in G and two nodes in G_a are adjacent if the corresponding two paths in G share a common link. Therefore the WAA problem is transformed into assigning wavelengths to nodes in G_a so that no two adjacent nodes are assigned the same wavelength. As such a set of paths in G can be assigned a common wavelength only if the nodes in G_a form an independent set.

Let L be the number of maximal independent sets in G_a , let w_i be the number of wavelengths which are assigned to the nodes in independent set i by a WAA algorithm and w the R -vector (w_i) .

Let $D=(d_{ij})$ be the $P \times R$ path-independent-set incidence matrix

$$d_{ij} = \begin{cases} 1, & \text{if independent set } j \text{ contains path } i \\ 0, & \text{otherwise} \end{cases} \quad (12)$$

The ILP whose value we denote as $T_o^\Lambda(\rho, p)$ can then be formulated as follows to maximize the carried traffic

$$T_o^\Lambda(\rho, p) = \max \sum_{i=1}^N m_i \quad (13)$$

subject to

$$w_i \geq 0, \text{ integer}, \quad i=1, \dots, L$$

the following capacity restriction implies that there are no more than Λ units of flow on a link

$$\sum_{i=1}^L w_i \leq \Lambda \quad (14)$$

and the traffic demands restriction

$$\begin{aligned} pf &\leq wD^T \\ n &\leq fA \\ n_i &\leq p_i \rho, \quad i=1, \dots, N \end{aligned} \quad (15)$$

4. RANDOM TRAFFIC DEMANDS

Let ρ_i denote the offered traffic to s - d pair i in Erlangs. If calls arrive at random and have random holding times, under the operation of an WAA algorithm the network is in a random state which we denote by $m = (m_1, m_2, \dots, m_N)$ where m_i is the number of calls in progress between pair s - d pair i . The set of feasible states for this network when the number of available wavelengths is Λ , which we denote by S_Λ , is the set of all non-negative integer N -vectors n for which the $T_o^\Lambda(\rho, p)$ ILP is feasible.

There exists non-negative integer vectors $w \in Z^L$ and $f \in Z^P$ such that

$$mA + (w \cdot f)B \leq \Lambda C \quad (16)$$

Where

$$A = (I_{N \times N} \quad 0_{N \times P} \quad 0_N^T) \quad (17)$$

$$B = \begin{bmatrix} 0_{L \times N} & -D^T & 1_L^T \\ -A & I_{P \times P} & 0_P^T \end{bmatrix} \quad (18)$$

and

$$C = (0_N \quad 0_P \quad 1)$$

Using the carried traffic for any WAA algorithm R for this network satisfies

$$\frac{1}{\Lambda} T_R(\rho, p) \leq T_o(r, p) \quad (19)$$

where $r = \rho/\Lambda$ and $T_o(r, p)$ is the value of the following linear program

$$T_o(r, p) = \max \sum_{i=1}^N s_i \quad (20)$$

subject to

$$\begin{aligned} sA + tB &\leq C \\ s &\leq pr \end{aligned} \quad (21)$$

The corresponding circuit-switching LP obtained by normalizing the objective function and each of the constraints in the $U_c(\rho, p)$ program by Λ and dropping the integrality constraints is

$$T_c(r, p) = \max \sum_{i=1}^N s_i \quad (22)$$

subject to

$$\begin{aligned} s &\leq tA \\ tB &\leq 1_M \\ s &\leq pr \end{aligned} \quad (23)$$

The blocking probability $B_R(\rho, p)$ for any WAA algorithm is related to its carried traffic by

$$T_R(\rho, p) = \rho(1 - B_R(\rho, p)) \quad (24)$$

Therefore

$$B_o(r, p) = 1 - \frac{T_o(r, p)}{r} \quad (25)$$

and

$$B_c(r, p) = 1 - \frac{T_c(r, p)}{r} \quad (26)$$

are the lower bounds for the blocking probability of any WAA algorithm in the wavelength-routing and circuit-switching cases.

Proposition 1. Let E be the total number of links in a circuit-switched network G . Let H denote the minimum number of edges in a shortest-path between all desired source-destination pairs between which there is nonzero traffic. Since a connection takes at least H circuits and there are a total of EA circuits, the total number of connections that can be supported is $\leq EA/H$.

Thus, the maximum number of connections that can be supported per wavelength is $T_c(r, p) \leq E/H$.

Proposition 2. Let's consider a circuit-switched network G with exactly one path between every s - d pair. Let ρ denote the total offered traffic to such a network G with traffic pattern vector p . Let ρ_j denote the offered traffic to link j in the network and let $\rho_{\max} = \max_j \rho_j$.

Let R be the maximum traffic offered per length so that the blocking probability is $\leq b$. Then

$$R_{I,p}(G) = \frac{\rho}{\rho_{\max}} \quad (27)$$

5. SIMULATION RESULTS

We simulated two networks, one with 5 nodes and the other with 20 nodes.

The 5-nodes network

Let's consider the network shown in Fig. 2. We will denote the pentagon network with G shown in Fig. 2.

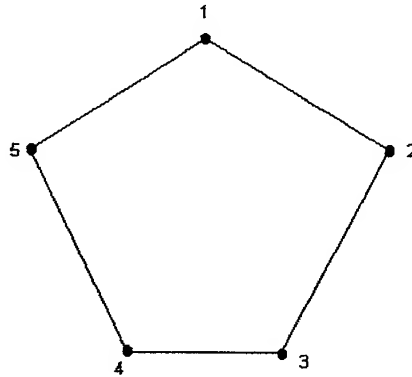


Fig. 2 The 5-nodes network

We easily identify the source-destination pairs of interest indexed from 1 to 5 to be (1, 3), (2, 4), (3, 5), (4, 1) and (5, 2), i. e. each node communicates with two other nodes in the network. The paths of interest are then 123, 1543, 234, 2154, 345, 3215, 451, 4321, 512, 5432, and will be indexed from 1 to 10.

The maximal independent sets in the path graph are {1, 2}, {3, 4}, {5, 6}, {7, 8}, {9, 10}, {1, 7}, {3, 9}, {5, 1}, {7, 3}, {9, 5}. For simplicity we will consider the uniform traffic case, i. e., $p_i = 1/5$, $i = 1, \dots, 5$.

Obviously the maximum cardinality of an independent set is 2 and hence $T_o(r, p) \leq 2$. The shortest path has two links ($H=2$) and there are $E=5$ links in the graph; hence, from Proposition 1 we get $T_{CP}(r, p) \leq 5/2$.

Solving the linear programs yield

$$T_o(r, p) = \begin{cases} r, & 0 \leq r \leq 2 \\ 2, & r > 2 \end{cases} \quad (28)$$

and

$$T_c(r, p) = \begin{cases} r, & 0 \leq r \leq 5/2 \\ 5/2, & r > 5/2 \end{cases} \quad (29)$$

Fig. 3 plots $T_o(r, p)$ and $T_{CP}(r, p)$ as a function of r .

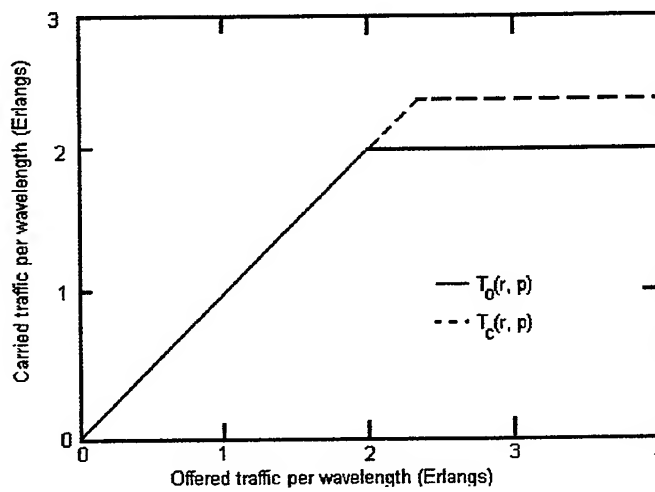


Fig. 3 Carried traffic versus offered traffic for the above five-node network. $T_o(r, p)$ is the upper bound without wavelength converters while $T_c(r, p)$ is the upper bound with wavelength converters

The 20-nodes network

We will consider now a larger network of 20 nodes which is close from a topology point of view to the original Arrant network.

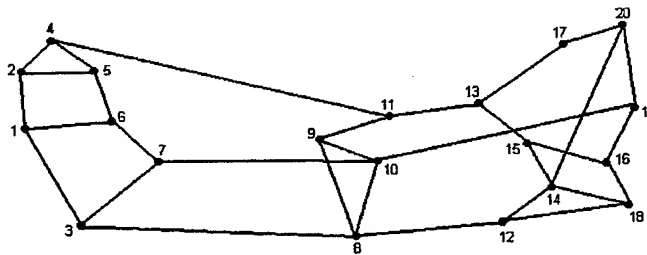


Fig. 4 A 20-node network

We will further consider the class of algorithms that use only shortest paths. Let the s - d pairs of interest be $\{1, 13\}$, $\{2, 7\}$, $\{3, 15\}$, $\{6, 8\}$, $\{11, 14\}$, $\{4, 20\}$, $\{5, 19\}$, $\{9, 18\}$, $\{10, 17\}$, $\{12, 16\}$. There are 14 shortest paths as follows: 3 shortest paths between s - d pairs $\{2, 7\}$ and $\{6, 8\}$ and a single shortest path between the other 8 s - d pairs. The path graph consists of 14 nodes corresponding to these shortest paths and has 43 maximal independent sets.

We will consider the uniform traffic case. Fig. 5 shows the carried traffic and blocking probability as a function of offered traffic.

$$\text{Hence, } T_c(r, p) = T_o(r, p) = \min(r, 7r/10 + 1, 3r/10 + 3, 6) \quad (30)$$

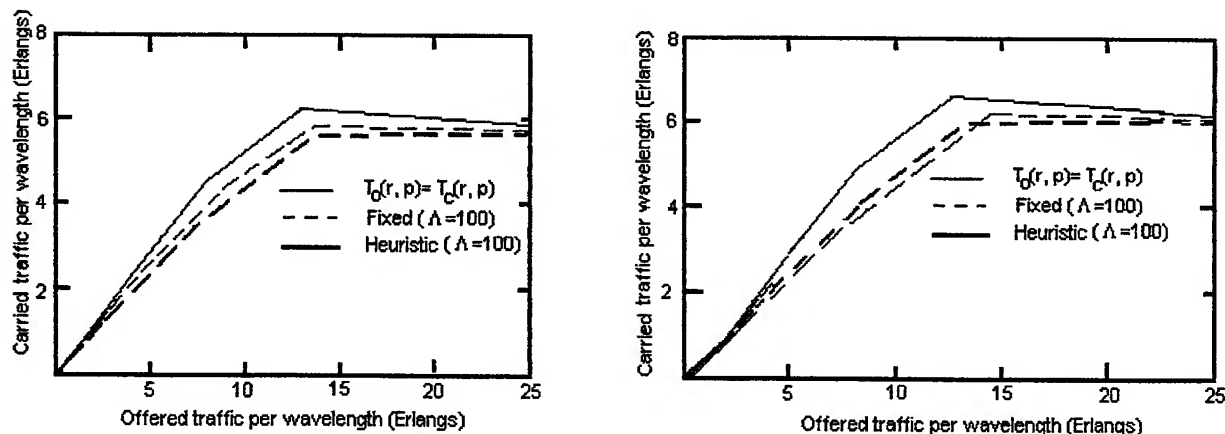


Fig. 5 Carried traffic versus offered traffic for a 20-nodes network assuming uniform traffic $T_o(r, p)$ is the upper bound on carried traffic without wavelength converters and $T_{CP}(r, p)$ is the upper bound with wavelength converters

6. CONCLUSIONS

Although the bound presented can be obtained by solving a linear program the number of variables in the linear program may be an exponential function of the number of source-destination pairs in the case of optical networks without wavelength converters. However, since the bound is on a per-wavelength basis, it need be computed only once and can be scaled easily with the number of wavelengths. It can be used as a metric against which the performance of different heuristics can be compared.

Using two examples we showed that this bound yields a better bound on the carried traffic than the bound for the corresponding circuit-switched network, or equivalently the corresponding optical network using dynamic wavelength converters.

We can infer the following from the above results:

- 1) One can build large all-optical networks without wavelength converters and support a modest number of connections per node with a reasonable number of wavelengths. From our simulation, for a 128 nodes network using 32 wavelengths we can support an average of 10 full-duplex connections per node. Another example shows that for a 1000 node random network we can support an average of 5 connections per node with average degree 4 using 32 wavelengths.
- 2) The wavelength converters offer a 10-40% increase in the amount of reuse achievable for our sampling with a range from 16 to 1000 nodes for a small number of nodes (10 to 32).

REFERENCES

1. K. Ball, "Routing in linear lightwave networks", PhD dissertation, Columbia Univ. 1993, CTR Tech.
2. R. Ramaswami, "Multi-wavelength lightwave networks for computer communications", *IEEE Commun. Mag.*, **31**, pp. 78-88, feb. 1993.
3. R. K. Pankaj, "Architectures for linear lightwave networks", PhD dissertation, MIT, Cambridge, MA, 1992.
4. K. C. Lee and V. O. K. Li, "A wavelength-convertible optical network", *IEEE/OSA J. Lightwave tech.*, **11**, pp. 962-970, May/June 1993.
5. M. Gondran and M. Minoux, *Graphs and Algorithms*, New York, Wiley, 1986.

SESSION IV

Technologies in Optoelectronics and Related Fields

ULTRASONIC INVESTIGATION OF PULSED LASER INTERACTION WITH SOLID TARGETS

I. Apostol^{* a}, R. Stoian^a, R. Dabu^a, A. Stratan^a, A. Serbanescu Oasa^b, C. Angelescu^a

^aNational Institute for Laser, Plasma and Radiation Physics,
Laser Dept., PO Box MG-36, R 76900, Bucharest

^bTechnical University, Sibiu

ABSTRACT

During the pulsed high power laser target interaction a local heating or material ablation takes place in function of incident laser energy. In both cases a stress wave is induced in the material volume with characteristics determined by the phenomena taking place in the interaction region. Analyses of the detected acoustic wave first peak amplitude (longitudinal wave) and especially of the region of the transversal wave appearance resulted in a method of interaction regime characterisation, ablation threshold determination and multipulse processes in-situ monitoring.

Key words: laser-material interaction, laser induced acoustic waves, ablation threshold, melting threshold, preablative phenomena

1. INTRODUCTION

The wide spread of laser applications in material processing is due to the very different phenomena that can be induced at the material surface under the action of laser radiation. We shall mention some of them: local heating, changes in surface morphology and microstructure, surface desorption, surface cleaning, surface melting, surface vaporisation and material ablation. The appearance of each of the mentioned phenomena depends of the intensity of the laser radiation incident on the target surface.

As a consequence in different applications of laser radiation the most important parameters to be selected are laser energy, fluence and intensity, because the complex processes taking place at the material surface in the interaction region depends on them. Between the material heating, appearing at lowest levels of laser intensity and plasma formation, as the phenomena appearing at the extremes of the energy scale, the other mentioned phenomena (surface modification, surface desorption, melting and vaporisation) are possible to appear. For a certain application to obtain a specific interaction regime is important and it can be controlled by incident laser beam parameters. So, the study of the threshold values for the appearance of these phenomena is important.

In our contribution we use the acoustic waves induced in the complex process of laser-matter interaction to analyse the phenomena taking place in the interaction region¹. The laser induced acoustic waves shape and amplitude depend on the phenomena that are taking place in the interaction region. As a consequence we have used the study of the shape and amplitude dependence on the incident laser energy and fluence to evidence the phenomena appearing at the surface and to estimate the ablation² and the melting threshold. We have studied the interaction of laser radiation with the most common metals used in industry, steel and aluminium.

^{*} Correspondence: Email: IAPOSTOL@ifin.nipne.ro

2. LASER GENERATION OF ACOUSTIC WAVES

2.1 Thermoelastic regime

The acoustic wave study was realised as a function of incident laser energy which is the parameter that controls the amplitude of the elastic waves induced in the interaction process, but also depending on the interaction regime. At small incident laser intensities at the surface of the material only a local absorption of radiation and a local material heating takes place. The calculation of the laser induced temperature variation induced at the target surface under the action of laser radiation ($\lambda = 266$ nm, $t_p = 15$ ns, incident energy of 15 mJ) the maximum value of temperature raise will be 96°K, at the end of the laser pulse³. The calculated temperature variation in depth, under the material surface, on the normal in the center of the irradiation spot, for the same irradiation conditions, at the end of the laser pulse, is given in Table 1. It is obvious that the temperature variation induced under the action of laser radiation decreases very fast with depth. To

compare, the calculated thermal diffusion length for an aluminium target [$l_T = (\frac{1}{4} \pi K t_p)^{1/2}$, where t_p is the laser pulse length] is of the order of $2 \cdot 10^{-6}$ m.

ΔT (°K)	96.04	53.71	26.81	11.81	4.56	1.52	0.44
Depth (cm)	0	0.0001	0.0002	0.0003	0.0003	0.0005	0.0006

Table 1

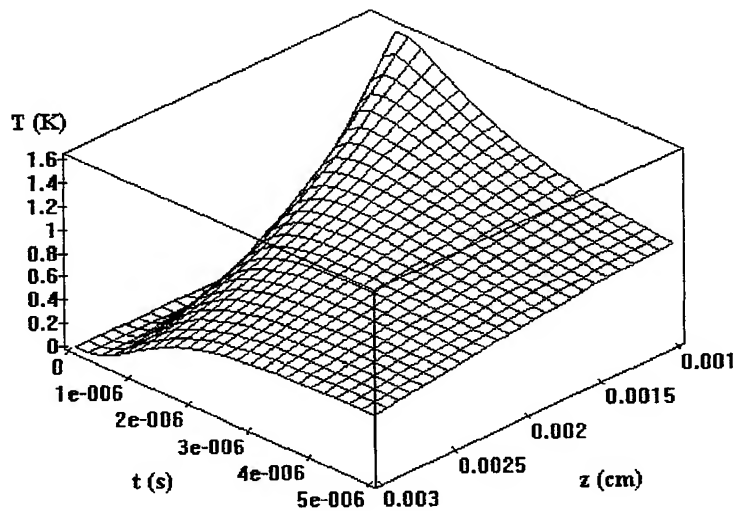


Fig. 1 The maximum temperature variation below the target surface

The calculated temperature variation, as a function of time after the quenching of the laser pulse ($t > t_p$) and position in the target depth situated between 10 and 30 μ m below the target surface on the normal in the irradiation spot centre is given in Fig.1. The short time temperature growth of the surface layer caused by the absorption of laser radiation is accompanied by thermal expansion that causes thermoelastic strains, equivalent to the sudden insertion of a volume ΔV of material immediately below the surface, that is proportional to incident energy E . This is the so called thermoelastic regime in which the local heating (without phase change) induces an elastic stress in the bulk of the material. In this case the acoustic wave source is created just under the material surface, in a volume limited by the laser radiation absorption depth and laser spot area. The source is pure expansion and can generate in the bulk of the material only compressional (longitudinal, L) waves equally in all directions. However the close proximity of the surface introduces some conversion of reflected waves to the shear modes (S). In case of the directivity patterns calculated for aluminium¹, there is no radiation normal to the surface; in this direction the source appears to cancel out with its reflection in the surface. Also, both L and S directivities gives lobes with cylindrical symmetry about the normal. The maximum longitudinal wave amplitude is radiated at an angle of $\approx 64^\circ$ and the maximum shear at $\approx 30^\circ$ and the shear is zero at 45° . So, in the epicentre the

propagation of the thermoelastic laser induced acoustic wave implies a depression of the back surface of the target, and a positive step appears at the arrival of the transversal (shear) acoustic wave. In this case the acoustic wave source is formed just under the material surface.

2.2 Ablation regime

For laser irradiation of target surface with high laser intensities, material removal from the target surface takes place. At more higher laser intensities ionisation of the expelled material is produced and a plasma is formed in front of the target. The interactions of laser pulse, plasma and surface are complex processes, but for the purposes of ultrasonic generation, ablation will be considered solely from the point of view of the material removal from the surface which induces an impulsive recoil force, by the transfer momentum from the surface. In this case the ultrasound source is formed just on the material surface. In calculations the ablation is modelled as a normal force with $\delta(t)$ time dependence. In this case most of the longitudinal wave energy is directed on the normal and the shear or the transversal mode has a maximum at 30° . This propagation geometry implies that the back surface of the metal rises away from the source. In this case the acoustic wave source is formed on the material surface.

From the short description it is obvious that the two regimes of acoustic source formation on the target surface under the action of laser radiation are corresponding to different phenomena taking place in the laser-target interaction region. Also the propagation directivity in the two cases is different. In our work laser ultrasonics has been used to evidence the interaction regime of the laser radiation with the target surface and to evaluate the thresholds separating the appearance of different phenomena, respectively the melting and the ablation threshold.

3. EXPERIMENTS

The experimental set-up permits irradiation of aluminium and steel targets with different irradiation wavelengths (Fig. 2). The laser beam was incident on the front surface of the target while at the opposite side a piezoelectric transducer was bonded. The transducer signal was displayed on a 200 MHz bandwidth Tektronix oscilloscope.

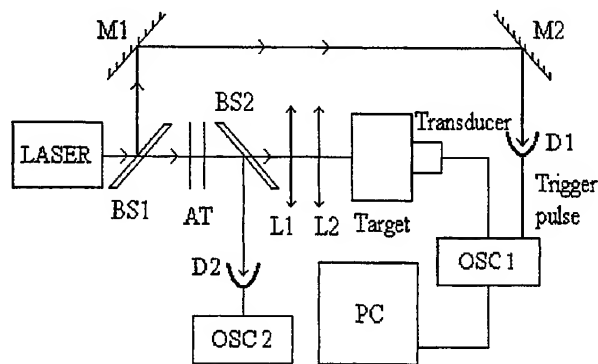


Fig. 2 The experimental set-up

We have worked with a YAG:Nd laser working on fundamental wavelength and armonics ($\lambda = 1.064 \mu\text{m}$, $\tau_p = 15 \text{ ns}$; $\lambda = 532 \text{ nm}$, $\tau_p = 12 \text{ ns}$; $\lambda = 266 \text{ nm}$, $\tau_p = 10 \text{ ns}$). The BS1 and BS2 beam splitters are deflecting the laser beam on a calorimeter and a pulse shape detector for energy value and laser beam time evolution monitoring. To select the proper range of incident laser energies calibrated attenuators (AT) are inserted on the beam path. The cylindrical targets were irradiated on the front surface and on the back surface was inserted the ultrasound detector. Signal acquisition was realised on the Tektronics oscilloscope coupled to a PC. The oscilloscope signal was triggered by the irradiation laser pulse front and the delay between the laser pulse and the acoustic signal represents the time required for propagation of the acoustic signal from the front surface of the target to the back surface of the target. The irradiation geometry permits a proper selection of the incident laser energy and laser intensity by choosing the laser beam energy and incident spot area. Some typical ultrasonic waves induced in aluminium targets under the action of laser radiation are given in Fig. 3, 4.

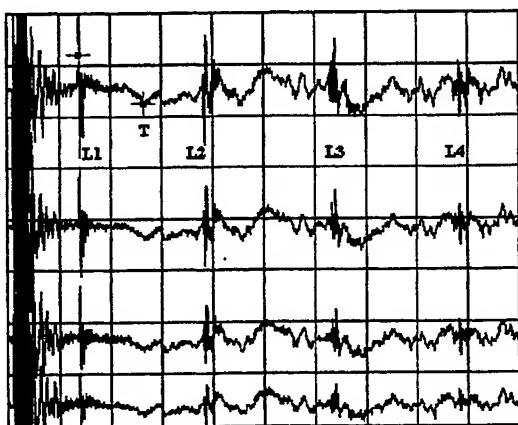


Fig. 3 Laser induced acoustic waves

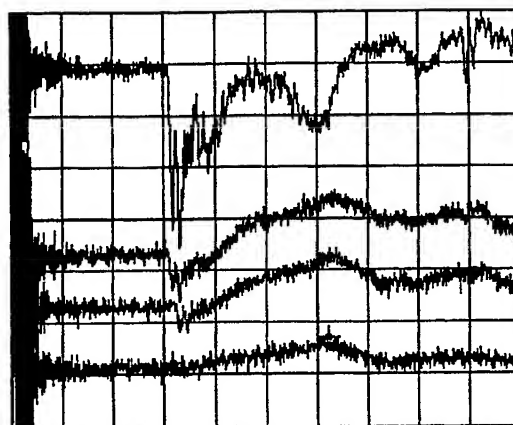


Fig. 4 Acoustic wave shape variation as a function of incident laser energy and fluence

In Fig. 3 are evident the reflections of the acoustic waves on the back and front surfaces of the target and the longitudinal and the transversal (shear) waves are marked. Fig. 4 represents the acoustic waves induced under the action of laser wavelength of 532 nm for incident laser energies of 3.2 mJ (1.99 J/cm^2), 8.39 mJ (5.92 J/cm^2), 14.52 mJ (8.9 J/cm^2) and 27.65 mJ (17.2 J/cm^2). It is evident that the amplitude of the acoustic waves depends on the incident laser energies, but also the pulse shape is changing. In this case only the lowest incident energy corresponds to a pure thermoelastic regime. For the highest presented incident energy we have pure ablation and for the other two waves we have a competition between the two phenomena.

3 RESULTS AND DISCUSSION

In the complex process of laser target interaction acoustic waves are created in the material volume and their shape and amplitude depend on the phenomena that take place in the interaction region, respectively on the mechanism of the acoustic wave generation.

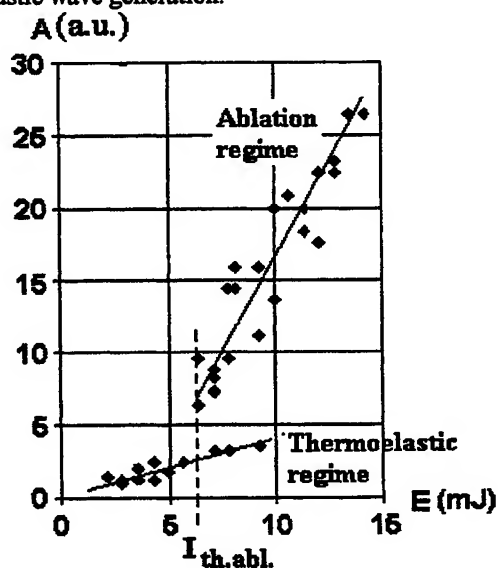


Fig. 5 Maximum amplitude of the longitudinal laser induced acoustic waves as a function of incident laser energy, for different spot area and respectively laser intensity

As we have presented the local heating of the material surface followed by a volume expansion produces essentially tangential stress¹, with no energy transport on the normal direction due to the reflection on the free surface. The longitudinal pulse induces a depression of the back surface of the target and the shear arrival induces an elevation of the surface. In the ablation regime also a plasma is formed on the target surface. On the back surface a positive step pulse of high amplitude is detected and the shear wave latter arrival has an opposite effect.

The dependence of the maximum amplitude of the longitudinal acoustic wave, in thermoelastic and in ablation regime, as a function of incident laser energy, for different spot area and respectively laser fluence, is given in Fig. 5. It can be observed that two regions of amplitude-energy dependence, with different slopes appear. A slow dependence on incident laser energy corresponds to the thermoelastic regime and a faster increase corresponds to the ablation regime. For a certain irradiation regime the acoustic wave amplitude depends only on the incident laser energy. But for the same incident energy the acoustic wave amplitude is much more higher if the laser fluence is higher than the ablation threshold. This result is evident if we consider the dependence of the longitudinal acoustic wave amplitude dependence on the laser fluence for a constant incident laser energy (Fig. 6).

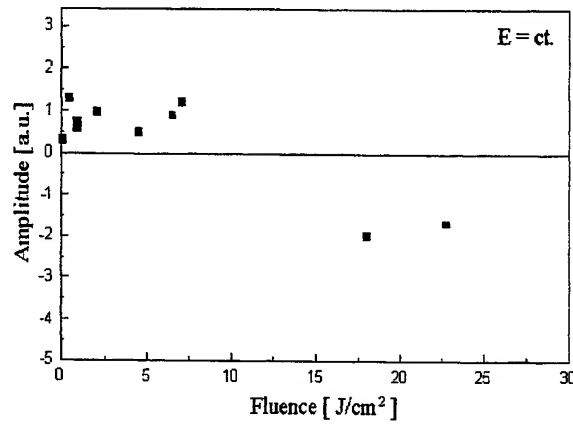


Fig. 6 Longitudinal acoustic wave amplitude dependence on the laser fluence for a constant incident energy

It can be observed that the acoustic wave amplitude is constant if the incident energy is constant, and only laser fluence is changed. But if also the interaction regime is changed, the amplitude of longitudinal acoustic wave becomes of opposite sign. By comparing the detected acoustic waveforms for different incident laser energies and fluences on the target surface, the ablation threshold was estimated as the domain for which the ablation acoustic source will compensate and then dominate the thermoelastic one.

It is considered that material ablation appears when laser intensity is high enough that material vaporisation takes place⁴.

$$I_{vap} = \frac{1}{2(1-R)} \left(\frac{\pi k \rho c_p}{\tau_p} \right)^{1/2} T_{vap}$$

where k -thermal conductivity, ρ -target density, c_p -heat capacity, R -target reflectivity and τ_p is the irradiation time equal with the laser pulse duration.

In Tab. 1 are given the calculated values for the vaporisation threshold and the ablation threshold fluence values estimated from the analyses of the acoustic waves for aluminium targets. A good agreement between them can be observed. Also a lower ablation threshold was determined for the targets with a low polishing quality.

In case of steel targets the calculated value for vaporisation threshold is $8 \cdot 10^7$ W/cm² and the ablation threshold values estimated from acoustic wave signal are situated between $4 \cdot 10^7$ W/cm² and $2 \cdot 10^8$ W/cm² and depend on the target surface quality.

In case of steel targets the calculated value for vaporisation threshold is $8 \cdot 10^7 \text{ W/cm}^2$ and the ablation threshold values estimated from acoustic wave signal are situated between $4 \cdot 10^7 \text{ W/cm}^2$ and $2 \cdot 10^8 \text{ W/cm}^2$ and depend on the target surface quality.

Tab. 1 Laser ablation threshold fluence and intensity estimation for an aluminium target

Wavelength (nm)	Vaporisation threshold fluence (J/cm^2)	Vaporisation threshold intensity (W/cm^2)	Threshold fluence (J/cm^2)	Threshold intensity (W/cm^2)	Observations
1 060	11.5	$7.9 \cdot 10^8$	10	$7 \cdot 10^8$	polished
532	6.4	$5.8 \cdot 10^8$	5.5	$5.2 \cdot 10^8$ $2 \cdot 10^8$	polished unpolished
248	11.5	$5.85 \cdot 10^8$	8 3	$4 \cdot 10^8$ $1.5 \cdot 10^8$	polished unpolished

Also laser induced melting of metals was proposed to be detected by analysing the photoacoustic signals induced in the sample⁴. It was considered that the limited ability of fluids to transmit shear stresses would result in a saturation of the transversal wave. If we consider the dependence of the amplitude of the transversal wave on the laser incident energy (Fig. 7) it presents a saturation region, corresponding, probably, to the melting of the material in the interaction region. This saturation corresponds to the region among $2.2 \cdot 10^8 \text{ W/cm}^2$ to $3.6 \cdot 10^8 \text{ W/cm}^2$. The calculated melting threshold intensity is in this case $1.7 \cdot 10^8 \text{ W/cm}^2$, very close to the lowest value. The region of lowering of the amplitude of the transversal wave, among 15-20 mJ, is considered to be due to the phenomena taking place for energies close to the ablation threshold like surface desorption, defects vaporisation, surface cleaning, melted particle expulsion, etc. It can be called as "preablative region". The ablation was considered to correspond to the negative region, with a threshold of $(5.2 \pm 0.2) \text{ J/cm}^2$, in good agreement with the value estimated from longitudinal acoustic waves analyses for the same wavelength. The acoustic wave induced under the action of laser radiation in the same irradiation conditions is very reproducible. From this reason the monitoring of the acoustic waves can give information about the reproducibility of the irradiation conditions (incident energy, surface quality, etc.). If a great number of laser pulses are incident on the same region from the material surface we have observed the lowering of the ablation threshold due to primary surface damages, which are improving surface absorption. This effect is very important for the optical components for high power lasers.

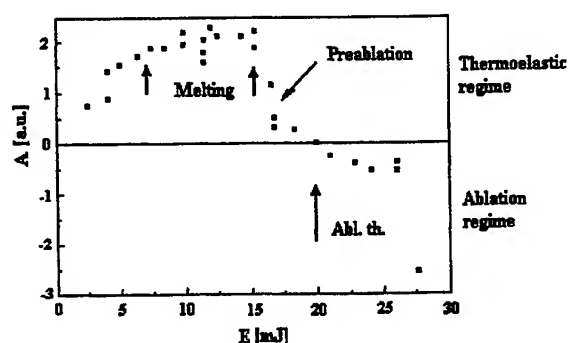


Fig. 7 Transversal wave amplitude of the laser induced acoustic waves as a function of incident laser energy

Laser cu excimer (248 nm)
 $E_{th} = (7 \pm 2) \text{ mJ}$, $\rho_{th} = (3.5 \pm 0.2) \times 10^8 \text{ J/cm}^2$
 $I_{th} = 1.7 \times 10^8 \text{ W/cm}^2$

4. CONCLUSIONS

Detection and analyses of acoustic waves induced in solid targets in the complex process of laser target interaction was used to evidence the interaction regime. Ablation and melting thresholds were measured for aluminium and steel targets and are in good agreement with the calculated values for the vaporisation and melting thresholds. It was evidenced that the threshold values depend very much on the quality of the irradiated surface and a very reproducible acoustic signal was registered for the same irradiation conditions.

REFERENCES

1. R.J. Dewhurst, D.A. Hutchins, S.B. Palmer and C.B. Scruby, Laser Generation of ultrasound in metals, *Res. Tech. in NDT*, v.7, ch. 8, *Read. Press*, New York, London, 1982
2. I. Apostol, G. Teodorescu, A. Serbanescu-Oasa, D. Dragulinescu, I. Chis and R. Stoian, Acoustic wave generation in the process of CO₂-TEA laser radiation interaction with metal targets in air, *SPIE Proc.*, vol. 2461, pp. 154-159, 1995
3. Anca Serbanescu Oasa, Generarea cu laser a ultrasunetelor in materiale, Doctoral theses 1997
4. K.S. Carslow, J.C. Jaeger, *Conduction of Heat in Solids*, Oxford Univ. Press. London, 1959
5. M. Mesaros, O.E. Martinez, C.M. Bilmes and J.O. Tocho, Acoustic detection of laser induced melting of metals, *J. Appl. Phys*, 81, pp. 1014-1021, 1997

Resonant-enhanced light transmission through metal nanochannels

S. Astilean^{*a}, Ph. Lalanne^b, M. Palamaru^a

^a Optics and Spectroscopy Dept., Babes-Bolyai University, 3400 Cluj-Napoca, Romania

^b Laboratoire Charles Fabry de l'Institut d'Optique, CNRS, B.P. 147, F-91403 Orsay Cedex, France

ABSTRACT

Zero-order transmission silver gratings of very narrow and deep enough slits exhibit exceptional transmission properties in visible and near-infrared light. By using a rigorous electromagnetic analysis of light diffraction, we show that the transmission enhancement occurs as a result of a resonant interaction of the incident light with surface plasmons located inside the grating slits.

Keywords: grating, metallic film, surface plasmon, waveguide

1. INTRODUCTION

Advances in materials processing technology now permit the production of highly regular structures on various substrates with well-defined profiles and periods of less than 100 nm. These structures can be integrated into optoelectronic devices adding a new dimension to device operation and control. A fundamental constraint in manipulating light in wavelength-scale structures is the extremely low transmittance of apertures smaller than the wavelength of the incident radiation. As predicted by Bethe¹, for an optically thick metal film perforated with a single hole, of which the diameter is less than the wavelength of light, the optical transmission is expected to be very small, and to be proportional to the fourth power of the ratio of the hole diameter and the optical wavelength $(r/\lambda)^4$, where r is the hole radius and λ is the wavelength of radiation impinging directly on the hole.

However, when the metal is perforated with an array of such subwavelength holes, the optical transmission is enhanced by several orders of magnitude. Indeed, it has been recently demonstrated that an array of cylindrical holes of sub-wavelength diameter perforated in optically thick, metallic films display highly unusual transmission spectra in the visible and near-infrared region^{2,3}. For radiation of wavelength as large as ten times the diameter of the holes, the absolute transmission efficiency calculated by dividing the fraction of light transmitted by the fraction of the surface area occupied by holes, is ≥ 2 . These unusual optical properties are apparently due to the coupling of light with plasmons on the surface of periodically patterned metal film. The surface-plasmon (SP) is a trapped electromagnetic wave, which propagates along the metal/dielectric interface and decays exponentially with distance away from the interface⁴. The excitation of SPs on metal reflection gratings is a well-known subject of gratings. For instance, several recent papers dealing with metal reflection gratings, have theoretically and experimentally identified particular local-field configurations in the form of 'stationary surface plasmons'⁵ or 'surface-shape resonances'⁶. In contrast with the widely investigated SPs propagating along corrugated metal surface, less attention has been paid to the electromagnetic interaction of SPs waves propagating inside of deep enough slits or holes of nanometric transversal dimensions existing in metal *transmission* structures.

In this paper we study the mechanism of transmission enhancement through very narrow slits (nanochannels) patterned in metallic films. The electromagnetic interactions of SPs 'located' in slits and their implications in the transmission will be demonstrated. Intuitively, inside the slit a stationary coupled-wave is generated by superposition of SPs reflected between walls. We will adopt the terminology of coupled-plasmon (CP) to call this coupled-wave confined inside the gap. Strong resonance effects can occur if the slit dimensions commensurate the spatial variations of CP field.

2. NUMERICAL RESULTS

Our approach is based on the analysis of light diffraction in a lamellar silver transmission grating of very narrow slits. The grating is a mono-periodic metallic structure consisting of spatially separated silver rods of rectangular cross section placed on silica substrate (see Fig. 1). The width of the air gap (slit) between rods is denoted by w , the period and the thickness of the grating are Λ and d , respectively. This periodic structure is illuminated at normal incidence ($\theta=0$) by a plane electromagnetic wave of TM polarization (the magnetic-field vector is parallel to rods). In response to the incident

field, the grating will give rise a diffracted field in the region above and below it and also a stationary field pattern inside it.

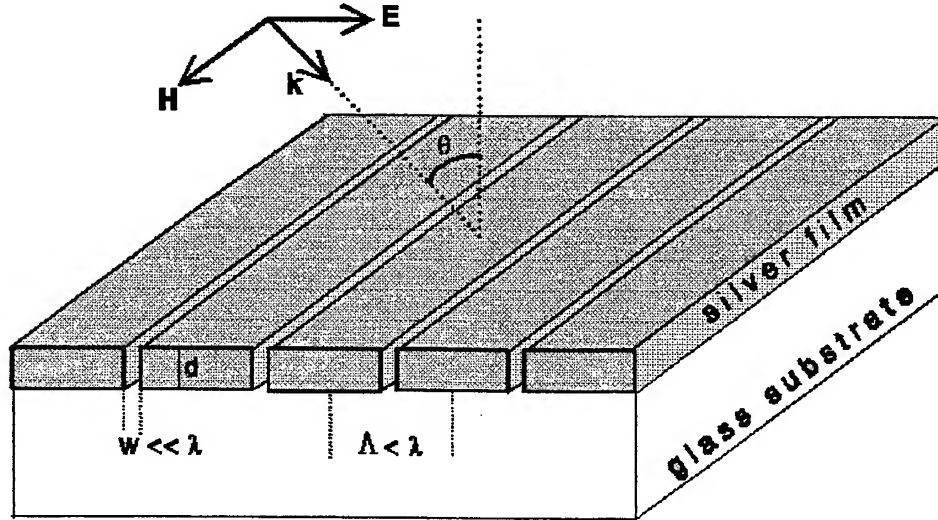


Fig. 1 Schematic view of the lamellar transmission metallic grating studied in this paper

2.1. Far-field optical response of gratings

In a first step, we focused on the computation of the far-field optical response (transmitted and reflected optical signals). For that purpose we have used the rigorous coupled-wave analysis (RCWA) of electromagnetic diffraction⁷. The RCWA is a versatile and efficient tool for describing the diffraction of electromagnetic waves by periodic structures. Recently the convergence performance of the RCWA to calculate the far-field optical response was substantially improved in the case of TM polarization⁷. Motivated by the results of Ref. [2] and [3], we investigated only the response of silver transmission gratings in the near infrared region of spectrum (between 0.9 μm and 2 μm). In order to theoretically isolate the grating response from the substrate effects, we consider both freestanding lamellar structures and grating structure on silica substrate of refractive index $n = 1.5$. The period of gratings was fixed at $\Lambda = 0.9 \mu\text{m}$. Therefore all freestanding structures are zero-order transmission gratings at wavelengths $\lambda > \Lambda = 0.9 \mu\text{m}$ and all structures on silica substrate are zero-order transmission gratings only at wavelengths $\lambda > n\Lambda = 1.35 \mu\text{m}$ (zero-order grating means that all diffracted orders, other than zeroth forward-transmitted and backward-reflected order are evanescent). This study considers silver as a metal of finite conductivity for which the dielectric response disperses with frequency and for the purpose of our calculations the dielectric functions of silver have been obtained by interpolation from values tabulated in Ref [8]. Losses to metal associated with the imaginary part of the refractive index, physically manifested as carrier heating in the metal, may be also extracted from RCWA by a relation of the form $A = 1 - T - R$, where T and R mean the transmission (T) and reflection (R) efficiencies, respectively and where the incident power is considered normalized to unity.

Fig. 2 shows the typical response of a freestanding grating with the slit width varying between 0 and 100 nm. The energy flow through grating (Fig. 2a) and the energy dissipation into metal (Fig. 2b) undergoes sharp modulation, contributing to dips in the reflected signal (Fig. 2c). The transmission displays some very sharp peaks for which the absolute efficiency is *greater than the unity*. The absolute efficiency is here calculated by dividing the zero-order transmission efficiency to the fraction of slit within one period. In particular, for strongest peak we found that the grating transmits 10 times more light of 1.433 μm wavelength than impinged directly on their slits. Note that the slit has only 32 nm width, nearly 45 times much smaller than the wavelength of incident light. That is what we call a very narrow slit or nanochannel.

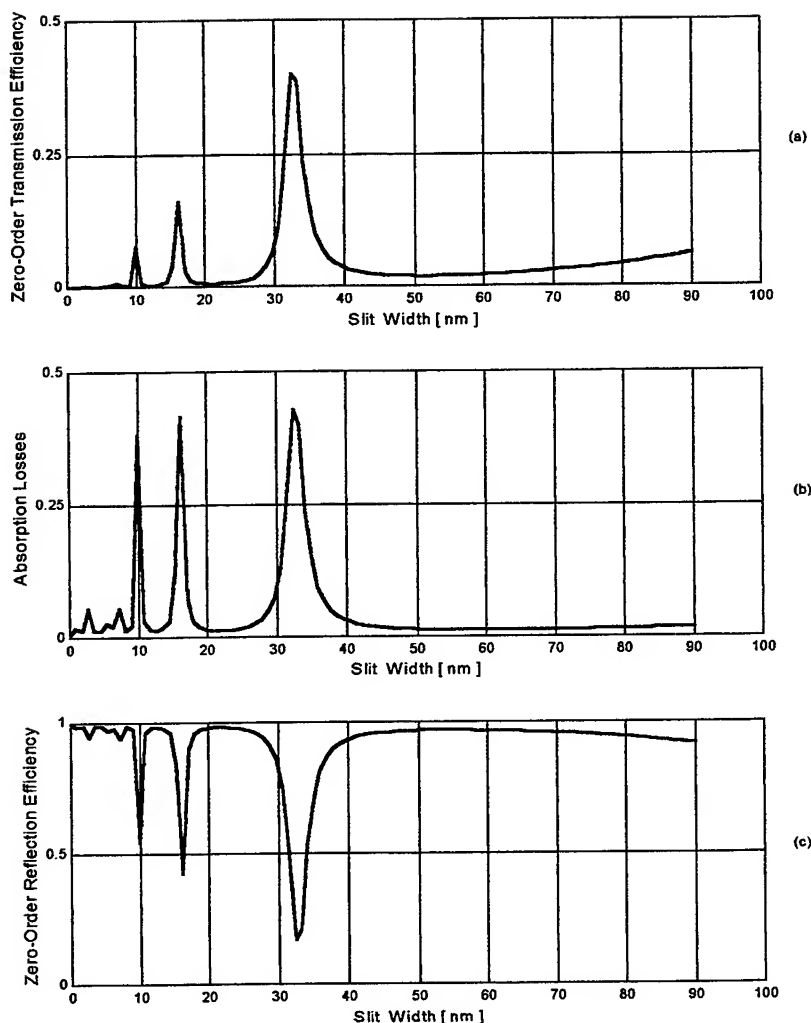


Fig. 2 Optical response of freestanding gratings as a function of the slit width: (a) transmission; (b) absorption; (c) reflection. The fixed grating parameters are: the period $\Lambda = 0.9 \mu\text{m}$, the thickness $d = 1.8 \mu\text{m}$ and the wavelength $\lambda = 1.433 \mu\text{m}$ (light is normally incident and TM-polarized).

Fig. 3 shows the transmission as a function of grating thickness for a fixed slit width ($w = 90 \text{ nm}$) and TM polarized light of $1.433 \mu\text{m}$ wavelength. Fig. 4 shows the transmission spectrum between $0.9 \mu\text{m}$ and $1.8 \mu\text{m}$ wavelength for a grating of fixed geometry ($d = 1.8 \mu\text{m}$, $w = 90 \text{ nm}$). One of the interesting features observed in Figs. 2 and 3 is the modulation of transmitted signals with the variation of geometrical and physical parameters. Note that the transmission resonances appear only at well-defined grating thickness and light wavelength.

Both freestanding gratings and gratings on a silica substrate are considered in Fig. 3 and Fig. 4. The substrate narrows and shifts the resonances to a lower grating thickness (see Fig. 3) but the most pronounced change is observed in Fig. 4 where the total forward-diffraction efficiency drops suddenly at the wavelength $\lambda = n\Lambda = 1.35 \mu\text{m}$. For $\lambda > n\Lambda$ the grating becomes a zero-order grating (Rayleigh-type anomaly) and the zero-order carries a considerable fraction of the incident energy (see the peak resonance located at $\lambda = 1.633 \mu\text{m}$).

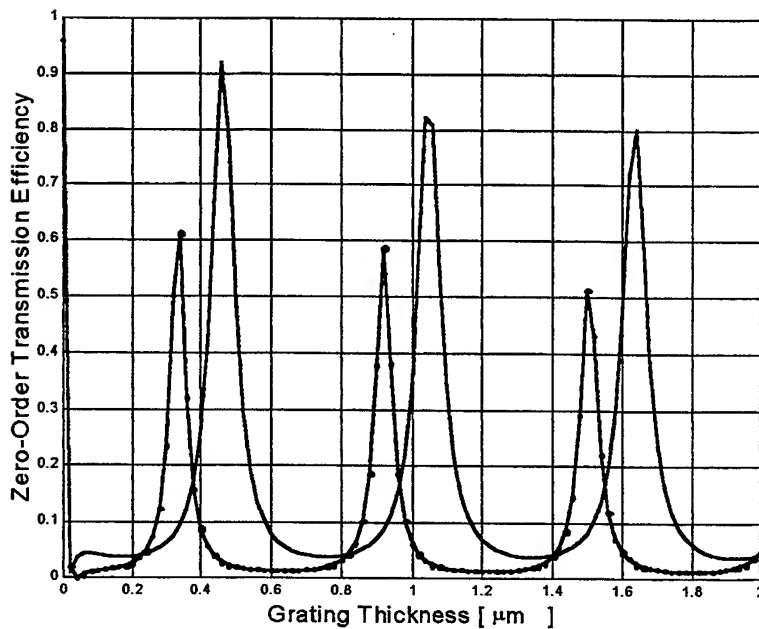


Fig. 3 Transmission response of zero-order gratings to the excitation with normally incident TM-polarized light of $\lambda = 1.433 \mu\text{m}$ wavelength as a function of the grating thickness (solid line: freestanding gratings; dash-dot line: gratings on silica substrate). The fixed grating parameters are: period $\Lambda = 0.9 \mu\text{m}$ and slit width $w = 90 \text{ nm}$.

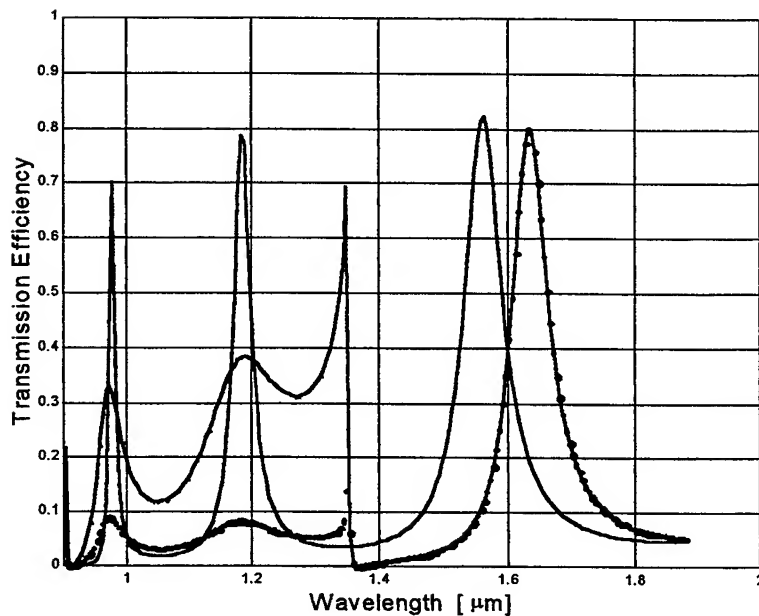


Fig. 4 Transmission spectra of a grating normally illuminated with TM-polarized light (solid line: freestanding grating; dash-dot line: grating on silica substrate). The fixed grating parameters are: period $\Lambda = 0.9 \mu\text{m}$, thickness $d = 1.8 \mu\text{m}$, and slit width $w = 90 \text{ nm}$.

2.2. Near-field optical response of gratings

In order to gain physical insight into this unusual behavior of gratings of very narrow slits, we examine the near-field electromagnetic responses of few particular gratings. The surface field of SP appears as a natural solution of Maxwell's equations in metal gratings. We will map this fields by using RCWA also. However, the standard RCWA is inappropriate to represent local fields quickly varying inside of gratings. Recently, a new approach to accurately calculate electromagnetic fields inside of metallic grating by RCWA has been proposed⁹. This new approach consists in Fourier

expanding the field components which are continuous at the grating boundaries. In our case these are the magnetic field H

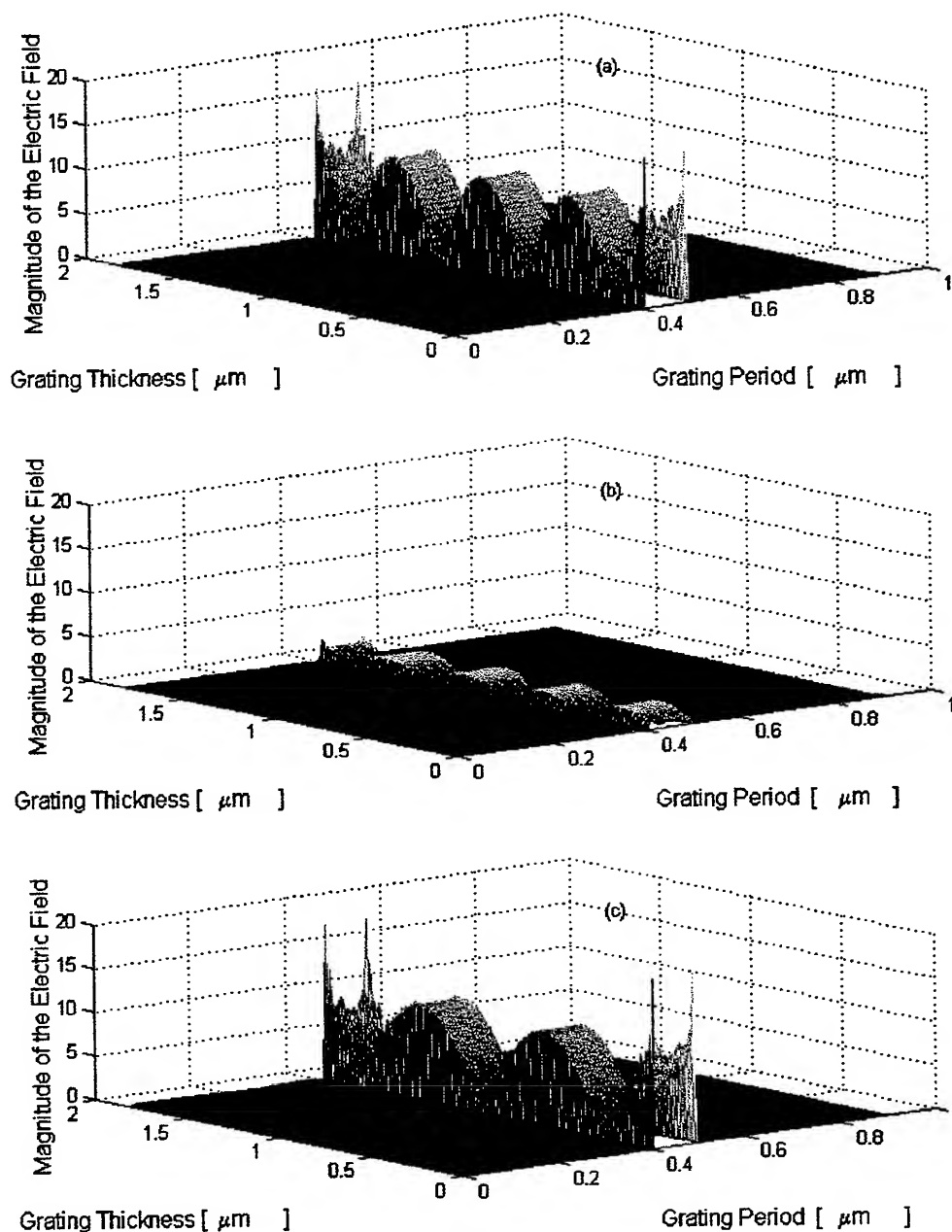


Fig. 5 Magnitude of the electric field $|E|$ computed in a rectangular grid of uniformly distributed points ($5 \times 5 \text{ nm}$) over the whole period and grating thickness: (a) freestanding grating at resonance ($\lambda = 1.183 \mu\text{m}$); (b) freestanding grating out of resonance ($\lambda = 1.053 \mu\text{m}$); (c) grating on silica substrate at resonance ($\lambda = 1.633 \mu\text{m}$). The grating parameters are $\Lambda = 0.9 \mu\text{m}$ (period), $d = 1.8 \mu\text{m}$ (thickness) and $w = 90 \text{ nm}$ (slit width).

(oriented parallel to the rods) and the electric displacement vector \mathbf{D} (oriented perpendicular to the rods). From the computation of \mathbf{D} , the electric field \mathbf{E} inside the slits (perpendicular to the metal walls) is simply derived by a constitutive relation. Finally we have computed the electric field $|\mathbf{E}|$ in a rectangular grid of uniformly distributed points (5×5 nm) over the whole period and grating thickness, with more densely sampled near and at the surface of grating, where the variation of wavefield is rapid (Fig. 5). We normalized the electric fields by taking the free-space impedance Z_0 ($Z_0=377 \Omega$) as a unity.

3. DISCUSSION

One interesting feature observed in Figs. 2, 3 and 4 is the series of maxima shown by the transmitted signal for some specific geometrical and physical parameters; the grating resonates only for some specific slit widths, depths and incident wavelengths. On the other hand, all maps of Fig. 5 illustrate also that the local field is practically confined inside of the slit and shaped as like the *fundamental mode* of a waveguide. Fig. 5a and 5b show the magnitude of the electric field $|\mathbf{E}|$ in two distinct cases: (a) the grating is excited at the resonance operating with 0.8 efficiency in transmission and (b) the grating is excited out of resonance operating practically in reflexion. There are distinct differences between the local field configurations in these two cases. As can be seen in Fig. 5a, the resonance is characterized by field antinodes at each open ends of the slit. The local field inside the slit is periodically enhanced up to 10 times. On the contrary, in Fig. 5b the local field exhibits nodes at the input side and antinodes at the output side of slits and any notable field enhancement exists, excepting the wedge singularities. However, the field singularities situated at the output side are removed due to the formation of nodes across the output boundary. Clearly, only some particular field configurations are responsible for the transmission enhancement. These configurations can occur whenever the slit contains an integral number of half-wavelength, a condition that may be expressed by a Fabry-Perot relation: $m \lambda_{cp} / 2 = d$, where λ_{cp} is the wavelength of the fundamental mode (CP mode), d is the thickness of the grating (cavity length) and m is an integer. From the thickness at which the slit becomes a resonant cavity, we can obtain the wavelength of CP mode. For example, freestanding gratings of $1.8 \mu\text{m}$ thickness excited at the resonance with light of $\lambda=1.183 \mu\text{m}$ can accommodate inside their slits CP of $\lambda_{cp} = 0.9 \mu\text{m}$ wavelength. It might seem conceivable, therefore, that when the width of the gap between the metal walls is much smaller than the transversal decay length of SP, the surface waves interact and form that standing coupled-wave (CP) inside the gap. As the slit width is increased, the electromagnetic coupling between rods are negligible and as a result an uniform 'electrostatic' field governs inside the slit. Other field distributions calculated when the lateral dimension of the slit is not much smaller than the transversal decay length of SP ($w > 200$ nm), show a superposition of SP field with an uniform field. Fig. 5c shows the distribution of the electric field $|\mathbf{E}|$ in the case for a grating on silica substrate at resonance.

The metallic grating being an efficient converter of incident light to oscillatory energy of electrons it is not surprising that an efficient incoupling of light into waveguiding structure is observed. However, for a finite conductivity metal there are two distinct processes able to operate: polarization (induction) surface currents across the rods and radiative damping of strongly localized surface plasmons (CP mode). We envision the interaction between light and the grating of very narrow slits ($w \ll \lambda$) as follows. The light of TM-polarization, normally incident on the metal transmission grating can excite *directly* only the SPs located on the lateral walls of the slit, \mathbf{E} being perpendicular to walls. For a gap sufficiently small, the SPs from each metal side interact and a CP state occurs in the gap. Our results prove strong resonant effects generated by the variation of this electromagnetic coupling. Indeed, CP modes can resonate and then mediate the light trapping into the slits, providing the enhancement of the light transmission through the metal structure. In fact, at the resonance, the field located over the input grating surface transfers its energy into a CP mode and then a concentrated energy stream can propagate through the grating plane. Consequently, although the transmission grating represents a periodical arrangement of isolated and opaque metal objects, a kind of transparency may be induced. Therefore the grating of very narrow slits can act for well-defined parameters as an open, resonant structure, tightly connected by the CP mode which carry and radiate almost all incident bulk light. This is a new phenomenon in the sub-wavelength scale metal structures. We emphasize that this phenomenon is present only where the gap between two metal walls is sufficiently small ($w \ll \lambda$), and where the optical properties of metal nanostructures appear to be dominated by very localized plasmon interactions. Here, due to the finite conductive of metal (on the contrary to the fundamental mode of perfect metallic gratings), the CP fundamental mode strongly depends on the aperture dimension, especially when apertures are much smaller than the wavelength. The net result is that the transmission properties of real metallic films perforated by small apertures strongly differ from those of perfect conductors.

4. CONCLUSIONS

In conclusion, a resonant cavity-enhanced light transmission mechanism is theoretically interpreted for operation with visible light. It is shown that under appropriate boundary conditions, the nanochannels behave as open Fabry-Pérot resonant cavities delivering a high photon flux, and that the coupling between the incident light and the CP mode supported by the channel is strongly controlled by waveguide resonances.

The wavelength at which the large transmission enhancement occurs can be tuned by making a proper choice of the grating period and slit width, by varying the refractive index of the dielectric medium adjacent to the metal, or by changing the incident angle. Such a tunability, together with the high transmission even at subwavelength scale, make such metallic structures very attractive in a number of applications, including subwavelength photolithography, near-field microscopy, wavelength-tunable filters, optical modulators, and flat-panel displays¹⁰.

Our theoretical results give quantitative support to the idea that the high transmission efficiency recently observed through sub-wavelength metal holes is an resonant effect mediated by the excitation of CP modes^{2,3}. Generally speaking, these effects must be also present in the visible spectrum for many composite and colloidal metallic media including nanometric cavities. Also they explain the dramatic changes observed in the optical response of a layer of random silver islands when interparticle separation distance is in the order of 100 nm. Moreover, local field enhancements are known to cause a variety of important optical effects, such as surface-enhanced Raman scattering and enhanced second harmonic generation. Further investigations will be necessary to determine the full potential of this phenomenon and its relation with the near-field molecular spectroscopy and nonlinear optical effects.

REFERENCES

1. H. A. Bethe, "Theory of diffraction by small holes", *Phys. Rev.* **66**, pp. 163-182, 1944.
2. T. W. Ebbesen, H. J. Lezec, H. F. Ghaemi, T. Thio, and P. A. Wolff, "Extraordinary optical transmission through sub-wavelength hole arrays", *Nature* **391**, pp. 667-669, 1998.
3. H. F. Ghaemi, T. Thio, D.E. Grupp, T. W. Ebbesen, and H. J. Lezec, "Surface plasmons enhance optical transmission through subwavelength holes", *Phys. Rev.* **58**, pp. 6779-6782, 1998.
4. H. Raether, *Surface plasmons on smooth and rough surfaces and on gratings*, Springer-Verlag, Berlin Heidelberg, 1986.
5. M. B. Sobnack, W.C. Tan, N. P. Wanstall, T. W. Preist, and J. R. Sambles, "Stationary surface plasmons on a zero-order metal grating", *Phys. Rev. Lett.* **80**, pp. 5667-5670, 1998.
6. T. López-Ríos, D. Mendoza, F. J. Garcia-Vidal, J. Sánchez-Dehesa, and B. Pannetier, "Surface shape resonances in lamellar metallic gratings", *Phys. Rev. Lett.* **81**, pp. 665-668, 1998.
7. Ph. Lalanne and G. M. Morris, "Highly improved convergence of the coupled-wave method for TM polarization", *J. Opt. Soc. Am. A* **13**, pp. 779-784, 1996.
8. E. D. Palik (ed.), *Handbook of Optical Constants of Solids*, Academic Press, Orlando, 1985.
9. Ph. Lalanne and M. P. Jurek, "Computation of the near-field pattern with the coupled-wave for transverse magnetic polarization", *J. Mod. Optics* **45**, pp. 1357-1374, 1998.
10. T. Kim, T. Thio, T. W. Ebbesen, D. E. Grupp, and H. J. Lezec, "Control of optical transmission through metals perforated with subwavelength hole arrays", *Opt. Lett.*, **10**, pp. 256-258, 1999.

Correspondence: e-mail: sastil@hera.ubbcluj.ro
tel.: +(40) 064405300

Modern procedures for chemical cleaning of corroded carbon steel equipment

Ileana-Hania Plonski^{a*}, Stefania-Floriana Spiridon^a, Maria Robu^a,
Carmen Doman^b, Mariana Tudorache^b, Mihaela Bobu^b, Emilian Mateescu^b,
Frank Schneider^c

^aInstitute of Optoelectronics, IOEL-SA, P. O. Box MG-22, Bucharest, Romania

^bS. C. THERMOELECTRICA S. A., Bucharest Electrocentral Branch, Bucharest, Romania

^cInstitute of Solid State and Material Research, IFW, D-01277, Dresden, Germany

ABSTRACT

Modern procedures have been elaborated taking into account the laboratory findings and developments of the past two decades concerning the factors increasing the solubility of iron oxides in the cleaning agent and conditioning improving the characteristics of the protective layer, both having in mind the present state of corrosion in romanian power energetic plants. The basic reagent formulae consists in citric acid, hidro-chloric acid, ferrous sulfate as dissolution activator and a corrosion inhibitor, operating at T 80-85 oC. The removal of thick corrosion deposits is achieved in a basic step-by-step procedure, the number of steps depending on the layer thickness and on the degree of damage of the underlying base metal. After chemical cleaning, a passive magnetite film will be formed under special conditioning of water with long-chained amines.

Keywords: corrosion, scale, crud, iron oxide deposits, chemical cleaning, heat transfer

1. INTRODUCTION

Corrosion is a damaging inevitable factor in every energetic plant; it represents the difference between trouble-free operation and costly down-time. The synergistic effect of corrosion deposits and mechano-thermic stress during operation lead to failures of the tubular arrangements simultaneously with a decrease of the heat transfer.

A practical approach to improve the heat transfer and to minimize losses due to replacement of damaged equipment is the periodic removal of the corrosion deposits using chemical agents and the formation of resistant-protective films at the metal surface.

2. STATE OF CORROSION AT CARBON STEEL COMPONENTS IN ROMANIAN POWER PLANTS

From the chemical cleaning standpoint the romanian thermoelectric power plants and heating stations can be divided in three categories resulted from the duration and the operating conditions.

1. Pre-operational mill-scale removal performed on new carbon steel components corroded in atmosphere during storage and in water during the hydraulic tests, when thin films of hematite cover the metal surface.
2. Chemical cleaning of deposits formed in operation under normal conditions as concerns the control and monitoring of water chemistry and fuel quality. Generally, the heating boilers of 1 Gcal/h in the Autonomous Administration of Thermal Energy Distribution (RADET) meet this case.
3. Eventually, the chemical removal of thick deposits (sludge and crud) grown on carbon steel on both fire and water sides due to improper operative conditions.

Severe situations arised in a Hot Water Boiler of 100 Gcal/h as that schematically shown in Fig. 1.

- a. Some romanian thermoelectric power plants use as fuel black oil with high content of sulphur which during combustion transforms in sulfuric acid; an acidic deposit of more than 3 cm thickness is formed attacking the material from the fireside and lowering the heat transfer. The local temperature increases from approximately 600 °C to more than

* Correspondence: Fax: (00401) 423.25.32, Phone: (00401) 780.34.69/1110, E-mail: plonski@k.ro

800 °C, transforming the corrosion products in an insulator, aggressive, deposit. At temperatures higher than 650 °C the carbon steel becomes an improper material and is highly corroded.

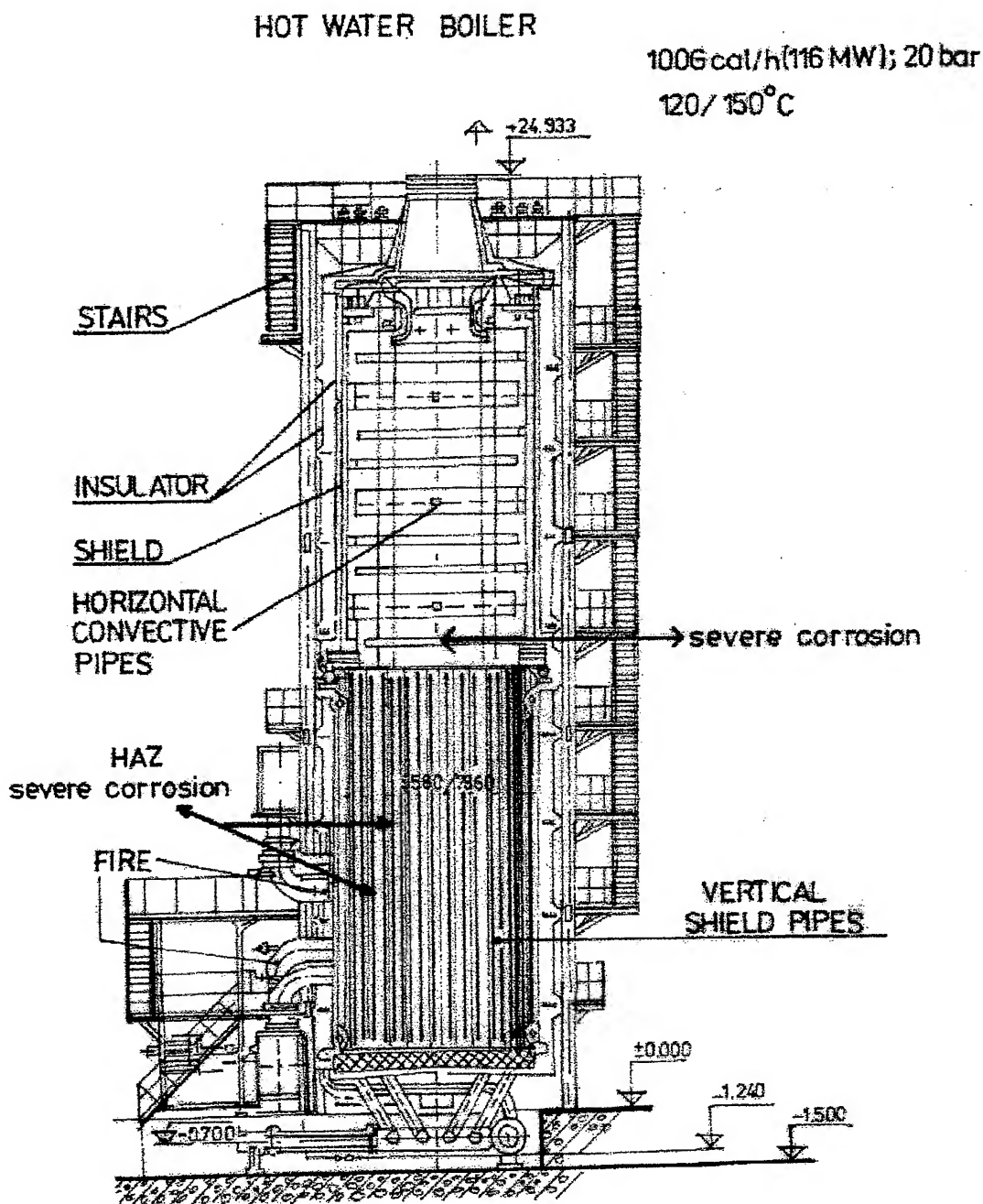


Fig. 1 Schematic view of a hot water boiler of 100 Gcal/h and the most corroded parts in service

- b. At the bottom of the convective zone at the water side, as a consequence of hot water corrosion thick layers of magnetite and hematite grow at the quasi-stagnant parts slowing down or even blocking the fluid circulation. Occasionally, on the top of iron oxides calcic carbonate is deposited. Under this non-protective deposit local wastage

followed by denting, cracking and pore formation occur. When the corrosion deposit blocking the pores and holes is detached, lackages of the circulating water appear and the plant must be shut down. A more severe situation appears when this type of attack is accompanied by local superheating followed by the pipe explosion (see Fig. 2 reproduced from ref. 1).

Corrosion damage occurred at the heat exchanger tubes for the drinking water circuit too (Fig. 3).



Fig. 2 Photographs of samples cut from pipes damaged in service¹ (corrosion + superheating → explosion)

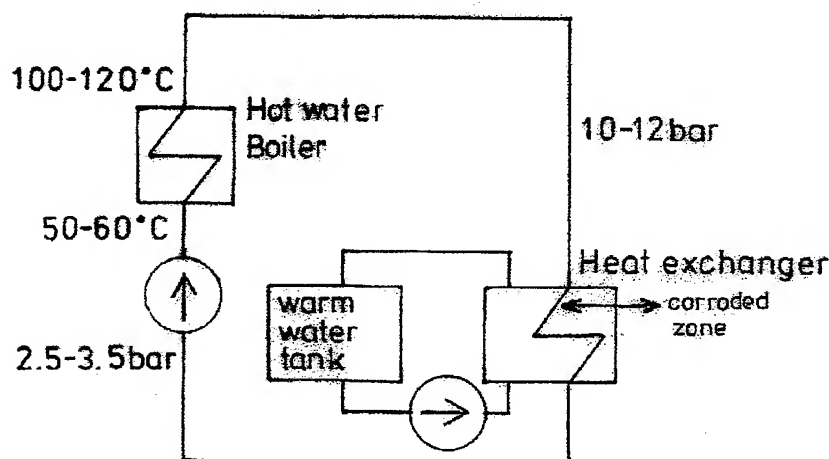


Fig. 3 Scheme of the warm water preparation in the Electric Heating Plant – Grozavesti and the most corroded zones

The primary cause of corrosion and deposition at the water side is the poor quality of the supplying feed water. Usually this water is thermally deaerated and not hard but occasionally tap water with high quantities of oxygen and CaCO_3 is deliberately used or accidentally penetrates into the primary circuit.

(Typically, the tap water contains CO_3^{2-} 100 mg/l, SO_4^{2-} 56 mg/l, Cl^- 27 mg/l; the minimum pH of the water in the heating circuit is 5.0 instead of 8.5 as recommended by standards and by the statutory audit Romanian limitations.)

In view of the elaboration of chemical cleaning procedures at the same time modern but facing the particularities mentioned above, a programme financially supported by the joint effort of the Romanian Company for Electrical Energy (CONEL), of the European Communittee via the TTQM-PHARE Project

No. 9602-02-02/Nov. 1997, of TECHNOPLANTS Impianti Industriali, Torino, and of the Institute of Optoelectronics, Bucharest, started in 1997. The agents, procedures and the precautions in their use will be shortly described below.

3. PROCEDURES FOR CHEMICAL CLEANING AND PASSIVATION OF CORRODED CARBON STEEL SURFACES

3.1. Chemical reagents and procedures actually in use

It is out the scope of this communication to analyse all the methods published in the literature. Only some aspects will be shown.

The usual procedure employed in Romania by factories laboratories or some small cleaning enterprises is the dissolution of iron oxide deposits in 5 – 10 % HCl in the presence of 1 % corrosion inhibitor at 65 °C. This agent has a pH value as low as – 0.5 to 0.0 being unacceptable aggressive for the underlying base metal and introducing a high degree of atmospheric pollution.

In the european western countries the most common reagent formulation for the chemical cleaning of steam generators or heat exchangers consist in a mixture of 1 to 5 % HF, 1 % NH_4HF_2 (ammonium hydrogen difluoride) and 0.1 to 1 % corrosion inhibitor of high efficiency (> 99.9), such as the french inhibitor trademark SOMAFER GV P9 or the english one ARMOHIB. Usually, in these countries the chemical cleaning is performed when the thickness of corrosion deposit is less than 100 μm and the equipment is hermetically closed so that there is no HF leakage in atmosphere. In view of the drawbacks of the old romanian plants and the economic difficulties this reagent is not suitable and consequently ruled out.

Other cleaning mixtures are also used for this purpose.

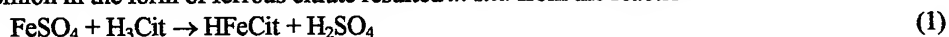
- 1.5 % citric acid + 0.15 % NH_4HF_2 + corrosion inhibitor
- 1.5 % sulfuric acid + 0.15 % NH_4HF_2 + corrosion inhibitor
- 1.5 % hydrofluoric acid + corrosion inhibitor
- 1.5 % sulfuric acid + corrosion inhibitor

3.2. Recommended practice for cleaning the romanian corroded energetic equipment

Literature references do not disclose exactly the reagent composition effectively used by the cleaning companies. As a result of extensive laboratory investigation and industrial testing the following specific agents and procedures have been elaborated suitable for the cleaning of romanian equipment.

Basically, the reagent consists in 1 – 2 % citric acid (H_3Cit), 1 % romanian inhibitor (trademark TRIAV M) and 0.1 – 0.2 % $\text{FeSO}_4 \cdot 7\text{H}_2\text{O}$. During the treatment the pH is controlled and adjusted at pH 2.2 to 2.6 by adding small portions of hydrochloric acid. The reason of this composition is explained below.

Because of the relative strength of Fe-O bonds in iron oxides, Fe^{II} is expected to be released quickly as compared to Fe^{III} , and the dissolution is probably governed by Fe^{III} phase transfer. This must be a slow process. The added ferrous ions act as dissolution activator^{2,3}, in our opinion in the form of ferrous citrate resulted *in situ* from the reaction



followed by the intermediary step in dissolution



In addition to this the dissolution process is favoured by the fact that the Fe^{3+} complex is stabilized in relation to the Fe^{2+} complex, or it is well known that ligands that stabilize the ferric ions are effective in bringing about dissolution.

The procedure is a many-step process, the number of steps and detailed reagent composition depending on the deposit characteristics and degree of damage of the basic underlying metal. In order to select the procedure, estimate the quantity of the corrosion products to remove following the method described in ref. 4. Prior to admission of any chemicals, samples cut from corroded pipes representative for the equipment as well as samples cut from new pipes must be welded at the entrance and the exit of the installation to observe the evolution of both deposit removal and metal attack during the treatment.

One-step procedure

Pre-operational mill-scale and thin layers of corrosion products (< 100 μm) can be removed in one-step process. In this case the pickling is immediately followed by a black oxide formation so that the presence of chloride ion in the scale removal formulation is prohibitive. Following is an outline of the procedure.

- I. Recirculate 1 % corrosion inhibitor long enough to obtain a homogeneous solution.
- II. Add 1 % citric acid and recirculate to homogenize.
- III. Add 0.1 % ferrous sulphate and recirculate to homogenize.
- IV. Increase the temperature to 75 – 85 °C and maintain constant forced circulation at the highest velocity consistent with tolerable corrosion rates. (Normally 3 to 4 hours should suffice for average cleaning.)
- V. Every hour measure the pH; when it reaches 3.5, adjust the pH to 2.2 by adding fresh citric acid to the depleted solvent or for economical reason sulfuric acid.
- VI. Continue recirculation up to constant pH which must not be higher than 4.
- VII. Displace the acidic solvent with hot water using the maximum practical velocity. Following this, hot water should be recirculated and repeated if necessary until pH >5.5.
- VIII. Flush to waste at high velocity.
- IX.a. Drain under nitrogen for dry storage or
- IX.b. Proceed to conditioning by formation of protective oxide layers as described further more.

Multi-step procedure

Thick deposits of operational corrosion products will be removed by a multi-step process. There are three reasons for this option. Experience has demonstrated that adverse situations can occur.

- precipitation of a grayish iron citrate from the solvent; it was demonstrated that precipitation occurs at pH values between 4.0 to 4.9 and an iron concentration of 0.45 % or higher⁵
- formation of a colored colloidal iron complex if rinsing and flushing are deferred⁵
- leakage of the pickling agent when the tube walls are penetrated through the pores, holes, and cracks formed in service but initially obturated by the deposit; in this case the chemical cleaning must be interrupted for welding the tubes and the solvent is wasted before complete depletion.

Following is an outline of this procedure.

A. Alkaline pre-treatment

This pre-treatment is recommended when thick adherent superheated layer is formed, in order to favorize the acid attack and to particulate the deposit.

- I. Recirculate 0.5 to 1.0 % sodium hydroxide long enough to obtain a homogeneous solution.
- II. Increase the temperature to 65 °C and maintain forced circulation for 12 hours.
- III. Displace the alkaline solution with water.
- IV. Flush to waste and drain.
- V. Repeat the last two operations up to pH <8.5.

B. Acid treatment

STEP I.

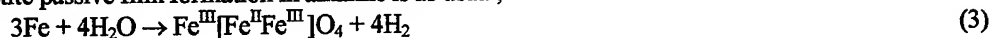
- I. Recirculate 1 % acid corrosion inhibitor long enough to obtain a homogeneous solution
- II. Add 0.07 – 0.08 % hydrochloric acid and recirculate to homogenize (it results approx. 0.02 N Cl⁻)
- III. Add 1 % citric acid and recirculate to homogenize
- IV. Add 0.1 % ferrous sulphate and recirculate to homogenize
- V. Increase the temperature to 75 – 85 °C and maintain constant forced circulation at the highest velocity consistent with tolerable corrosion rate
- VI. Measure the pH at the exit of the boiler. If the pH value reaches 3.5 or more adjust at 2.2 by adding small quantities of hydrochloric acid
- VII. When the concentration in chloride ions reaches 0.5, displace the acid solvent with hot water using the maximum practical velocity. Following this, hot water should be recirculated, flushed to waste and displaced with fresh water.
- VIII. Cut 15 cm from the inserted samples and observe the degree of the deposit removal. If the thickness is higher than 50 % from the initial one, repeat the step I, stages I to VII.

STEP II

Repeat the stages I-VII as above but at the stage II substitute the pH adjustment with HCl using small portions of sulfuric or citric acid.

3. 3. Corrosion protection by means of conditioning with octadecylamine (ODA)

The basic reaction of magnetite passive film formation in alkaline is as usual,



The conditioning with long-chained amines prevents corrosion by assisting the building of protecting oxide layers instead of the unprotecting ones, as those formed in service at ODA absence, which must be removed in the preceeding procedures. It acts via the following ways.

- Because of his active effect, the ODA removes loose adherent deposits and rust from metal surface. (It has been observed in practical application that at high concentration of ODA the detaching of the deposits was so high that the result was plugging of heat exchanger tubes by the loosened deposits.)
- Due to ODA barrier properties, the formed oxide layers are thinner, more fine grained and adherent. ODA impedes the access of the oxide forming water to the phase boundary metal water. Therefore the growth rate of the oxide is reduced and thinner layers are formed. Thinner layers have a higher resistance against mechanical stresses, because can be elastically deformed during mechanical stresses arised especially during shut-down and heating periods as a consequence of different thermic extension between metal and oxide layers. At variance, thick brittle oxide layers will crack.
- The film-forming ODA forms an additional layer on the top of the growing oxide laer. This additional ODA layer is a diffusion barrier for aggressive anions and water. In this manner the ODA layers prevent the attack of corrosive anions like chloride or sulphate on the oxide layer.
- The thin hydrophobic film initially formed at the metal surface is protective enough for temporary corrosion in water under static conditions at 20 to 230 °C. Additionally, the same thin hydrophobic layer formed on the top of the oxide retards erosion-corrosion^{6,7}.

Following is an outline of this procedure⁶.

- I. Use deionized water as supplying feed water and increase the pH to 8.5 by untotoxic NaOH (approx. 0.1 mg/kg).

If deionized water is not available, Na₃PO₄ (0.5 mg/kg) can be applied for pH increase of the supplying tap water without deposition of CaCO₃. Instead of CaCO₃ deposition Ca₃(PO₄)₂*Ca(OH)₂ originates from Ca²⁺, according to the reaction



This compound forms a noncrystalline surface complex which does not grow up but precipitates as sludge which has to be removed. The possible entry of phosphate into the drinking water has to be under control.

- II. Add 1 – 2 % octadecylamine emulsion
- III. Continuous control of ODA in water is necessary. The concentration must be maintained between 0.5 and 1.0 mg ODA/kg. The possible entry of ODA into the drinking water has to be under control.

REFERENCES

1. P. Marian and L. Damian, "Expertizarea a trei mostre de teava de cazan," *Buletin de Analize Nr.22*, Metallurgical Research Institute, Bucharest, 1998.
2. I. G. Gorichev, L. V. Malov, and V. S. Dukhanin, "Formation and Dissolution Constants of Active Centres on Magnetite and Hematite in Sulphuric Acid," *Russian Journal of Physical Chemistry* **52**, pp. 681-684, 1978.
3. E. Baumgartner, M. A. Blesa, H. A. Marinovich, and A. J. G. Maroto, "Heterogeneous Electron Transfer as a Pathway in the Dissolution of Magnetite in Oxalic Acid Solution," *Inorg. Chem.* **22**, pp. 2226-2228, 1983.
4. I. H. Plonski, "Cleaning Corroded Material; Recommended Practice for Cleaning Corroded Specimens," *Electrochemical Applications*, **1**, p. 6, 1996.
5. E. B. Morris, "Precautions in Use of Citric Acid for Chemical Cleaning," *J. of Engineering for Power*, October, pp. 367-370.
6. R. Bassler, M. Uhlemann and K. Mummert, *Materials and Corrosion*, **50**, p. 146, 1999.
7. "Combined Heat and Electric Stations, Temporary Corrosion Protection of Steam and Hot Water Generators and Heatexchangers, Corrosion Protection by Means of Conditioning with Octadecylamine," *Fachbereichstandard, DK 621.18:620197, TGL 190-52/09, Gruppe 934 200*, June 1990.

Evaluating smoke screens' masking ability in infrared using thermovision equipment

M. Tomescu^{1*}, R. Marginean¹, E. Nitis², M. Negosanu², M. Vizireanu²

¹ Institute of Optoelectronics, 76900 111 Atomistilor Str., Bucharest

² UM 02512C, Sos. Oltenitei, Bucharest

ABSTRACT

In the process of development new chemicals to be used for generating smoke screens, a method for evaluating the masking ability for the infrared spectral domain was needed. The experimental set-up, involving a thermovision equipment and a reference body is presented. The experiments were carried out for different types of chemical mixtures, both in laboratory and field conditions and the attenuation coefficients were calculated. The relevant thermal images, processed using dedicated software, are also presented.

Keywords: smoke screens, masking, thermovision

1. INTRODUCTION

Smoke screens are produced by burning a special chemical mixture and are currently used by military forces for protecting themselves, avoiding from being detected by the enemy. Because masking in visible can be easily obtained with smoke screens, the Gordian knot in developing such a mixture is to obtain one that is able to ensure protection against detection using equipment working in infrared domain. The thermal radiation emitted by all the natural and artificial bodies in infrared and transmitted by the atmosphere can be detected using thermovision equipment^{1,2}. Because atmosphere is transparent in infrared only for few spectral bands, thermovision equipment can be of two kinds: those with detectors for the 3-5.4 μm spectral band and those with detectors for the 8-14 μm spectral band.

In order to evaluate the masking ability in infrared of some smoke screens developed by a team from UM 2512- C, some measurements using thermovision equipment were made, for both the infrared spectral bands.

2. EQUIPMENT

For measurements in the infrared domain we used a Thermoteknix for Windows (ThermaGRAM) system³, having different types of thermal equipment as thermal sensor, depending on the spectral band. The Thermoteknix ThermaGRAM system has the following structure:

Hardware: Thermoteknix GRAM (or ThermaGRAM) is a board for real-time processing (subtract, average, filter, etc) of the thermal images. It has a high-precision analogue-digital converter, a 12-bits input and an electronic digital PLL that ensures video synchronization without a jitter and with a high tolerance to signal variations induced by analogue recording media (VCRs). The use of average is a very important feature for images with analogue input, because it allows reducing the noise level in the signal. The programmable amplification and the control over the offset ensure obtaining precise and real-time measurements of the input video signal.

Software: ThermaGRAM for Windows is a sophisticated software for acquisition and analysis of thermal images. The acquired images can be loaded in files or can be visualised ("live") on the computer's monitor by connecting a video camera or a VCR. The "live" images can be "frozen" and saved on the disk. An "incremental save" command allows to the user to easily successively save the images under some filenames that can suggest the fact that these files represent different moments of the same process, registered by sampling. The modernised GRAM board allows to "live" acquire and save a set of images at two seconds intervals. The successive files obtained using one of these methods can be automatically loaded in a Windows "super-image", in order to be analysed afterwards using some pre-established procedures.

* Correspondence: Phone: (401) 780.66.40; Fax: (401) 423.25.32

The thermal images loaded in files can be visualised using a large scale of various pseudo-colour palettes; for every palette, the temperature interval can be manually changed or optimised by the computer.

The analysis possibilities are the followings:

- Displaying punctual temperatures (at a pixels level);
- Tracing isothermes for individualising with a specific colour band the portions from the images that have a temperature within a specific interval;
- Tracing contours that can be used afterwards as graphic entities ("objects") for establishing the "intervals dividers" (as means of display the minimum, maximum and median temperature along a line) or for tracing temperature profiles along a line in a distinct graphic window;
- Tracing temperature profiles over the displayed image;
- Tracing rectangular, elliptic and polygonal contours that can be used afterwards as "objects" for displaying the minimum, maximum and mean temperatures in a specific region, using histograms;
- Displaying the differences between temperatures using various other means;
- Using labels for identification of "objects", etc.

2.1. Thermal equipment for the 3 - 5.4 μm spectral band

For measurements in the 3 - 5.4 μm spectral band we used an AGA Thermovision thermal camera type 660 - S - 525. This type of thermal camera has the following characteristics:

- | | |
|--|---|
| - focusing: | from 0.5 m to infinity; |
| - field of view: | 5 x 5 grade; |
| - frame rate: | 16 frames/sec; |
| - thermal resolution: | 0.2 ° C; |
| - domain of measured object's temperature: | -20 - 200 ° C |
| - detectors' type: | InSb; |
| - cooling: | liquid nitrogen; |
| - display of the information | thermal images are displayed on an oscilloscope screen. |

In order to be processed, the thermal images displayed by the thermal camera were recorded on videotape using a CCD camera and a usual VCR. The CCD camera is a JVC type TK 1085E and has a 10-mm objective.

2.2. Thermal equipment for the 8- 14 μm spectral band

For measurements in the 8 - 14 μm spectral band we used a LORIS thermovision equipment, type 445L. This equipment has a performant very good telescope for infrared, with two fields of view. Both the thermal sensor and the telescope are integrated in a protected metallic body. The video signal obtained from the equipment is in accordance with the TV CCIR-625 standard. The equipment can be remote controlled using a panel. The others characteristics are:

- | | |
|--|--|
| - fields of view: | 7° x 5°, 2.3° x 1.2° plus the possibility of using the electrooptic zoom and optical zoom (x2, x4) |
| - detectors: | 4 detectors, CdHgTe |
| - thermal resolution | 0.01 ° C |
| - domain of measured object's temperature: | -195 ° C – 100 ° C without use of a diaphragm to be needed; up to 1500 ° C with a diaphragm; |
| - cooling: | down to 77 K; miniaturised cryogenerator (Stirling cycle with He as a cooling agent) |
| - scanning: | bidimensional |
| - controls on the remote control panel; | polarity, level of signal, changing the field of view, focusing |

3. EXPERIMENTAL SET-UP

The first step in our experiments was to make measurements in laboratory conditions.

In order to obtain the optimal concentration for the gases composing the smoke screen, the mixtures produced by UM 2512-C were burned inside a parallelepipedic (4 m x 1,35 m x 0,95 m) box made of sheet iron. The box has two windows on its small sides and one window on its upper side; the first of the windows was used as an aiming window and was maintained open during experiments; the second window was used for fastening the thermal reference and closed afterwards; the third window (from the upper side of the box) was used for ventilation.

The thermal reference is a thermal source electrically heated to a temperature of 70 °C; the emissive surface has a 1cm² area. The distance between the thermal reference and the equipment was 4.03 m.

The thermal images registered using the LORIS equipment (for the 8 - 14 µm) were visualised in real-time on the computer's monitor and saved on the hard-disk at a constant time interval (20 seconds), starting from the initial moment of the probe's burning. In order to have a reference image, before starting probe's burning, an image was recorded, for every probe. The images were processed using the dedicated software. The thermal images obtained using the Thermovision 660 AGA equipment (for the 3 - 5.4 µm) were visualised in real-time on the oscilloscope's screen and filmed with a CCD JVC mini-camera connected to a VCR. In this way, the registration of the entire masking regime, for every probe, was ensured.

Because the signal displayed on the oscilloscope and filmed by the camera was very weak and because it had a frequency of 16 Hz (not 50 Hz, as the TV standard requires), a chain for amplifying and control the signal had to be realised.

The output signal from the video-player (that plays the tape containing the thermal images) enters in a preamplifier, from which is transmitted to a monitor and then to the VCR and to the computer (that has installed the ThermoGRAM board). In this manner, the signal was amplified and re-registered on a new videotape in order to be processed.

After this step of experiments, some specific mixture was selected for the next step of experiments. In this next stage, a military car was filmed (with thermovision equipment of LORIS type) during the process of smoke screen's development. The distance between the car and the equipment was about 40m; the mixtures were burned in a point situated off-axis, at 30 m from the equipment and 10m from the car. The meteorological conditions were:

- ⇒ Air temperature: 1 °C;
- ⇒ Atmospheric pressure: 7- mm col Hg;
- ⇒ Speed of the wind: 1.5-4 m/s;
- ⇒ Direction were from the wind blew: variable ;

4. EXPERIMENTAL RESULTS

For the case of measurements made using LORIS equipment (8-14 µm), thermal images were recorded and processed for 18 types of mixtures, named Pi in the table 1. For every mixture, the attenuation induced by the presence of smoke was calculated as:

$$A = 100 - Ti (\%); \quad Ti = 100 * Pi / Ref$$

where: Ref = the intensity of the reference source without the smoke (100% transmission);

Pi = the intensity of the reference source with the smoke obtained by burning the "i" mixture;

Ti = the transmission of the medium for the spectral domain with the smoke obtained by burning the "i" mixture.

For the case of measurements made using AGA equipment (3-5.4 µm), thermal images were recorded and processed for 7 types of mixtures. Again, for every probe, the attenuation was calculated.

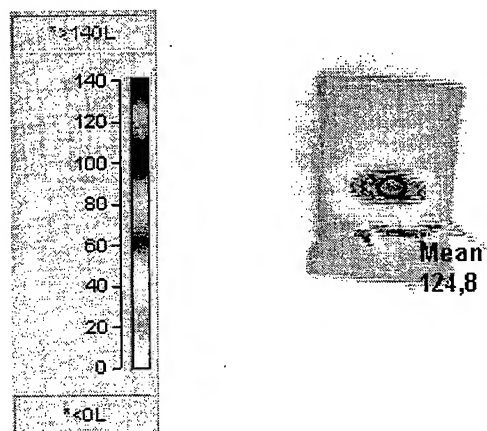


Fig.1 Thermal reference without the masking smoke screen, recorded using LORIS (8-14 μm)

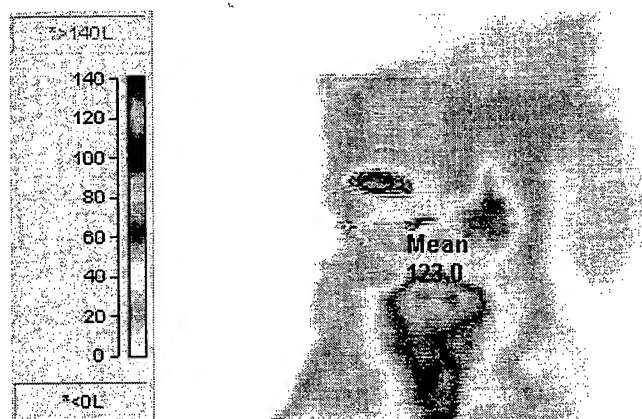


Fig.2 Thermal reference masked by the flame of burning the II mixture, recorded using LORIS

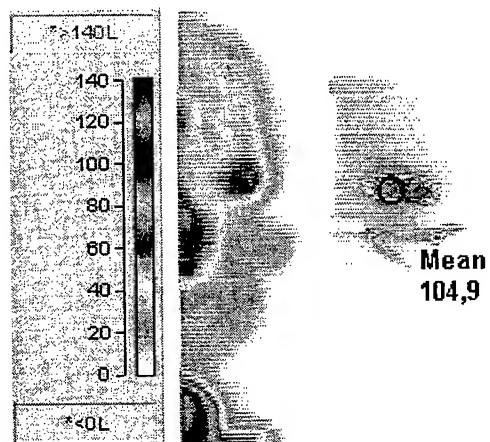


Fig.3 Thermal reference masked by the smoke screen, recorded using LORIS (8-14 μm); in the left side of the image, the flame can be observed

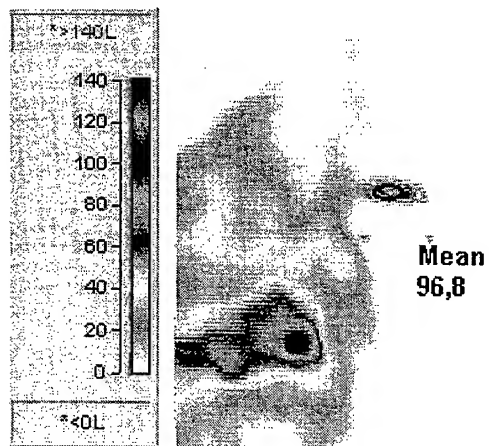


Fig.4 Thermal reference masked by the smoke screen and flames, recorded using LORIS (8-14 μ m)

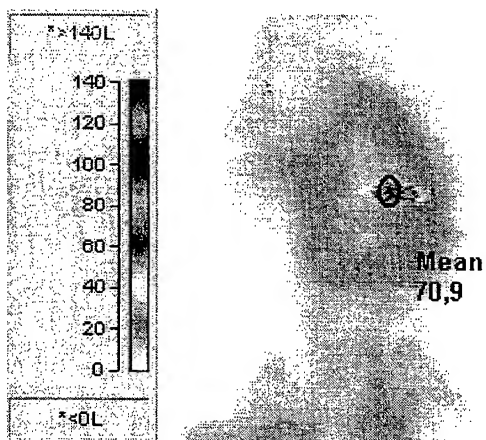


Fig.5 Thermal reference masked by the hot smoke, recorded using LORIS (8-14 μ m)

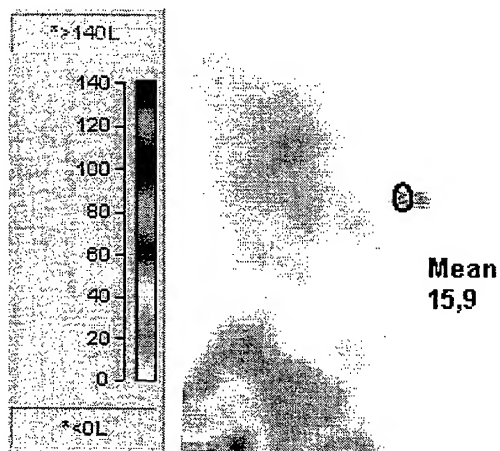


Fig.6 Thermal reference - the process of completely masking is started, recorded using LORIS

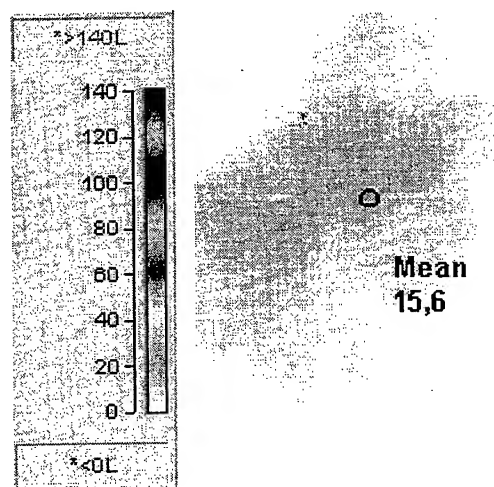


Fig.7 Thermal reference almost completely masked by the smoke screen, recorded using LORIS

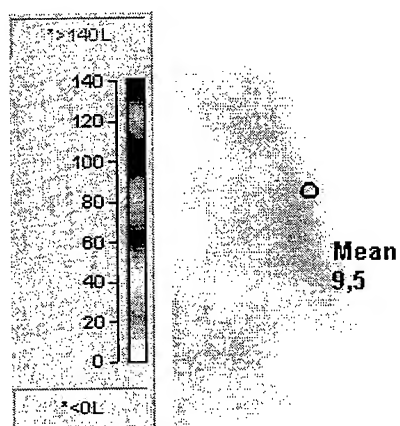


Fig.8 Thermal reference almost completely masked by the smoke screen, recorded using LORIS

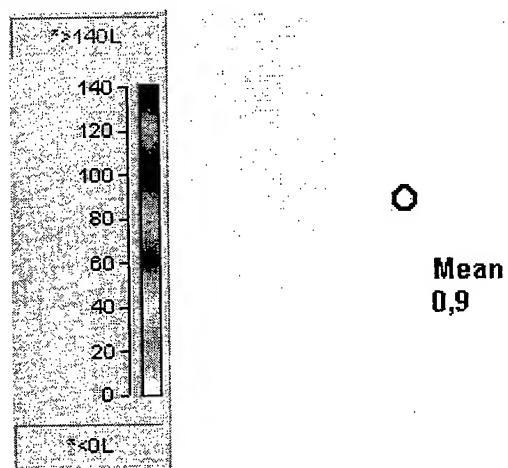


Fig.9 Thermal reference completely masked by the smoke screen, recorded using LORIS (8-14 μ m)

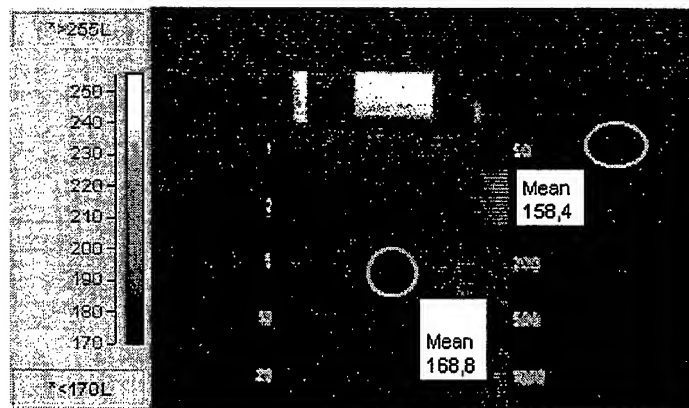


Fig.10 Thermal image of the reference body masked by burning the R14 mixture recorded in the 3-5.4 μm spectral domain

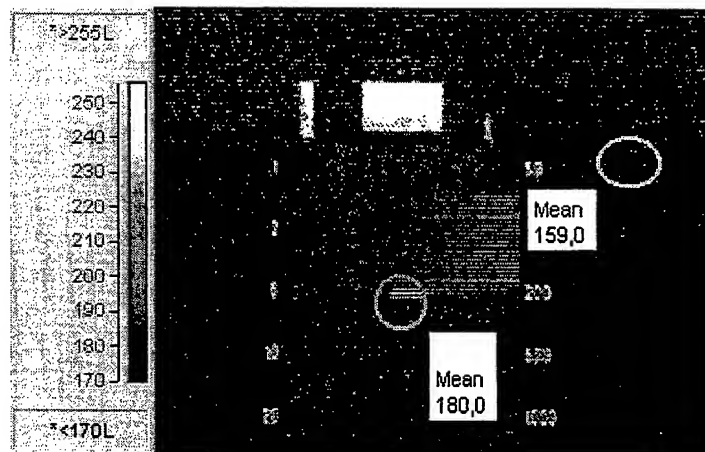


Fig.11 Thermal image of the reference body masked by burning the R19 mixture recorded in the 3-5.4 μm spectral domain

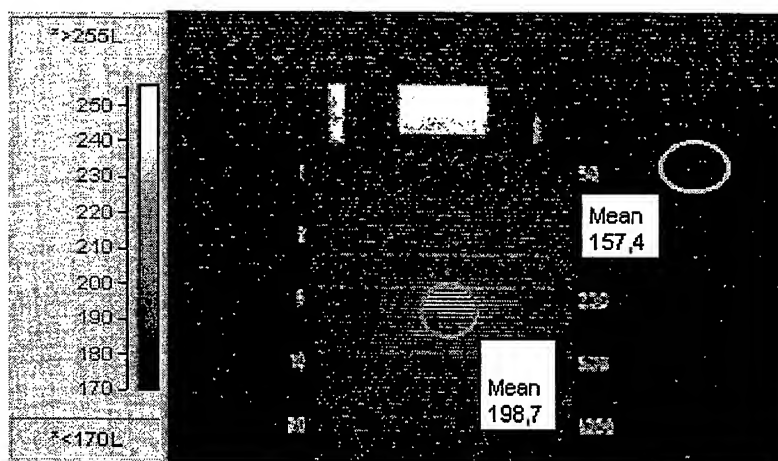


Fig.12 Thermal image of the reference body masked by burning the Rd mixture recorded in the 3-5.4 μm spectral domain



Fig. 13 Thermal reference of the military car, before burning the mixture, recorded using LORIS (8-14μm); the temperature profile along a line can be seen

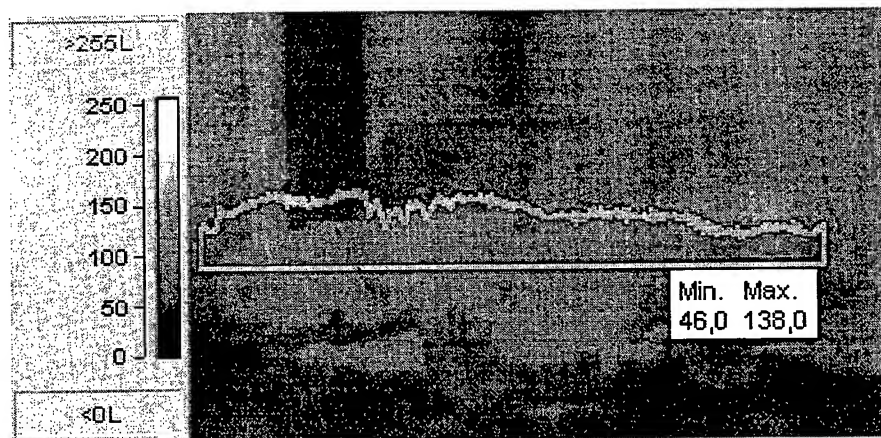


Fig. 14 The military car masked by the smoke screen; recorded using LORIS (8-14μm); the temperature profile along a line can be seen

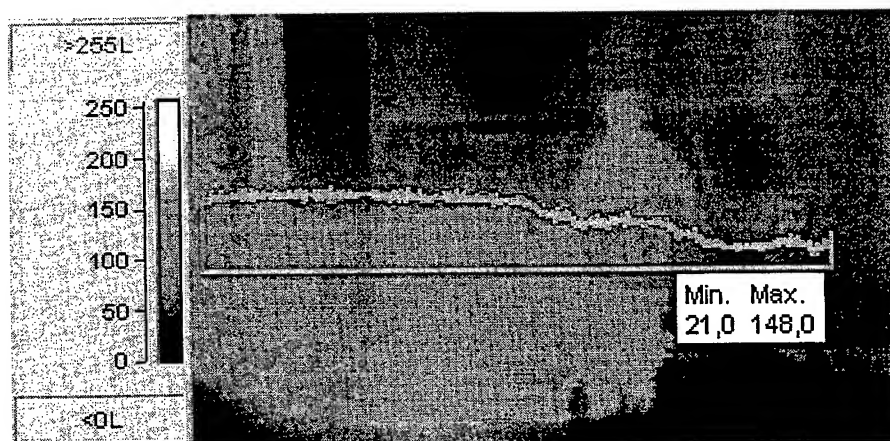


Fig. 15 The military car masked by the smoke screen; recorded using LORIS (8-14μm); the temperature profile along a line can be seen

In the Tab. 1, the values for attenuation A in the 8-14 μm spectral domain and duration D (representing the time interval between the initial moment of producing the smoke and the moment when the reference value is again obtained) are presented, for every probe. In the Tab. 2, the values for attenuation A in the 3-5.4 μm spectral domain and duration D are presented, for every probe.

Tab. 1 The values for attenuation A in the 8-14 μm spectral domain and time duration D

Probe	A (%)	D(min.)
Ref=130	0	
P1=78,8	39,39	4
P2=100,7	22,54	4
P3=37	69,17	4
P4=12,1	91	5
P5=71	40,83	3.6
P6=37	69,17	4.2
P7=20	83,33	5
P8=58	55,39	2,5
P9=0,6	98	4,5
P10=0,3	99	3
P11=62	55	2,5
P12=12	90	3.7
P13=61,8	52,5	2,5
Pab=127,5	2	2,5
PB=126,4	2,5	1,7
PC=115,8	11	4,5
PD=61	55	3,5
PE=116,7	10,3	1,25

Tab. 2 The values for attenuation A in the 3-5.4 μm spectral domain and time duration D

Probe	A (%)	D (sec)
Ref=55		
R 1=32	42	25
R 6=8	85,5	20
R 14=10,5	81	30
R 18=39	29	20
R 19=20	63,2	35
R d=41,3	25	25
SMD 2=20,5	62,7	30

We also present some thermal images recorded with LORIS equipment (Fig. 1 - 9) at the first stage of our experiments. The images presented the whole cycle of masking, starting from the reference image and ending with the image representing the reference body completely masked. Some images recorded using the AGA equipment during the first stage of our experiments are also presented in Fig. 10 - 12. Some of the thermal images of the military car masked by the smoke screen are presented in Fig. 13-15.

REFERENCES

1. J.M.Lloyd, *'Thermal Imaging Systems'*, pp.14, 18-30, 329, Plenum Press, New York, 1975
2. The Infrared Handbook, pp. 1.27-1.35, 3.3-3.19, 20.4-20.17, The Infrared Information Center - Environmental Research Institute of Michigan, 1989
3. ThermaGRAM User Manual, Thermoteknix Systems Ltd, issue 1.2, 1995

Computer designing of the shot range order structure of the vitreous $\text{As}_2(\text{S}, \text{Se})_3\text{Sn}_{0.1}$ semiconductors before and after illumination

A.Andriesh^b, A.Buzdugan^{*a}, V.Dolghier^a, M.Iovu^b, A.Popescu^b

^aCenter of Metrology, Automation & Scientific Research Work,

^bCenter of Optoelectronics, Institute of Applied Physics,
3/2 Academiei str., MD-2028, Chisinau, Moldova;

ABSTRACT

Experimental data of mass spectrometric analysis of vitreous $\text{As}_2(\text{S}, \text{Se})_3$ chalcogenide glasses shows the perceptible difference in the values of $\text{As}_m(\text{S}, \text{Se})_n$ ion currents before and after laser illumination. Data of the computational calculation of the stableness of molecular units are in good correlation with obtained experimental mass spectrometric data. After laser illumination we detect new kinds of molecular units as As_m , S_n and Se_n . The observed changes of the ion currents in the mass spectrum may be explained in view of some re-arrangement in the shot-range order of the component atoms under illumination. We propose for discussion the results of computational modeling of molecular units such as $\text{As}_m(\text{S}, \text{Se})_n$ observed experimentally in the $\text{As}_2(\text{S}, \text{Se})_3\text{Sn}_{0.1}$ alloys by their mass spectrometric analysis before and after laser illumination. In this report we suppose that a study of the composition of condensed molecules by the intermediacy of mass spectrometry and HyperChem Computational Chemistry Program may harvest complementary information useful in orders to building structural models of chalcogenide glasses. In result of this work we also conclude that tin atoms in the $\text{As}_2(\text{S}, \text{Se})_3\text{Sn}_{0.1}$ network are bonded in two mode: before illumination as $2(\text{S}, \text{Se})=\text{Sn}=2(\text{S}, \text{Se})$ - type and after illumination as $(\text{S}, \text{Se})-\text{Sn}-(\text{S}, \text{Se})$ - type.

Keywords: chalcogenide glasses, mass spectrometry, computational calculation, thin films, modeling.

1. INTRODUCTION

A great interest for vitreous materials is the appearance of new possibilities for its application as optical and photoelectric media, planar waveguides, active and passive elements for optoelectronics.

The interaction of laser radiation with vitreous chalcogenide semiconductor leads both irreversible and reversible changes of the atomic and the electronic structures. These changes are manifesting in the experiment through changes of mechanical, thermal, optical, photoelectrical and other characteristics¹.

Under the laser illumination the structure of the chalcogenide thin films changes, new defects appear, film crystallization or amorphization take place, phase transition or transition from one unstable state to another unstable state are observed¹. However there are several conception with something in view not understanding of their microstructure mechanism, mainly in the case of irreversible and reversible photostructural changes. This position is greatly caused by the difficulties of direct observation of local atomic structure transformation in disordered solids using ordinary techniques for vitreous structure.

In difference with the crystalline state distinguish by *long range order* (LRO), i.e. by the existence of correlation between the position of every two atoms situated as far as possible one from another, the vitreous states of chalcogenide glasses is distinguish by the absence of the *long range order* (LRO). The chalcogenide glasses are not a total disorder but a certain limited order called *shot range order* (SRO) defined by the inter-atomic correlation in the first coordination spheres of an arbitrary atom, i.e. up to the maximum distance where the bonding forces are acting. In vitreous chalcogenide glasses the order extends up to larger inter-atomic distances. On this basis a new type of order was defined the medium range order (MRO)².

In this article we submit that an analyze of the composition of condensed molecules by means of mass spectrometry may harvest complementary information important in building structural models in SRO and MRO chalcogenide glasses and explaining the mechanism of the photostructural changes in vitreous semiconductors³⁻⁶.

*Correspondence: E-mail dulgheru@as.md, Fax: (+3732)-737411, Phone: (+373-2)-737431

2. EXPERIMENTS

The bulk samples of As_2S_3 and As_2Se_3 doped with tin were synthesized using elementary As, S, Se and Sn of high purity. Thin films were obtained by thermal deposition (vaporization of the bulk samples) in a vacuum on the preliminary cleaned oxide glass substrates and on the oxide glass capillaries (for mass spectroscopy analysis of thin films obtained in the same condition).

Mass spectrums were registered using MX 1320 mass spectrometry. The measurements were made at ionizing electron energy 70 eV and vaporization temperature 453 K for As_2S_3 and 543 K for As_2Se_3 .

The identification of the species was made according to the relative abundance of the sulfur isotopes they contain. The intensity of peaks were measured with an error of $\approx 1\%$.

For the illumination of the thin films Ar-laser ($\lambda=514$ nm) was used. Data of mass spectrometric analysis of As_2S_3 and As_2Se_3 doped with tin chalcogenide glasses before and after illumination shows the perceptible difference in quota of As_mS_n and As_mSe_n molecular units⁴.

Using HyperChem Computational Chemistry Program we realized 3D structures, with minimum potential energy (Kcal/mol) conformation for the molecules: As_4 [3.47]; S_8 [4.44]; As_4S_3 [11.87]; As_2S_5 [14.36]; As_2S_4 [17.62]; As_2S_6 [19.11]; As_4S_4 [21.88]; As_4S_5 [24.98]; As_2S_3 [25.81]; As_4S_6 [43.13]; As_4Se_3 [80,26]; As_4Se_4 [177,29]; As_4Se_5 [150,07]; As_4Se_6 [184,33]; As_2Se_3 [97,18]; As_2Se_4 [115,42]; As_2Se_5 [148,03]; As_2Se_6 [191,09].

The total energy of the molecule configurations we obtained using Single Point Calculation of the HyperChem Computational Chemistry Program. A single point calculation performs the static properties of a molecule. The properties include potential energy, derivatives of the potential energy, molecular orbital energies, and the coefficients of molecular orbitals for excited states. The molecular structure data for a single point calculation usually reflects the coordinates of a stationary point on the potential energy surface, typically a minimum or transition state.

As regards a geometry optimization, HyperChem starts with a set of Cartesian coordinates for a molecule and tries to find a new set of coordinates with minimum potential energy.

The potential energy is very complex, even for a molecule containing only a few dihedral angles. Since minimization calculations can't cross or enter potential energy barriers, the molecular structure found during an optimization may be a local and not a global minimum. The minimum represents the potential energy closest to the starting structure of a molecule. Frequently are using minimizations to generate a structure at a stationary point for a subsequent single point calculation or to remove extreme force in a molecule, preparing it for a molecular dynamics simulation.

3. RESULTS

The Tab. 1 presented bellow gives the results of the mass spectrometric analysis of vaporization from thin films of As_2S_3 and As_2Se_3 doped with 2 % of tin before and after Ar-laser illumination.

Mass spectrums of the thin films of As_2S_3 doped with 2 % of Sn before and after Ar-laser illumination are presented on chart 1(before illumination) and chart 2 (after illumination). Visible there are perceptible difference in the intensity of the ion currents.

For thin films of As_2S_3 doped with 2 % of Sn before illumination we registered the following ions: As_mS_n^+ ($m=1-4$; $n=1-5$), As_m^+ ($m=1-4$), S_n^+ ($n=1-2$) and SnS_2^+ . After illumination of thin films new kinds of ions are present on the mass spectrum: S_n^+ ($n=3-8$), As_2S_6 and SnS^+ . Also increases the intensity of the As_m^+ .

Mass spectrums of the thin films of As_2Se_3 doped with 2% of Sn before and after Ar-laser illumination are presented on chart 3(before illumination) and chart 4 (after illumination). Visible there are perceptible difference in the intensity of the ion currents.

For thin films of As_2Se_3 doped with 2% of Sn before illumination we registered the following ions: As_mSe_n^+ ($m=1-5$; $n=1-4$), As_m^+ ($m=1-4$), Se_n^+ ($n=1-2$) and SnSe_2^+ . After illumination of thin films new kind of ion is present on the mass spectrum: SnSe^+ . Also increase the intensity of the As_m^+ ions.

As results of computational modeling we obtained sticks & dots models of the As_mS_n , As_4 and S_8 molecules that are presented bellow. There are also given the model of the As-S-Sn bonds before and after Ar-laser illumination.

Also there are presented sticks & dots models of the As_mSe_n molecules and the model of the As-Se-Sn bonds before and after Ar-laser illumination.

Tab. 1 Results of the mass spectrometric analysis of vaporization from thin films of As_2S_3 and As_2Se_3 doped with 2 % of Sn. The measurements were made at ionizing electron energy $V=70$ eV and vaporization temperature 453 K for As_2S_3 . The measurements for As_2Se_3 were made at ionizing electron energy $V=70$ eV and vaporization temperature 543 K

Ion for As-S-Sn	m/z	Intensity before radiation	Intensity after radiation	Ion for As-Se-Sn	m/z	Intensity before radiation	Intensity after radiation
S	32	5	10	As	75	80	90
S ₂	64	16	26	Se	80	78	85
As	75	36	49	As ₂	150	64	75
S ₃	96	-	1	AsSe	155	100	100
AsS	107	100	100	Se ₂	160	32	50
S ₄	128	-	41	SnSe	200	-	2
AsS ₂	139	11	13	As ₃	225	22	33
As ₂	150	19	42	As ₂ Se	230	40	25
SnS	152	-	2	AsSe ₂	235	9	4
S ₅	160	-	1	SnSe ₂	280	5	-
AsS ₃	171	2	11	As ₄	300	10	20
As ₂ S	182	29	17	As ₃ Se	305	68	34
SnS ₂	184	2	-	As ₂ Se ₂	310	28	15
S ₆	192	-	1	AsSe ₃	315	2	1
As ₂ S ₂	214	34	16	Se ₄	320	2	2
S ₇	224	-	8	As ₃ Se ₂	385	10	5
As ₃	225	14	24	As ₂ Se ₃	390	5	-
As ₂ S ₃	246	17	-	As ₄ Se ₂	460	5	3
S ₈	256	-	30	As ₃ Se ₃	465	8	5
As ₃ S	257	19	23	As ₄ Se ₃	540	14	20
As ₂ S ₄	278	18	-	As ₅ Se ₃	615	8	20
As ₃ S ₂	289	16	12	As ₄ Se ₄	620	3	25
As ₄	300	6	21				
As ₂ S ₅	310	9	-				
As ₃ S ₃	321	30	19				
As ₂ S ₆	342	-	5				
As ₃ S ₄	353	80	4				
As ₄ S ₃	396	8	37				
As ₄ S ₄	428	29	19				
As ₄ S ₅	460	19	5				

Chart 1. Mass spectrum of the As-S-Sn semiconductor system before Ar-laser radiation.

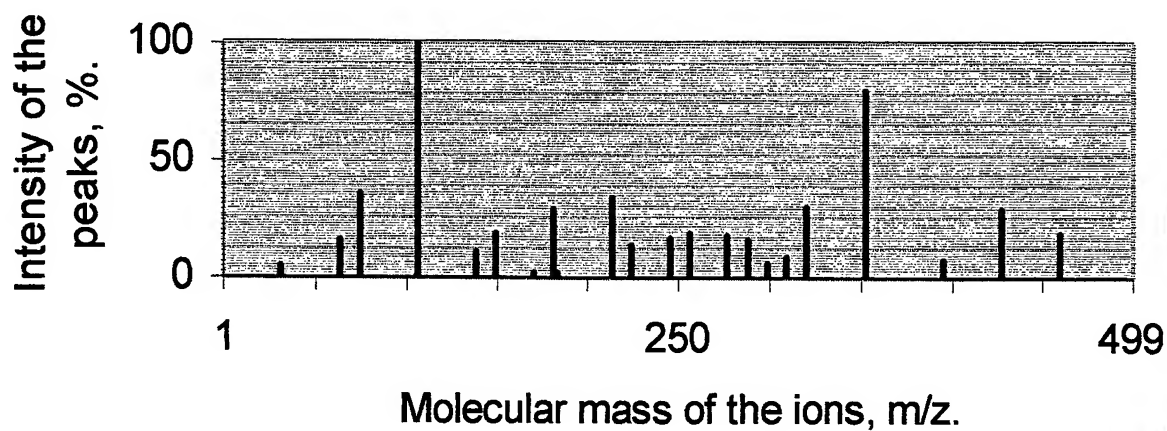


Chart 2. Mass spectrum of the As-S-Sn semiconductor system after Ar-laser radiation.

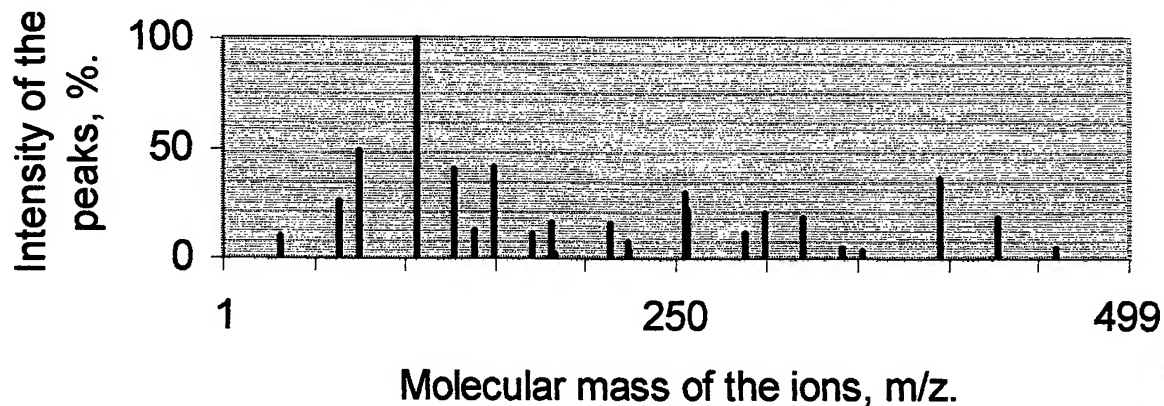


Chart 3. Mass spectrum of the As-Se-Sn semiconductor system before Ar-laser radiation.

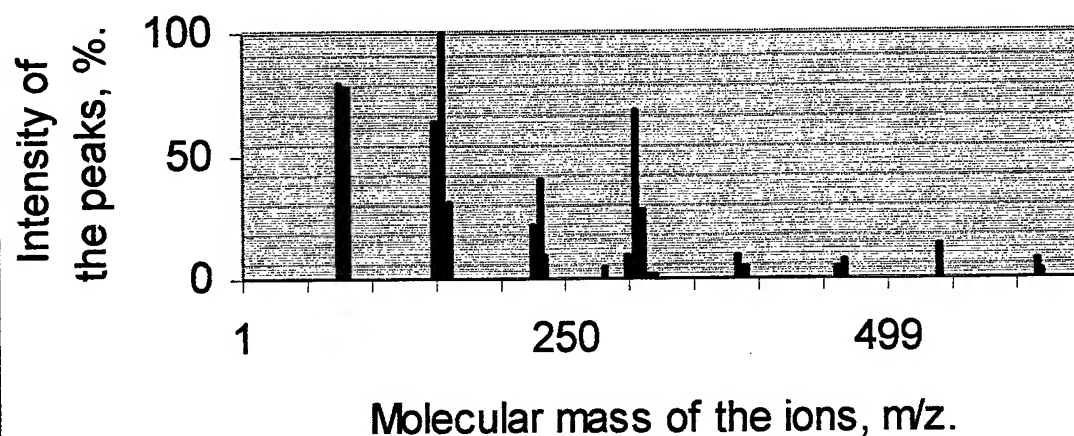
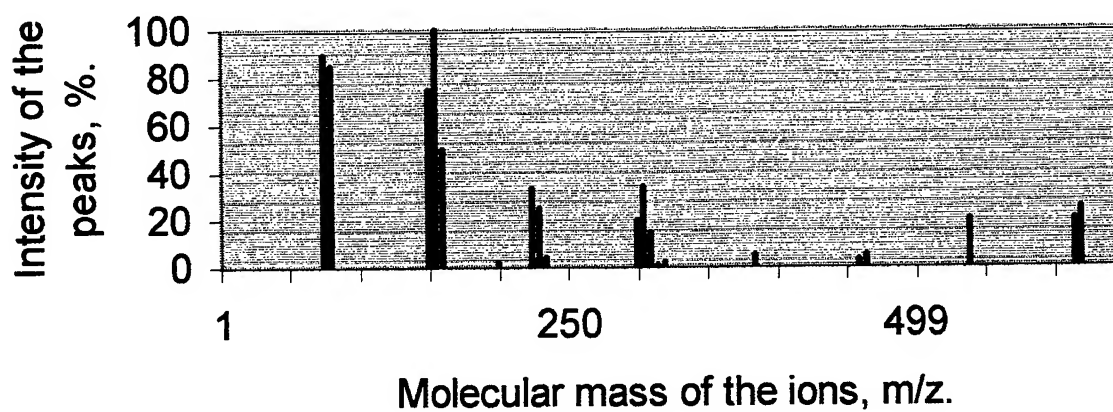


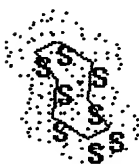
Chart 4. Mass spectrum of the As-Se-Sn semiconductor system after Ar-laser radiation.



Sticks & Dots models of the As-S molecules.



As_4
E=3,47 Kcal/mol



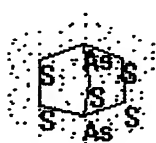
S_8
E=4,44 Kcal/mol



As_2S_3
E=25,81 Kcal/mol



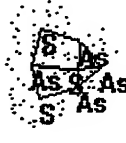
As_2S_4
E=17,62 Kcal/mol



As_2S_5
E=14,36 Kcal/mol



As_2S_6
E=19,11 Kcal/mol



As_4S_3
E=11,87 Kcal/mol



As_4S_4
E=21,88 Kcal/mol

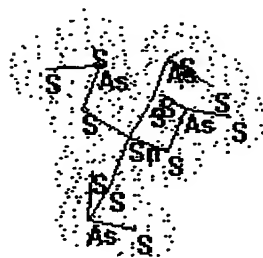


As_4S_5
E=24,98 Kcal/mol

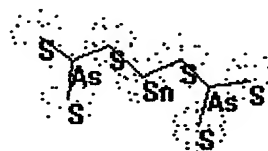


As_4S_6
E=43,13 Kcal/mol

Model of the As-S-Sn bonds.

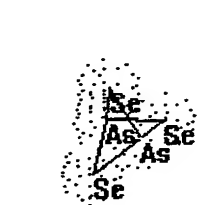


before laser illumination

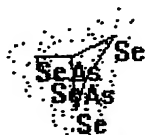


after laser illumination

Sticks & Dots models of the As-Se molecules.



As_2Se_3
E=97,18 Kcal/mol



As_2Se_4
E=115,42 Kcal/mol



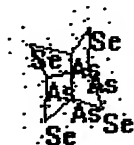
As_2Se_5
E=148,03 Kcal/mol



As_2Se_6
E=191.09 Kcal/mol



As_4Se_3
E= 80,26Kcal/mol



As_4Se_4
E=177.29 Kcal/mol



As_4Se_5
E= 150.07Kcal/mol

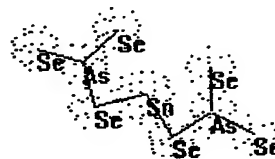


As_4Se_6
E= 184.33Kcal/mol

Model of the As-Se-Sn bonds..



before laser illumination



after laser illumination

4. DISCUSSION

Taking into account that molecules have tendency to formed evidently with minimum of the potential energy may be explained the appearance after illumination molecules that contain homogeneous As-As, S-S or Se-Se bonds. That fact respectively influences the physical proprieties of the thin films.

The observed changes in the mass spectra may be explained in view of some re-arrangement of the component atoms in the shot-range order. After the illumination the fragments of the form $[As_mS_n]^+$ & $[As_mSe_n]^+$ differ from the same before illumination. After illumination increased the intensities of the peaks, corresponding to the particles that contain As-As, S-S and Se-Se homogeneous bonds (As_4 , S_8 , As_4S_3 , As_4Se_3).

Molecules As_2S_3 and As_4S_6 contain only heterogeneous bonds As-S and molecules As_2Se_3 and As_4Se_6 contain only heterogeneous bonds As-Se. Molecules As_4 , S_8 , Se_4 contain only homogeneous As-As, S-S and Se-Se bonds. Molecules As_2S_4 , As_2S_5 , As_2S_6 contain respectively one, two and three homogeneous S-S bonds. Molecules As_4S_5 , As_4S_4 , As_4S_3 contain respectively one, two and three homogeneous As-As bonds.

The As_2Se_4 , As_2Se_5 , As_2Se_6 molecules contain respectively one, two and three homogeneous Se-Se bonds. The As_4Se_5 , As_4Se_4 , As_4Se_3 molecules contain respectively one, two and three homogeneous As-As bonds.

Molecules that contain only homogeneous As-As or S-S bonds have got a minimum of the potential energy. Thus As_4 molecule has got the potential energy 3,47 Kcal/mol and S_8 molecule has got the potential energy 4,44 Kcal/mol.

If the molecules contain homogeneous bonds As-As their have got a loss potential energy, for example As_4S_3 , As_4S_4 , and As_4S_5 have got respectively the potential energy 11,87 Kcal/mol; 21,88 Kcal/mol; 24,98 Kcal/mol. But the molecules As_4S_6 , that contain only heterogeneous As-S bonds have got respectively potential energy 43,13 Kcal/mol.

Modeling based on the mass spectroscopy data shows the appearance for As_2S_3 thin films after illumination the homogeneous As-As & S-S bonds and for As_2Se_3 thin films As-As & Se-Se homogeneous bonds. That fact leads to more compact packing of the component atoms. As result this fact caused the increase of the density of the films.

5. CONCLUSIONS

That behavior under the illumination may be connected with the characteristic of the structure of the thin films of As_2S_3 and As_2Se_3 doped with 2% of tin. For that reason, as a result of photostructural transformation under illumination the tin atoms change their valence from IV to II. In a like manner the illumination changes the coordination number of the tin atoms and that make the structure of the doped thin films more stable. That one permit us to conclude that the As_2S_3 and As_2Se_3 doped with tin alloys are more perspective for holographic and optical recording than the chalcogenide glass alloys without tin.

REFERENCES

1. A.M. Andriesh, *Physics and Application of Non-Crystalline Semiconductors in Optoelectronics*, Ed. by Andrei Andriesh and Mario Bertolotti, NATO ASI Series, **36**, pp. 17-30, 1997.
2. M.Popescu, *Physics and Application of Non-Crystalline Semiconductors in Optoelectronics*, Edited by Andrei Andriesh and Mario Bertolotti, NATO ASI Series, **36**, pp. 215-231, 1997.
3. V.T.Dolghier, *Physics and Application of Non-Crystalline Semiconductors in Optoelectronics*, Edited by Andrei Andriesh and Mario Bertolotti, NATO ASI Series, **36**, p. 457, 1997.
4. T.P. Martin, *Solid State Communication*, **47**, pp. 111-114, 1983.
5. A.Andriesh, A.Buzdugan, V.Dolghier and M.Iovu, *Proceedings of SPIE, ROMOPTO '97*, **3405**, pp. 258-261, 1998.
6. M. Lee, M.A. Paesler and D.E. Sayers, *J. Non-Crystalline Solids*, **123**, p. 295, 1990.

Fiber gyroscopes for strapdown technology

Octavian Novac*, Florina Jitescu

Military Equipment and Technologies Research Agency
P. O. Box 51-16, Bucharest, Romania, Code 76550

ABSTRACT

The gyroscopes are defined as devices, which can measure, autonomously, rotational motions relative to inertial space. They are of central importance for flight control, for navigation / orientation in the air, at sea and on land, and also for stabilization / guidance of smart weapon systems. Benefiting from advances in semiconductor technology, the basis of gyro systems has changed from mechanical platforms to strapdown technology. For strapdown use, new types of gyroscopes, such as optical gyros, have been developed. This paper presents optical gyros, emphasizing the fiber gyro and its principal advantages such as solid-state operation, light weight, small size, low power consumption, rapid turn-on time and high reliability, that are important considerations for many high-performance application areas.

Keywords: Strapdown technology, ring laser gyroscopes, fiber optic gyroscopes.

1. INTRODUCTION

The gyroscopes are defined as devices that can measure, autonomously, rotational motions relative to inertial space; consequently, gyroscopic systems are of central importance for flight control, for navigation / orientation in the air, at sea and on land, and for stabilization / guidance of smart weapon systems. Benefiting from advances in semi-conductor technology, the basis of gyro systems has changed from mechanical platforms to strapdown technology in which mechanical components are replaced by digital computers and software.

In the past, inertial navigation gyro systems contained a mechanical platform which carried the necessary gyroscopes and accelerometers and which was isolated from the vehicle's rotational motion by a system of gimbal.

This platform was aligned to the horizontal and north, and stabilized by the gyroscope signals. Acceleration in east-west and north-south directions was measured on the stabilized platform while the velocity and instantaneous position of the vehicle were computed.

Since the stabilized platform was voluminous, heavy and generating errors, more recently gyros and accelerometers have been fixed on the vehicle frame. In these strapdown systems (Fig.1), the acceleration is measured in the vehicle frame and the mechanical platform is effectively replaced by a computer software. In the system's digital computer, integration of the measured gyroscope signals is used to calculate a transformation matrix, which defines the instantaneous position of the vehicle relative to the earth and represents the mathematical analogue to a mechanical platform. The acceleration vector measured for the vehicle is multiplied by the transformation matrix and thus provides the acceleration in east-west and north-south directions, so that, as in stabilized mechanical platform systems, the velocity and instantaneous positions can then be computed.

In a strapdown system, the gyros are no longer rotationally isolated by gimbaling but are exposed to the full movement of the vehicle which, in aircraft, can be up to 400 °/s. This results in a very high dynamic range for strapdown gyros. Otherwise, high accuracy (0,01°/h) in this wide measurement range calls for excellent gyroscope linearity. Therefore, the change to strapdown technology forced new development of gyros to achieve the necessary dynamic range and linearity. Ring-laser and fiber-optic gyros have proved themselves suitable for strapdown applications.

* Correspondence: Phone: 401 423.30.58

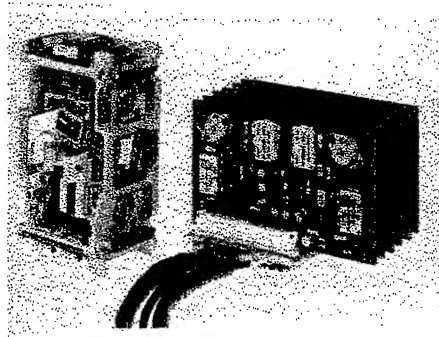


Fig.1 Strapdown system containing a sensor package with gyros and accelerometers (a), and a sensor electronics with digital computer (b)

2. RING-LASER GYROSCOPES

The ring-laser gyroscope (RLG) is an optical gyro in which light is guided by mirrors along a closed path, so that a beam of light encloses an area. If the rig laser is rotated, then two light beams which start at the same time but travel around the enclosed area in opposite directions, will show differences in transit times (Sagnac effect). This time difference provides a measure of the rotation that has occurred, and increases with the size of the area enclosed. The RLG consists of an HeNe laser, the beam of which is guided around the area by mirrors. Fig. 2 shows a RLG built by *Litton Guidance and Control Systems Division*, which uses four mirrors.

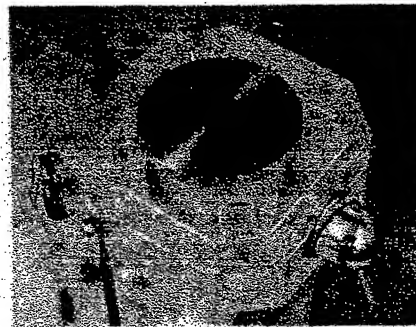


Fig.2 Ring-laser gyroscope

The difference in transit times in the RLG causes the laser to split into two modes with slightly different frequencies which overlap in the resonating chamber. This causes the formation of a standing light wave in which light (crests) and dark zones (nodal points) alternate. This standing wave in the RLG remains fixed in its position while the instrument rotates, and is thus the analogue to the moment of inertia of a mechanical gyro. The inertia of a rotating mass is thus replaced by the inertia of an electromagnetic wave field. These light and dark zones are scanned during rotation, not directly, as this is not possible due to the very small divergence of the laser beam. They are scanned indirectly, using an interference prism, to combine the beams from both directions onto a photodiode where interference fringes are measured.

The RLG has significant *advantages*:

- -the gyro doesn't contain any rotating mass since the inertia of a rotating mass is replaced by the inertia of an electromagnetic wave field;
- -there are no moving mechanical components, the function of which generates friction forces;
- -there are no needs to equilibrate moving parts;

- -the RLG has rapid turn-on time, high accuracy ($0,01^\circ/\text{h}$) and high reliability even under harsh environmental conditions.

In spite of this success, the RLG present some *technical drawbacks*:

- -it is necessary to ensure the rigidity of the optical path, so that it cannot be distorted;
- -the "lock-in effect" which occurs at a threshold of $100^\circ/\text{h}$. The back-scatter of the mirrors can lead to a type of friction between the wave field and the mirror so that, at small rates of rotation, even with high quality mirrors, the wavefield is dragged with the body of the instrument. This is known as the "lock-in effect" and must be overcome in all applications by using dither technique and rate bias technique. In dither technique each RLG of a gyro system is suspended in the center, on a spoked spring, and shaken by piezo elements with an amplitude of about $0,2^\circ$ about the axis of the spring. The springs are flexible elements and represent a source of error that degrades accuracy. In the rate bias technique, which avoids this source of error, the RLGs of a gyro system are mounted on a rotating table and are operated outside the lock-in threshold by continuously turning the table back and forth through a fixed angle.

3. FIBER-OPTIC GYROSCOPES

The fiber-optic gyroscope (FOG) is an optical gyro and uses light conducting fibers in place of mirrors. Its high sensitivity, ruggedness and the absence of lock-in effects permit its substitution for mechanical or laser gyros, even in rough environments.

Like the RLG, the FOG is based on the Sagnac effect, which produces a phase difference between two counterpropagating electromagnetic waves in a rotating frame of reference. The most commonly used configuration of a FOG is known as the Sagnac interferometer and its configuration is shown in Fig. 3.

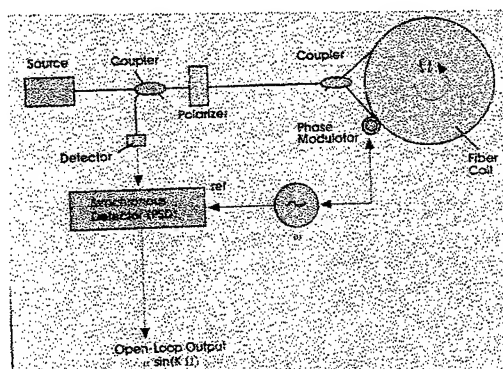


Fig.3 Basic minimum-configuration FOG

Light from an optical source is split into two components by a coupler and directed into a fiber loop of N turns to form optical fields that propagate around the loop in opposite directions. After passing through the fiber loop, the two optical components are recombined by the coupler and the interference between them is detected by the detector.

In a rotating frame, the Sagnac effect causes the effective optical path through the loop to increase for one beam, while for the other it becomes shortened. The resultant phase difference between the two optical components is given by:

$$\theta_s = 4 \pi R L \Omega / (\lambda_o c) \quad (1)$$

where R is the radius of the fiber coil, L is the total length of fiber in the loop, λ_o is the vacuum wavelength of the source radiation, c is the velocity of light, and Ω is the rotation rate. The phase θ_s is known as the Sagnac phase shift. The Sagnac effect is extremely small (the measurement of rotation rates on the order of $0,01^\circ/\text{h}$ using such a gyro requires a phase-shift-detection sensitivity of 10^{-7} rad) and can be easily overwhelmed by other physical effects that affect the optical path length and the phases of both waves equally. To eliminate phase shifts other than those that are due to rotation, the optical paths of the two beams must be identical when the gyro is in a nonrotating frame, that is, the system must exhibit reciprocity. To

achieve the reciprocity in the fiber loop it is crucial to have the same geometrical path for both waves and to select a single state of polarization for the input and the output waves since, because of their birefringence, the single-mode fibers used for optical gyros permit the propagation of two states of orthogonal polarization at different velocities and provide, consequently, two parallel optical path, in each direction, for the two independent polarization states. The geometrical path of both waves is made the same by deriving the output from the same coupler port that is used as the input and a single state of polarization is selected by using a polarizer at the input to the fiber loop.

The detector gives an electrical signal whose amplitude is proportional to the incident intensity of the detected interference signal. Since the counterpropagating waves have traveled identical optical path, they add in phase to a maximum value; at a maximum, the interference signal has low sensitivity to small phase differences between the interfering waves. To optimize gyroscope sensitivity, especially for low rotation rates, a phase-modulation technique is used. It consists of modulating the phase of each of the counterpropagating waves, by applying a time-varying modulation

$$\Phi = \Phi_m \sin \omega_m t \quad (2)$$

at one end of the fiber loop by means of a phase modulator. The phase modulation results in a nonreciprocal phase difference Φ_{NR} between the two waves, and also results in the intensity modulation of the interference signal. The intensity modulation of the interference signal is given in the following form:

$$P_m(t) = K \cos \{ \Phi_m \sin(\omega_m t) - \Phi_m \sin[\omega_m(t-\tau)] + \theta_s \} \quad (3)$$

where K is a coefficient proportional to the optical power and τ is the propagation time through the fiber loop- and can be expressed in terms of a Bessel function expansion which underlines that the interference signal without phase modulation ($\Phi_m = 0$) includes the Sagnac phase shift θ_s only through the form of $\cos \theta_s$, whereas the terms including $\sin \theta_s$ appear as a result of the phase modulation. These are the terms that assure the optimum or linear response of a gyro in a region of low rotation rate $\Omega \approx 0$. The component that oscillates at the fundamental frequency ω_m and has a sinusoidal dependence on Sagnac phase shift, θ_s , represents the output signal of FOG and varies proportionally to the Sagnac phase shift (to the measured rotation rate) for low rotation rates.

The output signal of FOG has a sinusoidal dependence on Sagnac phase shift and varies proportionally to the Sagnac phase shift (and thus, to the measured rotation rate), especially for low rotation rates, if a sinusoidal phase modulation technique is applied in order to optimize gyroscope sensitivity.

There are two basic modes of operation of the fiber gyros: open-loop and closed-loop. Fig. 4 shows the basic configurations used to implement the two modes.

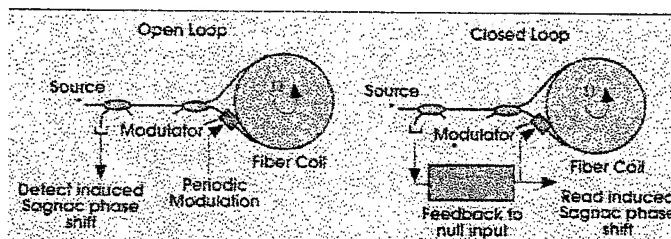


Fig.4 Configuration of open and closed-loop operations

In the first, the magnitude of Sagnac phase shift is determined directly, from the output signal of the FOG, while in the closed-loop configuration, the gyroscopes employ nonreciprocal phase shift devices, in a feedback loop, to compensate for the Sagnac phase shift, so that the FOG is operated at null.

Open-loop gyro offers a lower-cost option for many medium-performance applications but are limited by a number of factors. The output of an open-loop FOG depends sinusoidally on the Sagnac phase shift, and thus, on rotation rate; this leads to nonlinearity and to a limited dynamic range. Furthermore, the scale factor depends directly on the source intensity and on the polarization changes in the fiber. In most cases, the polarization problem is overcome by using high-birefringence, polarization-maintaining (PM) fibers, although this increases the cost of the optical head. The polarization

problem can also be overcome using a depolarized gyro configuration with a non-PM fiber coil, thus lowering the system cost.

Closed-loop gyro offers the potential of high-performance rotation-rate sensing with low drift, wide dynamic range and high scale-factor stability. Closed-loop signal processing is, however, considerably more complex, both optically and electronically, typically involving high-speed digital electronics. These systems are aimed at high-precision, low-drift and wide-dynamic-range sensing applications, such as inertial navigational system. In general, this type of system cannot provide very low cost options for less-demanding applications, where minimum detectable rotations (1 to $10^\circ / \text{h}$) and linearities (0.1 to 1 percent) may be adequate.

To improve the limited dynamic range of an open-loop gyro, an analog phase-tracking demodulator has been developed, that simulates the operation of a true closed-loop gyro, but the phase-shift nulling is done electronically, not optically. The scheme can be implemented using very low-cost analog electronics, and, when combined with a depolarized optical head, provides a system with low-cost optics and electronics.

The optical configuration of this electronically closed-loop system is basically that of a conventional open-loop gyro using phase modulation technique (Fig. 5).

In this scheme, the gyro output is fed to an analog multiplier, which mixes the harmonic components of the gyro output with an electronically synthesized interferometric signal S_e , of relative phase shift Ψ_r and modulation $\Delta\Psi \sin \omega t$, to produce a signal:

$$S_o = A \sin (\theta_s - \Psi_r) \quad (4)$$

where A is a constant dependent on the optical parameters of the system and the phase-modulation amplitude. This signal is dependent on the sine of the difference in phase between the gyro and the electronically synthesized interferometric signal $(\theta_s - \Psi_r)$. This is the form of signal generated with true closed-loop gyro configurations, where the phase Ψ_r is optically introduced in the fiber loop to directly null the Sagnac phase shift. In the system described here, the output of equation (4) is electronically synthesized from the output of an open-loop gyro. By using S_o as an error signal in a control loop, the output S_o can be nulled and the Sagnac phase shift (and, thus, the rotation rate) can be read via Ψ_r .

The output is linear over a range $\sim \pm 2\pi$ range in Sagnac phase shift, a range much greater than that obtainable from a direct open-loop gyro. This type of system can be configured for a range of rotation rates but typically will perform best with resolutions of $\sim 10^\circ / \text{h}$ and maximum rates of $\sim 1000^\circ / \text{s}$.

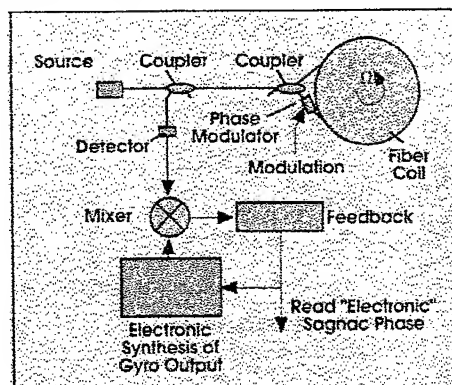


Fig. 5 Fiber gyro with electronically closed-loop operation

4. ADVANTAGES AND APPLICATIONS OF FIBER-OPTIC GYROSCOPES

As a sensor with no moving parts, the FOG has a number of advantages over conventional mechanical gyroscopes: high reliability even under harsh environmental conditions; no spin-up time; maintenance free; high shock resistance; high vibration resistance; extremely high bandwidth; no acceleration dependent drift; long shelf life; long service life; low cost of ownership; high Mean Time Between Failure (MTBF), light weight, small size, low power consumption. These are

important considerations for many high-performance application areas; adding to these advantages the potential for very low cost, the application areas for fiber gyros expand considerably.

The area of land navigation, and, in particular, the development of fiber gyros for navigational / guidance systems as part of intelligent vehicle systems, is generating considerable interest. Low-accuracy gyros can be used in such applications as positional updates from GPS (satellite) and ground-based reference beacons, and electronic maps can be used to augment the system. Companies in Japan, such as Sumimoto, Matsubishi are producing a large numbers of fiber gyros for such applications. Typical specifications include a resolution of $\sim 0,01^\circ/\text{s}$ and an accuracy of $< 0,25$ percent for rotations $< 70^\circ/\text{s}$. These devices are being installed in Nissan and Toyota cars sold in Japan as part of a navigation system that uses GPS and CD ROM maps.

Other potential applications of these low-cost fiber gyros include robotics, missile guidance, gyrocompasses and navigational systems for light aircraft. FOGs have the potential to provide a higher performance and greater reliability than conventional rate gyros, combined with lighter weight and lower power consumption. Litton Guidance and Control System, one of several companies working in this field, realized a production- standard inertial measurement unit (IMU)- comprising three FOGs, three accelerometers and the associated electronics – that can be packed into a pyramid measuring less than 7,6 cm per side and weighing under 340 g. This compares with typically 11,4 kg for an IMU based on conventional gyros, and 6,8 kg for one using ring-laser gyros.

Litton Guidance and Control Systems had test-flown what was claimed to be the first all-solid-state IMU. This Attitude and Heading Reference System employs three FOGs, microminiature silicon accelerometers and circuitry in a system weighing 2,3 kg. Also, the company developed the LN-200 IMU, in collaboration with LITEF in Germany and LITAL in Italy, as a candidate for use in missiles; the LN-200 IMU measures 12,7 cm x 12,7 cm x 10 cm and weighs less than 2,3kg

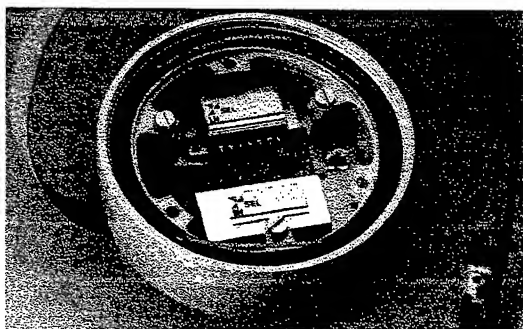


Fig. 6 Fiber-optic gyro

Litton has also built prototype FOGs for the US Army's Picatinny Arsenal, which is working on smart munitions for large calibre guns on tanks and howitzers; the company has also delivered engineering development models of high-accuracy FOGs to the US Naval Air Development Center, to demonstrate their feasibility for aircraft navigation system and shipboard gyrocompasses.

5. CONCLUSIONS

Ruggedness and long service life make the FOG a first choice for every application where it has to survive in a harsh environment. Such applications include turn indicators, platform stabilization, control of robots, navigation systems for vehicles and airplanes, stabilization of antennas and sensor packages, Attitude and Heading Reference Systems, hybrid GPS (Global Positioning System), aided navigation systems, and Inertial Navigation Systems (INS).

REFERENCES

1. Kersey, A. and Burns, W., "Fiber Optic Gyroscopes Put a New Spin on Navigation", *Photonics Spectra*, 27, pp. 72-76, (1993).
2. Handrich, Eberhard, "Gyroscope Technology: From Mechanical to Optical Gyros", *Military Technology*, 12, pp. 40, (1988).

Peculiarities of solidification mechanism of steel after Nd:YAG long pulse laser welding

V. Iov, F Costache*, A. Marian, D.M. Buca,

National Institute of Laser, Plasma and Radiation Physics

ECS Laboratory, P.O. Box M.G.-36, Bucharest, RO-76900, Romania

ABSTRACT

The hot cracking problem encountered when 1 mm thick stainless steel sheets are seam welded using a long pulse Nd:YAG laser is studied. Cracks are observed only in regions where the primary austenite was formed in the cooling phase, depending on its amount in the weld. The initiators of cracks were found between the heat affected zone and base metal as a band of segregate. High repetition rates decrease the crack formation at constant average power and welding speed. The primary austenite dendrites are strongly influenced by cooling rate. Melt thickness increases with pulse energy when pulse duration and repetition rate are kept constant. The optimum focus position was approximately 0.5 mm below the level of the workpiece front face and produced good quality seam welds.

Keywords: laser welding, long pulse Nd:YAG laser, solidification structure.

1. INTRODUCTION

Fusion welding is one major fabrication process where the laser has found a large field of applications. Production rate and yield, welding of materials with different melting points in inaccessible areas and different environments through transparent enclosures and external fields are the more obvious advantages of laser welding. Because of the short time factor associated with this source of heat, welds adjacent to heat sensitive elements could be effected. The heat affected zone, distortion and shrinkage of the weldment are very small and in many situations could be neglected.

In recent years, major advantages have taken place in our understanding of welding processes and welded materials. The high complexity of laser welding process requires an interdisciplinary approach. Until recently, descriptions of solidification of liquid alloys have focused on the near-equilibrium limit in which the solidification speed is largely controlled by the rate of transport of latent heat away from interface. However, if the temperature gradient becomes steeper, the growth rate increases to a point where the finite interface mobility can not be ignored. The maximum cooling rate (that is the product of temperature gradient and growth rate) encountered within the weld pool may range from 10^2 to 10^7 °C sec⁻¹. As a result of rapid solidification the structure of the fusion zone is changed.

2. WELDMENT STRUCTURE AND PROPERTIES

In laser welding the coherent beam of laser light can be focussed to a very small spot giving rise to high power densities of over 10^6 W cm⁻². Fusion welding processes lead to three distinct regions in the weldment as it is shown in Fig. 1. In the fusion zone is developed melting and solidification. The heat affected zone is characterised by thermal exposure and solidification transformation, without melting. The base metal zone is unaffected by the welding process.

As the laser beam strikes the workpiece, it quickly evaporates the substrate, produces plasma and creates a "keyhole" surrounded by molten metal. The driving force of keyhole formation is the evaporation pressure caused by local evaporation. The evaporation pressure is created locally where the intensity of the laser beam is high enough to heat the

* Correspondence: E-mail: florenta@pluto.infim.ro

material above the boiling temperature. The evaporation pressure of the metal balances the surface tension and the hydrostatic pressure of the molten metal to keep the keyhole from collapsing. Once the keyhole has become stable, it acts a black body and absorbs most of the incident radiation. The energy absorption efficiency can be improved dramatically to a value much higher than before, owing to multiple reflections of the beam in the cavity. As a result, laser welding produces welds with a high aspect ratio (depth-to width ratio) and narrow heat affected zone. In the keyhole mode of welding, the estimation of the absorption coefficient depends on the depth of the keyhole, which is difficult to determine, in practice.

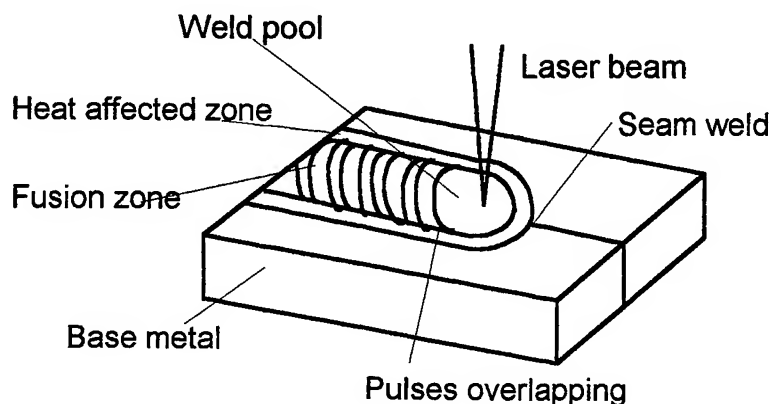


Fig. 1: Schematic diagram of the fusion welding process

The process-microstructure-property relationships are important for the understanding of the structure, properties and performances of the welded materials. Unfortunately, many of the basic principles relating to these relationships are not well understood, mainly because of the complexities inherent in fusion welding, such as unknown melt-pool shape, formation of non-equilibrium microstructures, and spatial variations of composition, microstructure and properties. Extensive local variations of composition and microstructures in a weldment are common and unique to welded structures. In addition, due to localised heating during welding, complex thermal and transformation stresses are generated that remain in the weldment as residual stresses¹.

The origin of microstructures and stress gradients and their influence on the weld performance is a largely unexplored field not only due to the lack of understanding of these gradients but also because the characterisation tools to probe these gradients on both macroscopic and microscopic scales have been developed fairly recently.

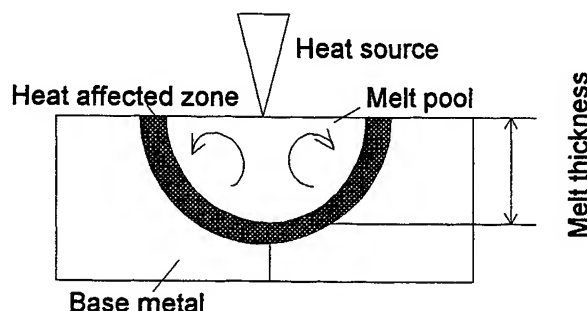


Fig. 2: The zones appeared at the laser beam - base metal interaction.

Currently, efforts are under way to study the fusion zone (FZ) and the heat affected zone (HAZ) characteristics and, in particular, the solidification behaviour of the weld-pool and the solid state transformations in welds (Fig. 2).

The critical parameters in determining the FZ microstructures are growth rate, temperature gradient, undercooling and alloy constitution. The temperature gradient and growth rate are important in combined forms and cooling rate as they influence the solidification morphology and the scale of the solidification substructure, respectively. Since the temperature gradients in solid could be easily estimated, the thermal gradient in the liquid is more critical in determining the morphology of the solid-liquid interface and its evaluation is complicated by the fact that it is strongly influenced by convection in the weld pool. Both of them play a significant role in determining the solidification substructure in the fusion zone.

Undercooling is a critical parameter that controls the solidification microstructure and segregation effects. It may be associated with the nucleation of a solid in a liquid or with the growth process during solidification. The effect of increased undercooling at the dendrite tips is to solidify at a composition closer to the overall alloy composition and thus reduce microsegregation. The stability of the solid/liquid interface in the fusion zone is critical in determining the microstructural characteristics of the weld metal. During the growth of the solid, the microscopic shape of the solid/liquid interface is determined by the thermal and constitutional conditions in the immediate vicinity of the interface. These factors determine whether growth occurs by planar, cellular or dendritic mode. Since in pure metals (suppose that any solute effects are developing) only thermal gradients control the stability of the solid/liquid interface, in alloys the solidification front stability is more complex, because composition gradient effects ahead the interface must be considered.

The effect of solute redistribution and build-up of solute at the solid/liquid interface on the morphological stability of the solidification front has been examined by considering the concept of constitutional supercooling. Depending on the actual thermal gradient in the liquid, the plane front will remain stable or will become unstable. As the growth conditions depart from planar stability, the interface morphology will change to cellular to dendritic. If the conditions are favourable, the dendrites will exhibit secondary and tertiary arms in crystallographically preferred growth conditions.

3. EXPERIMENTAL SET-UP AND PROCESS PARAMETERS INVOLVED

The laser used for performing welding experiments is a long pulse Nd:YAG with average power up to 100 W, repetition rate ranging among 1-10 Hz. Laser parameters used in this experiment are listed in Table 1.

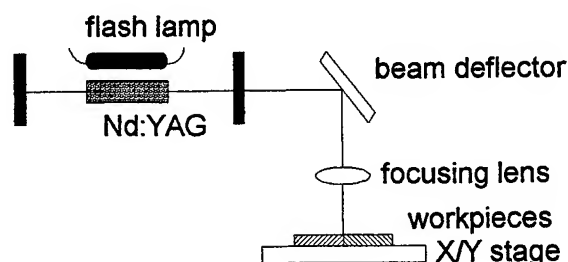


Fig. 3: Experimental arrangement for laser welding.

The welding material was a 1 mm thick plate made of AISI 316 stainless steel and the joint geometry used was seam (butt) weld. The pulsed seam weldments were performed with overlapping pulses. The variable overlapping degree (defined as $(1-d/d_s) \times 100$ where d -successively spot distance and d_s - spot diameter) were 70-90 % and was acquired by fitting the pulse repetition rate with the speed of the computer controlled translation stage. For beam focusing a lens with 90 mm focus length were used. In Fig. 3. is presented a schematic diagram of the laser welding experimental set-up. The melt thickness was measured using an optical microscope.

A check on the optimum position of the focus was made. The results showed that when the focus point was positioned inside the workpiece, a V shaped weld resulted so that it is necessary to align more precise the two pieces to be welded. When the beam was focused well above the level of workpiece front face, a large "nail head" was formed with a consequent loss of penetration. The optimum focus position was approximately 0.5 mm below the level of the workpiece front face and produced welds with little or no "nail head" and near parallel sides.

Tab. 1 Melt thickness obtained for laser parameters and overlapping degree used

<i>Pulse energy (J)</i>	<i>Pulse duration (ms)</i>	<i>Repetition rate (Hz)</i>	<i>Overlapping degree (%)</i>	<i>Melt thickness (μm)</i>
1.5	1	1	90	550
1.5	1	5	90	540
1.5	1	10	90	530
1.5	4	5	90	170
2.1	4	5	90	220
3.7	4	5	90	470
4.6	4	5	90	800
1.5	4	0.5	90	140
2.1	4	5	85	200
2.1	4	5	70	190

4. RESULTS, DISCUSSION AND CONCLUSIONS.

During welding, as the weld pool undergoes transformation from liquid to solid, the solidification behaviour controls solute redistribution², solidification structure, the size and shape of grains, and the distribution of inclusions and defects, such as porosity and hot cracking.

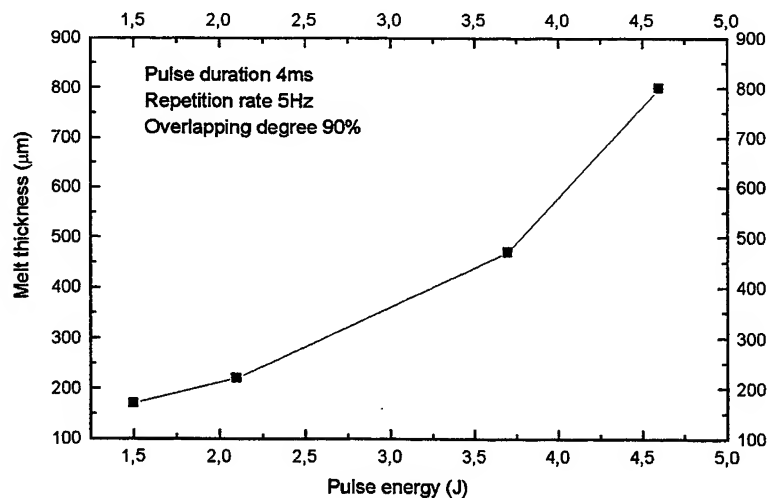
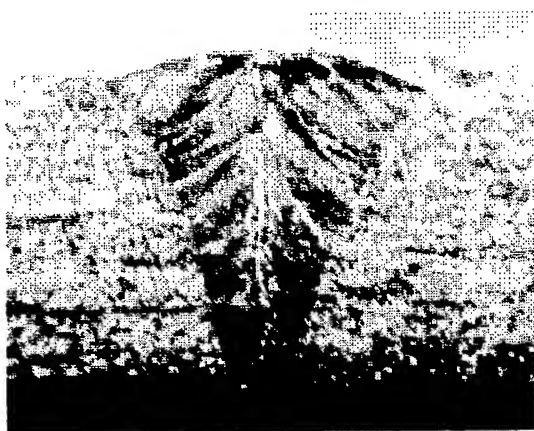


Fig. 4: Melt thickness versus pulse energy.

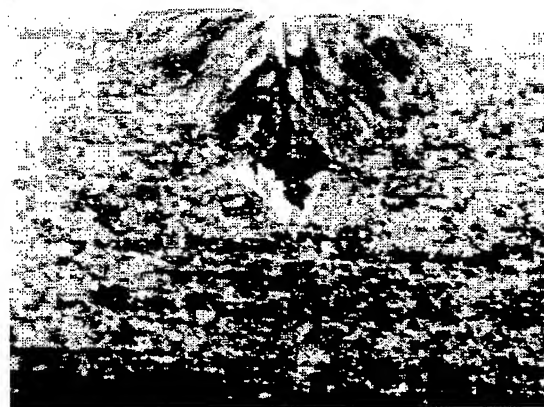
The melt thickness is strongly influenced by laser parameters. The results show that melt thickness increases with pulse energy when pulse duration and repetition rate are kept constant (Fig. 4.). Moreover, melt thickness increases with overlapping degree at constant pulse energy, pulse duration and repetition rate.

The problem encountered within this material was hot cracking, phenomenon that depends upon the cooling rate in the weld material. The AISI 316 type stainless steel consists mainly of austenite with a small amount of ferrite. During cooling down, the material in the joint solidifies either as a primary ferrite or primary austenite³. When cooling further down, most of the primary ferrite is then transformed into austenite. This behaviour of the microstructure has the origin into a change in the mode of freezing⁴. The various factors that control this nonequilibrium effect and the extent to which nonequilibrium phases form in welds cooled under rapid solidification conditions are not yet fully understood.

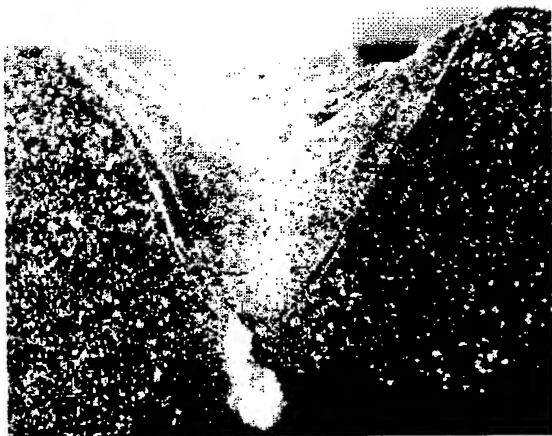
The metallographic examination revealed that solidification cracking had occurred in all of the welds and the initiators of cracks were found between the heat affected zone and base metal as a band of segregate. Primary austenite dendrite (PAD) was observed in all the specimens tested, with variations in pattern occurring as a result of differences in the rate of cooling. PAD readily grows, starting from the liquidus down to the eutectic temperature. Growth of dendrites continues concurrently with the eutectic range of the solidus. Thus, undercooling may lead to higher dendritic interaction. Because the dendrite arm spacing is controlled by diffusion and not by heat transfer, the decrease in the spacing between dendrites with increase in the cooling rate can be explained by the fact that there is insufficient time available for the diffusion solute.



a.



b.



c.

Photo 5: Transverse sections of weldments (the photos were performed by using an optical microscope)

Weld parameters:

a. $E = 1.5 \text{ J}$; $\nu = 5 \text{ Hz}$;

b. $E = 1.5 \text{ J}$; $\nu = 0.5 \text{ Hz}$;

c. $E = 1.5 \text{ J}$; $\nu = 10 \text{ Hz}$;

Overlapping degree: 90 %.

In conclusion, the results of these studies about hot cracking are:

1. The cracks are seen only in regions where the primary austenite was formed in the cooling phase, and depends upon it amount in the weld (Photos 5. a, b.);
2. Crack formation increased when the cooling rates were increased;
3. Cooling rates are increased if:
 - a) Welding depth is decreased. In this case the keyhole is small or does not exist (Photo 5. b.);
 - b) The overlapping of the pulses is decreased.
 - c) Welding speed is increased
4. At constant average power and welding speed, high repetition rates were reducing the crack formation.

In the Photo 6 is presented the Nd:YAG long pulse laser with a beam delivery system used for welding.

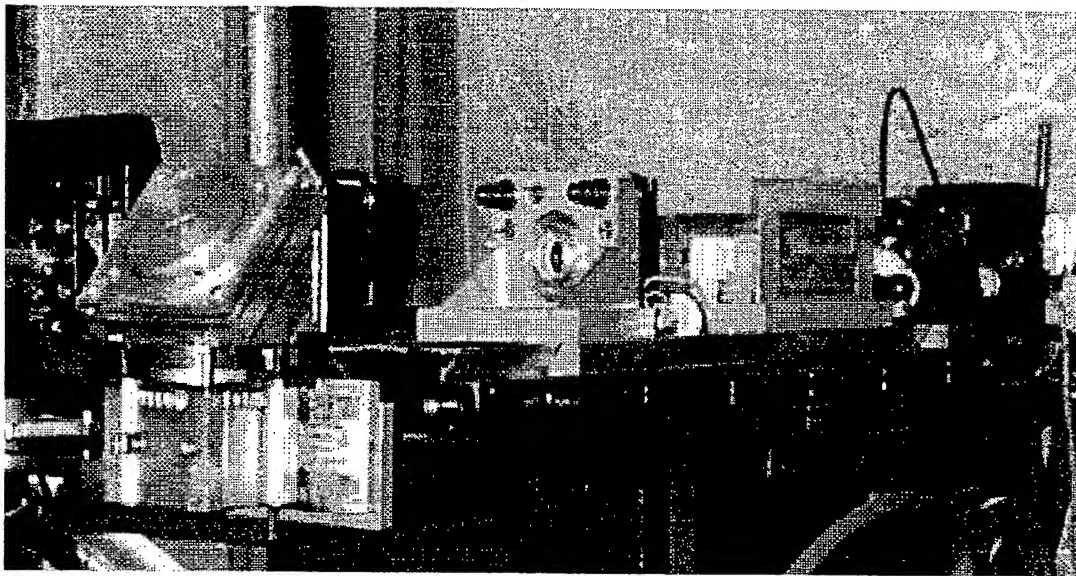


Photo 6: The experimental set-up for laser welding.

REFERENCES

1. S.A.David and S.M.Vitek, *International Trends in Welding Science and Technology*, ASM International, Materials Park, OH, 1982.
2. T. Deb Roy and S. A. David, *Physical processes in fusion welding*, Rev. Mod. Phys., **67**, No. 1, pp. 85-112, 1995;
3. K. Mukherjee and J. Mazumder, *Lasers in Metallurgy*, The Metallurgy Society of AIME, Warrendale, PA, 1982.
4. R. W. Cahn and P. Haasen, *Physical Metallurgy*, Part 1, Elsevier-New York, 1987.
5. J. Kroos, U. Gratzke, M. Vicaneck and G. Simon, "Dynamic of the keyhole in laser welding", *J. Phys. D: Appl. Phys.*, **26**, pp. 481-486, UK, 1993.

Selective laser sintering processing of metallic components by using a Nd:YAG laser beam

F. Costache*, A. Marian, D.M. Buca, V. Iov

National Institute of Laser, Plasma and Radiation Physics

Quantum Electronics Laboratory

P.O. Box MG-36, RO-76900 Bucharest, Romania

ABSTRACT

The development of the selective laser sintering (SLS) technique used for rapid building of 3D models from metal powders is presented. The aim of research efforts in laser sintering is to create strong and dense models with no need post-machining. The feasibility of SLS is demonstrated by the mechanical properties of models obtained, which nearly the equivalent to the products formed by sintering in conventional way. However, the range of the materials available to SLS technique is limited to weldable metals and alloys. The main benefit of this laser application is the exact control of process parameters.

A Nd:YAG laser working in CW regime was used. It was obtained sintered powder parts with a fine accuracy up to 0.4 mm. The shrinkage degree on height was lower than 10 %. The microstructure and mechanical properties of SLS processed materials are similar with those of conventionally processed material. The strength and the bulk hardness of the sintered material were tested.

Keywords: SLS, Nd:YAG laser, metallic powder, process parameters

1. INTRODUCTION

The wide variety of graphical models computer assisted was allowed to introduce on the market efficient and productive methods. Rapid prototyping is one of this methods rely on computer graphics technology. The feature of this method is the ability to produce freeform with complex geometry.

A brief description of the computer generated model procedures, the key of the rapid prototyping technique, is given below. The 3D model is created on computer assisted design (CAD) system and then is sliced into multiple 2D parts. The data, which describe the model surface, are used to reproduce a 2D slice of the model. The initial model prototype is built up again slice by slice through a linking procedure. For the rapid prototyping systems the build time is mainly dependent on the number of slices used and it can be significantly reduced through the use of a thicker slice. Methods of the rapid prototyping technique are SLS, which is used to generate 3-dimensional objects directly from CAD data by laser irradiation of a thin powder bed on a precise contour.

This paper aims to identify the optimal parameters of the sintering process in order to achieve accurate objects with good mechanical properties. Surface structure examination of sintering area shows a grained texture. Hardness of material after laser irradiation was evaluated and compared with material obtained by conventional ways. The influence of the laser power density and overlapping degree on surface roughness and tensile strength of sintered parts were discussed.

2. SELECTIVE LASER SINTERING

The part is grown by powder using the selectively melting (sintering) of the powder particles. A laser beam scans the powder bed and heats the powder grains to its melting point, so that they melt and stick together. After that the base plate is displaced slightly, and the next layer of powder is spread across the surface by a rotating roller. The next powder layer will be at the same working surface to the laser. The surrounding unscanned powder serves as a natural support for sintered

*Correspondence: e-mail: florenta@pluto.infim.ro

powder, therefore it is not necessary an extra supporting structures for the next layer of the powder. At the end of the build process, the entire amount of powder, sintered and unsintered, is lifted out of the machine. The part is built from successive layers of sintered powder. The final object can be sanded down, if required, to obtain smooth surfaces.

There are two phase transitions: from solid state to fluid state and back to solid state again. The materials used or investigated in this paper are metals. To obtain densities near 90 percents in compare with material nominal density, optimal process parameters were determined.

The parameters that potentially affect sintered part quality are layer thickness, powder particle sizes, laser power are scanning speed. Last researches examine also the sinter front's propagation effects in sintered layers and the influence of the relative densities of the sintered and unsintered powders during SLS process¹.

By melting and linking the metallic particles tend to be together due to superficial forces. The sintering process is affected by inhomogeneous heating of powder, dilatations and solidification mechanisms. These effects lead to porosity increasing and tensile strength decreasing of the parts. The surface roughness is higher when particles powder size is smaller. It can be obtained pieces with the lowest porosity and the mechanical strength very good. Hardening effect is determined by local heating high speed processes followed by cooling result from flow heat into cold base material. The features of these transforms are determined by temperature distribution in heat affected zone and its variation speed.

3. EXPERIMENTAL SET-UP

The SLS technique has been developed for stainless steel. The extension of this technique to metals has been the goal in order to create parts and particularly tools of high strength and hardness. In order to achieve a high density the powder has to be completely melted.

The goal of this research is to obtain pieces from iron cast sintered powders nearly to conventional way. This goal can be reached using a laser Nd:YAG because many materials, especially metals, have a very good absorptivity at 1.06 μm .

The SLS process can be described in few steps. First, a thin powder layer from fusible materials was predeposited on a tin base plate. An initial object was selectively "drawn" on the powder bed by local irradiation with a Nd:YAG laser beam. An additional powder layer was deposited over the previous one. A slide-roller mechanism made this powder layer uniform and it was scanned with the laser beam after the same contour. Each layer has been fused with the layer below it. The process was repeated until the piece is finished.

The powder used was from iron cast with particle sizes up to 100 μm . the optimal thickness layer was found about 100 μm , nearly to powder particles size. This value has been chosen from flow heat reason, fact that will be seen afterwards.

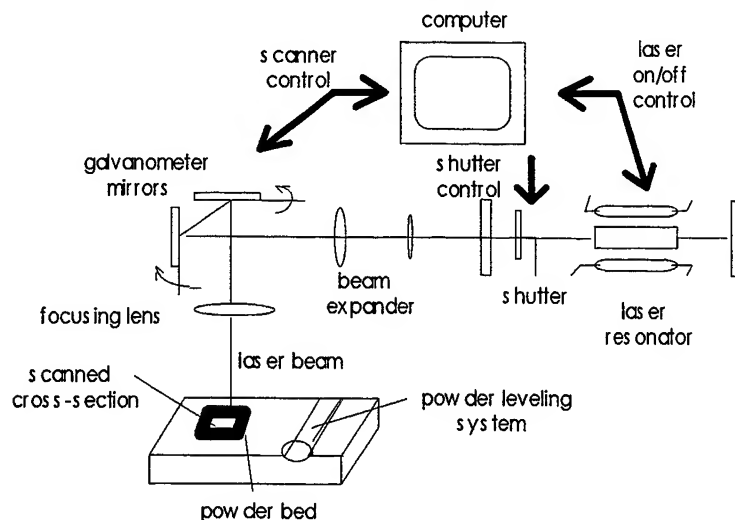


Fig. 1: The experimental set-up used for selective laser sintering of powders.

The experimental set up is shown in Fig. 1. The experimental arrangement contains a Nd:YAG laser working in CW regime with output power up to 150 W. Inside the laser cavity there is shutter commanded by the computer. So it is controlled the start-time and stop-time of laser irradiation.

The main computer commands the shutter to stop the laser radiation before effective scanning starting and immediately after laser scanning. This shutter assures the velocity vector accuracy. At scanning start the shutter is commanded to open and the mirror begin to move. One process delay lead to structural discontinuities, the mirror beginning the movement before laser starting. An earlier shutter opening leads to supra-exposure of powders at laser radiation and determines, as result, undesirable melting powder extension in scanning start point. System with no shutter needs a high scanning speed to reduce the radiation influence over unsintered powder parts.

The fourth process in the laser beam delivery system is the laser scanning system. The scanning system is the key of possibility to "drawing" the surface piece. The scanner configuration for SLS consists of two galvanometer-driven scanner mirrors controlled by two servo-controllers. The vector position commanded by computer is fragmented into incremental steps and is used to generate position profiles. This assures the beam scanning with a constant speed. The ability to maintain a constant scanning speed along the scanned surface is a critical matter because the sintering depends on the laser power density. A complex research gives solutions for improving the geometric accuracy; to reduce the staircase effect which is characteristic of layered components with square edges, and closely matched the designed surface⁴.

After focusing through a focusing system, aberrations free, the laser beam is lead to the process chamber. The sintering process has been made under the nitrogen atmosphere. The gas was introduced into the chamber through a nozzle. It's necessary to isolate the work zone because of the way that atmospheric oxygen affects the irradiated surface. In spite the fact that the oxides resulted by irradiation increase radiation-material coupling is much easier to control the process with no take this ones into account.

The scanning was made through successive contours. Important parameters are overlapping between contours due to inhomogeneous heating in laser spot. Scanning mirrors programming command was taken into account the shape of surfaces in according with the sizes of the objects obtained and the mirrors rotating angles with respect with focusing system.

In order to obtain optimal sintering processes parameters in the command program of scanning system was included the possibility to vary the overlapping passes degree and the scanning speed of sintering for a settled spot laser size and the choice the maximal mirrors rotating angle. Process parameters were resulted from the correlation between these ones and power laser density. The scanning speed was determined by ratio between two successive mirror movements' distance and the time allocated for that. This last one can be defined as a ratio between computer measured time necessary to describe the surface and the number of steps necessary to fill the chosen surface, respectively. That number of steps depends of the surface sizes, number of contours, overlapping passes degree and laser spot size.

4. RESULTS AND DISCUSSIONS

Parameters like laser working regime, power density, scanning speed, overlapping passes degree is decisive for sample density. Those parameters depend on each other and its must be properly adjusted. Though for a power laser and a scanning speed known the thickness and the depth of the melting pool have values that must be correlate with overlapping passes degree and laser spot size.

The layer thickness can be varying in order to find the optimal thickness value. It depends on the sintering depth correlate with laser power and laser spot size for a matched scanning speed. To do this it's need that the powder component particles have well known diameter. First, it must take into account the optical, thermal and mechanical characters of material used such as material absorbtivity at laser wavelength, melting point, thermal conductivity, density, thermal difusivity, sintering depth under an irradiation time established.

The quality of parts obtained by SLS, a major advantage of the SLS process depends heavily upon the ability to build accurate, high quality parts on a repeatable basis. The accuracy of the sintered surface was obtained by measuring the thickness of the sintered zone at one laser scanning contour on the powder bed at laser power density and scanning speed settled. It was established that the laser spot size must be 2-3 times higher than the powder particle size. The layer thickness was taken comparable with the powder particle size. It was necessary to establish a proper layer thickness to achieve a

linkage between layers due to enough laser energy. Level of the laser power determines the severity of temperature gradients, which introduce deviation due to thermal modes on parts. As a result, the laser power is a significant contributor at the sintering depth and the surface quality. The diagrams from Fig. 2, 3 present the dependencies between these parameters versus laser density powder at different focusing distances and at two chosen scanning speed programming settled. The graphics from below was raised at the same laser powers, only the focusing distance being changed.

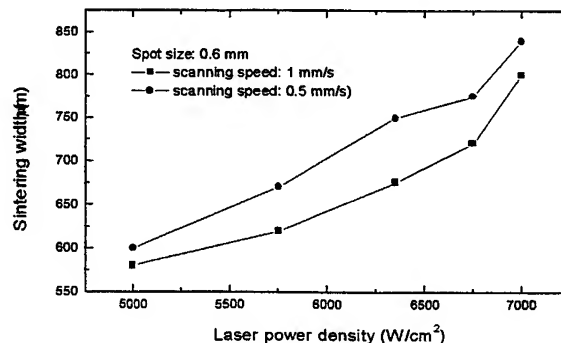
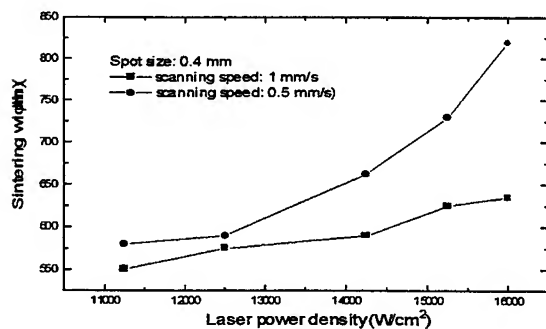


Fig. 2: Sintering width vs. laser power density for different sintering scanning speeds.

These diagrams conclude that at lower scanning speed the sintering zone widths are increased. These values were introduced in scanning program for to raise accuracy of parts.

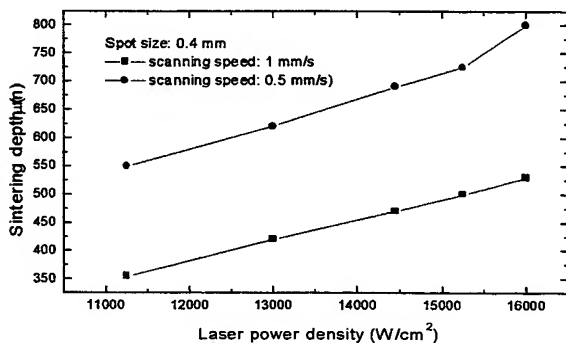


Fig. 3: Sintering depth vs. laser power density for different scanning speeds.

The conclusion result from this diagrams is that thickness layer must be chosen lower than 300 μm for to remain an amount of laser energy to heat in volume for assure the linkage between layers. As it was expected the sintering depth is lower at high scanning speeds.

Both the accuracy and the surface finish of parts are degraded as layer thickness increases. The choice of layer thickness is a compromise between built time and accuracy. From the stainless steel powder, finally, the objects accomplished was very accurate (dimensional tolerances was about 0.2-0.4 mm). A serious problem whose solution was actively research was the appearance of shrinkage on every layer after laser scanning. The pieces obtained in this experiment have been with a shrinkage degree on height by 10 percent, in the case that the thickness layer was about 100 μm .

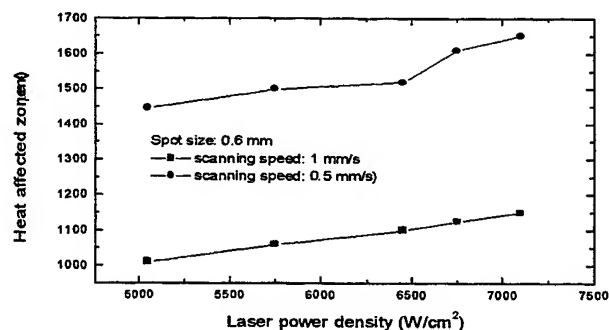
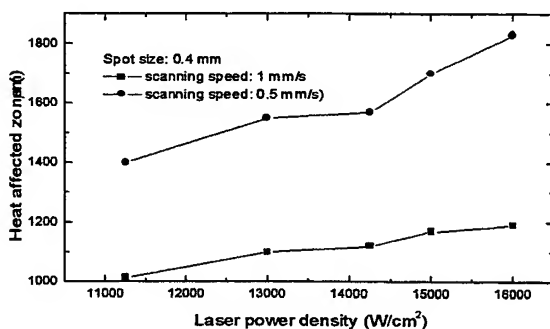


Fig. 4: Heat affected zone width vs. laser power density for different scanning speeds.

The shrinkage degree values are reproducible at the parts, which are created in the same conditions, with the same process parameters. To prove this was made few copies in the same process conditions. The sizes between programming object and the object produced by SLS result from errors in scanning mirrors movements in accord with commands and errors provide by the values of some measured parameters included into calculations from the command scanning program.

As it mentioned before, it's necessary to isolate the work zone from the atmospheric oxygen to avoid oxide creation, the main factor, which provoke the heat affected zone. To justify this statement it is presented the thickness heat affected zone measured at a single pass of laser beam over the powder bed with a settled scanning speed with respect to laser density power in the case of the work with or without nitrogen atmosphere (Fig. 4, 5) As it was observed, in nitrogen atmosphere, the heat affected zone, and the oxide zone are more reduced and here the work conditions not interfere at all.

As it was expected the heat affected zone width rapidly increases with increasing of laser energy amount on length unit given by the scanning speed variation.

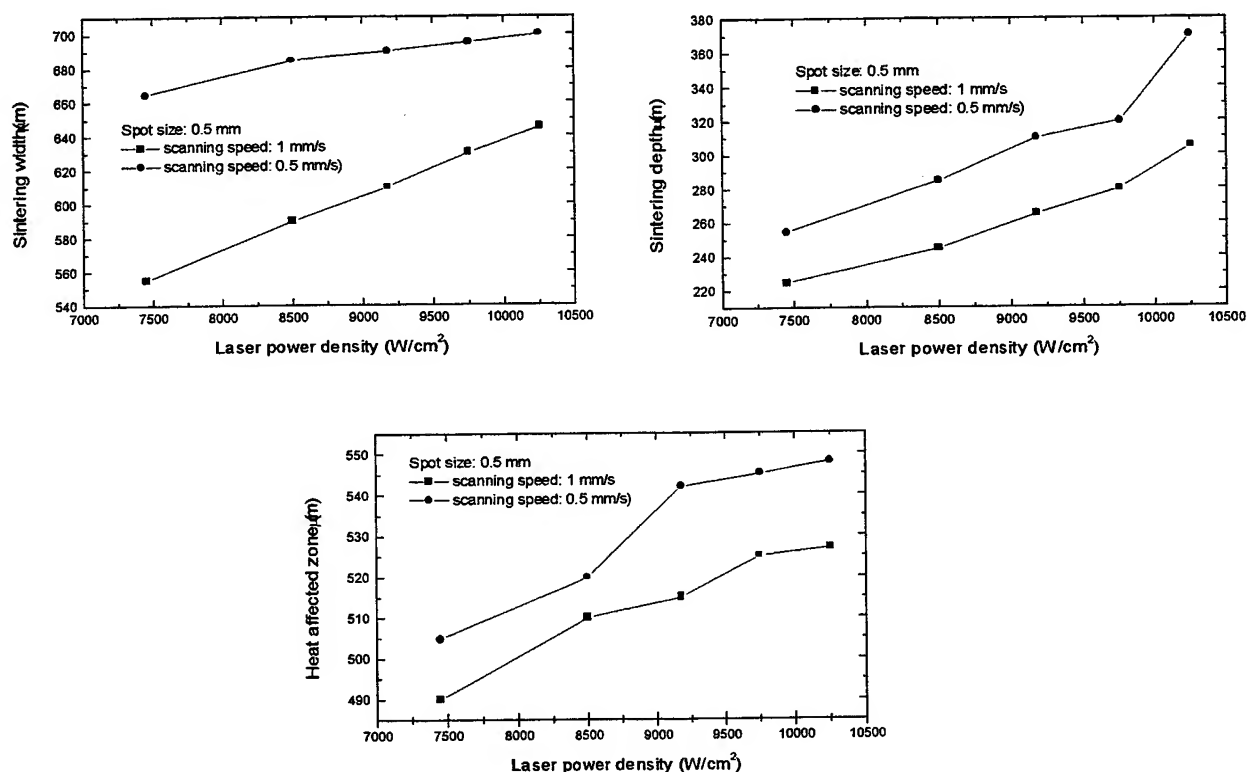


Fig. 5: Sintering zone width, sintering depth and heat affected zone width vs. laser power density, for different scanning speeds. The SLS process was applied in nitrogen atmosphere

Despite of the fact that the radiation-material coupling is higher in the case of work in nitrogen atmosphere, the sintering width and the sintering depth is decreased. The heat affected zone width is much lower in this case in comparison with work in free atmosphere. An important problem for multiple layer sintering is induced stresses. They change the form of the future volume model and don't allow depositing uniform layer by layer on the sintering surface. The photos below prove this statement. Fig. 6 - a, b represents objects where multiple stresses appeared. The layers are not enough bonded. In comparison Fig. 6 - c, d shows objects built up at the optimal parameters. The stresses is more reduced.

In addition appear a new problem, specific in SLS process. The curling phenomenon appear after solidification due to solidification mechanisms and due to induced stresses, and especially due to the difference between the energy amount given to center in compare with edges, caused by defocusing through laser beam tilting. This fact implies limitation in surface scanned sizes because defocusing rise with center departure.

The Vickers hardness was evaluated and in comparison with conventionally processed material. Data obtained was showed a new material. At metalographic microscope it was observed structural modification specific to annealed iron (Table 1). In the first case presented in this table it have been observed changing in Vickers hardness values due to appearance of the gray zones with higher hardness.

Tab. 1. Vickers hardness values for parts obtained by SLS

Particle size (μm)	Layer thickness (μm)	Laser power density (W/cm^2)	Overlapping passes degree	Scanning speed (mm/s)	Vickers hardness HV0.1
≤ 200	200	91.83×10^2	30%	0.5	230
≤ 200	200	91.83×10^2	30%	1	120

The tensile strength analyses was made. The results indicated that the tensile strength specification was nearly with the conventionally processed material. That depends on the choice of the involved parameters.

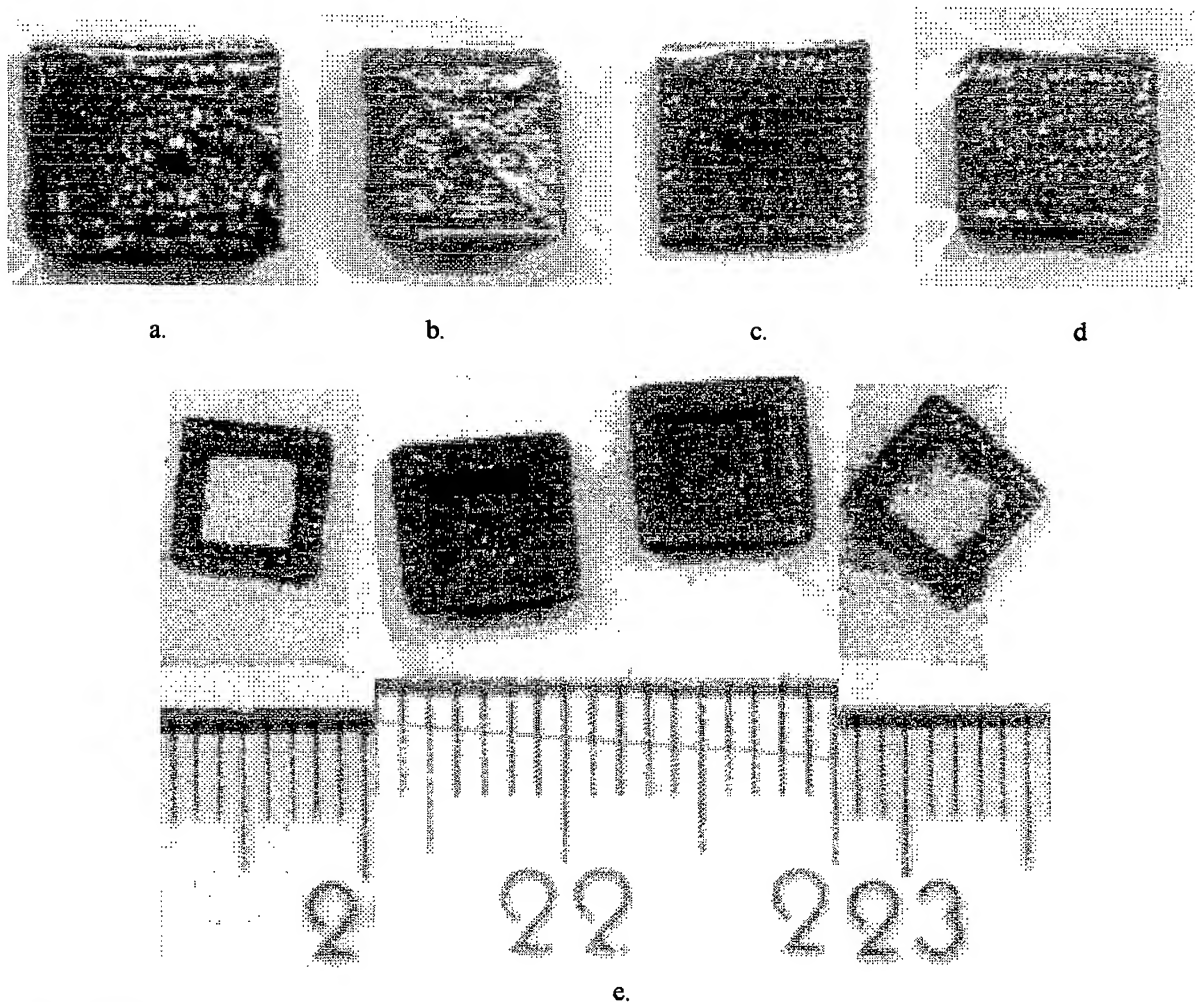


Fig. 6. Objects obtained by selective laser sintering of iron cast powder. Process parameters: $D_p = 75 \times 10^2 \text{ W}/\text{cm}^2$, $G = 50\%$, $v_{sc} = 1 \text{ mm}/\text{s}$ (a); $D_p = 100 \times 10^2 \text{ W}/\text{cm}^2$, $G = 70\%$, $v_{sc} = 1 \text{ mm}/\text{s}$ (b); $D_p = 100 \times 10^2 \text{ W}/\text{cm}^2$, $G = 30\%$, $v_{sc} = 1 \text{ mm}/\text{s}$ (c); $D_p = 100 \times 10^2 \text{ W}/\text{cm}^2$, $G = 30\%$, $v_{sc} = 0.5 \text{ mm}/\text{s}$ (d) where D_p is laser power density, G is overlapping passes degree and v_{sc} is scanning speed.

4. CONCLUSIONS

The studies were showed that SLS depends on a lot of technical parameters, which are specific to the objects achieved. By using an adequate scanning program for surface description, it was obtained pieces from stainless steel with sharp edges. The experiments was performed with a Nd: YAG laser working in CW regime and a level power used was no higher than 20 W. Depending on the desired sintering contour design a 2D scanner system and a process computer control were used. A powder delivery system assures a homogenous and uniform powder layer. Laser parameters (working regime, power density, laser spot size) and process parameters (scanner speed, powder particle size, layer thickness) were varied in order to obtain the optimal processing parameters which assure a satisfactory tensile strength of sintered pieces. The processing parameters were properly adjusted to avoid differences in heat conduction that lead to a narrower heat affected zones and melting out of the edges. It was established a optimal power laser up to 20 W, a laser spot size 2-3 times the average diameter powder particle, an overlapping degree between beam laser passes up to 30 percent at 1,5 mm/s scanning speed.

The parts obtained had a porous structure with aspect of grained texture, appreciable fracture toughness at first. By using powders with smaller particles size the part aspect have been improved.

The optimal parameters is obtained by a compromise in order to obtaining parts with decreased porosity, decreased surface roughness, higher hardness and tensile strength decreased. As a result of this compromise the overlapping passes degree was settled $< 30\%$, laser power density level was established higher than 10^4 W/cm^2 at scanning degree by 0.5 mm/s. Increasing of the laser power density lead to structural modifications which determine the beginning of annealing.

The major advantage of SLS technique remains the possibility to build up 3D objects freeform from powders. The photos from Fig. 6-e illustrate this advantage.

REFERENCES

1. Franco E. DeAngelis, "Laser generated 3-D prototypes", *SPIE*, **1598**, pp. 61-69, 1991.
2. Irem Y. Tumer, David C. Thompson, Kristin L. Wood and Richard H. Crawford, "Characterization of surface fault pattern with application to a layered manufacturing process", *The Journal of Manufacturing Systems*, **17**, No. 1, 1999.
3. Suman Das, Martin Wohler, Joseph J. Beaman and David L. Bourell, "Producing metal parts with selective laser sintering/ Hot isostatic pressing", *JOM*, **50** (12), pp. 17-20, 1998.
4. Hope, R. L. Roth and R. N. & Jacobs P. A., "Adaptive slicing with sloping layer surfaces", *Rapid Prototyping Journal Paper*, **3**, 1999.

Optical Refractive Synchronization Frequency Sampling Ratio Amplitude Ratio Between The Clock Frequency And The Modulated Frequency

by

J. R. Palmer

SilkRoad, Inc.
9707 Waples St., San Diego, CA 92121

Abstract

This paper addresses the equations necessary to evaluate the required sampling frequency as a function of the ratio of amplitudes between the clock frequencies and the frequencies that are modulated onto the respective clock frequencies. A key ingredient that is also involved in the appropriate selection of the sampling frequency is the base band noise level that is indicated for each of the channels that are provided in the protocol from the information providers. By using the techniques associated with thermal signature and imaging processing, one is able to use a multiplicity of Fast Fourier Transforms to subtract out images from background and noise and to recreate the image in a clean and noise free environment. In so doing one is able to maintain the image without subjection to outside disturbance or distress.

Introduction

As I have indicated in my paper, *Verisimilitude-Homodyne Laser Transmitter - Receiver*, this laser transmitter and receiver will have the ability to transmit and receive approximately 16 thousand channels, as presently organized. This amounts to approximately 100 GHz of modulation capability required. However, there is yet an additional set of problems that need to be addressed, viz., even if one is able to have a bandwidth of 100 GHz, how does one select the appropriate Sampling Frequency? This paper addresses the equations necessary to evaluate the required sampling frequency as a function of the ratio of amplitudes between the clock frequencies and the frequencies that are modulated onto the respective clock frequencies. A key ingredient that is also involved in the appropriate selection of the sampling frequency is the base band noise level that is indicated for each of the channels that are provided in the protocol from the information providers.

Basic Concept

At the risk of repeating myself, I need to refresh the reader as to some of what I have said in the paper, *Verisimilitude-Homodyne Laser Transmitter-Receiver*. Again, I need to begin with a bit of history. In the early part of this century it was not uncommon to talk to people that would build a crystal set in order to tune their new fangled radios. Even the term

"tuning to" a certain frequency to receive one's radio broadcast channel is riven with meaning. Truly, these people were tuning to the frequency of their crystal oscillator. In like fashion, we will be tuning into the clock frequencies that contain the information that is to be transported. In order to accomplish this task, one must be able to sort the various clock frequencies from one another and, then, to be able to recover the information from the modulated signal off of the clock frequencies.

As it happens, there are some correlative techniques that are used in image analysis and scanning technology that apply directly to the problem at hand. The first correlation relates to *Reticle Modulation*. And so we begin. A reticle system is essentially a mask or pattern placed in the image plane of an optical system. The transmission of this mask varies spatially. In most cases the mask transmits certain portions of the image scene and completely blocks other portions of the scene. The radiation from the transmitted portions is focused upon the detector. The detector output is assumed proportional to the total incident radiation. The reticle mask may be moved in the image plane, the imaged scene may be moved over a fixed reticle mask, or both.

The reticle mask in scene coordinates is specified by a real valued function $r(x, \tau)$. The function $r(x, \tau)$ specifies the transmission coefficient for the intensity of the image scene point x and time τ . The radiation distribution of the image scene, in scene coordinates is represented by a real valued function $s(x)$. Since the transmitted fluxes are integrated, the

output $v(\tau)$ from a reticle system is , (1)

$$v(\tau) = \int_{-\infty}^{\infty} r(x, \tau) s(x) dx$$

Consequently, the scene $s(x)$ is encoded into a temporal signal, $v(\tau)$, by a reticle system. *Eq. (1)* is a general model for a reticle system.

The assumption of periodicity is shown is *Eq. (2)* and does not restrict the class to a realizable reticle system. Since we are dealing with a circular aperture for our purpose, we

will be using polar coordinates. (2)

$$r(x, \tau) = r\left(x, \tau + \frac{2\pi}{\omega_0}\right)$$

The optimal scanning aperture is the two dimensional counterpart of the matched filter of electronics. This result supports the feeling that a scanning aperture should essentially be matched to the target shape but modified by the spatial characteristics of the

background. If the target is assumed to be a Gaussian pulse, (3)

$$(x_1, x_2) = a e^{-\left(\frac{x_1^2 + x_2^2}{2b}\right)}$$

where;

- ω_0 = Fundamental frequency = $\frac{2\pi}{\tau}$
- a = Peak radiance of Gaussian pulse
- b = Second moment of radiance density of Gaussian pulse
- ρ = $\sqrt{2 \left\{ 1.22 (N.A.) \lambda \right\}^2 (0.1743533)}$, cm [7],[8]
(Note: The central lobe carries 84% of the total flux density. The remainder is contained in the outer lobes.)
- N. A. = Numerical Aperture

$$\lambda = \frac{\text{Focal Length}}{\text{Diameter of Optic}} = \text{Wavelength, cm}$$

The Wiener spectrum of the background is given by, [4],[5],[6]

$$W_b(k_1, k_2) = \frac{b}{k_1^2 + k_2^2} \quad (4)$$

The optimal scanning aperture is given by, [4],[5],[6]

$$a(\rho) = \left(1.0 - \frac{\rho^2}{2b}\right) e^{-\left(\frac{\rho^2}{2b}\right)} \quad (5)$$

If the aperture is defined so that the center of pattern is pointed in turn at every scene point (x) , the function $g[x(\tau)]$ may be considered as a filtered version of the original imaged scene $s(x)$.

The Wiener spectrum, $W_g(k)$, of $g(x)$ is given by, [4],[5],[6]

$$W_g(k_1, k_2) = |A(k_1, k_2)|^2 W_s(k_1, k_2) \quad (6)$$

where;

$$\begin{aligned} A(k_1, k_2) &= \text{Fourier transform of } a(x) \\ W_s(k_1, k_2) &= \text{Weiner spectrum of the scene} \end{aligned}$$

For our problem, it is interesting to note that this formulation of the scanning aperture model permits an optimization of the scanning aperture. Most important is the criterion of optimization which is the maximization of the ratio of instantaneous target signal squared to the mean squared background signal, that is, the maximization of

$$\frac{\int |A^*(\xi) T(\xi)|^2 d\xi}{\int |A(\xi)|^2 W_b(\xi) d\xi} \quad (7)$$

where;

$$\begin{aligned} A^*(\xi) &= \text{Aperture Fourier transform} \\ T(\xi) &= \text{Target Fourier transform} \\ W_b(\xi) &= \text{Weiner spectrum of the background} \end{aligned}$$

Using, then, the Schwarz inequality, one finds the aperture, $A^*(\xi)$, which maximizes the ratio,

$$\int |g(x) s(x)|^2 dx \leq \int |g(x)|^2 dx \int |s(x)|^2 dx \quad (8)$$

The upper bound is obtained when $g(x) = s(x)$ and is written,

$$\begin{aligned}
 & \frac{\int |A^*(\kappa) \sqrt{W_b(\kappa)} \frac{T(\kappa)}{\sqrt{W_b(\kappa)}} d\kappa|^2}{\int |A(\kappa)|^2 W_b(\kappa) d\kappa} \leq \frac{\int |A(\kappa)|^2 W_b(\kappa) d\kappa \int \frac{T^2(\kappa)}{W_b(\kappa)} d\kappa}{\int |A(\kappa)|^2 W_b(\kappa) d\kappa} \\
 & = \int_{-\infty}^{\infty} \frac{T^2(\kappa)}{W_b(\kappa)} d\kappa
 \end{aligned} \tag{9}$$

The reticle and its motion are completely specified by ω_0 and the set $\beta_m(\tau)$. The harmonics of ω_0 are the carrier frequencies and $\beta_m(\tau)$, the modulation placed upon the m th harmonic by the interaction of scene and reticle patterns.

Using the Parseval relation and the convolution theorem, one may write,

$$\beta_m(\tau) = \int_{-\infty}^{\infty} A_m^*(\kappa) S'(\kappa) d\kappa \tag{10}$$

where $A_m^*(\kappa)$ = the conjugate of the Fourier transform of $a_m(x)$ and ,

$$S'(\kappa) = \int_{-\infty}^{\infty} S'(\kappa') O(\kappa - \kappa') d\kappa' \tag{11}$$

The transform of a circular aperture of radius (a) is found from,

$$A^*(\kappa) = A(k_1, k_2) = \frac{a J_1 \{ 2 \pi a \sqrt{k_1^2 + k_2^2} \}}{\sqrt{k_1^2 + k_2^2}} \tag{12}$$

where;

J_1 = is a Bessel function of the first order

At this point we can look at the analytical model for the amplitude modulation of the intensity of a point source in order to evaluate the maximum and minimum of the amplitude ratios of the scene and background that would appear to the sensor. The delta function representation for a point source in polar coordinates $I \delta \frac{\rho - \rho_T}{\theta - \theta_T}$ provides a modulation from, [9],[10],[11],[12]

$$\begin{aligned}
 & \tau = \frac{I(\rho_T)}{2} + I(\rho_T) \sum_{k=-\infty}^{\infty} \frac{e^{-(i(2k+1)\pi\delta)} e^{-(i\theta_T)} (2k+1)\rho e^{-(i(2k+1)\rho\tau\omega_0)}}{i\pi(2k+1) \frac{((\rho_T)(\rho_T e^{-b}) - b)}{(\rho_T)^2 + b^2 - 2b\rho_T \cos \theta_T}} e
 \end{aligned} \tag{13}$$

This is the amplitude modulation of the carrier, ω_0

We now have the amplitude modulation and the ratio of background to scene systems evaluated. We very often hear of the Nyquist sampling frequency as the time bandwidth product. Additionally, the Gaussian-pulse signal provides the minimum time bandwidth

[13],[14],[15] product. Effectively, the argument goes, that the minimum sampling frequency [13],[14],[15] must be,

$$T \leq \frac{1.0}{2B} \quad (14)$$

where;

B = The highest bandwidth to be sampled

However, this is less than accurate when dealing with an optical or electro-optical system. Based upon the work and equations shown above, it follows that the sampling frequency follows the requirement for that of an optical system that must have a suitable Modulation Transfer Function. Based on the foregoing equations I can build a mathematical relationship for the *Refraction Synchronization* Transmission technique that is to be used in the Transmitter-Receiver that is composed of the Refraction Synchronization technology.

[16],[17],[18] Based upon the foregoing equations and experimental data taken by the author, we can build a mathematical relationship between the optical *Modulation Transfer Function*, which provides for a suitable contrast ratio and brightness to provide the resolution of line pairs with optical components that meet the Rayleigh criteria, and the sampling frequency as a function of the ratioed amplitudes of the Clock frequency and the Modulated frequency. Based upon these ratios we find the *Sampling Modulation Transfer Function*,

$$\text{for } \left(\frac{A}{A_0} \right) < 1.0 \quad (15)$$

$$f_{\text{Osample}} = \frac{2}{\pi} \left\{ \cos^{-1} \left(\frac{A}{A_0} \right) - \left\{ \left(\frac{A}{A_0} \right) \sqrt{1.0 - \left(\frac{A}{A_0} \right)^2} \right\} \right\}$$

where;

A = Modulated frequency amplitude

A₀ = Clock frequency amplitude

$$M = \frac{8 \pi \delta A}{A_0}$$

$$\delta = \frac{\text{Baseband noise amplitude}}{2 * A_0}$$

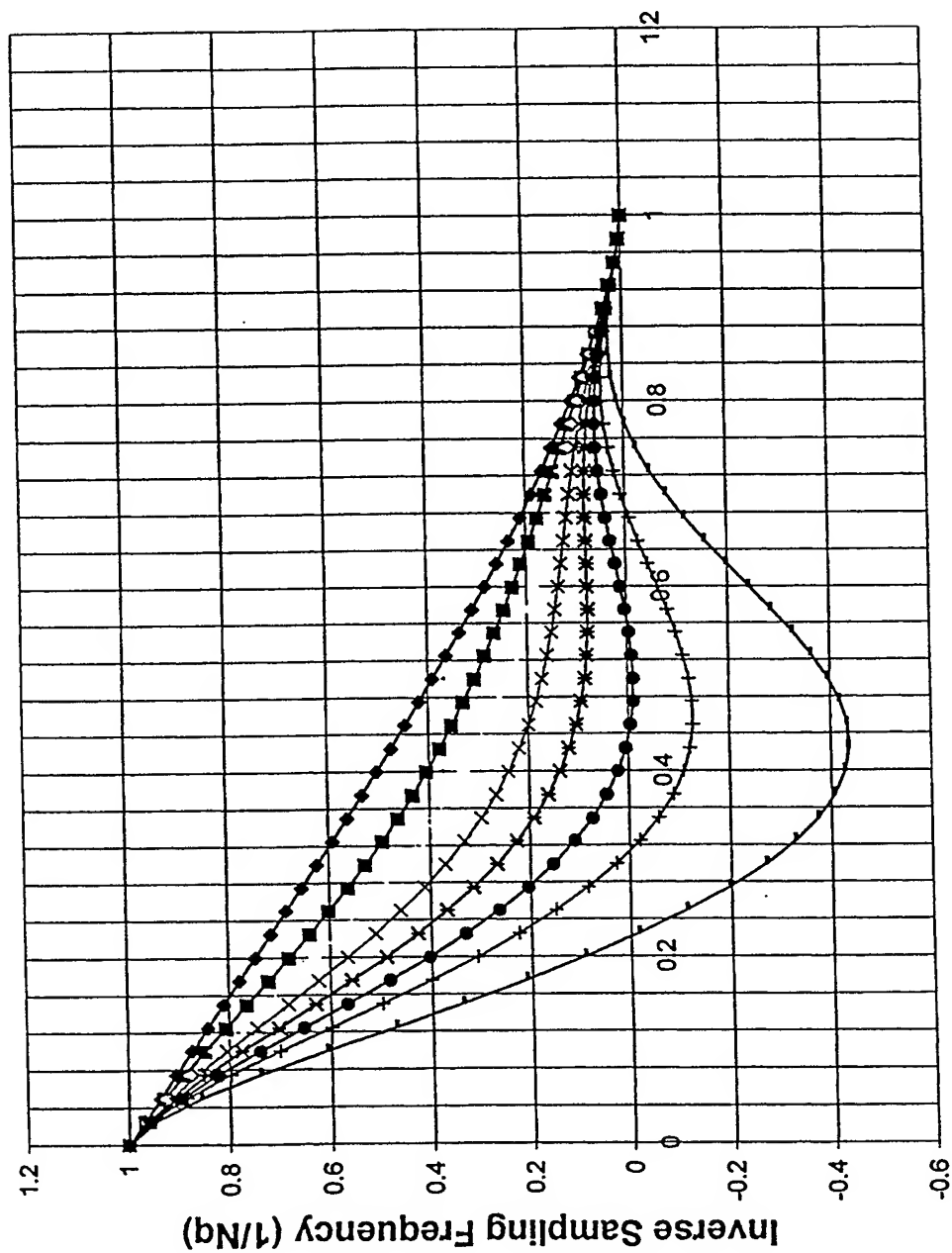
For the case where there is a noise level involved as a baseband Eq. (15) is modified according to,

$$f_{\text{osample}} = \frac{2}{\pi} \left\{ \cos^{-1} \left(\frac{A}{A_0} \right) - \left\{ \left(\frac{A}{A_0} \right) \sqrt{1.0 - \left(\frac{A}{A_0} \right)^2} \right\} \right\} \left\{ \frac{2 J_1(M)}{M} * \left\{ 1.0 - \left(\frac{A}{A_0} \right) \right\} \right\} \quad (16)$$

$$\text{The sampling frequency} = \frac{1.0}{f_{\text{Osample}}}$$

The following is a graph that reflects the amplitude ratio and the sampling frequency as a function of this ratio.

Inv. Sampling Frequency vs. Signal/Clock Amplitude Ratio



Signal/Clock Amplitude Ratio (A/A0)

References

1. L. M. Biberman, *Reticles In Electrooptical Devices*, Pergamon Press, Elmsford, N.Y., 1966.
2. S. Sterberg, J. Ulrich and R. Hamilton, "Analysis And Testing Of A Special Rotating - Translating Reticle," Willow Run Laboratories, University Of Michigan, Ann Arbor, MI, Report No. 7102-T, June 1967.
3. R. Swift, R. B. Wattson, J. A., Decker, R. Paganetti and M. Harwit, "Hadamard Transform Imaging And Imaging Spectrometer," *Applied Optics*, Optical Society Of America, Washington D. C., Vol. 15, No. 6, June 1976, pp. 1595-1609.
4. R. Lgault, "Reticle And Image Analysis", *The Infrared Handbook*, W. Wolfe and G. Zissis, ed., Office Of Naval Research, Washington D. C., 1978.
5. D. Peterson and D. Middleton, "Sampling And Reconstruction Of Wave Number Limited Functions in N-Dimensional Euclidean Spaces," *Information And Control*, Academic Press, New York, NY, Vol. 15, No.4, Dec. 1962.
6. J. P. Ulrich, W. D. Montgomery and J. L. Alwar, "Analysis Of Reticle Systems," Background Analysis Center, Willow Run Laboratories, University Of Michigan, Ann Arbor, MI, Report No. 6054-2-T, October 1965.
7. W. J. Smith, "Image Formation: Geometrical And Physical Optics", *Handbook Of Optics*, W. Driscoll and W. Vaughan, ed., McGraw-Hill Book Company, New York, NY, 1978.
8. J. R. Palmer, W. M., Steen and S. Martellucci, , "Analytical Model For Aberrated Diffraction In High Power CW Laser Beam Trains: Laser Cavity To Work Piece," *Laser Applications For Mechanical Industry*, Series E: Applied Sciences - Vol. 238, NATO ASI Series, Kluwer Academic Publishers, London, England, (1992).
9. W. D. Montgomery, "Some Consequences Of Sampling In FLIR Systems," *Institute For Defense Analyses*, Arlington, VA, Research Paper P-543, September 1969.
10. F. Oberhettinger, *Fourier Expansions: A Collection Of Formulas*, Academic Press, New York, NY, 1973.
11. H. J. Ryser, "Combinatorial Mathematics," *Carus Mathematical Monographs*, No. 14, John Wiley and Sons, New York, NY, 1963.
12. W. D. Davenport and W. L. Root, *Random Signals And Noise*, McGraw-Hill Book Co., New York, NY, 1960.
13. R. L. Shrader, *Electronic Communication*, 6th. ed., Macmillan/Mcgraw-Hill, New York, NY, (1991).
14. R. Blake, *Basic Electronic Communication*, West Publishing Co., New York, NY, 1993.

15. F. G. Stremmer, *Introduction To Communication Systems*, 3rd. ed., Addison-Wesley Publishing Company, Reading, MA., 1992.

16. J. R. Palmer, "Analytical Model For Transient Strehl Ratio Distribution In Soft X-Ray Optical Systems," *Proc. International Conference On Soft X-Ray Optics And Technology*, SPIE No 733, Berlin, Germany, 1986.

17. J. R. Palmer, "The Use Of A Cat's Eye Optic In A Round Lens System For Reading Horizontal Bar Codes On A One Dimensional Rectangular Charge Coupled Device," *Lecture Note* Given at Trinity College - Dublin, Ireland, 1991.

18. J. R. Palmer, *High Power Laser Optics*; 2nd ed., Pro Se Publishing Co., San Diego, CA., 1995.

For Further Author Information:

Email: james.palmer@silkroadcorp.com
Telephone: (858) 457*6767ticket
Web Site: <http://www.silkroadcorp.com>
Fax: (858) 457-6757
U.S.A.

Polishing of optical fibers using a CO₂ laser

Hamdi Orun^a, Mircea Udrea^{b*}, Ali Alacakir^c

^aMiddle East Technical University, Physics Department, 06531 Ankara, Turkey

^bNational Institute for Laser, Plasma and Radiation Devices, MG-6, Bucharest, Romania

^cAnkara Nuclear Research And Training Center, 06105 Besevler, Ankara, Turkey

ABSTRACT

A new application of glass surface treatment is presented here. Fine polishing of optical fiber end, core/cladding surface, is performed. A small power monomode longitudinal 10 W cw CO₂ laser is used. A decrease of the roughness from about 5 microns to hundreds of nanometres was achieved. The microstructure of the surfaces has been studied using atomic force microscopy. Applications of polished fiber surfaces are given.

Keywords: laser, material processing, optical fibers, atomic force microscopy.

1. INTRODUCTION

Laser processing of glass surfaces as cutting, etching, polishing and forming of microstructures is a wide field of applications. The radiation of CO₂ laser is strongly absorbed in silicate glasses and it is converted to thermal energy. If the temperature is carefully monitored high thermal stress are avoided. Glass surface treatment has been already intensively studied¹. A new application of glass treatment is presented here. It consists of the polishing of optical fiber end by using a small power CO₂ laser.

The optical fiber is a dielectric waveguide that proceeds in optical frequencies. This fiber is usually cylindrical in form. It confines energy in the form of electromagnetic waves in its surfaces and guides the light parallel to its axes. The structure establishes the information-carrying capacity of the fiber and influences the response of the waveguide to environmental perturbations. Optical fibers in commercial use consist of a solid dielectric cylinder (core), which is surrounded by another solid dielectric cylinder (cladding) that has a slightly smaller refractive index than the core. Moreover, these two structures are encapsulated in an elastic, abrasion resistant plastic material that is a polymer epoxy acrylate. The fibers used in commercial applications are made of glass that consists of silica (SiO₂) or a silicate. The largest category of optically transparent glasses from that optical fibers are made consists of the oxide glasses, and of these the most common is silica that has a refractive index of 1.458 for 850 nm. Furthermore, to produce two similar materials that have slightly different index of refraction for the core and the cladding, fluorine or different oxide such as B₂O₃, GeO₂, P₂O₅ are added to the silica. The principal raw material for silica is sand. Glass composed of pure silica is referred to silica glass, fused silica, or vitreous silica. Some of its important properties are a resistance to deformation for high temperature (1000 °C), a high resistance to breakage from thermal effects due to its low thermal expansion, good chemical durability, and high transparency in the visible and infrared regions for fiber optic communication systems².

In our experiment, single-mode fibers with a core/cladding diameter of 8/125 µm are used. The polishing of the end surface of the optical fiber, such that the surface of the core/cladding region can be useful in the applications with connectors, particularly with the FC/PC type connectors.

Demountable connectors are used to connect fibers to the terminal equipment. Sources and detectors are bonded permanently to a short length of fiber (pigtail). This usually connects to a standard, bulkhead, fiber to fiber connector mounted on the output panel of the device, into that the main fiber link can be plugged. Such a system permits different units and components to be tested separately and, if required, can be replaced. Connector performance varies with the precision of the mechanical location of the fiber, angular alignment, and end separation. When one of these (or all) occurs, such that a misalignment between the two fiber's core to core happens, than an optical loss results, since there is a

*Correspondence: Email: udrea@newton.physics.metu.edu.tr

redistribution of power among the modes for a mismatched connector. The optical losses can be given as the effects of mismatch in the mode field diameters, the effects of misalignment, and the Fresnel reflection losses for the fiber end faces. The most common connectors in commercial use are the FC, HMS-10, PC, D4, SMA, DIN, ST, and Biconic. In the connector, the most important component is the ferrule, since it holds the fiber and provides the alignment positioning. It is made from metallic or ceramic material, and has usually a diameter of 2.5 mm. The glass fiber with its 125 μm diameter is centered in the ferrule and it exits on the end face, in that the holding material and fiber are together mechanically polished to achieve a smooth endface. The differences in connector types are due to the differences in the mechanical part³.

The PC (physical contact) connector is polished by a flexible polishing disc, such that the total endface, including the glass-fiber tip, ends with a slight convex shape. This slight rounding (using radius of 25 mm) brings the fiber up to as the highest point on the endface and results in glass to glass connection, as can be seen in Fig. 1.

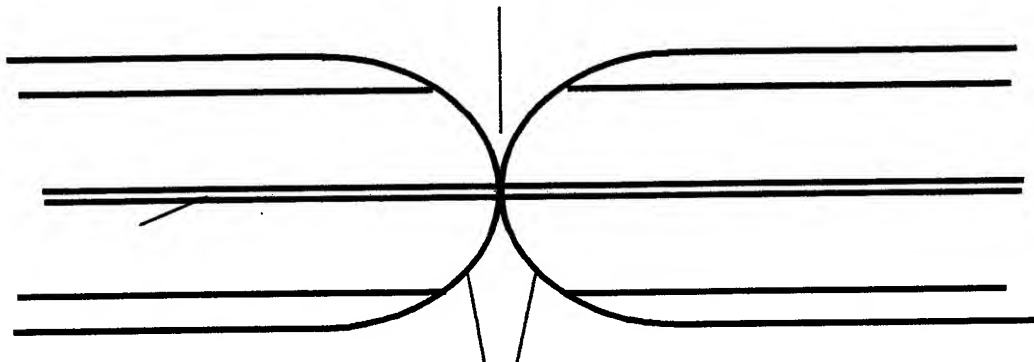


Fig. 1 Fiber glass connection

When the fiber and ferrule are sustained in the same surface and the surfaces of the two glass fibers are clean then the glass to glass connection removes the air gap induced reflections (Fresnel reflections) and the return loss is improved by several dB. The FC/PC, ST, SC, APC, and DIN are physically contacting connectors that use the same 2.5 mm diameter ferrule and ferrule construction style. The differences between these connectors are in the mechanical holding system that holds the ferrule. Since applications get more demanding of lower reflections, this PC contact is improved by better polishing the glass surface, because a smoother surface results in a better glass contact, and hence a lower reflection loss. We considered that the use of a CO₂ laser may lead to a better polishing effect of the two glass surfaces. If the surface of the glass is analysed in the micron scale, then it can be seen that hills and valleys with height of 300 nanometres till 1 micron constitute the surface, as it can be seen in the Fig. 2.



Fig. 2 Glass surface of the core/cladding region

It is known that using different laser sources (varying with the material to be polished) can polish such rough surfaces (particularly, thin films). When such a polishing effect is accomplished onto glass surfaces, then a highly smooth surface is achieved, and hence a very precise contact between the two glass surfaces results.

For a fiber optic communication application, such polished connectors are very important when the OTDR (optical time-domain reflectometer which measures round trip losses) is used. The measured response exhibits three types of

features, such that straight lines caused by Rayleigh backscattering, positive spikes caused by discrete reflections, and steps that can be positive or negative that varies with the physical fiber properties. When such a measurement is done, then the first peak that can be seen on an OTDR trace is the reflection of the front connector that mates the OTDR to the fiber. Since this reflection covers the near-end measurement region, it is not a wanted result, because it hides information on the fiber. Therefore, a clean, high quality connector with a smooth surface and low reflectance is necessary to achieve good results.

Structure modifications of the irradiated material are studied using both ordinary optical microscopy and atomic force microscopy (AFM). AFM has become the most popular type of microscopy using a probe mounted on a very small spring cantilever. When the probe is scanned across the sample, the force between the probe tip and sample changes as the surface features encountered, causing the spring cantilever to deflect. In order to obtain the magnitude of the height displacement, a laser and four-quadrant detector are used to detect the motion of spring cantilever and provide a feedback signal as it is scanned across the sample.

2. EXPERIMENTAL SET-UP

A longitudinal small power 10 W CO₂ laser is used⁴. The laser was designed to deliver a monomode beam. The divergence of the beam was about 0.7 mrad. In addition to the good uniformity of the beam, the laser beam was spatially filtered to increase the beam uniformity. The beam was focused by means of a 20 cm focal length ZnSe lens. The time duration of the laser exposure was optimised in the range of several seconds. The samples were glued onto a special holder. As it is usual in fiber optics technology, the samples were mechanically polished (we call this procedure pre-polishing) before irradiation using 5 microns diameter alumina powder. The optical fibers we have irradiated consist of 8 μ m diameter core and 125 μ m diameter cladding. Moreover, the plastic coating (epoxy acrylate) is removed from the fiber, so that just the end-surface of the core/cladding material is irradiated by the laser (the fiber materials were supplied by the Turk Telekom A.S. and the fiber samples were prepared in the Turk Telekom A.S., R&D Center).

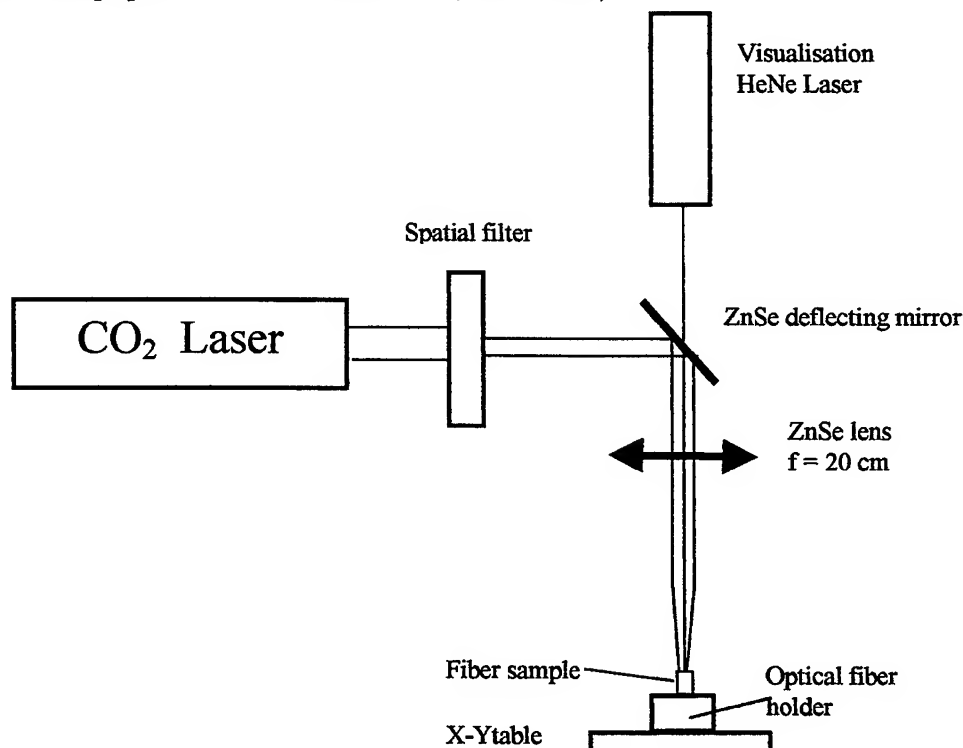


Fig. 3 Experimental set-up

3. RESULTS

The surfaces of the sample were photographed both before and after irradiation. The image of the optical fiber end was taken by means of an Leitz optical microscope and an TopoMetrix atomic force microscope. The optical microscope image was lead to a computer connected CCD camera.

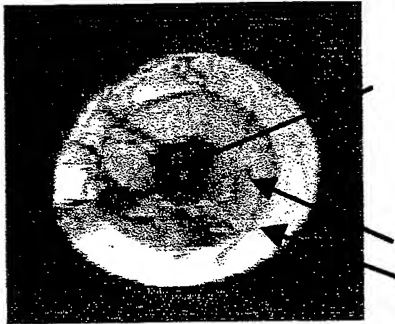


Fig. 4 Optical microscope picture of the optical fiber end, before irradiation (mechanically cut, no pre-polishing, x 3.5 magnification)

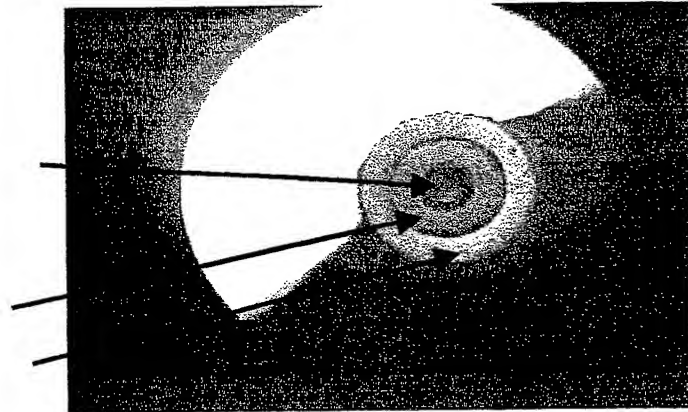


Fig. 5 Optical microscope picture of the optical fiber end, before irradiation (mechanically cut, 5 μm alumina powder pre-polishing, x 3.5 magnification)

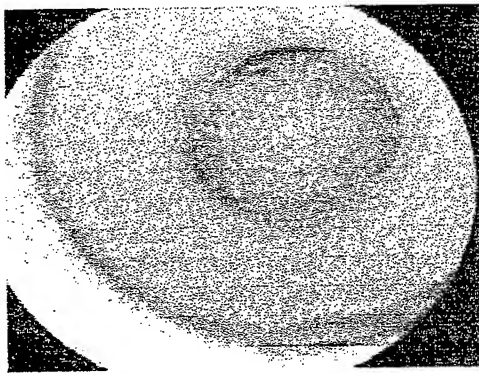


Fig. 5 Optical microscope picture of the optical fiber end, before irradiation (mechanically cut, 5 μm alumina powder pre-polished, x 10 magnification)

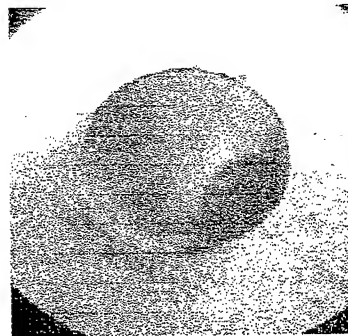


Fig. 6 Optical microscope picture of the optical fiber end, after irradiation (x 10 magnification)

In Fig. 6 it is observed that the core-cladding surface looks much smoother. This region was deeply investigated by means of an atomic force microscope and the results are given in Figs. 7 and 8.

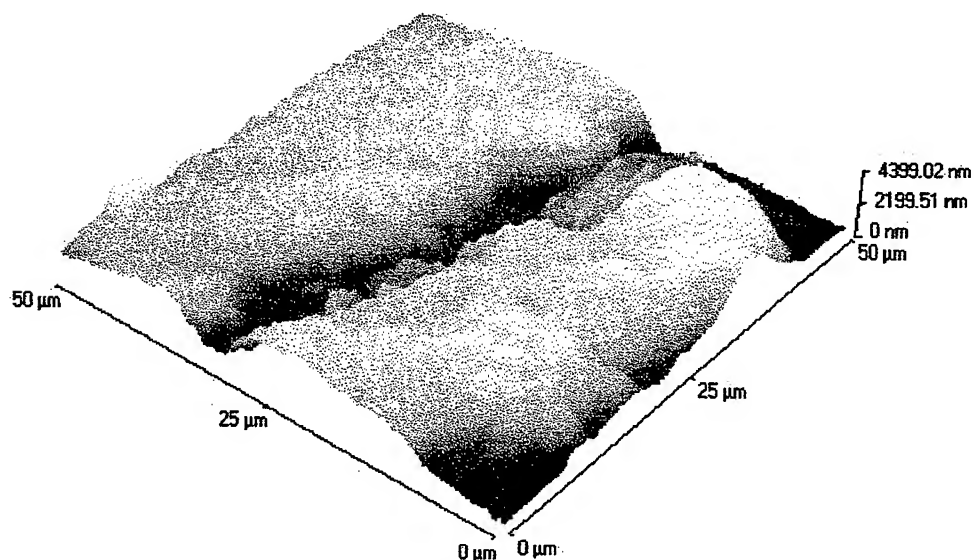


Fig. 7 Atomic force microscope picture of the sample, before irradiation

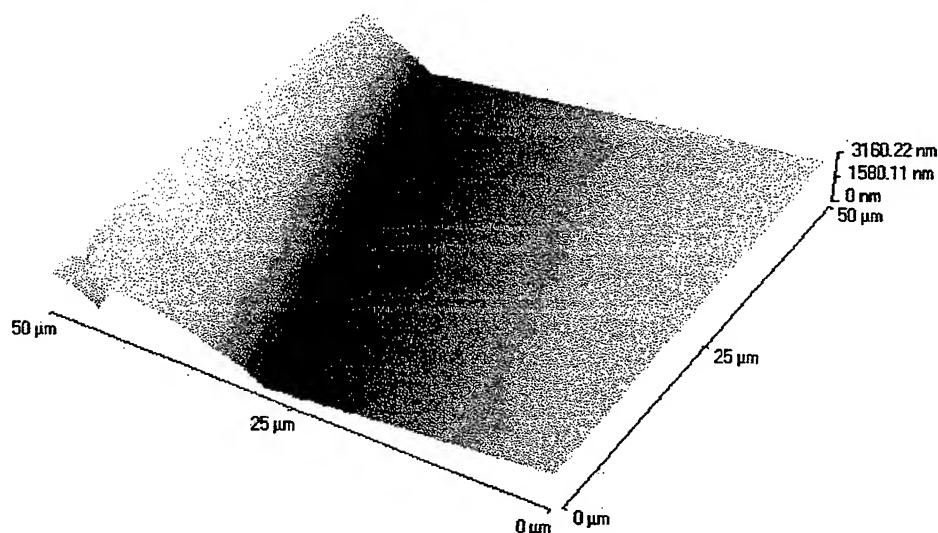


Fig. 8 Atomic force microscope picture of the sample, after irradiation

It might be easily seen from the atomic force microscope picture how the hills are melted and disappeared after a proper laser irradiation. Furthermore, the plastic coatings around the core-cladding structure are completely evaporated for several millimeters depth along the fiber. This means that the removal of the plastic coating might be achieved the same time as the polishing is performed. Investigations regarding the core-cladding structure modifications due to the melting of the plastic are studied. The plastic removal is exactly what a much more expansive laser, the excimer laser, is doing as an industrial method to eliminate the plastic coatings near the end of the fiber in order to put the fiber into connectors.

In conclusion, the use of a low power, reliable and cheap laser, as CO₂ laser is, leads to a high quality polishing of the optical fibers ends. The study of the transmission through this laser-polished optical fiber is now our aim.

ACKNOWLEDGEMENTS

Hamdi ORUN's fiber optic work is supported by the Turk Telekom A.S., R&D Center, 06095 Ahlatlibel, Ankara, Turkey. Dr.Mircea Udrea is supported by TUBITAK, The Turkish Scientific and Technical Research Council. He is on leave from the National Institute for Laser, Plasma and Radiation, Lasers Department, Bucharest, Romania.

REFERENCES

1. C.Buerhop, B.Blumenthal, R.Weissmann, N.Lutz, and S.Biermann "Glass surface treatment with excimer and CO₂ lasers", *Applied Surface Science*, 46, pp.430-434, 1990.
2. Gerd E. Keiser, *Optical Fiber Communications*, McGraw Hill College Div., 1991
3. D.Derickson, *Fiber Optic Test and Measurement*, Prentice-Hall Inc., 1998.
4. Mircea Udrea, Ali Alacakir, Sinan Bilikmen, Ozgul Kusdemir and Oguz Pervan, "Monomode Hybrid Longitudinal CO₂ Laser for Material Processing", *Proc.IL'99, International Conference on Industrial Lasers*, October 25-27, Wuhan, China, 1999.

Plume behavior and thin film deposition by laser ablation using an helicoidal shadow mask

A.Marcu^{*a}, C. Grigoriu^a, W.Jang^b and K.Yatsui^b

^aGas Pulsed Lasers Laboratory, National Institute of Lasers,
Plasma and Radiation Physics, P.O.Box M.G.36,Bucharest, Romania

^bLaboratory of Beam Technology, Nagaoka University of Technology,
Nagaoka, Niigata, Japan

ABSTRACT

The laser ablation is one of the best ways to obtain smooth thin film deposited on various substrates. However, to obtain a 'droplets-free' surface some special experimental setups are necessary. One of them is the 'eclipse' method, using a plane shadow mask. Based on studies on the plume behavior in a 'standard' deposition and in a plane shadow mask eclipse deposition, we propose a new shadow mask having an helicoidal shape, which permit to obtain a better film quality - maximum droplets size about 10 time smaller than for the plane shadow mask. The plume behavior and thin film quality are presented and discussed.

Keywords: PLD, film quality, shadow mask, plume propagation,

1. INTRODUCTION

Many and various methods for thin film deposition have been developed. For some particular materials (e.g. superconductors) the laser ablation^{2,3} seems to be the one, which give the best film quality. However, for some particular technological application - like microelectronics - even for deposition by laser ablation some special techniques^{1,4} have to be used in order to reduce "big" particle's size and number. The 'eclipse' method using a plane shadow mask is one of methods, which lead to a better film quality. By using such a plane shadow mask, could be obtain 'droplets free' film area on film surface. However, the 'droplets' does not disappear completely. In order to try to decrease more the droplets size and number, we analyzed the plume behavior in a 'standard' deposition and in a plane shadow mask deposition.

Measuring the plume luminous longitudinal movement on 'x' direction (perpendicular to the target) and transversal movement on 'z' direction (parallel with target) we obtained the data presented in Fig. 1 As could be observed, immediately after being expelled from the target, the plume particles have a speed mainly oriented on longitudinal direction. The longitudinal (maximum) speed is much bigger then transversal (maximum) one. In the interval 1.5 μ s and 3 μ s the transversal speed is still bigger but comparable with the transversal one. After 3 μ s - 4 μ s the longitudinal and transversal speed is about same and the expansion could be approximated with a spherical one, but the speed is already much lower then beginning.

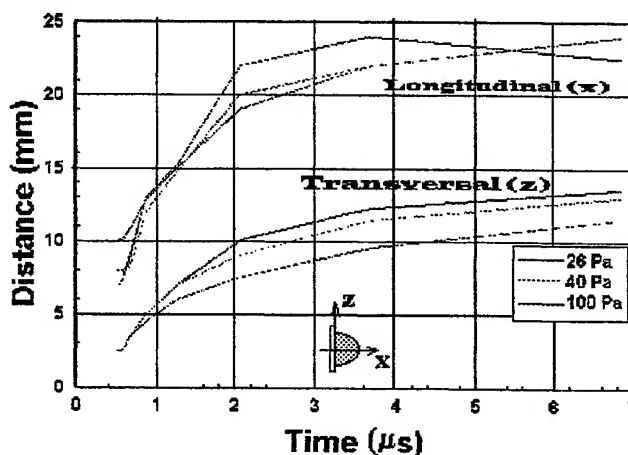


Fig. 1. Longitudinal and transversal movement of plume luminous front.

* Corresponding author: Fax: +40 1 423 14 70; Email : marcu@ifin.nipne.ro.

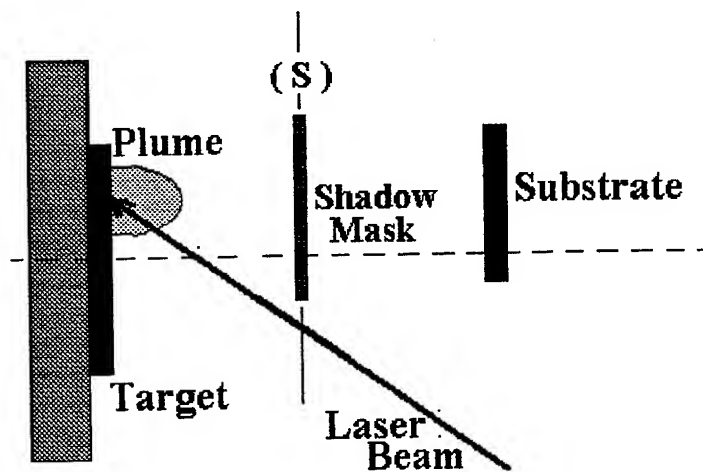


Fig. 2. Experimental setup for plane shadow mask.

Table 1. Main system parameters

LASER	Wavelength	1.064 μm
	Energy	200 mJ
	Density	2 mJ/cm ²
TARGET	Material	YBCO
AMBIENT GAS	Composition	O ₂
	Pressure	25 Pa
SHADOW MASK	Diameter	1 cm
	Material	Cu
	Distance from target	2 cm
SUBSTRATE	Material	MgO
	Distance from target	4 cm

Disposing an obstacle on the plume trajectory we should expect for first interval of 0.5 μs - 0.8 μs (which for a 25 Pa ambient pressure should correspond to a 0.7 cm - 1.2 cm) to have a very strong reflection of plume and if obstacle is large a very small number of particle should go around it. Also if the plume should meet the obstacle after 3-4 μs (which should mean for a 25 Pa ambient pressure about 3 cm distance from target) the particle speed being to low the interaction between the plume and obstacle is expected to do not go around the plane mask.

In Fig. 2 we present the case of a plane shadow mask of 1 cm diameter disposed at 2 cm from target.

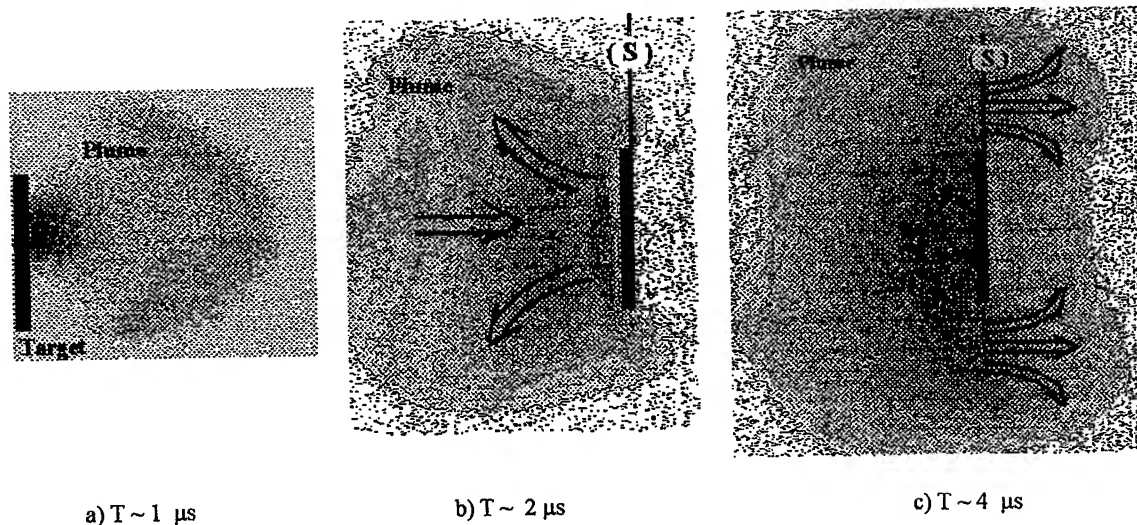


Fig.3 Plume behavior with plane shadow mask

In plume behavior (Fig. 3) we can distinguish 3 zones. First one (Fig. 3a) till 1 - 1.5 cm from target where the plume behavior is similar with the 'standard' one. The plume does not "fill" yet any influence from the shadow mask. The interval 1.5 - 2.5 μ s is the time interval in which the plume will interact with the shadow mask. As could be seen from Fig. 3b part of the plume will reach the shadow mask surface and will be deposited or reflected back. The reflected plume will interact with the incident one the result will be a stronger lateral expansion of the plume (Fig. 4) This expansion will enlarge the transversal size of the plume, and will increase the number of particles which will reach the (S) plane outside of the shadow mask zone, that means will pass around plane shadow mask. The particles that reach the (S) plane outside of the shadow mask area will not just go forward due to the high longitudinal speed, but, due to the interaction among them they will also expand in transversal direction, covering the zone behind the shadow mask.

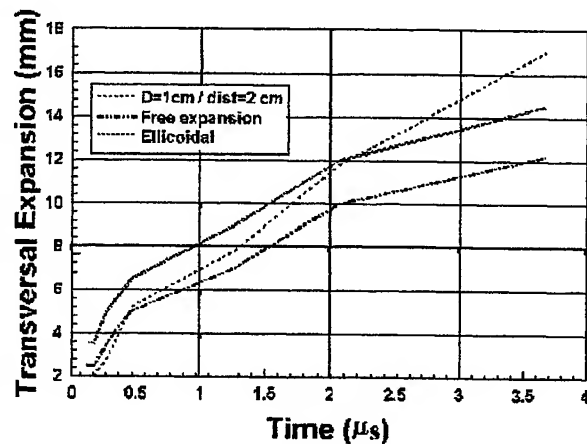


Fig. 4. Plume transversal expansion.

The ablation process is a complex phenomenon resulting from direct and indirect interaction of laser radiation with target material. One of the indirect ablation processes is the local "explosion" of target material due to the hitting by absorption of laser radiation. This process is considered to be one of the most important for expulsion of big clusters from target. But this process is a "slow" one and the apparition of such 'big particles' is considered to be later than the initial plume. The main difference between the 'droplets' and small particles should be not just the size, but also the mass. The plume small particles could be assimilated to behave like a "fluid" they being able to go around the shadow mask, but 'big' droplets, due to their 'big' mass will move more like a solid corp. The 'droplets' movement (simplified presented in Fig. 5.) will following the (a) or (b) trajectory, function of their initial speed orientation. (Any other external forces except the friction one is considered to be insignificant - including the gravitational one, due to the small distance between target and substrate and high initial speed.). However some droplets could be expelled from target together with the initial plume and. If that droplet size and mass is "small enough", the pressure of small particles, it could pushed it around the shadow mask (c trajectory). The fact that such a trajectory is possible and what exactly means "small enough" could be observed in Fig. 6 where we present a SEM picture of a substrate deposited using such an experimental setup. (The main system parameters are presented in Table 1) We chosen a area having such a 'big' droplets (about 3.3 μ s diameter) which passed around such a shadow mask Such big particles, because of their mass needs time to be accelerated and pushed inside the substrate area, behind the shadow mask. For a bigger particle - that also should mean a bigger mass - is necessary a bigger time, which taking into consideration the longitudinal sped - which statistically have to be still considerable bigger that the maximum transversal one - should mean a bigger distance "d". These considerations suggested, as a

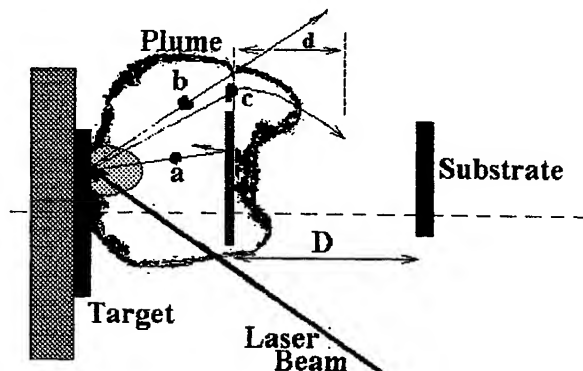


Fig. 5. 'Droplets' movement with a plane shadow mask.

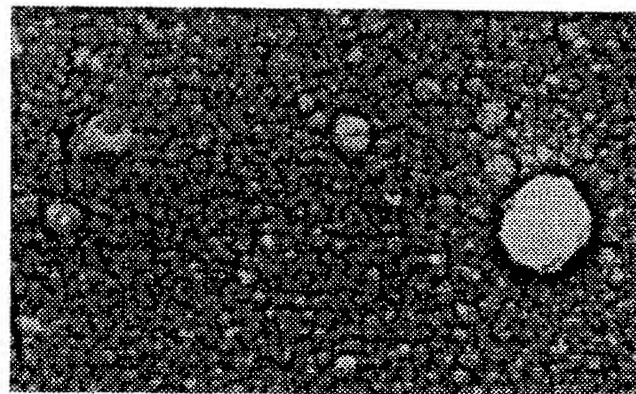


Fig. 6. - SEM for the thin film deposited by plane shadow mask setup.

possibility, to control the droplets size by controlling the distance "d". Such a system is presented in Fig. 7. In case that a "big" droplet should pass by the first shadow mask element, if the forces are not "big enough" for accelerating such a mass in a distance "p" corresponding to the distance between to consecutive mask elements (trajectory "a") the droplet should be reflected and pushed outside of substrate area by next shadow mask element (trajectory "b"). And the phenomena should be same for all shadow mask elements. However, considering that after 3-4 μs (which should correspond for a 2.5 - 3 cm from target the expansion of plume could be considered spherical and because the plume (small) particles density will drastically decrease with distance, the pressure exerted on the big particles will be much reduced, such that we consider that the step "p" between to consecutive obstacle could be increased without being affected the maximum 'droplets size' accepted inside the substrate area, such that the proposed experimental model have and unequal step.

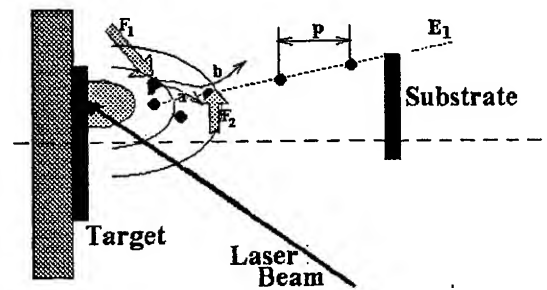


Fig. 7.- Theoretical consideration of 'droplets' penetration through a multi-element shadow mask system.

2. EXPERIMENTAL SYSTEM - HELICOIDAL MASK -

The experimental system for a "eclipse" deposition using an helicoidal shadow mask is presented in Fig. 8. The main system parameters are same like the plane shadow mask system described in Table. 1

Some optimizations of the helicoide parameters (Fig. 9) where necessary. The plume penetration through the mask was studied by an Ultra-Nac High Speed Camera. We briefly present the main consideration in choosing the helicoide parameters:

-spire diameter Φ -is inverse proportional with the mask length. Also an increasing of mask length should mean, besides the increasing of substrate distance an increasing of the mask total area. A $\Phi = 2$ mm have been chosen;

vertical step Δp_y - minimum value is 0. Decreasing to limit (0) of the vertical step the sensitivity of system alignment increase dramatically. Increasing vertical step Δp_y plume penetration will be strongly diminuated. We have chosen $\Delta p_y = 0.5$ mm and tried to control the plume penetration from longitudinal step Δp_x ;

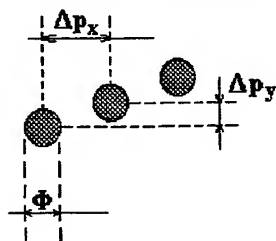


Fig 9. Helicoid parameters.

longitudinal step Δp_x - have been used to control the plume penetration. A decreasing of step increase the plume reflection which diminuate the plume penetration (Fig 10.a). An increasing of step will enlarge the substrate distance from target. No significant influence in plume

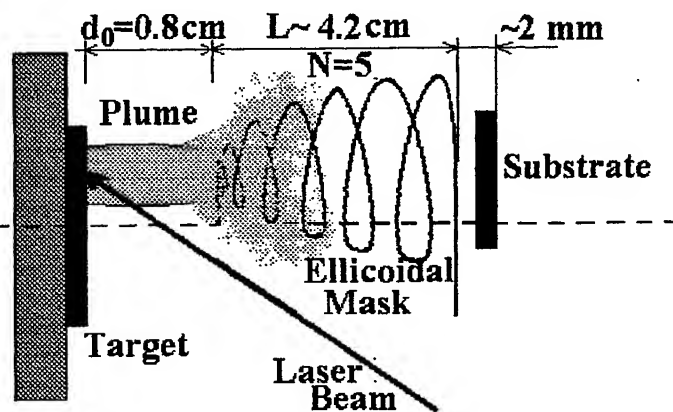


Fig. 8 Helicoidal shadow mask -experimental setup-

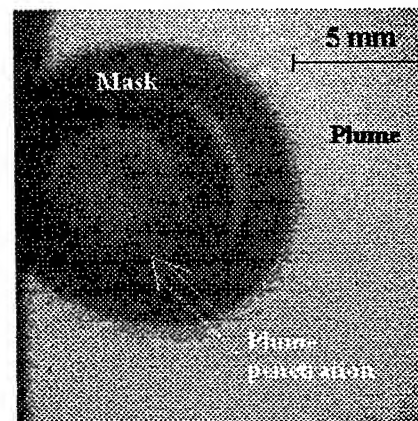


Fig. 10. Plume behavior with a helicoidal shadow mask (frontal view) $T = 2.5 \mu\text{s}$.

propagation with increasing of step over 5 mm have been modified, so, the minimum size $p_x = 5$ mm have been chosen;

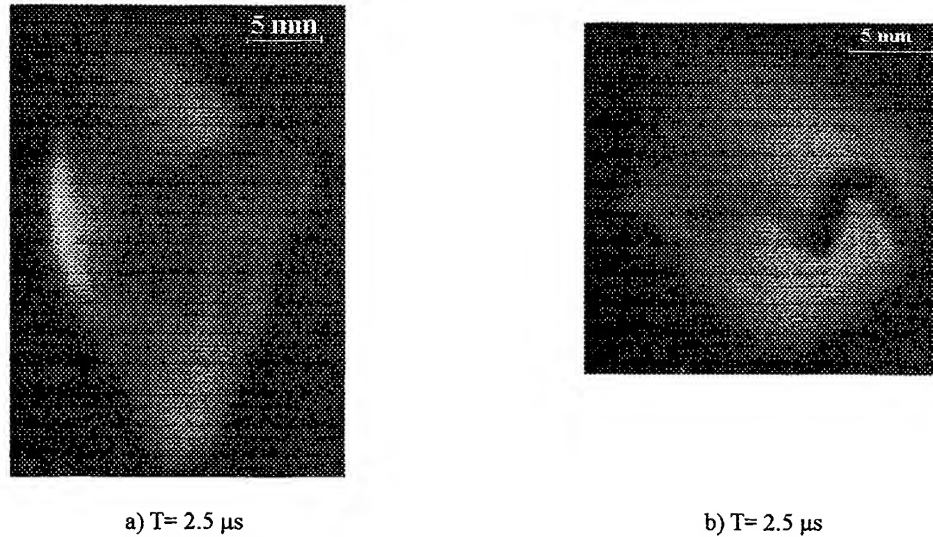


Fig. 11. Plume behavior with a Helicoidal shadow mask -lateral view
a) $\Delta p_x = 2$ mm; b) $\Delta p_x = 5$ mm.

distance from target d_0 - affect the plume reflection on helicoide tip. For distance d_0 bigger the 8 mm no longer strong reflection has been observed, so the minimum distance $d_0 = 8$ mm have been chosen.

The increasing of helicoide step have been made linear at ~ 2 mm/step.

With these helicoide parameters, the plume behavior is presented in frontal view (Fig. 10) and from lateral view (Fig. 11.b). A deposition with this helicoidal shadow mask and using the experimental system presented in Fig. 8 have been realized and analyzed.

3. RESULTS

The pictures of a thin film deposited helicoidal shadow mask system are presented in Fig. 12. In Fig 12a we present a SEM picture of a 'droplet'. The maximum size of "droplet" able to penetrate such a system could be estimated at about 300 nm. Number of "droplets" is considerable smaller for such a deposition than for a plane electrode shadow mask one, and also the maximum 'droplets size' is about 10 times smaller. This is considered to be the main advantage of such a deposition system. However, the deposition rate have been reduced about 4 times in comparison with the plane shadow

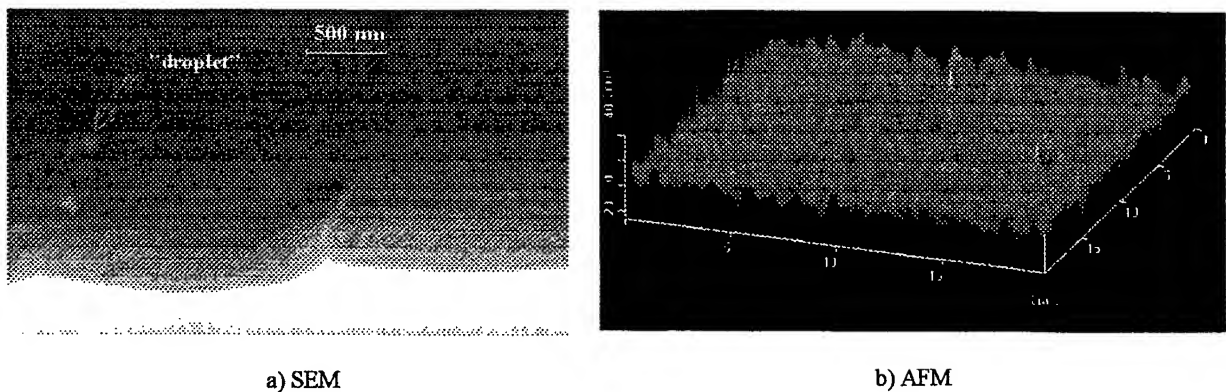


Fig. 12. YBCO thin film deposited with helicoidal shadow mask (18 000 pulses)
a) - SEM for a "droplet"; b) AFM.

mask system deposition rate In comparison with a standard deposition system by laser ablation (no shadow mask) deposition rate for such a system is about 10 % An AFM picture of a droplets-free area is presented in Fig 12b.

4. CONCLUSIONS

Based on a simplified approximation of the 'droplets' movement in a plane shadow mask deposition system, we propose a new shadow mask having an helicoidal shape. After studying plume behavior in such a system and after optimizing the helicoide parameters we was able to obtain a better film quality, having maximum droplets size about 10 times smaller than the one deposited with a plane shadow mask one.

5. REFERENCES

1. S.G. Lee, D.Hwang, Y.K.Park and J.Park, "Deposition Angle-Dependent Morphology of Laser Deposited $\text{YBa}_2\text{Cu}_3\text{O}_7$ Thin Film", *Appl Phys. Lett*, **65**, pp. 764-766, 1994.
2. A.Cohen, P.Allenspacher, M.M.Brieger, I.Jeuck and H.Opower, "Beam Target Interaction Growth of $\text{YBa}_2\text{Cu}_3\text{O}_{7-x}$ by Laser Ablation Techniques", *Appl Phys. Lett*, **59**, pp. 2186-2188, 1991.
3. S.R.Foltyn, R.C.Dye, K.C.Ott, E.Peterson, K.M.Hubbard, W.Hutchinson, R.E.Muenchauser, R.C.Estler and X.D.Wu, "Target Modification in the Excimer Laser Deposited $\text{YBa}_2\text{Cu}_3\text{O}_{7-x}$ Thin Films", *Appl Phys. Lett*, **59**, pp. 594 -596, 1991.
4. B..Holzaphel, B.Roas, L.Schultz, P.Bauer and G.Saemann-Ischenko, "Off-Axis Laser Deposition of $\text{YBa}_2\text{Cu}_3\text{O}_{7-x}$ Thin Film", *Appl. Phys.Lett.* **61**, pp. 3178 - 3180, 1992.

SESSION V

Optoelectronic Devices

Combinational logic circuits with photonic devices

Paul Schiopu^a, Vasile Degeratu^{*b}, Stefania Degeratu^c,

^a"Politehnica" University Bucharest, Romania, ^bS.C. Baneasa S.A., Bucharest, Romania,

^cUniversity of Bucharest, Faculty of Physics, Romania

ABSTRACT

In actual systems the optic signal are detected, processed and electronic recorded. These hybrid systems diminish considerably the processing speed of optical signals. So, it's absolute necessary to implement the processing signals of optic systems which have to be competitive with the actual electronic systems. In this paper, the authors present from theoretical point of view, the realization of some logical gates (AND, OR, NOT) with photonic devices and combinational logic circuits with photonic devices as decoder, demultiplexer and multiplexer.

Keywords: combinational logic circuits, logical circuits with photonic devices, optical logic circuits, optical computer.

1. INTRODUCTION

The interaction of laser ray with matter goes to a wide spectrum of physics phenomenon in nonlinear optics¹. The photonic microdevices with inferior power threshold which permit the propagation of laser pulses over a certain value of incident power can be realized using nonlinear optical mediums which are self-focusing. It can be realized optical power limiters using nonlinear guided waves if one or both mediums which bounds a linear dielectric film are characterized as optical self-defocusing which are not linear. Using both nonlinear effects, which is threshold power and power limiters, it results that only optic pulses with the values of power into a certain interval can be transmitted through an optic wave guide which is not linear².

A general definition for a combinational logic circuit (CLC) would be circuit which has n input (x_1, x_2, \dots, x_n) and m outputs (y_1, y_2, \dots, y_m) and where the output could be as functions only by the input variations^{3,4}.

$$\begin{aligned} y_1 &= f_1(x_1, x_2, \dots, x_n) \\ y_2 &= f_2(x_1, x_2, \dots, x_n) \\ &\dots\dots\dots \\ y_m &= f_m(x_1, x_2, \dots, x_n) \end{aligned} \quad (1)$$

In a CLC's structure doesn't exist memory circuits and reaction bounds because the mathematical model (1) doesn't involve free variables time and output (output variables cannot be applied on input). Output values are functions depending on input values, and input-output transfer is instantly (the propagation time is neglected in logical gates). A combinational logic circuit could be mathematically described by:

$$C = (X, Y, F) \quad (2)$$

where: $X = x_1, x_2, \dots, x_n$, input variables multitude; $Y = y_1, y_2, \dots, y_m$, output variable multitude; $F: X \rightarrow Y$, input-output function; it's noticed that time variation doesn't appear.

2. LOGICAL GATES

The logical circuits physically realized the transformation of the variables from the input into the output variables of the circuit according to a given logical function. That means, they realized practically the operations of the given logical function. The elementary logical circuits are static switching circuits and are called logical gates⁵.

*Correspondence: Email: valid@joe.tehfi.pub.ro; Telephone: 40-1-4908039; Fax: +40-1-4908125

In Fig. 1 there are given the representation symbols of the optical devices with inferior power threshold and with power limiter. For making easier the understanding of phenomena, there will not be given nominal values of the laser incident ray, but numbers (Roman or Arabic digits) that will emphasize only a qualitative difference between the different powers of the laser ray. Therefore, in Fig. 1a, there is represented the symbol of an optical device with inferior power threshold, showing that the incident power of laser ray must have at least the value "1" such as the light ray to propagate forward. Of the laser pulse has an incident power smaller than the value "1", then it will not pass forward, it will be stopped by the optical device. The difference between two optical devices having the values of incident power "1" and "2" respectively consists in the fact that, for the light ray to pass forward, the incident power of the laser pulse should be bigger when meeting the second optical device with inferior power threshold (the one that has the incident power represented by "2") as compared to the situation when it meets the first optical device (the one that has the symbol "1").

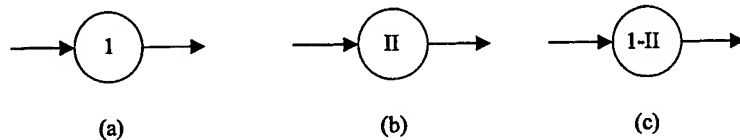


Fig. 1. Symbols: (a) optical device with inferior power threshold; (b) optical device with superior power limitation; (c) optical device with inferior and superior power threshold (the power varies only in a certain interval).

In Fig. 1b there is represented the symbol of an optical device with superior power threshold (optical power limiter), showing that the incident power of the laser ray should have at most the value "II" such as the light ray to propagate forward. If the laser pulse has an incident power bigger than the value "II", then the light will not pass forward, it will be stopped by the optical device. The difference between two devices having the values of incident power "II" and "III" respectively consists in the fact that, for the light ray to pass forward, the incident power of the laser pulse should be smaller when meeting the first optical device with superior power threshold (the one that has the incident power represented by "II") as compared to the situation when it passes through the second optical device (the one that has the symbol "III").

In Fig. 1c there is represented the symbol of an optical device with inferior and superior power limitation, showing that the incident power of the laser ray should be in the interval "I-II" such as the light ray to propagate forward. If the laser pulse has an incident power smaller than the value "1" or bigger than the value "II", the light will not pass forward, it will be stopped by the optical device.



It is to be noticed the fact that any light ray, no matter what symbol it has (A - showing that the light ray comes from a laser diode with emission in blue, V - green, G - yellow, R - red etc.), is considered as having the incident power with the value "1". That is also for making easier the understanding of phenomena.

Fig. 2. "AND" circuit with photonic devices.

In Fig. 2 there is represented an "AND" circuit having two gates (Fig. 2a) and four gates respectively (Fig. 2b) made by optical devices that use nonlinear optical effects. In Fig. 3, an "OR" circuit with two gates (Fig. 3a) and four gates (Fig. 3b) respectively is represented. It is realized from optical nonlinear devices.



For this work we will use only four light rays with different wavelengths (R - red, O - orange, G - yellow, A - blue). This is for making easier the understanding of the phenomena, because we can use light rays with some other wavelengths.

Fig. 3. "OR" circuit with photonic devices.

In electronics, from all the possibilities of representing binary digits, the most usual is by two distinct levels of the voltage. In this work, because photonic devices are used, the binary digits will be represented on some other principles. In the same way as the representation of binary digits in the most usual electronic circuits, there could be considered that, for the light ray symbolized by R (red), the "1" state, "1" logic, is when this ray exists and is transmitted, and the "0" state, "0" logic is when this ray doesn't exist, is missing from the spectrum transmitted through the light guide. Similarly for the light rays

symbolized by O, G and V. There is an inconvenience when the spectrum transmitted through the light guide all light rays are missing. This inconvenience is, in fact, the difficulty of realizing logical circuits. For this, a fifth light ray could be used. It is denoted by V (green) and it will show in the light guide when the other rays (A, G, O and R) are missing.

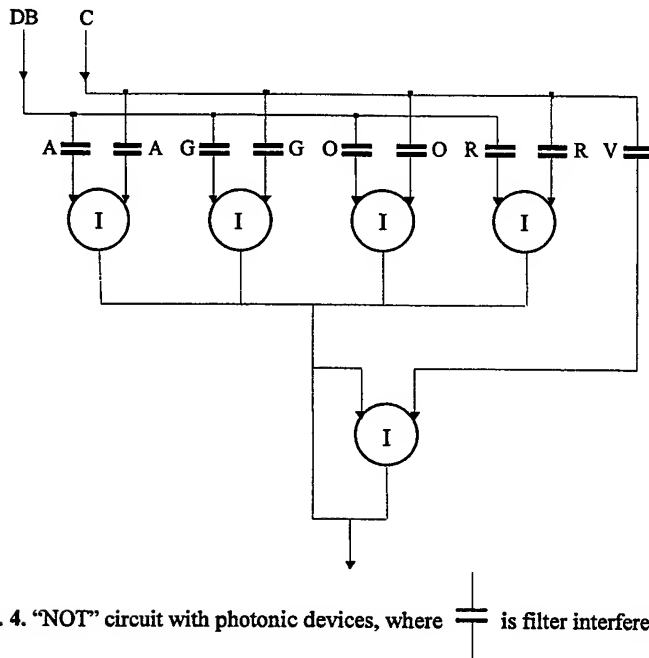


Fig. 4. "NOT" circuit with photonic devices, where \parallel is filter interferential.

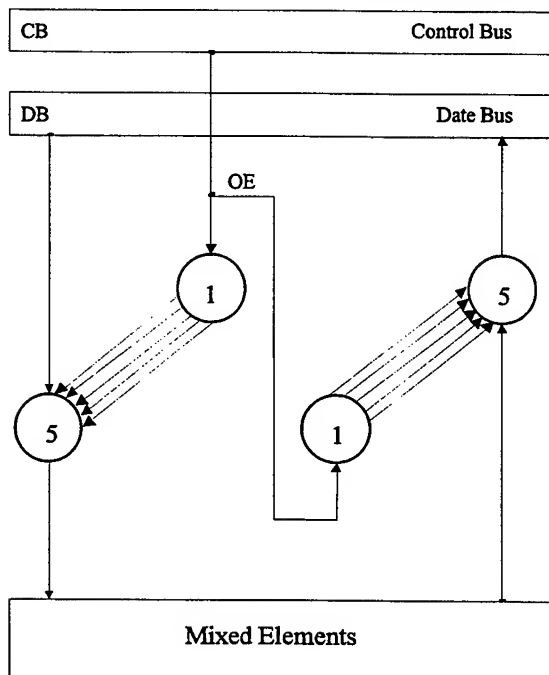
Therefore, through a light guide we could transmit simultaneously five light rays (because of the restriction imposed). When four of them exist (A, G, O, R) the "1" logic state is obtained; when only one, V (green), exists, the other four missing, the "0" logic state is obtained. For being I Boolean algebra, it is considered that each light ray expresses one bit from the word that could be transmitted through the light guide. The most significant bit is the bit expressed by the light ray symbolized by R.

In Fig. 4 a "NOT" circuit is represented. It is realized from optical nonlinear devices.

It has been denoted by DB (Data Bus) the bus with data. Another notation is C that represents a bus on which there are transmitted all the time the five light rays (A, G, O, R and V respectively). This bus is called refresh bus.

3. BUSES

A complex numerical system can be looked as logical blocks assembly interconnected conform of one architecture.



In this paper, the bus is a way for photonic and lighted signals transfer, and is built in general case from n lines.

At buses' lines are connected some transmitters (sources), receivers and mixed elements (source-receiver). Also must be existing gates elements which have to permit the access of data to and from these elements.

For the transmitting a correct information on bus is necessary to respect the following rule: at one moment the access on bus can have only one transmitter, theoretically the number of receivers being unlimited. In usual electronic circuits this rule has to be satisfied with high impedance state, HZ.

For circuits with photonic devices this rule can be fulfilled like in Fig. 5. So, like we can observe the access of transmitter at data bus (DB) can be realized only if the output is authorized (validated). Authorized by signal OE (Output Enable) which is sent using control bus (CB).

Fig. 5. The realization of access on bus at one moment using only one transmitter.

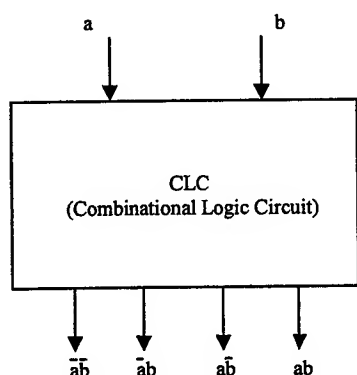
Data bus (DB) is the way where information is something like words of n bites. Address bus (AB) is necessary in microsystem for the addressing of different components.

Each point of microsystem, in which there is a necessary information, must be addressed with an address word. The generating by microprocessor on bus of an address word is selected a source circuit (which write the info) and a receiver circuit (which read the info). For microprocessor, address bus is unidirectional, this means that the address can be only write and not read by microprocessor.

Control bus (CB) synchronize the operations between microprocessor and addressed exterior circuits.

Refresh bus (C) as we already mentioned, is a bus which is used for the transmitting of that five ray light (A, G, O, R and V).

4. DECODER CIRCUIT



Let implement a combinational logic circuit with multiple outputs like in Fig. 6, where:

$$f=(f_0, f_1, f_2, f_3)=(\bar{a}\bar{b}, \bar{a}b, a\bar{b}, ab)$$

But these terms are disjunctive. So, for a certain combination of input variables we'll have an output and only one which will be activated (in this case in "1" logic). The name of such a circuit is decoder^{4,5}.

Fig. 6. Model of a combinational logic circuit (CLC).

Structure of four bits decoder and the truth table is represented in Fig. 7 and respectively in Table 1.

Table 1. The truth table of decoder.

A	G	O	R	f_0	f_1	...	f_{15}
0	0	0	0	V	0	...	0
0	0	0	1	0	R	...	0
.....							
1	1	1	1	0	0	...	A,G,O,R

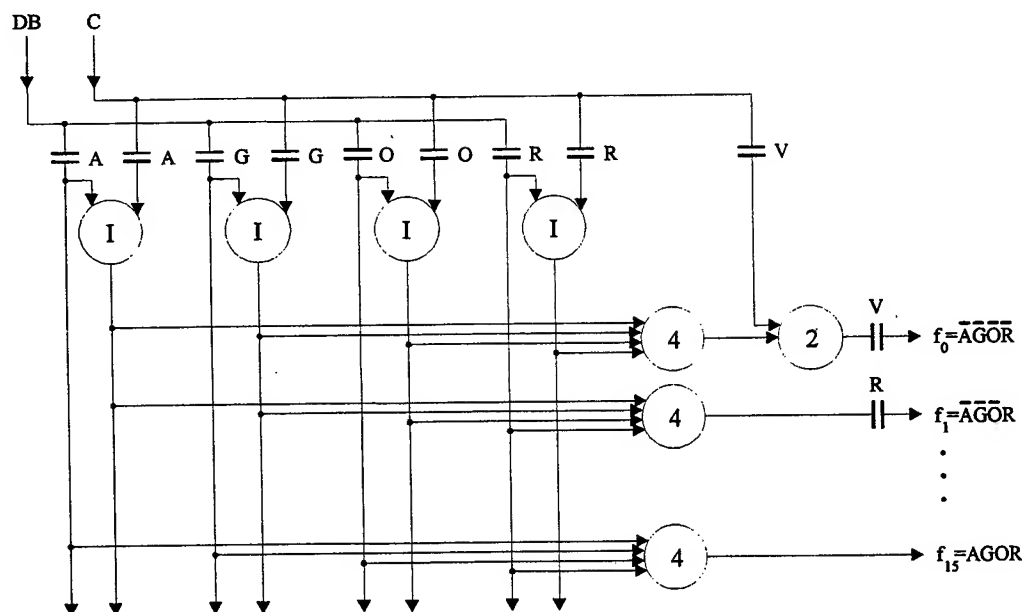


Fig. 7. Four bits decoder with photonic devices.

DB is a data bus. C is a refresh bus on which all the time is transmitted those five rays of light (A, G, O, R and V).

5. DEMULTIPLEXER CIRCUIT

In many applications it is useful that working of decoder circuit could be permitted or blocked using a supplementary input named "ENABLE" validity input^{4,5}. The validity function can be obtained introducing one supplementary input at the decoder gates. The name of this obtained circuit is demultiplexer (DMUX). The models of demultiplexer circuits are represented in Fig. 8.

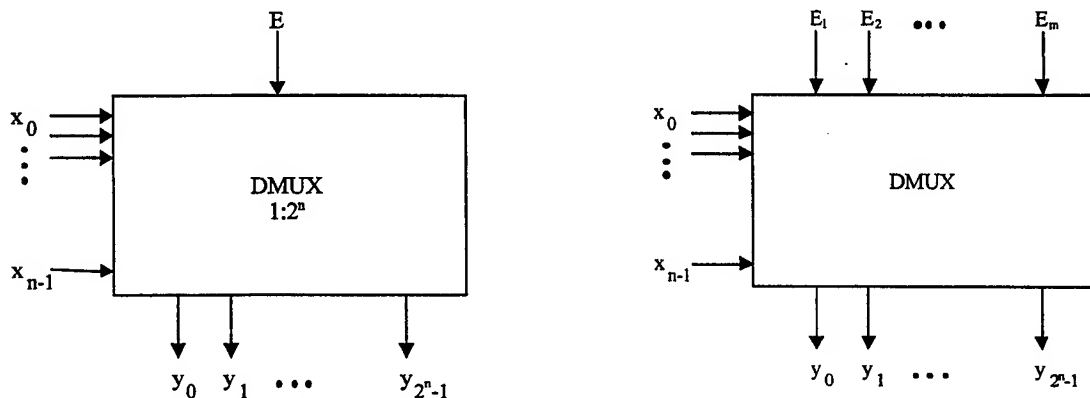


Fig. 8. Models of demultiplexer.

The truth table of the circuit from Fig. 9 is represented in Table 2.

Table 2. The truth table of demultiplexer.

A	G	O	R	f_0	f_1	...	f_{15}
0	0	0	0	E	0	...	0
0	0	0	1	0	E	...	0
.....							
1	1	1	1	0	0	...	E

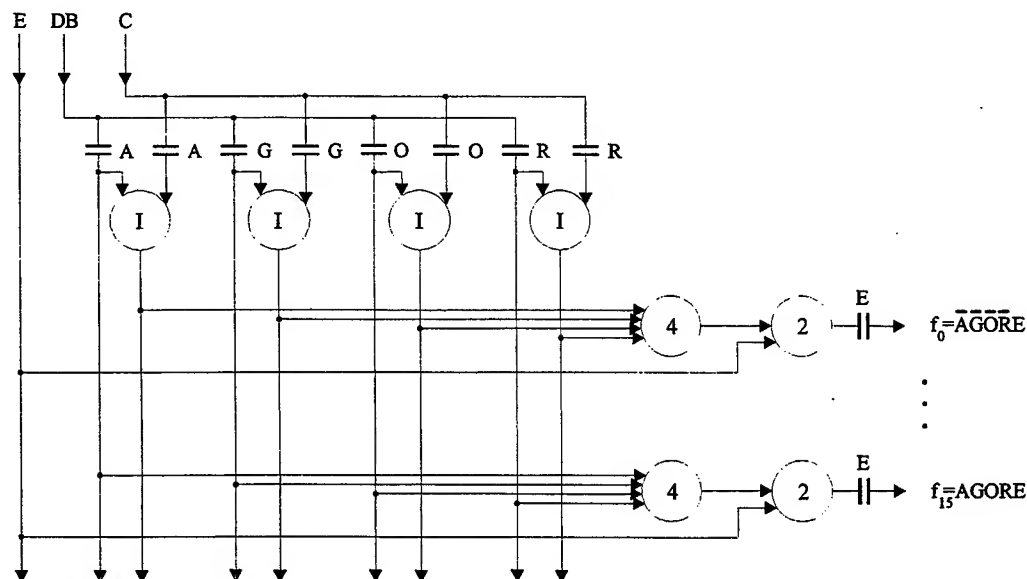
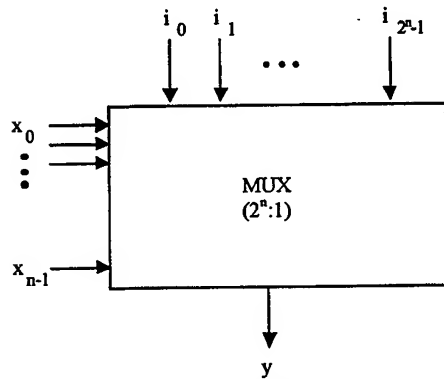


Fig. 9. Four bits demultiplexer with photonic devices.

6. MULTIPLEXER CIRCUIT



In 2 lines usual electronic multiplexer circuits is connected direct to the output only one from the input lines^{3,5}. Selection of the wanted line from the input to output is realized using a selection word of n bits transmitted through n input lines, like in Fig. 10.

Fig. 10. Model of multiplexer circuit (MUX).

For photonic circuits, if it's used a coded word with 4n bits length transmitted through n input lines x_0, x_1, \dots, x_{n-1} from 2^{4n} variables, transmitted through 2^{4n-2} lines, at input is connected direct to output only one, transmitted using only one line.

Structure of four bits multiplexer and the truth table is represented in Fig. 11 and respectively in Table 3.

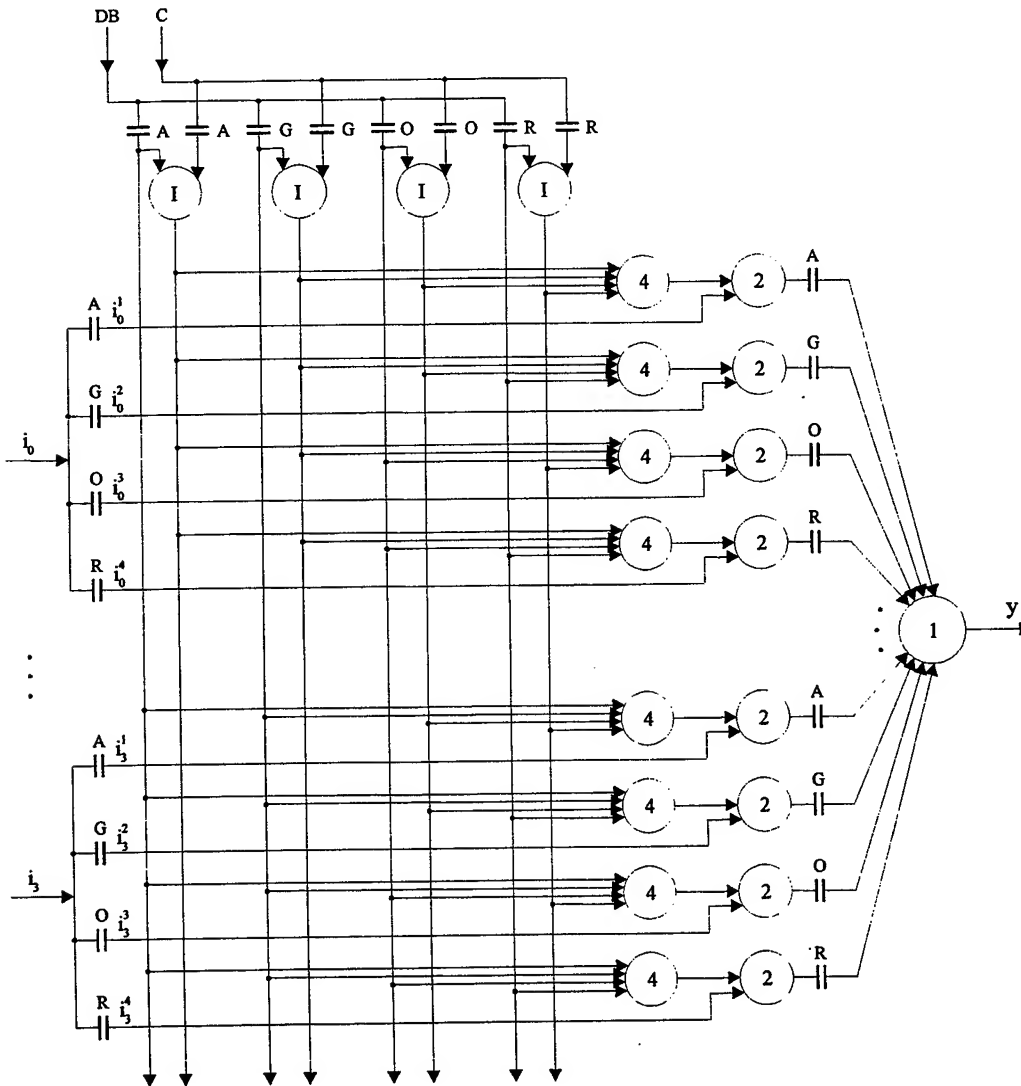


Fig. 11. Four bits multiplexer with photonic devices.

Table 3. The truth table of multiplexer.

x_3	x_2	x_1	x_0	y
0	0	0	0	i_0^1
0	0	0	1	i_0^2
.....				
1	1	1	1	i_3^4

7. READ-ONLY MEMORY

Memories circuits, when are viewed as structures that can implement logical functions under disjunctive canonic form (DCF), are enclosed in combinational circuits class too, although some of them have in their structures cells which are sequential circuits^{3,4}. In Fig. 12 is represented a read-only memory with photonic devices.

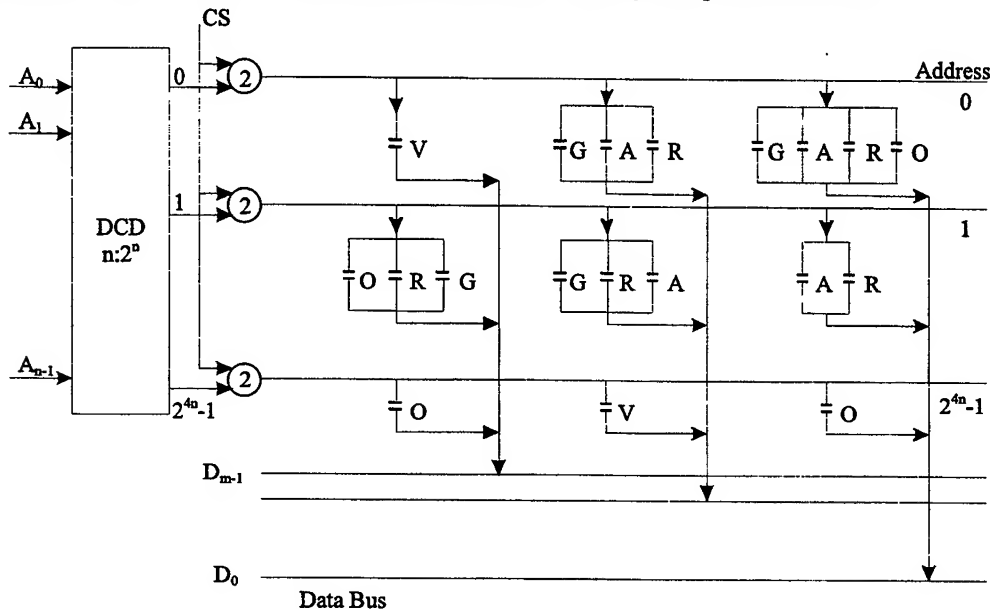


Fig. 12. Read-only memory with photonic devices.

8. CONCLUSIONS

In this work there has been tried, from the theoretical point of view, the realization of some logical circuits with photonic devices, competitive with the actual electronic systems.

The use of photonic devices instead of electronic devices has the following advantages:

- the switching time of photonic devices (10^{-12} - 10^{-14} s) is much smaller than the switching time of electronic devices;
- the possibility of transmitting simultaneously on a line many lights pulses having different wavelengths;
- the photonic signals are not perturbed by extern electrical and magnetic fields.

As disadvantages there are the facts that the integration degree of photonic circuits is smaller and the cost price is higher. Some new materials and architectures and technologies will eliminate these disadvantages.

REFERENCES

1. G. Nemeş, *Introducere în optica neliniară*, Editura Academiei Române, Bucureşti, 1972.
2. D. Mihalache and D. Mazilu, *Ghiduri de undă optice neliniare planare*, Editura Academiei Române, Bucureşti, 1990.
3. Gh. Toacşe, *Introducere în microprocesoare*, Editura Stiinţifică şi Enciclopedică, Bucureşti, 1986.
4. I. Spânulescu and S. I. Spânulescu, *Circuite integrate digitale şi sisteme cu microprocesoare*, Editura Victor, Bucureşti, 1996.
5. M.Ch. Gilmore, *Introduction to microprocessors*, McGraw-Hill, New-York, 1981.

Optimization of the number of detectors for the laser irradiation alert station

Mihai Olariu*

Military Equipment and Technologies Research Agency

ABSTRACT

In this paper the author presents a laser irradiation alert station which uses the directivity characteristic of the photosensible element in order to determine the direction of the irradiation beam. In order to solve this problem, the author considers a certain number of photodetectors obtained after the average optimization of the medium value of the square estimation error in different directions of the space. The M measure matrix is obtained as a result of this optimization. Having the values of the measure matrix elements, the error which occurs in determining the direction can be calculated taking into consideration different values of the error with which the sensor determines the direction of the radiation beam.

1. INTRODUCTION

In present days, most of the laser irradiation alert stations determine the arriving direction of a laser fascicle with a certain error of $\pm 15^\circ, \dots, \pm 45^\circ$ caused by the photodetector window. Some warning stations have a better precision of $\pm 1.5^\circ$ only for a specific area. In order to accomplish this, an increased number of photodetectors is required, but this is not the most convenient way to solve the problem.

2. THE SENSORS POSITIONING OPTIMISATION AND DEDUCTION OF MEASURING MATRIX (M)

This work tries to offer a solution and comes with the idea of using a station with a decreased number of photodetectors in order to realize an almost semispherical surveillance. Because the photodetectors are displayed in a certain configuration they provide the determination of the azimuth and of the wave direction in a vertical plan. The sensor of such a station exploits the photodiode answer dependence on the angle between the radiation and the normal to the surface of the photodiode (the directivity characteristic).

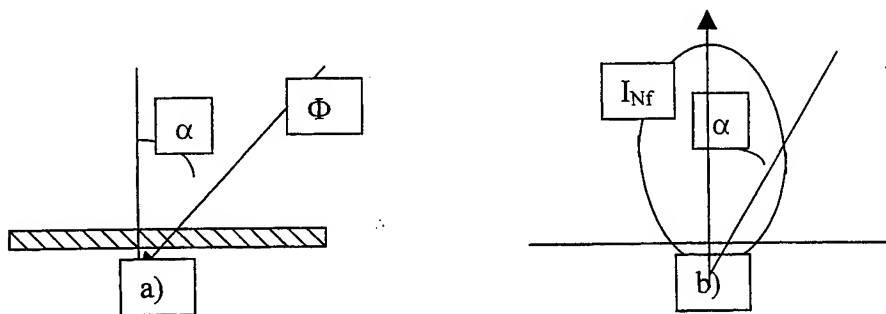


Fig.1 The directivity photodiode characteristic

- a) The radiation wave falls on the photodiode surface under the angle α ;
- b) The answer dependence of a photodiode on the incident angle of the radiation

For a certain level of radiation, the photocurrent given by the optoelectronic device depends on the angle under which the wave falls on the surface. If the photocurrent which the device gives when the wave falls normally is known, then the ratio $I_{\alpha fd}/I_{Nfd}$ gives us information on the incidence angle of the radiation (Fig. 1). Having such information from two or more sensors it is possible to determine the direction where the radiation came from.

* Correspondence: Phone: (401) 423.30.50; Fax: (401) 423.30.53

In the following we try to determine the position of the sensor support axes so that the vectorial measure X (direction) be estimated with a minimum error. Let's assume that the vectorial measure is determined with p sensors which give information on the measurement as it follows:

- \bar{u}_i is a unit normal which coincides with the normal to the surface of the photodetector;

$$y_i = \bar{u}_i \cdot \bar{X} + \varepsilon_i, \quad i = 1, \dots, p \quad (1)$$

ε_i – is the error with which the sensor determines the input measure ;

y_i – is the out-put measure given by the sensor.

The first relation can also be given under the form:

$$Y = MX + \varepsilon \quad (2)$$

Y – column vector of the p dimension, $Y \in M_{p \times 1}(R)$, being the p sensors' response when X matrix is applied on the input;

ε – column vector of the measurement errors which are assumed as being independent

and of values equal to zero, $\varepsilon \in M_{p \times 1}(R)$;

If the p number of measurements exceeds the dimension of the unknown vector X , then a unique relation for the X vector cannot be established. There for we tend to determine an X estimation for which the square of the Euclidean norm corresponding to the error vector is minimum²:

$$\tilde{Y} = Y - M\hat{X} \quad (3)$$

The functional which must be minimized is:

$$J(\hat{X}) = \|\tilde{Y}\|^2 = \tilde{Y}^T \tilde{Y} \quad (4)$$

The condition to obtain a minimum corresponds to the values which revoke the derivative of the functional $J(X)$ with respect to the vector X :

$$\frac{\partial J(\hat{X})}{\partial \hat{X}} = \frac{\partial}{\partial \hat{X}} (\tilde{Y}^T \cdot \tilde{Y}) = 0 \quad (5)$$

After proceeding with the calculus in relation (5), for the estimated \hat{X} vector we obtain the following expression which minimizes the functional³ from (4):

$$\hat{X} = (M^T M)^{-1} M^T Y \quad (6)$$

The solution, which minimizes the (6) functional depends on the values of the M matrix elements and on the Y output measures. The elements of the M measure matrix will be determined through the minimization of the functional:

$$\bar{\sigma}^2 = \frac{1}{\Omega} \iint_S \sigma_u^2 dS \quad (7)$$

σ_u^2 – the medium square deviation of the estimation error of the X vectorial measure in u direction, having the form: $\sigma_u^2 = u^T (M^T M)^{-1} u$, u being the unit normal of a random direction;

dS – the surface element on the sphere with the radius equal to 1;

$\bar{\sigma}^2$ – the medium value of the square average of the estimation error in different directions of the space, no region being privileged in comparison to others;

Ω – the solid angle covered by the warning station.

For the M matrix we consider an explicit representation having the form:

$$M = \begin{pmatrix} m_{11} & m_{12} & m_{13} \\ m_{21} & m_{21} & m_{31} \\ \cdot & \cdot & \cdot \\ m_{p1} & m_{p1} & m_{p1} \end{pmatrix} \quad (8)$$

If we consider for the station architecture a display of the axes after two concentric cones with the same vertex, the M matrix elements can be expressed using four parameters which are going to be determined. The M matrix elements are going to be determined so that the (7) functional be minimum.

In¹ it is proved that σ^{-2} , is minimum when :

$$(M^T M)^{-1} = \frac{p}{3} I_3 \quad (9)$$

If in the (9) system we substitute with the corresponding values of the measure matrix we obtain:

$$\cos^2 \varphi_1 + \cos^2 \varphi_2 = \frac{4}{3} \quad (10)$$

Let $\varphi_1=15^\circ$ and we obtain $\varphi_2=50.74^\circ$ so that we can determine a most propitious structure for the sensor system. What is important and must be taken into consideration is the fact that the resulted structure is most adequate and also not the only one; others can be obtained, too.

If the M measure matrix is associated to an optimum display, the $M^T M$ and $(M^T M)^{-1}$ are diagonal matrices.

For the upper determined parameter values, the measure matrix has the form:

$$M = \begin{pmatrix} 0.9659 & 0 & 0.2588 \\ -0.4829 & 0.8365 & 0.2588 \\ -0.4829 & -0.8365 & 0.2588 \\ 0.3164 & 0.548 & 0.7743 \\ -0.6328 & 0 & 0.7743 \\ 0.3164 & -0.548 & 0.7743 \end{pmatrix} \quad (11)$$

Finally we can find the error in determining the wave direction as a function of the error $\Delta\alpha$ which characterizes the determination of the direction of each sensor. Let us consider a random direction having the azimuth $\theta=60^\circ$ and the vertical angle $\varphi=15^\circ$. We further calculate the error of estimation as a function of various errors of the sensors.

From Tab. 1 we can see that in order to precisely determine the laser wave direction it is required that the elementary sensors be determined with minimum measurement errors.

Because the unknown direction is determined through calculus we can correct the information from the sensors so that the precision in determination may increase, if the errors of the sensors are known.

Tab. 1 Values of azimuth angles (θ) and elevation calculated for diverse own errors of 1 and 4 sensors.

The sensors own error		The azimuth angle	The elevation angle	The error in determining the direction
$\Delta\alpha_1$ [o]	$\Delta\alpha_4$ [o]	θ [o]	φ [o]	$\Delta\epsilon$ [o]
-0.5	-0.5	59.552	15.502	0.662
0.5	0.5	60.444	14.502	0.658
-1.5	-1.5	58.645	16.517	2.001
-1.5	1.5	58.198	13.529	2.283
1.5	-1.5	61.804	16.531	2.314
1.5	1.5	61.323	13.516	1.962
-5	-5	55.321	20.223	6.866
-5	5	53.978	10.303	7.521
5	-5	66.045	20.372	7.874
-10	-10	49.924	26.181	14.614
-10	10	47.843	6.14	14.866
10	-10	72.318	26.773	16.442
10	10	68.427	5.547	12.567

3. THE STUDY OF ESTIMATING ERRORS VARIATION, FUNCTION OF OWN ERRORS FOR 1 AND 4 SENSORS

In the following, the author analyses the variation of the error of estimations as a function of the sensor's own measurement error. The error of estimation depends, in the considered case, on two variables; the error in determination of the two sensors, $\Delta\alpha_1$ and $\Delta\alpha_4$. The way the error of estimation $\Delta\epsilon_2$ changes is presented in Figs. 2 and 3. It can be observed that when the sensor's own error is zero the error of estimation is also zero, but as the value of the sensor's error increases, the error of estimation increases too.

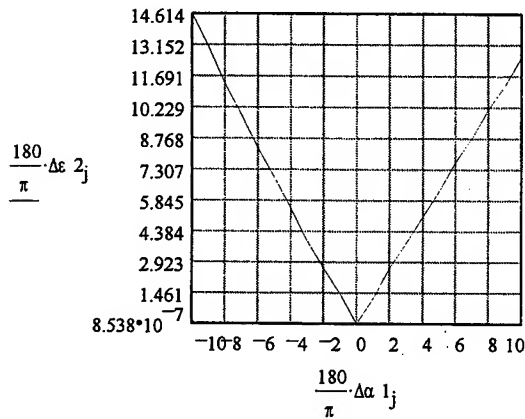


Fig. 2 The variation of the error in estimating the direction according to the sensor's own error. The sensor considered is the number 1 sensor

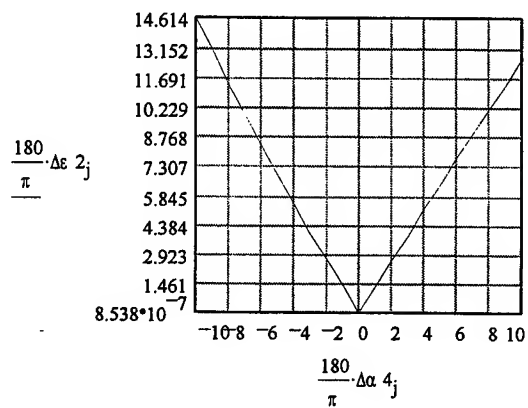


Fig. 3 The variation of the error in estimating the direction according to the sensor's own error. The sensor considered is the number 4 sensor

For the direction given by $\theta = 60^\circ$ and $\varphi = 15^\circ$ and the domain of variation of the sensor's error

$\Delta\alpha_1 \in [-10^\circ, 10^\circ]$, $\Delta\alpha_4 \in [-10^\circ, 10^\circ]$, the Fig. 4 illustrates the variation of the error of estimation, $\Delta\epsilon_2$, in a

three - axes system of co - ordinates.

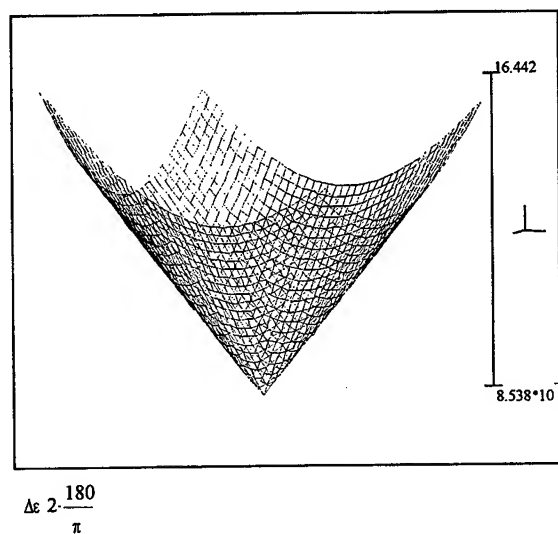


Fig. 4 The variation of the error in estimating the direction when both sensor number 1 and 4

are considered. The sensors errors are in the domain: $\Delta\alpha_1 \in [-10^\circ, 10^\circ]$, $\Delta\alpha_4 \in [-10^\circ, 10^\circ]$.

For the same direction, the Figs. 5 and 6 show the way the angles θ and φ vary. As it is known, the two above angles characterize the direction of the laser beam. The diagrams confirm the importance of building up sensors with low errors. If the sensor's error is below 1° , the precision in determining the direction increases very much. (see Tab. 1)

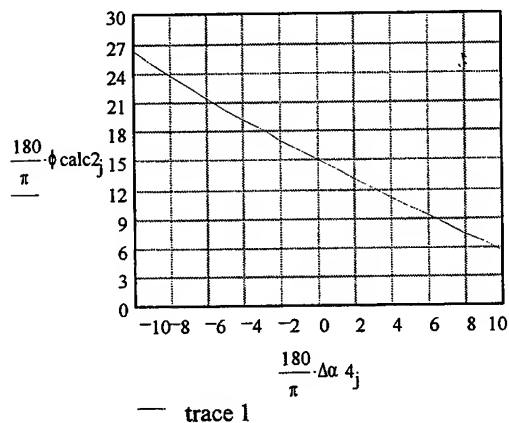


Fig. 5 The variation of the determined value of the angle φ considering the error of the sensor number 4

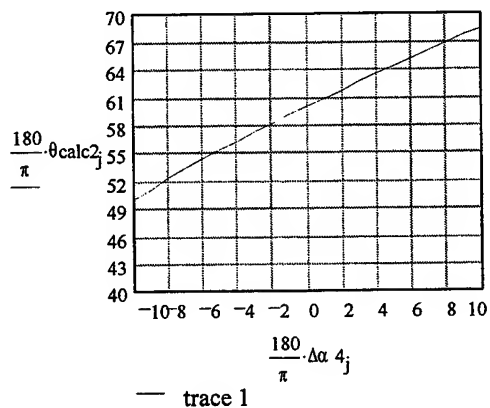


Fig. 6 The variation of the determined value of the azimuth, considering the error of the sensor number 4

4. CONCLUSIONS

We have demonstrated that there exists the possibility of building an alert station for determining the azimuth and the vertical angle of the laser wave with precision, but a microprocessor is needed in order to process the information. Through the calculus program we can eliminate false alarms meaning that information is processed even if it comes from more sensors at the same time and not from only one as it happens in most of present-day stations. In the analyzed example we

used 7 sensors (photodiodes) and we determined the error in estimating the direction taking into consideration the individual error of each sensor, which influences the resolution in determining the direction. For example an alert station which determines the angle under which we can find the wave with a precision of $\pm 15^\circ$, needs a number of 12 sensors for a circular covering.

The precision required above can be realized easily with such a station with only 7 sensors, and whose errors may be above 10° , which is considered an advantage.

For the given station it is not necessary to calculate the window in front of the photodiode, so that it receive the radiation only in a certain solid angle.

REFERENCES

1. Sabac, Gh., *Special Mathematics*, Didactic and Pedagogic Publishing House, Bucharest, 1981.
2. Raul, M. and Grozeanu, I., *Sequence Estimation Applied to Chemical Systems*, Technical Publishing House, 1985.
3. Olariu, M., *Master's Degree Thesis*, Military Technical Academy Library, 1998.

Resonant cavity light-emitting diodes: modeling, design and optimization

M. Dumitrescu*, P. Sipilä, V. Vilokkinen, L. Toikkanen, P. Melanen, M. Saarinen,
S. Orsila, P. Savolainen, M. Toivonen and M. Pessa

Optoelectronics Research Centre, Tampere University of Technology,
P.O. Box 692, 33101 Tampere, Finland

ABSTRACT

Monolithic top emitting resonant cavity light-emitting diodes (RCLEDs) operating in the 650 and 880 nm ranges have been prepared using solid-source molecular beam epitaxy (SSMBE) growth. Transfer matrix based modelling together with a self-consistent model have been used to optimise the devices' performances. The design of the layer structure (distributed Bragg reflector (DBR) mirrors, microcavity, quantum wells (QWs), barriers, current spreading and cap layers) and doping profile was assisted by computer simulations that enabled many device improvements. Among the most significant ones intermediate-composition barrier-reduction layers were introduced in the DBR mirrors for improving the I-V characteristics and the cavity and mirrors were detuned aiming at maximum extraction efficiency. The fabricated devices showed line widths below 15 nm, CW light power output of 8 and 22.5 mW, and external quantum efficiencies of 3% and 14.1% in the 650 nm and 880 nm ranges, respectively - while the simulations indicate significant performance improvement possibilities.

Keywords: Resonant Cavity-LED, Solid-Source MBE, modeling, optimization, detuning

1. INTRODUCTION

The resonant cavity light emitting diodes present several advantages compared to conventional light emitting diodes such as narrow linewidth, better directionality, high brightness and increased efficiency. The enhancements result from the alteration of the spontaneous emission pattern and depend on the structure ability to direct the cavity modes into the escape cone defined by the interface with the highest contrast (usually the last semiconductor-to-air or semiconductor-to-epoxy interface).

The basic RCLED structure that we investigated consisted of a cosine-type $1-\lambda$ -thick cavity delimited by AlGaAs DBR mirrors and having an active region (with 3 to 5 QWs) centred at the cavity antinode. Top emission was considered because of the GaAs substrate absorption in the working spectral ranges and monolithic structures were chosen since they enable integration and have reduced fabrication complexity.

Several software tools were used in the process of designing and optimizing the RCLED. Besides using a self-consistent model (to evaluate spontaneous emission spectrum, bandstructure, absorption edge, potential barriers, etc.) several transfer matrix based programs have been developed to help the design process. Apart from enabling a faster and more effective design and optimization the modeling and simulation also assisted some conceptual device improvements.

The structures were grown by SSMBE¹ that is suitable for the fabrication of many abrupt composition steps (like in the RCLED structures). Rapid thermal annealing (RTA) and burn-in tests improved significantly the RCLED efficiency in both spectral ranges. The structures were processed into circular, top-emitting mesas and the current aperture was formed by wet thermal oxidation. The processed devices were bonded on TO-46 cans with silver filled epoxy and a few of these devices were encapsulated by transparent epoxy. The measured static characteristics together with the near-field and far field distributions indicate good electrical and optical properties although the devices are not fully optimized. An incipient dynamic property investigation reveal that RCLEDs are significantly faster than LEDs but the dynamic behavior issue is just beginning to be tackled. The preliminary lifetime tests are very encouraging still showing a residual trend of improvement. We believe that, once fully optimized, our devices are suited for many applications like sources for plastic optical fiber based communications systems for LAN and automotive areas, miniature displays, imaging technologies, measurement and detector systems, optical printing.

* Correspondence: Mircea.Guina%ORC@semi.ee.tut.fi

2. MODELING AND SIMULATION

In a first modeling and simulation step the QW composition and thickness together with the barrier thickness are chosen, using a self-consistent model, so that the resulted spontaneous emission spectrum is peaked at the desired wavelength. The self-consistent model uses interband transition; strained QWs are treated using the k-p theory and valence band mixing effects are included. It has to be mentioned that since the spontaneous emission spectrum depends strongly upon bias and temperature while the active region temperature and the relation between injected current and QW carrier densities (used in the model) are highly uncertain, the calculated spontaneous emission spectrum must be fitted to measurements. Typical emission spectra for the 650 and 880 nm ranges are shown in Fig. 1 and 2, respectively. In Fig. 1 the emission spectrum asymmetry with respect to the emission peak and the emission spectrum dependence on bias can be observed while Fig. 2 shows a comparison between the spectra of one of our 880 nm RCLED and a commercial LED for two bias current values.

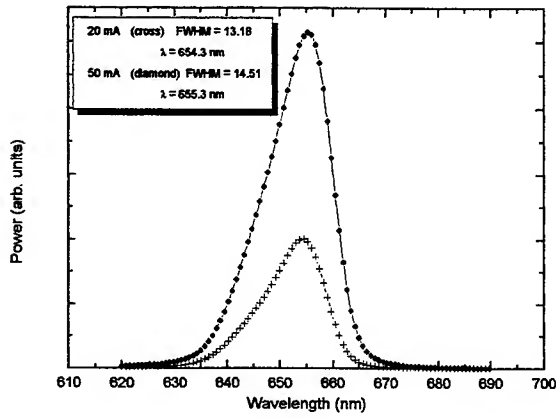


Fig. 1 Emission spectrum for a 650 nm range RCLED at two bias currents

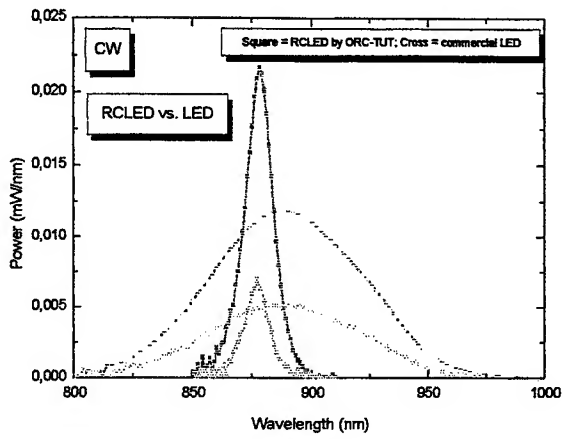


Fig. 2 Comparison between the emission spectrum of an 880 nm range RCLED and a commercial LED in the same wavelength range for two bias currents

If, based on a plane wave decomposition of the propagating field, only 1D propagation at a given wavelength and angle is analyzed, the field can be represented by a 2×1 column vector having the complex amplitudes of the forward propagating wave (Ψ^+) and backward propagating wave (Ψ^-) as elements. In an optically linear and isotropic propagation medium the optical fields in two planes z_i and z_{i+1} are linked by the matrix equation:

$$\begin{bmatrix} \Psi_{i+1}^+ \\ \Psi_{i+1}^- \end{bmatrix} = \begin{bmatrix} M_{11} & M_{12} \\ M_{21} & M_{22} \end{bmatrix}_{i+1} \cdot \begin{bmatrix} \Psi_i^+ \\ \Psi_i^- \end{bmatrix} \Leftrightarrow \tilde{\Psi}_{i+1} = \|M\|_{i+1} \cdot \tilde{\Psi}_i \quad (1)$$

It can be easily observed that the overall transfer matrix for a sequence of propagation sections (between successive z_i planes) can be obtained by multiplying the sections' transfer matrices – starting with the farthest on the direction of propagation:

$$\tilde{\Psi}_N = \|M\|_{(i=1..N)} \cdot \tilde{\Psi}_0 = \|M\|_N \cdot \|M\|_{N-1} \cdots \|M\|_2 \cdot \|M\|_1 \cdot \tilde{\Psi}_0 \quad (2)$$

Any longitudinal index profile $n(z)$ can be expressed as a staircase-like succession of constant-refractive-index layers. For a continuous $n(z)$ variation the narrower the staircase steps are the more accurate is the approximation of the real refractive index variation. Only two types of sections are needed for a transfer matrix representation of a structure with staircase

refractive index variation : the type corresponding to the interface between two constant-refractive-index layers and the type corresponding to a constant refractive index layer. The transfer matrix for the interface between two constant-refractive-index layers (denoted by the indices 1 and 2), assuming no optical loss at the interface, is:

$$\|R_{12}\| = \begin{vmatrix} 1/t_{21} & -r_{12}/t_{21} \\ -r_{12}/t_{21} & 1/t_{21} \end{vmatrix} \quad (3)$$

where $r_{12} = \frac{n_1 \cdot \cos \theta_1 - n_2 \cdot \cos \theta_2}{n_1 \cdot \cos \theta_1 + n_2 \cdot \cos \theta_2}$ and $t_{21} = 1 + r_{21}$ for TE polarisation while $r_{12} = \frac{n_2 \cdot \cos \theta_1 - n_1 \cdot \cos \theta_2}{n_2 \cdot \cos \theta_1 + n_1 \cdot \cos \theta_2}$

and $t_{21} = n_1 \cdot (1 + r_{21}) / n_2$ for TM polarisation, θ_1 and θ_2 being the incidence and refraction angles.

The transfer matrix for the constant-refractive-index layer is:

$$\|T\| = \begin{vmatrix} \exp\{[(g - \alpha) - j\beta]L\} & 0 \\ 0 & \exp\{-(g - \alpha) - j\beta\}L\} \end{vmatrix} \quad (4)$$

where g and α are, respectively, the gain and loss per length unit, L is the layer length on the direction under analysis and β the propagation constant.

The reflection and transmission coefficient of a succession of sections can be easily obtained if the sections' transfer matrices are known. Considering a normalized forward propagating wave entering the first section and no backward propagating wave entering the last one, the transmission and reflection coefficient for the whole structure are related by the matrix relation:

$$\begin{vmatrix} t_{(i=1 \dots N)} \\ 0 \end{vmatrix} = \|M\|_{(i=1 \dots N)} \cdot \begin{vmatrix} 1 \\ r_{(i=1 \dots N)} \end{vmatrix} = \begin{vmatrix} M_{11}^{(i=1 \dots N)} & M_{12}^{(i=1 \dots N)} \\ M_{21}^{(i=1 \dots N)} & M_{22}^{(i=1 \dots N)} \end{vmatrix} \cdot \begin{vmatrix} 1 \\ r_{(i=1 \dots N)} \end{vmatrix} \quad (5)$$

from which the reflection and transmission coefficient of the whole succession of sections can be derived:

$$r_{(i=1 \dots N)} = -\frac{M_{21}^{(i=1 \dots N)}}{M_{22}^{(i=1 \dots N)}} \quad \text{and} \quad t_{(i=1 \dots N)} = M_{11}^{(i=1 \dots N)} - M_{12}^{(i=1 \dots N)} \cdot \frac{M_{21}^{(i=1 \dots N)}}{M_{22}^{(i=1 \dots N)}} \quad (6)$$

The optical analysis of the RCLED layer structure is very much based on the determination of the reflectivity dependence upon wavelength, incidence angle, polarization, layer contrast, layer thickness, number of DBR periods. The example given in Fig. 3 shows a contrast dependence calculation pointing out that a 30-period $\text{Al}_{0.95}\text{Ga}_{0.05}\text{As}/\text{Al}_x\text{Ga}_{1-x}\text{As}$ DBR mirror should have at least a 0.42 contrast between high and low refraction index layers in order to obtain a reasonable reflectivity at 650 nm. Unfortunately high contrast in AlGaAs layers is limited in the red range by significant absorption at reduced aluminum content.

Since the devices electrical characteristics are as much important as the optical ones an electrical analysis is performed in conjunction with the optical analysis. The absorption edge (bandgap) and potential barriers' variation with layer composition, thickness and bias are analyzed at this stage with the aid of the self-consistent model. In order to alleviate the adverse effects of the DBR potential barriers, intermediate composition layers and/or delta doping regions were used before each high bandgap material layer (in the direction of majority carrier flow). Also structures having superlattice layers of high and low bandgap materials before each high bandgap layer (in the direction of majority carrier flow) were tried but with reduced effectiveness. The composition and thickness of the intermediate DBR layers were adjusted by analyzing the bandstructure profile calculated with the self-consistent model. The resulted optimum composition was roughly in the middle of the composition gap between low and high bandgap layers. Supplementary the doping and thickness was adjusted

to yield a smooth band-profile on the path of both majority carriers and to reduce/eliminate the notches induced by bandgap discontinuities. In order to keep the optical properties of the mirrors unaffected the intermediate composition layer thickness was kept much smaller than the emission wavelength and the thickness of the high bandgap layer was adjusted so that the optical thickness of the combined intermediate composition and high bandgap layer is $\lambda_0/4$. Also in order to improve the electrical device characteristics the bottom DBR was made of N (and not the typical $N+1/2$ periods) starting with high refractive index (low bandgap) layer on the substrate side. This was done since on one hand the number of periods in the bottom mirror was high enough (so that the contrast on the interface with the GaAs substrate is not important from the optical point of view) and on the other hand the GaAs to low-bandgap material interface produces a favorable barrier reduction step for electrons. In a similar attempt to introduce a barrier reduction step at the first potential barrier for holes the current spreading layer was made of low bandgap (high refractive index) material.

Once the DBR layer composition, order and thickness are established the remaining variable to adjust the DBR mirror reflectivities is the number of periods. The dependence of an $\text{Al}_{0.2}\text{Ga}_{0.8}\text{As}/\text{Al}_{0.9}\text{Ga}_{0.1}\text{As}$ DBR mirror reflectivity upon the number of periods at 895nm, presented in Fig. 4, is indicating that at least 20 periods should be used in the bottom mirror of the RCLED.

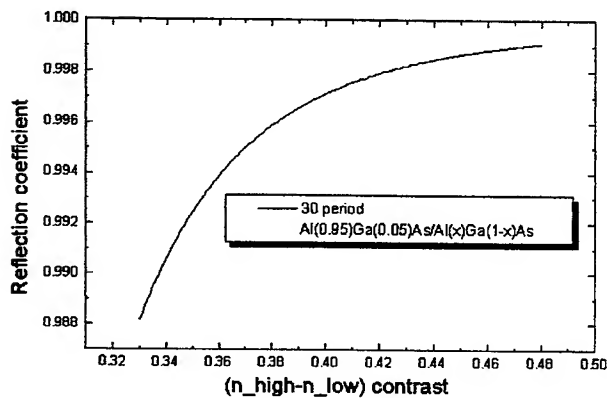


Fig. 3 Calculated 30-period $\text{Al}_{0.95}\text{Ga}_{0.05}\text{As}/\text{Al}_x\text{Ga}_{1-x}\text{As}$ DBR mirror reflectivity dependence upon layer contrast (at 650 nm and normal incidence).

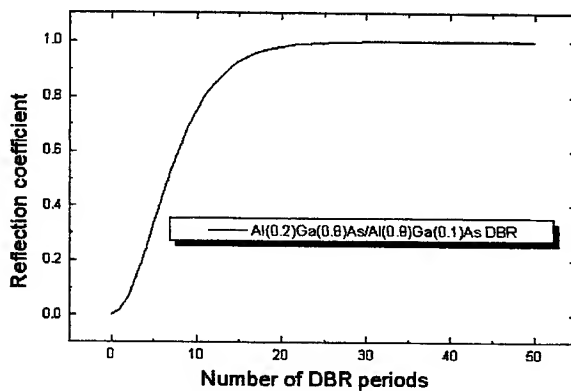


Fig. 4 Calculated $\text{Al}_{0.2}\text{Ga}_{0.8}\text{As}/\text{Al}_{0.9}\text{Ga}_{0.1}\text{As}$ DBR mirror reflectivity dependence upon the number of periods (at 895 nm and normal incidence)

In order to adjust the refractive index values used in simulations, comparisons between the calculated and experimental spectral reflectivities were carried out. Fig. 5 shows such a comparison for a 10-period $\text{Al}_{0.9}\text{Ga}_{0.1}\text{As}/\text{Al}_{0.2}\text{Ga}_{0.8}\text{As}$ DBR mirror at normal incidence. The differences on the short wavelength side lobes are due to the fact that the simulations assumed no absorption throughout the whole spectrum. The close match between the simulation and experiment indicates not only that the refractive index values used in simulation were fairly accurate but also that the control of the growth process was very good.

Since simply using an overall cavity optical thickness equal to the wavelength of the aimed cavity mode gives rather poor results we also used the transfer matrix approach to evaluate more accurately the spectral position of the cavity mode and adjust the cavity thickness. Fig. 6 presents the calculated spectral reflectivity of the top and bottom DBR mirrors of a 880nm RCLED together with the calculated spectral reflectivity of the whole RCLED structure at normal incidence - showing the cavity mode position. Several design elements can be analyzed in Fig. 6. For top high extraction efficiency, while the bottom mirror reflectivity is aimed at values as close as possible to unity, the top mirror reflectivity must be adjusted to significantly lower values - so that the cavity modes over the whole emission spectrum occupy as much as possible of the escape window. The top mirror reflectivity and the narrow cavity dip indicate that the number of top DBR mirror periods for the analyzed structure is above optimum. Another important fact that can be observed in this example is that both mirrors and the cavity mode were detuned with about 20 nm from the maximum emission wavelength ($\lambda_{\text{max}}=880$ nm). The detuning was aimed to increase the extraction efficiency into air. Unfortunately the high extraction efficiency is contradictory to good directivity since a rabbit ear far field (FF) pattern is associated with maximum extraction.

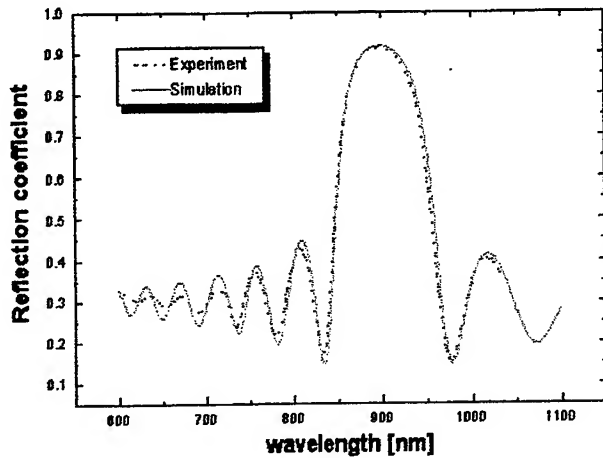


Fig. 5 Comparison between the measured and the calculated spectral reflectivity for a 10-period $\text{Al}_{0.9}\text{Ga}_{0.1}\text{As} / \text{Al}_{0.2}\text{Ga}_{0.8}\text{As}$ DBR mirror at normal incidence

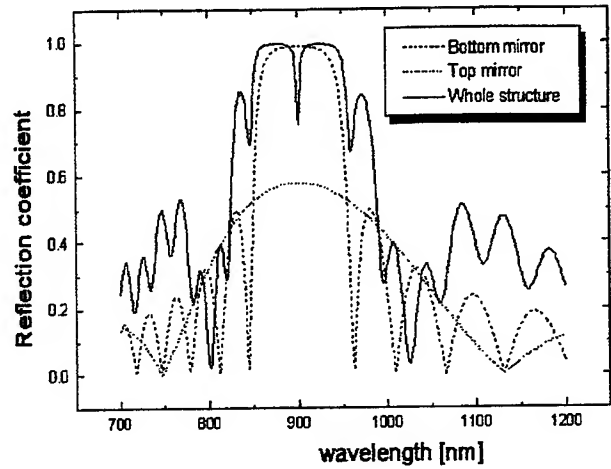


Fig. 6 Calculated spectral reflectivity of the whole structure, top and bottom DBR mirrors for a 880 nm range RCLED at normal incidence

The light extraction efficiency – defined as the amount of optical power emitted by the active region source that can be extracted outside the structure within a given collection angle – is an important design parameter. In order to optimize the extraction efficiency the DBR mirrors and the cavity must be detuned with respect to the emission spectrum peak. The detuning $\Delta\lambda$ is given by the difference between the cavity resonance wavelength ($\lambda_{\text{FP}} = 2 \cdot n_c \cdot L_c / m_c$, with n_c the cavity refractive index, L_c the cavity length and m_c the cavity order) – that should be aligned with the DBR stopband center ($\lambda_{\text{DBR}} = \lambda_{\text{FP}}$) – and the emission spectrum peak wavelength (λ_{max}): $\Delta\lambda = \lambda_{\text{FP}} (= \lambda_{\text{DBR}}) - \lambda_{\text{max}}$. For a monochromatic source emission and no limits on the collection angle the extraction efficiency is optimum when the cavity mode is centered in the middle of the escape window (corresponding to an emission lobe maximum at 45° from the surface) and the cavity finesse is low enough so that the cavity mode fills the whole escape window. However in the practical case the source has an emission spectrum not only of finite width but also not symmetrical with respect to the emission peak wavelength. In this situation detailed modeling and simulation is needed to find out the optimum detuning. The procedure we have applied to evaluate the optimum detuning is also based on the transfer matrix formalism, but instead of using gain in the active layers introduces source terms^{2,3}. The procedure starts from the estimated or from the directly measured active-region emission spectrum. For each emission spectrum sample the dipole-source angular emission pattern for each polarization case should be considered. However, since our RCLEDs have compressive strained QWs (leading to dominant electron-heavy hole recombination and TE emission) and since vertical dipole emission is poorly coupled to the cavity mode we took into account, in a first approximation, just the TE emission of the (arbitrarily oriented) horizontal dipoles. Because the device structure is invariant to rotation around an axis perpendicular on the grown layers (Oz) all the calculations are restricted in a xOz plane without loss of generality. The result of all these is a horizontal-dipole TE source term of a certain value^{2,3} for each wavelength sample and angular orientation. This source term is placed successively in source planes situated in the middle of each QW layer. A simple transfer matrix equation system then links (for each wavelength sample and angular orientation) the fields emerging progressively from the top (Ψ^+) and regressively from the bottom (Ψ^-) of the structure with the progressive (Ψ^+) and regressive (Ψ^-) source terms :

$$\begin{pmatrix} \Psi^+_t(\lambda, \theta) \\ 0 \end{pmatrix} = MU \times \begin{pmatrix} \Psi^+_{s+\varepsilon}(\lambda, \theta) \\ \Psi^-_{s+\varepsilon}(\lambda, \theta) \end{pmatrix} \quad (7)$$

$$\Psi^+_{s+\varepsilon}(\lambda, \theta) = \Psi^+_{s-\varepsilon}(\lambda, \theta) + \Psi^+_s(\lambda, \theta) \quad (8)$$

$$\Psi^-_{s-\varepsilon}(\lambda, \theta) = \Psi^-_{s+\varepsilon}(\lambda, \theta) + \Psi^-_s(\lambda, \theta) \quad (9)$$

$$\begin{pmatrix} 0 \\ \Psi^-_b(\lambda, \theta) \end{pmatrix} = MD \times \begin{pmatrix} \Psi^+_{s-\varepsilon}(\lambda, \theta) \\ \Psi^-_{s-\varepsilon}(\lambda, \theta) \end{pmatrix} \quad (10)$$

In the previous equation system the + and – upper indices indicate progressive (towards the top) and regressive (towards the bottom) propagation; the s, s+ε and s-ε lower indices correspond to the source plane and planes just above and just below the source plane; the MU transfer matrix corresponds to the structure from just above the source plane up to the top output medium and the MD transfer matrix corresponds to the structure from just below the source plane down to the bottom output medium.

When the cavity mode fits inside the escape window over the whole emission spectrum the optimum detuning leads to two separate emission lobes (with zero emission both at 0° and 90°). In this case the optimum detuning is roughly equal to the difference between the long wavelength edge and the peak emission wavelength of the emission spectrum. As the detuning is increased above the optimum value the emission lobes separate further apart (decreasing the coupling efficiency) and the extraction efficiency is decreased as shorter wavelength emission exits the escape window. When the detuning is decreased below the optimum value the emission lobes come closer together (increasing the coupling efficiency) and as they ‘overlap’ the extraction efficiency is reduced due to long wavelength emission exiting the escape window. At zero detuning a single emission lobe is obtained and this emission lobe gets narrower and the extraction efficiency is further decreased as the detuning is going farther in the negative domain. Fig. 8 shows the measured emission lobes for three 650 nm range RCLED structures for which the intended detuning was 0, 6 and 14 nm. It can be seen that the measured emission lobes are not far from those of Fig. 9, obtained by simulation, the differences being not only due to the model inaccuracies but also due to the inherent differences between the designed and realized structures.

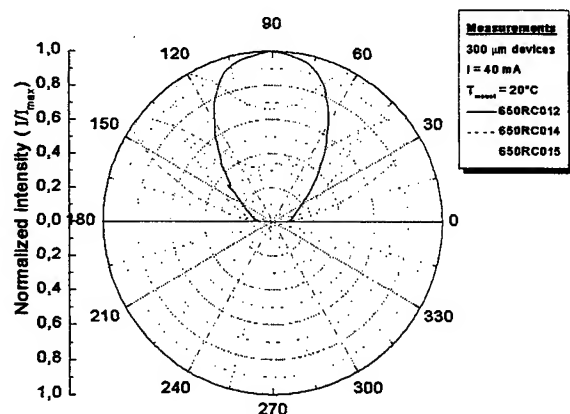


Fig. 7 Far-field emission measured for three 650 nm range RCLEDs having different intended detuning :
 $\Delta\lambda(650RC012) \approx 0\text{nm}$, $\Delta\lambda(650RC015) \approx 6\text{nm}$,
 $\Delta\lambda(650RC014) \approx 14\text{nm}$

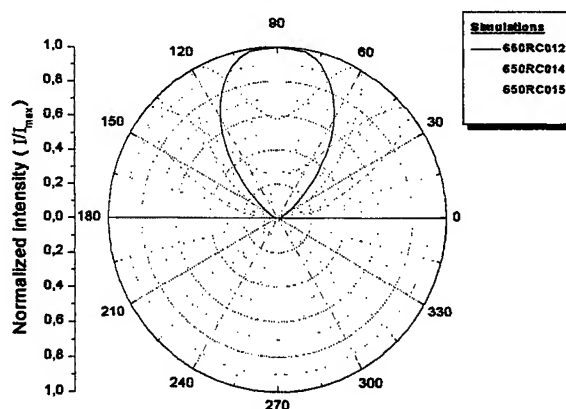


Fig. 8 Simulated far-field emission for the three 650 nm range RCLED structures whose measured far-field emission is given in Fig. 7

As the emitted spectrum, the DBR mirror stopband center and the cavity resonance wavelength depend on temperature and bias the optimum detuning regime is achieved at a particular bias and temperature of the active region. Temperature influences both the emission spectrum (which is red shifted with increased temperature) and the cavity resonance (which is also red-shifted due to thermal expansion and to the temperature dependence of the refractive index). As a consequence increased temperature brings the emission lobes closer together. The bias influences both the cavity resonance (as the refractive index depends on carrier density) and the emission spectrum (which is blue shifted with increased bias). A general tendency of the emission spectrum and angular far field distribution with bias cannot be determined since inherent temperature variation with bias – depending on the particular device structure – should be included.

Based on the same transfer matrix formalism the study of optical field longitudinal distribution enabled us to compare sine and cosine cavities, analyse the QW placement and evaluate doping profiles to reduce the free carrier absorption. Fig. 9 shows the refractive index and the optical field profile for a 1-λ cosine cavity 650 nm RCLED. In this case, only one of the QWs can be placed at the single antinode available; the additional QWs being less effectively coupled with the cavity mode. The optimum number of QWs is odd – to have one QW placed exactly at the antinode – and in the range of 3 to 7 depending on the QW and barrier thickness. Higher number of QWs induces reduced and non-uniform carrier injection into the QWs besides bad coupling to the cavity mode for the QWs farther from the antinode.

The refractive index and optical field longitudinal profiles for a $1-\lambda$ sine cavity 650 nm RCLED are shown in Fig. 10. In this case two QW groups can be centred at the two antinodes in the cavity. No sine-type cavity RCLEDs have yet been prepared although there are reasons to expect that by increasing the number of QWs without increasing the cavity length some of the device characteristics will improve. The device characteristic with highest improvement expectations in sine-type cavity devices is the modulation bandwidth due to increased photon density. The main drawback of the sine-type cavity devices is the degradation of QW carrier injection efficiency. The carrier injection is impaired not only by the increased number of QWs (leading to non-uniform injection) but also by degraded carrier confinement (the low-bandgap high refraction index layers bordering the sine cavity do not provide potential barriers for carrier confinement as were the high-bandgap low refraction index layers bordering the cosine cavity). The carrier confinement problem can be alleviated by using low-refraction-index high-bandgap spacers on the outer limits of the cavity (and lower bandgap barriers and spacers inside the cavity) and by optimising the doping profile in the region. The optical simulations in Fig. 9 and 10 indicate that for similar QW injection the relative optical field intensity is significantly higher in the sine-type cavity.

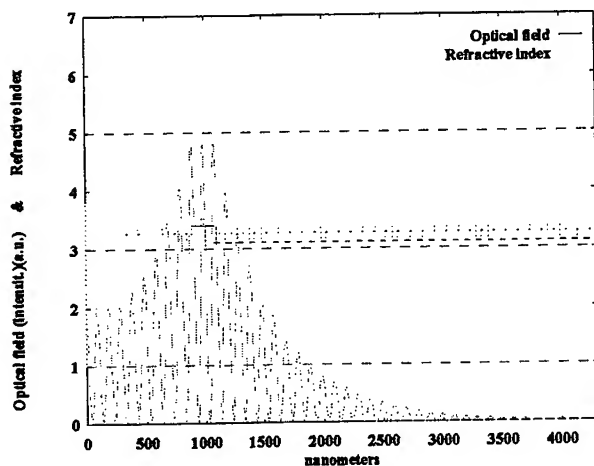


Fig. 9 Refractive index and optical field intensity profiles along a $1-\lambda$ cosine cavity RCLED

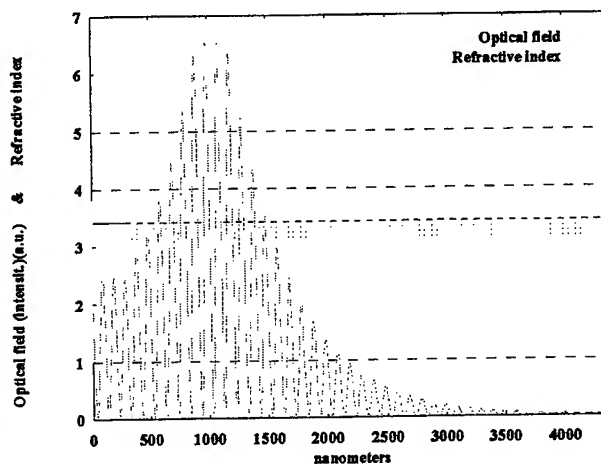


Fig. 10 Refractive index and optical field intensity profiles along a $1-\lambda$ sine cavity RCLED

3. DEVICE GROWTH, PROCESSING AND CHARACTERIZATION

Our RCLED structures were grown by solid-source molecular beam epitaxy (SSMBE)¹. Besides being suitable for the fabrication of many abrupt composition steps, SSMBE has the advantage of being toxic-gas-free and having a reduced growth temperature (as compared with MOCVD growth). Furthermore the SS-MBE grown AlGaInP material used for the red RCLED cavity does not suffer from alloy ordering to the same extent as in MOCVD growth^{4,5,6}, enabling the use of exactly cut substrates for RCLED structures in both spectral ranges. Valved cracker cells were used for arsenic and phosphorus, whereas group III (aluminum, gallium and indium) fluxes were generated by conventional effusion cells. Beryllium and silicon were used as *p*- and *n*-type dopants, respectively. The growth temperature and the phosphorus beam pressure for growing the active region were adjusted to yield maximum photoluminescence (PL) intensity.

The 650 nm RCLED structure consisted of a 32 period *n*-doped $\text{Al}_{0.5}\text{Ga}_{0.5}\text{As}/\text{AlAs}$ bottom DBR mirror (with $\text{Al}_{0.75}\text{Ga}_{0.25}\text{As}$ intermediate composition layers), a $1-\lambda$ cosine cavity with three $\text{Ga}_{0.45}\text{In}_{0.55}\text{P}$ QWs and $(\text{Al}_{0.5}\text{Ga}_{0.5})_{0.51}\text{In}_{0.49}\text{P}$ barriers and semicavities, a 5 to 12 period *p*-doped $\text{Al}_{0.95}\text{Ga}_{0.05}\text{As}/\text{Al}_{0.5}\text{Ga}_{0.5}\text{As}$ top DBR mirror (also with $\text{Al}_{0.75}\text{Ga}_{0.25}\text{As}$ intermediate composition layers) and an $\text{Al}_{0.5}\text{Ga}_{0.5}\text{As}$ current spreading layer with a thin p^{++}GaAs contact layer on top. The $\text{Al}_{0.98}\text{Ga}_{0.02}\text{As}$ wet thermal oxidation layer was placed one DBR period away from the cavity in order to avoid oxide modes and strain propagation into the cavity. The 880 nm RCLED structure consisted of a 20 period *n*-doped $\text{Al}_{0.2}\text{Ga}_{0.8}\text{As}/\text{Al}_{0.9}\text{Ga}_{0.1}\text{As}$ bottom DBR mirror, a $1-\lambda$ cosine cavity with three $\text{Ga}_{0.96}\text{In}_{0.04}\text{As}$ QWs and $\text{Al}_{0.2}\text{Ga}_{0.8}\text{As}$ barriers and semicavities, a 5 to 7 period *p*-doped $\text{Al}_{0.9}\text{Ga}_{0.1}\text{As}/\text{Al}_{0.2}\text{Ga}_{0.8}\text{As}$ top DBR mirror having a $\text{Al}_{0.97}\text{Ga}_{0.03}\text{As}$ wet thermal oxidation layer in the second period from the cavity and an $\text{Al}_{0.2}\text{Ga}_{0.8}\text{As}$ current spreading layer with a thin p^{++}GaAs contact layer on top. No barrier reduction layers were used in the 880 nm RCLEDs.

A rapid thermal annealing (RTA), done at 890°C for 1 s, was found to improve significantly the RCLED efficiency in both spectral ranges by removing some of the non-radiative recombination centres⁷. Electro-annealing (EA) produced a similar significant improvement as can be seen from the comparison between the V-I and L-I characteristics for devices with and without EA. The structures were processed into circular, top-emitting mesas with window diameters ranging from 80 μm to 500 μm . The current aperture was formed by wet thermal oxidation at 375°C for 135 minutes. The mesa edge and the oxide layer penetration can be observed in the scanning electron microscope image of a 650 nm range RCLED shown in Fig. 12. The arrow indicates the current aperture made by selective wet thermal oxidation.

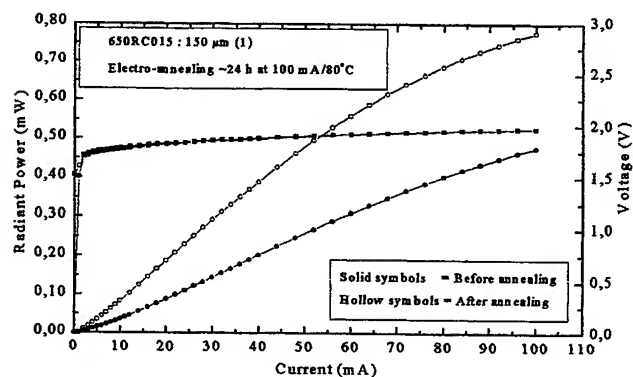


Fig. 11 L-I and V-I characteristics for 650 nm range RCLEDs with and without electro-annealing

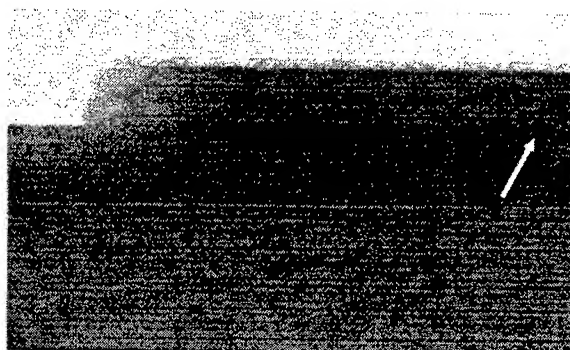


Fig. 12 Scanning electron microscope image of a 650 nm range RCLED showing the mesa and the oxide aperture

Initially a ring-shape top contact was used and near-field measurements indicated highly non-uniform transverse optical field distribution. Fig. 13 shows the non-uniform transverse near optical field distribution measured from a 80 μm diameter mesa structure having a top ring contact. Under the assumption that the transverse optical field non-uniformity was mainly caused by poor transverse current spreading, honeycomb 3 μm wide metal stripes were run through the window area to enhance current spreading. The resulted near field distribution is shown in Fig. 14. A more uniform transverse optical field distribution is obtained except from the areas shadowed by the metal stripes. The optical field gap in the lower left corner is probably due to the wire bonding extending over the aperture.

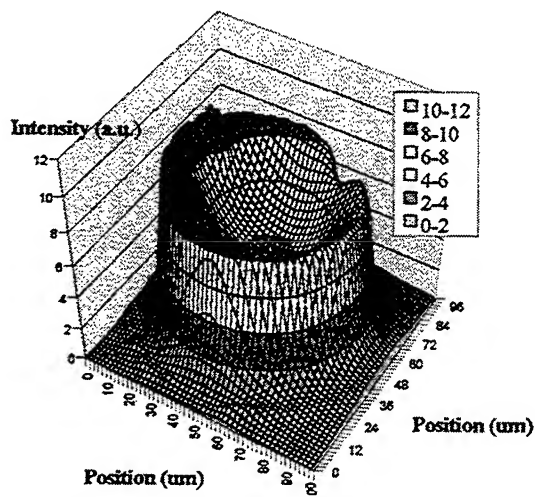


Fig. 13 Measured near optical field for a 650nm range RCLED with a ring contact of about 80 μm

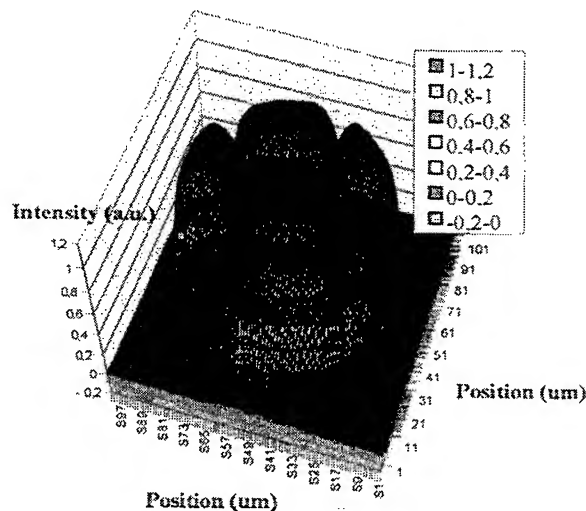


Fig. 14 Measured near optical field for a 650nm range RCLED having honeycomb metal stripes over the output aperture

The processed devices were bonded on TO-46 cans with silver filled epoxy. Some of these devices were encapsulated by transparent epoxy to protect the surface and to improve the light extraction from the device. The epoxy encapsulation decreased the refractive index difference at the semiconductor to output medium interface, thus enlarging the escape cone. Figs. 15 and 16 show the current-light-voltage (I-L-V) characteristics and external quantum efficiencies (QE) deduced from the experiments for encapsulated 500- μm devices (with $\Delta\lambda_{\text{det}} \approx 15 \text{ nm}$). The 650 nm device (Fig. 15) exhibits a maximum power in excess of 8 mW at $I = 200 \text{ mA}$ dc drive current and bias voltage $V_f = 2.20 \text{ V}$. The external QE has a maximum of 2.5% at $I = 60 \text{ mA}$, and it is slightly decreased at higher injection currents due to thermal effects. Our QE values are somewhat smaller than those of 202 μm wide red RCLEDs reported by a Swedish group⁸, indicating that our 650 nm RCLED structure may require further optimization. The 880 nm device (Fig. 16) exhibits a maximum power of 22.5 mW at $I = 130 \text{ mA}$, and V_f is 2.25 V. Some reduction of the forward voltage and series resistance can be expected when barrier reduction layers are introduced in the DBR mirrors and the layer succession is optimized. The maximum external QE is 14% obtained at $I = 30 \text{ mA}$. The external QE decreases, as injection current is increased, due to thermal effects. To the best of our knowledge, there exists no publication on RCLEDs emitting exactly at this wavelength for a close comparison with our results, but there are studies on 860 nm RCLEDs in the literature⁹. The reported 860 nm RCLED had an order of magnitude lower QE than that of our 880 nm device.

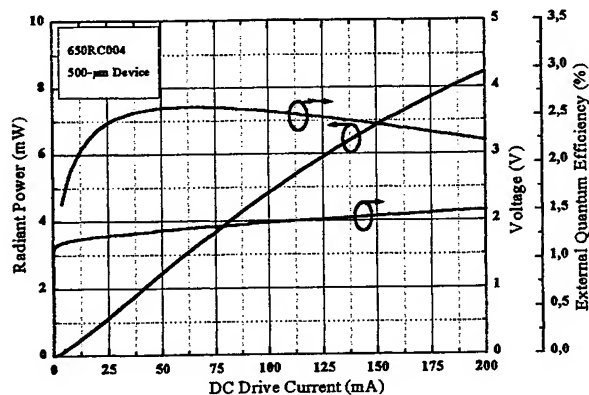


Fig. 15 Radiant power, forward voltage and external QE as a function of injected dc current for a 650 nm RCLED

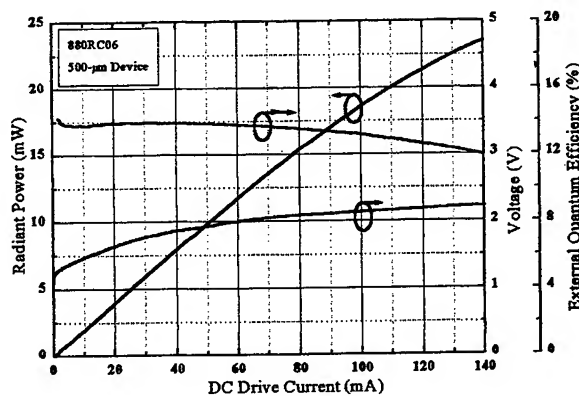


Fig. 16 Radiant power, forward voltage and external QE as a function of injected dc current for a 880 nm RCLED

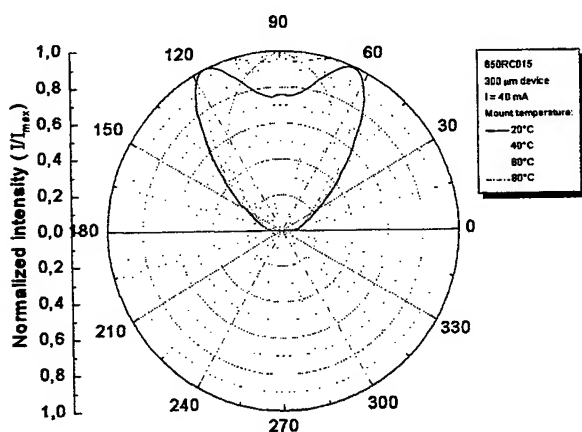


Fig. 17 Far field change with mount (ambient) temperature for a 650 nm RCLED designed with 6 nm detuning at room temperature

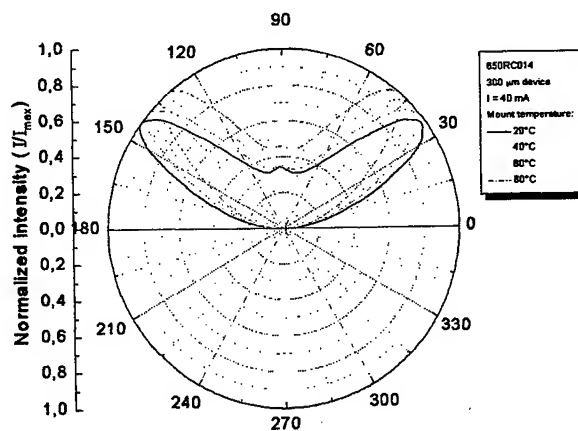


Fig. 18 Far field change with mount (ambient) temperature for a 650 nm RCLED designed with 14 nm detuning at room temperature

The temperature dependent device behavior was studied by performing measurements at various mount temperatures. The shift of the peak emission wavelength with temperature was found to be about 0.14 nm/°C for the 650 nm RCLEDs and about 0.22 nm/°C for the 880 nm RCLEDs. The angular emission pattern narrowed with increased temperature as both the emission spectrum and the cavity resonance were red-shifted. The effect of the mount (ambient) temperature increase on the far field pattern can be observed in Figs. 17 and 18. Fig. 17 shows the far field change with temperature for a 650 nm RCLED with intended 6 nm detuning for the cold device and Fig. 18 shows the far field change with temperature for a 650 nm RCLED with intended 14 nm detuning.

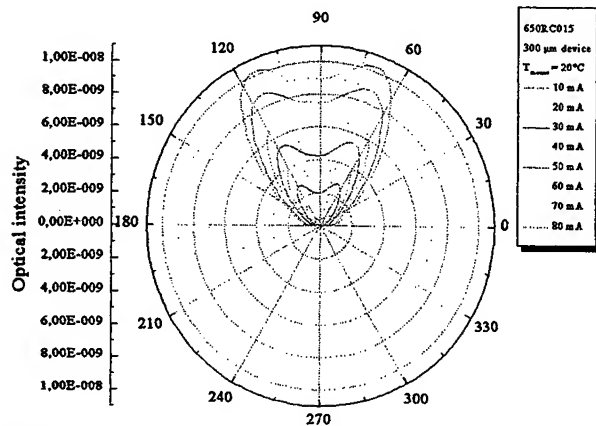


Fig. 19 Far field change with injected current for a 650 nm RCLED designed with 6 nm detuning

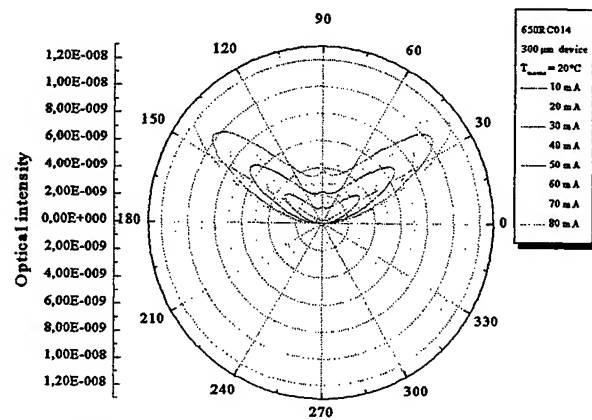


Fig. 20 Far field change with injected current for a 650 nm RCLED designed with 14 nm detuning

When the bias dependence was analyzed the angular emission pattern was more stable due to the combined effects of increased bias and associated increased temperature as can be observed in Figs. 19 and 20. Also the peak emission wavelength and the emission spectrum full width at half maximum show a relative stability with increased bias – as shown, for a 650 nm device, in Fig. 21. As a result of the temperature and bias dependencies the optimum extraction efficiency regime is achieved only at a certain bias and ambient temperature. This, together with other thermal effects, lead to the radiant power dependence on bias depicted in Fig. 22 exhibiting a clear maximum at a device-dependent injected current.

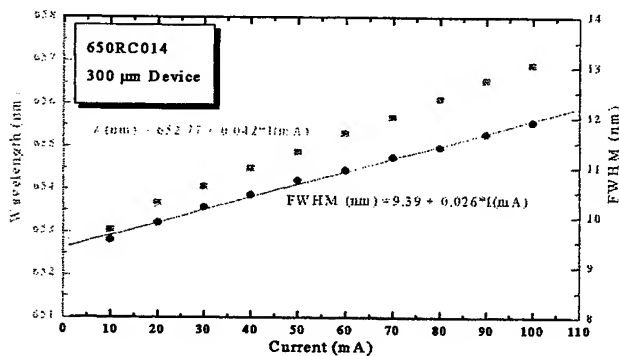


Fig. 21 Emission peak and spectrum extension dependence on injected current for a 650 nm RCLED

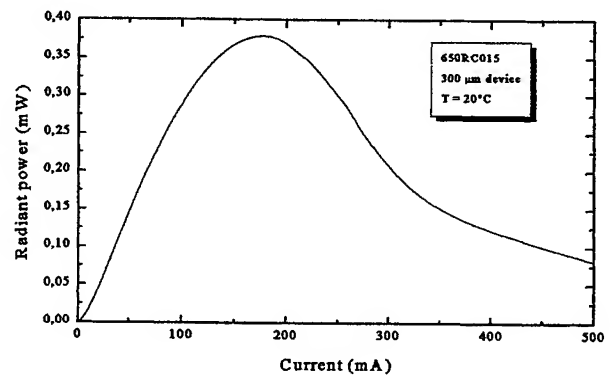


Fig. 22 Radiant power dependence on injected current exhibiting an optimum working regime

Dynamic properties have been investigated to some extent, but it is clear that much more work is needed to clarify the ultimate performance. It has turned out that RCLEDs are significantly faster than LEDs although their speed is limited by the photon recycling and by the carrier diffusion effects for large diameter devices. The measured modulation speeds for our 650 nm RCLEDs – shown in Fig. 23 – vary from 190 to 150 MHz as the device diameter is increased from 150 to 500 μm .

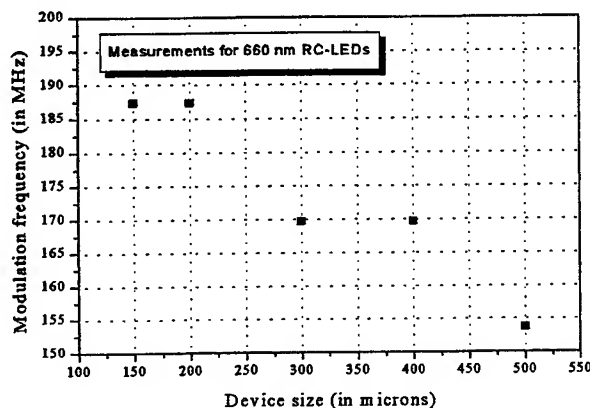


Fig. 23 Measured maximum modulation frequency

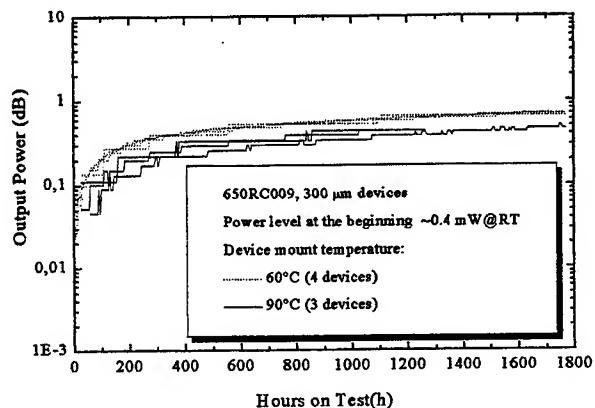


Fig. 24 Lifetest results for 7 650 nm RCLED devices

Owing to the lack of availability of SS-MBE grown RCLEDs, lifetime performance cannot have been explored previously and is only now being tackled. Fig. 24 shows the results from a group of seven 650 nm \varnothing 300 μ m RCLEDs, which have been undergoing life test for 12,600 device-hours at the time of writing. The devices are being driven under constant current at temperatures of 60 °C (4 devices) and 90 °C (3 devices) to accelerate their ageing. The power level was initially set at $P_{out} \approx 0.4$ mW at room temperature. The data shows an overall picture of no degradation. Indeed, all devices are still showing a residual trend of improvement and emitting at about 10 % higher P_{out} than they did initially. Lifetime tests over a longer period and for an increased number of devices are needed to evaluate the device lifetime since the projected lifetime calculated from the present measurements is infinite.

REFERENCES

1. M. Pessa, M. Toivonen, M. Jalonen, P. Savolainen, and A. Salokatve, "All-solid-source molecular beam epitaxy for growth of III-V compound semiconductors", *Thin Solid Films*, **306**, pp. 237-243, 1997.
2. H. Benisty, R.P. Stanley, M. Mayer, "Method of source terms for dipole emission modification in modes of arbitrary planar structures", *J. Opt. Soc. Am. A*, **15**, pp. 1192-1201, 1998.
3. K.A. Neyts, "Simulation of light emission from thin film microcavities", *J. Opt. Soc. Am.*, **15**, pp. 962-971, 1998.
4. A. Gomyo, T. Suzuki, K. Kobayashi, S. Kawata, I. Hino and T. Yuasa, "Evidence for the existence of an ordered state of Ga_{0.5}In_{0.5}P grown by metalorganic vapor phase epitaxy and its relation to band-gap energy", *Appl. Phys. Lett.*, **50**, pp. 673-675, 1987.
5. T. Tanaka, S. Minagawa, T. Kawano, and T. Kajimura, "Lasing wavelengths of index-guided AlGaInP semiconductor lasers as functions of off-angle from (100) plane of GaAs substrate", *Electron. Lett.*, **25**, pp. 905-907, 1989.
6. H. Hamada, M. Shono, S. Honda, R. Hiroshima, K. Yodoshi and T. Yamaguchi, "AlGaInP visible laser diodes grown on misoriented substrates", *IEEE J. Quantum Electron.*, **27**, pp. 1483-1490, 1991.
7. M. Jalonen, M. Toivonen, P. Savolainen, J. K ng s, and M. Pessa, "Effects of rapid thermal annealing on GaInP/AlGaInP lasers grown by all-solid source molecular beam epitaxy", *Applied Physics Letters*, **74**, no 24, pp. 479-481, 1997.
8. K. Streubel, U. Helin, V. Oskarsson, E. B cklin, and  . Johansson, "High Brightness Visible (650 nm) Resonant-Cavity Light-Emitting Diode", *IEEE Photonics Technology Letters*, **10**, no. 12, pp. 1685-1687, 1998.
9. E. F. Schubert, Y. -H. Wang, A. Y. Cho, L.-W Tu, and G. J. Zydnik, "Resonant cavity light-emitting diode", *Applied Physics Letters*, **60**, pp. 921-923, 1992.

MQW laser dynamic behavior analysis based on small signal modulation regime simulation

M. Guina^{*a}, M. Dumitrescu^a, O. Iancu^b

^aOptoelectronics Research Centre, Tampere University of Technology,
P.O. Box 692, Tampere, Finland

^bOptoelectronics Research Center, 'Politehnica' University of Bucharest
Iuliu Maniu 1-3, 77202 Bucharest, Romania

ABSTRACT

A comprehensive analysis of the small-signal direct modulation response (f_{3dB} limit), based on quantum well (QW) laser rate equations model is presented. This theoretical model is first analytically analyzed in order to estimate the influence of the phenomenological parameters taken into account on the modulation bandwidth. We show theoretically that the leakage current increases the low frequency parasitic-like roll-off effect and degrades the differential gain. Results from modulation measurements of a 5 QW AlInGaAs/InP structure are presented. The measurements are fitted with the theoretical model evaluation and the modulation response figures of merit are deduced. The modulation bandwidth limitation mechanisms are related to the extracted parameters and explained by means of carrier transport effects. Simulation results are used in order to assess the carrier capture/escape time ratio influence and leakage current influence on the modulation response.

Keywords: MQW laser, small-signal analysis, simulation, carrier transport, laser parameter extraction

1. INTRODUCTION

Quantum-well (QW) laser technology is developing towards high-speed operation improvement. The potential increase of the optical communications systems overall performance channeled a lot of effort in understanding the physical effects involved in laser dynamics. The most important processes affecting the modulation response of QW lasers are: carrier transport, photon population decay, spectral hole burning (SHB) and carrier heating.

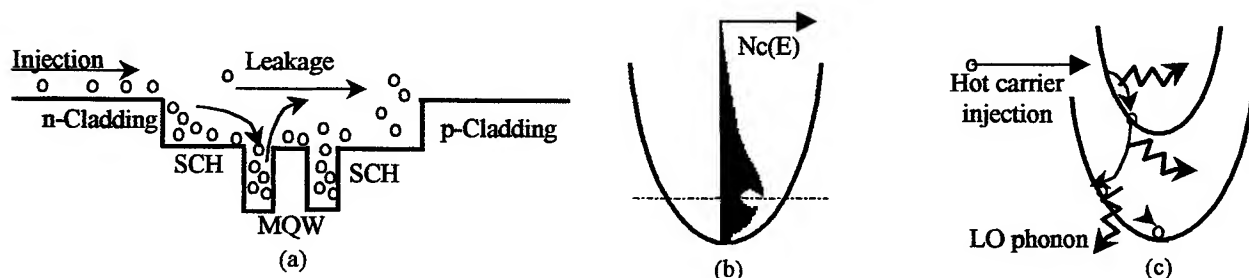


Fig. 1 (a) carrier diffusion-capture-escape times in carrier transport, (b) carrier dephasing time in SHB, and (c) carrier energy relaxation time in carrier heating

Each of these processes can be expressed by means of some phenomenological parameters like carrier drift-diffusion time in the separate confinement heterostructure (carrier transport), QW carrier capture and escape time (carrier transport), dephasing time (spectral hole burning) and carrier relaxation time (carrier heating). The differential gain and gain compression factor are other two important parameters involved in the phenomenological description of laser dynamics. First a theoretical study of the laser phenomenological parameters' effects on the small-signal response emphasizing on carrier transport influence is performed. A three-rate equation model describing the evolution of the carrier density in the quantum wells, of the carrier density in the confinement region and of the photon density is used. The well-known factors of merit that describe laser frequency response are introduced in connection with the phenomenological parameters involved in

* Correspondence: Mircea.Guina%ORC@semi.ee.tut.fi

the model. Microwave measurements for a 5 QWs AlGaInAs/InP structure are used for laser parameter extraction. Small-signal simulations using the model that takes into account transport effects and laser non-linear gain influence are realized and the results are analyzed in order to find out which are the mechanisms that degrade the modulation response.

2. THEORETICAL MODEL

Our theoretical model is based on the previously reported work of Nagarajan¹. For simplification this model takes into consideration just one carrier type and reduces the MQW to a single QW with equivalent phenomenological parameters. The laser model is described by a set of three rate equations for the carrier density in quantum-well N_w , carrier density in confinement region N_c , and photon density. The rate equations are:

$$\frac{dN_c}{dt} = \frac{I}{qV_{act}} - \frac{N_c}{\tau_c} - \frac{N_c}{\tau_{leak}} + \frac{N_w}{\tau_{esc}} \quad (1)$$

$$\frac{dN_w}{dt} = \frac{N_c}{\tau_c} - \frac{N_w}{\tau_{esc}} - \frac{N_w}{\tau_{nr}} - \frac{N_w}{\tau_n} - v_g g_0 \frac{N_w - N_0}{1 + \epsilon S} S \quad (2)$$

$$\frac{dS}{dt} = \Gamma v_g g_0 \frac{N_w - N_0}{1 + \epsilon S} S - \frac{S}{\tau_p} + \beta_{sp} \frac{N_w}{\tau_n}, \quad (3)$$

where I is the injected current into the active volume V_{act} , τ_c is the capture time in the QW, τ_{esc} is the escape time out of QW, $1/\tau_{leak}$ is carrier density reducing rate due to the leakage over SCH, τ_{nr} is the nonradiative recombination lifetime in the quantum-well active area, τ_n is the bimolecular recombination lifetime, τ_p is the photon lifetime, v_g is the optical mode velocity, g_0 is differential gain factor, ϵ is the nonlinear gain compression factor and β_{sp} is the spontaneous emission factor. Compared with other models introduced so far^{1,2,3} we take into account a new term for modeling the influence of the leakage current. The carrier transport time along the SCH is considered negligible because it was shown that for most of the structures (having not very long SCH) the carrier capture time dominates over the drift/diffusion time along the confinement region in the overall transport/capture process⁴.

2.1 Small-signal analysis

An analytical approach for the analysis of the small-signal response is presented in the following. The analysis is performed in order to relate the new terms introduced in equations (1) and (2) to the figures of merit that characterize the high-speed operation of semiconductor lasers: resonance frequency, damping factor, K factor and D factor.

In a direct current modulation scheme of semiconductor lasers, the injection current consists of a dc bias current I_0 and an ac modulation current $\Delta I = i \cdot e^{j\omega t}$, where $\omega/2\pi$ is the modulation frequency. Corresponding to this variation the carrier population density and photon density are given by: $N_c(t) = N_{c0} + n_c \cdot e^{j\omega t}$, $N_w(t) = N_{w0} + n_w \cdot e^{j\omega t}$ and $S(t) = S_0 + s \cdot e^{j\omega t}$. Following the calculation way described in literature¹ we obtained the relation between the modulating current and the optical signal including the new terms introduced in (1) and (2) for the leakage current and nonradiative recombination:

$$H(\omega) = \frac{s(\omega)}{i} = \left(\frac{\tau_{eff}}{1 + j\omega\tau_c\tau_{eff}} \right) \frac{\frac{\Gamma v_g g_0 S_0}{qV_{act}}}{\left[j\omega \left(1 + \frac{\tau_c\tau_{eff}}{1 + j\omega\tau_c\tau_{eff}} \frac{1}{\tau_{esc}} \right) + \frac{v_g g_0 S_0}{1 + \epsilon S_0} + \frac{1}{\tau_{nr}} + \frac{1}{\tau_n} \right] \left[j\omega(1 + \epsilon S_0) + \frac{\epsilon S_0}{\tau_p} \right] + \frac{1}{\tau_p} \frac{v_g g_0 S_0}{1 + \epsilon S_0}} \quad (4)$$

In the above equation the influence of the leakage factor is included within $\tau_{eff} = 1 + \frac{\tau_c}{\tau_{leak}}$. One can observe that the two factors representing the non-radiative recombination and bimolecular recombination have the same influence on $H(\omega)$. Due

to this they can be replaced by an equivalent recombination time $\frac{1}{\tau_{neff}} = \frac{1}{\tau_{nr}} + \frac{1}{\tau_n}$ and only this overall recombination time should be included in equation (2).

2.2. Small-signal modulation factors of merits

Assuming that in equation (4) we can neglect the frequency dependence in $\frac{\tau_c \tau_{eff}}{1 + j\omega \tau_c \tau_{eff}}$ and using some algebraic transformations we obtain:

$$H(\omega) = \left(\frac{\tau_{eff}}{1 + j\omega \tau_c \tau_{eff}} \right) \frac{A}{\omega_r^2 - \omega^2 + j\omega \gamma} \quad (5)$$

$$\omega_r^2 = \frac{(v_g g_0 / \chi) S_0}{\tau_p (1 + \varepsilon S_0)} \left(1 + \frac{\varepsilon}{v_g g_0 \tau_{neff}} \right) \quad (6)$$

$$\gamma = \frac{(v_g g_0 / \chi) S_0}{1 + \varepsilon S_0} + \frac{\varepsilon S_0 / \tau_p}{1 + \varepsilon S_0} + \frac{1}{\chi \tau_n}, \quad (7)$$

where a new notation was introduced by: $\chi = 1 + \frac{\tau_c \tau_{eff}}{\tau_{esc}} = 1 + \frac{\tau_c}{\tau_{esc}} \Big|_{\tau_{leak} \gg \tau_c}$. With ω_r was noted the most important figure of merit for high-speed modulation – the resonance frequency, and with γ was noted the damping factor. The damping effect depends on the resonance frequency and decreases the response peak corresponding to the resonance. The damping factor can be related to the resonance frequency by a frequency independent device parameter, the K factor:

$$\gamma = K f_r^2 + \frac{1}{\chi \tau_{neff}}; \quad K = 4\pi^2 \left(\tau_p + \frac{\varepsilon}{v_g g_0 / \chi} \right) \quad (8)$$

Another very useful relation for estimating the modulation features of semiconductor lasers relates the resonance frequency to the bias current:

$$f_r = \frac{1}{2\pi} \sqrt{\frac{\Gamma \frac{g_0}{\chi} v_g (I - I_{th})}{q V_{act}}} = D \sqrt{I - I_{th}} \quad (9)$$

A high resonance frequency and low damping factor are required in order to have a good modulation response. High resonance frequency is achieved at high photon density for lasers with high differential gain (high D) and short photon lifetime. Small non-linear gain factor and high differential gain lead to low damping of the resonance peak (small K) at a certain resonance frequency.

From these analytic expressions some effects on the modulation bandwidth are evident. It is obviously that the new factor introduced in (1) for modeling the leakage current increase the roll-off in the modulation response besides the influence due to carrier capture/escape time. The differential gain is reduced to g_0 / χ because if χ is high then the carriers are in the barrier region and not in the wells, and will not contribute to the gain. This results in the reduction of the resonance frequency for the same power levels. The gain compression factor remains unmodified so it is not dependent on carrier transport time.

A better understanding of carrier/escape time and leakage current influence on the modulation bandwidth will come from the simulation results presented in the end of the paper.

3. MEASUREMENTS RESULTS AND THEORETICAL MODEL FITTING

The modulation bandwidth of an AlGaInAs/InP laser structure⁵ was measured using the set-up and procedure previously described in literature⁶. The phenomenological laser parameters were extracted from the measurement results.

The modulation response – measured for several bias current values and normalized – is presented in Fig. 2.

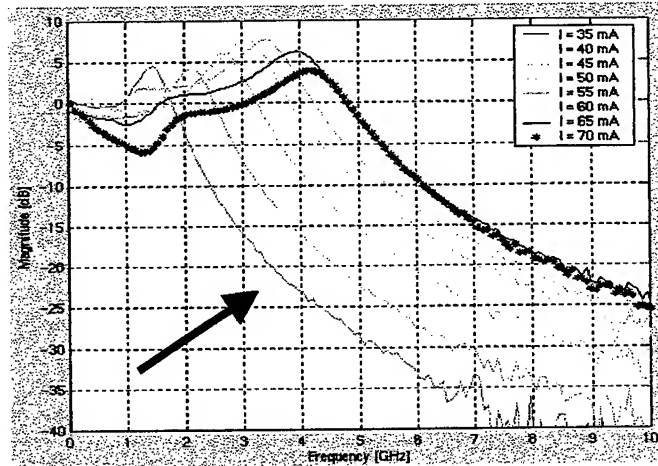


Fig. 2 Normalized transfer function at different bias current

The laser response can be accurately fitted to a transfer function containing two complex-conjugate poles corresponding to the relaxation peak and an additional parasitic-like real pole⁶:

$$\hat{H}(\omega) = \frac{\text{const.}}{(1 + j\omega\tau_{\text{par}})(\omega_r^2 - \omega^2 + j\omega\gamma)} \quad (10)$$

The f_r , γ and τ_{par} are deduced after fitting equation (10) with the measured transfer function (Table 1).

The differential gain is extracted from the $f_r^2(I)$ curve (Fig. 3). Using the relation between damping factor and resonance frequency the K factor is also deduced (Fig. 4) - $K=0.201$ ns. The gain compression factor can be easily derived from the value of K. Using this procedure we found out the values for the equivalent differential gain, $g_0/\chi = 8 \times 10^{-12} \text{ m}^2$, gain compression factor $\varepsilon = 3 \times 10^{-23} \text{ m}^3$, equivalent recombination time $\chi\tau_{\text{neff}} = 0.29 \text{ ns}$ (considering an active volume $V_{\text{act}} = 10 \times 10^{-17} \text{ m}^3$) and photon lifetime $\tau_p = 1.5 \text{ ps}$.

The parameter extraction procedure can be affected by error since at higher bias current the laser exhibits multi-mode operation causing higher roll-off at low frequency and unreliable value of the resonance frequency. Fig. 4 presents two fitting functions for the $\gamma(f_r^2)$ curve and one can see that K can be either 0.201 ns or 0.236 ns, depending on how many measured points are taken into account. Another error source is related to the value of the active volume that is not properly evaluated since this particular laser has a ridge guiding structure. The errors in the parameter extraction procedure can determine unreliable value for the differential gain and the gain compression factor.

We can relate the maximum possible intrinsic bandwidth to the K factor¹ by $f_{\text{max}} \approx 8.8 \times K$. The extracted K value gives a 44 GHz theoretical modulation bandwidth. The huge difference between the intrinsic modulation bandwidth and the measured one is mostly due to the small value of the D factor ($0.7123 \text{ GHz}/(\text{mA})^{1/2}$). Consequently the resonance frequency doesn't increase much when the bias current value increases. Analyzing the equation (9) we can explain the diminished D

value by means of reduced differential gain due to the carrier transport effects (capture/escape, leakage). The transport effects' influences on the modulation response are analyzed in the next chapter.

Tab. 1 Modulation response figures of merit extracted from measurements

I [mA]	f_r [GHz]	γ [GHz]	f_{3dB} [GHz]	$f_{3dB, par}$ [GHz]
35	1.47	4.15	2.02	1.98
40	2.18	4.48	2.97	2.47
45	2.75	4.75	3.71	2.84
50	3.13	5.52	4.19	3.11
55	3.47	5.96	4.59	3.14
60	3.79	6.65	4.98	3.29
65	3.98	7.56	5.40	4.41
70	4.27	7.70	5.57	3.55

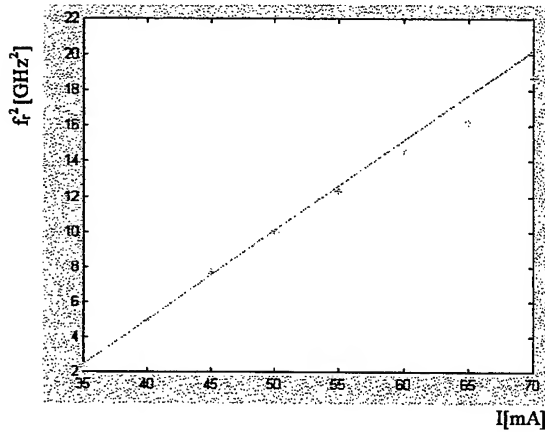


Fig. 3 Resonance frequency versus bias-current

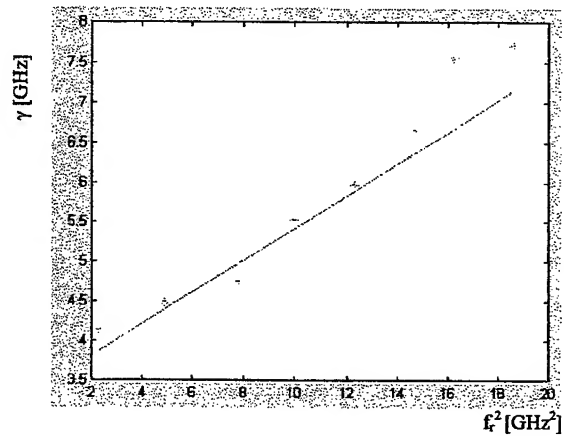


Fig 4 Damping factor versus resonace frequency

4. SIMULATION STUDY OF THE TRANSPORT EFFECTS

A simulation program based on the comprehensive three-rate equation model presented in the beginning was implemented. The simulations were performed aiming at a computer-aided analysis of the modulation bandwidth. Due to the fact that the described parameter extraction procedure cannot discriminate all the parameters (parameters like carrier capture/escape time, leakage time are included under extracted effective parameters) some of the input parameters were chosen from literature as typical MQW semiconductor laser parameters. Table 2 is presenting the values used for the input parameters.

First of all we supposed that our structure doesn't exhibit any leakage. Thus we can discriminate the effect of the capture to escape time ratio on the modulation response (Fig. 6). The observed dependence is corresponding to the theoretical analysis showing degraded response for high carrier capture to escape time ratio. This can be explained by differential gain

reduction with the factor $\chi = 1 + \frac{\tau_c}{\tau_{esc}} \bigg|_{\tau_{leak} \gg \tau_c}$. It is observed that for different capture/escape time values but same ratio the

modulation response is the same because χ has an unchanged value.

Tab. 2 Intrinsic MQW laser parameters used in simulation

Parameter	Description	Used value
V_{act}	active volume	$1 \times 10^{-17} \text{ m}^3$
Γ	optical confinement factor	0.08
τ_c	carrier capture time	1 ps - changed during simulation
τ_{esc}	carrier escape time	100 ps - changed during simulation
τ_{leak}	carrier leakage time	0.1 ns - changed during simulation
τ_{nr}	Nonradiative recombination time	0.1 ns - changed during simulation
τ_n	Bimolecular recombination time	1 ns
τ_p	Photon lifetime	1 ps
$g_0 = dg/dn$	Differential gain	$5 \times 10^{-20} \text{ m}^2$
ε	gain compression factor	$2 \times 10^{-23} \text{ m}^3$
N_0	carrier density at $g=0$	$1 \times 10^{24} \text{ m}^{-3}$
β_{sp}	Spontaneous emission factor	1×10^{-5}

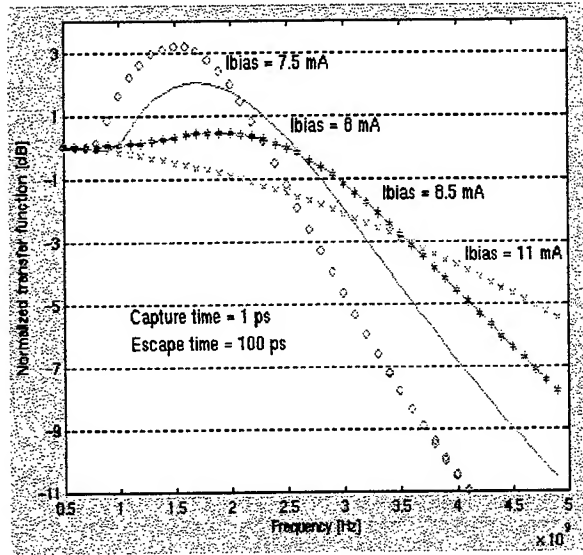


Fig. 5 Small signal direct modulation response of a MQW laser for different bias current values

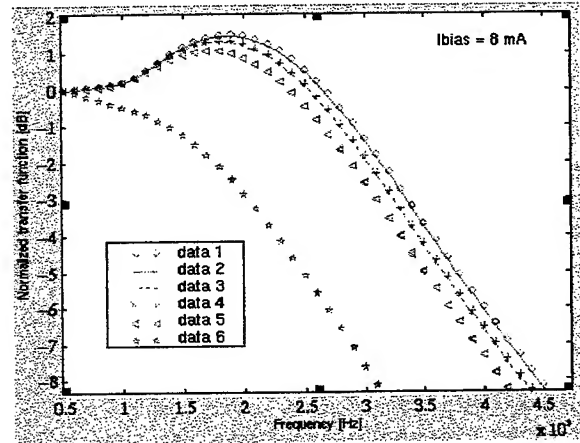


Fig. 6 Small signal direct modulation response for different values of the carrier capture time and the carrier escape time:

	data 1	data 2	data 3	data 4	data 5	data 6
τ_{cap} [ps]	1	1	1	5	10	20
τ_{esc} [ps]	500	100	20	100	100	40
τ_{cap} / τ_{esc}	0.002	0.01	0.05	0.05	0.1	0.5

In a second analysis stage we assumed that we have leakage. Considering that the modulation response is not impaired by the carrier capture/escape effects (from the last analysis we choose the carrier capture time 1 ps and carrier escape time 100 ps) we analyzed the influence of τ_{leak} on the modulation response.

The observed dependence depicted in Fig. 7 corresponds to the induced leakage influence, expressed in equation (4) by

$$\tau_{eff} = 1 + \frac{\tau_c}{\tau_{leak}}.$$

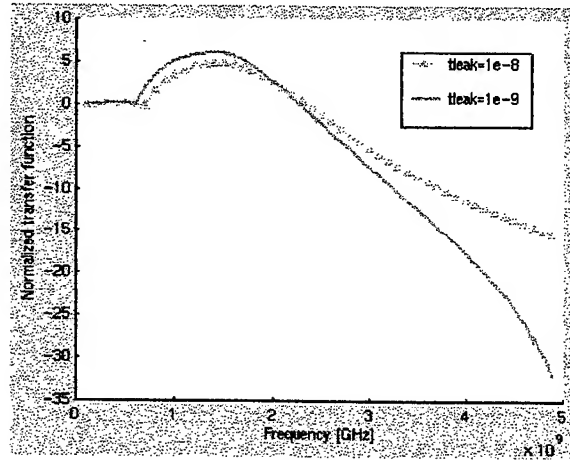


Fig. 7 Leakage influence on the modulation response

5. CONCLUSION

An improved 3-rate equation model was introduced and an analytical expression for the modulation response was deduced. Transfer function measurements and parameter extraction were performed for a 5 QWs, AlGaInAs/InP laser. The simulation results were used to assess the influence of carrier capture/escape time and leakage current on the modulation response. All simulation results are physically meaningful and in good agreement with the analytical solution and show that the carrier transport processes play an important role in the modulation response.

ACKNOWLEDGEMENTS

This work was supported, in part, by a grant from the Centre for International Mobility Finland. We want to thank to R. Schatz, O. Kjobe, and D. Soderström from Royal Institute of Technology, Laboratory of Photonics and Microwave Engineering, Sweden, for their assistance with modulation response measurement set-up and theoretical discussions.

REFERENCES

1. R. Nagarajan, "High Speed Quantum-Well Lasers and Carrier Transport Effects", *J.Q.E.*, **28**, pp.1601-1608, 1992.
2. R. Nagarajan, "Effects of Carrier Transport on Injection Efficiency and Wavelength Chirping in Quantum-Well Lasers", *IEEE J.Q.E.*, **29**, pp.1601-1608, 1993.
3. D. McDonald, "Comparison of Two- and Three- Level Rate Equations in the Modeling of Quantum-Well Lasers", *IEEE J.Q.E.*, **31**, pp. 1927-1934, 1995.
4. B. Romero and I. Esquivias, "Carrier Capture and Escape Process in InGaAs-GaAs Quantum Well Lasers", *IEEE P.T.L.*, **11**, pp. 779-781, 1999.
5. P. Savolainen, M. Toivonen, S. Orsila and M.Dumitrescu, "AlGaInAs/InP Strained-layer Quantum Well Lasers at 1.3 μm grown by Solid Source Molecular Beam Epitaxy", *Journal of Electronic Materials*
6. O.Kjobe, R.Schatz, S. Lourudoss and B. Stalnacke, "Modulation Response measurements and evaluation of MQW InGaAsP lasers of various design" *Proc. SPIE* **2684**, pp.138-152, 1996.

Magnetic field sensors utilising diluted magnetic semiconductors

A. Gh. Podoleanu^a, R.G. Cucu^{a*}, D.A. Jackson^a

^aApplied Optics Group, School of Physical Sciences, University of Kent,
Canterbury, Kent CT2 7NR, UK

ABSTRACT

We present two different AC magnetic field sensing configurations exploiting the Faraday effect in the semiconductor compound $\text{Cd}_{0.57}\text{Mn}_{0.43}\text{Te}$. The first configuration is a typical polarimetric set-up; the periodic magneto-optic polarisation rotation of a linearly polarised input in the transducer crystal is converted into intensity modulation by means of a polarisation analyser. In the second configuration, the Faraday modulation appears in the electronic spectrum of the interference signal at the output of a hybrid Mach-Zender interferometer. Both set-ups include noise rejection schemes (although different in principle and operation) to improve the signal to noise ratio.

Keywords: diluted magnetic semiconductor, Faraday sensor, common-mode noise rejection scheme, modulation, low coherence interferometry in transmission and reflection

1. INTRODUCTION

The development of optical sensors based on the Faraday magneto-optic effect is important for the power distribution industry as they offer several attractive features when compared with conventional current measuring transformers such as: immunity to both high voltages and electromagnetic interference, freedom from saturation effects, high speed response, potential for manufacturing of compact and low cost devices.

The Faraday transducers currently used range from monomode low birefringence optical fibres to various bulk materials (crystals and glasses)¹. Diluted magnetic semiconductors (DMS), also known as semimagnetic semiconductors are a new class of Faraday materials discovered and investigated since the middle of the eighties. Typical examples of DMS are the compounds $\text{Cd}_{1-x}\text{Mn}_x\text{Te}$, $\text{Hg}_{1-x}\text{Mn}_x\text{Te}$, $\text{Zn}_{1-x}\text{Mn}_x\text{Te}$, $\text{Cd}_{1-x}\text{Mn}_x\text{Se}$, $\text{Hg}_{1-x}\text{Mn}_x\text{Se}$, $\text{Cd}_{1-x-y}\text{Hg}_y\text{Mn}_x\text{Te}$ ¹⁻⁴. The prospects for extending the capabilities of Faraday sensors with the advent of diluted magnetic semiconductors are extremely good due to their high Verdet constant² (≈ 0.9 rad/mmT for $\text{Cd}_{0.55}\text{Mn}_{0.45}\text{Te}$ compared to 0.071 rad/mmT for FR-5 glass), large sensing bandwidth³ (up to 4 GHz for $\text{Cd}_{0.55}\text{Mn}_{0.45}\text{Te}$ at 633 nm), negligible dependence of the Verdet constant on temperature⁴ ($dV/dT \approx 0$ for $\text{Cd}_{0.57}\text{Mn}_{0.43}\text{Te}$), chemical and mechanical stability, compactness. Scientific investigations have been carried out to optimise the molar ratio of Mn and Hg in the DMS for maximum magneto-optic sensitivity at certain wavelengths of the incident light beam currently used in applications³: $\text{Cd}_{0.57}\text{Mn}_{0.43}\text{Te}$ at 633 nm, $\text{Cd}_{0.64}\text{Mn}_{0.36}\text{Te}$ at 670 nm, $\text{Cd}_{0.7}\text{Hg}_{0.1}\text{Mn}_{0.2}\text{Te}$ at 850 nm and $\text{Hg}_{0.6}\text{Mn}_{0.4}\text{Te}$ at 1300 nm.

The fibre optic sensors developed using DMS are extrinsic fibre optic sensors i.e. the transducer is a sensitive DMS monocrystal and monomode fibre links are used to convey the light to the sensing head. In the polarimetric sensor configuration the intensity of the linearly polarised light emerging from the input polariser varies due to the linear and circular birefringence induced in the fibre links by random environmental vibrations in the up-lead fibre. This corrupts the detected Faraday signal.

In order to reduce these perturbations, various common-mode noise rejection schemes (CMR) have been reported⁵⁻⁷. These usually need two down-leads. The polarimetric set-up we describe requires only one down-lead and contains a CMR scheme based on the creation of two replicas of the photodetector output signal and subsequent electronic processing that includes relative electronic delaying, time selection, rectification and subtraction/division. The sensor has improved performance in comparison with previously reported systems⁵⁻⁷ due to a very sensitive transducer (5 mm long $\text{Cd}_{0.57}\text{Mn}_{0.43}\text{Te}$ monocrystal)

* Correspondence: Phone: 44 1227 764000/3771; Fax: 441227827558; e-mail: R.G.Cucu@ukc.ac.uk

and due to the use of a longer single mode fibre delay line. This introduces a delay of about 100 ns which greatly relaxes the high speed requirements in the processing electronics.

In the low coherence interferometers, the output intensity noise arises from random modifications of the optical path imbalance (OPD) between the two interferometer arms due to vibrations and local thermal variations. The noise rejection in this case can be achieved by balanced detection.

2. POLARIMETRIC SYSTEM

The schematic diagram of the polarimetric set-up is shown in Fig. 1. Light from a pigtailed 1mW pulsed laser diode LD of 850 nm centre wavelength was injected into a 5 metres long single mode fibre. The output light from the fibre was passed through a linear polariser P and a non-polarising beam splitter BS to the sensing DMS crystal. The up-lead was wound around a PZT cylinder to simulate environmental vibrations that may occur in the fibre links of a remote operating device.

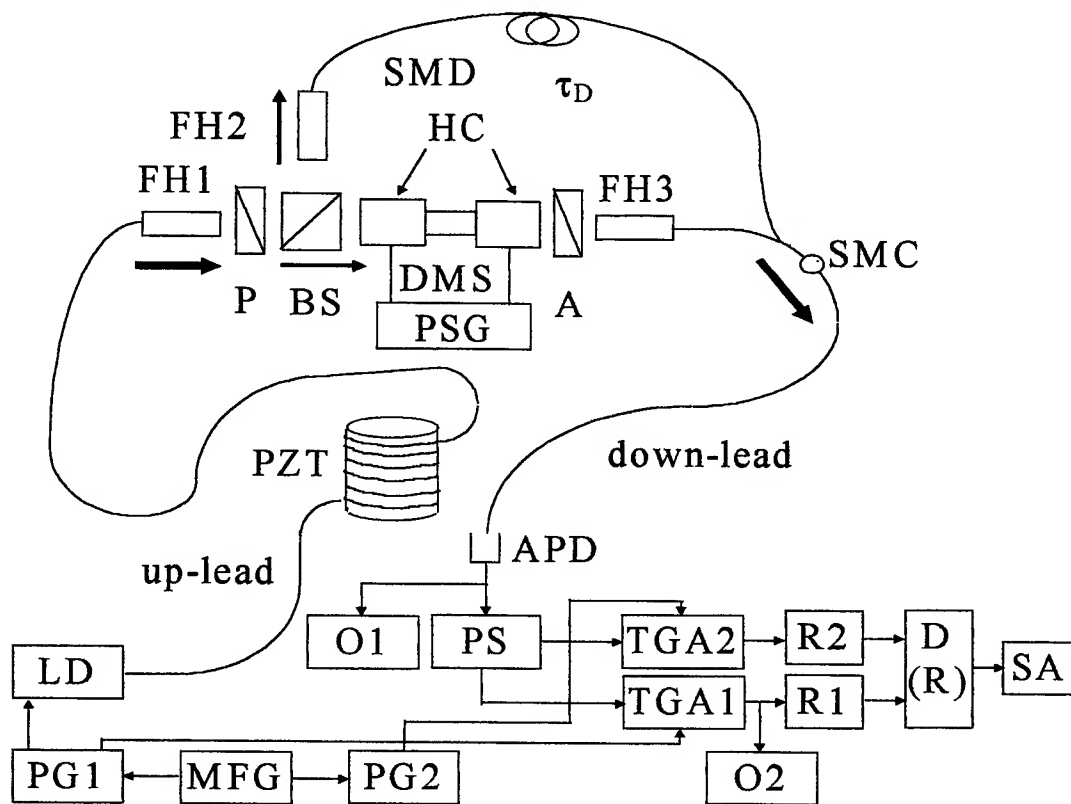


Fig.1 Experimental arrangement: LD: laser diode; PG 1,2: pulse generators; MFG: master function generator; PZT: piezo-electric cylinder; FH 1,2,3: fibre holders; BS: beam splitter; SMC: single mode coupler; HC: Helmholtz coils; DMS: sensing crystal; P: polariser; A: analyser; APD: avalanche photodiode; PS: pulse splitter; TGA1,2: time gated amplifiers; R1,2: rectifiers; O1,2: oscilloscopes; SA: spectrum analyser; D(R): divider/difference amplifier

The PZT operation induced periodic birefringence changes into the up-lead causing variations of the polarisation state at the input to P and hence intensity modulation of the linearly polarised light beam emerging from P. The laser diode was driven by 2 ns pulses with a repetition period of 190 ns. Half of the optical signal travelled through the DMS transducer placed in the middle of a pair of Helmholtz coils, HC and thus was encoded with the Faraday modulation and optical intensity noise induced by the PZT vibration (F&N). An analyser A was placed after the DMS crystal to convert the polarisation modulation into intensity modulation. The cross polarisation angle between the transmission directions of P and A was set at 45°. The other half of the optical signal carrying only the optical noise component N was injected into a single-mode fibre delay line (SMD). The delay τ_D introduced by SMD was about 115 ns. The optical signals emerging from the Faraday cell

arm and the delay line arm were injected into the input ports of a single-mode coupler, SMC. One of the output ports of the coupler was spliced to a 5 metres long single-mode fibre (the down-lead). An avalanche photodiode APD was placed at the output of the down lead. The signal detected by the APD consisted of two series of pulses of the same period. The APD output signal was divided by an electronic pulse splitter PS into two signals of equal magnitude which were processed separately in two electronic channels. The pulses encoded with the magneto-optic modulation and optical noise (F&N) from the Faraday cell arm and the pulses encoded with the optical noise component (N) from the delay line could be selected in the two channels of the electronic processing unit by applying suitably delayed TTL pulses to the inputs of the time gated amplifiers TGA 1,2 from the pulse generators PG 1,2. The master function generator MFG was used to trigger the generation of series of pulses of a given period by the pulse generators PG1,2. The pulse generator PG1 has two outputs. The signals at the two outputs could be relatively delayed by using the built-in function of the generator. The series of pulses from one output were used to drive the LD and the other output signal was applied to the TTL input of TGA1 to select the F&N pulses in the first electronic channel. PG2 has only one output which was connected to the TTL input of TGA2 to select the pulses N in the second electronic channel. The time selection was achieved by changing the period of the pulses generated by MFG and adjusting the built-in electronic delay between the two outputs of PG1. The selected pulses were rectified by rectifiers R1,2, then subtracted (divided) by a differential amplifier D (electronic ratiometer, R) to reduce the optical intensity noise.

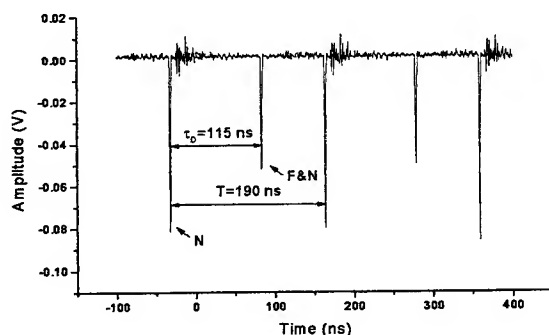


Fig. 2 Typical APD output. The two successions of pulses from the Faraday cell (F&N) and from the delay line (N) are relatively delayed by $\tau_D = 115$ ns

The two series of pulses F&N and N in the APD output signal are shown in Fig. 2 as displayed by the oscilloscope O1. The repetition time of the pulses generated by MFG is 190 ns. The time gated pulses at the outputs of TGA1 and TGA2 in the two channels of the electronic processing unit are displayed in Fig. 3.

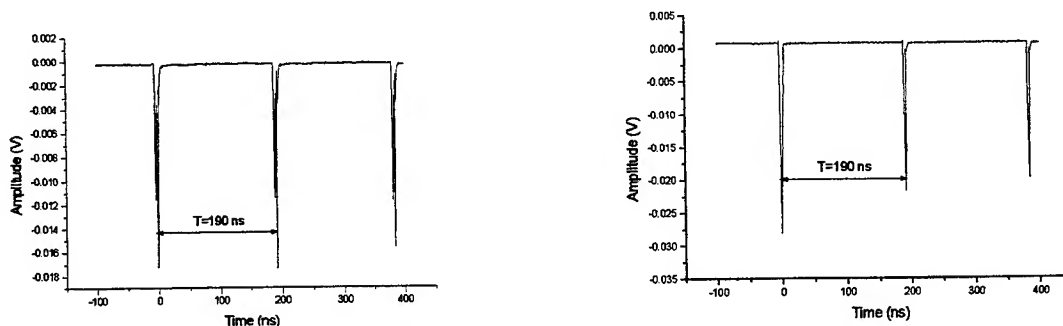


Fig. 3 Pulses selected by time gating: Faraday modulated pulses (left), delayed unmodulated pulses (right)

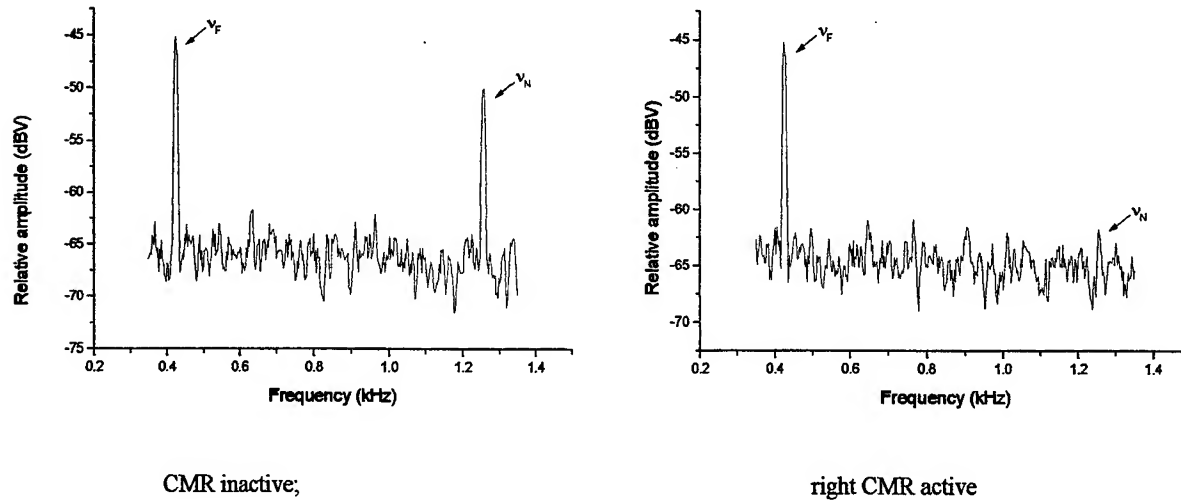


Fig. 4 Spectrum of D output for CMR by subtraction

Fig. 4 illustrates the performance of the CMR noise rejection scheme by subtraction to reject the optical induced noise in the up-lead as recorded from the electronic spectrum analyser SA with CMR active and inactive. The frequency of the applied Faraday modulation was 475 Hz. The peak at 1250 Hz is due to the harmonic PZT vibration used to simulate the vibration induced optical noise in the fibre links. The noise reduction figure relative to the white noise floor is more than 17 dBV for both CMR by division and CMR by subtraction.

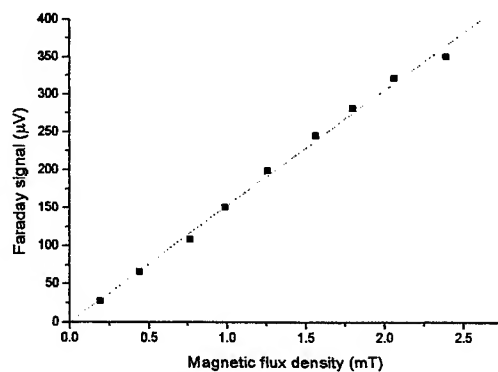


Fig. 5 System calibration curve

In practical terms, the division operation is more difficult to implement than subtraction and once implemented the mere process of division can introduce additional sources of noise and instability. The system calibration curve is plotted in Fig. 5 which shows a sensitivity of approximately 153 $\mu\text{V}/\text{mT}$. The minimum voltage which could be measured at the output was 10 μV which gives a minimum measurable signal of 0.06 mT rms. The sensitivity is dependent on the stability of the laser diode and of the APD power supply.

3. MAGNETIC FIELD MONITORING BY LOW COHERENCE INTERFEROMETRY

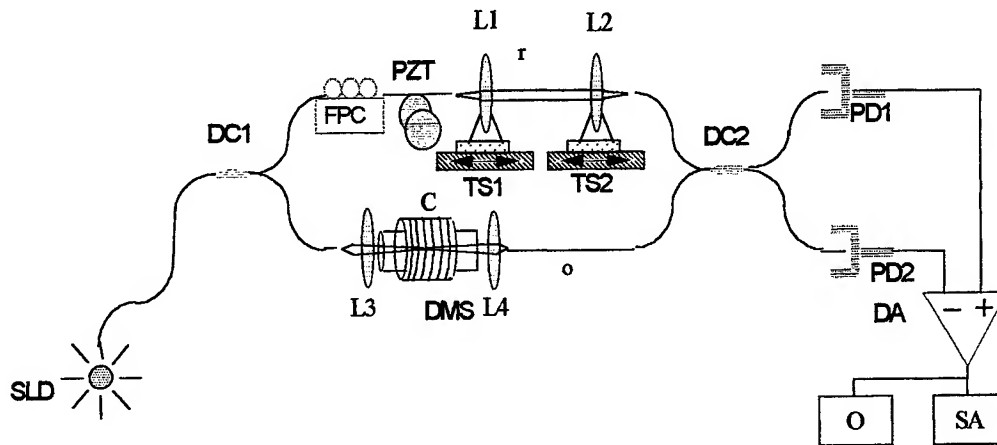


Fig. 6 The Mach-Zender interferometer used to measure the Faraday rotation; SLD: super luminescent diode, o: object arm; r: reference arm; DC 1,2: directional couplers, PZT: piezo-electric phase modulator, TS1,2: manual translation stages; DMS: transducer crystal; C: coil; L1,2,3,4: lenses; FPC: fibre polarisation controller; PD1,2: photodetectors; DA: differential amplifier; SA: electronic spectrum analyser; O: oscilloscope

As shown in Fig. 6., a hybrid Mach-Zender interferometer is used. The set-up is illuminated by a Superlum superluminescent diode SLD with a center wavelength 860 nm and 20 nm FWHM. The sensing crystal DMS was placed in the object arm o. No polarisation element was used to generate a linearly polarised input state at the transducer level. The reference arm r includes an adjustable air gap to bring the system to zero path imbalance (OPD). The length of the air gap could be modified by displacing longitudinally the two manual translation stages TS1,2. Balanced detection was used to reduce the excess photon noise⁸ due to the source and the noise caused by environmental factors (vibrations, local thermal variations) that takes the system out of coherence. The PZT vibrations in the reference arm created a carrier component at 12.8 kHz in the spectrum of the interference signal.

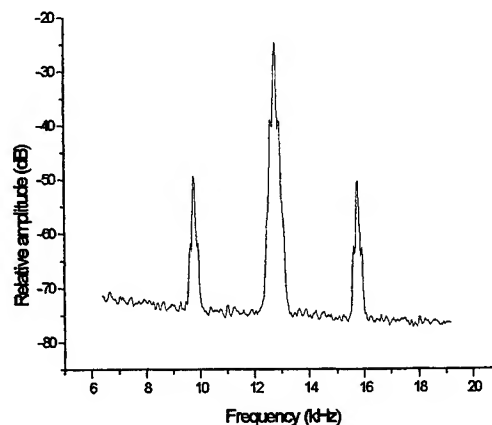


Fig. 7 Spectrum of the photodetected signal

The spectrum in Fig. 7 shows the PZT phase modulation of 12.8 kHz and the side bands due to the magnetic field applied at 3.3 kHz. Without the reference signal, both the carrier and the side bands go to zero showing that the effect appears as result of phase modulation. The Faraday modulation signal values recorded for different rms amplitudes of the applied magnetic flux density is shown in Fig. 8. The system sensitivity is approximately 145 $\mu\text{V}/\text{mT}$ rms. The minimum detectable field is 0.07 mT (very close to the sensitivity of the polarimetric system). The recording time of each point in the calibration curve was rather long as 100 average points were necessary for accurate measurement results.

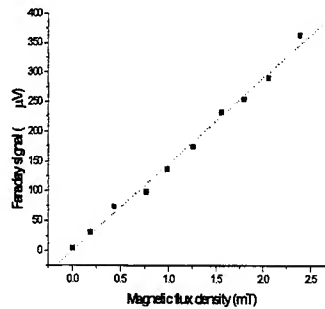


Fig. 8 Calibration curve for the magnetic field measuring system based on low coherence interferometry in transmission.

4. CONCLUSIONS

New sensor configurations are demonstrated using semimagnetic crystals. A RF techniques, using pulse modulation and time selection allows only one down-lead sensor for low cost. Low coherence interferometry is also exploited in a different configuration, which could open ways towards multiplexing of such sensors in path imbalance with possible remote interrogation.

ACKNOWLEDGEMENTS

We thank the European Commission, INCO-COPERNICUS IN15-CT96-0820 (DG12-MUYS) for financial support. We also thank the Department of Physical Electronics, Chernivtsy State University, Ukraine for supplying the DMS crystals, the General Physics Institute, Academy of Sciences of Russia for scientific collaboration and the Optoelectronics Laboratory, Radioelectronics Department, Technical University of Moldova, Chisinau for supplying the laser diode module.

REFERENCES

1. D.U. Bartolomew, J.K. Furdyna and A.K. Ramdas, "Interband Faraday rotation in diluted magnetic semiconductors: $\text{Zn}_{1-x}\text{Mn}_x\text{Te}$ and $\text{Cd}_{1-x}\text{Mn}_x\text{Te}$ ", *Physical Review B*, **34**, pp. 6943-6950, 1986.
2. P.I. Nikitin and A.I. Savchuk, "The Faraday effect in semimagnetic semiconductors", *Sov. Phys. Usp.* **33**, pp. 974-989.
3. P.I. Nikitin, A.N. Grigorenko and A.I. Savchuk, "Faraday Rotation Materials for Fiber-Optic Magnetic Field and Electric Current Sensors", *Sensors and Materials*, **4**, pp. 205-215, 1993.
4. P.I. Nikitin, A.N. Grigorenko, A.I. Savchuk, A.N. Lyakhovich and S.A. Medynski, "New Multinary Semiconductors for Faraday Rotation Magnetic Field Sensors", *Jpn. J. Appl. Phys.* **32**, Suppl 32-3, pp. 375-377, 1993.
5. Adrian Gh. Podoleanu, Norman E. Fisher and David A. Jackson, "A single fibre-optic down-lead Faraday current sensor", *Sensors and Actuators A*, **58**, pp. 225-228, 1997.
6. N.E. Fisher and D.A. Jackson, "A common-mode optical noise-rejection scheme for an extrinsic Faraday current sensor", *Meas. Sci. Technol.*, **7**, pp. 796-800, 1996.
7. N.E. Fisher and D.A. Jackson, "Vibration immunity and Ampere's circuital law for a near perfect triangular Faraday current sensor", *Meas. Sci. Technol.*, **7**, pp. 1099-1102, 1996.
8. K. Takada, "Noise in Optical Low-Coherence reflectometry", *IEEE J. Quantum. Electron.*, **34**, pp. 1098-1108, 1998.

LabVIEW remote control for a laser power/energy meter

Gabriel Ivan*, Dan Sporea

National Institute for Lasers, Plasma and Radiation Physics, Magurele,
Atomistilor St. 111, RO-76900, Romania

ABSTRACT

LabVIEW is a consistent development and execution environment that provides a method to implement various tests and measurements' systems containing stand alone laboratory instruments. This paper describes a virtual instrument created in LabVIEW that facilitates the control of a dual channel laser power/energy meter through a computer serial port, for accurate laser power/energy data logging and handling. The program has a modularity structure and could be easily used in conjunction with the device in any application involving laboratory laser power/energy measurements. The program was tested with very good results for the characterization of different types of lasers (semiconductor laser diodes, gas lasers for low level laser therapy and industrial metrology).

Keywords: virtual instrumentation, remote control, real time laser power/energy monitoring

1. INTRODUCTION

Most of the aerospace, industrial and medical applications based on laser systems or devices require at a certain point the exact knowledge of the power/energy within the experiment. For example, laser diodes used in conventional optical data-storage and -retrieval systems must have very well-known power properties: optical recording is based on focusing a certain amount of power into a diffraction limited spot, the optical power density of that spot being a factor that influence the maximum rate at which data can be recorded¹. In nonlinear optics field, frequency-doubling and -tripling efficiency in nonlinear crystals is determined by measuring second- and third-harmonic output as a function of fundamental input energy². In medical field, the heat from absorbed laser energy can cause small arteries to contract and close, the blood losses during surgery being greatly reduced³. Also in the medical field, power stability related problems that occur at devices using batteries are very critical and must be well known in order to avoid them. In the applications mentioned above, as in the majority of the laboratory experiments working with lasers, real results and correct conclusions are made possible just through a complete knowledge of the lasers' characteristics, including power and/or energy, power/energy density, their stability, etc.

Because a dedicated laboratory set-up is very complex and signals that must be acquire or simultaneously monitored could be in a large number, a complete control is difficult to made. Also, the instruments used could have proprietary software that works alone and cannot be synchronized with the rest of the experiment. An elegant solution is to integrate the whole system in a graphical interface program that accomplish a full remote control for the instruments and a real time data collection/processing. LabVIEW⁺ was design for such controls/data acquisitions and could be used to create instrument interfaces for various modern equipment's. LabVIEW programs, or VIs, are characterized by a modularity and hierarchy structure because any VI can run by itself or be used as part of another VI⁴. In this way could be design more VIs or subVIs that accomplish different tasks and could be quickly modified or combined for any experiment.

2. EXPERIMENTAL SET-UP

A simple laser power/energy measuring set-up is schematically represented in Fig. 1. An Ophir Optonics Laserstar dual channel laser power/energy meter is used to monitor the power and/or energy of various laser sources. Operating with

* Correspondence: Email: givan@ifin.nipne.ro; Telephone: +40-1-7805385 / 1817; Fax: +40-1-4231791

⁺ LabVIEW is a registered trademark of National Instruments

thermopile, pyroelectric and photodiode heads, the device could measure laser sources emitting at wavelengths from UV to far IR domain, at powers within $2\text{nW} \div 150\text{W}$ range and energies between 0.1mJ and 100J ⁵. The PD300-UV, 3A-P-CAL, F150A and PE25BB measuring heads were calibrated^{6,7} at National Physical Laboratory and Swedish National Testing and Research Institute, in the frame of the cooperation the Laser Metrology and Standardization Laboratory have with those institutions⁸⁻¹⁰.

The instrument is programmed and controlled remotely with LabVIEW through an RS-232 serial port^{11,12}. A second head could be optionally connected, so that the Laserstar can work with two heads at once. Depending on application or experimental set-up, a focusing optics and different type of filters must be used in front of the measuring heads.

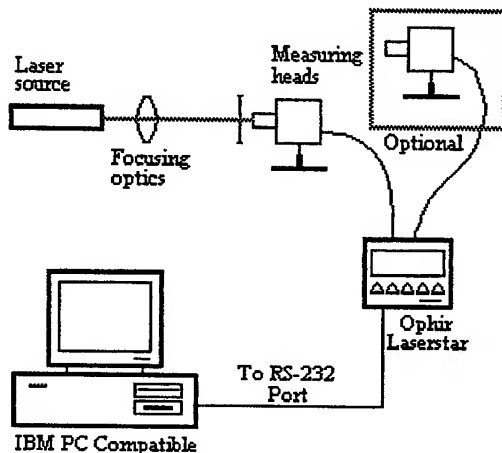


Fig. 1 An integrated laser power/energy measuring set-up

The goal in the development of this program, was to create an intuitive virtual instrument that simulates the physical device, virtual instrument that could be easily adapted practically to any laboratory laser applications. The developed program is used to configure, control and read from the laser power/energy meter, and to allow the user to analyze present or previous data regarding laser power/energy behavior.

3. USER INTERACTION AND PROGRAM EXECUTION

Before the initiation of the monitoring process the user enters the serial port number to which the laser power/energy meter is connected, as well as the baud rate utilized in the communication between computer and device. Depending on application, the user then makes the option to use a single or a dual channel configuration. If the device has two measuring heads connected, each channels could be use independent, which means that when a head measure power, the other can measure energy and viceversa. Next the user choose if the monitoring process takes place with or without data logging, in the first case being specified a data storage interval. The program could be used not only for real time laser power/energy monitoring and logging, but also for the visualization of the previously logged data. The user can make a choice in this way, before running time.

When the program is started, it initializes the RS-232 communications according to the user specifications regarding the serial port number and the baud rate. There are available different communications rates, the maximum being 38400 bps. If the initiation of the communication process failed, at runtime the program displays a dialog box with buttons that the user can use to either continue or stop the execution. When the initiation of the communication process complete successfully, the program configures the device for one of the several measuring options: power or energy on channel A, power or energy on channel B, the difference/ratio between the two channels, power on channel A and energy on channel B, or energy on channel A and power on channel B. The commands for the configurations mentioned above are transmitted to the instrument through a dedicated subVI called "Serial command" which manage the communication port

(write, read, buffer clear) for any instrument command, generate values for two error indicators, "Serial Error" and "Read Timeout", and return the instrument response to the user.

Using two push buttons, "Log to File" and "Data View", the user can set-up the program to record currently monitored data in *.txt files type respectively to view previously logged files. The data currently monitored as well as previously logged data could be view on the front panel of the virtual instrument on two different chart like displays, an eventually comparison being very easy to made. If "Log to File" button is pressed, at runtime the program asks the user to specify a file to create or replace where data must be recorded, and then begin the monitoring process. If "Data View" button is pressed, at runtime the program prompts the user for a file to open, read and display the data on the front panel then stops the execution.

When the program is running, any changes regarding the device configuration could be made through the part of the virtual interface shown in Fig. 2, which is in fact, the simulated front panel of the stand alone device. With this interface, the user can configure the power/energy meter depending on the laser or lasers involved in the experiment and can choose power or energy screens 'on the run'. Each of the five triangle buttons could be used, exclusively, for sending to the instrument "soft key" type commands.

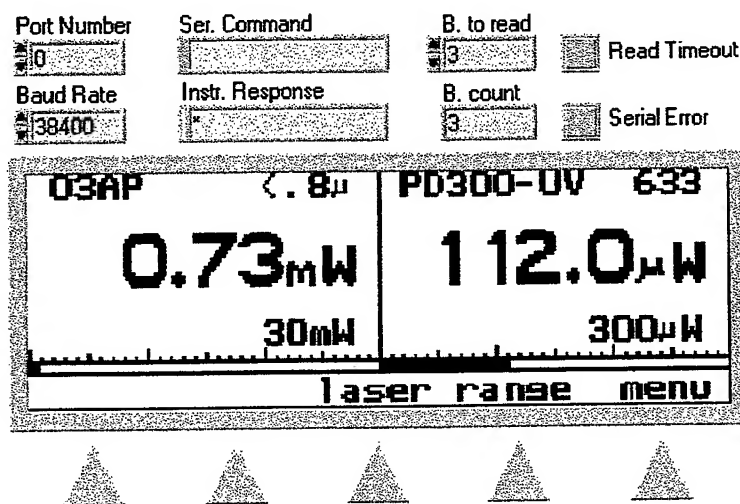


Fig. 2 Part of the virtual instrument representing the front panel of the stand alone device

For this purpose, a simple but very efficient subVI called "Serial sk-x" was build. If any of the five buttons is pressed, the specific command displayed in the menu placed at the bottom of the simulated device screen is transmitted to the instrument. A second specially design subVI, called "Serial screen-dump", working in conjunction with "Serial sk-x", proceed at an immediate update of the displayed interface. In this way, using only the virtual interface from the PC screen, the user can make a full remote control of the device. If none of the five triangle buttons is pressed but the user still wants to make a screen update, he can use the "Get Screen" button placed on the front panel of the virtual instrument.

Because the simulated interface of the stand-alone device is one of the main features of the program, in the following we focus on the way that "Serial screen-dump" subVI was build. The device LCD has 64 rows and each row has 240 pixels. One of the Laserstar command could request the image data of one row and could return the corresponding 240 pixels in groups of 4 and encoded as hexadecimal digits. In conclusion, the device returns 74 characters from which 60 encrypt the LCD row image data and 14 are used as delimiters.

When the "Serial screen-dump" is called by the main program, it initializes the serial port and then sends a command that stops the instrument writing to the display. This operation is necessary especially when the power and/or energy monitored change rapidly. In the case that LCD is updated frequently and the instrument must respond to an image data request, the encryption process would be impossible. If the initialization of the serial port or the communication with the instrument failed, at runtime the program displays a dialog box with buttons which prompt the user to either continue or stop the

execution If the freezing operation is completed successfully, the subVI send to the instrument the request for the image bitmap data of all 64 rows of the LCD. A while loop iterates 64 times and send commands, receive and convert the data until all the LCD image could be reproduce on the front panel of the virtual instrument. After the program receives first set of strings representing the encrypted image of the first LCD row, the delimiter characters are extracted, the remain 60's are converted from hexadecimal to binary representation and the process is rerun. A 'build array' function places the converted resulting data of all 64 rows in top to bottom order in this way being obtained the exact screen of the device. When the screen update is complete, the subVI send to the instrument a command that restarts the instrument writing to the display. As an example of LabVIEW graphical programming, in Fig. 3 is shown the part of the block diagram that extract the delimiter characters and convert the strings from hexadecimal to binary representation.

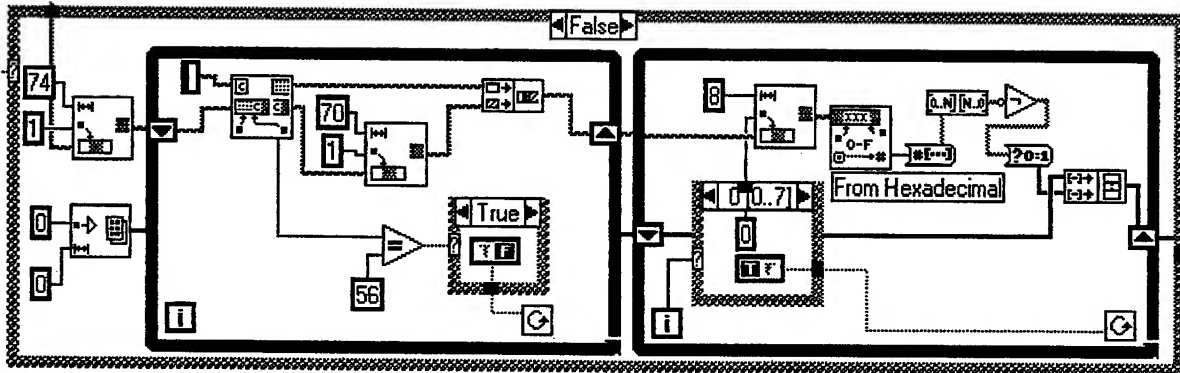


Fig. 3 Part of the "Serial screen-dump" subVI block diagram

Returning at the main virtual instrument execution, when the monitoring process takes place, the program waits until the user clicks the "Get Power/Energy" button place on the front panel. Once this is pushed, he sends the command to the device that previously was configured for a specific type of measurement. The stand-alone instrument respond to the request and begin to transmit the power and/or energy readings to the virtual instrument. The process takes place with or without data logging for a specified time interval or until the user stops the program. Other two dedicated subVI were built, "Serial p/e string-chart conversion" and "Serial log-view file", one for an intuitive interpretation of the device response and the other for an easy management of the data that must be recorded or read in/from files.

4. PROGRAM FEATURES

Ophir Optronics provides a data interface program (running in Windows) for the Laserstar instrument, but this software application does not include an interface similar to the physical instrument as in our case. Other advantages of the virtual instrument developed here are:

- a friendly user interface that allow to control and optimize a monitoring process just through mouse 'point and click' actions;
- a full access to any of the stand alone device configurations or settings;
- a modularity structure based on six specially design subVI which make our program easy to modify depending on application and which could be exported as a library to other Windows platform;
- a simultaneously graph-like visualization of the currently monitored and previously logged data;

The power or energy currently monitored is displayed in both digital and analog form at the same time. Statistical parameters like mean and standard deviation are calculated and displayed for power as well as for energy measurements. In power measurements, a second digital indicator displays the values corresponding to a logarithmic scale (dBm). Fig. 4 presents the part of the virtual interface that contain the buttons and controls mentioned in section three, and the analog/digital indicators for both channels of the instrument.

Apart from the two principal modes of operation, "Data Visualization" and "Real Time Power/Energy Monitoring", the program has a third type of running. "Terminal" mode enables the user to verify the communication between computer and instrument and to make brief tests before the beginning of any measurement procedure. The "Terminal Mode" push-like button, placed on the front panel of the virtual instrument, makes this operation mode available. A string-type control called "Command" is used for sending to the instrument one command at a time, a corresponding indicator returning to the user the instrument response.

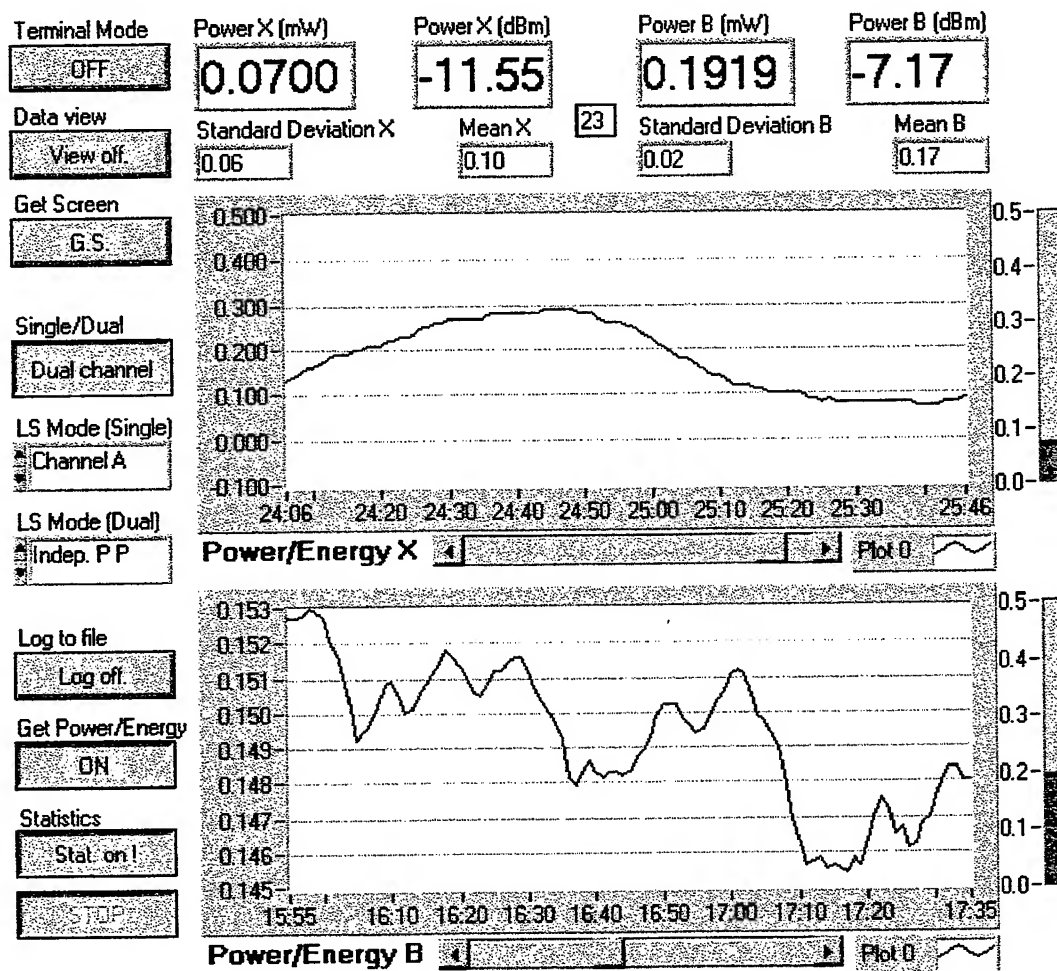


Fig. 4 The power or energy currently monitored is displayed in both digital and analog form

The data is recorded in columns by the program in ASCII text format file, and could be easily exported to spreadsheets. The program could be integrate in a more complex laboratory application and could be configure to control other devices or processes.

5. A SET-UP FOR LASER METROLOGY

In Fig. 5 is depicted a complex set-up to be used for the characterization of different types of lasers: CW lasers and pulse lasers. The main parameters to be assessed are: laser power/energy, wavelength, longitudinal mode structure, transversal mode structure, temporal pulse variation.

The set-up, as it is built, includes in fact several experimental structures, which could be combined according to practical needs. The radiation source can be a CW or a pulse operating one, emitting one or several wavelengths simultaneously

(i.e. He-Ne, He-Cd, CO₂, CW semiconductor or solid-state lasers), or can be a tunable laser (semiconductor or solid-state). The set-up accommodate also the evaluation of some semiconductor laser for optical communication use.

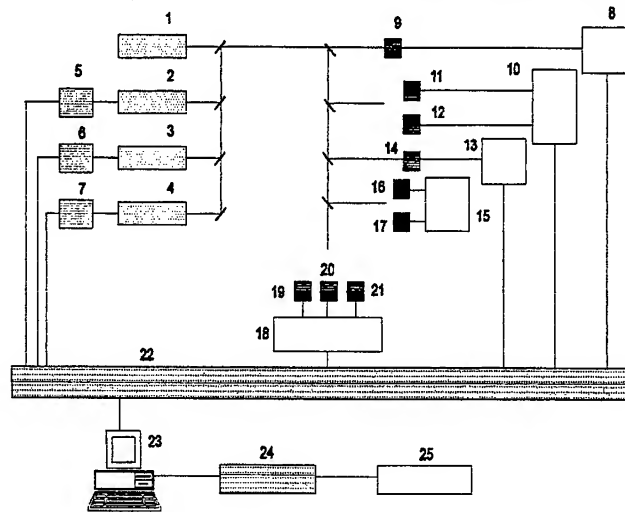


Fig. 5 1 - CW laser; 2 - pulse laser; 3 - tunable laser; 4 - semiconductor laser; 5 - triggering/synchronization system; 6 - wavelength selector; 7 - driver/controller; 8 - digital oscilloscope; 9 - fast detector; 10 - optical spectrum analyzer; 11 - low noise detector; 12 - wide-band detector; 13 - wavelength meter; 14 - detecting system; 15 - laser beam analyzer; 16 - broad-band CCD camera; 17 - pyroelectric camera; 18 - power/energy meter; 19 - Si detector; 20 - thermopile detector; 21 - pyroelectric detector; 22 - serial/GPIB interface; 23 - PC; 24 - network interface; 25 - Internet connection

To evaluate temporal characteristics of some laser products adequate detectors with special characteristics (rise time, spectral response, noise, etc.) are used, working in conjunction with a DSO, for data acquisition and processing. The DSO operation can be also remotely controlled by the PC, through special LabVIEW procedures for instrumentation (serial or GPIB, as appropriate). In order to estimate the spatial distribution of the laser power or energy for medical or industrial applications, or to evaluate the power/energy density characteristics of some components for optical communication, a laser beam analyzer is recommended. For a stand alone analyzer, special VIs for instrumentation control through a GPIB connection were developed. The most used investigations on laser systems are those related to power/energy evaluations. The LabVIEW control just described fits this niche.

ACKNOWLEDGMENTS

This work was partially supported by the European Union PHARE contract E&Y/PHASE II/C2.1.

REFERENCES

1. Donald B. Carlin, "Optical recording drives diode-laser technology", *Laser Focus World*, **28**, No. 7, pp. 77-84, 1992.
2. Jesse Buck, "Joulemeter displays pulse in laser experiments", *Laser Focus World*, **27**, No. 8, pp. 123-126, 1991.
3. Marcia W. Patchan, "Medical applications call for selectivity in laser performance", *Laser Focus World*, **27**, No. 4, pp. 85-104, 1991.
4. *LabVIEW User Manual*, National Instruments Corporation, Austin, 1996.
5. *Laser power/energy monitor user manual*, Ophir Optronics Ltd., Jerusalem, 1997.
6. Burt Mooney and Carrie O'Connor, "NIST traceability ensures power-meter accuracy", *Laser Focus World*, **35**, No. 6, pp. 121-128, 1999.
7. Michael Barret, "Calibration ensures detector accuracy", *Laser Focus World*, Vol. 33, No. 9, pp. 129-134, 1997.
8. SP Swedish National Testing and Research Institute, Calibration Certificate 01-F98937/1998.
9. National Physical Laboratory, Calibration Certificate EU0204/1999.
10. National Physical Laboratory, Calibration Certificate EU0207/1999.
11. *LabVIEW Instrument I/O VI Reference Manual*, National Instruments Corporation, Austin, 1996.
12. *StarCom for Windows and RS232 Data Interface*, Ophir Optronics Ltd., Jerusalem, 1997.

Multi-configuration optical system, with applications in night vision devices

Marinica Mirzu^{*a}, George Copot^b

^aMilitary Equipment and Technology Research Agency, PO Bragadiru, Bucharest

^bInstitute of Optoelectronics, Bucharest-Magurele, PO BOX MG-22, 76900

ABSTRACT

In optical design applications for night vision systems they are situations when an optical system have to work in multiple configurations. This paper speak about such a situation when an eyepiece have to combine the image from the image intensifier screen with the image of the symbology needed for gun aiming. We use the Multi-Config Zemax facility, with the accent on the necessary operations and delicate points of the optical design process. We present some results for a real situation.

Keywords: night vision, optical system, image intensifier tube (IIT), optical design, merit function, multi-configuration, optimization, tolerances, RMS spot, MTF.

1. INTRODUCTION

Generally speaking, in night vision sights appears the necessity to inject some informations and symbology in the field of view. If these are optically injected in the eyepiece, then the eyepiece have to be designed to work in the same time for two, three or more different configurations, for different fields and wavelengths. Also, the optimization process for the eyepiece optical system have to take in account the necessity to correlate the parameters for all the configurations, in such a way that all the technical specifications to be meet, in efficient conditions of price-quality.

For this purpose we used the Multi-Config facility of the Zemax optical design program, on the base of a correct constructed merit function. This Zemax capability is used for defining, analyzing and optimizing optical system that are used in multiple configurations¹. Multi-configurations are used to design zoom lenses, or to optimize lenses tested and used at different wavelengths, or optical systems used in various configurations, to name a few¹. However, it requires a little more care and practice to become proficient.

2. WORK CONDITIONS AND SYSTEM OPTIMIZATION

Let's be our problem to design an eyepiece system for night vision sights, that work in three different configurations (Fig. 1): one direct way A, for the observation of the target from the image intensifier screen, and one way B, with other two different ways, in two different wavelengths and fields, for the observation of the symbology used for aiming. For all these configurations we have: EFFL of the eyepiece (f' , in mm), exit pupil diameter of the eyepiece (d , in mm), exit pupil position of the eyepiece (z , in mm). For A way, we have: image field w_1 (mm), image field radius of curvature (r_{IIT} , in mm), wavelength (λ_1 , in nm). For B way, we have: image fields (w_2 and w_3 , in mm), image fields radius of curvature (r_{grat} , in mm), wavelengths (λ_1 and λ_2 , in nm). Also, there are some more configurations for each diopter adjustment position between -4 and +4 Dpt. At the end, we have 14 different configurations to optimize.

The first step is to define the configurations. It is a good idea to start with the most complex configuration first. In our case, the basic configuration is the way A, at 0 Dpt¹.

Once we have the basic configuration defined, it is time to define the rest of the configurations that are variations of the first. The first configuration does no need to be optimized yet; we will optimize across configurations later.

* Correspondence: E-mail: acttm@icda.mta.ro; Telephone/fax: 004014233052

Because the system is intended to be use in a night vision device, after an initial optimization process based on the RMS spot criteria, we will use a MTF based merit function, especially for the direct way A². It is very important to well define the merit function and the variables. Also, it is important to keep the same parameters values for different diopter adjustment positions, using pick-up facility.

The optical system will be oriented to the desired target if the merit function is well build and if the designer takes the control during the optimization process.

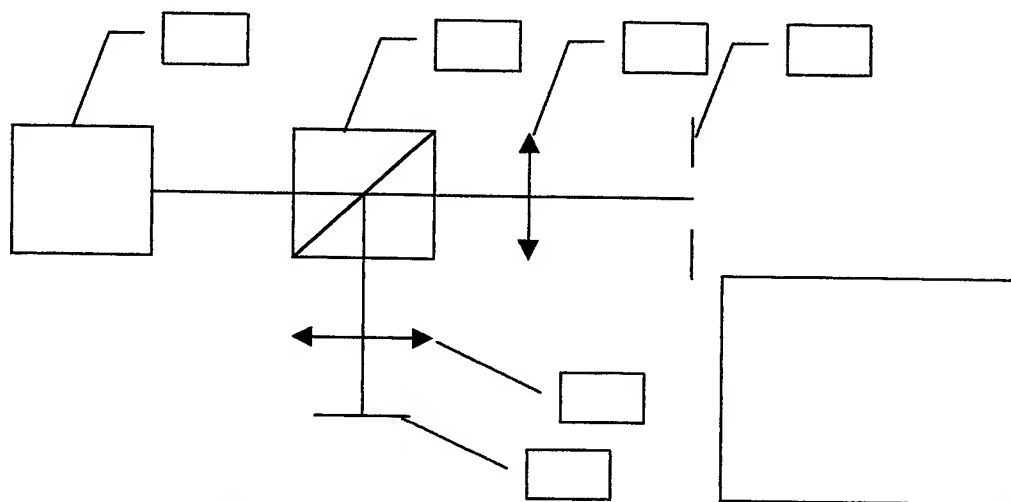


Fig.1 Eyepiece system with three configurations

3. RESULTS

In the earlier presented conditions, for $f'=30\text{mm}$, $d=10\text{mm}$, $z=30\text{mm}$, $r_{\text{III}}=40\text{mm}$, $w_1=17.5\text{mm}$, $w_2=6.5\text{mm}$, $w_3=7.5\text{mm}$, $r_{\text{grat}}=\text{infinity}$, $\lambda_1=500\text{...}590\text{nm}$, $\lambda_2=550\text{nm}$, $\lambda_3=655\text{nm}$, we have obtained the configurations from Figs. 2 and 3. There is a common portion of the system (first five lenses), moveable for diopter adjustment, and a variable portion, different for each of three basic configurations (the beamsplitter and the last lens). Only two types of glass were used for lenses: SK5 and SF4. The beamsplitter glass type is BK7.

The optimization process was based on the RMS spot criteria, along the entire 14 configuration in the same time.

The most important image quality indicators (MTF, Spot Diagram, Encircled Energy Diagram), obtained after the optimization, for the A and B configurations at 0 Dpt, are presented in Figs. 4, 5, 6, 7, 8 and 9.

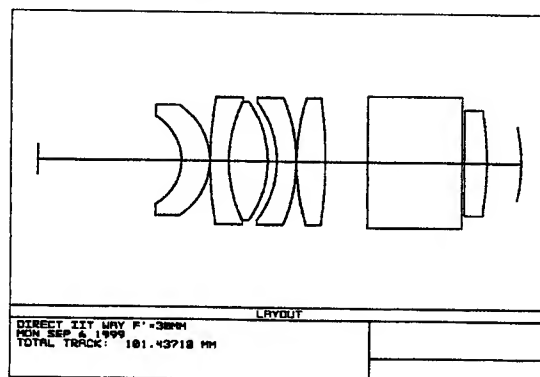


Fig.2 Direct IIT way configuration

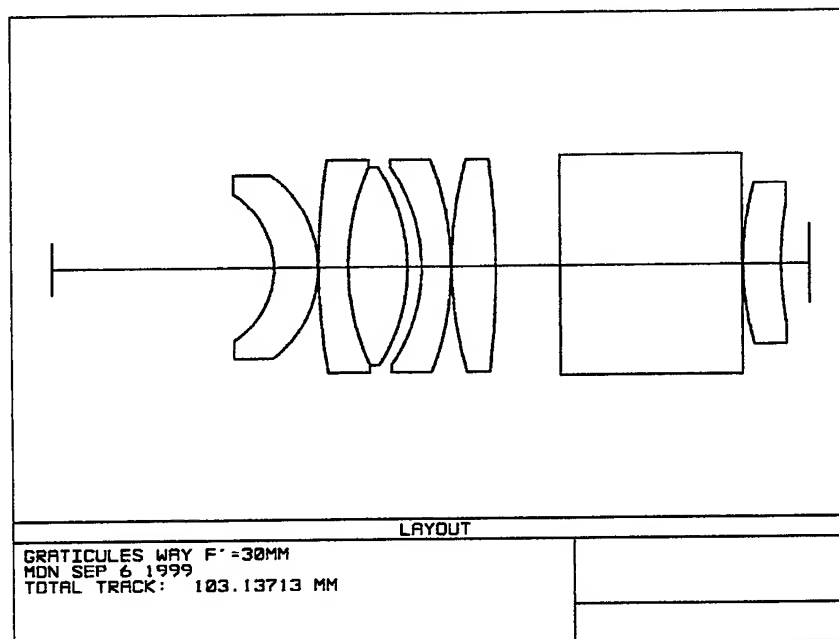


Fig.3 Graticules way configuration

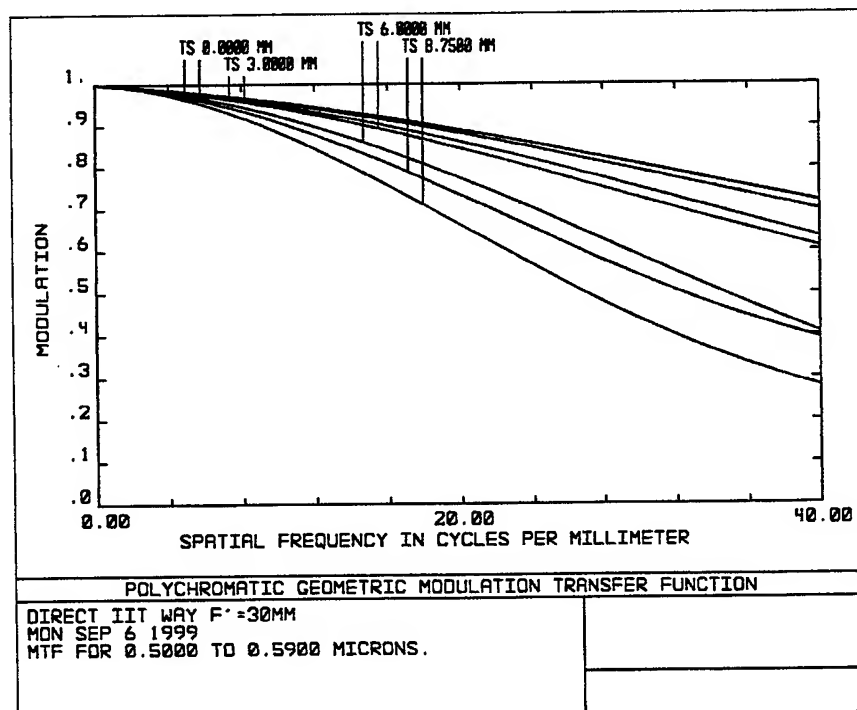


Fig. 4 Polychromatic MTF for direct IIT way configuration

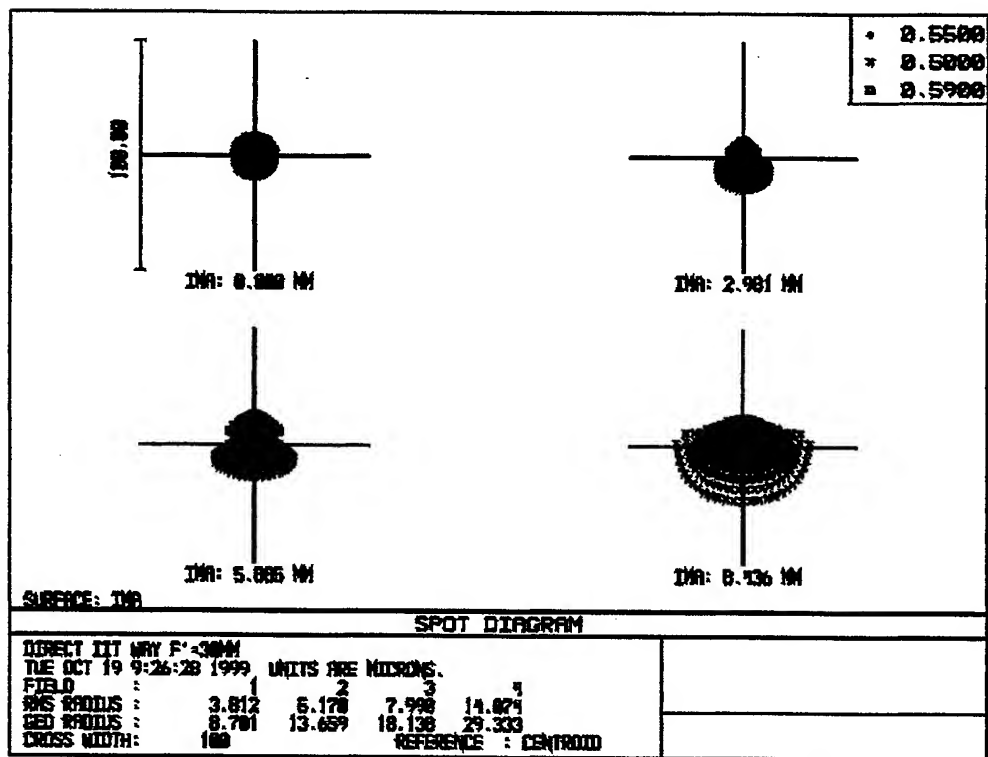


Fig.5 RMS Spot radius for direct IIT way configuration

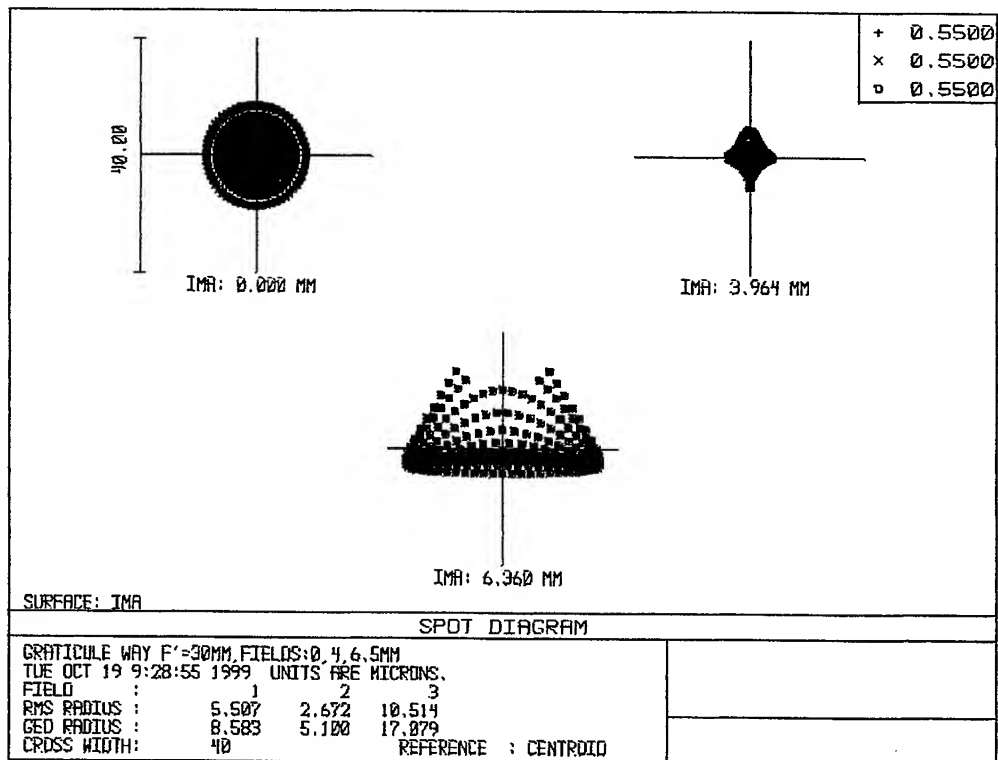


Fig.6 RMS spot radius for graticule way configuration

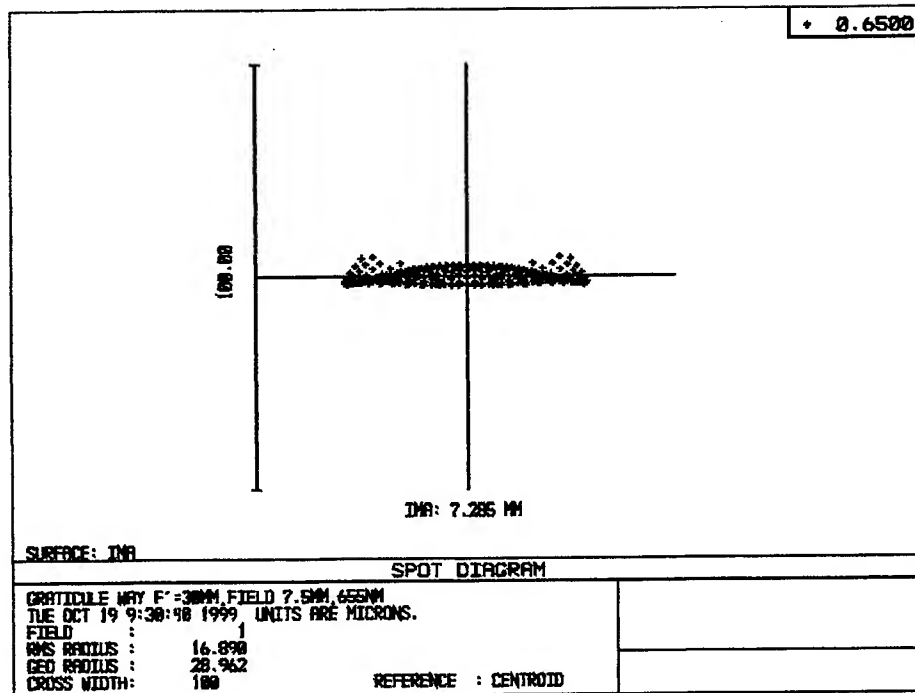


Fig.7 RMS spot radius for graticule way configuration. 8mm field and 655nm

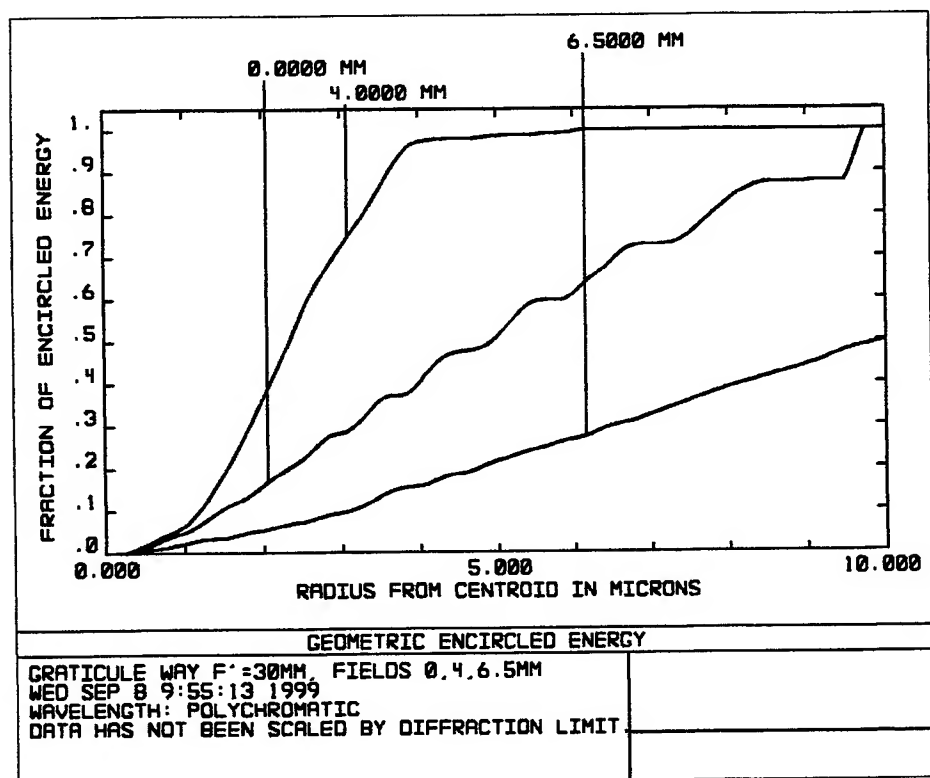


Fig.8 Fraction of encircled energy for graticule way configuration

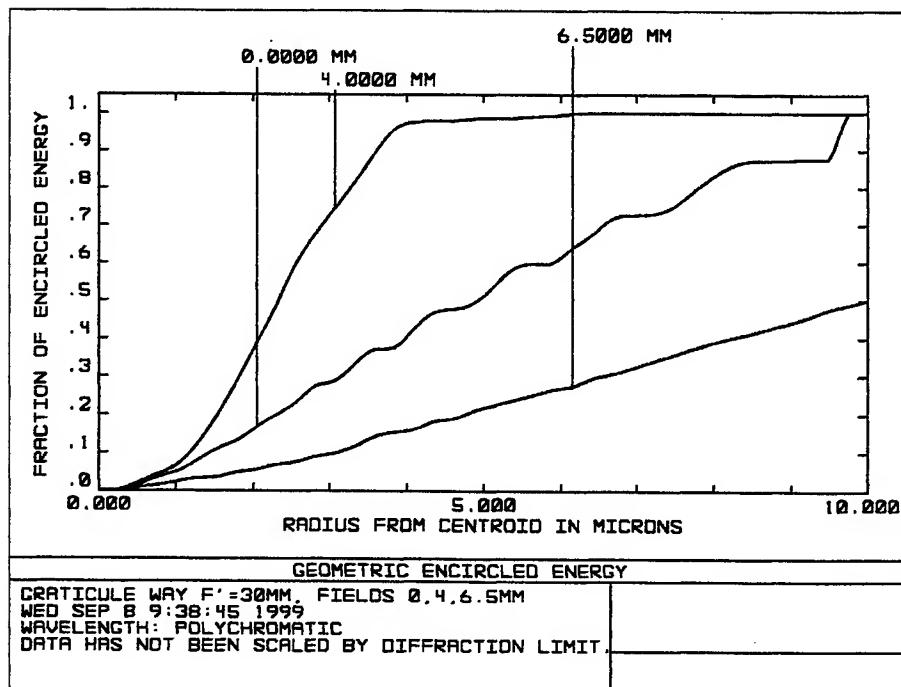


Fig.9 Fraction of encircled energy for graticule way configuration. 8mm field and 655nm

4. CONCLUSIONS

The multi-configuration optical systems can be designed using the Multi-Config Zemax program facility. The attention of the designer have to be concentrated to establish correctly the configurations, to well define the merit function and the variable parameters for optimization and to correlate the system characteristics over all the configurations in such a way that the final system to correspond for its destination.

REFERENCES

1. Zemax Optical Design Program, User's guide.
2. Mirzu M. and Necsoiu T., *Metode moderne ale opticii pentru calculul sistemelor optoelectronice de vedere pe timp de noapte*, Ed. Inst. de Optoelectronica, Buc., 1998.

Some aspects concerning optically powered intelligent sensors

Monica-Anca Chita^{*a}, Sorin Anghel^b, Ion Iorga-Siman^b

^a University of Pitesti, Electronic Department, Street Targul din Vale, No. 1, Pitesti, 0300

^b University of Pitesti, Physics Department, Street Targul din Vale, No. 1, Pitesti, 0300

ABSTRACT

This paper investigates the feasibility of using of an optically power sensor head as part of an intelligent sensor by means of a model realised using MSI (medium-scale integration) CMOS integrated circuits, with a view to a future ASIC (application-specific integrated circuit) version. Measurements was made under control of commands transmitted along the optical power line and digital data returned. This was achieved with an electrical power at the sensor head of less than 100 μ W, enabling the system to operate with an optical power of 1 mW.

Keywords: Intelligent sensors, optical fiber sensors, medium-scale integration (MSI), optical power, sensor head.

1. INTRODUCTION

The modern instrumentation intelligence and the technological possibilities offered by the microelectronics development have contributed to the appearance of the intelligent sensor concept. An intelligent sensor mainly corresponds of the integration in his body of an internal calculation unit (microprocessor, controller), a signal conditioning system (programmable or controlled) and a communication interface⁷. Therefore the intelligent sensors are devices capable to detect, measure, transform, date and process the collected data with a view of them communication to other units of the system in which they are integrated. In recent years intelligent sensors have developed from an academic idea into practical and powerful devices and in this way concepts such as reconfiguration allow them to be self testing and auto-calibrating¹, thereby overcoming the reliability problems associated with complexity.

Optical fiber sensor are not longer a subject for laboratory research only, but a very attractive solution for different industrial applications, because of their advantages: small size, immunity to interference from electrical and magnetic fields, total safety in explosive environments, chemical inertness, intrinsic galvanic isolation. The general structure of an optical fiber sensor is presented in Fig. 1.

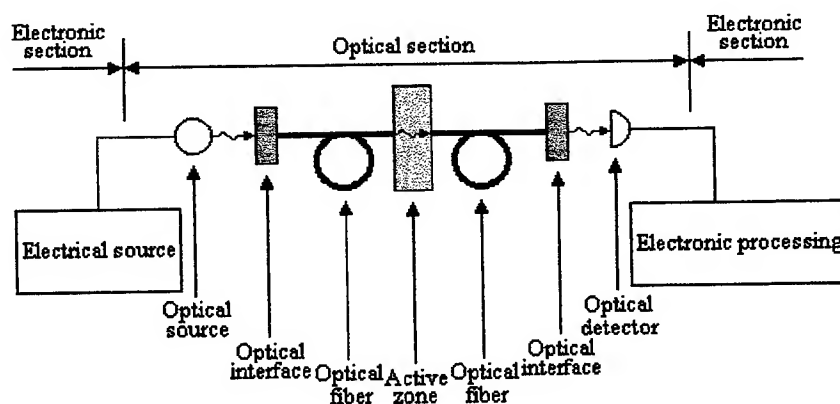


Fig. 1 The general structure of an optical fiber sensor

* Correspondence: E-mail: monica @electra.upit.ro; Telephone: 00 40 48 222949; Fax: 00 40 48 216448

One can delimit two sections: the optical section, where the measurand produces the variation or modulation of one of the light parameters and the electronic section, where the optical modulated signal is converted to an electrical signal which may be further electronically processed. There is an active zone in the optical section on which the size of measuring will act, creating changes of propagation the light radiation. The active zone may be a section of the optical fiber or other optical medium outside the fiber. That is why one prefers the name of "optical fiber sensors" to other variants as "optical sensors" or "sensors of optical fibers".

Thus the optical fiber sensors are useful where is an intrinsic safety requirement, where electromagnetic interference is rife or where is need to operate at an elevated electrical potential. If intelligence is to be provided, at least some sort of electrical subsystem must be at a sensor head and power must be supplied to it.

Hybrid optical fibre sensors in which power is supply optically to power a sensor, which then returns an optical signal, have been proposed as a method of overcoming the limitations of the all optical fibre sensors and enable the advantages of well - established, conventional sensor types to be combined with the advantages of galvanic isolation derived from the use of optical fibres². Some of these schemes have used an electrically excited sensor to act directly as a light modulator, but more usually the electrical power has been used to excite the sensor, make the measurement using conventional electronic technique and then convert the data back to a modulated optical signal. The sensor concept described here uses this latter approach, but extends the function of the sensor head to permit other operations to be performed to enable calibration or compensation of the sensor under the control of a sub-controller at the other end of the optical link.

2. OVERVIEW OF THE OVERALL SYSTEM CONCEPTS

While it is possible to deliver several watts of optical power down an optical fiber, in practice it is generally desirable to limit the power to a much lower level. This is certainly true if the system is to be used where there is risk of an explosive or flammable atmosphere. Laser sources capable of supplying a power of the order of 1 W continuously, but are very expensive, while lower-power laser-diode sources that produce 1-20 mW are very much cheaper. The efficiency with which optical power may be converted to electrical power is typically about 10 %, so that a realistic figure for the electrical power available for the sensor is less than 1 mW.

For an optically power sensor, the limited electrical power available severely restricts the scope for providing significant processing power at the sensor head. It has been demonstrated that a low-power microcontroller may be operated using power supplied optically, but the power required is very much greater than considered here. The alternative approach is to modify the intelligent sensor concept somewhat and to separate the sensor from the microcontroller which performs the intelligent control functions, the two parts of the system being linked by optical fibers to supply power and provide bidirectional data communications between the controller and the sensor head, this being illustrated in Fig.2.

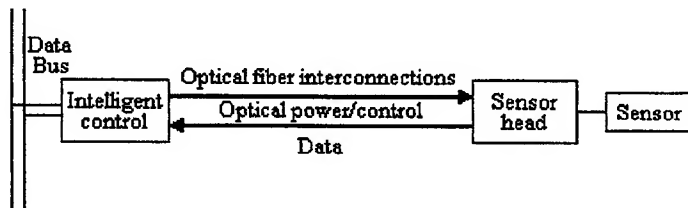


Fig. 2 An optically powered sensor system

As shown in Fig. 2, a single sensor is connected to its power source and controllers using two optical fibers, one to carry power and control data to the sensor head and a second fiber to return the data. While in principle the two functions could use bidirectional transmission down a single fiber, the added complexity and cost associated with the bidirectional optical couplers and the need avoid cross-talk would not be justified in view of the relatively small cost of a second fiber. The data communications to the sensor head are easily multiplexed with the power delivery. Although in Fig. 2 only one sensor is shown associated with the sensor head, in practice several sensors may be multiplexed onto the fiber data link. This may be required to provide compensation to correct for across-sensitivities of the sensor (s), e.g. temperature compensation.

Intelligent controller to perform measurement, calibration or testing routines may control the configuration of the sensors and their sampling sequence.

A key question is whether to return data from the sensor head in analogue or digital format. Analogue transmission can be achieved with good power efficiency by using pulse modulation, using the time separation of two short pulses to represent the analogue data. By using pulses that are short compared with the time separation of the pulse pair, and short compared with the time between data samples, the mean power required for data transmission can be kept very small. Digital transmission of the data requires the transmission of more pulses, but again they may be of short duration. In practice the power required for digital data transmission may be much less than the needed for making the measurement. The main overhead associated with digital data transmission, as far as the power consumption is concerned, is the analog-to-digital conversion. However, CMOS successive approximation converters using balancing techniques are able to provide good performance with low consumption and have the merit of providing serial data in a ready form for transmission.

The decision whether to adopt analogue or digital data transmission is not clear-cut. Either form of data transmission could provide a satisfactory solution. In the event, digital transmission has been chosen for the demonstrator since it avoids degradation of the signal by noise during transmission and it minimizes the need for analogue signal processing in the sensor head. Suitable micropower ADCs are readily available.

3. THE DEMONSTRATOR SYSTEM

As discussed previously, bidirectional transmission of power and data analog a single fiber is generally undesirable. Hence it is proposed that two optical fibers should be used: one to transmit power and data to the sensor head, and one to return the data. Data may easily be encoded onto the optical power line with little loss of power transfer. If a photocell array is used as the power converter, then the power supply may be modulated either with pulses of increased power superimposed on the optical power supply, or, more practically, as short notches of decreased power. If the single photocell with power converter is chosen as the power conversion system, the optical power supply must be chopped. In this case the easiest way to superimpose control data is to modulate the chopping frequency.

The optical power delivered to the sensor head must be converted to electrical power using a photovoltaic diode, or an array of such diodes. The light should have a wavelength in the near infrared region (800-1000 nm) to ensure that the loss in the optical fibers is small. This range of wavelengths permits the use of Si or GaAs photovoltaic cells that have an efficiency of about 10-20 %. The terminal voltage for a Si photovoltaic cell is about 0.4-0.5 V when the cell is producing maximum power; for a GaAs cell it is about 0.6 V. The voltage from a single cell is too small to be of direct use to power an electronic circuit, so it is therefore necessary to use some either an array of cells in series, or some form of up-conversion.

The use of photovoltaic arrays for powering sensors has been described by a number of authors^{3, 4}. This approach has the advantage of simplicity, but needs a suitable array of small-area diodes, electrically connected in series. A disadvantage is that the current is limited by the photodiode with the smallest output, either due to its low efficiency or unequal distribution of illumination⁵. The alternative approach is to use a single photodiode and an electronic power converter to step up the voltage. The use of a converter leads to some decrease in overall efficiency, but no more than is incurred in diode arrays. The principle disadvantage of using a d.c.-d.c. power converter is that it requires an inductance or transformer, which is relatively bulky and in the event of a fault may present an increased hazard if the system is to be used in a flammable or explosive atmosphere.

The demonstrator system⁶ uses a single photocell and power converter; hence, digital commands are transmitted to the sensor head by modulating the chopping frequency of the power supply. Doubling the period while maintaining the duty ratio modulates the frequency. Each data bit lasts for one cycle of the power modulation. A lengthened cycle corresponds to a '1', while a normal-length cycle corresponds to a '0'. The control data are transmitted as a serial word with one start bit and three data bits. Longer words could of course be used, but initially it was felt that eight codes would be sufficient for simple control. The change of period has only a small effect on the efficiency of the power conversion.

The modulation of the optical sources is picked off from the power converter and is converted to a logic signal, which is monitored to detect and decode the data transmitted to the sensor head. The mark-to-space ratio of the modulation is about 9:1. With a peak optical power of 2 mW delivered to the photodiode, the electrical power is about 160 μ W after conversion

to 2.5 V. The signal is demodulated using a very simple period detection circuit, which is based, upon charging a capacitor while the optical power is on and discharging the capacitor while it is off. When the period is long the capacitor charges above a preset level and a '1' is registered. When the first '1' is detected, it and the next three bits are stored in a shift register. When the shift register is full the sequence required by command is implemented. The modulation signal is also used as an internal clock, with a nominal frequency of 2 kHz, for controlling the operation of the sensor head.

The data are transmitted back to the controller as a serial data stream. The key requirement is that the data must be sent in a form that keeps the total power required within the available power budget. The power necessary to drive an LED is about 20 mW (2 V at 10 mA); thus it is necessary to use a pulse-encoded modulation that requires a small duty ratio in order to bring the mean power consumption down to a few microwatts. This could be achieved using analogue encoding with the separation of the two short pulses to encode the data. This is probably the most energy-efficient method. However, analogue data transmission is always vulnerable to degradation, so there is considerable advantage in transmitting the data in digital form where possible. Digital data must again be sent as a train of short pulses with a low duty ratio. The data may be encoding using either a simple scheme in which the presence of a pulse represents a '1' and the absence a '0', or if greater checking of data validity is required, a pulse position modulation scheme might be preferred.

A simplified schematic diagram of the demonstrator system⁶ is shown in Fig. 3.

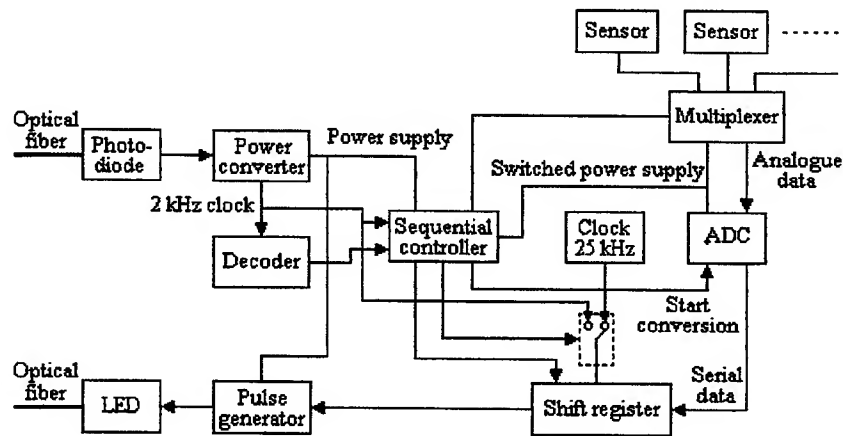


Fig. 3 The schematic diagram of the demonstrator system

The objective is to produce a system, which implement bidirectional communications, using the optical power line to transmit commands to the sensor head and a second fiber to return digital data. The range of eight commands is used to select a sensor, perform a zero-level measurement, monitor the power supply voltage, etc. as required. The system has been implemented using standard CMOS integrated circuits for the logic (HC series), while the DC is an LTC 1298. The LTC 1298 is a micropower circuit, which provides a 12-bit conversion using the digital data in serial form as the conversion proceeds.

In operation the sensor head is normally in a quiescent state power supplied only to those parts of the system necessary to monitor the power bus and receive and decode incoming commands. On receipt of a command the 25 kHz clock is energized, the data channel appropriate to the command is selected (a sensor, supply-line voltage, zero offset, etc.), the sensor is energized if necessary and power is supplied to the ADC. After 16 cycles of the 25 kHz clock the start conversion signal is provided for the ADC, the conversion performed and the data transferred to the shift register. The clock is stopped as soon as the conversion is complete (after 32 cycles) to minimize power consumption. This sequence is illustrated in Fig. 4, the whole conversion taking 1.28 ms.

One the conversion is complete the final phase of the measurement cycle is to step the data out from the shift register using the 2 kHz clock derived from the power supply line. The data from the shift register are passed to a pulse generator that

generates short pulses, in synchrony with the modulation of the power supply line. These pulses are converted to an optical signal using an LED, and returned to the main system controller.

The data are transmitted with a word length of 12 bits and a single start bit. Since the transfer of data from the shift the 2 kHz clock, the data pulses are synchronous with the clock, which could be used in the receiver to improve the checking of data validity, controls register. With a pulse length of 1 μ s the total energy required to send a single word is around 0.25 μ J. Hence, at a data rate of 10 words per second the power requirement for data transmission is around 2.5 μ W, a reasonable figure when compared with the available power budget of around 150 μ W.

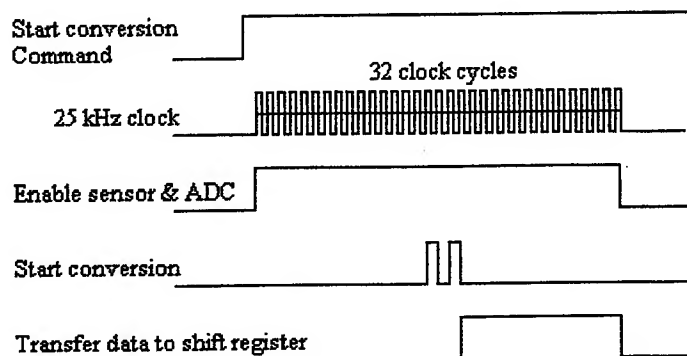


Fig. 4 Sequence to convert data

The sensor used during the development of the demonstrator has been a load cell with a thick-film strain-gauge bridge, although a wide range of sensor types is possible provided they can be powered up for a period of around 1 ms and settle in a time of around 0.5 ms. Obviously the more energy required for the measurement, the lower the maximum repetition rate.

The power consumed by system is modest at around 57 μ W (22 μ A at 2.6 V) at a sampling rate of 10 samples per second. A significant fraction of the power consumed from this part of the circuit rises with the data rate. There is also significant power consumption by those parts of the circuit that must operate continuously, the 2 kHz and the circuit for decoding incoming commands, but useful savings should be possible here.

4. CONCLUSIONS

The more and more stressed automation of the consumer products was disturbed by the lagging behind of the sensors development and in this way was diffused the new concept of the intelligent sensor for to compensate this lagging behind of the sensors development. The research in the intelligent sensors domain requires a team of experts from several disciplines, this multidisciplinary effort being characterized by long development times, in this way the co-operation between industry and research being desirable.

The demonstrator system has shown that the concept of an optically powered sensor head as part of an intelligent sensor system is feasible, even when the optical power is restricted to only a few milliwatts. A practical implementation of the system, would, however, require the development of a low-voltage ASIC to provide the logic for the control and data communications. This would not only reduce the size greatly; it would also help reduce power consumption. With the available of low-voltage CMOS processes this would appear to be a practical proposition. To be viable such an ASIC would have to be flexible, so that one design could operate with a range of sensors, and for a wide range of applications.

The decision to use a single photocell with an up-converter for power conversion was prompted by the simplicity of the scheme. However, the inductor that is required for efficient voltage conversion is inevitably rather large (with a volume of order 10^4 mm³). Increasing the frequency of the modulation of the power supply reduces the required inductance, and hence the inductor size, but the conversion efficiency then falls owing to the stray capacitance of the photocell and other

components. The other cause for concern is that in a flammable atmosphere. The stored energy is small, 2-3 μJ , but if the current path through the inductor is broken the voltage could rise to sparking potential.

Current work on the development of an ASIC version of the system is aimed at mitigating some of these problems.

REFERENCES

1. A. H. Taner and J. E. Brignell, "Aspects of intelligent sensor reconfiguration", *Sensors and Actuators A*, 46-47, pp. 525-529, 1995.
2. A. Ohte, K. Akiama and I. Ohno, "Optically-powered transducers with optical-fibre data link", *SPIE Proceedings*, 478, pp. 33-38, 1984.
3. W. Gross, "Fibre-optic hybrid sensor with optical power supply", *Siemens Forsch. Entwicklungsber*, 17, pp. 13-17, 1988.
4. W. Gross, "Optical power supply for fibre-optic hybrid sensors", *Sensors and Actuators A*, 25-27, pp. 465-480, 1991.
5. H. Kirkham and A. R. Johnston, "Optically powered data link for power-system applications", *IEEE Trans. Power Delivery*, 4, pp. 1997-2004, 1989.
6. M. R. Al-Mohanadi, J. N. Ross and J. E. Brignell, "Optical power and intelligent sensors", *Sensors and Actuators A*, 60, pp. 142-146, 1997.
7. M. Robert, M. Marchandiaux et M. Porte, *Capteurs intelligents et méthodologie d'évaluation*, Edition Hermes, Paris, 1993.

Staring infrared focal plane arrays for thermal imaging technology

Florina Jitescu*, Octavian Novac

Military Equipment and Technologies Research Agency
P. O. Box 51-16, Bucharest, Romania, Code 76550,

ABSTRACT

Thermal imaging converts the infrared (IR) radiation of a scene into a live picture of that scene; the thermal image is a pictorial representation of temperature differences. One of the most promising new sensors for thermal imaging is the infrared focal plane array (IR FPA). The infrared focal plane array consists of a large number of minuscule IR detectors which can resolve targets as little as one tenth of a degree warmer than their surroundings, and offer enormous gains in data throughput per unit time without mechanical scanning. Imaging arrays are the most advanced infrared detectors and commonplace in products ranging from hand-held IR cameras for industry and security use, to sophisticated systems for military applications

Keywords: thermal imaging, infrared detectors, focal plane arrays.

1. INFRARED DETECTORS

Infrared detectors are an integral part of fiberoptic systems and the remote controls found in nearly every household. At the same time, they serve in many more specialized niches in environmental monitoring, industrial process control, night-vision systems, and astronomy. IR detectors are used to monitor air temperature from satellites, check the cooling of electronic wafers and steel ingots, scan for burglars, and observe stars being born. These detectors also function as power meters for various types of laser systems.

IR detectors cover a wide range of the electromagnetic spectrum, from the near IR (0.8-2 μ m) to the far IR (20-400 μ m). Each region spans more than four octaves of frequency, compared with only a single octave for the visible light.

Detection of IR radiation can be based on many different technologies. These technologies have generated many types of IR sensor elements, each with its own characteristics.

There are two basic types of IR detectors in use today: photon (quantum) detectors and thermal detectors:

Photon detectors employ photon-detection mechanism in which absorption of an incident IR photon, with sufficient energy, produces excess of free carriers in a semiconductor structure. To absorb IR photons, the detector material must have the band-gap energy less than the energy of the incoming photons; thus, sensing longer wavelengths requires the use of small band-gap materials.

Small band-gap materials yield devices sensitive to low energy IR photons, but the electron carriers are then more easily generated in the semiconductor from random thermal excitation, and this degrades sensitivity through increased dark current and noise. One way to reduce these effects is to reduce the operating temperature of the detector:

- -by thermoelectric (TE) cooling to operating temperature below (-70°C), for applications at near and mid-IR wavelengths;
- -by cryogenic cooling with liquid-nitrogen filled Dewars;
- -with Joule-Thomson coolers;
- -with expansion-engine coolers (Stirling-cycle refrigerators) to operating temperatures of 100 K or less, in the mid or long-wave IR spectral regions.

* Correspondence: Phone: 401 423.30.58

Thermal detectors, such as thermopiles, bolometers, and pyroelectric detectors, measure the change in a physical property of the active element, induced by a temperature change. The temperature change is caused by heat generation from the absorption of IR radiation.

Resistive bolometers depend upon a change in resistance of a material due to a temperature rise when IR radiation is absorbed. The thermoelectric effect is familiar in the form of a thermocouple that generates an output voltage when the temperature of the junction between two metals changes with respect to the temperature of a reference junction. Both the resistive bolometer effect and the thermoelectric effect are found in metals and semiconductors. The pyroelectric effect, usually found in ferroelectric materials, is manifested by the generation of an external current in the absence of electrical bias by a time-dependent temperature change caused by the use of a radiation chopper to modulate the incident infrared radiation.

Thermal detectors can be used uncooled and are, therefore, compact and relatively inexpensive. By their nature, thermal detectors have a flat response over a wide range of wavelengths and, unlike photon detectors, they exhibit lower sensitivity and slower response time. For many applications that do not require high sensitivity or very long wavelengths (beyond 100 μm), thermal detectors are often the best choice.

2. INFRARED-SENSITIVE PHOTON DETECTORS

The most widely IR detectors are photon-detectors; although the basic operating principle of all photon-detectors is similar, the material properties are not.

Currently, four classes of IR sensitive photon-detectors are based on semiconductors, each having characteristic strength and weakness that make it useful for various applications:

- The dominant approach today uses intrinsic semiconductors which consist of pure, undoped materials. The bandgap of the semiconductor defines the longest wavelength that can be detected. As the energy bandgap in the semiconductor becomes smaller, the wavelength of the light to be detected gets longer. Intrinsic detectors may be constructed to operate in the photoconductive, photovoltaic, or photoelectromagnetic mode.

In *photoconductive* detectors an external battery maintains a current. Incident photons free additional charge carriers from atoms of the crystal lattice, thereby increasing the current. With steady radiation an equilibrium is established between new charge carriers being generated and those being immobilized by recombination.

In *photovoltaic* detectors an electric field is built into the element by way of a *p-n* junction. Photons incident on the junction create hole-electrons pairs which are separated by the action of the field before they can recombine. A voltage is thus set up at the opposite ends of the crystal.

In the *photoelectromagnetic* mode, radiation falling onto the crystal generates electrons and holes at the surface. Those which do not recombine drift toward the interior of the crystal. A magnetic field, set up at right angles to the movement of the charge carriers, separates holes from electrons and causes them to move to opposite sides of the crystal, thereby establishing a potential difference between these sides.

For short wavelengths, the commonly used materials are silicon and germanium. Intrinsic silicon IR detectors are limited to the detection of radiation at 1.1 μm , which corresponds to the minimum energy needed for valence band electrons to cross the bandgap to enter the conduction band.

For longer wavelength detection, the primary materials are ternary compounds in which the composition can be adjusted to fine-tune the bandgap. The fiberoptic industry relies heavily on indium gallium arsenide (InGaAs), while for a wide range of other applications the dominant material is mercury cadmium telluride (HgCdTe). This compound has a bandgap that can be varied to give a long-wavelength cutoff from 2 to 30 μm , providing great versatility.

- For sensing IR radiation that ternary intrinsic semiconductors cannot detect, extrinsic (impurity-activated) semiconductors are used.

Impurity-activated detectors operate only in the photoconductive mode. Charge carriers are freed from impurities which were deliberately added to the host crystal lattice. When impurities are added, it takes less energy to free charge carriers from these impurities, and the spectral response is extended by an amount depending on the type of impurity.

Extrinsic semiconductors are generally based on silicon or germanium doped with impurities. Dopants, such as boron, arsenic, gallium, mercury or gold, with their extravalence electrons, can have appropriate energy levels lying in the host-material bandgap. Thus, electrons can be knocked off the dopants at energies far below the cutoff for silicon or germanium itself, or even for the ternary compounds.

Extrinsic silicon detectors were actually used for IR detection before the development of ternary intrinsic compounds but these devices had significant drawbacks:

* They need to be cooled well below liquid-nitrogen temperature, and they operate somewhat unreliably. Cooling improves the detectivity. The amount of cooling required increases with increasing threshold wavelength. The necessity for cooling becomes apparent when one considers that charge carriers may be freed either by incoming photons or by lattice vibrations. Cooling will reduce the number freed by lattice vibrations, a process competing with the freeing of charge carriers by the radiation to be detected.

* Electrons knocked off of dopants left behind a positively charged ion, which could only slowly get an electron to neutralize its charge. A positive charge built-up prevents electrons from leaving the semiconductor and entering the electrode to be detected. The electrons can move out only when a sufficient local negative charge builds up near the electrode to overcome the positive ion's attraction. Current extrinsic semiconductors overcome this problem by greatly increasing the dopant density, thereby allowing electrons to jump more easily from one closely packed dopant ion to another, canceling the positive charges. These extrinsic detectors are termed blocked-impurity-band detectors and are finding application in such demanding disciplines as infrared astronomy.

- To avoid the extreme cooling demands of extrinsic semiconductor detectors and in some cases to reach even longer wavelengths, there is a third approach: photoemissive detectors. In these detectors, a metallic compound, for example, platinum silicide (PtSi), is overlaid by doped silicon. A photon bounces an electron or a hole, out of the conductor into the silicon.

The advantage of such devices is that response does not depend on the characteristics of the semiconductor but on those of the metal, which are extremely uniform, so that high uniformity of response is much easier to achieve. However, absorption is proportional to the square of the wavelength, so for wavelengths of a few microns, efficiency and sensitivity are much less than for extrinsic devices. At very long wavelengths, beyond 100 μm , these detector types are quite useful.

- The fourth main type of IR detector is the quantum-well IR photoconductor (QWIP). The operating principle in these devices is similar to that for extrinsic detectors-the dopants are used to alter the band structure. But in QWIPs, the dopants are concentrated into microscopic regions, creating quantum wells, where the band structure has shifted. Detection occurs when a photon knocks an electron or hole out of the quantum well into the neighboring band.

As with extrinsic semiconductor detectors, QWIPs can be tailored to reduce the energy a photon needs for detection. But QWIPs are much more sensitive than extrinsic types, because the entire quantum well, not just an individual dopant atom, acts as an absorber. Because the quantum wells are 10-100 atoms across, their effective absorption area is much higher.

Research is advancing rapidly in these devices, concentrating on gallium arsenide based systems, such as GaAs / AlGaAs, with the latter compound being used to create the quantum well.

In the wavelength range from 8 to 10 μm , QWIPs have been approaching HgCdTe performance, although at longer wavelengths the ternary compounds still have an edge. Like the extrinsic detectors, QWIPs generally have to be cooled below liquid-nitrogen temperature for background-limited performance.

3. THERMAL IMAGING

Thermal imaging converts the infrared radiation of a scene into a live picture of that scene. The IR image resembles a real time television picture of the scene with contrast differences, which represent the radiation differences in the scene, and can be computer processed to color-code temperature ranges.

The focused IR image is mechanically scanned across a detector, whose output is converted electronically into a visual image. Depending on the performance required, the detector may consist of one or many elements. The optics, the mode of scanning, and the signal processing electronics are closely interrelated.

Originally, developed to extend the scope of night-vision systems, thermal imagers, at first, provided an alternative to image intensifiers. As the technology has matured, its range of applications has expanded and now extends into fields that have little or nothing to do with night vision, but benefit from real-time thermal evaluation. Due to their high sensitivity and their resulting high detection range, their good resolution and the associated high identification range as well as the good penetration of the atmosphere under fog and smog conditions, thermal imaging sights are currently the technically optimal night vision equipment.

The two major regions of the IR spectrum used for thermal imaging are 3-5 and 8-12 microns. These wavelengths are used because they are commonly generated by both natural and manmade objects and are not completely absorbed by the atmosphere.

The 3-5 micron band's principle advantage is its operating temperature range. All conventional thermal imagers must include a mechanism to cool the sensor array which otherwise would generate an unacceptable signal-to-noise ratio. For imagers in the 3-5 micron region, however, the required temperature is around -90°C as compared to -200°C for systems operating in the 8-12 micron region. This is because of the inherently higher energy levels of photons in the 3-5 micron region.

On the other hand, the 8-12 micron region is more thermally active in the natural environment. The ambient temperature of most objects is between 0° and 30°C and, although the total amount of IR energy emitted is not large, it generally peaks in the 10 micron region. Low winter temperatures also have a more adverse affect on signal strength in the 3-5 region than in the 8-12. For these reasons, despite the additional cooling requirements of 8-12 micron range systems, they are more often pursued for general IR surveillance applications.

The construction of thermal imaging equipment requires very demanding technologies, particularly with highly sensitive IR detectors.

4. IMAGING ARRAYS-NOVEL IR DETECTORS

One of the most promising new sensors for thermal imaging is the infrared focal plane array (IR FPA). The infrared focal plane array consists of a large number of minuscule IR detectors (pixels) which can resolve targets as little as one tenth of a degree warmer than their surroundings.

Infrared focal plane arrays are commonplace in products ranging from hand-held infrared cameras for industry and security use, to ultra sophisticated devices for IR astronomy or military applications. IR FPAs have great potential for a wide variety of devices, such as fast pyrometers, analytical instruments, homing heads, guidance of intelligent munitions, laser threat-warning receivers, that demand performance, speed of response and temperature of operation. Made up of a large number of IR detector elements, IR arrays sense thermal energy, or heat, and are able to capture a two-dimensional image of a scene that results from emitted energy.

The thermal radiation emitted by the objects reaches the detectors through an IR objective lens. The detectors convert the incoming thermal energy to proportional electric signals. These signals, after they have been intensified, are processed and shown on a suitable display device (monitor).

Like the individual IR detectors that arrays are made up of, arrays operate on two different physical principles: quantum arrays react to individual photons, while thermal arrays measure the total energy absorbed by each element.

The most common IR imaging arrays are based on photon detectors. Such array is a single chip containing a mosaic of numerous IR detectors, each 30 microns square on one side, with a corresponding number of minute signal processing elements, known as charge couple devices (CCDs), on the opposite side. In operation, the detectors accumulate photon energy, which is then transferred to a signal processor for subsequent multiplexing off the chip. The photosensitive array delivers signals corresponding to the absolute value of the illumination at each point in an image (pixel).

Not only quantum arrays but also thermal arrays can be used for imaging. Thanks to the sensitivity gain obtainable with multiple elements, systems using arrays of thermal detectors can give useful performance. Though not equal to the best that can be obtained with quantum detectors, such systems have the advantage of not requiring cooling.

The appropriate figure of merit describing the sensitivity of the FPA detector is the noise equivalent temperature difference (NETD). The NETD is the change in the temperature of a large blackbody in the scene being viewed, which causes a change in the signal-to-noise ratio of unity in the output of the array. Typical values for single pixels and small arrays are 0,1 to 0,3 °C; large FPAs have NETD values of 0,01 to 0,02 °C.

Although the sensitivity of a pixel of a thermal-detection array is far less than that of one pixel of a photon-detection array, a large thermal-detection array could exhibit equal or better sensitivity than a small photon-detection array.

In contrast to most photon detectors, where the speed of response is dictated by the free-carrier lifetime (typically in the range of a microsecond or less) the speed of response of thermal detectors is governed by their thermal time constant (typically in the millisecond range). The thermal time constant is the ratio of the pixel heat capacity to the thermal conductance associated with heat flow from the pixel to its surroundings.

With the advancement of fabrication technology, arrays of microbolometers, the leading thermal array type, are challenging the more developed quantum arrays for many application areas and are leading to the development of room-temperature thermal imagers.

Most of the systems in use today employ FPAs of mercury cadmium telluride (HgCdTe), a semiconductor whose composition is adjusted to provide optimum response in the 8 to 12 μm atmospheric window. The operating temperature of 77 K is usually provided by Stirling-cycle cryocoolers. Other thermal-imaging approaches employ FPAs of indium antimonide (InSb) (fig.1) and platinum silicide (PtSi). Both types operate in the 3 to 5 μm atmospheric window and require cryogenic operation. Moreover, FPAs of HgCdTe and quantum-well infrared photodetectors (QWIPs) based upon aluminum gallium arsenide / gallium arsenide (AlGaAs / GaAs) multiple-quantum-well structures. These also require cryogenic operation.

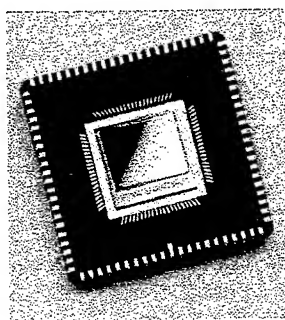


Fig.1 320 x 256 InSb array

5. SIGNIFICANT ADVANTAGES OF INFRARED FOCAL PLANE ARRAYS

Focal plane arrays for infrared imaging provides significant advantages in both applications and performance:

1. -Basically, any attempt to increase sensitivity in scanned systems has meant getting more signal to the detector. This in turn meant either increasing optics size or slowing scanning speed, both of which have undesirable consequences. Larger

optics mean higher cost, while slower scan speeds mean frame rates that stretch the definition of real-time imagery. An FPA detector electronically observes an entire scene at one time without having to scan the scene through an arrangement of oscillating, or rotating mirrors. An FPA is thus a staring array, as opposed to a scanning mechanical / optical device, which means that an FPA can be used with very simple, small-size optics, allowing size and weight-reduction benefits for small-diameter designs.

2. -The image acquisition rate of scanning imagers is limited by scanning frame rate, which can be anywhere from 10 to 60 Hz. Since each detector element of an IR FPA continuously views its assigned target pixel, the device can record full-field high-speed phenomena at an image acquisition rate limited only by detector-preamp response; 1000 Hz can be obtained with IR FPA imagers. For the first time, high-speed infrared imagery at 100 frames / s can be realized by using FPAs.

3. -Spatial resolution-the ability to image and measure the temperature of a single spot on the target surface at any given distance-provides IR FPA imagers with another big advantage over scanners. Because of the element isolation inherent in the design each image element has far less influence on the next than is the case for mechanical scanning. A properly calibrated FPA imager will provide three to five times as much measurement spatial resolution as a scanning system with the same specified instantaneous field of view.

4. -An FPA detector has greater sensitivity in detecting and supplies improved scene informations, generated by the larger number of detectors.

5. -An other advantage derives from mounting CCDs on the same chip with detectors. This drastically reduces the number of output wires that would otherwise be required, thus simplifying assembling and reducing chances of mechanical failure, and eliminating optical interlace functions and components.

6. -In FPA systems, dwell time (the time any one part of the scene could be imaged onto the detector) is increased over a scanned single-element detector by the larger number of elements in the array. For example, a 256x256 element array has more than 65,000 times more signal available to it than a single-element scanned one.

7. -R FPA technology can benefit of advances, such as region of interest multiplexers (ROI), that provide enhanced functionality and improved performance while relieving the data-transfer and data-processing burden from the data transmission lines and downstream processor.

More pixels are a benefit during initial target surveillance and acquisition modes for applications like missile tracking. However, once a target has been acquired, the tracking and terminal-homing process requires more frequent scene updates and more downstream processing.

FPA multiplexers may provide an ROI capability where selected subsets of pixels, or windows, of the full field are transmitted to the downstream processor. Pixels outside of the ROI windows are simply not read out from the FPA. This technique increases the effective frame rate during terminal homing and reduces the amount of transmitted data, thus reducing the computational demand on the downstream mission processor.

6. CONCLUSIONS

Thanks to improved manufacturing techniques, two-dimensional staring focal plane arrays for infrared imaging have become better and easier to use. Thermal imagers with large staring FPAs do not require any moving parts, which reduces system size and complexity. Thermal resolution of less than 0,003 K has been already reported for imagers operated at 95K in the 3,4-4,8 μm band. Future generation of infrared systems will require high-performance, cost-effective staring arrays providing enhanced functionality and improved performance.

REFERENCES

1. Lerner, Eric J., "Infrared detectors offer high sensitivity", *Laser Focus World*, 6, pp. 155-164, 1996.
2. Wauters, Jan, "Novel IR detectors operate at room temperature", *Laser Focus World*, 5, pp 175-179, 1998.

The first results on the cesium atomic fountain in INFLPR

Cipriana Mandache , T. Acsente* , M. Ungureanu

National Institute for Laser, Plasma and Radiation Physics, Nuclear Fusion and Plasma Physics
Laboratory, R-76900 , Bucharest, Magurele, P.O.Box MG-36, Romania

ABSTRACT

The atomic fountain is a new high-performance primary frequency standard where the stability is of the order of 10^{-17} and the accuracy of the order of 10^{-16} . Our goal is to realize such a standard in our laboratory. In an atomic fountain we can distinguish three basic part: the cesium atom source, the microwave and the C-field region, and the detection area. In this paper we briefly recall an atomic fountain operation and present the first research results obtained in our laboratory concerning the atomic cesium fountain.

Keywords: atomic fountain, optical molasses, laser cooling, magneto-optical trap (MOT), time of flight (TOF), extended laser cavity,

1. DESCRIPTION AND OPERATION OF AN ATOMIC FOUNTAIN.

The scheme of a fountain frequency standard is shown in fig. 1. We can distinguish three basic parts: the cold atom source, the microwave and the C-field region, and the detection zone.

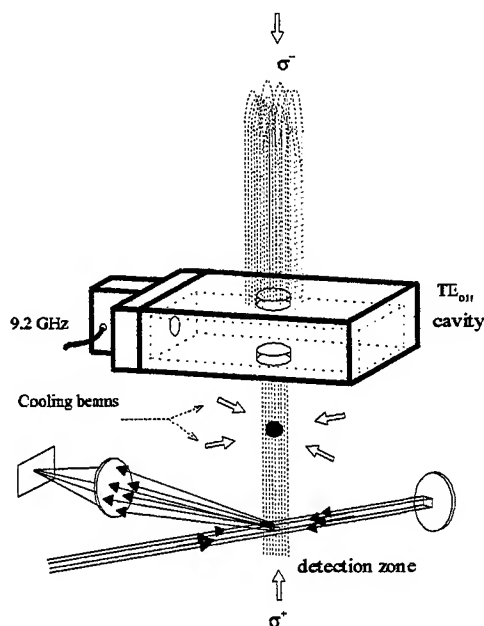


Fig. 1. Experimental setup of an Atomic Fountain

* Correspondence: Email: tomy@alpha2.inflpr.ro; Telephone: 789 38 65; Fax: 423 17 91;

In the following we briefly describe the operation of an atomic fountain ^{1,2}.

The cesium atoms are first cooled for about 0.3 to 0.5 s in the cold atomic source. Six independent laser beams capture and cool cesium atoms in a low-pressure ($\sim 10^{-8}$ Torr) Cs cell. Between 10^5 and a few 10^8 atoms can be cooled down to 2.5 μ K by a 3-D σ^+ - σ^- magneto-optical trap or lin \perp lin optical molasses. After cooling the 1-D moving molasses method is used to upward launch the atoms. The atoms pass through a high Q ($\sim 30,000$) cylindrical TE₀₁₁ cooper microwave cavity situated 30 cm above the cooling zone, where they experience a first $\pi/2$ pulse. They then continue their ballistic flight in the C-field region, where a highly homogeneous static magnetic field is produced by a solenoid and compensation coils. In this region of the fountain the pressure is kept low ($5 \cdot 10^{-10}$ Torr) in order to reduce collisions with background gases. Three μ -metal magnetic shields surround the microwave cavity and C-field region. The C-field region is thermally isolated and temperature controlled in order to frequency tune the microwave cavity. The atoms fall back through the cavity, undergoing a second microwave interaction, so that the Ramsey separated oscillatory field method is effected.

Finally in the detection zone the atomic populations are measured and the time-of-flight (TOF) technique is used to determine the vertical velocity.

The fountain operation is pulsed with a cycle time of about 1.1 s.

A 852 nm laser diode, in an extended cavity configuration provides the required laser frequencies. Are used the $F=4 - F'=5$ transition of the D₂ line to cool and detect the atoms. The frequency and the intensity of beams are controlled via acousto-optical modulators. All the beams are spatially filtered and expanded up to 2 cm in diameter. The maximum optical intensity is about 10 mW/cm² for the cooling beams and 1 mW/cm² for detection. During the microwave interaction, all the laser beam are blocked by electromechanical shutters to avoid light shifts.

2. RESULTS OBTAINED IN INFLPR.

2.1. The magneto-optical trap (MOT)

The most efficient device for cooling atoms is the magneto-optical trap (MOT) whose schematic is depicted in fig.2. MOT consists of three mutually orthogonal, retro-reflected laser beams interacting at the center of a quadrupolar magnetic field. In practical realization (fig.3) it is a main fused silica cylinder with four orthogonal arms, each one ended with optical windows to allow the infrared laser radiation to pass. The cesium reservoir is attached to the glass envelope in a "cold finger" configuration allowing us to change the concentration of thermal atom in the trap to the optimum value for cooling.

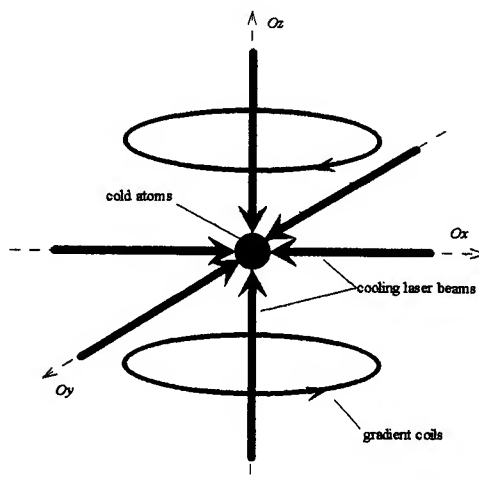


Fig.2 Schematic of a magneto-optical trap (MOT)

To obtain cold atoms, the partial pressure of thermal, high velocity cesium atoms in the trap must be of 10^{-8} hPa. Measurement of the thermal atoms concentration is realized using an saturated absorption experiment

The trap and cesium source are coupled together to an ionic pump. Two anti-Helmholtz coils disposed on the main cylinder produces the quadrupolar magnetic field. By varying the current injected in these coils, we are able to produce a magnetic gradient field between 5 and 15 G/cm. On the trap arms compensation coils are also attached to eliminate the effect of terrestrial magnetic field .

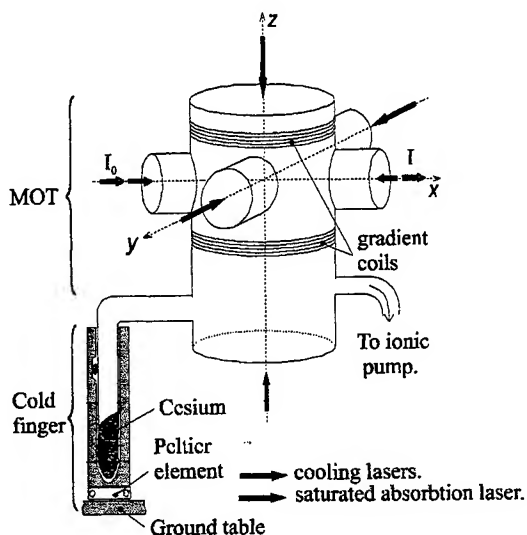


Fig.3 Practical realization of the magneto-optical trap (MOT)

2.2. The extended laser cavity.

The trapping laser beams come from an SDL 5402 laser diode (852 nm) in an extended cavity configuration. The linewidth of a single laser diode is larger than few MHz because of the dimension of the resonator. We use extended cavity operation, because it is the simplest and most robust method of achieving a linewidth narrower than the linewidth of the caesium transition.

An extended cavity semiconductor laser is a laser diode in which the resonant cavity is longer than the diode itself. In our case the total cavity length is 4 cm and is formed by the highly-reflecting rear facet of the diode and a diffraction grating. The 1200 lines/mm grating is mounted in the Litrow geometry, with the first order beam retroreflected to the diode. In order to adjust the cavity length the grating is glued onto a piezoelectric ceramic, held in a mirror mount. This enables to reflected beam to be aligned and the frequency to be selected.

The laser diode, collimating optics, and grating mount are mounted on an aluminium base plate, around which is constructed an aluminum box which is temperature stabilized to better than 0.1°C .

The linewidth of the free running laser mounted in an extended cavity ranging from 5MHz to 100kHz and the tuning range obtained with thermal compensation is about 15- 20 GHz³.

2.3. Gradient and compensation coils.

The quadrupolar magnetic field used for cooling cesium atoms is obtained using two anti-Helmholtz coils, placed on the trap chamber (fig.3). This coil configuration provides a uniform magnetic field gradient of about 10 Gauss/cm, which

leads to the appearance of Zeeman energy sub-levels of moving atoms. The coils have a diameter of about 30-cm and the space between the two coils is about 11 cm.

To compensate the effect of terrestrial magnetic field in the trapping region we use three pairs of coils, each pair mounted in Helmholtz configuration.

The power supplies consist of adjustable current generators for both gradient and compensation coils.

2.4. The resonant cavity .

In an atomic fountain, after launching, the atoms pass through a cylindrical TE₀₁₁ cavity, with the diameter of 5 cm. For the theoretical computation of the Q we used the following relations ^{4,5}:

$$Q_c = \frac{\nu_0}{\Delta\nu} = \frac{\sqrt{\frac{\mu}{\epsilon} \left[\left(\frac{x'_{mn}}{R} \right)^2 + \left(p \frac{\pi}{h_c} \right)^2 \right]^{3/2}}}{2R_s \left[\frac{1}{R} \left(\frac{x'_{mn}}{R} \right)^2 + \frac{2}{h_c} \left(p \frac{\pi}{h_c} \right)^2 \right]} \quad (1)$$

and we obtained Q= 25 200.

The experimental determination of the Q cavity gives us: Q_{exp}= 21 370

In order to assure the proper resonant frequency we studied the variation of the resonant frequency as a function of temperature (Fig. 4)

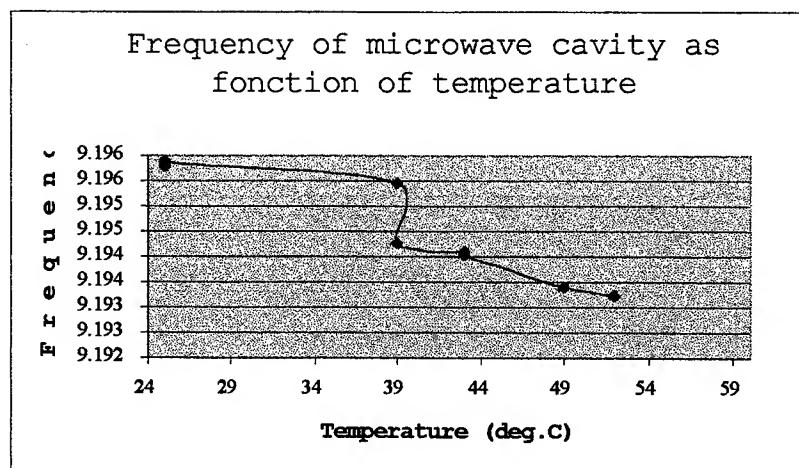


Fig.4 The frequency of the μ -cavity as function of temperature

2.5. Electric devices for photo-detectors.

During the ballistic flight, the atomic cloud expands and in typical conditions, less then 10% of the atoms pass two times through the microwave cavity. The time distribution of the fluorescence signal allows the atomic velocity distribution

(TOF) and the temperature of the atoms to be measured. The time of flight spectrum gives us information about the temperature and the density in the molasses. The TOF measurements are performed on the bottom part of the fountain, in the detection area.

We have realized the detection electronic devices, which provides a high amplification and very low noise for all 4 photo-detectors. In practical realization the photo-detector consist of a PIN photodiode and a transimpedance amplifier.

2.6. Laser diode current supply.

Much of current atomic physics research involves the interaction of atoms and light in some way. Laser sources that can be tuned to particular atomic transitions are now a standard tool in most atomic physics laboratories. The main difficulty in using diode lasers in most atomic physics experiments is the problem of tuning them to the desired wavelength, usually that of some atomic transition. The accord of a laser diode can be made in two steps: the control of temperature and then the accord of diode current supply.

In fig. 5 is presented the block structure of the current supply for the laser diodes used in our experiment.

The day-to-day repeatability of the laser system performance is determined primarily by the temperature stability. The last important element in setting up a diode laser is the current control circuit. For according the laser diode on Cesium D2 line wavelength, we are using a current supply with special performances. The output current can be adjusted between 0 mA and 200 mA, for a proper laser accord on the resonance frequency.

In the electronic design we used high-performance components like OP 27 and OP 470 and we obtained a noise density of $5.14 \text{ nA}/\sqrt{\text{Hz}}$.

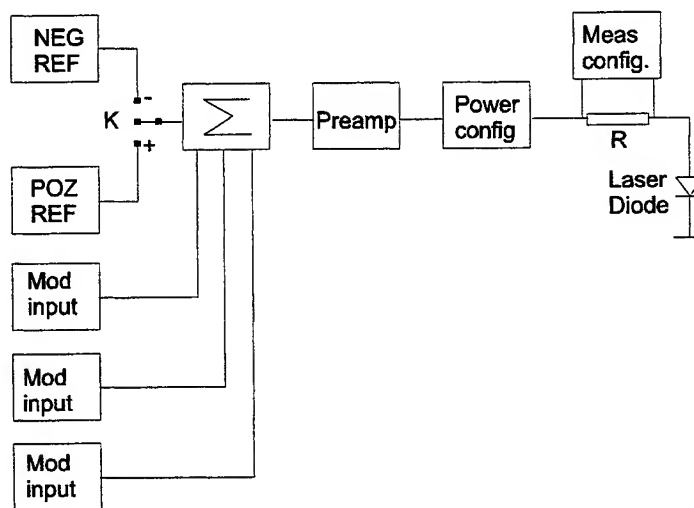


Fig. 5. Block diagram of current supply for the laser diode

2.7. Thermostated caesium cell .

In order to stabilize the frequency of the laser diode and to reduce acoustic noise, the extended laser cavity must be locked to the D2 line of Cs. This will be achieved using a saturated absorption technique.

We realized a miniaturized, compact, and temperature stabilized mount for a caesium cell which will be used to perform the saturated absorption experiment. This cell is shown in fig.6.

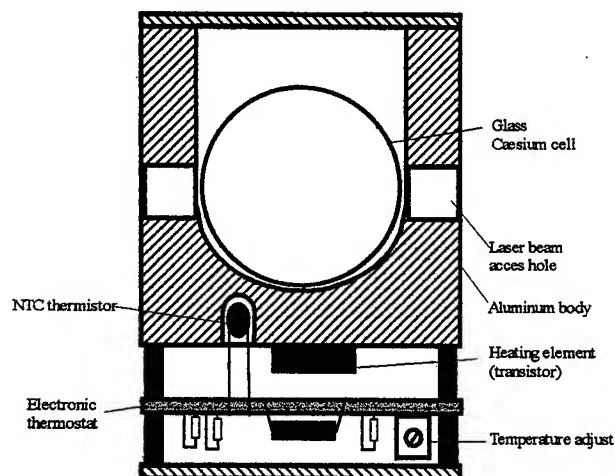


Fig.6. Thermostated caesium cell.

2.8. 3-D motion of cesium atoms.

We have performed numerical computations taking into consideration the actual sub-levels structure of the $F=4 \rightarrow F=5$ transition in Cesium, the gradient of magnetic field and the exact structure of the laser electric field. As the MATLAB routine for solving ordinary differential equations (ODE) we are using deals only with real numbers, and the coherence really. We can choose as variables in our system of ODE's the three coordinates x, y, z and the three components of the velocity of the atom together with the superior diagonal components of the density matrix.

ACKNOWLEDGMENTS

This work was supported by the National Agency for Science, Technology and Innovation.

REFERENCES

1. Bize S. et al., "High-accuracy measurement of the ^{87}Rb ground-state hyperfine splitting in an atomic fountain", *Europhys. Lett.* 45, 558 (1999).
2. Clairon A. et al., "A Cesium fountain frequency standard: preliminary results", *IEEE Trans. on Instr. and Meas.* 44, 128 (1995).
3. C. Mandache, P. Thomann, "Miniaturized, extended cavity for laser diode", *European Space Agency Reports*, CEC CIPA 3510PL (1993)
4. C. Mandache, T. Acsente, M. Bengulescu, "Research on the cesium cold atoms at IFTAR, in Bucharest, Romania" published in "Frequency Standards and Metrology", *Applied Physics Books*, World Scientific, editor J.C.Bergquist ,Part XVII, p.415 (1996)
5. C. Mandache, T. Acsente, "Research on the cesium magneto-optic trap in IFTAR", *Romanian Reports in Physics*, vol.49, nr.3-4, p223-228 (1997)

The measurement of the ^{87}Rb ground-state hyperfine splitting in an atomic fountain

S. Bize^a, Y. Sortais^a, M. S. Santos^b, C. Mandache^{*c}, A. Clairon^a and C. Salomon^d

^aBureau National de Métrologie, Laboratoire Primaire du Temps et des Fréquences, Observatoire de Paris, 61 Av. Denfert-Rochereau, 75014 Paris, France

^bInstituto de Fisica de Sao Carlos-USP, Departamento de Fisica e Ciencia dos Materiais, P.O.Box369, Av. Dr. Carlos Botelho, 1465, Sao Carlos, SP, 13560-970, Brazil

^cInstitutul National de Fizica Laserilor, Plasmei si Radiatiei, P.O. Box-MG36, Bucuresti, Magurele, Romania

^dLaboratoire Kastler Brossel, Ecole Normale Supérieure, 24 rue Lhomond, F-75231 Paris Cedex 05, France

ABSTRACT

The new atomic Rb-Cs fountain should confirm the recent theoretical calculations relating to the collisions of rubidium atoms. According to this theory, the displacement of the frequency of clock due to the collisional shift was predicted to be 15 times lower for ^{87}Rb than for ^{133}Cs at equal density. Using Rb instead of Cs in a fountain standard may lead to an order of magnitude improvement in frequency stability together with an excellent accuracy.

In this paper we describe the operation of a laser cooled ^{87}Rb frequency standard and present a new measurement of the ^{87}Rb ground state hyperfine frequency with a relative accuracy of $2.4 \cdot 10^{-15}$ by comparison with a Cs fountain atomic standard. In order to measure this, first we determined the absolute frequency of the reference H-maser by comparison with the LPTF's Cs fountain. Second, we corrected the measured frequency to take into account different systematic shifts: magnetic field, black body, microwave leakage, collisions. The measured frequency is 6 834 682 610.904 333 (17) Hz. This value differs from previously published values^{1,2} by about 2-3 Hz and is 10^4 times more accurate.

Keywords: time and frequency, optical cooling, trapping, fine and hyperfine structure, atomic fountain

1. THE EXPERIMENTAL APPARATUS

The construction of an atomic fountain operating with ^{87}Rb atoms has been motivated by two reasons. First, because the collisional shift is one of the dominant terms in the uncertainty budget of Cs fountains, in the new fountain this frequency shift was predicted to be 15 times^{3,4} lower for ^{87}Rb than for ^{133}Cs . The second point of interest is the fact that accuracy in the 10^{-16} range should make it possible to search for possible drift of the fine structure constant $\alpha = e^2/\hbar c$ with time⁵.

The operation of this new fountain is similar to that of the fountain with cesium⁶ FO1. The experimental set-up is described in more details in other papers⁷, and we briefly recall its operation (Fig.1). About 10^8 rubidium atoms are caught^{8,9} in Lin \perp Lin optical molasses (MOT) from a vapour cell at room temperature, at a pressure of $\sim 10^{-8}$ Torr in one second. The molasses cloud has a Gaussian shape with a $e^{-1/2}$ diameter, measured with a CCD camera. Using laser diodes and a tapered optical amplifier providing up to 25 mW per cooling beam, we trap up to 7.5×10^8 atoms spread among the F=2 Zeeman sublevels. Using the moving molasses technique^{10,11}, the atoms are launched in the (1,1,1) direction with respect to the cooling beams. They are adiabatically cooled¹² in the moving frame by slowly turning down the laser intensities after

* Correspondence: E-mail: cipriana@alpha1.infm.ro; Fax: 40 1 423 17 91

launch. The atomic cloud temperature is on the order of $1.4 \mu\text{K}$. The launch velocity is $3\text{--}4 \text{ m/s}$. The atoms are selected in the $F = 1$, $m_F = 0$ Zeeman sublevel by means of microwave and laser pulses. Passing twice through a cylindrical TE_{011} microwave cavity¹³, they undergo a Ramsey interrogation. The microcavity is made of copper and has a quality factor of ~ 15000 . The populations of the two hyperfine levels are finally measured by laser induced fluorescence. The density of atoms selected in $m_F = 0$, and averaged along the flight above the cavity, reaches $2 \times 10^8 \text{ at.cm}^{-3}$.

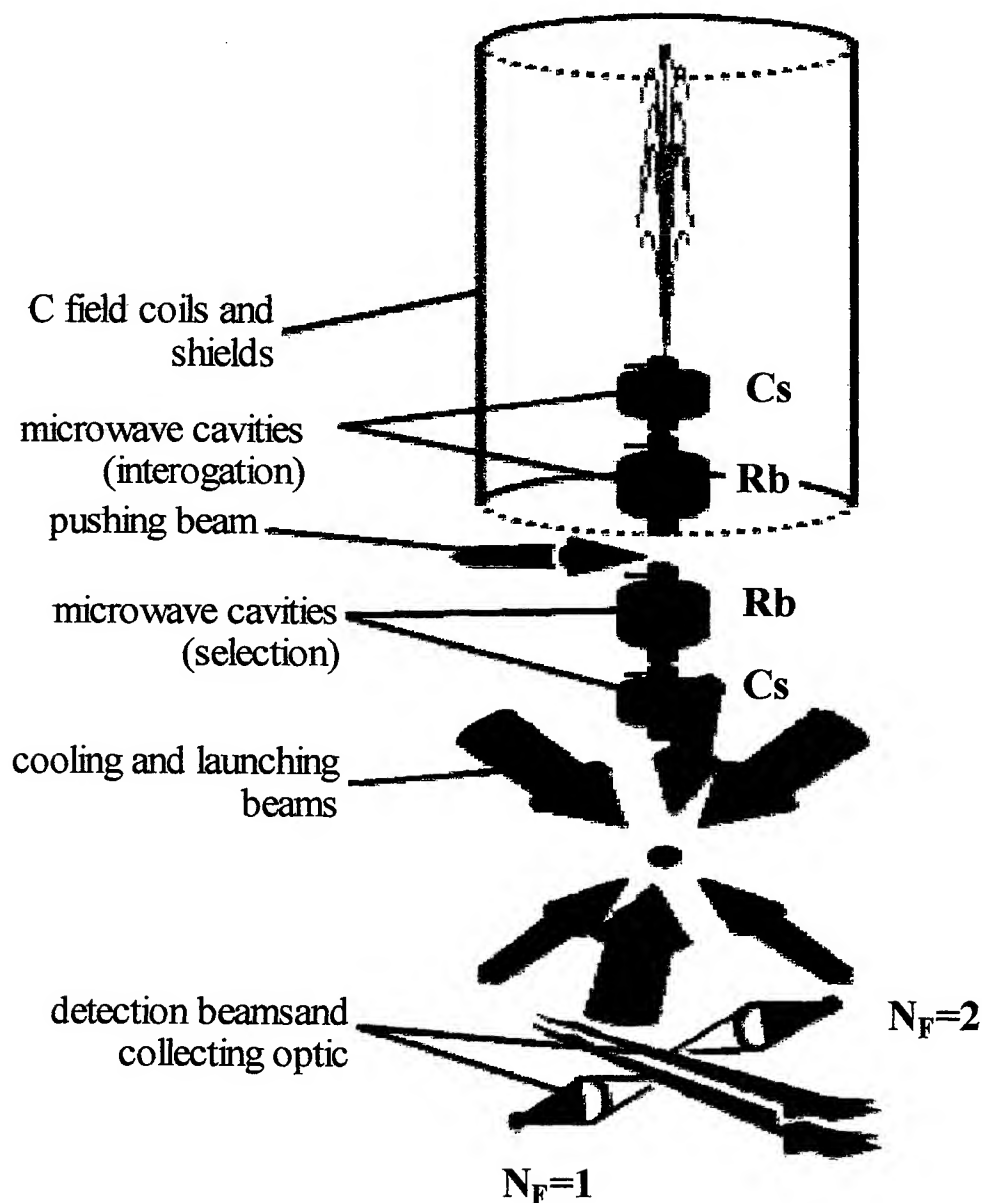


Fig.1 Rb-Cs fountain. The atomic population $N_{F=1}$ (and $N_{F=2}$) in $F=1$ (respectively $F=2$) are measured by light induced fluorescence.

The atomic temperature is also deduced from the width of the time of flight peak⁵. From the measured populations as a function of microwave detuning, an error signal is produced to lock the microwave frequency to the atomic resonance.

Magnetic- field fluctuations are reduced by four μ -metal shields surrounding the Ramsey cavity and actively compensated by external coils. In this way, the external magnetic perturbations are attenuated by more than 5 orders of magnitude in the interrogation region.

Light is guided from the optical bench to the vacuum chamber by polarising optical fibers and collimators mechanically prealigned with a few 10^{-4} rad accuracy. This ensures a good reliability of the set-up.

The Ramsey resonance as a function of the microwave frequency is plotted in Fig.2. The central fringe has a 1.2 Hz FWHM, corresponding to a launching height of 20 cm above the microwave cavity.

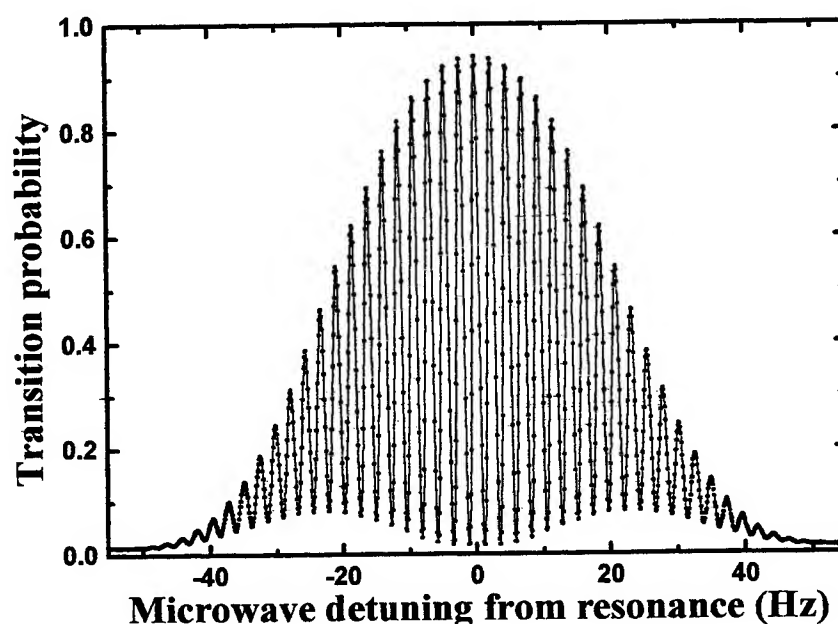


Fig. 2 Ramsey fringes of the rubidium fountain. The transition probability $N_{F=2} / (N_{F=1} + N_{F=2})$ is plotted as a microwave frequency detuning.

The noise on the transition probability at half-central fringe is 1/800 per shot and results from the phase noise of the local oscillator. We become insensitive to this noise source by working at resonance and applying $\pi/4$ microwave pulses in the cavity. The noise then drops down to 1/2400. The noise measured on resonance indicates a potential stability of $5 \times 10^{-14} \tau^{-1/2}$. The present frequency stability is clearly limited by the phase noise of the microwave-interrogating signal.

We measure the Allan standard deviation¹⁴ of the frequency fluctuations by comparison to an H-maser. The short-term stability is $1.5 \times 10^{-13} \tau^{-1/2}$, where τ is the integration time in seconds. The stability decreases down to 1×10^{-15} after a 20000 s interrogation (Fig.3).

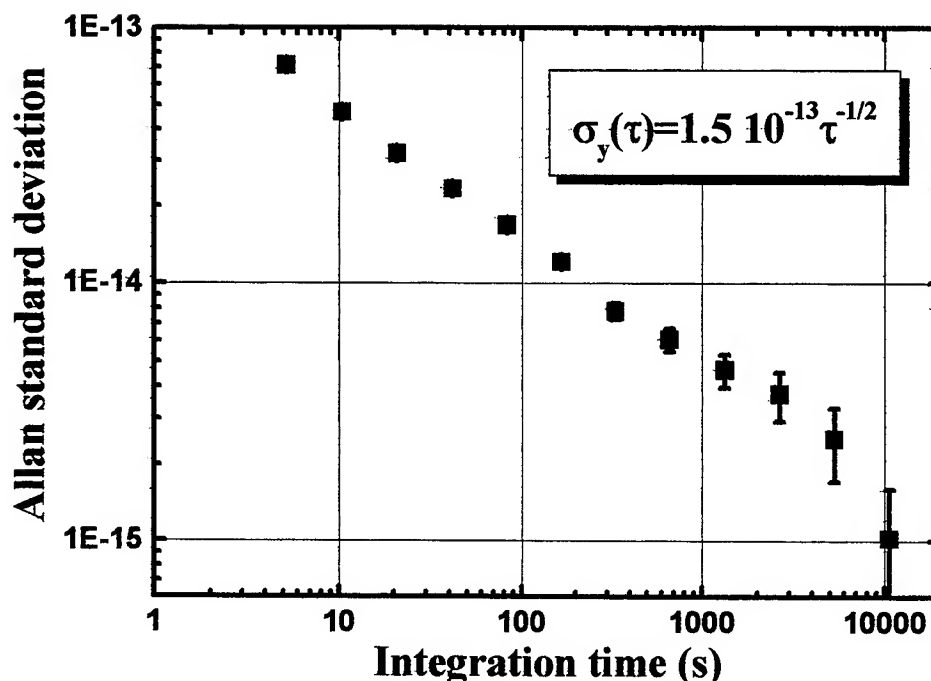


Fig.3 Allan standard deviation, $\sigma_y(\tau)$ of the rubidium fountain against H-maser.
The short stability is limited by phase noise of the local oscillator.

2. MEASUREMENT OF THE ^{87}Rb GROUND STATE HYPERFINE SPLITTING

As shown in Fig.4, in the BNM-LPTF two Cs fountains^{15,16}, the present Rb fountain, and a Cs thermal beam¹⁷ are operating. The interrogating microwave frequency of each clock is generated from the same local oscillator, which delivers a 100 MHz frequency with a low phase noise. This frequency is synthesised from a 5 MHz low noise BVA quartz¹⁸ weakly locked on the H-maser. Thus, it is possible to compare directly each clock with one of the others and reject the noise induced by the H-maser frequency variations, of the order of 3×10^{-15} per day. Using one Cs fountain we track the H-maser frequency with a 1.4×10^{-15} accuracy.

In order to measure the rubidium ground – state hyperfine frequency against the cesium primary standard, we first determine the absolute frequency of the reference H-maser by comparison with the LPTF's Cs fountain. This comparison being made with a resolution better than 1×10^{-15} , the H-maser frequency is known with the cesium fountain 2×10^{-15} absolute accuracy. Second, we correct the measured frequency to take into account different systematic shifts^{19,20} listed in Table I.

Our new value for the ^{87}Rb hyperfine frequency is 6 834 682 610.904 333 (17) Hz. The resulting accuracy of our measurement of the ^{87}Rb ground state hyperfine splitting is 2.4×10^{-15} . This measurement is in agreement with the value we previously published⁵. Its accuracy has been improved by a factor 6, by reducing microwave leakage and magnetic field fluctuations in the interrogation region.

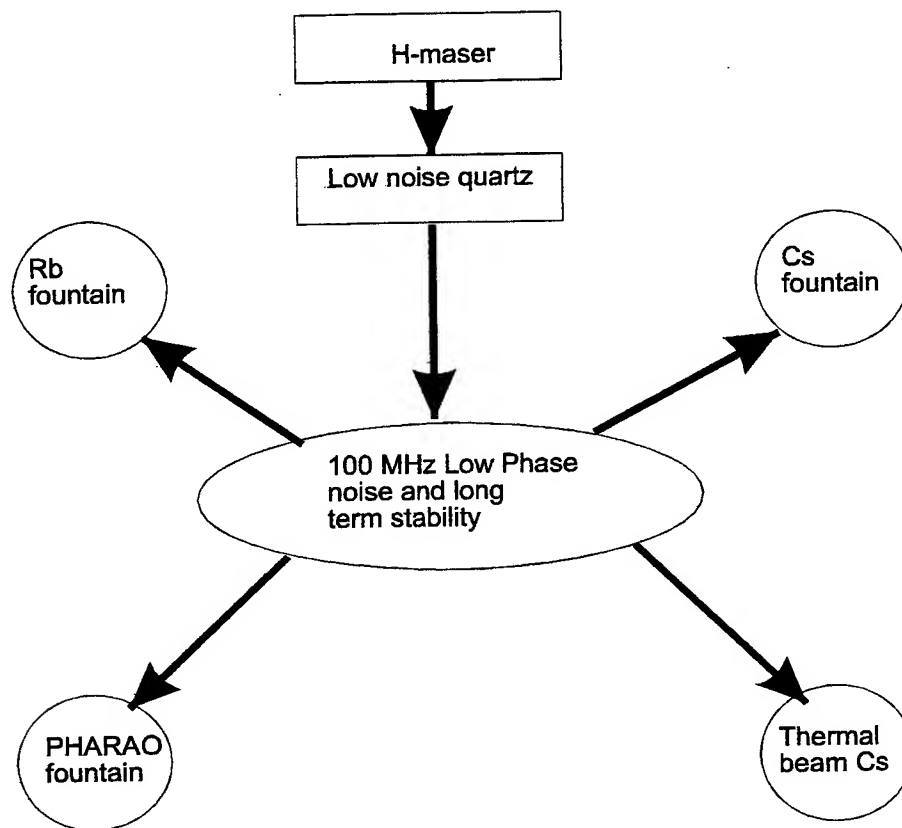


Fig.4 LPTF's clock ensemble

Tab. I Frequency shifts and related uncertainties for a set-up temperature $T = 296$ K, a magnetic field $B = 50$ nT, an average density $n = 2.5 \times 10^7 \text{ cm}^{-3}$ and an atomic resonance quality factor of 6.2×10^9 . The redshift correspond to a height above the geoid of 65(5) m.

Effect	Frequency shift (10^{-5} Hz)	Uncertainty (10^{-5} Hz)
First order Doppler	0.0	0.5
Gravitational Redshift	+ 5.2	0.5
Second order Zeeman	+14.1	0.5
Black body radiation	- 8.1	0.5
Microwave leakage, Ramsey and Rabi pulling...	0	1.5
Collisions	- 0.13	0.6
Total uncertainty	-	1.9

The achievement of high-precision Rb clocks also opens the way for several new experiments. A search for a possible drift of the fine-structure constant can be done^{4, 20, 21} by comparison of the hyperfine energies of alkali atoms with different Z numbers over an extended period of time (~ year). We estimate that using Rb and Cs fountains, $\dot{\alpha}/\alpha$ can be tested at a level of 10^{-16} per year, which would represent a 100-fold improvement compared to the present best laboratory tests. In conclusion, we have operated a ⁸⁷Rb fountain. The present short stability of this Rb clock is $1.5 \cdot 10^{-13} \tau^{-1/2}$. Given its small collisional shift, ⁸⁷Rb seems to be able to surpass the ¹³³Cs primary frequency standard and reach the 10^{-17} accuracy range.

3.CONCLUSIONS

We have operated a ⁸⁷Rb fountain. The present short stability of this Rb clock is $1.5 \cdot 10^{-13} \tau^{-1/2}$. Given its small collisional shift, ⁸⁷Rb seems to be able to surpass the ¹³³Cs primary frequency standard and reach the 10^{-17} accuracy range. The second point of interest is the fact that accuracy in the 10^{-16} range should make it possible to search for possible drift of the fine structure constant $\alpha = e^2/\hbar c$ with time.

ACKNOWLEDGE

This work was supported by BNM and CNRS. We are grateful to M. Lours, M. Dequin, P. Aynie, A. Legrand, A.H. Gerard and L. Volodimer for useful contributions. BNM-LPTF is Unité Associée au CNRS (UMR 8630). Laboratoire Kastler Brossel is Unité Associée au CNRS (URA 18) et à l'Université Paris 6.

REFERENCES

1. Essen L. et al., *Nature*, **189**, p.298, 1961.
2. Arditi M. et al., *IEEE Trans. Instrum. Meas.*, **IM-21**, p.391, 1972.
3. Kokkelmans S. J. et al., "Predictions for laser-cooled Rb clocks", *Phys. Rev. A*, **56**, p.4389, 1997.
4. Fertig C. et al., "Laser-cooled Rb clocks", *Proceedings of the 52th Frequency Control Symposium*, p.18, 1998.
5. Prestage J. D. et al., "Atomic clocks and variations of the fine structure constant", *Phys. Rev. Lett.*, **74**, p.3511, 1995.
6. Ghezali S., "Première évaluation de l'exactitude d'une fontaine d'atomes froids de césium à $2 \cdot 10^{-15}$ et perspectives", *Thèse*, Paris, 1997.
7. Bize S. et al., "High-accuracy measurement of the ⁸⁷Rb ground-state hyperfine splitting in an atomic fountain", *Europhys. Lett.*, **45**, p.558, 1999.
8. Kasevich M. et al., "RF spectroscopy in an atomic fountain", *Phys. Rev. Lett.*, **63**, p.612, 1989.
9. Raab E. et al., "Trapping of neutral Sodium atoms with radiation pressure", *Phys. Rev. Lett.*, **59**, p.2631, 1987.
10. Lea S.N. et al., "Laser cooling and trapping of atoms : New tools for ultra-stable caesium clocks", *Physica Scripta*, **T51**, p.78, 1994.
11. Clairon A. et al., "Ramsey Resonance in a Zacharias Fountain", *Europhys. Lett.*, **16**, p.165, 1991.
12. Kastberg A. et al., "Adiabatic cooling of cesium to 700 nK in an optical lattice", *Phys. Rev. Lett.*, **74**, p.1542, 1995.
13. Vanier J and Audoin C, *The Quantum Physics of Atomic Frequency Standards*, Adam Hilger ed. IOP Publishing Ltd., Bristol, England, 1989.
14. Santarelli G., "Contributions à la réalisation d'une fontaine atomique", *Thèse*, Paris, 1998.
15. Clairon A. et al., "A Cesium fountain frequency standard: preliminary results", *IEEE Trans. on Instr. and Meas.*, **44**, p.128, 1995.
16. Laurent Ph. Et al., "A cold atom in absence of gravity", *Eur. Phys. J. D.*, **3**, p.201, 1998.
17. Makdissi A., "Traitement du signal appliqué aux étalons primaires de fréquence: amélioration de leur exactitude et de leur stabilité", *Thèse*, Paris (1999)
18. Simon E. et al., "Experimental measurement of the shift of Cs hyperfine splitting due a static electric field", *Proceedings of the 11th European Frequency and Time Forum*, p.43, 1997.
19. Rovera G.D. et al., "Frequency synthesis chain for the atomic fountain primary frequency standard", *IEEE Trans. Ultrason., Ferroelec., Freq. Contr.*, **UFFC 43**, p.354, 1996.
20. Ghezali S. et al., "An experimental study of the spin-exchange frequency shift in a laser cooled cesium fountain frequency standard", *Europhys. Lett.*, **36**, p.25, 1996.
21. J.K. Webb et al., "Search for time variation of the fine structure constant", *Phys. Rev. Lett.*, **82**, p.884, 1999.

Small power pulsed and continuous longitudinal CO₂ laser for material processing

Mircea Udrea^{a*}, Ali Alacakir^b, Akif Esendemir^c, Ozgul Kusdemir^b, Oguz Pervan^b,
Sinan Bilikmen^c

^aNational Institute for Laser, Plasma and Radiation Physics, MG-6, Bucharest, Romania

^bAnkara Nuclear Research And Training Center, 06105 Besevler, Ankara, Turkey

^cMiddle East Technical University, 06531 Ankara, Turkey

ABSTRACT

A small average power CO₂ laser for some industrial applications is presented. The laser might operate both in a continuous regime and in a pulsed one or in a combination of two. Average power up to 20 W and peak power of several hundreds of kW has been achieved. The advantages of the good optical quality beam of a longitudinal discharge laser and of a high peak power pulsed regime are simultaneously achieved. A high voltage capacitor, which is switched on by means of a rotary spark gap, sustains the pulsed regime. The commutation between the two regimes might be easily done and a mixed operation is obtainable. By superposition of the two regimes, a continuous heating of the material by the continuous beam as well as an evaporation due to high peak power are obtainable. Drilling, cutting and marking of different types of glasses as well as different plastic materials were performed.

Keywords: laser, material processing, atomic force microscopy.

1. INTRODUCTION

The low cost operation of the CO₂ laser continues to recommend it to be an attractive tool for much specific application. The small power (10... 50 W) lasers are still widely used. Some of the applications of these lasers need an average high power level other ones need a high peak power. A hybrid small power CO₂ laser for material processing is presented here. Average power up to 20 W, peak powers of hundreds of kW and beam divergence of 0.7 mrad have been obtained. The pulse operation is sustained by means of a rotary spark gap. The radiation of CO₂ laser is strongly absorbed in glasses. As a consequence, CO₂ laser sustained cutting, etching, polishing, forming of microstructures are possible¹. Fine polishing of glass is reported here. Also, fine polishing of optical fiber ends was accomplished.

Structure modifications of the irradiated material are studied using atomic force microscopy (AFM). AFM has become the most popular type of microscopy using a probe mounted on a very small spring cantilever. When the probe is scanned across the sample, the force between the probe tip and sample changes as the surface features encountered, causing the spring cantilever to deflect. In order to obtain the magnitude of the height displacement, a laser and four-quadrant detector are used to detect the motion of spring cantilever and provide a feedback signal as it is scanned across the sample.

2. EXPERIMENTAL DEVICE

A hybrid longitudinal CO₂ laser is presented² (Fig. 1). The laser might operate in a continuous wave regime, in a pulsed regime or in a superposition of two. The laser tube is a 60 cm length 11 mm internal diameter pyrex glass tube. The cooling water flows through a plastic pipe which is put in windings around the laser tube. No additional water filled glass envelope is necessary. The discharge electrodes consist of a hollow anode A and a hollow cathode K. The continuous regime is sustained by the high voltage supply HV₁ and the ballast resistor R₁. A simple rotary spark gap (RSG) rapidly switches the discharge of the capacitor C through the gas mixture. The capacitor value was varied in the range of 5...20 nF. The high voltage supply HV₂ charges the capacitor by the resistor R₂ up to 25 kV. The pulse repetition rate might be continuously varied by varying the rotation speed of the central plate of the rotary spark gap till several tenth of Hz. Six symmetrically placed pins multiply by six the rate of repetition of the pulses. The divergence of the laser beam was found to be 0.7 mrad.

*Correspondence: Email: udrea@newton.physics.metu.edu.tr

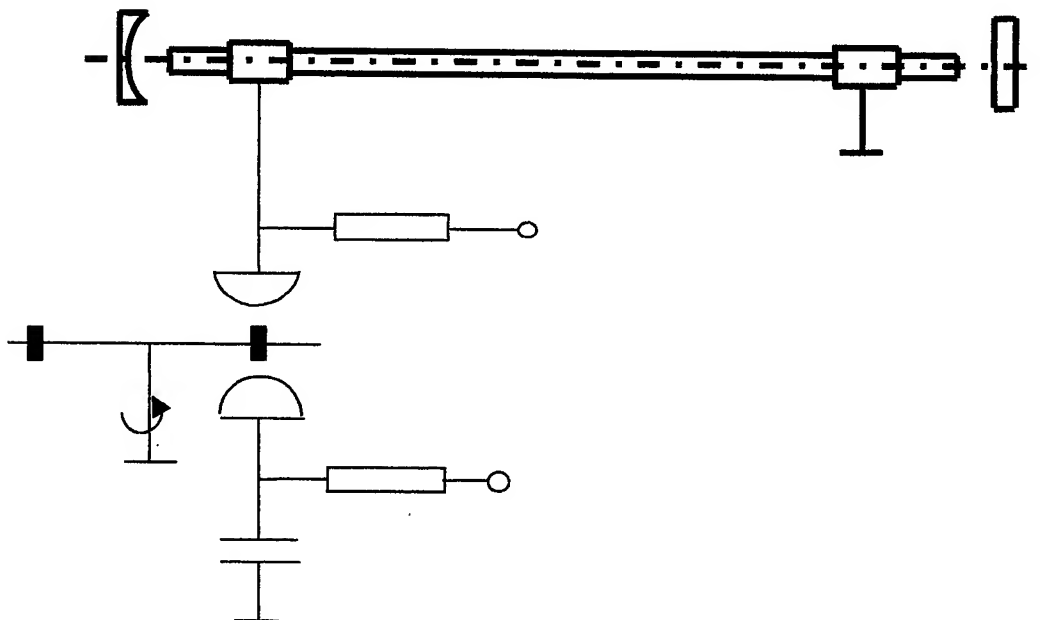


Fig. 1 Experimental device

Fig. 2 represents the interaction of the beam with a plastic sheet placed in front of the laser. The monomode beam profile might be observed. The divergence was measured over a 15-m distance. The results are plotted in Fig. 3.

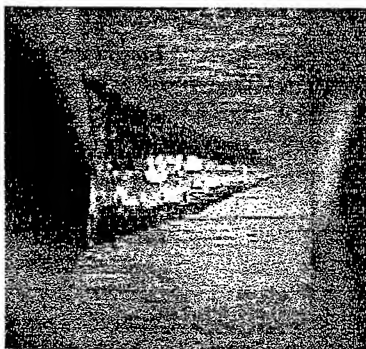


Fig. 2 Near field beam profile

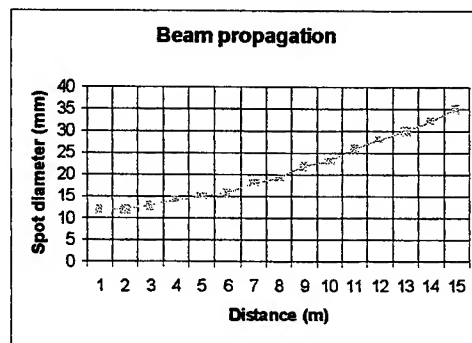


Fig. 3 Beam propagation

3. MATERIAL PROCESSING USING THE CO₂ LASER

3.1. Hole drilling

Many industrial applications of lasers involve the creation of an extended cavity within a material. Laser hole drilling can be successfully employed to produce components such as ink jet nozzle. Low ablation threshold, minimal thermal damage and high optical resolution have made excimer lasers the favoured tool for these applications. However, from the standpoint of low operating cost and industry acceptability, pulsed CO₂ lasers are attractive if suitable hole quality can be obtained¹. Laser radiation enters the drill hole and is dissipated at its surface. A temperature gradient exists between the interface where the laser radiation is absorbed and the surrounding solid. Due to this temperature gradient, microcracking of glass by CO₂ laser irradiation is occurring (see Fig. 4). The study of microcracking production and the use of some methods to avoid or to limit cracking are very important for practical applications. The hole quality depends on the limitation of cracking.

Our experiments consist of the irradiation of a glass sample till a hole is achieved. The diameter of the hole was found to be about 300 microns (Fig. 5). An air fan was used to cool the sample during the irradiation.

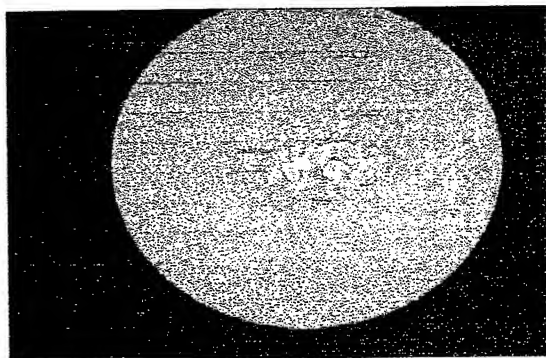


Fig. 4 Microcracking initiation
(power density $< 40 \text{ W/cm}^2$)

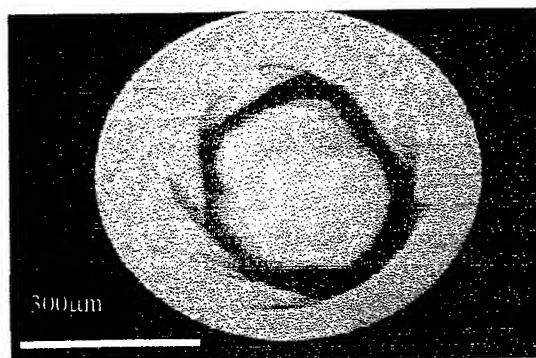


Fig. 5 Hole drilling in glass
(3 mm thin glass sample)

The cracking development was limited by using a cooling unit. This allows us to prevent after irradiation thermal stress. This thermal stress is responsible for cracking occurring. By moving the sample in front of the beam at a constant speed a chain of cracking is developing as it might be seen in Fig. 6.

No cooling is necessary in hole drilling when we have used a mixed regime (the superposition of the continuous regime and the pulsed one). The material is heated by the cw beam and it is evaporated by the pulses.

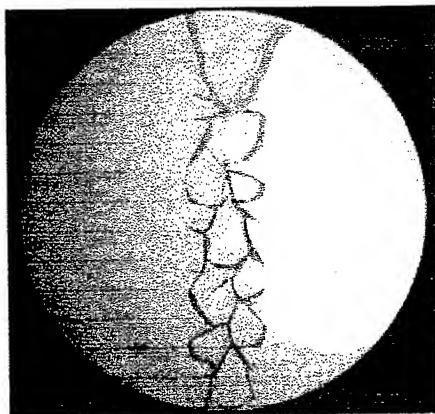


Fig. 6 Microcracking development (speed 0.8 mm/s , 3 mm thin glass, 20 W/cm^2 power density)

3.2. Glass cutting

The cutting of glasses has a lot of applications. Even the glass cutting was one of the first industrial laser applications, recent advances to laser glass cutting were presented this year to different top international meeting (Society for Information Display, San Jose, California, USA, 1999; CLEO'99, Munchen, Germany, 1999).

For example, Accudyne laser system passes light from a 200 W CO_2 laser through an optical path of four zinc selenide elements. During the cutting process, the beam is followed by a cooling stream of helium gas (that can also be mixed with water) to quench the substrate and facilitate the glass separation. The laser provided by the Schott Company uses a $10,6 \mu\text{m}$ CO_2 laser to heat the glass along the desired scribe line, followed immediately by a jet stream of cooling air. The cutting speeds for different types of glasses of 1-mm width vary from 7 cm/s to 20 cm/s .

The primary current application is cutting thin glass panel for plasma displays. Other applications include automotive glass, vacuum tubes, and glass tubes for medical and chemical applications.

In spite of the fact that the power of our laser is not so high we were able to get some useful results regarding the interaction of the laser beam with different types of glasses and to develop a new method to cut glasses that will be presented below. An example of cutting 3-mm glass at .8 mm/s speed is shown in Fig. 7.



Fig. 7 Glass cutting without cooling
speed: 0.8 mm/s; 3 mm thin glass

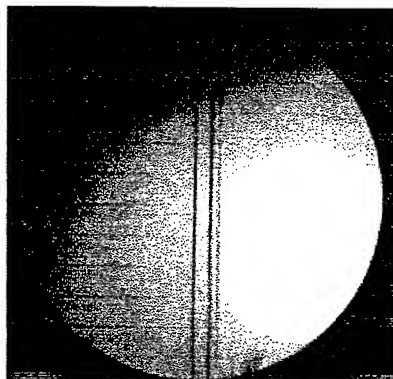


Fig. 8 Glass cutting under water
speed 0.8 mm/s; 3 mm thin glass

An innovative method of cutting without cracking has been developed. It consists of the introducing of the sample into water in such a manner that only a thin layer of water is covering the glass surface. So, a good cooling of the whole sample is accomplished. In Fig. 8 a perfect cut which was obtained using this method is shown.

3.3. Fine polishing of glasses

For a given small power density, the aspect of the irradiated surface is a very specific one. We call it UFO like. Its microscopic picture is given in Fig. 9. A fine polished surface is revealed. The surface, which is shown in Fig. 9, was investigated also using atomic force microscopy. A clear difference between the quality of the glass before and after irradiation might be observed. So, a method to fine polishing of glass surfaces was put into evidence. A power density threshold of about 20 W/cm² was found. The irradiation time was about 15 seconds. For larger surfaces two methods might be used: a laser scanning of the surface and the use of a more powerful laser which is able to assure a uniform power density in the given time onto the whole surface. The parameters which we have found to be the optimal ones means an energy density of about 300 J/cm².

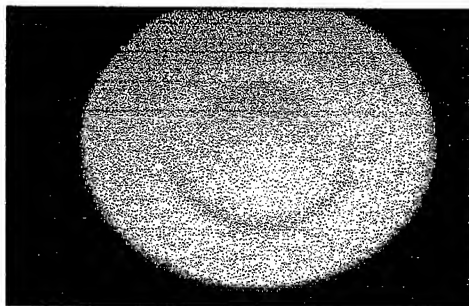


Fig. 9 UFO like polished surface (power density 20 W/cm²)

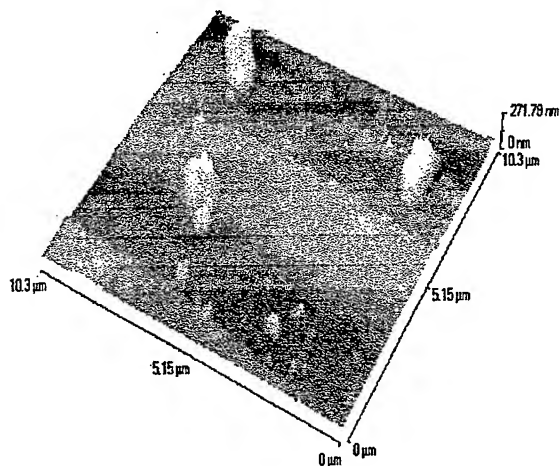


Fig. 10 Glass surface before laser polishing

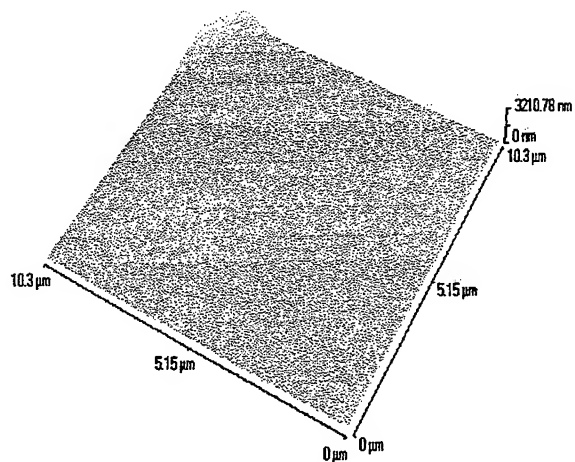


Fig. 11 Glass surface after laser polishing

3.4. Optical fiber polishing

Taking into account the results we have obtained by laser glass polishing we have performed the polishing of the ends of optical fibers. The surfaces of the sample were photographed both before and after irradiation. The image of the optical fiber end was taken by means of an Leitz optical microscope and an TopoMetrix atomic force microscope. The optical microscope image was lead to a computer connected CCD camera as in the previous experiments.

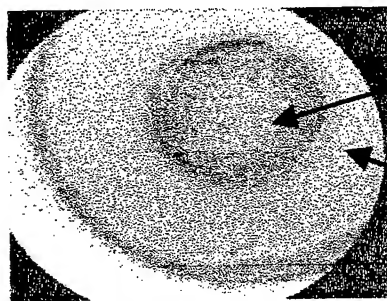


Fig. 12 Optical microscope picture of the optical fiber end, before irradiation (mechanically cut, 5 μ m alumina powder pre-polished, x 10 magnification)

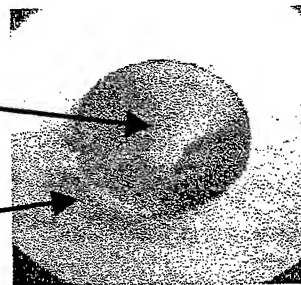


Fig. 13 Optical microscope picture of the optical fiber end, after irradiation (x 10 magnification)

This part was deeply investigated by means of an atomic force microscope and the results are given in Figs. 14 and 15.

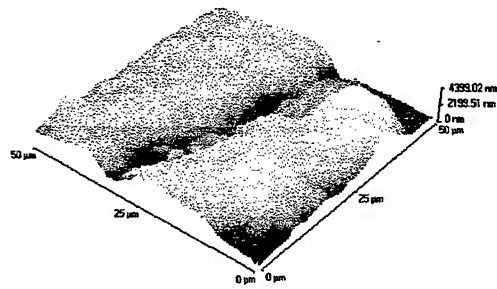


Fig. 14 Atomic force microscope picture of the sample, before irradiation

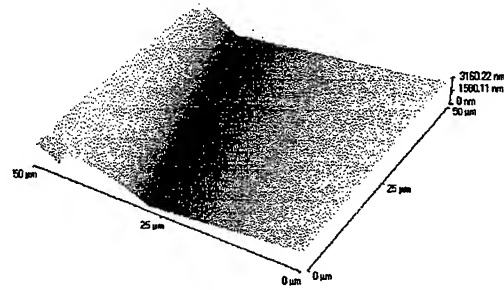


Fig. 15 Atomic force microscope picture of the sample, after irradiation

It might be easily seen from the atomic force microscope picture how the hills are melted and disappeared after a proper laser irradiation. Also, the plastic coatings around the core-cladding structure are completely evaporated for several millimeters depth.

In conclusion, the use of a low power, reliable and cheap laser, as CO₂ laser is, is still an efficient method of material processing. We have investigated here the capability of this laser to perform glass processing as drilling, cutting, polishing. A lot of plastic materials find in the CO₂ laser a convenient tool.

The superposition of the continuous wave beam and the pulsed beam delivered by the same laser tube increased significantly the quality of the holes which were performed in glass.

ACKNOWLEDGEMENTS

Dr.Mircea Udrea is supported by TUBITAK, The Turkish Scientific and Technical Research Council. He is on leave from the National Institute for Laser, Plasma and Radiation, Lasers Department, Bucharest, Romania.

REFERENCES

1. C.Buerhop, B.Blumenthal, R.Weissmann, N.Lutz, and S.Biermann "Glass surface treatment with excimer and CO₂ lasers", *Applied Surface Science*, **46**, pp.430-434, 1990.
2. Mircea Udrea, Ali Alacakir, Sinan Bilikmen, Özgül Kusdemir and Oguz Pervan, "Monomode Hybrid Longitudinal CO₂ Laser for Material Processing", *Proc.IL'99, International Conference on Industrial Lasers*, October 25-27, Wuhan, China, 1999.

Wide band acoustic transducer

Robu Octavian^a, Robu Maria^{b*}

^aMarine Equipment Scientific Research Centre Constanta

^bInstitute of Optoelectronics, Bucharest, Romania

ABSTRACT

One of our latest developments regards the achievement of an omnidirectional acoustic transducer able to work in marine environment in a wide band of frequency. Our research has involved allowing a fairly linear variation of the impedance active component. This paper presents some aspects concerning the effective achievement of the acoustic transducer and the compensation of the impedance reactive component in order to obtain a maximum transfer of power. The acoustic transducers have a specific construction and are made of PZT-type piezoelectric ceramic obtained in laboratory. Some essential aspects of the measurement methodology and the results obtained are also addressed.

Keywords: PZT ceramics, acoustic transducer

1. INTRODUCTION

The paper presents the way of development of a transducer for noise simulation of a ship, which is moving with variable speed, in a given frequency range.

Mainly, the noise radiated by a ship could be seen as a white noise, amplitude modulated by the propeller frequency¹.

The first figure presents principle scheme of such a simulator, its load being the wide band acoustic transducer.

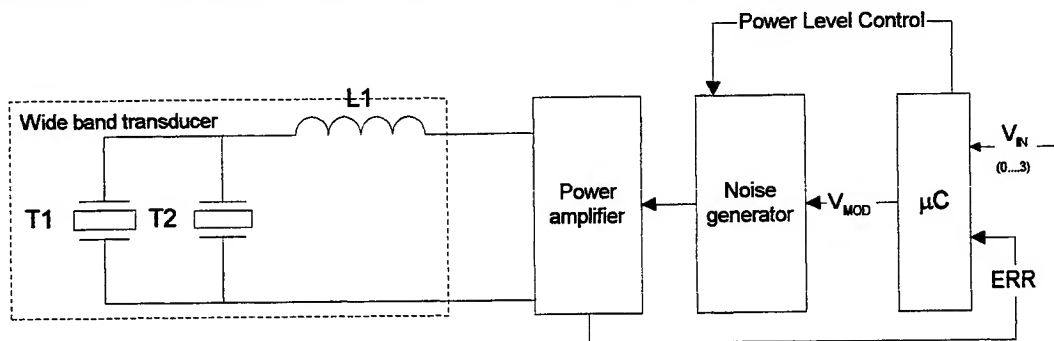


Fig. 1 Scheme of the noise simulator

The simulator of the ship noise contains the following items:

- the wide band acoustic transducer, built to operate in marine environment, with maximum transfer of the energy;
- the power amplifier, which ensures the required acoustic pressure level;
- the signal generator, which provides white noise in the given band, modulated by the propeller frequency;
- the microcontroller which makes data acquisition in form of a DC voltage, proportional with the propeller speed, and controls the signal generator modulation.

The propeller frequency depends on the number of propeller blades and the reduction ratio of the gear, as follows:

* Correspondence:

Phone: 780.66.40, Fax: 423.25.32

$$f\left(\frac{\text{rounds}}{\text{sec}}\right) = N_p \cdot R_r \cdot 1000 \cdot \frac{V}{V_{\max}} \cdot \frac{1}{60}$$

where: N_p - number of blades;

R_r - reduction ratio of the gear,

V - voltage of the tat-generator that measures the propulsion engine speed.

The micro-controller (μC) makes acquisition of data from max. 4 engines, computes the frequency of each propeller and then it generates the modulation tension for the signal generator.

Thus, the white noise on the transducer is amplitude modulated by the signal given by the following relationship:

$$U_m = \frac{3}{4} \sum_{i=0}^3 a_i f_i$$

where: a_i takes 0 or 1 values.

In order to provide the required acoustical pressure level, the μC controls the electrical power generated through the power amplifier.

The variation of the electrical power applied to the transducer is controlled by changing the power supply tension, performed by a software based on loading current surveillance.

2. THE CONSTRUCTION OF THE BROAD FREQUENCY RANGE TRANSDUCER

In order to reach the proposed aim, as we presented above, a study on the transducer presented in Fig. 2 was performed⁴. The transducer contains the main elements:

- the acoustic envelope (1);
- the ensemble of the piezo-ceramic elements (2);
- the coupling fluid (3).

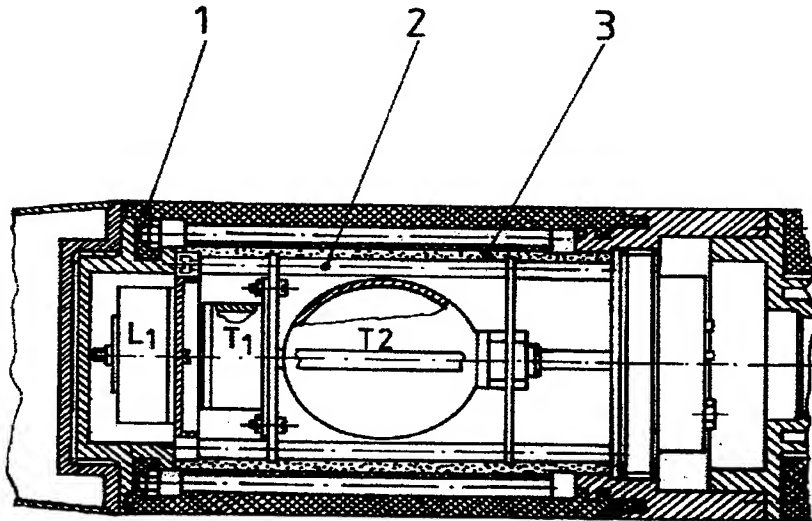


Fig. 2 Scheme of the transducers ensemble

The ensemble of the piezo-ceramic element (2) contains a spherical (T1) and cylindrical (T2) piezo-ceramic elements, parallel coupled.

The inductance L1 makes a compensation of the reactive part of the transducer impedance, in the middle of the band, in order to obtain a uniform variation of the active part of it.

The piezo-ceramic elements and the compensation inductance are located on a mechanical structure, and they are covered by an acoustic transparent envelope (1). This envelope is made of a mechanical structure, covered by rubber and has the acoustic impedance of the working environment³.

The ensemble of the piezo-ceramic element (2) is sunk in the coupling fluid (3), which nearly has the same impedance as the working environment. The transducer built as above mentioned, is a rigid and water-tight body and can work in the marine environment, with maximum energy transfer.

The aim of this way of building is to provide a coupling element between the piezo-ceramic elements and the working environment, which would be able to prevent major loss of energy. In this case, the coupling element contains two layers: one of them is made of castor oil in which the element (2) was sunk, and the second layer made of a rubber mixture. Both layers have the same acoustic impedance. The thickness of the rubber layer is equal to $\lambda/2$, in order to take into account the transparency and reflection coefficients, in the middle of the band⁴.

The piezo-ceramic elements are of PZT type in a structure: $\text{Pb}(\text{Zr}_{0.53} \text{Ti}_{0.47})\text{O}_3$ obtained through classical technology from oxide powders (ZrO_2 , TiO_2 and PbO), in laboratory.

These piezo-ceramic elements have the following properties:

- mass density - 7.5 g/cm³
- electromechanical coupling coefficient - $K_p = 0.55$
- loss factor - $\text{tg}\delta = 0.01$
- permittivity coefficient $\epsilon = 1000$.

3. EXPERIMENTAL RESULTS

There were three stages in manufacturing the wide band acoustic transducer.

During the first stage, the ensemble of piezo-ceramic elements was obtained from spherical and cylindrical elements to cover the required frequency band. Impedance measurements for both air and oil were performed and thus the value of compensation inductance of the reactive part was computed and adjusted in such a way that the active part of the ensemble impedance to be approximately a line and to minimise the loss of power.

During the second stage a coupling system between acoustic ensemble with the environment was obtained. The aim was that the power loss to be the least. Thus a rubber mixture with "pc" almost equal to those of seawater was studied. Finally, both layers, castor oil and rubber, should ensure a maximum transparency coefficient.

The following table presents the main characteristics of that "pc" rubber in comparison with castor oil and sea water: (Tab. 1)

Tab. 1 Comparative features for different types of fluids

	"pc" rubber	Castor-oil	Sea water
Mass density ρ (kg/m ³)	1050	950	1026
Sound speed c (m/sec)	1466	1540	1500
Acoustic impedance pc (rayls)	$1.54 \cdot 10^6$	$1.45 \cdot 10^6$	$1.54 \cdot 10^6$

During the third stage, measurements of the whole transducer were performed, as follows:

- a) impedance vs. frequency (the three voltmeter method , keeping the same output voltage on the generator).

The scheme is presented by Fig. 3:

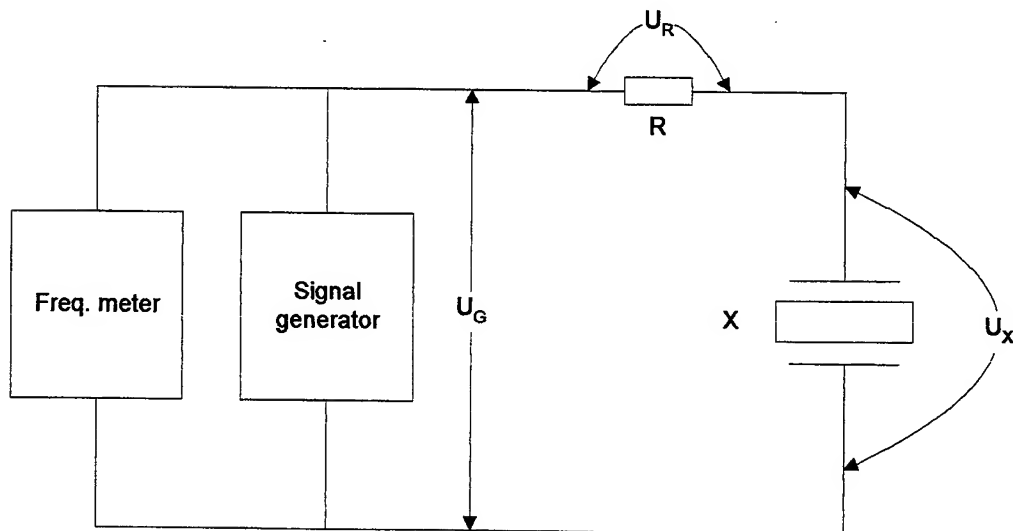


Fig. 3 Impedance measuring circuit for the transducers ensemble

Fig. 4 presents the variation of the active part of transducer impedance:

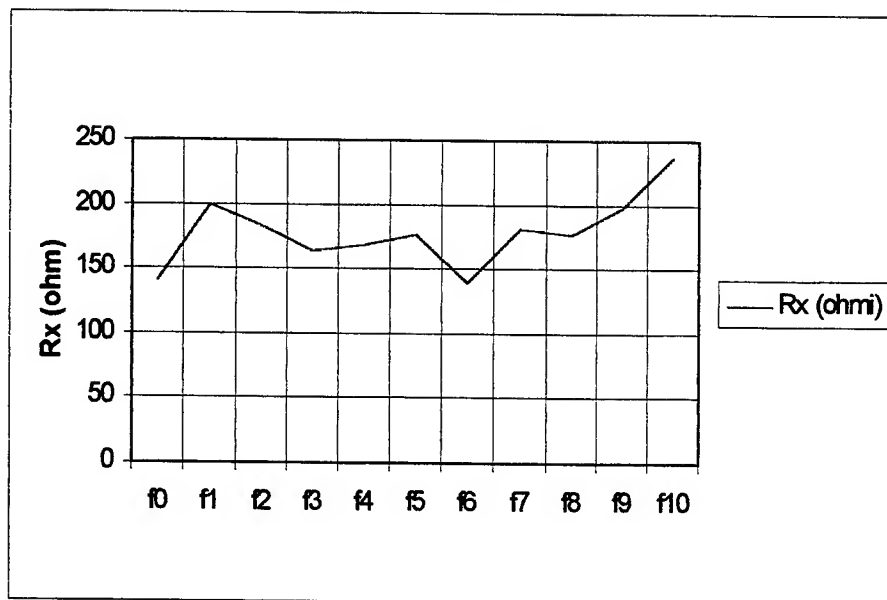


Fig. 4 Impedance active resonance oscillation with frequency of the transducers ensemble

b) plotting the directive diagram of the transducer in a horizontal plane. The directive diagram plotting was performed in a phono-absorbant tank, using the scheme in Fig. 5².

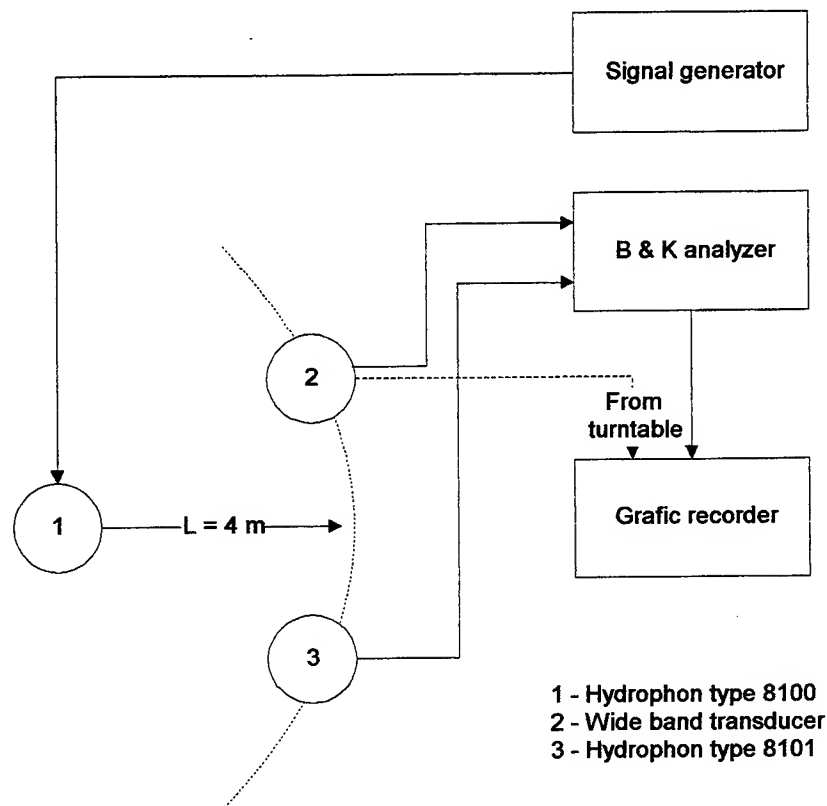


Fig. 5 The measuring scheme of the directivity diagram of the transducers ensemble

Fig. 6 presents the results obtained from plotting the directive diagram of the transducer, for the central frequency of the working band, in rectangular co-ordinates⁴:

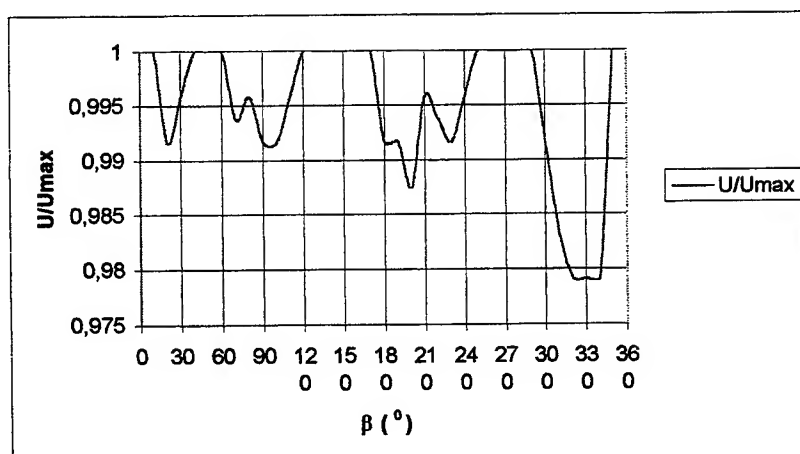


Fig. 6 The directivity diagram of the transducers ensemble

c) measurement of the acoustic pressure generated by whole transducer in frequency band. The measurement scheme is presented by Fig. 7:

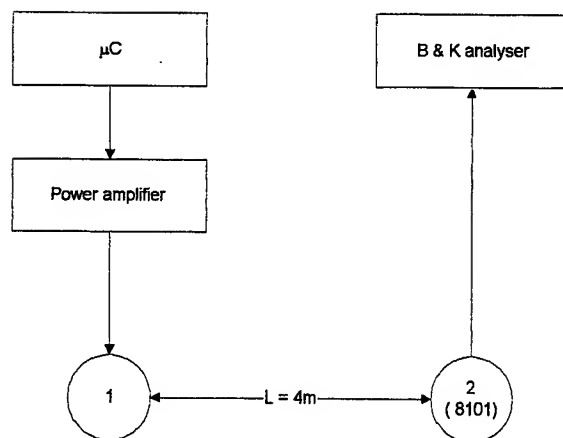


Fig. 7 The measuring scheme of the acoustic pressure level

Wide band transducer- WBT was fed as the Fig. 1 presented. The measurement took place in a phono-absorbant tank. The variation of the acoustic pressure in dB (reference – 1 μPa) is presented in Fig. 8:

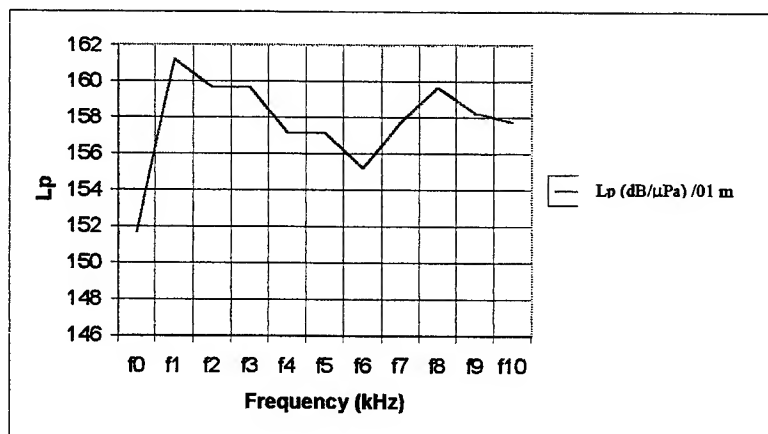


Fig. 8 The oscillation of the acoustic pressure level in the working (wave) band

The results met the proposed aim.

4. CONCLUSIONS

This paper presents certain technological aspects regarding the achievement of piezoceramic transducers to be used within a one-way acoustic transducer for a maximum transfer of power. The methodology measuring of them as well as the results obtained are equally summarised below.

REFERENCES

1. R.J.Urick, *Principles of underwater sound*, Mc. Graw-Hill Company, 3d edition, 1983.
2. R.J. Bobber, *Underwater electroacoustic measurements*, Peninsula Publishing, Los Atlas, California, USA, 1988.
3. O.B. Wilson, *Introduction to Theory and Design of Sonar Transducers*, Peninsula Publishing, Los Atlas, California, USA, 1988.
4. O. Robu, *Methods and Arrangements for Non-Destructive Multi-Parametric Control. Sonar Devices for Marine Environment Control*, Ph. D. Thesis, Central Institute of Physics, Bucharest, 1990.

Equipment for gluing the parts of an optoelectronic detector

Brindus Comanescu^{a*}, Adelina Ighigeanu^a, Daniel Oancea^a, Mihai Petcu^a, Bogdan Tatulea^a,
Gueorgui Chelkov^b, Dmitri Dedovich^b, Petr Evtoukhovitch^b, Alexi Gongadze^b, Serguei Podkladkin^b,
Edisher Tskhadadze^b, Dan Vasile^c, Melu Vlad^c

^aInstitute of Optoelectronics, 111 Atomistilor St, PO Box MG 22, Bucharest, Romania

^bJoint Institute for Nuclear Research, 141980 Dubna, Russia,

^cElectronics and Automatics Company, 242 Calea Floreasca, Bucharest 2, Romania

ABSTRACT

This paper describes equipment used for gluing the parts of an optoelectronic detector¹. Two rails compose this equipment and a dispenser and electronically system for control the moving of dispenser in two directions and the start/ stop of the glue. For rails we use modular components. The moving on the X direction is realized with two long shaft and bushing. For transversal moving we use a special guiding and bushing. This equipment will fixed on a granite table using special support. Electronic system will fixed on a control panel near a granite table and will link with thin and very flexible cable with equipment.

Keywords: Gluing equipment, devices for gluing Al tubes

1. INTRODUCTION

The optoelectronic detector - drift chamber will be used in muon system of Atlas collaboration at CERN. This chamber is composed by:

1. frame;
2. two multilayer with Al drift tubes;
3. optoelectronic system;

The frame is composed by two long beams and three cross plates.

The multilayers are composed by three layers of Al drift tubes each and glued on the both side of the chamber frame.

The optoelectronic system is composed by an optic system connected to a computer. This system can monitoring and controls the correct position of detector.

During the fabrication of detector we are need to use special tools. This tool was realized with a very high accuracy and with the respect of the technical restriction^{1,2}.

For fabrication we are need a granite table where we put all the tools and a dedicated chamber for this application with special condition for environment. This restriction was impose by the granite table and other tools and devices because if we don't use this condition of environment the surface of a granite table and other systems will be not in the range.

On the granite table we have:

1. support for detector frame;
2. support for Al drift tubes;
3. gluing equipment.

The support for detector frame is composed by six high precisions towers, three for each long side of detector. Three towers are fixed on the support for Al tubes and three towers can be moved on the granite table.

* Correspondence: Email: brindus.comanescu@yahoo.com; Phone: 00401.780.66.40; Fax: 00401.423.25.32

The support for tubes is a suction equipment used for keep the tubes during the gluing procedure of the tubes on the chamber frame.

Gluing equipment is used for gluing the tubes on the frame. Is fixed on the granite table with supports.

2. DESCRIPTION OF EQUIPMENT

Gluing equipment (Fig. 1) is electromechanical equipment fixed with support on the granite table used for gluing the tubes on the chamber frame.

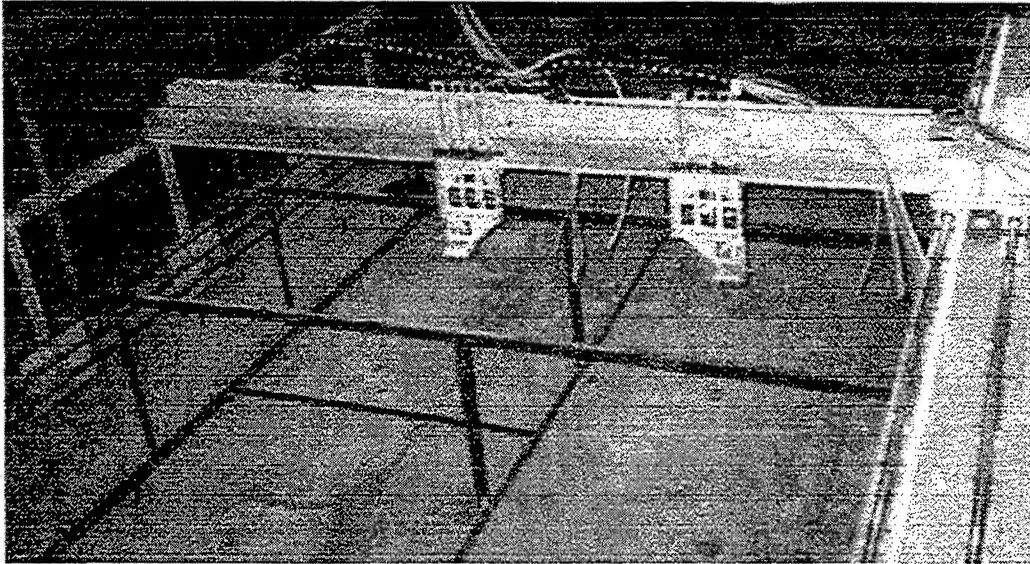


Fig. 1 Glue Machine

This equipment is composed by:

- supports;
- rail for x axis;
- rail for y axis;
- electronic system.

The direction for moving is:

- X direction for moving along tubes;
- Y direction for moving in a perpendicular direction to the tubes;
- Z direction for moving in the direction perpendicular to X and Y.

The support are made from modular aluminum profile, connected with special connectors and nuts and fixed on the granite table.

Rail for X-axis is composed by:

- base;
- guiding system;
- car;
- actuator.

The base is made from aluminum and is mounted on the modular aluminum support. Guiding system is mounted on the base. Using this system the friction is insignificant and we can use a small, usual and not powerful actuator. Two shafts and four bushing compose the guiding system.

The car is mounted on the guiding system. On the plate we mounted a rack for moving the transversal car along the Y-axis, the pieces for mechanical stop, two switchers for stop the actuator on the X-axis (Fig. 2).

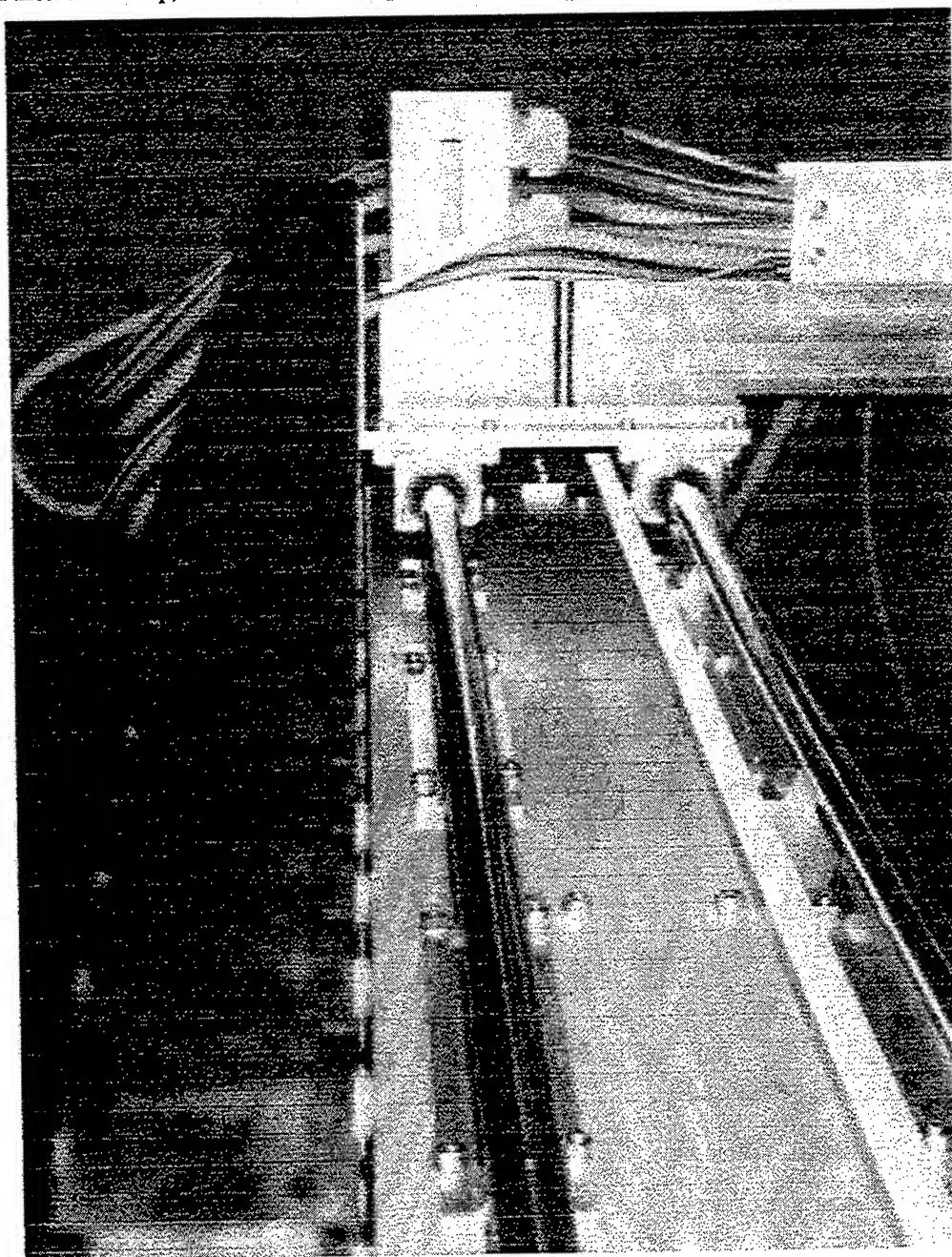


Fig. 2 Rails for Glue Machine

The rail for Y-axis is composed by:

- long beam for support the Y moving;
- two special guiding;
- wheel assembly;
- two dispensers;

Long beam is mounted on car. On the long beam is mounted the special guiding system, the wheel assembly and the dispensers. Wheel assembly is made from aluminum profile and the wheel. The diameter of the wheel and distance between two wheels is the similar with the distance between two tubes on the support on the granite table.

The dispenser (Fig. 3) is composed by:

- frame;
- three actuator for pushing the glue;
- two actuator for stop glue;
- an actuator with gear box for transversal moving;
- three cylinder for pushing glue;
- special wheel assembly;
- guiding for moving along Z axis;
- nozzle.

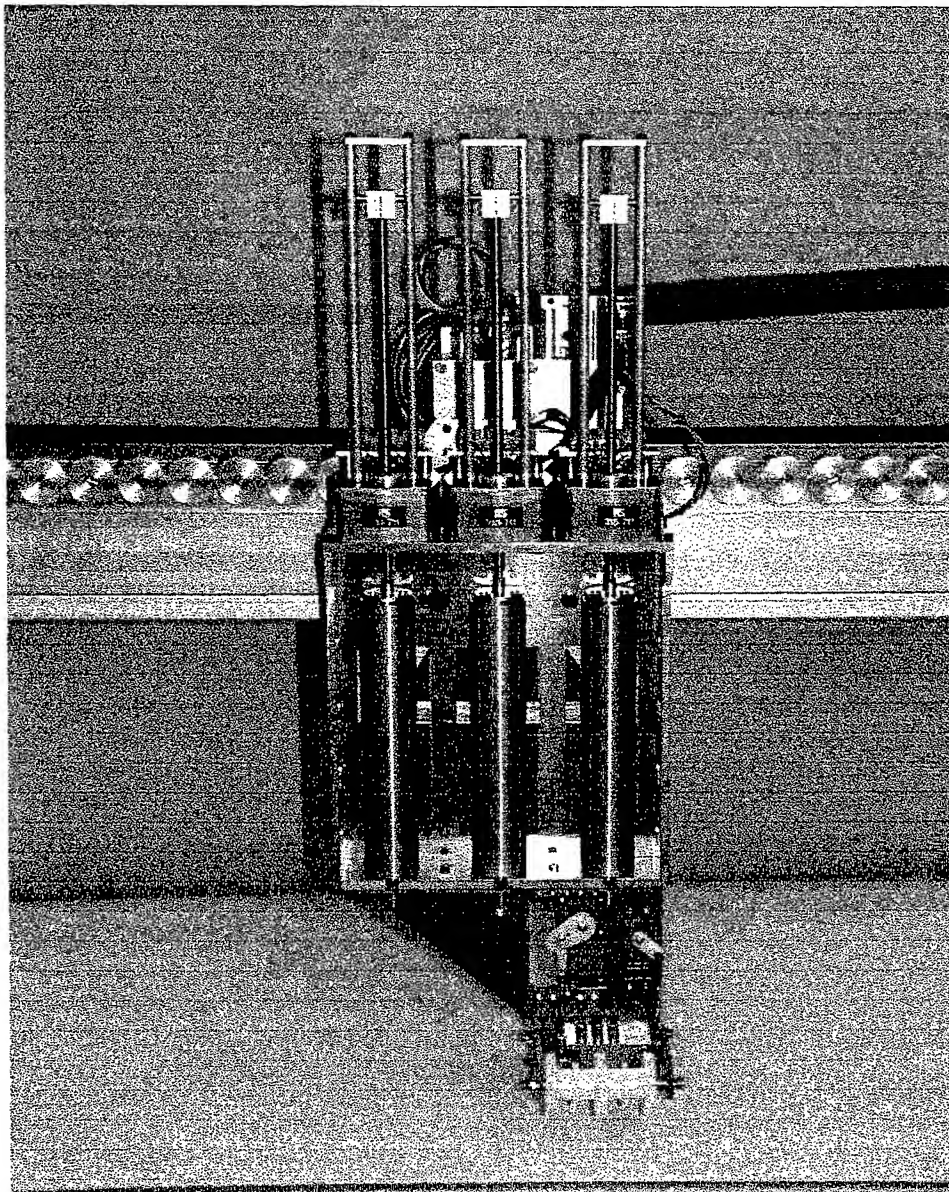


Fig. 3 Dispenser

The dispenser can be moved on the transversal direction using an actuator with a gearbox. The dispenser is moved step by step using the wheel assembly (Fig. 4 a and 4 b).

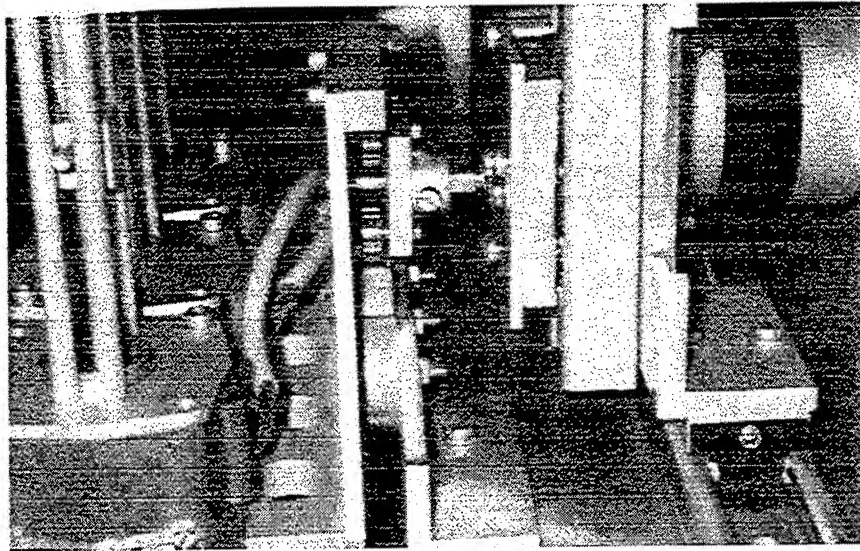


Fig. 4 a) Moving of dispenser, first step

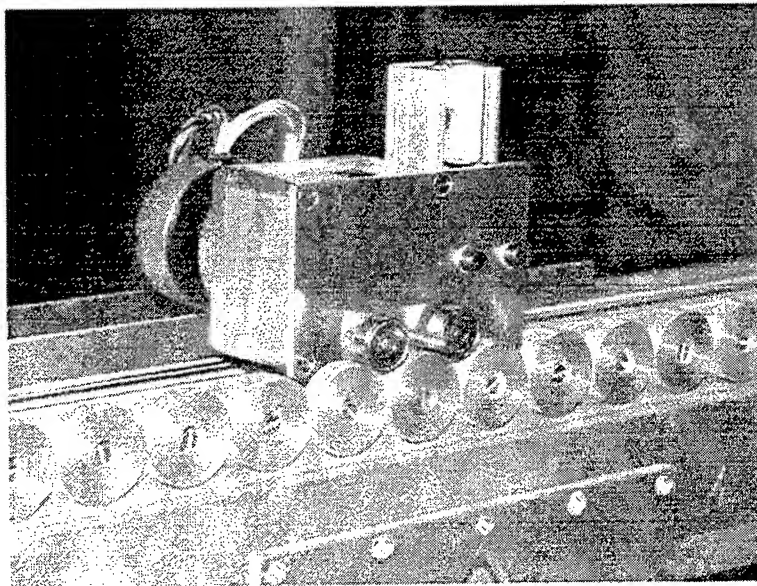


Fig. 4 b) Moving of dispenser, second step

The frame is made from aluminum. On the frame are mounted three actuators for pushing the glue through cylinders and two actuators for stop the glue through nozzle. The special wheel assembly is used for positioned the dispenser on the tube (Fig. 5).

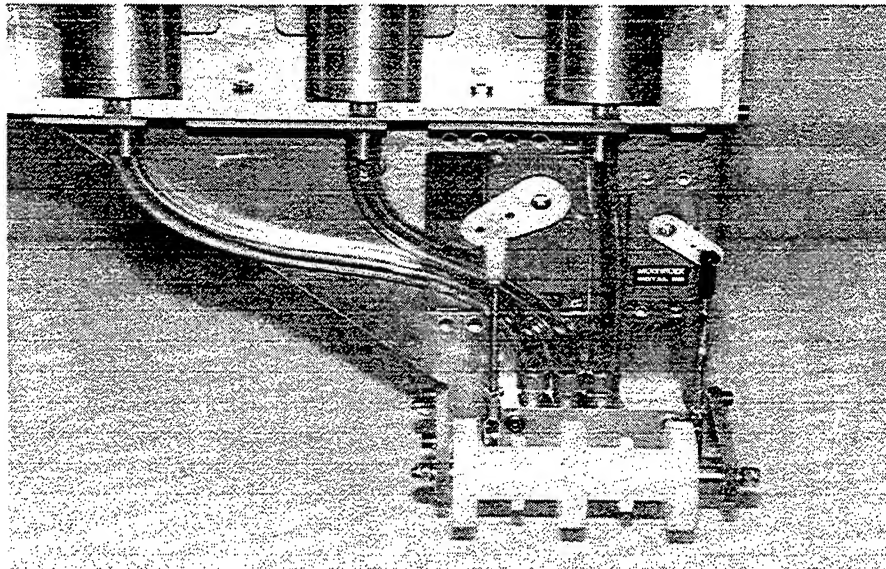


Fig. 5 Wheel assembly

The nozzle is special designed for this application. Is made from brass.

In Fig. 6 is presented a nozzle composed by:

- outlet;
- body;
- special shaft;

The outlet is designed after research regarding gluing the tubes.

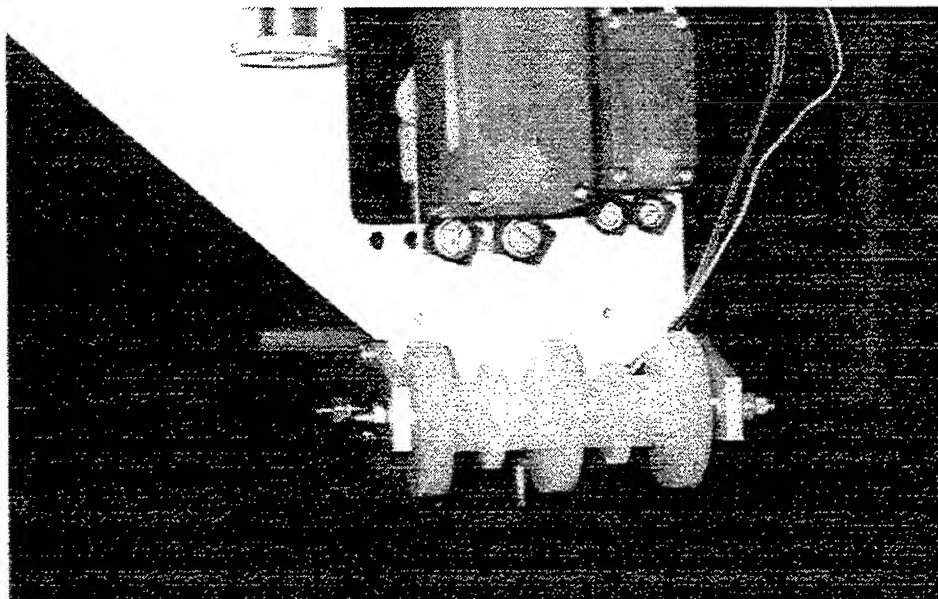


Fig. 6 Nozzle

3. METHOD FOR OBTAIN THE NOZZLE

As we mentioned for gluing the tube is very important how we design the outlet and how we tuning the speed of the car along X-axis, a speed of the actuator for push the glue through the cylinder.

For glue the tubes we get two lines of glue at 60 and 120 degree and one glue line has to be applied to the gap between two tubes. For this reason the nozzle will be provided with three outlets.

A cross sectional area of a rope of glue 0.5 mm^2 is enough to produce a good fixation of a next layer. The width of rope is 3 mm. For obtain a good fixation of the tubes we choose araldit for glue and after research we find that the speed of the dispenser is 0.25 m/ sec^3 .

The force that we are need to push the glue through the cylinder for obtain a good rope is 125 N. For fabrication the detector we have a limits of the time for gluing a layer, 75 min. This is the reason for that we use two headers in parallel and with this solution we obtain an considerable reduction of time for gluing a layer³.

4. CONCLUSIONS

The equipment for gluing the parts of an optoelectronical detector was designed as a modular system. For this reason, the components of equipment can be very assembled and disassembled using common tools.

This is an semiautomatic machine. Using photo gates, switchers, the machine glue the components of an optoelectronical detector, controlling the moving of dispensers in 2 axis.

ACKNOWLEDGEMENTS

We would like to thank Atlas muon group members of MPI (Munich, Germany) for the very useful discussions on the engineering aspects of design and the procedure for controlling of the system.

REFERENCES

1. ***, *Atlas Technical Design Reports and Proposal*, 1997.
2. C. Capoccia, S. Cerioni, M. Curatolo, B. Esposito, M.L.Ferrer and G. Maccarrone, *B M L Assembly Manual*, INFN- LNF Frascati, Italy, 1999.
3. H. Kroha, A. Nonz and D. Kaltenbrenner, *Glue Dispenser*, 1999.

Method for calculus of the sag of frame of an optoelectronic detector

Brindus Comanescu^{a*}, Adelina Ighigeanu^a, Daniel Oancea^a, Mihai Petcu^a, Bogdan Tatulea^a,
Gueorgui Chelkov^b, Dmitri Dedovich^b, Petr Evtoukhovitch^b, Alexi Gongadze^b, Serguei Podkladkin^b,
Edisher Tskhadadze^b

^aInstitute of Optoelectronics, 111 Atomistilor St, PO Box MG 22, Bucharest, Romania

^bJoint Institute for Nuclear Research 141980 Dubna, Russia

ABSTRACT

An optoelectronic detector is composed by a frame where we assemble all the parts. Technical condition, 20 μm on the wire positioning requires a high level of mechanical precision in the assembly procedure. During the procedure of fabrication the frame of detector is fixed on a special support. For obtain high assembly precision compensation of this deformation is necessary. The equipment for compensate this deformation is composed by a pneumatic system, with sensor for measurement the force and a PC for monitoring and controlling. This paper describes the method for measurement the sag of frame of an optoelectronic detector using pneumatic equipment.

Keywords: calculus of the sag, electropneumatical equipment

1. INTRODUCTION

For muon system of Atlas collaboration at CERN an optoelectronic detector - drift chamber will be used. This detector is composed by a frame and two multilayers of Al drift tubes glued on the both side of the frame. The frame is design from two long beams and three cross plate. In the frame is inserted optic and electronic system¹.

Technical condition, 20 μm on the wire positioning requires a high level of mechanical precision in the assembly procedure. The drift chamber will be supported in the general assembly of experimental set up at the ends of the long beams.

During procedure of fabrication the chamber will be supported to a mechanical system by using six high precision towers by the ends of three cross-plates. In order to glue the layers of tubes to the frame of detector with high precision, the cross plate have to be precisely positioned with respect to the jig, which determines the position of the layers of tubes to be glued. This is achieved by holding in precise position the end of the cross plates. In this configuration, the cross plate of the detector would sag more than when is mounted in the general assembly of detector, where they are supported in the "Bessel point", by a factor 48. As a result, a cross plate satisfying the sag specification of the design could however have unacceptable sag during the assembly procedure.

As cross-plates are supported differently during chamber fabrication than when installed in the experimental set up, a cross-plate sag compensation system is necessary. This problem was solve using a special equipment assisted by computer who support the frame in the "Bessel point" (Fig. 1a, 1b), gaining back the factor 48, so that cross plate support correctly the tube in detector, would also meet the requirement during the assembly. This device is special designed to compensate the sag of the frame of detector and finally the frame will be in plane in range of technical restriction.

From simple beam calculations in the case of uniform load, with the optimal support described above, a reduction in the sag with a factor 252 with respect to the case of a simple support at the ends is obtained. Such a large factor will allow reducing even large sags to acceptable values of a few microns².

* Correspondence: E-mail: brindus-comanescu@yahoo.com; Telephone: 00401.780.66.40; Fax: 00401.423.25.32

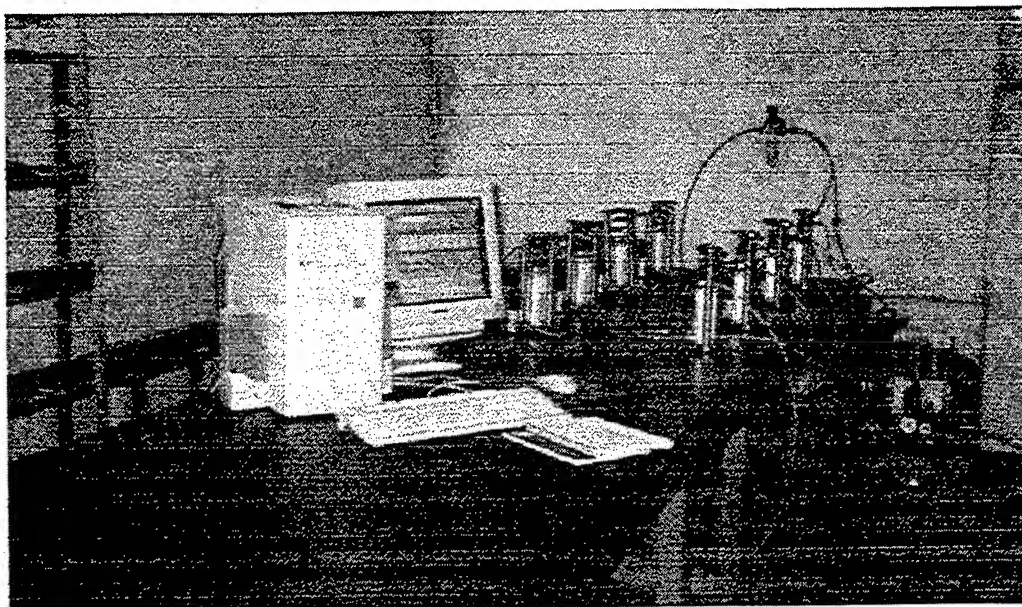


Fig. 1 a) Sag Compensation Equipment

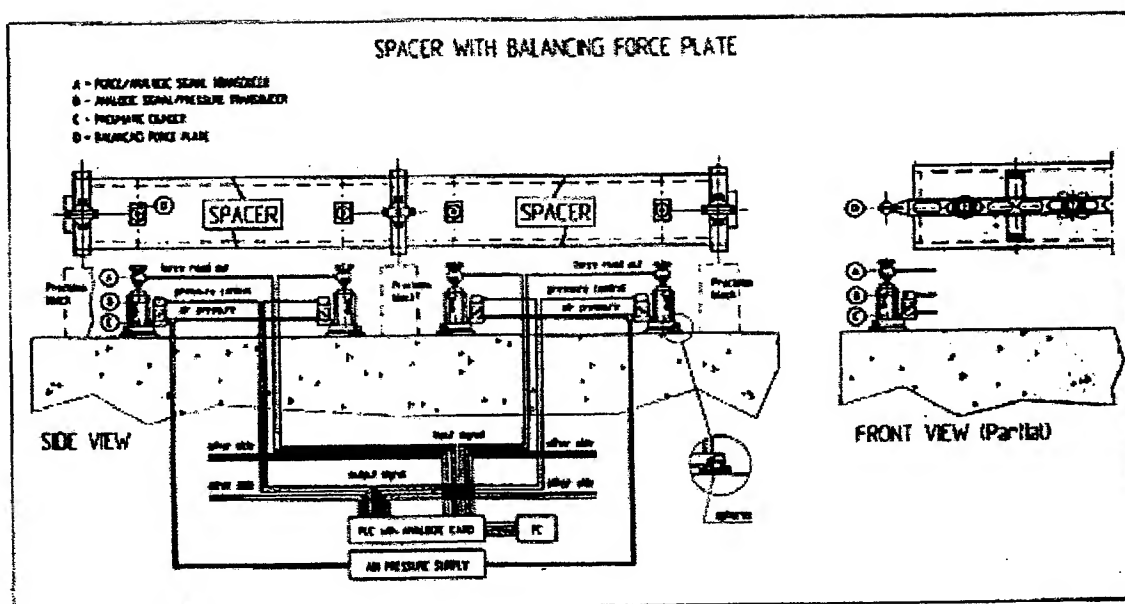


Fig. 1 b) Illustration of the pneumatic supporting system for the cross-plates

1.1. Description of method for compensate the sag of frame

In the Fig. 2 two forces are applied on the long beams, supporting the full weight of the cross plates plus long beam plus tube load. In this configuration the cross plate shape will be exactly the same as when the chamber is mounted in the apparatus. At two ends a high precision sphere is attached to the cross plate, with a symmetric bracket. The deflection of a cross plate will be exactly the one produced by the "Bessel Support"

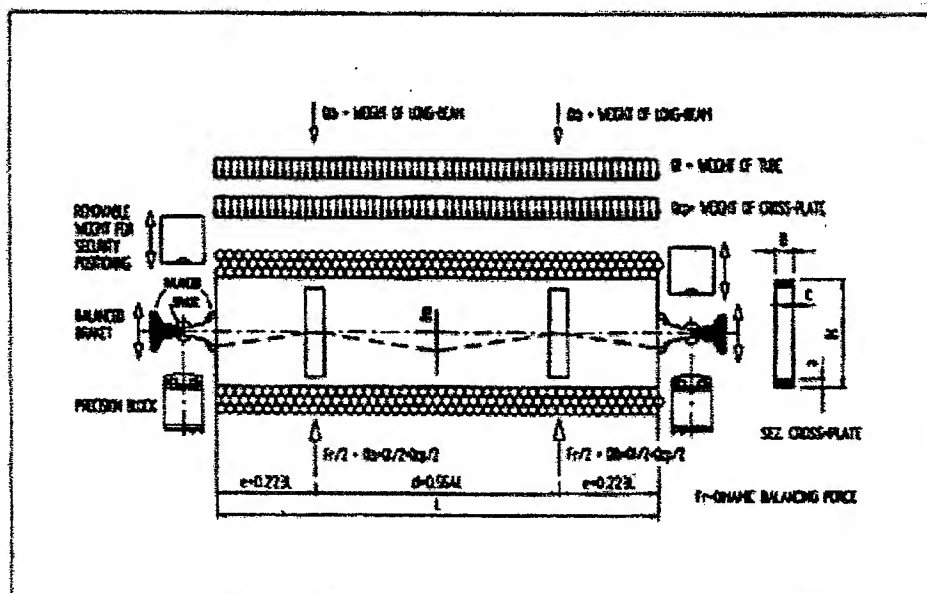


Fig. 2 A schematic drawing of the cross-plate supporting scheme

A bar on one side of the end cross plate and two bars at two sides of a middle cross plate are connected to the long beams and are supported at their ends on pneumatic push-up group (Fig. 3a). The pressure inside the pneumatic pistons determines the forces, which through the bars are transmitted to the long beams and through the long beams to the cross plates (Fig. 3c). The positions of the pistons and of the bars will adjust according to the position of the cross plate determined by spheres. The deflection of the bar is irrelevant.

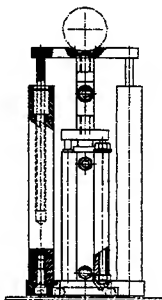


Fig. 3 a) Push-up group designed

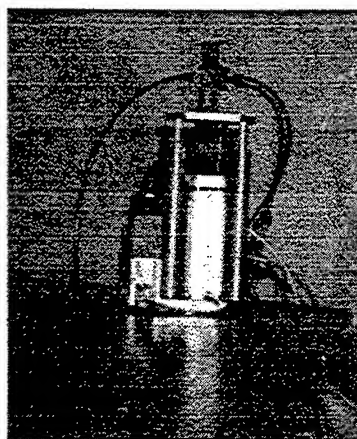


Fig. 3 b) Push-up group realised

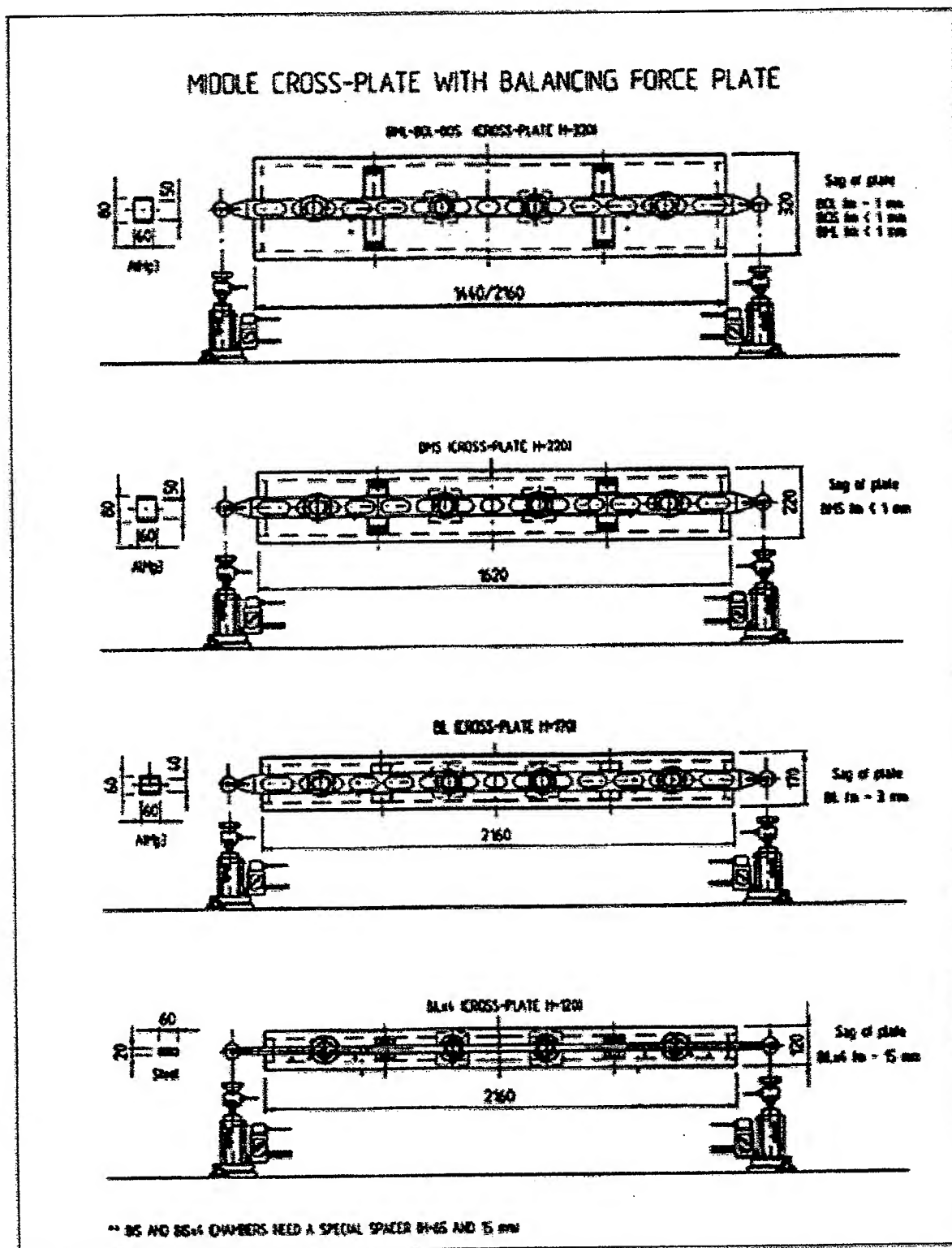


Fig. 3 c) Middle cross-plate sags for various barrel chambers, with the additional forces applied

1.2 Description of equipment

The equipment used for compensate the sag during the fabrication is composed by:

- 8 push-up group;
- Sag bars;
- Electronically - pneumatically system for monitoring and control the deformation;

The push -up group is composed by:

- Pneumatic cylinder;
- Force sensor;
- Mechanical pieces.

Sag bar is an Al profile used for transmitted the force to the frame of detector. System for control is composed by:

- Valve;
- Tubes;
- Reduction;
- PC board for input and output;
- Signal amplifier;

At the end of the sag bars we have the push - up group. If is pressure in the pneumatic system, the cylinder push the sag bar with a force and the sag bar push the frame. The sensor measures the force and the signal is input using a PC board for special data acquisition software. With this software the computer processed the input and send by a PC board to a valve. This valve controls the pressure through pneumatic cylinder and the force.

For first step we introduce the force that we calculate using the software and the method that we present in this paper. If the force is good the force read by sensor is ok and we stop the loop of software here. If the force read by sensor is different by the force read from data base, the software send an output signal to valve and we can modify the force through the cylinder until we obtain the good value of the force. This is the force that we can obtain a good compensation of the sag.

2. CALCULATION OF THE SAG

The equation for profile of the beam $v(z)$ is:

$$EJv'' = pz^2/2 - Rz - F(z-a) \quad (1)$$

Where:

E - modulus of elasticity

J - momentum of inertia

C_1 and C_2 are constant of integration

After integration we obtain:

$$EJv = pz^4/24 - Rz^3/6 - F(z-a)^3/6 + C_1z + C_2 \quad (2)$$

With the condition $z > a$

We put the following condition for obtain the constants:

$$v' = 0 \text{ (symmetry)} \quad (3)$$

$$v(0) = 0 \quad (4)$$

So the constant of integration is:

$$C_1 = - \{p(a+b)^3/6 - R(a+b)^2/2 - Fb^2/2\} \quad (5)$$

$$C_2 = 0 \quad (6)$$

We introduce the adimensional coordinate:

$$\varepsilon = z/(L/2) \quad (7)$$

and the following adimensional parameters:

$$x = a/(L/2) \quad (8)$$

$$y = F/(pL/2) \quad (9)$$

with this notation the equation of beam profile (2) is now:

$$v(\varepsilon) = 5pL^4/384 \{ 1/5 [\varepsilon^4 - 4(1-y)\varepsilon^3 + 8\varepsilon + 12y(-2x+x^2)\varepsilon] - 4/5y(\varepsilon-x)^3 \} \quad (10)$$

Where $0 < \varepsilon < 1$ corresponding to the half length of the beam and the term $4/5(\varepsilon-x)^3$ has to be considered only for $\varepsilon > x$.

The multiplying factor is the maximum sag for a beam only supported at the ends (i.e. for $x = 0$ and v calculated at $\varepsilon = 1$) Therefore the function:

$$f(\varepsilon) = 1/5[\varepsilon^4 - 4(1-y)\varepsilon^3 + 8\varepsilon + 12(-2x+x^2)\varepsilon] - 4/5y(\varepsilon-x)^3 \quad (11)$$

represents the profile of the beam in units of the maximum sag when the beam is supported at the two ends and describes a beam of any length subject to any uniform load of any elasticity module and any constant momentum of inertia.

$f(\varepsilon)$ gives also the dependence of the deformation on the parameters x and y describing where the force is applied and what fraction of the load it balances.

From function 11 we studied two cases:

1. $y = 1$

This is the case when only two supporting force are applied to the beam in the points specified by x . In this case by minimizing the difference between maximum and minimum deformation $f_{\max} - f_{\min}$ we found the optimal value for x where the sag is minimum. The value is $x = 0.1163$ and corresponds to "Bessel points". In such condition the maximum deformation is (sag for end support only)/ 48.

2. $y < 1$

This correspond to the case when 4 force are applied to the beam at the two ends and in two internal points, specified by the parameter x . By minimizing the maximum deformation one can estimate the optimal value for x and y . They are $x = 0.62226$ and $y = 0.7658$. In such a condition the maximum deformation is (sag for end support only)/ 252.

The profile of the beam for cases considered above is shown in Figs. 4, 5 and 6. In those figures the full length of the beam is represented with an adimensional coordinate going from 0 to 1.

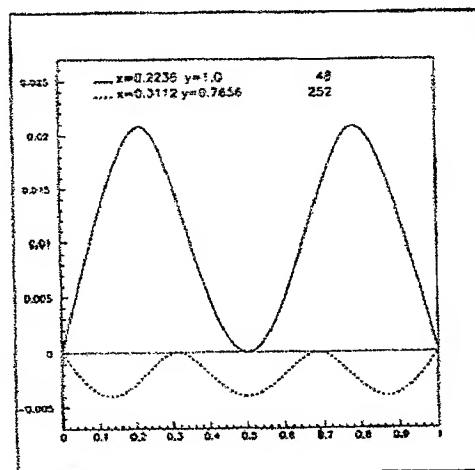


Fig. 4 The profile of the beam supported at the Bessel points (full line) and at four points, two internal plus the two ends (dashed line)

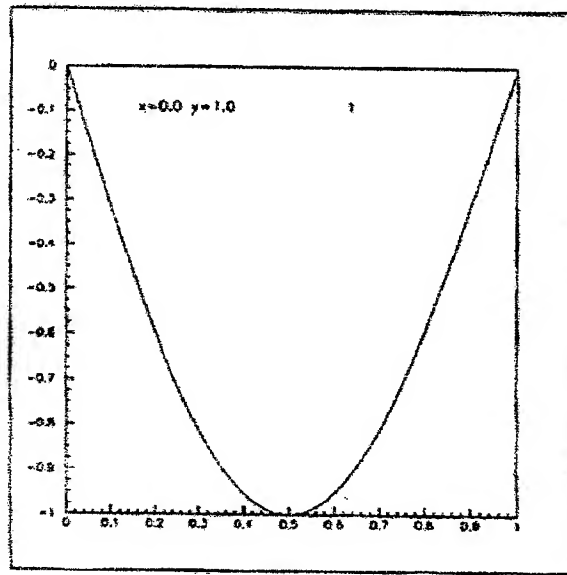


Fig. 5 The profile of the beam supported at the two ends only

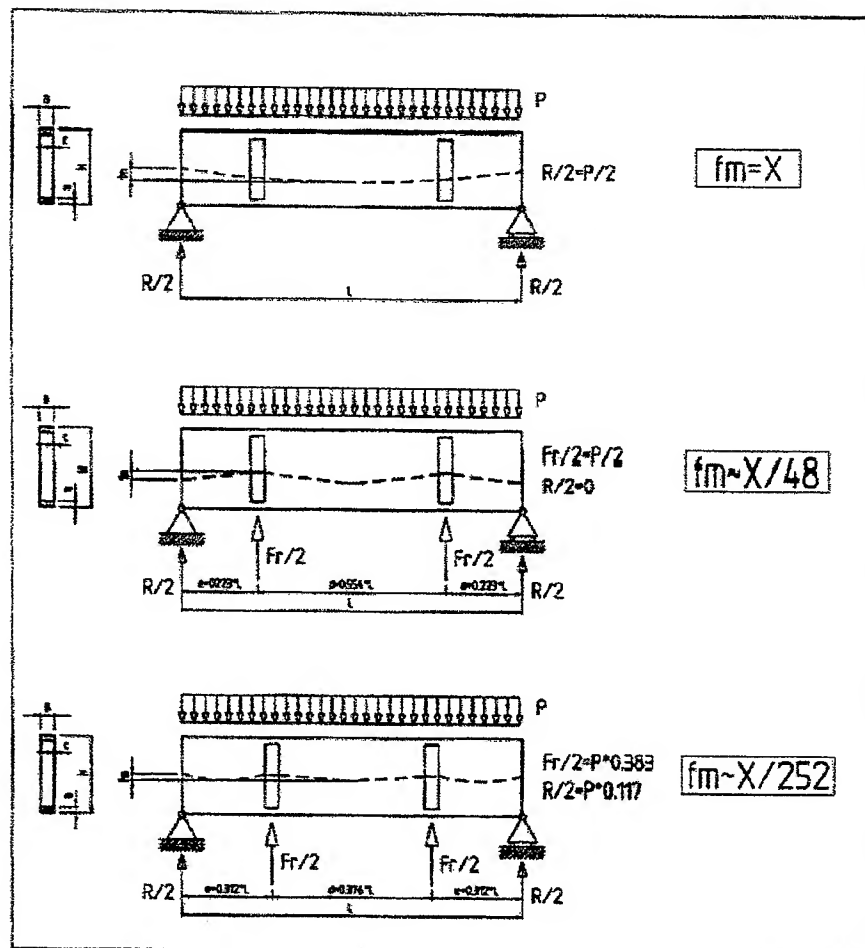


Fig. 6 The profile of the beam when supported in the ends only, in the Bessel points and in four points (two internal plus the two ends)

3. CONCLUSIONS

For compensate the sag of frame of an optoelectronic detector, we use a special equipment assisted by computer. This equipment using sensors can controlling and monitoring in real time the sag of frame.

ACKNOWLEDGEMENTS

We would like to thank muon group members of LNF INFN (Frascati, Italy) for the very useful discussions on the engineering aspects of the calculus of the sag and the procedure for controlling of sag compensation system.

REFERENCES

1. ***, *Atlas Technical Design Reports and Proposal*, 1997.
2. C. Capocchia, S. Cerioni, M. Curatolo, B. Esposito, M.L. Ferrer, G. Maccarrone, F. Linde, P. Werneke, K. Ackermann, A. Manz, *Cross plate sag compensation in the assembly of MDT chambers*, 1998.

SESSION VI

**Optoelectronics in Analytical Instrumentation
and Medicine**

Advances in low coherence interferometry for tissue imaging

Adrian Gh. Podoleanu and David A. Jackson

School of Physical Sciences, University of Kent, Canterbury, CT2 7NR, UK

ABSTRACT

We present fiberised OCT systems developed to image biological tissue with high depth resolution. The systems can deliver transversal as well as longitudinal OCT images. When in the transversal mode, the systems provide a confocal image simultaneously with the OCT image. Design particularities in adopting the system for imaging either the skin or the retina in vivo are presented. They refer to the interface optics, power to the tissue and imaging speed. Images from retina and skin in vitro and in vivo are shown. When applied to the eye, line rates up to 1 kHz and frame rates up to 5 Hz can be used. In order to improve the penetration depth in skin, lower scanning rates are used. Also, flow of milk into a vessel simulator is investigated using Doppler OCT. In this case, no transversal scanning is applied. The laminar profile of the velocity inside the vessel is determined with the depth accuracy of the OCT.

Keywords: scanning laser, ophthalmoscopy, low coherence interferometry, tomography

1. INTRODUCTION

Optical coherence tomography (OCT) as a new tool for imaging the tissue was developed for two reasons: (i) based on interference, low level signals reflected by the tissue are enhanced by the power in the reference arm of the interferometer¹; (ii) using a source with low coherence length, depth resolved images can be produced (depth sampling interval is 10 - 20 μm when using SLDs² and below 4 μm when using Kerr lens mode-locked lasers³). The OCT technique applied to ophthalmology has evolved rapidly in the last few years, as it can deliver a much better depth resolution than scanning laser ophthalmoscopes (SLO) based on the confocal microscopy principle. Initially, different set-ups for measurement of intraocular distances¹ were devised and lately, the emphasis has shifted steadily towards imaging. Laboratories throughout the world have reported notable results in the OCT longitudinal imaging of the eye. OCT has successfully been applied to detect and image abnormalities such as diabetic retinopathy, the congenital pit of the optic nerve head, vitreous detachment, central serous chorioretinopathy, inflammatory optic neuropathy, macular holes and retinal pigment epithelium (RPE) detachment⁴.

An increased interest is now manifested towards extending the OCT technique to skin imaging⁵ and to determine the flow in micro-capillaries. However, all the reports in literature refer to longitudinal OCT images, i.e. slices in the object which contain the optical axis. This is explained by the easiness in their production in comparison with transversal OCT images. To produce longitudinal OCT images, the same device scanning the object in depth produces the carrier for the image bandwidth. This is no longer the case in the transversal OCT, where the reference mirror is kept at rest and a carrier has to be produced by other means. We have been interested to produce transversal OCT images with high depth resolution and developed an OCT system where both transversal and longitudinal modes of operation are possible. We apply such a system to image the retina, the skin and characterise the flow in vessel simulators.

For further author information:

Phone: 44 1227 764000/3762; Fax: 441227827558; e-mail: A.G.H.Podoleanu@ukc.ac.uk

The depth resolution in the OCT channel is 20 μm and in the confocal channel 2.5 mm when measuring the eye and less than 0.2 mm when measuring skin. For the eye investigation, the gap in the range of depth resolution between the OCT and the confocal channel is covered in two ways: by using a source with adjustable coherence length and by software superposing OCT transversal images collected at different depths.

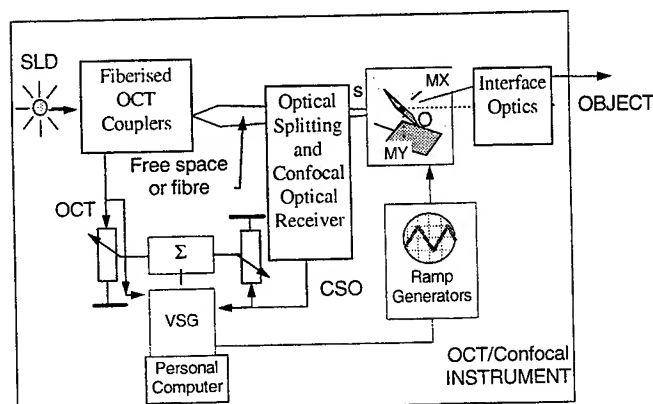


Figure 1. Basic set up of the stand alone OCT/confocal system where a separate confocal receiver diverts parts of the light returned from the object.

SLD: Superluminescent diode (Superlum SLD-361)⁸VSG: variable scan frame grabber; C1, C2, C3: microscope objectives; DC1, DC2: directional couplers; PM: phase modulator (fiber wrapped piezocylinder); G: sinusoidal generator; SXY: orthogonal scanning mirror pair; MX(MY): mirror of the X(Y) scanner; RX, RY: ramp generators; L1: convergent lens; PD1, PD2: photodetectors; DA: differential amplifier; FPC1,2,3: polarizer controllers; PE: processing electronic block; PC: personal computer; VSG: variable scan frame grabber

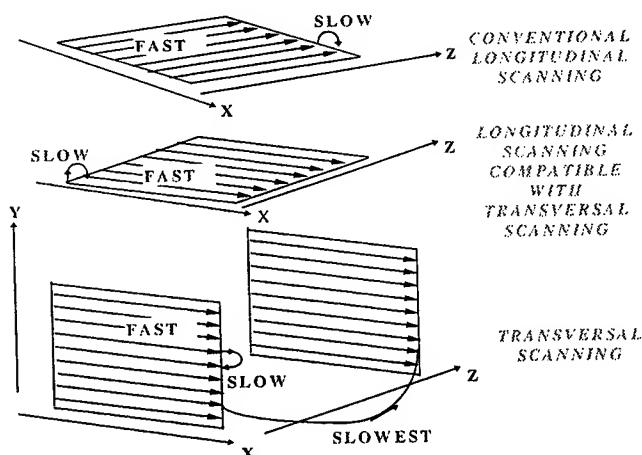


Figure 2. Three modes of operation of the OCT

2. CONFIGURATION

Our configuration is based on two fiberised single mode couplers published elsewhere⁶. In order to image different objects, adjustable interface optics was designed. A powerful Superlum SLD is used, at 850 nm, delivering 100 μW to the eye. The system can collect a large number of transversal images at successive depths or a large number of longitudinal images for different orientations in the transversal plane.

3. TRANSVERSAL VERSUS LONGITUDINAL

Figure 2 shows three possibilities of building OCT images. The majority of reports in literature refer to the longitudinal imaging procedure as shown at the top of the Fig. 2, where the fast lines in the image are in depth and the transversal scanner advances at a slower pace. We reversed this in our system, where the transversal scanner does the fast lines in the image and the longitudinal scanner advances slower, as shown in Fig. 2 middle. This allows to produce OCT transversal images for a fixed reference path, as illustrated in the Fig. 2 bottom. One of the transversal scanner does the fast lines in the image, the other transversal scanner advancing a second coordinate in the transversal plane at a slower rate. Different transversal slices are collected for different depths, either after each transversal slice is collected or at an advancing speed for which the depth position for the point in the top left corner of the image and the depth position in the bottom right corner of the image do not differ by more than half the depth resolution. This imposes the slowest pace for the advancement of the scanner in depth.

The immediate disadvantage of such a procedure is that a supplementary phase modulation method has to be employed, contrary to all the OCT imaging reports in literature which took advantage of the

Doppler signal created by longitudinal scanning at a constant speed.

For convenience, let us consider that the time to scan in depth, say 2 mm when doing conventional longitudinal imaging and the time to scan transversally the same 2 mm using our method is the same, $T_z = T_x = 1$ ms. We will also consider the same pixel size $\delta z = \delta x = \delta y = 20 \mu\text{m}$, (both the transversal and the longitudinal pixel size could be lower). In this case, for the, the same number of pixels $N_x = N_z = 100$ result which gives the image bandwidth: $B_i = 50$ kHz. This is the bandwidth which modulates in intensity the OCT signal on the carrier frequency introduced by the constant shift of the mirror in the longitudinal OCT or by the phase modulation introduced in the transversal OCT system. However, the frequency of the piezo-modulators is relatively low or comparable with the bandwidth as worked out above. Therefore, we employ a combination of the modulation introduced by the galvanometer scanner^{7,8} and the modulation introduced by a piezo-modulator stretching the fiber in the reference arm of the OCT, as explained in the reference⁶.

4. IMAGES FROM RETINA

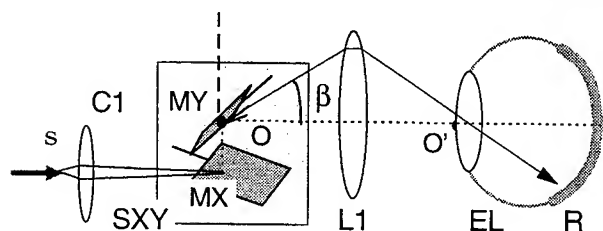


Figure 3. C1: collimator; SXY: transversal scanning head; MX, MY: mirrors; L1: lens; HE: patient's eye; EL: eye lens; R: human retina.

Figure 3 shows the interface optics when imaging the retina. The points O and O' are conjugate by virtue of the lens L1. All the images presented here were obtained at a 700 Hz line rate and 2 frames/second. The power was 125 μW to the eye, at a wavelength of 860 nm and depth resolution estimated as 20 μm .

Procedures we apply refer to: simultaneous presentation of confocal and OCT transversal images, collection of a number of transversal OCT images for different depths in the eye and then building of longitudinal OCT images at different transversal orientations, OCT transversal images with adjustable depth resolution, animations and rendering of 3D images.

4.1. REAL TIME IMAGES

4.1.1. TRANSVERSAL IMAGES

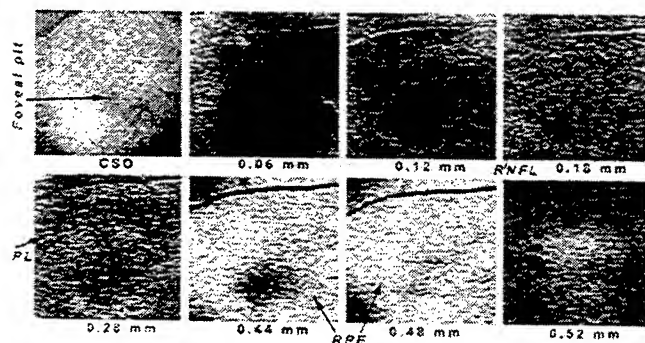


Figure 4. Confocal image (top corner left) and OCT images collected simultaneously from the fovea in the living eye.

The voltage applied on the galvanometer scanners were such to cover 3 mm x 3 mm at the back of the eye lens, EL. Shifting the translation stage at 50 $\mu\text{m/s}$ for 1 mm, 45 images at 30 μm depth interval were collected. Seven such OCT transversal images and the confocal image from the fovea are shown in Fig. 4. It can be noticed that due to the high depth resolution, the OCT images look fragmented. Also, if the retina is out of coherence, the image is completely dark. This is why the confocal image⁹ is important, it shows the part of the eye the system is pointing at, which might not be evident from the OCT images at some depths. As the OCT images have very good depth resolution, it is acceptable to work with a much larger depth resolution in the confocal channel, but sufficient to eliminate the reflections from the eye lens.

In our case, we adjusted the depth resolution of the confocal channel to 3.5 mm, which allowed us to work with only 4% light derived from that reflected by the eye, living most of the power in the OCT channel.

4.1.2. Longitudinal images

By slowly shifting the translation stage for 0.8 mm in 0.5 s (one frame duration), (the procedure shown at the middle of Fig. 2) the OCT longitudinal image of the fovea was obtained as shown in Fig. 5. The MX was driven to cover 3 mm on the retina and MY was kept at rest. Retinal nerve fibre layer (RNFL), photoreceptor layer (PL) and the retinal pigment epithelium (RPE) layer are visible.

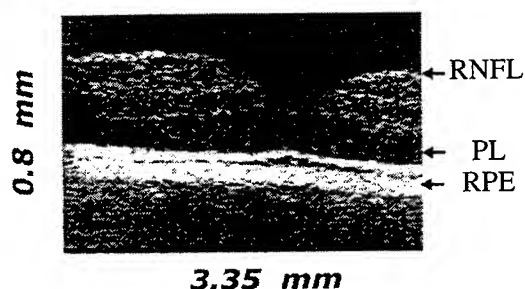


Figure 5. Longitudinal OCT image of the retina of a volunteer.

3 mm (horizontal=100 pixels) x 0.8 mm (vertical=40 pixels) corresponding to depth, measured in the air.

4.2. SOFTWARE PROCESSED IMAGES

By software means, the OCT transversal images can be processed to obtain (i) longitudinal images at any desired direction in the transversal plane when using stacks of transversal images or transversal images at any desired depth when processing stacks of longitudinal images; (ii) intensity images by superposing all the transversal images collected; (iii) 3-D profiles; (iv) animation, scrolling through the object volume.

4.2.1. Weighted superposition of transversal OCT images

Varying the number of images superposed, the effective depth sectioning interval of the superposed image could be altered. In this way, the sectioning interval width could be varied from the minimum given by half of the

coherence length of the source, to a maximum, approximately given by half of the range covered by

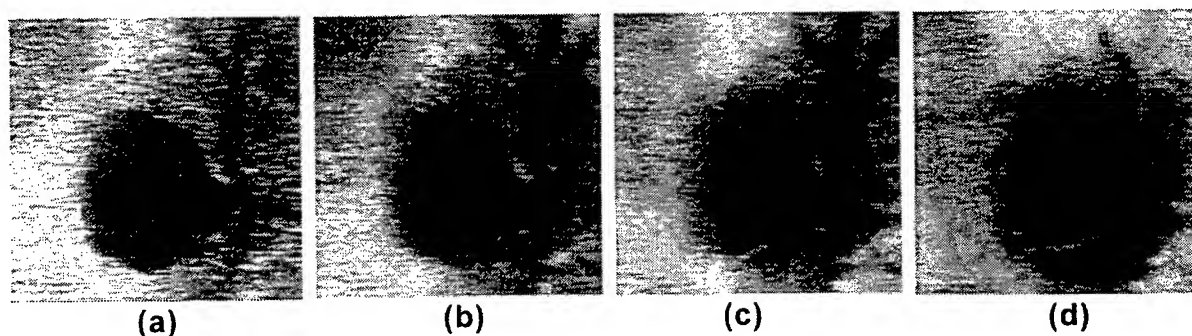


Figure 6. Different ways of presenting images with different depth resolution from the optic nerve area (volunteer B).

(a): OCT image in the middle of the set of 45 images, 18 μm depth resolution; (b): equivalent confocal image of the image in (a) with 150 μm depth resolution; (c): equivalent confocal image of the image in (a) with 300 μm depth resolution; (d): superposition of all 45 OCT images.

the data collection. We demonstrate this by processing images from a set of 45 OCT transversal images, collected from the optic nerve area, at 30 μm step interval between adjacent images. The

retina size displayed is 3 mm x 3 mm. Superposing all 45 images, an intensity image is obtained as shown in the Fig. 4(d). This may be considered as an image with $30 \times 45 = 1350 \mu\text{m}$ depth sectioning interval. In order to get confocal equivalent images, the images in the set have been squared. The image in Fig. 4(a) shows the OCT image at the position 22 in the set of 45 images. Then, Fig. 4b and 4c show weighted superpositions of all the squared images using a Gaussian profile for the weighting coefficients. For the image in Fig. 4b, a Gaussian profile with $\text{FWHM} = 150 \mu\text{m}$ was used while for the Fig. 4c, a Gaussian profile with $\text{FWHM} = 300 \mu\text{m}$. Fig. 4b and 4c present images which we would expect to be similar with images displayed by SLOs with equivalent depth resolution. However, no SLO exist to supply confocal images with less than $300 \mu\text{m}$ depth resolution. We can only compare the images with those obtained by the confocal channel in our standalone system, where for the time being the depth resolution is set to a few millimeters. In this way, the gap between the depth resolution insured by optical coherence tomography ($5\text{--}30 \mu\text{m}$) and the minimum achievable by SLOs ($300 \mu\text{m}$) can be filled.

Above, we eliminated 15 images which were very disturbed by eye movements. We have not attempted to align the remaining images, so we expect a level of blurring due to inadvertent eye movements.

Fig. 7a shows a software inferred longitudinal cut from a set of 120 OCT transversal images collected from the optic nerve region. Fig. 7b shows the OCT longitudinal image from the same transversal position obtained in real time. Although no alignment was applied to eliminate the disturbances of the eye movement, the image in Fig. 7a bears strong resemblance with the hardware image in Fig. 7b.



Figure 7a. Software inferred longitudinal OCT image from the retina.
3 mm x 1 mm



Figure 7b. OCT longitudinal image from the same part of the retina
3 mm x 1 mm

The collection of images was also used to produce an animation, which can be seen at the URL in reference¹⁰.

5. IMAGES FROM THE SKIN

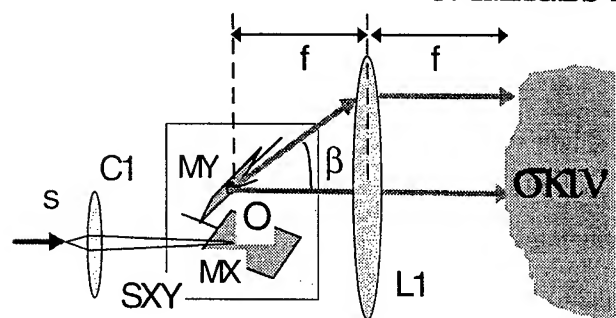


Figure 8. Interface optics to image the skin.

C1: microscope objective; SXY: transversal scanning head; MX, MY: mirrors; L1: lens.

OCT can provide high depth resolution images from skin without staining or using sophisticated image-processing techniques. With $1.3 \mu\text{m}$ probing light, structures up to 1 mm below the surface of the skin could be imaged¹¹, with a lateral and depth resolution of $10 \mu\text{m}$. We present OCT images from the skin with $\lambda = 860 \text{ nm}$, for which the penetration depth is smaller. However, this is the same wavelength as that recently successfully used to image skin using confocal microscopy¹². As the microscope objective can be placed very close to the tissue, both transversal and longitudinal pixel sizes can be very small using confocal microscopy only. However, it is expected that better penetration depth is achieved using OCT, as shown in

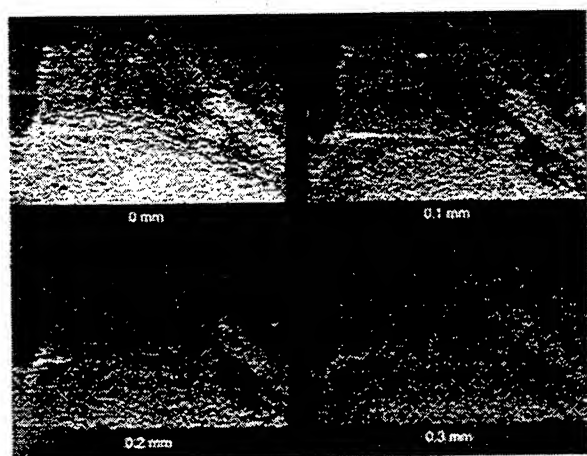


Figure 9. Images from melanoma at four depths.

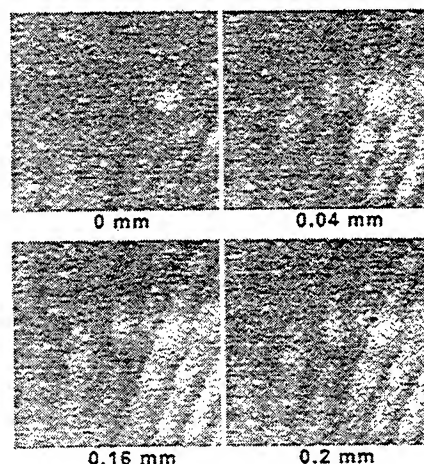


Figure 10. Transversal OCT images from finger.

references^{13,14}. As OCT longitudinal images have already been reported¹¹, we present here only transversal OCT images.

For skin and DOCT experiments, the lens L1 is mounted at f instead at $2f$ from the scanner, as shown in Fig. 8. Transversal OCT images from a histological section showing a melanoma are in Fig. 9. The border between normal tissue and the melanoma (on the left hand side of the images) is very visible.

Images from a finger are shown in Fig. 10 for four different depths. The white dotted spots represent sweat ducts. The finger pattern is the most visible in the slice at 0.2 mm depth (in air).

6. DOCT FROM VESSEL SIMULATORS

Determination of blood flow in retinal vessels and in tiny vessels inside skin tumours may offer relevant information about the tissue and the illness. This technique, termed optical Doppler tomography (ODT)¹¹ combines laser Doppler flowmetry with optical coherence tomography (OCT). A version of this technique, the color Doppler optical coherence tomography (CDOCT)¹² uses color to show the sense of flow movement. DOCT allows to superpose the velocity mapping over the anatomical image.

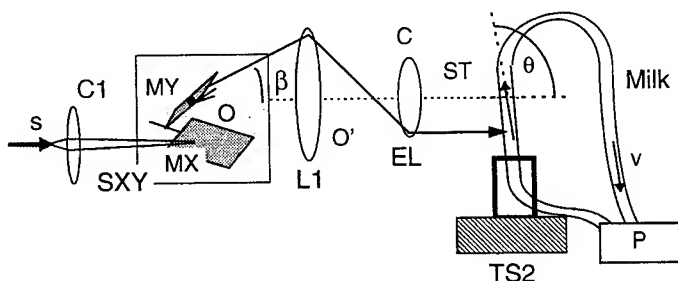


Figure 11. The interface optics to address the flow in DOCT experiments.

In comparison with laser anemometry, where two beams (of weak power) at an angle are used and the interference takes place between two object beams, ODT has the advantage of interfering the object light from the sensing arm with a very powerful beam, from the reference arm of the interferometer. In our case, a silicone tube, ST, with internal diameter of 0.8 mm is used, as shown in Fig. 11 which can be suitably angled at angles θ with the ray direction.

Using a pump, P, the flow can be set at different speeds between 0 - 3 mm/s. The tube is mounted on a controlled translation stage TS2. However, the immediate disadvantage of ODT lays with the need to tilt the flow object, as the Doppler shift frequency ν is proportional with the cosine of the angle θ between the ray direction and the flow direction:

$$\nu = \frac{2v \cos \theta}{\lambda} \quad (1)$$

where v is the flow velocity and λ the wavelength in air. The measurement volume is scanned by varying the position of the translation stage, TS1 (not shown) carrying the reference mirror in the OCT system. Let us consider the light focused at δ from the wall within the vessel (measured without the liquid), i.e. after shifting the stage TS2 by the same amount towards the lens L1. The waist of the beam moves further away to $n\delta$ measured in air) from the tube wall, after introducing the liquid. Consequently, in order to keep the waist at coherence, for each δ movement of the translation stage

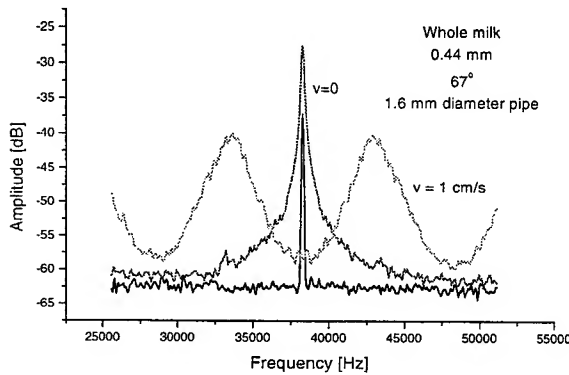


Figure 12. Spectra of the photodetected signal for: outside the liquid at the interface air-rubber; from 0.44 mm inside the liquid at $v=0$ cm/s and from the same position when $v=1$.

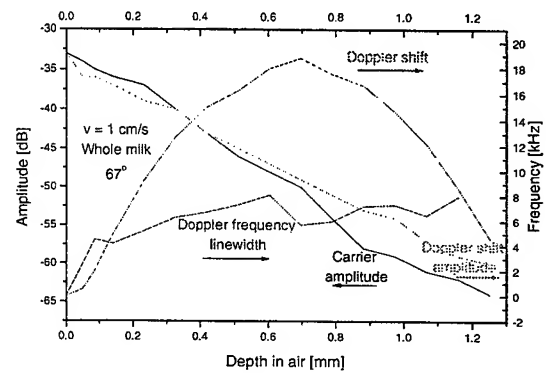


Figure 13. Frequency versus depth for $v=1$ cm/s and the amplitude of the carrier signal (for no flow) and the amplitude of the DOCT signal.

TS1, the translation stage TS2 has to be moved towards increasing the reference path by $(\delta n)n - \delta = \delta(n^2 - 1)$. The procedure is called dynamic focus¹. Without dynamic focus, the amplitude of the signal is lower and if the numerical aperture of the lens L1 is large, the range of depths is largely reduced.

Fig. 12 shows how the spectra of the photodetected signal differs, depending whether the point at coherence is outside or inside the liquid, whether the liquid is flown or not. When the point is outside the liquid, at the interface air-rubber the linewidth is very narrow. In the liquid, the linewidth is larger, due to the Brownian motion. When the liquid is flown, supplementary enlargement occurs due to the flow. Both the linewidth and the frequency shift are useful for tissue diagnosis.

Fig. 13 shows the frequency resolved depth which demonstrates that the flow is laminar. The attenuation of the signal when penetrating deeper into the milk is shown also.

Fig. 14 shows a longitudinal OCT cut through the vessel and Fig. 15 the map of the flow within the same section using the DOCT method. A special processing electronics was used to create a signal proportional with the frequency shift. However, the circuit is not capable yet to distinguish the sense of flow movement.

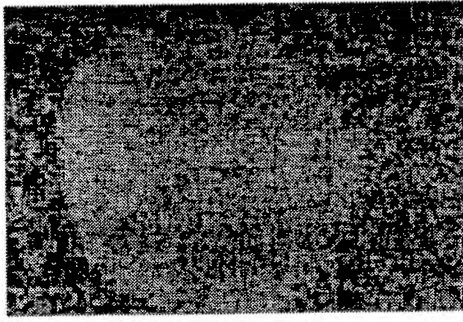


Figure 14. Longitudinal OCT section in the 0.8 mm pipe filled with milk.

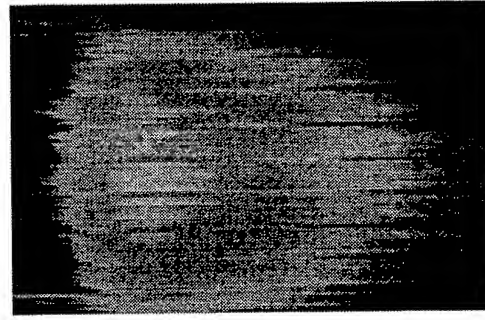


Figure 15. Flow map constructed by DOCT.

7. Signal to noise ratio in the OCT

According to reference¹⁴, as balance detection is used in our OCT, the mean square photodetector current fluctuation is given by:

$$\langle \Delta I_p^2 \rangle = 2eB \langle I \rangle_{\text{REF}} + 2(1 + \Pi^2) \frac{B}{\Delta\nu} \langle I \rangle_{\text{FER}} \langle I \rangle_{\text{Ref}} = \langle \Delta I_{\text{sh}}^2 \rangle + \langle \Delta I_{\text{ex}}^2 \rangle \quad (2)$$

where $\langle I \rangle_{\text{REF}}$ represents the cumulated photocurrent due to the reference power and $\langle I \rangle_{\text{FER}}$ the cumulated photocurrent for the two photo-detectors, due the fiber end reflection, e is the electron charge, B the electrical bandwidth, Π represents the polarization degree of the light and $\Delta\nu$ the effective optical line-width. The shot noise photocurrent due to the object can be neglected in comparison with the noise due to the reference power. Hence:

$$\frac{S}{N} = \frac{2(\alpha\gamma P)^2 \xi_F (1 - \chi)(1 - \gamma)^{-1} \sigma \Gamma_0^2 O}{2e\alpha P \gamma \sigma (1 - \gamma)^{-1} + 2(1 + \Pi^2)(\Delta\nu)^{-1} \gamma \sigma (1 - \gamma)^{-1} R \alpha^2 P^2 + I_a^2} \quad (3)$$

where $\alpha = 0.5$ is the pin photodetector responsivity, $R \approx 1.7 \cdot 10^{-5}$ cumulates for the reflectivity of the fiber end reflection in the object arm and Rayleigh backscattering noise. $\gamma = 0.75$ is the DC1 coupler efficiency from the port "s" to the coupler DC2 considered ideally even. $\xi_F = 0.44$ represents the single mode fiber collection efficiency of the object signal. $\sigma = 0.3$ is the efficiency for the light being coupled from port "r₁" to port "r₂". It is assumed that the two OCT couplers DC1 and DC2 have zero losses, the loss in transferring the power from the port "s" to the object is neglected and the balanced receiver is perfect. χ represents the reflectivity of the plate beamsplitter used to divert light to the confocal receiver in Fig. 1 and Γ_0 represents the maximum of the normalized correlation function. For an ideal match of the polarizations of the two interfering beams (object and reference), Γ_0 is unity. However, in our case we obtained a maximum $\Gamma_0 = 0.5$. The photodetector and amplifier have a cumulative $\sqrt{\langle \Delta I_a^2 \rangle} / B \approx 3 \text{ pA/Hz}^{1/2}$. With $\Delta\nu = 11 \text{ THz}$ and powers P less than $120 \text{ }\mu\text{W}$, the shot noise dominates in (3). Considering a minimum of the S/N ratio of 9 as indicated in reference⁹, with $B = 100 \text{ kHz}$ and $P = 120 \text{ }\mu\text{W}$, the sensitivity results as:

$$O_{\text{min,sys}} = 9 \frac{eB}{P \alpha \gamma (1 - \chi) \xi_F \Gamma_0^2} \quad (4)$$

which gives $1.74 \cdot 10^{-8} / (1 - \chi)$. When no beam-splitter is introduced in the set-up (no confocal channel), $\chi = 0$ and (16) gives -77.6 dB . For the skin imaging, larger power are allowed. In this case the excess photon noise cannot be neglected.

$$O_{\text{min,skin}} = 9 \frac{2e\alpha P \gamma \sigma (1 - \gamma)^{-1} + 2(1 + \Pi^2)(\Delta\nu)^{-1} \gamma \sigma (1 - \gamma)^{-1} R \alpha^2 P^2 + I_a^2}{2(\alpha\gamma P)^2 \xi_F (1 - \gamma)^{-1} \sigma \Gamma_0^2} B \quad (5)$$

Neglecting the contribution to noise of the background from the tissue, with $P = 50$ mW, (5) gives -89 dB.

7. CONCLUSIONS

OCT systems for tissue investigations were presented. The systems are capable of producing transversal as well as longitudinal images using fast transversal scanning and slow or stepped longitudinal scanning. First transversal OCT images from the retina, skin and vessel simulators are presented.

8. ACKNOWLEDGMENTS

The authors acknowledge the support of the UK Engineering and Physical Sciences Research Council and also the support of Superlum, Moscow.

9. REFERENCES

1. A. F. Fercher, "Optical coherence tomography", *J. Biomed. Opt.*, 1(2), pp. 157-173, 1996.
2. S.A. Safin, A.T. Semenov, V.R. Shidlovski, "High-Power Superluminescent Diodes with extremely small Fabry- Perot Modulation Depth", *Electron. Lett.*, v. 28, No. 2, pp. 127-129, 1992.
3. B. Bouma, D. J. Tearney, S. A. Boppart, M. R. Hee, M. E. Brezinski, J. G. Fujimoto, "High-resolution optical coherence tomographic imaging using a mode-locked $\text{Ti:Al}_2\text{O}_3$ laser source", *Opt. Lett.*, vol. 20, No.13, pp.1486-1488, 1995.
4. C. Puliafito, *Optical coherence tomography of ocular diseases*, Thorofare, NJ, SLACK Inc., 1996.
5. A. Pagnoni, A. Knuettel, P. Welker, M. Rist, T. Stoudemayer, L. Kolbe, I. Sadiq and A. M. Kligman, "Optical coherence tomography in dermatology", *Skin Research and Technology*, (1995), 5, No. 2, pp. 83-87.
6. A. Gh. Podoleanu, M. Seeger, G. M. Dobre, D. J. Webb, D. A. Jackson and F. Fitzke "Transversal and longitudinal images from the retina of the living eye using low coherence reflectometry", *J. Biomed Optics*, 3(1), pp. 12-20, 1998.
7. A. Gh. Podoleanu, G. M. Dobre and D. A. Jackson, "En-face coherence imaging using galvanometer scanner modulation", *Opt. Lett.*, 23, pp. 147-149, 1998.
8. A. Gh. Podoleanu, G. M. Dobre, D. J. Webb, D. A. Jackson, 'Coherence Imaging by Use of a Newton Rings Sampling Function', *Opt. Lett.* 21, pp. 1789-1791, 1996.
9. A. Gh. Podoleanu and D. A. Jackson, Noise Analysis of a Combined Optical Coherence Tomograph and Confocal Scanning Ophthalmoscope, *Applied Optics*, vol. 38, no. 10, (1999), pp. 2116-2127.
10. http://www.ukc.ac.uk/physical-sciences/aog/Low_Cohe/
11. J. M. Schmitt, M. J. Yadlowsky, R. F. Bonner, "Subsurface imaging of living skin with optical coherence microscopy", *Dermatology*, 191(2), pp. 93-98, 1995.
12. M. Rajadhyaksha, R. R. Anderson and R. Webb, "Video-rate confocal scanning laser microscope for imaging human tissues in vivo", *Appl. Opt.*, Vol. 38, No. 10, (1999), pp. 2105-2115.
13. J. A. Izaat, M. R. Hee, G. M. Owen, E. A. Swanson and J. G. Fujimoto, "Optical coherence microscopy in scattering media", *Opt. Lett.*, Vol. 19, No. 8, (1994), pp. 590-592.
14. M. Kempe, A. Z. Genack, W. Rudolph and P. Dorn, "Ballistic and diffuse light detection in confocal and heterodyne imaging systems", *JOSA*, Vol. 14, No. 1, (1997), pp. 216-223.
15. Z. Chen, T. E. Milner, X. J. Wang, S. Srinivas, J. S. Nelson "Optical Doppler Tomography: Imaging in Vivo Blood Flowing Pharmacological Intervention and Photodynamic Therapy", *Photoch. and Photob.*, 67(1), pp. 56-60, 1998.
16. Z. Chen, T. E. Milner, S. Srinivas, X. J. Wang, A. Malekafzali, M. J. C. vanGemert, J. S. Nelson "Noninvasive Imaging of In Vivo Blood Flow Velocity Using Optical Doppler Tomography", *Opt. Lett.*, Vol.22, No.14, pp.1119-1121, 1997.
17. J. A. Izatt, M. D. Kulkarni, S. Yazdanfar, J. K. Barton, A. J. Welch "In Vivo Bidirectional Color Doppler Flow Imaging of Picoliter Blood Volumes Using Optical Coherence Tomography", *Opt. Lett.*, Vol.22, No.18, pp.1439-1441, 1997.
18. K. Takada, "Noise in Optical Low-Coherence reflectometry", *IEEE J. Quantum. Electron.*, vol. 34, (1998), pp. 1098-1108.

Digital speckle-interferometry camera for non-destructive testing

D. Apostol*, V. Damian, A. Dobroiu, V. Nascov

National Institute for Laser, Plasma and Radiation Physics, Laser Department

Măgurele, P.O.Box MG-36, Bucharest 76900-Romania

ABSTRACT

Speckle interferometry for non destructive testing of out of plane or in-plane stresses or deformations of rough mechanical parts is a powerful and modern technique. Basics of speckle phenomena and interferometry in speckled light are reviewed. Electronic speckle pattern interferometry for vibration analysis and a Duffy-Young digital camera for in plane measurement are presented.

Keywords: speckle pattern, interferometry

1. INTRODUCTION

In the last years classical and holographical interferometry were replaced by electronic speckle pattern interferometry in many applications. This changement was produced in two steps:

- the first step was imposed by the necessity to replace the time consuming photograhic recording and TV technique was the answer;

- the second step was produced by the evolution of digital acquisition and digital fringe pattern measurement techniques.

In the meantime vidicon camera was replaced by CCD camera, and the coherence of gas laser was obtained from minute diode laser for much more power and much more coherence length. Small and rugged interferometers are now available to the engineers for high interferometric sensitivity non-destructive testing. We will present the basics of speckle phenomenon an ESPI set-up for vibration analysis: the optical set-up, the digital recording and the fringe pattern analysis for a simple application, and a digital camera for in-plane deformation visualisation and measurement.

2. BASICS OF SPECKLE PHENOMENA

2.1. History

As J. M. Burch¹ pointed out when interference phenomena are described in text books it is usual to find them classified in two groups: those in which the interfering beams are derived by division of amplitude at partial reflector (Michelson) and those in which a spatially coherent wavefront is sampled by laterally separated apertures (Young). An intermediate possibility whereby division of the light is accomplished by means of processes of diffraction or scattering is possible.

A short history of the diffused light interference is reviewed by M. Francon²: "The phenomenon of interference in diffused light was observed for the first time by Newton. A mirror, with a reflecting back surface was illuminated by a point source of light placed at its center of curvature. A beautiful system of colored rings centered on the source was then observed. Continuing the experiments of Newton, the duc de Chaulnes showed in 1775 that the visibility of the rings could be increased by using a mirror with partially diffusing front surface. Further studies of this subject were made by Young and Herschel. Fabry and Perot observed a similar system of rings in transmited light. Their system consisted of a semi-reflecting plate with parallel faces one of which was diffusing. Burch for the first time, applied the interference phenomenon in diffused light for the construction of an interferometer".

I cannot refraine myself to give a small text in an antique romanian language published by a Romanian professor and scientist,, member of the Romanian Academy, Emil Bacaloglu as early as 1870³:

"Asemenea coloratiuni sau inele se producu cu lame grose, candu atunci elle sunt mai mari si mai intensivu luminate. Aceste inele le potemu produce lesne, asediendu intr'ua camera intunecosa inaintea gaurei A a oblonului,

* Correspondence: E-mail: apostold@ifin.nipne.ro

pre unde patrundu radiele soarelui, ua oglinda de sticla concava XY (fig 269) astu-feliu incatu centrulu seu de curbatura sa fie langa gaura. Feci'a oglindei trebue sa fie prafuita, seu acoperita cu un stratu de aburi seu de lapte cu apa, ca sa dea numai lumina diffusa. Atunci vom vedea in giurulu gaurei innee colorate mari si intensivu lumnate". (It is describe the Newton experiment and recomand to use a dusty, or milk or water vapour covered front surface).

When TV camera and video processing were used to record and generate interference pattern in diffused light the Electronic Speckle Pattern Interferometry or ESPI was born. ESPI was first demonstrated by Butters and Leendertz⁴. Many review papers and books are now available⁵⁻⁸.

2.2. Main ideas about speckle

2.2.1. Speckle appearance and localization

When coherent laser light is diffusely reflected by a rough surface a speckled appearance of light is observed. The speckle pattern is seen sharply when the eye is focused on any plane in space and with maximum contrast; the light scattered from a rough surface sets up a complicated, standing wave field in space because of the high coherence of the laser beam.

By interference of the light waves coming from different points on the rough object we have statistically distributed field amplitudes and thus also field intensities at different points in space. Hence the speckle phenomenon is brought about by statistical multiple beam interference. We simulated this in Fig 1: on the upper side of the paralelipiped we placed the punctiform light coherent sources with random positions and phases. On the down side face of the paralelipiped we consider the observation plane and studied the result of the interference of the many random coherent sources.

2.2.2. Speckle distribution

When looking at a speckle pattern Fig 2, we notice that darker parts obviously occur more often than bright spots. At a point P in space the individual speckle amplitude is:

$$E_n = \frac{A_n}{r_n} \exp(ikr_n) \quad (1)$$

sum to the total amplitude

$$E_n = \sum_n \frac{A_n}{r_n} \exp(ikr_n) \quad (2)$$

The result of the intensity obtained in the lower part of the paralelipiped is illustrated in Fig.3g for a different number of random distributed point-like sources in the upper plane. On the lateral plane the result of the interference is illustrated in Fig.3e. Fig. 3a and 3b are histograms of the phase distribution (Fig.3f) and intensity distribution respectively in a speckle pattern.

The probability density $p(I)$ for the intensity may be obtained analitically⁶ as

$$p(I) = \frac{1}{\langle I \rangle} \exp\left(-\frac{I}{\langle I \rangle}\right) \quad \text{for } I \geq 0 \quad (3)$$

in good concordance with our simulation. This is illustrated in Fig.3d. Indeed the intensities near zero occur more often. For the phase θ of $E_p = |E_p| \exp(i\theta)$ the probability distribution density

$$p(\theta) = \frac{1}{2\pi} \quad \text{for } \theta \in [-\pi, +\pi] \quad (4)$$

and the phase is indeed homogeneously distributed. (Fig.3c)

2.2.3. Speckle contrast

The fringe contrast is unity because the most probable intensity in the pattern is the null one (Fig.3d)

2.2.4. Speckle size - the aperture dependence

The speckled appearance of the difused light by a rough surface is a coherent effect. It is was pregnantly observed in the time coherent laser light appeared, but already known by a few bunch of scientists as early as when radar technique was promoted. It is fundamentally an interference effect. Let us consider o coherent laser beam illuminating a rough surface (Fig4.)

Every point of the surface becomes a secondary punctual Huygens spherical source of radiation, (or the source of a divergent bunch of rays diffusing (radiating) in all directions). The waves superpose in space and being higly coherent between them are interfering. The wavelet coming from the point P will have a different phase as reported to the corresponding wavelet coming from the point P' because of the microgeometry of the surface. For this reason the eye pupil P will receive a random phase distributed bunch of rays making different angles between them; the maximum angle is determined by the apperture P dimension. The eye will observe a random fringe interference system called speckle. The dimensions of the speckles will be also randomly distributed but is obviously depending of the pupil P of the eye. This is easily proved observing a laser illuminated object through a iris aperture, or increasing our distance from the object. The magnitude of the speckles depends also on the illuminated area on the object. A first distinction must be made to classify the speckle patterns.

2.2.4.1. Objective speckle pattern

It is the pattern obtained when diffused light produced by an $L \times L$ laser illuminated area is detected and measured on a screen z length units appart. The medium size grain is, for this case:

$$\sigma \equiv \frac{\lambda z}{L} \quad (5)$$

A simple physical explanation of this value could be the following: the highest density fringes will corespond to the rays coming from the points separated by L , and the minimum density fringes corresponds to tyhe rays coming from points separated at the confusion limit. Remembering the Young interference experiment (Fig.5), the corresponding fringe frequency on the observing plane will be:

$$f_{\max} = \frac{L}{\lambda z} \text{ and } f_{\min} = 0 \quad (6)$$

so the mean value will be somewere between them.

2.2.4.2. Subjective speckle pattern

Subjective speckle pattern is obtained when an object which is illuminated by laser light is projected by a lens. In the image plane the object is covered by a distribution of spots (Fig.6)

The dimensions of these spots are determined by the diffraction limit of the imaging system. In geometric optics light rays emanating from a point would be imaged back into a point. In practice because of the diffraction, the point image cannot be arbitrarily small. The limit, or the smallest point image produced by a physical lens is generally accepted as defined by the Rayleigh criterion; it states that the image is resolved if the central maximum in the diffraction pattern of a point image coincides with the first dark fringe of its adjacent point. For example if the lens L with a diameter D were used in the imeging as shown in Fig.6, the point object P_1 would be focused into a diffraction pattern in the form of a first-order Bessel function. The distance between the central peak and the first zero would be

$$\delta = 1,22 \frac{\lambda p'}{D} \quad (7)$$

and by the Rayleigh criterion, the minimum distance between two resolvable object points would therefore be of this magnitude. If points Q_1 and Q_2 in the image plane correspond to the points P_1 and P_2 at the limit of resolution we can consider that a point further away from P_1 than P_2 will contribute a small amount of light to the amplitude Q_2 but since the secondary maxima of the diffraction pattern are very much smaller than the primary maxima, such contribution can be neglected. We consider the intensity at a given point, say the center of a bright spot. The speckle is bright because a great number of waves from neighboring object points happen to interfere constructively at that point. The image of any object

point is a diffraction pattern that is significant only over a region whose radius is about equal to Rayleigh limit. On average the intensity will be great over an area equal to that of the Airy disk.

$$d = 2,4 \frac{\lambda p'}{D} \quad (8)$$

Because of the random phases the speckle are not round, but very irregular. The dependence of the size of the subjective speckle dimensions of the aperture viewing lens can be observed by comparing the size of the speckle when an object is viewed directly by eye and when an aperture smaller than the eye pupil is placed in front of the eye. In this case the speckle size will be seen to increase. This can be understood considering the Young double slit interference experiment. The fringe separation of the interference pattern depends on the angle between the two slits as seen from the the *observing* point Q :

$$i = \frac{\lambda z}{L} \approx \frac{\lambda}{\alpha} \quad (9)$$

The smaller this angle the larger the fringe separation.

Subjective speckle is always seen sharply because it results from statistical interference of coherent waves entering the eye. While the mean speckle size cannot be quantified it can be related to the autocorrelation function $R(\vec{r}_1 \vec{r}_2)$ of the intensity distribution defined as

$$R(\vec{r}_1 \vec{r}_2) = \langle I(\vec{r}_1) I(\vec{r}_2) \rangle \quad (10)$$

where the average is performed over many speckles. When $\vec{r}_1 = \vec{r}_2$, $R = \langle I^2 \rangle$. As $(\vec{r}_1 - \vec{r}_2)$ increases, intensities $I(\vec{r}_1)$ and $I(\vec{r}_2)$ are different, and eventually become totally unrelated to one another. In this case $R(\vec{r}_1 \vec{r}_2) = \langle I(\vec{r}_1) \rangle \langle I(\vec{r}_2) \rangle$.

The distance at which the intensities are unrelated is an estimate of the speckle dimensions. Goodman⁹ realized rigorous calculations for subjective and objective speckle, calculating the autocorrelation function of the scattered intensity. Subjective speckle produced by an area of dimension $L \times L$ uniformly illuminated by a coherent (laser) beam has an autocorrelation function

$$R(\Delta x, \Delta y) = \left\langle \langle I \rangle^2 \left[1 + \text{sinc}^2 \left(\frac{L \Delta x}{\lambda z} \right) \text{sinc}^2 \left(\frac{L \Delta y}{\lambda z} \right) \right] \right\rangle \quad (11)$$

The average size of a speckle will be the value for which the sin function first becomes zero:

$$(\Delta x) = \frac{\lambda z}{L} \quad (12)$$

The autocorrelation function of the image-plane speckle was also calculated by Goodman as:

$$R(r) = \langle I \rangle^2 \left[1 + \left(2J_1 \left(\frac{\pi a r}{\lambda v} \right) / \left(\frac{\pi a r}{\lambda v} \right) \right) \right] \quad (13)$$

and the speckle size is taken as the separation between the first two minima of the Bessel function:

$$d = \frac{2,4 \lambda v}{a} \quad (14)$$

3. SPECKLE INTERFEROMETRY

The basic principles of speckle interferometry is to optically combine a *speckle-pattern* either with a *second speckle-pattern* or with a *smooth reference wave* of comparable brightness. One can no longer expect to observe recognizable fringe patterns, but if the two superposed disturbances are mutually coherent they will produce a new single well-developed

speckle-pattern. If the two disturbances remain coherent in relation to the integration time of the eye (or camera) but their mutual phase changes slowly, this will become apparent to the observer in terms of a pronounced local twinkling of the individual speckles. If the changes of phase occur too rapidly the amplitude cross-products between the two disturbances give a vanishing time average and it is addition of intensity rather than of amplitude which determines the resultant pattern.

3.1. Speckle over speckle.

A plane optically rough surface D lying in the (x, y) plane is viewed normally in the z direction by a lens L of focal length f and aperture diameter a . The surface is illuminated by a divergent wavefront, and a photograph of the image-plane speckle pattern is recorded in the plane S (screen). If the photographic plate is exposed once only, the intensity distribution of the speckle pattern can be represented as the sum of a set of sinusoidal gratings whose spatial frequencies vary between zero and upper limit, which is determined by the viewing lens aperture and the lens - to recording plane distance. When the developed plate is illuminated by a plane wave front and the diffracted light is observed in a Fourier plane, it will form a circle whose diameter is determined by the maximum spatial frequency.

When the plate is exposed first to light scattered from the undisplaced object, and then to light scattered from the object after it has been displaced by an amount Δx in the Ox direction, two identical (intensity) speckle patterns are obtained which are displaced with respect to one another by an amount Δx (if we consider the magnification of the optical system to be unity)⁶.

After double exposure the photographic plate has a transmission proportional with the sum of the transmittivities of the individual speckle patterns:

$$t(x, y) \propto I(x, y) + I(x + \Delta x, y) \quad (15)$$

The intensities $I(x, y)$ and $I(x + \Delta x, y)$ denote the nonshifted and shifted speckle pattern respectively (The photographic plate model is obsolete; a digital recorded image of the two intensities were recorded, memorized and added).

If we consider the speckle pattern intensity distribution in the camera plane as a sum of Dirac delta function properly pondered by a local (point) depending intensity (convolution with Dirac delta function):

$$I(x, y) = (I * \delta)(x) = \int I(\xi, y) \cdot \delta(x - \xi) d\xi \quad (16)$$

$$I(x + \Delta x, y) = (I * \delta)(x + \Delta x) = \int I(\xi, y) \cdot \delta(x + \Delta x - \xi) d\xi \quad (17)$$

and after translation by an amount Δx (1D case) the total intensity in the registration plane will be

$$I_r = I(x, y) + I(x + \Delta x, y) = \int I(\xi, y) \cdot [\delta(x - \xi) + \delta(x + \Delta x - \xi)] d\xi \quad (18)$$

The Fourier transform of the above intensity distribution become from the convolution theorem

$$\tilde{I}_r(f_x, f_y) = FT[I_r(x, y)] = FT[I(x, y)] \cdot FT[\delta(x) + \delta(x + \Delta x)] \quad (19)$$

Or it is well known that

$$FT[\delta(x) + \delta(x + \Delta x)] = 2 \cdot \cos\left[\frac{\pi}{\lambda} \Delta x \sin \alpha\right] \exp\left[-i \frac{\pi}{\lambda} \Delta x \sin \alpha\right] \quad (20)$$

so that the intensity of the light diffracted at an angle α in the Fourier plane is

$$\tilde{I}_r = FT[I(x, y)] \cdot 4 \cdot \cos^2\left(\frac{\pi}{\lambda} \Delta x \sin \alpha\right) \quad (21)$$

Thus, the diffraction halo will contain fringes with minima occurring when

$$\sin \alpha = (2n + 1) \frac{\lambda}{\Delta x} \quad n = 0, 1, 2, 3 \dots \quad (22)$$

The spacing of these fringes can be seen to be equivalent to those obtained with two slits and for this reason are often referred to as Young's fringes. Such fringes are known as diffraction halo fringes (Fig 7).

3.2. Speckle pattern over smooth reference wave. Vibration fringe formation

A basic arrangement of ESPI for vibration analysis is shown in Fig.8. The object under test is illuminated by a coherent light beam - called object beam - and imaged by a lens on a CCD camera. A second coherent lens beam - the uniform reference - is directed to the same CCD camera to produce an interference pattern. The two waves are very well directed on exactly the same way, and coming on different paths from the same coherent source. Their path length from the laser source to the CCD camera are within the coherence length of the laser. If letting¹⁰

$$E_o(x, y) = A_o(x, y) \exp[i\Phi_o(x, y)] \quad (23)$$

$$E_r(x, y) = A_r(x, y) \exp[i\Phi_r(x, y)] \quad (24)$$

represent the optical field of the object beam and the reference beam in the CCD matrix, the detected intensity is the interference pattern:

$$\begin{aligned} I(x, y) &= \langle [E_o(x, y) + E_r(x, y)][E_o(x, y) + E_r(x, y)]^* \rangle \\ &= A_o^2(x, y) + A_r^2(x, y) + 2\langle E_o(x, y)E_r^*(x, y) \rangle \end{aligned} \quad (25)$$

When the object vibrates sinusoidally the optical phase distribution of the object wave is given by:

$$\Phi_o(x, y) = \Phi'_o(x, y) + \frac{4\pi}{\lambda} a_o(x, y) \cos \omega t \quad (26)$$

If the frame frequency of the CCD camera is lower than the vibration frequency of the object the interference term in equation could be developed as:

$$\begin{aligned} \langle E_o(x, y)E_r^*(x, y) \rangle &= A_o A_r \frac{1}{\tau} \int_0^\tau \exp \left\{ \left[\Phi'_o(x, y) - \Phi_r(x, y) + \frac{4\pi}{\lambda} a_o(x, y) \cos \omega t \right] \right\} dt \\ &= A_o A_r J_0 \left[\frac{4\pi}{\lambda} a_o(x, y) \cos \Phi(x, y) \right] \end{aligned} \quad (27)$$

where

$$\Phi(x, y) = \Phi'_o(x, y) - \Phi_r(x, y) \quad (28)$$

is the phase difference between the object and reference wave in the static state of the object (the random phase of the speckle pattern produced by the interference between the speckle pattern produced by the object and the uniform reference). The intensity of the interference pattern will be now

$$I(x, y) = I_o(x, y) + I_1(x, y) \cdot J_0 \left[\frac{4\pi}{\lambda} a_o(x, y) \right] \cdot \cos \Phi(x, y) \quad (29)$$

$$I = I(x) + I(x + \Delta x) = \Sigma I_o(x) \cdot [\delta(x) + \delta(x + \Delta x)] \quad (30)$$

To observe such an intensity displayed on the monitor we must make two steps: high pass filtering and quadric rectifying. Indeed the signal has negative and positive values. The television monitor will however display negative-going signal as area of blackness; to avoid this loss of signal, the intensity signal is rectified before being displayed on the monitor. High pass filtering of the signal is found to give improved visibility fringes by removing low frequency noise together with variations in mean speckle intensity. The final resultant fringe intensity displayed on the monitor is expressed by:

$$I(x, y) \cong J_0^2 \left[\frac{4\pi}{\lambda} a_0(x, y) \right] \cos^2 \Phi(x, y) \quad (31)$$

A conventional vibration fringe pattern of the flat disk centrally excited is shown in Fig.9.

4. IN PLANE DISPLACEMENT MEASUREMENT USING YOUNG SPECKLE INTERFEROMETRY

As early as 1972 D. E. Duffy¹¹ proposed a method relating moiré gauging of in plane displacement using speckle pattern interferometry. In his method the surface is illuminated with only one laser beam. A description of the Duffy's method considers a scattering surface illuminated by a coherent light beam as shown in Fig.10.

A lens is positioned to form an image of the scattering surface on a CCD camera. An opaque stop containing two apertures of width d and separated by a distance D is placed in front of the lens. If either of the aperture is blocked, the other will form a speckled patterns image of the scattering surface. As we already know the width of the speckle is inversely proportional to the aperture size. When light is passed by both aperture, interference fringes will be formed within a speckle when the two pattern overlap, like in the classical Young double slit experiment. Thus a periodic grid structure is introduced within each speckle cell (Fig. 11). The grid lines run perpendicular to the line joining the aperture centers, so that by rotating the aperture, one can change the orientation of the lines in any direction over the image. If 2α is the angle under the lens is viewed from the camera, the spacing of the Young fringes on the CCD camera is:

$$i = \frac{\lambda}{2 \sin \alpha} \cong \frac{\lambda}{2\alpha} = \frac{D}{2p'} = \frac{\lambda p M}{D} \quad (32)$$

if the lens magnification is $M = p/p'$, $i = \frac{\lambda p M}{D}$ on the camera and $i_0 = \frac{\lambda p}{D}$ on the object. The distribution of the speckles within the image is a function of the size and location of the double apertures with respect to the object and must be carefully chosen as do not overpass the resolution of the CCD camera. On the other side the displacement of the object must be small enough as to produce Young fringes within the speckle and also the fringe distance must be larger than the resolution of the camera. The sensibility of the moiré technique depends on the grating pitch on the object

$$i_0 = \frac{\lambda p}{D} \quad (33)$$

or on the angle subtended at the object by the two apertures. For a given distance between the object and camera lens, the limiting sensitivity is the determined by the diameter of the camera lens. From the viewpoint of the coherence of the light source only the spatial coherence requirements is relevant. A powerfull laser diode is usually good enough for illuminating the object. A Duffy-Young diode laser camera is presented in Fig.12, and the usual illustration of the in plane displacement of the object illustrated by an in plane rotation is presented in Fig.13. The method was developed to a greater extent by Sirohi¹².

5. CONCLUSIONS

Electronic speckle pattern interferometers are complex optoelectronic devices including lasers, digital cameras, optics, computers, frame grabbers and specialized software for digital handling of data. Their impact on the engineering is growing up constantly. We presented the basic of speckle phenomena, the physics of applications and a short presentation of two set ups for out of plane and in plane deformation evidence and measurement.

REFERENCES

1. J. M. Burch, *Interferometry with Scattered Light, Optical Instruments and Technique*, ed. J. Home Dickson, Oriel Press, 1970.
2. M. Francon, "New method of optical processing using a random diffuser", *Optica Acta*, , 20, (1) pp.1-17,1973.
3. E. Bacaloglu, *Elemente de fisica*, Bucuresti, Typografia Curtii, pp. 308-309, 1870.
4. M. Francon, *Granularite laser. Speckle. Applications en Optique*, Masson, Paris, 1978.
5. M. Francon, *Laser Speckle and Applications in Optics*, Academic Press, N. Y, 1979.

6. R. Jones, C. Wykes, *Holographic and Speckle Interferometry*, Cambridge University Press, London, NY, 1983.
7. J.C. Dainty (ed), *Laser Speckle and related phenomena*, Topics in Applied Physics, Vol. 9, Springer Verlag Berlin, 1975.
8. W. Lauterborn, T. Kurz, M. Wiesenfeldt, *Coherent Optics*, Springer Verlag, Berlin, Heidelberg, 1993.
9. J.W. Goodman, *Laser speckle and Related Phenomena*, chapter 2, ed. J. C. Dainty, Springer, 1975.
10. Yaotang Li, "ESPI vibration fringe enhancement by laser diode wavelength modulation", SPIE, Vol. 1553, *Laser Interferometry IV: Computer-Aided Interferometry*, ed. R.J.Pryputniewicz, pp. 150-159, 1991.
11. D.E. Duffy, "Moiré Gauging of In-Plane Displacement Using Double Aperture Imaging", *Applied Optics*, 11(8), pp. 1778-1781, 1972.
12. R.S. Sirohi, "Speckle Metrology: Some Newer Techniques and Applications", pp. 318-327, in *International Trends in Optics and Photonics ICO IV*, ed. T. Asacura, Springer, Berlin, 1999.

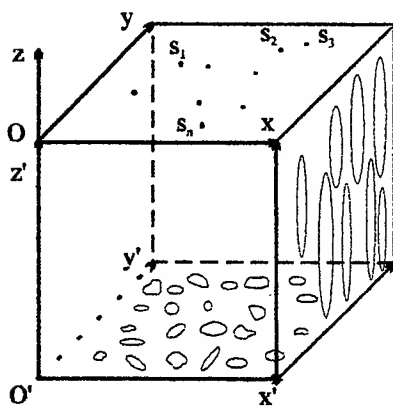


Fig. 1 Simulation geometry of speckle pattern production

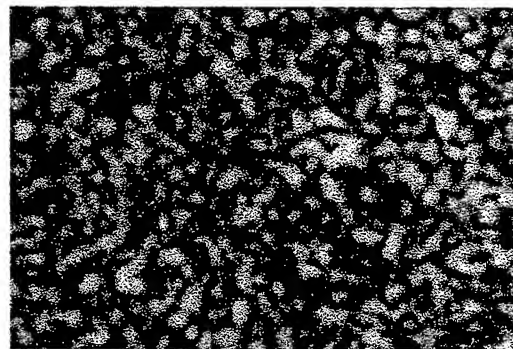
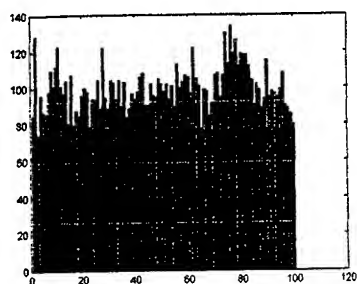
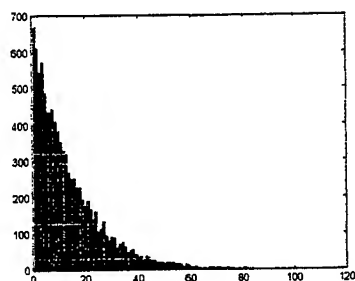


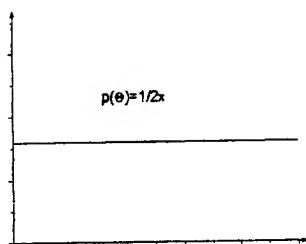
Fig. 2 Speckle pattern photography



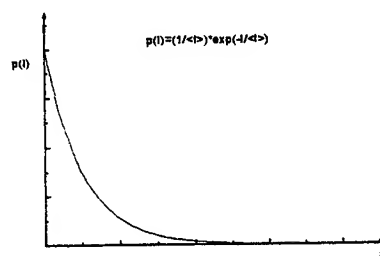
3a Phase histogram



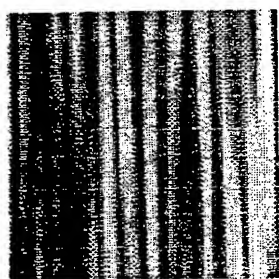
3b Intensity histogram



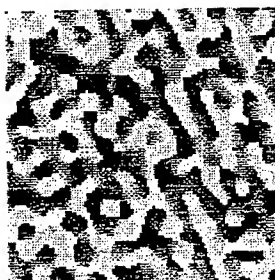
3c Phase distribution



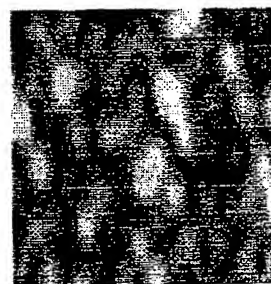
3d Intensity distribution



3e Simulated speckle pattern on a lateral side of the parallelepiped



3f Simulated phase distribution in a speckle pattern



3g Simulated objective speckle pattern

Fig. 3 Simulation results of an objective speckle pattern

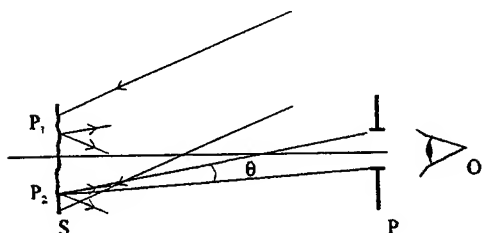


Fig. 4 Observation of a coherent laser beam illuminated rough surface

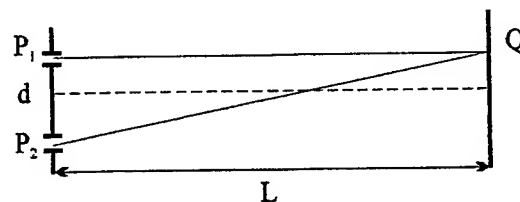


Fig. 5 Young double slit experiment geometry

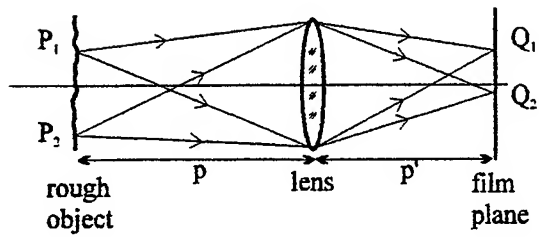


Fig. 6 Optical set-up for subjective speckle pattern production

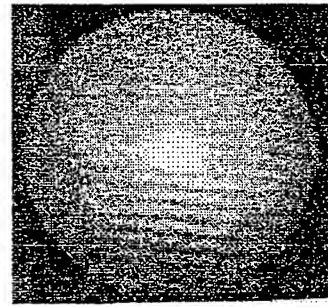


Fig. 7 Diffraction halo fringes

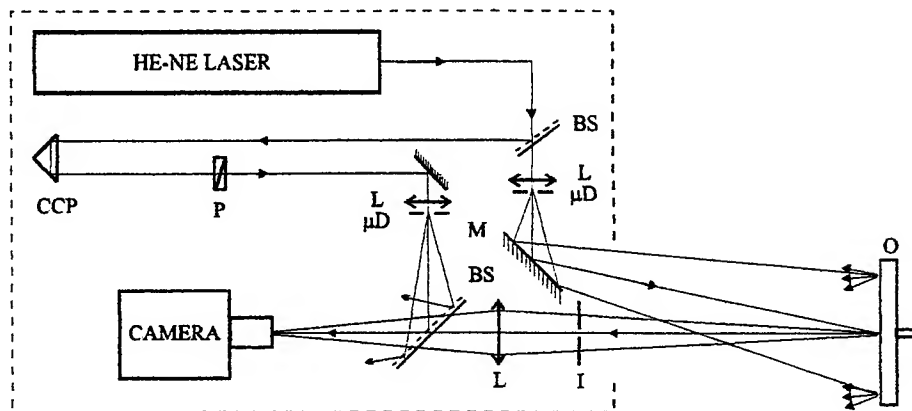


Fig. 8 Optical set-up of a ESPI

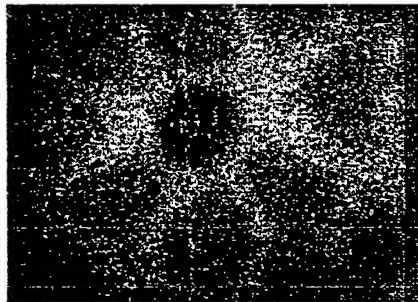


Fig. 9 Vibration fringe pattern of a flat centrally excited disc

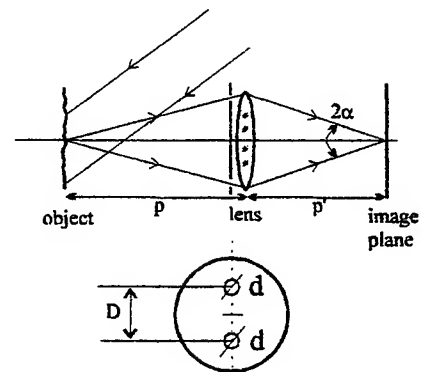


Fig. 10 Geometry of the Duffy double slit experiment

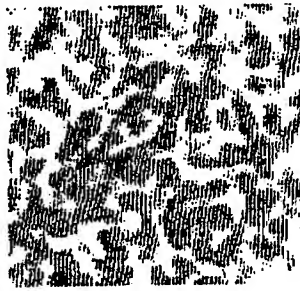


Fig. 11 Young fringes in speckle pattern (zoomed image)

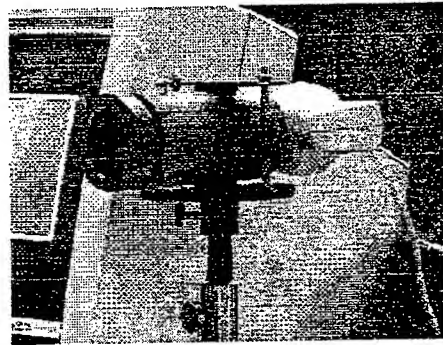


Fig. 12 Photography of a ESPI digital camera

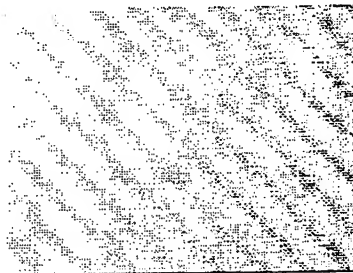


Fig. 13 In plane rotation of a rough metallic plate;
typical fringes

Holographic interferometry study of phenol diffusion

Mona Kurzluk ^{*a}, Anicuta Guzun^b, Levai Stefan^c,

^aTechnical University of Construction, Physics Department, Bv. Lacul Tei 124, sect.2, Bucharest.

^b"Polytechnica" University, Chemical Engineering Department.

^cUniversity of Bucharest, Physics Department.

ABSTRACT

Phenol exists in wastewater streams for many industrial processes. The toxicity of phenolic effluents is well known and their treatment must be accomplished. Among the methods of recovery, the technique of adsorption provides a convenient way with low cost. For modelling the diffusion process it is necessary to know the diffusion constant. The technique of double-exposure holographic interferometry (HI) is used to study phenol diffusion in water in the presence and in the absence of activated carbon. The diffusion constant is calculated by a simple and direct measurement of interferograms.

Keywords: holographic interferometry, diffusion.

1. INTRODUCTION

Although it was discovered in early 18 th century, the diffusion phenomenon is still intensely studied because it is essential in understanding and controlling any inter-phase mass transfer phenomena. The precise determination of the diffusion coefficients is necessary for the design of separation devices in chemical industry. Optical methods for diffusion study have some advantages (precision, versatility and reduced measure time) over the classical¹⁻⁴ ones (Stokes diffusion cell). Optical methods based on free diffusion are generally preferred to classical ones, in the determination of liquid-phase mutual diffusion coefficients, due to their high accuracy. The technique of HI can be used not only for small molecular substance diffusion study, but also for macro-molecular system in gels. The diffusion study of macro-molecular system in gels is of great interest in human tissue engineering (drugs transfer in gels, membranes and human tissue). Protein diffusion is also a subject of active investigation⁵. Phenol is a major pollutant under strict effluent restriction. The concentration of phenol in polluted wastewater streams is high enough to be recovered. Among the methods of recovery, the technique of adsorption from an aqueous solution on activated carbon is a separation process widely used in industry and environmental technology. From the materials used as adsorbents, granular activated carbon has been widely used in environmental pollution control due to its capability to adsorb a broad range of organic and inorganic compounds. Column adsorber packed with granular activated carbon (GAC) is used to treat ground water and industrial wastewater contaminated with organic compounds. To properly design a GAC column, information regarding adsorption equilibrium and kinetics are required. Equilibrium data can be easily collected from batch experiments. On the other hand, accurate kinetic data including film transfer rate and interparticle diffusion rate parameters are more difficult to obtain.

The aim of this paper is to present experimental results for phenol diffusion in two cases: in pure water and in the presence of granular activated carbon using double - exposure HI.

2. EXPERIMENTAL TECHNIQUES

In order to obtain interferograms that show phenol diffusion, we made a classical holographic interferometry set-up, presented in Fig. 1. The laser beam, emerging from a He-Ne laser (6 mW), is split in reference and object beams by means of the beam-splitter BS. Both the transmitted and the reflected beams are expanded and filtered with lenses L1 and L2, and with pinholes MD1 and MD2. The reflected beam represents the object beam and passes through the diffusion cell having 10 X 100 X 100 mm, after the reflection on the mirror M. In front of the diffusion cell one puts a

* Correspondence: Email: monak@hidro.utcb.ro / Email: a.guzun@oxy.pub.ro

diffusing glass. The reference beam passes through the beam splitter BS and, after being expanded and filtered meets the holographic plate HP. The object and the reference beams overlap on the holographic plate, generating a system of interference fringes.

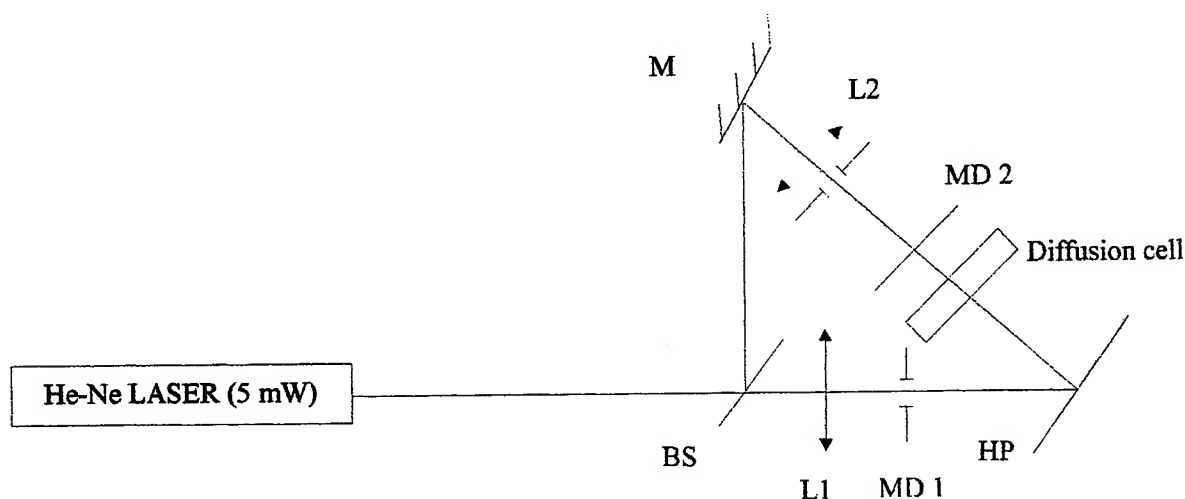


Fig. 1 Experimental set-up for double-exposure holographic interferometry for visualising diffusion of phenol.

As granular activated carbon was used Filtrasorb® 300 produced by Chemviron Carbon. The effective size is in the range 0.80 to 1.00 mm.

3. RESULTS

3.1 Refractive index gradient determination for phenol diffusion in water.

Using the set-up presented in Fig.2, we obtained a series of interferograms, one of them being given in Fig 3.

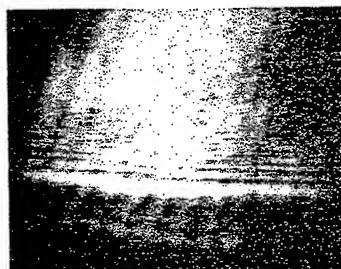


Fig. 2 Interferogram for phenol diffusion in water.

Holographic interferometry with double-exposure implies the recording of two holograms of the studied object on the same holographic plate. The fringes of interference obtained reveal the change of the object state between the two exposures. In our experiment we made the first exposure after 15 min from the beginning of the diffusion, and the second one after 2h. The fringes presented in Fig. 3 represent isoconcentration planes. By processing these fringes one can determine the concentration gradient, the refractive index gradient and the diffusion constant.

For a large number of substances and for a wide range of concentration values there is a linear dependence of the refractive index on concentration, so one may consider that⁶ :

$$n(y, z) = n_0 + \frac{dn}{dC} C(y, z) \quad (1)$$

where, $n(y, z)$ is the refractive index of the solution, n_0 is the refractive index of the solvent, $C(y, z)$ is the concentration due to the diffusion given by:

$$C(y, z) = (2N_{y,z} + 1) \frac{\lambda}{2l} \left(\frac{dn}{dC} \right)^{-1} \quad (2)$$

where, l is the width of the cell, $\frac{dn}{dC}$ is the slope of the dependence $n = n(C)$, λ is the wavelength of the laser beam (633 nm).

Using a Pulfrich refractometer we have determined the dependence of refractive index on concentration for phenol-water

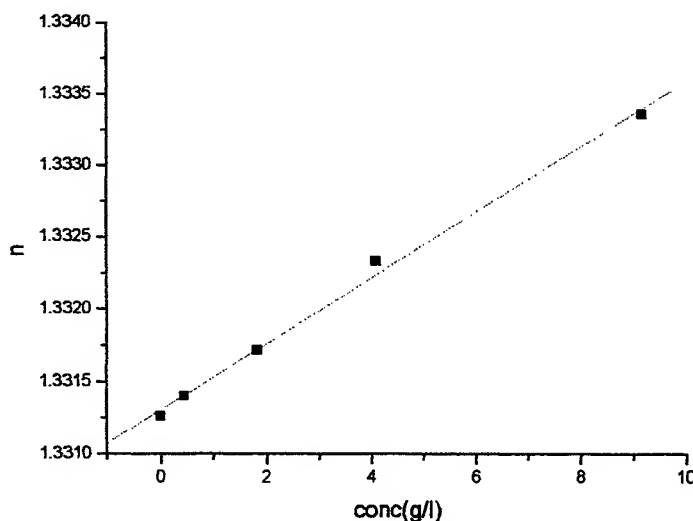


Fig.3. Refractive index dependence on concentration for phenol-water system.

Let be the first black interference fringe closest of the interface counted like fringe of zero order. So, the concentration C_0 of the plane containing this fringe and being parallel with the interface is:

$$C_0 = \frac{\lambda}{2l} \left(\frac{dn}{dC} \right)^{-1} = 0.27 \text{ kmol/m}^3$$

$$n = n_o + \frac{dn}{dC} C_o = 1.337578$$

$$\frac{dC}{dz} = 9.73 \frac{\text{kmol}}{\text{m}^3} / \text{mm}$$

$\frac{dn}{dz} = 0.204 \text{mm}^{-1}$, where dn/dC is the slope experimentally determined, $\lambda = 6328 \text{ \AA}$, $l=5\text{mm}$ is the width of the diffusion cell, n is the refractive index corresponding to the first black fringe, n_o is the refractive index of solvent (distilled water) and z is the distance between the bottom of the diffusion cell and the position of the first black fringe after two hours from the beginning of the diffusion phenomenon.

3.2 Diffusion constant determination for phenol -water diffusion.

The diffusion process is ruled by Fick's second law, which for 1-D diffusion can be expressed as:

$$\frac{\partial C}{\partial t} = D_{AB} \left(\frac{\partial^2 C}{\partial z^2} \right) \quad (3)$$

where D_{AB} , the diffusion coefficient, is independent of the concentration in the interval of concentrations considered. The solution of this equation, in the case of two liquids initially separated at the point $z=0$ and with concentrations C_{oi} and C_{os} , is⁷.

$$C(z, t) = \frac{(C_{oi} + C_{os})}{2} + \frac{C_{oi} - C_{os}}{\sqrt{\pi}} \int_0^{z/2\sqrt{D_{AB}t}} \exp(-\eta^2) d\eta \quad (4)$$

Due to the diffusion phenomenon taking place in the cell, the concentration gradient changes as a function of time, so the concentration variation between times t_1 and t_2 will be:

$$C(z, t_1) - C(z, t_2) = \frac{C_{oi} - C_{os}}{\sqrt{\pi}} \int_{z/2\sqrt{D_{AB}t_2}}^{z/2\sqrt{D_{AB}t_1}} \exp(-\eta^2) d\eta \quad (5)$$

If the refractive index varies linearly with the concentration between C_{oi} and C_{os} we can express the change of the index of refraction as:

$$n(z, t_1) - n(z, t_2) = A \int_{z/2\sqrt{D_{AB}t_2}}^{z/2\sqrt{D_{AB}t_1}} \exp(-\eta^2) d\eta \quad (6)$$

where A is a constant.

Through holographic interferometry it is possible to record on a holographic plate information concerning the state of the system at times t_1 and t_2 . When the interferogram is reconstructed, a series of interference fringes appear superimposed on the image of the cell whenever the following conditions is fulfilled:

$$n(z, t_1) - n(z, t_2) = \frac{(2k+1)\lambda}{2l} \quad (7)$$

where k is the interference order, λ is the wavelength of the light used, and l is the thickness of the diffusion cell. Combining the previous equations one obtains for the diffusion coefficient the following simplified expression (2):

$$D_{AB} = \frac{(z_1^2 - z_2^2)}{4t_1} \left[\frac{\ln(2p+1)z_1}{(2m+1)z_2} \right]^{-1} \quad (8)$$

Equation (8) allows us to obtain the diffusion coefficient using times t_1 and t_2 , which have elapsed, since the start of the diffusion, and the distances z_1 and z_2 from the interface position, at which the m th and p th order fringes, appear. The mean value of the diffusion coefficient that we obtained is $(8.9 \pm 0.02) \cdot 10^{-9} \text{ m}^2/\text{s}$. Formula (8) is valid only for $(t_2 - t_1) \ll t_1$. Ruiz-Bevia et al.³ consider a general formula having no restriction:

$$\left[\frac{\frac{z_1}{2} \sqrt{D_{AB} t_1}}{\frac{z_1}{2} \sqrt{D_{AB} t_2}} \int_{\frac{z_1}{2} \sqrt{D_{AB} t_2}}^{\frac{z_1}{2} \sqrt{D_{AB} t_1}} \exp(-\eta^2) d\eta / (2m+1) \right] - \left[\frac{\frac{z_2}{2} \sqrt{D_{AB} t_1}}{\frac{z_2}{2} \sqrt{D_{AB} t_2}} \int_{\frac{z_2}{2} \sqrt{D_{AB} t_2}}^{\frac{z_2}{2} \sqrt{D_{AB} t_1}} \exp(-\eta^2) d\eta / (2p+1) \right] = 0 \quad (9)$$

In order to apply the above formula, further experiments are needed.

3.3 Diffusion constant determination for phenol -water in presence of GAC

To determine the diffusion constant for phenol in water in the presence of GAC in the diffusion cell, granular activated carbon has been used as powder. This powder has been situated at the top of the cell. The interferogram obtained in this case is presented in Figure 4.

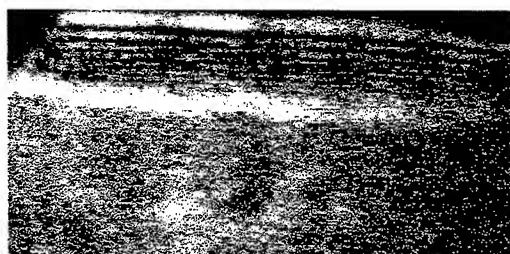


Fig.4. Interferogram for phenol diffusion in water in presence of granulated activated carbon

Pore diffusion is the mechanism by which adsorbates move within the pores of the adsorbent before being adsorbed onto the surface of the pores. The adsorbate movement is controlled by the liquid-phase concentration gradient. The pore diffusion is basically the same as the adsorbate's molecular diffusion except it is modified by adsorbent porosity and pore tortuosity. Surface diffusion occurs along the pore surface of the adsorbent after adsorption has taken place. The driving force for the surface diffusion is the difference in the amount adsorbed on the pore surface. Experimental results have shown that the values of surface diffusivity are a function of the solid phase concentration and temperature.

A concept of the apparent diffusion has been used to lump together the effects of surface and pore diffusions. The model for the apparent interparticle diffusion is ⁷:

$$\frac{\partial q}{\partial t} = \frac{1}{r^2} \frac{\partial}{\partial r} \left(D_e r^2 \frac{\partial q}{\partial r} \right) \quad (10)$$

Where, q is the solid phase concentration (g/m^3), r is radius (m) and D_e is the effective diffusivity (m^2/s). A relationship between the apparent diffusivity and the surface (D_s) and pore (D_p) diffusivity can be derived⁸. In liquid-phase adsorption, pore diffusivity is equal to the molecular diffusivity D_{AB} modified by the physical properties of the adsorbent. The physical properties include adsorbent pore porosity ϵ_p and pore tortuosity κ_p . The tortuosity of the pore has a negative effect on pore diffusivity. As tortuosity increases, pore diffusivity decreases. A model to correlate pore diffusivity with molecular diffusivity, adsorbent porosity, and tortuosity has been proposed:

$$D_p = \frac{\epsilon_p}{\kappa_p} D_{AB} \quad (11)$$

The ratio $\frac{\epsilon_p}{\kappa_p}$ should be a constant for a particular adsorbent and can be determined from others experiments. So that,

the relation (11) can be used to determine the pore diffusivity. Using equation (8) we have calculated the diffusion constant of phenol in water D_{AB} and we have obtained practically the same value as in the first series of experiments.

4. CONCLUSIONS

The main aim of this study was to obtain and to process interferograms in order to compute some physical quantities involved in the diffusion phenomenon, as refractive index, concentration gradients, and diffusion coefficient for the phenol - water system. Two cases have been studied. One is concerning phenol diffusion in water, and the second is focused on the phenol diffusion in water in the presence of granulated activated carbon. This experiment can be used to determine the pore diffusivity if adsorbent pore porosity ϵ_p and pore tortuosity κ_p are known. The value obtained for diffusion coefficient for phenol-water system is in good agreement with those given in literature.

REFERENCES

1. N. Bochner and J. Pipman, "A simple method of determining diffusion constants by holographic interferometry," *J. Phys. D: Appl. Phys.* **9**, pp. 1825-1830, 1976.
2. L. Gabelmann-Gray and H. Fenichel, "Holographic interferometric study of liquid diffusion," *Applied Optics*, **18**, pp. 343-345, 1979.
3. F. Ruiz-Bevia, A. Celdran-Mallol, C. Santos-Garcia, and J. Fernandez-Sempere, "Holographic interferometric study of free diffusion: a new mathematical treatment," *Applied Optics* **24**, pp. 1481-1484, 1985.
4. F. Ruiz-Bevia, J. Fernandez-Sempere, and N. Boluda-Botella "Variation of phosphoric acid diffusion coefficient with concentration," *AIChE J.* **41**, pp. 185-189, 1995.
5. D. D. Kong, T. F. Kosar, S. R. Dungan, and R. J. Phillips, "Diffusion of proteins and nonionic micelles in agarose gels by holographic interferometry," *AIChE J.* **43**, pp. 25-32, 1997.
6. I. Cucurezeanu, R. Chisleag, P. Suciuc and D. Borza, *Aplicatii ale holografiei optice*, Editura Tehnica, Bucuresti, 1984.
7. J. Crank, *The mathematics of diffusion*, Oxford U. P., London, 1975.
8. D. Gu, L. Nguyen, C. V. Philip, M. E. Huckman, R. G. Anthony, J. E. Miller, and D. E. Trudell, "Cs⁺ Ion exchange kinetics in complexe electrolyte solutions using hydrous crystalline silicotinates," *Ind. Eng. Chem. Res.* **36**, pp. 5377-5383, 1997.
9. E. G. Furuya, H. T. Chang, Y. Miura, H. Yokomura, S. Tajima, S. Yamashita, and K. E. Noll, "Interparticle mass transport mechanism in activated carbon adsorption of phenols," *J. Envir. Eng.* **122**, pp. 909-915, 1996.

Spectrophotometric characterization of useful dyes in laser photodynamic therapy

L. Danaila^a, M. L. Pascu^{*b}, A. Popescu^b, M. Pascu^c, R. Ion^d

^aInstitute of Cerebrovascular Diseases, Neurosurgery Department, Bucharest;

^bNational Institute for Lasers, Plasma and Radiation Physics, Laser Department, Bucharest;

^c"Prof. Dr. Dimitrie Gerota" Hospital, Neuropsychiatry Department, Bucharest;

^dZECASIN SA, Bucharest.

ABSTRACT

This paper presents the physico-chemical properties of some synthetic porphyrin dyes obtained at ZECASIN SA. We have measured the absorption, excitation and fluorescence spectra of these dyes in different solvents. From them we have concluded that the most reliable dye for our studies concerning the photodynamic therapy with UV lasers is Zn II - tetrakis-sulfonatophenyl porphyrin (Zn - TSPP).

Keywords: porphyrins, DMSO, natural saline, distilled water, photodynamic therapy, photosensitizers

1. INTRODUCTION

Due to the fact that the photodynamic therapy (PDT) is an innovative and attractive modality for the treatment of small and superficial tumors, it was long time studied. PDT as a treatment procedure requires both a selective photosensitizer and a powerful light source which matches the absorption spectrum of the photosensitizer ¹. As a photosensitizer Photofrin II was long time studied and used in photodynamic therapy of cancer. The major drawbacks of this product are the lack of chemical homogeneity and stability, skin phototoxicity, unfavourable physico-chemical properties and low selectivity with respect to uptake and retention by tumor versus normal cells. Second-generation photosensitizers, including the phthalocyanines, show an increased photodynamic efficiency in the treatment of animal tumors and reduced phototoxic side effects ¹.

Major limiting factors for the usefulness of PDT have been the limited penetration of light into the tissues and the low absorbance of the currently used sensitizers at wavelengths larger than those specific for hemoglobin (the main absorber in most tissues) ².

Most available data suggest a common mechanism of action. Following excitation of photosensitizers to long lived excited singlet and/or triplet states, the tumor is destroyed by reactive singlet oxygen species (type II mechanism) and/or radical products (type I mechanism) generated in an energy transfer reaction ^{1,3}.

As a function of the photosensitizer physical properties, the access towards tumoral cells, in vivo or in vitro, is different. First, it is necessary to find a solvent which could dissolve the dye. For hydrophilic sensitizers the most used solvent is water and deuterated water. This solvent is also consistent with the cell, because water is one of the major components of living cells. But these hydrophilic compounds are less sensitive than the lipophilic compounds.

In general, the solvents used in PDT are dimethylsulfoxide (DMSO), ethyl alcohol, water, phosphate buffer, natural saline, etc; the most used solvent for lipophilic dyes is DMSO which is a strongly coordinating solvent with a high donor number. It has both a "hard" site (the oxygen atom) and a "soft" one (the sulphur atom) and it is able to coordinate most transition metal ions and also the central metal from porphyrins or phthalocyanine macrocycles ⁴. After dissolving in DMSO, it is

*Correspondence: E-mail: pascu@ifin.nipne.ro; Fax: (401)4231719

necessary to minimize the toxic effects by mixing the solution with water or natural saline, in order to bring the DMSO concentration down to less than 5%.

Tumors differ in a number of ways from most normal tissues, which is particularly the case of the malignant tumor cells ⁴. The main differences between tumors and tissues include the following:

- a. solid tumors retain somewhat selectively a variety of dyes at concentrations higher than those found in many kinds of normal tissues, perhaps as a result of differences in the properties of the microvasculature, stroma, etc.
- b. the mitochondria of carcinoma cells differ from those in normal cells in that they accumulate very high concentrations of certain photosensitizing cationic dyes, such as some cyanine derivatives.
- c. the membrane of leukemic lymphocytes have high affinity binding sites for merocyanine 540 anionic photosensitizing dye.
- d. malignant tumor cells have some cell surface antigens that are different from those of normal cells. Monoclonal antibodies directed towards tumor cell antigens can be covalently coupled to photosensitizing dyes ⁵.

2. PHYSICO-CHEMICAL AND SPECTRAL PROPERTIES OF DYES

The dyes we studied are prepared at ZECASIN S. A., Bucharest, using appropriate methods ⁴.

The porphyrins and phthalocyanines represent two classes of chemically very versatile compounds. Depending on the central metal and/ or the peripheral substituents, a wide range of photophysical and photochemical properties can be obtained [4]. We have chosen these dyes because their absorption is strong along a large spectral range either, which made it possible to excite their fluorescence at 337.1 nm, the wavelength of the N₂ pulsed laser. The physico-chemical and spectral properties of these dyes are summarized in Table 1.

We measured the absorption, excitation and fluorescence spectra of TNP, TPP and TSPP (Figs. 1, 2 and 3). Then, we have studied porphyrin derivatives with metals, such as Zn -TNP, Zn - TSPP, Pb - TSPP and Mn II-TSPP (Figs. 4 - 12).

From the absorption, excitation and fluorescence spectra, that we have recorded with a SPECORD UV-VIS spectrophotometer and respectively with a classical photofluorimeter, we concluded that Zn-TSPP, which has a more intense fluorescence intensity could best fit our purpose concerning PDT. The absorption, excitation and fluorescence spectra of Zn-TSPP are presented in Figs. 9 and 10.

Tab. 1 Photosensitizer dyes

No.	Dye	Solvents used	Comments
1.	tetra-naphtyl porphyrin (TNP)	- DMSO - water with 5% DMSO	-porphyrin derivative -important absorption at 337.1 nm -good selectivity -high fluorescence intensity
2.	tetra-phenyl porphyrin (TPP)	- DMSO - water with 5% DMSO	-porphyrin derivative -important absorption at 337.1 nm; -good selectivity -high fluorescence intensity
3.	tetra-sulfonatophenyl porphyrin (TSPP)	- distilled water - DMSO - water with 5% DMSO	-porphyrin derivative -aggregation tendency in watery medium -high absorption at 337.1 nm -good selectivity
4.	Zn-tetrakis-naphtyl porphyrin (Zn-TNP)	- DMSO	-porphyrin derivative -high absorption at 337.1 nm -good selectivity -high fluorescence intensity

No.	Dye	Solvents used	Comments
5.	Zn II-tetra-sulfonatophenyl porphyrin (Zn-TSPP)	- distilled water - DMSO - water with 5% DMSO	-porphyrin derivative -reduced aggregation tendency in watery medium -high absorption at 337.1 nm -good selectivity -high fluorescence intensity
6.	Pb II-tetra-sulfonatophenyl porphyrin (Pb-TSPP)	- DMSO	-porphyrin derivative -high absorption at 337.1 nm -good selectivity -high fluorescence intensity
7.	Mn II-tetra-sulfonatophenyl porphyrin (Mn II-TSPP)	-distilled water -physiological serum	-porphyrin derivative -insoluble in DMSO -low absorption at 337.1 nm

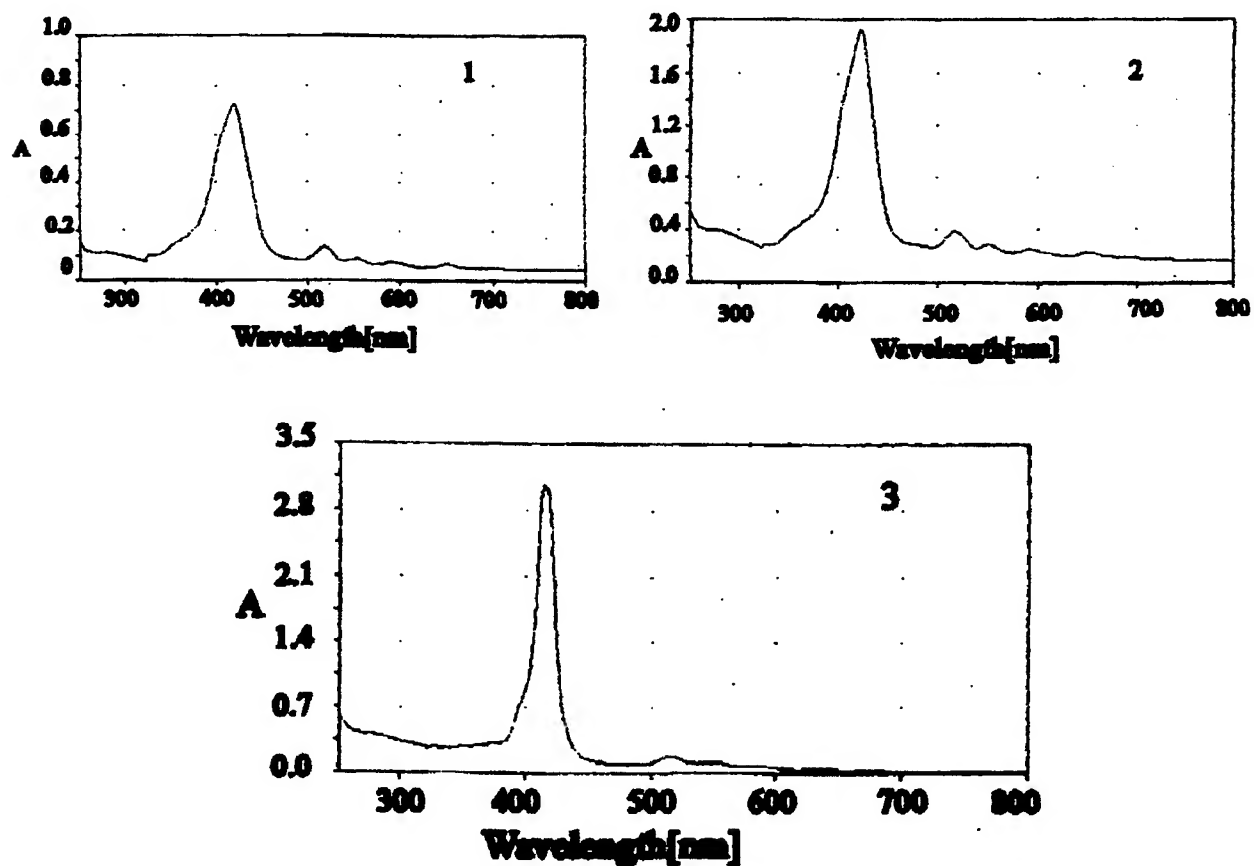


Fig.1 Absorption spectra of 1) TNP in 5% DMSO; 2) TPP in 5% DMSO; 3) TSPP in water.
(A - absorption measured as extinction)

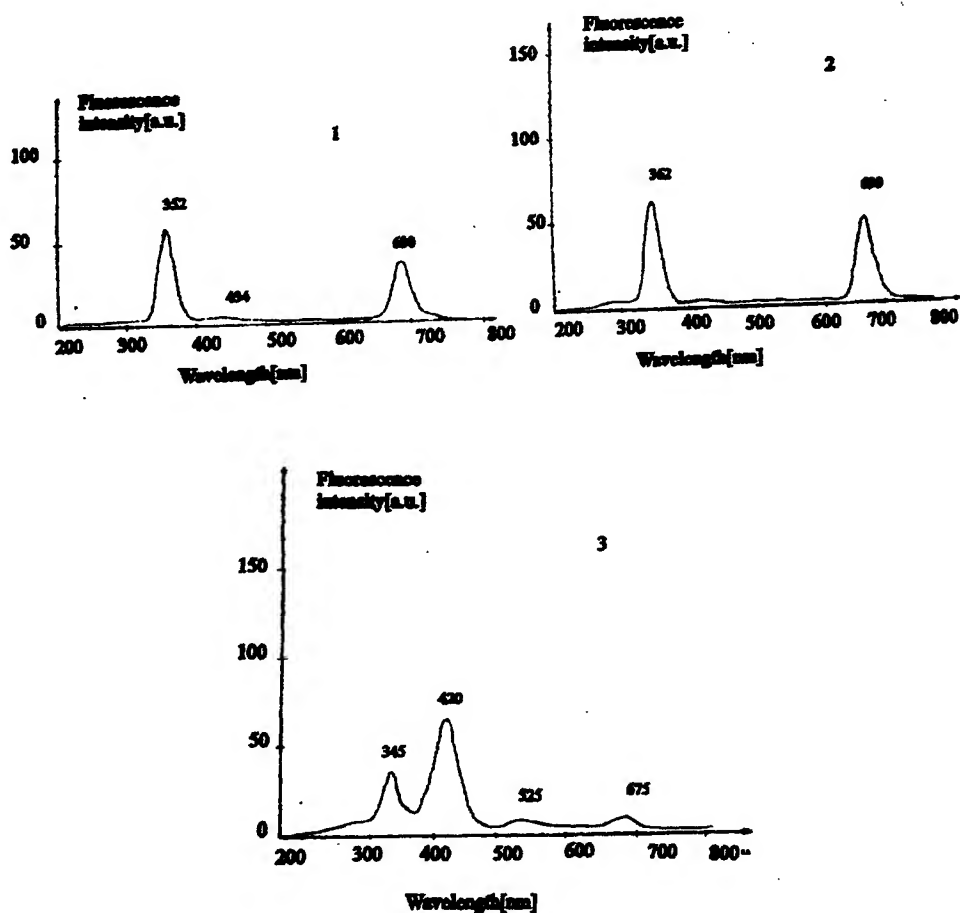


Fig. 2 Excitation spectra of
 1) TNP in 5% DMSO;
 2) TPP in 5% DMSO;
 3) TSPP in water.

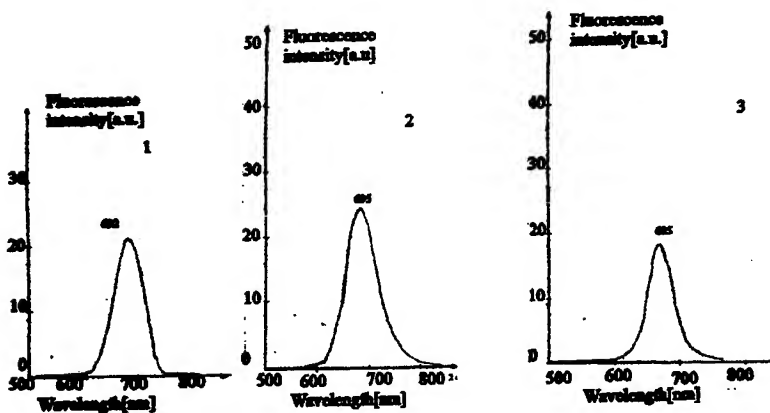


Fig. 3 Fluorescence spectra of 1) TNP in 5% DMSO; 2) TPP in 5% DMSO; 3) TSPP in water.
 Excitation wavelength: 337.1 nm.

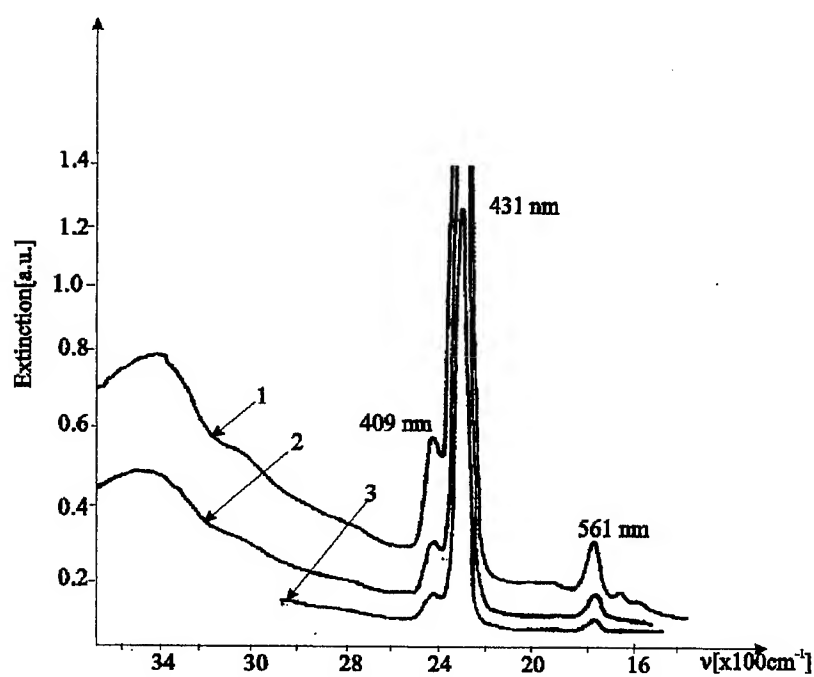


Fig. 4 Extinction spectra of Zn - TNP in DMSO at
1) 5×10^{-5} M; 2) 2.5×10^{-5} M; 3) 1.75×10^{-5} M

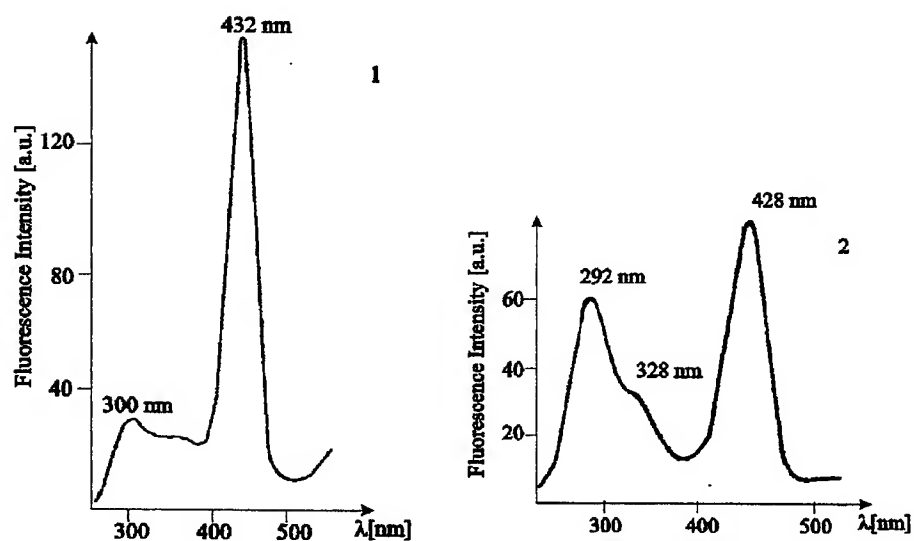


Fig. 5 Excitation spectra of Zn-TNP in DMSO at $c=10^{-5}$ M,
at 610 nm (1) and at 655nm (2) emission wavelengths

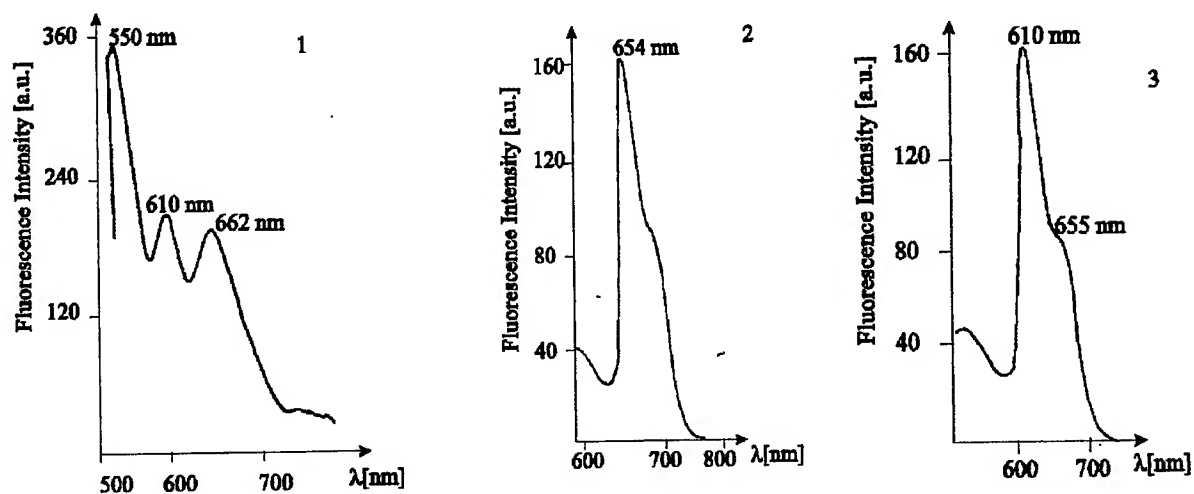


Fig. 6 Emission spectra of Zn-TNP in DMSO with $c=10^{-5}$ M at 337 nm (1), 436 nm (2) and 440 nm (3) excitation wavelengths

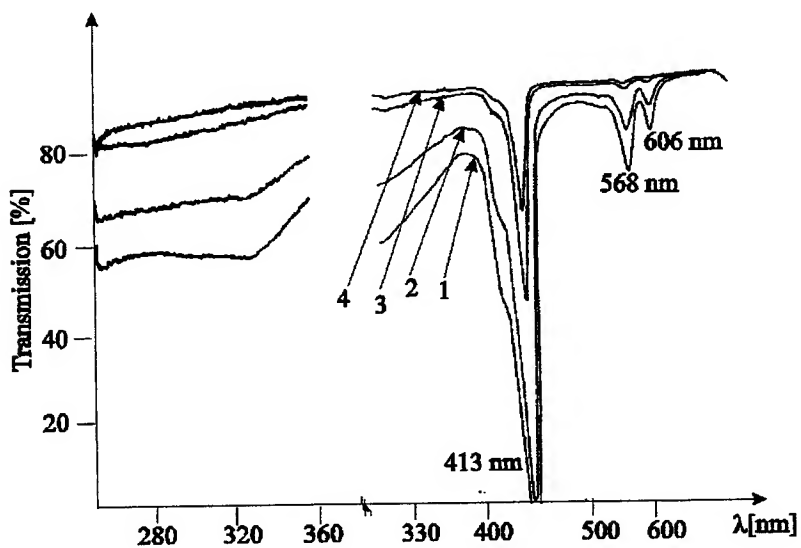


Fig. 7 Transmission spectra of Pb-TSPP in DMSO at 1) 10^{-5} M; 2) 5×10^{-4} M; 3) 10^{-4} M; 4) 5×10^{-5} M

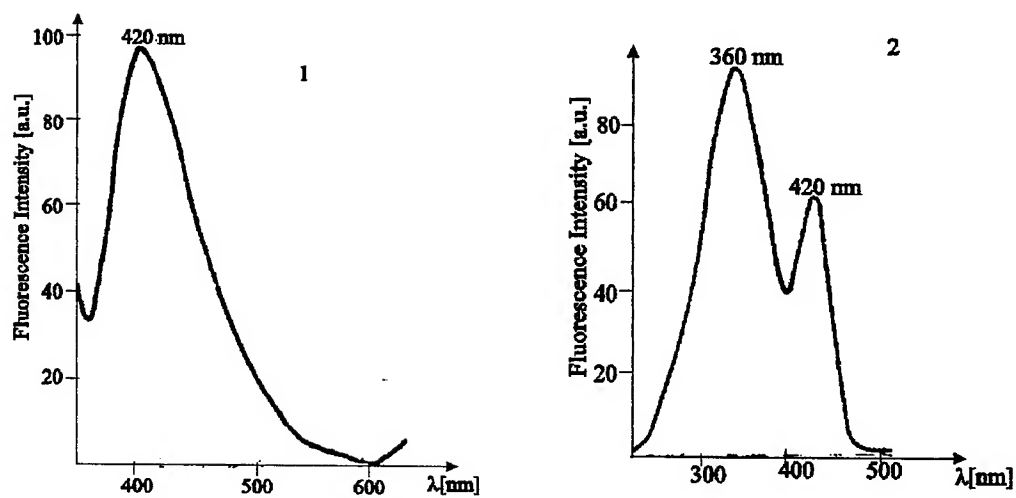


Fig. 8 Emission (1- $\lambda_{\text{ex}}=337$ nm) and excitation (2 - $\lambda_{\text{em}}=420$ nm) spectra of Pb-TSPP in DMSO at 10^{-5} M

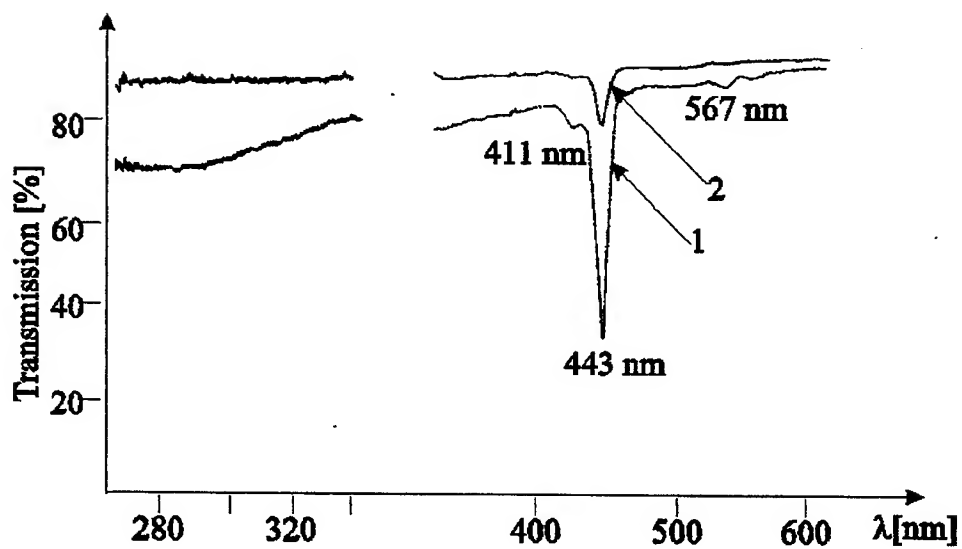


Fig. 9 Transmission spectra of Zn - TSPP in DMSO:
1). $c=10^{-3}$ M; 2). $c=10^{-4}$ M

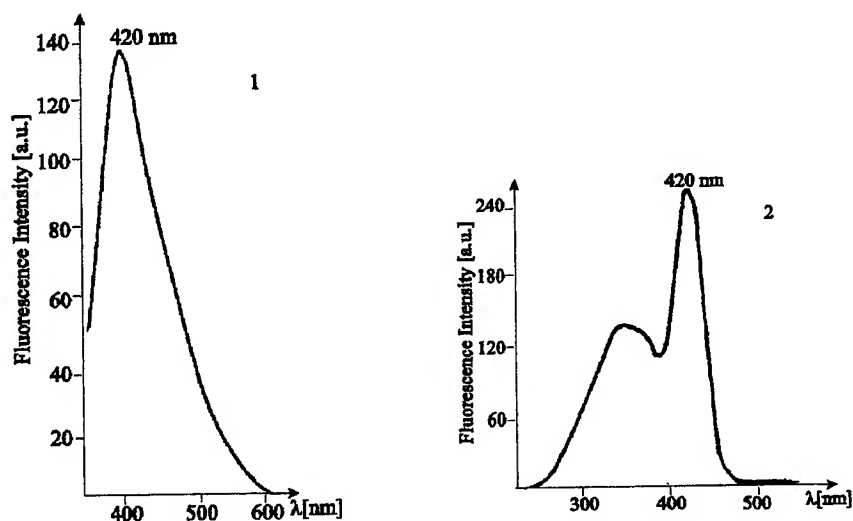


Fig.10 Fluorescence (1 - $\lambda_{\text{ex}}=337$ nm) and excitation (2 - $\lambda_{\text{em}}=420$ nm) spectra of Zn - TSPP in DMSO at $c=10^{-5}$ M

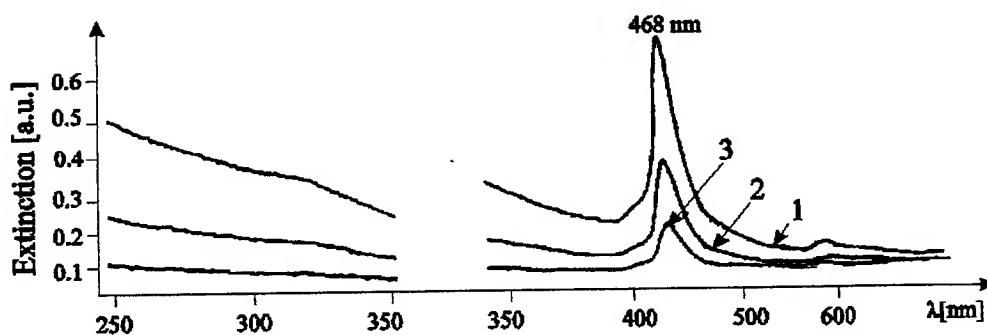


Fig. 11 Absorption spectra of Mn II-TSPP in distilled water at 1) $c=10^{-3}$ M; 2) $c=2.5 \times 10^{-4}$ M; 3) $c=10^{-4}$ M.

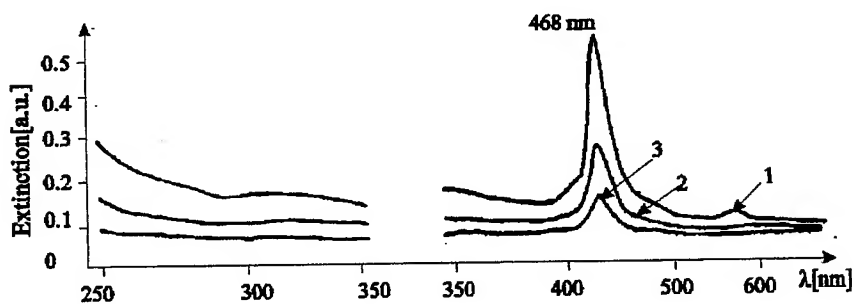


Fig. 12 Absorption spectra of Mn II TSPP in natural saline at 1) $c=10^{-3}$ M; 2) $c=2.5 \times 10^{-4}$ M; 3) $c=10^{-4}$ M.

3. RESULTS OF TOXICITY TESTS ON EXPERIMENTAL MICE

For obtaining sterile solutions that would be injected to mice, we have irradiated at a home made microwave installation working at a current intensity $I = 210\text{mA}$, samples containing solutions of 5% DMSO in natural saline. The advantage of using natural saline is that it is sterile at the beginning and it is very well tolerated by the organism. We have irradiated the first sample 10s, the second 15s, the third 20s, the fourth two times 15s and the fifth three times 15s. The samples no.4 and 5 were irradiated in series of two, respectively 3 times 15 seconds in order to avoid overheating. From UV-VIS spectra we have concluded that there are no significant differences between samples before and after microwave sterilization. With the same purpose to measure the sterile character of the solutions we also have made samples investigation using an optical microscope. Since all these studies did not give any evidence about viruses, bacteria or other microorganisms, we have concluded that our samples are sterile after microwave irradiation.

The second stage was to study the toxicity of the solutions on experimental mice. We have used two mice with 100 g weight. We have injected the mice with 0.25 ml solution of DMSO in natural saline at 5 % concentration and with 2.5 ml solution of DMSO in natural saline at 0.5 % concentration, respectively. These mice did not present special symptoms, so that we have concluded that the solutions are not toxic. We have done another injection with 0.25ml of 10% DMSO solution in natural saline. The mouse injected did not present unusual symptoms, either.

We have injected another two experimental mice with solutions of Zn-TSPP dye in 5% DMSO in distilled water with dye concentration of 10^{-4} M and 10^{-3} M, respectively. Neither these mice did present symptoms which can be bound with solution toxicity.

4. CONCLUSIONS

The absorption, excitation and fluorescence spectra of the studied dyes show that the UV radiation, especially that emitted by a N_2 pulsed laser at 337.1nm may be used for PDT. This class of photosensitisers would allow mainly, in principle to obtain the same kind of effects for PDT as in the hematoporphyrins case were the absorption takes place in red; the advantage of exciting the photosensitisers in UV is that the available sources in that range are more powerful than those with emission in red and we could obtain a more efficient effect for PDT.

From our measurements it results, that the most recommended dye is Zn TSPP in DMSO at 0.5% concentration, but the other dyes have characteristics which made them interesting for PDT studies.

The toxicity experiments done on mice have shown that the Zn - TSPP and DMSO solutions are tolerated by animal organisms and it is expected to be accepted for use on human patients.

From the obtained results it appears advisable to continue the studies following two directions:

- to study other types of porphyrins in order to identify even more convenient photosensitizers;
- to begin the phototoxicity and PDT studies on human patients.

REFERENCES

1. M. Ochsner, "Photophysical and Photobiological Processes in the Photodynamic Therapy of Tumours", *Journal of Photochemistry and Photobiology B*, **39**, pp. 1-18, 1997.
2. K. Berg, E. Hovig and J. Moan, "Sister Chromatid Exchanges Induced by Photodynamic Treatment of Cells in the Presence of Photofrin II, Aluminium Phthalocyanine Tetrasulfonate and Tetra (3-hydroxyphenyl) Porphyrin", *Light in biology and medicine*, **1**, Plenum Press, New York and London, pp. 95-103.
3. D.J. Ball et al., "A Comparative Study of the Cellular Uptake and Photodynamic Efficacy of Three Novel Zinc Phthalocyanines of Differing Charge", *Photochemistry and Photobiology*, **69** (3), pp. 390-396, 1999.
4. R. M. Ion, I. Yilmaz and O. Bekaroglu, "Supramolecular assemblies of pyridyl porphyrin and diazadithia phthalocyanine", *J. Serb. Chem. Soc.* **64** (7-8), pp. 453-462, 1999.
5. J. D. Spikes, "The Role of the Anatomy, Physiology and Biochemistry of Tumors in the Selective Retention of Sensitizers and the Mechanisms of Photosensitized Tumor Destruction", *Light in biology and medicine*, **1**, Plenum Press, New York and London, pp. 105-113, 1989.

Medical diagnosis using thermal fluxes sensors of a thermoelectric type

R. Marginean*, V. Hutanu

Institute of Optoelectronics, 76900, 111 Atomistilor Street, Bucharest

ABSTRACT

Researches on thermal processes developed inside the human body and on the quantity of heat emitted by the body in its environment allowed obtaining important information about the equilibrium between the human body and its environment and about the body's biological activity and state of health. Methods like thermography and thermovision, involving measuring human body's temperature, are presently used at present as medical diagnose methods for diseases even in their early stages of development. A very accurate piece of information about the thermal processes that are developing inside the human body can be obtained from direct measurements of the heat emitted by the body's surface using thermal flux sensors of a thermoelectric type. Thermoelectric effects occurring in anisotrope and inhomogeneous media are involved in functioning of this type of sensors that can detect heat fluxes up to 10^{-8} W/cm².

Keywords: thermoelectric sensors, medical equipment, thermal flux

1. INTRODUCTION

In this paper, we propose the use of thermoelectric sensors that detect the heat flow emitted by the body's surface and also measure its temperature, in order to develop a more accurate method for medical diagnosis.

As evidenced by the results of various medical studies, the temperature anomalies at some points of human body often results from functional and organic problems and in certain stages of development of the disease, especially in its early one, the information obtained from temperature anomalies can be used for medical diagnosis. From all the methods for medical diagnosis involving the use of such information, thermography is the best known.

However, the distribution of temperature over the skin can give only a limited information about the thermal processes developed inside the body. This fact is related to the distortion of the temperature data induced by the auto-thermo-regulating mechanism of the body. For example: in a steady state, the human body emits a caloric flux of almost 50 W at a normal temperature of 36,6 °C. In the case of a physic effort, the caloric emission can grow up to 500 – 1000 W, but the temperature is maintained at its normal value by the thermo-regulating mechanism. In this case, the conclusion is that the temperature is not a reliable source of information about the thermal processes developed inside the body.

A more accurate information can be obtained by direct measuring the heat flow emitted by the body. These measurements can be done using thermoelectric sensors, taking into account the fact that the newest types of these sensors can measures heat flows up to 10^{-8} W/cm².

The thermoelectric sensors for measuring heat flows can be a very reliable source of information regarding the energetic balance of the interaction between the human body and its surrounding medium. The use of a system composed of such sensors over body's surface allows obtaining data about this energetic balance and about the energetic reaction of the body when an external factor varies.

In order to be able to measure such energetic modification we propose the development of medical equipment containing in a chain of thermoelectric sensors placed on the patient's skin. The electrical signals obtained from all the sensors will be integrated and processed in order to obtain the energetic (caloric) balance, and by comparing the individual signal obtained from one sensor to the signals obtained from the others sensors, we'll be able to find out which regions of the body can be seen as preferential channels in the energy exchange between the body and the surrounding medium.

* Correspondence: Phone: (401) 780.66.40; Fax: (401) 423.25.32; e-mail: nmarg@ifin.nipne.ro

The proposed sensors are also devices that can precisely measure the temperature. In this way, the equipment will do a thermographic and a calorimetric investigation of the human body. This task will involve solving the mathematical problem of calculating the distribution of temperature and heat flow inside the body, thing that can be done only by using a powerful computer.

2. MEASURING THE HEAT FLOW USING THERMOELECTRIC SENSORS

The microcalorimeters with thermoelectric sensors are devices that measure the density of the thermal flow. Their constructive structure depends on their domain of use and the method of heat's (heat flow's) transport (materials' thermoconductivity, exchange of heat in terms of convection or emission).

Such a device¹ uses the reference method - the introduction along the direction of the heat flow of a standard barrier having a known thermoconductivity coefficient. In this way, the intensity of the heat flow produces an easy measurable temperature difference on the barrier (see Fig.1). A measuring device is connected to the thermoelectric sensor and, if it is proper graduated, the value of the heat flow is measured.

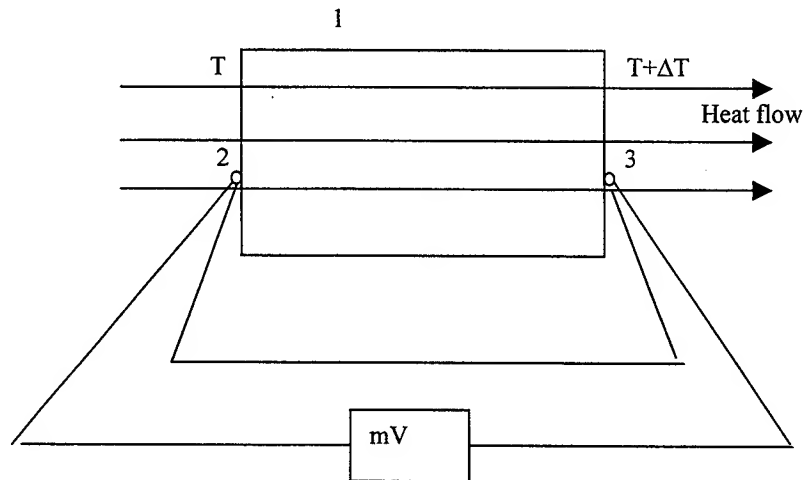


Fig. 1 Scheme for measuring heat flow, where:

- 1 is the reference barrier,
- 2 is the thermocouple that measures the temperature T
- 3 is the thermocouple that measures the temperature $T+\Delta T$

The main parameters of such a device are:

- Sensibility S_0
- Working coefficient k_p
- Thermal resistance R_T
- Thermocouple's/ thermobattery's resistance Ω
- Time constant τ
- Working domain of temperatures
- Area of the working surface

The thermoelectromotive force produced at the sensor's surface is proportional with the heat flow Q_w :

$$E = k Q_w$$

- where:
- $k = I (\alpha_1 - \alpha_2) / \chi$
 - α_1 and α_2 are the Seebeck coefficients of the materials from which the arms of the thermocouple are made,

- l is the thickness of the reference barrier,
- χ is the thermoconductivity coefficient of the barrier.

The sensibility of the thermoelectric sensor is its most important parameter. The sensibility is defined as the thermoelectromotive force produced at the sensor's surface by a heat flow equal to unity:

$$S_0 = E / Q_w = l (\alpha_1 - \alpha_2) / \chi$$

The working coefficient is defined as:

$$K_p = 1 / S_0$$

When some inhomogeneities in the heat flow appear, the results of measurements can be affected; that is why the contact wires are mounted in the central part of the electrodes.

3. MEASURING THE HEAT FLOW USING MULTIPLE THERMOELECTRIC SENSORS

The use of a singular thermoelectric sensor allows making measurements of heat flow in the range of $10^3 - 10^6 \text{ W/m}^2$. In comparison, devices with multiple sensors have a higher sensibility. The devices that use the thermobattery as a reference barrier have the maximum sensibility.

Depending on the concrete conditions of use, different materials can be used for the reference barrier: rubber, paronite, glass fiber, asbestos, etc. For reducing the errors induced by the device, the material for the reference barrier is chosen in such a way to have for the thermoconductivity coefficient a value as near as possible from the value corresponding to the material crossed by the heat flow.

The thermobatteries² are made from metallic alloys and are used for thermocouples. The most used are the batteries with galvanic films made of Cu deposited on constantan or Ni deposited on Cr. It can be also used: constantan-Ag, coppel-Ag, coppel-Cu, coppel-Au, alumel-Fe, coppel-Fe, nikelina-Ni, and rodiplatinum-platinum.

In a sensor having an area of $17 \times 17 \text{ mm}^2$ we can have between 3000 and 3500 thermocouples glued in an epoxi resin or in a thermoresistive lacque. The epoxi (ED4) resin can't be used for temperatures higher than 100°C ; the ED - 6 resin has as a maximum temperature the value of 120°C and the FEAD - 13 resin, the temperature of 150°C . For higher temperatures, enamel is used.

In table 1, the parameters of some devices used for heat flows measurements are presented.

Tab. 1 Parameters of usual sensors used for heat flow measurements

Type of the device	Domain of measured heat flow (W/m^2)	Sensibility ($\text{mV m}^2/\text{W}$)
DTP-02-01	$0.2 - 3 \times 10^4$	1.5×10^{-2}
DTP-02-4	$0.1 - 2 \times 10^4$	7×10^{-3}
DTP-02-5	$0.1 - 2 \times 10^4$	8×10^{-3}
DTP-02-7	$10^{-3} - 10^4$	1
DTP-02-8	$10^{-2} - 10^4$	1×10^{-1}
DTP-02-9	$10^{-1} - 10^4$	2×10^{-2}
DTP-02-10	$10^{-1} - 10^4$	4×10^{-2}

4. EQUIPMENT WITH ANISOTROPIC THERMOELECTRIC SENSORS FOR MEDICAL APPLICATIONS

The main requirements of such a medical equipment³, i.e. the method simplicity combined with a high sensitivity and low errors were fulfilled at this stage of work by differential switching of two identical sets of sensors which allows to find both the absolute temperature values at a given point and its overheat with respect to the design. By using such a method, the sensitive elements were electrically switched in an anti-parallel way, and the sensors were mechanically fixed by partial evacuation of the volume enclosed between the receiving pad and the controlled surface.

The results of the first investigations have shown that the use of these sensors permits to control temperature anomalies at symmetric points of human body and clearly diagnose such diseases as mastitis, myomas, onco-diseases, bruises, closed, fractures, etc.

The sensor consists of a housing made of dielectric material of low thermal conductivity in the form of a hollow truncated cone, with its lower part fixed to heat dissipating Al radiator by means of inner threaded connection. The inner cone surface has a convex form and on its lateral surface there is an opening with a rubber member fixed to it by means of a coupling. At the output of the coupling on the inner cone surface in a circle there is a neck serving as a restricting protrusion determining the distance between the receiving pad and the surface of the measured object. Thermoresistive element based on the anisotropic thermobattery is situated between the receiving pad made of black copper and the dissipating radiator. The working faces of the battery are electrically insulated using the layer made of deposited SiO_2 and the gasket made of ceramics based on Al_2O_3 . The electrical leads of the thermoelectric battery are flexible wires passing through the opening in the center of radiator.

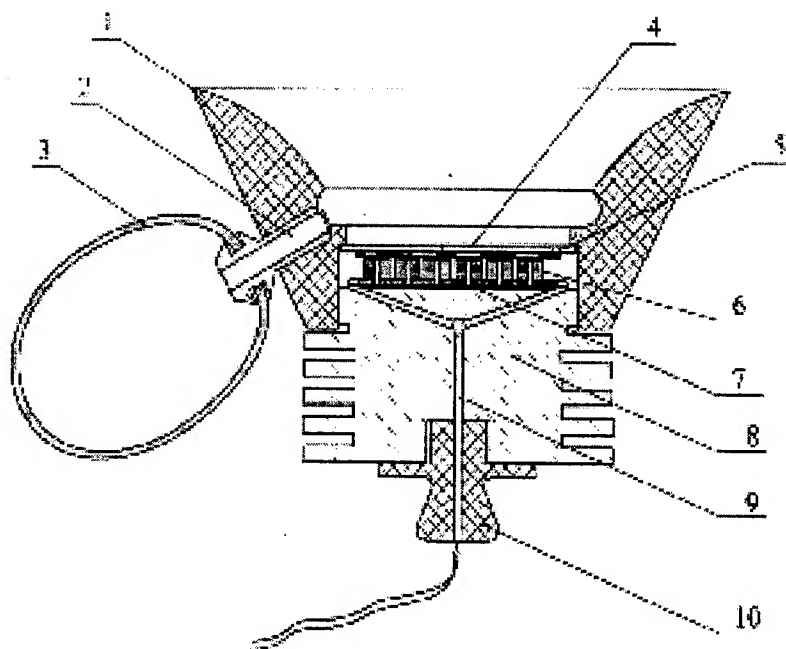


Fig.1 Anisotropic sensor for medico-biological investigations

1 is the housing, 2 is the coupling, 3 is the rubber member, 4 is the receiving pad, 5 and 7 are the gasket, 6 is the thermopile, 8 is the Radiator, 9 are the electric leads and 10 is the heat insulating handle

The choice of the number of anisotropic sensors and of their dimensions was governed by the requirements for the equipment's characteristics. In our case, the equipment comprises the thermoelectric battery ($0.7 \times 0.7 \text{ cm}^2$) consists of 16 sensors 0.1 cm high and has the followings parameters:

- $S = 0.36 \text{ V/W}$;
- $R = 7. \text{ K}\Omega$;
- $\tau = 3 \text{ s}$
- temperature control with an accuracy of 0.3 K

5. CONCLUSIONS

In order to develop a more accurate method for medical diagnosis we proposed the use of thermoelectric sensors that can detect both the heat flow emitted by the body's surface (up to 10^{-8} W/cm^2) and its temperature. In this way, the thermal anomalies for some points of the human body can be detected and interpreted in terms of functional and organic problems associated with diseases in various stages of development. Better results can be obtained using the proposed method than using thermography (the best known method for medical diagnosis involving the use of thermal information), taking into account the fact that the distribution of temperature over the skin can give only a limited information about the thermal processes developed inside the body. This fact is related to the distortion of the temperature data induced by the auto-thermo-regulating mechanism of the body. A more accurate information can be obtained by direct measuring the heat flow emitted by the body.

In order to be able to measure such energetic modification we proposed the development of a medical equipment containing in a chain of thermoelectric sensors placed on the patient's skin. The electrical signals obtained from all the sensors are integrated and processed in order to obtain the energetic (caloric) balance, and by comparing the individual signal obtained from one sensor to the signals obtained from the others sensors, we'll be able to find out which regions of the body can be seen as preferential channels in the energy exchange between the body and the surrounding medium.

The choice of the number of anisotropic sensors and of their dimensions was governed by the requirements for the equipment's characteristics. In our case, the equipment comprises the thermoelectric battery ($0.7 \times 0.7 \text{ cm}^2$) consists of 16 sensors 0.1 cm high and has the followings parameters: sensibility $S = 0.36 \text{ V/W}$, thermal resistance $R = 7. \text{ K}\Omega$, time constant $\tau = 3 \text{ s}$ and temperature control with an accuracy of 0.3 K.

REFERENCES

1. L.I. Anatyshuk, *Thermoelements and Thermoelectric Devices Handbook*, p. 714, Haykoba d ymka, Kiev, 1999
2. A.A. Ascheulov, I.V. Gutsul, A.I. Rarenko and N.K. Voronka, "Thermoelectric batteries based on Cadmium Antimonide", *Journal of Thermoelectricity*, 3, pp.65-68, 1999
3. A. A. A. Ascheulov and L. Kushneryk, "Anisotropic sensor for medico-biological Investigations", *Journal of Thermoelectricity*, 2, pp.94-95, 1999

Soil-vegetation discrimination and assessment in satellite imagery

A. Caramizoiu^{1*}, C. Aiftimiei, A. Stoica

Remote Sensing Department,
Institute of Optoelectronics – S.A., 111 Atomistilor St., Magurele-Bucharest, Romania

ABSTRACT

This paper presents an analysis of the remote sensing methods of extracting information on soils and land cover. For this purpose we selected Danube Delta, a complex ecosystem, with an important role in Romanian environment and economy. Several types of satellite images were used; in order to assess their suitability in land cover and vegetation changes detection. Landsat MSS and TM, ERS1&2 images were used. Were applied contrast enhancing and special filtering procedures to improve image and remove speckle (linear, root filtering, destriping, Frost and Lee filters). At the end of this phase, we obtained good quality images with not significant information losses. On these images we performed unsupervised and supervised classifications, (vegetation classes were established during “in situ” ground truth collection campaigns). The result of this application was the confirmation that only combined sets of images (optical, IR and microwave) can be a useful tool for land cover assessment, vegetation and soil discrimination. Beside the multi sensor approach, another condition for a complete observation is the multitemporal approach, by using several images acquired at different intervals of time, in this way we can obtain a good vegetation discrimination on seasonal basis.

Keywords: Remote Sensing, soil, land cover

1. INTRODUCTION

An important advantage that Remote Sensing is providing is that ensures a continuous monitoring for large areas, even at global scale. Remote Sensing can be used in a wide variety of disciplines and fields of interest of the economic activity.

There are discussions about a proper definition of Remote Sensing, a more accurate and a simple definition can be: Remote Sensing is a complex of disciplines oriented on spatial and physical characteristic detection of objects without direct contact. Depending on platforms used for sensors we have terrain, air and satellite remote sensing and depending on the domain of the sensors there is optic, radar, lidar, IR etc. In the past 30 years great progress were achieved in spatial and radiometric resolution of the remote sensed data and a large area of applications were identified. Land use and vegetation discrimination are some of these applications(1).

An analysis of the remote sensing methods of extracting information on soils and land cover. For this purpose we selected Danube Delta, a complex ecosystem, with an important role in Romanian environment and economy.

Several types of satellite images were used; in order to assess their suitability in land cover and vegetation changes detection(2). Landsat MSS and TM, ERS1&2 images were used. Were applied contrast enhancing and special filtering procedures to improve image and remove speckle (linear, root filtering, destriping, Frost and Lee filters). At the end of this phase, we obtained good quality images with not significant information losses.

On these images we performed unsupervised and supervised classifications, (vegetation classes were established during “in situ” ground truth collection campaigns).

*Correspondence: alex@ioel.nipne.ro

The use of combined optical and radar domain images provided the necessary information to assess different soil types and to classify the vegetal canopy in cultivated and spontaneous classes of vegetation.

Another important source of information is AVIRIS data(8), Using multivariate analysis techniques, can be observed that soils of different types can be discriminated with high accuracy.

An important factor the use of remote sensing in soil and vegetation discrimination is the resolution. In more detail, a scene is characterized by four key parameters: spectral, spatial, and temporal resolution and view angle (Duggin 1985). The spectral resolution of the sensor is given by the wavelengths of the electromagnetic spectrum used, the size of the area on the ground represent the spatial resolution and is restricting the field of applications and the measurements that can be performed on the image. The spatial resolution relative to the spatial structure of the scene objects determines the appropriate analysis methods for scene inference (Woodcock and Strahler 1987). The frequency with which images are obtained in time is referred as the temporal resolution specifies. View angle is also an important component of the imaging geometry.

2. TEST SITE DESCRIPTION

We located a zone near Bucharest (Romania) to perform land cover detection procedures, mainly because the terrain recognition was easy to make and also because for this zone we had several images from Landsat MSS, Landsat TM and from SAR-ERS 1.

The study zone is intensively cultivated and the vegetal cover is complex and representative for a larger geographical area. Forests are also presented in a good proportion. The Cernica zone, at North East of Bucharest is an example of cultivated landscape and here the human interference with the Nature is most visible, as is one of the most densely populated zones.

Danube Delta was the other test site. Its vegetal canopy characteristics are special, the spontaneous vegetation being dominant. In the winter season, soil classification can be performed if there is no snow coverage and the vegetation is no more covering the surface except for the dead leaf layer. In this case cultivated fields can be simply delimited from the spontaneous vegetation by using multitemporal images.

3. DATA PROCESSING

Digital image processing involves several procedures of preprocessing, enhancement, analyze and information extraction. To eliminate the atmospheric influence on the radiometric signal of the image, several radiometric correction procedures can be applied. In this way, together with other image enhancement procedures, in the end of the preprocessing stage, we can obtain a corrected image of a good quality, ready to be analyzed in order to extract the useful information.

As we are interested in soil and vegetation discrimination, the best way to achieve the maximum precision in the thematic map with soil and vegetation types distribution over the selected test sites it would be best not to perform any preprocessing on the images in order not to alter the information contained. In this case we choose to perform several correction before the classification, mostly because we were interested also in the interpretation of the images and also we wanted a good geospatial referencing for these images as we intended to use the results as data entries in a Geographic Informational System.

In Fig. 1-3 are presented several atmospheric corrections performed on Landsat TM image of Cernica zone for each image channel. It can be observed a significant improvement of the image and minor information losses.



Fig. 1 Atmospheric correction applied on a Landsat TM image ch. 3 - Cernica zone

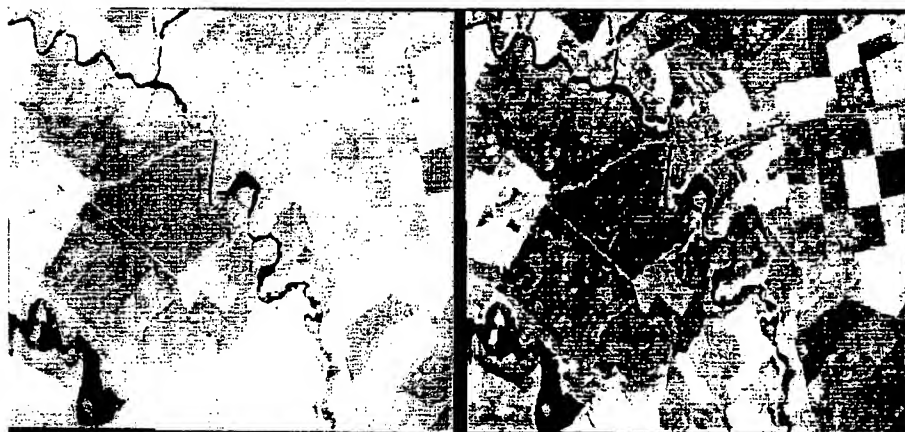


Fig. 2 Atmospheric correction applied on a Landsat TM image ch. 2 - Cernica zone



Fig. 3 Atmospheric correction applied on a Landsat TM image ch. 5 - Cernica zone

The geometric correction are the next step in preprocessing and as different types of images are affected of different types of geometric errors, specialized geometric corrections must be performed accordingly to the type of image.

Precision correction removes the rest of the geometric errors, caused by the position and the altitude of the spatial platform of the sensor. The necessary corrections to obtain an image compatible with the desired map projection (in this case UTM) will "force" the image to follow the longitude/latitude grid of the projection. But this correction is not enough in the case of

high relief. The topographical distortion can be removed for the SAR images by using digital terrain models. For the selected test areas, the relief displacement was not a problem due to the fact that both zones were on flat terrain.

For this purpose we used the map registration technique. A digitized map of the study area was used to select ground control points and the correspondent points were identified on the image. With this set of pair of control points (road intersections or a distinct feature) selected we measured the displacement of these ground control points between the uncorrected image and the master data set (in this case a map). In order to determine the two coordinate coefficients for the transformation equations we use a least square regression analysis. These coefficients relate the distorted image to the map.

The geometric correction can be performed in two step process:

- Transformation of pixel coordinates- a corrected pixel matrix is generated accordingly to the map geometry.

The transformation model requires that polynomial equations to be fitted to the ground control points selected on the map using least squares method to compute the corrections without identifying the source of distortion. The most suitable polynomial equation is a second order polynomial transform, which is best and with acceptable precision describing the way the uncorrected image will be warped to register to the master image.

$$\begin{aligned} X_1 &= a_0 + a_1x + a_2y + a_3xy + a_4x^2 + a_5y^2 \\ Y_1 &= b_0 + b_1x + b_2y + b_3xy + b_4x^2 + b_5y^2 \end{aligned} \quad (1)$$

- Resampling: to determine the pixel values to fill into the corrected matrix from the uncorrected image.

By resampling we interpolated the gray values of each pixel of the original, distorted image and to relocate the pixel with its corresponding gray value in an appropriate location in the corrected matrix. There are several methods that can be applied (Nearest neighbor, Bilinear interpolation and cubic convolution). In this case we did not choose the cubic convolution, that is using the weighted average of the sixteen surrounding pixels of the uncorrected image to approximate the intensity value.

The most rapid method of resampling is the nearest neighbor, that determines the gray level from the closest pixel in the input coordinate specified and assigns that value to the output coordinate, in order not to alter the gray level real distribution.

Image enhancement involves the application of procedures designed to facilitate the interpretation of images. In attempting to identify the types of soil and the vegetation type by using their gray level we performed unsupervised and supervised classification procedure over the same area test- i.e. Cernica zone, near the Bucharest. As the reflectance of each type of an object behaves different across the wavelength spectrum it is enough to perform a spectral discrimination for every type of land cover.

The parameter estimation process for spectral classifiers can be generalized as being supervised or unsupervised (Swain and Davis 1978, Schowengerdt 1983). A supervised classification uses a sample of image elements for each land cover class to estimate parameters, the classifier is usually a mean vector and covariance matrix.

For unsupervised classification, we used clustering algorithm group the spectral responses of the data in several populations of pixels within a determined domain of reflectance, which are referred to as spectral classes and parameters estimated for these spectral classes (Richards and Kelly 1984). Training to establish a correspondence between the spectral classes and the land-cover classes. The maximum likelihood classification proved to be a less probability error method of unsupervised classification. To enhance the standard output from the maximum likelihood classification can be created a raster for each land-cover class wherein the pixel value would be the a posteriori probabilities of membership for the category. As a result we obtain a probabilistic digital map of the geographic distribution for every land-cover class in the image.

Once the land cover classes determined a precision of the classification can be performed on the field, at a test site, chosen as to be representative for all the classes.

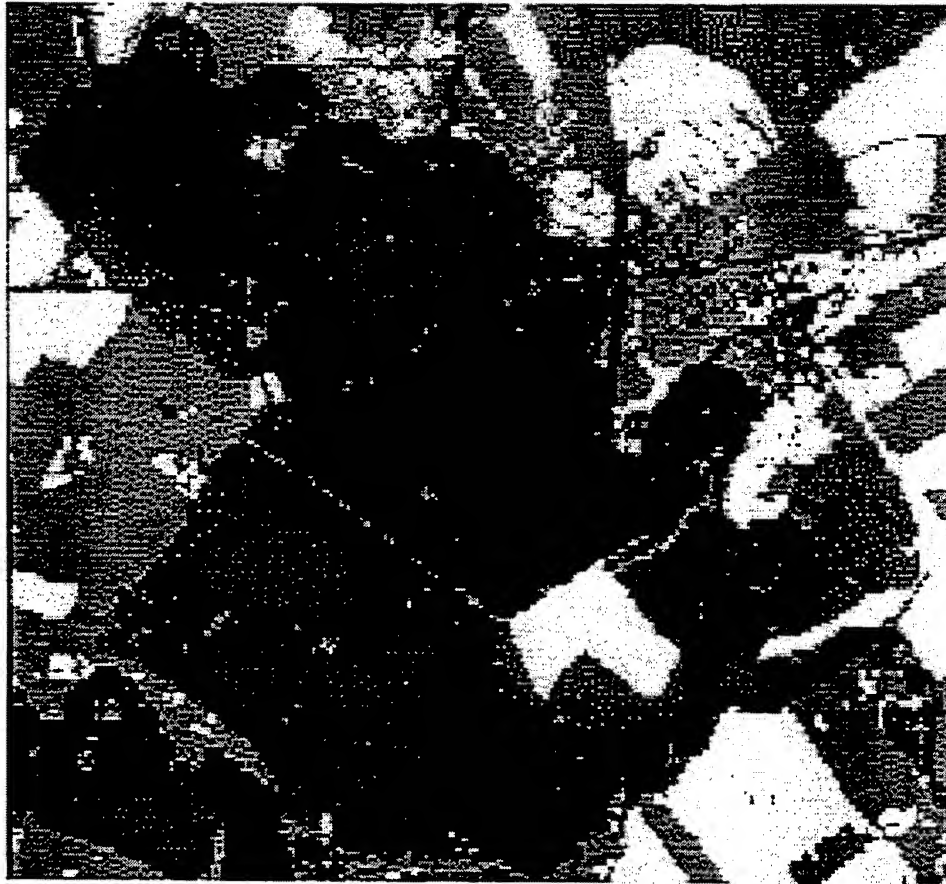


Fig. 4 Unsupervised classification – 8 classes. Cernica zone

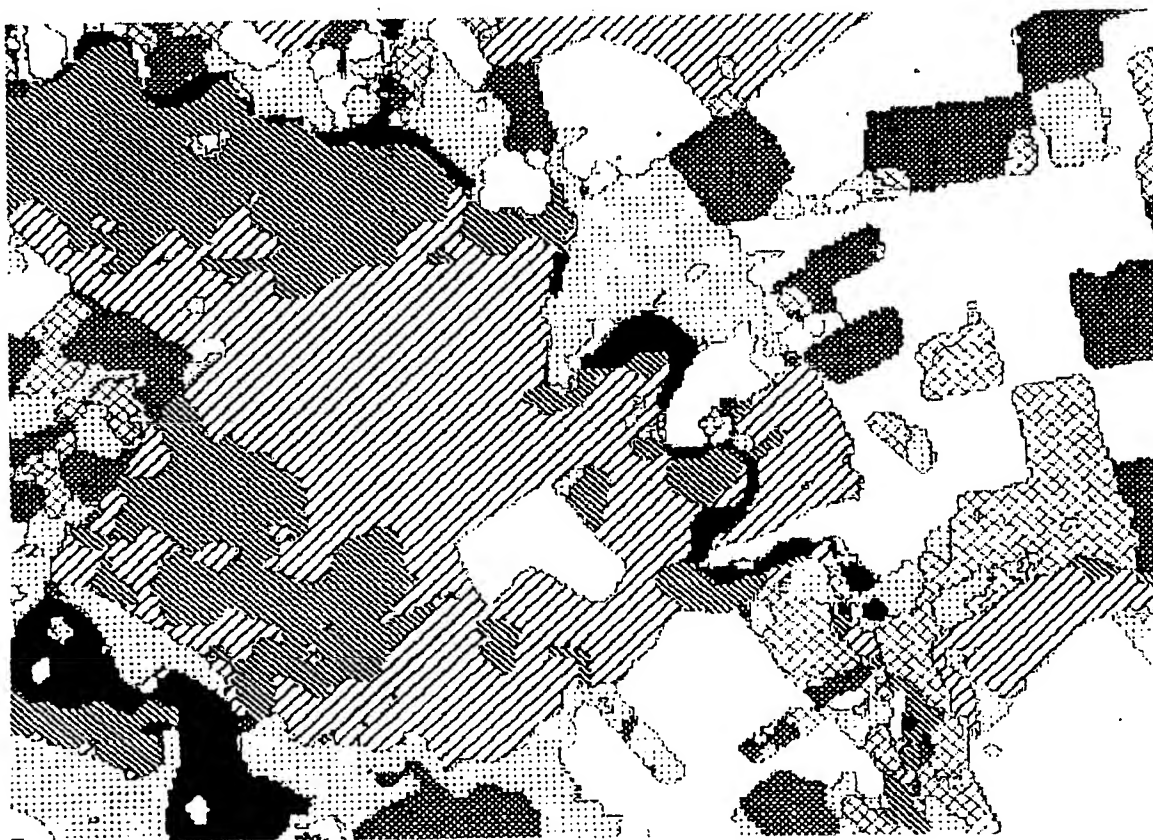
The supervised classification requires aprioric information regarding the spectral reflectance of different classes of land cover and the use of this parameters to instruct the classifiers to group the appropriate pixels with similar reflectance responses in the identified land cover classes.

Using the unsupervised classification results, we compared to the reality in field and an accuracy of more of 85% of cover type proved to be correct. The rest of misclassification results were due to the lack of homogeneity of the land cover.

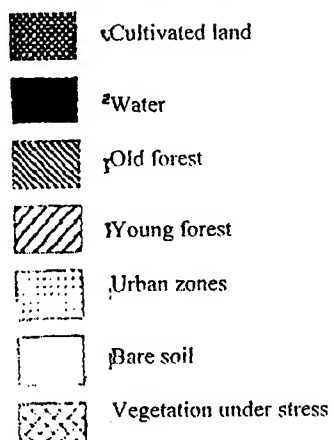
The main steps were:

- Defining the database channels, visual reference and training channels
- Signature Generation /editing: Training area acquisition, signature generation, trial classification, signature separability measures, scatterplot generation and histogram generation.
- Data classification, saving results.

The result of this classification is presented in Fig. 5. It can be observed that the output is similar to the one obtained from the unsupervised classification : there is a clear distinction between young and mature forest, the bare soil is neatly differentiated from the constructed zones and the cultivated land is represented with high accuracy. The confusion appeared only in forested regions where tree population (8) was not homogenous.



Legend:



4. CONCLUSIONS

From the data analysis a good quality soil-vegetation discrimination can be obtain by using images in the visible domain. The radar data can also be of great help, especially when we are interested in water content and stressed vegetation. The radar images can be useful for roughness surface assessment, which is an important parameter also in land cover studies. As the spatial and the radiometric resolution is improving day by day and new satellites with new, performant sensors, which are scheduled to be, launched in the near future, a more complex and accurate data will flow on the desk of the remote-sensing specialists. The only way to handle this large amount of information is to use a GIS frame and utilities of dynamic

databases. Another problem is the access to land use information for all those involved in land and living resources management. The cost of this information is not yet fully accessible and also not all the land use specialists are accustomed with the remote sensing specific methods.

If we use only ground observations of seasonal characteristics we can obtain information concerning specific plants over a limited spatial area. But satellite data analysis is able to provide the broad-scale measure of changes in plant canopy at a regional level. Multitemporal satellite-derived vegetation observations have allowed researchers to quantify seasonal events and to characterize vegetation according to its seasonal patterns and to its soil substrate in the context of humidity level. (Reed and others 1994, Loveland and others 1993).

5. REFERENCES

1. Belward A. S., and Loveland. T.R., "Use with Remote Sensor Data", 964, The IGBP-DIS 1-km Land Cover Project: Remote Sensing in Action. *Proceedings of the 21st Annual Conference of the Remote Sensing Society*, Southampton, United Kingdom. 1995.
2. Brown, J.F., Loveland, T.R., Merchant, J.W., Reed, B.C., and Ohlen, D.O., "Using Multisource Data In Global Land Cover Characterization: Concepts, Requirements and Methods", *Photogrammetric Engineering and Remote Sensing*, 1993,
3. Brown, J.F., Reed, B.C. and Huewe L., "Advanced Strategy for Multi-Source Analysis and Visualization in Land Cover Characterization, *Human Interactions with the Environment: Perspectives From Space Pecora 13*.
4. Daughtry, C.S.T., K.D. Gallo, and M.E. Bauer, "Spectral estimates of solar radiation intercepted by corn canopies", *AgRISTARS Tech. Report SR-PZ-04236*, Purdue University, West Lafayette, IN., 1983.
5. Keeling, C. D., Chin, J. F. S. & Whorf, T. P., "Increased activity of northern vegetation inferred from atmospheric CO₂ measurements", *Nature*, 1996.
6. Loveland, T.R., J.W. Merchant, D.O. Ohlen, J.F. Brown, "Development of a land-cover characteristics data base for the conterminous", *U.S. Photogrammetric Engineering and Remote Sensing*, 1991.
7. Loveland, T.R., Merchant, J.W., Brown, J.F., Ohlen, D.O., Reed, B.C., Olson, P., and Hutchinson, J., "Seasonal Land-Cover Regions of the United States", *Annals of the Association of American Geographers*, 1995.
8. Reed, B.C., J.F. Brown, D. VanderZee, T.R. Loveland, J.W. Merchant, and D.O. Ohlen, "Measuring phenological variability from satellite imagery", *Journal of Vegetation Science*, 1994.
9. Anderson, J.R., Hardy, E.E., Roach J.T., and Witmer R.E., "A Land Use and Land Cover Classification System for Tucker", *Remote Sensing of Environment*, 1976.
10. C.J., B.N. Holben, J.H. Elgin, Jr., and J.E. McMurtrey, "Remote sensing of total dry-matter accumulation in winter wheat", *Remote Sensing of Environment*, pp. 11:171-189, 1981.

Optoelectronic associative neural network for some graphical patterns recognition

Ioan Ileană^a, Ovidiu Corneliu Iancu^b

^a"1 Decembrie 1918" University, Alba Iulia

^b"Politehnica" University, București

ABSTRACT

This paper presents an autoassociative memory built for graphic pattern recognition. The network was designed for the validation of handwritten signatures from bank documents. Neurons interconnections are considered to be implemented optically by computer generated holograms (CGH). The network functioning was simulated on computer and the paper presents the results of simulations on a data set and a CGH layout for neuron interconnections.

Keywords: pattern recognition, artificial neural network, autoassociative memory, computer generated hologram.

1. INTRODUCTION

There are, in human society, activity areas which daily imply the processing of a huge quantity of written documents, like post services and bank institutions. Consequently, the automation of these activities is very important and there is, since the sixties, a constant interest for this field. The main problem consist in the extraction and then in the recognition of certain handwritten items from a typified form. There are many references^{3, 7, 9, 11} concerning the processing of financial and bank documents.

This problem belongs to the larger field of pattern recognition where cursive script is only a particular case. Pattern recognition has been attempted with many different systems and algorithms⁹: Fourier transform, matching unknowns against templates (including here the neural approach), Hidden Markov Models, syntactic pattern recognition etc.

The main difficulty in automatic handwriting recognition appears due to the fact that cursive script is very unstable in which shape and quality of component features are concerned. The complexity of recognition depends on the following factors:

- the acquisition type of the items to be recognized (on-line or off-line)
- the type and quality of the handwriting (words in separated or joined characters)
- the number of subjects (one, few, many)
- the size of the used vocabulary (small- up to 100 words, intermediate - 100 to 500 words, large - over 500 words).

This paper approaches a limited segment of bank documents handwriting recognition, namely signature recognition and validation. This type of recognition belongs, according to previous considerations, to the off-line mode, with many subjects and large vocabulary (notifying that, instead of words, we use graphic patterns representing signatures). The main requests to such a recognition system are :

- the recognition of authentic signatures, uninfluenced by the variableness of their aspect
- the rejection of forgeries. From the point of view of error costs, accepting a false signature can cause more damage then rejecting an authentic one.

In order to recognize signatures, we used an autoassociative memory, synthesized basing on a certain number of original signatures (prototypes). We have considered that the signatures to be recognized are supplied to the network, so that it doesn't have to extract these items from the documents (for this extraction, the model described in¹ can be used).

Section 2 presents the model of the used neuronal network, and section 3 describes an optical interconnection of neurons through a computer generated hologram (CGH). Section 4 shows the simulation results, predictable difficulties and approaches in order to overcome these difficulties.

Correspondence: +(40)058812630

2. THE ARTIFICIAL NEURAL NETWORK MODEL

In this section we'll briefly introduce the main theoretical elements concerning associative memories and recurrent neural networks, elements that will be used in section 4 in order to build an associative memory for signature recognition.

We'll call 'pattern' a multidimensional vector with real components. An associative memory is a system that accomplishes the association of p pattern pairs $\xi^\mu \in \mathbb{R}^n$, $\zeta^\mu \in \mathbb{R}^m$, ($\mu=1, 2, \dots, p$) so that when the system is given a new vector $x \in \mathbb{R}^n$ such as

$$d(x, \xi^i) = \min_j d(x, \xi^j) \quad (1)$$

the system responds with ξ^i ; in (1) $d(a, b)$ is the distance between patterns a and b .

The pairs (ξ^i, ζ^i) , ($i=1, 2, \dots, p$) are called prototypes and the association accomplished by the memory can be defined as a transformation $\Phi: \mathbb{R}^n \times \mathbb{R}^m$ so that $\zeta^i = \Phi(\xi^i)$.

The space $\Omega \subset \mathbb{R}^n$ of input vectors x is named configuration space and the vectors ξ^i , ($i=1, 2, \dots, p$) are called attractors or stable points. Around each attractor, there is a basin of attraction B_i such that $\forall x \in B_i$, the dynamics of the network will lead to the stabilization of (ξ^i, ζ^i) pair. For the autoassociative memory $\xi^i = \zeta^i$, ($i=1, 2, \dots, p$) and if some vector x is nearest ξ^i , then $\Phi(x) = \xi^i$.

In section 4 we will use for graphic pattern recognition a neural network whose model is presented below. Let's consider the single-layer neural network built from totally connected neurons, whose states are given by $x_i \in \{-1, 1\}$, $i=1, 2, \dots, n$, (Fig. 1).

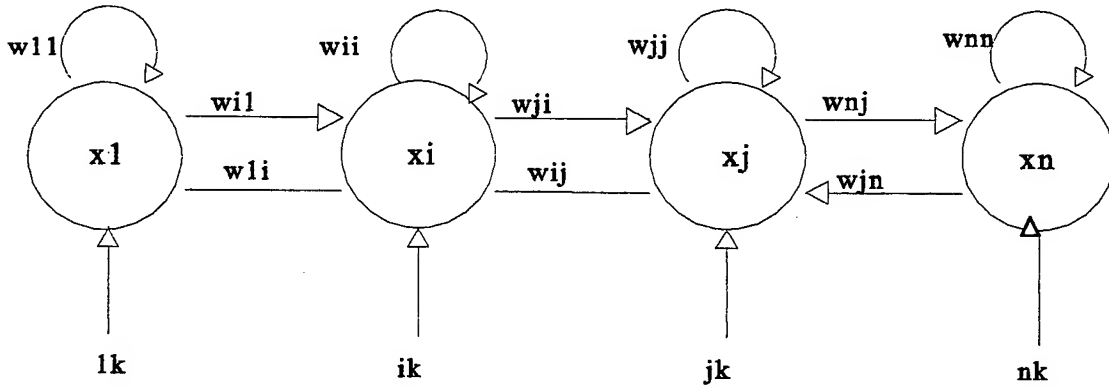


Fig. 1 Single layer recurrent neural network

We denote: $W=[w_{ij}: 1 \leq i, j \leq n]$ the weights matrix
 $\theta=[\theta_1, \dots, \theta_n]^T \in \mathbb{R}^n$ the thresholds vector
 $x(t)=[x_1(t), \dots, x_n(t)]^T \in \{-1, 1\}^n$ the network state vector

The evolution in time of the network is described by the following dynamic equation⁵:

$$x_i(t+1) = \text{sgn} \left[\sum_{j=1}^n w_{ij} x_j(t) - \theta_i \right] \quad i=1, 2, \dots, n \quad (2)$$

with the convention:

$$\sum_{j=1}^n w_{ij} x_j - \theta_i = 0, \quad x_i(t+1) = x_i(t) \quad (3)$$

where:

$$\text{sgn}(x) = \begin{cases} 1 & \text{if } x > 0 \\ -1 & \text{if } x < 0 \end{cases} \quad (4)$$

Notes:

1. We may consider networks where the neurons' state is not bipolar: $\{-1, 1\}$, but binary: $\{0, 1\}$. A relation between the two representations can be easily found⁵:

$$n_i(t+1) = H\left[\sum_{j=1}^n w_{ij} n_j(t) - \hat{\theta}_i\right] \quad i = 1, 2, \dots, n \quad (5)$$

where n_i , $H(x)$ are the neurons outputs, respectively the Heaviside function, and for the thresholds we find:

$$\theta_i = 2 \hat{\theta}_i - \sum_{j=1}^n w_{ij} \quad (6)$$

2. In many situations we may give up the neural network threshold θ_i and we'll do this whenever it doesn't affect the results.

For the autoassociative memory described in this paper, the weight matrix W will be built as follows:

Given a set of n -dimensional prototype vectors $X = [\xi^1, \xi^2, \dots, \xi^p]$, we establish the synaptic matrix W and the threshold vector θ , so that the prototype vectors become stable points for the associative memory, that is:

$$\xi^i = \text{sgn}(W \xi^i - \theta) \quad i = 1, 2, \dots, p \quad (7)$$

where the sgn function is applied to each component of the argument.

Several classical rules for determining the weights matrix proved successful in time:

- the 'Hebb' rule
- the projection rule
- the delta projection rule (the gradient method)

3. THE OPTICAL INTERCONNECTION OF THE NEURONS IN THE AUTOASSOCIATIVE NETWORK

Due to the fact that the neural network presented in this paper is destined to the recognition of 2D images, it was conceived for an optoelectronic implementation, using as processing elements laser diodes (DL) and photodetectors (PD) and for synaptic signal transmission, optical connections.

Optical interconnections are useful for neural network as far as one can take advantage of the special potential of 3D connection through free space. This involves the organizing of the neurons layer in 2D configurations (planar), where the optical interconnections realise the desired links between the two planes. Such a connection also materialises the synaptic weight corresponding to neuron j from the input plane and the neuron i from output plane (Fig. 2).

The interconnection network accomplishes the following function:

$$\beta(k, l) = \sum_{ij} \alpha(i, j) \cdot T_{ijk} \quad (8)$$

In order to connect the two neuron planes one may use computer generated holograms which, by light waves diffraction, assure the desired connections. Due to the fact that generally the connections differ from neuron to neuron, the interconnection system will be a spatial variant system, each point from the input plane being connected differently to the output plane. This spatial variance can be realised in several manners.

The reference⁶ suggests an optoelectronic neural network where spatial variance is assured by attaching to every neuron output (in the input plane) a hologram that stores all the connections between this output and the other neurons' inputs.

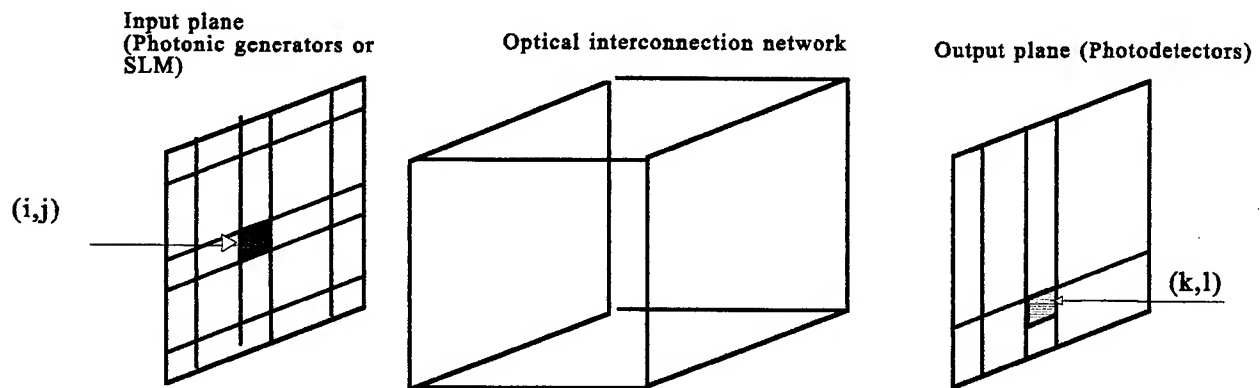


Fig. 2 Optical interconnection of two neural planes

In order to use CGH for neural interconnections we have considered the case described in the above reference, using one hologram for each neuron. The neurons are disposed in a 2D grid, and different planes are considered for input and output. The hologram for ij neuron was synthesised starting from the calculated synaptic weights, including all the weights of the connections between the ij neuron and the others. The hologram generation process is illustrated for a single neuron, the whole hologram containing a number of such elementary holograms equal to the number of neurons in the recurrent network.

To synthesise a Fourier amplitude hologram we started from the synaptic interconnection matrix W , from which we selected a column, corresponding to the connections from the output of a neuron to the inputs of all the others. We organised this column in a 2D array, corresponding to the spatial configuration of the neurons. The weights w_{ij} will represent the amplitude distribution in the output plane of the optical system (the input neuron plane). This weights matrix was used to calculate the Fourier transform. The layout of the obtained CGH is shown in Fig. 3.

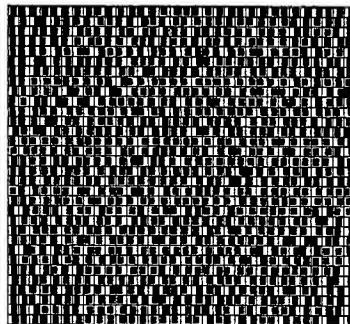


Fig. 3 Layout example of a CGH obtained by "detour phase" method

4. EXPERIMENTAL RESULTS

In the following, we will present the results obtained in the software simulation of an associative memory of discrete autocorrelator¹⁰ (DA) type, implemented with neural networks as described in section 2. The DA is a single layer, symmetric, non-linear, autoassociative network, that stores binary or bipolar patterns, uses for recall the nearest neighbour criteria, learns off-line and operates in discrete time.

In order to synthesise and simulate the network, we developed a Turbo Pascal 7.0 program, that ran on an IBM compatible Pentium II/350. The software simulator is very easy to use because of its friendly G U I.

For the network training we used a set of eight signatures (Fig. 4), as prototypes. We used this relatively small number of prototypes because we intended for this stage, only an investigation of the viability of this solution. In fact, the storing capacity of the network is much higher (hundreds of prototypes). The signatures were represented as BitMap (BMP) files. The digitization was realised by a 300 DPI resolution scanner. In a real application, using a digital camera is probably more efficient.

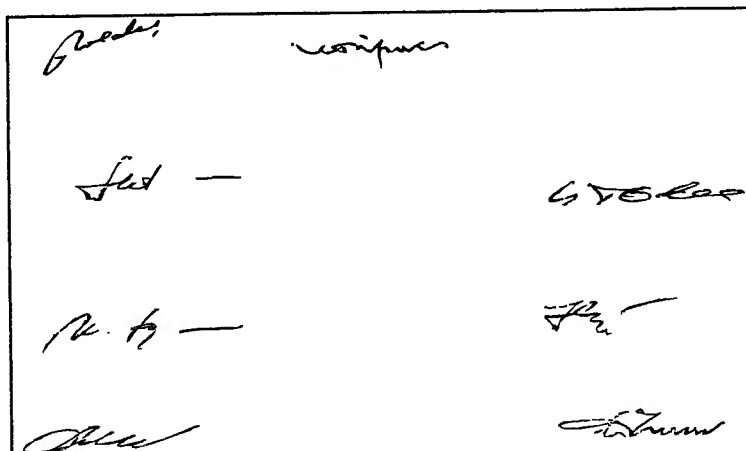


Fig. 4 The prototypes used to build the associative memory

After building the network with the help of specified prototypes, it has been tested, being asked to recognize several types of images:

- I. Prototypes affected by noise signals or degraded by absence of a certain part of the signature.
- b) Signatures of the same persons, generated in different contexts (having more or less significant variations from the prototypes)
- c) Images representing copies of the original signatures (forgeries).

The results we obtained are exposed in the following, for each simulation category.

- I. When recognizing noisy or incomplete prototypes the memory works very well, some results being shown in Fig. 5 and

Fig. 6.

- b) The recognition of authentic signatures written in various contexts (having therefore a certain variability) has also shown a good functioning of the network (Fig.7).
- c) We also performed a number of simulations having as input data forged signatures- written by persons, other than the one that provided the prototype. In this case the results were more nuance. Thus, in most situations, those entries weren't recognize, the network failing in a stable state different from any prototype. There were, though, situations when the network recognized as authentic a false signature. Some ways to avoid such situations will be discussed below.

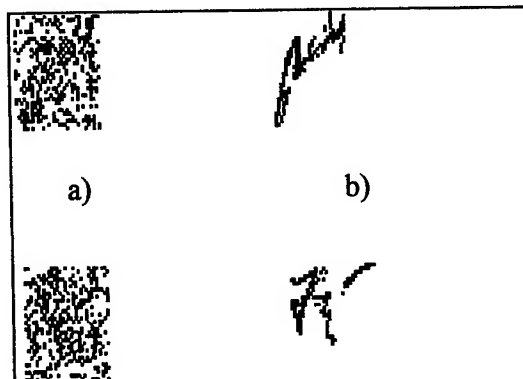


Fig. 5 Prototypes affected by 30 % noise a) and the recognition result b)

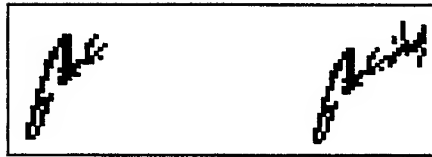


Fig. 6 Recognition of incomplete prototypes

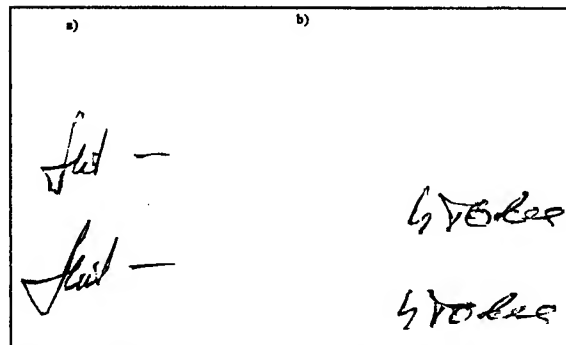


Fig. 7 Authentic signatures a) and recognized prototypes b)

5. CONCLUSIONS

The present paper describes the using of neural networks for recognizing signatures from documents. The simulations performed have shown that such a system can be viable, but we also noticed several complications that may occur:

- I. In our simulation we represented each signature as a 32×32 pixels array (which leads to a features vector with 1024 components and a $\approx 10^6$ components interconnection matrix). This dimension has been chose because of two reasons: the size of the memory required for storing synaptic connections (9)⁴, and the computing time required for network stabilisation (10).

$$M_{RAM} \cong 4n^2 \text{ bytes} \quad (9)$$

$$T_{rec} \approx O(n^2 N_{medit}) \quad (10)$$

where N_{medit} signifies the average iterating number until the network stabilises to an attractor.

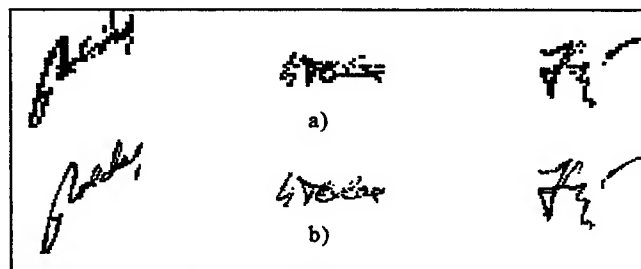


Fig. 8 Prototypes represented by 32×32 pixels: a) or by 64×32 pixels: b)

It is obvious that using finer granulations leads to a more accurate representation of the signature structure, therefore to a better individualisation. In fig. 8. we show the same signature in 32×32 pixels and 64×32 pixels representation. In this situation it will be an increase in the number of neurons and in the number of synaptic weights. In software simulations these will need more memory and more computing time.

- II. We noticed the existence of a contradiction between the selectivity of the network, needed in order to reject the

forgeries, and the generality of the recognition, necessary for validation of various original signatures with slight variations. A possible solution could be, besides increasing the dimension of features vector, to use as prototypes not a single signature but an average of a larger number of original signatures. Also, if the acquisition of signatures were on-line one could use the pressure and acceleration informations for validation of authentic signatures.

III. It is possible sometimes that there are, in the entry set, two prototypes so resembling one to the other (in terms of Hamming distance) that authentic samples or forgeries of a signature end up by being recognized as the other. We consider that this anomaly can be overcome, in a practical signature recognition system, by grouping the set of signatures to be recognized in subsets whose components keep among them a specified minimum Hamming distance. Each subset will then have its own recognition system. The recognition system can thus be called in accordance with the pattern to be recognized.

REFERENCES

1. Cote M., Lecolinet E., Cheriet M. and Suen C. Y., "Lecture automatique d'écriture cursive utilisant des concept perceptifs", *Actes du congrus de l'Association canadienne-franzaise pour l'avancement de la science*, pp. 183-193, Montreal, Canada, 1996.
2. Cote Myriam, *Utilisation d'un module d'accus lexical et de concepts perceptifs pour la reconnaissance d'images de mots cursifs*, These pour le grade de Docteur, Ecole Nationale Superieure des Telecommunications, Paris, 1997.
3. Guilevic Didier and Suen Ching Y., "Cursive Script Recognition Applied to the Processing of Bank Cheques", *Int. Conf. On Document Analzsis and Recognition (ICDAR)*, Montreal, Canada, pp. 11-14, August 1995.
4. Ileană Ioan, *Refele neuronale on tehnologia optoelectronică. Interconexiuni optice*, Referat de doctorat, București, 1999.
5. Kamp Yves and Hasler Martin, *Reseaux de neurones rúcursifs pour mûmoires associatives*, Presses polytechniques et universitairea romandes, Lausanne, 1990.
6. Keller Paul and Gmitro F. Arthur, "Design and analisys of fixed planar holographic interconnects for optical neural networks", *Applied Optics* **31**, pp.5517-5526, 1992.
7. Liu Ke, Suen Ching Y. and Nadal Christine, "Automatic Extraction of Items from Cheque Images for Payment Recognition", *International Conference on Pattern Recognition*
8. Lohman A. W., Paris D., "Binary Fraunhofer Holograms Generated by Computer", *Applied optics*, **7**, pp. 651-655, April 1968.
9. Scattolin Patrice, *Recognition of Handwritten Numerals Using Elastic Matching*, D. Thesis, Concordia University, Montreal, 1995.
10. Patrick Simpson, *Artificial Neural Systems. Foundations, Paradigms, Applications and Implementations*, Pergamon Press, 1990.
11. Suen C. Y., Liu K. and Strathy N. W., "Sorting and Recognizing Cheques and Financial Documents", *The 3rd LAPR Workshop on Document Analysis Systems*, pp. 1-18, Nagano, Japan, November 1998.
12. Webber Chris J. S., "Emergent componential coding of a handwritten image database by neural self-organisation", *Network: Comput. Neural Syst.* **9**, p.433-447, (1998).

Stabilisation system for the viewing field of sighting optical devices installed on vehicles

Axente Stoica*, Alexandra Caramizoiu, Cristina Aiftimiei

Dept. of Remote Sensing, Institute of Optoelectronics

ABSTRACT

The functioning principles, hardware and software structures are presented, and on this basis, the essential differences between the usual optical systems at which the sighting direction is stabilised and an optical system of a special type whose stabilised element is its viewing field are brought to evidence. The principal applications these optical systems with viewing field stabilised by using of some referential elements of inertial type can have are also presented. In those situations in which is oriented upon some fixed target the ISVFS (the Inertial System for Viewing Field Stabilisation) presents some functioning similarities with those opto-electronic devices that achieve the stabilisation of the image received on a monitor screen by "point by point" analysis of this image.

Keywords: Stabilised sight, sight direction, viewing field, inertial navigation system, gyroscopic reference, laser telemetry

1. INTRODUCTION

As it is generally known, by sighting direction stabilisation of some optical devices, the maintaining at a constant value of this direction tilting angles in respect to the reference inertial space is ensuring.¹ In this manner, the influence of the angular oscillations of the carrying vehicle (airship, terrestrial or marine vehicle) upon the image received by the observer is eliminated. In such an image are taken over only the vehicle's linear displacements which make the viewing field "to parade" in front of the operator in tight dependence to the vehicle's displacement speed. In contrast with these sighting direction stabilisation systems which achieve, as was mentioned above, the decoupling of this direction from the rotational movements of the carrying vehicle, the viewing field stabilisation system, which constitutes the object of this report, ensures the independence of the received image from both the rotational and translational movements of the vehicle. In this manner, in the moment a zone of "interest" is reaching, the proposed system can achieve the "fixation" of the viewing field upon the respective zone, independently to the fact that the carrying vehicle continues its displacement or, in the case of a fight airship, effects different manoeuvres for avoiding the enemy fire.

The functioning of a such viewing field stabilisation system is basing upon that that at the entrance of the numeric processor, which achieves in cvasi-real time the computing of the general stabilisation function, beside the angular reference signals delivered by the gyrometric transducers block and the sighting direction orientation signals transmitted by the control handle, the signals that represent the components on three orthogonal axes of the vehicle's current displacement is applying also; this displacement at its turn being determined, for an example, by means of an inertial navigation system. Moreover, in the specialised processor must be introduced also the value of distance at which was situated relative to the vehicle, in the moment of its selection, the objective sighted in the centre of the viewing field, value that is determinable by a single laser ranging.² However, the computing program of the system permits that that laser ranging to be replaced by a simple operation of "resetting" of the sighting device upon the selected objective, by a manual command, at two different moments of time. On the basis of this data, the computing program ensures the elaboration of the control signals for the actuating blocks of the optical element from the system entrance; these control signals have the necessary size and sense for the above mentioned optical element, by means of its rotations, to maintain unchanged in the operator's field of view, the terrain zone selected by this, independently from the carrying vehicle manoeuvres.

Such a stabilising system for the viewing field, (ISVFS - Inertial System for Viewing Field Stabilisation), can find itself an immediate application, for example, in the fotogrammetric recording operations of the terrain and in those that offer the

* Correspondence: Email: axente99@yahoo.com; Telephone: 0040-1-780.66.40 ; Fax: 0040-1-432.25.32

possibility of relief perception in the photo-interpretation activities. In the standard mode, to obtain the necessary in these activities stereoscopic pairs of images, two video-cameras are using, placed on the same carrying vehicle, at a certain distance one from another. Since this distance is limited by the size of the respective vehicle, the image pairs obtained in this manner, as a rule, do not assure a proper locating accuracy for the more far situated in terrain objectives. This drawback can eliminate if the proposed stabilising system is adopting; this system has the possibility that by using a single video-camera, to sight and, respectively, to record the same terrain objective, in two different moments of the displacement.

This viewing field stabilisation function is certainly remarkable useful also for some applications with military character, in the "reconnaissance" phase and, when it is the case, for some objectives of interest photographing. In the fixed targets case, the Inertial System for Viewing Field Stabilisation (ISVFS) can find itself a new application in the operation of maintaining an illuminating laser beam upon the respective targets. In this mode it is possible to use a more simple laser illuminating device that is not equipped with its own automatic tracking system of the target, system that is based on the reflected by the target laser beam. Certainly, an another application of the ISVFS system can be constituted also by its direct connection to the orientation mechanism of a piece of artillery which, in this way, can be automatically maintained upon the selected target, all the period of time which normally is necessary for its distroyment, independently from the carrying airship evolution.

Concerning the mobile target one can say that the "immobile" maintaining of the viewing field facilitates in a great measure also the discovering and the "catching" of mobile targets, especially for those systems with video-cameras with automatic tracking whose functioning is based on the detection of the mobile elements in a TV image contained, by numeric processing of the respective image. Related to this one must emphasise here also the delimitation that exists between the inertial systems for viewing field stabilisation - ISVFS - and the systems with automatic tracking based on the numeric processing of the digital images.

So, it should be precised that in the case that the initially adopted target as a positional reference is a fixed target, the image that can be obtained with the ISVFS system likens to that delivered by an electronic system which achieves the stabilisation of the image received on a monitor, by "point by point" numeric processing of that image. But in contrast with the electronic system for the stabilisation of the image from a monitor, ISVFS system which achieves the inertial stabilisation of the viewing field can be applied both in some installations that assure the image visualisation on an electronic monitor and in classic optic-mechanic installations where the sighting is effected through eyepieces with glass lens.

At the end, it should be also added that the viewing field inertial stabilisation constitutes the optimal solution when it is desiring to achieve simultaneous observation of many targets with close weight in respect to its contrast relative to landscape, the distance from the observer, geometrical dimensions and its tactical importance.

Essential differences between the two stabilisation systems of the sighting direction and viewing field respectively will be more clear emphasised, after the following presentation of the functioning principle and computing algorithm on which the functioning of each of these systems is basing.

2. SIGHTING DIRECTION STABILISATION. FUNCTIONING PRINCIPLE AND THE COMPUTING ALGORITHM.

An essential constructive peculiarity of the stabilisation systems which constitute the object of this report is also that, being not equipped with an own reference inertial element, respectively, in this case, an incorporated gyroscopic block,^{3, 4} the system can overtake the signals that represents the current angular values of the carrying vehicle rotations, from the gyroscopic station of the vehicle. Such system configuration is commonly known as "strap-down". In the frame of such a system, on the basis of both, the gyroscopic station delivered signals and those introduced by means of a controle handle connected to the stabilisation system, a built-in computing block continuously elaborates and transmits to some actuator blocks of the opto-mechanical sighting element the necessary signals to ensure the rotation of this element with respect to three of its reciprocally perpendicular axes, with the angular values that ensure the wished stabilisation mode irrespective

of the disturbing movements of the carrying vehicle. By means of the control handle, the operator can effect, the controlled changing of the stabilisation direction, with a continuously variable angular speed.⁵

To establish now the computing algorithm on which the viewing direction stabilising function is basing the followings will be referred also to the Fig. 1 which represent the vectors diagram defining the orientations of the airship direction Av and of the target direction T , with respect to the direction N of the local magnetic meridian adopted as reference.

As results also from the vectorial diagram in the Fig. 1, the sighting stabilised system is brought on the direction on which it is currently orientated as a result of the rotations made by the carrying airship with respect to an inertial reference system, rotations to that are added those made by the system or the stabilised element itself with respect to the airship. The inertial system of co-ordinates adopted as reference has the origin "O" bound to the airship, and two of its axes disposed in the horizontal plane of the site, one of the two axes being oriented along the local direction North of the magnetic meridian.

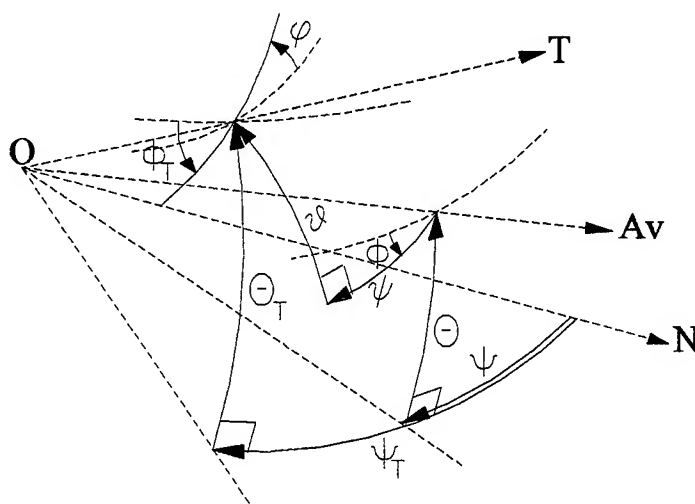


Fig. 1. Diagram of the vectors defining the orientations of parameters involved in the stabilisation system functioning.

Taking into consideration the current orientations, with respect to the north direction N of the local magnetic meridian adopted as reference, presented by the flying direction Av of the airship and by the direction T of the target on which the sighting element is oriented, one may consider that the airship has reached its current direction Av by effecting a series of rotations with respect to the reference system, as follows:

- an yaw rotation within the local horizontal plane by the angle Ψ , which is taken as positive if the rotation is made clockwise with respect to the N direction of the magnetic meridian;
- a pitch rotation within the local vertical plane by the angle Θ , which is taken as positive if the rotation is made towards nadir direction with respect to the horizontal plane;
- a roll rotation around the longitudinal axis of the airship by the angle Φ , which is taken as positive if the rotation corresponds to the forwarding rotation of a right screw along the flying direction.

These angles, Ψ , Θ and Φ , defined in the above presented mode, can be directly determined by the aid of the gyroscopic equipment of the airship. This equipment can consist of either an azimuth and elevation gyroscopic station (CCV), or a gyrovertical device and a gyromagnetic compass.

To reach the direction T of the target starting from the direction Av of the airship, the sighting system must make in its turn three rotations, as follows:

- a yaw rotation within the horizontal plane of the airship by an angle ψ , which is taken as positive if the orientation direction of the stabilised system is made clockwise;
- a pitch rotation within a vertical plane of the airship by an angle ϑ , which is taken as positive if the rotation of the sighting direction is made towards nadir direction;
- a roll rotation around the orientation direction of the stabilised system by an angle φ , which is taken as positive if the rotation corresponds to the forwarding rotation of a right screw along the sighting direction.

The rotational angles ψ , ϑ and φ of the stabilised element can be directly determined by the aid of some rotational transducers located onto the corresponding rotation axes of the sighting system.

On the other hand, the direction T of the target can be defined not only by the six rotation angles, directly measurable, Ψ , Θ , Φ , ψ , ϑ and φ , above precised, but also directly by three absolute angular co-ordinates corresponding to some hypothetical rotations of the sighting direction, starting from N reference direction, as follows:

- an azimuth rotation within the local horizontal plane by an angle Ψ_T , which is taken as positive if the rotation is made clockwise with respect to the N reference axis;
- an elevation rotation within a local vertical (meridian) plane by an angle Θ_T , which is taken as positive if the rotation is made towards nadir direction;
- a roll rotation by an angle Φ_T around the sighting direction, which is taken as positive if the rotation corresponds to the forwarding rotation of a right screw along this direction.

Both, these imaginary rotations corresponding to the three absolute angular co-ordinates, on one side, and the six real rotations listed above (as being made by the carrying airship and the sighting system, respectively), on the other side, by different ways, lead from the N reference direction towards the same direction T of the target. This means that there is a perfect equivalence between the successive transforms that the co-ordinates system of the sighting element gets through on each of the two aforementioned ways. This fact can be expressed in a synthetic manner by the following matricial equation:

$$[\varphi][\vartheta][\psi][\Phi][\Theta][\Psi] = [\Phi_T][\Theta_T][\Psi_T] \quad (1)$$

where the matrices corresponding to each rotation of the co-ordinates system of the sighting element have the following expressions:

$$[A] = \begin{bmatrix} \cos A & \sin A & 0 \\ -\sin A & \cos A & 0 \\ 0 & 0 & 1 \end{bmatrix}; [B] = \begin{bmatrix} \cos B & 0 & -\sin B \\ 0 & 1 & 0 \\ \sin B & 0 & \cos B \end{bmatrix}; [C] = \begin{bmatrix} 1 & 0 & 0 \\ 0 & \cos C & \sin C \\ 0 & -\sin C & \cos C \end{bmatrix}. \quad (2)$$

where the following notations have been used:

A for parameters Ψ_T , Ψ and ψ ;

B for parameters Θ_T , Θ and ϑ ;

C for parameters Φ_T , Φ and φ .

By solving the matricial equation (1) on the basis of the known values of six of the parameters that enter in the content of this equation, the values of the other three parameters can be determined. So, based both on the values of the absolute angular co-ordinates of the target, Ψ_T , Θ_T and Φ_T , and on the values of the current angles, Ψ , Θ and Φ , describing the orientation of the airship, the values of the angular rotations, ψ , ϑ and φ , can be determined. As was mentioned before, these angular rotations must be effected by the stabilisation system with respect to the airship in order to ensure, in every moment, the maintaining of the sighting element on the target direction.

3. VIEWING FIELD STABILISATION. FUNCTIONING PRINCIPLE AND COMPUTING ALGORITHM

Sighting device functioning in the viewing field stabilisation regime, - ISVFS - , involves the achievement by the operator of the following initialisation phase:

After terrestrial objective selection, in the moment when, by control handle actuation, the operator succeeded its framing in the sighting device collimator, the simultaneous recording of the relative co-ordinates of the target is effecting. These co-ordinates are determining, in respective initially moment $t = 0$, by the sighting device in respect to the location of the airship:

Ψ_{T_0} - azimuth angular co-ordinate of the target, measured in the horizontal plane of the airship, in respect to the North local magnetic meridian;

Θ_{T_0} - elevation angular co-ordinate of the target, measured in its vertical plane and having as reference the horizontal plane in which the airship is situated;

Δ_0 - the direct distance to the target determined by laser remote ranging.

Beginning also with the initial moment $t = 0$, the airship geographic co-ordinates values, latitude - φ_{Av} and longitude - λ_{Av} , are recording, as well its flying heights - h . These values are continuously delivered by the airship's inertial navigation system, in cvasi-real time. The computing algorithm on which the functioning of the ISVFS is basing contains three principal sequences:

- The group of relations defining the target relative positioning in the local vertical plane;
- The group of relations by which the target geographic co-ordinates are computing;
- The group of relations by which the relative to airship target angular co-ordinate are computing.

3.1. Relations for the target positioning in the local vertical plane.

The principal angular parameter for in vertical plane positioning of the sighted terrestrial target is, as it is presenting also in Fig. 2, the angle σ between the R' radius of the terrestrial sphere in the point T where the sighted terrestrial target is located and the direction of the site vertical that passes both through the C centre of the terrestrial sphere and the Av current point in which the observing airship is situated. The other parameters that appear in the schema from Fig. 2 are:

R - terrestrial sphere average radius;

Θ_T - in the vertical plane inclination angle of the target sighting direction; its value is delivered by the sighting stabilised system;

h - the airship flying height delivered also by its inertial navigation system;

Δ - The direct distance between the airship and the target; this distance can be measured by laser remote ranging.

Consequently, in the common triangle $CAvT$ from the Fig. 2, the values of two sides, $R + h$ and Δ , as well the value of the angle Θ_T between these sides, are directly measurable. On this basis, one can immediately obtains the computing relations for the angular co-ordinate σ and for the target absolute height R' , respectively. For the sighting initial moment, $t = 0$, these relations have the following form:

$$\tan \sigma_0 = \frac{\Delta_0 \cdot \cos \Theta_{T_0}}{R + h_0 - \Delta_0 \cdot \sin \Theta_{T_0}} \quad (3)$$

and

$$R' = \frac{\Delta_0 \cdot \cos \Theta_{T_0}}{\sin \sigma_0} \quad (4)$$

or:

$$R' = \frac{(R + h_0) \cdot \cos \Theta_{T_0}}{\cos(\sigma_0 - \Theta_{T_0})} \quad (5)$$

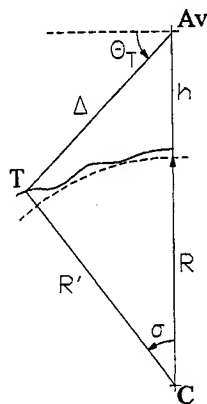


Fig. 2. The defining in the vertical plane of the terrestrial target T position relatively to the airship Av

3.2. Relations for the target angular geographic co-ordinates computing.

In this phase, as it is resulting also from the diagram presented in Fig. 3, the target angular geographic co-ordinates, latitude φ_T and longitude λ_T respectively, can be computed depending both on the target relative angular co-ordinates, Ψ_{T_0} and σ_0 respectively, that are determined in respect with the observing airship position Av_0 , in the initial moment of sighting, and on the latitude and longitude, φ_{Av_0} and λ_{Av_0} respectively, of this airship position. The last two co-ordinates are delivered in real time by the airship's inertial navigation system.

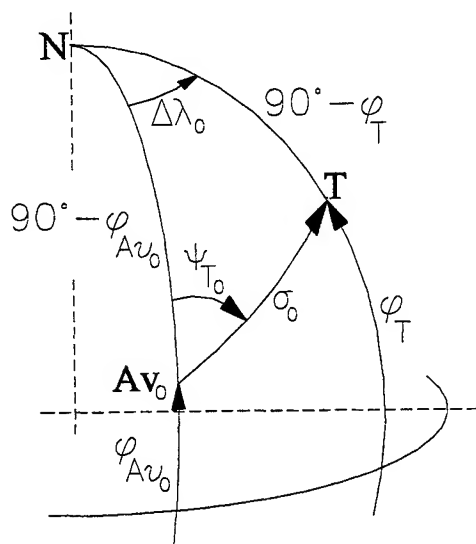


Fig. 3 Diagram for the target geographic co-ordinates establishing.

Therefore, in the common triangle NAv_0T traced on terrestrial sphere from the Fig. 3, two sides represented by the arcs of the R radius circle, $N\hat{A}v_0 = 90^\circ - \varphi_{Av_0}$ and $T\hat{A}v_0 = \sigma_0$ respectively, are known, as well the angle Ψ_{T_0} between these sides. With the relations of the trigonometry on sphere one can determine the other parameters of the NAv_0T triangle, namely the angle $\Delta\lambda_0 = \lambda_T - \lambda_{Av_0}$ of the longitude differences, as well the other side, $N\hat{T} = 90^\circ - \varphi_T$, that corresponds to the target latitude. So, one can obtain:

$$\tan \Delta \lambda_0 = \frac{\sin \Psi_{T_0} \cdot \sin \sigma_0}{\cos \varphi_{Av_0} \cdot \cos \sigma_0 - \sin \varphi_{Av_0} \cdot \sin \sigma_0 \cdot \cos \Psi_{T_0}} ; \quad (6)$$

so that:

$$\lambda_T = \lambda_{Av_0} + \Delta \lambda_0 , \quad (7)$$

and:

$$\cos \varphi_T = \frac{\sin \sigma_0 \cdot \sin \Psi_{T_0}}{\sin \lambda_T \cdot \cos \lambda_{Av_0} - \cos \lambda_T \cdot \sin \lambda_{Av_0}} . \quad (8)$$

3.3. Relations for the computing of the target current angular co-ordinates in respect to the airship.

The last sequence of this algorithm contains the group of relations with which one must repeatedly calculates the target angular co-ordinates in respect to the airship, Ψ_T and Θ_T , in order to, on these values basis, to achieve the continuously re-orientation of the sighting device on the respective target direction, in conditions in which the airship is displacing or effects different flight manoeuvres. To establish these relations one must refer to the diagram from the Fig. 4 in which on the terrestrial sphere the triangle $NAvT$ is traced.

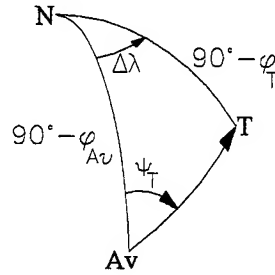


Fig. 4 Diagram for the target current angular co-ordinates relative to airship establishing.

This triangle binds the current position Av of the on sphere projection of the airship to the position T on the same sphere of the sighted target and to the geographic north N . In this triangle two sides, one constituted by the arc of circle $NAv = 90^\circ - \varphi_{Av}$ and the other by the arc of circle $NT = 90^\circ - \varphi_T$, are known, as well the angle $\Delta \lambda$ between these sides; (the current geographic co-ordinates φ_{Av} and λ_{Av} of the airship are delivered in real time by its inertial navigation system, and the geographic co-ordinates, φ_T and λ_T of the target, have been calculated in the previous sequence). On this basis, with the equations of the trigonometry on sphere applied to the triangle $NAvT$, the following computing relations for both the Ψ_T angle and the third side, the σ arc respectively, are establishing:

$$\tan \Psi_T = \frac{\sin \Delta \lambda \cdot \cos \varphi_T}{\cos \varphi_{Av} \cdot \sin \varphi_T - \sin \varphi_{Av} \cdot \cos \Delta \lambda \cdot \cos \varphi_T} \quad (9)$$

and:

$$\sin \sigma = \frac{\sin \Delta \lambda}{\sin \Psi_T} \cdot \cos \varphi_T \quad (10)$$

with:

$$\Delta \lambda = \lambda_T - \lambda_{Av} \quad (11)$$

To establish the computing expression, also for the angular co-ordinate Θ_T , one must refer again to the diagram presented in the Fig. 2, respectively to the plane triangle $CAvT$. For this once, in this triangle two sides, $R+h$ and R' , as well the angle σ between these sides, are known. On this basis one can obtain:

$$\tan \Theta_T = \frac{R+h-R' \cdot \cos \sigma}{R' \cdot \sin \sigma} \quad (12)$$

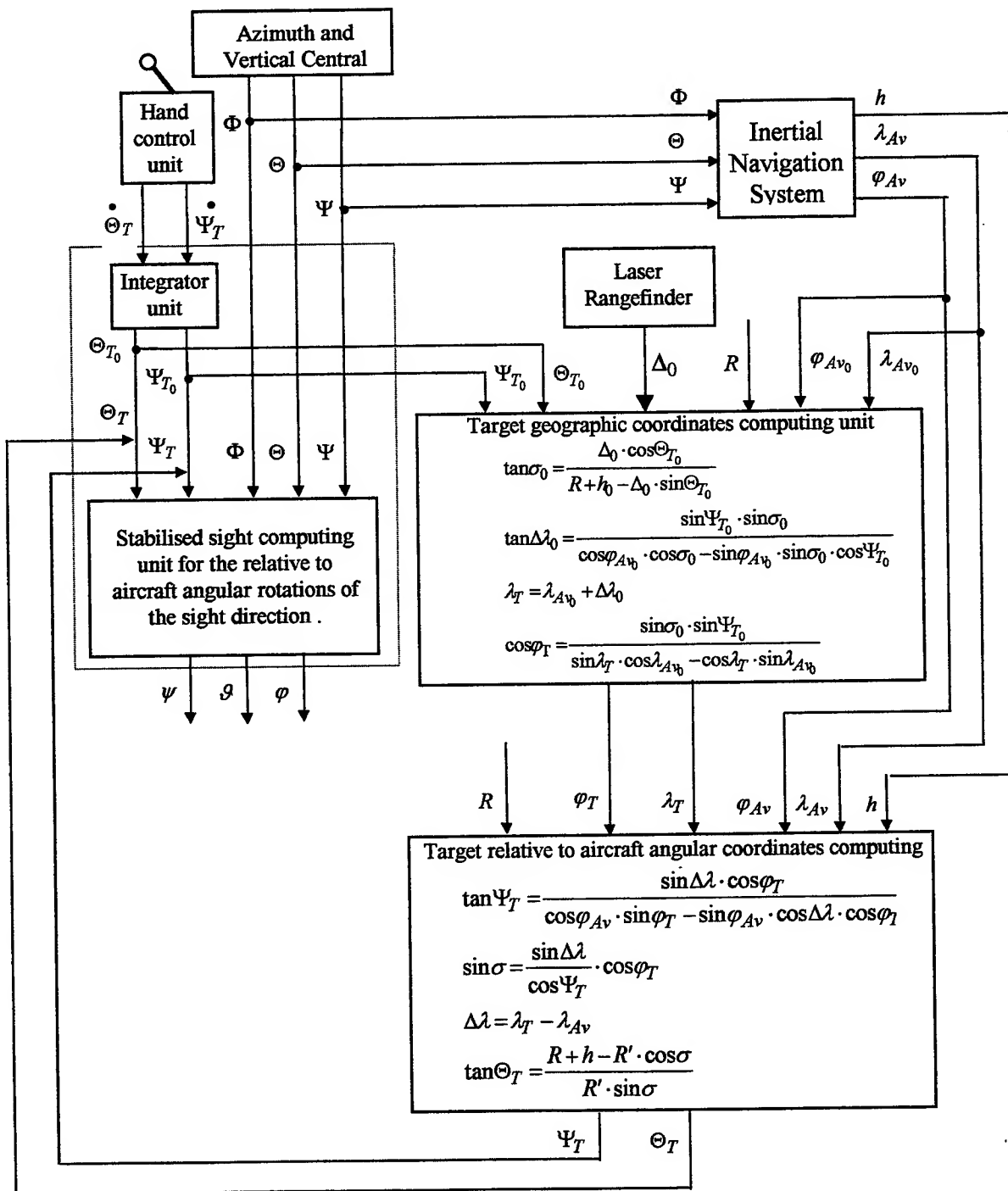


Fig. 5 Block schema of the general computing algorithm on which the functioning of the sighting system with stabilised viewing field - ISVFS - is basing.

3.4. Integration of the computing relations in the general algorithm on which the functioning of the viewing field stabilisation system (ISVFS) is basing.

Further, the two relative angular co-ordinate values, Ψ_T and Θ_T , of the terrestrial target, which are obtained as a result of passing through the above presented computing cycle, will replace, at the entrance of the computing system of the sighting device, the initial values of the same co-ordinates obtained by time integration of the signals, $\dot{\Psi}_T$ and $\dot{\Theta}_T$, delivered by the control handle M.C., until the moment of target framing in the collimator.

In this way, on the basis of current values, Ψ_T and Θ_T , of the target angular co-ordinates, the "strap-down" type sighting system is able to determine, as it was presented in the paragraph 2 of this report, the angular values group, ψ , ϑ and φ , with which its optical elements must be rotated to maintain the viewing field unchanged in the collimator, irrespective of the carrying airship evolution.

The closed computing cycle that includes all the above presented operations and which must be repeated by the built-in numeric processor, with a high enough frequency to ensure a proper quality for the sighting field stabilising process, is presented in the block schema from the Fig. 5.

4. DETERMINATION OF THE DISTANCE BETWEEN THE AIRSHIP AND THE TARGET ON TWO SUCCESSIVE SIGHTINGS BASIS

As it is resulting from the presentation of the viewing field stabilisation system, its functioning involves the determination of the initial distance between the sighted terrestrial target and the observer. But it can happen to be not possible to determinate this distance by means of a laser measurement, due to at least one of the following causes: the sighting device is not equipped also with a laser range finder, the nature of sighted objective makes that the laser beam reflected by this to have not the necessary level for a correct distance measurement and finally, the masking necessity against the hostile objective does not allow the use of laser.

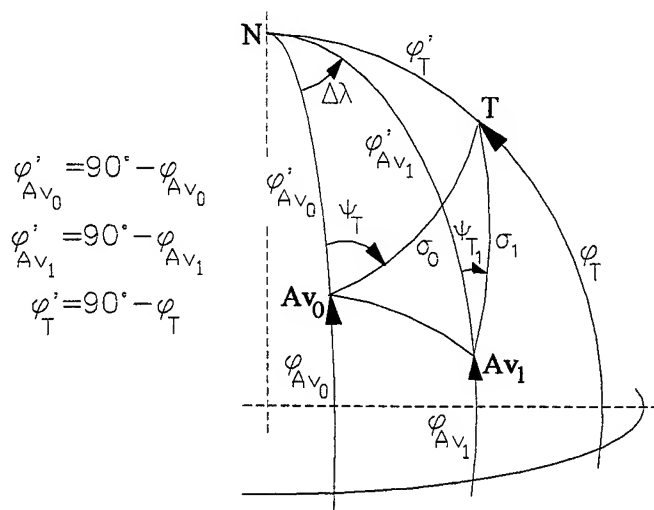


Figure 6 Diagram for the establishing of the computing relations of the target distance from the airship

However, for these situations exist the possibility, as already was mentioned in the introductory paragraph that the determination of the distance between the airship and the target to be achieved by means of two successive sights of the target. In each of these sightings the airship geographic co-ordinates, φ_{Av} and λ_{Av} , as well the target relative angular co-ordinates, Ψ_T and Θ_T , are marked. In order to establish the relations by means which, on the basis of the above mentioned parameters, one can compute the target distance Δ , it is necessary to make reference to the diagram of

triangulation on the terrestrial sphere surface from the Fig. 6 in which the two successive airship positions, Av_1 and Av_2 , and fixed target position T , are marked.

To establish the computing relations of the distance it is necessary to pass successively through the following phases:

a. - In a first phase one is making reference to the triangle Av_0NAv_1 traced on the terrestrial sphere surface; in this triangle two sides $N\hat{A}v_0 = \varphi'_{Av_0} = 90^\circ - \varphi_{Av_0}$ and $N\hat{A}v_1 = \varphi'_{Av_1} = 90^\circ - \varphi_{Av_1}$, as well the angle $\Delta\lambda = \lambda_{Av_1} - \lambda_{Av_0}$ between the two sides, are known.

On this basis and by means of the equations of the trigonometry on sphere one can compute the two other angles of this triangle, - the angle α with the tip in the point Av_0 and the angle β with the tip in the point Av_1 -, as well the third side, $\delta = Av_0\hat{A}v_1$:

$$\tan \alpha = \frac{\sin \Delta\lambda \cdot \cos \varphi_{Av_1}}{\cos \varphi_{Av_0} \cdot \sin \varphi_{Av_1} - \sin \varphi_{Av_0} \cdot \cos \varphi_{Av_1} \cdot \cos \Delta\lambda} \quad (13)$$

$$\sin \beta = \frac{\cos \varphi_{Av_0} \cdot \sin \alpha}{\cos \varphi_{Av_1}} \quad (14)$$

$$\sin \delta = \frac{\sin \Delta\lambda}{\sin \beta} \cdot \cos \varphi_{Av_0} \quad (15)$$

b. - In the following phase one is passing to the triangle Av_0TAv_1 that is traced also in the diagram from the Fig. 6 on the terrestrial sphere surface; in this triangle, two angles, respectively the angle " $\alpha - \Psi_{T_0}$ " with its tip in the point Av_0 and the angle " $\beta + \Psi_{T_1}$ " with its tip in the point Av_1 , as well the side $\delta = Av_0\hat{A}v_1$ commune to these angles, are known. For this configuration, the equations of trigonometry on sphere permit to obtain the following computing relation for the side represented by the relative angular co-ordinate σ_0 of the target:

$$\tan \sigma_0 = \frac{\sin(\beta + \Psi_{T_1}) \cdot \sin \delta}{\sin(\alpha - \Psi_{T_0}) \cdot \cos(\beta + \Psi_{T_1}) + \cos(\alpha - \Psi_{T_0}) \cdot \sin(\beta + \Psi_{T_1}) \cdot \cos \delta} \quad (16)$$

This last expression obtained for the angular co-ordinate σ_0 can replace in this case the relation (3) with which the co-ordinate σ_0 is computing in function of the distance Δ_0 obtained by laser remote ranging. In the frame of the general computing algorithm of the system, for the situation in which this system is not equipped with a laser remote ranger, the relation (3) is replaced by (13), (14), (15) and (16) group of relations.

c. - For the applications in which it is necessary to know also the distance value to the target, this can be obtained now from the relation (3) depending on the angular co-ordinate σ_0 whose value is given by the relation (16):

$$\Delta_0 = \frac{(R + h_0) \cdot \tan \sigma_0}{\cos \Theta_{T_0} + \sin \Theta_{T_0} \cdot \tan \sigma_0} \quad (17)$$

4. CONCLUSIONS

An optical device which is equipped with an usual gyroscopic system for stabilisation of its sighting direction and for the goniometry of the sighted target can be transformed in a sighting system whose stabilised element is for this once its viewing field selected in an initial moment. To do this the including of the respective optical device in a closed control circuit is necessary; in this circuit a micro-processor is delivering, with a cadence corresponding to the respective application necessity, the successive values of the target angular co-ordinates relative to the observing vehicle, in conditions in which this is displacing or effects different manoeuvres. These values of the target relative co-ordinates, which are continuously variable, under the form of some controlling electrical signals, are applying to the electromechanical actuators which achieves the rotation of the mobile optical elements of the sighting device in the necessary mode to ensure the stabilising type presented here.

Besides of the optical sighting device, of its stabilising and goniometring system, another essential element of the above mentioned controlling circuit is constituted by the inertial navigation system (INS) which is used here to deliver in a continous manner the data reffering to the displacement of the observing vehicle. To be able to achieve this, as it is resulting from the general schema of the stabilising system presented in the Fig. 5, besides the signals received from its accelerometric block, the INS system overtakes also the reference gyroscopic signals delivered by the heading and vertical central (CCV) of the carrying vehicle, central to which is also directly connected the sighting stabilised device⁶.

Finally, it is mentioning also that to determine the observing vehicle displacement one is not resorting to the satellitary system of the global positioning (GPS), although this system is able to deliver at a higher precision level, the absolute values of the position co-ordinates of the vehicle. The motive of this option is that that the cadence of one measurement per second generally ensured by the GPS system is not satisfactory for the most of the applications of the stabilised sighting system for which the continuous fluxes of relative positioning data delivered by the inertial navigation systems are preferable.

REFERENCES

1. *Viseur gyrostabilisé APX-M334-04* - S.F.I.M. Catalogue, France
2. A. Stoica et al. "Modular System for Gyrostabilised Sighting, Goniometry and Laser Telemetry", Romanian Journal of Optoelectronics, 7, nr.1, pp.77-84, 1999
3. David John Cann and Ronald Whalley "Dispositif de stabilisation, notamment pour un viseur gyroscopique", Invention Patent no. 7.632.574, 1988, France
4. A. Stoica "Device for gyroscopic stabilisation of an optical sight". Inv. Patent no.103.115/1991, Romania
5. A. Stoica et al. "Sight Direction Stabilising System in strap-down configuration", Romanian Journal of Optoelectronics, 5, 4, pp.25-30, 1997.
6. A. Stoica et al, "Inertial Navigation System (INS) conceived for the complementation of the GPS systems used in position determinations on vehicles". Romanian Journal of Optoelectronics, 6, 3, pp.49-56, 1998.

Analysis of some specific errors in infrared thermometry

Catalin A. Spulber*, Gabriel E. Constantinescu

Research and Design Institute for Optical Industry "ProOptica S.A."

4, Bucovina St., RO-74404 Bucharest, Romania

ABSTRACT

This paper studies the influence of radiation thermometer optical system properties on the total radiating energy upon an optoelectronic detection device when the measuring distance is variable. The first part is a brief analysis of characteristics of concentrating infrared radiation through the thermometer objective. The sources used are smaller, larger or equal than the detection device field of view. When using the equal sources, the specific shape of the measuring area was taken into account, and included in the total field of view (the measuring area upon background). Catoptric objective (Cassegrain assembly) was used. In addition, this paper presents the main error sources on concentrating IR radiation on the detection device in following conditions: the calibration is performed at a finite and infinite distance, the radiation source is assumed to be perfectly Lambertian and the objective is catoptric (using a central diaphragm).

Keywords: Infrared, temperature measurements, optics systems.

1. RADIATION COLLECTION

An infrared thermometer has 4 component functional modules, encased in a box: an *optical module* (collects IR radiation in specific wavelength), a *detection module* (detection and conversion of passive IR radiation emitted in the measurable spectrum), an *electronic module* (amplification, processing, recording and display of data received from the detection module) and a *power supply module*. This paper studies the influence of the optical module characteristics upon the thermometer performance.

In order to obtain the maximum power (energy) value for the radiating source, the detector 1 must be situated at a distance q from this, which can be calculated using the following formula¹ (see Fig.1 and Fig.2):

$$q = \frac{L \cdot f_{ob}}{L - f_{ob}} \quad (1)$$

where L – distance to object plane 3 and f_{ob} – focal length of objective 2 of the thermometer.

Temperature measurements using a device calibrated for a image distance $L = L_0$ leads to errors when $L \neq L_0$ because the maxim radiant energy will not fall on the detector, but either in front or behind it. The relationship between this offset and the distance (L) can be described as follows:

$$\frac{dq}{dL} = - \frac{f_{ob}^2}{(L - f_{ob})^2} \quad (2)$$

* Correspondence: Email: prooptic@fx.ro

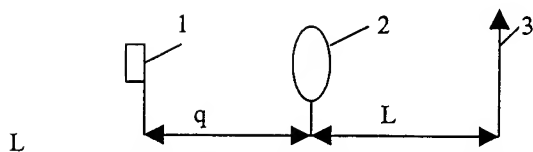


Fig.1 Optical data of a radiation thermometer

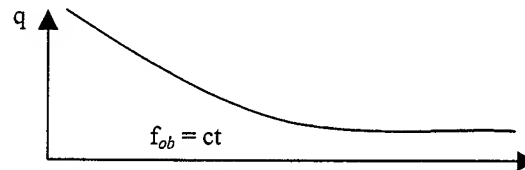


Fig.2 Diagram of image distance variation related to the change of the L object distance

1.1. Objective influence

Let us consider a simple optical system consisting of an objective (with entrance pupil area A_{ob} focal length of f_{ob} and a diameter D_{ob}) and a detection element (having a useful sensitive surface area A_d). Let us assume that source S (with a surface area A) is located at a large distance L facing the objective, and its image is in the focal plane where the detection element is located. The radiant flux Q falling onto the detection element from source S can be calculated using the following formula²:

$$Q = \frac{W \cdot A_{ob} \cdot A}{L^2} \quad (3)$$

when object (source) S is smaller than the visual field of the detection element, or, when object (source) S is larger than the visual field of the detection element, by the following relationship:

$$Q = W \cdot \omega \cdot A_{ob} = \frac{W \cdot A_d \cdot A_{ob}}{f_{ob}^2} \quad (4)$$

1.2 .Radiation collection using dioptric objectives

In order to simplify, we assumed that radiant emitancet from the object field can be derived form Stefan-Boltzamans law. In addition, we considered that, since the targeted object is at a large enough distance from the detector, the distance L between the detector and the object can be approximated as being equal with that to background.

Based on the above assumptions, q , the distance between the detector and the objective, can be calculated using the following formula (1); the image D , located in the object plane of a detection element with a size D_d can be expressed as follows:

$$D = \frac{D_d \cdot L}{f_{ob}} \quad (5)$$

If $L \gg f_{ob}$, obviously $q = f_{ob}$.

But D can be much more accurately calculated using the following relationships¹:

$$D = \left(\frac{D_{ob} - D_d}{L_0} + \frac{D_d}{f_{ob}} \right) \cdot L - D_{ob} \quad (6)$$

if $L_0 < L$, and

$$D = \left(\frac{D_d}{f_{ob}} + \frac{D_{ob} + D_d}{L_0} \right) \cdot L + D_{ob} \quad (7)$$

if $L_0 > L$.

Diameter D is indicated in Fig. 3:

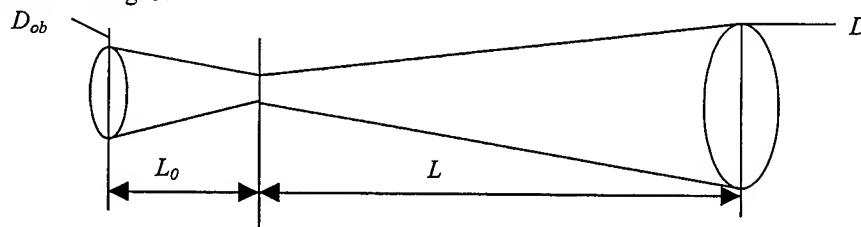


Fig.3 Diagram for variation of the D object field related to the change of the L distance

The following is a presentation of 3 extreme cases:

- The total visual field α of the detection element is smaller than the measured field
 - The total visual field α of the detection element is larger than the measured field
 - The total visual field α of the detection element is equal to or smaller than the measured field, but the latter has distinctive shape, and a part of the background remains visible.
- To easy understanding of the energetic phenomena, the objective is represented as a simple lens, and the fields are considered for beginning, as a circular shape.

1.2.1 The total visual field α of the detection element is smaller than the measured field

The radiance received by the objective (W), and forwarded to the detector (W_d) can be calculated as follows³:

$$W = \frac{\pi^2 \cdot \tau_a \cdot \tau_{ob} \cdot \sigma \cdot \varepsilon \cdot T^4 \cdot D_{ob}^2 \cdot D_d^2}{16 \cdot f_{ob}^2} \quad (8)$$

$$W_d = \frac{\pi^2 \cdot \tau_a \cdot \tau_{ob} \cdot \sigma \cdot \varepsilon \cdot T_d^4 \cdot D_{ob}^2 \cdot D_d^2}{16 \cdot f_{ob}^2} \quad (9)$$

with "d" stands for "detector"; therefore we can rewrite the expression as follows:

$$\Delta W = \frac{\pi^2 \cdot \tau_a \cdot \tau_{ob} \cdot \sigma \cdot D_{ob}^2 \cdot D_d^2 (\varepsilon \cdot T^4 - \varepsilon_d \cdot T_d^4)}{16 \cdot f_{ob}^2} \quad (10)$$

Based on the Stefan-Boltzman law assumption:

$$\Delta W = \frac{\pi^2 \cdot \tau_a \cdot \tau_{ob} \cdot D_{ob}^2 \cdot D_d^2 (W - W_d)}{16 \cdot f_{ob}^2} \quad (11)$$

Moreover, if we assume the size of the detection element to be a and b :

$$\Delta W = \frac{\pi^2 \cdot \tau_a \cdot \tau_{ob} \cdot D_{ob}^2 \cdot a \cdot b \cdot (W - W_d)}{4 \cdot f_{ob}^2} \quad (12)$$

1.2.2 The total visual field α of the detection element is larger than the measured field

The initial assumption is that upon the detector falls radiation exclusively from background and visual field of the detector is smaller than the measure field, therefore:

The irradiance of the objective by the background (W_f) can be expressed³:

$$W = \frac{\pi^2 \cdot \tau_a \cdot \tau_{ob} \cdot \sigma \cdot \varepsilon_f \cdot T_f^4 \cdot D_{ob}^2 \cdot D_d^2}{16 \cdot f_{ob}^2} \quad (13)$$

The objective radiation towards the detector (W_d) can be expressed:

$$W_d = \frac{\pi^2 \cdot \tau_a \cdot \tau_{ob} \cdot \sigma \cdot \varepsilon_d \cdot T_d^4 \cdot D_{ob}^2 \cdot D_d^2}{16 \cdot f_{ob}^2} \quad (14)$$

The net radiance of the detector (W_d) – when it visualises the screen only, can be expressed:

$$\Delta W = W_f - W_d = \frac{\pi^2 \cdot \tau_{ob} \cdot \sigma \cdot D_{ob}^2 \cdot D_d^2 (\tau_a \cdot \varepsilon_f \cdot T_f^4 - \varepsilon_d \cdot T_d^4)}{16 \cdot f_{ob}^2} \quad (15)$$

In a combined situation, object – screen, combining the above relationships (12 – 15) can derive the net detector radiation:

$$\Delta W = \frac{\pi^2 \cdot \tau_a \cdot \tau_{ob} \cdot \sigma \cdot D_{ob}^2 \cdot D_d^2 (\varepsilon \cdot T^4 - \varepsilon_f \cdot T_f^4)}{16 \cdot f_{ob}^2} \quad (16)$$

A particularly interesting situation is when the temperature of the object field (T) is close to that of the background (T_f); in such an instance, since $T \approx T_f$

$$T^4 - T_f^4 = (T^2 + T_f^2)(T + T_f)(T - T_f) \quad (17)$$

and by assuming

$$T^2 + T \cdot T_f^2 \approx 2T^2; T + T_f \approx 2T; T - T_f \approx \Delta T$$

we get $T^4 - T_f^4 \approx 4T \cdot \Delta T$ and:

$$\varepsilon T^4 - \varepsilon_f T_f^4 = \varepsilon (T^4 - T_f^4) + T_f (\varepsilon - \varepsilon_f)$$

Substituting these values in the (3.11) relationship, the following result is obtained:

$$\Delta W (T \approx T_f) = \pi^2 \tau_a \tau_{ob} \sigma D_{ob}^2 D_d^2 (4 \varepsilon T^3 \Delta T + \Delta \varepsilon T^4 / 16 f_{ob}^2) \quad (18)$$

where $\Delta \varepsilon = \varepsilon - \varepsilon_f$

Assuming that $\Delta T > 1^\circ\text{C}$ and $\varepsilon \gg \varepsilon_f$

$$\Delta W (T \approx T_f) = \frac{\pi^2 \cdot \tau_a \cdot \tau_{ob} \cdot \sigma \cdot D_{ob}^2 \cdot D_d^2 \cdot \varepsilon \cdot T^3 \cdot \Delta T}{4 \cdot f_{ob}^2} \quad (19)$$

This way we can rewrite Stefan – Boltzmann's law hypothesis:

$$\Delta W (T \approx T_f) = \frac{\pi^2 \cdot \tau_a \cdot \tau_{ob} \cdot D_{ob}^2 \cdot D_d^2 \cdot W \cdot \Delta T}{4 \cdot T \cdot f_{ob}^2} \quad (20)$$

and if we assume the size of the detection element to be $a \times b$

$$\Delta W (T \approx T_f) = \frac{\pi^2 \cdot \tau_a \cdot \tau_{ob} \cdot D_{ob}^2 \cdot a \cdot b \cdot W \cdot \Delta T}{T \cdot f_{ob}^2} \quad (21)$$

1.2.3 The total visual field α of the detection element is equal to or smaller than the measured field, but the latter has distinctive shape, and a part of the detecting area remains visible

In this situation the image of the measured field does not cover completely the whole sensitive area of the detection element, therefore, one must derive the surface area of the screen and the object field image on the detection element².

- the surface area of the object field image: $\frac{A \cdot f_{ob}^2}{L^2}$

- the surface area of the screen: $\frac{\pi \cdot L^2 \cdot D_d^2}{4 \cdot f_{ob}^2} - A$ or $\frac{a \cdot b \cdot L^2}{f_{ob}^2} - A$

(the latter one assuming the radiating surface area to be $A = a \cdot b$)

Through a similar reasoning:

$$\Delta W = \frac{(W - W_f) \cdot A \cdot D_{ob}^2}{4 \cdot L^2} \quad (22)$$

1.3 Radiation collection using catoptric objectives

In catoptric systems, the secondary mirrors (diameter D_s) blocks the radiation in the central portion; therefore the radiation reaching the primary mirror (D_p) has the aspect of a corona (missing the central area). In such an instance, the radiation reaching the sensitive portion of the detection module is weaker when compared to dioptric systems, where this obscuring of the central portion does not occur. A second disadvantage is due to the angular variation of the intensity of the incoming radiation; in the case of a Lambertian source, this variation is easily measurable, but in the case of a specular source, it is impossible to quantify.

The missing portion surface area in the radiation reaching the primary mirror is directly proportional to the distance between the object and the objective. A correction coefficient K_1 must be used for the radiance onto the detector⁴:

$$K_1 = \frac{\frac{D_s^2 \cdot L^2}{(L - l_s)^2}}{D_p^2 - D_s^2} \quad (23)$$

such that the detection element radiance becomes:

$$\Delta W = \Delta W (1 - K_1) \quad (24)$$

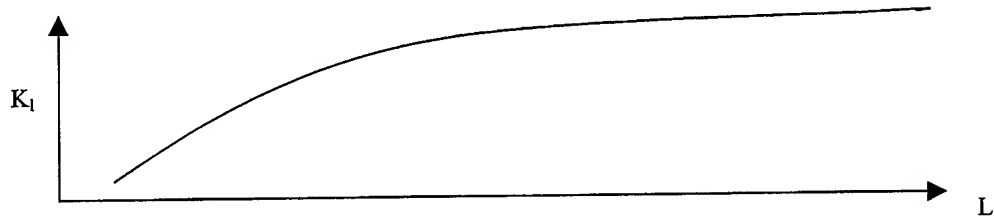


Fig.4 Diagram for variation of K_1 correction coefficient related to the change of object distance in the case of the obstruction of the primary mirror

The correction coefficient (K) expresses the total error and has a different value for:

- dioptric systems

$$K = K_0 \cdot K_1 \quad (25)$$

- catoptric systems

$$K = K_0 \cdot K_1 \cdot K_2 \quad (26)$$

This will generate a shape such the one in Fig. 5.

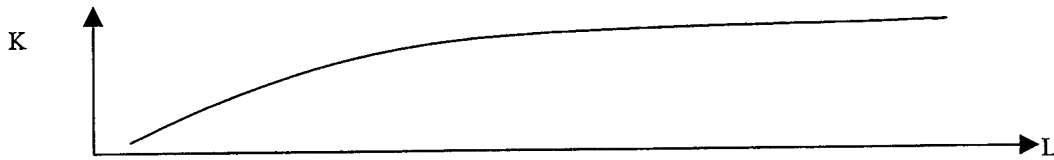


Fig.5 Diagram for variation of K total correction coefficient related to the change of L object distance

2. MAIN ERROR SOURCES ENCOUNTERED IN IR COLLECTION

If the calibration is performed on a determined distance L_0 , while the source is located at a distance $L \neq L_0$, the power of the collected radiation varies with a coefficient derived from the following formula: $K_0 = \Phi / \Phi_0$, derived from (29) (see Fig.6), where:

Φ - the collected power of the radiation when the source is at a distance L

Φ_0 - the collected power of the radiation when the source is at the L_0 calibrating distance ⁴

$$K_0 = \frac{L_0^2 \cdot (L - f_{ob})^2}{L^2 \cdot (L_0 - f_{ob})^2} \quad (27)$$

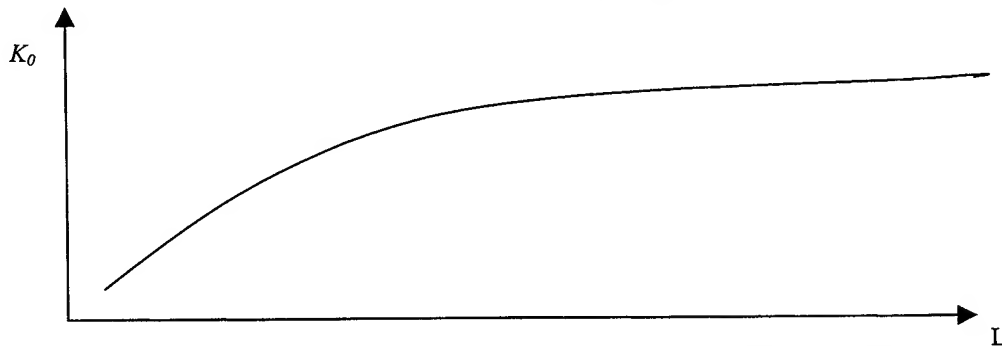


Fig.6 Diagram for variation of K_0 correction coefficient of the power captured by the detector related to the changed of L object distance

Ideally, K_0 should be independent of the distance L .

The (26) and (27) relationships are true only when the size of the radiating surface is larger than the surface covered by the visual field corresponding to the detection element.

It is also interesting to notice that, if the calibration is performed using $L_0 = \infty$, the detector will receive less energy and the measured temperature will be less than the real temperature. Actually, as L increases when compared to L_0 , K_0 (the error coefficient) is larger. Even if the source is perfectly Lambertian (no reflections, completely diffused in all directions in a uniform manner), by the variation of the distance L , the objective receives a modified radiation since the diffusion angles vary by distance. The total influence is expressed as K_2 , from (27): (see Fig. 7)

$$K_2 = \frac{\cos[2 \arcsin \frac{D_s}{2(L-l_s)}] - \cos[2 \arcsin \frac{D_p}{2L}]}{4 \cos[\arcsin \frac{D_s}{2(L-l_s)}] - \cos[\arcsin \frac{D_p}{2L}]} \quad (28)$$



Fig.7 Diagram for variation of K_2 correction coefficient dependent on the source type related to the change of L object distance

3. EXAMPLES REGARDING SPECIFICS OF THE MAIN ERRORS ANALYSED FOR DISCRETE VALUES OF CERTAIN OPTICAL SYSTEMS

Tab.1 shows variation by distance L of the image plane (dq/dL), of the collected power (K_0) by the detector, the reduction in the optical signal due to the secondary mirror (K_1) as well as the variation by source type (K_2). The starting points were $D_p = 50$ mm, $D_s = 22$ mm, $l_s = 7$ mm, $f_{ob} = 90$ mm, $L_0 = 400$ mm.

Tab.1 Influence of the L distance on some optoelectronic parameters

L [m]	0,2	0,4	0,6	0,8	1	1,2	1,4	1,6	1,8	2
dq/dL [%]	66,9	4,8	2,2	1,2	0,8	0,6	0,4	0,3	0,2	0,1
K_0	0,5	1	1,2	1,31	1,38	1,42	1,46	1,48	1,50	1,52
K_1	0,98	0,99	1	1	1	1	1	1	1	1
K_2	0,56	0,53	0,52	0,52	0,51	0,51	0,51	0,51	0,51	0,51

4. CONCLUSIONS

- The main error sources in collecting radiation by an IR thermometer are:
 - the measuring distances are different from the calibration distance;
 - measuring areas that are smaller than the visual field of the instrument;
 - incoordination between real measuring source and Lambertian emission source (black body standard) on the basis of which the calibration is performed.
- Using improved software for processing data from the electronic module leads to an increased precision measurement.

REFERENCES

1. C. Spulber, and M. Arton, "On a IR temperature measurement using a radiation ratio pyrometer", *Revista Romana de Mecanica Fina si Optica, Bucuresti, Oct. 1994*
2. R. W. Astheimer, and E. M. Wormser, "High-Speed Infrared Radiometers", J.O.S.A, vol. 49, no.2, pp. 179-183, 1959
3. C. Spulber, M. Marzu, and E. Cretu: "Sisteme optoelectronice de vedere pe timp de noapte", pp. 162-163, pp. 165-166, Ed. Militara, Bucuresti, iunie 1999
4. R. G. Driggers and all "Long-range radiometer measurements with a close-range reference, Applied Optics, vol.32, no.30, pp. 6072-6076, 1993

Biostimulation effects of the low energy laser radiation on the yeast cell suspensions

Sorin Anghel^{*a}, Constantin Stănescu^a, Dana Giosanu^a, Ionica Neagu^b, Geta Săvulescu^c,
Ion Iorga-Simăn^a

^aDept. of Physics, University of Pitești, Romania

^bDept. of Biology, University of Pitești, Romania

^cWine-growing Research Station, Ștefănești-Argeș, Romania

ABSTRACT

This paper presents our work to determine the effects produced by low energy laser radiation on the metabolism and growth of a yeast (*Saccharomyces ellipsoideus*) cell suspension. As experimental material, we used young (18 – 24 hours) yeast culture in liquid medium, then distributed on a solid medium, to obtain isolated colonies. As laser source, we used a He-Ne laser ($\lambda = 632,8$ nm, $P = 6$ mW), and the irradiation was made with different exposure times. From each irradiated material, a sample of white grape sterile must was sowed, that has fermented at $18 \div 20$ °C for $10 \div 15$ days, after that some properties was tested (alcoholic generation power, volatile acidity, total acidity). Some microscopic studies were also made. The results prove some influence of low energy laser irradiation, which can induce mutations, with new properties of the irradiated material. These mutations can be obtained in a positive sense, with new and important perspectives in wine industry. Also, we observed an inhibitory effect of the laser radiation on the yeast cell growth, due, probably, to the too high values of the exposure.

Keywords: low energy laser (LEL), biostimulation, yeast cells, cell growth

1. INTRODUCTION

The low energy laser radiation (LEL) can produce on the biological systems various effects. More than 30 years ago, the unique known effect of the laser radiation was the thermal one, used, as a matter of fact, in different surgical applications. Since then, much other kind of effects, defined as non-thermal, i.e. non-concerning the temperature increase was observed in vitro, as well in vivo. While the interaction mechanism electromagnetic field - biological system is well known in the case of thermal effects, not the same is the case of non-thermal effects. For that reason, in the last years, the general tendency is to move the study from macroscopic level to microscopic one, and here the attention is guided to the cells and constitutive elements that can represent possible interaction sites¹. The study of the interaction between low energy laser radiation and living systems involves aspects of both physical and biological science that are less than perfectly understood.

The reported effects of low-energy laser irradiation are manifested in alterations in cellular and extracellular biochemical constituents and reactions, as well as in changes in cell division rates. These bioeffects were observed in both in vivo and in vitro experiments². In this context, we have made some experiments, concerning the action of a low-energy laser beam on the yeast cell suspensions, and the eventuality of the induced mutations. These mutations consist in some modifications concerning the DNA molecule distortion, which affects the fermentation properties of the yeast. The hypothesis of the explain these modifications is based on bioeffects as a function of the photoinduction of biochemical processes. This approach is not the only one, an alternative view to understanding the bioactivity of laser exposure being that such cells activity is an adaptive response to stress action. The adaptive reaction is characterized by a specific threshold in sense that the monochromatic laser radiation (stress action) becomes stimulus only if its energy exceeds a threshold value. That represents the minimum threshold, but also there is a maximum threshold; at higher values after that, the stimulus may not have any effect, or may have an opposite one, or the cell response is no more dependent to the stimulus intensity.

* Correspondence: Phone/fax 048-216448, e-mail: sanghel @ electra.upit.ro

2. MATERIAL AND METHODS

The must and wine micro-flora is very diverse, including a great number of bacteria and fungi, that determine the wine's qualities. Among the fungi, a remarkable importance has the *Saccharomyces cerevisiae* var. *ellipsoideus* and therefore we choose them to determine the mutagenic action of the visible laser light on it.

The material for irradiation was prepared as it follows:

- liquid culture medium - YEPG (yeast extract - 10 g/l, peptone - 10 g/l, glucose - 20 g/l, distilled water tile 1 l), sterilised 20 minutes at 1.5 atm.
- solid culture medium (yeast extract - 10 g/l, peptone - 10 g/l, glucose - 20 g/l, agar - 25 g/l, distilled water tile 1 l), sterilised 20 minutes at 1.5 atm.

The young yeast cell culture (18 ÷ 24 hours) in liquid medium was sowed on plates with solid medium, to obtain isolated colonies (temperature = 28 ÷ 30 °C). The irradiation have been made with a laser source, a He-Ne laser ($\lambda = 632,8$ nm, $P = 6$ mW), continuous wave, focused laser beam, at different exposure times. The first experiment stage consists in cell colonies exposure to the visible laser light from a laser source (He-Ne laser with $\lambda = 632,8$ nm, $P = 6$ mW), for different exposure times and the study of a range of properties of the irradiated cell colonies. The exposure time values for different samples are presented in Tab. 1.

Tab. 1 Exposure time of the first group samples

Sample	1	2	3	4	5	6	7	Control
Exposure time (minutes)	0.5	1	3	5	8	12	18	0

From each irradiated colony, a sample of white grape sterile must (minimum 250 g/l sugars refractometrically determined, 10 minutes boiling sterilised) was sowed, that has fermented at room temperature, 18 ÷ 20 °C, for 10 ÷ 15 days; after that some properties was tested (alcoholic generation power, total acidity, volatile acidity).

In the second stage, another set of colonies was irradiated at different doses (exposure times) and the growth-time dependence post-irradiation was studied. The exposure time values for the samples in this second stage of the experiment are presented in Tab. 2.

Tab. 2 Exposure time of the second group samples

Sample	1	2	3	4	5	6	Control
Exposure time (minutes)	2	5	8	12	18	25	0

From each irradiated colony, a sample was sowed in a liquid culture medium (YEPG). The samples was left at room temperature, 18÷20 °C, in closed test tubes, for the cell multiplication.

To measure the growth rate-time dependence, we have made the following considerations: the cellular growth rate is proportional to the yeast cell density in culture medium at that moment. If the extinction of the cell medium non-sowed is considered 0, the extinction of the culture medium in which was sowed a yeast strain, at a time t is $E(t)$. But, from Lambert-Beer law of the alternation of the light crossing a solution, $I = I_0 \cdot \exp(-\epsilon cz)$, where I_0 is the intensity of the incident light, I - intensity of the light at the depth z , ϵ - the extinction coefficient and c - the concentration of the absorbent in solution, one can note the ratio: $\tau = I/I_0$ as the transmission coefficient and $E = \ln(I_0/I) = \ln(1/\tau)$ is the extinction of the substance. It is obvious from the previous relation that extinction E is proportional to concentration c ; measuring the extinction at different times it is possible to follow the variation of the concentration, i.e. the variation of the number of yeast cell in colony.

We have measured the extinction-time dependence for every sample irradiated at different doses (after stirring for solution homogenisation), in order to point out the possible influence of the irradiation on the yeast cell culture growth. The determination of the extinction was made with a photocolorimeter SPECOL.

3. EXPERIMENTAL RESULTS

The first stage microscopic studies during the fermentation can be synthesised as follows:

- 1 day after the sowing of the irradiated and control colonies in 250 ÷ 300 ml white grape sterile must, the microscopic observation show spherical - oval cells, with normal aspect and dimensions; the 5th sample (8 minutes exposure) manifests a tendency for cell agglomeration; no morphological cell modifications was observed. At that time, a sample from every colony was selected for later fermentation, to see if the fermentative properties maintain in time.
- 2 days after the sowing: start of the fermentation.
- 4 days after the sowing: the 5th sample reveals a foam level approximately 2 times lower than the control sample.
- one week after the sowing: the morphologic observations revealed no significant cell modifications; the 3rd sample showed lightly greater cell dimensions and the 5th sample showed lightly smaller cell dimensions than the control; the foam level in the 5th sample remain approximately 2 times lower than the control sample.
- two weeks after the sowing: in the 5th sample the wine clear up starts; after one day, follows the 4th sample and after another day, the 3rd sample; for all samples, the yeast fall out is compact for all samples; none of them formed a film.

After two weeks fermentation, some properties was tested (alcoholic generation power, total acidity, volatile acidity). The results are presented below:

Tab. 3 Properties of the irradiated samples after two weeks fermentation

Sample	1	2	3	4	5	6	7	Control
Exposure time (minutes)	0.5	1	3	5	8	12	18	0
Alcohol (% vol.)	16.4	16.3	16.4	16.3	16.4	16.3	16.4	16.2
Volatile acidity pH	0.76	0.8	0.8	0.8	0.8	0.8	0.8	0.76
Total acidity pH	6.2	6.2	6.2	6.2	6.2	6.2	6.2	6.2

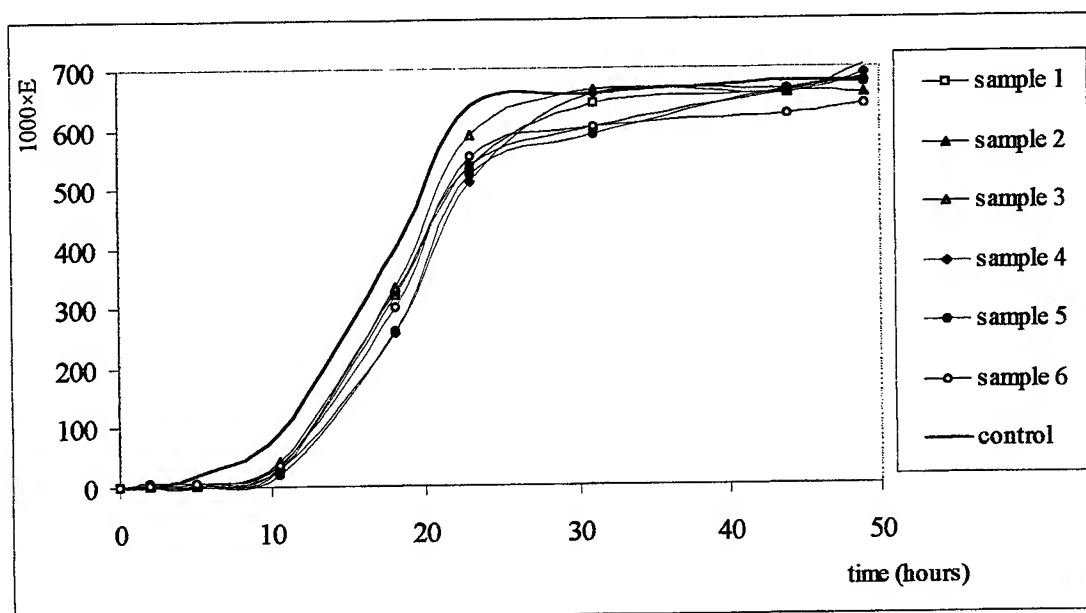
After some time (6 months at least), we will test the maintenance or change in time of these properties. Also, a determination of the presence or the modification of the "killer" or sensible character of the strains will be made.

In the second stage, the results of the extinction measurements at different times are presented in Tab. 3. The table contains the values of the relative extinction of the solution samples (multiplied by 10³) at different times. The culture solution extinction is related to the extinction of the non-sawed culture liquid medium (YEPG).

Tab. 4 Extinction values of the solutions during the growth period

Sample		time (h)								
		0	2	5	10,5	18	23	31	44	49
1	E X T I N C T I O N × (10 ³)	0	0	0	28	319	535	640	660	703
2		0	4	8	41	328	538	602	658	658
3		0	4	4	32	333	588	664	664	685
4		0	8	8	28	258	510	656	656	690
5		0	5	5	19	263	525	589	665	675
6		0	4	8	36	301	553	602	620	638
Control		0	0	18	92	398	638	658	678	678

The results are plotted in Fig. 1. After a short latency period, the extinction of the solution (i.e. the yeast cell concentration) shows an initial exponential increase, followed by a saturation of the concentration, after 20 ÷ 30 hours, due to the fact that the nutritive substance in the solution is exhausted. After about 50 hours, the extinction decreases slowly. All the samples were maintained in the same conditions, therefore the influence of the temperature on the growth rate is out of the question.



4. CONCLUSIONS

The study of the interaction between laser radiation and the human body involves many physical and biological aspects. On one hand, it was demonstrated that there is a "threshold stimulus", in sense that the laser radiation becomes stimulus only if its energy exceeds a threshold value. On the other hand, all observed biological effects of this laser radiation action originate from the changes in cellular membrane potentials, resulting from changes in membrane permeability and microviscosity. These changes are caused by the action of the excitation that provoke charge separations, which generate concentration gradients and potential gradients⁸.

Also, the electromagnetic-induced biological effects may be characterised as adaptive or compensatory. The electromagnetic action determine an integrative response: after the electromagnetic wave detection, information is communicated to the central nervous system which then activates the physiological mechanisms to determine a compensatory response.

The results of our experiments indicate primarily the existence of certain parameters of light beam for biostimulation effects; the most important is the time exposure for a constant intensity, i.e. the dose exposure. Considering the laser beam cross-section equal to 1 mm², the intensity of the beam is about 0.6 W/cm². For exposure times in 1 ÷ 25 min. range, the energetic exposure dose (specific energy fluence) is 30 ÷ 700 mJ/cm², which corresponds to the photochemical interaction domain³. From the microscopic observations for the first stage, we can see some important facts, all regarding the 5th sample:

- 1 day after the sowing of the irradiated and control colonies the 5th sample (8 minutes exposure) manifests a tendency for cell agglomeration;
- 4 days after, the 5th sample reveals a foam level approximately 2 times lower than the control.

- one week after, the 5th sample showed lightly smaller cell dimensions than the control; the foam level in the 5th sample remain approximately 2 times lower than the control.
- two weeks after the sowing: in the 5th sample the wine clear up starts;

All of that show an important modification of the fermentation properties for the 5th sample, modifications that are in the positive sense (especially the reduced foam level and the earlier clear up time). These are sustained by the results in alcohol and acidity determinations. A rise from 16,2 % alcohol in control sample to an average of 16,4 % for the most of the irradiated samples is significant and with an important perspective for wine industry, if these results can conduce to mating types with better fermentation characteristics.

From the second stage determinations, we can emphasise the fact that it is an evident action of the laser light on the yeast cell culture. Comparing the evolution of the cell number in all irradiated samples with the control sample (non-irradiated), we can see that the irradiation have an inhibitor effect on the yeast cell growth (it is a retardation in the mitotic process).

That light-induced inhibition of biological activity may be explain by the existence of two competing processes: the formation by photosensitization of reactive oxygen species, which stimulate the redox activity of the respiratory chain, and, on the other hand, the intramolecular electronic-vibrational energy transfer from an endogenous photosensitizer to an enzyme of the respiratory chain, thereby bringing this enzyme into an inactive configuration and paralysing the respiratory chain⁵. The second process must be more intense, having as result the inhibition of the growth.

However, we could not determine a quantitative relationship between the exposure dose and the retardation time. It is necessary to make some new experiments in order to find that relationship. In fact, this experiment will continue and will be repeated in various conditions, to confirm the mutagenic action of laser beam and to obtain a strain with new, good and stable fermentation properties. Another kind of laser (diode laser) also will be used, the type of laser source, even at comparable wavelengths, could be an important factor⁶.

The fact that the previous discussed result is a result of the enhancement of the proliferation of the cells may be due to the exposure time and power density values, which determine the effects of the laser irradiation. Both stimulation and inhibition of the cell properties can be obtained with the same laser on the same cells⁷.

We can, also conclude, while the exposure dose was similar in the first and second stage experiments and the other conditions (preparation, maintaining) was the same, that one cannot establish a relationship between the influence of the laser radiation on the multiplication process (cell growth) on the one hand and mutagenic effects of the laser radiation and some properties modifications on the other hand. This conclusion is due to the fact that, in same exposure conditions, the fermentation properties was enhanced, while the cell growth was inhibited.

Finally, we think that the existence of the minimum and maximum threshold is proved in our experiment by the fact that, in the first stage of experiment, only the samples irradiated at the exposure time about 8 min. have presented properties modifications.

ACKNOWLEDGEMENTS

The authors thank Prof. Dr. Ioan Moisa for his valuable remarks and suggestions on this paper. This work was possible with the help of Wine-growing Research Station, Stefanesti-Arges, Romania.

REFERENCES

1. F. Franck, "Laser light and tissue. Biophysical aspects of medical laser application", *SPIE Proceedings – Lasers and Medicine*, **1353**, pp. 37-45, 1989
2. T. I. Karu, "Biophysical basis of low-power laser effects", *SPIE Proceedings – Lasers Chemistry, Biophysics, and Medicine*, V.N. Zadkov (editor), **2802**, pp. 142-151, 1996
3. G.J. Müller, K. Dörschel and B. Schaldach, "Main Problems and New Results on Dosimetry in Laser Medicine", *SPIE Proceedings – Lasers and Medicine*, **1353**, pp. 2-10, 1989

4. T. I. Karu and O. Tiphlova, "Regulation of cellular metabolism with low-intensity monochromic visible light", *SPIE Proceedings*, **1353**, pp. 68-78, 1989.
5. H. Friedmann and R. Lubart, "Competition between activating and inhibitory processes in photobiology", *SPIE Proceedings – Effects of Low-Power Light on Biological Systems*, Tiina I. Karu, Antony R. Young, **2630**, pp. 60-64, 1996.
6. Adelina Grigorovici, Sanda-Ilinca Despa and Teodor-Gabriel Paunescu, "Laser effects on yeast cell suspensions", *SPIE Proceedings – ROMOPTO '94*, V.I. Vlad, D.C. Dumitras (editors), **2461**, pp. 411-413, 1995.
7. H.H. van Breugel and R.P. Bar, "Power density and exposure time of the He-Ne laser irradiation are more important than total energy dose in photo-biostimulation of human fibroblasts in vitro", *Lasers in Surgery & Medicine*, **12**, pp. 528-37, 1992.
8. Greguss P., "Biostimulation of tissue by laser irradiation" *SPIE Proceedings, Lasers and Medicine*, **1353**, pp. 79-91, 1989.
9. N. Ben-Dov N et al., "Low energy laser irradiation affects satellite cell proliferation and differentiation in vitro", *Biochimica et Biophysica Acta*, **1448**, pp. 372-380, 1999.
10. T. Karu, L. Pyatibrat and G. Kalendo, "Irradiation with He-Ne laser increases ATP level in cells cultivated in vitro", *Journal of Photochemistry & Photobiology. B Biology*, **27**, pp. 219-223, 1995.
11. I.L. Daniels and T.I. Quickenden, "Does low-intensity He-Ne laser radiation produce a photobiological growth response in *Escherichia coli*?" *Photochemistry & Photobiology*, **60**, pp. 481-5, 1994.
12. T. Karu, O. Tiphlova, R. Esenaliev and V. Letkhov, "Two different mechanisms of low-intensity laser photobiological effects on *Escherichia coli*", *Journal of Photochemistry & Photobiology. B – Biology*, **24**, pp. 155-161, 1994.
13. T. Karu, L.V. Piatibrat and G.S. Kalendo, "The effect of the He-Ne laser radiation on the adhesive properties of the cell membrane", *Biulleten Eksperimentalnoi Biologii i Meditsiny*, **115**, pp. 622-3, 1993.
14. H.H. van Breugel and P.R. Bar, "He-Ne laser irradiation affects proliferation of cultured rat Schwann cells in a dose-dependent manner", *Journal of Neurocytology*, **22**, pp. 185-90, 1993.

Design consideration and performance of digital lock-in amplifier with 68HC11 microcontroller

Ioan Burda*, Simion Simon, Mihai Todica, Gheorghe Cristea,
Georgeta Cerbanic, Lavinia Cociu

"Babes-Bolyai" University, Department of Physics, 3400 Cluj-Napoca, Romania

ABSTRACT

The lock-in amplifier technique is frequently used in characterization of optoelectronic devices. A digital lock-in amplifier and a digital direct synthesis signal generator are implemented with a general purpose 68HC11E1FN microcontroller. The resolution in frequency is less than 1 Hz. The digital lock-in amplifier operates over a frequency range from 1 Hz to 1 kHz and can measure signal at any harmonic of the reference signal. Typical error is less than 0.5% for the range of frequencies reported. This digital lock-in technique is inexpensive and can be used in experiments with low frequency response.

Keywords: Digital lock-in amplifier, Optoelectronic devices, Digital direct synthesis, Microcontroller

1. INTRODUCTION

Many kinds of analyses are performed on complex periodic signals to extract a particular component from the composite signal. This is easily done by lock-in amplification providing the frequency of the component of interest is synchronous with that of the phase-locked loop's reference. The digital lock-in amplifier technique can be used to study of semiconductor materials or optoelectronic devices.

In an analog lock-in amplifier, the signal of interest is mixed both in-and out-of-phase with a reference and fed through low-pass filters. In this manner, an analog lock-in amplifier can measure both the amplitude and phase of the signal while effectively filtering out broadband noise. In a digital lock-in, both the signal and reference are digitized at a rate much greater than the reference frequency and then transferred to the computer. The computer then performs the Fourier analysis to measure the amplitude of both and the relative phase shift between them. This technique is called digital lock-in analysis because it performs the same measurement as an analog lock-in amplifier, although in a somewhat different fashion.

The recent advances in the capabilities of high-resolution analog to digital converter and data processing with dedicated microcontrollers have allowed us to develop digital lock-in techniques that surpass the capabilities of analog lock-in amplifiers.

The term dual-channel refers to the number of digitizer channels used in the measurement. Dual-channels digital lock-in digitize the signal and reference in parallel using two separate channels.

The published versions fall into distinct categories¹. First, there are the hardware-based versions that are capable of measuring signals up to fairly high frequencies but require the construction of specific electronics. Second, then are the software-based versions but operating only at low frequencies.

2. PRINCIPLE OF OPERATION

The objective of the measurements is to obtain both the magnitude of the signal and its phase relative to the given reference signal. The arithmetic sum of products that defines the response of linear, time invariant networks, can be expressed as

* Correspondence: E-mail: iburda@phys.ubbcluj.ro; Telephone: +40 064 191315; Fax: +40 064 191906

$$y(n) = \sum_{k=1}^K A_k x_k(n) \quad (1)$$

where; $y(n)$ is response of network at time n , $x_k(n)$ is k th input variable, and A_k is weighting factor of k th input variable that is constant for all n , and so it remains time-invariant.

In filtering applications the constant, A_k , are the filter coefficients and variables, x_k , are the prior sample of a single data source (for example, an analog to digital converter). In frequency transforming (whether the discrete Fourier or the fast Fourier transform) the constants are the sine/cosine basis functions and the variables are a block of samples from a single data source. Example of multiple data source may be found in image processing. The multiply intensive nature of equation 1 can be appreciated by observing that a single output response requires the accumulation of K products terms.

The block diagram of the lock-in amplifier and a typically application is shown in Fig. 1. The signal response and the reference signal are fed into the channels of an analog to digital converter, where they are synchronously sampled and stored at the measurement frequency f_m . The number of samples for each channel is denoted by N . The signal period is $T = 1/f$, and $\tau = 1/f_m$ is the measurement interval. To resolve signals at frequency f_r , it is necessary to sample the signals at least as fast, i.e., $f_m > 2 f_r$.

$$N\tau = qT, \quad q = \text{integer}, \quad (2)$$

The signals are acquired over an integer number of signal periods. This condition is met if where q is the number of signals periods contained in the N points sample. Equation (1) can be rewritten as It is important to note that since both N and q are integers, the ratio f_m / f_r is a ratio of integers. In the others words, the

$$f_m / f_r = N / q. \quad (3)$$

measurement frequency is commensurate with the signal's frequency.

The signal and reference vectors take the general form

$$\text{Sig}(k) = S_x \cos(2\pi qk / N) + S_y \sin(2\pi qk / N), \quad k = 1, 2, 3, \dots, N, \quad (4)$$

$$\text{Ref}(k) = R_x \cos(2\pi qk / N) + R_y \sin(2\pi qk / N), \quad k = 1, 2, 3, \dots, N. \quad (5)$$

Once the digitizer obtains the data, it is transferred to the computer where the analysis commences. We want to determine S_x , S_y , R_x , and R_y ; if we know these four quantities, then we can determine the amplitudes of the signal and reference and the relative phase shift between them. The program that analyzes the data has previously generated and stored internal sine and cosine vectors using same values of N and q

$$\hat{c}(k) = \cos(2\pi qk / N), \quad k = 1, 2, 3, \dots, N, \quad (6)$$

$$\hat{s}(k) = \sin(2\pi qk / N), \quad k = 1, 2, 3, \dots, N. \quad (7)$$

To obtain S_x , we calculate the normalized dot product of the signal and the cosine vector

$$S_x = 2 / N \sum_{k=1}^N \text{Sig}(k) \times \hat{c}(k). \quad (8)$$

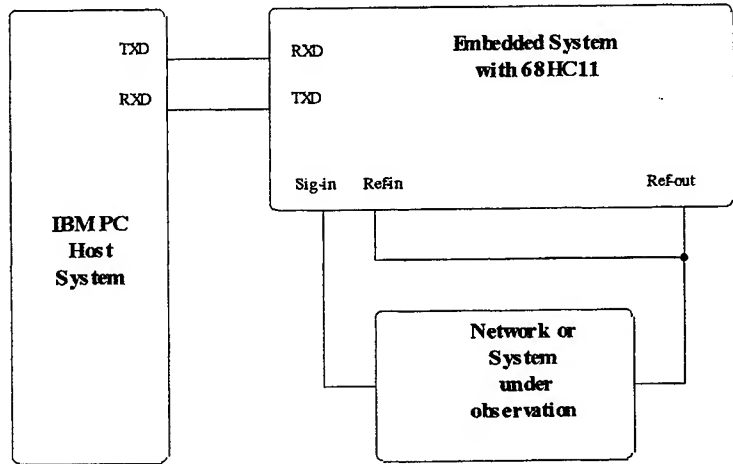


Fig. 1 The block diagram of the digital lock-in amplifier

This expression can be demonstrated if we use the orthogonality relationships³. We obtain by performing the same sum with $Ref(k)$; S_y and R_y are obtained using equation 7 in an equation with close form of the equation 8. The magnitudes of the signal and reference can be obtained using

The relative phase shift of the signal with respect to the references is

It is important when calculating the relative phase shift the arctangent will be defined within the same half-plane. This technique is capable of measuring signals at any harmonic of the reference signals. The generalization of the measurement for harmonic analysis requires only a few modifications. If information is required for more than a few signal frequencies, it is faster to use a fast Fourier transform routine to calculate the signal components.

With a general purpose 68HC11 microcontroller² the signal generator and data acquisition for digital quadrature lock-in detection are implemented.

Fig. 2 The circuit diagram of the embedded system.

3.2. Software

Phase-sensitive detection is a well-known and widely used technique. Digital lock-in amplifiers, first proposed by Cova³, are very stable because of the digital nature of design. The instrument, in fact, measures the correlation between the two signals. In a digital lock-in amplifier, both the signal and the reference are digitized at a rate much higher than the reference frequency and then transferred to the computer.

Very important for this application is the output-compare function (TIMER) which is used for the generated PWM signal with duty cycle specified in a buffer memory (maximal 8192 bites, sine wave). Any waveforms can be obtained with this technique (DDS-Direct Digital Synthesizer)⁴.

The acquisition data and control of PCFRS is performed by the embedded system. The time critical task showed in Table 1, performed by the embedded system generates the PWM signal (Ref-out), reads the value of the signal response of the semiconductor sample (Sig-in), reads the value of the reference signal (Ref-in) and stores these data in two internal memory buffers.

The PWM signal (OC1 and OC2 is used together to produce one PWM output) with period of 128 μ s and resolution of 500ns is generated with a duty cycle specified ($128/0.5 = 256$ which is the resolution for duty cycle of 0 to 100 percent) in a buffer memory. This task only produces duty cycles of 50 to 100 percent.

When a smaller duty cycle is specified, it is automatically changed to 100 percent minus the specified duty cycle, and the polarity of the output is switched. To perform all these functions, only 128 μ s is available; the real performance of the task is 116 μ s. An auxiliary square wave signal is available at the PA4/OC4/OC1 pin for testing, or eventually, for external chopper synchronization. The maximal resolution in frequency in this configuration is less than 1 Hz and can be customized over a large range.

The maximum measurement points are 8192 (N) and the same number is available for the PWM buffer memory (limited by RAM memory of the embedded system, 24 K-byte all buffers). The particular situations are important in practice; if the resolution in frequency must be equal to 1 Hz (0.999936 Hz), 7812 measurement points

```
*****
* PRODUCES HIGH OR LOW GOING PWM SIGNALS, READ SIGNAL *
* AND REFERENCE VIA A/D CONVERTER IN BUFFERS *
*****

...
data initialization
...
CLI
NVERST LDY PIVOT [6] TEST END ACQUISITION
CPY ENDBUFF [7] (NREG) X 3 + BOTBUFF
BNE NVERST [3]
LDY #BOTBUFF [3]
STY PIVOT [5]
BRA NVERST FOR EVER
* SVOC1 - OUTPUT COMPARE 1 SERVICE ROUTINE, >> 128 uS
* 16 cycles for flight at SVOC1 service
SVOC1 LDX #REGBAS [3]
LDD TOC1,X [5] CURENT PWM % INITIALIZE
ADDD PROCNOU [6] 128 < PROCNOU < 255
STD TOC2,X [5] TIME FOR % PART
* max. 64uS - (19 + 16) x .5 = 17.5 uS
LDD TOC1,X [5] NEXT PULSE
ADDD PWMPER [6] FOR 128 uS, PWMPER = 00FF
STD TOC1,X [5] TIME FOR NEXT PULSE
LDAA ADR1,X [4] READ CURENT VALUE
LDY PIVOT [6]
INY [4]
STAA ,Y [5] WRITE SIGNAL DATA
LDAA ADR2,X [4]
INY [4]
STAA ,Y [5] WRITE REFERENCE DATA
INY [4] PERFORM NEXT PWM
STY PIVOT [6]
LDAB OC1D,X [2] IF < or > 50% next pulse
ANDB #%00010000
LDAA ,Y [5]
CMPA #$80 [2]
BLS ARNZOC [3] jump for < 50%
ADDB #%01000000 [2]
ARNZOC EORB #%00010000
STAB OC1D,X [4] H/L or L/H ok
CMPA #$80 [2]
BHI NUSCAD [3]
TAB [2]
LDAA #$FF [2]
SBA [2]
NUSCAD TAB [2]
CLRA [2]
STD PROCNOU [5]
BCLR TFLG1,X $7F [7]
RTI [12]
* 24 + (115 x .5) = 57.5 + 17.5 = 75 uS
* End SVOC1 routine
```

Table 1 TT

(1s/128 μ s = 7812.5) are

necessary. In this situation, the PWM signal with frequency equal to 1 Hz is composed of 7812 samples ($q = 1$). For a PWM signal with frequency equal to 1 kHz for each signal period ~ 8 samples are used ($q = 1000$); in other words, in the wrong case $f_m \approx 8 f_s$. If the frequency resolution can be 10 Hz (10.0096 Hz) only, 782 points of measurement are necessary. In this particular case the measurement is very fast. The host system performs the next sequence: initialize the number of point measurements (N), perform and transfer duty cycles for the sine wave to the PWM buffer memory of the embedded system and command the acquisition task. After loading all the data, these are performed in accordance with Fourier analysis⁴.

4. NOISE ANALYSES

The digital lock-in responds to noise can be appreciated in approximation of the signal at a frequency different than the chosen signal frequency⁷, f_s . The effective white noise bandwidth of the measurements is $\sim f_s/q$; this is the inverse of the total sampling time. It is important to note that the in-phase and quadrature response have zeros at the frequencies

$$f_n = f_s (1 \pm p/q), \quad p = 1, 2, 3, \dots \quad (11)$$

The discrete nature of the sampling in a digital lock-in introduces another possible source of noise; aliasing. The aliasing noise⁷ components will appear to be at a frequency

$$f = |f_n - j f_m|, \quad j = 1, 2, 3, \dots, \quad (12)$$

where f_n is the actual noise frequency and j refers to the closed harmonic of the sampling frequency. The standard way to deal with this problem is to pass the signal through a low-pass filter at or below $f_m/2$ before digitizing to attenuate the aliasing components.

The real noise of digital lock-in amplifier presented in this paper can be evaluated for signal response at amplitude and phase shift of the signal by deconvolution⁵. In Fig. 3 is plot the response of the digital lock-in amplifier at a complex signal. The signal response at amplitude (fig. 3(B)), all amplitude noise of the experiment (fig. 3 (C)) and in Fig. 3 (D) is shown the amplitude noise of the digital lock-in amplifier extracted by the experimental noise.

The phase shift noise of the digital lock-in amplifier is shown in Fig. 3(G). The same experimental condition with amplitude measurement is ensuring for this evaluation. Of course the low resolution of analog to digital converter (8 bits) is the basic source of the noise in this application. In other hand the very good stability and flexibility of the digital lock-in amplifier may be an important point of view.

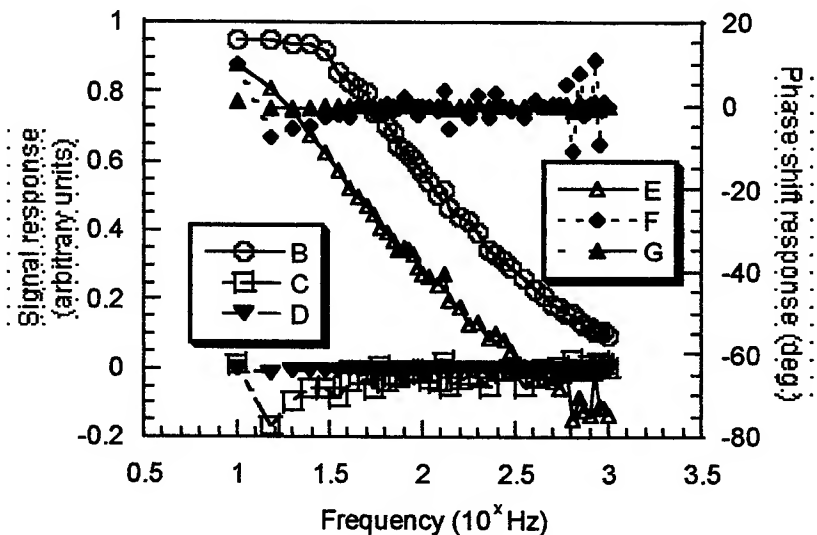


Fig. 3 The signal response (B), all noise of signal (C) and the signal noise of digital lock-in (D); the phase-shift response (E) all phase-shift noise F) and phase shift noise of the digital lock-in (G).

5. CONCLUSIONS

A digital lock-in amplifier and a digital direct synthesis signal generator are implemented with a general propose 68HC11E1FN microcontroller. The resolution in frequency is less than 1 Hz. The digital lock-in amplifier operates over a frequency range from 1 Hz to 1 kHz and can measure signal at any harmonic of the reference signal. Typical error is less

than 0.5 percent for the range of frequencies reported. This performance is possible though the mode of synchronization between the signal generator and the measurement and is limited by the 8-bit resolution of the ADC subsystem. Typical error is less than 0.5% for the range of frequencies reported. The low resolution of analog to digital converter is the basic source of the noise in this application. The very good stability and flexibility of the digital lock-in amplifier may be an important point of view. This digital lock-in technique is inexpensive and can be used in experiments with low frequency response.

ACKNOWLEDGMENTS

It is a pleasure to acknowledge to Motorola literature center for documentation and software support. This material is based upon work supported by the CNCSU under grant No. CNCSIS - 212.

REFERENCES

1. L.G. Rubin, *Sci. Instrum.* **59**, pp. 514, 1988.
2. M68HC11RM/AD, *Reference Manual*, Motorola INC., Rev.3, 1991.
3. S. Cova, A. Longoni and I. Freitas, *Sci. Instrum.* **50**, p. 296, 1979.
4. Rohde Ulrich, *Digital Frequency Synthesizers, Theory and Design*, Pentice-Hall, 1983.
5. D. Goldfarb, and A. Idnani, "A numerically stable dual method for solving quadratic programming," *Math. Programming*, **27**, pp. 1-33, 1983.
6. Dream Machine, *Application Reference Book*, Philips Semiconductor 8-11, 1996.
7. E.G. Woschni, "Minimising aliasing error of sensor with digital output," *J.Phys.Instrum.* **20**, pp. 119-124, 1987.

The environmental diagnosis and supervision mobile system for emergency cases

Maftai Rosca^a, Stefan Geanta^a, Gheorghe Manoliu^{*a}, Octavian Logofatu^b

^aCivil Protection Command, 19 Ceasornicului Street, Sector 1, Bucharest, Romania

^bArsenalul Armatei, 5B Timisoara Blvd., Sector 6, Bucharest, Romania

ABSTRACT

“The environmental diagnosis and supervision mobile system for emergency cases” it’s a flexible system which support the decision and the management of the risks. To optimise the time reaction, in case of emergency, is synonymous to save the maximum possible lives. The decision in such a case must be strongly supported by a wide information pictures, information needed in a command center both for the acting operators and civilian people. The system described bellow try to clarify the general architecture necessary to be adopted in order to respond at a such a need. The authors inform with this occasion that this architecture it is a very flexible one and could be configured upon request.

Keywords: environmental diagnosis and supervision, mobile system, emergency cases, flexible system, decision, risk management, , acting operators, civilian people, flexible architecture,.

1. INTRODUCTION

In the last decade, vast region from different places in the world were damaged by natural catastrophic phenomena such as earthquake, hurricanes, floods, etc.; along the time, Romania was hitted several times by natural disasters, doubled in couple of cases by important damages and great loss of people life.

Scientifically community in the whole world make some efforts to support the realisation of the prediction for a such a kind of phenomena and for perfecting technical abilities and the social background, so that a prepared society could be able to face off the consequence of some disastrous experiences.

To optimise the time reaction in the case of emergency it is necessary to assist the decision, who is imperative to be receipted and processed in real time for all the volume of different information, communications and data transmissions from and/or to decision center, data which are essential elements for the modern management of emergency and risks.

“The environmental diagnosis and supervision mobile system for emergency cases“ is conceived to be an optimised and in “live” reaction time transmission system in case of emergency for difficult access and very dangerous zones.

2. THE SYSTEM

The system is disposed on a small vehicle (a mobile command platform¹) which can rich, in principle, any dangerous or damaged zone; the vehicle can be self-propelled or a wheeled one.

The crew is composed by:

- a driver;
- a main operator which operate the robot;
- an assistant.

The platform is equipped with:

- a radio station for data and voice transmission;
- a command desk with one or more monitors for environmental and robot surveillance;
- a remote control for commanding the robot;

*Correspondence: Email: dragosp@ro.pims.org; Telephone: 00 40(1) 400 39 26; Fax: 00 40(1) 232 20 08

- different tools with several destinations;
- the robot himself.

The platform could be equipped with LIDAR unit (LIght Detecting And Ranging) based on the well known laser radiation good characteristics:

- divergence;
- monochromaticity;
- coherence;
- higher intensity.

Laser radiation characteristics recommend the laser beam as an ideal source of radiation in LIDAR systems for the detection of the distance.

LIDAR unit suppose a laser transmitter for distance detection. IR radiation emitted or absorbed, diffused or reflected by toxic substance molecules could be detected and analysed using proper detectors (e.g.: for explosive substance are used optical IR detectors).

3. THE ROBOT

The robot has 2 video transmitting channels in VIS/IR working on day/night time; the robot can penetrate calamitated and/or polluted areas, taking pictures of the access place or making panorama of the area.

The robot can also make some meteorological, chemical and radioactivity (radiometry) analyses.

If the decision to take need more information such as those who can result after a more detailed analyse, the robot could take some samples (gaseous, liquid or solid) to be later analysed.

Optional, the robot could be also equipped with a LIDAR unit, but the presence of a such unit on the vector (robot) lead to a more complicated robot and, for sure, at a very high price; the LIDAR unit lead also to a greater robot which it is not suitable.

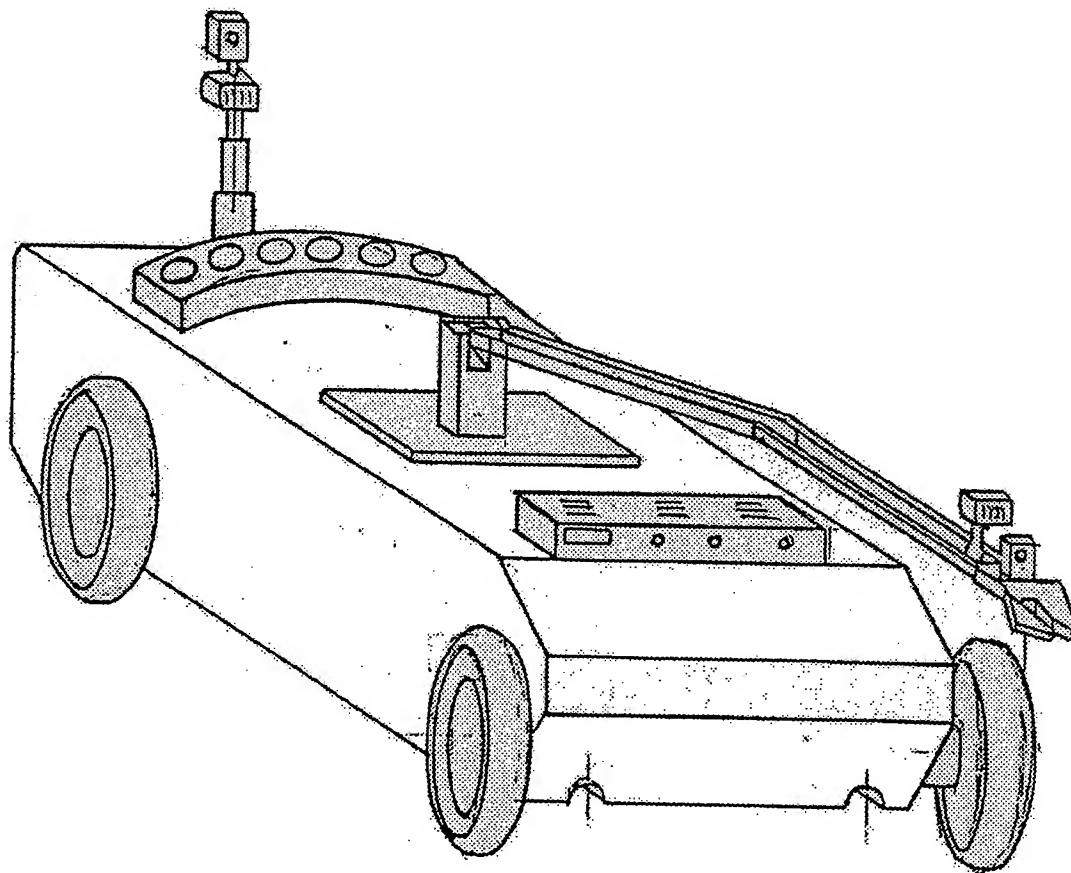
Infrared radiation emitted or absorbed, diffused or reflected by toxic substance molecules generated as a result of a calamity and/or an accident could be a very good support (working agent) for the quantitative and/or qualitative determinations (measurements) by the means of the own detectors.

- 1st figure show us the robot's general organisation with its main components in general view:
 - a) the vector itself, which has the possibility to move on the ground and in water too, has the following subassemblies:
 - the chassis;
 - ground propulsion system;
 - water propulsion system;
 - power supply;
 - central process unit (CPU).
 - b) the arm has the possibility to move in gyration $\pm 90^\circ$ and in elevation between -10° to $+80^\circ$ (as shown in Fig.2).
 - c) the sensor battery consist of:
 - chemical unit (one of the sensors is shown in Fig. 3; a such a cell can measure both values – absolute or relative – as is necessary);
 - meteorological unit (such a unit will deliver all the essential parameters of the local atmosphere: humidity, pressure, temperature, speed and wind direction);
 - radiometric unit (consist of cell battery measurement for α , β , and γ radiation);
 - video unit.
 - d) tank samples:
 - e) command and data transmission unit.

The chemical and radiometric units could give all the absolute level of the checked parameter or the moment when a concentration threshold a value; to fit the robot with a type or another of this sensors it is a matter of philosophy and price, and do not implies major differences in the structure of the control process unit.

- Just to have an idea of the size of the robot it can be specified:
 - length-----830 mm;
 - width -----820 mm;
 - height-----600 mm;
 - clearance-----upon request; typical 100 mm;
 - weight-----approx. 60 kg.
- To complete the upper idea, down are presented few of the performances and characteristics of the robot:
 - speed (ground // water)-----0-6 km/h // 0-3 km/h;
 - maximum inclination-----35°;
 - gyration radius-----> 610 mm;
 - operational range-----approx. 200 m;
 - working diagram for the mobile arm-----see fig. 2;
 - maximum weight lifted up by the arm-----1 kg;
 - power supply (battery)-----24 V;
 - sensors number-----3-6.

Fig.1 General view of the robot



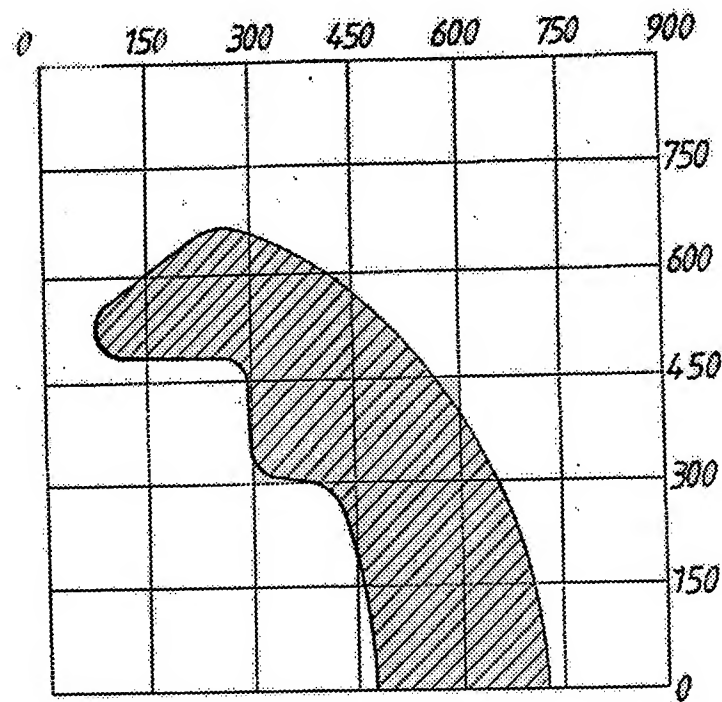


Fig.2 Working diagram for the mobile arm.

The robot could move in open or closed area, on arrange or disarrange territory, and also in water. It could attack consistent obstacles due to the clearance, ampathament and ecartment².

The work arm could lift up samples or it could mark the interest area.

Used video cameras are sensible on visible/infrared radiation spectra during the day - night time operation and will be located as follows:

- one to the end of the mobile arm;
- one on the robot.

Each camera has its own illuminate installation.

Weather, chemical and radioactivity units has miniature sensors without moving parts. Chemical unit has in it own composition optic infrared sensors which measures the gas concentration of the environmental atmosphere. (see 3rd figure).

Measurement results are memorised by the robot board or are transmitted to the command base.

The robot is control remotod from the command desk through a coaxial cable of approx. 200 m; from the command-desk we could transmit maximum 32 command km/h with 3 Hz. On the same cable, opposite of direction (from the robot to the command-desk) is transmitted the audio-video signal take-it over by one of the two video camera.

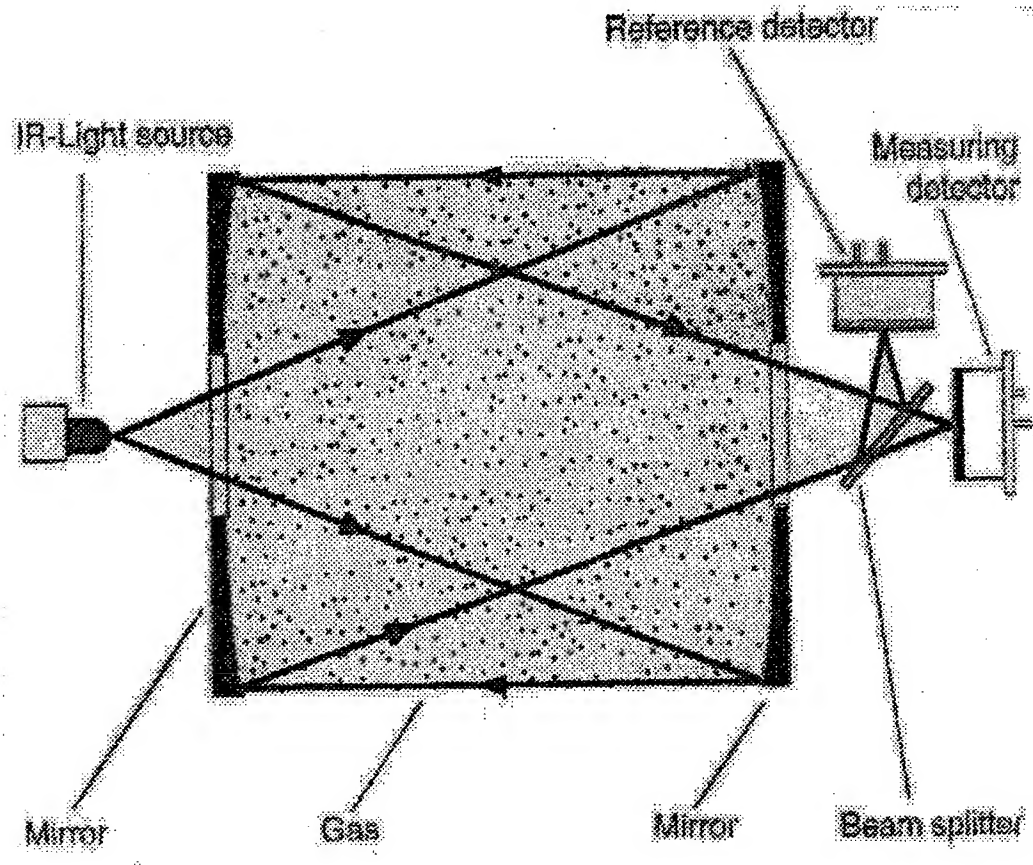


Fig.3 Gas concentration measurement principle

The cable link in another configuration could be made by the means of a fibre-optic cable; that solution has the advantage of the increasing transmitting speed of data and decreasing weight of the coil for the same length or, a much more length for the same weight.

The architectural structure of the robot is conceived to be a modular one; this modularity could give the possibility, in function of the moment need, to use a dedicated measurement module, for example, which not made part from the base structure.

Otherwise, if in a mission, when appears the necessity to take two times much more samples as in the basically structure, the operator has the possibility to remove, let's saying, the radiometric module with an additional sample module knowing the fact that in the working area it's no danger for radiation contamination.

By the means of video-mixing pictures delivered by the two cameras it is possible to work on a fixed point with the arm of the robot and having, in the same time, a panorama of the area with the other camera.

4th figure present the general robot organisation:

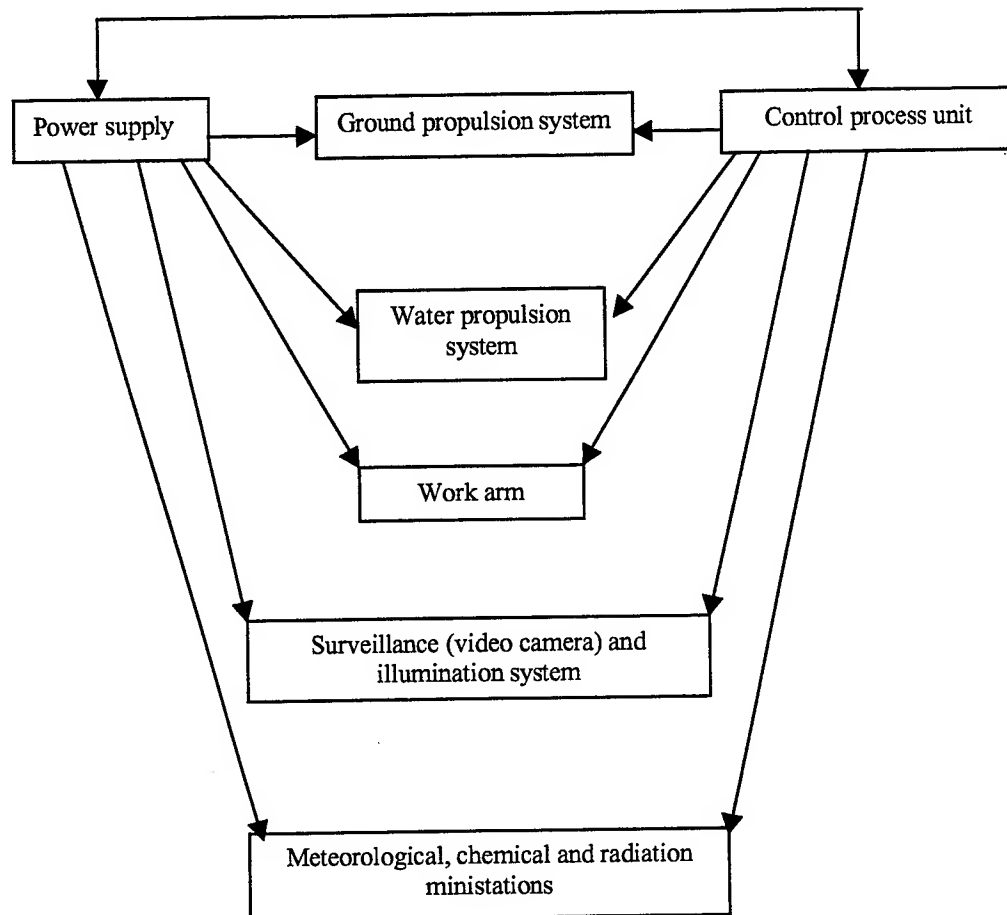


Fig.4 General robot organisation

4. CONCLUSION

“The environmental diagnosis and supervision mobile system for emergency cases” is conceived to be an optimised and in “live” reaction time transmission system in case of emergency for difficult access and very dangerous zones.

REFERENCES

1. Liegeois, L. Fagegaltierg, *Terrain-Tolerant Motion Planning of Wheeled Robotic Vehicles*, Milan catalogue, 1995.
2. Cox Wilfong, *Autonomous Robot Vehicles*, Springer verlag, New York, 1990.

Low power radio frequency capacitively coupled plasma in air An alternative spectral source ?

Sorin - Dan Anghel^{*a}, Alpar Simon^a, Tiberiu Frentiu^b, Emil A. Cordos^b

^aDept. of Physics, Babes-Bolyai University, M. Kogalniceanu 1, 3400 Cluj, ROMANIA

^bDept. of Chemistry, Babes-Bolyai University, Arany J. 11, 3400 Cluj, ROMANIA

ABSTRACT

The low power radio frequency capacitively coupled plasma sustained in air at atmospheric pressure is described with the aim of using it as spectral source for atomic emission spectroscopy of pneumatically nebulised liquid samples and the direct analysis of non-conductive solid samples. The plasma was generated at a frequency of 13.56 MHz, absorbed RF powers of 20-70 W and air flow rates of 0.1-1 l/min, being intrinsic part of the resonant circuit of a free-running oscillator. The liquid samples were pneumatically nebulized using a Meinhard nebulizer and introduced into the plasma via a 4-roller peristaltic pump. The rotational temperature and the intensity ratio of ion to atom lines for Ca were determined experimentally. Detection limits were determined using the "3 σ method" given by Boumans for 11 elements (Ag, Ca, Cr, Cu, Mg, Mn, Na, Li, Ba, Pb, Sr) at an RF power of 50 W and air flow-rate of 0.7 l/min. The same plasma was used for the direct analysis of non-conductive solid samples. All measurements have been carried out on cylindrical sample pellets of chalk, pressed in a steel press at a pressure of $87 \cdot 10^5$ Pa, at an RF power of 40 W and air flow-rate of 0.5 l/min.

Keywords: capacitively coupled plasma, spectral source, atomic emission spectroscopy, RF sputtering

1. INTRODUCTION

Over the last few decades, plasma excitation sources at atmospheric pressure for analytical atomic emission spectrometry (AES) have been well characterized as sensitive spectral sources. Most of these sources are inductively coupled plasmas (ICPs). The radiofrequency (RF) capacitively coupled plasma (CCP) as physical phenomenon, was studied before ICPs.

The principle of capacitive coupling to generate a plasma has been known since late 1920s. In 1941, Cristescu and Grigorovici¹ reported that an RF CCP could be obtained at atmospheric pressure between two electrodes, one of them being a platinum tip. Between 1949 and 1961 they made the first steps in consecrating the CCP sustained at atmospheric pressure as excitation source for spectral analysis^{2,3}.

The interest on plasma spectral sources was shifted to the ICPs in the early 1960s, when Greenfield and al.⁴ reported almost simultaneously with Wendt and Fassel⁵ the successful application of an argon ICP in spectrochemical analysis. Since then, until the mid 80's the world of spectrochemical analysis was dominated by the ICPs.

After 1988, Blades et al.⁶⁻¹⁰ "rediscovered" the RF CCP in different electrode geometry for spectrochemical analysis. Probably they were attracted by both low RF power and argon consumption compared to the ICPs.

In the last decade, our attention was directed to the construction of RF generators able to generate CCPs at low and very low absorbed RF powers. Firstly, we have built¹¹ an RF generator for maintaining an argon CCP at atmospheric pressure. The working frequency was 27.12 MHz and the RF powers were in the range of 100-300 W. Two electrodes configurations have been used to maintain the plasma: tip-ring and tube-ring electrode geometries. This generator was coupled with a sequential monochromator, resulting an atomic emission spectrometer. It has been used for analysis of liquid samples introduced into the plasma by pneumatic nebulization and of conductive solid samples. The obtained results were promising¹²⁻¹⁸. Secondly,

* Correspondence: E-mail: anghels@phys.ubbcluj.ro; Phone: + 40 - 64 - 405 300; Fax: + 40 - 64 - 191 906

the RF generator built with the aim of studying the CCP in argon and air at atmospheric pressure at very low RF powers (20-70 W and 13.56 MHz)¹⁹ was used to generate an argon plasma as spectral source for direct analysis of non-conductive samples²⁰.

In the present work, the second RF generator is used to maintain an air CCP at atmospheric pressure. This plasma is studied as atomization and excitation source for liquid samples introduced into the plasma by pneumatic nebulization and as possible sampling and excitation source for non-conductive solid samples. Two kind of plasma devices are presented. A torch with two electrodes (the sustaining tip of the plasma and a tip like grounded counterelectrode) for analysis of liquid samples and a torch for direct analysis of non-conductive samples. The second device, a sputtering chamber, was built by modifying the previous torch to provide the sampling and excitation conditions for non-conductive solid samples.

2. INSTRUMENTATION

2.1. Experimental setup

The construction of the RF generator used for sustaining the very low power capacitively coupled plasmas at atmospheric pressure, is described elsewhere¹⁹. The plasma was generated at a frequency of 13.56 MHz, at various absorbed RF power levels (20-70 W). The main characteristic of our capacitively coupled plasma is that it is an intrinsic part of the tuned circuit of the radio-frequency generator. The oscillator is one of the inductive reaction type having the tuned circuit placed in the control grid network of the active element (pentode tube). The presence of the adjustable inductive coupling in the reaction circuit offers the possibility of the maximisation the RF power transferred to the plasma. It was experimentally proved that this plasma could be successfully used for the analysis of liquid samples^{15, 17} by atomic emission spectroscopy technique and for the direct analysis of both conductive¹⁴ and non-conductive solid samples²⁰.

The experimental setup, for both techniques, is schematically outlined in Fig. 1. and Fig. 2. Details of the equipment used and the operating conditions are provided in Table 1.

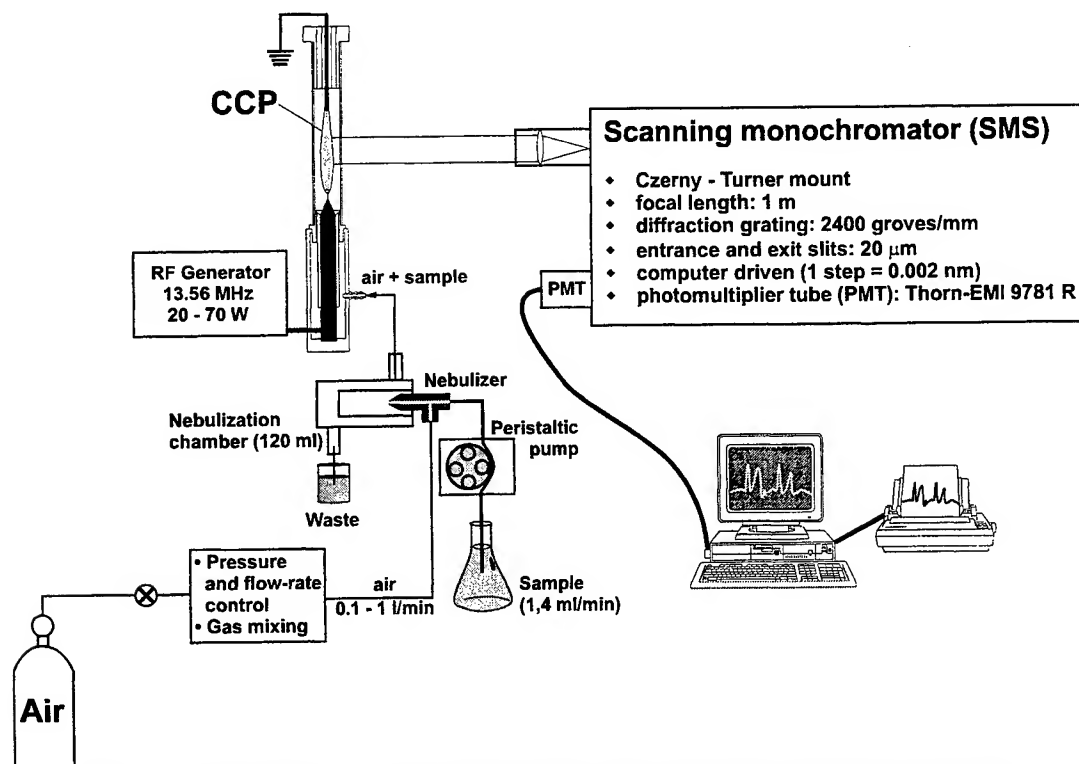


Fig. 1. The experimental set-up for liquid sample analysis by atomic emission spectroscopy

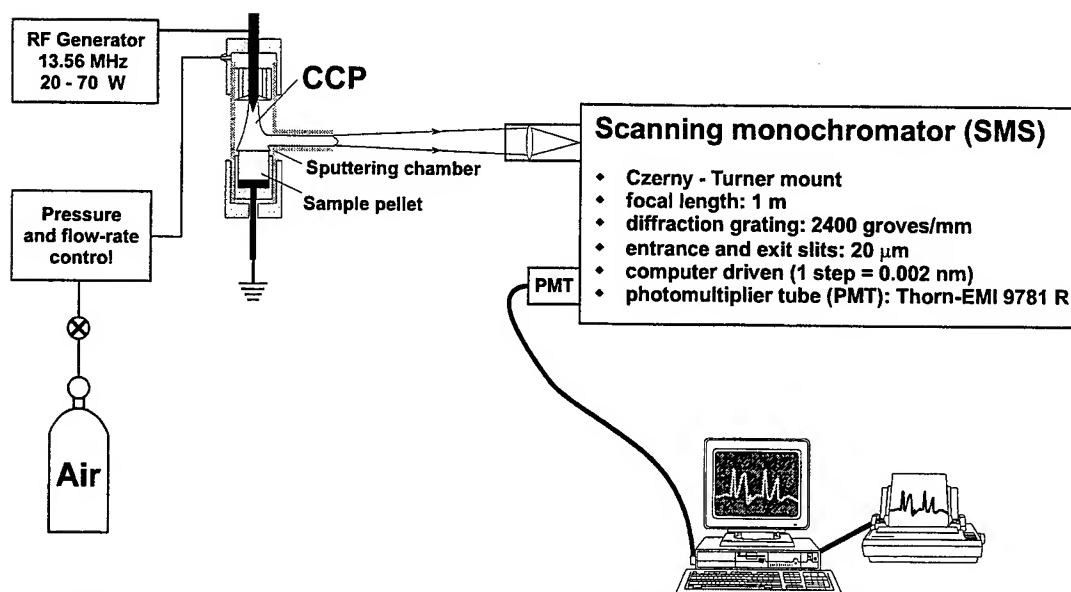


Fig.2. The experimental set-up for the direct analysis of non-conductive solid sample by atomic emission spectroscopy

Table 1. Equipment and operating conditions

Plasma generation:	RF oscillator (13.56 MHz; 20 - 60 W). Laboratory constructed. <i>Babes-Bolyai University, Faculty of Physics, Cluj-Napoca, Romania</i> Stabilised Power Supply BS 452 E type (2 × 500 V; max. 400 mA). <i>TESLA, Czech Republic</i> Stabilised Power Supply I 4104 type (40 V; 5 A). <i>IEMI, Bucharest, Romania</i>
Plasma torch:	Laboratory constructed (Fig.3.)
Sputtering chamber:	Laboratory constructed (Fig.4.)
Plasma support gas:	High purity, compressed air (0.1 - 1 l/min)
Optics:	110 mm focal length, 30 mm diameter fused silica lens
Monochromator:	Computer driven scanning type (1 step = 0.002 nm), 1 m focal length, Czerny-Turner mount, with 2400 grooves·mm ⁻¹ diffraction grating and 20 μm slits (internal wavelength calibration with an Al hollow cathode lamp). <i>Research Institute for Analytical Instrumentation, Cluj-Napoca, Romania</i>
Detector:	9781 R photomultiplier tube operated at 700 V. <i>Thorn EMI Ltd., England</i>
Data acquisition and processing:	Digital data acquisition and monochromator driving carried out by an IBM-PC equipped with a laboratory constructed interface (64 μs data acquisition time); data processing with an appropriate in-house software. <i>Research Institute for Analytical Instrumentation, Cluj-Napoca, Romania</i>

Internal calibrations were done with an Al hollow cathode lamp and the corrections for the spectral response of the spectrometric system (optics and photomultiplier) were made with a spectral irradiance standard lamp EPI 1604.

2.2. The CCP torch and sample preparation for liquid sample analysis

The low power CCP for liquid sample analysis is sustained on a kanthalum tip (20 - 24 % Cr, 5 - 6 % Al, 2 % Co, 68 - 73 % Fe). For a greater stability of the plasma the presence of the second (counter) electrode is required. The tip is part of the CCP torch presented in Fig.3.

The main parts of the CCP torch are: a quartz tube /1/ (14 mm i.d., 16 mm o.d., 150 mm length); a brass electrode as support of a kanthalum tip /2/ (0.8 mm in diameter and 4 mm in length); an electrode holder made out of PTFE /3/ (with 12 concentric holes of 1 mm in diameter, providing the sample entrance to the plasma) and a PTFE chamber /4/ (volume = 10 ml); RF coupling /7/ and the air and sample introduction inlet /6/. The counter electrode is grounded and made out of copper /9/ (2 mm thickness and 100 mm length). A PTFE electrode holder /8/ (with 6 concentric holes of 2.5 mm in diameter for gas outlet) is providing the joining with the remain of the torch. The plasma gas is air, and flows in a laminar motion through

the quartz tube with a flow-rate of 0.1-1 l/min. At these flow-rates the plasma has a candle flame-like with an orange like colour.

Stock solutions (1000 µg/ml element) were prepared by dissolution of the high-purity metals or their salts in HNO₃ (1+1) or in HCl (1+1) (FLUKA). Single element working standard of 50 µg/ml were obtained by diluting the stock solutions with high purity 2 % v/v HNO₃. These solutions were used for the analysis of liquid samples by atomic emission spectroscopy technique. A blank solution of 2 % (v/v) HNO₃ was used.

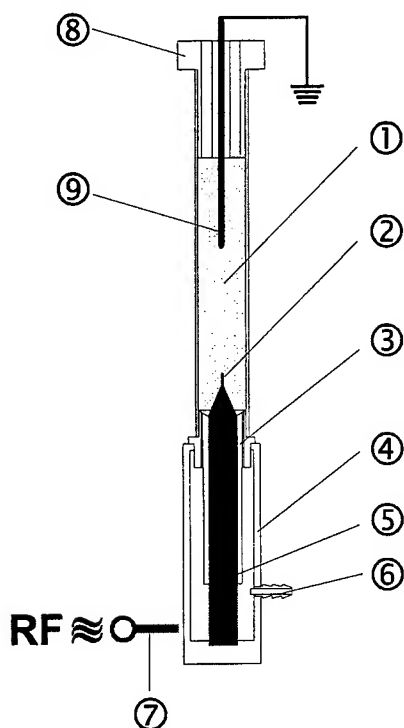


Fig.3. The CCP torch

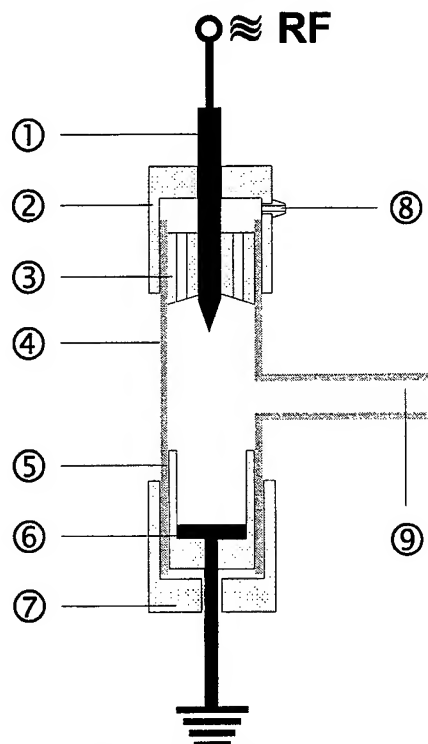


Fig.4. The sputtering chamber

2.3. The sputtering chamber and sample pellet preparation

The capacitively coupled plasma used for RF sputtering of non-conductive solid samples was obtained inside of a tubular quartz chamber /4/ (14 mm i.d., 100 mm length, with a lateral port, 5 mm i.d., 50 mm length) on a tungsten electrode /1/ (4 mm in diameter, with the tip sharpened at 45°) (see Fig.4.). The plasma gas was introduced inside the chamber via a gas inlet /9/ and a PTFE electrode holder /3/ (12 concentric, 1 mm i.d. holes). The sample pellet was placed inside of a PTFE sample holder cup /5/ on plate brass counter electrode /6/. The RF electrode and the sample holder were placed at the opposite sides of the quartz tube and fixed with two PTFE lids /2/ and /7/. The plasma viewing is insured by the lateral port /10/.

The experimental measurements were carried out on cylindrical sample pellets of chalk (CaCO₃). The raw materials necessary for pellet preparation were mixed with 30 ml ethyl alcohol in a mortar and stirred until homogeneity. This procedure was done until the whole quantity of the added alcohol was evaporated and this procedure was repeated twice. Drying at 105 °C was followed by 7 h of sintering in furnace at 1000-1100 °C. After a new set of grinding and sifting, the sample was homogenised again. A quantity from the powders obtained this way was pressed in a steel press at a pressure of 87·10⁵ Pa for 10 minutes. The resulting analytical sample pellets had cylindrical shape, with a 11 mm diameter and were used for the direct analysis of non-conductive solid samples.

3. RESULTS AND DISCUSSION

The study of physical and analytical of a plasma discharge properties (temperatures, line intensity ratios, signal to background

ratios, dynamic range, detection limits) represents a very important preliminary step toward understanding the mechanisms and processes that occur within the plasma used as spectral source and provides for the possible users an indication as to whether samples at low levels can be analyzed with some desired level of precision.

As far as the plasma support gas was air, the rotational temperature (T_{rot}) seems to be the most important physical property of this type of plasmas. It was calculated via the Boltzmann plot method, from the slope of a regression line fitted to the appropriate data according to Eqn.1, using six lines from the R2 branch of the (0,0) transition of the OH radical (307.1; 307.3; 307.4; 307.7; 308.4 and 308.9 nm).

$$\log\left(\frac{I}{g \cdot A \cdot 2 \cdot (J+1)}\right) \sim \frac{E_{rot}}{k_B \cdot T_{rot}} \quad (1)$$

where: I = relative intensity of the OH line; g = statistical weight; A = transition probability; k_B = Boltzmann constant, E_{rot} = excitation energy of a rotational level. The spectroscopic data were taken from the paper of Kornblum and De Galan²¹.

The temperature measurements were performed at an RF power of 50 W and air flow-rate of 0.7 l/min, in two situations: for pure but not dried air plasma without distilled water, and for an air plasma with pneumatically nebulised distilled water, introduced via devices described in Fig.1. and Table 1., respectively. Thus, temperatures of 2240 K and 2210 K were obtained, respectively. This results and the plasma spectra in those two situations, presented in Fig.5a. and Fig.5b., demonstrate that the water provides extra OH radicals, meaning higher relative intensities in the band and has a coolant action, lowering the rotational temperature.

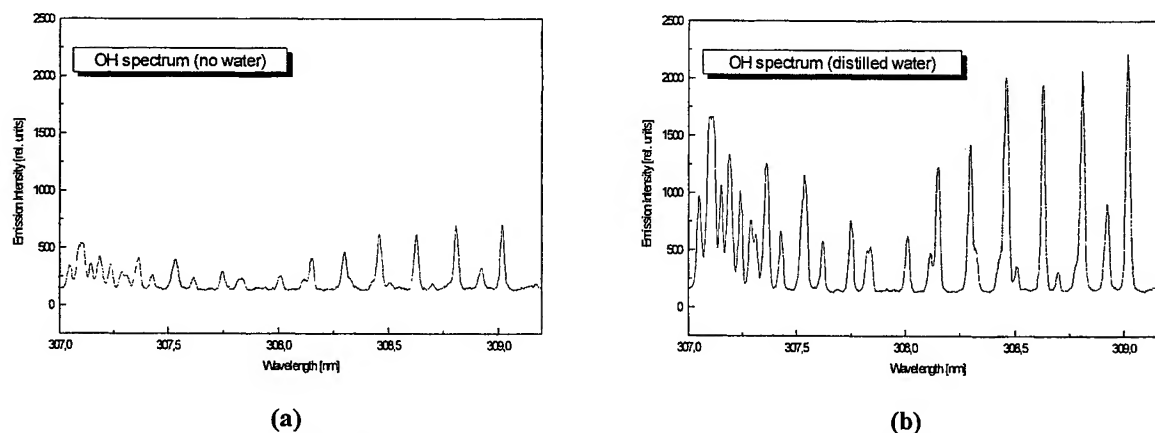


Fig.5. The R2 branch of the (0,0) transition of the OH radical

The intensity ratio of ion to atom lines for a certain element (Ca in our case) is an indicator of the existing species (ions, atoms or both) within a plasma discharge. This intensity ratio depends on the electron number density, ionization temperature and ionization potential of the elements in question. For our spectral source, the ratio was determined experimentally using the 393.367 nm ionic and the 422.673 atomic lines of Ca and was found to be 1 : 13. Thus, our plasma contains more atomic species than ions.

Without any doubt, the most important analytical characteristic of a spectral source is the detection limit. The detection limit of the concentration (LOD or c_L) according to Boumans²² is:

$$c_L = k \cdot \frac{B}{x_B} \cdot \frac{c_0}{x_A/x_B} = k \cdot 0.01 \cdot RSDB \cdot \frac{c_0}{SBR} \quad (2)$$

where: x_A = net analyte signal; x_B = net analyte signal; $SBR = x_A / x_B$ = signal-to-background ratio (SBR); σ_A = standard deviation of the background signal; RSDB = relative standard deviation of the background signal and k = const.

If $k = 2\sqrt{2} (\approx 3)$ the formalism presented above is called "3 σ method" and it is the most commonly used technique of detection limit determination. By using this method the SBR and LOD for a number of 11 elements (Ag, Ba, Ca, Cr, Cu, Li, Mg, Mn, Na, Pb and Sr) were determined at an observation height of 10mm above the tip by introducing 50 $\mu\text{g/ml}$ aqueous working standard solutions of each element. These results are presented in Table 2., in comparison with the results for the same elements, obtained with an Ar plasma, operated at the same RF power and gas flow-rate parameters²³.

Table 2. Detection limits for the low power air CCP

Element	Analytical wavelength [nm]	LOD [$\mu\text{g/ml}$]	
		air CCP 40 W	argon CCP 40 W
Na	588.90	0.014	0.107
Ca	422.67	0.650	0.170
Pb	405.78	28.920	1.400
Ag	328.07	1.670	0.114
Cu	324.75	24.100	0.166
Mg	285.21	5.850	0.100
Cr	425.43	42.400	4.200
Mn	403.08	1.310	0.520
Ba	493.41	66.100	142.000
Sr	460.70	1.310	0.078
Li	670.79	0.063	0.130

The detection limits listed in Table 2. for the air CCP at 40 W were found to be in the range of 0.014 - 66 $\mu\text{g/ml}$. These results are comparable of those of the low power Ar CCP. For alkali metals (Na and Li) the detection limits are better in the air plasma. The results from Table 2. are in a good agreement with the theory according to what a molecular plasma, the low power air CCP in our case, is better for the analysis of a refractory element (e.g., Ba) than an Ar plasma.

The dynamic range of the plasma source was determined by plotting a calibration curve for Ag. It is about 3 orders of magnitudes. The correlation coefficient for the calibration curve is about 0.999 for this dynamic range and the standard deviation of its slope is 2.8 % (Fig.6.)

The influence of RF power on the background and on the emission intensity was studied for Na doublet (588.995 nm/589.59 nm) and the dependences are presented in Fig.7. A linear increase of the emission intensities and a constant background could be concluded.

The behavior of Na atoms in a plasma spectral source could provide some other important informations about that source. The self-absorption is a phenomenon which occurs when on its path through the plasma the emitted radiation is absorbed by the atoms in ground state. It is estimated as the ratio of the two emission intensities of the Na doublet, $I_{\text{I}}/I_{\text{II}}$. In the absence of this phenomenon this ratio has to be 2, and below 2 when the self-absorption is present. For our plasma source the ratio was found to be between 1.9 and 2.0. These results shows that the self-absorption is lower compared to the reference value of 1.8, the self-absorption constant in an arc source²⁴.

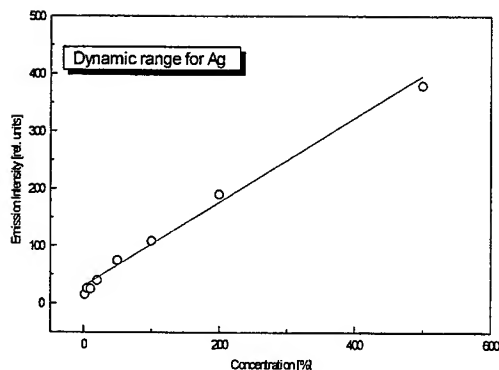


Fig.6. Dynamic range for Ag

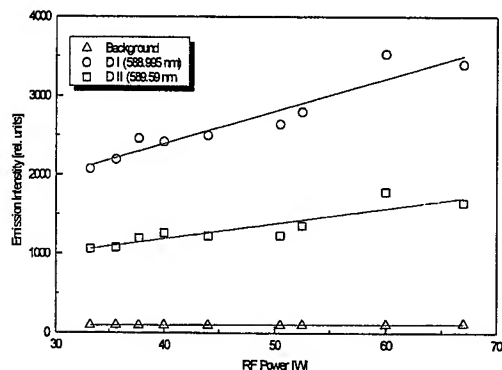


Fig.7. Effect of RF power on background and signal

The low power air CCP is a versatile tool for real liquid sample analysis. The emission lines for Na and Ca from drinking water are presented in Fig.8. and Fig.9.

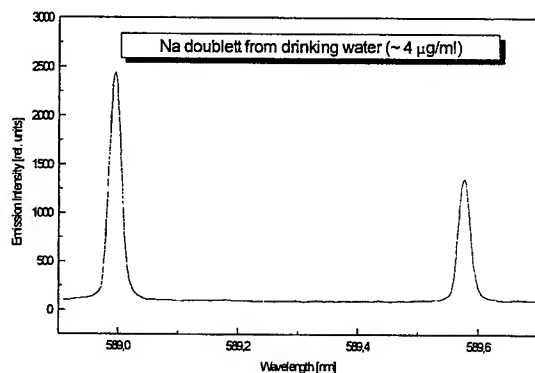


Fig.8. Na doublet in drinking water

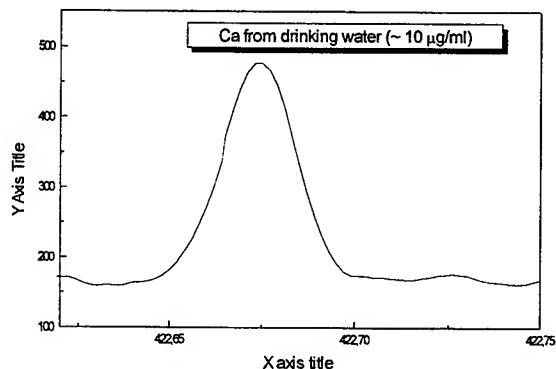


Fig.9. Ca atomic line in drinking water

The possibility of using a capacitively coupled plasma for RF sputtering of non-conductive solid samples was one of the purposes of our research work and the preliminary results are presented in this paragraph. The main characteristic of our low power capacitively coupled plasma is that it is an intrinsic part of the tuned circuit of the radio-frequency generator (Fig.10.).

The automatic grid bias network ($R_g C_g$) develop a negative voltage on the grid in the range of 150 - 200V. Its value is function of the anode positive bias. Over this negative dc component, the RF component is superimposed, the amplitude of oscillation being 15-20% greater than the dc potential of the control grid. Because the oscillator works under resonant conditions, the amplitude of the RF oscillations on the sustaining electrode of the plasma is in the range of 2000-3000V. Due to the DC component the RF wave is translated toward negative values, its form being asymmetric with respect to ground. During a full cycle of the RF wave, the plasma sustaining electrode has a negative potential a time interval longer than a half-cycle. This fact, combined with the lower mobility of the positive ions relative to the electrons, cause an accumulation of positive charge greater than the negative charge close to the sustaining plasma electrode. This accumulation of positive charge has two consequences: (a) - an excess of negative charge that appears toward the free end of the plasma where the sample is placed, and (b) - the electrostatic shielding of the sustaining electrode of the plasma. Consequently, an internal DC electric field appears in the plasma.

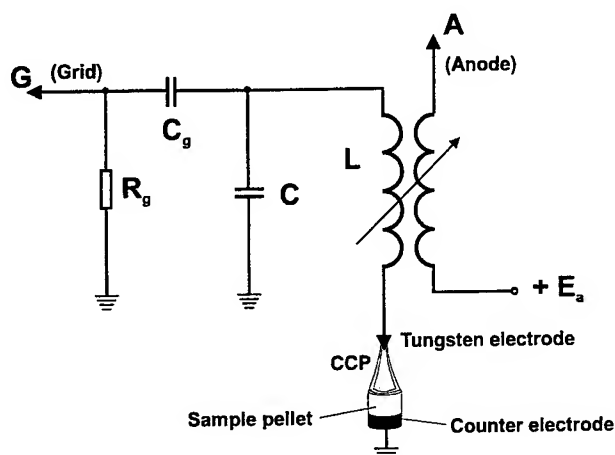


Fig.10. The CCP intrinsic part of the RF oscillator's tuned circuit

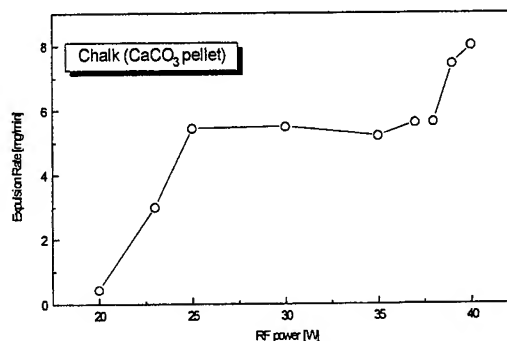


Fig.11. Expulsion rate as function of RF power

At a critical distance between the plasma electrode and the sample (about 2 - 4 mm) the electrical field is sufficiently intense to accelerate the positive ions towards the sample and to induce sputtering of the sample, causing sample atomisation. Sputtered atoms are then available to enter the plasma for subsequent excitation and ionization. At sufficiently high RF powers (above 50 W in the case of an air plasma), the heating of the sample is so high that it is tending to incandescence. We suppose that the increase of the sample temperature causes the thermal evaporation on its surface. This can be a supplementary atomisation mechanism which will cause an increase in the number of the sample atoms in the plasma. These affirmations are supported by the plots from Fig. 11., Fig.12. and Fig.13.

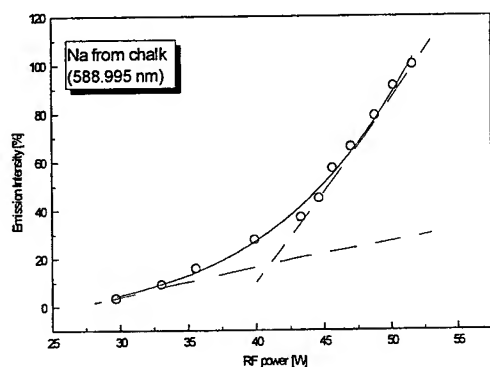


Fig.12. Effect of RF power on the Na emission intensity at an air flow-rate of 0.5 l/min

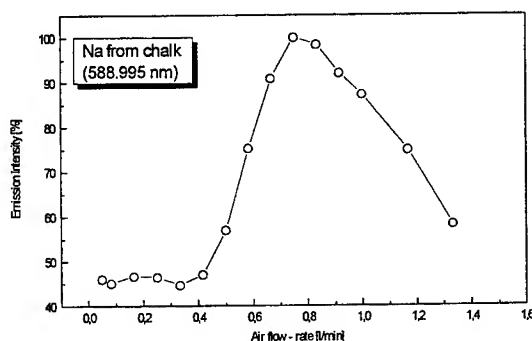


Fig.13. Effect of air flow-rate on the Na emission intensity at an RF power of 40 W

Fig.11. presents the dependence of the expulsion rate on the RF power absorbed by the plasma. The expulsion rate was calculated as being the difference between the chalk sample weight before and after exposure to collisions with ions. Nine replicate sample pellets were used. At powers lower than 20 W, the sputtering rate is low since the intensity of the dc internal field is low. In the range of 20 - 40 W, the sputtering rate is nearly constant which means the intensity of the accelerating field remains nearly constant. An explanation of this phenomenon could be the complementary effects of the increase of the RF voltage amplitude and of the electrostatic shielding, respectively. In this power range the sample atomisation is produced only by the sputtering process. At powers higher than 50 W, the thermal evaporation will be present because of heating of the sample by energised ions. Such, an increase of the atomisation rate appears.

In Fig.12. the effect of RF power on the emission intensities of Na (588.99 nm) from the CaCO_3 matrix is presented. As one can notice, each plot is composed of two straight lines with different slopes. The first line corresponds to the sputtering mechanism and the second to the combination of sputtering and thermal evaporation. Observing that the increase of the slope

takes place at the RF power of 42-45 W which is the same as when the atomisation rate begins to increase, the thermal evaporation assumptions seem to be plausible.

In Fig.13., the effect of the gas flow rate on the Na (588.99 nm) emission line from the CaCO_3 matrix is presented, at an RF power of 40 W is shown. The plot has a maximum at a gas flow rate that can be considered optimum (0.5 l/min). At this gas flow rate, the number of sputtered atoms entering the plasma, where the excitation and atomisation processes take place, are maximal. At gas flow rates greater than the optimum, the residence time of atoms in the plasma decreases, and as a result, the net intensities of the emission line decrease too. Mg impurities were found in the chalk. The Mg emission line (285.21 nm) is presented in Fig.14.

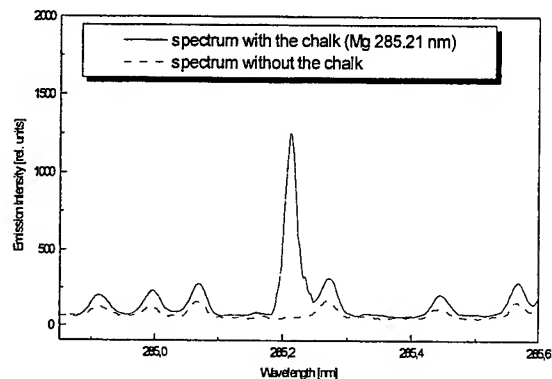


Fig.14. Emission line of Mg from chalk

CONCLUSIONS

It has been shown that an air RF CCP operated at atmospheric pressure and very low power could be a valuable spectral source for atomization and excitation of liquid samples and for sampling and excitation of non-conductive solid samples. A very stable air plasma could be maintained at a power of 50 W and a gas flow-rate of 0.7 l/min. The LODs for liquid samples were in the 0.014 ppm to 66 ppm range. For some elements they are comparable or better than the LODs obtained in the Ar RF CCP at the same power. If some constructional and functional optimization will be made, the air RF CCP obtained with the described sputtering chamber could be successfully used as spectral source for trace element determination in chemical reagents and geological samples. The main advantage of this spectral source is the very low price of the plasma gas.

ACKNOWLEDGEMENTS

The authors wish to thank to Dr. A. Popescu and C. Dem for their valuable help in the experimental work. They are also indebted to H. Mioscu and I. Marginean for the interface and the in-house software. This research was supported by Research Grant 32575/1999, CNCSIS 117.

REFERENCES

1. G. D. Cristescu and R. Grigorovici, "Temperaturbestimmungen an einer hochfrequenten Fackelentladung aus der Intensitätsverteilung in N_2 - und OH-banden, sowie durch Linienumkehr", *Bull. Soc. Roum. Phys.* **42**, 37-51, 1941.
2. G. D. Cristescu and R. Grigorovici, "Untersuchungen über die Hochfrequenz-Fackelentladung", *R. Rev. Phys.* **1**, 103-126, 1956.
3. G. D. Cristescu and R. Grigorovici, "Studiul tortei de inalta frecventa IV. Observatii spectroscopice", *Com. Acad. RPR* **5**, 515-520, 1955.

4. R. H. Wendt and V. A. Fassel, "Induction-coupled plasma spectrometric excitation source", *Anal. Chem.* **37**, 920-922, 1965.
5. S. Greenfield, I. L. Jones and C. T. Berry, "High pressure plasmas as spectroscopic emission sources", *Analyst* **89**, 713-720, 1964.
6. D. C. Liang and M. W. Blades, "Atmospheric pressure capacitively coupled plasma atomizer for atomic absorption spectrometry", *Anal. Chem.* **60**, 27-31, 1988.
7. D. C. Liang, D. Huang, and M. W. Blades, "Capacitively coupled plasma detector for gas chromatography", *J. Anal. At. Spectrosc.* **4**, 789, 1991.
8. D. Huang and M. W. Blades, "Evaluation of a 13.56 MHz capacitively coupled plasma as a detector for gas chromatographic determination of organotin compounds", *J. Anal. At. Spectrosc.* **6**, 215-219, 1991.
9. D. C. Liang and M. W. Blades, "An atmospheric pressure capacitively coupled plasma formed inside a graphite furnace as a source for atomic emission spectrometry", *Spectrochim. Acta.* **44B**, 1059-1063, 1989.
10. B. M. Patel, J. P. Deavor and J. D. Winefordner, "Solution nebulization of aqueous samples into the tubular-electrode torch capacitively-coupled microwave plasma", *Talanta* **35**, 641-645, 1988.
11. S. D. Anghel, "An RF Generator for capacitively coupled plasma at atmospheric pressure", *Studia Univ. "Babes-Bolyai" Cluj, Physica*, **XXXVIII**, nr.1, pp. 39-51, 1993.
12. E. A. Cordos, S. D. Anghel, T. Frentiu, and A. Popescu, "Capacitively coupled plasma with tip-ring electrode geometry for atomic emission spectrometry. Analytical performance and matrix effect of sodium chloride and potassium chloride", *J. Anal. At. Spectrom.* **9**, pp. 635-641, 1994.
13. S. D. Anghel, E. Darvasi, T. Frentiu, A. M. Rusu, A. Simon, and E. A. Cordos, "Characteristic temperatures and electron number densities in an RF capacitively coupled plasma", *Fresenius Journ. Anal. Chem.* **355**, pp. 250-251, 1996.
14. S. D. Anghel, T. Frentiu, A. M. Rusu, L. Bese, and E. A. Cordos, "The analysis of conductible solid samples by RF capacitively coupled plasma at atmospheric pressure", *Fresenius Journ. Anal. Chem.* **355**, pp. 252-253, 1996.
15. T. Frentiu, A. M. Rusu, M. Ponta, S. D. Anghel, and E. A. Cordos, "Analytical performances of an RF capacitively coupled plasma for atomic emission, with tip-ring electrode geometry", *Fresenius Journ. Anal. Chem.* **355**, pp. 254-255, 1996.
16. E. A. Cordos, T. Frentiu, A. M. Rusu, S. D. Anghel, A. Fodor, and M. Ponta, "Analytical characterization of CCP torch with central tube electrode", *Talanta* **48**, pp. 827-837, 1999.
17. S. D. Anghel, T. Frentiu, A. M. Rusu, A. Popescu, A. Simon, and E. A. Cordos, "Figures of merit and physical characteristics of a capacitively coupled radiofrequency argon plasma sustained at atmospheric pressure in tip-ring electrode geometry", *Acta Chimica Hungarica - ACH Models in Chemistry* **136**, pp. 131-148, 1999.
18. T. Frentiu, A. M. Rusu, S. D. Anghel, A. Popescu, S. Negoescu, A. Simon, and E. A. Cordos, "Radiofrequency CCP torch with central tubular electrode and outer ring electrode", *Acta Chimica Hungarica - ACH Models in Chemistry* **136**, pp. 119-129, 1999.
19. E. Tataru, S. D. Anghel, and I. I. Popescu, "A Stabilized low power RF torch for analytical spectrometry", *Rev. Roum. Phys.* **39**, pp. 29-44, 1991.
20. S. D. Anghel, E. A. Cordos, T. Frentiu, A. Popescu, and A. Simon, "Atmospheric pressure capacitively coupled plasma source for direct analysis of non-conductive solid samples", *J. Anal. At. Spectrom.* **14**, pp. 541-545, 1999.
21. G. R. Kornblum and L. de Galan, "Arrangement for measuring spatial distributions in an argon induction coupled RF plasma", *Spectrochim. Acta.* **29B**, 249-261, 1974.
22. P. W. J. M. Boumans, "Measuring detection limits in inductively coupled plasma emission spectrometry using the 'SBR-RSDB approach' - I. A tutorial discussion of the theory", *Spectrochim. Acta.* **46B**, 431-445, 1991.
23. S. D. Anghel, A. Simon, T. Frentiu and E. A. Cordos, "A spectral source with very low power radio frequency capacitively coupled plasma. Physical characteristics and detection limits", *to be published*.
24. *Tablitsi Spektralnikh Linii*, Izdatelstva Nauka, Moskow, 1977.

Spectral study of some fatty acid - cholesterol mixtures

Maria Honciuc*, Eugenia Carbunescu, Carmen Popa, Elena Slavniciu,
Iulian Badragan

Department of Physics, University Politehnica of Bucharest

ABSTRACT

This paper analyses the behavior of fatty acid-cholesterol mixtures, components of biological membranes, under the influence of the electromagnetic field.

The mixtures acid lauric-cholesterol, prepared in thin layers of 24 μm , have a liquid crystal behavior at room temperature.

Spectra obtained in the range (330 \div 800) nm put into evidence some regions of resonance between the oscillatory system characterising the textures and the electromagnetic field.

The results are discussed in terms of Maxwell's formalism. A good agreement between experiment and theory was obtained for the lauric acid. The impurification with cholesterol leads to a greater disorder in the system and the agreement with the theory is no more satisfactory.

Keywords: biological membrane, fatty acid - cholesterol mixture, transmissivity, effective dielectric constant.

1. INTRODUCTION

Based on structure, properties and functional similarities, the great number of chemical different macromolecules that build living systems is divided into some main classes: proteins, glucids, fatty acids, nucleic acids. A main role in the understanding of the organization and functions of living systems is played by cellular membranes. Depending on the place and role they have, cellular membranes are strictly specialised^{1,2}.

The spatial disposal of a membrane, determinant for its functions, corresponds to a minimum of the free energy of the system constituted by the membrane for a given temperature and surroundings.

The basic structure of any cellular membrane is given by a double lipidic layer. That is why the knowledge of the physical properties of fatty acids that are components of cellular membranes is of great importance for clearing up the behavior of any cellular membrane.

In this paper we present the results of the optical transmission studies of some systems formed by one of the fatty acids of interest, the lauric acid (L), and the mixtures lauric acid-cholesterol in weight percentage 2 \div 1 (A_2C_1) and 1 \div 1 (A_1C_1).

Optical microscopy and phase transition studies by the thermoelectret method³ put into evidence the mesomorphic behavior of these systems.

The optical transmission of the samples was studied in the range (330 \div 800) nm. The influence of the impurification with cholesterol which is a constitutive component of any lipidic layer is also discussed.

* Correspondence: Email: proto@physics.pub.ro

2. EXPERIMENTAL CONDITIONS AND CHARACTERISTICS OF THE SAMPLES

The saturated lauric acid, $\text{CH}_3(\text{CH}_2)_{10}\text{COOH}$, is a polycrystalline powder at room temperature, with the melting point at $t = 45^\circ \text{C}$.

The samples, with an active layer of $24 \mu\text{m}$ in thickness⁴, were pulled out from melt and sealed in cells with plane parallel plates. The liquid crystal orientation of the samples is smectic *A* type, with the director vector \vec{n} perpendicular to the plates that have transparent electrodes laid on (Fig. 1). The incident light is normal to the electrodes. The transmission spectra in the range $(330 \div 800) \text{nm}$ were registered with a spectrophotometer SPECORD UV-VIS. The reference beam passed through a witness cell, identical with the cell containing the samples.

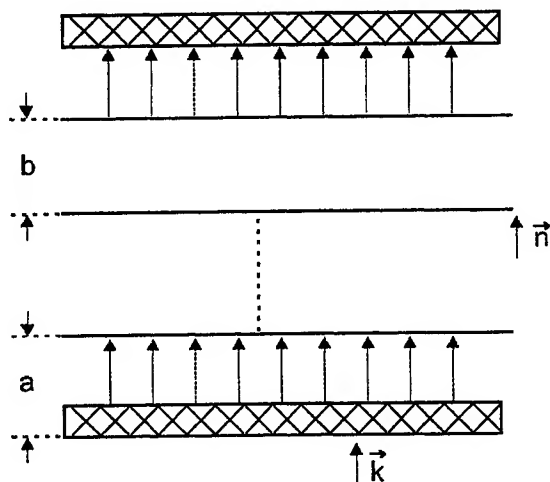


Fig. 1. Smectic A - liquid crystal: large density layers - a, the space between two layers with large density - b, \vec{n} - the director vector, and \vec{k} - the wave vector.

3. THEORETICAL CONSIDERATIONS

In order to characterise the propagation of light through the systems of interest we use the Maxwell formalism, assuming that there are no free charges and no free currents and that the magnetic susceptibility is zero.

For the beginning, assuming that the medium is uniform and isotropic, the Fourier transforming Maxwell's equations in time⁵ leads to (in cgs units):

$$\begin{aligned} \nabla \vec{D} = 0, \quad \nabla \times \vec{E} &= \frac{i\omega}{c} \vec{B} \\ \nabla \vec{B} = 0, \quad \nabla \times \vec{H} &= -\frac{i\omega}{c} \vec{D} \end{aligned} \quad (1)$$

with the constitutive relations:

$$\vec{D} = \epsilon \vec{E}, \quad \vec{B} = \vec{H}. \quad (2)$$

As in this case the dielectric constant is independent of the spatial variables, by eliminating \vec{D} and \vec{B} , we get:

$$\nabla^2 \vec{E} + \frac{\varepsilon \omega^2}{c^2} \vec{E} = 0 \quad (3)$$

$$\nabla^2 \vec{H} + \frac{\varepsilon \omega^2}{c^2} \vec{H} = 0 \quad (4)$$

where \vec{E} and \vec{H} are the electric and magnetic wave field vectors and c is the speed of light in vacuum. The solutions to equations (3) and (4) are

$$\vec{E}(\vec{r}, \omega) = \vec{E}_0 e^{i\vec{k} \cdot \vec{r}} \quad (5)$$

$$\vec{H}(\vec{r}, \omega) = \vec{H}_0 e^{i\vec{k} \cdot \vec{r}} \quad (6)$$

in which \vec{E}_0 and \vec{H}_0 are constants and \vec{k} is the wave vector related to ω by:

$$\omega(k) = \frac{c}{\sqrt{\varepsilon}} \cdot k, \quad k = |\vec{k}| \quad (7)$$

Nevertheless, in smectic type systems, the dielectric constant of the layers with large molecular density (Fig. 1, regions a) is different from that of the layers with small molecular density (Fig. 1, regions b), and consequently:

$$\varepsilon = \varepsilon(\vec{r}) \quad (8)$$

Therefore, light propagates through such systems in a more complicated manner than equations (5) and (6) tell us. Assuming a periodic function for $\varepsilon(\vec{r})$ along the direction of \vec{k} , these equations can be solved using photonic band structure methods⁶.

The solution for the electric field of the light propagating through the sample is written in the form:

$$\vec{E}(\vec{r}, \omega) = \vec{u}(\vec{r}) \cdot e^{i\vec{k} \cdot \vec{r}} \quad (9)$$

where $\vec{u}(\vec{r})$ is a periodic function with the periodicity of the structure. Based on this method, D.B. Ameen et alia⁷ calculated the frequencies of light that propagates through the cornea of the mammalian eye, supposed to be a periodic ordered system with smectic liquid crystal type structure, and found that cornea is, such as it was expected, transparent in the visible range while sclera, which is a less ordered system, is not transparent.

They supposed that light in the visible range propagates in the ordered system (cornea) like in a uniform medium with an effective dielectric constant ε_{eff} given by:

$$\omega = \frac{c}{\sqrt{\varepsilon_{eff}}} \cdot k \quad (10)$$

In our case, based on the effective medium approximation, we can obtain the transmission through the samples in the visible range by means of the fraction of light reflected by a slab of uniform medium 2 (the active layer), when the incident light comes from medium 1 and emerges into medium 3, given by⁵:

$$R = \frac{r_{12}^2 + r_{23}^2 + 2 r_{12} r_{23} \cos \beta}{1 + r_{12}^2 r_{23}^2 + 2 r_{12} r_{23} \cos \beta} \quad (11)$$

where r_{ij} is the Fresnel coefficient on passing from medium i to j and β is a phase factor specific to the interference between the two interfaces.

For light at normal incidence, the Fresnel coefficient and the phase factors are:

$$r_{ij} = \frac{\sqrt{\epsilon_i} - \sqrt{\epsilon_j}}{\sqrt{\epsilon_i} + \sqrt{\epsilon_j}} \quad (12)$$

$$\beta = 2 \omega d \frac{\sqrt{\epsilon_{eff}}}{c} \quad (13)$$

where d is the thickness of the active layer.

Then, at normal incidence the fraction of the light that is transmitted through the sample is given by:

$$T = 1 - R. \quad (14)$$

4. EXPERIMENTAL RESULTS AND DISCUSSIONS

The transmissivity of the lauric acid and of the mixtures A_2C_1 and A_1C_1 is presented in Fig. 2.

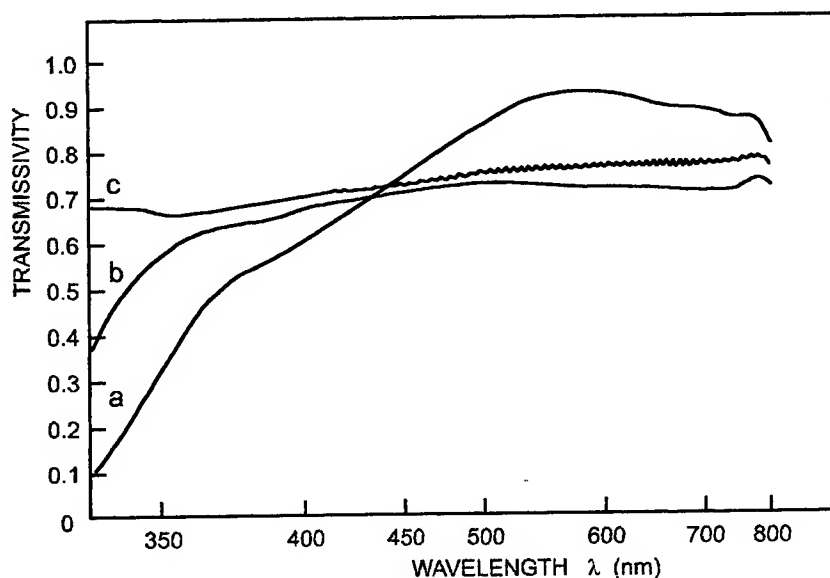


Fig. 2. The dependence $T = T(\lambda)$ for: pure lauric acid - a, A_2C_1 - b and A_1C_1 - c

We see that the transmissivity of the lauric acid in the range $(330 \div 370)$ nm (near ultraviolet) is small, less than 50%, while in the visible range the transmissivity T increases until 93% for $\lambda = 580$ nm and then it decreases slowly in the near infrared region ($\lambda > 750$ nm). The transmissivity of the mixture A_2C_1 is greater than the transmissivity of the pure acid in the range $(330 \div 425)$ nm, with a rate of increasing more important for the region $(330 \div 365)$ nm. In the visible range $(400 \div 700)$ nm, T has a constant value of about 70%. The presence of cholesterol in the system A_1C_1 determines a relatively constant level of the transmissivity for the whole range $(450 \div 800)$ nm. The curve $T = T(\lambda)$ for A_1C_1 presents a series of oscillations in the range $(430 \div 780)$ nm that may be associated with multiple reflections of light between the surfaces of the sample.

In Fig. 3 is presented the transmissivity of the samples as a function of the energy of the incident photons.

We see that for photons with energies greater than 2.8 eV the transmissivity of pure lauric acid decreases rapidly while for the mixtures decreases slowly (the rate for A_2C_1 is greater than for A_1C_1).

According to ⁷, the decrease of the transmissivity of the samples for energies greater than 2.8 eV may be associated with the existence of forbidden photonic bands due to the modification of the order in the system determined by the modification of the distance among molecules on the one hand, and, on the other hand, by the modification of the distance among the layers with large molecular density (a in Fig. 1).

From relation (10) the phase factor results to be:

$$\cos \beta = \frac{R(1 + r_{12}^2 r_{23}^2) - (r_{12}^2 + r_{23}^2)}{2(1 - R)} \quad (15)$$

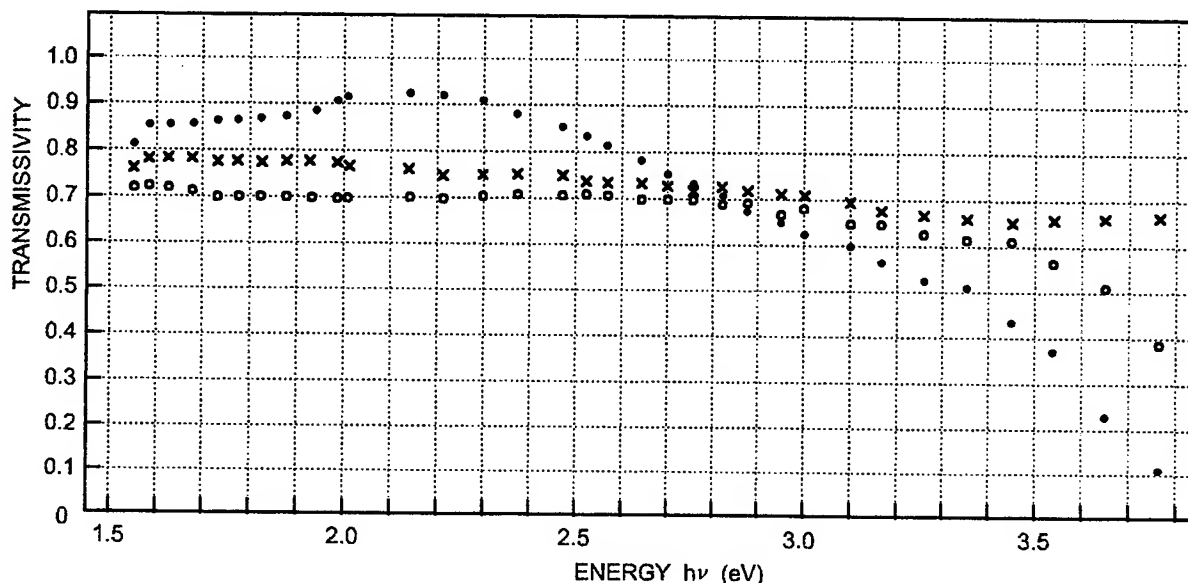


Fig. 3. The dependence $T = T(h\nu)$; • lauric acid; × lauric acid - cholesterol 1:1; ■ lauric acid - cholesterol 2:1.

For the configuration of the sample presented in Fig. 1, it is obvious that $r_{12} = r_{23} = r$, so that:

$$\cos \beta = \frac{R(1 + r^4) - 2r^2}{2(1 - R)} \quad (16)$$

The dependence of $\cos \beta$ upon R for the studied systems is presented in Fig. 4 for the minimum value of the transmissivity obtained for $\lambda = 330$ nm. We see that the absolute value of $\cos \beta$ increases with the decrease of the reflection factor, R , which is produced by the increase of the percentage of cholesterol.

Thus the refraction index n , given by $n = \sqrt{\epsilon_{eff}}$, increases with the percentage of cholesterol. In fact ϵ_{eff} increases with one order of magnitude when passing from the lauric acid to the mixture A_2C_1 and the same when passing from A_2C_1 to A_1C_1 .

These results are in good agreement with the results obtained by electrical measurements for the same systems ⁸.

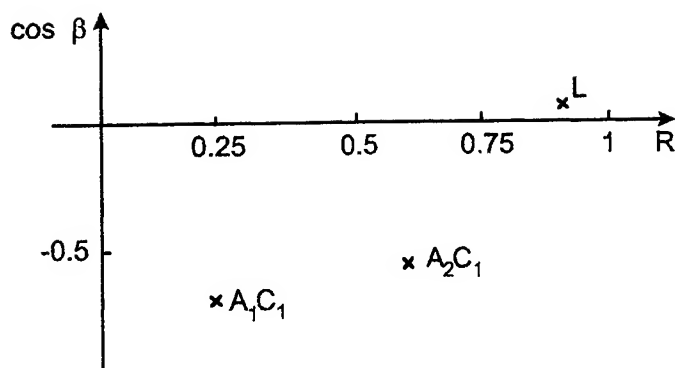


Fig. 4. The dependence $\cos \beta = f(R)$

5. CONCLUSIONS

Pure lauric acid has the best transmissivity in the visible range ($T_{\max} > 90\%$). The impurification with cholesterol decreases the transmissivity of the mixtures in the visible range: $T_{\max} > 75\%$ for A_1C_1 and $T_{\max} > 70\%$ for A_2C_1 , while in the near ultraviolet the transmissivity increases with the percentage of impurification with cholesterol. We see that light propagates through the lauric acid like in a uniform medium.

In what concerns the mixtures A_2C_1 and A_1C_1 , the transmission of light is more complex so that the model proposed is no more valid and this subject is to be treated in the future. The results obtained by electrical measurements show that the impurification with cholesterol leads to an important increase of the electric charge density which can no more be neglected when solving the Maxwell equations. In this case, the solution is more complex and it is necessary to take care of the absorption effects (the Berr law).

REFERENCES

1. R. J. Cherry, *Biological membranes*, Academic Press, London, 1975.
2. P. J. Quinn, and D. Chapmann, "Fluidity of biological membranes", *Rev. Biochem.* **8**, pp. 81-95, 1981.
3. Maria Honciuc, Iuliana Cuculescu, Maria Socaciu, Rodica Bena, and V. Stoian, "Build up of thermoelectronics at phase transitions in fatty acids", *Phase Transitions*, **51**, pp. 231-239, 1994.
4. Maria Honciuc, "The influence of electric and magnetic fields upon liquid crystals", Doctoral thesis, University of Bucharest, 1977.
5. J. R. Reitz, F. J. Milford, and R. W. Christy, *Foundations of Electromagnetic Theory*, Addison - Wesley, Reading, 1993.
6. A. A. Maradudin, and A. R. McGurn, *Photonic Band Gaps and Localization*, C. M. Soukoulis, editor, Plenum Press, New York, 1993.
7. D. B. Ameen, M. F. Bishop, and T. McMullen, "A lattice model for computing the transmissivity of cornea and sclera", *Biophys. Journal*, **75**, pp. 2520 - 2531, 1998.
8. Maria Honciuc, Cornelia Motoc, Mihaela Dumitru, R. Mitroi, Lidia Sterian, and Raluca Honciuc, "Electrical properties of some fatty acids - cholesterol mixtures", *MCLC*, **215**, pp. 229 - 236, 1992.

The single-particle optical sensing (SPOS) using optical fiber intensity modulation sensors

Traian Nicula *

Military Chemistry Application School, Str. Marasti 48, Campulung-Argeș, 0425 Romania

ABSTRACT

The ability to accurately measure the particle size distribution (PSD) of particle suspensions and dispersions has proven to be crucial for ensuring the success of a wide process material and final products.

We propose two optical fiber sensors that exploit light intensity modulation in optical fibers. One of them is constructed in a typical reflection-sensing configuration but it uses the backscattering effect on particles in suspension. The other one is based on intensity modulation of the transmitted light through optical fibers. In this case, the diffusing particle acts as a tiny lens deflecting the light away from incident beam. Furthermore, we have presented the theoretical framework concerning the light scattering on dielectric spheres (Mie scattering) and colloidal aggregates. The relevant experimental data are also shown in order to prove the sensors reliability.

Keywords: SPOS, fractal structure, Mie scattering, kinetic aggregation, particle size distribution, optical fiber sensors

1. INTRODUCTION

The single -particle optical sensing (SPOS)^{1,2,3} technique was originally developed for particular contamination analysis. Particles in liquid suspension are made to flow across a small "view volume" - a narrow, slab - like region of uniform illumination, typically produced by a laser diode. The flowing particle suspension is made sufficiently dilute that the particles pass through the "view volume" one at a time, thus avoiding coincidences. Passage of a particle through the zone of detection gives rise to a signal pulse, the height of which depends on the mean particle diameter and the physical method of detection - either light scattering or light extinction (or "blockage").

For particles smaller than about 1.3 μm , the method of light scattering provides the high sensitivity required for detecting and sizing such ultra-fine particles. For particles larger than about 1.3 μm , the method of light extinction is preferred. When a particle enters the active "view volume", a small fraction of the area of illumination is effectively blocked. The optics is designed so that the pulse height increases monotonically and smoothly with the particle diameter. The population distribution is constructed in real time using specialized digital circuits and software, by comparing the measured pulse heights with a standard calibration curve.

1.1 Advantages of SPOS over ensemble techniques

The SPOS techniques have several distinctive characteristics, which make them attractive for a wide diversity of applications. The most obvious, of course, is its single-particle resolution. The only technique, which provides comparable resolution, is the classical electrozone method.

There are two important attributes of the SPOS method that allow its particle size distribution (PSD) results to be generally superior to those produced by ensemble techniques. First, by definition, SPOS yields a true population, or number-weight, PSD. Second, the PSD, which is generated, is stable and reproducible. The particles that are sized by SPOS are also counted.

The only significant disadvantage of the SPOS method is that it ceases to be practical or effective below approximately 0.5-1 μm .

* Telephone: +40-048812500; Fax: +40-048823679

2. INTENSITY MODULATION OPTICAL FIBER SENSOR

The intensity modulation optical fiber sensors are based on the physical phenomena like: light transmission through optical fibers, light reflection, light scattering and fiber microbending. The main advantages of the intensity modulation sensors are their simplicity, accuracy and the low price.

A typical reflection-sensing configuration is presented in figure no. 1.

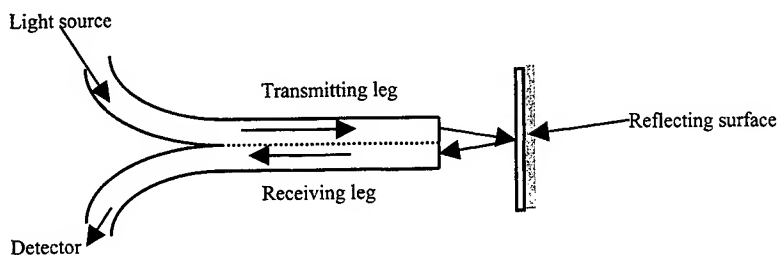


Fig. 1. Sensor arrangement

We used as a light source a well-stabilized in intensity laser diode that emits in visible spectrum. The detector output was transformed into digital signal by means of an ordinary analogous-digital (AD) converter (38000 sample/s and 12 bits). Moreover, the signal was computer processed recording both pulse height and its time span. Thus, one measures in the same time the particle size and its passage time through the "view volume".

One of SPOS sensors tested by us exploits the backscattering effect on the particles in suspension. In this kind of experimental arrangement, detected light intensity depends on the distance between reflecting target and probe fiber. Thus, the sensing range for a pair of optical fibers was found to be of about $40\mu\text{m}$. It can be achieved a better optical efficiency and an enhanced signal on detector using a monomode fiber as light source and a multimode fiber as sensing fiber. An additional improvement can be obtained if the light source fiber end is melted to form a tiny lens, which will focus the light in a small "view volume". We found this sensor suitable for colloid PSD measurements.

Another sensing configuration developed by us is based on light transmission phenomenon between two optical fibers with the same optical axis. In order to obtain a better sensing efficiency we chose the frustrated total internal reflection arrangement. This configuration has the advantage to reduce the internal reflection between the ends of fibers, which are polished to an angle of 50° in regard to optical axis. (Fig. no. 2)

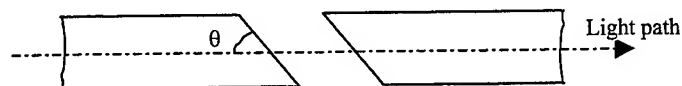


Fig. 2. Sensor arrangement

Passage of a particle through the zone of detection gives rise to a signal pulse due to light extinction, the height of which depends on the mean particle diameter. The maximum sensing range for this kind of sensor is about $30\mu\text{m}$. This sensor was used with very good results for emulsion PSD determinations as it will be shown further in this paper.

The two types of sensors described above have the advantage that permits measurements of PSD without any disturbance of the suspension. However, it is required that the suspension concentration to be reduced enough to avoid coincidences in the "view volume". Using this kind of sensors it is possible to monitor different points in the suspension (or colloid) observing subtle phenomena like local concentration fluctuation or local kinetic aggregation rate. Such experimental data can be very useful in the study of colloidal aggregation kinetics and some results will be presented below in this paper.

3. SHORT REVIEW OF MIE SCATTERING ON A SPHERE

The SPOS unlike dynamic light scattering (DLS) needs to compare the measured pulse heights with a standard calibration curve in order to obtain particle size. The most useful relations for calibration computations are presented briefly in the subsequent paragraphs. The concise Mie considerations presented below in this section apply very well for emulsion PSD measurements.

Mie scattering calculations are useful tools in many science fields involving scattering. In order to describe the scattering process it is necessary to evaluate the expressions for the radiation scattered by a sphere of radius r and index of refraction m ^{4,5,6}. The quantities required are

$$Q_{\text{ext}} = \frac{2}{x^2} \sum_{n=1}^N (2n+1) \text{Re}(a_n + b_n) \quad (1)$$

$$Q_{\text{sca}} = \frac{2}{x^2} \sum_{n=1}^N (2n+1) (|a_n|^2 + |b_n|^2) \quad (2)$$

$$g = \frac{4}{x^2 Q_{\text{sca}}} \sum_{n=1}^N \left[\frac{n(n+2)}{n+1} \text{Re}(a_n a_{n+1}^* + b_n b_{n+1}^*) + \frac{2n+1}{n(n+1)} \text{Re}(a_n b_n^*) \right] \quad (3)$$

$$S_1(\mu) = \sum_{n=1}^N \frac{2n+1}{n(n+1)} [a_n \pi_n(\mu) + b_n \tau_n(\mu)] \quad (4)$$

$$S_2(\mu) = \sum_{n=1}^N \frac{2n+1}{n(n+1)} [a_n \tau_n(\mu) + b_n \pi_n(\mu)] \quad (5)$$

which are, respectively, the extinction efficiency, scattering efficiency, asymmetry factor, and complex scattering amplitudes for two orthogonal directions of incident polarization. The phase functions $\pi_n(\mu)$ and $\tau_n(\mu)$ are expressed in terms of Legendre polynomials. Size parameter x is equal to the sphere's circumference $2\pi r$ divided by the wavelength λ . The complex-valued Mie coefficients a_n and b_n depend on x and the complex refractive index $m = n_1 - i n_2$. μ is the cosine of the scattering angle.

The extinction efficiency Q_{ext} is defined as the ratio between extinction cross section C_{ext} and geometrical cross section of the particle, πa^2 . We have computed the extinction efficiency for dielectric spheres with refractive index m in the range 1.2-1.7 and particle size in 1-20 μm range. The computational results are plotted in figure no. 3.

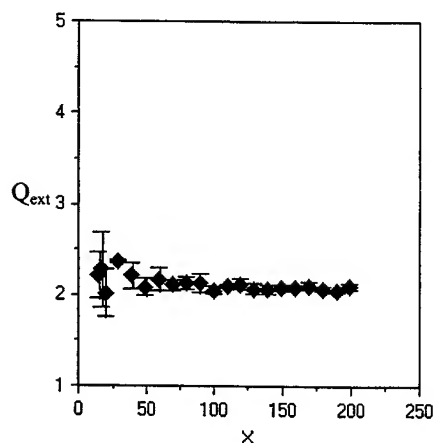


Fig. 3. The mean extinction efficiency Q_{ext} and its standard deviation for dielectric sphere with m in the 1.2-1.7 range and particle size in 1-20 μm range.

One can notice from fig. 3 that for $x > 50$ the extinction efficiency is approximately two. Thus, the pulse height, which is proportional with extinction cross section, will be function of square of the particle diameter for particle smaller than the thickness of the "view volume". The transmission sensor is based on the light extinction method described above.

Now we will describe shortly the special case of backscattering on spheres. The backscattered intensity from spheres is the same for each of the plane-polarized components of the incident radiation.

The relation below gives the backscatter efficiency or backscatter gain

$$G = (4/x^2) |S_1(\cos(180^\circ))|^2 \quad (6)$$

Computing the function $|S_1(\cos 180^\circ)|^2$ one observes that it is very sensitive to variations of x and refractive index m . Moreover, the function has a complex shape and it is difficult to calibrate, based on it, the experimental arrangement. A regular behavior is observed for small values of x towards the Rayleigh scattering range. We have plotted $|S_1(\cos 180^\circ)|^2 ((m^2 + 2)/(m^2 - 1))^2$ as function of x in figure 4.

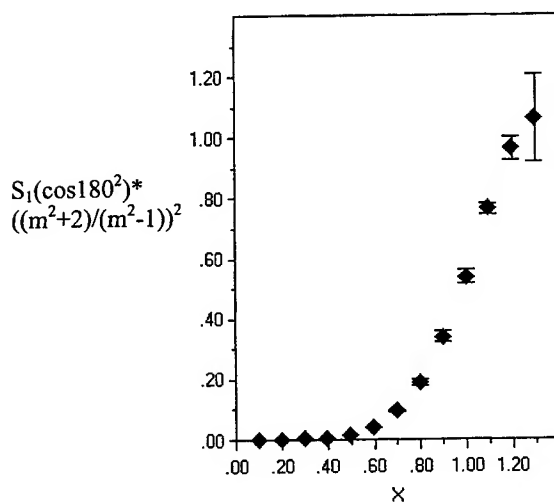


Fig. 4. The mean value and the standard deviation of the function $|S_1(\cos 180^\circ)|^2 ((m^2 + 2)/(m^2 - 1))^2$ for dielectric sphere with m in the 1.2-1.7 range and x in 0.1-1.3 range.

From figure 4, it is obvious that the backscattering sensor can be calibrated and used to measure the small sphere diameter if one knows the refractive index m of the emulsion. Although, the function shape is rather simple and regular, the signal level is too low and detection becomes difficult. Hence, we did not use this type of sensor for emulsion PSD measurements.

4. RANDOM WALK CONSIDERATIONS

Another think that must be taken into account is the flight time through the "view zone". There can be large particles which walk tangent to the "view volume" giving rise to fake signal at the detector. These fake signals can be filtered knowing the relation between the mean time for the particle to cross the "view volume" and its size.

Particles in liquid suspension carry out a diffusion motion. The diffusion and diffusive phenomena can be modeled in terms of random walk. Let $p_n(r)$ be the probability density for the location of a random walker after n steps. The lowest order approximation to $p_n(r)$ furnished by the central limit theorem is a Gaussian whose mean is $n\langle x \rangle$ and whose variance is equal to $\sigma^2 n$. The Gaussian can also be regarded as the solution to a diffusion equation provided one replaces the factor $2\sigma^2 n$ by $4Dt$, where D is the diffusion constant⁷. Thus, the linear time dependence of the mean squared displacement of a particle in a homogeneous medium is obvious.

The particle diffusivity, D , is inversely proportional to the mean particle radius, r , according to the Stokes-Einstein relation,

$$D = kT/6\pi\eta r \quad (7)$$

where k is Boltzmann's constant, T the temperature (K) and η the shear viscosity of the solvent. The diffusion constant, D , in aqueous solution at room temperature is given approximately by relation $D \sim 2 \times 10^{-13} r^{-1}$, r being the particle radius.

Exploiting the above considerations about random walk we concluded that mean time for particle to cross the view volume is given by relation

$$t \approx 2 \cdot 10^3 \cdot r \quad (8)$$

where r is the particle radius in meters. Thus, the time range for particle to cross the "view volume" extend from 1 ms to 50 ms. Therefore, it is possible to utilize an AD converter for detector signal processing. One has the possibility not only to register the pulse height as in standard SPOS multichannel techniques but the pulse duration. Thus, one can deduce supplementary information about diffusion constant D and has the possibility to filter particle after the time spent in the "view volume" and to eliminate pulses produced by particle that pass tangent to it.

Making use of possibility to measure directly the random walk time in the "view volume", one can compute the shear viscosity of the solvent η knowing the particle size.

The absolute nature of the method can be proved observing the particle size distribution (PSD) for polystyrene latex standard, 5 μm , obtained with transmission sensor (Fig. 5). We can see that the size of standard latex beads of 5 μm is obtained accurately. In order to achieve the required statistical accuracy, the counted particle number was 72400.

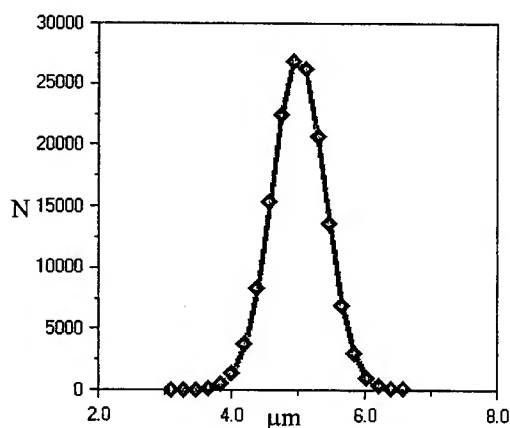


Fig. 5. Population distribution PSD for standard latex of 5 μm obtained with transmission sensor. The total particle number counted was 72400.

5. COLLOIDAL AGGREGATION

5.1. Fractal structure, cluster-cluster aggregation model (CCA)

In order to present the sensors utilization in the case of colloidal aggregates, we will make a short review of the fractal structure and the kinetic aggregation.

The clusters produced by colloidal aggregation appear universally to possess dilation symmetry and this property is typical for fractal structures⁸⁻¹². There are two natural length scales that can be associated with each aggregate, the radius of the individual particles, a , and the size of the whole cluster, R . However, the structure of the aggregates is invariant, in a statistical sense, under any scale change between these two characteristic lengths. Thus, the mass of the clusters scales with their characteristic size as $M \sim R^{D_f}$, where D_f is the fractal dimension typically non-integer and less than the Euclidean dimension of the space¹³.

In addition, the mass-mass correlation function within the cluster also exhibits power law behavior,

$$c(r) \approx r^{-\alpha} \quad (9)$$

where $\alpha = d - D_f$.

Let's suppose a particular case when energy barrier between individual clusters is very small, $E_b \ll k_B T$, so diffusion is the only phenomenon limiting the aggregation kinetics. This specific situation is described by cluster-cluster aggregation model (CCA) ^{8,10}. The cluster-cluster aggregation model is one of the most studied problems of fractal growth because it describes a large amount of interesting physical phenomena in the field of colloids, polymer solutions and gels. The CCA model is usually defined on a square lattice with periodic boundary conditions in which N initial particles are distributed randomly. These particles diffuse by performing a Brownian motion on the lattice and, if they occupy adjacent sites at a given time, they stick irreversibly and give rise to larger clusters. The classical understanding of CCA focuses on the mean distribution as given by the mean-field Smoluchowski equation ¹⁰. In this equation, the approximation used is to neglect the space dependencies of all physical quantities, so it cannot provide any information about the geometrical characteristics of clusters i.e., the fractal dimension. The value of the fractal dimension of clusters obtained from computer simulation is

$$D_f \approx 1.75 \pm 0.05 \quad (d=3) \quad (10)$$

where d is space dimension.

An important amount of information on the CCA process is given by the knowledge of the mass distribution of the aggregates, both as a function of time and in the steady-state regime. One can numerically find how the mean cluster-size increases with time and even, more precisely, how the entire cluster-size distribution evolves. The cluster size distribution i.e., the number of clusters of i particles, n_i , can be written under the reduced form ¹⁰:

$$n_i \approx i^{-2} f(i/\langle i \rangle) \quad (11)$$

where $f(x)$ is the scaling function and is independent of time. One finds that the mean cluster-size varies as a power-law with time:

$$\langle i \rangle \approx t^\gamma \quad (12)$$

where exponent γ depends on the exponent α and on the dimension of space. The exponent α was introduced as a starting parameter in the cluster-cluster model and specifies how the velocities of the clusters vary with their mass, $v_i \approx i^\alpha$. The parameter α has no effect over fractal dimension of the aggregates, but has a direct influence on the kinetics and the size distribution function. Jullien and Botet ¹⁰ have shown that the reduce size distribution function is given by:

$$f_\omega(x) = x^{-2\omega} e^{-(1-2\omega)x} \quad (13)$$

with $2\omega = \alpha + (d-2)/D_f$ smaller than one. After long enough time, the time dependence $n_i(t)$ disappears and we observe a power-law behavior ⁸.

$$n_i \approx i^{-2} \quad (14)$$

This is actually the behavior predicted by the Smoluchovski theory.

5.2. Light scattering on fractal aggregates

The scattered light intensity can be obtained starting from the fractal correlation function of the particle centers. The correlation function must be multiplied by a function $g(r/R)$ that accounts for the finite extent, R , of the cluster. Function $g(x)$ has the property that $g(x) \sim 0$ for $x > 1$ and $g(x) \sim \text{const.}$ for $x < 1$. Thus, one obtains for the correlation function

$$c(r) = r^{-\alpha} g(r/R) \quad (15)$$

The scattered intensity is proportional with Fourier transform of the correlation function. It is given for $q \gg 1/R$ by relation¹⁴.

$$S(q, R) \approx (qR)^{-D_f} \quad (16)$$

and for $q \ll 1/R$ (Guinier regime)

$$S(q, R_g) = \exp(-q^2 R_g^2 / 3) \quad (17)$$

where $q = (4\pi/\lambda)\sin(\theta/2)$ is the modulus of the scattering vector and R_g is the cluster radius of gyration. Of course one need to take into account the fact that unlike the DLS techniques the correlation function is computed over a single cluster and not over a statistical ensemble.

We have chosen to use backscattering sensor since one can calibrate easily the sensor and data analysis does not require mathematical manipulation.

The relation (16) is valid in case of backscattering sensor for entire range of measurements i.e., $1/q \approx 0.2 < 1-20 \mu\text{m}$. Furthermore, the light scattered intensity for the cluster is given by relation

$$I(q) \approx M^2 S(q, R) \quad (18)$$

Bearing in mind that $M \sim R^{D_f}$, equation (18) becomes

$$I(q) \approx M q^{-D_f} \quad (19)$$

Consequently, it can be measured the aggregate mass or cluster size making use of equation (19) and knowing the aggregate fractal dimension D_f . The fractal dimension of the aggregates D_f can be obtained experimental by means of usual light scattering techniques.

We used backscattering sensor for PSD determination of an AgI colloid. The colloidal state corresponding CCA model has been achieved adding a salt into colloid that has increased the electrostatic screening and reduced the energy barrier. Fractal dimension of the aggregates has been obtained using light scattered methods and is in accord with the value resulted from the computer simulation $(1.72 \pm 0.05)^{8,10,15}$. We have waited long enough until the particle size distribution has reached the steady state behavior described by equation (14). The experimental data are plotted in figure 6 and they follow clearly the expected behavior. The number of particle counted is sufficiently large that the statistical fluctuation is negligible. The shape of PSD obtained corresponds to a power law with exponent equals to $-3.44 \pm 0.05 \approx -2D_f$. We notice a very good accord with CCA model predictions.

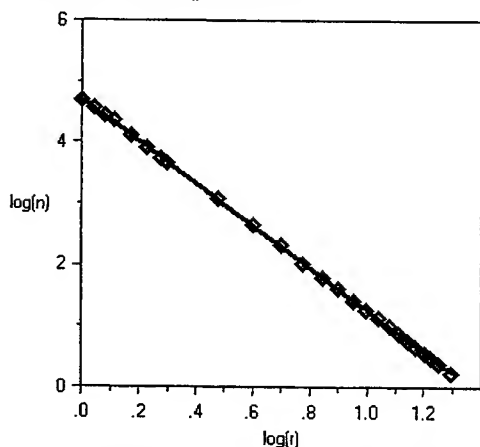


Fig. 6. The PSD obtained for AgI colloid. The slope is equal to $-3.44 \pm 0.05 \approx -2D_f$ and it satisfies the CCA model predictions.

6. CONCLUSIONS

The SPOS is ideal for measuring the detailed structure of the PSD. In the case of mostly submicron emulsions, this includes quantitative determination of the population of oversized primary particles or aggregates, located well above the mean diameter. The only significant disadvantage of the SPOS method is that it ceased to be practical or effective below approximately 0.5-1 μm , depending on the specific application in question.

The particles that are sized by SPOS are also counted. Hence, the absolute particle volume contained within a given range can be determined easily and with high accuracy.

The sensing arrangements presented in this paper, although not clearly mentioned, can work with autodilution method. The computations and experiment recommend the transmission sensor as well-suited for emulsion PSD determination while the backscattering sensor gives best results in colloid PSD measurements. We preferred to use the sensors directly immersed in solution in order to avoid suspension disturbance. Besides, one acquires spatial information about suspension locating sensors in different points in solution volume. This kind of sensors can be used to monitor different kinetic processes and to get subtle information about local fluctuation of particle size and concentration. Thus, the sensors described above are useful research tools for a wide diversity of phenomena especially in the submicron particle field.

ACKNOWLEDGMENTS

This work has greatly benefited from many enlightening discussions with Prof. Iancu Iova from Physics Faculty-Bucharest and Mihaela Stoica from National Institute for Laser-Bucharest.

REFERENCES

1. T. Provder, *Particle size distribution I and II: assessment and characterization*, , ed, Washington, DC: ACS symp. Series, 1987 and 472, 1991.
2. T. Allen, *Particle size measurement*, Third ed, New York, Chapman and Hall, 1891.
4. H. C. Van de Hulst, *Light Scattering by a Small Particles*, John Wiley&Sons, New York, 470 (1957).
5. M. Born and E. Wolf, *Principles of Optics*, Pergamon Press, New York, 808 (1959).
6. M. Kerker, *The Scattering of Light and Other Electromagnetic Radiation* (Academic, New York, 1969).
7. A. Bunde and S. Havlin, *Fractals and Disordered Systems*, Springer Verlag, Heidelberg 1991.
8. T. Vicsek, *Fractal Growth Phenomena* (World Scientific, Singapore, 1992).
9. Weitz D. A., Huang J. S., Lin M. Y. and Sung J., *Phys. Rev. Lett.* **54**, pp. 1416 (1985).
10. R. Jullien and R. Botet, *Aggregation and Fractal Aggregates*, World Scientific, Singapore, 1987.
11. P. Meakin, *Phys. Rev. Lett.* **51**, pp. 1119 (1983).
12. M. Kolb, R. Botet and R. Jullien, *Phys. Rev. Lett.* **51**, 1123 (1983).
13. B. B. Mandelbrot, *The Fractal Geometry of Nature*, Freeman, San Francisco, 1982.
14. S. K. Sinha, T. Freltoft and J. Kjems, *Kinetics of Aggregation and Gelation*, ed. F. Family and D. P. Landau, Elsevier, Amsterdam, 1984.
15. D. A. Weitz and M. Y. Lin, *Phys. Rev. Lett.* **57**, pp. 2037 (1986).

Remote sensing studies on seismic activity

Cristina Aiftimiei^{*a}, Alexandra Caramizoiu^a, Axente Stoica^a,
Aurelian Aiftimiei^b

^a Department of Remote Sensing, Institute of Optoelectronics, 111 Atomistilor Str.,
PO Box: MG-22, Romania

^b Codification Department, Ministry of Defense, Romania

ABSTRACT

This study presents the result of the application of remote sensing techniques to the seismic area analysis and monitoring. Remote sensing methodology and field studies of active faults can provide a geologic history that overcomes many of the shortcomings of instrumental and historic records. We present the result of comparing ERS-1 and optical data, and we analyze if the structural inventory (faults, lineaments) can be traced more accurately, by the help of ERS-1 data. First results show that lineaments in Landsat-TM images appear denser in shorter distances whereas ERS-1 images are dominated by the principal structures.

Keywords: remote sensing techniques, geologic applications, lineaments, seismic activity

1. INTRODUCTION

Geology and geomorphology are between the applicative disciplines most interested in remote sensing in general. The interest and efficiency of satellite remote sensing techniques can be appreciated by their contribution to the fundamental knowledge's in applicative sciences. The Earth's sciences regard the processes and multi-temporal, multi-scale objects that can be analyzed first at the elementary level.

It was proven the utility of remote sensed images in major applications as oil and mineral exploration, hydrology, geologic hazards (seismic hazards, faults, volcanoes, floods, soil erosion) and land use.

Geologists have used aerial photographs for decades as data bases on which to map rock units (stratigraphy), study the expression and modes of origin of landforms (geomorphology), determine the structural arrangements of disturbed strata (folds and faults), evaluate dynamic changes from natural events (floods, volcanic eruptions), and seek surface clues (such as alteration and other signs of mineralization) to subsurface deposits of ore minerals, oil and gas, and groundwater. With the advent of satellite imagery, geoscientists now can extend that use in two important ways:

1. large area or synoptic coverage allows them to examine (in single scenes or in mosaics) the geological portrayal of the Earth on a regional basis;
2. analyze narrowly defined spectral bands quantitatively.

These quantitative analyses can be carried out in terms of numbers either raw digital counts, (DNs), radiance and reflectance.

These special computer processing routines can merge different types of remote sensing products (reflectance images with radar or with thermal imagery) or combine these with topographic elevation data and with other kinds of information (thematic maps, geophysical measurements, chemical sampling surveys). While these new space-based approaches have not yet revolutionized the ways in which geoscientists conduct their field studies, they have proven to be indispensable techniques for improving the mapping process and carrying out practical exploration for natural resources on a grand scale.

*Correspondence: E-mail: caifti@yahoo.com; Fax: 423.25.32; Tel: 780.66.40

2. SEISMIC CHARACTERIZATION OF ROMANIAN TERRITORY

An earthquake is a very complex physical phenomenon, characterized by a chaotic and violent movement of earth superficial layers, and because of his devastating consequences on peoples and material assets it represent one of the biggest natural calamity known in our days. Because of their unforeseeable appearance and generating causes, men couldn't control the earthquakes, which, in a very short period of time, can produce huge damages and disasters on works that took centuries for men to build up.

The alpino-charpatian region represents 63 % of Romanian territory and consists of mountainous areas (Carpatii Orientali, Carpatii Meridionali, Apuseni mountains), bounded by depressions (Avanfosa Carpatica, intermountain depression of Transilvania, the eastern limit of Panonian Depression).

From the point of view of plate tectonics, the Moldova platform represents the edge of the euro-asiatic plate, the Moesian platform is a sub-plate placed in front of Carpathian and Balkan Mountains, the Transilvania's depression is a sector of a inter-alpine sub-plate, continued by the edge of Panonic Depression (Fig. 1).

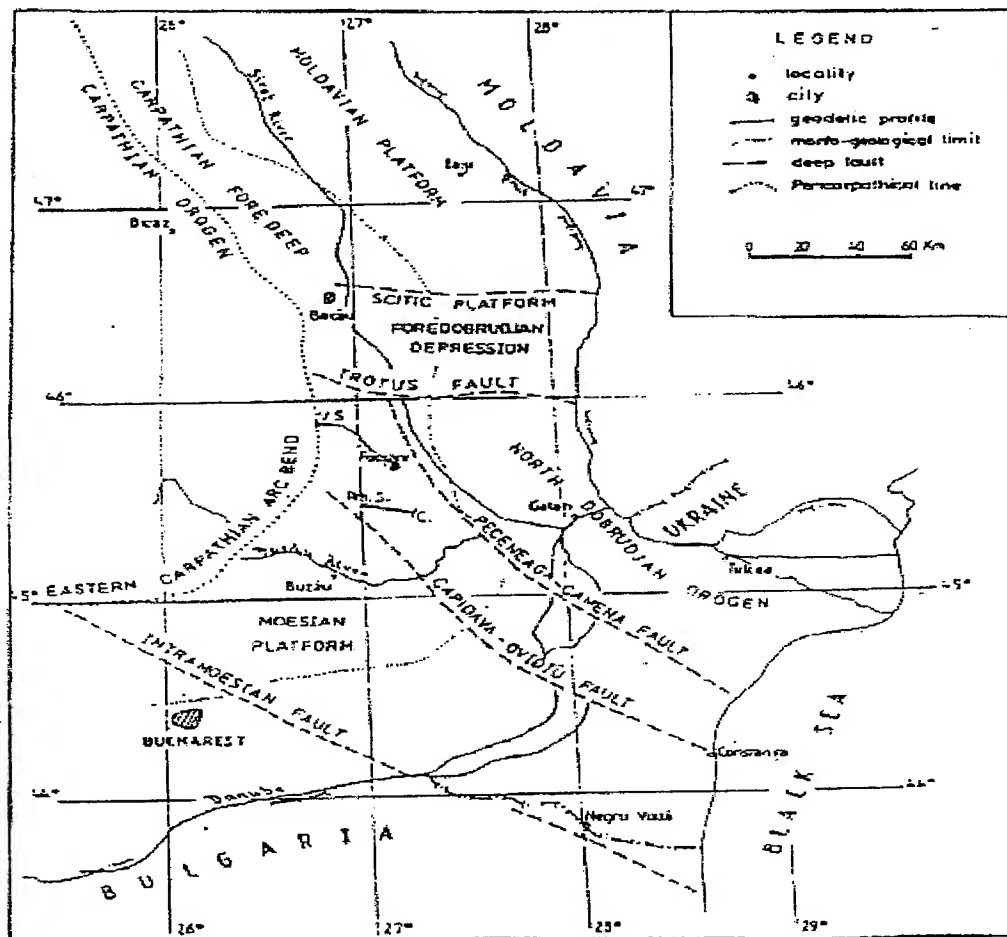


Fig. 1 Neighbours of Moldavian platform

The most important epicentre zone of Romania is the Vrancea region, characterised by the frequent production of intermediate depth earthquakes (90-180 km), the most frequent been at 130-150 km.

The position of Vrancea epicentre zone is related to the sub-crust processes, whose character results indirectly from the regional geologic structures, which agrees with the idea of heterogeneity of earth's crust. Indication about this are given by:

- the emphasised curve of the Carpati Orientali;
- the fact that in front of the SW corner of east-European platform intersect two lineaments with continental dimensions – Podolic, direction NW-SE, and Tetys direction, oriented SW;
- the extension to SE of the neogenic volcanic chain crosses the same region;
- the identification of a major change in the distribution of gravitational anomalies.

In this situation it looks normal the position, on seismic plane, of earthquakes, and, on structural level, of a tendency of axial plunging of old geologic structures.

Fig. 2 present a Landsat (TM4/TM2/TM1) image of Vrancea region.



Fig. 2 Landsat (TM) image

3. THE USE OF REMOTE SENSING TECHNIQUES FOR SEISMIC STUDIES

The main use of remote sensing techniques in geologic exploration is based on a landscape analysis with methods inherited from photo-geology. Remote sensing techniques allows the discrimination of geologic objects and emphasises some singularities.

Remote sensing techniques are a set techniques that differentiate by vector type (plane, satellite or space ship), the acquisition way (analogical or numerical, active or passive), spatial resolution, spectral domain, and the observed surface.

Having in view the number of satellites in orbit, geologists have a certain freedom in choosing the data type best suited to solve their problems. There are a number of criterions that can guide this choice. First of all, there are general criterions, geographic and climateric, studied surface, scale. There are also, thematic criterions, application type, and studied indices.

There are some examples that can guide the choice of data type:

- when the study area is big and the scales are of the order 1/500000 or 1/250000, the proper data are Landsat TM and MSS data;
- when the area is small or medium, and the scales of the order 1/100000, 1/50000 or 1/25000, is reasonable to use SPOT-HRV (20 m resolution) or Landsat TM data (30 m resolution);
- if the research is based on a wide spectral range from blue to thermal IR, then the TM data are well suited. After the nature of searched objects, the specificity of spectral bands is as follows:
 - band 1 (0,45-0,52 μm): penetrate water, materials in suspension, soil-vegetation;
 - band 2 (0,52 – 0,60 μm): vegetation strength;
 - band 3 (0,63 – 0,69 μm): structural analysis;
 - band 4 (0,76 – 0,90 μm): vegetation stress assessment determined by geologic phenomenon, detection of iron oxides;
 - band 5 (1,55 – 1,75 μm): indices of vegetation and soil water content;
 - band 6 (10,40 – 12,50 μm): discrimination of silicate and non-silicate rocks, soil water content, vegetation stress assessment;
 - band 7 (2,08 – 2,35 μm): discrimination of some rock types.
- When the research needs a three-dimensional observation, the only space source is the HRV instrument on SPOT satellite, which allows the acquisition of a stereoscopic couple;
- When the study is placed in a equatorial area or with a big nebulosity, the acquisition characteristics in any moment of radar makes of him a privileged instrument (ERS-1, 2, RADARSAT).

Until now, the methods for investigating the earth movements were based on photo interpretation, used as a completion of in-situ measurements. Remote sensing techniques were little used because the spatial data, before SPOT satellite was on orbit, didn't have the needed characteristics, their spatial resolution not been consistent with the pixel dimension (MSS), where the system doesn't allow stereoscopic acquisition (TM).

A new method, called "Q & D" method, was developed for earthquake prediction in China. The data from the thermal infra-red channels of AVHRR instrument undergoes density slicing to determine the brightness temperature and then undergoes geometric correction using information on the atmospheric temperature and pressure. The data is then geo-referenced and calibrated in order to produce a thermal infra-red map. Analysis of these maps is performed in order to identify temperature anomalies which may be indicative of future earthquake activity. From an anomaly's character, the time, location and magnitude of an earthquake may be predicted.

The main steps of the process are as follow:

- identify isolated area of thermal infra-red increase;
- track the direction of the development and movement of the thermal infra-red increase area;
- identify the temperature increase phenomenon as a precursor of earthquake by taking into consideration the effects of topography, geotectonics and present tectonics stress field;
- provide a three element prediction (earthquake time, location and magnitude) by considering the distribution of active fractures and seismic belts.

In Fig. 2 we can see the lineament present in the Vrancea region image, which we obtained with an edge detection algorithm (Sobel algorithm).

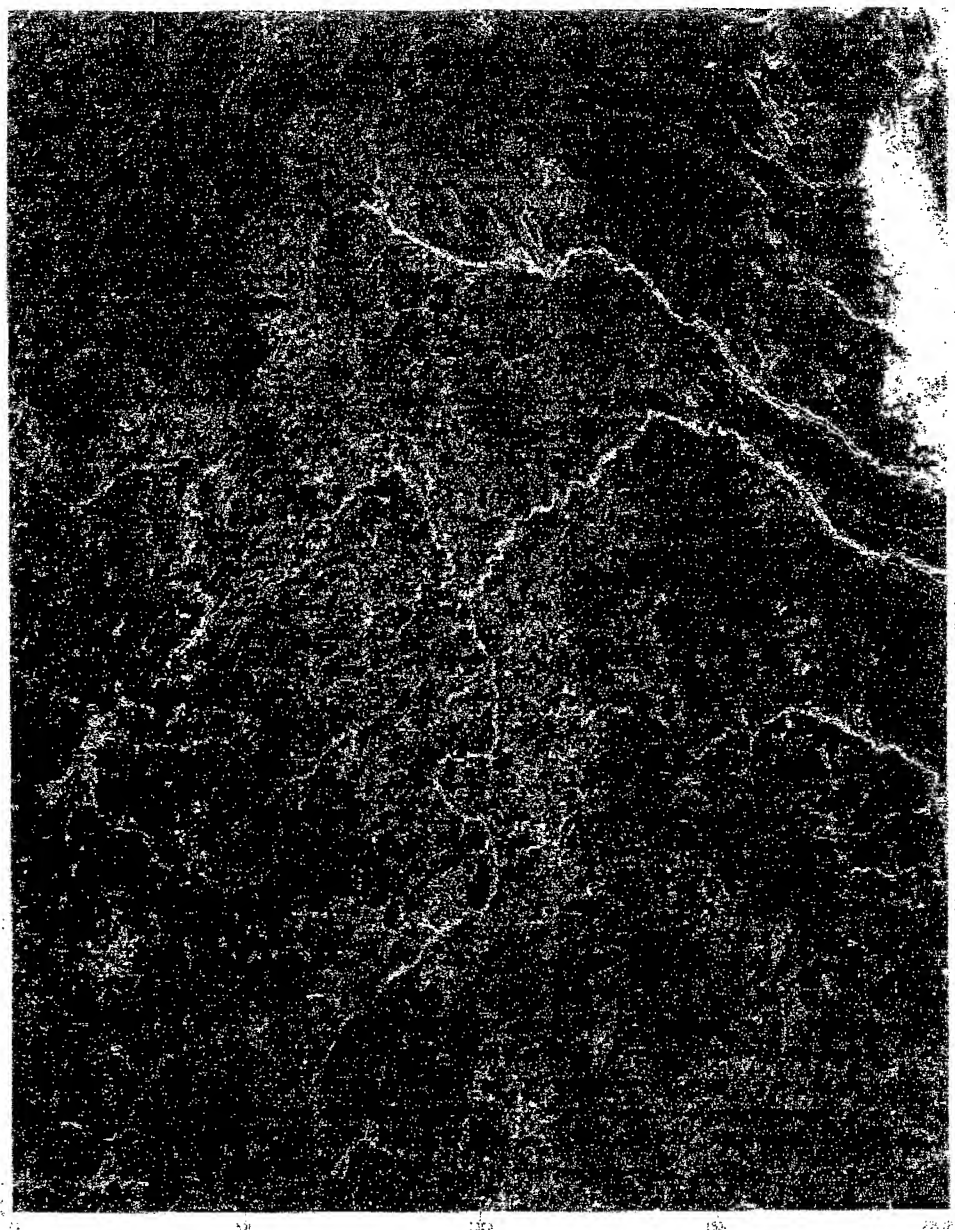


Fig. 3 Edge detection on the image of Vrancea region

4. CONCLUSIONS

Satellite data in the optical range (visible – IR) supplied by Landsat MSS and TM sensors, as well as those from microwave domain, supplied by ERS-1&ERS-2, SPOT, JERS, etc, facilitate geological structure analysis and allow the surveillance of global and regional faults. Satellite remote sensing images allows the seismo-tectonic maps up-dating, on areas with a high risk of earthquakes: deep and young quasi-tectonic faults, the change of the direction of movement of tectonic plates, etc.

The comparative analyse of these images in different spectral domains, completed with geologic and geophysical information allow the seismic risk assessment. It is then necessary to create an integrated system of satellite data, completed with geologic information, for monitoring the spatio-temporal evolution of seismo-tectonic phenomenon's, with the purpose of facilitating the identification of vulnerable area, possible earthquakes generators, as a result of gradual gain of tension due to tectonic plate and sub-plate movement.

REFERENCES

1. John Richard, *Remote Sensing Digital Image Analysis, An Introduction*, Springer Verlag, 1986
2. Pratt William K., *Digital image processing*, John Wiley & Sons, NY, 1978
3. Stephen P. Banks, *Signal processing, image processing and pattern recognition*, Prentice Hall, London, 1990

Neural networks for vegetation stress assessment

Cristina Aiftimiei^{*a}, Alexandra Caramizoiu^a, Axente Stoica^a,
Aurelian Aiftimiei^b

^a Department of Remote Sensing, Institute of Optoelectronics, 111 Atomistilor Str.,
PO Box: MG-22, Romania

^b Codification Department, Ministry of Defense, Romania

ABSTRACT

In digital imagery, picture elements which contain two or more land cover classes are called mixed pixels. Small strips or patches of woody vegetation, typical landscape features in many farming areas, are frequently not detected by standard computer-assisted classification of digital imagery because such landscape features are smaller than the pixel size of the image and are mixed with other classes.

Development of advanced techniques for improving remote sensing image classification accuracy is essential for deriving reliable land cover information for natural resource applications. Artificial neural networks are among the optimal tools for this type of application. Neural network techniques were developed for processing two dates of Landsat TM data, and a measure of image texture for the purpose of deriving more accurate land use and land cover information. Classification results derived from the neural network approach overall were nearly 10% more accurate than those derived previously using a conventional maximum likelihood approach.

Keywords: artificial neural networks, remote sensing, classification, land use, land cover, filtering

1. INTRODUCTION

The general objectives of this paper were to describe, demonstrate and test the capability of artificial neural networks for satellite image classification of forest areas. For this paper we have used two Landsat images and one SAR image.

Artificial neural networks can be seen as highly parallel dynamical systems consisting of multiple units that can perform transformations by means of their state response to their input transformation. How the transformation is carried out depends on the neural network model and its way of learning the transformation. Neural networks learn by examples. Usually, a neural network is presented iteratively with a set of samples, known as the training set, from which the network can learn the values of its internal parameters.

A lot of effort has been done in laying the theoretical foundations of neural networks and the links between statistical and neural methodologies. There are some approaches that differentiate neural networks and statistical methods:

- problems and model complexity
- goal of modeling
- no assumption about data distribution/robustness and quality of prediction estimates

There are at least four main aspects that should be considered in any neural network application:

1. preparing the data;
2. designing the network architecture;
3. estimating the parameters, i.e. training a network for a given problem;
4. assessing the performances of the network.

^{*}Correspondence:

E-mail: caifti@yahoo.com; Fax: 423.25.32; Phone: 780.66.40

2. TEST SITE DESCRIPTION

The ecological potential of Bucharest and especially of the Ilfov county allows the development of different vegetal associations, which can be integrated to the deciduous forests zone. Human activities lead to the replacement, on large areas, of the natural vegetation with agriculture cultures, buildings, etc. The studied zone is situated in the east of Ilfov county, represented by "islands" of oak forests, which alternate with cultivated areas. The Cernica forest, situated in the north-east of Bucharest was chosen taking into consideration that we were interested to follow the changes of a deforested zone



Fig. 1 Initial image of Cernica forest

3. DATA AND DEVICES USED

In order to better manage all the information available on the study area, data acquired have been integrated in a unique database. This information consists of thematic maps from cartography, land use map from classification of remotely sensed data and ground radiometric profiles.

- The study has used two Landsat TM data of 20/08/93 and two ERS-1 SAR data of 27/04/93. The ERS-1 image was acquired in PRI format and Landsat TM image at "system corrected" level.
- Topographic maps over the selected area.
- TITAN 3000 Super computer, running PCI – EASI/PACE software.

4. INPUT DATA AQUISITION AND PREPROCESSING

4.1 Registration

The registration and geocoding were first carried out between existing maps (topographic maps) and the Landsat TM data. It was produced by digitizing (collecting) ground control points – GCP's on the maps and on the TM data. 28 GCP's were used for the third order polynomial coefficient calculations, with cubic convolution as resampling method. The RMS error was 0,71 pixel. The relative accuracy of the geocoding was verified by scanning parts of the topographic maps and superimposing TM band 4 on them.

The ERS-1 SAR PRI data registration was done in two steps. One image was chosen as reference. Due to the very good geometry, only translations in X and Y directions were necessary to achieve a satisfactory fit. Since the ERS-1 satellite has a very stable orbit, images from repetitive orbits can be registered with only few match points.

Difficulties were encountered at the second step, during the ERS-1 SAR PRI data geocoding, in identify enough GCP's. For this reason, the topographic/SAR image GCP collection was difficult despite the topographic maps recently updated. 18 GCP's were selected with RMS error of 0,73 pixel.

Finally the ground radiometric profiles were included into the database by using a registration between known points on map and users coordinates.

4.2 Speckle filtering

From the light coherency theory, the probability density function (pdf) of an image of pure speckle is an exponential decreasing function. The mean and the standard deviation of this pdf are identical and thus the coefficient of variation $C_\mu = \sigma/\mu$ is equal to unity. C_μ represent a certain measure of the image homogeneity and can be used as a textural index. However, the convolution of single looks (three looks in SAR PRI) changes the exponentially decreasing pdf to a Gamma function. In most cases a multiplicative speckle model is assumed. Different methods have been tested on the selected zone.

The *Lee filter* is an adaptive filter based on different noise models. The Lee filter for multiplicative noise has for the resulting gray level value R of the smoothed pixel the following implementation:

$$R = 1 + K(CP - UI) \quad (1)$$

where

$$K = 1 - (MVAR/U^2)/(QVAR/I^2) \quad (2)$$

The multiplicative noise variance is calculated from local statistics in the filter window: $MVAR = (SD/I)^2$. The value of mean multiplicative noise is usually 1. QVAR is the variance of filter window, I is the mean gray level in the filter window, U is the mean multiplicative noise, CP is the central pixel in filter window, MVAR is the multiplicative noise variance and SD is the standard deviation of the noise in the filter window. *The results are presented in Figure 2.b.*

Frost filter uses an adaptive filtering algorithm which is an exponentially damped convolution kernel which adapt itself to features by using local statistics. The adaptive filter computes a set of weight values for each pixel within the filter window surrounding each pixel. The Frost filter differs from the Lee filter with respect that the scene reflectivity is estimated by convoluting the observed image with the impulse response of the SAR system. The impulse response of the SAR system is obtained by minimizing the mean square error between the observed image and the scene reflectivity model which is assumed to be an auto-regressive process. The damping factor for adaptive filtering depends on the non-filtered image and require trial-an-error experiments to determine the best value. *The results are presented in Fig. 2.c.*

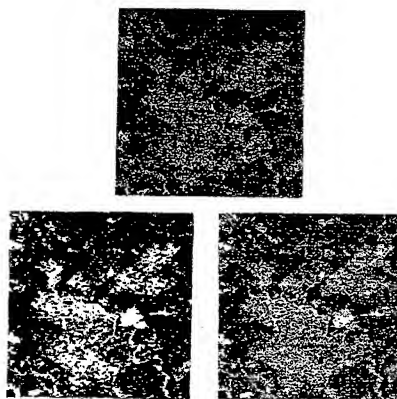


Fig. 2 Results of filtering algorithms

5. DATA ANALYSIS

5.1 Optical data calibration

Rectifying image data to remove as much as possible the degrading effects of the atmosphere entails modeling the scattering and absorption processes that take place and establishing how this determine both the transmittances of the various paths and the different components of sky irradiance and path radiance. When available this can be used to relate the digital count values given for the pixels in each band of data, to the true reflectance of the surface being imaged. A method to estimate the reflectance R is described by Richards [1] for the case of Landsat MSS data. It needs the atmospheric conditions – temperature, relative humidity, atmospheric pressure, visibility – at the time of overpass. Froster [2] gives source materials and tables to assist in the computations. We have used the same algorithm for the Landsat TM data.

5.2 Optical data classification

Maximum Likelihood was the first method used in order to classify the Landsat TM data. The results of this classification are used as a reference image for the neural network approach. *The classification results are presented in Fig. 3.*

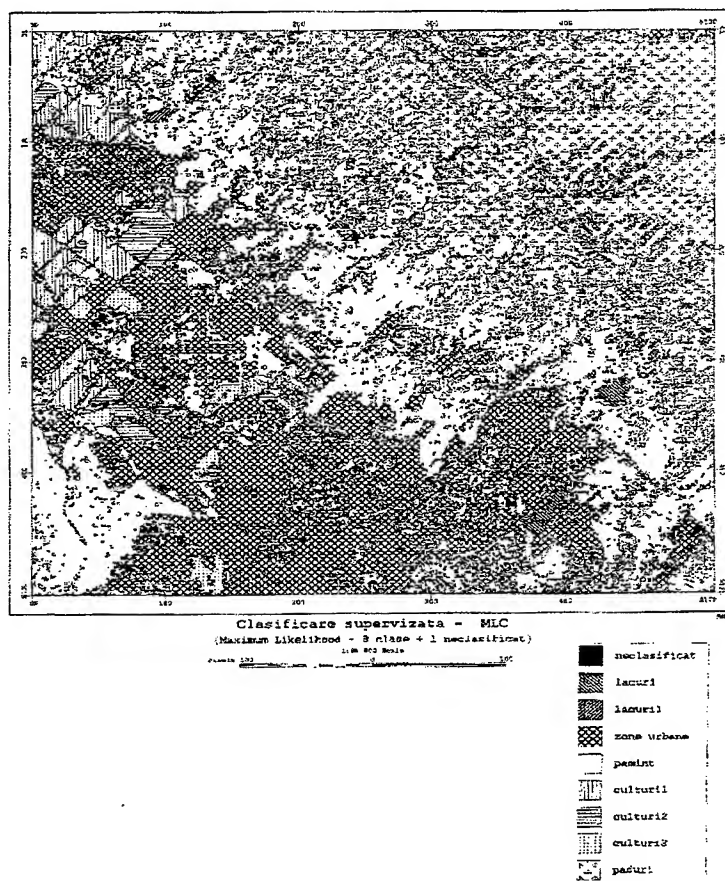


Fig. 3 Unsupervised classification

5.3 Neural network classification

One of the first papers to appear in the literature concerning the application of neural networks in the analysis of remotely sensed images was published by Key et. al. They described a system to classify merged 5-channel AVHRR data and 2-

channel SMMR data over Arctic regions into four regions and eight cloud classes using back-propagation neural networks. They compared their results to those from a maximum likelihood procedure and manual interpretations and discussed the various merits and drawbacks of neural networks.

Gualtieri and Withers and Kamagar-Parisi et al. Described a second important application of neural networks in remote sensing: clustering of multi-spectral data and indicated the potential of these approaches for clustering very high-dimensional imagery such as from imaging spectrometers. Kamagar-Parisi et al. used the Hopfield model of neural networks to perform clustering in a multidimensional feature space.

Foody et. al employed neural networks trained with the back-propagation algorithm to classify agricultural crops from SAR data. Their results show that in general neural networks perform better than statistical classifiers. However when a priori information about class occurrence was available to the discriminate analysis the performance of both methods was comparable.

Neural networks are computational systems, either hardware or software, which mimic the computational abilities of biological systems by using simple, interconnected artificial neurons. A neuron is the fundamental building block of the nervous system. Artificial neurons are simple emulations of biological neurons. They take input information, perform very simple operations on this data, and selectively pass the results on to other artificial neurons.

The back-propagation network (or back-propagation perceptron) is probably the most well known and widely used neural network system. The term "back-propagation" refers to the training method by which the connection weights of the network are adjusted. The back-propagation network is a type of multilayer feed-forward network. Other types of feed-forward networks are the perceptron, the ADALINE and MADALINE networks, the Boltzmann machine, and the Cauchy Machine.

The neural network programs NNCREAT, NNTRAIN, and NNCLASS process for multi-spectral image classification based on training sites. The neural network classifier provides an alternative to using the maximum likelihood classifier program (MLC) and other classifiers from the PACE Multispectral Analysis package. Neural network classifiers process imagery by pattern recognition. The programs use a back-propagation network that learns using the Generalised Delta Rule.

NNCREAT creates and initializes a new neural network segment for back-propagation neural network processing. This neural network segment can be trained to recognize classes with the NNTRAIN program. Once the neural network has been trained, it can be used to classify imagery with the NNCLASS program. The NNREP program is used to produce a report for a neural network segment.

NNTRAIN trains an existing neural network segment created by NNCREAT for back-propagation neural network processing using sample data from training sites. When the neural network training reaches a specified maximum acceptable error or the maximum number of iterations, training terminates. NNCLASS would use the trained neural network to classify the image.

Back-propagation neural networks need to be trained to learn the input patterns of interest. When the neural network segment is first created by NNCREAT, the weights for the inter-unit connections are initialized to random values in the range of -0.5 to $+0.5$. If a classification will be performed with NNCLASS before training the neural network with NNTRAIN, the classification results would be completely random. (NNCLASS does check the number of training iterations and will not run if the neural network is untrained).

Typically, back-propagation neural networks require a number of iterations (100 to 1000) before the interconnection weights stabilize enough to recognize the input patterns. If NNTRAIN exits when the specified number of iterations (MAXIT) have run and the specified error (MAXTERR or MAXIERR) has not been met, then the network may have to be trained again with NNTRAIN. If it still does not converge, the neural network may have to be redefined (using different input channels, more accurate bitmaps, more input and hidden units, or more samples). The learning and momentum rates affects how quickly the neural network stabilizes. A high learning rate (0.9) would converge quickly, but may exit prematurely. A low learning rate (0.1) would take more iterations to train, but should not exit prematurely.

NNCLASS classifies multispectral imagery using a back-propagation neural network created by the NNCREAT program and trained by program NNTRAIN. *The classification results are presented in Fig. 4.*

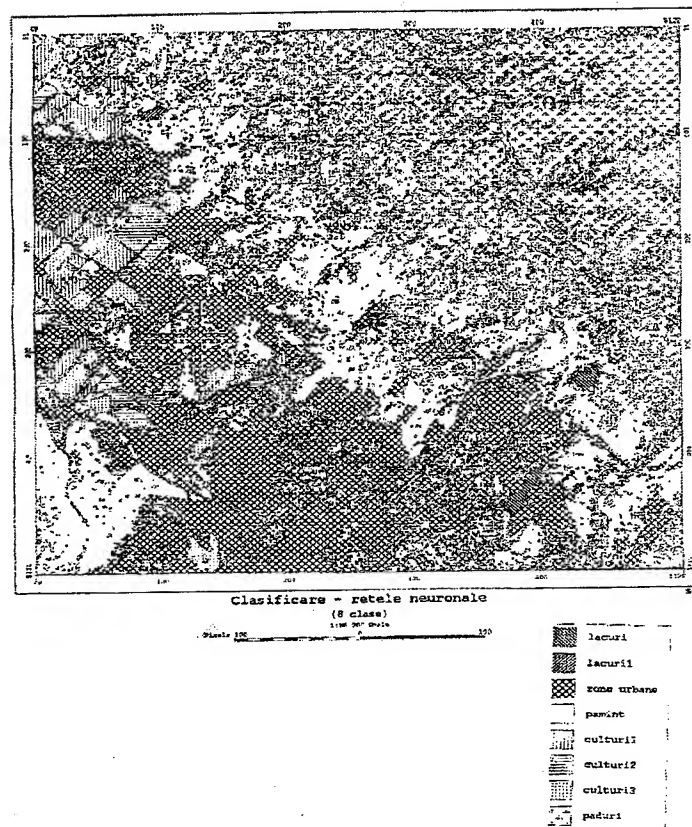


Fig. 4 Neural network classification

6. CONCLUSIONS

The paper has demonstrated the possibility of classifying remote sensed images from different sources by using back-propagation neural network based processing techniques. For this reason we have developed a methodology for automatic classification of multi-temporal, multi-sensor satellite data. Neural networks offer a number of advantages over the conventional statistical classifiers, for example are distribution free and more robust. They also offer a reliable way for combining multi-sensor imagery and can potential be used to integrate auxiliary data into satellite image analysis.

REFERENCES

1. John Richard, *Remote Sensing Digital Image Analysis, An Introduction* Springer Verlag, 1986
2. Pratt William K., *Digital image processing*, John Wiley & Sons, NY, 1978
3. Stephen P. Banks, *Signal processing, image processing and pattern recognition*, Prentice Hall, London, 1990
4. D. Dumitrescu and H. Costin, *Rețele Neuronale. Teorie și Aplicații*, Ed. Teora, 1996
5. P. Antognetti and V. Milutinovic, *Neural Networks. Concepts, Applications and Implementations*, 1-4, Prentice Hall, 1991

Quality audit of optoelectronics systems

Letitia Tanase*

Institute of Optoelectronics IOEL-S.A., Str. Atomistilor nr.1, Bucharest – Magurele

ABSTRACT

The quality audit of a product (optoelectronic system) serves to evaluate the accordance of its quality characteristics with customer's requirements or specified in references documents. On this occasion the reference documents are verified, in order to establish if these are proper to achieve the stipulated objectives in the domain of products quality. The audit is not a simple examination of product's quality, but it is and effective evaluation quality measures concerning the respective product. Based on the results of quality audit it can be settle necessary improvement measures. The process quality audit serves to evaluate the accordance of the process with customer's requirements or with specified requirements in the references documents. In order to establish if the reference documents are proper to achieve the stipulated objectives, these documents are verified, just like in the case of the quality audit of product. The quality audit of a process presents also the effective measures to ensure the quality of the process, establishing the necessary corrective and improvement measures. In order to perform the quality audit of the product/process, the procedures of quality system, the specification of the product, the documents, the manufacture and inspection means, the documents concerning the development, supervision and inspection of the process and also the requirements which refer to the qualification of the involved personal are verified.

Keywords: quality audit, quality control, quality assurance

1. INTRODUCTION

Quality audit: It is a systematic and independent examination having the aim to determinate is the activities concerning the quality and the results satisfy the dispositions established, the dispositions are effectively implemented and if these are proper to attain the objectives (Fig.1).

1. *The quality audit applies in a typical mode, but not only, to a quality system or to some to its elements, to the processes or services. This kind of audits are named "quality system audit", "quality audit of the process", "quality of the product", "quality audit of the service", etc.*
2. *The quality audits are performed by personal don't having responsibilities in the audited areas, but it is rather that they cooperate with the personal who work in these areas.*
3. *One of quality audit aims is to estimate the improving necessity or corrective actions. The audit doesn't have to be mixed up with "supervision" or with "inspection", activities, which are performed in order to control the process or to accept the product.*
4. *The quality audits can be performed internal or external aims.*

The internal quality audits serve especially to ensure and to improve the capability for quality of an organization. *The external quality audits* serve to demonstrate the capability for quality (Fig.2)^{1,5}.

The systematic and independent examination^{3, 6} performed about the activities and the results concerning the quality of products and processes has the mission to offer data, information's and to establish causes and suitable measures to attain a be of the following aims:

1. Determination of the conformity level of products/processes with the conditions specified in the reference documents (standards, technical specifications, manufacture documents, etc.).
2. Determination/ evaluation of the efficiency of the quality assurance measures concerning measures concerning the respective product (optoelectronic system).
3. Improving the quality of product/ process by implementation of corrective and preventive resulted measures.
4. To offer to the management the data in order to analyze the nonconformities and their causes.
5. To determine the adequate moment to require the certification of the product.

* Correspondence: Phone: (401) 780.66.40; Fax: (401) 423.25.32

Quality audit_{is}

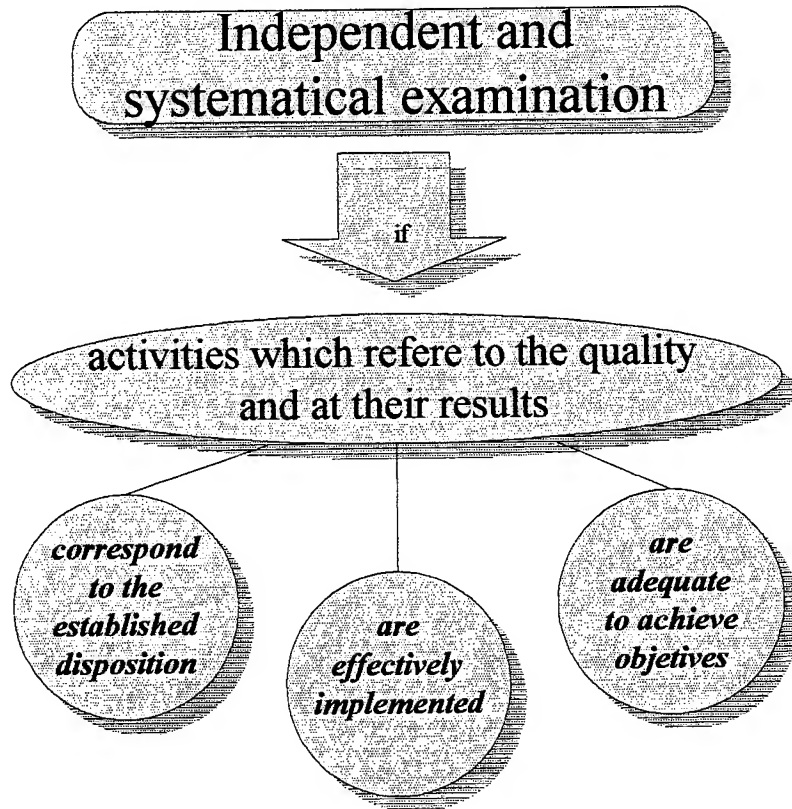


Fig. 1 Quality audit definition

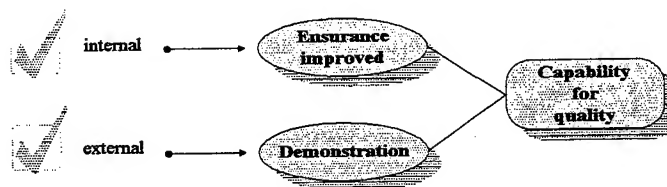


Fig. 2 The audits serve first

The audits can have different forms: 2, 8, 10

- **The system audit**, verify if the quality system is in accordance with the reference standard from SR EN ISO 9000 series. The system audit is composed of the audit documentation and the audit of implementation.
- **The audit of organization** verifies if the organization has the necessary equipment and resources to implement the politics and to achieve the declared objectives.
- **The audit of documentation** verifies if the documented practices implement the approved politics and the most important requirements of standard.

- **The audit's implementation** verify if the documented practices are respected and if some undocumented practices which influence the quality exist; it is formed by two parts :
 - the first is addressed to the management and to the implementation of the strategic plans ;
 - the second is addressed to the personal and to the implementation of the procedures.
 - **The audit of process** verifies if the processes, which have as, result products or services are performed in defined limits.
 - **The audit of product or service** verifies if the resulted products or services achieve the specified requirements.
- The quality audit of an opoelectronic system is an audit of quality of product.*

We have to make a distinction between the preliminary analysis (1) and the audit on a certain location (2), which is the right audit of quality (Fig.3). The preliminary analysis consists in a verification of the concordance between the product's documentation and the specified requirements/ customer's requirement^{7,11}.

According to the definition of the AUDIT, an audit made at a certain location establish the activities and the results concerning the quality fulfill the basic requirements and are effectively implemented and are proper to fulfill the tasks. We start form the assumption that based on a set of good preliminary results, the activities referring the quality respects the requirements of the standards. There is a difference between the preliminary analysis and the audit. So, during the preliminary analysis we have to make a complete check of documentation. The audit at a specified component of an organization can be made by "pick sample" procedure (Fig.4).

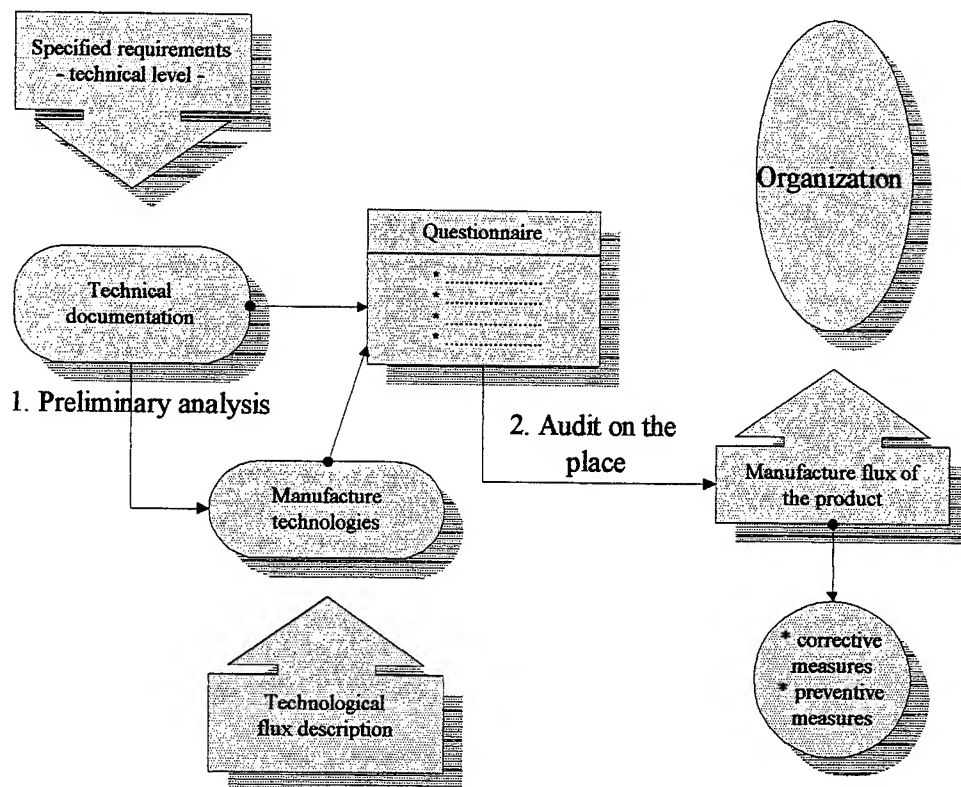


Fig. 3 A way to perform a quality audit

PRELIMINARY ANALYSIS AND THE AUDIT MADE AT A CERTAIN LOCATION

- **PRELIMINARY ANALYSIS**
All the existent documentation is verified
- **THE AUDIT MADE AT A CERTAIN LOCATION**
It is a type of examination by sampling
 - ✓ A sample of a population
For example drawings, etc.
 - ✓ A sample from life cycle of the product
For example a command, etc.

Fig. 4 The audit made at a certain location – of examination by sampling

A type of examination by sampling is, for example:

- The identification of documentation of the components, etc;
- Calibration's registering for inspection and testing tools;
- Checking of the endorsement of drawings, specifications, inspections plans
- The existence of the inspection instructions at the inspected zones;
- The existence of the work instructions at the work position.

A different type of examination by sampling is the representative selection for example:

- Sampling of a series or of a type of row material supplied and tracking on it during the manufacturing process till to the delivering of the final product, through the whole life cycle of the product.
- We can choose for example an assembly drawing which will be check concerning all the detail drawings, including analysis and endorsement, modifications, the distribution process, the with draw all process of the unvalued drawings and the products manufactured according to this assembly drawing.

During the audit at a certain location there is perform an examination (Fig. 5) using an intensive asking procedure together with the analysis of the documents and activities observations and a final meeting we can find correct data or collect proofs.

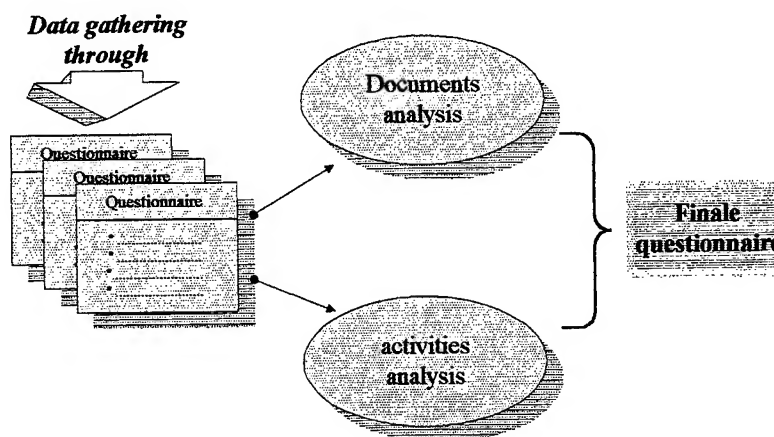


Fig. 5 Examination during an audit at a certain location

2. THE DETERMINATION OF THE EFFICIENCY OF THE SYSTEM

There are two dimensions of the efficiency: the results you get and the efficiency of the method you use to establish the efficiency. There are few methods which can be used to establish the efficiency:

- The audit of the quality
- The tracking of the performance
- The costs of the quality
- Feed-back from customers

Efficiency means to fulfill in good conditions the correct activities.

The audits have to be continually repeated based on a certain reason. There is well known and proved by a large experience that the efficiency of the quality management diminishes in time because the procedures are not very carefully tracked. This evolution is represented by a curve "saw teeth" which justifies the supervision audits (Fig.6). The supervision audits lead to an improvement of the quality through small steps.

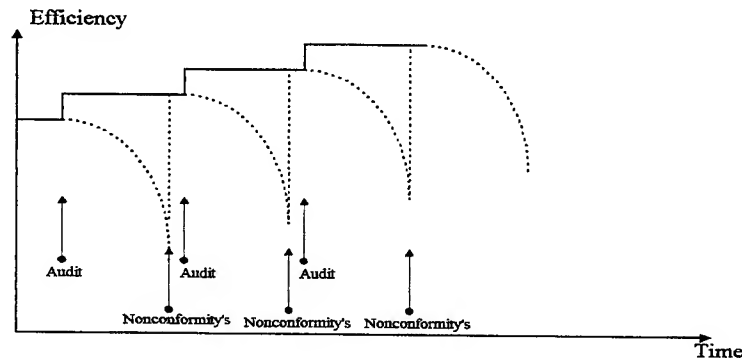


Fig. 6 The "saw teeth" effect

If the system allows to the management to stop the manufacture of some products unnecessary on the marked, to anticipate the customers' needs before the competitors, to reduce the losses (50 %), to achieve all the delivery conditions established with the customer, we can appreciate that the system is efficient.

2.1 Importance of the activity

The importance of the activity has to be established concerning the effect, which the nonconformity could have regarding the planning. For example: if the modality to complete the specifications (for provisioning) is fundamental, this activity has to be audited. The importance is applied too for something, which can seem a minor decision in the planning or design activity, if these decisions are wrong some major problems can appear later^{10, 12}. Each audit is an examination process of a product to establish if it achieve or not the requirements. The achievement makes possible the acceptance or the certification (when any nonconformity's don't was founded) - Fig. 7. The statute and the importance of activities determine the periodicity of the audits.

2.2 The independence of auditors

Auditor: A person who has the skill to perform quality audits.

1. In order to perform a quality audit, the auditor has to be authorized for that audit.
2. Any auditor who is nominated to lead a quality audit is named "chief auditor".

It is essential that the auditor have direct responsibilities in the audited activity. There are many alternatives:

- the auditors can be from the same department in which the activities are audited with the condition that they aren't responsible for the audited activities ;
- independent departments can be organization which have qualified auditors ;
- the implementation audits can be performed by specialized the personal, supervised by a qualified auditor.

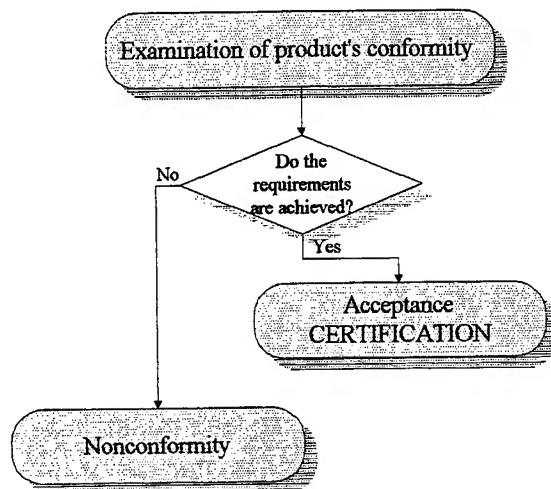


Fig. 7 Examination of conformity

3. THE PRESENTATION OF THE AUDIT'S CONCLUSIONS

The audit report must contain the audit's conclusions, the conformities and the nonconformity's, as well, and has to be presented to the manager of the audited zone, an also to his superior manager. A finding of the audit is a situation, established during the quality audit and demonstrated by an objective proof. (**Objective proofs:** information, records or the realization of the facts whether qualitative or quantitative, which refer at the quality of an entity or a service, or at the existence of a quality system element's implementation, which is based on observations measurements or trials that can be verified)^{3, 7, 10}. This kind of situation can be established by completing questionnaires, analyzing the documents, observing the activities and verifications (Fig. 8).

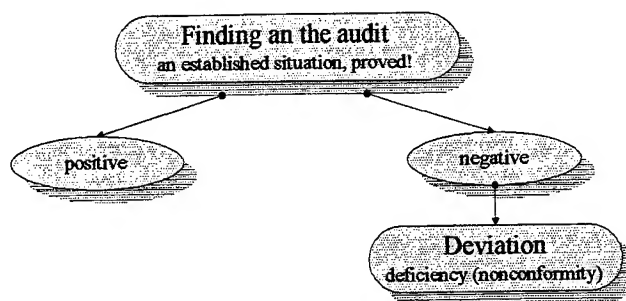


Fig. 8 Finding an the audit

There are different kinds of nonconformities (**Nonconformity:** unsatisfaction of the specified conditions) - Fig. 9:

- not carrying out the standard's requirements;
- a disposition which is not suitable (to attain the objectives);
- an activity which doesn't correspond to the dispositions;
- an unimplemented disposition effectively.

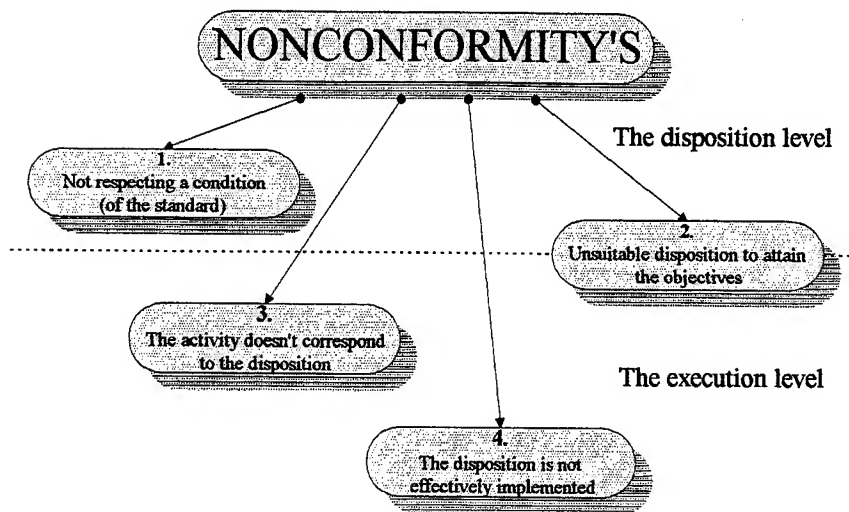


Fig. 9 Different kinds nonconformity's

The auditor's responsibility is to identify the nonconformities. All the findings/nonconformity's, which are pointed out, are clearly established based all objective proofs (**Observation**: a finding of the facts, made during an audit and proved by objective proofs). The proofs are obtained by:

- discussions;
- the documents' examination;
- observing the activities and the situations.

Un example of possible causes of nonconformity is presented in Fig. 10.

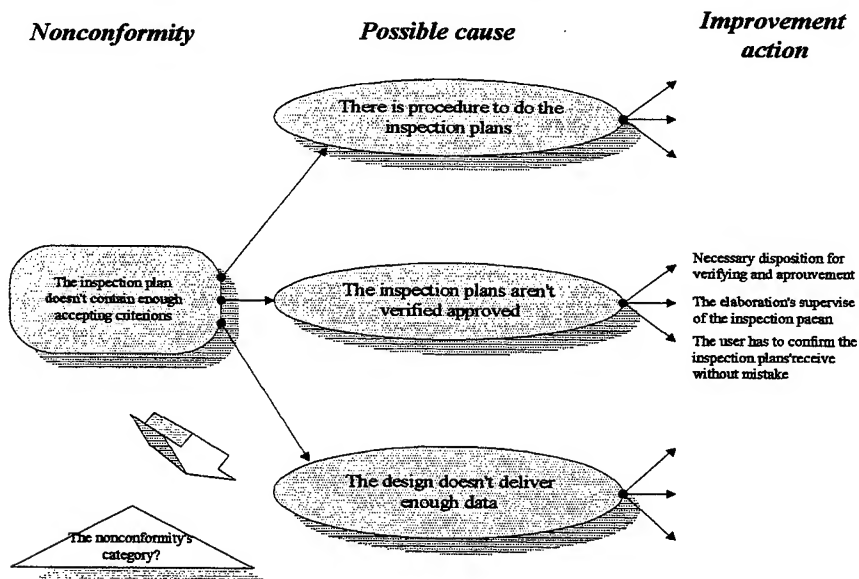


Fig. 10 The possible causes of an nonconformity

In order to evaluate a nonconformity it is necessary to have large and considerable knowledge in specialty and experience concerning the interpretation and understanding the requirements (Fig. 11).

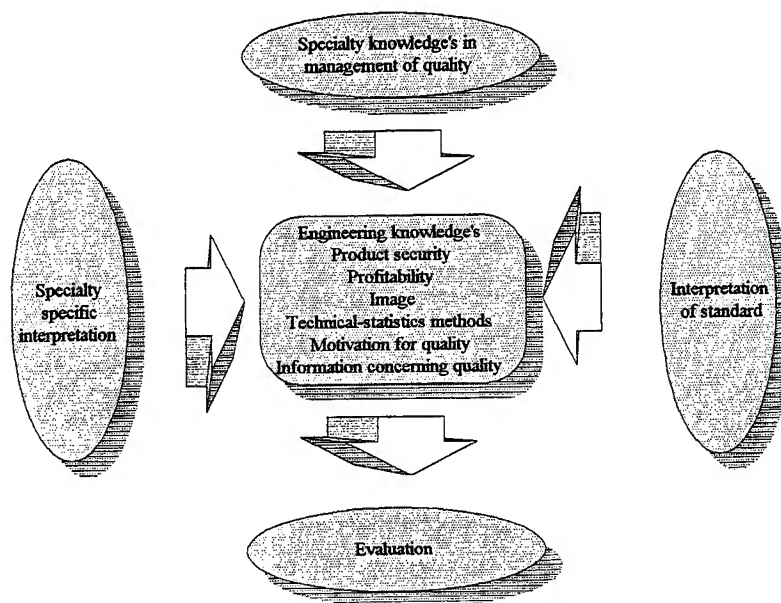


Fig. 11 Evaluation of nonconformity

The nonconformities are written in special forms, respecting the things in Fig. 12.

NONCONFORMITY REPORT	
Well-informed requirements	<ul style="list-style-type: none"> ➤ customer, number of report ➤ reference to the audit protocol ➤ audited organization period ➤ participants ➤ auditor, data ➤ signatures
Structure	<ul style="list-style-type: none"> ➤ chapter of standard, standard's requirements ➤ finding/ nonconformity ➤ weight of nonconformity, evaluation ➤ presumptive cause of nonconformity ➤ (improvement measure if it is necessary)
Distribution	<ul style="list-style-type: none"> ➤ distribution list
Terms	<ul style="list-style-type: none"> ➤ solution of corrective measures ➤ supplementary audit
Form/ volume	<ul style="list-style-type: none"> ➤ 1-2 pages

Fig. 12 Nonconformity report

There are three actions that the responsible manager has to apply:

- remedy actions to correct a certain nonconformity;
- search other examples of nonconformity's and decision about the proportion of nonconformity;
- finding the cause of nonconformity and prevention of its repetition.

The audited has the responsibility to initiate and to perform all the necessary corrective measures to eliminate the nonconformity's at established terms. The audited organization has the task to inform about the phase of corrective actions and about their solution. By this kind of audits it is verified if:

- the established corrective action was implemented;

- the nonconformity was eliminated.

The auditors who perform the supervision audit have to be the same who has performed the initial audit. When all the nonconformity's was eliminated, the audit report can be closed. The audit is incomplete till all the corrective actions were implemented. The unfolding and the phases of an audit are presented in Fig 13.

4. THE OBJECTIVES OF PRODUCT'S AUDIT

The quality audit of a product serves to evaluate the conformity of quality characteristics of the finished product or its subassemblies with customer's requirements, or with the requirements specified in reference documents (standards, technical specifications, manufacture documents, etc.). On this occasion, the reference documents are verified in order to establish if these are adequate to achieve the stipulated objectives in the quality area. The audit doesn't resume only to a simple examination of the product's quality, but it wants to evaluate the efficiency of the quality ensurance measures, concerning the respective product. Based on the result of quality audit, the necessary improvement or corrective measures regarding the audited product can be established.

In order to perform the quality audit, the system's quality procedures, product's specification, documents and means of manufacture and inspection are verified^{4, 7, 12}. A quality audit of a product suppose usually the following important phases (Fig.14):

- examination of the product in relation with the reference documents the processes involved in its manufacture and with the materials used.
- elaboration of the "examination report" clearly specifying the nonconformity's discovered;
- analysis of the nonconformity's and their causes;
- stipulation of necessary improvement or corrective measures;
- supervision of the established corrective improvement measures application.

It is recommended that the necessity and the frequency of the products' audits to be mentioned in the audit plan and their effective planning in relation with the types of products to be made by the quality compartment of the organization. It is necessary to ensure the possibility to perform some audits when it is necessary, independently of the planning, for example in the case of the products denounced by the customers or which have major nonconformities. The report elaborated at the end of the audit has to contain all the results of inspections or tests performed, identifying the nonconformity's and their causes, in order to can establish the best corrective measures or measures to improve the quality of product.

5. THE OBJECTIVES OF PROCESS AUDIT

Process' quality audit serves to evaluate the conformity of quality characteristics of a finished product or its subassemblies with customer's requirements, or with the requirements specified in reference documents (standards, technical specifications, manufacture documents, etc.). As in the case of quality audit of a product, the reference documents regarding the audited process are verified too, in order to establish if these are adequate to achieve the stipulated objectives.

The quality audit of a process has the aim to establish the efficiency of the quality ensurance measures concerning the respective process, establishing the corrective measures or the necessary improvements. The quality audit of a process is based on the adequate procedures of the quality system concerning the development, supervision and inspection of the process. The requirements referring to the qualification of personnel involved in the audited process are verified too.

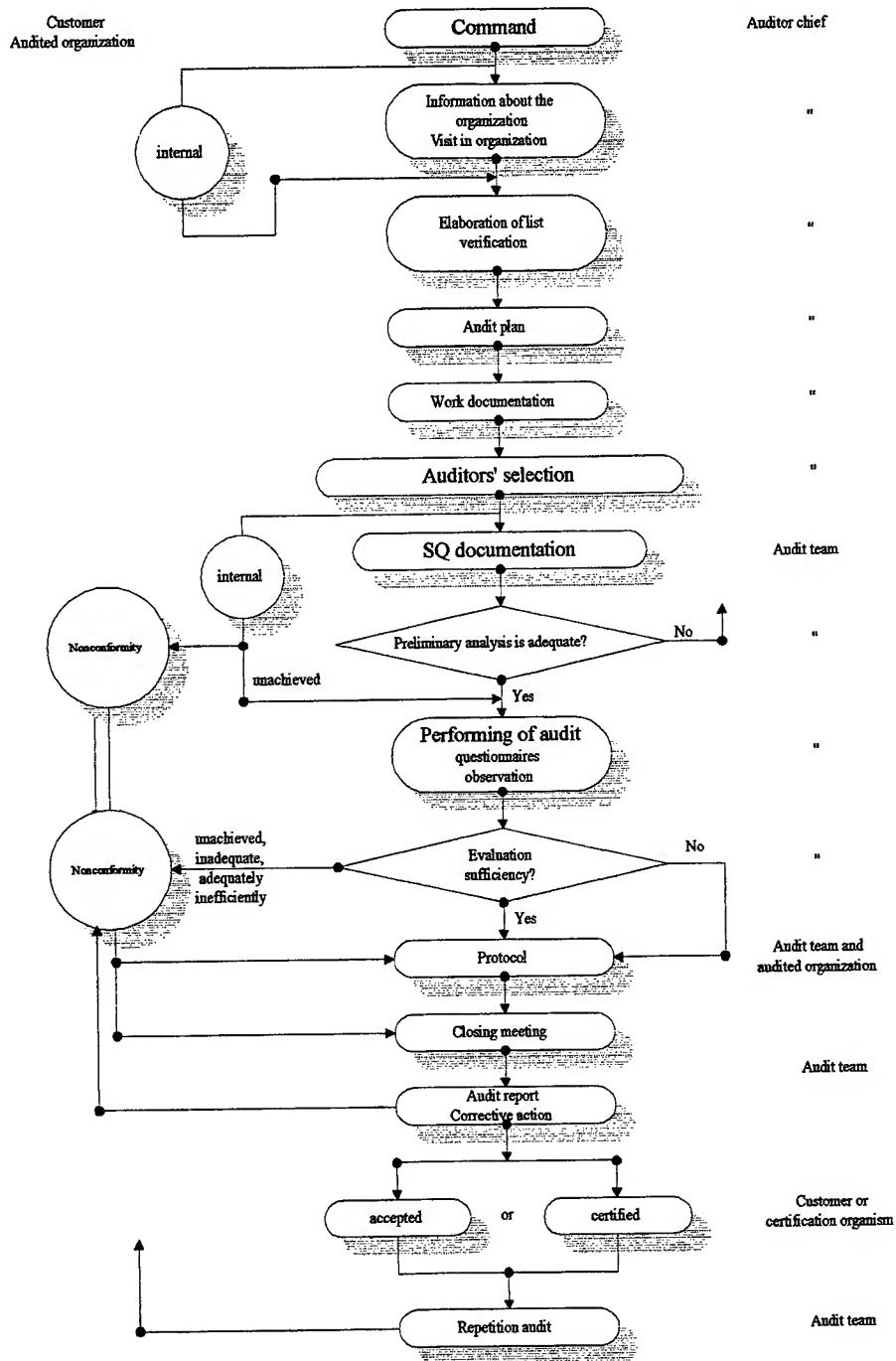


Fig. 13 Phases of an audit

A quality audit of a process usually supposes the following important phases (Fig.15):

- examination of all important elements for the quality of the audited process;
 - ✓ the validity of the documents referring to the process (work instructions, inspection instructions, drawings, etc.);
 - ✓ the capacity of the equipment (machines, installations) to achieve the necessary quality;

- ✓ the situation of the inspection equipment and the correctness of their use;
- ✓ the analysis concerning the raw materials;
- ✓ the results of the tests performed with the components, which are subduced to the self-control.
- elaboration of the intermediary documents, which include the results of the examinations of the mentioned elements (verification lists, examination report, etc.);
- elaboration of the "audit report", clearly specifying the nonconformity's discovered;
- analysis of the nonconformity's and their causes;
- decision about the necessary corrective or improvement measures - it can be made proposals concerning:
 - ✓ modification of equipment in respective process;
 - ✓ improvement of manufacture planning;
 - ✓ structure's modification of manufacture;
 - ✓ improvement of quality assurance methodology of raw materials and processed materials;
 - ✓ correction of development of certain phases of the process;
- supervision concerning the application of the established corrective or improvement measures.

It is recommended that the planning of these audits to be made and performed systematically, at least once a year, for all the processes of the organization, according a special priority to the complex processes which have many intermediary components manufactured or having certain technological particularities^{2, 5, 11}. The conclusions of the audit report must to be known by the chiefs of audited compartments in order to apply the necessary corrective or improvement measures.

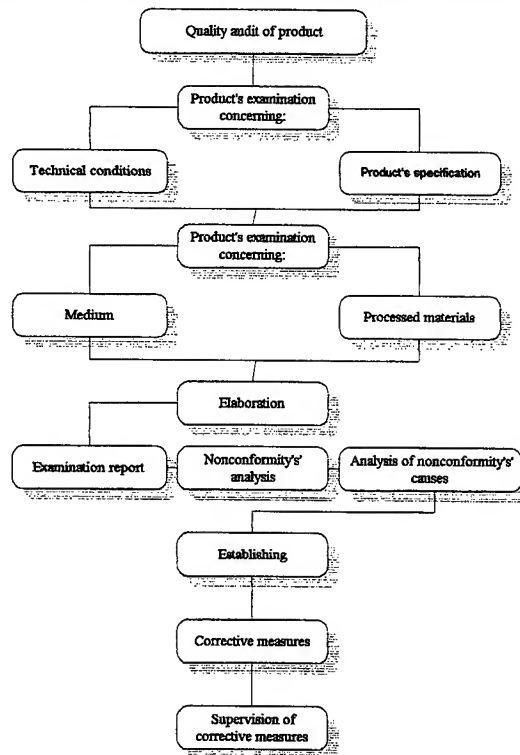


Fig. 14 The general methodology of a quality audit of product

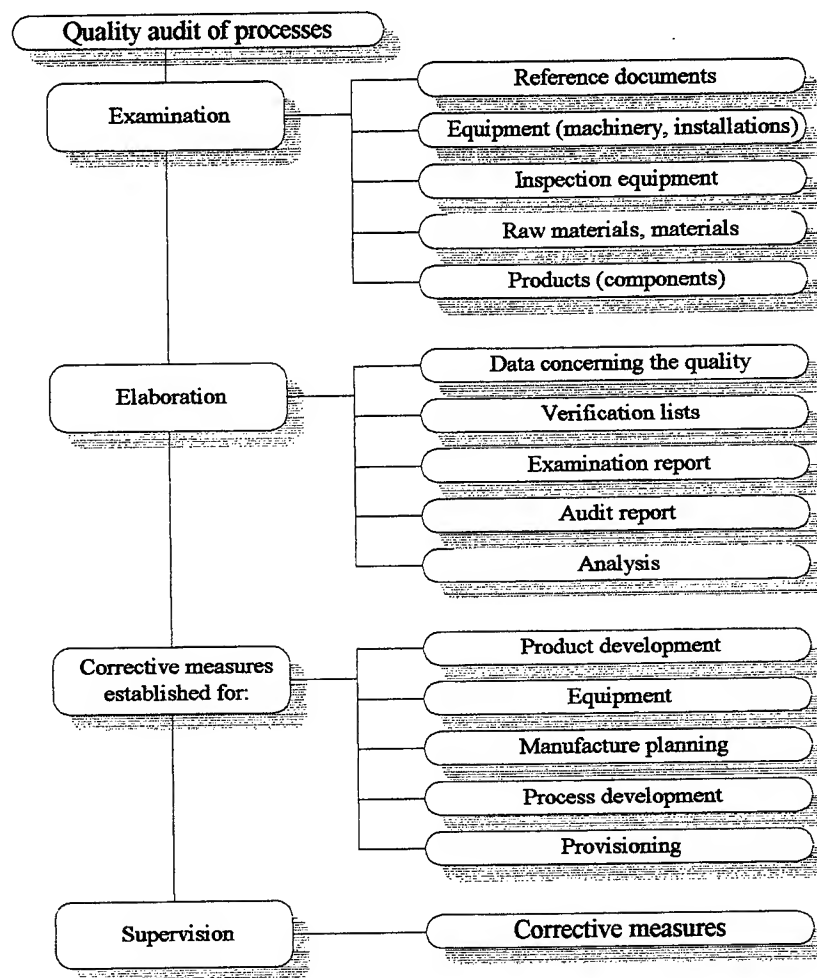


Fig. 15 The general methodology of quality audit of process

REFERENCES

1. V. Antonescu and D. Constantinescu, *Managementul Calitatii Totale*, OID-MICM, 1993.
2. W. Brakhahn and U. Vogt, *ISO 9000 pentru servicii-Rapid si sigur spre certificare*, Ed. Tehnica, Bucuresti, 1998.
3. P. Candu, *Audit des associations*, Les Editions d'Organisation, Paris, 1990.
4. B. Froman, *Manualul Calitatii instrument strategic al abordarii calitatii*, Ed. Tehnica, Bucuresti, 1998.
5. K. Ishikawa, *The quality control audit*, Quality Progress, 1987.
6. J. M. Juran and F. M. Gryna, *Quality Control Handbook*, Mac Graw Hill Co, 4e edition, 1988.
7. J. M. Juran, *Planifier la Qualite*, Afnor Gestion, 1989.
8. H. Mitonneanu, *Réussir l'audit qualité*, Editia a 2-a, Afnor, Paris, 1994.
9. M. Olaru, *Managementul Calitatii*, Ed. Economica, Bucuresti, 1995.
10. A. Pereira, *Quality audits and international standards*, Quality Progress 1987.
11. M. Perigord, *Reussir la Qualite totale*, Les éditions d'Organisation, 1990.
12. Gh. Zgura, Gh. Solomon and A. Szuder, *Elemente de asigurarea calitatii*, Ed. Tehnica, Bucuresti, 1998.

Mobile system for vehicles in distress locating and tracking

Giuliano Landi^{*a}, Axente Stoica^b

^aHAL 9000 ID systems s.r.l. (Italy)

^bRemote Sensing Depart., Institute of Optoelectronics (Romania)

ABSTRACT

This report relates to a mobile system for tracking and protection of vehicles owned by some banking organisations, security institutions or by some social service for fire, medical rescue or taxicabs, by an operator placed also aboard of a vehicle in which he have at his disposal all the necessary means (Satellitary System for Global Positioning - GPS and the telecommunication system) for precise determination of the position and the state of each vehicle from the fleet that is under his surveying. Therefore in contrast to the operating mode of the localisation systems known in present and which have in its composition a stable centre for permanent surveying, the operator of the system presented in this report can intervene personally and in an efficient mode in the aid of the vehicle in distress.

Keywords: Global Positioning System, World Geodetic System 1984, vehicles locating and tracking, inertial navigation system, gyroscopic system, computing unit

1. INTRODUCTION

The endowing of the valuable vehicles (or those that transport values) with means that permit its rapid recovery in the event of some infrafractional overtaking of these vehicles, constitutes an important objective which many speciality firms proposed itself, more or less recently.

Related to this, the creation and the settlement in operational state of the American satellitary system NAVSTAR for global positioning (GPS) has as a result the appearance in the endowment of some guard and protection services from many countries of different systems and devices for the vehicles centralised locating based on GPS system.

As it is generally known, the satellitary system GPS makes it possible to compute the position of any point on the surface of the earth with high precision. These GPS systems, devised for military purposes, are now widespread within civil sphere and are based on the reception of signals from a number of satellites orbiting the earth. On this basis, the GPS systems can provide the geographic fix and also the absolute altitudes with respect to sea level, with medium or high accuracy for civil uses.

Computation of a GPS receiver position is performed using three or four satellites, each of which provides a distance value. By applying a system of equations in four unknowns, three for the coordinates X, Y, Z and the fourth C for the clock and solving by Taylor's method, the required solution for the position is obtained. Corrections for relativistic effects, ionospheric and tropospheric distortion are then applied in the known manner. The position is provided by the processor installed on the standard GPS Board in several formats such as the Cartesian coordinates in meters from the centre of the Earth and the geographical coordinates, that is to say latitude and longitude in radians.

Usually, the average deviation of determinations is contained between 25 and 50 meters, but the accuracy of determinations can be enhanced in an important measure if the GPS system is used in a "differential" regime, that is to say, if the effected determinations are related to those obtained with a fixed reference GPS station, placed on a point whose coordinates are precisely known. The only drawback of these differential systems is that, that in this case, data acquisition for position determination is relatively slow.

* Correspondence: Telephone: +39 578 267154 ; Fax: +39 578 267160

The locating systems currently in use in fact utilise an operations centre manned around the clock by an individual watching the monitor of a computer for the raising of an alarm. This computer needs to be furnished with electronic mapping to allow the pinpointing of the position of the vehicle from which the alarm emanated.

It is obvious that such a system, which in present is used by many international organisations for goods and assets transport, as well by some public services for medical rescue, fire or banks, assumes the existence of the facilities offered by the operations centre, among which can be mentioned and the possibility to use the general electronic mapping of the surveyed region.¹

However, these facilities offered by the operations centre involve very high costs of manning, machinery, logistic set up, and the adoption of the digital mapping entails, apart from the intrinsic inaccuracies, high purchase and maintenance costs. Moreover, electronic mapping of many large, medium-sized and small cities, to say nothing of villages, is not yet available for a great part of them.

Another problem connected with the currently available national mapping derives from its non-compliance with the WGS 84 (World Geodetic System 1984) reference system used by the GPS satellite system.

2. MOBILE AUTONOMOUS SYSTEM FOR VEHICLES LOCATING AND TRACKING - SMALUV.

The mobile (autonomous) system for vehicles locating and tracking, which is the subject of this presentation and which was conceived and patented by the Italian company "HAL 9000", obviates the aforesaid drawbacks, that is to say the costs due to the operations centre and to the mapping, insofar as neither the one nor the other is required.² As it results also from its name, the system is conceived to assure to the owner of the vehicle or someone on his behalf the possibility not only to locate, but also to personally track and search the vehicle in distress within a definite geographical area.

To achieve the above mentioned functions, the proposed system on principle contains an installation in which are included a GPS receiver and a system for remote communication on board the vehicle or object whose position is intended to determine and a similar locating installation constituted from a GPS receiver and a system for remote communication and placed both with the person which effect the searching on board of the "seeker" or "pursuer" vehicle.

As it is presented in the Fig. 1, in the event that the target is a motor vehicle, on this is disposed also an alarm device (1), such as for example an anti-theft system.

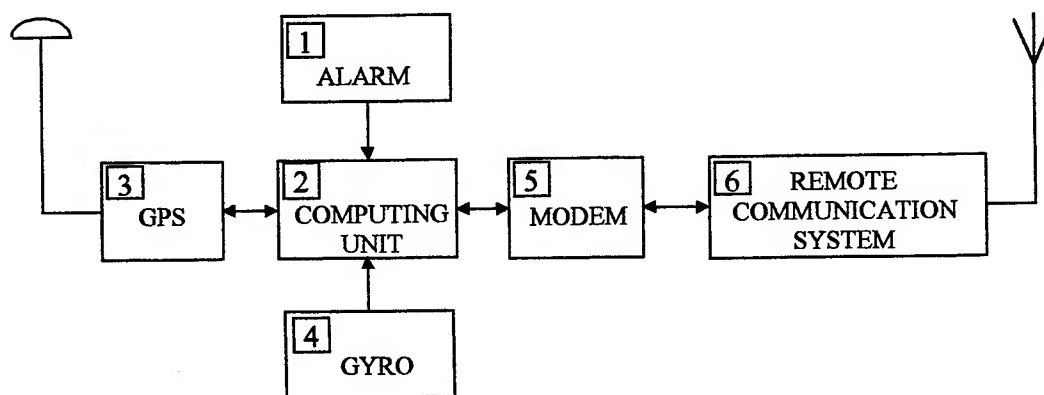


Fig. 1 Block scheme of the portable system component disposed on board of the target vehicle.

The alarm device (1) is connected to a computing unit CU (2), which is disposed for starting up the whole of the system following the detection of an alarm condition such as a theft or an unauthorised use of the vehicle.

To the computing unit (2) is connected also the system (3) for geographic terrestrial position locating, namely the "Global Positioning System" (GPS).

The computing unit (2) is also associated with a gyroscope system (4) for immediate detection of variations in the direction of travel of the target vehicle. In the installation achieved by the Italian company "HAL 9000" the gyroscope system is fitted with a solid-state "rate gyro" based on the Coriolis effect and marketed by the Japanese company "Murata" under the name "Gyrostar".

The computing unit (2) is furthermore connected through a modem (5) to a system (6) for remote communication. The system (6) can be a straightforward radio transceiver or a cellular telephone. In the latter case, a cellular telephone system of the GSM type is preferred on account of the ease of interfacing between GSM cellular telephone and modem (5).

Under normal conditions both the GPS subsystem (3) and the GYRO subsystem (4) and also the computing unit CU (2) are active by the fact that these subsystems continuously compute the geographical position of the target vehicle in which they are installed and communicate this to the computing unit (2) updating it, for example, once a second. The computing unit (2) stores the new position datum, constantly checking on the input of the alarm device (1) for the existence of conditions which require the transmission of the position data to the seeker device.

The remote communication system (6) with which the CU (2) is associated is on standby for calls. The computing unit (2) furthermore has a non-volatile memory device in which several useful telephones numbers are recorded.

The seeker device is in the form of a computer of the "Lap Top" type comprising provision for a mass memory module which carries a store of the positions relating to the localities from the respective region, either on a global scale, or on a reduced scale, according to need.

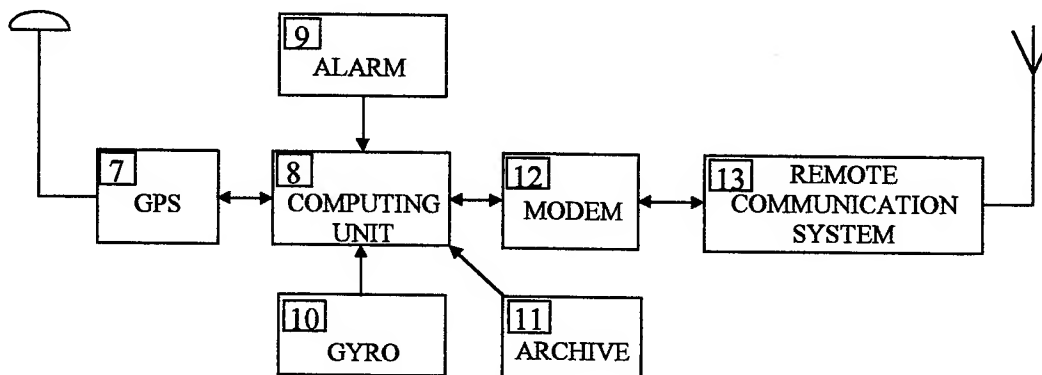


Fig. 2 Block scheme of the portable system component disposed on board of the seeker vehicle.

With reference to Fig. 2, the device on board the seeker comprises:

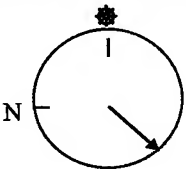
- a GPS subsystem (7) similar to that mentioned in the description of the target installation;
- a computing unit (8) connected to a display (9);
- a gyroscope device (10) similar to that mentioned with reference to Fig. 1;
- an archive (11) of known positions, preferably in the form of an interchangeable memory module;
- a modem (12) and a remote communication system such as a GSM rig as explained with reference to Fig. 1.

The seeker device can locate any target device so long as it knows its telephone number. If the vehicle is abandoned by the driver with the seeker on board, a strong acoustic warning signal is brought into operation. Similarly, a strong acoustic signal is emitted also in the event that the motor car is abandoned by the owner somewhere outside of the coverage of the GPS or GSM signal.

In the event that the seeker receives a call from the target, it then activates the devices for determining its own position, receives and stores the position of the target vehicle and, when it is certain of the reliability of the datum received, sends the confirmation message to the called target.

When the actual GPS device has computed the position of the seeker, the direction with respect to true North (bearing) to be taken in order to reach the target is computed and flagged in the form of an analog compass. This information is provided and flagged in degrees. Furthermore, the GPS device consults its own internal archive and the position of the target with respect to the nearest locality (distance and bearing), is indicated.

DIRECTION OF MOTION OF THE SEEKER

SEEKER DATA	SATELLITE COMPASS	TARGET DATA
DATE : 01/01/99 TIME : 13:15:18 LAT : 42°51'16" LONG : 011°58'00" SATELLITES USED : 4 STATE : NAV 3D SPEED 80 Km/h	 RECEDING BEARING 135° DISTANCE 6925 m TARGET AT 3200 m SOUTH OF CHIUSI	DATE : 01/01/99 TIME : 13:15:19 LAT : 42°47'10" LONG : 011°55'03" SATELLITES USED : 3 STATE : NAV 2D SPEED 50 Km/h

LEGEND:

- ✱ indicates the direction of motion of the seeker
- N indicates the direction of the true North with respect to the seeker
- indicates the direction to be followed to reach the TARGET
- BEARING is the angle between the direction ✱ followed by the seeker and the direction ➤ in which the target lies.

Fig. 3 The graphics appearance of the display available to the seeker.

At this point the manager of the seeker procures the means adapted for the pursuit and location of the target and, on beginning the pursuit, will call the target via the seeker. When the two devices are once again in mutual communication, the seeker receives, every second, the position data of the target and hence has the possibility of computing and highlighting the following information using its own position and the archive (11) of known positions:

- The seeker and the vehicle carrying it are provided for, respectively oriented in the direction of travel, in the top quadrant of the software-constructed satellite analog compass, in which at 12 o'clock is marked an asterisk to indicate the direction of movement of this seeker. (see Fig. 3). True North is thus also marked on the quadrant together with the bearing of the target in the form of an arrow which in the search movement always indicates the direction of the target with respect to the seeker;
- The updated position with respect to the nearest locality or district is found;
- The distance in metres to the target is computed and kept constantly updated (Great-Circle course); and
- Visual and acoustic indication is flagged of target approaching, target receding and target dead ahead.

Besides the above mentioned, from the GPS processor other information can be obtained also, such as:

- data and UTC time (Universal Time Coordinate);
- receiver altitude in metres;
- number and the identifiers of the satellites used;

- data concerning the accuracy;
- various correction factors;
- state of the receiver.

This last item of information is useful in that it makes it possible to decide if and when to pass from the main position determining system, that is to say that based on GPS, to the secondary system (GYRO).

It should be pointed out at this juncture that the system provides the values of Cartesian or geographical coordinates referred to the WGS-84 ellipsoid which is the model adopted by the United States. All the information deduced by computation of the CU and that provided directly by the GPS system are therefore also referred to WGS-84.

To correspondingly assure all the above presented functions, in the SMALUV system a GPS receiver achieved in a sub-miniaturised form by the Rockwell company from United States was incorporated. Among other performances, it should be mentioned that after about 60 seconds from its start, this receiver can deliver the first positioning data, the respective information being presented on one of the serial ports of the computing units.

The position information is normally received by a GPS type multi-channel circuit, although it sometimes happens that particular local conditions do not allow visibility of a sufficient number of satellites to compute a position. Therefore, both the target system and the seeker system avail themselves of a fibre optic or piezoelectric gyroscope circuit which makes it possible, as stated, to compute position even if with the passage of time the effect of precession renders a data item gleaned in this way less accurate.

So, the GYRO subsystem intervenes on request from the computing unit as backup device for the determination of position when, for various reasons, GPS loses the ability to navigate and enters a defined "acquisition" state, which can occur essentially because the antenna is obscured by tunnels, other buildings, foliage, etc.³

In each case, the seeker is informed about the status of all the circuits for computing the position, both of the target and its own ones.

The GYRO subsystem provides the computing unit merely with variations in the angular velocity of the vehicle on which it is placed, using in this aim a gyroscopic device with optic fiber or of a miniaturised piezoelectric type, such as the above mentioned "Gyrostar" device.

The Gyrostar device is connected to an A/D (analog/digital) converter which in turn offloads the angular velocity variation data onto the port of the computing unit at a sampling frequency of for example 50 data per second. On this basis, in the absence of the positioning data provided by GPS it is possible to compute new positions with the data from Gyrostar device, if the value of the vehicle velocity is also available. This latter data item can be obtained directly from the cars on which the SMALUV system is sited.

It should be mentioned here the fact that the inertial navigation techniques (of "dead reckoning" type) are based on time integration of the signals delivered by gyrometric and/or accelerometric transducers, so the errors in determination of the passed distance are increasing continuously in time. Therefore the intervention duration of the GYRO subsystem must be limited to 1 - 2 minutes. As a consequence, the position computed with the GYRO system should therefore be regarded as indicative for maintaining an acceptable space-time correlation between the target and the seeker during GPS blackout.⁴

The state of the radiocommunications is likewise monitored and checked: Cutting of the connection gives rise to automatically repeated calls until normal communications are resumed.

3. CYCLES TRACKED BY THE INFORMATION FLUXES

Accordingly to its functioning general algorithm, computing block on "the target" continually computes its own position, keeping track of the latest reliable position, the mean velocity for the latest minute, for the latest quarter of an hour and for the latest hour. As it continues to "cycle" it carries out some checks such as:

- the presence of incoming calls;
- the presence of the alarm system (in the widest sense);
- the proximity to "danger" zones.

The occurrence of one or more of the above events allows the despatching of the data relating to its own position by the target to the seeker, which works only if called by a target or if a target's call function is activated.

In both cases the data received from the target are compared by the seeker with those received from its own GPS subsystem and the results of this comparison, whether in digital or analog form, are flagged in the display of the seeker.

It will furthermore be noted that as far as the target is concerned the following particulars are complied with:

- In the case of incoming calls, the target will verify, through the sending by the seeker of a ten-digit keyword which constitutes the permission by this seeker to talk, for the purpose of preventing other seekers or other users of a seeker from being able to have recourse to the system;
- The activation of the alarm system has as a result the fact that the computing unit of the target will be able to interface with one or more communication channels;
- The signalisation "approach to danger zones" appears in situations in which the positions occupied by the target for more than 5 minutes fall within areas recorded in the non-volatile memory of the target. For example, 64 such positions are provided for and within a 5 km vicinity each of these points is regarded as a "danger zone". Purely by way of example, the following may be regarded as such; frontier crossings, harbours or airports;
- The data are transmitted and received only in encrypted form, the algorithm for which is known only to the constructor.

More exactly, the functioning of the SMALUV devices is resulting from the Fig. 4 and Fig. 5 where the flowcharts of the software resident in the computing unit on board the target and respectively on board the seeker are presented.

As it is resulting from the flowchart in Fig. 4, in the moment in which the initialisation of the target computer is effected, the internal database is read, this being composed of the data relating to the danger areas, the "time out" for the calls of the seeker, the telephone numbers to be selected, the seeker and operator codes permitted to communicate with the target, the configurations of the modem and the maximum time of stay in danger zones.

In continuation, the computing unit executes the test of the GPS subsystem, and if the result of the test is negative, the procedure for communication with a seeker is activated immediately and as soon as the communication channel is activated, a suitable message of failure of the operation of the GPS is sent. After sending this message and receiving the response message, the GPS is deactivated and the system remains on standby.

If the result is positive, calculation continues and configuration of the modem is undertaken, concomitantly with the test of correct operation of the modem. If the result is negative, it actually becomes impossible to communicate; from this moment onwards the computing unit will keep track in rows of the positions occupied until the reserves of the memory peripheral units are refilled, discarding the oldest data and recording the most recent, so long as they are reliable and are characterised by a velocity greater than 5 km/h, that is to say by means in motion.

Hence, the target will cycle continuously until one of the initially mentioned conditions obtains:

- the presence of arriving calls;
- the activation of the alarm system;
- the proximity to "danger" zones.

In the first case, the module which is dealing with the communications takes control of the computing unit after having ascertained the presence of the ringing telephone, and orders the handset to be lifted and handshaking to be set up. Once the communication is connected, the admissibility of the incoming call is checked: the target places itself on standby for data and in particular for the message that contains the machine code of the seeker and that of the operator. If the check on the codes is positive, the communication can continue: Otherwise the computing unit orders the modem to replace the handset, interrupting the communication.

In the second case, should the signal present on the parallel port become ON and remain so for 10 seconds, the communication procedure is activated.

In the third case, to determine entry into danger zones, a counter is activated every time the point computed by the GPS subsystem lies within a 5 km radius of one of the points loaded in the initialisation phase. If the counter reaches the value defined in the initialisation phase, for example currently defined as 5 minutes, the procedure for communication with the seeker is activated automatically. In these situations in which the order to activate the communication procedure issues from the target, there will be no check or exchange of messages of recognition via software.

The communication procedure consists in dialling up in order, as they are listed in the initialisation phase, the stored numbers; with each telephone number will be associated the number of attempts to be made before passing to the next. The exchange of data will take place with the first seeker with which communication is successfully established.

Normally, communication takes place with a message which contains the own target data identifier, the data relating to its position, UTC time, velocity, course, elevation and state of the GPS receiver. After sending the message and receiving confirmation of receipt, the target suspends communications and places itself on standby for other calls.

As regards the seeker and related initialisation, as results also from the flowchart of the seeker vehicle software presented in Fig. 5, the internal database is read first of all, consisting in loading the positions of the localities, the seeker's own code and the configurations of the modem; the password is then requested from the operator assigned to the use of the seeker.

Then, the computing unit executes the test of the GPS and if the result of the test is negative, the operator is immediately notified via a message on the display of the non-functioning of the GPS.

If the result is positive, calculation continues and the configuring of the modem is undertaken, concomitantly with the test of correct operation of the modem. If the result of this last test is negative, so that it in fact becomes impossible to communicate, the operator is immediately notified via a message on the display of the non-functioning of the modem.

The operator can activate the system in order to communicate with a target or await the arrival of a call.

In the first case, the number of the target to be called is requested from the operator: once the number is typed in, the computing unit instructs the modem to dial up the number in order to attempt to establish the connection.

After having verified active connection, the seeker will have to send, through an initial message, its own machine code and that of the active operator.

Unless the communication is cut on its volition, the target transmits a message relating to its own identifier data, in addition to the UTC time available with the indication of whether or not this is a valid time. After the confirming by the seeker about the receiving of the first message, the target sends the message about the position and status data. Comparison between these data and those gleaned directly from its own GPS subsystem, will enable the computing unit of the seeker to flag on the display the information relating to distance and to bearing.

In the second case, namely the case of receiving a call from some of the tracked targets, calculation will proceed as soon as the modem notifies the computing unit of the presence of an incoming call, which will follow the instruction to the modem to lift the handset and establish the communication.

From this moment onwards the behaviour will be identical to that described above.

The seeker can determine for the target also the optimal satellitary configuration for its GPS subsystem and will send through a special message which satellites and which elevation value to use.

For the recovery of vehicles in distress the manager of the seeker follows the indications of the satellite compass and constantly checks that the value of the distance to the target is decreasing.

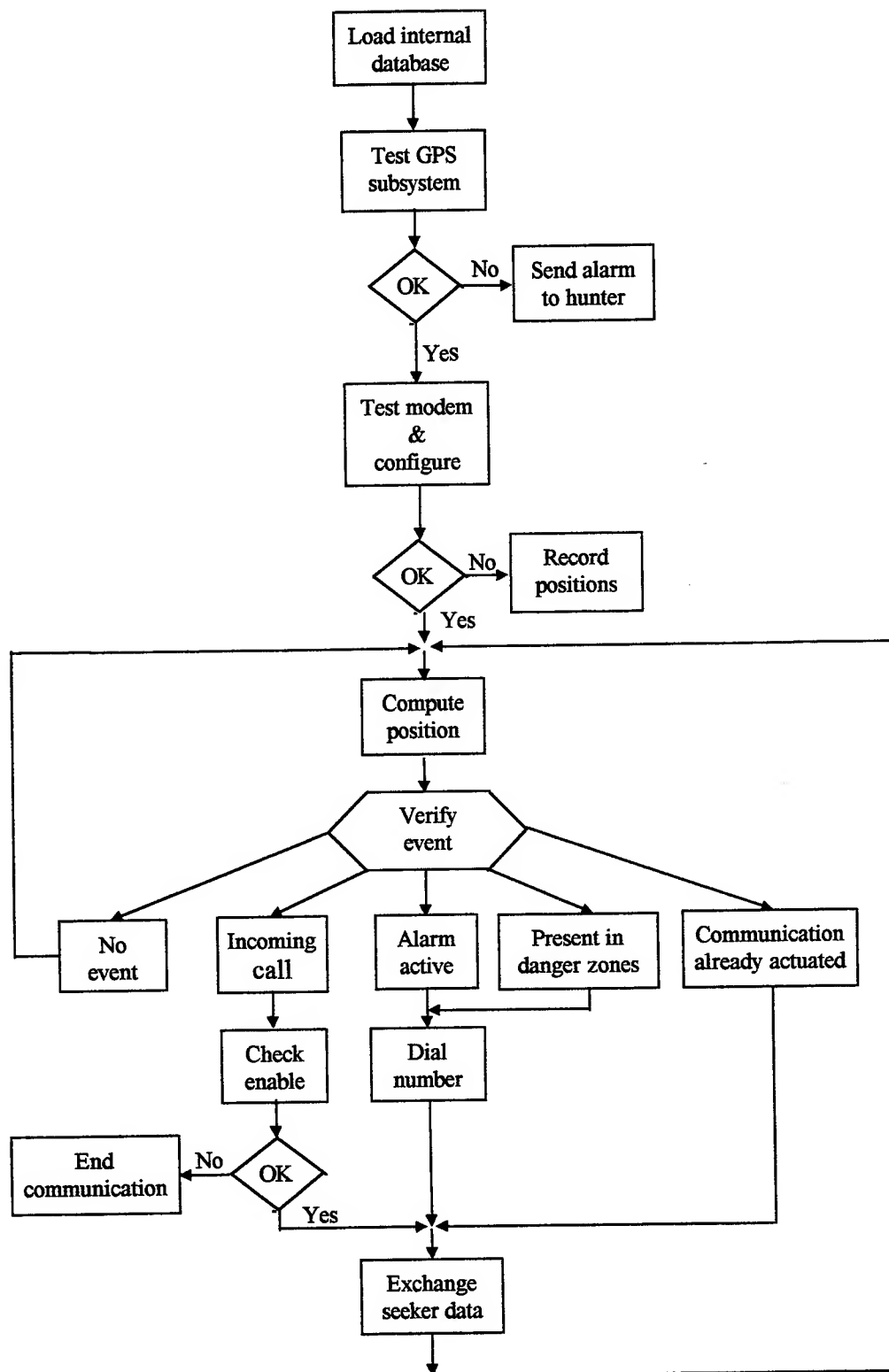


Fig. 4 Flowchart which synthetises the functioning of the installation on board the target vehicle

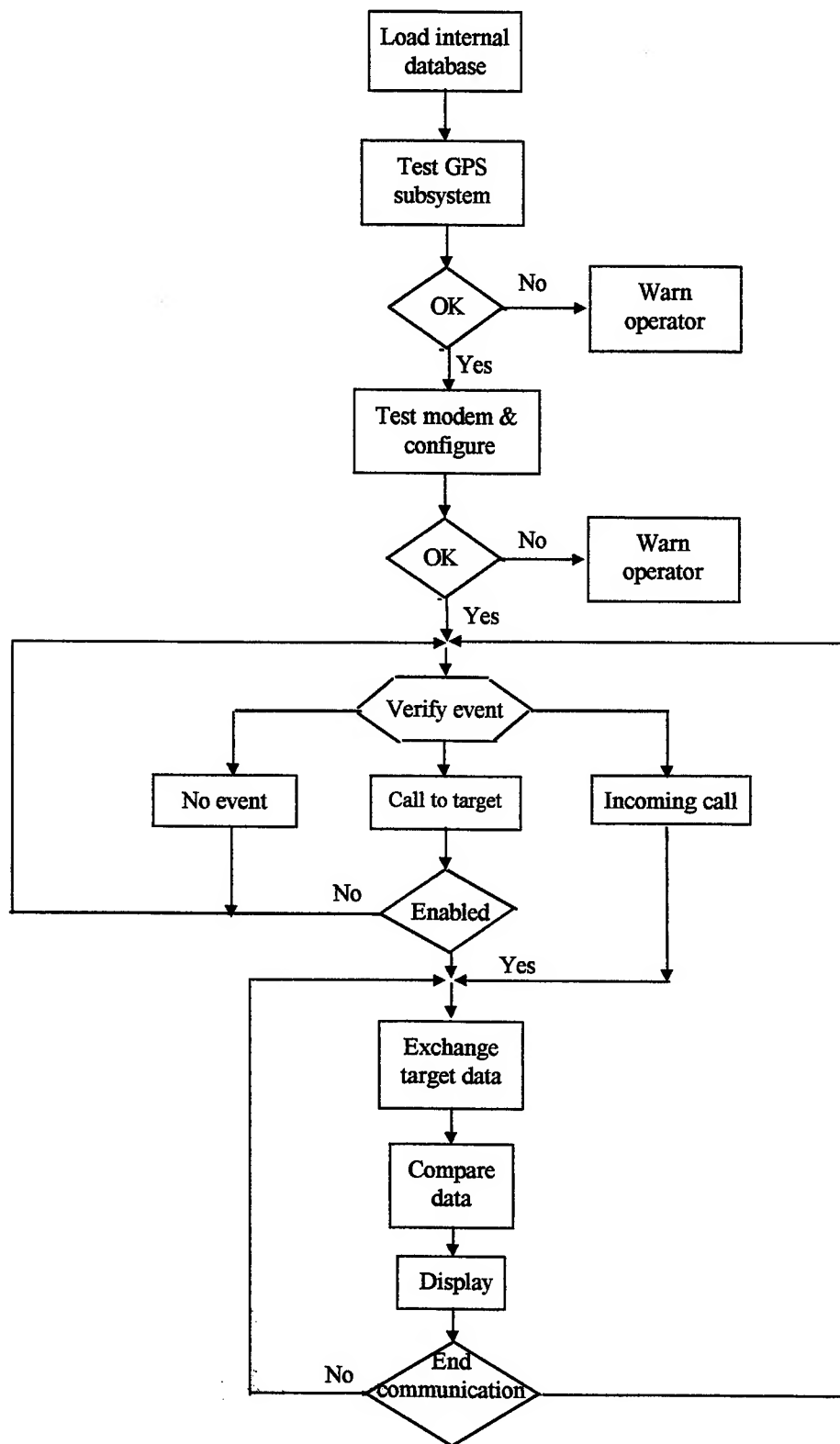


Fig. 5 Flowchart which synthesises the functioning of the installation on board the seeker vehicle

4. CONCLUSIONS

The mobile (autonomous) system for vehicles locating and tracking - SMALUV -, conceived and patented by the Italian company "HAL 9000", represents an original and efficient solution for the protection assurance of vehicles existing in the endowment of a fleet. As it was resulted from the above presented, the system is designed to assure to an operator the possibility not only to locate, but also to track and search personally the vehicle in distress, obviating in this way the necessity of an operational tracking centre on which the functioning of other surveying systems for vehicles fleets is based. The autonomous searching system provides, in real time and directly, the data referring to the target vehicle, like the distance in meters, direction, speed, exact geographic position, the closest locality, etc. Optionally, the position data can be transferred to a common mapping allowing subsequent display.

Moreover it should be mentioned that the data relating to the great-circle distance (shortest path between two points on the earth's surface), the bearing angle or direction, etc. provided by the autonomous system, are to be regarded as exact insofar as both the seeker device and the target device use the same WGS 84 reference system. In this manner, although it makes not use of the Differential GPS system (DGPS), the proposed autonomous system obtains locating accuracy which are comparable with those which can be obtained with DGPS system,⁵ with only remark that in this case, the locating is not achieved in absolute coordinates, but in relative ones, in respect to the seeker vehicle.

REFERENCES

1. E.J. Krakiwsky *"Innovations in Vehicle Tracking and Navigation"* GPS World February, pp.42-46, 1994.
2. G. Landi *"System for locating moving vehicles or objects"* Patent PCT/IT/97/00072, The International Bureau of WIPO, April 1997.
3. L.J. Levy *"The Kalman Filter: Navigation's integration Workhouse"* GPS World September, pp.65-71, 1997.
4. A. Stoica *"Inertial Navigation System (I.N.S.) conceived for the complementation of the GPS systems used in position determinations on vehicles"*, Romanian Journal of Optoelectronics, 3, pp.49-56, 1998.
5. T.Necsoiu and A. Stoica *"GPS relative guidance of the aviation bombs"* Tehnica Militara, 2, pp.58-62, 1998.

Temporal resolution spectroscopy applied in the study of a LTE arc plasma

I. Iova*, S. Levai, Floriana Iova, C. Biloiu, Gh. Ilie, M. Băzăvan, M. Bulinski
University of Bucharest, Faculty of Physics
76900 Bucharest - Măgurele, P.O. BOX MG - 11, Romania

ABSTRACT

A method for local thermodynamic equilibrium (LTE) plasma diagnostics by vibrational structure of diatomic molecule electronic states is elaborated. On this purpose is adopted a model of plasma temperature determination from the relative intensities of the molecular vibrational band head incompletely spectrally resolved. The relative intensities were determined using the temporal integrated profile (the peak intensity multiplied by temporal half width of the intensity pulse) instead of peak or integrated spectral profile of a band head. This more accurate method of vibrational temperature determination (estimated at about 6100 K) allows obtaining new data about the plasma internal processes (the role of electrons in the excitation of the vibrational levels, the role of molecular ions in LTE plasmas etc).

Keywords: plasma spectroscopy, vibrational spectra, plasma diagnostics

1. INTRODUCTION

The so-called violet band system of CN is observed in the spectra of most sources of moderate excitation, which contain carbon such as arcs, flames, jets and certain classes of stars.

The frequent occurrence of these bands makes them potentially useful in determining the excitation temperature of the sources. Temperature could be obtained from the relative intensities of the individual rotational lines of a band using highly resolved spectra. However, when a low dispersion spectrograph is used or when the rotational structure is badly blended with lines of other molecules or atoms as in most stellar spectra it is practically impossible to use the rotational lines for this purpose.

Nevertheless, it is often still possible to make fairly accurate temperature determinations from the relative peak intensities measurements of the unresolved band heads if the relative vibration transition probabilities of the bands are known.

Some difficulties can be encountered in attempting to use the relative peak intensities of unresolved band heads as temperature indicator as follows.

Basically, the relative peak intensities are not usually a truly measure for the relative strengths of the vibrational transitions giving rise to the bands because of the different rotational structure in each unresolved band. Furthermore, the peak intensities are affected by overlapping of rotational lines of neighboring bands, by self-absorption or by self-reversal. Moreover, the probabilities of determining the excitation temperature from the relative intensities of band heads measurements are strongly limited by the scarcity of data on relative vibrational transition probabilities.

The temperature knowledge of a thermodynamic or local thermodynamic equilibrium arc plasma containing CN molecules allows the vibrational and rotational energy levels to be calculated and the relative vibrational transition probabilities to be derived from the measurement of intensities.

Reciprocally, such probabilities can be used to determine the excitation temperature.

The approximation taken into consideration for the measurements of the relative band heads intensities leads us to a correct evaluation of the temporal evolution of the vibrational excited states correlated with some collision processes in LTE plasmas.

* Correspondence: Phone home: 682.57.53

2. A PRACTICAL RELATIONSHIP FOR THE BAND HEADS RELATIVE INTENSITIES DETERMINATION IN THE CASE OF AN INCOMPLETELY SPECTRAL RESOLUTION

As it is known the total relative intensity in emission of a vibrational band arising from a vibrational transition $v' \rightarrow v''$ can be expressed by:

$$I_{v'v''} \approx N_{v'} \nu^4 R_{v'v''}^2 \quad (1)$$

where $N_{v'}$ is the number of molecules in the upper electronic state with the vibrational quantum number v' , i.e. the sum of populations of all rotational levels associated with the vibrational level v' , $R_{v'v''}^2$ is proportional to the vibrational transition probability $v' \rightarrow v''$ and ν is the frequency of the emitted radiation.

In a LTE arc plasma, the relative values of $N_{v'}$ for different vibrational states are proportional to $\exp(-W_{v'}/kT)$, where $W_{v'}$ is the energy of the upper vibrational state involved in the transition.

Thus the total intensity of a band emitted in such plasma becomes:

$$I_{v'v''} \approx \nu^4 R_{v'v''}^2 e^{-\frac{W_{v'}}{kT}} \quad (2)$$

In spite of the fact that the equation (2) holds for the total intensity of a band, it can not be used to compare the peak intensities of the unresolved band heads, unless the differences in the rotational structure of each band are so small to be negligible.

Such differences arise in the variation from band to band of three factors: the intensity distribution among the rotational lines in the band head, the effective average rotational quantum number $J_h(v'v'')$ representing the lines blended in the band head peak and the number of rotational lines ΔJ forming the head.

In this paper, an equation incorporating these factors is derived, relating the relative vibrational transition probabilities to the relative peak intensities of the unresolved heads of violet bands. We are dealing with the violet band system, which arises from the $[B^2\Sigma - X^2\Sigma]$ transition, where $X^2\Sigma$ is the ground state of CN.

Although in this type of transition, the rotational lines are doublets, however in CN molecule spectra the doublet splitting cannot be resolved until very high rotational quantum number are reached. It is the reason why the CN violet bands have been cited as examples of singlet bands¹.

For the low and intermediate values of J the rotational lines of the violet bands may be accurately represented by the formula for singlet transitions¹, which in the P branch ($\Delta J = -1$) where the heads of violet bands are formed, is:

$$\tilde{\nu} = \tilde{\nu}_0 + (B_{v'}' + B_{v''}'')J - (B_{v'}' - B_{v''}'')J^2 \quad (3)$$

where $\tilde{\nu}_0$ is the wave number of the origin of the band, $B_{v'}'$ and $B_{v''}''$ are the rotational constants associated with the upper and the lower vibrational states, respectively.

It must be outlined that B_v is approximately a linear function of the vibrational quantum number.

Under the conditions of thermal equilibrium the intensities of rotational lines in a P branch are proportional to:

$$J e^{-\frac{W_r'}{kT}} = J e^{-\frac{B_{v'}' J(J+1)hc}{kT}} \quad (4)$$

where W_r' is the rotational energy of the molecule in the upper electronic state.

In terms of the rotational quantum numbers the position of the head of the band $J_h(v'v'')$ is that value of J for which the first derivative of eq. (3) with respect to J is zero. Thus:

$$\frac{d\tilde{\nu}}{dJ} = (B_{v'}' + B_{v''}'' - 2J(B_{v'}' - B_{v''}'')) = 0 \quad \text{and}$$

$$J_h(v'v'') = \frac{(B_{v'}' + B_{v''}''))}{2(B_{v'}' - B_{v''}''))} \quad (5)$$

are generally not integers and are different for each band head.

They closely represent the average quantum number of the lines forming the peak of each band head.

Consequently, if the intensities of these fictitious average lines in different band heads could be directly compared, they would be proportional to: $\nu^4 R_{v'v''}^2 J_h(v'v'') \cdot \exp\left[-\left(W_{v'}' + W_{v''}''/kT\right)\right]$.

In fact, what are measured at the band head are not the intensity of a single rotational line but the sum of the intensities of a number ΔJ of blended lines, which comprise the head. The value of ΔJ for each band must be determined.

If the range of wave numbers over which the rotational lines are added together to form the head is $\Delta\tilde{\nu}$ and correspondingly of J values is ΔJ , an equation relating $\Delta\tilde{\nu}$ and ΔJ may be derived from eq. (3) with the aid of eq. (5) as follows:

$$\tilde{\nu} + \Delta\tilde{\nu} = \tilde{\nu}_0 + (B_{v'}' + B_{v''}'')J + \Delta J_{v'v''} - (B_{v'}' - B_{v''}'')J^2 \quad \text{or}$$

$$\tilde{\nu} + \Delta\tilde{\nu} = \tilde{\nu}_0 + (B_{v'}' + B_{v''}'')J - (B_{v'}' - B_{v''}'')J^2 + (B_{v'}' + B_{v''}'')\Delta J_{v'v''} - 2(B_{v'}' - B_{v''}'')J\Delta J_{v'v''} - (B_{v'}' - B_{v''}'')\Delta J_{v'v''}^2 \quad (6)$$

Then:

$$\Delta\tilde{\nu} = \Delta J_{v'v''} \left[(B_{v'}' + B_{v''}'') - 2 \cdot (B_{v'}' - B_{v''}'')J \right] - (B_{v'}' - B_{v''}'')\Delta J_{v'v''}^2$$

Replacing the value of J with the expression from eq. (5), we finally obtain:

$$\Delta\tilde{\nu} = (B_{v''}'' - B_{v'}')\Delta J_{v'v''}^2 \quad (7)$$

and consequently:

$$\Delta J_{v'v''} = \pm \sqrt{\frac{\Delta\tilde{\nu}}{(B_{v''}'' - B_{v'}')}} \quad (8)$$

Our measurements, to be described in the followings, were made with a plane grating monochromator characterized by an almost constant linear dispersion in wavelength over the range covered by the CN red and violet bands.

By taking into consideration the relationship:

$$\frac{\Delta\nu}{\nu} = -\frac{\Delta\lambda}{\lambda} \quad \text{and therefore} \quad \Delta\nu = \frac{(\text{const})^2}{\lambda^2}$$

eq. (8) becomes:

$$\Delta J_{v'v''} = \pm \frac{\text{const}}{\lambda_h(v'v'')} \frac{1}{\sqrt{(B_{v''}'' - B_{v'}')}} = \pm \frac{\text{const}}{\lambda_h(v'v'')} S_{v'v''} \quad (9)$$

where $\lambda_h(v'v'')$ is the wavelength of the head of the band.

Therefore the number ΔJ affects the intensity of the band head as a statistical weight, representing the number of unresolved rotational lines involved in the head. Relative values of ΔJ may be computed by using eq. (9).

The intensities of band heads arising from a single electronic transition and observed with a spectral instrument having a constant dispersion are therefore:

$$I_{v'v''} \approx \nu^4 R_{v'v''}^2 J_h(v'v'') \Delta J_{v'v''} e^{-\frac{W_{v'}' + W_{v''}''}{kT}} \quad (10)$$

If we take the transition probability of $0 \rightarrow 0$ band and R_{00}^2 as unity, the intensity of unresolved head of the $v' \rightarrow v''$ band relative to that of the $0 \rightarrow 0$ band is given by:

$$\frac{I_{v'v''}}{I_{00}} = \left(\frac{\nu_{v'v''}}{\nu_{00}} \right)^4 R_{v'v''}^2 \frac{J_h(v'v'')}{J_h(00)} \frac{\Delta J_{v'v''}}{\Delta J_{00}} e^{-\frac{W_{v'} + W'_{r(v')} - W_0 - W'_{r(0)}}{kT}} \quad (11)$$

In the terms of wavelength and with the notation defined by eq. (9) this equation becomes:

$$\frac{I_{v'v''}}{I_{00}} = \left(\frac{\lambda_{00}}{\lambda_{v'v}} \right)^5 R_{v'v''}^2 \frac{J_h(v'v'')}{J_h(00)} \frac{S_{v'v''}}{S_{00}} e^{-\frac{W_{v'} + W'_{r(v')} - W_0 - W'_{r(0)}}{kT}} \quad (12)$$

where:

$$W'_{r(v')} = hc B_{v'} J_h(v'v'') [J_h(v'v'') + 1] \quad (13)$$

Taking the common logarithm of both sides of eq. (11) and transposing, we get:

$$\lg \left[\left(\frac{\lambda_{00}}{\lambda_{v'v}} \right)^5 \frac{J_h(v'v'')}{J_h(00)} \frac{S_{v'v''}}{S_{00}} R_{v'v''}^2 \right] = \lg \frac{I_{v'v''}}{I_{00}} + \frac{\lg e}{kT} (W_{v'} + W'_{r(v')} - W_0 - W'_{r(0)}) \quad (14)$$

By contracting the coefficients of $R_{v'v''}^2$ in one constant:

$$C_{v'v''} = \left(\frac{\lambda_{00}}{\lambda_{v'v}} \right)^5 \frac{J_h(v'v'')}{J_h(00)} \frac{S_{v'v''}}{S_{00}} \quad (15)$$

and designating the net difference in energies of the upper state as:

$$\Delta W_{v'v''} = \frac{1}{hc} (W_{v'} + W'_{r(v')} - W_0 - W'_{r(0)}) \quad (16)$$

the relationship between the logarithms of the relative vibrational transition probabilities and the relative band head intensities may be written as:

$$F_{v'v''} = \lg(C_{v'v''} R_{v'v''}^2) - \lg \frac{I_{v'v''}}{I_{00}} = \frac{A_{v'v''}}{T} \quad \text{with} \quad A_{v'v''} = \frac{hc}{2.3k} \Delta W_{v'v''} \quad (17)$$

Values of $C_{v'v''}$ and $A_{v'v''}$ for the CN violet bands are given by Acey *et al.*²

The values of the relative transition probabilities $R_{v'v''}^2$ for $[B^2\Sigma - X^2\Sigma]$ bands of CN molecule are given in Tab. 1³.

It must be outlined that eq. (17) is valid when conditions of thermal equilibrium exists between CN radicals and their surroundings. While the electric arc plasma satisfies these conditions to a high degree, eq. (17) cannot be applied to band head intensities observed in such a plasma until the effects of overlapping bands, self-absorption and self-reversal have either been eliminated or corrected.

Tab. 1 Relative transition probabilities $R_{v'v''}^2$ for $[B^2\Sigma - X^2\Sigma]$ violet bands of CN molecule

$v'-v''$	λ_h	$R_{v'v''}^2$
0-1	4216.0	0.092
1-2	4197.2	0.133
2-3	4181.0	0.141
3-4	4167.8	0.124
0-0	3883.4	1.000
1-1	3871.4	0.813
2-2	3861.9	0.736
3-3	3854.7	0.732
4-4	3850.0	0.776
1-0	3590.4	0.083
2-1	3585.9	0.165
3-2	3583.9	0.194
4-3	3582.5	0.205

To discuss these effects it is necessary to describe the method used in measuring the relative intensities of the bands in our arc discharge plasma.

3. EXPERIMENTAL AND RESULTS

The experimental set-up is represented in the Fig. 1.

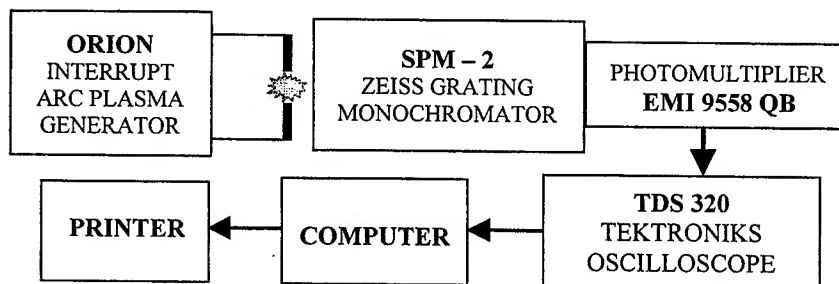


Fig. 1 Experimental set-up

The unstable diatomic CN molecules were obtained by a thermal synthesis reaction between carbon element sputtered from the coal arc electrodes burning at the atmospheric pressure and the atmospheric nitrogen. The power supply used was of type ORION for the interrupt arc regime generating the pulses presented in Fig. 2.

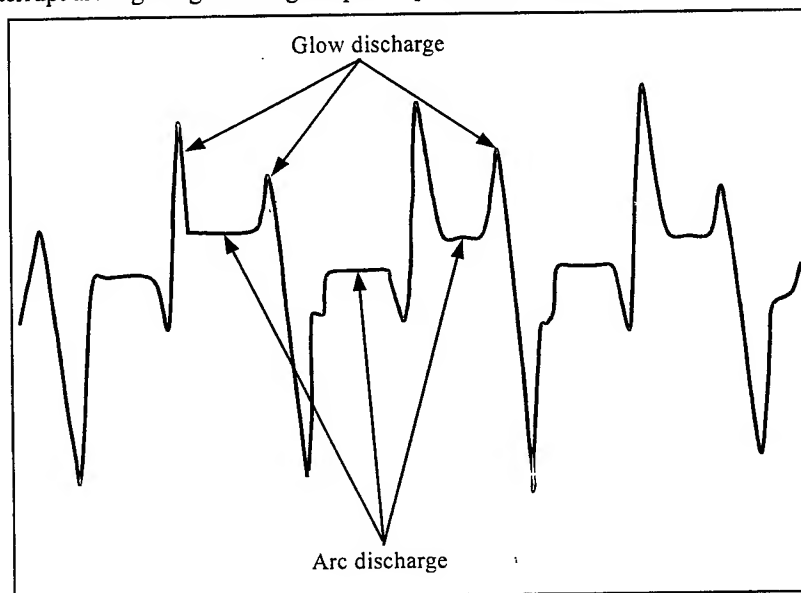


Fig. 2 The voltage oscillogramme of an electric discharge which periodically transits from a glow discharge in an arc discharge and reciprocally [Meek J. M. and Craggs J.D. - Electrical Breakdown of Gases, Oxford 1953]

The operating parameters of the plasma generator were those presented in Tab. 2 (see also ⁵).

Tab.1 Operation parameters of the interrupt arc plasma generator

Discharge current (A)	2	4
Peak voltage (V)	(+) 316 (-) 318	(+) 326 (-) 330
Profile width (ms)	10	10
Voltage on landing (V)	50	50
Repetition frequency (s ⁻¹)	90	100

The measurements of these parameters for different discharge current values were performed using a TEKTRONIKS TDS - 350 oscilloscope. The spectra were obtained with a ZEISS SPM - 2, 600-lines/mm, plane-grating monochromator characterized by a constant linear dispersion in the spectral range of interest (3500 Å to 4500 Å).

We have supposed for this monochromator a triangular slit function of the form⁴:

$$\rho = 1 - \left(\frac{\nu - \nu'}{s} \right) \quad (18)$$

for

$$\nu - \nu' \leq s \quad (19)$$

and a linear dependency between peak intensity, half bandwidth and the slit. In the relationships (18) and (19) ν is the frequency on the peak of the profile in cm⁻¹, ν' is the current frequency on the profile and s is the instrumental slit width in cm⁻¹.

The band heads taken into consideration were those corresponding to the transitions $\Delta\nu = +1$ and $\Delta\nu = -1$.

The molecular spectral parameters corresponding to these transitions $C_{v'v''}$ and $R_{v'v''}$ were taken from ³. In order to correlate the band head intensities and the vibrational temperature with some other plasma processes, we have recorded the temporal band head profiles for these transitions using a TEKTRONICS TDS-320 oscilloscope, characterized by a 100 MHz frequency and a time rise of 5 ns. Each profile was averaged over 256 pulses.

Because the positive column plasma diameter was smaller than 1 mm and we have used the spectral band heads with the terminal levels $v'=1$ and $v'=2$ and not the fundamental vibrational levels, the self-absorption was neglected.

The values of the peak intensities for the transitions of interest corresponding to three different plasma current intensities are presented in Fig. 3

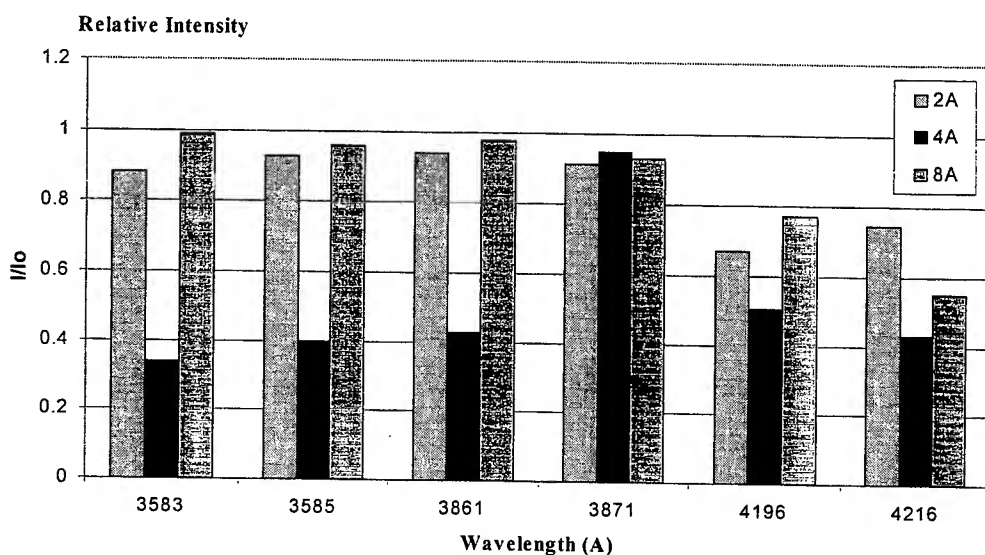


Fig. 3 Values for the peak intensities.

In order to reduce some possible intensity fluctuations during the peak intensity measurements, we have used for temperature measurements the temporal integrated profiles i.e. the product between the temporal half width of the band heads and their intensities (Fig. 4).

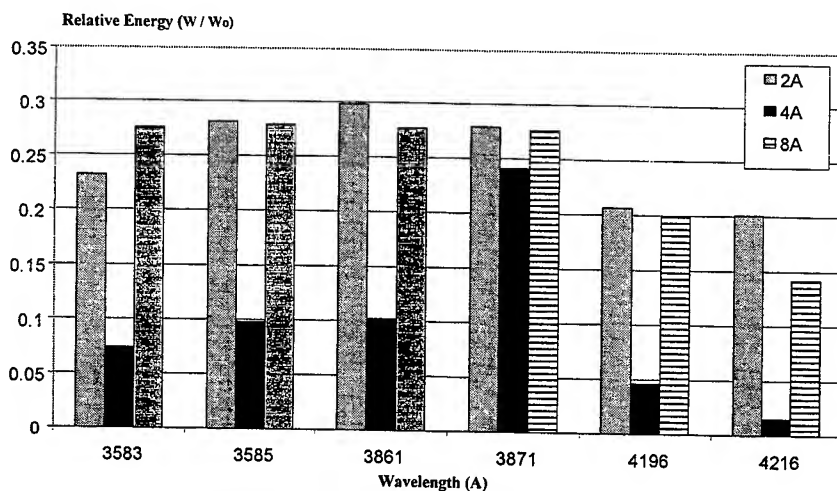


Fig. 4 Values for the temporal integrated profiles

The heterochromatic correction of the band head peak intensities was made using the quantum efficiency of the EMI 9558QB photomultiplier used to measure the spectra.

Using the experimental data and the values of the tabulated coefficients $C_{v'v''}$, $A_{v'v''}$ and $R_{v'v''}^2$ we have plotted $F_{v'v''}$ as a function of $\Delta v'v''$. This is the known Ornstein's diagram presented in Fig. 5.

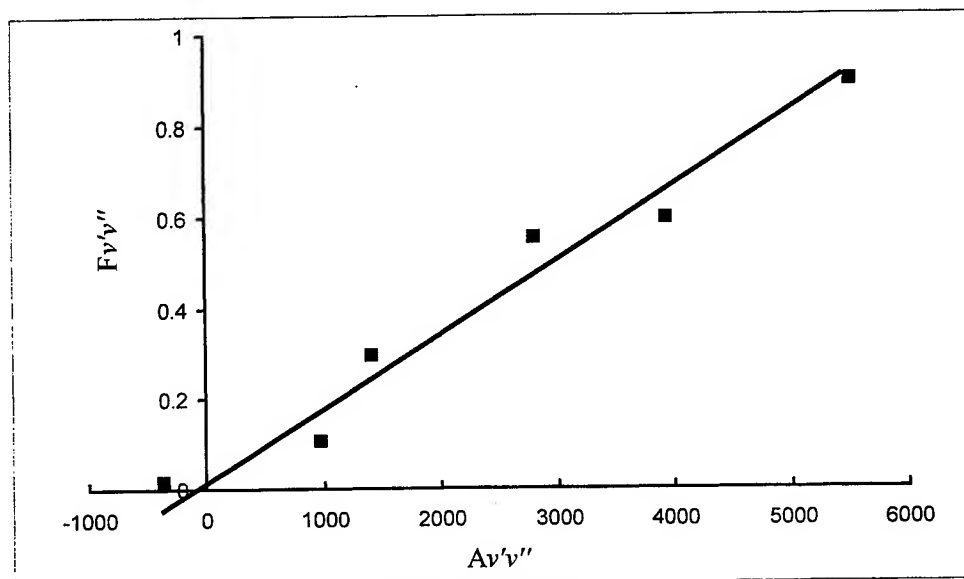


Fig. 5 Ornstein's Diagram

From the slope of this curve we obtain an average vibrational temperature of 6100 K.

As we have outlined in a previously published paper⁵ the practical independence of this temperature on the current intensities, characterizes a LTE arc plasma. Nevertheless the spectral lines intensities depend significantly on the current values. In this case the excitation of the CN molecule vibrational levels is due to the direct electron collision processes.

We have reported in previous papers^{6,7} the presence, in the plasma spectrum obtained in similar conditions, of an important number of Ti II spectral lines having the excitation energy in the range of 3.60 to 5.69 eV. This means that the energy of the exciting particles is not efficient enough to produce the CN molecule dissociation.

The spectral lines of C and N atoms resulting from the CN molecule dissociation are not relevant. Consequently, the electric arc current in these conditions consists essentially of electrons and molecular ions.

The reasonable temperature determined in LTE offers the possibility to make an evaluation of some localization of the arc plasma processes⁸ too.

4. CONCLUSIONS

The adopted phenomenological formula for LTE plasma temperature determination concerning the linear dependency between the relative intensities of the incompletely resolved molecular band heads and the upper level energies of the considered transitions has allowed us to obtain a plausible vibrational temperature of 6100 K by using instead of relative intensities "classically" used, the relative values of the temporary integrated profiles.

An oscilloscope characterized by 100 MHz frequency band and with a rise time of 5 ns, adequate to obtain the temporal profiles of the spectral lines by averaging the pulse shape over 256 pulses allows us to apply this method in very good conditions.

ACKNOWLEDGEMENT

This work was sponsored by the CNCSIS Romania under the grant no. 226.

REFERENCES

1. G. Hertzberg, *Spectra of Diatomic Molecules*, I, p.42, D. Van Nostrand Company Inc., New York, 2nd edition, 1950.
2. L. Acey, F.B. King and R.B. King, *J. Opt. Soc. Am.* **45**, pp. 249-255, 1955.
3. L. L. Danylewych and R. W. Nicholls, *Proc. R. Soc. Lond.*, **A 360**, pp. 557 - 573, 1978
4. H. I. Bernstein, G. Allen, *J. Opt. Soc. Am.*, **45**, 4, p. 237, 1955.
5. I.Iova, M. Bazavan, C. Biloiu, M. Ganciu, C. Ristoscu, M.C. Penache and D. Penache, *Rom. Rep. Phys.* **49**, 3-4, p. 245, 1997.
6. I. Iova, C. Biloiu, M. Bazavan and Gh. Ilie, *Proc. Suppl. Balkan Physics Letter*, **5**, pp. 1520-1923, 1997.
7. I. Iova, M. Bazavan, C. Biloiu, Gh. Ilie and M. Bulinski, *SPIE*, **3405**, pp. 636 – 639, 1998.
8. M. Cristea, C. Cristescu, I. Iova and J. J. Damelincoirt, *XXIV ICPIG*, **2**, pp. 189-190, 11-16 July 1999.

Author Index

- Accente, T., 645
 Aiftimiei, Aurelian, 800, 806
 Aiftimiei, Cristina, 726, 740, 800, 806
 Alacakir, Ali, 570, 657
 Albu, Ana-Maria, 59
 Alexandrescu, Adrian, 342
 Andriesh, Andrei M., 535
 Angelescu, C., 506
 Angelescu, D., 130
 Anghel, Sorin-Dan, 633, 758, 776
 Apostol, Dan, 290, 342, 695
 Apostol, Ileana, 226
 Apostol, Ion G., 506
 Astilean, Simion, 466, 513
 Atanasiu, C. V., 271
 Badragan, Iulian, 786
 Balint, Agneta M., 33
 Balint, Ștefan, 33
 Baltateanu, N., 448
 Bălțean, Diana G., 33
 Băzăvan, M., 834
 Bela, A., 17
 Belea, Andrei, 375, 429
 Bena, Rodica, 45
 Berseth, Claude-Albert, 2, 166
 Bilikmen, Sinan, 657
 Biloiu, Costel, 834
 Bize, S., 651
 Blejan, Marian, 348
 Bobu, Mihaela, 520
 Bolognesi, Luca, 6
 Buca, Dan M., 549, 555
 Budau, P., 52
 Bulaceanu, Claudiu, 497
 Bulinski, M., 17, 375, 429, 834
 Burda, Ioan, 336, 764
 Buzdugan, Arthur I., 535
 Calian, Violeta, 454, 460, 485
 Caliman, Andrei N., 310
 Caramizoiu, Alexandra, 407, 726, 740, 800, 806
 Carbunescu, Eugenia G., 786
 Catriniciu, Marinela, 219
 Cerbanic, Georgeta, 336, 764
 Chelkov, Gueorgui, 172, 669, 676
 Chita, Monica-Anca, 633
 Ciocan, Cristina, 124, 130
 Clairon, A., 651
 Cociu, Lavinia, 336, 764
 Comanescu, Brindus, 172, 348, 669, 676
 Cone, Gabriela, 247
 Constantinescu, Gabriel E., 330, 751
 Constantinescu, Radu D., 255
 Copot, George, 401, 627
 Copot, Rodica, 401
 Cordos, Emil A., 776
 Corsi, Michela, 6
 Costache, F., 549, 555
 Cotirlan, C., 278
 Cristea, Gheorghe, 336, 764
 Cristea, M., 104
 Cristescu, Constantin P., 26
 Cristescu, Simona M., 261
 Cucu, Maria, 355
 Cucu, R. G., 615
 Dabu, Razvan V., 506
 Damian, Victor, 290, 342, 695
 Danaile, Leon, 712
 Dedovich, Dmitri, 172, 669, 676
 Degeratu, Stefania, 584
 Degeratu, Vasile, 584
 Dinca, C. D., 303
 Dobroiu, Adrian, 290, 342, 695
 Dolghier, V., 535
 Dolocan, Voicu, 143, 149
 Doman, Carmen, 520
 Dragulinescu, Dumitru, 226
 Drumea, Petrin, 348
 Dumitras, Dan C., 261
 Dumitrescu, Mihail M., 297, 413, 597, 608
 Dutu, Doru C. A., 261
 Elisa, Mihai, 90
 Enache, Ioana, 348
 Enachescu, M., 52
 Esendemir, Akif, 657
 Evtoukhovitch, Petr, 172, 669, 676
 Facina, M., 303
 Fenic, Constantin G., 478
 Filoti, G., 17
 Florea, C., 156
 Forgaci, Flavia, 124, 130
 Franke, Hilmar, 17
 Frentiu, Tiberiu, 776
 Furlani, Maurizio, 45
 Geanta, Stefan, 770
 Gearba, Alina, 247
 Georgescu, Serban, 156, 284
 Gheorghe, L., 423
 Giosanu, Dana, 758
 Gongadze, Alexi, 172, 669, 676
 Grecu, Rodica, 117
 Grigoriu, Constantin, 226, 576
 Guina, Mircea D., 297, 608
 Guzun, Anicuta, 706
 Hapenciu, Claudiu, 156, 284

Honciuc, Maria, 786
 Hutanu, Vladimir M., 143, 149, 721
 Iakovlev, V. P., 2, 166, 310
 Iancu, Ovidiu Corneliu, 413, 608, 733
 Ighigeanu, Adelina, 172, 669, 676
 Ileană, Ioan, 733
 Ilie, Gheorghe, 834
 Iliescu, Brandusa, 278
 Indrea, Emil, 117
 Ion, Rodica-Mariana, 712
 Ionescu, Carmen, 255
 Iorga-Simăn, Ion, 633, 758
 Iov, Valentin, 549, 555
 Iova, Floriana, 834
 Iova, Iancu, 17, 834
 Iovu, Mihai S., 535
 Ivan, Gabriel, 621
 Jackson, David A., 615, 686
 Jang, W., 576
 Jianu, Angela, 491
 Jinga, Sorin, 72, 78
 Jitescu, Florina, 543, 639
 Kapon, Eli E., 2, 166
 Karabarbounis, A., 303
 Karam, Jean-Michel, 413
 Kevorkian, Antoine P., 26
 Kuncser, V., 17
 Kurzeluk, Mona, 706
 Kusdemir, Ozgul, 657
 Lalanne, Philippe, 513
 Landi, Giuliano, 824
 Lazar, Marian V., 136
 Lengyel, Edit, 104
 Levai, Stefan, 834
 Logofatu, Octavian, 770
 Lupascu, Alexandru I., 26
 Lupei, Aurelia, 232, 423
 Lupei, Voicu, 156, 207, 232, 423
 Macarovici, D., 111
 Manaila-Maximean, Doina, 45, 59
 Mandache, Cipriana, 645, 651
 Manoliu, Gheorghe, 770
 Manu, V., 303
 Marcu, A., 226, 576
 Marculescu, Bogdan, 59
 Margaritescu, Mihai, 364
 Marginean, Raluca-Maria, 526, 721
 Marian, A., 549, 555
 Marin, Mihai, 348
 Mateescu, Emilian, 520
 Melanen, Petri, 597
 Mereuta, Alexandru Z., 2, 310
 Mihailovici, Monica, 33
 Miron, I. G., 271
 Mirzu, Marinica, 627
 Mocofanescu, Anca, 478
 Nascov, Victor, 290, 342, 695
 Naud, C., 156
 Neagu, Ionica, 758
 Neculae, Adrian, 33
 Negosanu, M., 526
 Negutu, C., 247
 Nicula, Traian, 792
 Niculescu, Ecaterina C., 104
 Nitis, E., 526
 Novac, Octavian, 543, 639
 Oancea, Daniel, 172, 348, 669, 676
 Olariu, Mihai, 591
 Onose, Carmen, 72
 Onose, Cristian, 72, 78
 Oprescu, Benedict, 442
 Orsila, Seppo L., 597
 Orun, Hamdi, 570
 Osiac, Eugen, 207, 232, 423
 Ougazzaden, Abdallah, 2
 Păcurar, Lucia, 117
 Palamaru, M., 466, 513
 Palleschi, Vincenzo, 6
 Palmer, James R., 381, 562
 Papadakis, I., 303
 Pascu, Ligia, 117, 130
 Pascu, M., 712
 Pascu, Mihai L., 712
 Pascu, Rovenă, 407
 Penciu, Paul, 219
 Pervan, Oguz, 657
 Pessa, Markus, 597
 Petcu, Mihai, 172, 669, 676
 Petrache, M., 423
 Petraru, A., 156, 232, 423
 Petrescu, Camelia, 219
 Petrescu, Emil, 219
 Petris, Adrian, 491
 Plonski, Ileana-Hania, 520
 Podkladkin, Serguei, 172, 669, 676
 Podoleanu, Adrian Gh., 615, 686
 Popa, Carmen, 491, 786
 Popa, Dragos, 491
 Popa, Razvan, 255
 Popescu, A., 712
 Popescu, Anatol N., 535
 Popescu, Gheorghe, 191
 Popescu, Ion M., 26, 247
 Popovici, Elisabeth Jeanne, 111, 117, 124, 130
 Porte, C., 156
 Postolache, C., 130
 Puscas, Niculae N., 240, 436
 Radu, G., 52
 Rahvalov, V., 65
 Ristici, E., 278
 Ristici, Marin, 278
 Rizea, Roxana, 226
 Robu, Maria, 520, 663
 Robu, Octavian, 663
 Rogojan, Rodica, 90
 Rosca, Maftai, 770

Rosu, Constantin, 45
 Rudra, Alok P., 2, 166
 Russo, U., 17
 Saarinen, Mika J., 597
 Sagnes, I., 2
 Salomon, C., 651
 Salvetti, Azenio, 6
 Sanduloviciu, Mircea, 442
 Santos, Marilde S., 651
 Sarbu, A. V., 310
 Sävöläinen, Pekka, 597
 Săvulescu, Geta, 758
 Scarlat, Florea, 303
 Schiopu, Carmen Liliana, 178, 184
 Schiopu, Paul, 178, 184, 198, 584
 Schneider, Frank, 520
 Serbanescu Oasa, Anca, 506
 Simion, Mariana, 84
 Simon, Alpar, 776
 Simon, Simion, 336, 764
 Sipilä, Pekko, 597
 Slavnicu, Elena, 786
 Socaciu, Margareta, 454, 485
 Sorop, T. G., 232
 Sortais, Yvan, 651
 Spiridon, Stefania-Floriana, 520
 Sporea, Dan G., 213, 621
 Spulber, Catalin A., 330, 751
 Stanculescu, Anca I., 84, 97
 Stanculescu, Florin G., 97
 Stănescu, Constantin S., 758
 Stefan, Levai, 706
 Sterian, Paul E., 90
 Stiliaris, E., 303
 Stoenescu, George, 324, 448, 460, 472
 Stoian, Razvan, 506
 Stoian, Victor, 45
 Stoica, Axente D., 726, 740, 800, 806, 824
 Stoicescu, C., 423
 Stratan, Aurel, 478, 506
 Suruceanu, Grigorie I., 166, 310, 317
 Syrbu, Alexei V., 2, 166
 Tanase, Letitia, 355, 364, 812
 Tatulea, Bogdan, 172, 669, 676
 Tilica, Maria, 84
 Tivarus, Madalina-Elena, 278
 Todica, Mihai, 336, 764
 Tognoni, Elisabetta, 6
 Toikkanen, L., 597
 Toivonen, Mika, 597
 Tomescu, M., 526
 Trikalinos, C., 303
 Trouillet, Alain, 59
 Tskhadadze, Edisher, 172, 669, 676
 Tudorache, Mariana, 520
 Udrea, Mircea V., 570, 657
 Ulmeanu, Magdalena, 52
 Ungur, Laura, 111, 124
 Ungureanu, M., 645
 Ursache, Marcela, 454, 485
 Vădan, Maria, 111, 124
 Vasile, Dan, 669
 Vasile, Florentin I., 198
 Vasilescu, Marilena, 111
 Vasilescu, Mihaela, 84
 Vieru, Stanislav F., 310
 Vilokkinen, Ville, 597
 Visan, Tiberiu, 213, 478
 Vizireanu, M., 526
 Vlad, Melu, 669
 Vlad, Valentin I., 491
 Yatsui, Kiyoshi, 576
 Zamfirescu, M., 478
 Zhitaru, R., 65